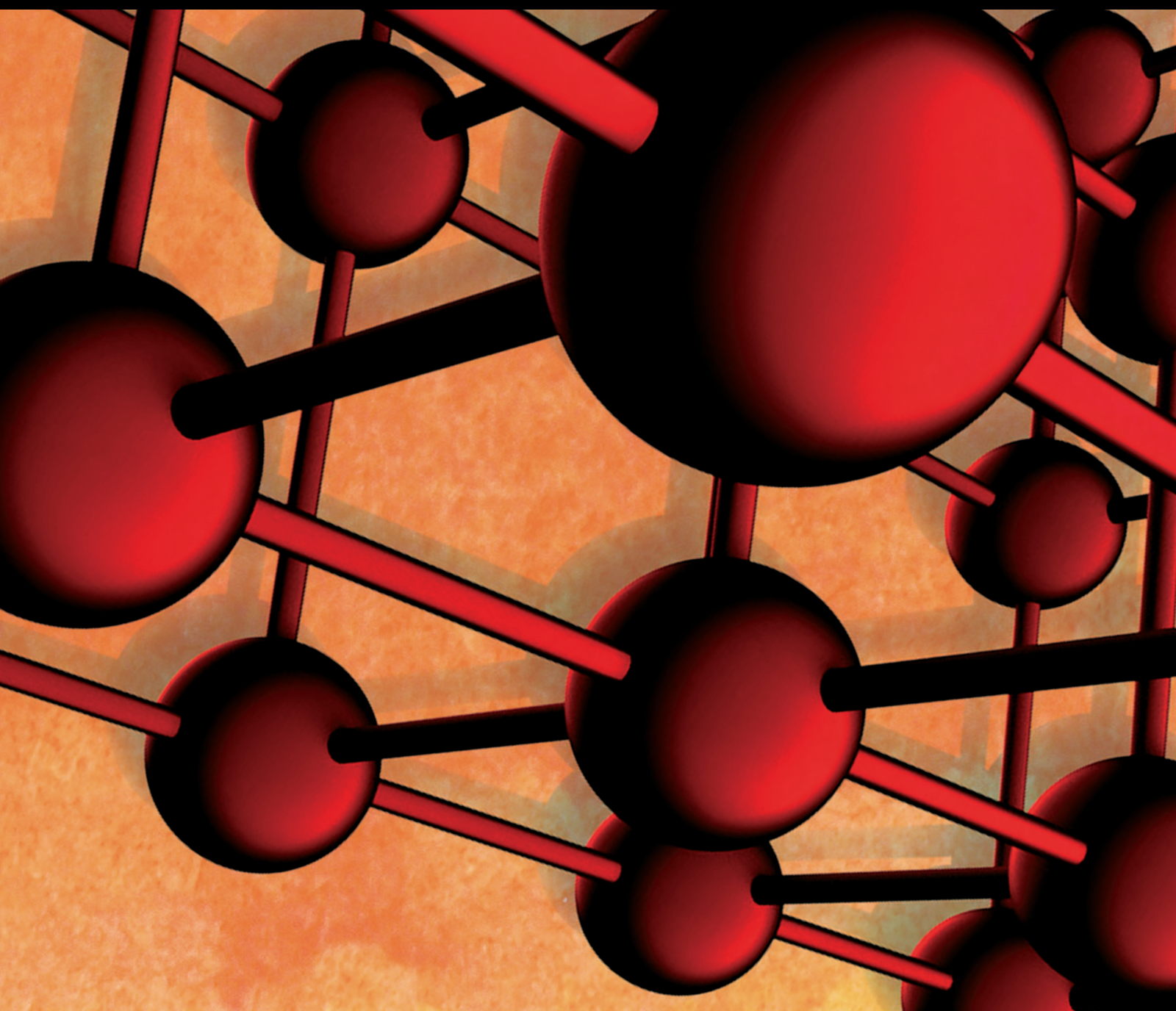


Advances in Materials Science and Engineering

Processing and Applications of Advanced Functional Materials

Lead Guest Editor: Samson Jerold Samuel Chelladurai

Guest Editors: Ramesh Arthanari and J. Paulo Davim





Processing and Applications of Advanced Functional Materials

Advances in Materials Science and Engineering

**Processing and Applications of
Advanced Functional Materials**

Lead Guest Editor: Samson Jerold Samuel
Chelladurai


Guest Editors: Ramesh Arthanari and J. Paulo
Davim



Copyright © 2024 Hindawi Limited. All rights reserved.

This is a special issue published in "Advances in Materials Science and Engineering." All articles are open access articles distributed under the Creative Commons Attribution License, which permits unrestricted use, distribution, and reproduction in any medium, provided the original work is properly cited.

Chief Editor




























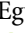

Amit Bandyopadhyay , USA

Associate Editors

Vamsi Balla , India
Mitun Das , USA
Sandip Harimkar, USA
Ravi Kumar , India
Peter Majewski , Australia
Enzo Martinelli , Italy
Luigi Nicolais , Italy
Carlos R. Rambo , Brazil
Michael J. Schütze , Germany
Kohji Tashiro , Japan
Zhonghua Yao , China
Dongdong Yuan , China
Wei Zhou , China

Academic Editors

Antonio Abate , Germany
Hany Abdo , Saudi Arabia
H.P.S. Abdul Khalil , Malaysia
Ismael Alejandro Aguayo Villarreal , Mexico
Sheraz Ahmad , Pakistan
Michael Aizenshtein, Israel
Jarir Aktaa, Germany
Bandar AlMangour, Saudi Arabia
Huaming An, China
Alicia Esther Ares , Argentina
Siva Avudaiappan , Chile
Habib Awais , Pakistan
NEERAJ KUMAR BHOI, India
Enrico Babilio , Italy
Renal Backov, France
M Bahubalendruni , India
Sudharsan Balasubramanian , India
Markus Bambach, Germany
Irene Bavasso , Italy
Stefano Bellucci , Italy
Brahim Benmokrane, Canada
Jean-Michel Bergheau , France
Guillaume Bernard-Granger, France
Giovanni Berselli, Italy
Patrice Berthod , France
Michele Bianchi , Italy
Hugo C. Biscaia , Portugal

Antonio Boccaccio, Italy
Mohamed Bououdina , Saudi Arabia
Gianlorenzo Bussetti , Italy
Antonio Caggiano , Germany
Marco Cannas , Italy
Qi Cao, China
Gianfranco Carotenuto , Italy
Paolo Andrea Carraro , Italy
Jose Cesar de Sa , Portugal
Wen-Shao Chang , United Kingdom
Qian Chen , China
Francisco Chinesta , France
Er-Yuan Chuang , Taiwan
Francesco Colangelo, Italy
María Criado , Spain
Enrique Cuan-Urquizo , Mexico
Lucas Da Silva , Portugal
Angela De Bonis , Italy
Abílio De Jesus , Portugal
José António Fonseca De Oliveira
Correia , Portugal
Ismail Demir , Turkey
Luigi Di Benedetto , Italy
Maria Laura Di Lorenzo, Italy
Marisa Di Sabatino, Norway
Luigi Di Sarno, Italy
Ana María Díez-Pascual , Spain
Guru P. Dinda , USA
Hongbiao Dong, China
Mingdong Dong , Denmark
Frederic Dumur , France
Stanislaw Dymek, Poland
Kaveh Edalati , Japan
Philip Eisenlohr , USA
Luis Evangelista , Norway
Michele Fedel , Italy
Francisco Javier Fernández Fernández , Spain
Spain
Isabel J. Ferrer , Spain
Massimo Fresta, Italy
Samia Gad , Egypt
Pasquale Gallo , Finland
Sharanabasava Ganachari, India
Santiago Garcia-Granda , Spain
Carlos Garcia-Mateo , Spain

Achraf Ghorbal , Tunisia
Georgios I. Giannopoulos , Greece
Ivan Giorgio , Italy
Andrea Grilli , Italy
Vincenzo Guarino , Italy
Daniel Guay, Canada
Jenő Gubicza , Hungary
Xuchun Gui , China
Benoit Guiffard , France
Zhixing Guo, China
Ivan Gutierrez-Urrutia , Japan
Weiwei Han , Republic of Korea
Simo-Pekka Hannula, Finland
A. M. Hassan , Egypt
Akbar Heidarzadeh, Iran
Yi Huang , United Kingdom
Joshua Ighalo, Nigeria
Saliha Ilican , Turkey
Md Mainul Islam , Australia
Ilia Ivanov , USA
Jijo James , India
Hafsa Jamshaid , Pakistan
Hom Kandel , USA
Kenji Kaneko, Japan
Rajesh Kannan A , Democratic People's
Republic of Korea
Mehran Khan , Hong Kong
Akihiko Kimura, Japan
Ling B. Kong , Singapore
Pramod Koshy, Australia
Hongchao Kou , China
Alexander Kromka, Czech Republic
Abhinay Kumar, India
Avvaru Praveen Kumar , Ethiopia
Sachin Kumar, India
Paweł Kłosowski , Poland
Wing-Fu Lai , Hong Kong
Luciano Lamberti, Italy
Fulvio Lavecchia , Italy
Laurent Lebrun , France
Joon-Hyung Lee , Republic of Korea
Cristina Leonelli, Italy
Chenggao Li , China
Rongrong Li , China
Yuanshi Li, Canada

Guang-xing Liang , China
Barbara Liguori , Italy
Jun Liu , China
Yunqi Liu, China
Rong Lu, China
Zhiping Luo , USA
Fernando Lusquiños , Spain
Himadri Majumder , India
Dimitrios E. Manolakos , Greece
Necmettin Maraşlı , Turkey
Alessandro Martucci , Italy
Roshan Mayadunne , Australia
Mamoun Medraj , Canada
Shazim A. Memon , Kazakhstan
Pratima Meshram , India
Mohsen Mhadhbi , Tunisia
Philippe Miele, France
Andrey E. Miroshnichenko, Australia
Ajay Kumar Mishra , South Africa
Hossein Moayedi , Vietnam
Dhanesh G. Mohan , United Kingdom
Sakar Mohan , India
Namdev More, USA
Tahir Muhmood , China
Faisal Mukhtar , Pakistan
Dr. Tauseef Munawar , Pakistan
Roger Narayan , USA
Saleem Nasir , Pakistan
Elango Natarajan, Malaysia
Rufino M. Navarro, Spain
Miguel Navarro-Cia , United Kingdom
Behzad Nematollahi , Australia
Peter Niemz, Switzerland
Hiroschi Noguchi, Japan
Dariusz Oleszak , Poland
Laurent Orgéas , France
Togay Ozbakkaloglu, United Kingdom
Marián Palcut , Slovakia
Davide Palumbo , Italy
Gianfranco Palumbo , Italy
Murlidhar Patel, India
Zbyšek Pavlík , Czech Republic
Alessandro Pegoretti , Italy
Gianluca Percoco , Italy
Andrea Petrella, Italy

Claudio Pettinari , Italy
Giorgio Pia , Italy
Candido Fabrizio Pirri, Italy
Marinos Pitsikalis , Greece
Alain Portavoce , France
Simon C. Potter, Canada
Ulrich Prah, Germany
Veena Ragupathi , India
Kawaljit Singh Randhawa , India
Baskaran Rangasamy , Zambia
Paulo Reis , Portugal
Hilda E. Reynel-Avila , Mexico
Yuri Ribakov , Israel
Aniello Riccio , Italy
Anna Richelli , Italy
Antonio Riveiro , Spain
Marco Rossi , Italy
Fernando Rubio-Marcos , Spain
Francesco Ruffino , Italy
Giuseppe Ruta , Italy
Sachin Salunkhe , India
P Sangeetha , India
Carlo Santulli, Italy
Fabrizio Sarasini , Italy
Senthil Kumaran Selvaraj , India
Raffaele Sepe , Italy
Aabid H Shalla, India
Poorva Sharma , China
Mercedes Solla, Spain
Tushar Sonar , Russia
Donato Sorgente , Italy
Charles C. Sorrell , Australia
Damien Soulat , France
Adolfo Speghini , Italy
Antonino Squillace , Italy
Koichi Sugimoto, Japan
Jirapornchai Suksaeree , Thailand
Baozhong Sun, China
Sam-Shajing Sun , USA
Xiaolong Sun, China
Yongding Tian , China
Hao Tong, China
Achim Trampert, Germany
Tomasz Trzepieciński , Poland
Kavimani V , India

Matjaz Valant , Slovenia
Mostafa Vamegh, Iran
Lijing Wang , Australia
Jörg M. K. Wiezorek , USA
Guosong Wu, China
Junhui Xiao , China
Guoqiang Xie , China
YASHPAL YASHPAL, India
Anil Singh Yadav , India
Yee-wen Yen, Taiwan
Hao Yi , China
Wenbin Yi, China
Tetsu Yonezawa, Japan
Hiroshi Yoshihara , Japan
Bin Yu , China
Rahadian Zainul , Indonesia
Lenka Zaji#c#kova# , Czech Republic
Zhigang Zang , China
Michele Zappalorto , Italy
Gang Zhang, Singapore
Jinghuai Zhang, China
Zengping Zhang, China
You Zhou , Japan
Robert Černý , Czech Republic

Contents

Retracted: Optimizing the Characteristics of the Laser Hardfacing Process Parameters to Maximize the Wear Resistance of Ni-Based Hard-Faced Deposits Using the RSM Technique

Advances in Materials Science and Engineering
Retraction (1 page), Article ID 9786960, Volume 2024 (2024)

Retracted: Detecting Distance between Surfaces of Large Transparent Material Based on Low-Cost TOF Sensor and Deep Convolutional Neural Network

Advances in Materials Science and Engineering
Retraction (1 page), Article ID 9780191, Volume 2024 (2024)

Retracted: Electrochemical Studies of WC-Flyash HVOF Coating Interface on SA209-T1 Steel under 3.5 NaCl Solution

Advances in Materials Science and Engineering
Retraction (1 page), Article ID 9898454, Volume 2023 (2023)

Retracted: Investigation on Dielectric Properties of Press Board Coated with Epoxy Resin, Quartz, and Rice Husk Ash

Advances in Materials Science and Engineering
Retraction (1 page), Article ID 9898059, Volume 2023 (2023)

Retracted: Industrial Waste Water Recycling Using Nanographene Oxide Filters

Advances in Materials Science and Engineering
Retraction (1 page), Article ID 9897310, Volume 2023 (2023)

Retracted: Effect of the Reinforcement Phase on Indentation Resistance and Damage Characterization of Glass/Epoxy Laminates Using Acoustic Emission Monitoring

Advances in Materials Science and Engineering
Retraction (1 page), Article ID 9897260, Volume 2023 (2023)

Retracted: Optimization of Remazol Black B Removal Using Biochar Produced from *Caulerpa scapelliformis* Using Response Surface Methodology

Advances in Materials Science and Engineering
Retraction (1 page), Article ID 9896204, Volume 2023 (2023)

Retracted: Improvement on Mechanical Properties of Submerged Friction Stir Joining of Dissimilar Tailor Welded Aluminum Blanks

Advances in Materials Science and Engineering
Retraction (1 page), Article ID 9896026, Volume 2023 (2023)

Retracted: Process Development for Edible Film Preparation Using Avocado Seed Starch: Response Surface Modeling and Analysis for Water-Vapor Permeability

Advances in Materials Science and Engineering
Retraction (1 page), Article ID 9895647, Volume 2023 (2023)

Retracted: A Comparative Study on Crack-Healing Ability of Al₂O₃/SiC Structural Ceramic Composites Synthesized by Microwave Sintering and Conventional Electrical Sintering
Advances in Materials Science and Engineering
Retraction (1 page), Article ID 9891324, Volume 2023 (2023)

Retracted: Mathematical Modeling and Analysis of Wear Behavior of AlTiN Coating on Titanium Alloy (Ti-6Al-4V)
Advances in Materials Science and Engineering
Retraction (1 page), Article ID 9879768, Volume 2023 (2023)

Retracted: Effect of Manganese Ions on Spectroscopic and Insulating Properties of Aluminophosphate Glasses
Advances in Materials Science and Engineering
Retraction (1 page), Article ID 9878420, Volume 2023 (2023)

Retracted: Experimental Study of Thermal and Mechanical Behaviour of Graphite-Filled UJF Composite
Advances in Materials Science and Engineering
Retraction (1 page), Article ID 9878410, Volume 2023 (2023)

Retracted: A Comprehensive Examination of Bandgap Semiconductor Switches
Advances in Materials Science and Engineering
Retraction (1 page), Article ID 9875806, Volume 2023 (2023)

Retracted: Impact of Different Electrolytes on the Machining Rate in ECM Process
Advances in Materials Science and Engineering
Retraction (1 page), Article ID 9874648, Volume 2023 (2023)

Retracted: Strength Enhancement Study on Composites of AA6066 Aluminium Alloy with Magnesium Oxide and Coal Ash
Advances in Materials Science and Engineering
Retraction (1 page), Article ID 9873561, Volume 2023 (2023)

Retracted: Empirical Investigation on Compressive Strength of Geopolymer and Conventional Concretes by Nondestructive Method
Advances in Materials Science and Engineering
Retraction (1 page), Article ID 9871638, Volume 2023 (2023)

Retracted: Mechanical Behavior of Silica Fume Concrete Filled with Steel Tubular Composite Column
Advances in Materials Science and Engineering
Retraction (1 page), Article ID 9870502, Volume 2023 (2023)

Retracted: Development of Novel Nano-Silver-Based Antenna for Green Agriculture
Advances in Materials Science and Engineering
Retraction (1 page), Article ID 9863035, Volume 2023 (2023)

Contents

Retracted: Analysis on Emissions and Performance of Ceramic Coated Diesel Engine Fueled with Novel Blends Using Artificial Intelligence

Advances in Materials Science and Engineering
Retraction (1 page), Article ID 9861010, Volume 2023 (2023)

Retracted: Characterization of Composite RFID Antennas Based on Thermal Properties: A Survey

Advances in Materials Science and Engineering
Retraction (1 page), Article ID 9849341, Volume 2023 (2023)

Retracted: Optimization of Reinforced Aluminium Scraps from the Automobile Bumpers with Nickel and Magnesium Oxide in Stir Casting

Advances in Materials Science and Engineering
Retraction (1 page), Article ID 9849280, Volume 2023 (2023)

Retracted: Multiobjective Optimization of Mechanical Properties on Sisal-Glass Fiber-Reinforced Hybrid Composites Using Response Surface Methodology and LINGO Analysis

Advances in Materials Science and Engineering
Retraction (1 page), Article ID 9846941, Volume 2023 (2023)

Retracted: Optimization of CNC End Milling Process Parameters of Low-Carbon Mold Steel Using Response Surface Methodology and Grey Relational Analysis

Advances in Materials Science and Engineering
Retraction (1 page), Article ID 9846872, Volume 2023 (2023)

Retracted: Comparative Analysis of Natural Fibre Reinforced Composite Material Using ANSYS

Advances in Materials Science and Engineering
Retraction (1 page), Article ID 9841768, Volume 2023 (2023)

Retracted: Steady-State Flow Characteristics and End Clearance Optimization of Internal Gear Grease Pump

Advances in Materials Science and Engineering
Retraction (1 page), Article ID 9839141, Volume 2023 (2023)

Retracted: Utilization of Red Mud-Fly Ash Reinforced with Cement in Road Construction Applications

Advances in Materials Science and Engineering
Retraction (1 page), Article ID 9836564, Volume 2023 (2023)

Retracted: Microstructure and Fatigue Properties of 6061 Aluminum Alloy Laser-MIG Hybrid Welding Joint

Advances in Materials Science and Engineering
Retraction (1 page), Article ID 9828097, Volume 2023 (2023)

Retracted: Experimental and Thermal Investigation on Powder Mixed EDM Using FEM and Artificial Neural Networks

Advances in Materials Science and Engineering
Retraction (1 page), Article ID 9826891, Volume 2023 (2023)

Retracted: Performance Analysis and Development of a Semiconductor Junction Rectifier with Multicolor Coding for Indoor Farm Applications

Advances in Materials Science and Engineering
Retraction (1 page), Article ID 9825682, Volume 2023 (2023)

Retracted: Computational Investigations of Fixed-Free and Fixed-Fixed Types Single-Wall Carbon Nanotube Mass Sensing Biosensor

Advances in Materials Science and Engineering
Retraction (1 page), Article ID 9825404, Volume 2023 (2023)

Retracted: Experimental Investigation and Optimization on Friction Stir Welding of Nylon 6A Using Taguchi and ANOVA with Microstructural Analysis

Advances in Materials Science and Engineering
Retraction (1 page), Article ID 9820953, Volume 2023 (2023)

Retracted: Experimental Analysis of Mechanical Properties and Durability of Cement-Based Composite with Carbon Nanotube

Advances in Materials Science and Engineering
Retraction (1 page), Article ID 9818232, Volume 2023 (2023)

Retracted: Optimization on Operation Parameters in Reinforced Metal Matrix of AA6066 Composite with HSS and Cu

Advances in Materials Science and Engineering
Retraction (1 page), Article ID 9817471, Volume 2023 (2023)

Retracted: Effect of Tool Profile Influence in Dissimilar Friction Stir Welding of Aluminium Alloys (AA5083 and AA7068)

Advances in Materials Science and Engineering
Retraction (1 page), Article ID 9813726, Volume 2023 (2023)

Retracted: Modified Mechanical Structure Electric Bike Design Computation and Prototype Model Implementation

Advances in Materials Science and Engineering
Retraction (1 page), Article ID 9812502, Volume 2023 (2023)

Retracted: Effects of the FR 4 Substrate Realized in a Circularly Polarized UHF-RFID Reader Antenna with Fractal Geometry for Enhancing Parameters

Advances in Materials Science and Engineering
Retraction (1 page), Article ID 9810579, Volume 2023 (2023)

Retracted: Structural Classification of Basalt FRP at High Temperatures

Advances in Materials Science and Engineering
Retraction (1 page), Article ID 9808402, Volume 2023 (2023)

Contents

Retracted: Green Machining Characteristics Study of Al-6063 in CNC Milling Using Taguchi Method and Grey Relational Analysis

Advances in Materials Science and Engineering
Retraction (1 page), Article ID 9808305, Volume 2023 (2023)

Retracted: Free Vibration Analysis of Thick Rectangular and Elliptical Plates with Concentric Cut-Out

Advances in Materials Science and Engineering
Retraction (1 page), Article ID 9805674, Volume 2023 (2023)

Retracted: Improving the Mechanical Properties of Natural Fiber Composites of Hemp Fiber with Ramie and Banana Fiber through Compression Molding Method

Advances in Materials Science and Engineering
Retraction (1 page), Article ID 9804915, Volume 2023 (2023)

Retracted: Investigation on V_2O_5 Thin Films for Field Effect Transistor Applications

Advances in Materials Science and Engineering
Retraction (1 page), Article ID 9804082, Volume 2023 (2023)

Retracted: Synthesis, Mechanical, and Tribological Performance Analysis of Stir-Casted AA7079: $ZrO_2 + Si_3N_4$ Hybrid Composites by Taguchi Route

Advances in Materials Science and Engineering
Retraction (1 page), Article ID 9803865, Volume 2023 (2023)

Retracted: Development of Smart Sensing Technology Approaches in Structural Health Monitoring of Bridge Structures

Advances in Materials Science and Engineering
Retraction (1 page), Article ID 9803564, Volume 2023 (2023)

Retracted: Parameters of Porosity and Compressive Strength-Based Optimization on Reinforced Aluminium from the Recycled Waste Automobile Frames

Advances in Materials Science and Engineering
Retraction (1 page), Article ID 9803238, Volume 2023 (2023)

Retracted: XRD Peak Profile Analysis of SiC Reinforced Al_2O_3 Ceramic Composite Synthesized by Electrical Resistance Heating and Microwave Sintering: A Comparison

Advances in Materials Science and Engineering
Retraction (1 page), Article ID 9795810, Volume 2023 (2023)

Retracted: Parameters Optimization of Dissimilar Friction Stir Welding for AA7079 and AA8050 through RSM

Advances in Materials Science and Engineering
Retraction (1 page), Article ID 9795165, Volume 2023 (2023)

Retracted: Continuous Sorption of Remazol Brilliant Orange 3R Using *Caulerpa scalpelliformis* Biochar
Advances in Materials Science and Engineering
Retraction (1 page), Article ID 9791609, Volume 2023 (2023)

Retracted: Evaluation of Microstructure, Hardness, and Tensile Properties: A Comparative Study of Stir Cast and Extruded Al7005/Glass-/Fly-Ash-Reinforced Hybrid MMCs
Advances in Materials Science and Engineering
Retraction (1 page), Article ID 9769382, Volume 2023 (2023)

Retracted: Studying the Effect of Metallic Precursor Concentration on the Structural, Optical, and Morphological Properties of Zinc Sulfide Thin Films in Photovoltaic Cell Applications
Advances in Materials Science and Engineering
Retraction (1 page), Article ID 9769253, Volume 2023 (2023)




Retracted: Flexural Behaviour of Chicken Mesh Ferrocement Laminates with Partial Replacement of Fine Aggregate by Steel Slag
Advances in Materials Science and Engineering
Retraction (1 page), Article ID 9765178, Volume 2023 (2023)

Retracted: Design and Implementation of SOC-Based Noncontact-Type Level Sensing for Conductive and Nonconductive Liquids
Advances in Materials Science and Engineering
Retraction (1 page), Article ID 9764235, Volume 2023 (2023)

Retracted: Effect of Grey and White Portland Cement Fillers on Flexural and Shear Strength of GFRP Composite Material
Advances in Materials Science and Engineering
Retraction (1 page), Article ID 9756064, Volume 2023 (2023)



Retracted: Mechanical Strength and Fatigue Fracture Analysis on Al-Zn-Mg Alloy with the Influence of Creep Aging Process
Advances in Materials Science and Engineering
Retraction (1 page), Article ID 9863267, Volume 2023 (2023)

Retracted: Effects of Novel Material Field Effect Transistor for Heterogeneous Energy and Traffic-Aware Secure Applications
Advances in Materials Science and Engineering
Retraction (1 page), Article ID 9781709, Volume 2023 (2023)





[Retracted] Green Machining Characteristics Study of Al-6063 in CNC Milling Using Taguchi Method and Grey Relational Analysis
R. Suresh Kumar , S. Senthil Kumar , K. Murugan, and Sintayehu Mekuria Hailegiorgis 
Research Article (12 pages), Article ID 4420250, Volume 2021 (2021)

Contents








[Retracted] Electrochemical Studies of WC-Flyash HVOF Coating Interface on SA209-T1 Steel under 3.5 NaCl Solution

D. Elango, A. Daniel Das , S. P. Kumaresh Babu, S. Natarajan, and A. Yeshitla 
Research Article (9 pages), Article ID 8706630, Volume 2021 (2021)



[Retracted] Parameters of Porosity and Compressive Strength-Based Optimization on Reinforced Aluminium from the Recycled Waste Automobile Frames

A. Parthiban, V. Vijayan , T. Sathish , S. Dinesh Kumar, L. Ponraj Sankar, N. Parthipan, Dawit Tafesse , and Mebratu Tufa 
Research Article (10 pages), Article ID 3648480, Volume 2021 (2021)



[Retracted] Optimizing the Characteristics of the Laser Hardfacing Process Parameters to Maximize the Wear Resistance of Ni-Based Hard-Faced Deposits Using the RSM Technique

S. Gnanasekaran , Samson Jerold Samuel Chelladurai , T. Ramakrishnan , S. Sivananthan , G. Padmanaban , Ramesh Arthanari , and V. Balasubramanian 
Research Article (15 pages), Article ID 3665631, Volume 2021 (2021)


Investigation on Microstructure and Tensile Properties of High-Strength AA2014 Aluminium Alloy Welds Joined by Pulsed CMT Welding Process

Rajendran Chinnasamy , Samson Jerold Samuel Chelladurai , and Tushar Sonar
Research Article (8 pages), Article ID 8163164, Volume 2021 (2021)







[Retracted] Performance Analysis and Development of a Semiconductor Junction Rectifier with Multicolor Coding for Indoor Farm Applications

E. D. Kanmani Ruby , M. Umadevi, C. Kanmani Pappa, W. Edwin Santhkumar, P. Janani, and P. Shanmugasundaram 
Research Article (12 pages), Article ID 6585680, Volume 2021 (2021)





[Retracted] Detecting Distance between Surfaces of Large Transparent Material Based on Low-Cost TOF Sensor and Deep Convolutional Neural Network

Rong Zou , Yu Zhang, Junlan Gu, and Jin Chen
Research Article (12 pages), Article ID 8340179, Volume 2021 (2021)


[Retracted] Empirical Investigation on Compressive Strength of Geopolymer and Conventional Concretes by Nondestructive Method

B. Ravali , K. Bala Gopi Krishna , D. Ravi Kanth , K. J. Brahma Chari , S. Venkatesa Prabhu , and R. Ramesh 
Research Article (10 pages), Article ID 9575964, Volume 2021 (2021)





[Retracted] Free Vibration Analysis of Thick Rectangular and Elliptical Plates with Concentric Cut-Out

Anjibabu Merneedi , Nalluri Mohan Rao, L. Natrayan , L. Yuvaraj , and Prabhu Paramasivam 
Research Article (14 pages), Article ID 7212075, Volume 2021 (2021)

[Retracted] Modified Mechanical Structure Electric Bike Design Computation and Prototype Model Implementation

K. Ramash Kumar, T. S. Anandhi, B. Vijayakrishna, Monalisa Mohanty, M. Siva Ramkumar, H. A. Shivappa, Belachew Zegale Tizazu , B. Kirubakaran, and E. Thinapakar
Research Article (7 pages), Article ID 3673172, Volume 2021 (2021)



Developing an Empirical Relationship to Predict the Wear Characteristics of Ni-Based Hardfaced Deposits on Nuclear Grade 316LN Austenitic Stainless Steel

S. Gnanasekaran , Samson Jerold Samuel Chelladurai , G. Padmanaban, Ramesh Arthanari , and V. Balasubramanian 
Research Article (10 pages), Article ID 3934787, Volume 2021 (2021)




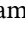


[Retracted] Effects of Novel Material Field Effect Transistor for Heterogeneous Energy and Traffic-Aware Secure Applications

C. Ambika Bhuvaneshwari , E. D. Kanmani Ruby , A. Manjunathan , R. Balamurugan , P. Jenopaul , and Belachew Zegale Tizazu 
Research Article (9 pages), Article ID 9085854, Volume 2021 (2021)




[Retracted] Design and Implementation of SOC-Based Noncontact-Type Level Sensing for Conductive and Nonconductive Liquids

J. L. Mazher Iqbal , Munagapati Siva Kishore, Arulkumaran Ganeshan , and G. Narayan
Research Article (12 pages), Article ID 7630008, Volume 2021 (2021)






[Retracted] Development of Novel Nano-Silver-Based Antenna for Green Agriculture

Subitha D. , Vani R. , Raja A. , Balasubramani S. , Manjunathan A. , and Kibebe Sahile 
Research Article (9 pages), Article ID 9065960, Volume 2021 (2021)



[Retracted] A Comprehensive Examination of Bandgap Semiconductor Switches

S. Siva Subramanian , R. Saravanakumar, Bibhu Prasad Ganthia, S. Kaliappan , Surafel Mustefa Beyan , Maitri Mallick, Monalisa Mohanty, and G. Pavithra
Review Article (8 pages), Article ID 3188506, Volume 2021 (2021)

[Retracted] Experimental Investigation and Optimization on Friction Stir Welding of Nylon 6A Using Taguchi and ANOVA with Microstructural Analysis






G. S. V. Seshu Kumar , Anshuman Kumar , S. Rajesh , Rama Bhadri Raju Chekuri , and Amsalu Gosu Adigo 
Research Article (12 pages), Article ID 7483393, Volume 2021 (2021)

[Retracted] Characterization of Composite RFID Antennas Based on Thermal Properties: A Survey

Chitra Varadhan , Fekadu Ashine Chamatu , and S. Arulsevi
Review Article (9 pages), Article ID 8905489, Volume 2021 (2021)










Contents

[Retracted] Structural Classification of Basalt FRP at High Temperatures

Sudhir Vummadisetti , Sessa Ratnam Pasalapudi , Santosh Kumar Gottapu , Kranthi Kumar Goriparthi , and Areda Batu 

Research Article (9 pages), Article ID 6917471, Volume 2021 (2021)

[Retracted] Multiobjective Optimization of Mechanical Properties on Sisal-Glass Fiber-Reinforced Hybrid Composites Using Response Surface Methodology and LINGO Analysis

S. Ragunath , A. N. Shankar , K. Meena , B. Guruprasad , S. Madhu , N. Rakesh , M. Hariprabhu , S. Balamuralitharan , and Nahom Daniel 

Research Article (10 pages), Article ID 2376148, Volume 2021 (2021)

[Retracted] Experimental and Thermal Investigation on Powder Mixed EDM Using FEM and Artificial Neural Networks

Venkata N. Raju Jampana , P. S. V. Ramana Rao , and A. Sampathkumar 


Research Article (12 pages), Article ID 8138294, Volume 2021 (2021)

[Retracted] Investigation on V₂O₅ Thin Films for Field Effect Transistor Applications

S. K. Suresh Babu , D. Jackuline Moni , D. Gracia , and Amsalu Gosu Adigo 

Research Article (7 pages), Article ID 2414589, Volume 2021 (2021)

[Retracted] Continuous Sorption of Remazol Brilliant Orange 3R Using *Caulerpa scalpelliformis* Biochar

Gokulan Ravindiran , Pradeepkumar Sugumar , and Elias G 

Research Article (7 pages), Article ID 6397137, Volume 2021 (2021)

[Retracted] Experimental Analysis of Mechanical Properties and Durability of Cement-Based Composite with Carbon Nanotube

Yubing Du , Peiwei Gao , Jianming Yang , Feiting Shi , and Mohammad Shabaz 





Research Article (12 pages), Article ID 8777613, Volume 2021 (2021)

[Retracted] Comparative Analysis of Natural Fibre Reinforced Composite Material Using ANSYS

K. G. Saravanan , R. Prabu , A. Sivapragasam , and Nahom Daniel 


Research Article (17 pages), Article ID 9391237, Volume 2021 (2021)

[Retracted] Impact of Different Electrolytes on the Machining Rate in ECM Process

K. G. Saravanan , R. Prabu , A. R. Venkataramanan , and Eden Tekle Beyessa 


Review Article (6 pages), Article ID 1432300, Volume 2021 (2021)

[Retracted] Utilization of Red Mud-Fly Ash Reinforced with Cement in Road Construction Applications

Sarath Chandra K, Krishnaiah S, and Kibebe Sahile 








Research Article (8 pages), Article ID 3728652, Volume 2021 (2021)

[Retracted] Effect of the Reinforcement Phase on Indentation Resistance and Damage Characterization of Glass/Epoxy Laminates Using Acoustic Emission Monitoring

C. Suresh Kumar, K. Saravanakumar, P. Prathap, M. Prince, G. Bharathiraja, S. Kannan, S. Madhu, and P. Kumaran 





Research Article (11 pages), Article ID 5768730, Volume 2021 (2021)

[Retracted] Development of Smart Sensing Technology Approaches in Structural Health Monitoring of Bridge Structures

Arvindan Sivasuriyan , D. S. Vijayan , A. LeemaRose , J. Revathy , S. Gayathri Monicka , U. R. Adithya , and J. Jebasingh Daniel 




Research Article (14 pages), Article ID 2615029, Volume 2021 (2021)

[Retracted] Flexural Behaviour of Chicken Mesh Ferrocement Laminates with Partial Replacement of Fine Aggregate by Steel Slag

Sridhar Jayaprakash , Jegatheeswaran Dhanapal , Vivek Deivasigamani , and Elias G 






Research Article (9 pages), Article ID 7307493, Volume 2021 (2021)

[Retracted] Optimization of CNC End Milling Process Parameters of Low-Carbon Mold Steel Using Response Surface Methodology and Grey Relational Analysis

R. Suresh Kumar , S. Senthil Kumar , K. Murugan, B. Guruprasad , Sreekanth Manavalla , S. Madhu , M. Hariprabhu , S. Balamuralitharan , and S. Venkatesa Prabhu 








Research Article (11 pages), Article ID 4005728, Volume 2021 (2021)

[Retracted] Process Development for Edible Film Preparation Using Avocado Seed Starch: Response Surface Modeling and Analysis for Water-Vapor Permeability

R. Ramesh , Hemalatha Palanivel , S. Venkatesa Prabhu , Belachew Zegale Tizazu , and Adugna Abdi Woldesemayat 



Research Article (7 pages), Article ID 7859658, Volume 2021 (2021)

[Retracted] XRD Peak Profile Analysis of SiC Reinforced Al₂O₃ Ceramic Composite Synthesized by Electrical Resistance Heating and Microwave Sintering: A Comparison

Madhan Mohankumar , S. Praveen Kumar, B. Guruprasad , Sreekanth Manavalla , Joshua Stephen Chellakumar Isaac JoshuaRamesh Lalvani , P. L. Somasundaram , P. Tamilarasu , and Prakash Singh Tanwar 

Research Article (7 pages), Article ID 8341924, Volume 2021 (2021)





[Retracted] Optimization of Reinforced Aluminium Scraps from the Automobile Bumpers with Nickel and Magnesium Oxide in Stir Casting

V. Vijayan, A. Parthiban, T. Sathish , L. Ponraj Sankar, S. Dinesh Kumar, S. Saravanakumar, and Dawit Tafesse 




Research Article (10 pages), Article ID 3735438, Volume 2021 (2021)

Contents




[Retracted] Mechanical Strength and Fatigue Fracture Analysis on Al-Zn-Mg Alloy with the Influence of Creep Aging Process

Muruganantham Ponnusamy , Bhanu Pratap Pulla, T. Sathish , Sivakumar Karthikeyan , S. Ravindran, Balachandra Pattanaik , and Ram Subbiah
Research Article (5 pages), Article ID 1899128, Volume 2021 (2021)

[Retracted] Mechanical Behavior of Silica Fume Concrete Filled with Steel Tubular Composite Column

Maganti Sandeep Kauthsa Sharma, S. Umadevi, Yerra Sai Sampath , K. Vasugi, K. J. N. Sai Nitesh, V. Swamy Nadh , and L. Natrayan 
Research Article (9 pages), Article ID 3632991, Volume 2021 (2021)



[Retracted] Optimization of Remazol Black B Removal Using Biochar Produced from *Caulerpa scalpelliformis* Using Response Surface Methodology

R. Gokulan , S. Balaji , and P. Sivaprakasam 
Research Article (8 pages), Article ID 1535823, Volume 2021 (2021)



[Retracted] Improvement on Mechanical Properties of Submerged Friction Stir Joining of Dissimilar Tailor Welded Aluminum Blanks

R. Suryanarayanan , V. G. Sridhar, L. Natrayan , S. Kaliappan , Anjibabu Merneedi , T. Sathish , and Alazar Yeshitla 
Research Article (6 pages), Article ID 3355692, Volume 2021 (2021)

[Retracted] Effects of the FR 4 Substrate Realized in a Circularly Polarized UHF-RFID Reader Antenna with Fractal Geometry for Enhancing Parameters

Chitra Varadhan , S. Arulsevi, and Fekadu Ashine Chamatu 
Research Article (7 pages), Article ID 8475621, Volume 2021 (2021)







[Retracted] Evaluation of Microstructure, Hardness, and Tensile Properties: A Comparative Study of Stir Cast and Extruded Al7005/Glass-/Fly-Ash-Reinforced Hybrid MMCs

Praveen Kumar Swamy , Shantharaja Mylraiah, and Dadapeer Basheer 
Research Article (7 pages), Article ID 8601484, Volume 2021 (2021)

[Retracted] Effect of Tool Profile Influence in Dissimilar Friction Stir Welding of Aluminium Alloys (AA5083 and AA7068)

S. Jayaprakash , S. Siva Chandran, T. Sathish , Bhiksha Gugulothu , R. Ramesh , M. Sudhakar, and Ram Subbiah
Research Article (7 pages), Article ID 7387296, Volume 2021 (2021)

[Retracted] Industrial Waste Water Recycling Using Nanographene Oxide Filters

P. Yuvarani , S. Vijayachitra , V. Ranganayaki, S. Sathish Kumar , K. Srujan Raju , M. Sivachitra , and Ishwarya Komalnu Raghavan 
Research Article (7 pages), Article ID 4528949, Volume 2021 (2021)

[Retracted] Parameters Optimization of Dissimilar Friction Stir Welding for AA7079 and AA8050 through RSM

M. Kavitha, V. M. Manickavasagam, T. Sathish , Bhiksha Gugulothu , A. Sathish Kumar, Sivakumar Karthikeyan , and Ram Subbiah





Research Article (8 pages), Article ID 9723699, Volume 2021 (2021)

Study of Complex Helical Drill with a “S” Type Chisel Edge Tip Orient to Carbon Fiber Reinforced Plastics

Yu He , Xiaolong Zhou , Ping Zou, and Kun Liu



Research Article (15 pages), Article ID 5175515, Volume 2021 (2021)

[Retracted] Experimental Study of Thermal and Mechanical Behaviour of Graphite-Filled UJF Composite

K. Manohar Reddy , D. Harsha Vardhan , Y. Santhosh Kumar Reddy, Gujjala Raghavendra , and Ramesh Rudrapati 



Research Article (7 pages), Article ID 3739573, Volume 2021 (2021)

[Retracted] Strength Enhancement Study on Composites of AA6066 Aluminium Alloy with Magnesium Oxide and Coal Ash

L. Ponraj Sankar, G. Aruna, T. Sathish , A. Parthiban, V. Vijayan, S. Dinesh Kumar, S. Rajkumar , Addisalem Mekonnen, and Mebratu Tufa





Review Article (8 pages), Article ID 2810106, Volume 2021 (2021)

[Retracted] Effect of Grey and White Portland Cement Fillers on Flexural and Shear Strength of GFRP Composite Material

D. Harsha Vardhan , D. Sai Chaithanya Kishore, Y. Santhosh Kumar Reddy, K. Manohar Reddy, Gujjala Raghavendra, and Ramesh Rudrapati 

Research Article (7 pages), Article ID 9586474, Volume 2021 (2021)

[Retracted] Optimization on Operation Parameters in Reinforced Metal Matrix of AA6066 Composite with HSS and Cu

Y. Sesharao, T. Sathish , Kumaran Palani , Anjibabu Merneedi, Natrayan L , Melvin Victor De Pours , and T. Maridurai

Research Article (12 pages), Article ID 1609769, Volume 2021 (2021)

[Retracted] Improving the Mechanical Properties of Natural Fiber Composites of Hemp Fiber with Ramie and Banana Fiber through Compression Molding Method

S. Dinesh Kumar , L. Ponraj Sankar , T. Sathish , V. Vijayan , A. Parthiban , R. Kamalakannan , and S. Rajkumar 

Research Article (8 pages), Article ID 7813634, Volume 2021 (2021)

[Retracted] Analysis on Emissions and Performance of Ceramic Coated Diesel Engine Fueled with Novel Blends Using Artificial Intelligence

Tarun Kumar Kotteda , Rama Bhadri Raju Chekuri , B. Naga Raju , Prasada Raju Kantheti , and S. Balakumar 

Research Article (13 pages), Article ID 7954488, Volume 2021 (2021)

Contents








[Retracted] Mathematical Modeling and Analysis of Wear Behavior of AlTiN Coating on Titanium Alloy (Ti-6Al-4V)

P. Sivaprakasam , A. Kirubel , G. Elias , P. Maheandera Prabu , and P. Balasubramani 
Research Article (9 pages), Article ID 1098605, Volume 2021 (2021)








[Retracted] Effect of Manganese Ions on Spectroscopic and Insulating Properties of Aluminophosphate Glasses

B. Kassa, J. Leta Tesfaye, B. Bulcha, R. Kiran, T. Deepak, Dayanand Lal, S. Venkatesh, and R. Krishnaraj 
Research Article (11 pages), Article ID 6253069, Volume 2021 (2021)


[Retracted] A Comparative Study on Crack-Healing Ability of Al₂O₃/SiC Structural Ceramic Composites Synthesized by Microwave Sintering and Conventional Electrical Sintering

Madhan Mohankumar , A. N. Shankar , T. S. Karthik , R. Saravanakumar , Hemakesavulu Oruganti , S. Venkatesa Prabhu , and N. Rakesh 
Research Article (8 pages), Article ID 3170697, Volume 2021 (2021)






[Retracted] Computational Investigations of Fixed-Free and Fixed-Fixed Types Single-Wall Carbon Nanotube Mass Sensing Biosensor

K. Umapathi , Yalamanchili Sangeetha , A. N. Shankar , P. Vidhyalakshmi , R. Ramkumar , S. Balakumar , and D. Magdalinmary 
Research Article (13 pages), Article ID 3253365, Volume 2021 (2021)

[Retracted] Synthesis, Mechanical, and Tribological Performance Analysis of Stir-Casted AA7079: ZrO₂ + Si₃N₄ Hybrid Composites by Taguchi Route

G. Jegan, P. Kavipriya, T. Sathish, S. Dinesh Kumar, T. Samraj Lawrence , and T. Vino
Research Article (15 pages), Article ID 7722370, Volume 2021 (2021)


[Retracted] Investigation on Dielectric Properties of Press Board Coated with Epoxy Resin, Quartz, and Rice Husk Ash

Banumathi S. , Karthik T. S. , Sasireka M. , Kiran Ramaswamy , Vishnu J. , Yuwan M. K. , Kavin R. R. , and Sathish Kumar S. 
Research Article (7 pages), Article ID 9839770, Volume 2021 (2021)

[Retracted] Microstructure and Fatigue Properties of 6061 Aluminum Alloy Laser-MIG Hybrid Welding Joint

Cong Fan , Shanglei Yang , Minqi Zhu, and Yishan Bai
Research Article (12 pages), Article ID 1933942, Volume 2021 (2021)

[Retracted] Studying the Effect of Metallic Precursor Concentration on the Structural, Optical, and Morphological Properties of Zinc Sulfide Thin Films in Photovoltaic Cell Applications

S. Abel, J. Leta Tesfaye, R. Kiran, T. Deepak, A. Usha Ruby, S. Venkatesh, and R. Krishnaraj 
Research Article (6 pages), Article ID 7443664, Volume 2021 (2021)

[Retracted] Steady-State Flow Characteristics and End Clearance Optimization of Internal Gear Grease Pump

Xinjian Li , Lingfeng Tang, and Ming Qian

Research Article (16 pages), Article ID 8293040, Volume 2021 (2021)

Retraction

Retracted: Optimizing the Characteristics of the Laser Hardfacing Process Parameters to Maximize the Wear Resistance of Ni-Based Hard-Faced Deposits Using the RSM Technique

Advances in Materials Science and Engineering

Received 23 January 2024; Accepted 23 January 2024; Published 24 January 2024

Copyright © 2024 Advances in Materials Science and Engineering. This is an open access article distributed under the Creative Commons Attribution License, which permits unrestricted use, distribution, and reproduction in any medium, provided the original work is properly cited.

This article has been retracted by Hindawi following an investigation undertaken by the publisher [1]. This investigation has uncovered evidence of one or more of the following indicators of systematic manipulation of the publication process:

- (1) Discrepancies in scope
- (2) Discrepancies in the description of the research reported
- (3) Discrepancies between the availability of data and the research described
- (4) Inappropriate citations
- (5) Incoherent, meaningless and/or irrelevant content included in the article
- (6) Manipulated or compromised peer review

The presence of these indicators undermines our confidence in the integrity of the article's content and we cannot, therefore, vouch for its reliability. Please note that this notice is intended solely to alert readers that the content of this article is unreliable. We have not investigated whether authors were aware of or involved in the systematic manipulation of the publication process.

Wiley and Hindawi regrets that the usual quality checks did not identify these issues before publication and have since put additional measures in place to safeguard research integrity.

We wish to credit our own Research Integrity and Research Publishing teams and anonymous and named external researchers and research integrity experts for contributing to this investigation.

The corresponding author, as the representative of all authors, has been given the opportunity to register their agreement or disagreement to this retraction. We have kept a record of any response received.

References

- [1] S. Gnanasekaran, S. J. S. Chelladurai, T. Ramakrishnan et al., "Optimizing the Characteristics of the Laser Hardfacing Process Parameters to Maximize the Wear Resistance of Ni-Based Hard-Faced Deposits Using the RSM Technique," *Advances in Materials Science and Engineering*, vol. 2021, Article ID 3665631, 15 pages, 2021.

Retraction

Retracted: Detecting Distance between Surfaces of Large Transparent Material Based on Low-Cost TOF Sensor and Deep Convolutional Neural Network

Advances in Materials Science and Engineering

Received 8 January 2024; Accepted 8 January 2024; Published 9 January 2024

Copyright © 2024 Advances in Materials Science and Engineering. This is an open access article distributed under the Creative Commons Attribution License, which permits unrestricted use, distribution, and reproduction in any medium, provided the original work is properly cited.

This article has been retracted by Hindawi following an investigation undertaken by the publisher [1]. This investigation has uncovered evidence of one or more of the following indicators of systematic manipulation of the publication process:

- (1) Discrepancies in scope
- (2) Discrepancies in the description of the research reported
- (3) Discrepancies between the availability of data and the research described
- (4) Inappropriate citations
- (5) Incoherent, meaningless and/or irrelevant content included in the article
- (6) Manipulated or compromised peer review

The presence of these indicators undermines our confidence in the integrity of the article's content and we cannot, therefore, vouch for its reliability. Please note that this notice is intended solely to alert readers that the content of this article is unreliable. We have not investigated whether authors were aware of or involved in the systematic manipulation of the publication process.

Wiley and Hindawi regrets that the usual quality checks did not identify these issues before publication and have since put additional measures in place to safeguard research integrity.

We wish to credit our own Research Integrity and Research Publishing teams and anonymous and named external researchers and research integrity experts for contributing to this investigation.

The corresponding author, as the representative of all authors, has been given the opportunity to register their agreement or disagreement to this retraction. We have kept a record of any response received.

References

- [1] R. Zou, Y. Zhang, J. Gu, and J. Chen, "Detecting Distance between Surfaces of Large Transparent Material Based on Low-Cost TOF Sensor and Deep Convolutional Neural Network," *Advances in Materials Science and Engineering*, vol. 2021, Article ID 8340179, 12 pages, 2021.

Retraction

Retracted: Electrochemical Studies of WC-Flyash HVOF Coating Interface on SA209-T1 Steel under 3.5 NaCl Solution

Advances in Materials Science and Engineering

Received 26 December 2023; Accepted 26 December 2023; Published 29 December 2023

Copyright © 2023 Advances in Materials Science and Engineering. This is an open access article distributed under the Creative Commons Attribution License, which permits unrestricted use, distribution, and reproduction in any medium, provided the original work is properly cited.

This article has been retracted by Hindawi, as publisher, following an investigation undertaken by the publisher [1]. This investigation has uncovered evidence of systematic manipulation of the publication and peer-review process. We cannot, therefore, vouch for the reliability or integrity of this article.

Please note that this notice is intended solely to alert readers that the peer-review process of this article has been compromised.

Wiley and Hindawi regret that the usual quality checks did not identify these issues before publication and have since put additional measures in place to safeguard research integrity.

We wish to credit our Research Integrity and Research Publishing teams and anonymous and named external researchers and research integrity experts for contributing to this investigation.

The corresponding author, as the representative of all authors, has been given the opportunity to register their agreement or disagreement to this retraction. We have kept a record of any response received.

References

- [1] D. Elango, A. Daniel Das, S. P. Kumaresh Babu, S. Natarajan, and A. Yeshitla, "Electrochemical Studies of WC-Flyash HVOF Coating Interface on SA209-T1 Steel under 3.5 NaCl Solution," *Advances in Materials Science and Engineering*, vol. 2021, Article ID 8706630, 9 pages, 2021.

Retraction

Retracted: Investigation on Dielectric Properties of Press Board Coated with Epoxy Resin, Quartz, and Rice Husk Ash

Advances in Materials Science and Engineering

Received 26 December 2023; Accepted 26 December 2023; Published 29 December 2023

Copyright © 2023 Advances in Materials Science and Engineering. This is an open access article distributed under the Creative Commons Attribution License, which permits unrestricted use, distribution, and reproduction in any medium, provided the original work is properly cited.

This article has been retracted by Hindawi, as publisher, following an investigation undertaken by the publisher [1]. This investigation has uncovered evidence of systematic manipulation of the publication and peer-review process. We cannot, therefore, vouch for the reliability or integrity of this article.

Please note that this notice is intended solely to alert readers that the peer-review process of this article has been compromised.

Wiley and Hindawi regret that the usual quality checks did not identify these issues before publication and have since put additional measures in place to safeguard research integrity.

We wish to credit our Research Integrity and Research Publishing teams and anonymous and named external researchers and research integrity experts for contributing to this investigation.

The corresponding author, as the representative of all authors, has been given the opportunity to register their agreement or disagreement to this retraction. We have kept a record of any response received.

References

- [1] B. S., K. T. S., S. M. et al., "Investigation on Dielectric Properties of Press Board Coated with Epoxy Resin, Quartz, and Rice Husk Ash," *Advances in Materials Science and Engineering*, vol. 2021, Article ID 9839770, 7 pages, 2021.

Retraction

Retracted: Industrial Waste Water Recycling Using Nanographene Oxide Filters

Advances in Materials Science and Engineering

Received 26 December 2023; Accepted 26 December 2023; Published 29 December 2023

Copyright © 2023 Advances in Materials Science and Engineering. This is an open access article distributed under the Creative Commons Attribution License, which permits unrestricted use, distribution, and reproduction in any medium, provided the original work is properly cited.

This article has been retracted by Hindawi, as publisher, following an investigation undertaken by the publisher [1]. This investigation has uncovered evidence of systematic manipulation of the publication and peer-review process. We cannot, therefore, vouch for the reliability or integrity of this article.

Please note that this notice is intended solely to alert readers that the peer-review process of this article has been compromised.

Wiley and Hindawi regret that the usual quality checks did not identify these issues before publication and have since put additional measures in place to safeguard research integrity.

We wish to credit our Research Integrity and Research Publishing teams and anonymous and named external researchers and research integrity experts for contributing to this investigation.

The corresponding author, as the representative of all authors, has been given the opportunity to register their agreement or disagreement to this retraction. We have kept a record of any response received.

References

- [1] P. Yuvarani, S. Vijayachitra, V. Ranganayaki et al., "Industrial Waste Water Recycling Using Nanographene Oxide Filters," *Advances in Materials Science and Engineering*, vol. 2021, Article ID 4528949, 7 pages, 2021.

Retraction

Retracted: Effect of the Reinforcement Phase on Indentation Resistance and Damage Characterization of Glass/Epoxy Laminates Using Acoustic Emission Monitoring

Advances in Materials Science and Engineering

Received 26 December 2023; Accepted 26 December 2023; Published 29 December 2023

Copyright © 2023 Advances in Materials Science and Engineering. This is an open access article distributed under the Creative Commons Attribution License, which permits unrestricted use, distribution, and reproduction in any medium, provided the original work is properly cited.

This article has been retracted by Hindawi, as publisher, following an investigation undertaken by the publisher [1]. This investigation has uncovered evidence of systematic manipulation of the publication and peer-review process. We cannot, therefore, vouch for the reliability or integrity of this article.

Please note that this notice is intended solely to alert readers that the peer-review process of this article has been compromised.

Wiley and Hindawi regret that the usual quality checks did not identify these issues before publication and have since put additional measures in place to safeguard research integrity.

We wish to credit our Research Integrity and Research Publishing teams and anonymous and named external researchers and research integrity experts for contributing to this investigation.

The corresponding author, as the representative of all authors, has been given the opportunity to register their agreement or disagreement to this retraction. We have kept a record of any response received.

References

- [1] C. S. Kumar, K. Saravanakumar, P. Prathap et al., "Effect of the Reinforcement Phase on Indentation Resistance and Damage Characterization of Glass/Epoxy Laminates Using Acoustic Emission Monitoring," *Advances in Materials Science and Engineering*, vol. 2021, Article ID 5768730, 11 pages, 2021.

Retraction

Retracted: Optimization of Remazol Black B Removal Using Biochar Produced from *Caulerpa scalpelliformis* Using Response Surface Methodology

Advances in Materials Science and Engineering

Received 26 December 2023; Accepted 26 December 2023; Published 29 December 2023

Copyright © 2023 Advances in Materials Science and Engineering. This is an open access article distributed under the Creative Commons Attribution License, which permits unrestricted use, distribution, and reproduction in any medium, provided the original work is properly cited.

This article has been retracted by Hindawi, as publisher, following an investigation undertaken by the publisher [1]. This investigation has uncovered evidence of systematic manipulation of the publication and peer-review process. We cannot, therefore, vouch for the reliability or integrity of this article.

Please note that this notice is intended solely to alert readers that the peer-review process of this article has been compromised.

Wiley and Hindawi regret that the usual quality checks did not identify these issues before publication and have since put additional measures in place to safeguard research integrity.

We wish to credit our Research Integrity and Research Publishing teams and anonymous and named external researchers and research integrity experts for contributing to this investigation.

The corresponding author, as the representative of all authors, has been given the opportunity to register their agreement or disagreement to this retraction. We have kept a record of any response received.

References

- [1] R. Gokulan, S. Balaji, and P. Sivaprakasam, "Optimization of Remazol Black B Removal Using Biochar Produced from *Caulerpa scalpelliformis* Using Response Surface Methodology," *Advances in Materials Science and Engineering*, vol. 2021, Article ID 1535823, 8 pages, 2021.

Retraction

Retracted: Improvement on Mechanical Properties of Submerged Friction Stir Joining of Dissimilar Tailor Welded Aluminum Blanks

Advances in Materials Science and Engineering

Received 26 December 2023; Accepted 26 December 2023; Published 29 December 2023

Copyright © 2023 Advances in Materials Science and Engineering. This is an open access article distributed under the Creative Commons Attribution License, which permits unrestricted use, distribution, and reproduction in any medium, provided the original work is properly cited.

This article has been retracted by Hindawi, as publisher, following an investigation undertaken by the publisher [1]. This investigation has uncovered evidence of systematic manipulation of the publication and peer-review process. We cannot, therefore, vouch for the reliability or integrity of this article.

Please note that this notice is intended solely to alert readers that the peer-review process of this article has been compromised.

Wiley and Hindawi regret that the usual quality checks did not identify these issues before publication and have since put additional measures in place to safeguard research integrity.

We wish to credit our Research Integrity and Research Publishing teams and anonymous and named external researchers and research integrity experts for contributing to this investigation.

The corresponding author, as the representative of all authors, has been given the opportunity to register their agreement or disagreement to this retraction. We have kept a record of any response received.

References

- [1] R. Suryanarayanan, V. G. Sridhar, L. Natrayan et al., "Improvement on Mechanical Properties of Submerged Friction Stir Joining of Dissimilar Tailor Welded Aluminum Blanks," *Advances in Materials Science and Engineering*, vol. 2021, Article ID 3355692, 6 pages, 2021.

Retraction

Retracted: Process Development for Edible Film Preparation Using Avocado Seed Starch: Response Surface Modeling and Analysis for Water-Vapor Permeability

Advances in Materials Science and Engineering

Received 26 December 2023; Accepted 26 December 2023; Published 29 December 2023

Copyright © 2023 Advances in Materials Science and Engineering. This is an open access article distributed under the Creative Commons Attribution License, which permits unrestricted use, distribution, and reproduction in any medium, provided the original work is properly cited.

This article has been retracted by Hindawi, as publisher, following an investigation undertaken by the publisher [1]. This investigation has uncovered evidence of systematic manipulation of the publication and peer-review process. We cannot, therefore, vouch for the reliability or integrity of this article.

Please note that this notice is intended solely to alert readers that the peer-review process of this article has been compromised.

Wiley and Hindawi regret that the usual quality checks did not identify these issues before publication and have since put additional measures in place to safeguard research integrity.

We wish to credit our Research Integrity and Research Publishing teams and anonymous and named external researchers and research integrity experts for contributing to this investigation.

The corresponding author, as the representative of all authors, has been given the opportunity to register their agreement or disagreement to this retraction. We have kept a record of any response received.

References

- [1] R. Ramesh, H. Palanivel, S. Venkatesa Prabhu, B. Z. Tizazu, and A. A. Woldesemayat, "Process Development for Edible Film Preparation Using Avocado Seed Starch: Response Surface Modeling and Analysis for Water-Vapor Permeability," *Advances in Materials Science and Engineering*, vol. 2021, Article ID 7859658, 7 pages, 2021.

Retraction

Retracted: A Comparative Study on Crack-Healing Ability of Al₂O₃/SiC Structural Ceramic Composites Synthesized by Microwave Sintering and Conventional Electrical Sintering

Advances in Materials Science and Engineering

Received 26 December 2023; Accepted 26 December 2023; Published 29 December 2023

Copyright © 2023 Advances in Materials Science and Engineering. This is an open access article distributed under the Creative Commons Attribution License, which permits unrestricted use, distribution, and reproduction in any medium, provided the original work is properly cited.

This article has been retracted by Hindawi, as publisher, following an investigation undertaken by the publisher [1]. This investigation has uncovered evidence of systematic manipulation of the publication and peer-review process. We cannot, therefore, vouch for the reliability or integrity of this article.

Please note that this notice is intended solely to alert readers that the peer-review process of this article has been compromised.

Wiley and Hindawi regret that the usual quality checks did not identify these issues before publication and have since put additional measures in place to safeguard research integrity.

We wish to credit our Research Integrity and Research Publishing teams and anonymous and named external researchers and research integrity experts for contributing to this investigation.

The corresponding author, as the representative of all authors, has been given the opportunity to register their agreement or disagreement to this retraction. We have kept a record of any response received.

References

- [1] M. Mohankumar, A. N. Shankar, T. S. Karthik et al., "A Comparative Study on Crack-Healing Ability of Al₂O₃/SiC Structural Ceramic Composites Synthesized by Microwave Sintering and Conventional Electrical Sintering," *Advances in Materials Science and Engineering*, vol. 2021, Article ID 3170697, 8 pages, 2021.

Retraction

Retracted: Mathematical Modeling and Analysis of Wear Behavior of AlTiN Coating on Titanium Alloy (Ti-6Al-4V)

Advances in Materials Science and Engineering

Received 26 December 2023; Accepted 26 December 2023; Published 29 December 2023

Copyright © 2023 Advances in Materials Science and Engineering. This is an open access article distributed under the Creative Commons Attribution License, which permits unrestricted use, distribution, and reproduction in any medium, provided the original work is properly cited.

This article has been retracted by Hindawi, as publisher, following an investigation undertaken by the publisher [1]. This investigation has uncovered evidence of systematic manipulation of the publication and peer-review process. We cannot, therefore, vouch for the reliability or integrity of this article.

Please note that this notice is intended solely to alert readers that the peer-review process of this article has been compromised.

Wiley and Hindawi regret that the usual quality checks did not identify these issues before publication and have since put additional measures in place to safeguard research integrity.

We wish to credit our Research Integrity and Research Publishing teams and anonymous and named external researchers and research integrity experts for contributing to this investigation.

The corresponding author, as the representative of all authors, has been given the opportunity to register their agreement or disagreement to this retraction. We have kept a record of any response received.

References

- [1] P. Sivaprakasam, A. Kirubel, G. Elias, P. Maheandera Prabu, and P. Balasubramani, "Mathematical Modeling and Analysis of Wear Behavior of AlTiN Coating on Titanium Alloy (Ti-6Al-4V)," *Advances in Materials Science and Engineering*, vol. 2021, Article ID 1098605, 9 pages, 2021.

Retraction

Retracted: Effect of Manganese Ions on Spectroscopic and Insulating Properties of Aluminophosphate Glasses

Advances in Materials Science and Engineering

Received 26 December 2023; Accepted 26 December 2023; Published 29 December 2023

Copyright © 2023 Advances in Materials Science and Engineering. This is an open access article distributed under the Creative Commons Attribution License, which permits unrestricted use, distribution, and reproduction in any medium, provided the original work is properly cited.

This article has been retracted by Hindawi, as publisher, following an investigation undertaken by the publisher [1]. This investigation has uncovered evidence of systematic manipulation of the publication and peer-review process. We cannot, therefore, vouch for the reliability or integrity of this article.

Please note that this notice is intended solely to alert readers that the peer-review process of this article has been compromised.

Wiley and Hindawi regret that the usual quality checks did not identify these issues before publication and have since put additional measures in place to safeguard research integrity.

We wish to credit our Research Integrity and Research Publishing teams and anonymous and named external researchers and research integrity experts for contributing to this investigation.

The corresponding author, as the representative of all authors, has been given the opportunity to register their agreement or disagreement to this retraction. We have kept a record of any response received.

References

- [1] B. Kassa, J. Leta Tesfaye, B. Bulcha et al., "Effect of Manganese Ions on Spectroscopic and Insulating Properties of Aluminophosphate Glasses," *Advances in Materials Science and Engineering*, vol. 2021, Article ID 6253069, 11 pages, 2021.

Retraction

Retracted: Experimental Study of Thermal and Mechanical Behaviour of Graphite-Filled UJF Composite

Advances in Materials Science and Engineering

Received 26 December 2023; Accepted 26 December 2023; Published 29 December 2023

Copyright © 2023 Advances in Materials Science and Engineering. This is an open access article distributed under the Creative Commons Attribution License, which permits unrestricted use, distribution, and reproduction in any medium, provided the original work is properly cited.

This article has been retracted by Hindawi, as publisher, following an investigation undertaken by the publisher [1]. This investigation has uncovered evidence of systematic manipulation of the publication and peer-review process. We cannot, therefore, vouch for the reliability or integrity of this article.

Please note that this notice is intended solely to alert readers that the peer-review process of this article has been compromised.

Wiley and Hindawi regret that the usual quality checks did not identify these issues before publication and have since put additional measures in place to safeguard research integrity.

We wish to credit our Research Integrity and Research Publishing teams and anonymous and named external researchers and research integrity experts for contributing to this investigation.

The corresponding author, as the representative of all authors, has been given the opportunity to register their agreement or disagreement to this retraction. We have kept a record of any response received.

References

- [1] K. M. Reddy, D. H. Vardhan, Y. S. K. Reddy, G. Raghavendra, and R. Rudrapati, "Experimental Study of Thermal and Mechanical Behaviour of Graphite-Filled UJF Composite," *Advances in Materials Science and Engineering*, vol. 2021, Article ID 3739573, 7 pages, 2021.

Retraction

Retracted: A Comprehensive Examination of Bandgap Semiconductor Switches

Advances in Materials Science and Engineering

Received 26 December 2023; Accepted 26 December 2023; Published 29 December 2023

Copyright © 2023 Advances in Materials Science and Engineering. This is an open access article distributed under the Creative Commons Attribution License, which permits unrestricted use, distribution, and reproduction in any medium, provided the original work is properly cited.

This article has been retracted by Hindawi, as publisher, following an investigation undertaken by the publisher [1]. This investigation has uncovered evidence of systematic manipulation of the publication and peer-review process. We cannot, therefore, vouch for the reliability or integrity of this article.

Please note that this notice is intended solely to alert readers that the peer-review process of this article has been compromised.

Wiley and Hindawi regret that the usual quality checks did not identify these issues before publication and have since put additional measures in place to safeguard research integrity.

We wish to credit our Research Integrity and Research Publishing teams and anonymous and named external researchers and research integrity experts for contributing to this investigation.

The corresponding author, as the representative of all authors, has been given the opportunity to register their agreement or disagreement to this retraction. We have kept a record of any response received.

References

- [1] S. Siva Subramanian, R. Saravanakumar, B. P. Ganthia et al., "A Comprehensive Examination of Bandgap Semiconductor Switches," *Advances in Materials Science and Engineering*, vol. 2021, Article ID 3188506, 8 pages, 2021.

Retraction

Retracted: Impact of Different Electrolytes on the Machining Rate in ECM Process

Advances in Materials Science and Engineering

Received 26 December 2023; Accepted 26 December 2023; Published 29 December 2023

Copyright © 2023 Advances in Materials Science and Engineering. This is an open access article distributed under the Creative Commons Attribution License, which permits unrestricted use, distribution, and reproduction in any medium, provided the original work is properly cited.

This article has been retracted by Hindawi, as publisher, following an investigation undertaken by the publisher [1]. This investigation has uncovered evidence of systematic manipulation of the publication and peer-review process. We cannot, therefore, vouch for the reliability or integrity of this article.

Please note that this notice is intended solely to alert readers that the peer-review process of this article has been compromised.

Wiley and Hindawi regret that the usual quality checks did not identify these issues before publication and have since put additional measures in place to safeguard research integrity.

We wish to credit our Research Integrity and Research Publishing teams and anonymous and named external researchers and research integrity experts for contributing to this investigation.

The corresponding author, as the representative of all authors, has been given the opportunity to register their agreement or disagreement to this retraction. We have kept a record of any response received.

References

- [1] K. G. Saravanan, R. Prabu, A. R. Venkataramanan, and E. T. Beyessa, "Impact of Different Electrolytes on the Machining Rate in ECM Process," *Advances in Materials Science and Engineering*, vol. 2021, Article ID 1432300, 6 pages, 2021.

Retraction

Retracted: Strength Enhancement Study on Composites of AA6066 Aluminium Alloy with Magnesium Oxide and Coal Ash

Advances in Materials Science and Engineering

Received 26 December 2023; Accepted 26 December 2023; Published 29 December 2023

Copyright © 2023 Advances in Materials Science and Engineering. This is an open access article distributed under the Creative Commons Attribution License, which permits unrestricted use, distribution, and reproduction in any medium, provided the original work is properly cited.

This article has been retracted by Hindawi, as publisher, following an investigation undertaken by the publisher [1]. This investigation has uncovered evidence of systematic manipulation of the publication and peer-review process. We cannot, therefore, vouch for the reliability or integrity of this article.

Please note that this notice is intended solely to alert readers that the peer-review process of this article has been compromised.

Wiley and Hindawi regret that the usual quality checks did not identify these issues before publication and have since put additional measures in place to safeguard research integrity.

We wish to credit our Research Integrity and Research Publishing teams and anonymous and named external researchers and research integrity experts for contributing to this investigation.

The corresponding author, as the representative of all authors, has been given the opportunity to register their agreement or disagreement to this retraction. We have kept a record of any response received.

References

- [1] L. Ponraj Sankar, G. Aruna, T. Sathish et al., "Strength Enhancement Study on Composites of AA6066 Aluminium Alloy with Magnesium Oxide and Coal Ash," *Advances in Materials Science and Engineering*, vol. 2021, Article ID 2810106, 8 pages, 2021.

Retraction

Retracted: Empirical Investigation on Compressive Strength of Geopolymer and Conventional Concretes by Nondestructive Method

Advances in Materials Science and Engineering

Received 26 December 2023; Accepted 26 December 2023; Published 29 December 2023

Copyright © 2023 Advances in Materials Science and Engineering. This is an open access article distributed under the Creative Commons Attribution License, which permits unrestricted use, distribution, and reproduction in any medium, provided the original work is properly cited.

This article has been retracted by Hindawi, as publisher, following an investigation undertaken by the publisher [1]. This investigation has uncovered evidence of systematic manipulation of the publication and peer-review process. We cannot, therefore, vouch for the reliability or integrity of this article.

Please note that this notice is intended solely to alert readers that the peer-review process of this article has been compromised.

Wiley and Hindawi regret that the usual quality checks did not identify these issues before publication and have since put additional measures in place to safeguard research integrity.

We wish to credit our Research Integrity and Research Publishing teams and anonymous and named external researchers and research integrity experts for contributing to this investigation.

The corresponding author, as the representative of all authors, has been given the opportunity to register their agreement or disagreement to this retraction. We have kept a record of any response received.

References

- [1] B. Ravali, K. B. G. Krishna, D. R. Kanth, K. J. B. Chari, S. V. Prabhu, and R. Ramesh, "Empirical Investigation on Compressive Strength of Geopolymer and Conventional Concretes by Nondestructive Method," *Advances in Materials Science and Engineering*, vol. 2021, Article ID 9575964, 10 pages, 2021.

Retraction

Retracted: Mechanical Behavior of Silica Fume Concrete Filled with Steel Tubular Composite Column

Advances in Materials Science and Engineering

Received 26 December 2023; Accepted 26 December 2023; Published 29 December 2023

Copyright © 2023 Advances in Materials Science and Engineering. This is an open access article distributed under the Creative Commons Attribution License, which permits unrestricted use, distribution, and reproduction in any medium, provided the original work is properly cited.

This article has been retracted by Hindawi, as publisher, following an investigation undertaken by the publisher [1]. This investigation has uncovered evidence of systematic manipulation of the publication and peer-review process. We cannot, therefore, vouch for the reliability or integrity of this article.

Please note that this notice is intended solely to alert readers that the peer-review process of this article has been compromised.

Wiley and Hindawi regret that the usual quality checks did not identify these issues before publication and have since put additional measures in place to safeguard research integrity.

We wish to credit our Research Integrity and Research Publishing teams and anonymous and named external researchers and research integrity experts for contributing to this investigation.

The corresponding author, as the representative of all authors, has been given the opportunity to register their agreement or disagreement to this retraction. We have kept a record of any response received.

References

- [1] M. Sandeep Kauthsa Sharma, S. Umadevi, Y. Sai Sampath et al., "Mechanical Behavior of Silica Fume Concrete Filled with Steel Tubular Composite Column," *Advances in Materials Science and Engineering*, vol. 2021, Article ID 3632991, 9 pages, 2021.

Retraction

Retracted: Development of Novel Nano-Silver-Based Antenna for Green Agriculture

Advances in Materials Science and Engineering

Received 26 December 2023; Accepted 26 December 2023; Published 29 December 2023

Copyright © 2023 Advances in Materials Science and Engineering. This is an open access article distributed under the Creative Commons Attribution License, which permits unrestricted use, distribution, and reproduction in any medium, provided the original work is properly cited.

This article has been retracted by Hindawi, as publisher, following an investigation undertaken by the publisher [1]. This investigation has uncovered evidence of systematic manipulation of the publication and peer-review process. We cannot, therefore, vouch for the reliability or integrity of this article.

Please note that this notice is intended solely to alert readers that the peer-review process of this article has been compromised.

Wiley and Hindawi regret that the usual quality checks did not identify these issues before publication and have since put additional measures in place to safeguard research integrity.

We wish to credit our Research Integrity and Research Publishing teams and anonymous and named external researchers and research integrity experts for contributing to this investigation.

The corresponding author, as the representative of all authors, has been given the opportunity to register their agreement or disagreement to this retraction. We have kept a record of any response received.

References

- [1] S. D., V. R., R. A., B. S., M. A., and K. Sahile, "Development of Novel Nano-Silver-Based Antenna for Green Agriculture," *Advances in Materials Science and Engineering*, vol. 2021, Article ID 9065960, 9 pages, 2021.

Retraction

Retracted: Analysis on Emissions and Performance of Ceramic Coated Diesel Engine Fueled with Novel Blends Using Artificial Intelligence

Advances in Materials Science and Engineering

Received 26 December 2023; Accepted 26 December 2023; Published 29 December 2023

Copyright © 2023 Advances in Materials Science and Engineering. This is an open access article distributed under the Creative Commons Attribution License, which permits unrestricted use, distribution, and reproduction in any medium, provided the original work is properly cited.

This article has been retracted by Hindawi, as publisher, following an investigation undertaken by the publisher [1]. This investigation has uncovered evidence of systematic manipulation of the publication and peer-review process. We cannot, therefore, vouch for the reliability or integrity of this article.

Please note that this notice is intended solely to alert readers that the peer-review process of this article has been compromised.

Wiley and Hindawi regret that the usual quality checks did not identify these issues before publication and have since put additional measures in place to safeguard research integrity.

We wish to credit our Research Integrity and Research Publishing teams and anonymous and named external researchers and research integrity experts for contributing to this investigation.

The corresponding author, as the representative of all authors, has been given the opportunity to register their agreement or disagreement to this retraction. We have kept a record of any response received.

References

- [1] T. K. Kotteda, R. B. R. Chekuri, B. Naga Raju, P. R. Kantheti, and S. Balakumar, "Analysis on Emissions and Performance of Ceramic Coated Diesel Engine Fueled with Novel Blends Using Artificial Intelligence," *Advances in Materials Science and Engineering*, vol. 2021, Article ID 7954488, 13 pages, 2021.

Retraction

Retracted: Characterization of Composite RFID Antennas Based on Thermal Properties: A Survey

Advances in Materials Science and Engineering

Received 26 December 2023; Accepted 26 December 2023; Published 29 December 2023

Copyright © 2023 Advances in Materials Science and Engineering. This is an open access article distributed under the Creative Commons Attribution License, which permits unrestricted use, distribution, and reproduction in any medium, provided the original work is properly cited.

This article has been retracted by Hindawi, as publisher, following an investigation undertaken by the publisher [1]. This investigation has uncovered evidence of systematic manipulation of the publication and peer-review process. We cannot, therefore, vouch for the reliability or integrity of this article.

Please note that this notice is intended solely to alert readers that the peer-review process of this article has been compromised.

Wiley and Hindawi regret that the usual quality checks did not identify these issues before publication and have since put additional measures in place to safeguard research integrity.

We wish to credit our Research Integrity and Research Publishing teams and anonymous and named external researchers and research integrity experts for contributing to this investigation.

The corresponding author, as the representative of all authors, has been given the opportunity to register their agreement or disagreement to this retraction. We have kept a record of any response received.

References

- [1] C. Varadhan, F. Ashine Chamatu, and S. Arulsevi, "Characterization of Composite RFID Antennas Based on Thermal Properties: A Survey," *Advances in Materials Science and Engineering*, vol. 2021, Article ID 8905489, 9 pages, 2021.

Retraction

Retracted: Optimization of Reinforced Aluminium Scraps from the Automobile Bumpers with Nickel and Magnesium Oxide in Stir Casting

Advances in Materials Science and Engineering

Received 26 December 2023; Accepted 26 December 2023; Published 29 December 2023

Copyright © 2023 Advances in Materials Science and Engineering. This is an open access article distributed under the Creative Commons Attribution License, which permits unrestricted use, distribution, and reproduction in any medium, provided the original work is properly cited.

This article has been retracted by Hindawi, as publisher, following an investigation undertaken by the publisher [1]. This investigation has uncovered evidence of systematic manipulation of the publication and peer-review process. We cannot, therefore, vouch for the reliability or integrity of this article.

Please note that this notice is intended solely to alert readers that the peer-review process of this article has been compromised.

Wiley and Hindawi regret that the usual quality checks did not identify these issues before publication and have since put additional measures in place to safeguard research integrity.

We wish to credit our Research Integrity and Research Publishing teams and anonymous and named external researchers and research integrity experts for contributing to this investigation.

The corresponding author, as the representative of all authors, has been given the opportunity to register their agreement or disagreement to this retraction. We have kept a record of any response received.

References

- [1] V. Vijayan, A. Parthiban, T. Sathish et al., "Optimization of Reinforced Aluminium Scraps from the Automobile Bumpers with Nickel and Magnesium Oxide in Stir Casting," *Advances in Materials Science and Engineering*, vol. 2021, Article ID 3735438, 10 pages, 2021.

Retraction

Retracted: Multiobjective Optimization of Mechanical Properties on Sisal-Glass Fiber-Reinforced Hybrid Composites Using Response Surface Methodology and LINGO Analysis

Advances in Materials Science and Engineering

Received 26 December 2023; Accepted 26 December 2023; Published 29 December 2023

Copyright © 2023 Advances in Materials Science and Engineering. This is an open access article distributed under the Creative Commons Attribution License, which permits unrestricted use, distribution, and reproduction in any medium, provided the original work is properly cited.

This article has been retracted by Hindawi, as publisher, following an investigation undertaken by the publisher [1]. This investigation has uncovered evidence of systematic manipulation of the publication and peer-review process. We cannot, therefore, vouch for the reliability or integrity of this article.

Please note that this notice is intended solely to alert readers that the peer-review process of this article has been compromised.

Wiley and Hindawi regret that the usual quality checks did not identify these issues before publication and have since put additional measures in place to safeguard research integrity.

We wish to credit our Research Integrity and Research Publishing teams and anonymous and named external researchers and research integrity experts for contributing to this investigation.

The corresponding author, as the representative of all authors, has been given the opportunity to register their agreement or disagreement to this retraction. We have kept a record of any response received.

References

- [1] S. Rangunath, A. N. Shankar, K. Meena et al., "Multiobjective Optimization of Mechanical Properties on Sisal-Glass Fiber-Reinforced Hybrid Composites Using Response Surface Methodology and LINGO Analysis," *Advances in Materials Science and Engineering*, vol. 2021, Article ID 2376148, 10 pages, 2021.

Retraction

Retracted: Optimization of CNC End Milling Process Parameters of Low-Carbon Mold Steel Using Response Surface Methodology and Grey Relational Analysis

Advances in Materials Science and Engineering

Received 26 December 2023; Accepted 26 December 2023; Published 29 December 2023

Copyright © 2023 Advances in Materials Science and Engineering. This is an open access article distributed under the Creative Commons Attribution License, which permits unrestricted use, distribution, and reproduction in any medium, provided the original work is properly cited.

This article has been retracted by Hindawi, as publisher, following an investigation undertaken by the publisher [1]. This investigation has uncovered evidence of systematic manipulation of the publication and peer-review process. We cannot, therefore, vouch for the reliability or integrity of this article.

Please note that this notice is intended solely to alert readers that the peer-review process of this article has been compromised.

Wiley and Hindawi regret that the usual quality checks did not identify these issues before publication and have since put additional measures in place to safeguard research integrity.

We wish to credit our Research Integrity and Research Publishing teams and anonymous and named external researchers and research integrity experts for contributing to this investigation.

The corresponding author, as the representative of all authors, has been given the opportunity to register their agreement or disagreement to this retraction. We have kept a record of any response received.

References

- [1] R. Suresh Kumar, S. Senthil Kumar, K. Murugan et al., "Optimization of CNC End Milling Process Parameters of Low-Carbon Mold Steel Using Response Surface Methodology and Grey Relational Analysis," *Advances in Materials Science and Engineering*, vol. 2021, Article ID 4005728, 11 pages, 2021.

Retraction

Retracted: Comparative Analysis of Natural Fibre Reinforced Composite Material Using ANSYS

Advances in Materials Science and Engineering

Received 26 December 2023; Accepted 26 December 2023; Published 29 December 2023

Copyright © 2023 Advances in Materials Science and Engineering. This is an open access article distributed under the Creative Commons Attribution License, which permits unrestricted use, distribution, and reproduction in any medium, provided the original work is properly cited.

This article has been retracted by Hindawi, as publisher, following an investigation undertaken by the publisher [1]. This investigation has uncovered evidence of systematic manipulation of the publication and peer-review process. We cannot, therefore, vouch for the reliability or integrity of this article.

Please note that this notice is intended solely to alert readers that the peer-review process of this article has been compromised.

Wiley and Hindawi regret that the usual quality checks did not identify these issues before publication and have since put additional measures in place to safeguard research integrity.

We wish to credit our Research Integrity and Research Publishing teams and anonymous and named external researchers and research integrity experts for contributing to this investigation.

The corresponding author, as the representative of all authors, has been given the opportunity to register their agreement or disagreement to this retraction. We have kept a record of any response received.

References

- [1] K. G. Saravanan, R. Prabu, A. Sivapragasam, and N. Daniel, "Comparative Analysis of Natural Fibre Reinforced Composite Material Using ANSYS," *Advances in Materials Science and Engineering*, vol. 2021, Article ID 9391237, 17 pages, 2021.

Retraction

Retracted: Steady-State Flow Characteristics and End Clearance Optimization of Internal Gear Grease Pump

Advances in Materials Science and Engineering

Received 26 December 2023; Accepted 26 December 2023; Published 29 December 2023

Copyright © 2023 Advances in Materials Science and Engineering. This is an open access article distributed under the Creative Commons Attribution License, which permits unrestricted use, distribution, and reproduction in any medium, provided the original work is properly cited.

This article has been retracted by Hindawi, as publisher, following an investigation undertaken by the publisher [1]. This investigation has uncovered evidence of systematic manipulation of the publication and peer-review process. We cannot, therefore, vouch for the reliability or integrity of this article.

Please note that this notice is intended solely to alert readers that the peer-review process of this article has been compromised.

Wiley and Hindawi regret that the usual quality checks did not identify these issues before publication and have since put additional measures in place to safeguard research integrity.

We wish to credit our Research Integrity and Research Publishing teams and anonymous and name external researchers and research integrity experts for contributing to this investigation.

The corresponding author, as the representative of all authors, has been given the opportunity to register their agreement or disagreement to this retraction. We have kept a record of any response received.

References

- [1] X. Li, L. Tang, and M. Qian, "Steady-State Flow Characteristics and End Clearance Optimization of Internal Gear Grease Pump," *Advances in Materials Science and Engineering*, vol. 2021, Article ID 8293040, 16 pages, 2021.

Retraction

Retracted: Utilization of Red Mud-Fly Ash Reinforced with Cement in Road Construction Applications

Advances in Materials Science and Engineering

Received 26 December 2023; Accepted 26 December 2023; Published 29 December 2023

Copyright © 2023 Advances in Materials Science and Engineering. This is an open access article distributed under the Creative Commons Attribution License, which permits unrestricted use, distribution, and reproduction in any medium, provided the original work is properly cited.

This article has been retracted by Hindawi, as publisher, following an investigation undertaken by the publisher [1]. This investigation has uncovered evidence of systematic manipulation of the publication and peer-review process. We cannot, therefore, vouch for the reliability or integrity of this article.

Please note that this notice is intended solely to alert readers that the peer-review process of this article has been compromised.

Wiley and Hindawi regret that the usual quality checks did not identify these issues before publication and have since put additional measures in place to safeguard research integrity.

We wish to credit our Research Integrity and Research Publishing teams and anonymous and named external researchers and research integrity experts for contributing to this investigation.

The corresponding author, as the representative of all authors, has been given the opportunity to register their agreement or disagreement to this retraction. We have kept a record of any response received.

References

- [1] S. C. K, K. S, and K. Sahile, "Utilization of Red Mud-Fly Ash Reinforced with Cement in Road Construction Applications," *Advances in Materials Science and Engineering*, vol. 2021, Article ID 3728652, 8 pages, 2021.

Retraction

Retracted: Microstructure and Fatigue Properties of 6061 Aluminum Alloy Laser-MIG Hybrid Welding Joint

Advances in Materials Science and Engineering

Received 26 December 2023; Accepted 26 December 2023; Published 29 December 2023

Copyright © 2023 Advances in Materials Science and Engineering. This is an open access article distributed under the Creative Commons Attribution License, which permits unrestricted use, distribution, and reproduction in any medium, provided the original work is properly cited.

This article has been retracted by Hindawi, as publisher, following an investigation undertaken by the publisher [1]. This investigation has uncovered evidence of systematic manipulation of the publication and peer-review process. We cannot, therefore, vouch for the reliability or integrity of this article.

Please note that this notice is intended solely to alert readers that the peer-review process of this article has been compromised.

Wiley and Hindawi regret that the usual quality checks did not identify these issues before publication and have since put additional measures in place to safeguard research integrity.

We wish to credit our Research Integrity and Research Publishing teams and anonymous and named external researchers and research integrity experts for contributing to this investigation.

The corresponding author, as the representative of all authors, has been given the opportunity to register their agreement or disagreement to this retraction. We have kept a record of any response received.

References

- [1] C. Fan, S. Yang, M. Zhu, and Y. Bai, "Microstructure and Fatigue Properties of 6061 Aluminum Alloy Laser-MIG Hybrid Welding Joint," *Advances in Materials Science and Engineering*, vol. 2021, Article ID 1933942, 12 pages, 2021.

Retraction

Retracted: Experimental and Thermal Investigation on Powder Mixed EDM Using FEM and Artificial Neural Networks

Advances in Materials Science and Engineering

Received 26 December 2023; Accepted 26 December 2023; Published 29 December 2023

Copyright © 2023 Advances in Materials Science and Engineering. This is an open access article distributed under the Creative Commons Attribution License, which permits unrestricted use, distribution, and reproduction in any medium, provided the original work is properly cited.

This article has been retracted by Hindawi, as publisher, following an investigation undertaken by the publisher [1]. This investigation has uncovered evidence of systematic manipulation of the publication and peer-review process. We cannot, therefore, vouch for the reliability or integrity of this article.

Please note that this notice is intended solely to alert readers that the peer-review process of this article has been compromised.

Wiley and Hindawi regret that the usual quality checks did not identify these issues before publication and have since put additional measures in place to safeguard research integrity.

We wish to credit our Research Integrity and Research Publishing teams and anonymous and named external researchers and research integrity experts for contributing to this investigation.

The corresponding author, as the representative of all authors, has been given the opportunity to register their agreement or disagreement to this retraction. We have kept a record of any response received.

References

- [1] V. N. R. Jampana, P. S. V. Ramana Rao, and A. Sampathkumar, "Experimental and Thermal Investigation on Powder Mixed EDM Using FEM and Artificial Neural Networks," *Advances in Materials Science and Engineering*, vol. 2021, Article ID 8138294, 12 pages, 2021.

Retraction

Retracted: Performance Analysis and Development of a Semiconductor Junction Rectifier with Multicolor Coding for Indoor Farm Applications

Advances in Materials Science and Engineering

Received 26 December 2023; Accepted 26 December 2023; Published 29 December 2023

Copyright © 2023 Advances in Materials Science and Engineering. This is an open access article distributed under the Creative Commons Attribution License, which permits unrestricted use, distribution, and reproduction in any medium, provided the original work is properly cited.

This article has been retracted by Hindawi, as publisher, following an investigation undertaken by the publisher [1]. This investigation has uncovered evidence of systematic manipulation of the publication and peer-review process. We cannot, therefore, vouch for the reliability or integrity of this article.

Please note that this notice is intended solely to alert readers that the peer-review process of this article has been compromised.

Wiley and Hindawi regret that the usual quality checks did not identify these issues before publication and have since put additional measures in place to safeguard research integrity.

We wish to credit our Research Integrity and Research Publishing teams and anonymous and named external researchers and research integrity experts for contributing to this investigation.

The corresponding author, as the representative of all authors, has been given the opportunity to register their agreement or disagreement to this retraction. We have kept a record of any response received.

References

- [1] E. D. Kanmani Ruby, M. Umadevi, C. Kanmani Pappa, W. Edwin Santhkumar, P. Janani, and P. Shanmugasundaram, "Performance Analysis and Development of a Semiconductor Junction Rectifier with Multicolor Coding for Indoor Farm Applications," *Advances in Materials Science and Engineering*, vol. 2021, Article ID 6585680, 12 pages, 2021.

Retraction

Retracted: Computational Investigations of Fixed-Free and Fixed-Fixed Types Single-Wall Carbon Nanotube Mass Sensing Biosensor

Advances in Materials Science and Engineering

Received 26 December 2023; Accepted 26 December 2023; Published 29 December 2023

Copyright © 2023 Advances in Materials Science and Engineering. This is an open access article distributed under the Creative Commons Attribution License, which permits unrestricted use, distribution, and reproduction in any medium, provided the original work is properly cited.

This article has been retracted by Hindawi, as publisher, following an investigation undertaken by the publisher [1]. This investigation has uncovered evidence of systematic manipulation of the publication and peer-review process. We cannot, therefore, vouch for the reliability or integrity of this article.

Please note that this notice is intended solely to alert readers that the peer-review process of this article has been compromised.

Wiley and Hindawi regret that the usual quality checks did not identify these issues before publication and have since put additional measures in place to safeguard research integrity.

We wish to credit our Research Integrity and Research Publishing teams and anonymous and named external researchers and research integrity experts for contributing to this investigation.

The corresponding author, as the representative of all authors, has been given the opportunity to register their agreement or disagreement to this retraction. We have kept a record of any response received.

References

- [1] K. Umaphathi, Y. Sangeetha, A. N. Shankar et al., "Computational Investigations of Fixed-Free and Fixed-Fixed Types Single-Wall Carbon Nanotube Mass Sensing Biosensor," *Advances in Materials Science and Engineering*, vol. 2021, Article ID 3253365, 13 pages, 2021.

Retraction

Retracted: Experimental Investigation and Optimization on Friction Stir Welding of Nylon 6A Using Taguchi and ANOVA with Microstructural Analysis

Advances in Materials Science and Engineering

Received 26 December 2023; Accepted 26 December 2023; Published 29 December 2023

Copyright © 2023 Advances in Materials Science and Engineering. This is an open access article distributed under the Creative Commons Attribution License, which permits unrestricted use, distribution, and reproduction in any medium, provided the original work is properly cited.

This article has been retracted by Hindawi, as publisher, following an investigation undertaken by the publisher [1]. This investigation has uncovered evidence of systematic manipulation of the publication and peer-review process. We cannot, therefore, vouch for the reliability or integrity of this article.

Please note that this notice is intended solely to alert readers that the peer-review process of this article has been compromised.

Wiley and Hindawi regret that the usual quality checks did not identify these issues before publication and have since put additional measures in place to safeguard research integrity.

We wish to credit our Research Integrity and Research Publishing teams and anonymous and named external researchers and research integrity experts for contributing to this investigation.

The corresponding author, as the representative of all authors, has been given the opportunity to register their agreement or disagreement to this retraction. We have kept a record of any response received.

References

- [1] G. S. V. Seshu Kumar, A. Kumar, S. Rajesh, R. B. R. Chekuri, and A. G. Adigo, "Experimental Investigation and Optimization on Friction Stir Welding of Nylon 6A Using Taguchi and ANOVA with Microstructural Analysis," *Advances in Materials Science and Engineering*, vol. 2021, Article ID 7483393, 12 pages, 2021.

Retraction

Retracted: Experimental Analysis of Mechanical Properties and Durability of Cement-Based Composite with Carbon Nanotube

Advances in Materials Science and Engineering

Received 26 December 2023; Accepted 26 December 2023; Published 29 December 2023

Copyright © 2023 Advances in Materials Science and Engineering. This is an open access article distributed under the Creative Commons Attribution License, which permits unrestricted use, distribution, and reproduction in any medium, provided the original work is properly cited.

This article has been retracted by Hindawi, as publisher, following an investigation undertaken by the publisher [1]. This investigation has uncovered evidence of systematic manipulation of the publication and peer-review process. We cannot, therefore, vouch for the reliability or integrity of this article.

Please note that this notice is intended solely to alert readers that the peer-review process of this article has been compromised.

Wiley and Hindawi regret that the usual quality checks did not identify these issues before publication and have since put additional measures in place to safeguard research integrity.

We wish to credit our Research Integrity and Research Publishing teams and anonymous and named external researchers and research integrity experts for contributing to this investigation.

The corresponding author, as the representative of all authors, has been given the opportunity to register their agreement or disagreement to this retraction. We have kept a record of any response received.

References

- [1] Y. Du, P. Gao, J. Yang, F. Shi, and M. Shabaz, "Experimental Analysis of Mechanical Properties and Durability of Cement-Based Composite with Carbon Nanotube," *Advances in Materials Science and Engineering*, vol. 2021, Article ID 8777613, 12 pages, 2021.

Retraction

Retracted: Optimization on Operation Parameters in Reinforced Metal Matrix of AA6066 Composite with HSS and Cu

Advances in Materials Science and Engineering

Received 26 December 2023; Accepted 26 December 2023; Published 29 December 2023

Copyright © 2023 Advances in Materials Science and Engineering. This is an open access article distributed under the Creative Commons Attribution License, which permits unrestricted use, distribution, and reproduction in any medium, provided the original work is properly cited.

This article has been retracted by Hindawi, as publisher, following an investigation undertaken by the publisher [1]. This investigation has uncovered evidence of systematic manipulation of the publication and peer-review process. We cannot, therefore, vouch for the reliability or integrity of this article.

Please note that this notice is intended solely to alert readers that the peer-review process of this article has been compromised.

Wiley and Hindawi regret that the usual quality checks did not identify these issues before publication and have since put additional measures in place to safeguard research integrity.

We wish to credit our Research Integrity and Research Publishing teams and anonymous and named external researchers and research integrity experts for contributing to this investigation.

The corresponding author, as the representative of all authors, has been given the opportunity to register their agreement or disagreement to this retraction. We have kept a record of any response received.

References

- [1] Y. Sesharao, T. Sathish, K. Palani et al., "Optimization on Operation Parameters in Reinforced Metal Matrix of AA6066 Composite with HSS and Cu," *Advances in Materials Science and Engineering*, vol. 2021, Article ID 1609769, 12 pages, 2021.

Retraction

Retracted: Effect of Tool Profile Influence in Dissimilar Friction Stir Welding of Aluminium Alloys (AA5083 and AA7068)

Advances in Materials Science and Engineering

Received 26 December 2023; Accepted 26 December 2023; Published 29 December 2023

Copyright © 2023 Advances in Materials Science and Engineering. This is an open access article distributed under the Creative Commons Attribution License, which permits unrestricted use, distribution, and reproduction in any medium, provided the original work is properly cited.

This article has been retracted by Hindawi, as publisher, following an investigation undertaken by the publisher [1]. This investigation has uncovered evidence of systematic manipulation of the publication and peer-review process. We cannot, therefore, vouch for the reliability or integrity of this article.

Please note that this notice is intended solely to alert readers that the peer-review process of this article has been compromised.

Wiley and Hindawi regret that the usual quality checks did not identify these issues before publication and have since put additional measures in place to safeguard research integrity.

We wish to credit our Research Integrity and Research Publishing teams and anonymous and named external researchers and research integrity experts for contributing to this investigation.

The corresponding author, as the representative of all authors, has been given the opportunity to register their agreement or disagreement to this retraction. We have kept a record of any response received.

References

- [1] S. Jayaprakash, S. Siva Chandran, T. Sathish et al., "Effect of Tool Profile Influence in Dissimilar Friction Stir Welding of Aluminium Alloys (AA5083 and AA7068)," *Advances in Materials Science and Engineering*, vol. 2021, Article ID 7387296, 7 pages, 2021.

Retraction

Retracted: Modified Mechanical Structure Electric Bike Design Computation and Prototype Model Implementation

Advances in Materials Science and Engineering

Received 26 December 2023; Accepted 26 December 2023; Published 29 December 2023

Copyright © 2023 Advances in Materials Science and Engineering. This is an open access article distributed under the Creative Commons Attribution License, which permits unrestricted use, distribution, and reproduction in any medium, provided the original work is properly cited.

This article has been retracted by Hindawi, as publisher, following an investigation undertaken by the publisher [1]. This investigation has uncovered evidence of systematic manipulation of the publication and peer-review process. We cannot, therefore, vouch for the reliability or integrity of this article.

Please note that this notice is intended solely to alert readers that the peer-review process of this article has been compromised.

Wiley and Hindawi regret that the usual quality checks did not identify these issues before publication and have since put additional measures in place to safeguard research integrity.

We wish to credit our Research Integrity and Research Publishing teams and anonymous and named external researchers and research integrity experts for contributing to this investigation.

The corresponding author, as the representative of all authors, has been given the opportunity to register their agreement or disagreement to this retraction. We have kept a record of any response received.

References

- [1] K. Ramash Kumar, T. S. Anandhi, B. Vijayakrishna et al., "Modified Mechanical Structure Electric Bike Design Computation and Prototype Model Implementation," *Advances in Materials Science and Engineering*, vol. 2021, Article ID 3673172, 7 pages, 2021.

Retraction

Retracted: Effects of the FR 4 Substrate Realized in a Circularly Polarized UHF-RFID Reader Antenna with Fractal Geometry for Enhancing Parameters

Advances in Materials Science and Engineering

Received 26 December 2023; Accepted 26 December 2023; Published 29 December 2023

Copyright © 2023 Advances in Materials Science and Engineering. This is an open access article distributed under the Creative Commons Attribution License, which permits unrestricted use, distribution, and reproduction in any medium, provided the original work is properly cited.

This article has been retracted by Hindawi, as publisher, following an investigation undertaken by the publisher [1]. This investigation has uncovered evidence of systematic manipulation of the publication and peer-review process. We cannot, therefore, vouch for the reliability or integrity of this article.

Please note that this notice is intended solely to alert readers that the peer-review process of this article has been compromised.

Wiley and Hindawi regret that the usual quality checks did not identify these issues before publication and have since put additional measures in place to safeguard research integrity.

We wish to credit our Research Integrity and Research Publishing teams and anonymous and named external researchers and research integrity experts for contributing to this investigation.

The corresponding author, as the representative of all authors, has been given the opportunity to register their agreement or disagreement to this retraction. We have kept a record of any response received.

References

- [1] C. Varadhan, S. Arulsevi, and F. Ashine Chamatu, "Effects of the FR 4 Substrate Realized in a Circularly Polarized UHF-RFID Reader Antenna with Fractal Geometry for Enhancing Parameters," *Advances in Materials Science and Engineering*, vol. 2021, Article ID 8475621, 7 pages, 2021.

Retraction

Retracted: Structural Classification of Basalt FRP at High Temperatures

Advances in Materials Science and Engineering

Received 26 December 2023; Accepted 26 December 2023; Published 29 December 2023

Copyright © 2023 Advances in Materials Science and Engineering. This is an open access article distributed under the Creative Commons Attribution License, which permits unrestricted use, distribution, and reproduction in any medium, provided the original work is properly cited.

This article has been retracted by Hindawi, as publisher, following an investigation undertaken by the publisher [1]. This investigation has uncovered evidence of systematic manipulation of the publication and peer-review process. We cannot, therefore, vouch for the reliability or integrity of this article.

Please note that this notice is intended solely to alert readers that the peer-review process of this article has been compromised.

Wiley and Hindawi regret that the usual quality checks did not identify these issues before publication and have since put additional measures in place to safeguard research integrity.

We wish to credit our Research Integrity and Research Publishing teams and anonymous and named external researchers and research integrity experts for contributing to this investigation.

The corresponding author, as the representative of all authors, has been given the opportunity to register their agreement or disagreement to this retraction. We have kept a record of any response received.

References

- [1] S. Vummadisetti, S. R. Pasalapudi, S. K. Gottapu, K. K. Goriparthi, and A. Batu, "Structural Classification of Basalt FRP at High Temperatures," *Advances in Materials Science and Engineering*, vol. 2021, Article ID 6917471, 9 pages, 2021.

Retraction

Retracted: Green Machining Characteristics Study of Al-6063 in CNC Milling Using Taguchi Method and Grey Relational Analysis

Advances in Materials Science and Engineering

Received 26 December 2023; Accepted 26 December 2023; Published 29 December 2023

Copyright © 2023 Advances in Materials Science and Engineering. This is an open access article distributed under the Creative Commons Attribution License, which permits unrestricted use, distribution, and reproduction in any medium, provided the original work is properly cited.

This article has been retracted by Hindawi, as publisher, following an investigation undertaken by the publisher [1]. This investigation has uncovered evidence of systematic manipulation of the publication and peer-review process. We cannot, therefore, vouch for the reliability or integrity of this article.

Please note that this notice is intended solely to alert readers that the peer-review process of this article has been compromised.

Wiley and Hindawi regret that the usual quality checks did not identify these issues before publication and have since put additional measures in place to safeguard research integrity.

We wish to credit our Research Integrity and Research Publishing teams and anonymous and named external researchers and research integrity experts for contributing to this investigation.

The corresponding author, as the representative of all authors, has been given the opportunity to register their agreement or disagreement to this retraction. We have kept a record of any response received.

References

- [1] R. Suresh Kumar, S. Senthil Kumar, K. Murugan, and S. M. Hailegiorgis, "Green Machining Characteristics Study of Al-6063 in CNC Milling Using Taguchi Method and Grey Relational Analysis," *Advances in Materials Science and Engineering*, vol. 2021, Article ID 4420250, 12 pages, 2021.

Retraction

Retracted: Free Vibration Analysis of Thick Rectangular and Elliptical Plates with Concentric Cut-Out

Advances in Materials Science and Engineering

Received 26 December 2023; Accepted 26 December 2023; Published 29 December 2023

Copyright © 2023 Advances in Materials Science and Engineering. This is an open access article distributed under the Creative Commons Attribution License, which permits unrestricted use, distribution, and reproduction in any medium, provided the original work is properly cited.

This article has been retracted by Hindawi, as publisher, following an investigation undertaken by the publisher [1]. This investigation has uncovered evidence of systematic manipulation of the publication and peer-review process. We cannot, therefore, vouch for the reliability or integrity of this article.

Please note that this notice is intended solely to alert readers that the peer-review process of this article has been compromised.

Wiley and Hindawi regret that the usual quality checks did not identify these issues before publication and have since put additional measures in place to safeguard research integrity.

We wish to credit our Research Integrity and Research Publishing teams and anonymous and named external researchers and research integrity experts for contributing to this investigation.

The corresponding author, as the representative of all authors, has been given the opportunity to register their agreement or disagreement to this retraction. We have kept a record of any response received.

References

- [1] A. Merneedi, N. Mohan Rao, L. Natrayan, L. Yuvaraj, and P. Paramasivam, "Free Vibration Analysis of Thick Rectangular and Elliptical Plates with Concentric Cut-Out," *Advances in Materials Science and Engineering*, vol. 2021, Article ID 7212075, 14 pages, 2021.

Retraction

Retracted: Improving the Mechanical Properties of Natural Fiber Composites of Hemp Fiber with Ramie and Banana Fiber through Compression Molding Method

Advances in Materials Science and Engineering

Received 26 December 2023; Accepted 26 December 2023; Published 29 December 2023

Copyright © 2023 Advances in Materials Science and Engineering. This is an open access article distributed under the Creative Commons Attribution License, which permits unrestricted use, distribution, and reproduction in any medium, provided the original work is properly cited.

This article has been retracted by Hindawi, as publisher, following an investigation undertaken by the publisher [1]. This investigation has uncovered evidence of systematic manipulation of the publication and peer-review process. We cannot, therefore, vouch for the reliability or integrity of this article.

Please note that this notice is intended solely to alert readers that the peer-review process of this article has been compromised.

Wiley and Hindawi regret that the usual quality checks did not identify these issues before publication and have since put additional measures in place to safeguard research integrity.

We wish to credit our Research Integrity and Research Publishing teams and anonymous and named external researchers and research integrity experts for contributing to this investigation.

The corresponding author, as the representative of all authors, has been given the opportunity to register their agreement or disagreement to this retraction. We have kept a record of any response received.

References

- [1] S. Dinesh Kumar, L. Ponraj Sankar, T. Sathish et al., "Improving the Mechanical Properties of Natural Fiber Composites of Hemp Fiber with Ramie and Banana Fiber through Compression Molding Method," *Advances in Materials Science and Engineering*, vol. 2021, Article ID 7813634, 8 pages, 2021.

Retraction

Retracted: Investigation on V₂O₅ Thin Films for Field Effect Transistor Applications

Advances in Materials Science and Engineering

Received 26 December 2023; Accepted 26 December 2023; Published 29 December 2023

Copyright © 2023 Advances in Materials Science and Engineering. This is an open access article distributed under the Creative Commons Attribution License, which permits unrestricted use, distribution, and reproduction in any medium, provided the original work is properly cited.

This article has been retracted by Hindawi, as publisher, following an investigation undertaken by the publisher [1]. This investigation has uncovered evidence of systematic manipulation of the publication and peer-review process. We cannot, therefore, vouch for the reliability or integrity of this article.

Please note that this notice is intended solely to alert readers that the peer-review process of this article has been compromised.

Wiley and Hindawi regret that the usual quality checks did not identify these issues before publication and have since put additional measures in place to safeguard research integrity.

We wish to credit our Research Integrity and Research Publishing teams and anonymous and named external researchers and research integrity experts for contributing to this investigation.

The corresponding author, as the representative of all authors, has been given the opportunity to register their agreement or disagreement to this retraction. We have kept a record of any response received.

References

- [1] S. K. Suresh Babu, D. Jackuline Moni, D. Gracia, and A. G. Adigo, "Investigation on V₂O₅ Thin Films for Field Effect Transistor Applications," *Advances in Materials Science and Engineering*, vol. 2021, Article ID 2414589, 7 pages, 2021.

Retraction

Retracted: Synthesis, Mechanical, and Tribological Performance Analysis of Stir-Casted AA7079: ZrO₂ + Si₃N₄ Hybrid Composites by Taguchi Route

Advances in Materials Science and Engineering

Received 26 December 2023; Accepted 26 December 2023; Published 29 December 2023

Copyright © 2023 Advances in Materials Science and Engineering. This is an open access article distributed under the Creative Commons Attribution License, which permits unrestricted use, distribution, and reproduction in any medium, provided the original work is properly cited.

This article has been retracted by Hindawi, as publisher, following an investigation undertaken by the publisher [1]. This investigation has uncovered evidence of systematic manipulation of the publication and peer-review process. We cannot, therefore, vouch for the reliability or integrity of this article.

Please note that this notice is intended solely to alert readers that the peer-review process of this article has been compromised.

Wiley and Hindawi regret that the usual quality checks did not identify these issues before publication and have since put additional measures in place to safeguard research integrity.

We wish to credit our Research Integrity and Research Publishing teams and anonymous and named external researchers and research integrity experts for contributing to this investigation.

The corresponding author, as the representative of all authors, has been given the opportunity to register their agreement or disagreement to this retraction. We have kept a record of any response received.

References

- [1] G. Jegan, P. Kavipriya, T. Sathish, S. Dinesh Kumar, T. Samraj Lawrence, and T. Vino, "Synthesis, Mechanical, and Tribological Performance Analysis of Stir-Casted AA7079: ZrO₂ + Si₃N₄ Hybrid Composites by Taguchi Route," *Advances in Materials Science and Engineering*, vol. 2021, Article ID 7722370, 15 pages, 2021.

Retraction

Retracted: Development of Smart Sensing Technology Approaches in Structural Health Monitoring of Bridge Structures

Advances in Materials Science and Engineering

Received 26 December 2023; Accepted 26 December 2023; Published 29 December 2023

Copyright © 2023 Advances in Materials Science and Engineering. This is an open access article distributed under the Creative Commons Attribution License, which permits unrestricted use, distribution, and reproduction in any medium, provided the original work is properly cited.

This article has been retracted by Hindawi, as publisher, following an investigation undertaken by the publisher [1]. This investigation has uncovered evidence of systematic manipulation of the publication and peer-review process. We cannot, therefore, vouch for the reliability or integrity of this article.

Please note that this notice is intended solely to alert readers that the peer-review process of this article has been compromised.

Wiley and Hindawi regret that the usual quality checks did not identify these issues before publication and have since put additional measures in place to safeguard research integrity.

We wish to credit our Research Integrity and Research Publishing teams and anonymous and named external researchers and research integrity experts for contributing to this investigation.

The corresponding author, as the representative of all authors, has been given the opportunity to register their agreement or disagreement to this retraction. We have kept a record of any response received.

References

- [1] A. Sivasuriyan, D. S. Vijayan, A. LeemaRose et al., "Development of Smart Sensing Technology Approaches in Structural Health Monitoring of Bridge Structures," *Advances in Materials Science and Engineering*, vol. 2021, Article ID 2615029, 14 pages, 2021.

Retraction

Retracted: Parameters of Porosity and Compressive Strength-Based Optimization on Reinforced Aluminium from the Recycled Waste Automobile Frames

Advances in Materials Science and Engineering

Received 26 December 2023; Accepted 26 December 2023; Published 29 December 2023

Copyright © 2023 Advances in Materials Science and Engineering. This is an open access article distributed under the Creative Commons Attribution License, which permits unrestricted use, distribution, and reproduction in any medium, provided the original work is properly cited.

This article has been retracted by Hindawi, as publisher, following an investigation undertaken by the publisher [1]. This investigation has uncovered evidence of systematic manipulation of the publication and peer-review process. We cannot, therefore, vouch for the reliability or integrity of this article.

Please note that this notice is intended solely to alert readers that the peer-review process of this article has been compromised.

Wiley and Hindawi regret that the usual quality checks did not identify these issues before publication and have since put additional measures in place to safeguard research integrity.

We wish to credit our Research Integrity and Research Publishing teams and anonymous and named external researchers and research integrity experts for contributing to this investigation.

The corresponding author, as the representative of all authors, has been given the opportunity to register their agreement or disagreement to this retraction. We have kept a record of any response received.

References

- [1] A. Parthiban, V. Vijayan, T. Sathish et al., "Parameters of Porosity and Compressive Strength-Based Optimization on Reinforced Aluminium from the Recycled Waste Automobile Frames," *Advances in Materials Science and Engineering*, vol. 2021, Article ID 3648480, 10 pages, 2021.

Retraction

Retracted: XRD Peak Profile Analysis of SiC Reinforced Al₂O₃ Ceramic Composite Synthesized by Electrical Resistance Heating and Microwave Sintering: A Comparison

Advances in Materials Science and Engineering

Received 26 December 2023; Accepted 26 December 2023; Published 29 December 2023

Copyright © 2023 Advances in Materials Science and Engineering. This is an open access article distributed under the Creative Commons Attribution License, which permits unrestricted use, distribution, and reproduction in any medium, provided the original work is properly cited.

This article has been retracted by Hindawi, as publisher, following an investigation undertaken by the publisher [1]. This investigation has uncovered evidence of systematic manipulation of the publication and peer-review process. We cannot, therefore, vouch for the reliability or integrity of this article.

Please note that this notice is intended solely to alert readers that the peer-review process of this article has been compromised.

Wiley and Hindawi regret that the usual quality checks did not identify these issues before publication and have since put additional measures in place to safeguard research integrity.

We wish to credit our Research Integrity and Research Publishing teams and anonymous and named external researchers and research integrity experts for contributing to this investigation.

The corresponding author, as the representative of all authors, has been given the opportunity to register their agreement or disagreement to this retraction. We have kept a record of any response received.

References

- [1] M. Mohankumar, S. Praveen Kumar, B. Guruprasad et al., "XRD Peak Profile Analysis of SiC Reinforced Al₂O₃ Ceramic Composite Synthesized by Electrical Resistance Heating and Microwave Sintering: A Comparison," *Advances in Materials Science and Engineering*, vol. 2021, Article ID 8341924, 7 pages, 2021.

Retraction

Retracted: Parameters Optimization of Dissimilar Friction Stir Welding for AA7079 and AA8050 through RSM

Advances in Materials Science and Engineering

Received 26 December 2023; Accepted 26 December 2023; Published 29 December 2023

Copyright © 2023 Advances in Materials Science and Engineering. This is an open access article distributed under the Creative Commons Attribution License, which permits unrestricted use, distribution, and reproduction in any medium, provided the original work is properly cited.

This article has been retracted by Hindawi, as publisher, following an investigation undertaken by the publisher [1]. This investigation has uncovered evidence of systematic manipulation of the publication and peer-review process. We cannot, therefore, vouch for the reliability or integrity of this article.

Please note that this notice is intended solely to alert readers that the peer-review process of this article has been compromised.

Wiley and Hindawi regret that the usual quality checks did not identify these issues before publication and have since put additional measures in place to safeguard research integrity.

We wish to credit our Research Integrity and Research Publishing teams and anonymous and named external researchers and research integrity experts for contributing to this investigation.

The corresponding author, as the representative of all authors, has been given the opportunity to register their agreement or disagreement to this retraction. We have kept a record of any response received.

References

- [1] M. Kavitha, V. M. Manickavasagam, T. Sathish et al., "Parameters Optimization of Dissimilar Friction Stir Welding for AA7079 and AA8050 through RSM," *Advances in Materials Science and Engineering*, vol. 2021, Article ID 9723699, 8 pages, 2021.

Retraction

Retracted: Continuous Sorption of Remazol Brilliant Orange 3R Using *Caulerpa scalpelliformis* Biochar

Advances in Materials Science and Engineering

Received 26 December 2023; Accepted 26 December 2023; Published 29 December 2023

Copyright © 2023 Advances in Materials Science and Engineering. This is an open access article distributed under the Creative Commons Attribution License, which permits unrestricted use, distribution, and reproduction in any medium, provided the original work is properly cited.

This article has been retracted by Hindawi, as publisher, following an investigation undertaken by the publisher [1]. This investigation has uncovered evidence of systematic manipulation of the publication and peer-review process. We cannot, therefore, vouch for the reliability or integrity of this article.

Please note that this notice is intended solely to alert readers that the peer-review process of this article has been compromised.

Wiley and Hindawi regret that the usual quality checks did not identify these issues before publication and have since put additional measures in place to safeguard research integrity.

We wish to credit our Research Integrity and Research Publishing teams and anonymous and named external researchers and research integrity experts for contributing to this investigation.

The corresponding author, as the representative of all authors, has been given the opportunity to register their agreement or disagreement to this retraction. We have kept a record of any response received.

References

- [1] G. Ravindiran, P. Sugumar, and G. Elias, "Continuous Sorption of Remazol Brilliant Orange 3R Using *Caulerpa scalpelliformis* Biochar," *Advances in Materials Science and Engineering*, vol. 2021, Article ID 6397137, 7 pages, 2021.

Retraction

Retracted: Evaluation of Microstructure, Hardness, and Tensile Properties: A Comparative Study of Stir Cast and Extruded Al7005/Glass-/Fly-Ash-Reinforced Hybrid MMCs

Advances in Materials Science and Engineering

Received 26 December 2023; Accepted 26 December 2023; Published 29 December 2023

Copyright © 2023 Advances in Materials Science and Engineering. This is an open access article distributed under the Creative Commons Attribution License, which permits unrestricted use, distribution, and reproduction in any medium, provided the original work is properly cited.

This article has been retracted by Hindawi, as publisher, following an investigation undertaken by the publisher [1]. This investigation has uncovered evidence of systematic manipulation of the publication and peer-review process. We cannot, therefore, vouch for the reliability or integrity of this article.

Please note that this notice is intended solely to alert readers that the peer-review process of this article has been compromised.

Wiley and Hindawi regret that the usual quality checks did not identify these issues before publication and have since put additional measures in place to safeguard research integrity.

We wish to credit our Research Integrity and Research Publishing teams and anonymous and named external researchers and research integrity experts for contributing to this investigation.

The corresponding author, as the representative of all authors, has been given the opportunity to register their agreement or disagreement to this retraction. We have kept a record of any response received.

References

- [1] P. K. Swamy, S. Mylraiah, and D. Basheer, "Evaluation of Microstructure, Hardness, and Tensile Properties: A Comparative Study of Stir Cast and Extruded Al7005/Glass-/Fly-Ash-Reinforced Hybrid MMCs," *Advances in Materials Science and Engineering*, vol. 2021, Article ID 8601484, 7 pages, 2021.

Retraction

Retracted: Studying the Effect of Metallic Precursor Concentration on the Structural, Optical, and Morphological Properties of Zinc Sulfide Thin Films in Photovoltaic Cell Applications

Advances in Materials Science and Engineering

Received 26 December 2023; Accepted 26 December 2023; Published 29 December 2023

Copyright © 2023 Advances in Materials Science and Engineering. This is an open access article distributed under the Creative Commons Attribution License, which permits unrestricted use, distribution, and reproduction in any medium, provided the original work is properly cited.

This article has been retracted by Hindawi, as publisher, following an investigation undertaken by the publisher [1]. This investigation has uncovered evidence of systematic manipulation of the publication and peer-review process. We cannot, therefore, vouch for the reliability or integrity of this article.

Please note that this notice is intended solely to alert readers that the peer-review process of this article has been compromised.

Wiley and Hindawi regret that the usual quality checks did not identify these issues before publication and have since put additional measures in place to safeguard research integrity.

We wish to credit our Research Integrity and Research Publishing teams and anonymous and named external researchers and research integrity experts for contributing to this investigation.

The corresponding author, as the representative of all authors, has been given the opportunity to register their agreement or disagreement to this retraction. We have kept a record of any response received.

References

- [1] S. Abel, J. Leta Tesfaye, R. Kiran et al., "Studying the Effect of Metallic Precursor Concentration on the Structural, Optical, and Morphological Properties of Zinc Sulfide Thin Films in Photovoltaic Cell Applications," *Advances in Materials Science and Engineering*, vol. 2021, Article ID 7443664, 6 pages, 2021.

Retraction

Retracted: Flexural Behaviour of Chicken Mesh Ferrocement Laminates with Partial Replacement of Fine Aggregate by Steel Slag

Advances in Materials Science and Engineering

Received 26 December 2023; Accepted 26 December 2023; Published 29 December 2023

Copyright © 2023 Advances in Materials Science and Engineering. This is an open access article distributed under the Creative Commons Attribution License, which permits unrestricted use, distribution, and reproduction in any medium, provided the original work is properly cited.

This article has been retracted by Hindawi, as publisher, following an investigation undertaken by the publisher [1]. This investigation has uncovered evidence of systematic manipulation of the publication and peer-review process. We cannot, therefore, vouch for the reliability or integrity of this article.

Please note that this notice is intended solely to alert readers that the peer-review process of this article has been compromised.

Wiley and Hindawi regret that the usual quality checks did not identify these issues before publication and have since put additional measures in place to safeguard research integrity.

We wish to credit our Research Integrity and Research Publishing teams and anonymous and named external researchers and research integrity experts for contributing to this investigation.

The corresponding author, as the representative of all authors, has been given the opportunity to register their agreement or disagreement to this retraction. We have kept a record of any response received.

References

- [1] S. Jayaprakash, J. Dhanapal, V. Deivasigamani, and E. G., "Flexural Behaviour of Chicken Mesh Ferrocement Laminates with Partial Replacement of Fine Aggregate by Steel Slag," *Advances in Materials Science and Engineering*, vol. 2021, Article ID 7307493, 9 pages, 2021.

Retraction

Retracted: Design and Implementation of SOC-Based Noncontact-Type Level Sensing for Conductive and Nonconductive Liquids

Advances in Materials Science and Engineering

Received 26 December 2023; Accepted 26 December 2023; Published 29 December 2023

Copyright © 2023 Advances in Materials Science and Engineering. This is an open access article distributed under the Creative Commons Attribution License, which permits unrestricted use, distribution, and reproduction in any medium, provided the original work is properly cited.

This article has been retracted by Hindawi, as publisher, following an investigation undertaken by the publisher [1]. This investigation has uncovered evidence of systematic manipulation of the publication and peer-review process. We cannot, therefore, vouch for the reliability or integrity of this article.

Please note that this notice is intended solely to alert readers that the peer-review process of this article has been compromised.

Wiley and Hindawi regret that the usual quality checks did not identify these issues before publication and have since put additional measures in place to safeguard research integrity.

We wish to credit our Research Integrity and Research Publishing teams and anonymous and named external researchers and research integrity experts for contributing to this investigation.

The corresponding author, as the representative of all authors, has been given the opportunity to register their agreement or disagreement to this retraction. We have kept a record of any response received.

References

- [1] J. L. M. Iqbal, M. S. Kishore, Arulkumaran Ganeshan, and G. Narayan, "Design and Implementation of SOC-Based Noncontact-Type Level Sensing for Conductive and Nonconductive Liquids," *Advances in Materials Science and Engineering*, vol. 2021, Article ID 7630008, 12 pages, 2021.

Retraction

Retracted: Effect of Grey and White Portland Cement Fillers on Flexural and Shear Strength of GFRP Composite Material

Advances in Materials Science and Engineering

Received 26 December 2023; Accepted 26 December 2023; Published 29 December 2023

Copyright © 2023 Advances in Materials Science and Engineering. This is an open access article distributed under the Creative Commons Attribution License, which permits unrestricted use, distribution, and reproduction in any medium, provided the original work is properly cited.

This article has been retracted by Hindawi, as publisher, following an investigation undertaken by the publisher [1]. This investigation has uncovered evidence of systematic manipulation of the publication and peer-review process. We cannot, therefore, vouch for the reliability or integrity of this article.

Please note that this notice is intended solely to alert readers that the peer-review process of this article has been compromised.

Wiley and Hindawi regret that the usual quality checks did not identify these issues before publication and have since put additional measures in place to safeguard research integrity.

We wish to credit our Research Integrity and Research Publishing teams and anonymous and named external researchers and research integrity experts for contributing to this investigation.

The corresponding author, as the representative of all authors, has been given the opportunity to register their agreement or disagreement to this retraction. We have kept a record of any response received.

References

- [1] D. H. Vardhan, D. Sai Chaithanya Kishore, Y. Santhosh Kumar Reddy, K. Manohar Reddy, G. Raghavendra, and R. Rudrapati, "Effect of Grey and White Portland Cement Fillers on Flexural and Shear Strength of GFRP Composite Material," *Advances in Materials Science and Engineering*, vol. 2021, Article ID 9586474, 7 pages, 2021.

Retraction

Retracted: Mechanical Strength and Fatigue Fracture Analysis on Al-Zn-Mg Alloy with the Influence of Creep Aging Process

Advances in Materials Science and Engineering

Received 11 July 2023; Accepted 11 July 2023; Published 12 July 2023

Copyright © 2023 Advances in Materials Science and Engineering. This is an open access article distributed under the Creative Commons Attribution License, which permits unrestricted use, distribution, and reproduction in any medium, provided the original work is properly cited.

This article has been retracted by Hindawi following an investigation undertaken by the publisher [1]. This investigation has uncovered evidence of one or more of the following indicators of systematic manipulation of the publication process:

- (1) Discrepancies in scope
- (2) Discrepancies in the description of the research reported
- (3) Discrepancies between the availability of data and the research described
- (4) Inappropriate citations
- (5) Incoherent, meaningless and/or irrelevant content included in the article
- (6) Peer-review manipulation

The presence of these indicators undermines our confidence in the integrity of the article's content and we cannot, therefore, vouch for its reliability. Please note that this notice is intended solely to alert readers that the content of this article is unreliable. We have not investigated whether authors were aware of or involved in the systematic manipulation of the publication process.

Wiley and Hindawi regrets that the usual quality checks did not identify these issues before publication and have since put additional measures in place to safeguard research integrity.

We wish to credit our own Research Integrity and Research Publishing teams and anonymous and named external researchers and research integrity experts for contributing to this investigation.

The corresponding author, as the representative of all authors, has been given the opportunity to register their agreement or disagreement to this retraction. We have kept a record of any response received.

References

- [1] M. Ponnusamy, B. P. Pulla, T. Sathish et al., "Mechanical Strength and Fatigue Fracture Analysis on Al-Zn-Mg Alloy with the Influence of Creep Aging Process," *Advances in Materials Science and Engineering*, vol. 2021, Article ID 1899128, 5 pages, 2021.

Retraction

Retracted: Effects of Novel Material Field Effect Transistor for Heterogeneous Energy and Traffic-Aware Secure Applications

Advances in Materials Science and Engineering

Received 11 July 2023; Accepted 11 July 2023; Published 12 July 2023

Copyright © 2023 Advances in Materials Science and Engineering. This is an open access article distributed under the Creative Commons Attribution License, which permits unrestricted use, distribution, and reproduction in any medium, provided the original work is properly cited.

This article has been retracted by Hindawi following an investigation undertaken by the publisher [1]. This investigation has uncovered evidence of one or more of the following indicators of systematic manipulation of the publication process:

- (1) Discrepancies in scope
- (2) Discrepancies in the description of the research reported
- (3) Discrepancies between the availability of data and the research described
- (4) Inappropriate citations
- (5) Incoherent, meaningless and/or irrelevant content included in the article
- (6) Peer-review manipulation

The presence of these indicators undermines our confidence in the integrity of the article's content and we cannot, therefore, vouch for its reliability. Please note that this notice is intended solely to alert readers that the content of this article is unreliable. We have not investigated whether authors were aware of or involved in the systematic manipulation of the publication process.

Wiley and Hindawi regrets that the usual quality checks did not identify these issues before publication and have since put additional measures in place to safeguard research integrity.

We wish to credit our own Research Integrity and Research Publishing teams and anonymous and named external researchers and research integrity experts for contributing to this investigation.

The corresponding author, as the representative of all authors, has been given the opportunity to register their agreement or disagreement to this retraction. We have kept a record of any response received.

References

- [1] C. Ambika Bhuvanewari, E. D. Kanmani Ruby, A. Manjunathan, R. Balamurugan, P. Jenopaul, and B. Z. Tizazu, "Effects of Novel Material Field Effect Transistor for Heterogeneous Energy and Traffic-Aware Secure Applications," *Advances in Materials Science and Engineering*, vol. 2021, Article ID 9085854, 9 pages, 2021.

Retraction

Retracted: Green Machining Characteristics Study of Al-6063 in CNC Milling Using Taguchi Method and Grey Relational Analysis

Advances in Materials Science and Engineering

Received 26 December 2023; Accepted 26 December 2023; Published 29 December 2023

Copyright © 2023 Advances in Materials Science and Engineering. This is an open access article distributed under the Creative Commons Attribution License, which permits unrestricted use, distribution, and reproduction in any medium, provided the original work is properly cited.

This article has been retracted by Hindawi, as publisher, following an investigation undertaken by the publisher [1]. This investigation has uncovered evidence of systematic manipulation of the publication and peer-review process. We cannot, therefore, vouch for the reliability or integrity of this article.

Please note that this notice is intended solely to alert readers that the peer-review process of this article has been compromised.

Wiley and Hindawi regret that the usual quality checks did not identify these issues before publication and have since put additional measures in place to safeguard research integrity.

We wish to credit our Research Integrity and Research Publishing teams and anonymous and named external researchers and research integrity experts for contributing to this investigation.

The corresponding author, as the representative of all authors, has been given the opportunity to register their agreement or disagreement to this retraction. We have kept a record of any response received.

References

- [1] R. Suresh Kumar, S. Senthil Kumar, K. Murugan, and S. M. Hailegiorgis, "Green Machining Characteristics Study of Al-6063 in CNC Milling Using Taguchi Method and Grey Relational Analysis," *Advances in Materials Science and Engineering*, vol. 2021, Article ID 4420250, 12 pages, 2021.

Research Article

Green Machining Characteristics Study of Al-6063 in CNC Milling Using Taguchi Method and Grey Relational Analysis

R. Suresh Kumar ¹, S. Senthil Kumar ², K. Murugan,³
and Sintayehu Mekuria Hailegiorgis ⁴

¹Department of Mechanical Engineering, Sri Eshwar College of Engineering, Coimbatore, Tamil Nadu, India

²Department of Mechanical Engineering, RMK College of Engineering and Technology, Puduvoyal, Tamil Nadu, India

³Government Polytechnic College, Valangaiman, Tamil Nadu, India

⁴Department of Chemical Engineering College of Biological and Chemical Engineering, Addis Ababa Science and Technology University, Addis Ababa, Ethiopia

Correspondence should be addressed to Sintayehu Mekuria Hailegiorgis; sintayehu.mekuria@aastu.edu.et

Received 4 August 2021; Revised 19 August 2021; Accepted 16 November 2021; Published 16 December 2021

Academic Editor: Samson Jerold Samuel Chelladurai

Copyright © 2021 R. Suresh Kumar et al. This is an open access article distributed under the Creative Commons Attribution License, which permits unrestricted use, distribution, and reproduction in any medium, provided the original work is properly cited.

Green machining strategies in the manufacturing sector help to maintain the product value by considering the environmental impacts. Also, improvisation in the quality contribution of the parts can minimize the environmental consequences by improving resource efficiency, specifically in terms of coolants used in machining. Certain hazardous impacts have been witnessed because of longer exposure to such a machining environment. To address it, many researchers have concentrated on providing a healthy machining environment either by introducing dry machining or by minimum quantity lubrication (MQL). The proposed study addresses this context. The influence of these tactics on the attained surface quality of Al-6063 is quantified in this paper in terms of surface integrity (R_a) and removal rate of material (MRR). The study involves single-response optimization using the Taguchi design and multiresponse optimization using grey relational analysis (GRA). The results reveal that the depth of cut (D_c) and spindle speed (S_s) have the greatest impact on R_a and MRR. The machinability of Al-6063 is examined by considering the key machinability parameters, such as the spindle speed (S_s), feed rate (F_r), and the depth of cut (D_c), to arrive at the best possible surface roughness and removal rate of the material. As a typical Taguchi approach cannot perform multiresponse optimization, grey relational analysis is used. The grey relational analysis combined with Taguchi gives a novel methodology for multi-optimization. The entire study is performed in dry condition and under minimum quantity lubrication. The results suggest that the responses are highly influenced by the depth of cut and spindle speed.

1. Introduction

Advancements in nonconventional machining technologies are now widely employed to address a variety of challenges in machining processes, such as machining high-strength materials, improving surface integrity, achieving high levels of precision, reducing surplus material, and shortening production time. CNC end milling is one of the most versatile machining processes in which a desired output can be achieved with reliability and accuracy. Many industries and researches are employing different techniques to understand the behavior of alloy materials during machining by monitoring R_a , MRR, etc. Many investigations and

studies are performed using optimization techniques to determine the effect of R_a , MRR, etc. on the machining performance of both brittle and ductile materials. Such studies usually incorporate the application of numerical and statistical models combined with the design of experiment (DoE). Generally, the surface roughness of the CNC end milling parameters is predicted using a mathematical model followed by the application of regression analysis for predicting the results. Such results are validated with the experimental values. The researcher used DoE to evaluate the R_a and MRR of the aluminum metal matrix composites. The quality achieved postmachining is compared with the projected values. The results attained are found to be

increased [1–7] based on Taguchi's prediction involving improvisations in the efficiency of resource management, energy consumption, parameter settings, and energy efficient systems. A study of machining factors is performed for estimating MRR by considering the spindle speed, coolant flow, and the depth of cut in a combination set framed by the central composite rotatable design [8].

Helu et al. [9, 10] proposed a process time reduction model. The model provides the total cost analysis based on the experimental data involving the tool wear and service costs. Derflinger et al. [11] investigated and found that the alloys of aluminum or steel, when subjected to dry machining, achieved positive results. Also, the test results depict that the tool coated with the hard and lubricant layers can significantly improve the tool's lifetime. Dry machining characteristic studies on aluminum alloys were performed on Al-5052 by Tatsuya et al. [12]. In this study, a cemented carbide cutting tool is used for machining aluminum alloys. In a few studies, MQCL (Minimum Quantity Cooled Lubrication) model was implemented [13–16]. The study employed biodegradable vegetable oil as a coolant. The result revealed a 1.57-time increase in the tool's life. The study used ceramic-bound cutting materials and CBN. The study revealed that the CBN tools are associated with high thermal conductivity compared to ceramics. Moreover, CBN effectively dissipated heat, and finally, the study concluded that CBN is highly suited for the dry machining of cast irons. These studies also emphasized the impact of dry machining on high-speed machining.

The impact of dry machining [17–22] studied by various researchers also provides a positive platform toward eco-friendly machining, involving studies on cutting forces, chip formations, heat dissipation, etc. Various simulation models [23–26] are developed for estimating the minimum energy consumption, minimum R_a , and maximum productivity. The study involved a minimum energy formulation by looking at the tactics and constraints for lowering the machine tool energy consumption, while maintaining the tool's life and parts' quality. While the approach seems to be beneficial in increasing the utilization of resource efficiency, they rarely consider component quality or different production outputs as alternatives for the improvisation of resource efficiency and ensuring successful marketable goods. Few researches on micro-milling also employed the application of optimization techniques in addressing effective utilization of resources [27–31]. Jawahir et al. [32] put forth an insight toward the research perspective that merely spotlighted the formulation of the predictive and measuring methods for surface integrity. The consistent study toward sustainability and machining with environmental consciousness [33, 34] is visible in such articles that aim to find solutions with the least impact on environmental issues. The parameter optimization for attaining required roughness R_a using different tools and techniques in machining aluminium and its alloys are elucidated with commendable outcomes [35–39]. The previous attempts made by researchers toward the implementation of green machining strategies and their impacts on the machining processes are commendable. As a result, an attempt has been made on the application of green machining strategy on Al-6063, which is one of the most successful architectural materials in today's scenario.

2. Aluminum Alloy Al-6063

Al-6063 contains magnesium and silicon as the main alloying elements. The composition standardization of the alloys is maintained by The Aluminum Association. Al-6063 possesses good mechanical properties and is heat treatable and weldable. Table 1 details the chemical composition of the selected material. This alloy is most commonly used for extrusions as complex shapes can be formed much easily. Few applications include window frames, door frames, roofs, and sign frames. The extensive use of the material in architectural applications elicited the idea of performing a study on providing a suitable solution for the machining of Al-6063 with the least effect on the environment, irrespective of demand. For this study, a rectangular work material of dimensions 75 mm × 30 mm × 12 mm is taken for machining. Based on the literature survey, the TiCN end mill cutter is taken as the cutting tool material with a Rockwell hardness of 88. The cutter selected is of 20 mm diameter with a total length of 74 mm. To avoid the effect of vibration and chatter while machining, an overhung length of 20 mm is maintained throughout the process.

3. Experimental Design

The experiments are based on Taguchi Robust Design. The L9 Orthogonal array is selected for the experimental run pattern with respect to the parameters and their levels assigned. In this study, three controllable factors are considered to study the pattern of behavior on two uncontrollable parameters, as shown in Table 2. The controllable parameters considered are the spindle speed (rpm), the depth of cut (mm), and the feed rate (mm/min). Each parameter is subjected to a three-level test as the parameters are multilevel factors. The responses considered for the analyses are surface roughness (R_a) and materials removal rate (MRR). In the machining process, the surface roughness is measured based on the outer profile texture attained. The attainment of the surface texture is commonly measured in terms of the arithmetic average of profile heights for the length under evaluation and is represented by the average surface roughness (R_a). The three levels for each factor are represented as S_s , F_r , and D_c , as given in Table 2. The response outputs for the experimentation are represented as R_a and MRR. Figure 1 shows the experimental runs conducted in a 3-axis vertical milling center. The surface tester Mitutoyo is employed for measuring the roughness of the machined. The surface tester has a resolution varying from 0.01 microns to 0.3 microns. The average roughness value (R_a) is considered for the analysis.

The machining process is performed in dry conditions and is also performed with the minimum quantity lubrication (MQL) method. The results of the experimental runs for both dry and MQL are depicted in Table 3.

4. Results and Discussion

The following sections provide an insight into the parametric influence of the machining parameters on the responses

TABLE 1: Chemical composition.

Si	Fe	Cu	Mn	Mg	Cr	Zn	Ti	Others	Al
1.12	0.15	0.04	0.01	0.53	0.01	0.03	0.06	0.05	98

TABLE 2: Machining parameters and their levels.

Control factors	Unit	Code	Levels		
			1	2	3
Spindle speed	rpm	S_s	1500	2300	3000
Feed rate	mm/min	F_r	10	20	30
Depth of cut	mm	D_c	0.4	0.5	0.6



FIGURE 1: Measurement of roughness.

TABLE 3: Experimental runs and responses.

Exp	Machining parameter levels			Dry run		MQL	
	S_s (rpm)	D_c (mm)	F_r (mm/min)	R_a (μm)	MRR (IPM)	R_a (μm)	MRR (IPM)
1	1500	0.4	10	0.91	0.787	0.76	0.779
2	1500	0.5	20	1.59	1.293	1.13	1.311
3	1500	0.6	30	2.28	2.038	2.14	2.042
4	2300	0.4	20	0.88	0.632	0.78	0.643
5	2300	0.5	30	1.63	1.378	1.42	1.412
6	2300	0.6	10	2.05	1.987	1.98	1.923
7	3000	0.4	30	0.76	0.236	0.71	0.265
8	3000	0.5	10	0.79	0.345	0.73	0.330
9	3000	0.6	20	1.49	0.989	1.37	1.115

considered. The capability of the function is also validated by the analysis of variance (ANOVA).

4.1. *Surface Roughness (R_a)*. Figures 2 and 3 depict the parametric interactions of the S/N ratios on R_a in the dry run conditions and the MQL method. The objective function is

taken as smaller-the-better. From the graph, it is evident that in the dry runs and the MQL method, D_c is the most significant parameter governing R_a , followed by S_s and F_r , respectively. On careful observation, it is notable to record that the application of coolant in the minimum level improves R_a .

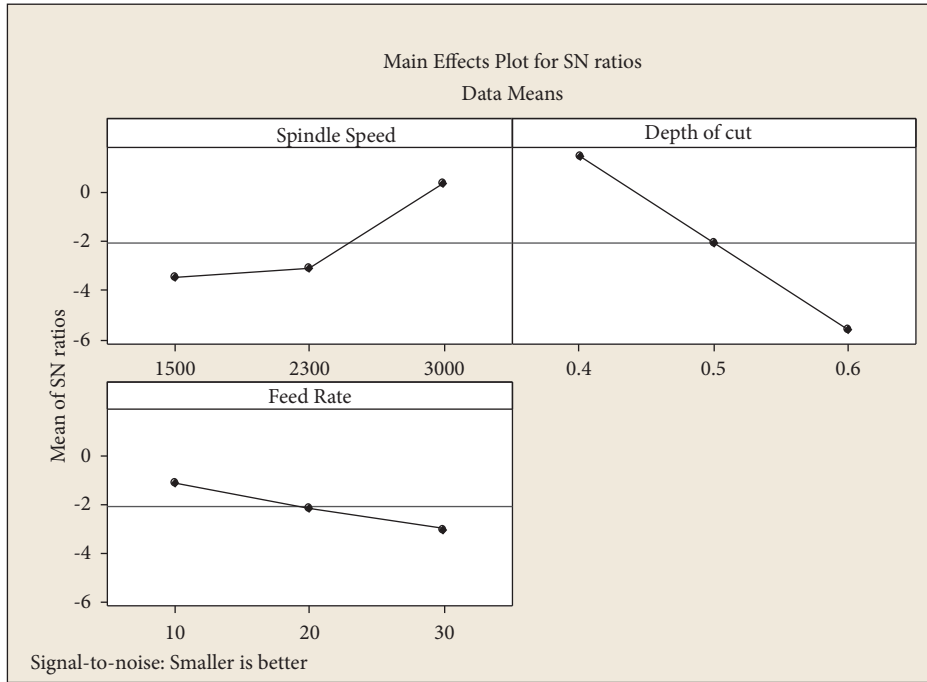


FIGURE 2: S/N ratio plot for R_a -dry runs.

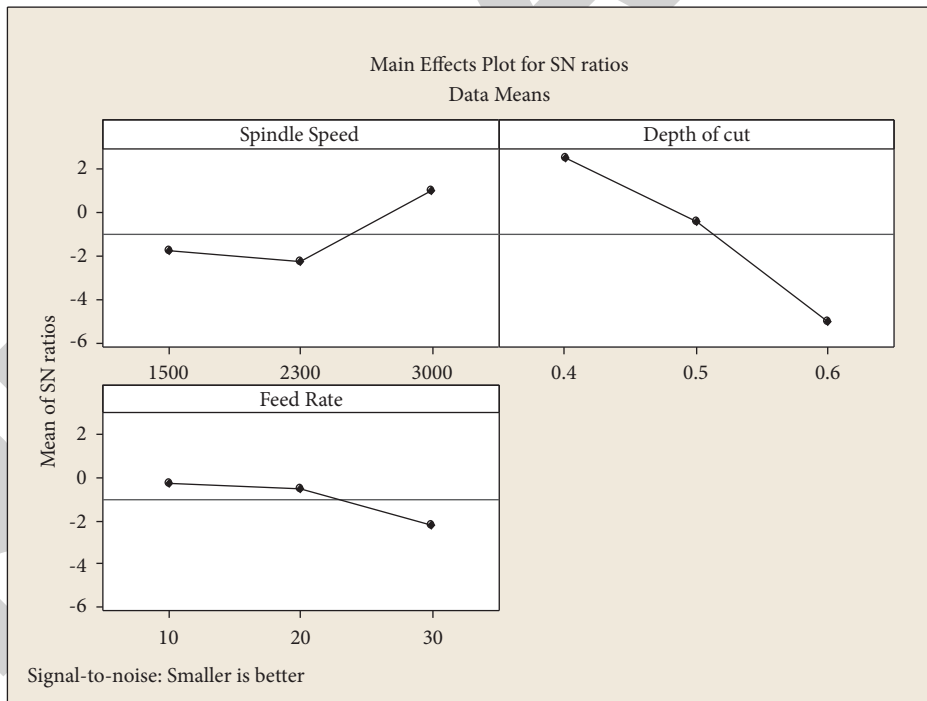


FIGURE 3: S/N ratio plot for R_a -MQL.

4.1.1. *Parameter Interaction Effects on Dry Runs and MQL.* Figures 4 and 5 highlight the parametric interaction of the means on R_a in the dry run condition and the MQL method. From the graph, it is clearly evident that in the dry runs and the MQL method, D_c is the most influencing parameter governing R_a , followed by S_s and F_r , respectively.

4.1.2. *ANOVA for Roughness under Dry Run.* The relevance of the desirability function is confirmed by the “F-value” of 27.60 and the “P value” of 0.035 as shown in Table 4. If the values are more than 0.10, the function is said to be insignificant. In other words, there is a 0.01% chance that the noise will cause an insignificant effect. Furthermore, the

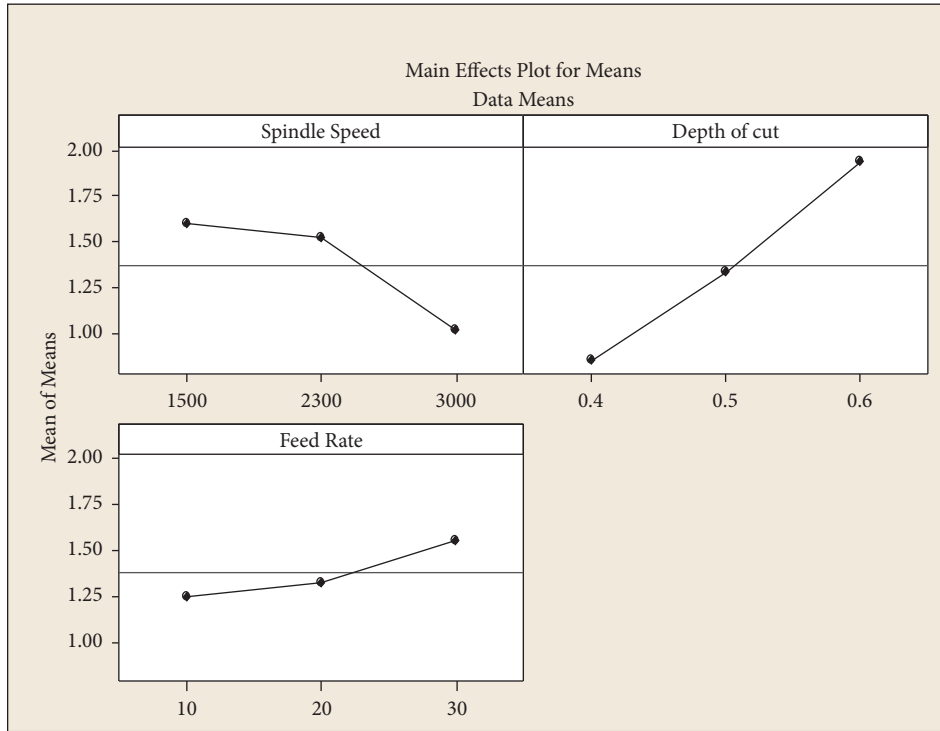


FIGURE 4: Means plot for R_a -dry runs.

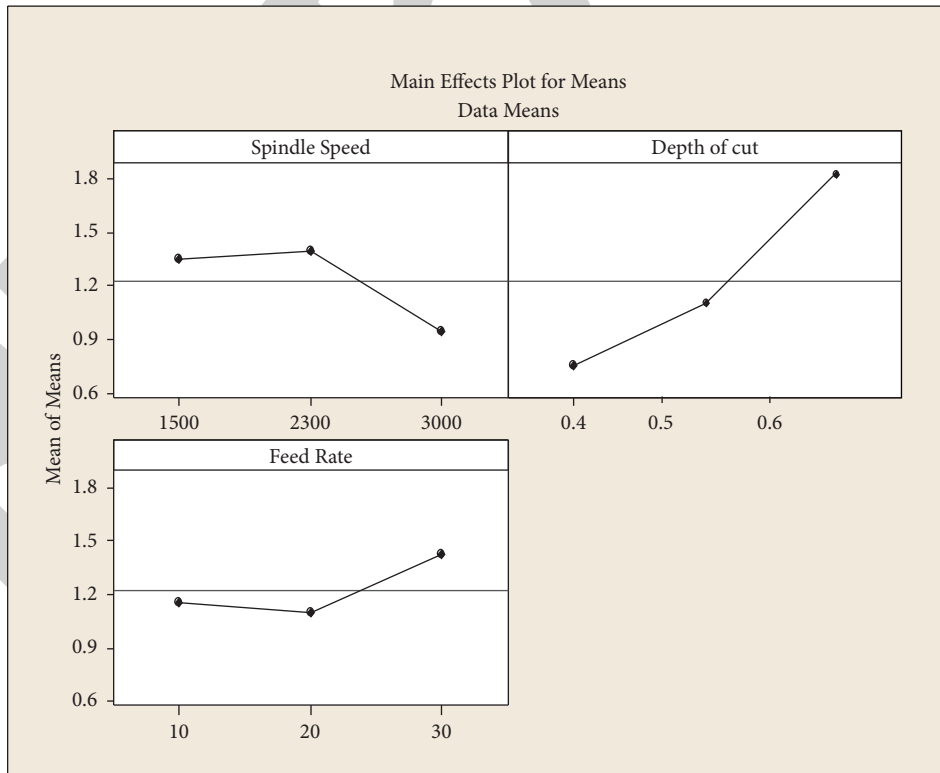


FIGURE 5: Means plot for R_a -MQL.

TABLE 4: ANOVA for S/N ratios (R_a -dry runs).

Response surface linear model						
Analysis of variance for S/N ratios-dry run						
Source	Df	Seq. SS	Adj. SS	Adj. Ms	F-value	P value
A	2	26.257	26.257	13.128	9.70	0.093
B	2	74.701	74.701	37.350	27.60	0.035
C	2	5.329	5.329	2.664	1.97	0.337
Residual error	2	2.707	2.707	1.353		
Total	8	108.993				
Standard deviation		1.163 (%)				
R^2		97.5				
Adj R^2		90.1				

values of R^2 and Adj R^2 indicate a favorable trend toward a higher efficacy.

4.1.3. ANOVA for Roughness under MQL. Table 5 shows a similar data of ANOVA comparison for R_a under the MQL condition. Here, we can find that the “F-value” of 92.98 and the P value of 0.011 show the significance level. Also, the values of R^2 and Adj R^2 indicate a favorable trend toward a higher efficacy.

4.1.4. Response Table for S/N Ratios for R_a . Table 6 is the response for S/N ratio for R_a and its influence. From the table, we can find that D_c is the major significant parameter influencing R_a , followed by S_s and F_r in the dry run condition and the MQL method. The delta values in both cases (dry runs and MQL) are found to be closer, which shows the capability of machining to attain the desired outcome in either condition.

4.2. Material Removal Rate (MRR)

4.2.1. Parameter Interaction Effects on Dry Runs and MQL. Figures 6 and 7 depict the parametric interaction of the S/N ratios on MRR in the dry run condition and the MQL method. The objective function is taken as larger-the-better. From the graph, it is evident that in the dry runs and the MQL method, D_c is the most influencing parameter governing MRR, followed by S_s and F_r , respectively. However, the presence of coolant enhances the desirability function.

Figures 8 and 9 highlight the parametric interaction of the means on MRR in the dry run condition and the MQL method. From the graph, it is evident that in the dry runs and the MQL method, D_c is the most influencing parameter governing R_a , followed by S_s and F_r , respectively.

4.2.2. ANOVA for MRR under Dry Run. The relevance of the desirability function is confirmed by the “F-value” of 16.69 and the “Pvalue” of 0.057 as shown in Table 7. If the values are more than 0.10, the function is said to be insignificant. In other words, there is a 0.01% chance that noise will cause an

TABLE 5: ANOVA for S/N ratios (R_a -MQL).

Response surface linear model						
Analysis of variance for S/N ratio-MQL						
Source	Df	Seq. SS	Adj. SS	Adj. Ms	F-value	P value
A	2	18.503	18.5028	9.2514	19.55	0.049
B	2	87.980	87.9796	43.9898	92.98	0.011
C	2	6.719	6.7186	3.3593	7.10	0.123
Residual error	2	0.946	0.9463	0.4731		
Total	8	114.147				
Standard deviation		0.6878				
R^2		99.2%				
Adj R^2		96.7%				

TABLE 6: Response table for S/N ratios (R_a).

Level	Dry runs			MQL		
	Response table-S/N ratios			Response table-S/N ratios		
	S_s	D_c	F_r	S_s	D_c	F_r
1	-3.4558	1.4377	-1.1228	-1.762	2.5056	-0.272
2	-3.1228	-2.0747	-2.1271	-2.2737	-0.4579	-0.546
3	0.3225	-5.6192	-3.0062	0.9913	-5.092	-2.2264
Delta	3.7788	7.0569	1.8834	3.265	7.5976	1.9544
Rank	2	1	3	2	1	3

insignificant effect. Furthermore, the values of R^2 and Adj R^2 indicate a favorable trend toward a higher efficacy.

4.2.3. ANOVA for MRR under MQL. Table 8 shows a similar data on ANOVA comparison for MRR under the MQL condition. Here, we can find that the “F-value” of 11.25 and the P value of 0.082 show a significance level. Moreover, the R^2 , Adj R^2 , and Pred R^2 values indicate a positive approach toward its higher efficacy, and the values are close to 1.

4.2.4. Response Table for S/N Ratios for MRR. Table 9 is the response for the S/N ratio of MRR and its influence. From the table, we can find that D_c is the major significant parameter influencing R_a , followed by S_s and F_r in the dry run condition and the MQL method. The delta values in both cases (dry runs and MQL) are found to be closer, which shows the capability of machining to attain the desired outcome in either condition.

4.3. Optimized Parameters. The optimized set of machining parameter is given in Table 10.

5. Grey Relational Analysis (GRA)

The steps followed to arrive at the optimal solutions are as follows.

5.1. Normalization. The preprocessing of data is done in this step based on the chosen objective function. If the normalization or data preprocessing is based on “larger-

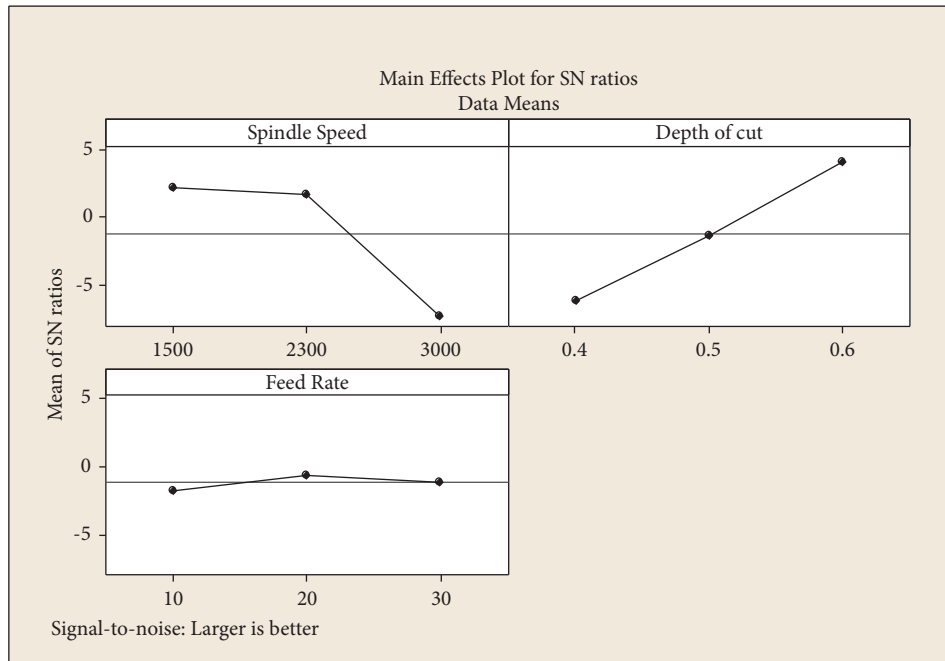


FIGURE 6: S/N ratio plot for MRR-dry runs.

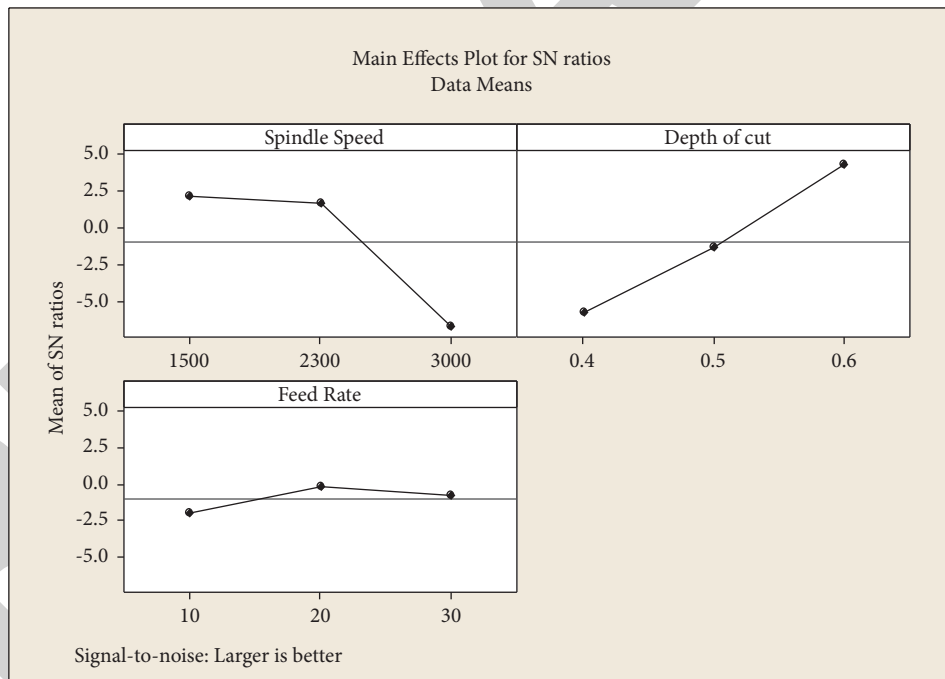


FIGURE 7: S/N plot for MRR-MQL.

the -better,” then equation (1) is used. If the data pre-processing or normalization is based on “smaller-the-better,” then equation (2) is used. Normalization is a technique for creating a comparable data set from a larger set of data by lowering the amount of variation for easier analysis.

$$Xi(k) = \frac{xi(k) - \min xi(k)}{\max xi(k) - \min xi(k)} \tag{1}$$

$$Xi(k) = \frac{\max xi(k) - xi(k)}{\max xi(k) - \min xi(k)} \tag{2}$$

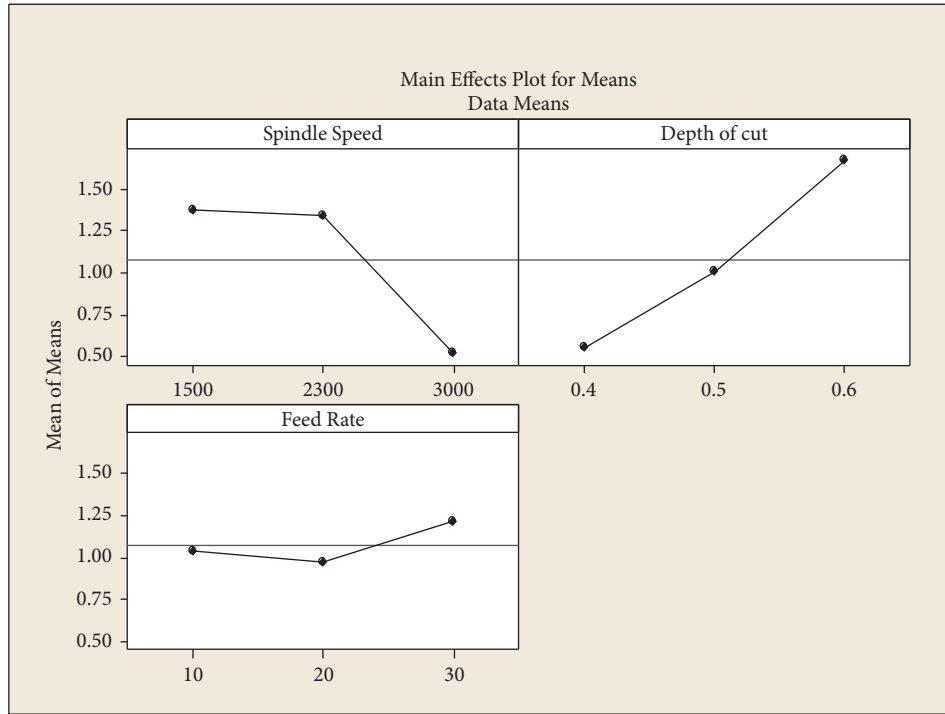


FIGURE 8: Means plot for MRR-dry runs.

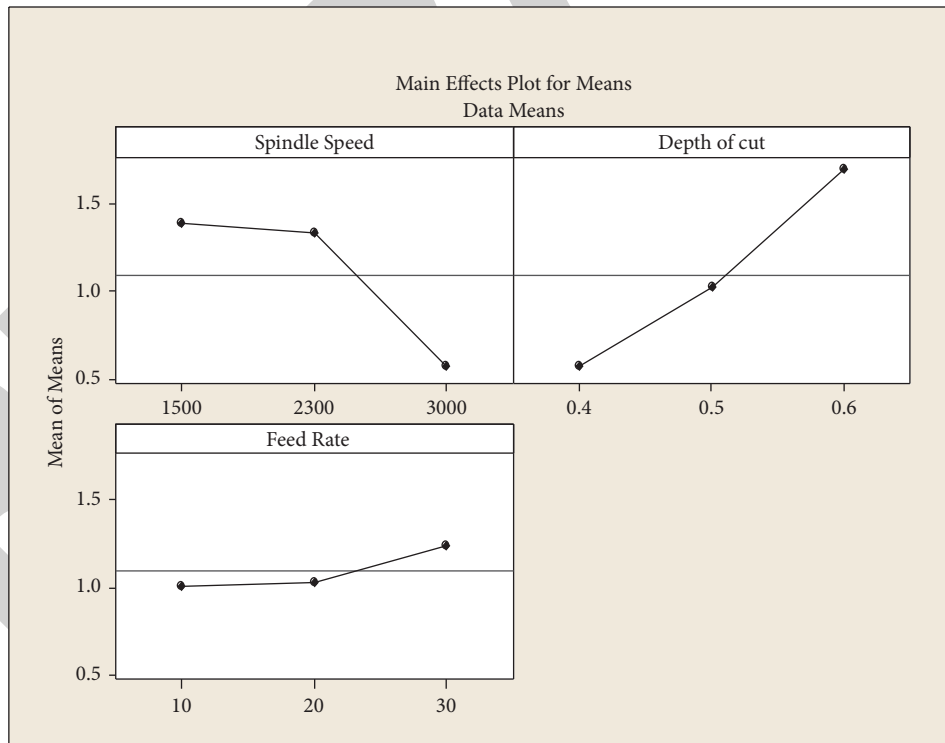


FIGURE 9: Means plot for MRR-MQL.

Here, $i = 1, \dots, m$; $k = 1, \dots, n$. m is the number of experimental data. n is the number of responses. $X_i(k)$ represents the value after data preprocessing. $x_i(k)$

represents the original sequence data. $\max x_i(k)$ is the largest value of $x_i(k)$. $\min x_i(k)$ is the minimal value.

TABLE 7: ANOVA for S/N ratios (R_a -dry runs).

Response surface linear model						
Analysis of variance for S/N ratios-dry runs						
Source	Df	Seq. SS	Adj. SS	Adj. Ms	F-value	P value
A	2	167.624	167.624	83.812	16.69	0.057
B	2	156.871	156.871	78.436	15.52	0.060
C	2	2.054	2.054	1.027	0.20	0.830
Residual error	2	10.045	10.045	5.023		
Total	8	336.595				
Standard deviation				2.241 (%)		
R^2				97.0		
Adj R^2				88.1		

TABLE 8: ANOVA for S/N ratios (R_a -dry runs).

Response surface linear model						
Analysis of variance for S/N ratios-MQL						
Source	Df	Seq. SS	Adj. SS	Adj. Ms	F-value	P value
A	2	148.679	148.679	74.339	10.82	0.085
B	2	154.508	154.508	77.254	11.25	0.082
C	2	5.410	5.410	2.705	0.39	0.717
Residual error	2	13.740	13.740	6.870		
Total	8	322.337				
Standard deviation				2.621 (%)		
R^2				95.7		
Adj R^2				82.9		

TABLE 9: Response table for S/N ratios (MRR).

Level	Dry runs			MQL		
	Response table-S/N ratios			Response table-S/N ratios		
	S_s	D_c	F_r	S_s	D_c	F_r
1	2.1118	-6.2026	-1.7867	2.1280	-5.8467	-2.0398
2	1.5878	-1.4089	-0.6166	1.6135	-1.4270	-0.1794
3	-7.2938	4.0173	-1.1909	-6.7398	4.2754	-0.7791
Delta	9.4057	10.2200	1.1701	8.8677	10.1221	1.8604
Rank	2	1	3	2	1	3

TABLE 10: Optimized parameter for both dry run and MQL.

Tool used	Condition	S_s (rpm)	D_c (mm)	F_r (mm/min)
Taguchi	R_a	3000	0.4	10
	MRR	1500	0.6	30

5.2. *Deviation Sequence.* Based on the responses, smaller-the-better is assigned for R_a , while larger-the-better option is assigned for MRR. The deviation for normalized values is calculated in this phase. The deviation for each response is recorded in relation to the highest normalized value reached.

5.3. *Grey Relational Coefficients (GRCs).* The grey regression coefficients are determined using equation (3). The grey relational coefficient $\xi_i(k)$ is used here. The absolute differences, lowest and maximum values are represented by minimum and maximum values. The difference taken here is 0.5, which is the identifying or distinguishing coefficient that typically varies from 0 to 1.

$$\xi_i(k) = \frac{\Delta \min + \psi \Delta \max}{\Delta o_i(k) + \psi \Delta \max} \quad (3)$$

5.4. *Grey Relational Grade (GRD).* The correlation level of the reference and comparison sequences is represented by GRD (γ). A multiobjective function is converted to a single-objective function at this point. The governing equation for achieving grey relational grade is shown as follows:

$$\gamma^i = \frac{1}{n \sum_{k=1}^n \xi_i(k)} \quad (4)$$

5.5. *Optimal Parameters.* In this stage, the rank of each set of values is determined. The optimized level is readily determined based on the achieved rank, which provides the best solution by combining all responses. Tables 11 and 12 show the grey regression analysis performed on the experimental values.

TABLE 11: Grey relational analysis-dry runs.

Exp	Dry runs		Normalization		Deviation sequence		Coefficients		Grade	Rank
	R_a	MRR	R_a	MRR	R_a	MRR	R_a	MRR		
1	0.91	0.787	0.901	0.694	0.099	0.306	0.835	0.621	0.728	4
2	1.59	1.293	0.454	0.413	0.546	0.587	0.478	0.460	0.469	6
3	2.28	2.038	0.000	0.000	1.000	1.000	0.333	0.333	0.333	9
4	0.88	0.632	0.921	0.780	0.079	0.220	0.864	0.695	0.779	3
5	1.63	1.378	0.428	0.366	0.572	0.634	0.466	0.441	0.454	7
6	2.05	1.987	0.151	0.028	0.849	0.972	0.371	0.340	0.355	8
7	0.76	0.236	1.000	1.000	0.000	0.000	1.000	1.000	1.000	1
8	0.79	0.345	0.980	0.940	0.020	0.060	0.962	0.892	0.927	2
9	1.49	0.989	0.520	0.582	0.480	0.418	0.510	0.545	0.527	5

TABLE 12: Grey regression analysis-MQL.

Exp	Dry runs		Normalization		Deviation sequence		Coefficients		Grade	Rank
	R_a	MRR	R_a	MRR	R_a	MRR	R_a	MRR		
1	0.76	0.779	0.965	0.711	0.035	0.289	0.935	0.634	0.784	4
2	1.13	1.311	0.706	0.411	0.294	0.589	0.630	0.459	0.545	5
3	2.14	2.042	0.000	0.000	1.000	1.000	0.333	0.333	0.333	9
4	0.78	0.643	0.951	0.787	0.049	0.213	0.911	0.702	0.806	3
5	1.42	1.412	0.503	0.355	0.497	0.645	0.502	0.437	0.469	7
6	1.98	1.923	0.112	0.067	0.888	0.933	0.360	0.349	0.355	8
7	0.71	0.265	1.000	1.000	0.000	0.000	1.000	1.000	1.000	1
8	0.73	0.33	0.986	0.963	0.014	0.037	0.973	0.932	0.952	2
9	1.37	1.115	0.538	0.522	0.462	0.478	0.520	0.511	0.516	6

TABLE 13: Optimized parameter by GRA.

S_s (rpm)	D_c (mm)	F_r (mm/min)
3000	0.4	30

TABLE 14: Confirmatory runs.

Tool	Type	Predicted				Achieved	Predicted	Achieved		
		Dry run R_a	Dry run MRR	Dry run R_a	Dry run MRR	MQL R_a	MQL MRR	MQL R_a	MQL MRR	
Taguchi	Single response (R_a)	0.76	—	0.81	—	0.71	—	0.73	—	
	Single response (MRR)	—	0.236	—	0.255	—	0.265	—	0.302	
GRA	Multiresponse	2.28	2.038	2.30	2.054	2.14	2.042	2.11	2.15	
% deviation										
	Single response (R_a)							2		
	Single response (MRR)								3.7	
	GRA multiresponse							3	4	

5.6. *Optimized Set of Parameters Using GRA.* From Table 13, the highest rank is contributed by the 7th experimental run that includes the combination of parameters as reflected in Tables 11 and 12, which is as follows:

6. Confirmatory Runs

To validate the above, confirmatory runs were conducted, and Table 14 shows the results attained.

The % deviation shown in Table 14 provides a lucid view on the performance of the optimization tool used. It is noteworthy to state that the above approach provides the

optimized results satisfactory and within the acceptance limit as the deviation recorded lies within the 10% level of acceptance.

7. Conclusion

This study focused on green machining characteristics while machining Al-6083 in two conditions, i.e., under dry condition and under MQL. The study is performed as single response and multi-response optimization. For single response, Taguchi design is followed, and for multiresponse, GRA is applied. The inferences noted in the entire study and

found to be acceptable in accord to the results attained in confirmatory runs are as follows:

- (i) For achieving minimum roughness, D_c plays the dominant role followed by S_s .
- (ii) The least contributing factor governing roughness in this case is found to be F_r .
- (iii) The above two statements stand true irrespective of whether the machining is dry run or MQL. However, it is acceptable that the application of coolant enhances in achieving the minimum roughness.
- (iv) From Table 14, minimum R_a achieved under the dry run is 0.76, while in MQL, it is 0.71, which proves that the application of coolant aids in achieving a better finish.
- (v) Also, it is evident that the MQL condition is sufficient for achieving the required roughness instead of the flooded machining, depending on the constraints to be considered while machining.
- (vi) For maximum MRR, D_c plays a prominent role with S_s assigned at its lower level.
- (vii) D_c and S_s are the significant factors in the dry run conditions and the MQL method.
- (viii) The presence of coolant also enhances MRR.
- (ix) In case of multiresponse optimization, GRA results align with the higher level of S_s and the medium level of D_c , followed by F_r .

The % deviation recorded depicts the significance of both dry machining and under MQL. As the deviation level is within 10%, dry machining also fulfills the objective function of achieving a minimum roughness.

From an environmental perspective, green machining is much required for the manufacturing sector. Industries will be required to practice dry machining to comply with environmental laws and health requirements. A few advantages of green machining are that it causes no pollution of the atmosphere, has lower disposal and cleaning cost, and is nontoxic in all aspects (health, skin, allergy).

Data Availability

The data used to support the findings of this study are included within the article.

Disclosure

The study was performed as a part of the Employment of Addis Ababa Science and Technology University, Ethiopia.

Conflicts of Interest

The authors declare that there are no conflicts of interest.

References

- [1] M. A. Azmir, A. K. Ahsan, and A. Rahmah, "Effect of abrasive water jet machining parameters on aramid fibre reinforced plastics composite," *International Journal of Material Forming*, vol. 2, no. 1, pp. 37–44, 2008.
- [2] N. R. Prabhuswamy, S. Srinivas, A. Vasli, M. V. Sheshashayan, S. Venkatesh, and Y. Roongta, "Machinability studies of aluminium 6061 cut by abrasive water jet," *Materials Today: Proceedings*, vol. 5, no. 1, pp. 2865–2870, 2018.
- [3] R. Neugebauer, R. Wertheim, and C. Harzbecker, "Energy and resource efficiency in the metal cutting industry," in *Proceedings of the 8th Global Conference on Sustainable Manufacturing*, pp. 247–257, Heidelberg ; New York, May 2011.
- [4] S. Kara and W. Li, "Unit process energy consumption models for material removal processes," *CIRP Annals*, vol. 60, no. 1, pp. 37–40, 2011.
- [5] N. Diaz, E. Redelsheimer, and D. Dornfeld, "Energy consumption characterization and reduction strategies for milling machine tool use," in *Proceedings of the 18th CIRP International Conference on Life Cycle Engineering*, pp. 263–267, Braunschweig, Germany, March 2011.
- [6] P. T. Mativenga and M. F. Rajemi, "Calculation of optimum cutting parameters based on minimum energy footprint," *CIRP Annals*, vol. 60, no. 1, pp. 149–152, 2011.
- [7] N. Weinert, S. Chiotellis, and G. Seliger, "Methodology for planning and operating energy-efficient production systems," *CIRP Annals*, vol. 60, no. 1, pp. 41–44, 2011.
- [8] I. Zohourkari, M. Zohoor, and M. Annoni, "Investigation of the effects of machining parameters on material removal rate in abrasive waterjet turning," *Advances in Mechanical Engineering*, vol. 6, p. 624203, 2014.
- [9] M. Helu, B. Behmann, H. Meier, D. Dornfeld, G. Lanza, and V. Schulze, "Total cost analysis of process time reduction as a green machining strategy," *Leveraging Technology for a Sustainable World*, pp. 299–304, 2012.
- [10] M. Helu, A. Vijayaraghavan, and D. Dornfeld, "Evaluating the relationship between use phase environmental impacts and manufacturing process precision," *CIRP Annals*, vol. 60, no. 1, pp. 49–52, 2011.
- [11] V. Derflinger, H. Brändle, and H. Zimmermann, "New hard/lubricant coating for dry machining," *Surface and Coatings Technology*, vol. 113, pp. 86–292, 1999.
- [12] S. Tatsuya, Y. Nishimoto, and T. Enomoto, "On-machine tool reshaping process for dry machining of aluminum alloys employing LME phenomenon," *Precision Engineering*, vol. 40, pp. 241–248, 2015.
- [13] S. B. Kedare, D. R. Borse, D. R. Borse, and P. T. Shahane, "Effect of minimum quantity lubrication (MQL) on surface roughness of mild steel of 15HRC on universal milling machine," *Procedia Materials Science*, vol. 6, pp. 150–153, 2014.
- [14] P. S. Sreejith and B. K. A. Ngoi, "Dry machining: machining of the future," *Journal of Materials Processing Technology*, vol. 101, no. 1-3, pp. 287–291, 2000.
- [15] M. S. Najiha, M. M. Rahman, and K. Kadrigama, "Performance of water-based TiO₂ nanofluid during the minimum quantity lubrication machining of aluminium alloy, AA6061-T6," *Journal of Cleaner Production*, vol. 135, pp. 1623–1636, 2016.
- [16] D. Dudzinski, A. Devillez, A. Moufki, D. Larrouquère, V. Zerrouki, and J. Vigneau, "A review of developments towards dry and high speed machining of Inconel 718 alloy," *International Journal of Machine Tools and Manufacture*, vol. 44, no. 4, pp. 439–456, 2004.
- [17] M. Nayak and R. Sehgal, "Environmentally benign metal machining technologies and concepts," in *Proceedings of the National Conference on Paradigm in Mechanical Engineering (PME-2014) on 20th Dec*, MRIU, Faridabad, December 2014.

Retraction

Retracted: Electrochemical Studies of WC-Flyash HVOF Coating Interface on SA209-T1 Steel under 3.5 NaCl Solution

Advances in Materials Science and Engineering

Received 26 December 2023; Accepted 26 December 2023; Published 29 December 2023

Copyright © 2023 Advances in Materials Science and Engineering. This is an open access article distributed under the Creative Commons Attribution License, which permits unrestricted use, distribution, and reproduction in any medium, provided the original work is properly cited.

This article has been retracted by Hindawi, as publisher, following an investigation undertaken by the publisher [1]. This investigation has uncovered evidence of systematic manipulation of the publication and peer-review process. We cannot, therefore, vouch for the reliability or integrity of this article.

Please note that this notice is intended solely to alert readers that the peer-review process of this article has been compromised.

Wiley and Hindawi regret that the usual quality checks did not identify these issues before publication and have since put additional measures in place to safeguard research integrity.

We wish to credit our Research Integrity and Research Publishing teams and anonymous and named external researchers and research integrity experts for contributing to this investigation.

The corresponding author, as the representative of all authors, has been given the opportunity to register their agreement or disagreement to this retraction. We have kept a record of any response received.

References

- [1] D. Elango, A. Daniel Das, S. P. Kumaresh Babu, S. Natarajan, and A. Yeshitla, "Electrochemical Studies of WC-Flyash HVOF Coating Interface on SA209-T1 Steel under 3.5 NaCl Solution," *Advances in Materials Science and Engineering*, vol. 2021, Article ID 8706630, 9 pages, 2021.

Research Article

Electrochemical Studies of WC-Flyash HVOF Coating Interface on SA209-T1 Steel under 3.5 NaCl Solution

D. Elango,¹ A. Daniel Das ,² S. P. Kumaresh Babu,³ S. Natarajan,³ and A. Yeshitla ⁴

¹Department of Metallurgical and Materials Engineering, National Institute of Technology, Tiruchirappalli, Tamil Nadu, India

²Department of Mechanical Engineering, Karpagam Academy of Higher Education, Coimbatore, Tamilnadu, India

³Department of Metallurgical and Materials Engineering, National Institute of Technology, Tiruchirappalli, Tamil Nadu, India

⁴Department of Biotechnology College of Biological and Chemical Engineering, Addis Ababa Science and Technology University, Addis Ababa, Ethiopia

Correspondence should be addressed to A. Yeshitla; alazar.yeshi@aastu.edu.et

Received 15 July 2021; Revised 10 August 2021; Accepted 20 October 2021; Published 9 November 2021

Academic Editor: Samson Jerold Samuel Chelladurai

Copyright © 2021 D. Elango et al. This is an open access article distributed under the Creative Commons Attribution License, which permits unrestricted use, distribution, and reproduction in any medium, provided the original work is properly cited.

In this present research, the coatings of SA209-T1 using high velocity oxygen fuel were employed for the application of boiler tubes. Due to the adaptation of corrosion easy in boiler material, the research of those properties is significant because of its criticality and functionality during the service time. A right coating was found and applied on the SA209-T1 surface against corrosive environments. Good corrosion resistance is achieved by WC-flyash coatings applied on SA209-T1 substrate. The 90% WC-10% flyash coatings were found to be more protective followed by SA209-T1 steel. WC-flyash covering was tracked down so that the covering is compelling to secure the SA209-T1 steel substrate. It is reasoned that the arrangement of NiO, Cr₂O₃, CoO, and NiCr₂O₄ could add to the advancement of consumption opposition in coatings. The steel of uncoated endured erosion as extraordinary stripping and spalling of the scale, which could be because of the development of Fe₂O₃ oxide scale unprotectively. This paper reveals the performance, applications, and development of 90wt.% WC and 10wt.% fly ash through HVOF coating in SA209-T1 for electrochemical corrosion studies at room temperature.

1. Introduction

HVOF showering is applied predominantly to metallic and cermet coatings due to the dissolving force of the HVOF splashing weapons and frameworks. Notwithstanding, because of the greater kinetic energy, more limited stay reason of particles in the fire, and lower fire temperature contrasted with the plasma splash, HVOF offers an intriguing mix to create thick coatings with controlled stage changes. For WC-Co-based material, it is noted that during the time of flight, showered particles soften to various degrees relying upon their density, size, and dwell time. Liquid Co breaks down the WC grains through carbon misfortune that happens by dissemination through the fluid followed by the response of oxygen to environmental factors. There can be a lot of carbon and tungsten broke down from the framework material, particularly from the external area of splashed particles. During the cooling time, Co-

rich liquid becomes supersaturated coming about because of the development of W₂C and other blended carbides. Substantial cooling rates can even be liable for the development of the formless/nanocrystalline network stage. At the time of cooling, precipitation of blended carbides, like the estimated time of arrival, carbide stage may happen in the co-rich material. These impacts are generally noticeable on the external center of the particles. In the little size particles, the entire molecule can be impacted by decarburization. On the chance that cooling is sufficiently quick, the lattice will remain indistinct and super-saturated with C and W. At the point when heat treatment of the coating occurs, the precipitation of the estimated time of arrival begins at a temperature of over 600°C bringing about the checked increment of hardness and a decrease in lingering stresses in the covering [1–3]. The erosion was characterized by Rapp and Zhang as the speed up of the oxidation of the material by temperature raise, prompted by a meager film of melded salt

stores [1]. The reasons for the disappointment of heater tube due to the fireside consumption in waste warmth recuperation evaporator using fumes of gas turbine terminated with fast diesel were investigated by Srikanth et al. [2]. Moreover, they revealed that the consumption happens on account of the response of sulfur species in the gas stage to the surface of the metals. The presence of sulfur in coal and fuel oils yielded SO_2 during ignition which might be a part of this way oxidized to SO_3 . The NaCl responds to SO_3 and fume when burning temperature yields Na_2SO_4 . Limited number of vanadium might be likewise has been available in oils which are ignition structures V_2O_5 . This could additionally respond to Na_2SO_4 low frame liquefying sodium vanadate, which is very destructive to substantial material temperature utilized in the burning framework [3, 4]. Evaporator prepared cannot meet the prerequisite for both high thermal consumption obstruction and high thermal strength. Covering gives a method of broadening the constraints of utilization of materials under good finish because of their presentation ability, through permitting the good mechanical strength of substrate metals to be kept while securing it against erosion and wear [5]. Nickel chromium compound has been utilized as a covering to manage oxidizing conditions at high temperature. At the point when nickel and chromium are alloyed, the component oxidizes Cr_2O_3 , which may make it reasonable for use up to around 1200°C . Nonetheless, its utilisation is restricted to temperatures under 800°C [6]. The warm splashed 50/50 nickel chromium composite is typically suggested as disintegration erosion insurance for heater tube in power age application [7]. Chuanxian et al. [8] and Lio et al. [9] have announced wide utilization of cermet warm splash coatings in clear circumstances since they consolidate a few benefits like protection from scraped area, high temperature, disintegration, and destructive airs. The HVOF measure is accounted for an adaptable innovation, and it is embraced by numerous enterprises because of its adaptability, cost adequacy, and predominant nature of covering created. The hypersonic speed of the fire abbreviates the hour of cooperation between the fire and powder, and less temperature of fire restricts the deterioration and grain development of coatings. Because of the great effect speed of particles, the covering shows a uniform microstructure, substantial cement strength, high thickness, low porosity, and substantial firm strength of separate splats [10]. The ultimate target of the current research is to describe the substantial temperature erosion systems for high velocity oxy fuel metallic coatings on heater steel to be specific ASTM SA 209-T1 grade Al in a forceful climate of liquid salt (Na_2SO_4 -60% V_2O_5). SEM/EDAX, XRD, and EPMA methods have been utilized to describe consumption items after hot erosion under cyclic conditions at 900°C .

2. Investigation of Experiment

2.1. Materials and Methods. The boiler tube steel with ASTM SA209-T1 grade Al (GrAl) compound structure as demonstrated in Table 1 has been utilized under the substrate steel. In north India, some power plants have utilized this

material as evaporator tube material. The steel tests were sliced to shape around $20\text{ mm} \times 20\text{ mm}$ measured samples. The samples were neatly cleaned and grit blasted with Al_2O_3 (coarseness 45) preceding use of the high velocity oxy fuel shower coatings. The examination has been performed for coated and uncoated specimens with the end goal of correlation [9]. The uncoated specimen was reflecting cleaned to one μm of alumina wheel fabric cleaning before erosion examination. The outside of the consumed workpieces was outwardly seen to record tone, stripping, and spalling of scale during electrochemical erosion. The specimen after erosion run has been analyzed by SEM analysis.

2.2. Thickness of Coverings. The covering thickness was measured through the BSE images which was normally around $300\mu\text{m}$. The deliberate estimations of the porosity for a splashed covering are shown in Table 2. The spray variables used during HVOF showering are shown in Table 3.

2.3. Specimens Arrangement for Corrosion. The hacksaw was used to cut the coated interface, and rough sheets were used for deburring the specimens. The parent metal was additionally ready for examination to connect the erosion conduct with the WC-flyash covered specimens [11]. The SiC 1200 grade emery paper having rough coarseness is used for setting up the surface of the metal, and refined water is used to clean the specimen and then dried at room temperature.

2.4. Electrochemical Studies. Figure 1 shows the Autolab electrochemical workstation; the consumption opposition is examined by the utilization of potentio-dynamic polarizing bends and electrochemical impedance spectroscopy at 28°C of ambient temperature. The examinations have been conducted through utilizing Autolab instruments, CECRI, Karaikudi, Tamil Nadu, India, with polarization forecast programming. Saturated calomel anode and platinum were used as cathode. On a superficial level zone, the examination has been performed for 2 cm^2 for every single time. At a time frame $\text{mV}-1.500\text{ mV}$, the curves of polarisation were estimated at a pace of scan of mV/s . A specimen of WC-flyash covered at OCP for sixty minutes was held with electrochemical impedances [3].

2.5. Surface Morphology Analysis by SEM and EDS. A cold cathode Hitachi S 4800 field electron SEM lens is utilized to identify the morphology of the surface. The thermo NORAN NSS power scatter X-beam (EDS) is matched with the field electron SEM which gave a best-in-class imaging gadget of value around 1 nm in goal at 15 kV of beam power. The component appropriation could be described utilizing EDS investigation. The yttrium aluminum garnet backscattered electron identifier is accessible alongside field electron SEM and is utilized to catch the contrast improved pictures of multistage materials [4].

TABLE 1: SA209-T1 chemical composition (OES method).

Elements	Mn	C	P	Si	S	Mo	Fe
Weight %	0.45	0.19	0.025	0.34	0.024	0.55	Balance

TABLE 2: Thickness of scale (average) and porosity of coverings.

Sl. no.	Depletion	K_p ($10^{-10} \text{g}^2 \cdot \text{cm}^{-4} \cdot \text{s}^{-1}$)	Thickness of scale (average) (μm)	Porosity (%)
1	Uncovered SA209-T1	6860.8	950	—
2	WC-flyash-coated	1515.3	850	1.35–1.5

TABLE 3: Spray variables utilized during HVOF showering.

Sl. no.	Spray variables	Hipojet-209-T10
1	Flow rate of oxygen	225 LPM
2	Flow rate of fuel (LPG)	65 LPM
3	Flow rate of air	6100 LPM
4	Diameter of wire/size of the particle	$-30 + 15 \mu\text{m}$
5	Wire/powder feed	30 g/min
6	Spray distance	200 mm

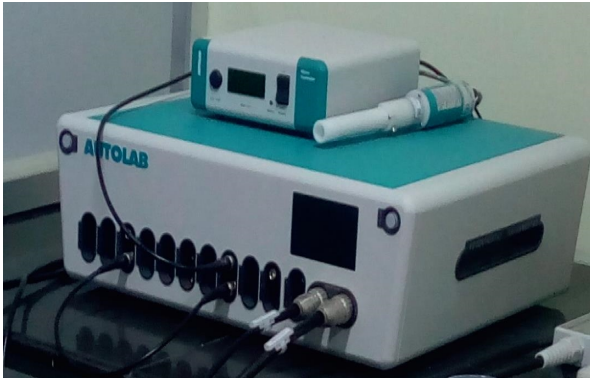


FIGURE 1: Electrochemical workstation to identify the utilization of potentiodynamic polarizing bends and electrochemical impedance spectroscopy.

2.6. *Optical Microscope.* Perception of the grain design of base materials and covering interface is performed by cutting-edge mechanical sorting on a large scale. It is likewise used to quantify the normal covering thickness statement utilizing direct block attempt strategy.

3. Discussion of Results

3.1. *EDS-Based Morphological Study.* The surface morphology of the coated and uncoated prepared after cyclic hot erosion was shown by the SEM images and is shown in Figure 2. Fe_2O_3 could be the dominating stage which demonstrates the uncoated steel by EDAX investigation. EDAX examination of size of WC-flyash covered example showed little amounts of Cr_2O_3 and Fe_2O_3 presence alongside largest level of NiO (96%). The coated specimen size has high level of NiO and Cr_2O_3 alongside other minor stages MnO, Fe_2O_3 , SiO_2 , and so on. The EDAX of the WC flyash coated steel scale showed CoO, Fe_2O_3 with an exceptionally small amount of WO_3 . The size of coated steel

stellite-6 shows the predominance of CoO alongside Cr_2O_3 and Fe_2O_3 .

Figure 3 shows the WC-flyash-coated steel EPMA planing analysis; it shows that the substrate diffuses Fe in to coatings whereas Si and Mn concentrated at the substrate and coating interface. Throughout the scale, Cr and Ni are present. Also, the coating shows the Ni-rich pockets. The nickel (Ni) rich region depletes the chromium (Cr) region. The uncoated steel EPMA mapping of scale shows Co-rich layer in the scale top and contains chromium. The presence of the tungsten-rich streaks was also seen in the scale. Si is precipitated out to the substrate boundary [12–15]. Whereas EPMA mapping for uncovered steel. Figure 4 shows that top layer to be Cr rich and below that presence of Ni in higher concentration. Notification of iron migration from the substrate to the top layer of the scale. The oxide scale mainly consisted of Fe_2O_3 has been indicated by WC-flyash-coated steel EPMA map. Fe has been diffused from substrate into the coating for all [16, 17].

3.2. *Optical Microscopic Studies.* By analyzing the proof of micrographs of the coating obtained by HVOF, the coatings deposited on GrA1 steel substrates shown in Figure 5 also show uniform thickness, $103 \pm 6 \mu\text{m}$, as well as good adhesion to the substrate.

3.3. *Potential Dynamic Polarization Studies.* The unique polarization is performed for uncoated steel at 28 °C room temperature as per ASTM G59-97(2020) standards. The checking of polarization at the rates between 0.01mVs^{-1} to 50mVs^{-1} and plotting of chart are shown in Figure 6. The outcome is derived from three separate sources: the uncoated base material, the WC-flyash-coated base material, and the interface. The run of the mill anodic terminal polarization conduct of SA209-T1 in NaCl arrangement comprises of dynamic disintegration, lack of involvement, and abrupt addition in the thickness of the current due to the pitting on the base material. Due to this abrupt augmentation of thickness of the current, the pitting is steady. The covered and uncoated examples are likewise tried at greatest output rate, neglected to show a stable pitting. Due to this reason, the Cr_2O_3 is present in the coated specimens [18–20]. The uncoated locales are the most noteworthy consumption district as opposed to the interface area of the WC-flyash covered SA209-T1 steel concentrate through polarization bends. The degree of pitting at the uncoated is too poor contrasted with the WC-flyash covered SA209-T1 steel.

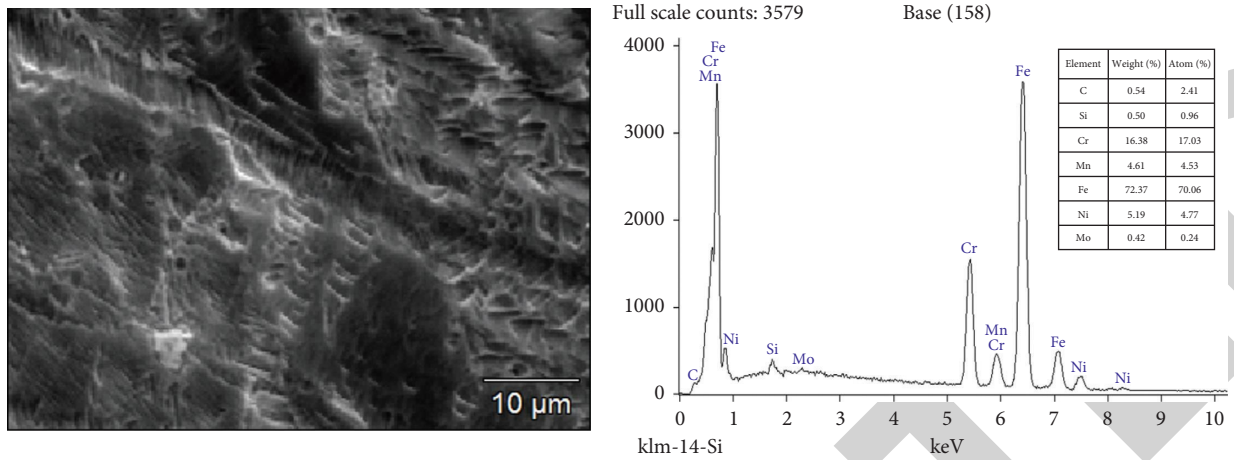


FIGURE 2: EDS and SEM investigation of the good material at dendritic multiperiod of 100 microns.

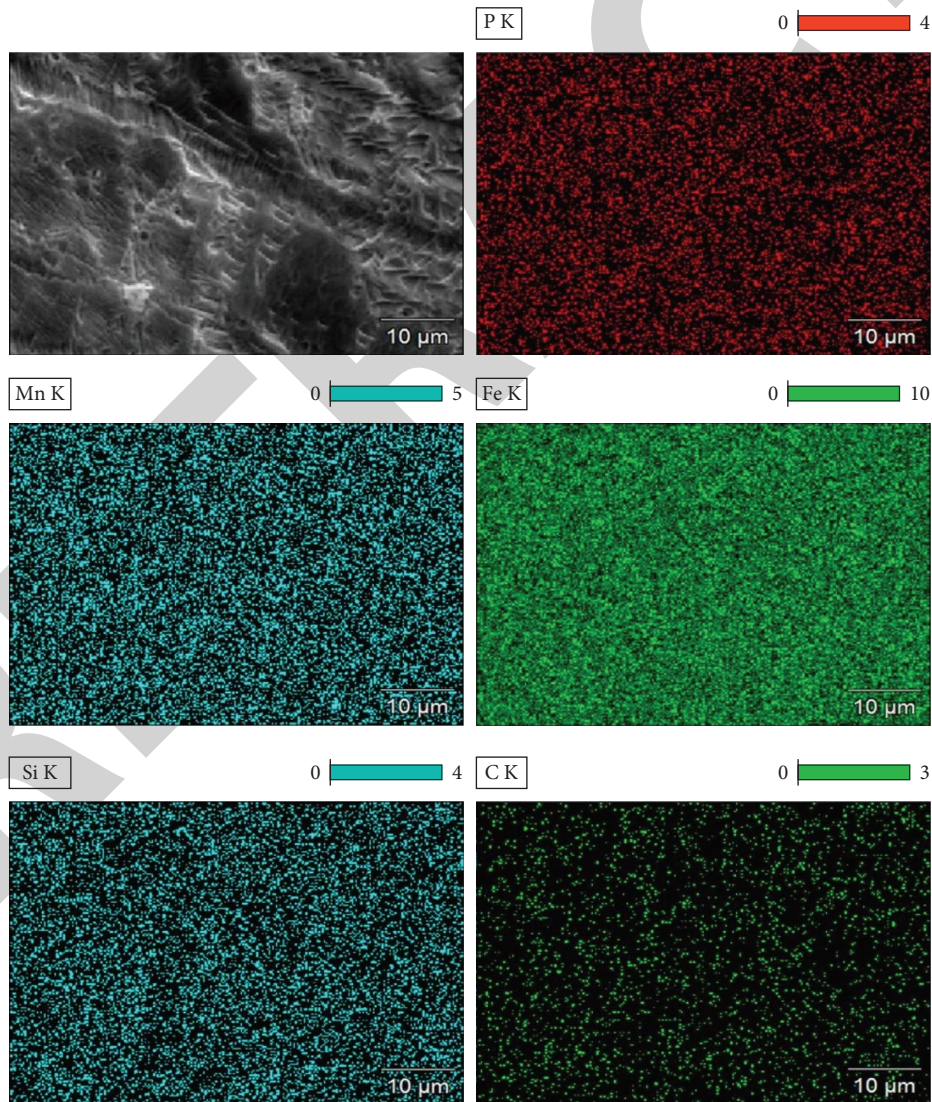


FIGURE 3: Arrangement picture BSEI and X-ray mapping of the cross segmentation of WC-flyash-covered GrA1 steel exposed to electrochemical consumption under 3.5%NaCl solution.

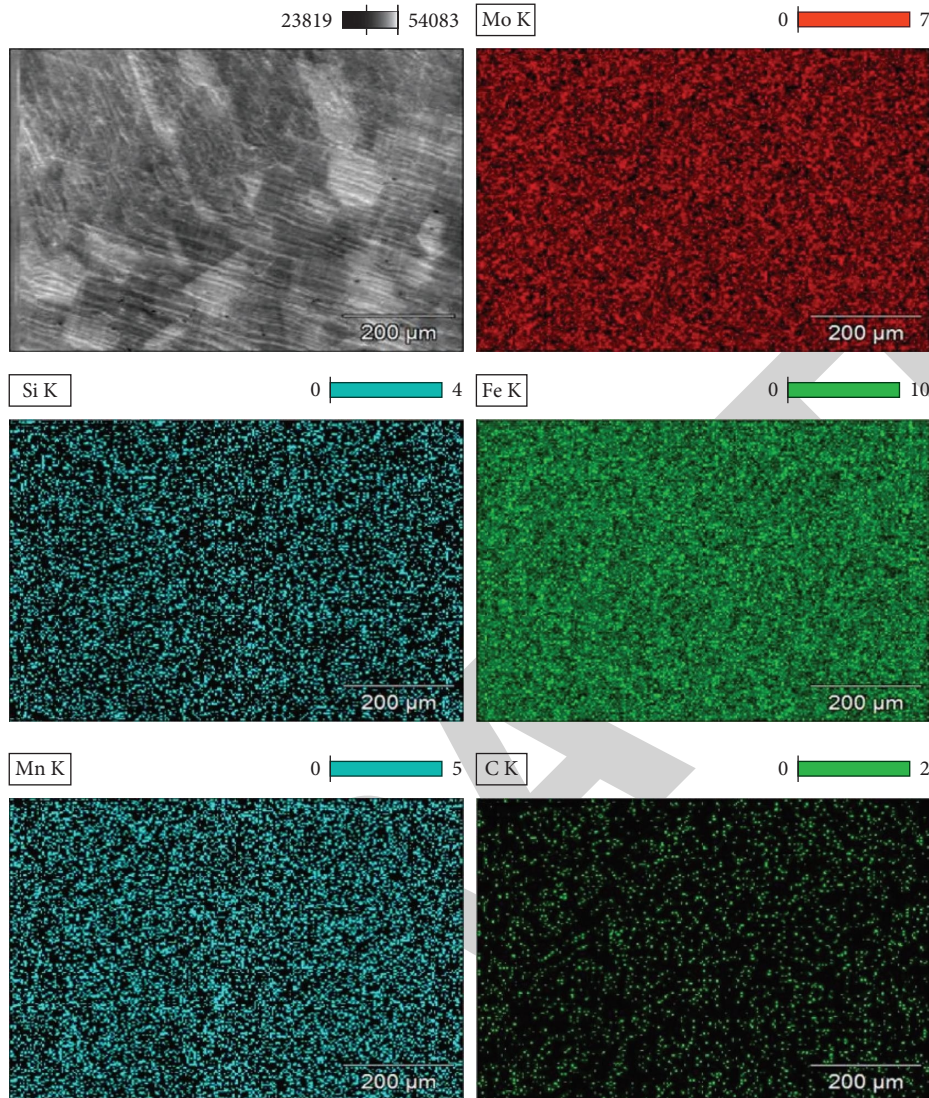


FIGURE 4: Arrangement picture BSEI and X-ray mapping of the cross portion of uncoated GrA1 steel exposed to electrochemical consumption under 3.5%NaCl solution.

3.4. Electrochemical Impedance Spectra. Affirmations of defensive film development on the surface of the metal, AC spectra (electro substance impedance range) have been utilized as per ASTM G106 standards. The obstruction of charge move (R_t) increments when the defensive film structures on the surface of the metal; the capacitance esteem diminishes with the twofold level. Variables of the AC impedance incorporate burden transmission obstruction (R_t) and twofold layer capacitance (CdL) from Nyquist plots of base metal (B), combination zone (F), and the influenced region (D), as demonstrated in Figure 7. The figure curves of EIS show that there is serious erosion happened on the zone of warmth influencing and base material and the combined zone [21]. WC-flyash covered GrA1 steel has better destructive obstruction, and uncoated has helpless destructive opposition. The genuine impedance segment (Z') speeds up to the greatest degree in the interface with varieties of the qualities at the primary

phase of erosion. Subsequently, compared with the uncoated and WC-flyash covered GrA1 steel climate, the warmth affecting climate's consumption power is low [22–24].

EIS was utilized to research the erosion insurance for the steel. Figure 7 shows the Nyquist plots and Bode plots recorded for the WC-flyash-covered GrA1 steel. As shown in Figure 7, the measurement of the crescent in the Nyquist circle of the example with in various environments is bigger than that of the covered GrA1 steel, demonstrating that the tempering interaction has upgraded the consumption obstruction. The biggest crescent breadth was noticed, for example, WC-flyash covered GrA1 steel, which affirms its best consumption hindrance execution among all specimens [25–27].

Figure 8 shows the phase angle plots of uncoated GrA1, interface, and WC-flyash-coated GrA1 steel. Another time steady was seen in the low recurrence area, and the first one was moved to a higher recurrence locale.

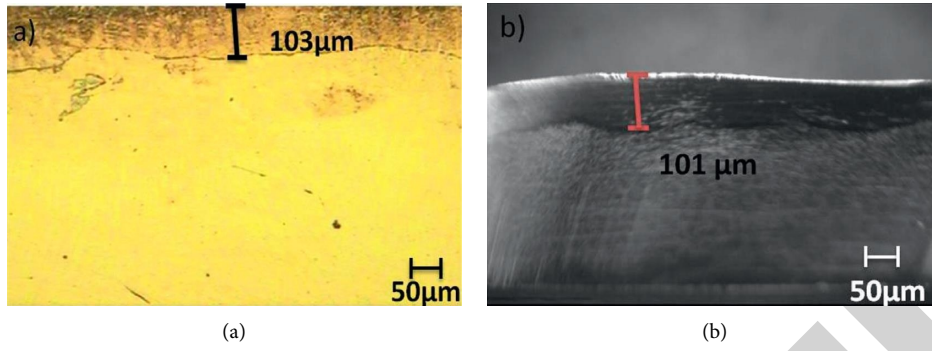


FIGURE 5: Micrographs of the coatings obtained by HVOF (a) and (b).

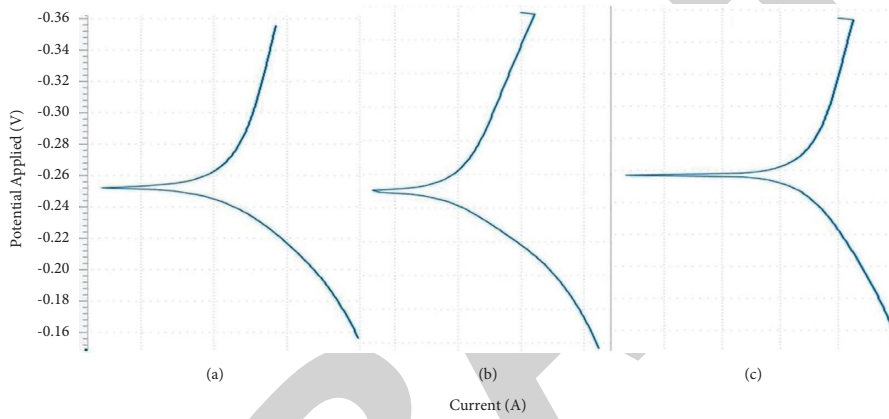


FIGURE 6: Polarization curves obtained on GrA1 steel specimen at uncoated GrA1, interface, and WC-flyash-coated GrA1 steel.

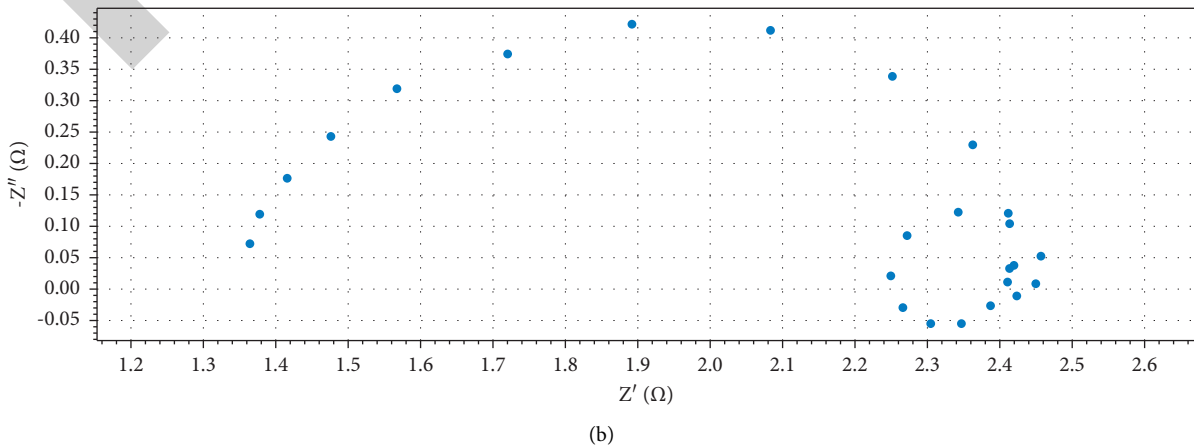
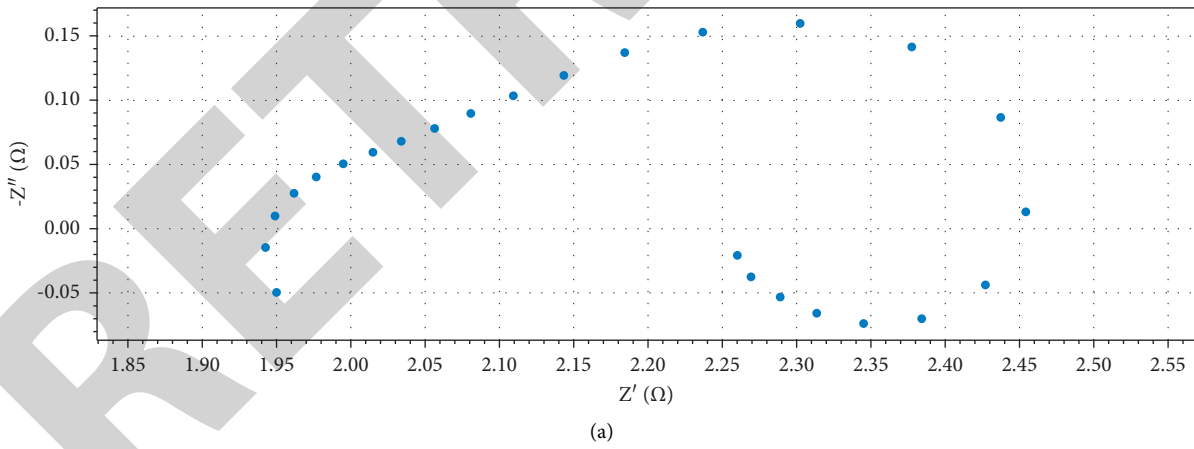
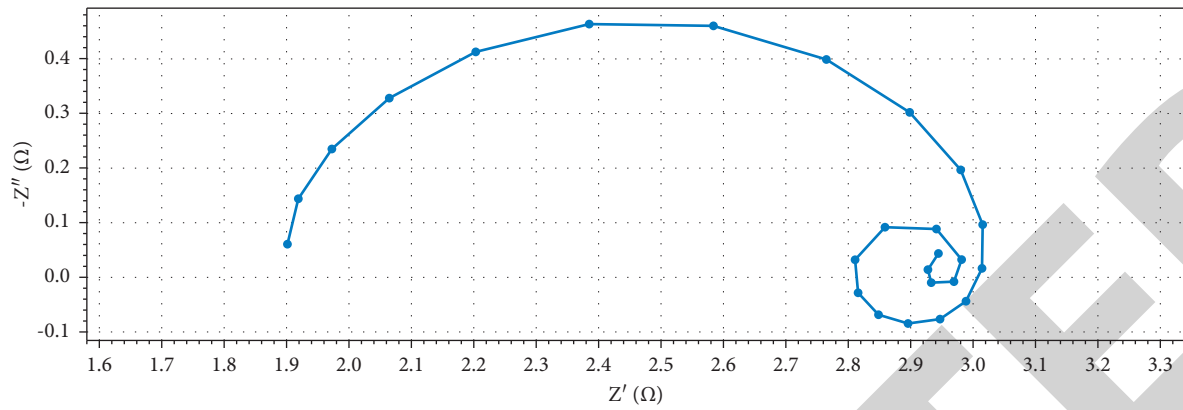
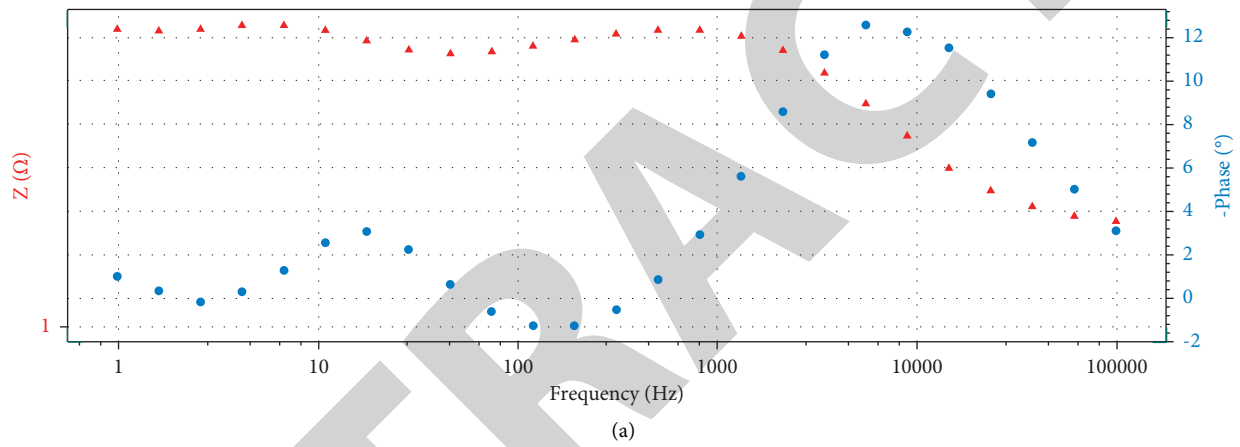


FIGURE 7: Continued.

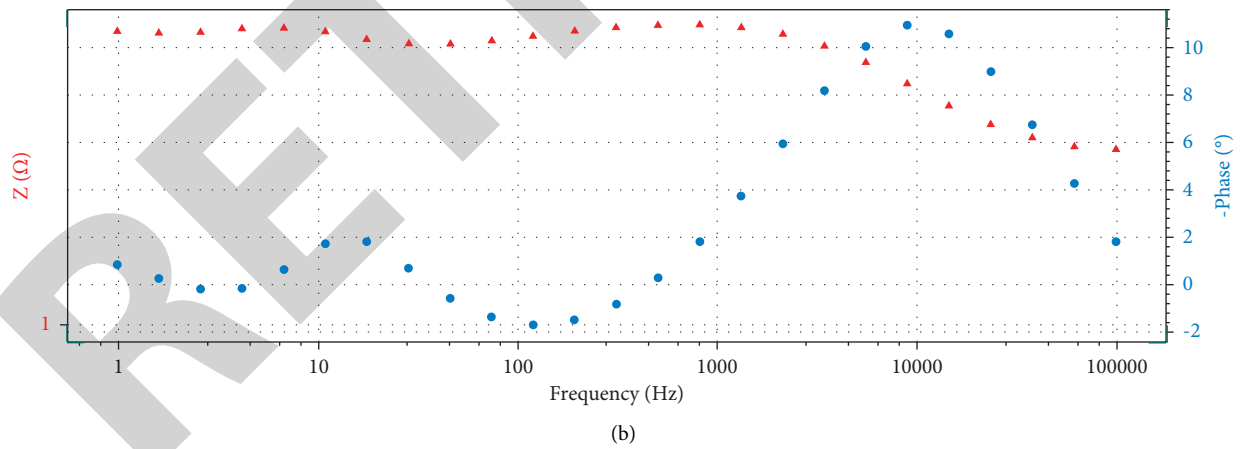


(c)

FIGURE 7: Electrochemical impedance spectra (Nyquist plot) of WC-flyash-coated GrA1 steel.



(a)



(b)

FIGURE 8: Continued.

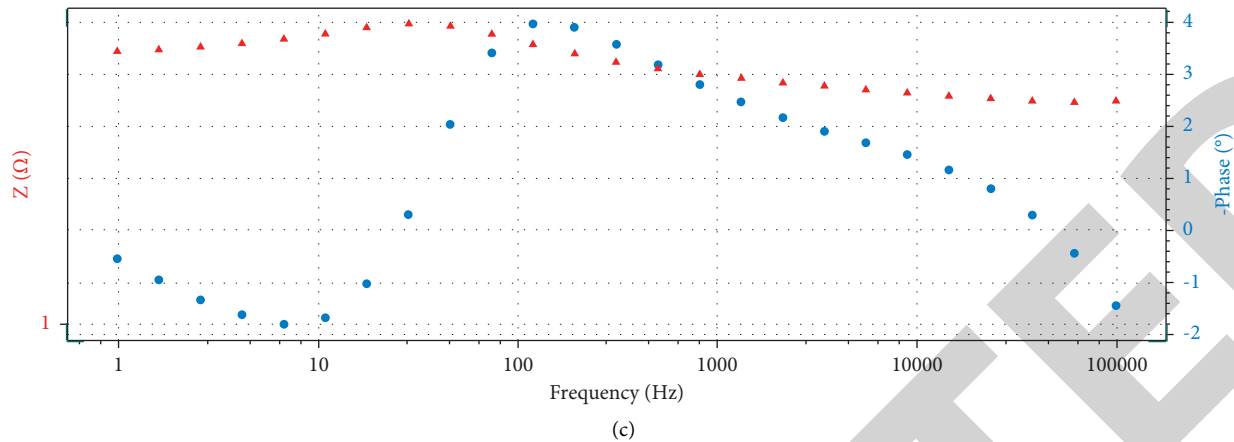


FIGURE 8: Phase angle plots of uncoated GrA1, interface, and WC-flyash-coated GrA1 steel.

4. Conclusions

The curiosity of this examination was promoted through the use of cathodic assurance to kill the impacts of erosion under 3.5% NaCl climate. The HVOF splash measure gives the chance of creating WC-flyash coatings on evaporator tube steel. The uncovered substrate steel shows extreme spalling, stripping off scale and weight acquired was substantial during electrochemical consumption concentrated under the climate of 3.5% NaCl arrangement. Fe_2O_3 was distinguished as the significant stage by SEM and EPMA investigation in the size of uncovered steel. The coating porosity lies between the scope of 1–3.5%, which was discovered to be helpful in creating consumption opposition in heater tube steel (GrA1). WC-flyash covering shows the least estimation of porosity and gave better protection from consumption. The arrangement of defensive oxides like NiCr_2O_4 , NiO , and C_2O_3 in the scale could be added to the better consumption opposition of coatings. Spalling of scale for WC-flyash coatings was nearly less. The associated dissipation with tungsten from the scale may have ascribed to the least consumption opposition as demonstrated by 90% WC-10% flyash covering.

Data Availability

The data used to support the findings of this study are included within the article.

Disclosure

This work was performed as a part of the employment of Addis Ababa Science and Technology University, Ethiopia.

Conflicts of Interest

The authors declare that there are no conflicts of interest.

References

- [1] R. A. Rapp and Y.-S. Zhang, "Hot corrosion of materials: fundamental studies," *Journal of the Minerals Metals & Materials Society*, vol. 46, no. 12, pp. 47–55, 1994.
- [2] S. Srikanth, Z. Wang, H. Tu et al., "Functional properties of the *Drosophila melanogaster* inositol 1,4,5-trisphosphate receptor mutants," *Biophysical Journal*, vol. 86, no. 6, pp. 3634–3646, 2004.
- [3] C. I. Walker, "Slurry pump side-liner wear: comparison of some laboratory and field results," *Wear*, vol. 250, no. 1–12, pp. 81–87, 2001.
- [4] K. Sugiyama, S. Nakahama, S. Hattori, and K. Nakano, "Slurry wear and cavitation erosion of thermal-sprayed cermets," *Wear*, vol. 258, no. 5–6, pp. 768–775, 2005.
- [5] L. Pawlowski, *The Science and Engineering of Thermal Spray Coatings*, Wiley, Hoboken, NJ, USA, 2008.
- [6] M. Ivosevic, R. A. Cairncross, and R. Knight, "3D predictions of thermally sprayed polymer splats: modeling particle acceleration, heating and deformation on impact with a flat substrate," *International Journal of Heat and Mass Transfer*, vol. 49, no. 19–20, pp. 3285–3297, 2006.
- [7] G. Bolelli, L. Lusvardi, and M. Barletta, "HVOF-sprayed WC-CoCr coatings on Al alloy: effect of the coating thickness on the tribological properties," *Wear*, vol. 267, no. 5–8, pp. 944–953, 2009.
- [8] D. Chuanxian, H. Bingtang, and L. Huiling, "Plasma-sprayed wear-resistant ceramic and cermet coating materials," *Thin Solid Films*, vol. 118, no. 4, pp. 485–493, 1984.
- [9] X. Ning, C. Wiraja, D. C. S. Lio, and C. Xu, "Al dmpffscoating," *Advanced healthcare materials*, vol. 9, no. 10, Article ID 2000147, 2020.
- [10] A. Ibrahim and C. C. Berndt, "Fatigue and deformation of HVOF sprayed WC-Co coatings and hard chrome plating," *Materials Science and Engineering A*, vol. 456, no. 1–2, pp. 114–119, 2007.
- [11] T. S. Sidhu, S. Prakash, and R. D. Agrawal, "State of the a coating investigations-A review," *Marine Technology Society Journal*, vol. 39, no. 2, pp. 53–64, 2005.
- [12] E. Sadeghi and S. Joshi, "Chlorine-induced high-temperature corrosion and erosion-corrosion of HVOF and HVOF-sprayed amorphous Fe-based coatings," *Surface and Coatings Technology*, vol. 371, pp. 20–35, 2019.

Retraction

Retracted: Parameters of Porosity and Compressive Strength-Based Optimization on Reinforced Aluminium from the Recycled Waste Automobile Frames

Advances in Materials Science and Engineering

Received 26 December 2023; Accepted 26 December 2023; Published 29 December 2023

Copyright © 2023 Advances in Materials Science and Engineering. This is an open access article distributed under the Creative Commons Attribution License, which permits unrestricted use, distribution, and reproduction in any medium, provided the original work is properly cited.

This article has been retracted by Hindawi, as publisher, following an investigation undertaken by the publisher [1]. This investigation has uncovered evidence of systematic manipulation of the publication and peer-review process. We cannot, therefore, vouch for the reliability or integrity of this article.

Please note that this notice is intended solely to alert readers that the peer-review process of this article has been compromised.

Wiley and Hindawi regret that the usual quality checks did not identify these issues before publication and have since put additional measures in place to safeguard research integrity.

We wish to credit our Research Integrity and Research Publishing teams and anonymous and named external researchers and research integrity experts for contributing to this investigation.

The corresponding author, as the representative of all authors, has been given the opportunity to register their agreement or disagreement to this retraction. We have kept a record of any response received.

References

- [1] A. Parthiban, V. Vijayan, T. Sathish et al., "Parameters of Porosity and Compressive Strength-Based Optimization on Reinforced Aluminium from the Recycled Waste Automobile Frames," *Advances in Materials Science and Engineering*, vol. 2021, Article ID 3648480, 10 pages, 2021.

Research Article

Parameters of Porosity and Compressive Strength-Based Optimization on Reinforced Aluminium from the Recycled Waste Automobile Frames

A. Parthiban,¹ V. Vijayan ,² T. Sathish ,³ S. Dinesh Kumar,⁴ L. Ponraj Sankar,⁵ N. Parthipan,⁶ Dawit Tafesse ,⁷ and Mebratu Tufa ⁷

¹Department of Mechanical Engineering, Vels Institute of Science Technology & Advanced Studies, Pallavaram, Chennai 600 117, Tamil Nadu, India

²Department of Mechanical Engineering, K. Ramakrishnan College of Technology (Autonomous), Samayapuram, Trichy 621 112, Tamil Nadu, India

³Department of Mechanical Engineering, Saveetha School of Engineering, SIMATS, Chennai 602 105, Tamil Nadu, India

⁴Department of Mechanical Engineering, St. Peter's Institute of Higher Education and Research, Avadi, Chennai 600 054, Tamil Nadu, India

⁵Department of Civil Engineering, CMR Institute of Technology, Hyderabad, India

⁶Department of Mechanical Engineering, M. Kumarasamy College of Engineering, Karur, Tamil Nadu, India

⁷Department of Mechanical Engineering, Faculty of Manufacturing, Institute of Technology, Hawassa University, Hawassa, Ethiopia

Correspondence should be addressed to T. Sathish; sathish.sailer@gmail.com and Dawit Tafesse; dawitt@hu.edu.et

Received 25 June 2021; Revised 22 July 2021; Accepted 16 October 2021; Published 8 November 2021

Academic Editor: Samson Jerold Samuel Chelladurai

Copyright © 2021 A. Parthiban et al. This is an open access article distributed under the Creative Commons Attribution License, which permits unrestricted use, distribution, and reproduction in any medium, provided the original work is properly cited.

Automobile industries were ready to recycle the waste old parts as well as the damaged parts of the old vehicles as much as possible. This study mainly focused on the recycling of the waste and damaged aluminium frames of the automobile bodies. These aluminium-based frames only collected the metal matrix composite created by reinforcement of 3% silicon carbide (SiC) and 3% high carbon steel. The stir casting method is chosen to make the composites. Optimization is done by Taguchi ANOVA technique. Three input parameters such as stir speed, time of squeeze, and the temperature of the preheating were considered. The outputs such as compressive strength and porosity were experimentally measured with the combination of nine (L9) experimental trails. The measured experimental results were analyzed and optimized with the help of Taguchi technique with different plots for clear identification. The optimized parameters based on low porosity and high compressive strength were recommended for conclusion.

1. Introduction

Nowadays, recycling the wastes is considered as the new production in the industrial world. In automobile industry, arrival of the new vehicles leads to increasing old vehicle scraps. Krishnan et al. [1] entirely studied about scrap of aluminium-used composites' metal matrix. The source aluminium is clearly collected and used from the wastes. They provide explanation and accomplishment suggestion concerning different methods bringing into play for creation

through those wastes as well as scraps. Furthermore, they explained the various composite material microstructure behavior and composite material mechanical properties with various experiment results.

Similarly, Gupta and Satyanarayana [2] completely discussed the solidification procedure on metal matrix composites of aluminium with the help of various researchers point of view. There are different methods, processes, combination of composite materials and corresponding parameters considered, and optimization

methods used for the metal matrix. They also mentioned individually in a clear manner. Gesing and Wolanski [3], without a doubt, argued on the subject of recycling the light metals from the used vehicles and spare parts of the automobiles and scraps. These suggestions afford assurance to generate research work related to this method.

Christy et al. [4] discussed the stir and squeeze casting input parameters optimization by using the technique of Taguchi with four different input and outputs for the experiments. They express the microstructures to identify the relation of the experimental result outcomes. They used the aluminium alloy wheel scrap for the formation of the composites by the method of stir casting. They optimized with help of the Taguchi method based on the preferable mechanical properties' outcomes and also explained them with optical microscopic images, scanning electron microscopic images, and diffraction of X-ray and X-ray spectroscopy. Importance of the porosity was explained.

The fundamental belongings to the optimization method for different reinforced composites such as Al reinforced to nanomaterials [5], Al reinforced to ZrC [6], and Al reinforced to silicon carbide [7] were discussed clearly. In the same way, various operations such as turning process [8], diffusion bonding [9], laser welding process [10], electrochemical machining [11], and A-GTAW welding [12] were experimentally tried in each article with different parameters and responses.

Mazahery and Shabani [13] undoubtedly investigated the composites of sintered Al matrix regarding the abrasive wear behavior and microstructure property with various experiments and clear comparison on results. Dai et al. [14] explained about the aluminium scrap details and aluminium content based on recycling and also expressed about the fibers of carbon materials. They also mentioned that the scrap of the aluminium material-based car parts was increased day by day due to the need of the increasing vehicles with different articles' reference.

Cullen and Allwood [15] explained about liquid aluminium-based product conversion into global usages. They created the recycled secondary products of aluminium by using the ancient scraps of aluminium collected from different places of the customers. They used recycling in the closed loop method. Oliveux et al. [16] reviewed various articles regarding the reinforcement of composites with various methods. They mentioned about the reuse and recycling of different composites.

Mishra and Srivastava [17] explained about the wear behavior of the composite of aluminium alloy with silicon carbide with the number of SEM images with respect to the load variation. They clearly mentioned the microstructures of the composites. Almadhoni and Khan [18] reviewed the metal matrix composite research article with different combinations and different compositions of various metals. They mainly focused the stir casting process with three major parameters such as temperature of the die and speed of the stirrer. They also conclude that the speed of the stirrer is directly proportional to the homogenous collaboration on the reinforcement matrix of aluminium alloys.

Chandla et al. [19] reviewed the stir casting process with the aluminium alloy-based composites. They mainly listed the various combinations of materials such as alumina, silicon carbide, barium carbide, red mud, iron oxide, aluminium oxide, frit, graphite, carbon nano tube, zirconium oxide titanium carbide, and other materials in different percentage volumes with aluminium alloy-based composites. They compared the considered parameter variations and mentioned the corresponding properties augmentations for single metal matrix composites and hybrid composite metal matrix. Silicon carbide-based stir casting parameters are also compared with their consequences.

Arulraj et al. [20], Manivannan and Sasikumar [21], M. K. Sahu and R. K. Sahu [22], and Aravindan et al. [23] clearly explained the following. Stir casting method retains numerous benefits over further conventional techniques such as less handling cost, high homogeneity between the particulates, absorption of moisture is low, and suitable for huge manufacture. It is also preferable for different sizes with various shapes and dimensions. Due to its simple method for the production, it is the most preferable one for the production industry. This can be used to reduce the cost of the production from 10% to 35% of the other methods used for production.

In this paper, reinforced composite was created from the waste automobile frames by recycling along with reinforcement materials such as silicon carbide and high carbon steel. These composite specimens were prepared by the stir casting method. The suitable stir casting parameters will be selected based on properties such as porosity and compressive strength by the optimization method.

1.1. Experimental Procedure. From the automobile industries, automobile service centres, and mechanic workshops, the samples of the aluminium frames were collected and converted into small scrap pieces. The scraps of aluminium having composition such as 0.95% of magnesium, 0.7% of silicon, 0.68% of iron, 0.39% of copper, 0.31% of zinc, 0.16% of manganese, 0.2% of titanium, and 0.4% of chromium, and then, the remaining have aluminium content in the percentage of weight basis. There is 92% of scrap particles reinforcement with two materials for the remaining percentage of volume concentrations.

There is 3% of silicon carbide, and the remaining 3% is utilized with the high carbon steel. All these materials were in the form of powder. The scrap aluminium material is powered by using the ball bearing pulveriser. Then, these materials were placed into the stir casting machine. This stir casting has the pouring method in the bottom side. The machine shown in Figure 1 has the electrical furnace, reinforcement preheating chamber, runway preheater, hydraulic sequence pressure ram, and electrical control panel.

In this optimization-based investigation, L9 ANOVA table is used as per Table 1. It contains variations in holding temperature which were 300°C, 400°C, and 500°C. The squeezing time considered were 20 sec deviation from the 20 sec to 60 sec. Then, the stir speed is maintained with 100 rpm variation starting with 400 rpm to 600 rpm. The holding pressure is



FIGURE 1: Stir casting machine.

TABLE 1: Details of experimental parameters (L9).

Trail of experiment no.	Holding temperature as temp (°C)	Time as t in sec	Stir speed as N in rpm
TE 1	300	20	400
TE 2	300	40	500
TE 3	300	60	600
TE 4	400	20	500
TE 5	400	40	600
TE 6	400	60	400
TE 7	500	20	600
TE 8	500	40	400
TE 9	500	60	500

maintained as 120 MPa throughout the process. The specimens were prepared for both desired properties such as porosity and compressive strength with the dimensions of 40 mm diameter and 30 mm height in small cylinders.

The porosity of the specimens was calculated with the traditional formula that if the ratio of the experimental and theoretical density values was multiplied by 100, then the total value is subtracted from the number one. By Archimedes principle, the experimental density of the individual sample specimen is obtained. Similarly, the theoretical density is obtained from the rule of the mixture on the specimen. Then, the compressive strength is measured by the traditional method in a universal testing machine with compressive strength analyzed as per the ASTM standards such as ASTM E9. Porosity and compressive strength of the individual specimen was tested as per Table 1.

2. Results and Discussion

2.1. Porosity. The experimentally measured values of porosity and the compressive strength are mentioned in Table 2

TABLE 2: Experimental results for the trails of experiments.

Trail of experiment no.	Porosity in %	Compressive strength CS in MPa
TE 1	12.328	319.44
TE 2	18.215	345.58
TE 3	24.102	371.72
TE 4	12.155	306.34
TE 5	18.042	332.48
TE 6	22.948	360.72
TE 7	11.982	293.24
TE 8	16.888	321.48
TE 9	22.775	347.62

in detail. There are nine trials which were conducted as per Table 1. Initially, porosity-based results were examined with minimum being the desirable condition. Then, the compressive strength was examined with maximum being the desirable condition. Then, both porosity and compressive strength values were examined with nominal being the suitable condition. All these three examinations were conducted with the help of the Taguchi analysis by using the Minitab 18 software.

Significant consequence diagram based on the SN ratio for experimental results of porosity is clearly mentioned in Figure 2. In this place, minimum porosity in needed condition is used. Significantly minimum results of porosity can be obtained at 500°C of the holding temperature with 20 sec of the holding time and 400 rpm speed of the stir in the stir casting process. Likewise, the significant consequence diagram based on the means of porosity is shown in Figure 3. The maximum porosity is obtained at the input parameters such as 300°C of the holding temperature with 60 sec of the holding time and 600 rpm speed of the stir. From these two diagrams, minimum and maximum porosity obtaining parameters were clearly obtained.

Comparison of porosity responses using contour plots is shown in Figure 4. There are three different contour plots such as time in competition with temperature, speed contrasted with temperature, and speed versus time available based on the porosity results. The variations on the contour plot were expressed in the form of the colour variation with the various ranges for the individual colours based on the intensity of the experimental results achieved from the experiments. Similarly, Figure 5 shows the surface plots comparison for porosity as the three-in-one diagram. In this diagram, porosity in the vertical direction and the remaining two directions in each diagram are time-contrasted with temperature, speed as opposed to temperature, and speed in competition with time, respectively.

Significant consequence table for porosity is clearly mentioned in Table 3 for both SN ratio and means response. The highest priority of the parameters reached as rank of one, two and three for the holding time, stir speed, and holding temperature in the same order. So, the holding time has the superior contribution when compared to other similar speed of the stir which has the least significant contribution based on the minimum porosity outcomes. The corresponding regression equation is given as follows for the considered parameter-based experimental results:

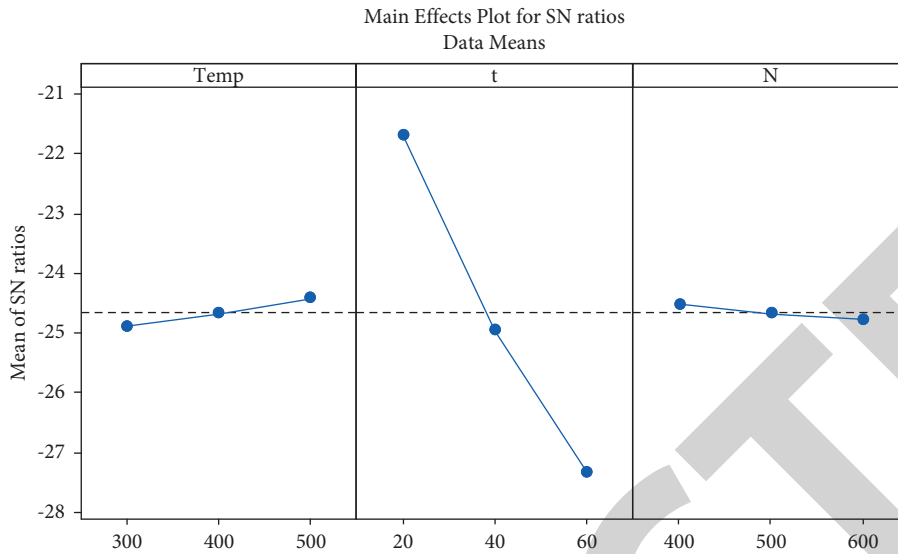


FIGURE 2: Significant consequence diagram based on the SN ratio for porosity (temp: temperature in °C; *t*: time in sec; and *N*: stir speed in rpm).

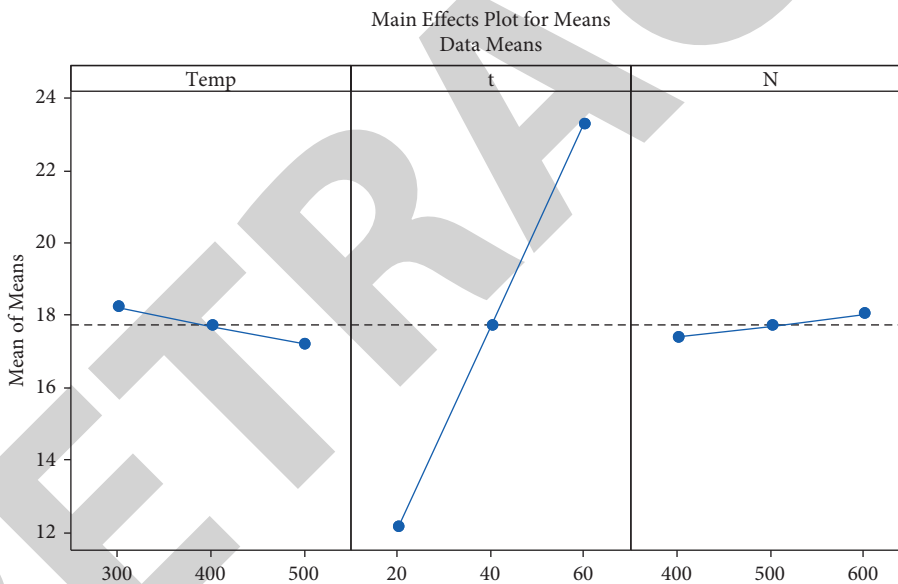


FIGURE 3: Significant consequence diagram based on means for porosity (temp: temperature in °C; *t*: time in sec; *N*: stir speed in rpm).

regression equation for porosity

$$= 6.960 - 0.005000 \text{ temp} + 0.2780 t + 0.003270 N. \quad (1)$$

2.2. *Compressive Strength.* Significant consequence diagram based on the SN ratio for compressive strength is evidently pointed out in Figure 5. Similarly, Figure 6 explains about the significant consequence diagram based on means for compressive strength. These two figures were supported each other with the same condition such that the greatest compressive strength is preferable. These two figures based on the experimental outcomes of the compressive strength results obviously point out that the uppermost compressive strength is obtained for the input parameters such as 300°C

of the holding temperature with 60 sec of the holding time and 400 rpm speed. Likewise, the lowest compressive strength is obtained for the input parameters such as 500°C of the holding temperature with 20 sec of the holding time and 600 rpm of stir speed of the stir in the friction stir operation.

Figure 7 unmistakably shows the contour plots comparison such as speed with respect to temperature, time with respect to temperature, and speed with respect to time for the compressive strength results with different colour intensities for different range of results in Figure 8. Similarly, Figure 9 demonstrates the surface plots comparison such as compressive strength in vertical axis and horizontal axis which were mentioned with speed versus temperature, time versus temperature, and speed versus time. Table 3 provides

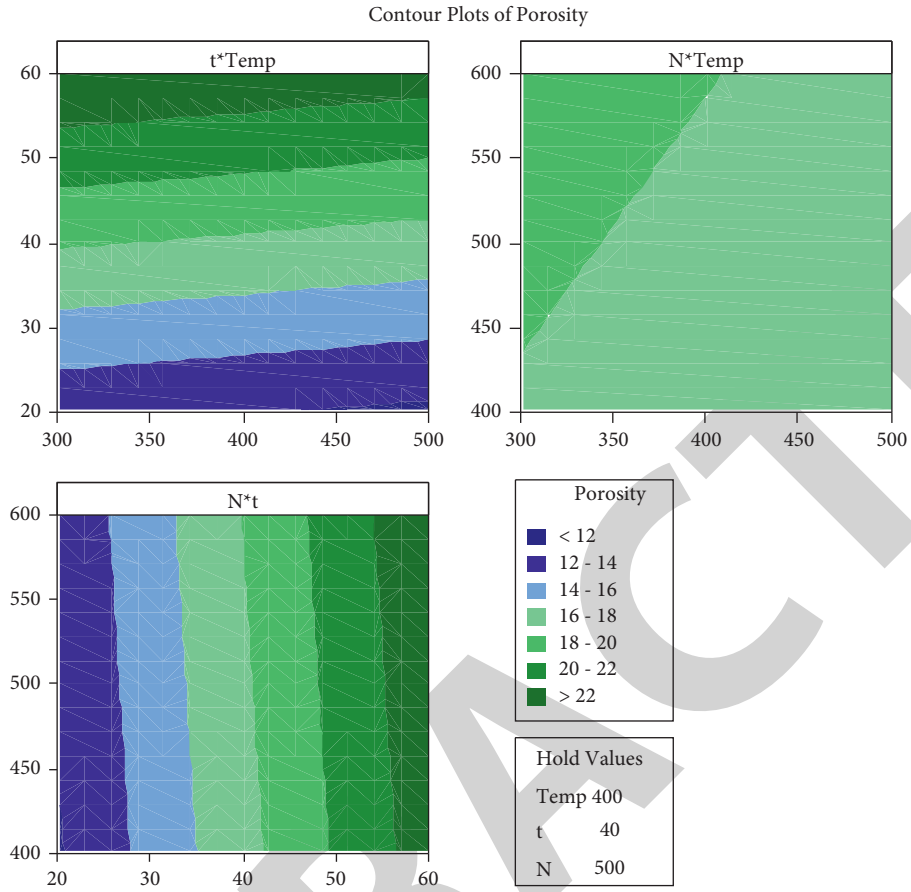


FIGURE 4: Contour plots comparison for porosity (temp: temperature in °C; t : time in sec; N : stir speed in rpm).

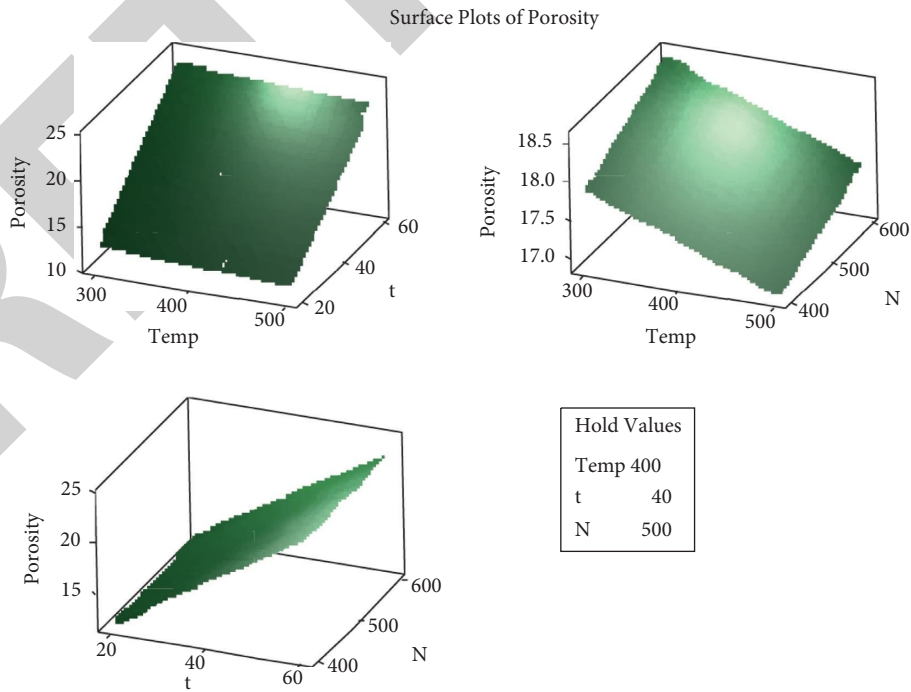


FIGURE 5: Comparison of surface plots for porosity (temp: temperature in °C; t : time in sec; N : stir speed in rpm).

TABLE 3: Significant consequence for porosity.

Level	Response for SN ratio			Response for means		
	Temperature (°C)	Time (sec)	Stir speed (rpm)	Temperature (°C)	Time (sec)	Stir speed (rpm)
1	-24.89	-21.69	-24.53	18.22	12.15	17.39
2	-24.68	-24.96	-24.68	17.72	17.72	17.72
3	-24.42	-27.34	-24.78	17.22	23.28	18.04
Delta	0.47	5.64	0.25	1.00	11.12	0.65
Rank	2	1	3	2	1	3

Temp: temperature in °C; t: time in sec; N: stir speed in rpm

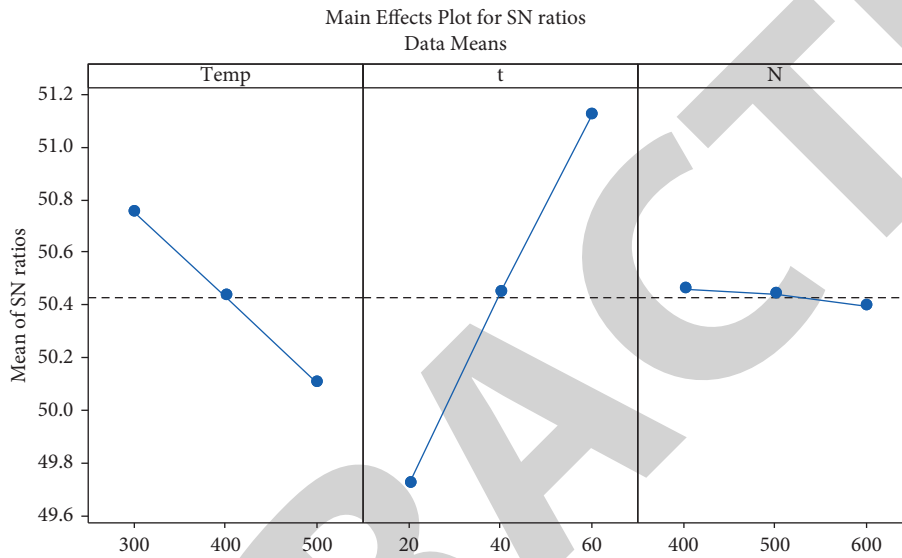


FIGURE 6: Significant consequence diagram based on the SN ratio for compressive strength (temp: temperature in °C; t: time in sec; N: stir speed in rpm).

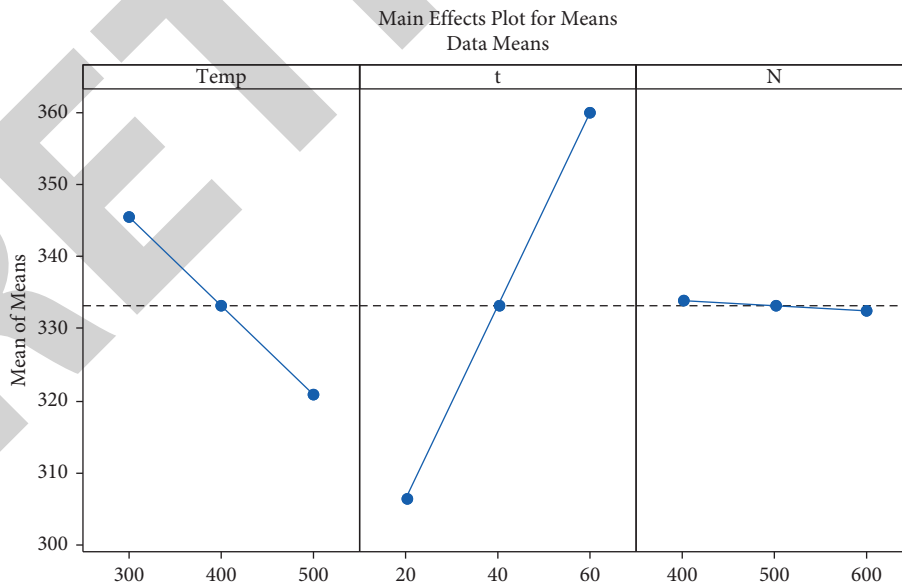


FIGURE 7: Significant consequence diagram based on means for compressive strength (temp: temperature in °C; t: time in sec; N: stir speed in rpm).

the response of the compressive strength based on SN ratio and means. Here, larger is better condition is used. The first, second, and third ranks are provided for time, holding

temperature, and stir speed, respectively and the corresponding regression equation is mentioned as follows for the compressive strength based on the input parameters used:

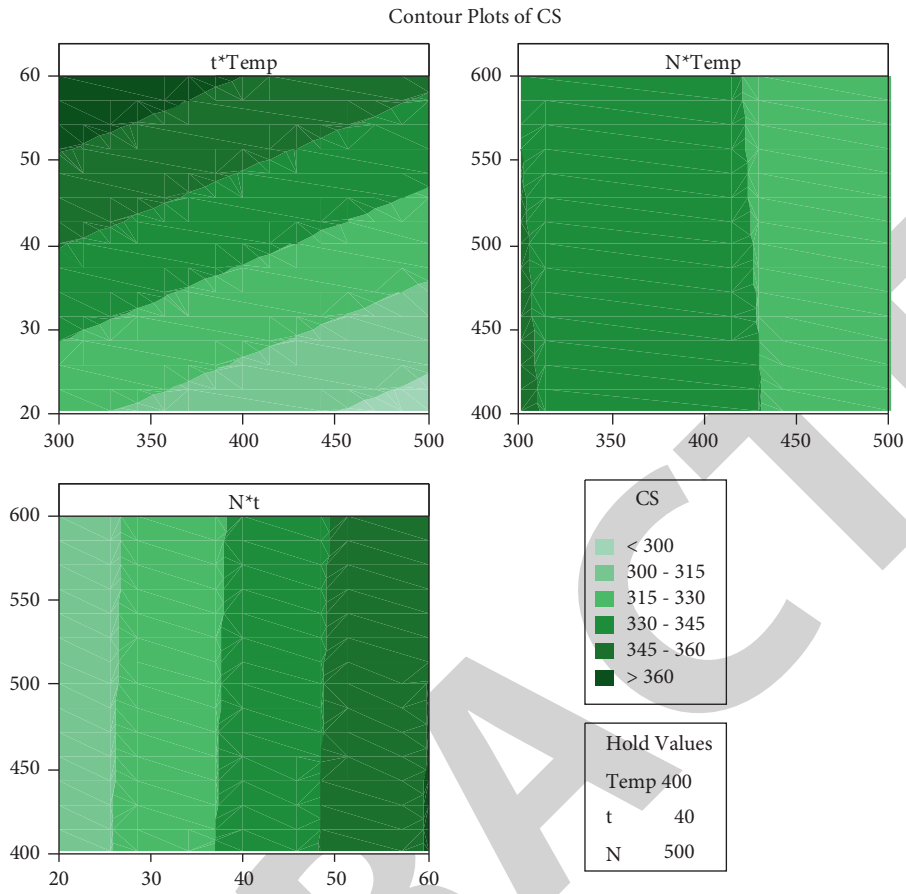


FIGURE 8: Comparison of the compressive strength using contour plots (temp: temperature in °C; t: time in sec; N: stir speed in rpm).

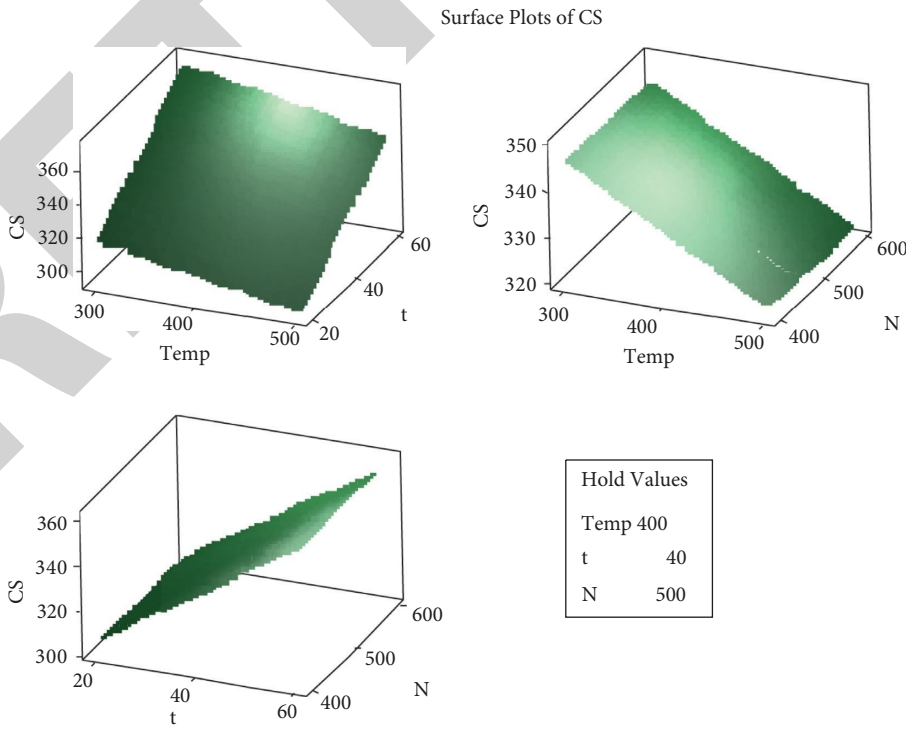


FIGURE 9: Comparison of the compressive strength using surface plots (temp: temperature in °C; t: time in sec; N: stir speed in rpm).

TABLE 4: Porosity and compressive strength-based responses.

Level	Temperature (°C)	Time (sec)	Stir speed (rpm)
1	-47.28	-46.36	-46.99
2	-46.95	-46.96	-46.96
3	-46.62	-47.53	-46.91
Delta	0.66	1.18	0.08
Rank	2	1	3

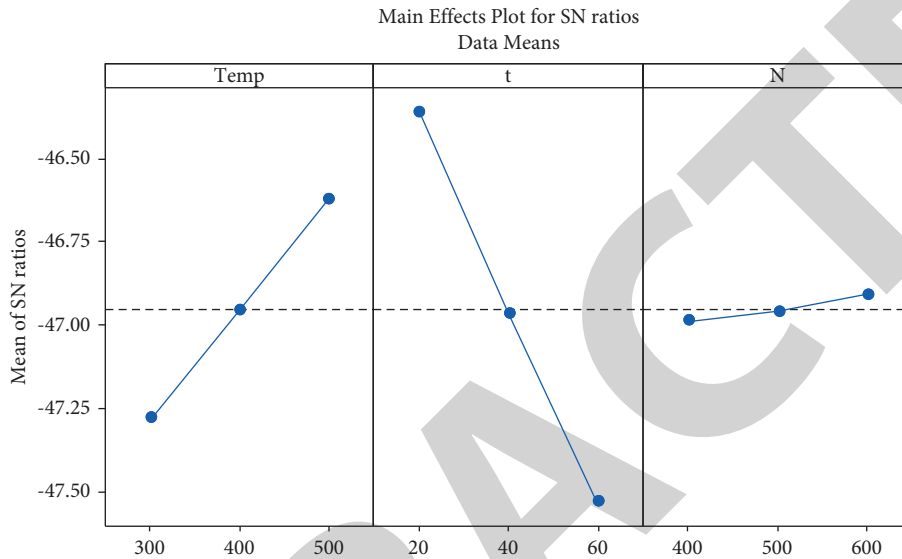


FIGURE 10: Significant consequence diagram based on the SN ratio for porosity and compressive strength (temp: temperature in °C; t: time in sec; N: stir speed in rpm).

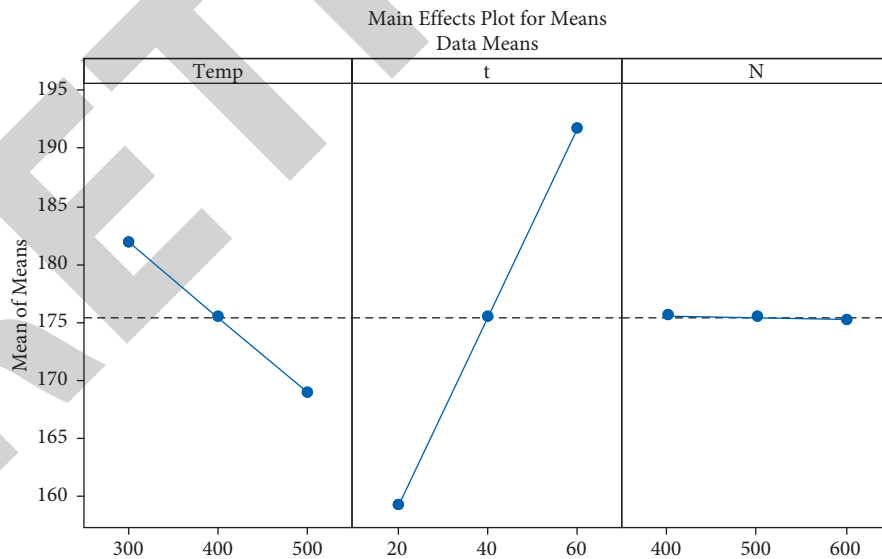


FIGURE 11: Significant consequence diagram based on means for porosity and compressive strength (temp: temperature in °C; t: time in sec; N: stir speed in rpm).

regression equation for compressive strength
 $= CS = 332.6 - 0.1240 \text{ temp} + 1.342 t - 0.007000 N.$

(2)

2.3. Porosity and Compressive Strength. After completing the individual optimization based on porosity and compressive strength values, the combination of these two was considered with nominal being the best condition in Table 4.

TABLE 5: Compressive strength response table.

Level	Response for SN ratio			Response for means		
	Temperature (°C)	Time (sec)	Stir speed (rpm)	Temperature (°C)	Time (sec)	Stir speed (rpm)
1	50.75	49.72	50.46	345.6	306.3	333.9
2	50.43	50.45	50.44	333.2	333.2	333.2
3	50.10	51.12	50.39	320.8	360.0	332.5
Delta	0.65	1.40	0.06	24.8	53.7	1.4
Rank	2	1	3	2	1	3

Figure 10 shows the significant consequence diagram based on the SN ratio for porosity and compressive strength. Similarly, Figure 11 shows the significant consequence diagram based on means for porosity and compressive strength. From Figures 10 and 11, the nominal results can be achieved for the input parameters such as 500°C of the holding temperature with 20 sec of the holding time and 600 rpm speed of the stir. Table 5 provides the porosity and compressive strength-based responses with the ranks such as first rank for time, second rank for holding temperature, and last rank for stir speed. Time is superior and most important parameter for porosity and compressive strength. Among these three cases, speed of stir obtained the very low preference for the responses.

3. Conclusion

This study on parameters of porosity and compressive strength-based optimization on reinforced aluminium from the recycled waste automobile frames can be possible, and the corresponding conclusions are as follows:

- (i) The lowest porosity-based optimum parameters were 500°C of holding temperature with 20 sec of holding time and 400 rpm speed of the stir
- (ii) The maximum compressive strength-based optimum parameters were 300°C of holding temperature with 60 sec of holding time and 400 rpm speed of the stir
- (iii) The porosity and compressive strength-based optimum parameters were 500°C of holding temperature with 20 sec of holding time and 600 rpm speed of the stir
- (iv) In future, the work was extended to conduct the impact test for checking the impact strength of the frame in the vehicle and also planned to conduct the corrosion test of the reinforced composites

Data Availability

The data used to support the findings of this study are included in the article. Further data or information which are required are available from the corresponding author upon request.

Disclosure

This work was performed as a part of the Employment Hawassa University, Ethiopia.

Conflicts of Interest

The authors declare that there are no conflicts of interest regarding the publication of this paper.

Acknowledgments

The authors appreciate the support from Hawassa University, Ethiopia. The authors thank Saveetha School of Engineering, SIMATS, Saveetha University, Chennai, Tamil Nadu, India, for the Technical Assistance to complete this experimental work.

References

- [1] P. K. Krishnan, J. V. Christy, R. Arunachalam et al., "Production of aluminum alloy-based metal matrix composites using scrap aluminum alloy and waste materials: influence on microstructure and mechanical properties," *Journal of Alloys and Compounds*, vol. 784, pp. 1047–1061, 2019.
- [2] N. Gupta and K. G. Satyanarayana, "Symposium review: solidification processing of MMCs," *Journal of Materials Science*, vol. 58, no. 6, pp. 91–93, 2006.
- [3] A. Gesing and R. Wolanski, "Recycling light metals from end-of-life vehicle," *Journal of the Minerals Metals & Materials Society*, vol. 53, no. 11, pp. 21–23, 2001.
- [4] J. V. Christy, R. Arunachalam, A.-H. I. Mourad et al., "Processing, properties, and microstructure of recycled aluminum alloy composites produced through an optimized stir and squeeze casting processes," *Journal of Manufacturing Processes*, vol. 59, pp. 287–301, 2020.
- [5] T. Sathish, K. Muthukumar, R. Saravanan, and V. Dhinakaran, "Study on temperature difference of aluminium nitride nanofluid used in solar flat plate collector over normal water," *AIP Conference Proceedings*, vol. 2283, no. No. 1, Article ID 020126, 2020.
- [6] T. Sathish and N. Sabarirajan, "Synthesis and optimization of AA 7175 - Zirconium Carbide (ZrC) composites machining parameters," *Journal of New Materials for Electrochemical Systems*, vol. 24, no. 1, pp. 34–37, 2021.
- [7] T. Sathish, N. Sabarirajan, and S. Karthick, "Machining parameters optimization of Aluminium Alloy 6063 with reinforcement of SiC composites," *Materials Today: Proceedings*, vol. 33, pp. 2559–2563, 2020.
- [8] S. P. Palaniappan, K. Muthukumar, R. V. Sabariraj, S. Dinesh Kumar, and T. Sathish, "CNC Turning process parameters optimization on Aluminium 6082 alloy by using Taguchi and ANOVA," *Materials Today: Proceedings*, vol. 21, pp. 1013–1021, 2020.
- [9] T. Sathish, S. Dinesh Kumar, K. Muthukumar, and S. Karthick, "Temperature distribution analysis on diffusion bonded joints of Ti-6Al-4V with AISI 4140 medium carbon

Retraction

Retracted: Optimizing the Characteristics of the Laser Hardfacing Process Parameters to Maximize the Wear Resistance of Ni-Based Hard-Faced Deposits Using the RSM Technique

Advances in Materials Science and Engineering

Received 23 January 2024; Accepted 23 January 2024; Published 24 January 2024

Copyright © 2024 Advances in Materials Science and Engineering. This is an open access article distributed under the Creative Commons Attribution License, which permits unrestricted use, distribution, and reproduction in any medium, provided the original work is properly cited.

This article has been retracted by Hindawi following an investigation undertaken by the publisher [1]. This investigation has uncovered evidence of one or more of the following indicators of systematic manipulation of the publication process:

- (1) Discrepancies in scope
- (2) Discrepancies in the description of the research reported
- (3) Discrepancies between the availability of data and the research described
- (4) Inappropriate citations
- (5) Incoherent, meaningless and/or irrelevant content included in the article
- (6) Manipulated or compromised peer review

The presence of these indicators undermines our confidence in the integrity of the article's content and we cannot, therefore, vouch for its reliability. Please note that this notice is intended solely to alert readers that the content of this article is unreliable. We have not investigated whether authors were aware of or involved in the systematic manipulation of the publication process.

Wiley and Hindawi regrets that the usual quality checks did not identify these issues before publication and have since put additional measures in place to safeguard research integrity.

We wish to credit our own Research Integrity and Research Publishing teams and anonymous and named external researchers and research integrity experts for contributing to this investigation.

The corresponding author, as the representative of all authors, has been given the opportunity to register their agreement or disagreement to this retraction. We have kept a record of any response received.

References

- [1] S. Gnanasekaran, S. J. S. Chelladurai, T. Ramakrishnan et al., "Optimizing the Characteristics of the Laser Hardfacing Process Parameters to Maximize the Wear Resistance of Ni-Based Hard-Faced Deposits Using the RSM Technique," *Advances in Materials Science and Engineering*, vol. 2021, Article ID 3665631, 15 pages, 2021.

Research Article

Optimizing the Characteristics of the Laser Hardfacing Process Parameters to Maximize the Wear Resistance of Ni-Based Hard-Faced Deposits Using the RSM Technique

S. Gnanasekaran ¹, Samson Jerold Samuel Chelladurai ², T. Ramakrishnan ³,
S Sivananthan ⁴, G. Padmanaban ⁵, Ramesh Arthanari ⁶ and V. Balasubramanian ⁵

¹Department of Mechanical Engineering, Sri Shakthi Institute of Engineering and Technology, Chinniyampalayam, Coimbatore, Tamil Nadu, India

²Department of Mechanical Engineering, Sri Krishna College of Engineering and Technology, Coimbatore, Tamilnadu, India

³Department of Mechanical Engineering, Sri Eshwar College of Engineering, Coimbatore, Tamilnadu, India

⁴Department of Mechanical Engineering, K. Ramakrishnan College of Engineering, Tamilnadu, India

⁵Centre for Materials Joining & Research (CEMAJOR), Department of Manufacturing Engineering, Annamalai University, Annamalaiagar, Tamil Nadu, India

⁶Department of Mechanical Engineering, Chennai Institute of Technology, Tamil Nadu, India

Correspondence should be addressed to Samson Jerold Samuel Chelladurai; samsonjeroldsamuel@skcet.ac.in

Received 5 August 2021; Revised 7 October 2021; Accepted 18 October 2021; Published 1 November 2021

Academic Editor: Angela De Bonis

Copyright © 2021 S. Gnanasekaran et al. This is an open access article distributed under the Creative Commons Attribution License, which permits unrestricted use, distribution, and reproduction in any medium, provided the original work is properly cited.

The nickel-based Colmonoy-5 hardfacing alloy is used to hard-face 316LN austenitic stainless steel components in fast reactors. The nominal composition (in wt%) was listed as follows: 0.01 C, 0.49 Si, 0.87 Mn, 17.09 Cr, 14.04 Ni, 2.56 Mo, 0.14 N, and balance Fe. Hardfacing is a technique of applying hard and wear-resistant materials to substrates that need abrasion resistance. The thickness of hardfacing deposit varies between 0.8 mm and 2 mm based on parameter combinations. In this study, laser hardfacing process parameters including laser power, powder feed rate, travel speed, and defocusing distance were optimized to reduce weight loss of laser hard-faced Ni-based deposit. The tribological characteristics of reactor-grade NiCr-B hard-faced deposits were investigated. The RSM technique was used to identify the most important control variables resulting in the least weight loss of the nickel-based alloy placed on AISI 316LN austenitic stainless steel. Statistical techniques like DoE and ANOVA are utilized. Changing the laser settings may efficiently track the weight loss of laser hard-faced nickel alloy surfaces. These are created using the response surface technique. The deposit produced with a laser power of 1314 W, powder feed rate of 9 g/min, travel speed of 366 mm/min, and defocusing distance of 32 mm had the lowest weight loss of 16.4 mg. Based on the F value, the powder feed rate is the major influencing factor to predict the hardness followed by power, travel speed, and defocusing distance.

1. Introduction

Prototype Fast Breeder Reactor (PFBR) is a 500 MWe pool type sodium-cooled nuclear reactor having two separate sodium circuits with the intermediate heat exchanger (IHX) providing thermal contact between the primary pool and the secondary circuit. The secondary sodium circuits transfer heat from the IHX to the steam generator (SG), the steam from which drives the conventional steam turbines. The

minimum sodium temperature in the primary pool during normal operation is 400°C, while the mean above-core temperature is 550°C. The minimum and maximum sodium temperatures in the secondary circuit are 355 and 525°C, respectively. The steam temperature is 490°C at 16.6 MPa pressure. Austenitic stainless steel (SS) is the major material of construction for PFBR. The Main Vessel, Inner Vessel, GridPlate, and Primary Piping, etc., whose service temperatures are above 427°C, are made of numerous austenitic

stainless steel components that come into touch with flowing liquid sodium at temperatures of up to 823 K. Due to the fact that flowing liquid sodium dissolves the oxide layer that typically forms on metallic surfaces, prolonged static contact between mating surfaces may result in self-welding. When components move in relation to one another, galling occurs. By hardfacing these components with nickel or cobalt-based alloy powders, self-welding and galling resistance are increased. While alloys based on Co are extensively used as high-temperature hardfacing materials [1–4], induced radioactivity from transmuted Co^{60} isotopes is generated in a nuclear reactor environment [5, 6]. Colmonoy grades, because of their high chromium and boron content, may be used in place of Co-based Stellite alloys for abrasive and adhesive wear resistance. Colmonoy alloys are tougher than Stellite alloys because they include chromium carbides and borides in the deposit, while Stellite contains just carbide precipitates [7, 8].

Wear resistance is a material's mechanical characteristic that allows it to withstand surface damage during sliding contact [9]. The chemical, physical, and mechanical characteristics of wear-generated scars vary throughout tribological testing. Changes in wear scar morphology may affect frictional force. Wear mechanisms on steel-based alloys are classified as adhesive, abrasive, oxidation, and plastic extrusion [10, 11]. In general, material wear resistance is inversely linked to hardness. This deposit's superior wear resistance to stainless steel extends the life of FBR components. Despite its improved mechanical characteristics, this alloy's friction and wear as a function of sliding distance remain unknown. Hardfacing process factors affect deposit quality. Few studies have examined the impact of laser process parameters on wear characteristics [5]. The softer dilution zone frequently exceeds the ultimate required hardfaced deposit thickness in conventional welding techniques like gas tungsten arc welding (GTAW) and plasma transferred arc welding (PTAW). So, the more flexible laser hardfacing method was selected to minimize the dilution zone by adjusting the deposition settings.

Zhang et al. [12] used a CO_2 laser to clad 316 L austenitic stainless steel with Colmonoy 6 powder. A reduced friction coefficient and higher wear resistance after laser cladding were observed, indicating that the laser cladding layer plays a significant role in wear resistance. Laser cladding microstructures include eutectic, boride, and carbide. Hemmati et al. [13] observed that specimens with laser and PTA hardfacing had friction values of 0.42–0.48 and 0.51–0.58. Laser and PTA hardfacing both lose mass (7 and 380 mg). Laser hardfacing has a lower friction coefficient and a lower wear mass loss than PTA hardfacing. Laser cladding and wear testing of nickel base hardfacing materials have process parameter effects on ASTM [14]. They found that two laser cladding samples with differing travel speeds had very distinct wear processes. The laser cladding process may adapt the hardfacing material quality to the tribology circumstances and applications by varying the process parameters.

As the process facts have not been revealed yet, selecting process parameters for nickel-based alloys is challenging. A many-factor analysis is a set of mathematical and statistical

methods used to model and analyze situations where the goal is to maximize the responses [15]. RSM reduced experimentation and improved process parameters for wear resistance (minimum weight loss). The hardfacing process settings are known to affect the deposits' mechanical and wear resistance. There is no literature available in optimizing the laser hardfacing parameters to attain maximum hardness on nickel-based hard-faced deposit on 316 LN austenitic stainless steel. Hence, in this study, an attempt has been made to optimize the important laser hardfacing parameters to attain maximum hardness in nickel-based hard-faced deposits on 316 LN austenitic stainless steel by RSM.

2. Materials and Methods

The current study's goals were designed as shown in the flow chart (Figure 1).

2.1. Identifying Important Laser Hardfacing Parameters. Choosing variables for the process under study is a first step in designing experiments. Many factors in laser hardfacing have been identified as possibly influencing the deposit's characteristics. It is not feasible to manage all potential parameter changes economically (time) and theoretically (parameter dependency). The following process parameters have been identified as having a greater impact on deposit characteristics: laser power (P), powder feed rate (F), travel speed (T), and defocusing distance (D). All of these factors affect the melting and flattening of powder particles and, therefore, the deposit properties of nickel-based hardfacing.

2.2. Feasible Working Range of Laser Hardfacing Parameters. To determine the possible working limits of laser hardfacing parameters, trial runs were conducted using a 12 mm thick 316 LN austenitic stainless steel plate and nickel-based alloy powder. The experimental tests were conducted using various combinations of factors. This was accomplished by varying the value of any one of the variables from lowest to highest while keeping the other parameters constant (Table 1). Macrostructure was used to determine the practical operating limits of various parameters (cross section of the deposits). The parameter level that produces a deposit with a smooth appearance devoid of visible macrolevel flaws such as fracture and pores was chosen as the parameter's practical working limit. Table 2 lists the selected levels of the specified process parameters, along with their units and notations.

2.3. Developing the Experimental Design Matrix. Taking into account the aforementioned circumstances, the parameter limitations were set so that flawless laser hard-faced deposits could be created. A second-order central composite rotatable design was determined to be the most effective tool in RSM for establishing the empirical connection of the response surface with the least number of trials [16]. To establish an empirical connection, four variables, five levels, and a core composite design matrix were used. The most common response surface technique design is the central

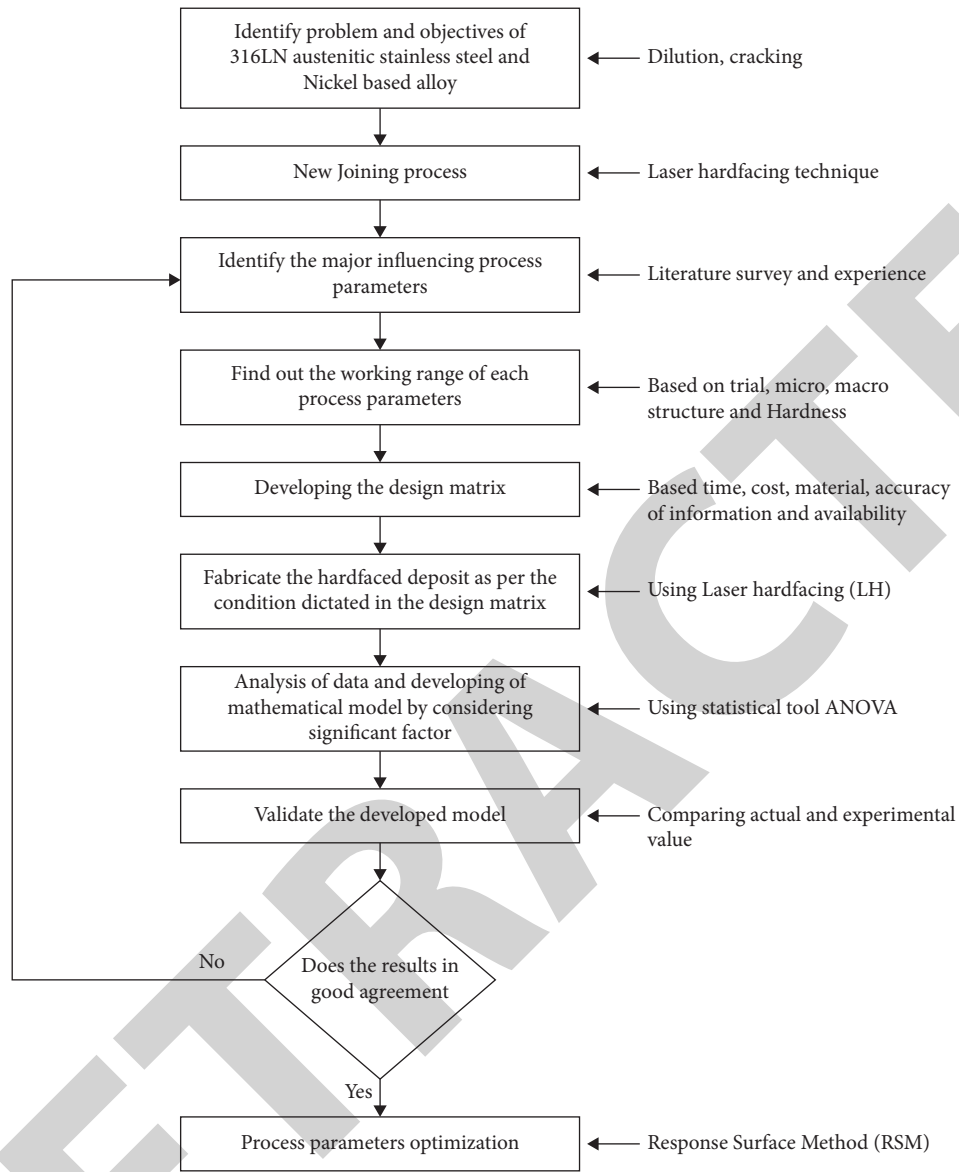


FIGURE 1: Flow chart for process optimization.

TABLE 1: Fixing the working range of laser hardfacing macrostructure analysis.

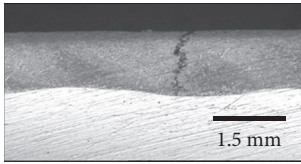
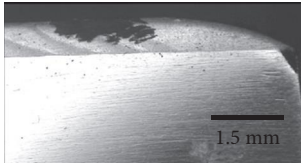
S. no.	Process parameters	Parameter range	Macrograph	Name of the defect
1	Laser power (P)	$P > 1900 \text{ W}$		Crack and high dilution
		$P < 1100 \text{ W}$		Pores and escaping of powder

TABLE 1: Continued.

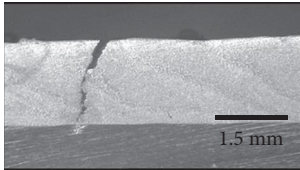
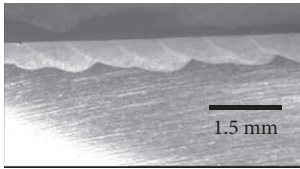
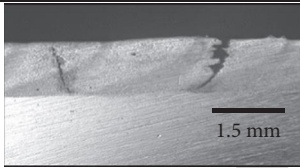
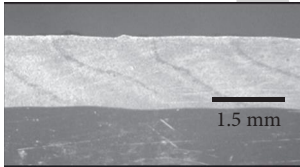
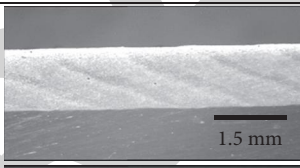
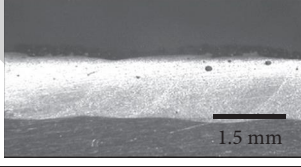
S. no.	Process parameters	Parameter range	Macrograph	Name of the defect
2	Powder feed rate (F)	$F > 11 \text{ g/min}$		Cracks
		$F < 3 \text{ g/min}$		High depth of penetration and high dilution
3	Travel speed (T)	$T > 500 \text{ mm/min}$		Cracks
		$T < 300 \text{ mm/min}$		Excess bead height
4	Defocusing distance (D)	$D > 37 \text{ mm}$		Poor bonding
		$D < 17 \text{ mm}$		Presence of pores

TABLE 2: Laser hard-faced processing parameters and their working range.

S. no.	Factor	Notation	Levels				
			-2	-1	0	1	2
1	Laser power (W)	P	1100	1300	1500	1700	1900
2	Powder feed rate (g/min)	F	3	5	7	9	11
3	Travel speed (mm/min)	T	300	350	400	450	500
4	Defocusing distance (mm)	D	17	22	27	32	37

composite design, which includes three sets of design points: factorial, axial or star, and center. The primary composite design's structure allows for successive experimentation, which is noteworthy. Table 3 displays the design matrix's coded conditions. The design matrix has 30 coded conditions, including 16 four-factor factorial points, 8 star points, and 6 center points.

The star points are formed by combining each process variable's lowest (-2) or highest (+2) level with the other 8 intermediate level variables. In this manner, the 30 experimental conditions enabled estimating the variables' linear, quadratic, and two-way interaction impacts on

microhardness and weight loss of laser hard-faced nickel-based deposits. Making such a matrix was previously discussed [17]. The upper and lower values of the variables are labeled as +2 and -2 for ease of collecting and processing experimental results.

2.4. Developing Empirical Relationships. For example, the hardness of the deposit is a function of power (P), powder feed rate (F), travel speed (T), and defocusing distance (D).

$$f = \text{responses}(P, F, T, D). \quad (1)$$

TABLE 3: Design matrix and experimental results.

Ex no.	Coded value				Actual value				Responses	
	P	F	T	D	P (W)	F (g/m)	T (mm/min)	D (mm)	Microhardness (HV)	Weight loss (mg)
1	-1	-1	-1	-1	1300	5	350	22	573	32.2
2	1	-1	-1	-1	1700	5	350	22	475	41.4
3	-1	1	-1	-1	1300	9	350	22	778	18.3
4	1	1	-1	-1	1700	9	350	22	603	31.3
5	-1	-1	1	-1	1300	5	450	22	475	39
6	1	-1	1	-1	1700	5	450	22	574	29.1
7	-1	1	1	-1	1300	9	450	22	794	25
8	1	1	1	-1	1700	9	450	22	703	18.2
9	-1	-1	-1	1	1300	5	350	32	743	23.8
10	1	-1	-1	1	1700	5	350	32	568	32.8
11	-1	1	-1	1	1300	9	350	32	820	16.4
12	1	1	-1	1	1700	9	350	32	602	32.2
13	-1	-1	1	1	1300	5	450	32	545	36.2
14	1	-1	1	1	1700	5	450	32	581	27.9
15	-1	1	1	1	1300	9	450	32	680	26.8
16	1	1	1	1	1700	9	450	32	648	24.9
17	-2	0	0	0	1100	7	400	27	727	26.2
18	2	0	0	0	1900	7	400	27	551	31.7
19	0	-2	0	0	1500	3	400	27	487	36.8
20	0	2	0	0	1500	11	400	27	770	19.8
21	0	0	-2	0	1500	7	300	27	799	27.7
22	0	0	2	0	1500	7	500	27	721	29.8
23	0	0	0	-2	1500	7	400	17	575	30.4
24	0	0	0	2	1500	7	400	37	681	25
25	0	0	0	0	1500	7	400	27	769	28.7
26	0	0	0	0	1500	7	400	27	766	27.9
27	0	0	0	0	1500	7	400	27	769	28.7
28	0	0	0	0	1500	7	400	27	770	27.9
29	0	0	0	0	1500	7	400	27	766	27.8
30	0	0	0	0	1500	7	400	27	766	27.7

The second-order polynomial (regression) equation for the response surface Y is

$$Y = b_0 + \sum b_i X_i + \sum b_{i_2} X_{i_2} + \sum b_{ij} X_i X_j \quad (2)$$

Selected polynomial could be expressed as

$$H = b_0 + b_1(P) + b_2(F) + b_3(T) + b_4(D) + b_{12}(PF) + b_{13}(PT) + b_{14}(PD) + b_{23}(FT) + b_{24}(FD) + b_{11}(P^2) + b_{22}(F^2) + b_{33}(T^2) + b_{44}(D^2) \quad (3)$$

B1, B2, B3, and B4 are linear interactions and factor square terms. The coefficient was estimated with 95% confidence using Design-Expert 7 software. The *t*-test and *P* values of each coefficient were computed. Model terms are significant when “Probe > *F*” is less than 0.05.

The important terms are *P*², *F*², and *D*². The final empirical connection of laser hard-faced deposit of colmonoy-5 alloy was developed utilizing just these coefficient.:

$$\begin{aligned} \text{hardness of the deposit (H)} &= \left(\begin{aligned} &772.50 - 41.92(P) + 69.17(F) - 13.25(T) + 17.67(D) - 23.62(P * F) \\ &+ 42.38(P * T) - 7.75(P * D) + 12.88(F * T) - 29.25(F * D) \\ &- 24.75(T * D) - 38.17(P^2) - 40.79(F^2) - 7.92(T^2) - 40.92(D^2) \end{aligned} \right) \text{HV.} \\ \text{weight loss} &= \left(\begin{aligned} &-83.403 + 0.1353(P) - 10.642(F) + 0.5610(T) - 4.410(D) \\ &+ 3.140E - 3(P * F) - 4.618E - 4(P * T) - 7.75(P * D) - 3.312E - 3(F * T) \\ &+ 0.1781(F * D) + 5.625 - 3(T * D) + 6.171E - 6(P^2) + 0.0210(F^2) + 3.750E - 6(T^2) - 2.625E - 3(D^2) \end{aligned} \right) \text{mg.} \end{aligned} \quad (4)$$

2.5. Checking Adequacy of the Developed Relationships.

The established empirical connections were tested using ANOVA. In this study, 95% confidence was sought. The connection is sufficient. The estimated F ratio of the generated model should not exceed the standard tabulated F ratio, and the calculated R ratio should surpass the standard tabulated R ratio for a specified degree of confidence. The model is determined to be sufficient. The likelihood $> F$ in Tables 4 and 5 is less than 0.05, indicating that the empirical connections are significant. The lack of fit was not substantial for all empirical connections. The model is sufficient if the computed F ratio of the generated relationship does not exceed the predicted F ratio for a given degree of confidence. Fisher's F -test with a low probability value shows the regression model's high significance. The determination coefficient measures the model's fit (R^2). The coefficient of determination was determined to be 0.99, meaning that 99 percent of the experimental results agree with the model's predictions. R^2 should always be 0-1. A statistically sound model has an R^2 near 1.0.

Then, we reconstruct the phrase using important terms. Adj. $R^2 = 0.981$ also shows the model's high relevance. To put it another way, the model could explain 82.2 percent of the variability in prediction. This is in line with the Adj. R^2 of 0.952. The coefficient of variation is 2.17, indicating that the difference between experimental and anticipated values is small. A signal-to-noise ratio higher than 4 is ideal. With a ratio of 34.47, the signal is sufficient. To utilize this model, go here. The correlation graph in Figures 2(a) and 2(b) illustrates anticipated and actual hardness of laser hard-faced deposit, indicating minimal variation between the two. Figure 3 shows the microhardness and weight loss of all thirty experiments with an error bar. Table 6 shows the ANOVA test result for weight reduction. The table shows that the created statistical model met the 95% confidence level. In this case, the predicted and experimental values were compared using R^2 . The " R^2 " score for the above-developed model shows a strong correlation between estimated and experimental values. As demonstrated in Figures 2(a) and 2(b), the established empirical connections may be successfully utilized for prediction.

2.6. Verification of Developed Empirical Relationships.

It is critical to check that the empirical connections established satisfy the requirements and the results are accurate. This is the procedure of validation. For validation, four alternative laser hardfacing process parameter combinations were used that were not specified in the design matrix (Table 3). Tables 6 and 7 show the experimental and anticipated findings. The anticipated values of microhardness and weight loss match well with the actual data, with only small deviations (5%).

3. Results and Discussion

3.1. Perturbation Plots.

By replacing process parameter values in the coded form, the empirical connections may be utilized to anticipate responses. The primary and interaction impacts of process factors on deposit characteristics were

calculated and shown as perturbation plots in Figures 4 and 5. The perturbation plot is a diagrammatic depiction of the response surface. The perturbation plot compares the impacts of all variables in the RSM design space.

In response to surface designs, the perturbation plot illustrates how the response varies as each component moves away from the reference point. The default reference point in Design-Expert software is in the design space (the coded zero level of each factor). A high slope or curve in a factor indicates a sensitive reaction. A generally flat line indicates insensitivity to change [18]. Using F values, one may also evaluate the main variables that have significant and small impacts on the answers. According to the F value analysis, the most important variables influencing the reactions are input power, stand-off distance, and powder feed rate. Figures 4–5 indicate a strong impact that agrees well with the anticipated model F values.

Figure 4 shows a perturbation plot for the deposit hardness response. Figure 4 shows the change of hardness when each laser hardfacing parameter travels away from the reference point, while all other parameters remain constant. The experiment's design places the reference point at the design space's center. The perturbation and response surface graphs show that when hardness rises, defocusing distance climbs to a point and then declines. Insufficient energy or low heat input causes powders and unmelted partials to escape from deposits. Laser power and travel speed reduce hardness. The increased heat input may enhance penetration depth and diluting of deposits [19].

3.2. Process Optimization.

The RSM was utilized to improve the laser hardfacing parameters in this research. RSM is a set of mathematical and statistical methods used for planning experiments, building mathematical models, determining optimum input parameter combinations, and displaying results visually [20]. As illustrated in Figure 6, two parameters in the midway tier and two parameters in the X -axis and Y -axis were used to construct surface and contour plots that indicate potential factor independence. In the design realm, contour plots assist us to anticipate reaction [21]. On the response plot, the apex represents maximal hardness.

To categorize a stationary point, we determine if it is a minimum, maximum, or saddle point using a contour plot. A contour plot is important in learning response surfaces. It is noticeable that as the powder feed rate rises, so does the defocusing distance and hardness. Three-dimensional diagrams are drawn for a specific processing condition to learn more about how process factors affect hardness. Surface and contour graphs for each process parameter are shown in Figure 6. Figure 6(a) shows that when process parameters like laser power and powder feed rate rise, the hardness decreases. Dilution and microstructure affect hardness. Laser power dissolves powder, and heat melts the substrate. As the laser intensity increases, more substrate material melts.

The deposit dilution may influence the hardness variation in laser hard-faced samples. Higher dilution reduces hardness. Increasing power (constant F , T , D) reduces

TABLE 4: ANOVA test results for microhardness of the deposit.

Source	Sum of squares (SS)	Degree of freedom	Mean square	F value	P value (prob > F)	Whether significant or not
Model	3.334 E + 005	14	23817.52	27.17	<0.0001	Significant
P	41417.04	1	41417.04	47.65	<0.0001	
F	1.226 E + 005	1	1.226 E + 5	129.73	<0.0001	
T	1751.04	1	1751.04	4.76	0.0118	
D	7245.38	1	7245.38	8.46	<0.0001	
PF	12265.56	1	12265.56	10.09	<0.0001	
PT	23485.56	1	23485.56	32.46	<0.0001	
PD	1580.06	1	1580.06	1.09	0.0157	
FT	6201.56	1	6201.56	3.00	<0.0001	
FD	14220.56	1	14220.56	15.47	<0.0001	
TD	10251.56	1	10251.56	11.07	<0.0001	
P ²	33380.36	1	33380.36	45.15	<0.0001	
F ²	36063.57	1	36063.57	51.57	<0.0001	
T ²	2480.86	1	2480.86	1.94	0.0039	
D ²	48696.50	1	48696.50	51.89	<0.0001	
Residual	3195.42	15	213.03			
Lack of fit	2608.08	10	260.81	1.51	0.1959	
Pure error	587.33	5	117.47	Pred. R ²	0.9529	
Cor total	3.366 E + 005	29		Press	15868.32	
Std.deviation	14.60			Mean	671.10	
R ²	0.9905			C.V %	2.17	
Adj. R ²	0.9816			Adeq. Precision	34.478	

TABLE 5: ANOVA test results for weight loss of the deposit.

Source	Sum of squares	Degree of freedom	Mean square	F value	P value (prob > F)	Whether significant or not
Model	968.18	14	69.16	140.87	<0.0001	Significant
P	40.30	1	40.30	82.74	<0.0001	
F	444.62	1	444.62	905.69	<0.0001	
T	0.35	1	0.35	10.52	0.0048	
D	24.60	1	24.60	50.76	<0.0001	
PF	25.25	1	25.25	51.80	<0.0001	
PT	341.33	1	341.33	695.82	<0.0001	
PD	5.18	1	5.18	10.40	0.0057	
FT	1.76	1	1.76	3.49	0.0814	
FD	50.77	1	50.77	103.27	<0.0001	
TD	31.64	1	31.64	64.30	<0.0001	
P ²	1.28	1	1.28	3.14	0.0968	
F ²	0.077	1	0.077	0.35	0.0519	
T ²	0.75	1	0.75	0.016	0.0418	
D ²	0.26	1	0.26	0.28	0.6044	
Residual	8.77	15	0.58			
Lack of fit	7.73	10	0.77	2.73	0.1399	
Pure error	1.05	5	0.21	Pred. R ²	0.9616	
Cor total	976.95	29		Press	46.01	
Std.deviation	0.76			Mean	28.39	
R ²	0.9910			C.V %	2.69	
Adj. R ²	0.9826			Adeq. Precision	45.511	

dilution. Less dilution means less hardness. Because more heat is used to melt the powder and less heat melts the substrate, increasing F (constant P, T, D) decreases dilution and increases hardness. Increasing T (constant P, F, D) reduces powder density per square area (g/mm^2), increasing dilution rate and decreasing hardness. Hardness increases when D (constant P, F, T) decreases. Increasing the defocusing distance reduces the energy density per unit of clad

pass available, reducing penetration depth and dilution. That is the greatest hardness and the lowest weight loss. Their use in predicting response (hardness and weight loss) in any zone of the experimental area [22] is recommended. The highest attainable hardness value is 820 HV, as illustrated in Figures 6(a)–6(f). Figures 7(a)–7(f) show the minimal weight loss value of 16.31 mg. The settings for maximum hardness and minimal weight loss are 1314 W power,

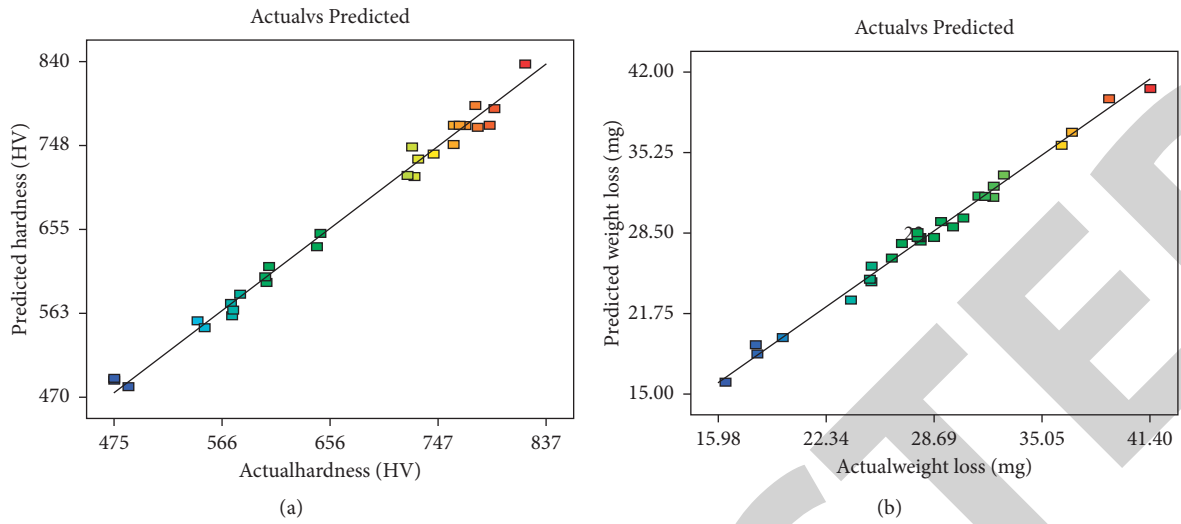


FIGURE 2: Correlation graphs. (a) Microhardness of deposit. (b) Weight loss of deposit.

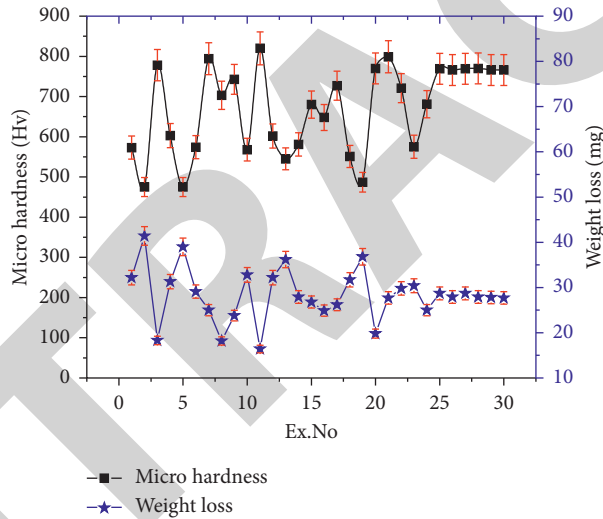


FIGURE 3: Microhardness and weight loss with error bar for all thirty experiments.

TABLE 6: Verification results for microhardness.

Sl. No	Power (W)	Powder feed rate (g/min)	Travel speed (mm/min)	Defocusing distance (mm)	Actual hardness (HV)	Predicted hardness (HV)	Error (%)
01	1386	8.5	353	30	815	828	2.7
02	1414	9	437	25	809	821	1.4
03	1329	9	361	32	820	829	1

TABLE 7: Verification results for wear test weight loss.

Sl. No	Power (W)	Powder feed rate (g/min)	Travel speed (mm/min)	Defocusing distance (mm)	Actual weight loss (mg)	Predicted weight loss (mg)	Error (%)
01	1100	4	325	20	30.7	29.6	3.58
02	1400	6	400	26	29.28	30	-2.45
03	1800	8	470	30	28.02	27.15	3.10

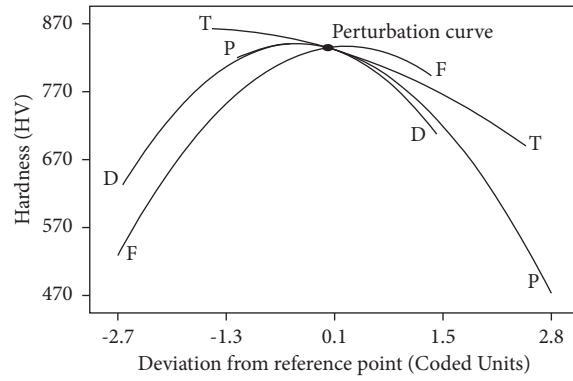


FIGURE 4: Effect of laser hardfacing processes parameters on hardness.

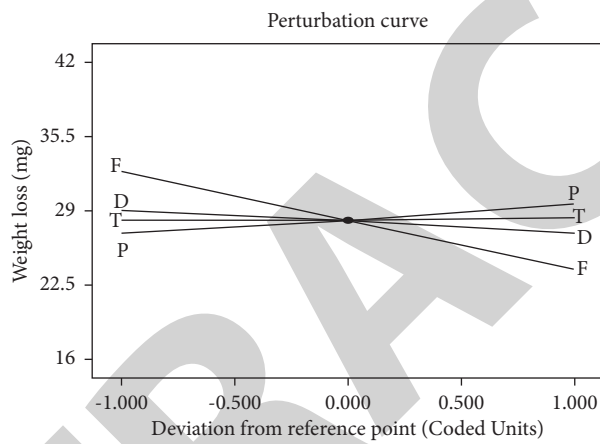


FIGURE 5: Effect of laser hardfacing processes parameters on weight loss.

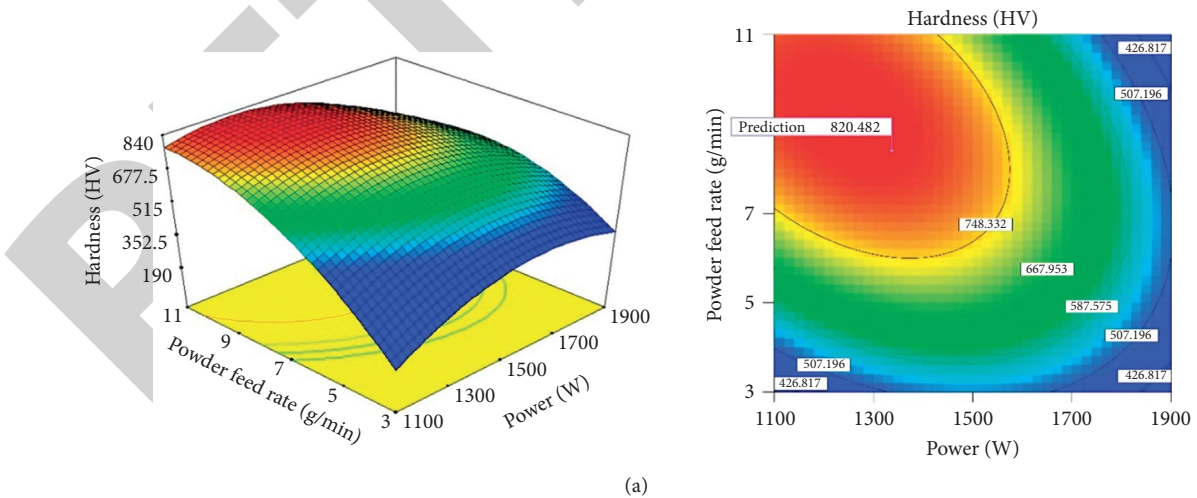
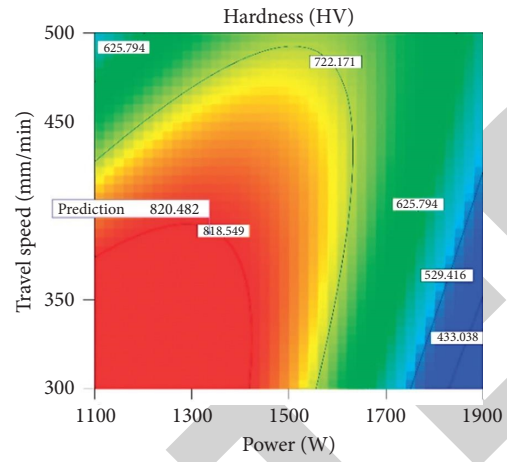
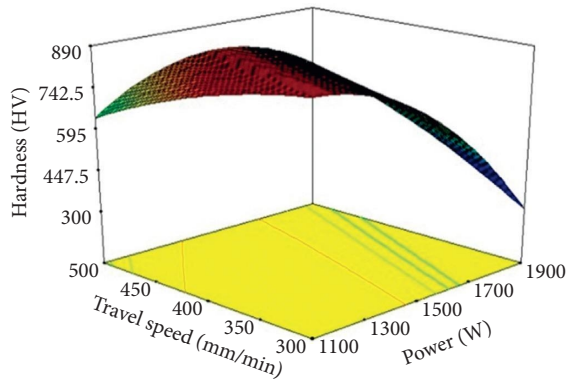
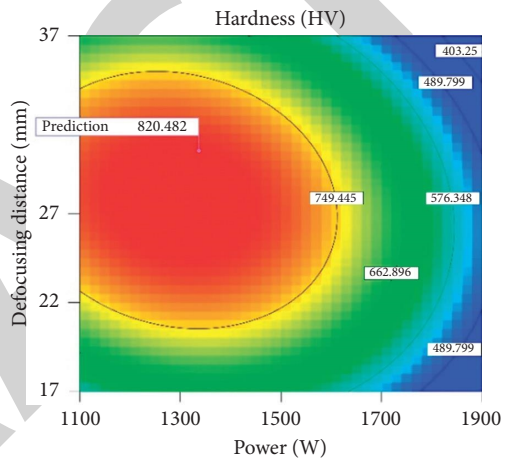
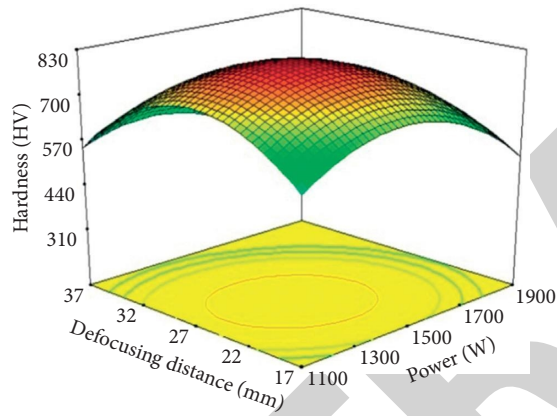


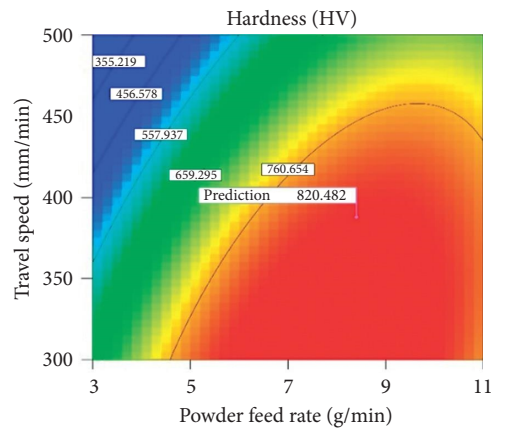
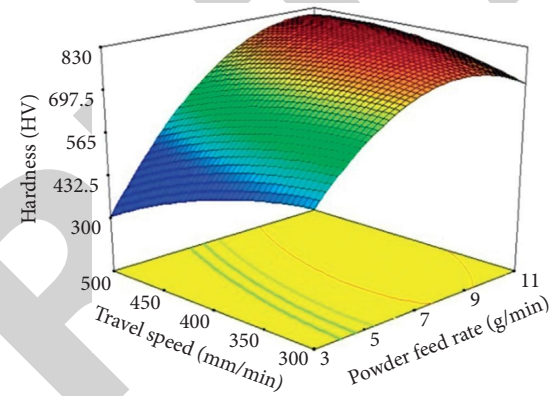
FIGURE 6: Continued.



(b)

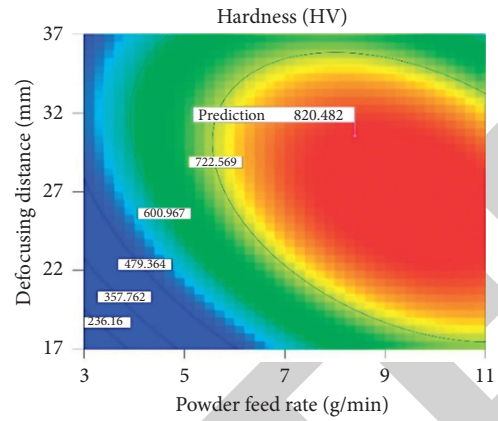
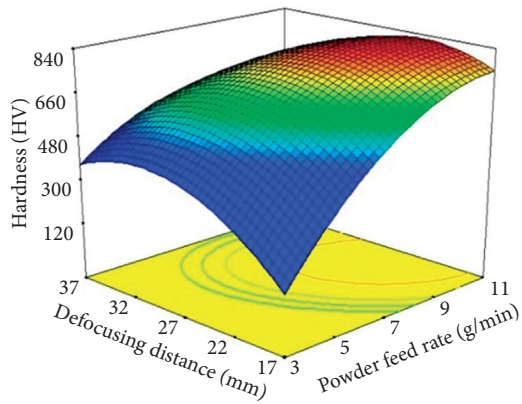


(c)

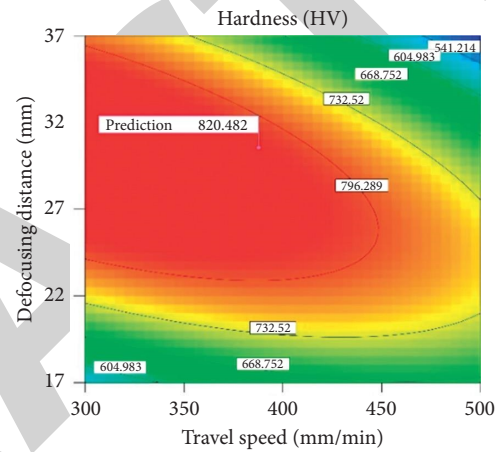
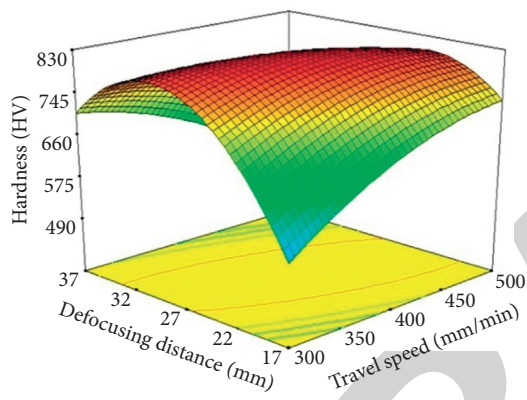


(d)

FIGURE 6: Continued.

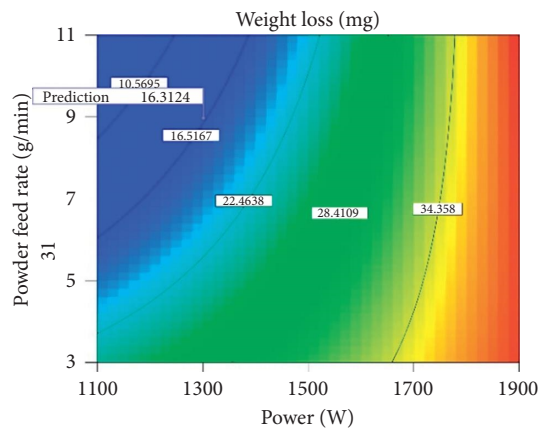
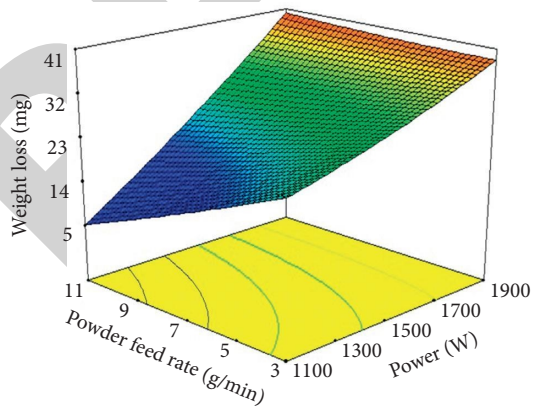


(e)



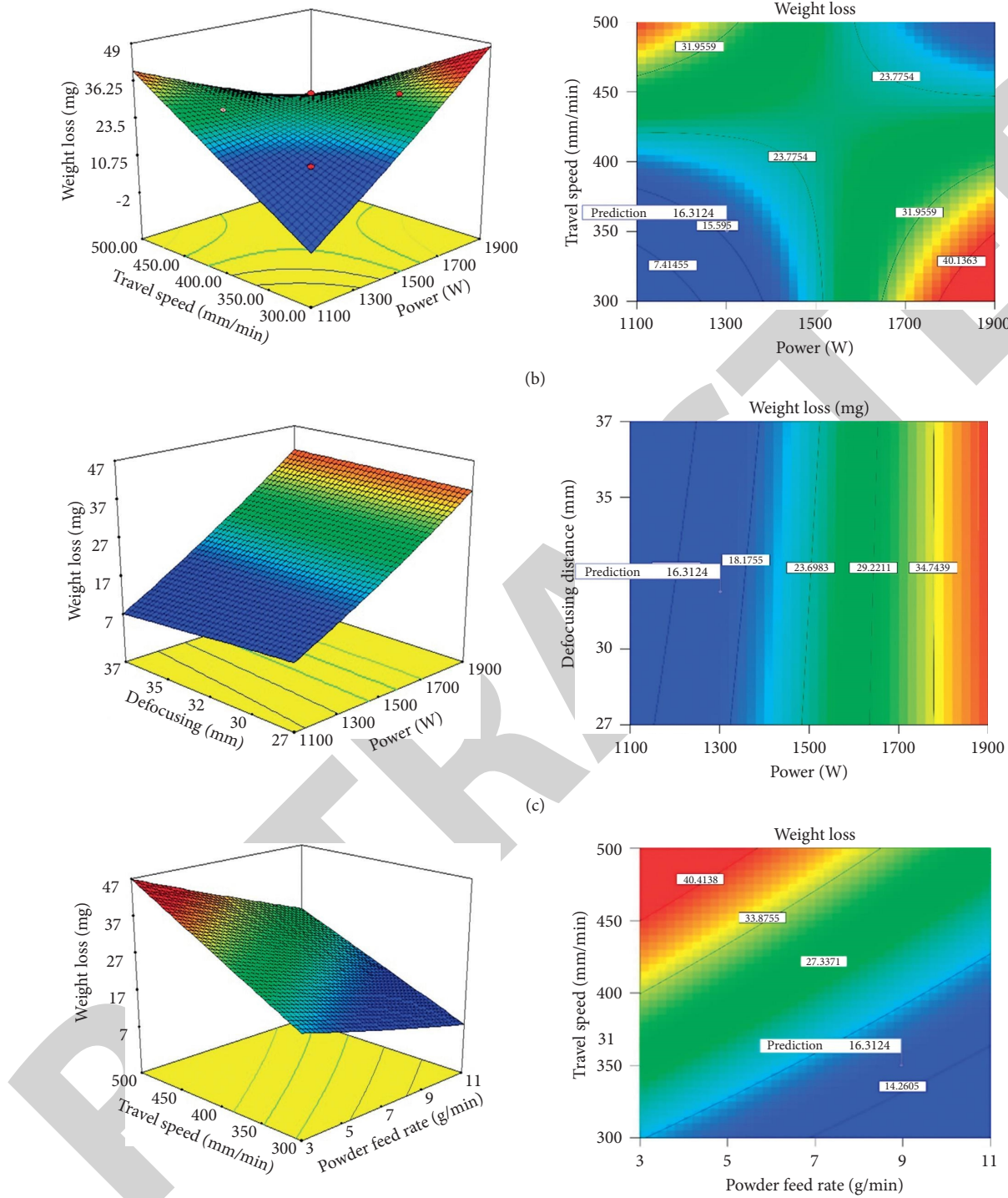
(f)

FIGURE 6: Response surface graphs and contour plots. The interaction between (a) laser power and powder feed rate, (b) laser power and travel speed, (c) laser power and defocusing distance, (d) powder feed rate and travel speed, (e) powder feed rate and defocusing distance, and (f) travel speed and defocusing distance is examined.



(a)

FIGURE 7: Continued.



(d)
FIGURE 7: Continued.

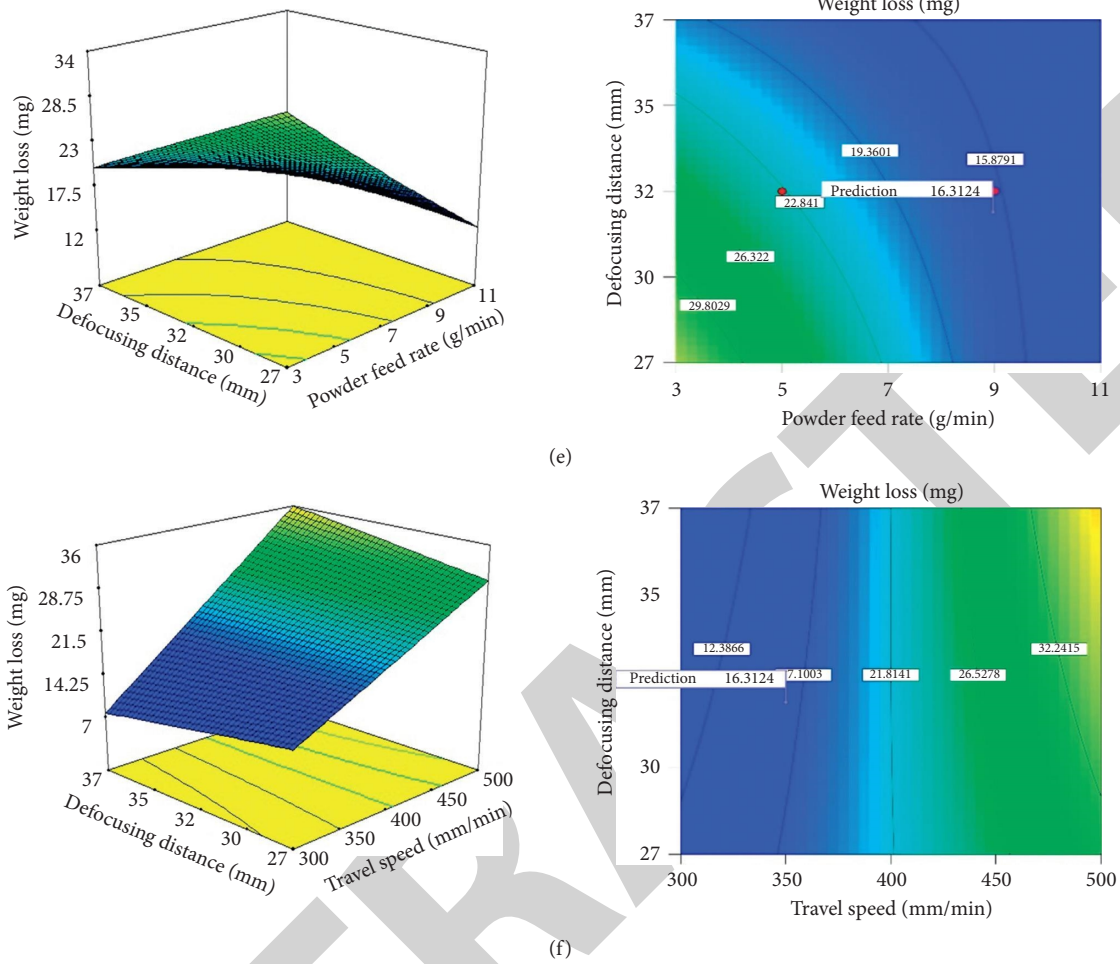


FIGURE 7: Response surface graphs and contour plots. The interaction between (a) laser power and powder feed rate, (b) laser power and travel speed, (c) laser power and defocusing distance, (d) powder feed rate and travel speed, (e) powder feed rate and defocusing distance, and (f) travel speed and defocusing distance is examined.

9 g/min powder feed, 366 mm/s travel speed, and 32 mm defocusing distance. There is a more important process parameter with a higher F ratio.

Using the F ratio, it can be inferred that the powder feed rate is the most important element in exploiting hardness, followed by power, defocusing distance, and travel speed [23]. To verify the empirical relationship's prediction abilities, three additional confirmation tests were run using hardfacing process parameters selected at random from the practical working range (Table 8). The actual answer was the mean of three findings. The produced findings show the empirical connection is accurate with a 5% variance. Table 9 lists optimized laser hardfacing parameters.

3.3. Graphical Optimization for Deposit Desired Quality Characteristics. Numerous responses are handled graphically by superimposing significant response contours on a contour map. Then, a visual search may provide the most accurate results. When confronted with a large number of answers, it is preferable to begin with numerical

optimization in order to identify a viable area. The graphical optimization procedure included the numerical optimization criteria, and the lower and upper bounds were determined using the numerical optimization findings. Overlay plots may be used to rapidly determine the values of the laser hardfacing process parameters required to obtain the desired response value for this kind of material [24, 25].

Given that deposit hardness is directly related to wear resistance (weight loss), linking microhardness and wear resistance is critical. Hardness improves wear resistance and therefore reduces weight loss. Deposit resistance typically reflects hardness. This leads to the study of microhardness and wear resistance combined [26–28]. Given the above, it is preferable to run a graphical optimization result and let the visual inspection choose the best deposit condition. The overlay plot's shaded regions do not meet the proposed criteria. Figure 8 shows the graphical optimization charts. To find the desired response within the design space, one can use this overlay plot. An optimization study finds optimal spraying conditions to achieve desired microstructural and mechanical properties [29-33].

TABLE 8: Validation test results for the developed empirical relationship.

S. no.	Power (W)	Powder feed rate (g/min)	Travel speed (mm/min)	Defocusing distance (mm)	Actual hardness (HV)	Predicted hardness (HV)	Error (%)
01	1400	4	325	20	585	570	-2.6
02	1600	6	375	24	658	635	-3.6
03	1800	10	450	35	783	797	1.7

TABLE 9: Optimal parameters for laser hardfacing.

S. no.	Main parameters	
1	Laser power (W)	1300
2	Traverse speed (mm/min)	350
3	Powder feed rate (grams/min)	9
4	Defocusing distance (mm)	32

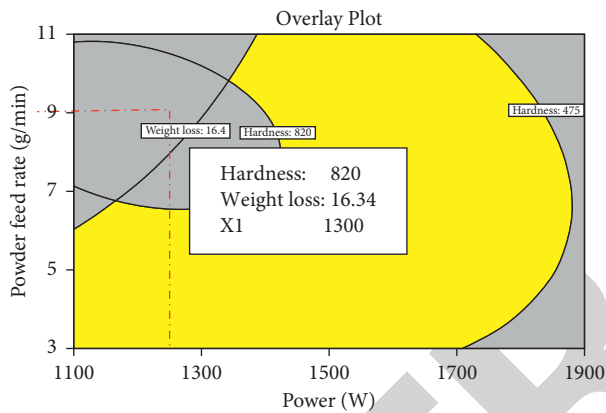


FIGURE 8: Graphical optimization plot shows the response of optimized process parameters for minimum weight loss and maximum hardness.

4. Conclusions

- (1) An empirical relationship was developed to predict the hardness of nickel-based layer deposited on 316LN austenitic stainless steel substrate with 95% confidence level by incorporating important laser hardfacing parameters
- (2) The laser hardfacing parameters (power, powder feed rate, travel speed, defocusing distance) were optimized for Ni-based deposit, by adopting multi-response optimization with the RSM approach. However, the illustrated approach and the methodology of the response surfaces are universal and can be applied for any specific application to tailor the deposit properties
- (3) A maximum hardness of 820 HV and minimum weight loss of 16.31 mg could be achieved in the deposit made using laser power of 1314 W, powder feed rate of 9 g/min, a travel speed of 366 mm/min, and defocusing distance of 32 mm
- (4) Of the four laser hardfacing parameters, the powder feed rate (based on F value) is the major influencing

factor to predict the hardness followed by power, travel speed, and defocusing distance [31–33]

Data Availability

The data used to support the findings of this study are included within the article.

Conflicts of Interest

The authors declare that they have no conflicts of interest.

Acknowledgments

The authors thank the UGC-DAE Consortium for giving financial support in order to conduct this research (Project No. CSR-KN/CRS-56/2013-14/656, dated 04.09.13). The authors would like to convey their heartfelt gratitude to M/s. Geometrix Laser Solutions Pvt Limited, Tada, for providing them with laser hardfacing services. The authors would also like to express their heartfelt gratitude to the Director, IGCAR, Kalpakkam, for providing the basic metal.

References

- [1] L. C. Lim, Q. Ming, and Z. D. Chen, "Microstructures of laser-clad nickel-based hardfacing alloys," *Surface and Coatings Technology*, vol. 106, no. 2-3, pp. 183–192, 1998.
- [2] A. K. Bhaduri, R. Indira, S. K. Albert, B. P. S. Rao, S. C. Jain, and S. Asokkumar, "Selection of hardfacing material for components of the Indian prototype fast breeder reactor," *Journal of Nuclear Materials*, vol. 334, no. 2-3, pp. 109–114, 2004, Frenk and W. Kurz: Mater. Sci. Eng. A, 1993, vol. 173, pp. 339–342.
- [3] S. L. Mannan, C. S. C. B. Raj, and S. B. Bhoje, *Materials R&D for Prototype Fast Breeder Reactor*, S. L. Mannan and M. D. Mathew, Eds., Indira Gandhi Centre for Atomic Research, Kalpakkam, 2003.
- [4] G. Chakraborty, S. K. Albert, and A. K. Bhaduri, "Effect of dilution and cooling rate on microstructure and magnetic properties of Ni base hardfacing alloy deposited on austenitic stainless steel," *Materials Science and Technology*, vol. 28, no. 2, pp. 454–459, 2012.
- [5] N. Jeyaprakash and C.-H. Yang, "Comparative study of NiCrFeMoNb/FeCrMoVC laser cladding process on nickel-based superalloy," *Materials and Manufacturing Processes*, vol. 35, no. 12, pp. 1383–1391, 2020.
- [6] N. Jeyaprakash, CH. Yang, M. Duraiselvam, Muthukannan, and S. Sivasankaran, "Comparative study of laser melting and pre-placed Ni-20% Cr alloying over nodular iron surface," *Archiv.Civ.Mech.Eng.*, vol. 20, no. 20, p. 0030, 2020.
- [7] N. Jeyaprakash, C.-H. Yang, S. Sivasankaran, and S. Sivasankaran, "Formation of FeCrMoVC layers on AA6061 by laser cladding process: microstructure and wear

Research Article

Investigation on Microstructure and Tensile Properties of High-Strength AA2014 Aluminium Alloy Welds Joined by Pulsed CMT Welding Process

Rajendran Chinnasamy ¹, Samson Jerold Samuel Chelladurai ¹ and Tushar Sonar²

¹Department of Mechanical Engineering, Sri Krishna College of Engineering and Technology, Coimbatore 641008, India

²Centre for Materials Joining and Research (CEMAJOR), Department of Manufacturing Engineering, Annamalai University, Annamalainagar 608002, India

Correspondence should be addressed to Samson Jerold Samuel Chelladurai; samsonjeroldsamuel@skcet.ac.in

Received 30 May 2021; Revised 16 August 2021; Accepted 2 September 2021; Published 23 October 2021

Academic Editor: Akbar Heidarzadeh

Copyright © 2021 Rajendran Chinnasamy et al. This is an open access article distributed under the Creative Commons Attribution License, which permits unrestricted use, distribution, and reproduction in any medium, provided the original work is properly cited.

High-strength AA 2014 aluminium alloys are broadly employed for many applications because of their good mechanical properties, high strength-to-weight ratio, and better resistance to corrosion and are recyclable. The major problems in welding of AA 2014 aluminium alloy using a traditional joining process are partially melted zone, hot cracking, and alloy segregation. Cold metal transfer-welding (CMT) process is an advanced variant of gas metal arc welding process characterized by reduced heat input in which the welding wire is retracted during the short circuit which allows sufficient time for the weld to cool before placing each drop. In this investigation, the pulsed CMT welding process was chosen to weld high-strength AA2014 aluminium alloy under T6 condition. The joint tensile properties were compared with the parent material and correlated to the microstructural features. The defect-free weld was achieved at constant welding speed of 450 mm/min, welding current of 110 A, and electrode feed rate of 5550 mm/min. The joint weld using pulsed CMT yields a maximum strength of 303 MPa, extending joint efficiency up to 67%. It mainly refers to the beneficial effects of welding wire pulsing and dip and retreat motion which causes refining of dendritic grains in weld metal and enhances the strength of joints.

1. Introduction

AA 2xxx alloy is precipitation hardening aluminium alloy preferentially employed in aerospace and automotive application owing to its good mechanical properties, resistance to general corrosion, high strength-to-weight ratio, and better formability. The light combat aircraft interstage skin and the automotive wheel are made from this alloy. The main problems encountered in welding high-strength age-hardened Al-alloys, including AA2014, are cracking in weld metal and partially melted zone, porosity, and alloy segregation which constrain the fusion welding of AA2014 aluminium alloy (Babu et al, [1–9]). Hence, novel methods have been developed and commercialized over few decades. The TIG-welded aluminium alloy joints disclosed inferior

strength properties which is almost half of the base material strength. It refers to high heat input requirement in TIG welding of aluminium alloy. This made researchers to practice low heat input solid state welding process popularly known as friction stir welding (FSW) process [10, 11] [12–16]. Several grades of aluminium alloys and dissimilar materials were fabricated using FSW. Moreover, the strength of friction stir welded joints is 75%–85% of the base material strength [17]. Even though, this process has limitations such as the exit hole at the end of the weld, CMT was invented in 2004 and is foreseen to be a breakthrough method in aluminium and its alloy welding. CMT is an advanced variant of GMAW in which the digital control detects the short circuit timing and detaches the drop by the retracting motion of welding wire during welding; the wire is moved forward and

again pulled back as the short circuit happens. Thus, CMT arc introduces heat input only during the burning phase of arc. This lowers the heat input than traditional dip transfer welds [18]. Shang et al. investigated the mechanical and metallurgical characteristics of CMT-welded dissimilar materials. The intermetallic compounds have considerably affected strength. Pickin and Young [19] reviewed the role of CMT welding process in thick materials and pulsed GMAW. Finally, the CMT welding process was compared with pulsed GMAW. CMT welding process deposited a small amount of filler material in the weld by pulse frequency. Gungor et al. [20] used AA5083 and AA6082 for CMT welding. The materials were joined using two welding processes such as pulsed robotic CMT welding and MIG welding. The test results showed that the CMT welded joints had good tensile and fatigue strength. Azar [21] proposed a model to predict the heat input and geometry of CMT weld. This model explained the behavior of weld pool and formation of weld pool with respect to heat input. [22] and analyzed the formation of weld defects in CMT welded 5083 plates and joint performance. In the fusion zone, a dendritic structure with a significant percentage of big pores was found. Inadequate surface cleaning before welding was the cause of the creation of big pores. The failure mechanism was also influenced by the existence of large pores, which dictated the fracture growth path. The crack propagated within the fusion zone by jumping from one pore to the next, resulting in brittle failure.

The research work on CMT welding of aluminium alloy is mainly reported on 5xxx, 6xxx, and 7xxx series grade. The information available on P-CMT welding of AA2014

aluminium alloy is scanty. It is necessary to investigate the strength properties and microstructural features of AA2014-T6 aluminium alloy and compare the joint performance with base material for its viability in the concerned applications. Hence, an attempt has been made to weld AA2014-T6 aluminum alloy using pulsed CMT welding.

2. Work Methodology

Cold rolled sheets (AA2014-T6) with a thickness of 2 mm were used in this work. The chemical properties and mechanical properties of the base material (BM) were presented in Tables 1 and 2, respectively. The mechanical properties of BM were evaluated using a tensile test. The grain size of BM was 50 μm (Figure 1(a)). A test coupon size of 150 mm \times 150 mm was prepared for the weld. CMT-2000x version machine (Figure 1(b)) was used to make a joint with a constant current of 110 A, a voltage of 12 V, welding speed of 45 cm/min, gas flow rate of 5 lpm, and wire travel speed of 555 cm/min (Table 3). The photograph of P-CMT welded joint is shown in Figure 1(c). Composite tensile specimens were extracted from the weld in accordance with the ASTM E8-M04 guidelines (Figure 1(d)). The process parameters were illustrated in Figure 1(e). The machined samples were used for tensile test. Tensile test was conducted using 100 kN electromechanically controlled UTM with a slide velocity of 0.15 cm/min. For metallography examination, a rectangular piece of the sample was cut from the middle portion of the weld line. Different grades of sand paper were used to polish the weld sample with alumina powder. The heat developed during welding was calculated using the following equation:

$$\text{Heat generation } Q (\text{kJ/mm}) = \frac{\text{Welding current } (A) \times \text{Thermal efficiency factor } (\eta) \times \text{Voltage } (V)}{1000 \times \text{Welding speed } (\text{mm/min})} \quad (1)$$

To reveal the structure of weld and other regions, the polished sample was etched with Keller's reagent. The hardness distribution across the weld was performed using Vickers microhardness test and was carried out as per the ASTM- E384, and the applied load of 0.5 N and dwell time of 15 sec were used. A scanning electron microscope was used to measure the type of failure pattern in the tensile tested sample. Moreover, EDS analysis was performed in the fractured region using energy dispersive spectroscopy.

3. Results

3.1. Tensile Test. The strength properties of AA 2014 P-CMT joints are presented in Table 4. The strength properties were taken from an average of three samples in tensile test. From the results, the welded joint yields inferior strength than the parent material in as received conditions because of the differences in microstructural features, orientation of grains, and sizes in different regions. It affects the plastic deformation behavior during tensile load. However, the temperature rises above 200 degrees, and it causes the reversion of precipitate (θ'') at WZ and HAZ on cooling. This may be

the reason for lower hardness and strength. P-CMT weld conceived a maximum tensile strength of 303 MPa, and it is 33% lower than the base material strength. The yield strength and percentage of elongation of CMT weld were 258 MPa and 6.5%, respectively (Figure 2). The reason for the material in as received condition possesses maximum strength is the presence of strengthening precipitates in its matrix and tempering condition. The P-CMT joint showed an efficiency of 67%.

3.2. Hardness Survey. The hardness measurement across the transverse direction of weld is shown in Figure 3. The hardness distribution in the materials depends on two criteria such as size and distribution of precipitates and size of the grains. It is an inverse proportion to the grain size and precipitate size. The formation of recrystallized grains and distribution of strengthening precipitates in CMT weld is carried out by the heating and cooling process during thermal cycle. Hence, the hardness distribution has a direct relationship with weld strength. The weld region conceived a peak hardness of 88 HV and HAZ was 72 HV. Moreover, the

TABLE 1: Elemental composition (wt. %) of AA2014-T6 alloy (base material).

Si	Cu	Fe	Mg	Cr	Zn	Mn	Ti	Al
0.871	4.812	0.131	0.732	0.004	0.061	0.811	0.011	Bal

TABLE 2: Mechanical properties of nonwelded parent metal.

Material	0.2%YS (MPa)	UTS (MPa)	% elongation (50 mm gauge length)	Microhardness (HV)
AA2014	430	454	8.5	162

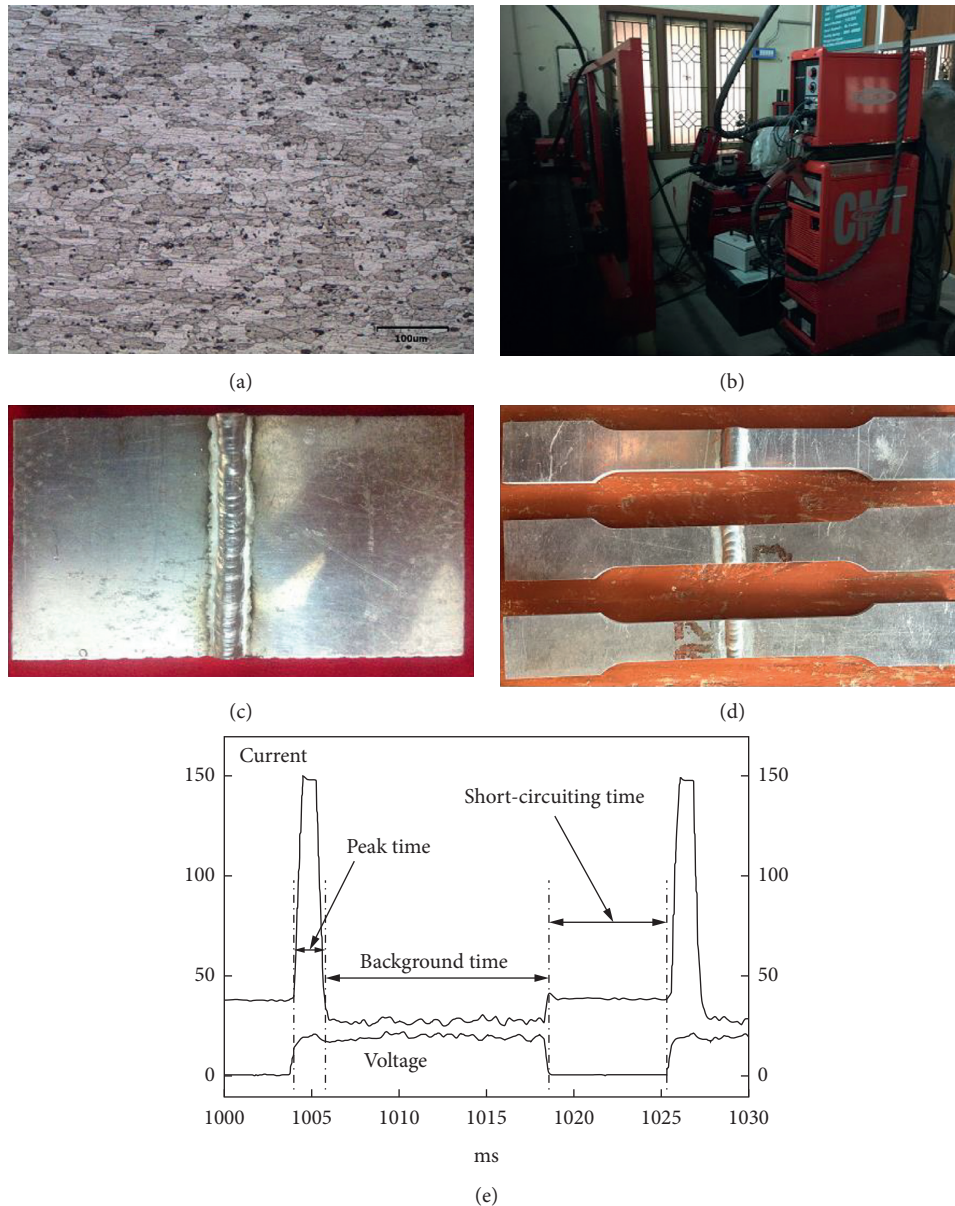


FIGURE 1: (a) Microstructure of base material. Photograph of (b) CMT machine, (c) fabricated P-CMT welded joint, (d) tensile specimens, and (e) process parameters [23].

HAZ is the weaker region irrespective of the welding process. Due to formation of the soft region [24], HAZ is adjacent to the fusion zone, where this zone experienced severe heat input followed by a slow cooling rate. As results, the

grains were coarsened. The precipitate in HAZ may be coarsened or partially destroyed. Moreover, the dispersion of strengthening precipitate was lower. Hence, the soft region was formed. This region will act as a crack initiation

TABLE 3: Optimized P-CMT welding parameters.

Joint no.	P-CMT parameters					Arc length	Heat input (KJ/mm)	UTS (MPa)	Probable reason
	Arc voltage (V)	Welding current (A)	Wire feed rate (mm/min)	Welding speed (mm/min)					
1	12	90	5500	450	15	0.121	—	Low heat input causes lack of fusion	
2	12	100	5500	450	15	0.188	255	Moderate heat causes coarse grain	
3	12	110	5500	450	15	0.223	303	Fine and recrystallized grains by an optimum heat	
4	12	120	5500	450	15	0.312	286	Coarse and long grains cause by high heat input	
5	12	130	5500	450	15	0.389	-	High heat input causes porosity and coarse grains	

TABLE 4: Tensile test results of PCMT welded aluminium alloy joint.

Joint No	Condition	Microhardness (HV)		0.2% YS (MPa)	% elongation (50 mm gauge length)	UTS (MPa)	Efficiency (%)
		WZ	HAZ				
1	P-CMT welded joint	88	75	258	6.3	303	67%
2	Base material	155	—	431	9	455	—

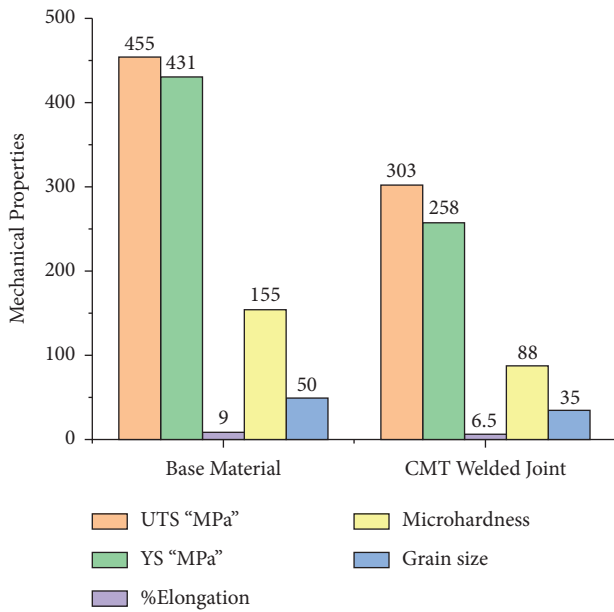


FIGURE 2: Tensile properties of P-CMT welded joint and base material.

point. Strengthening precipitate in as received condition is sensitive to the heat input during the welding cycle. It reduces the strength properties of joint, particularly, in the HAZ region. During artificial ageing of precipitation hardening aluminum alloy (AA2014-T6), the primary precipitates are needle-like (θ''), which is the main strengthening precipitate in α -aluminum [25]. The spread of precipitate is uniform in the matrix. Due to thermal driving forces, the needle-like precipitate was transferred into a metastable (θ') precipitate whose presence along with

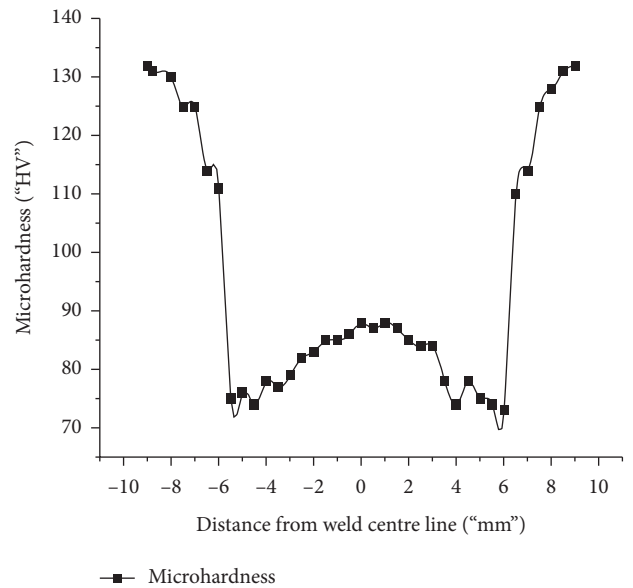


FIGURE 3: Microhardness profile.

aluminum becomes predominant in the WZ. This phenomenon is the main factor to reduce the hardness and strength. Moreover, the precipitate changes from θ'' to θ' , causing a soft zone in the WZ [26].

3.3. *Microstructure.* The macrograph of P-CMT joint is revealed in Figure 4(a). No visible flaws were observed in the welded joints. The fusion zone of the weld showed brighter appearance than the other region due to recrystallization of grains and the geometry of the weld exhibits in elliptical shape. The mean value of grains in the weld (Figure 4(b)),

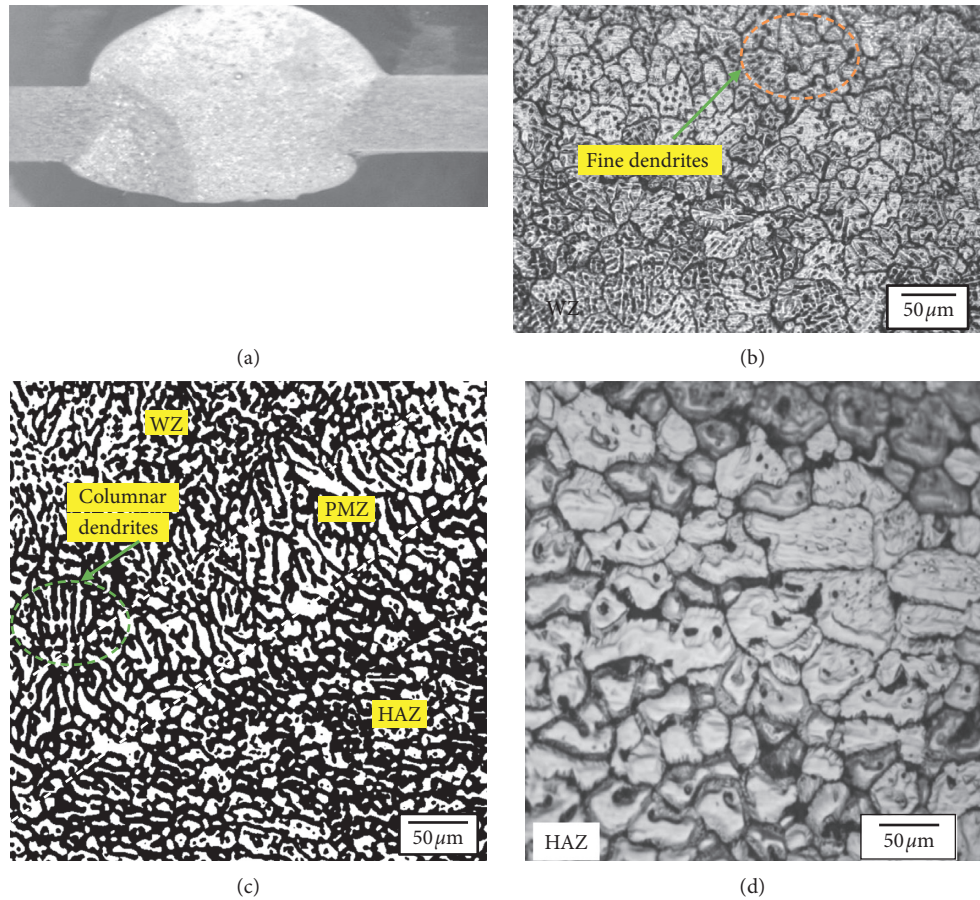


FIGURE 4: (a) Macrograph. Micrograph of (b) fusion zone, (c) FZ and PMZ interface, and (d) HAZ.

partially melted zone (Figure 4(c)), and heat affected (Figure 4(d)) zone was $35\ \mu\text{m}$, $38\ \mu\text{m}$, and $45\ \mu\text{m}$, respectively. The fusion zone of P-CMT weld is framed with columnar grains with the dendritic structure. The grain morphology varies in the order of equiaxed dendrites and coarse dendrite. The equiaxed dendrites begin from the fusion line to the center of the weld and are perpendicular to the fusion line and parallel to the weld line. As the rate of solidification slows down, the amount of solute in the solution increases. Furthermore, the field of constitutional super cooling significantly expands. When the size of equiaxed dendrites and its respective volume present in liquid weld metal exceed a certain stage, columnar dendrites stop growing and turn into equiaxed dendrite.

3.4. Fractography. The SEM (JEOL India Pvt. Ltd. Type: 6610LV JSM Oh, Japan) analysis was conducted primarily to clarify the failure mode (i.e., both brittle or ductile). The fracture morphology of tested specimens is shown in Figure 5. The fractography does provide useful information about the role of microvoids on strength properties of joint. The fracture surface of high-strength aluminium alloy in as received condition showed fine and deep dimples (Figure 5(a)), whereas wider and shallow dimples were found in the joint welded with P-CMT. It suggests the larger

fracture energy stored during tensile load. Although, the fracture was propagated along the grain boundary, it suggests the fracture mode was intergranular.

4. Discussion

The P-CMT welded AA2014-T6 joint revealed maximum tensile strength of 303 MPa compared to 455 MPa of parent metal. This extends joint efficient up to 67%. By short circuiting and current pulsing, the highest weld strength is due to wire retraction, resulting in the development of refined dendritic grains in weld metal, enhancing the tensile properties of CMT joint in the pulsing mode. Coarse grain formation with partial destruction or size variation in harder precipitates in the HAZ area and is the cause for the breaking point in the HAZ zone [24]. As compared to arcing and short circuiting, the welded metal microstructure of P-CMT joints yields refined dendritic grains that are columnar in shape since the process is connected to a pulse stage with adequate heat input [19]. This pulsing effect, along with the faster cooling rate, helps the grains refine thoroughly. The microstructure of the welding metal is not as refined as it is for CMT joints [27]. The hardness properties in different regions of the joint were based on its microstructural behavior due to the unavailability of pulsation compared to the P-CMT joint [28]. Its high hardness was given by various

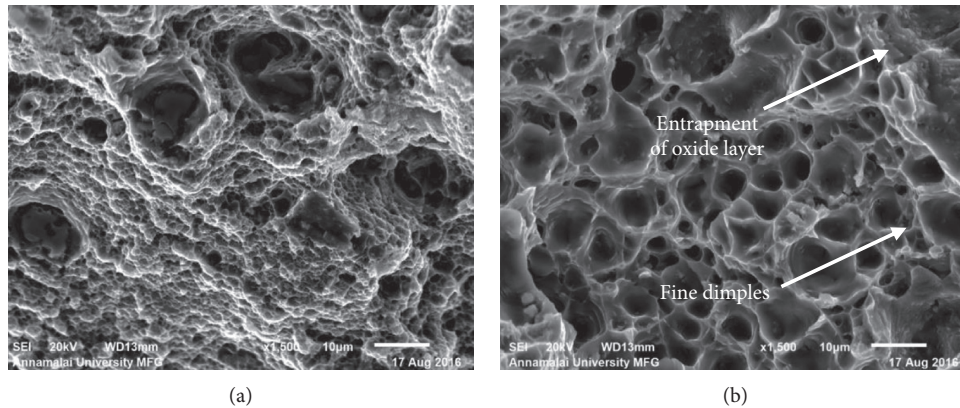


FIGURE 5: SEM fractography of (a) BM and (b) PCMT welded joint.

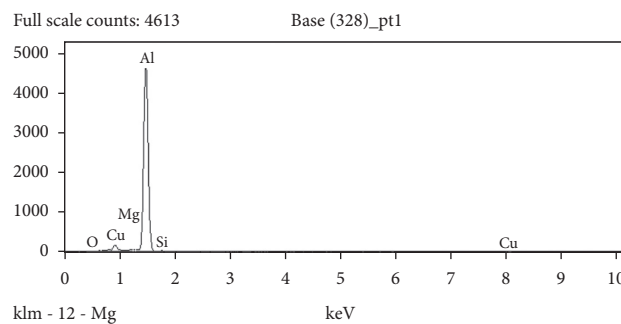


FIGURE 6: EDS analysis of the partially melted zone.

intermetallic compounds of Mg, Cu, and Al or by two of them produced near the fusion region [29, 30]. The weld metal revealed somewhat higher hardness associated to the HAZ zone; although dissolution of precipitate in the weld zone was completely. The region adjacent to the fusion zone is a soft region. Due to the microsegregation of brittle eutectic (α -Al) + θ''), when the grain boundary is heated above the eutectic temperature, the liquation will partially form [31]. This eutectic microsegregation weakens the PMZ, and in the tensile strains, it can result in intergranular cracking. The PMZ is differentiated in the fusion welding process by the formation of equiaxed to columnar grains caused by high heat input. And, the volume of microsegregated eutectic rises as the peak temperature increases, while the concentration of solutionized Cu in the alpha aluminium decreases. In addition, the high concentration electromagnetic force produces a constitutional super-cooling effect to the P-CMT process in the fusion region, which helps regulate phase division tremendously. The hardness of the fusion zone was, therefore, superior to the other zones.

The mechanism behind the formation of weld in high-strength aluminum alloy is the enhancement of the solid solution with Cu and Mn. In the softened area, the minimum hardness was by coarsening or complete destruction of harder phases (precipitates) [24, 32–34]. The greater electromagnetic force contributes the P-CMT process to a constitutional faster-cooling impact that helps to regulate the division of stages immensely. In P-CMT, the pulsing effect is similar to the CMT

process, which helps to dramatically monitor the degree of phase segregation and distribution in the weld region. By the low heat input (0.164 KJ/mm) during the welding cycle, brittle phase and variation in precipitate intensity were reduced considerably. With the formation of weld metal, a common soluble zone was created between the α -aluminium and the welded metal. To disclose the cause behind the fracture point in the welded joint, EDS analysis was performed on the fractured sample. Most researchers claimed that HAZ was the fracture region of the fusion welding process. This area has since lost its precipitate reinforcement due to heat sensitivity during the welding cycle. EDS analysis (Figure 6) result showed that HAZ was composed of Si, Mg, Si, Cu, and O with aluminium. In addition, it consists of 94.97 percent (atom) of Al, 2.44 percent of Cu, 0.75 percent of Mg, 0.43 percent of Si, and 1.4 percent of O, which showed that Al-based solid solution and $\text{Al}_2\text{CuMgSiO}_2$ eutectic structure were composed of this region.

5. Conclusions

The microstructural features and tensile properties of AA2014-T6 joints developed under optimized condition of P-CMT welding were evaluated, and conclusions were made as follows:

- (i) The AA2014-T6 aluminium alloy can be welded successfully using pulsed mode of cold metal transfer-welding (CMT) process without defects of cracking and porosity.

- (ii) The P-CMT AA2014 joints developed using a welding current of 110 A, a welding speed of 450 mm/min, a voltage of 12 V, and a wire feed rate of 5500 mm/min disclosed a maximum tensile strength of 303 MPa compared to 455 MPa of parent metal. This extends joints efficiency up to 67%.
- (iii) The enhancement in strength of P-CMT AA2014 joint is attributed to the combination of the wire's withdrawal motion and pulsing effect in the P-CMT process. The related pulsing mechanism, as well as the arcing and short-circuiting phases, help in refining the dendritic grains in weld metal which aids in controlling the eutectic phase segregation. This enhances the hardness of the weld metal region.
- (iv) The failure occurred at the HAZ of P-CMT AA2014 joint due to the formation of lower eutectic elements in the HAZ and grain growth which lowers the hardness of HAZ compared to weld metal.

Data Availability

The data used to support the findings of this study are included within the article.

Conflicts of Interest

The authors declare that they have no conflicts of interest.

References

- [1] G. Buffa, J. Hua, R. Shivapuri, and L. Fratni, "A continuum based fem model for friction stir welding—model development," *Materials Science and Engineering A*, vol. 419, no. 1–2, pp. 389–396, 2006.
- [2] Z. W. Cen and S. Yazdani, "Friction stir lap welding: material flow, joint structure and strength," *Journal of Achievements in Materials and Manufacturing Engineering*, vol. 55, pp. 629–637, 2012.
- [3] H. Jamshidi, S. Serajzadeh, and A. Kokabi, "Theoretical and experimental investigation in to friction stir welding of AA5086," *International Journal of Advanced Manufacturing Technology*, vol. 52, no. 5, pp. 531–544, 2011.
- [4] R. S. Mishra and Z. Y. Ma, "Friction stir welding and processing," *Materials Science and Engineering: A R*, vol. 50, no. 1–3, pp. 1–78, 2005.
- [5] Y. Tian, J. Shen, S. Hu, Z. Wang, and J. Gou, "Effects of ultrasonic vibration in the CMT process on welded joints of Al alloy," *Journal of Materials Processing Technology*, vol. 259, pp. 282–291, 2018.
- [6] E. Ünel and E. Taban, "Properties and optimization of dissimilar aluminum steel CMT welds," *Welding in the World*, vol. 61, no. 1, pp. 1–9, 2017.
- [7] Y. Liang, S. Hu, J. Shen, H. Zhang, and P. Wang, "Geometrical and microstructural characteristics of the TIG-CMT hybrid welding in 6061 aluminum alloy cladding," *Journal of Materials Processing Technology*, vol. 239, pp. 18–30, 2017.
- [8] Z. Xin, Z. Yang, Z. Han, and Y. Chen, "Comparative study on welding characteristics of laser-CMT and plasma-CMT hybrid welded AA6082-T6 aluminum alloy butt joints," *Materials*, vol. 12, Article ID 3300, 20 pages, 2019.
- [9] Q. Sun, J. Li, Y. Liu, Y. Jiang, K. Kang, and J. Feng, "Arc characteristics and droplet transfer process in CMT welding with a magnetic field," *Journal of Manufacturing Processes*, vol. 32, pp. 48–56, 2018.
- [10] Y. J. Kwon, I. Shigematsu, and N. Saito, "Dissimilar friction stir welding between magnesium and aluminium alloys," *Materials Letters*, vol. 62, pp. 3827–3829, 2008.
- [11] J. C. Yan, Z. W. Xu, Z. Y. Li, L. Li, and S. Q. Yang, "Microstructure characteristics and performance of dissimilar welds between magnesium alloy and aluminium formed by friction stirring," *Scripta Materialia*, vol. 53, pp. 585–589, 2005.
- [12] F.-y. Shu, T. Ze, L. ü. Yao-hui, and W.-x. He, L. ü. Fei-yang, J.-j. Lin, H.-y. Zhao, and B.-s. Xu, "Prediction of vulnerable zones based on residual stress and microstructure in CMT welded aluminum alloy joint," *Transactions of Nonferrous Metals Society of China*, vol. 25, no. 8, pp. 2701–2707, 2015.
- [13] X. Fang, L. Zhang, H. Li, C. Li, K. Huang, and B. Lu, "Microstructure evolution and mechanical behavior of 2219 aluminum alloys additively fabricated by the cold metal transfer process," *Materials*, vol. 11, no. 5, p. 812, 2018.
- [14] H. Liu, S. Yang, C. Xie, Q. Zhang, and Y. Cao, "Mechanisms of fatigue crack initiation and propagation in 6005A CMT welded joint," *Journal of Alloys and Compounds*, vol. 741, pp. 188–196, 2018.
- [15] Z. Silvayeh, B. Götzinger, K. Werner, M. Hartmann, and C. Sommitsch, "Calculation of the intermetallic layer thickness in cold metal transfer welding of aluminum to steel," *Materials*, vol. 12, no. 1, p. 35, 2019.
- [16] B. Cong, R. Ouyang, B. Qi, and J. Ding, "Influence of cold metal transfer process and its heat input on weld bead geometry and porosity of aluminum-copper alloy welds," *Rare Metal Materials and Engineering*, vol. 45, no. 3, pp. 606–611, 2016.
- [17] C. Rajendran, K. Srinivasan, V. Balasubramanian, H. Balaji, and P. Selvaraj, "Evaluation of load-carrying capabilities of friction stir welded, TIG welded and riveted joints of AA2014-T6 aluminium alloy," *Aircraft Engineering & Aerospace Technology*, vol. 19, no. 9, 2019.
- [18] R. R. Ambriz, G. Barrera, R. García, and V. H. López, "The microstructure and mechanical strength of Al-6061-T6 GMA welds obtained with the modified indirect electric arc joint," *Materials & Design*, vol. 31, no. 6, pp. 2978–2986, 2010.
- [19] C. G. Pickin and K. Young, "Evaluation of cold metal transfer (CMT) process for welding aluminium alloy," *Science and Technology of Welding & Joining*, vol. 11, no. 5, pp. 583–585, 2006.
- [20] B. Gungor, E. Kaluc, E. Taban, and A. Sik Ş, "Mechanical and microstructural properties of robotic cold metal transfer (CMT) welded 5083-H111 and 6082-T651 aluminum alloys," *Materials & Design*, vol. 54, pp. 207–211, 2014.
- [21] A. S. Azar, "A heat source model for cold metal transfer (CMT) welding," *Journal of Thermal Analysis and Calorimetry*, vol. 122, no. 2, pp. 741–746, 2015.
- [22] L. Yin, J. Wang, H. Hu, S. Han, and Y. Zhang, "Prediction of weld formation in 5083 aluminum alloy by twin-wire CMT welding based on deep learning," *Welding in the World*, vol. 63, no. 4, pp. 947–955, 2019.
- [23] S. Selvi, A. Vishvakshnan, and E. Rajasekar, "Cold metal transfer (CMT) technology-An overview," *Defence technology*, vol. 14, no. 1, pp. 28–44, 2018.
- [24] R. R. Ambriz, D. Chicot, and N. Benseddiq, "Local mechanical properties of the 6061-T6 aluminium weld using micro-traction and instrumented indentation," *European Journal of Mechanics-A/Solids*, vol. 30, pp. 307–315, 2011.

- [25] S. Babu, G. D. Janaki ram, and P. V. Venkatakrishnan, G. Madusudhana Reddy, K. Prasad Rao, "Microstructure and mechanical properties of friction stir lap welded aluminium alloy AA2014," *Journal of Materials Science & Technology*, vol. 28, no. 5, pp. 414–426, 2012.
- [26] A. Ramaswamy, S. Malarvizhi, and V. Balasubramanian, "Effect of variants of gas metal arc welding process on tensile properties of AA6061-T6 aluminium alloy joints," *International Journal of Advanced Manufacturing Technology*, vol. 108, no. 9, pp. 2967–2983, 2020.
- [27] B. Gungor, E. Kaluc, E. Taban, and S. I. K. Aydin, "Mechanical and microstructural properties of robotic Cold Metal Transfer (CMT) welded 5083-H111 and 6082-T651 aluminum alloys," *Materials & Design*, vol. 54, pp. 207–211, 2014.
- [28] J. Shang, K. Wang, Q. Zhou, D. Zhang, J. Huang, and G. Li, "Microstructure characteristics and mechanical properties of cold metal transfer welding Mg/Al dissimilar metals," *Materials & Design*, vol. 34, pp. 559–565, 2012.
- [29] R. R. Ambriz, G. Barrera, R. García, and V. H. López, "Effect of the weld thermal cycles of the modified indirect electric arc on the mechanical properties of the AA6061-T6 alloy," *Welding International*, vol. 24, no. 4, pp. 321–328, 2010.
- [30] L. M. Liu, X. J. Liu, and S. H. Liu, "Microstructure of laser-TIG hybrid welds of dissimilar Mg alloy and Al alloy with Ce as interlayer," *Scripta Materialia*, vol. 55, pp. 383–386, 2006.
- [31] S. Y. Chang, L. C. Tsao, T. Y. Li, and T. H. Chuang, "Joining 6061 aluminum alloy with Al-Si-Cu filler metals," *Journal of Alloys and Compounds*, vol. 488, pp. 174–180, 2009.
- [32] C. Rajendran, K. Srinivasan, V. Balasubramanian, H. Balaji, and P. Selvaraj, "Effect of post weld heat treatment on strength and microstructure of friction stir welded lap joints of AA2014-T6 aluminum alloy," *Metal Science and Heat Treatment*, vol. 61, no. 5, pp. 305–310, 2019.
- [33] C. Rajendran, K. Srinivasan, V. Balasubramanian, H. Balaji, and P. Selvaraj, "Effect of tool tilt angle on strength and microstructural characteristics of friction stir welded lap joints of AA2014-T6 aluminum alloy," *Transactions of Non-ferrous Metals Society of China*, vol. 29, no. 9, pp. 1824–1835, 2019.
- [34] M. L. Zhu and F. Z. Xuan, "Correlation between microstructure, hardness and strength in HAZ of dissimilar welds of rotor steels," *Materials Science and Engineering*, vol. A527, pp. 4035–4042, 2010.

Retraction

Retracted: Performance Analysis and Development of a Semiconductor Junction Rectifier with Multicolor Coding for Indoor Farm Applications

Advances in Materials Science and Engineering

Received 26 December 2023; Accepted 26 December 2023; Published 29 December 2023

Copyright © 2023 Advances in Materials Science and Engineering. This is an open access article distributed under the Creative Commons Attribution License, which permits unrestricted use, distribution, and reproduction in any medium, provided the original work is properly cited.

This article has been retracted by Hindawi, as publisher, following an investigation undertaken by the publisher [1]. This investigation has uncovered evidence of systematic manipulation of the publication and peer-review process. We cannot, therefore, vouch for the reliability or integrity of this article.

Please note that this notice is intended solely to alert readers that the peer-review process of this article has been compromised.

Wiley and Hindawi regret that the usual quality checks did not identify these issues before publication and have since put additional measures in place to safeguard research integrity.

We wish to credit our Research Integrity and Research Publishing teams and anonymous and named external researchers and research integrity experts for contributing to this investigation.

The corresponding author, as the representative of all authors, has been given the opportunity to register their agreement or disagreement to this retraction. We have kept a record of any response received.

References

- [1] E. D. Kanmani Ruby, M. Umadevi, C. Kanmani Pappa, W. Edwin Santhkumar, P. Janani, and P. Shanmugasundaram, "Performance Analysis and Development of a Semiconductor Junction Rectifier with Multicolor Coding for Indoor Farm Applications," *Advances in Materials Science and Engineering*, vol. 2021, Article ID 6585680, 12 pages, 2021.

Research Article

Performance Analysis and Development of a Semiconductor Junction Rectifier with Multicolor Coding for Indoor Farm Applications

E. D. Kanmani Ruby¹, M. Umadevi,² C. Kanmani Pappa,¹ W. Edwin Santhkumar,³ P. Janani,¹ and P. Shanmugasundaram⁴

¹Vel Tech Rangarajan Dr. Sagunthala R & D Institute of Science and Technology, Chennai, Tamilnadu, India

²Er Perumal Manimegalai College of Engineering, Hosur, India

³Sri Sakthi Institute of Engineering and Technology, Coimbatore, India

⁴Mizan-Tepi University, Tepi, Ethiopia

Correspondence should be addressed to E. D. Kanmani Ruby; bewinbewin54@gmail.com

Received 4 August 2021; Revised 18 August 2021; Accepted 8 September 2021; Published 18 October 2021

Academic Editor: Samson Jerold Samuel Chelladurai

Copyright © 2021 E. D. Kanmani Ruby et al. This is an open access article distributed under the Creative Commons Attribution License, which permits unrestricted use, distribution, and reproduction in any medium, provided the original work is properly cited.

This paper aims to build a smart lighting system with applications such as remote for controlling power supply and optimizing heat management in the metal body of the semiconductor diode and with a printed circuit board for agriculture. The semiconductor diode strips with multiple colors are lined up and configured as a LED lamp with proper casing and heat sink. It has a driver circuit with required power regulation that is able to control the intensity of light for photosynthesis and plant growth requirements. The system uses hydroponics to plant the water, thus decreasing the usage of fertilizers. The entire system is controlled remotely using necessary communication interface application.

1. Introduction

The most important mutable factor with respect to plant growth and development is light. The lights in green house application are advantages for plant growth research. The purpose for using grow lights differs and includes increasing light levels for plant photosynthesis or altering the photoperiod [1]. The photoperiod is defined as the period of light a plant perceives. The different lighting sources that growers can use include incandescent (INC) lamps, tungsten-halogen lamps, fluorescent lamps, and high-intensity discharge (HID) lamps. Light-emitting diodes (LEDs) are fourth-generation lighting sources and are an emerging technology in horticulture.

Lead-wire, surface-mounted, and high-power LEDs are three main structural types. LEDs are solid-state semiconductors and when turned on or off, the action is instant and is about 70 percent from initial installation which can

operate up to 50,000 hours. It is not necessary to replace single diodes or lamps constantly because LEDs do not burn out. Factors such as design, materials used, and heat release affect life expectancy. As for consumption of energy, LEDs are more efficient and use less energy than any other traditional greenhouse lights [2]. In addition, operating costs and carbon emissions are lowered when using LEDs.

2. Related Works

The authors in [1] have devised a new digital control strategy that is presented for a bridgeless single-stage multioutput AC/DC converter previously proposed as an semiconductor diode grow light. The proposed control system can regulate the output current flowing through each individual diode string, perform power factor correction at the AC side, and provide zero-voltage switching characteristics for all power semiconductors, and the new method reduces conduction

losses associated with transformer windings and power semiconductors by adaptively varying the DC bus voltage; thus, the new control system can result in superior transient response.

The relationship between LEDs and plant growth with respect to a small hydroponic plant is described in [3]. The global population growth and the ongoing climate crisis pose immense risk to the stable food supplies in the future. So, it is necessary to develop a small hydroponic plant cultivation system to ensure supply of nutrients even in extreme circumstances. To build a sustainable system, they have utilized an LED lighting system together with conserved energy generated by sunlight. Such hydroponic plant cultivation systems have to operate at an affordable yet efficient principle.

The authors in [4] specified how we can use Internet of Things (IoT) and build smart garden systems. Internet of Things (IoT) consists of devices that connect to the Internet and communicate with each other. It enables these devices to collect and exchange data with a consumer. This paper presents an IoT-based Smart Garden with Weather Station system, which can be used to monitor the growth of plants every day and predict the probability for raining. Many people interested in growing plants always forget to water the plants. Hence, in this study, the device is equipped with a water pump, where it can be monitored and controlled by using a smartphone. In addition, the device also consists of four main sensors, which are a barometric pressure sensor, a DHT11 temperature and humidity sensor, a soil moisture sensor, and a light intensity module sensor. The soil and light intensity sensor is used to measure the value in percentages. Besides, two actuators, which are the water pump and LED light, can be used remotely or by using a button on the device. The LED is purposely used to replicate the sunlight and make the plant grow faster. This IoT-based Smart Garden with Weather Station System can record the data and send the result to the user through the smartphone application named "Blynk apps." This research is beneficial, and the system can be easily managed by all users such as researchers, farmers, and children.

The way the light supplementation can increase the crop yield in greenhouses by promoting photosynthesis and plant growth has been explained by the authors in [5]. However, the high energy costs associated with light supplementation are a predominant factor that limits development and profit improvement of controlled environment agriculture.

In [6], the authors studied an effective way of light usage for plant growth. The light types included LED, grow light, and natural light. Investigated periods are germination and growth. A plant nursery of $1.2 \times 1.2 \times 1.5$ m in dimension was used. The structure was made up of PVC tubes. It was covered by black canvas. The system was controlled by a micro-controller. The sensor module DHT22 detected both temperature and humidity. The plant nursery was separated into two rooms for LED and grow light testing. Cooling pads and water dispenser were used for the cooling system. A fan was installed for flowing air. The plant was watered automatically. From the experimental results, it was observed that the plant under LED light had the fastest rate of germination.

In [7], the current agriculture and its advancement are explained, with sustainable food production and security in a demographically obese world, and considered to be the challenging issue. Different technologies were employed to enable farming practices to adapt and build resilience against irregular microclimate shifts. Alternate farming technologies like hydroponic culture technique and integration of smart artificial light and IoT system are deemed promising solutions to the aforementioned problems.

The authors in [8] discussed how to develop a smart LED lighting system [8], which is remotely controlled by Android apps via handheld devices, e.g., smartphones, tablets, and so forth. The status of energy use is reflected by readings displayed on a handheld device, and it is treated as a criterion in the lighting mode design of a system. The wireless data communication is designed to operate in compliance with the ZigBee standard, and signal processing on sensed data is made through a self-adaptive weighted data fusion algorithm. A low variation in data fusion together with a high stability is experimentally demonstrated in this work.

In [9], the authors described how light-emitting diodes (LEDs) have tremendous potential as supplemental or sole-source lighting systems for crop production both on and off earth. Their small size, durability, long-operating lifetime, wavelength specificity, relatively cool emitting surfaces, and linear photon output with electrical input current make these solid-state light sources ideal for use in plant lighting designs.

3. Designing of LEDs: Manufacturing Process

3.1. Frame Precuring for Die Bond. To begin, it all starts with the precuring of the LED frames [1] in oven 1 for 1 hour at 150 degrees. This is because the metal becomes soft, and it will be easy to do the die bond.

3.2. Expanding Crystal. Now, the LED crystals are taken; initially, they are all placed very close to each other, so a compression machine is used to expand the spaces between them. Before that, the LED crystals should be exposed to polarized air for a couple of seconds.

3.3. Die Bonding. Die bonding is a manufacturing process used in the packaging of semiconductors, as shown in Figure 1. It is the process of attaching a die (or chip) to a substrate or package by epoxy or solder, also known as die placement or die attach. The process starts with picking a die from a wafer or wafer pack and then placing it at a specific location on the substrate. The die is placed into a previously dispensed epoxy or placed into solder.

The die-attach material plays a key role in the performance and reliability of mid, high, and super high-power LEDs. [10] The selection of the suitable die-attach material for a particular chip structure and application depends on several considerations. These include the packaging process (throughput and yield); performance (thermal dissipation and light output); reliability (lumen maintenance); and cost. Eutectic gold-tin, silver-filled epoxies, solder, silicone, and



FIGURE 1: Die-bonding machine.

sintered materials have all been used for LED die-attach. The use of a particular technology platform often results in trade-offs between different attributes. Mid- to super high-power LEDs are operated at increasing current and power levels (for lighting and mobile ash applications, among others). This trend has brought to the forefront the need for robust thermal dissipation. If the heat is not managed properly [11], the LED performance can degrade significantly, resulting in loss of radiant flux, increase in forward voltage, wavelength shift, and consequently, reduced lifetime. Figures 1 and 2 show the die-bonding machine and mechanism of die bonding, respectively.

3.4. Die-Bonded Frame for Curing. After the die bonding is performed, the frames are again placed in oven 2 at 175 degrees for 2 hours. Thus, the LED gets well settled and becomes rigid in place.

3.5. Wire Bonding. Wire bonding [9, 12, 13] is the process of creating electrical interconnections between semiconductors (or other integrated circuits) [14] and silicon chips using bonding wires, which are fine wires made of materials such as gold and aluminum. The sample diagram is represented in Figure 3.

Compared to aluminum wedge bonding, gold ball bonding is significantly faster due to being nondirectional, resulting in its widespread use in plastic packaging [15]. However, gold ball bonding on aluminum bond pads cannot be used in hermetic packages due to the high sealing temperatures used in such packages, as these temperatures greatly accelerate the formation of gold-metal intermetallic, which can result in early life failures. Conversely, gold ball bonding on gold bond pads can be utilized in hermetic packages. Figure 4 shows the process of wire bonding.

Gold-aluminum ball bonding requires the use of heat to enable the bonding process [16]. Good bonding between the aluminum bond pad and the gold ball bond without causing damage to the wire, bond pad, or silicon substrate through solely ultrasonic methods is impossible due to the aluminum bond pad being harder than the gold ball bond. The aluminum bond pads are softened by applying thermal energy to them, which encourages the aluminum and gold atoms to interdiffuse, which forms the gold-aluminum bond [17]. The application of thermal energy also improves the bonding

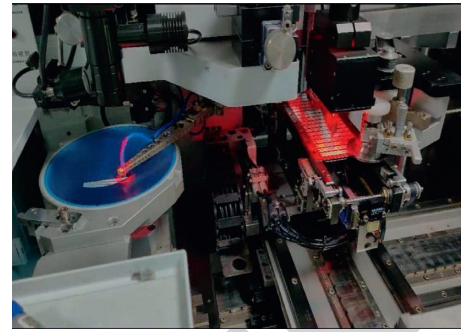


FIGURE 2: Mechanism of die bonding.



FIGURE 3: Wire bonding.

process by eliminating organic contaminants on the surface of the bond pad. Recent transitioning in the wire bonding industry has seen a preference in copper over gold for use in the wire bonding process, with the reason being that the cost of gold is rising. Although there are concerns that copper is less reliable due to its hardness and susceptibility to corrosion, copper wire can be used at smaller diameters, making it more cost-effective.

3.6. Wire-Bonded Curing. After the wire-bonding process is complete, the frames are once again placed in oven 1 for pre-curing for half an hour before they go to the dispenser. This in turn settles the wire-soldered material to remain in its place [18].

3.7. Planetary Mixture. Planetary mixers [19] are industrial noncontact mixers for all liquids, pastes, powders, and fillers and any combination of liquids or liquids/solids. This includes engineering compounds, pharmaceutical or cosmetic formulations, and nanoparticle dispersions. They mix, disperse, and degas your materials in seconds to minutes, in a sealed or lid-less container such as a jar, beaker, syringe tube, or cartridge [20]. The noncontact mixing principle makes it possible to formulate or combine compounds from very small amounts such as 0.5 ml to large-scale production. By means of both rotation and revolution of the material in a container, materials are mixed and degassed. The materials are placed under an acceleration of 400 G, in which even materials of very high viscosity can be mixed and deaerated or degassed at the same time [21].

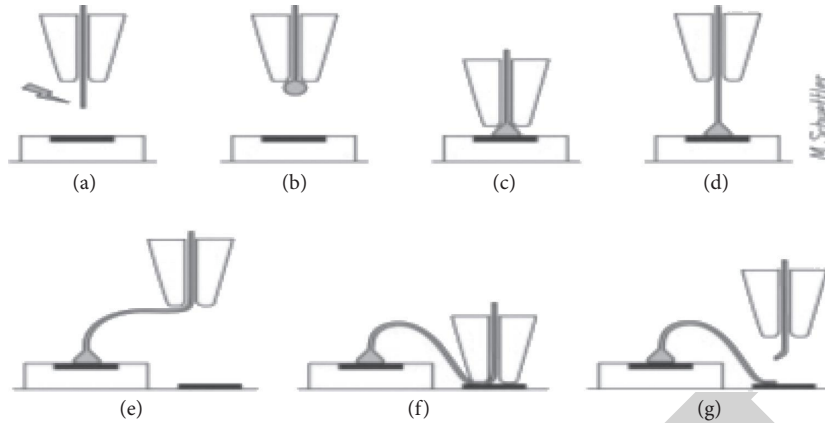


FIGURE 4: Process of wire bonding.

Figure 5 shows the principle in action of two slabs of modelling clay that are completely mixed in a couple of minutes. The stages illustrate the mixing action imparted to the materials by the planetary forces. Lower viscosity materials can mix much faster. All sorts of powders or fillers can be mixed into liquids or pastes in the same way.

3.8. Dispenser. The dispensing machine [19, 22] is used to apply high viscous liquids paste material on LED bulbs as well as other round applications. These dispensers are portion-controlled, delivering accurate amounts of the product configured to the preset value, commonly used quantities, or quantities specified by the company. Process selections are made using buttons on the front panel using our unique, state-of-the-art control technology. The dispenser uses a manually operated push switch or cycle start switch to deliver products in a desired quantity. The dispenser consists of a syringe-like device that secretes the required amount of portion onto the LED to give the required wavelength or color [23]. The features of the dispenser include clean dispense, quick cutoff avoiding messy spills, high accuracy and efficiency, increased productivity, continuous and controlled calibrated HMI display, manually and automatically controlled machine, standard high pressure safety valve, and calibrated gauges, designed with ergonomics and aesthetic consideration, reduced labor cost, simplicity of use, and easiness in cleaning.

Different colors can be achieved by the LEDs by using different semiconductors:

- (i) Red: wavelength 625 to 760 nm (AlGaAs)
- (ii) Orange: wavelength 600 to 625 nm (GaAsP)
- (iii) Yellow: wavelength 577 to 600 nm (AlGaInP)
- (iv) Green: wavelength 492 to 577 nm (GaN)
- (v) Blue: wavelength 455 to 492 nm (ZnSe)
- (vi) Violet: wavelength 390 to 455 nm (InGaN)

3.9. Dispenser Frames Curing. Once the dispenser completes dispensing the required portions onto all the LEDs, the LEDs are then placed in oven 3 for 1 hour at 100°C and then in oven 4 for 4 hours at 150°C [24].

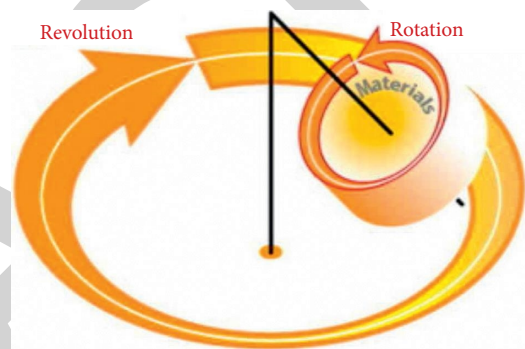


FIGURE 5: Rotation and revolution in a planetary mixture.

3.10. Frame Tester. The frame tester is a device that will test the electricity flow in the frame and check whether each and every LED is glowing or not. It will place two metal sticks at the terminals of the LED and give the required voltage to turn it on [25].

3.11. Single Cutting. It is a device that will cut the LEDs out of the frame.

3.12. Bin Sorting. The device, as shown in Figure 6, will separate all the LEDs according to their wavelength and temperature. A spectrometer is present at the entrance, where every LED will pass through it, and it will detect which wavelength the LED has and will place it in the respective bin; it is the same for the temperature of the LED also. If a LED does not work, it will be placed in a separate bin.

3.13. LED Precuring for Packaging. Here, the LED will be heated one last time before being packed.

3.14. Packaging and Reeling. Here, the LEDs are placed in a machine that will test them and place them onto a casing that will be reeled automatically. The machine will automatically cut the chain of LEDs when they reach the reel limit [26].

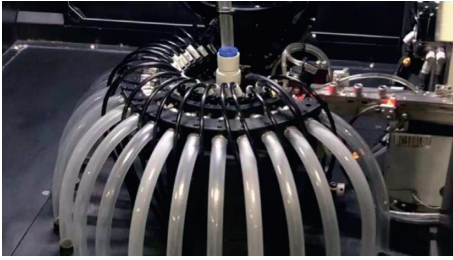


FIGURE 6: Mechanism inside a bin-sorting machine.

3.15. *Packing.* The reels are placed in a cover and then using a vacuum, the air is sucked out and sealed.

4. LED Grow Lights

An LED grow light is an electric light source, which helps plants to grow [1–5]. Grow lights either attempt to provide a light spectrum similar to that of the sun or a spectrum that is more tailored to the needs of the plants being cultivated. Outdoor conditions are mimicked with varying colors, temperatures, and spectral outputs from the grow light, as well as varying the intensity of the lamps. Depending on the type of plants being cultivated, the stage of cultivation, and the photoperiod required by the plants, the specific ranges of spectrum, luminous efficacy, and color temperature are considered to be desirable parameters for some specific plants.

Energy-efficient LED grow lights are the lighting of the future of agriculture [6]. They not only are economic in their use, but produce better plants as well, in comparison to all traditional lighting options.

LEDs outperform incandescent lights in many ways, especially when it comes to energy efficiency. According to Energy Star, the LEDs can save energy at a rate of 90 percent more than incandescent bulbs. The way LED lighting works is when the light source is turned on, it is directional. This means that the LED light aims in a certain direction to provide illumination. But in a compact fluorescent lamp or CFL as well as incandescent bulbs, the light travels in all directions, which decreases energy efficiency due to dispersion of light unnecessarily. Not only do LEDs make a smarter choice for the environment then, but for our wallets as well. Most LED lights will last about 50,000 hours.

4.1. *LED Grow Lights.* These do not solely have to be LED lights. We may also choose to grow your plants with high-intensity discharge lights or HIDs, fluorescents, and incandescent grow lights. No matter which we choose, grow lights generate the right amount of light, so a plant can photosynthesize [27]. This means of conversion gives the plant the energy. Most grow lights are electric, and all are artificial. Plant owners will use grow lights if a plant needs an extra light source besides the sun or if the plant cannot get access to the sun for any reason. For instance, maybe we grow a plant in a cubicle, grow lights, although artificial, try to mimic the sun as naturally as possible. In doing this, we typically have a varying light spectrum available for our grow

lights. Besides the color spectrum, it is also possible to have control over the color temperature and the luminous efficacy with grow lights.

5. Hydroponics

Hydroponics is a method of growing plants indoors without using any soil [3–5, 7]. Instead of pulling mineral nutrients needed for growth from the ground, plants get all of their nutrition through a nutrient solution supplied to their roots. Hydroponics works in a variety of scenarios from growing a small collection of herbs in a kitchen all the way up to numerous plants in a large-scale commercial operation. People with limited or no outdoor space, such as urban residents, apartment dwellers, or renters who cannot have an outdoor garden, find hydroponic growing especially useful [28–33].

The advantages of hydroponics are as follows [8, 9, 34]: firstly, it requires far lesser space than plants grown in soil, and the roots do not have to spread out to search for nutrients and moisture as in hydroponics water, and nutrients are delivered to the roots directly, either intermittently or constantly. Secondly, it conserves a lot of water when compared to soil growing plants. Thirdly, it requires less labor, as it does not require tilling, weeding, and herbicide and insecticide application, as the user is just required to make sure to change water time to time. Fourthly, as it does not require artificial fertilizers, the plants are more natural and organic and have higher quality. Finally, the reason to choose this technology is that the customer using this device can grow his/her own plants or vegetables anywhere they want, and also it is very easy to control it as it is equipped with Wi-Fi and its own app with easy settings. It grows the plants with the highest quality without compromising on the best form of its organic, natural, and nutritious state [35].

5.1. *Selection of Wavelength.* The LEDs selected are 450 nm, 660 nm, 730 nm, and 3000 CCT [9]. The amount of light affects the photosynthesis process in the plant. This process is a photochemical reaction within the chloroplasts of the plant cells, in which CO₂ is converted into carbohydrate under the influence of the light energy. The spectral composition of the different wavelength regions (blue, green, yellow, red, far red, or invisible, e.g., UV or IR) is important for the growth, shape, development, and flowering (photomorphogenesis) of the plant. Figure 7 shows the illumination with various wavelengths. Table 1 shows various wavelengths, vegetative growth, and its effects.

5.2. *Design of the Body.* The body of the design consists of 2 plant holders, a container with partitions for the components, a lid to close the container, and a tube to hold and support the LED profile.

- (i) The dimensions of the container are $35 \times 20 \times 10$ cm ($l \times b \times h$)
- (ii) The dimensions of the plant container are $30 \times 17 \times 10$ cm ($l \times b \times h$)

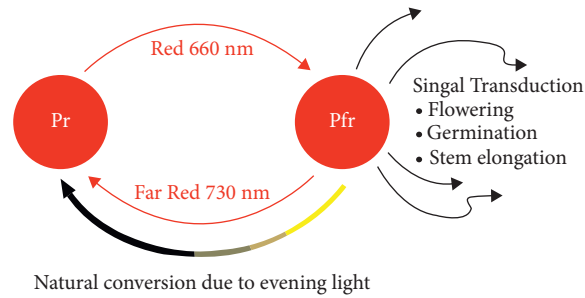


FIGURE 7: Illumination with 660 nm and 730 nm.

TABLE 1: Effects of the particular wavelengths.

Wavelength (nm)	Photosynthesis	Vegetative growth	Effects
450 nm	✓	✓	Leaf expansion, stomatal openings
660 nm	✓	✓	Flowering, budding, stem elongation
730 nm	✓	✓	Germination, leaf building, flowering
3000 CCT white	✓	✓	Boosts the plant growth

- (iii) The dimensions of the holders are 5×7 cm ($r \times h$)
- (iv) The dimensions of the LED profile are $30.5 \times 5 \times 3.5$ cm ($l \times b \times h$)
- (v) The dimensions of the tube are 2×35 cm ($r \times h$)

The material used for the body is aluminum, and the body of the device will be welded.

5.3. Component Selection: Node MCU. Node MCU is an open-source Lua-based firmware and development board [35] specially targeted for IoT-based applications. It includes firmware that runs on the ESP8266 Wi-Fi SoC from Express if it is based on the ESP-12 module. Figures 8 and 9 represent the images of drivers and motor, respectively.

- (i) Microcontroller: Tensilica 32-bit RISC CPU Xtensa LX106
- (ii) Operating voltage: 3.3 V
- (iii) Input voltage: 7–12 V
- (iv) Digital I/O pins (DIO): 16
- (v) Analog input pins (ADC): 1
- (vi) UARTs: 1
- (vii) SPIs: 1
- (viii) I2Cs: 1
- (ix) Flash memory: 4 MB
- (x) SRAM: 64 KB
- (xi) Clock speed: 80 MHz
- (xii) USB-TTL based on CP2102 is included onboard, enabling plug and play
- (xiii) PCB antenna
- (xiv) Small-sized module to fit smartly inside your IoT projects

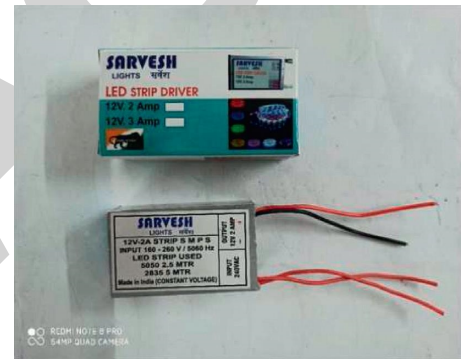


FIGURE 8: 12 V/2 A driver.



FIGURE 9: 1500 rpm motor.

5.4. Circuit Design. The LED positive is connected to the power supply positive. The LED negative is connected to the drain of the MOSFET1. The MOSFET1 gate is connected to the microcontroller, and the source is connected to the power supply negative and ground of the microcontroller. The motor positive is connected to the power supply positive. The motor negative is connected to the drain of the MOSFET2 [33]. The MOSFET2 gate is connected to the microcontroller, and the source is connected to the power supply negative and ground of the microcontroller. The 230/

12 V adapter positive wire is connected to a terminal pin in the PCB. The 12 V pin is connected to 3 separate pins on the board. The 3 pins are connected to the positive wire; one of them is connected to the positive terminal of the $10\ \mu\text{F}$ capacitor that is in turn connected to the input pin of the LM7805 MOSFET. Figure 10 shows the circuit design of MOSFET [34].

The output pin of the LM7805 MOSFET is connected to the positive pin of the $1\ \mu\text{F}$ capacitor. The negative of the $10\ \mu\text{F}$ and $1\ \mu\text{F}$ capacitor, ground of the LM7805 MOSFET, are commonly connected to node MCU 5 V is obtained at the positive pin of the $1\ \mu\text{F}$ capacitor. This is connected to the Vin pin on the node MCU to power it up. The other pins are connected to the 12 V positive wire; one is connected to the LED strip positive wire, and the other pin is connected to the motor positive wire. A total of 4 LED strips are used; all the positive wires are joined together and given a voltage of 12 V; it is the same for the motor also, as the motor is 12 V and 1500 rpm. Now, the negatives of the LED strips and motor each are connected to each 2N7000 MOSFET's drain pin, and the gate is connected to each PWM pin on the node MCU; here, the pins are D1, D2, D3, and D4. The overall block diagram is represented in Figure 11.

- (i) The 2N7000 MOSFET's source is all commonly connected to the ground on the node MCU

5.5. *LED Strip Design.* 4 LED strip designs are used. The LEDs used in this project are as follows:

- (1) 6–450 nm LEDs (blue), 10 cm
- (2) 6–660 nm LEDs (deep red), 10 cm
- (3) 6–730 nm LEDs (far red), 10 cm
- (4) 6–3000 CCT LEDs (warm white), 10 cm

Figure 12 shows the images of the LED strip. The LEDs are placed in a combination of 3S, 2P, that is, 2 sets of 3 LEDs in series, and both sets are connected in parallel. A LED strip is 5 cm and consists of 3 LEDs each, and each LED is 3 V/150 mA. They are placed in series. In series, the voltage adds and the current stays constant; thus, the LED strip is 9 V/150 mA. Each wavelength has 2 LED strips, that is, 6 LEDs, which is 2 strips set in parallel. In parallel, the current adds and the voltage stays constant; thus, each wavelength LED strip is 9 V/300 mA. The input voltage given is 12 V, and as the required voltage is 9 V, a resistor is used to cause a voltage drop. Voltage drop is $12 - 9 = 3\ \text{V}$. Current = 300 mA. Resistance = $V/I = 3\ \text{V}/300\ \text{mA} = 10\ \text{ohms}$. Thus, a 10-ohm resistor is used.

For a red LED, the specification is 2 V/150 mA. Thus, each strip of 3 LEDs is 6 V/150 mA. The red wavelength strip consists of 6 LEDs that are 2 strips in parallel, so the specification is 6 V/300 mA. The input voltage is 12 V, and the required voltage is 6 V. Voltage drop = $12 - 6 = 6\ \text{V}$. Current = 300 mA. Resistance = $V/I = 6\ \text{V}/300\ \text{mA} = 20\ \text{ohms}$, and thus a 20-ohm resistor is used.

The profile is made of aluminum, and its dimensions are $300 \times 50 \times 35\ \text{mm}$. All these strips are attached to the profile,

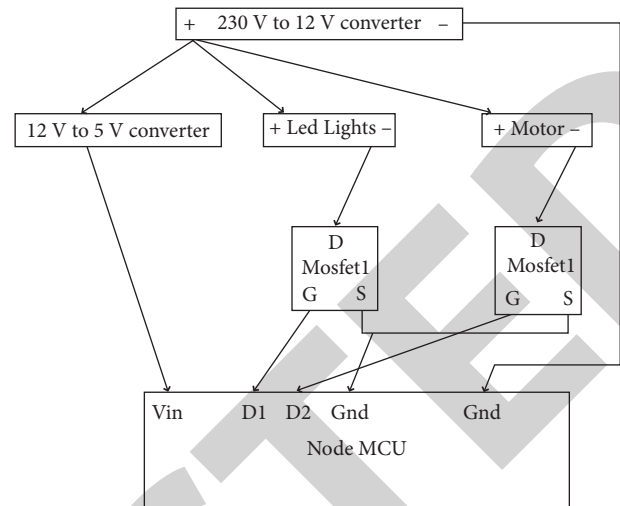


FIGURE 10: Circuit design.

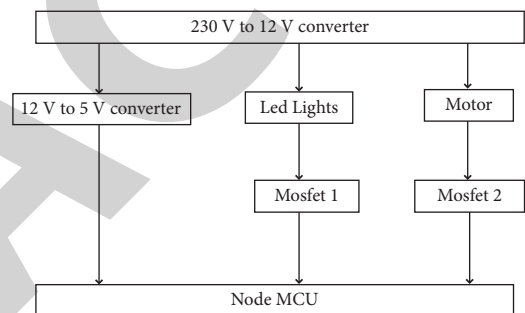


FIGURE 11: Block diagram.



FIGURE 12: LED strip.

which is equipped with a heat sink design. The strips are first glued to the profile using thermal paste and then screwed to them.

5.6. *Outer Body.* The 3D model of the body is shown in Figures 13–15. The outer body of the device consists of 4 parts. The material used is 2 mm aluminum metal sheet. They are (1) plant holder part, (2) electronic component holder part, (3) LED profile, and (4) the goose neck pipe.

5.6.1. *The Plant Holder Part.* The plant holder part consists of 3 plant holders with a diameter of 5 cm. The dimensions are $300 \times 100 \times 100\ \text{mm}$.

5.6.2. *The Electronic Component Holder Part.* Its dimensions are $300 \times 50 \times 100\ \text{mm}$. Here, the PCB and the motor are placed separately. Front view, side view, and back view of the

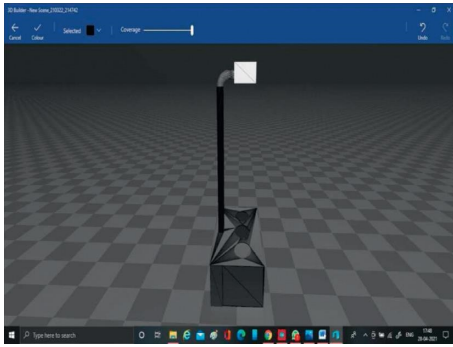


FIGURE 13: Front view of the body.

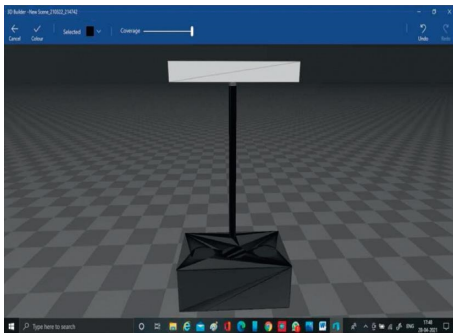


FIGURE 14: Side view of the body.

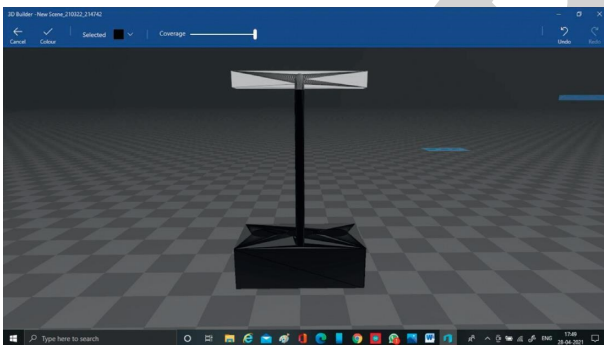


FIGURE 15: Back view of the body.

body are represented in Figures 13–15, respectively. Figures 16 and 17 represent the plant holder part.

Figure 18 depicts the electronic component part, and Figure 19 shows the electronic setup of the entire parts.

5.6.3. The LED Profile. The LED profile consists of heat sink on the top. It also has the LEDs stuck to them with thermal paste and screws as shown in Figure 20. Its dimensions are $300 \times 50 \times 35$ mm.

5.6.4. The Goose Neck Pipe. It is a 450 mm long flexible metal pipe with a diameter of 14 mm. It will connect the LED profile to the lower body of the device. Figure 21 shows the goose neck pipe model.

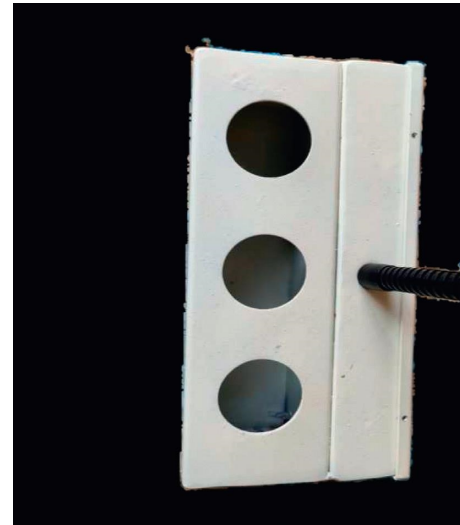


FIGURE 16: Plant holder part.

5.7. Printed Circuit Board. Its dimensions are $60 \times 40 \times 2$ mm. It consists of the respective components: LM7805, $0.1\text{--}1\ \mu\text{F}$ capacitor, $1\text{--}10\ \mu\text{F}$ capacitor, 4-2N7000 MOSFET, and 1-node MCU (ESP8266). The LM7805 and the 2 capacitors make the 12 V to 5 V converter, which is represented in Figure 22.

Figures 23 and 24 represent the schematic circuit diagram and PCB diagram, respectively. The 230/12 V adapter positive wire is connected to a terminal pin in the PCB. The 12 V pin is connected to 3 separate pins on the board. The 3 pins are connected to the positive wire; one of them is connected to the positive terminal of the $10\ \mu\text{F}$ capacitor that is in turn connected to the input pin of the LM7805 MOSFET. The output pin of the LM7805 MOSFET is connected to the positive pin of the $1\ \mu\text{F}$ capacitor. The negative wire connected to the negative terminal of the $10\ \mu\text{F}$ capacitor, the ground of the LM7805 MOSFET, and the negative of the $1\ \mu\text{F}$ capacitor are all commonly connected to the ground on the node MCU.

5 V output is obtained at the positive pin of the $1\ \mu\text{F}$ capacitor. This is connected to the Vin pin on the node MCU to power it up. The other pins are connected to the 12 V positive wire; one is connected to the LED strip positive wire, and the other pin is connected to the motor positive wire.

A total of 4 LED strips are used; all the positive wires are joined together and given a voltage of 12 V; it is the same for the motor also, as the motor is 12 V and 1500 rpm. Now, the negatives of the LED strips and motor each are connected to each 2N7000 MOSFET's drain pin. The 2N7000 MOSFET's gate is connected to each PWM pin on the node MCU; here, the pins are D1, D2, D3, and D4. The 2N7000 MOSFET's source is all commonly connected to the ground on the node MCU.

6. Results

This work aims to find a solution for indoor plant growth using LED lights and hydroponics. The LEDs are a highly

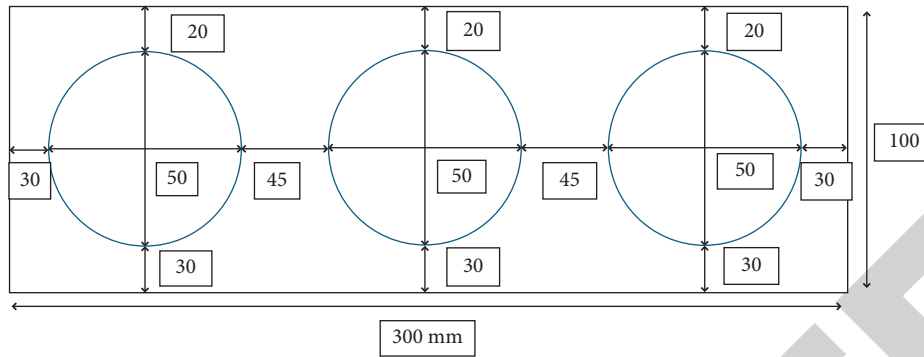


FIGURE 17: Plant holder part.

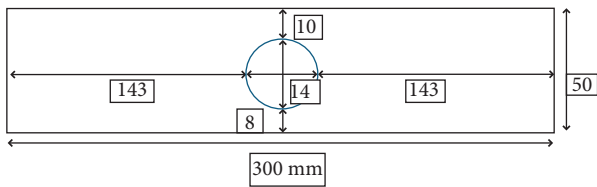


FIGURE 18: Electronic component part.

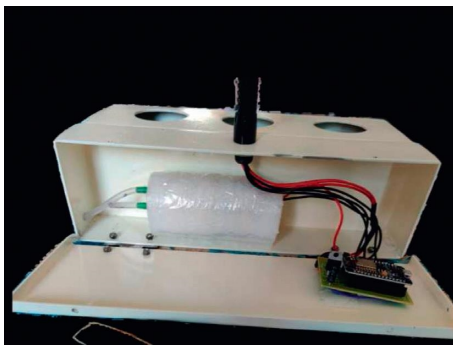


FIGURE 19: Electronic setup.



FIGURE 20: Profile of the LED system.

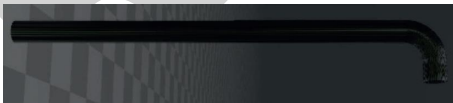


FIGURE 21: Goose neck pipe.

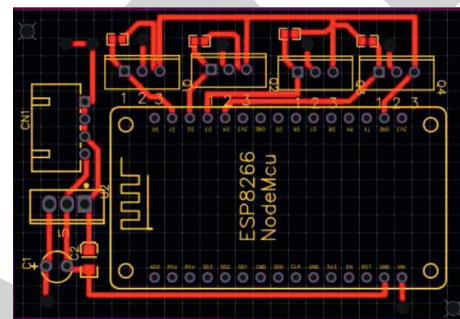


FIGURE 23: Schematic circuit diagram.

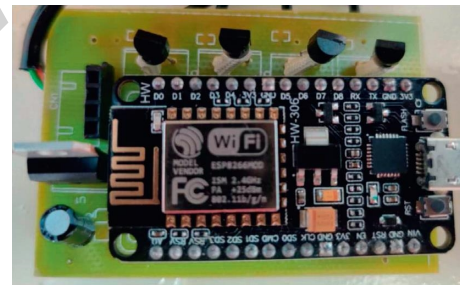


FIGURE 24: PCB.

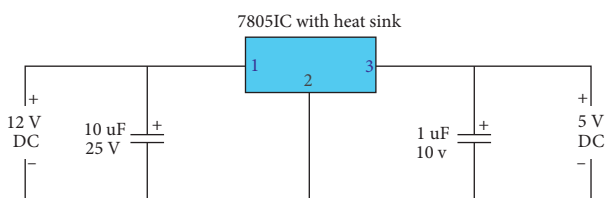


FIGURE 22: 12 V to 5 V converter.

efficient replacement for sunlight, and hydroponics is good replacement for growing plants without soil. The reason LEDs are used for grow lights is as follows. A 10 W LED bulb produces about 1000 to 1250 lumens, and for the same amount of lumens to be produced by an incandescent bulb, we need a 120 W bulb. Now, the lifetime of a LED bulb is 25,000 hours, and the lifetime of incandescent bulbs is 1200 hours. LED life = 25000 hours and incandescent life = 1200 hours, i.e., 4.8 per cent of 25000 is 1200.

Thus, LED bulb is 95.2 per cent more efficient than incandescent bulb in lifetime. The cost of 10 W LED bulb is around 550 rupees. The cost of 120 W incandescent bulb is around 250 rupees. The cost of LED is 45 per cent more than incandescent bulbs. The yearly power consumption is 1 10 W LED bulb, when it is on 24 hours a day in kWh.

LED bulb:

(i) $1 \text{ bulb} \times 10 \text{ W} = 10 \text{ W}$ or 0.01 kW

(ii) $24 \text{ hours daily} \times 365 \text{ days a year} = 8670 \text{ hours}$

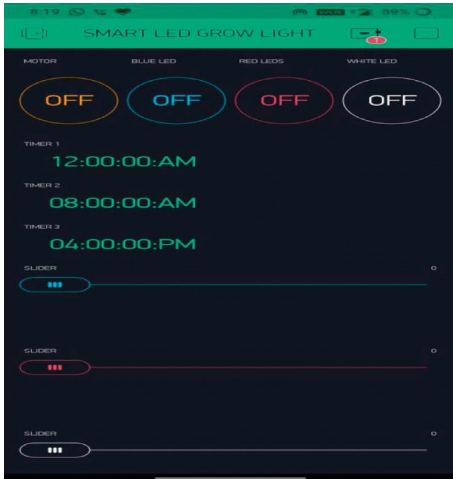


FIGURE 25: Simulation done in Blynk app.

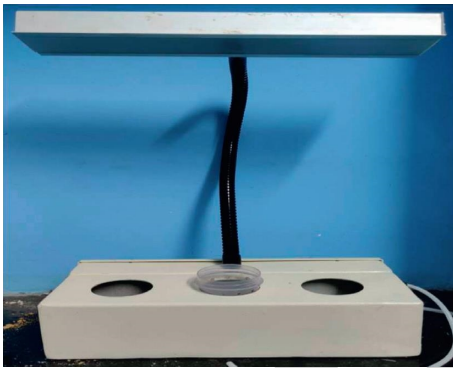


FIGURE 26: The device.

- (iii) $0.01 \text{ kW} \times 8760 \text{ hours} = 87.6 \text{ kWh}$
- (iv) So, in one year 87.6 kWh is consumed.

Incandescent bulb:

- (i) 7 bulbs are needed to run for 1 year continuously
- (ii) $7 \text{ bulb} \times 120 \text{ W} = 840 \text{ W}$ or 0.84 kW
- (iii) $24 \text{ hours daily} \times 365 \text{ days a year} = 8760 \text{ hours}$
- (iv) $0.84 \text{ kW} \times 8760 \text{ hours} = 7358.4 \text{ kWh}$
- (v) So, in one year, 7358.4 kWh is consumed. Thus, when compared, the LED bulb is 84 per cent more efficient than the incandescent bulb. This is the solution that is achieved through this project. Figure 25 shows the simulation result of the work.

6.1. Different Modes of Lightings. Figure 26 shows the entire device diagram. Figures 27–30 represent the device with various LEDs such as blue, red, white, and all colors LEDs switch ON together. The blue LED with 450 nm lights helps in leaf expansion and stomatal openings, photosynthesis, and leaf expansion. In Figure 28, the red LED lights are turned ON, and if the plant is illuminated with 660 nm, it feels like it is illuminated in the direct sun, and thus, it helps

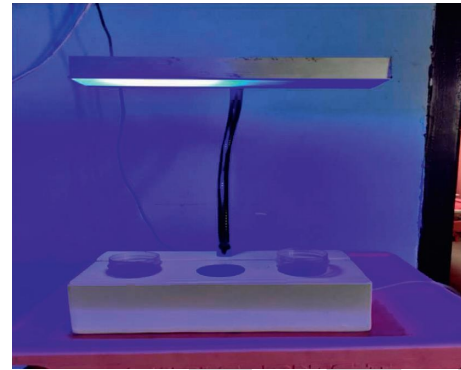


FIGURE 27: LED system with blue (450 nm) LED ON.

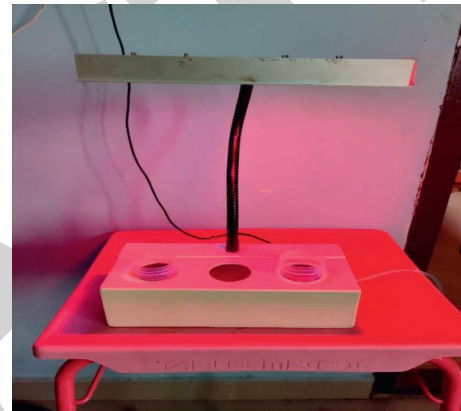


FIGURE 28: LED system with red (660 nm and 730 nm) LED ON.

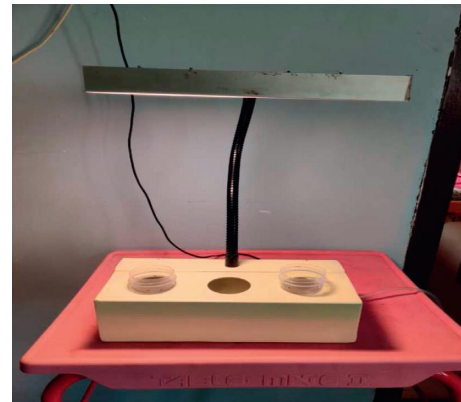


FIGURE 29: LED system with white (3000 CCT) LED ON.

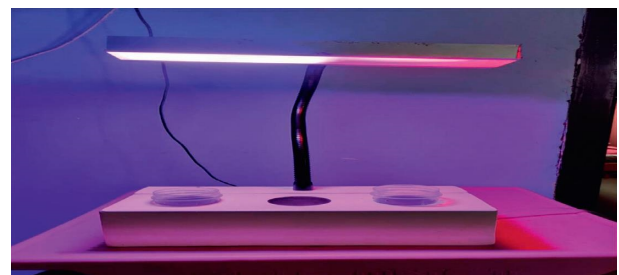


FIGURE 30: LED system with all the LEDs ON.

in stem elongation, and if the plant is illuminated mainly with 730 nm, it feels like it is growing in the shadow of another plant that shades the sun light, thus helping in leaf expansion. In Figure 29, the white LED with 3000 CCT light boosts the photosynthesis and plant growth.

7. Conclusion

The goal of this work is to find a solution for indoor plant growth using LED lights and hydroponics that can be used by any plant growing person other than industries. The device comes with 4 modes of lightings and a hydroponics supported body design that enhances the growth of the plants. The LEDs are a highly efficient replacement for sunlight. The wavelengths used in this project are 450 nm blue light, 660 nm deep red light, 730 nm far red light, and 3000 CCT white light. Each wavelength has its own advantages for the growth of the plant. The 450 nm blue light increases chlorophyll production, resulting in healthier foliage, boosts the stem elongation, and increases the stomata openings. The 660 nm deep red and 730 nm far-red light promote growth and flowering; specifically, the 660 nm deep red is very bright and gives plant the feeling that it is growing right under the sun and helps in stem elongation and overall growth of the plant, whereas the 730 nm far red is dim and gives the plant the feeling that it is growing under a shade causing the leaves to expand to absorb more light. It is proved from the analysis that the hydroponic system is good replacement for growing plants without soil. The motor changes the water in the container every 8 hours, which in turn replenishes the plant with fresh water, thus boosting the plant growth and always having abundant water. With this device, any common person who has no prior experience also can use the device to grow their plants without worrying about sunlight or water.

When compared in terms of power consumption of normal grow lights like incandescent to LED grow lights, there is gain up to 80 percentage of efficiency when an LED grow light is used. Even though the LED lights are costlier by 45 percentage than the normal ones, the lifetime of the LED is more by 95 percentage, thus saving the costs by a lot in the long run. That is the solution this proposed methodology aims to achieve.

Data Availability

The data used to support the findings of this study are included within the article.

Disclosure

This study was performed as a part of the employment of Mizan Tepi University, Ethiopia.

Conflicts of Interest

The authors declare that there are no conflicts of interest to publish this article.

References

- [1] R. Samani, M. Zareie, D. Shekari, L. Wrubleski, and M. Pahlevani, "A hybrid digital control system for LED grow lights," in *Proceedings of the 2019 IEEE Applied Power Electronics Conference and Exposition (APEC)*, March 2019.
- [2] Z. Xu, S. Ansari, M. A. Amir, M. Ali Imran, and Q. H. Abbasi, "IoT enabled smart security framework for 3D printed smart home," in *Proceedings of the 2020 IEEE International Conference on Smart Internet of Things (SmartIoT)*, Beijing, China, August 2020.
- [3] T. Namgyel1, C. Khunarak1, S. Siyang1, T. Pobkrut2, J. Norbu1, and T. Kercharoen, "Effects of supplementary LED light on the growth of lettuce in a smart hydroponic system," in *Proceedings of the 2018 10th International Conference on Knowledge and Smart Technology (KST)*, Chiang Mai, Thailand, February 2018.
- [4] T. Namgyel, S. Siyang, C. Khunarak et al., "IoT based hydroponic system with supplementary LED light for smart home farming of lettuce," in *Proceedings of the 2018 15th International Conference on Electrical Engineering/Electronics, Computer, Telecommunications and Information Technology*, Chiang Mai, Thailand, July 2018.
- [5] L. Promratrak, "The effect of using LED lighting in the growth of crops hydroponics," *International Journal of Smart Grid and Clean Energy*, vol. 6, no. 2, April 2017.
- [6] N. Ohe, M. Ishihara, H. Yonemori, S. Kitagami, M. Inoue, J. Sawamoto et al., "A method of prototype construction for the active creation of IoT application ideas and its evaluations," *International Journal of Internet of Things*, vol. 5, pp. 1-8, 2016.
- [7] K. Kobayashi, T. Amore, and M. Lazaro, "Light-emitting diodes (LEDs) for miniature hydroponic lettuce," *Optics and Photonics Journal*, vol. 3, 2012.
- [8] S. Wang, H. Ji, Z. Zhu, Y. Zhang, and H. Chen, "An intelligent control-ling system for LED plant supplemental lighting greenhouse," in *Proceedings of the 2012 Symposium on Photonics and Optoelectronics*, Shanghai, China, May 2012.
- [9] Y. Eka Nugraha, B. Irawan, and R. Erfa Saputra, "System design and implementation automation system of expert system on hydroponics nutrients control using forward chaining method," in *Proceedings of the IEEE Asia Pacific Conference on Wireless and Mobile (APWiMob)*, Bandung, Indonesia, November 2017.
- [10] T. Nishimura, Y. Okuyama, A. Matsushita, H. Ikeda, and A. Satoh, "A compact hardware design of a sensor module for hydroponics," in *Proceedings of the IEEE 6th Global Conference on Consumer Electronics (GCCE 2017)*, Nagoya, Japan, October 2017.
- [11] T. Okumura, K. Takano, Y. Saito, N. Satta, and T. Fujio, "Development and pilot test of sterilization system using discharge reactor for hydroponics solution," in *Proceedings of the 2016 IEEE International Conference on Plasma Science (ICOPS)*, June 2017.
- [12] Dr.D. Saraswathi, P. Manibharathy, R. Gokulnath, E. Sureshkumar, and K. Karthikeyan, "Automation of hydroponics green house farming using IOT," in *Proceedings of the 2018 IEEE International Conference on System, Computation, Automation and Networking (ICSCA)*, July 2020.
- [13] A. W. Phutthisathian, N. Pantasen, and N. Maneerat, "Ontology-based nutrient solution control system for hydroponics," in *Proceedings of the International Conference on Instrumentation, Measurement, Computer, Communication and Control*, Beijing, China, October 2011.

Retraction

Retracted: Detecting Distance between Surfaces of Large Transparent Material Based on Low-Cost TOF Sensor and Deep Convolutional Neural Network

Advances in Materials Science and Engineering

Received 8 January 2024; Accepted 8 January 2024; Published 9 January 2024

Copyright © 2024 Advances in Materials Science and Engineering. This is an open access article distributed under the Creative Commons Attribution License, which permits unrestricted use, distribution, and reproduction in any medium, provided the original work is properly cited.

This article has been retracted by Hindawi following an investigation undertaken by the publisher [1]. This investigation has uncovered evidence of one or more of the following indicators of systematic manipulation of the publication process:

- (1) Discrepancies in scope
- (2) Discrepancies in the description of the research reported
- (3) Discrepancies between the availability of data and the research described
- (4) Inappropriate citations
- (5) Incoherent, meaningless and/or irrelevant content included in the article
- (6) Manipulated or compromised peer review

The presence of these indicators undermines our confidence in the integrity of the article's content and we cannot, therefore, vouch for its reliability. Please note that this notice is intended solely to alert readers that the content of this article is unreliable. We have not investigated whether authors were aware of or involved in the systematic manipulation of the publication process.

Wiley and Hindawi regrets that the usual quality checks did not identify these issues before publication and have since put additional measures in place to safeguard research integrity.

We wish to credit our own Research Integrity and Research Publishing teams and anonymous and named external researchers and research integrity experts for contributing to this investigation.

The corresponding author, as the representative of all authors, has been given the opportunity to register their agreement or disagreement to this retraction. We have kept a record of any response received.

References

- [1] R. Zou, Y. Zhang, J. Gu, and J. Chen, "Detecting Distance between Surfaces of Large Transparent Material Based on Low-Cost TOF Sensor and Deep Convolutional Neural Network," *Advances in Materials Science and Engineering*, vol. 2021, Article ID 8340179, 12 pages, 2021.

Research Article

Detecting Distance between Surfaces of Large Transparent Material Based on Low-Cost TOF Sensor and Deep Convolutional Neural Network

Rong Zou , Yu Zhang, Junlan Gu, and Jin Chen

School of Mechanical Engineering, Jiangsu University, Zhenjiang 212013, China

Correspondence should be addressed to Rong Zou; zr@ujs.edu.cn

Received 5 August 2021; Accepted 6 October 2021; Published 18 October 2021

Academic Editor: Aniello Riccio

Copyright © 2021 Rong Zou et al. This is an open access article distributed under the Creative Commons Attribution License, which permits unrestricted use, distribution, and reproduction in any medium, provided the original work is properly cited.

Detecting distance between surfaces of transparent materials with large area and thickness has always been a difficult problem in the field of industry. In this paper, a method based on low-cost TOF continuous-wave modulation and deep convolutional neural network technology is proposed. The distance detection between transparent material surfaces is converted to the problem of solving the intersection of the optical path and the transparent material's front and rear surfaces. On this basis, the Gray code encoding and decoding operations are combined to achieve distance detection between surfaces. The problem of holes and detail loss of depth maps generated by low-resolution TOF depth sensors have been also effectively solved. The entire system is simple and can achieve thickness detection on the full surface area. Besides, it can detect large transparent materials with a thickness of over 30 mm, which far exceeds the existing optical thickness detection system for transparent materials.

1. Introduction

Distance detection between surfaces of transparent materials has always been a research hotspot in the field of industry. The traditional contact distance detection method between surfaces is the simplest and lowest cost method, such as the use of vernier calipers or micrometers. The disadvantage is that it can only detect the single surface point near the edge of the surface. It needs to perform manually and cannot automate. So, it is inefficient and gradually eliminated.

Currently, noncontact distance detection methods between surfaces are widely used, which can be roughly divided into optical and nonoptical methods. The typical capacitance method [1–3] is a nonoptical distance detection method between surfaces. This method is based on the principle that the transparent material causes the capacitance change to detect the distance between surfaces of the transparent material. The entire system is simple, but it is extremely susceptible to space electromagnetic interference and changes in the distributed capacitance between lines. The fluorescent immersion method [4–6] is an indirect

optical detection method. The transparent material is immersed in a special liquid. The liquid will emit fluorescence after being irradiated by a laser. Since the transparent material does not emit light, a sharp boundary can be obtained. The optical image is recorded by a camera. The distance between the surfaces of the transparent material can be obtained after the calculation and processing. This method has a complicated system structure and requires the use of fluorescent liquid to cause inconvenience to the user.

Direct optical methods include grating spectroscopy and light triangulation. Grating spectroscopy is designed based on the principle of grating spectroscopy [7]. The system uses white light illumination. The light obtained after being reflected by the transparent material is decomposed by the concave grating. The decomposed spectrum is received by the sensor. The data is sent to the computer for spectral analysis. The distance between the surfaces of the transparent material is obtained. The drawback of this method is that the distance detection system is very difficult to adjust and correct. The optical triangulation method [8–11] uses the principle of the difference in displacement between the

upper and lower surfaces of the transparent material. The system is simple, convenient, and effective. So, it is the most used method at present. Nevertheless, this method is easily affected by stray light. At least for now, there is a common shortcoming of these existing methods for detecting the distance between surfaces of the transparent material; that is, they can only measure a very limited small area at a time [12]. It is impossible to give an objective evaluation of the distance change between the entire surfaces of the transparent material. Besides, the thickness detected by these methods is limited, and the maximum cannot exceed 15 mm.

To develop a method that can detect the distance between the entire surfaces of the large transparent material at a time, we also refer to a variety of transparent object surface reconstruction methods. Murase [13] provided a new idea for recovering shapes from pattern distortions for transparent fluid materials. The geometric information of transparent materials is speculated from the distortion of known or unknown calibration patterns caused by light refraction. This method is mainly aimed at the problem of water surface shape reconstruction. Morris and Kutulakos [14] considered the water surface reconstruction with time on this basis. His method can not only obtain the refractive index but also accurately estimate the depth and normal vector of each pixel. It is not dependent on the surface mean and is highly robust. Kutulakos and Steger [15] analyzed the possibility of using triangulation to realize the three-dimensional reconstruction of the surface of transparent materials. They proposed a light direct measurement method. But the common feature of the above measurement methods is that passive visual sensors are used to passively capture light on the surface of transparent materials.

In recent years, active time-of-flight (TOF) depth sensors are being widely used in the field of 3D digital modeling with the advantages of high efficiency and wide adaptability. Therefore, a small number of researchers also conducted some preliminary studies on the active TOF sensor used in the surface reconstruction of transparent materials [16]. The modulated light emitted by the TOF depth sensor travels in a transparent material at a slower speed than the air, so the so-called distortion phenomenon occurs. This distortion phenomenon carries relevant thickness information. This provides a new idea for our distance detection method between entire surfaces of the large transparent material. However, these current exploratory methods have many shortcomings, especially the hole problem in the depth map generation process, which has a huge impact on the distance detection between surfaces of the transparent material. It should be noted that, in order to reflect that our method can realize the thickness detection of the entire surface area of the object, we use the phrase “distance between surfaces” to replace the commonly referred term “thickness” in this article.

Here, we propose a novel method of optics. This method uses low-cost TOF sensors and deep convolutional neural network technology to achieve distance detection between the surfaces of the large transparent material. It can effectively reduce the cost of the system. The main idea is to transform the distance detection between transparent material surfaces into front and rear surface reconstruction

problems. We further demonstrated that surface reconstruction of the transparent material can also be converted to the problem of searching for the intersection of the light path and the front and back surfaces of the transparent object and its surface normal. Combining a series of Gray code patterns, the entire detection system is simple and easy to implement. Another contribution of this paper is the introduction of deep convolutional neural networks into the field of active vision. Thereby, the performance of the low-cost TOF sensor is used to the limit. Our method can detect the large transparent material with a thickness of over 30 mm.

2. Methodologies

TOF depth sensors are divided into a single-photon counting measurement method and a continuous-wave modulation measurement method according to the form of emitted light waves. In the continuous-wave modulation method, a sinusoidal signal is invoked as the signal of the optical transmitter. Depth measurement is achieved by calculating the phase difference between the received and emitted waves, as shown in Figure 1. It is easy to implement at a low cost [17]. The basic measurement equation is expressed as

$$\begin{aligned} \text{Depth} &= \frac{c}{2} \cdot t \\ &= \frac{c}{2} \cdot \frac{\Delta\phi}{2\pi f}, \end{aligned} \quad (1)$$

where Depth represents the distance between the camera and the object, c is the speed of light, t represents the travel time of the round-trip light, $\Delta\phi$ shows the phase difference between the returned signal and the received signal, and f is the natural frequency.

The principle of distance detection between the surfaces of the transparent material is shown in Figure 2. O is the coordinates of the optical center of the sensor. A_1 and A_2 represent the points on the front and rear surfaces of the transparent material. B_1 and B_2 represent a set of distorted three-dimensional points when the reference plate is moved back and forth corresponding to the image pixels. The direction of the light emitted by the TOF depth sensor is OA_1 . When the reference board is placed in the first reference position, the TOF depth sensor is used to collect infrared images and depth data of the surface position of the transparent material. It mainly includes two sets of data without the transparent material and transparent material. Based on these two sets of data, the distorted three-dimensional point of the first position $\overrightarrow{OB_1}$ can be obtained. The current position of the reference board is also recorded. By moving the platform, the reference board is moved to the second position. Repeating the detection step of the previous position, we get the distorted three-dimensional point $\overrightarrow{OB_2}$ in the second position. Similarly, the position and moving distance of the reference board are recorded at this time. The difference between the distorted three-dimensional points of the two positions can be obtained as the reference light direction $\overrightarrow{B_1B_2}$. A series of Gray code patterns are used in the reference board [18], as shown in Figure 3. According to the sensor light

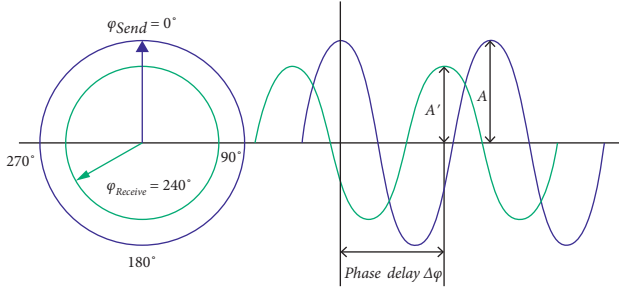


FIGURE 1: The continuous-wave modulation measurement method of TOF.

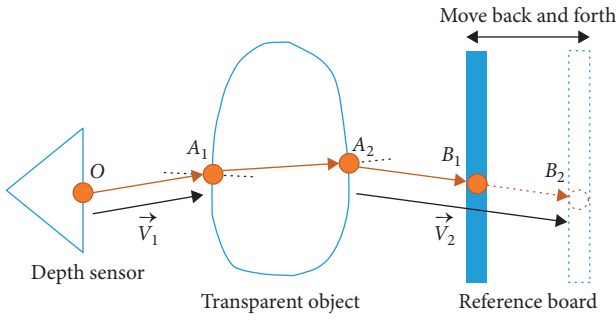


FIGURE 2: Detecting distance principle between surfaces of the transparent material.

direction $\overrightarrow{OA_1}$, the reference light direction $\overrightarrow{B_1B_2}$, and the corresponding depth data, the front and back surface points of the transparent material can be obtained by using related algorithms. Finally, the distance between the surfaces of the transparent material is obtained. It should be noted that $\overrightarrow{V_1}$ and $\overrightarrow{V_2}$ represent the sensor light direction and the reference light direction, which need to be converted into their unit vectors to participate in the calculation.

2.1. Estimation of Transparent Material Surface Points. Figure 4 shows Snell's normal law in refracted light. At a point i on the rear surface, Snell's norm is defined as

$$\begin{aligned} \overrightarrow{SN}_i &= \frac{\overrightarrow{V_2} - n\overrightarrow{A_1A_2}}{|\overrightarrow{V_2} - n\overrightarrow{A_1A_2}|} \\ &= \frac{\overrightarrow{B_1B_2} - n\overrightarrow{A_1A_2}}{|\overrightarrow{B_1B_2} - n\overrightarrow{A_1A_2}|} \end{aligned} \quad (2)$$

where \overrightarrow{SN}_i is the Snell normal vector at point i on the rear surface, $\overrightarrow{A_1A_2}$ represents the space vector at the intersection of the refracted light path and the front and rear surfaces of the transparent material, and n is the refractive index of the transparent material.

The surface normal at the point is expressed as

$$\overrightarrow{N}_i = \frac{\partial(\overrightarrow{OB_1} - |\overrightarrow{A_2B_1}|\overrightarrow{V_2})/\partial u \times \partial(\overrightarrow{OB_1} - |\overrightarrow{A_2B_1}|\overrightarrow{V_2})/\partial v}{\left| \partial(\overrightarrow{OB_1} - |\overrightarrow{A_2B_1}|\overrightarrow{V_2})/\partial u \times \partial(\overrightarrow{OB_1} - |\overrightarrow{A_2B_1}|\overrightarrow{V_2})/\partial v \right|} \quad (3)$$

where \overrightarrow{N}_i is the surface normal at the point i , $|\overrightarrow{A_2B_1}|$ is the distance from the point on the back surface of the transparent material to the corresponding point on the first position reference plate, u, v are the image horizontal axis and vertical axis, and ∂ is partial differential calculation.

From equations (2) and (3), the two normals should coincide; that is, the summation term has a minimum value in the following equation:

$$|\overrightarrow{A_2B_1}| = \arg \min_{|\overrightarrow{A_2B_1}|} \sum_{i \in I} \|\overrightarrow{SN}_i - \overrightarrow{N}_i\|_2^2 \quad (4)$$

2.2. Measurement Model Based on TOF Continuous-Wave Modulation. There are multiple variables in expressions of \overrightarrow{SN}_i and \overrightarrow{N}_i . Combined with the inherent model of the TOF continuous-wave modulation principle, we get

$$D = |\overrightarrow{OA_1}| + n|\overrightarrow{A_1A_2}| + |\overrightarrow{A_2B_1}|, \quad (5)$$

where D represents the actual distance between the sensor lens and the reference plate, which are directly read by the depth sensor. $|\overrightarrow{OA_1}|, |\overrightarrow{A_1A_2}|, |\overrightarrow{A_2B_1}|$ are three unknowns in equation (5). According to the calculation rule of the vector, the relationship between the three unknowns can be obtained:

$$\begin{cases} \overrightarrow{OA_1} = |\overrightarrow{OA_1}|\overrightarrow{V_1}, \\ \overrightarrow{OB_1} = \overrightarrow{OA_2} + |\overrightarrow{A_2B_1}|\overrightarrow{B_1B_2}, \\ = \overrightarrow{OA_2} + |\overrightarrow{A_2B_1}|\overrightarrow{V_2}, \\ \overrightarrow{A_1A_2} = \overrightarrow{OA_2} - \overrightarrow{OA_1}. \end{cases} \quad (6)$$

Substituting equation (6) into equation (5), we can get

$$|\overrightarrow{OA_1}| = \frac{-\left(D - |\overrightarrow{A_2B_1}| - n^2\overrightarrow{OB_1}^T * \overrightarrow{V_1}\right) \pm \sqrt{\left(D - |\overrightarrow{A_2B_1}| - n^2\overrightarrow{OB_1}^T * \overrightarrow{V_1}\right)^2 - (n^2 - 1)\left(n^2|\overrightarrow{OB_1}|^2 - \left(D - |\overrightarrow{A_2B_1}|\right)^2\right)}{n^2 - 1} \quad (7)$$

Therefore, after putting equations (6) and (7) in equation (5), there is only one unknown $|\overrightarrow{A_2B_1}|$. According to equation (4), the back surface depth data corresponding to

each pixel of the rear surface can be estimated. Combined with equation (6), the surface points of the front and back of the transparent material can be estimated:



FIGURE 3: Gray code sequence.

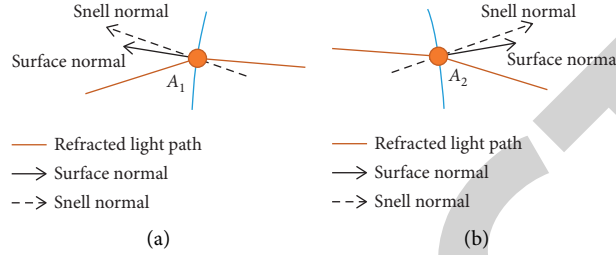


FIGURE 4: Normal diagram of a surface point of the transparent material. (a) Normal distribution at a point on the front surface. (b) Normal distribution at a point on the rear surface.

$$\begin{cases} \overrightarrow{OA_2} = \overrightarrow{OB_1} - |\overrightarrow{A_2B_1}| \overrightarrow{V_2}, \\ \overrightarrow{OA_1} = |\overrightarrow{OA_1}| \overrightarrow{V_1}. \end{cases} \quad (8)$$

So, the normal map can be resolved by equation (2) or equation (3). The depth data used in equation (4) only comes from the depth value directly read by the depth sensor. In practice, as the depth sensor usage time becomes longer during the experiment, the noise also increases [19]. We propose using a regularization method to reduce noise interference. A regularization term is introduced for each pixel. d_i is the estimated noise-free TOF optical length and $d_{i'}$ is the actual depth value reads. The noise suppression optimization equation is given by

$$|\overrightarrow{A_2B_1}| = \arg \min_{|\overrightarrow{A_2B_1}|} \sum_{i \in I} \left(\|\overrightarrow{SN_i} - \overrightarrow{N_i}\|_2^2 + \lambda \sum_{i' \in N_i} \|d_i - d_{i'}\|_2^2 \right). \quad (9)$$

The above equation can be interpreted as an estimate of the shape of the rear surface because $|\overrightarrow{A_2B_1}|$ corresponds to the depth data of the rear surface. To avoid calculating the second derivative with high computational complexity, the L-BFGS method [20] is utilized here. It only uses approximate Hessian matrices instead of calculating them specifically.

2.3. Patching Holes in Low-Resolution Depth Maps. In the above measurement model, the integrity of the transparent material depth data acquisition is critical. The low-cost TOF depth sensor has a lower resolution. Besides, the depth map obtained is usually affected by complex factors so that holes often appear at the edges and occlusions of the object. It seriously affects subsequent processing and information

extraction [21]. Figure 5 is an example of holes in a depth map, where too bright (Gray value of 255) and too dark (Gray value of 0) are the positions of holes. Generally, the area where the transparent material is located is prone to holes, including small and large areas. The depth value represented by the hole position is not valid. In other words, the lack of depth data occurs. Patching the holes in the depth map is an important part of using low-cost TOF depth sensors to detect the distance between the surfaces of the transparent material.

A hole patching method based on a convolutional neural network is proposed. First, the depth map is generated and the hole position is detected to generate a hole mask map. Then, the hole mask map and original depth map are fed into the deep convolutional neural network to achieve unsupervised hole patching.

Untrained deep convolutional neural networks are used, in which the weights are randomly initialized. In the autonomous unsupervised learning process, the network weight parameters needed for depth map patching are generated. That is, based on the given damaged depth map and task-dependent observation model, a randomly initialized convolutional neural network is given. The model parameters are provided by iterations to make it close to the maximum likelihood value. In this paper, the depth map patching task is represented as a problem of energy minimization, given by

$$x^* = \min_x E(x; x_0) + R(x), \quad (10)$$

where x, x_0 are the depth map generated by the neural network and the original depth map with holes. $E(x; x_0)$ depends on the specific application scenario, which mainly compares the difference between the generated data and the original data. In equation (10), it is necessary to find the value of x that minimizes $E(x; x_0)$ and as the output x^* of



FIGURE 5: Examples of holes in the depth map. The object in the red box is transparent materials.

the final network. $R(x)$ is a priori knowledge of the depth map, which is often captured by training a convolutional neural network with a large sample. But here, the implicit prior information captured by the convolutional neural network is used to replace $R(x)$. The convolutional neural network learns from the input randomly coded image to the mapping of the original depth map with holes. x^* is reconstructed from the optimal solution θ^* obtained by learning. So, equation (10) becomes

$$\begin{cases} x^* = f_{\theta^*}(z), \\ \theta^* = \arg \min_{\theta} E(f_{\theta}(z); x_0), \end{cases} \quad (11)$$

where θ is the network parameters and θ^* is the optimal solution of the parameters obtained by Adam gradient descent algorithm training based on the random initialization network. The random vector z is the input code of the network. Once the optimal parameters are obtained, the input z can be calculated to obtain the optimal x . Therefore, the idea of the algorithm is essentially the process of searching for the optimal θ in the feasible space. Use the gradient descent [22] method to randomly initialize the parameters to obtain the (local) minimizer θ .

Figure 6 is the network structure of the depth map patching algorithm. The overall structure is an Encode-Decode network structure. Input random code z , original depth maps containing holes, and hole mask maps and then let the convolutional neural network autonomously learn the mapping from original pixel values of the input randomly coded z to the original depth map containing the holes according to the areas without holes in the hole mask map. The model network is formed by the cascade of encoding compression (encoder) and decoding reconstruction (decoder). The sampling unit of each layer includes a convolution layer (convolution), a batch normalization layer (BN, batch normalization) [23], and the nonlinear activation function layer (LReLU, Leaky ReLU) [24]. As shown in Figure 6, the downsampling unit uses a convolution layer and the upsampling unit uses nearest-neighbor interpolation convolution. We use the ‘‘Meshgrid’’ image as the input code. Subsequent experiments show that this type of input will increase the smoothness. It is useful for hole patching.

The number of filters in the downsampling unit and the upsampling unit is 16, 32, 64, 128, 128, and 128. The kernel size is 3 and 5. These are all fixed values. After each convolutional layer, there is a BN layer to normalize the data to improve the details of image restoration. In the convolutional neural network, it is necessary to utilize the activation function as a nonlinear transformation. Complex mapping relationships can be learned. In the algorithm, there is a Leaky ReLU activation function after each BN layer, given by

$$\text{Leaky ReLU}(x_i) = \begin{cases} x_i, & x_i \geq 0, \\ ax_i, & x_i < 0. \end{cases} \quad (12)$$

3. Experiment Verification

To verify the effectiveness of our method, this paper builds an experimental setup as shown in Figure 7. The large transparent material is thick glass with a flat and smooth surface. A low-cost TOF depth sensor based on the continuous-wave modulation measurement method is Microsoft’s Kinect V2, which costs less than \$150.

3.1. Patching Algorithm Experiment and Result Analysis.

To verify the performance of the algorithm, the built experimental device was used to collect the depth map of the transparent glass cylinder, as shown in Figure 5. The image resolution is 512×424 pixels. Figure 8 indicates the iterative patching process of depth maps based on convolutional neural networks.

As can be seen from Figure 9, not only is it effective for small and larger holes in the transparent materials we care about but also it is possible to patch larger holes at the loading platform. Another advantage of our method is to obtain a good patching effect without affecting the clarity of the original image.

The comparison experiment of the patching effect is adopted to compare the traditional median filtering method, Gaussian filtering method, bilateral filtering method, joint bilateral filtering method, and the method in this paper. Some key parameters of these algorithms in the experiment are set as follows: the filtering window in the median filtering method is 4×4 . The filtering window in the Gaussian filtering method is 10×10 . The standard deviation of the filter is 1 pixel. The filtering radius of the bilateral filtering method is 5. The filtering variance is 5, and the local variance is 0.5. The processing effect is illustrated in Figure 10.

Figure 11 further shows the hole patching effect of the transparent glass cylinder and the corresponding error distribution diagram. A comprehensive comparison of the hole patching effects of traditional algorithms shows that the proposed algorithm has obvious advantages. The median filtering method can better fill the small holes. But it is not appropriate for the large area of the hole because the pixel value of this part will be replaced by the median value of the neighboring pixels. This will lead to a larger depth error, thereby losing the original depth information of the object. Although the Gaussian filtering method patches some of the holes, it leads to the edge information of the measured object

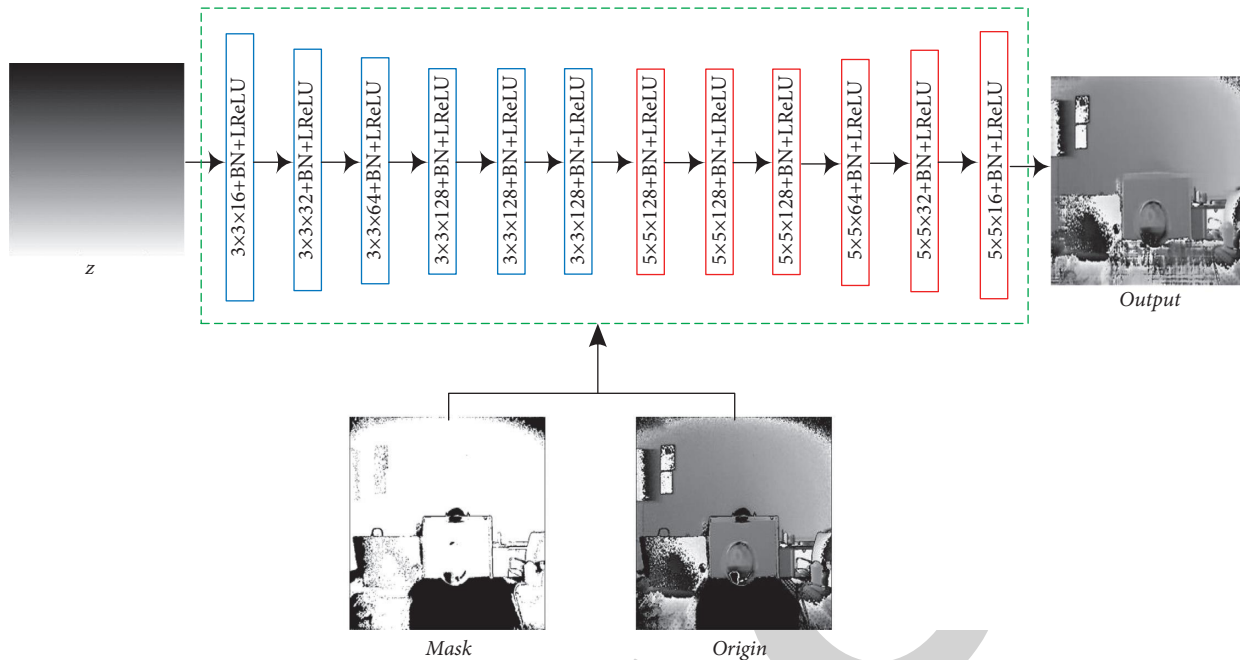


FIGURE 6: The network structure of the depth map patching algorithm.

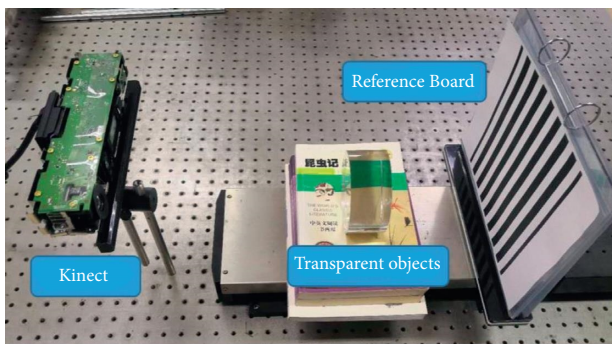


FIGURE 7: Experimental setup.

in the image be too blurred. It will bring greater calculation errors. Bilateral filtering can reduce the loss of depth information at the edges. However, a large area of the hole cannot be patched. The joint bilateral filtering method can patch some small and a part of the larger holes. However, holes on the edges of transparent objects cannot be patched. Even if the parameters are manually adjusted for patching, the transparent objects in the depth map after patching will be blurred to a certain extent.

3.2. Experimental Evaluation of the Measurement Model.

For the calibrated Kinect depth sensor, a set of Gray code images was collected at two different distances. The two distances selected in the experiment are 60 mm and 75 mm away from the Kinect depth sensor. Figure 12 shows a set of Gray code images at a distance of 75 mm from the transparent material and the Kinect depth sensor.

The Gray code image sequence taken in this experiment is illustrated in Figure 12. The vertical Gray code image sequence encodes the horizontal coordinate position of the image. The

horizontal Gray code image sequence encodes the vertical coordinate position of the image. Due to the near-infrared camera resolution limitations of the low-cost Kinect depth sensor, only 7 different Gray code images were selected in the experiment.

Figure 13 shows a single image in the Gray code image sequence. For the decoding of Gray code images, we take vertical Gray code fringe images as an example. We observe the pixels in the blue and red circles in Figure 13(a). Assuming that there is only one pixel in the circle. A pixel in the blue circle is located in the white area and the corresponding Gray code value is 0. A pixel in the red circle is in the black area and the corresponding Gray code value is 1. After the sequence changes according to this rule, the code in the blue circle is 1000010 and the code in the red circle is 0101101. The two codes are translated into decimals of 66 and 45, respectively. These are the horizontal coordinate values corresponding to the two pixels at their respective positions. Use the same method to find the vertical coordinate values, and traverse each pixel in the image to get the corresponding decimal coordinates. The decimal coordinates of each pixel in the image without transparent objects are also achieved in the same way. Finally, the two decimal coordinates of each pixel are correspondingly subtracted to obtain the three-dimensional distortion point of the position.

The three-dimensional distortion point at a distance of 60 mm from the depth sensor is acquired using the same process. The difference between the three-dimensional distortion points at two different distances is the reference light direction. Depending on the theoretical analysis in Chapter 2, point cloud images of the front and back surfaces of the transparent material can be obtained. Figure 14 shows a point cloud image that is issued by the Gray code image sequence.

For the transparent object with flat surfaces, the distance between surfaces is detected by the corrected corresponding

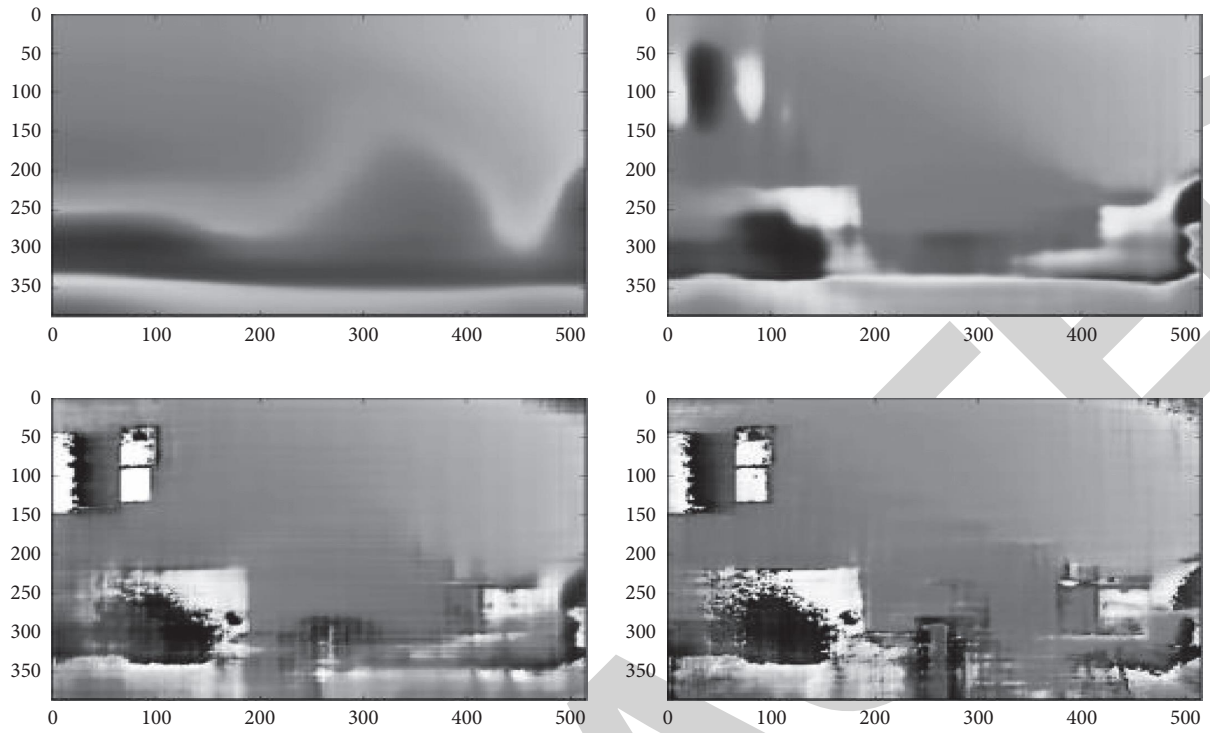
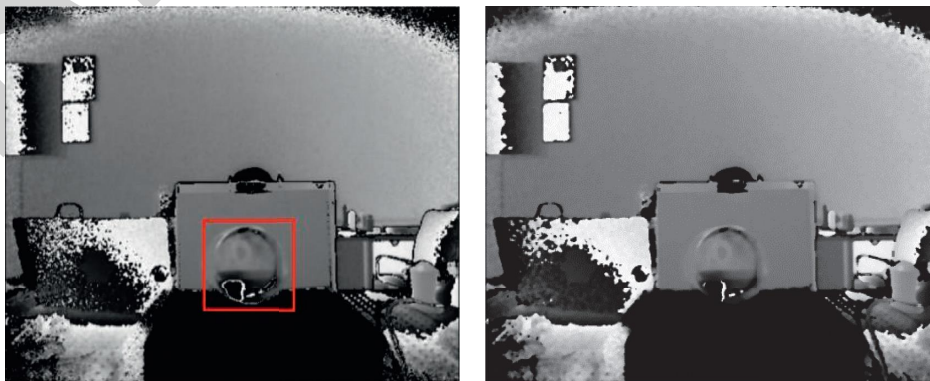


FIGURE 8: Depth map generated during the convolutional neural network patching process.



FIGURE 9: Convolutional neural network patching effect.



(a)

(b)

FIGURE 10: Continued.

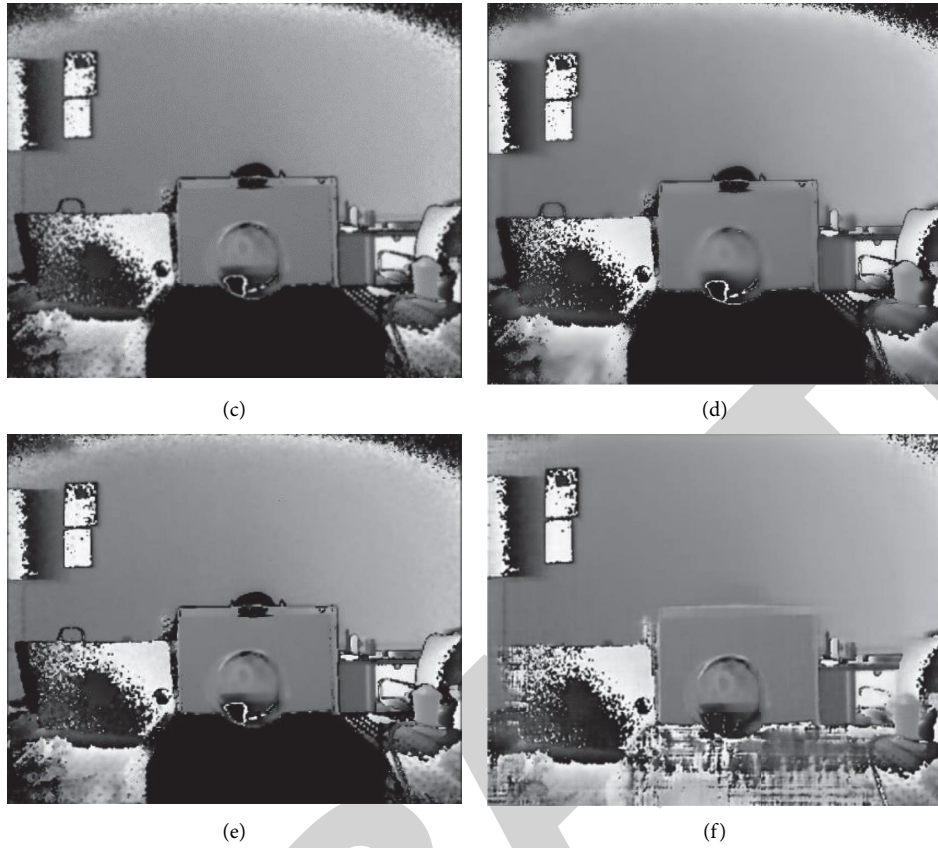


FIGURE 10: Comparison of various algorithms for hole patching. (a) Original depth map. (b) Median filtering method. (c) Gaussian filtering method. (d) Bilateral filtering method. (e) Joint bilateral filtering method. (f) Convolutional neural network method.

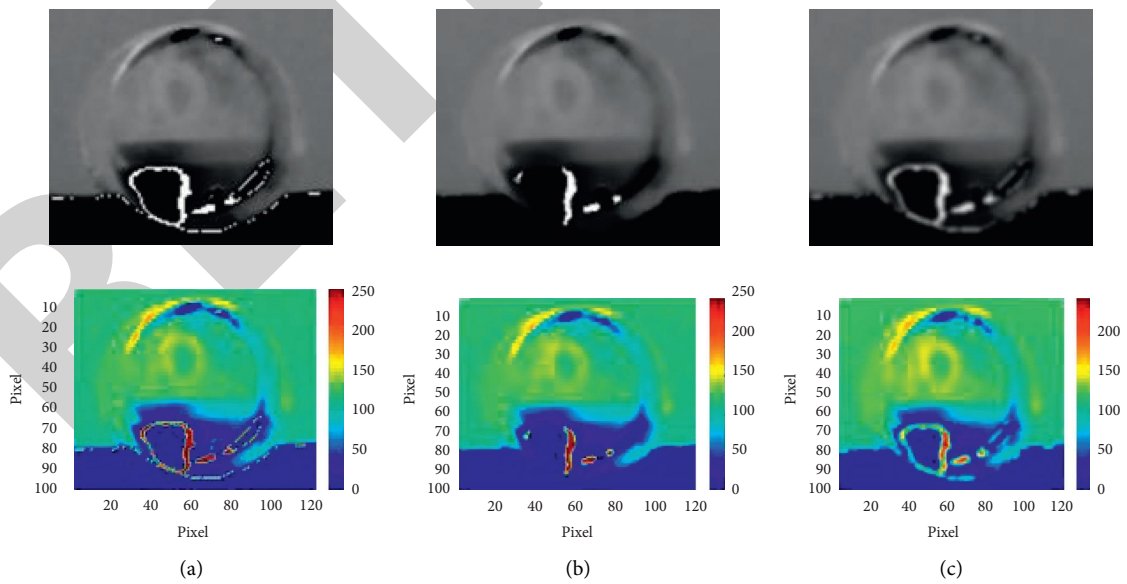


FIGURE 11: Continued.

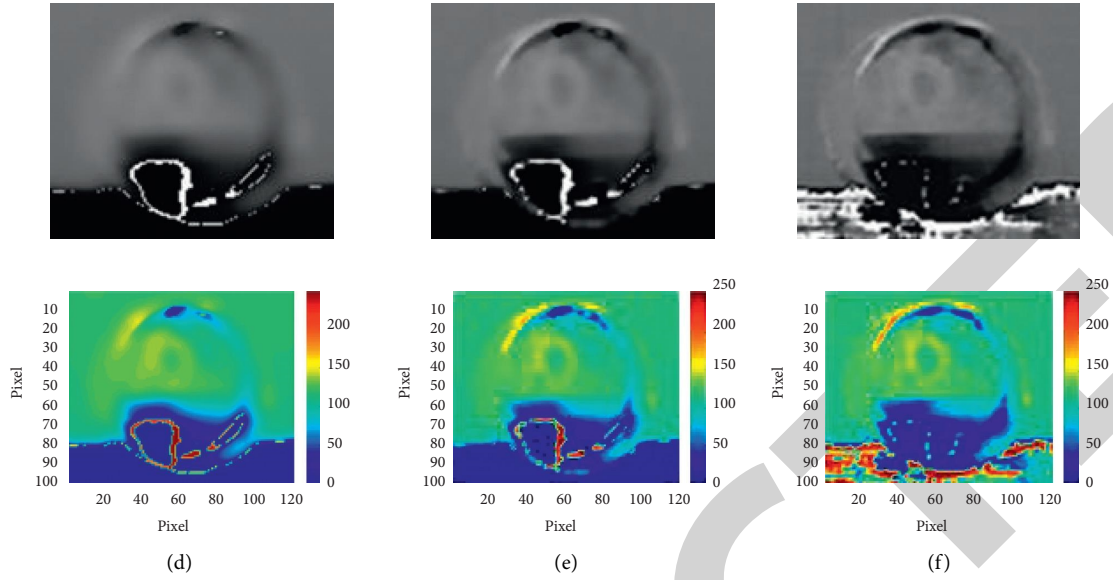


FIGURE 11: The corresponding error distribution map of hole patching. (a) Original depth map. (b) Median filtering method. (c) Gaussian filtering method. (d) Bilateral filtering method. (e) Joint bilateral filtering method. (f) Convolutional neural network method.

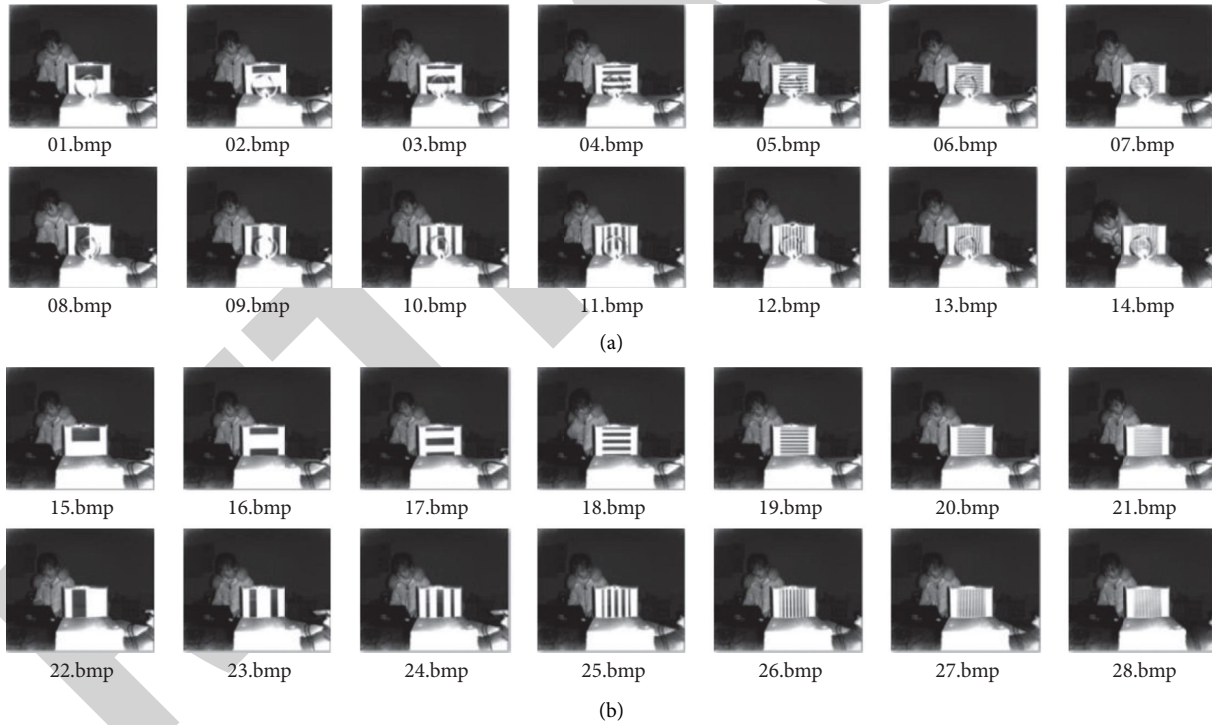


FIGURE 12: A set of Gray code original images. (a) A set of Gray code images with transparent objects. (b) A set of Gray code images without transparent objects.

points on the front and back surfaces. Table 1 is part of the distance data between surfaces (unit: mm). The true thickness is 30.000 mm.

To verify the performance of our method, two transparent objects with large flat surfaces differing only in thickness were used for the detection. This experiment evaluates the method by

obtaining the root mean square error (RMSE) between the surface spacing and the true thickness as follows:

$$RMSE = \sqrt{\frac{1}{m * n} \sum_i^{m*n} (y_i - \hat{y}_i)^2}, \quad (13)$$

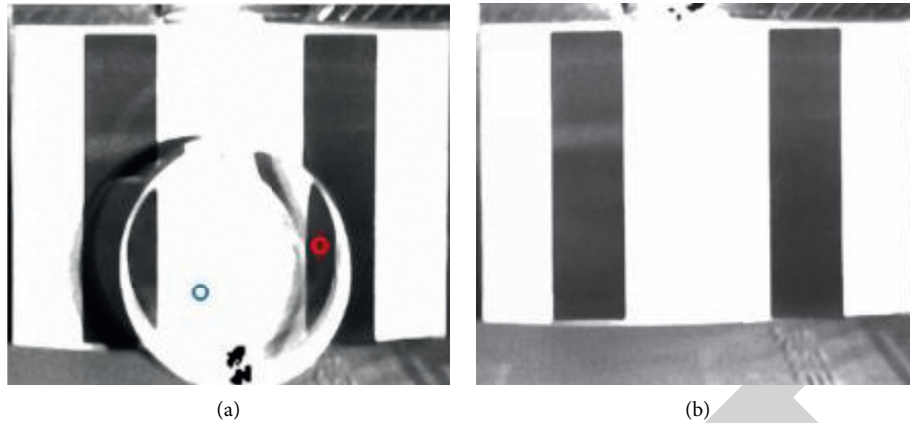


FIGURE 13: A Gray code image. (a) A single Gray code image with transparent objects. (b) A single Gray code image without transparent objects.

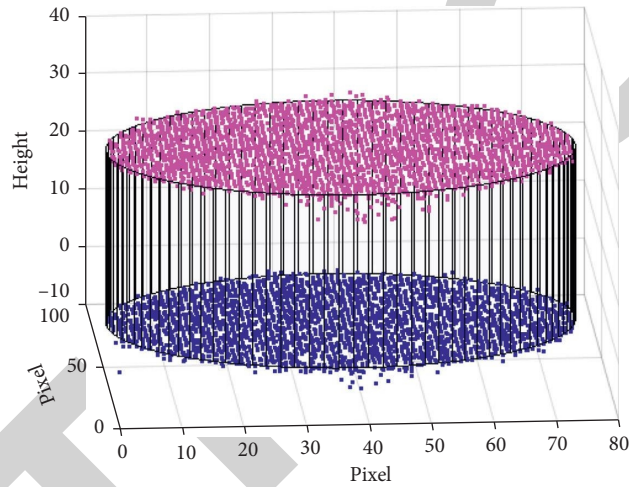


FIGURE 14: Point clouds of transparent material.

TABLE 1: Part of the distance data between surfaces (mm).

	Point 1	Point 2	Point 3	Point 4	Point 5	Point 6	Point 7	Point 8	Point 9	Point 10
Distance value	29.772	29.927	30.362	29.896	30.172	30.019	30.229	29.965	30.136	30.121

where $m * n$ represents the image size, i is i th pixel in the image, y_i is the true thickness of a transparent object, \hat{y}_i represents the actual distance between surfaces, and $y_i - \hat{y}_i$ represents the error value between the two data.

Figure 15 shows the RMSE distribution curve of transparent objects of 30 mm and 25 mm thicknesses. It shows the error range of the detection results. In our method, RMSE of the 30 mm and 25 mm transparent objects are 0.2586 mm and 0.3417 mm, respectively. Relative minimum errors can reach 0.86% and 1.3668%, respectively. The reason for different detection accuracy is primarily the optical path length of the refracted light inside the transparent material becomes longer as the thickness of the transparent material increases. Because the

degree of deformation of the Gray code will be more obvious, low-resolution cameras can record better. So, the detection result is more accurate. The experimental data are given in Table 2.

Experimental results show that the proposed image quality is comparable to [17]. The denoising method proposed in this paper can effectively avoid the adverse effects of noise on reconstruction results. It is worth noting that the reconstruction accuracy is higher than that of [9, 10] mainly because the length of the refracted light path inside the transparent object becomes longer with the increase of the thickness of the transparent object, and the deformation degree of the Gray code becomes more obvious.

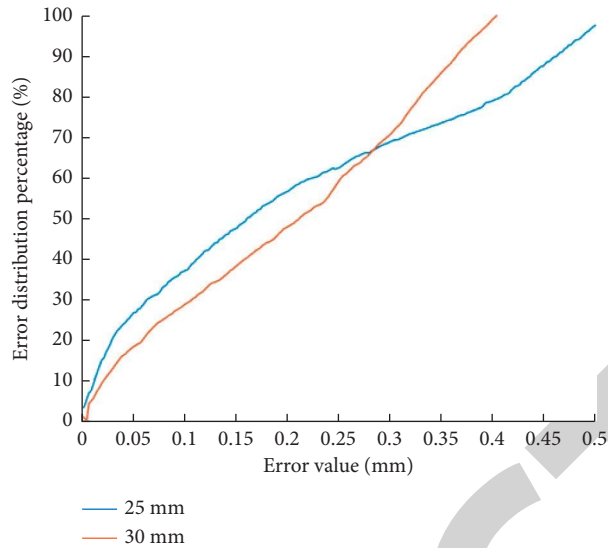


FIGURE 15: RMSE distribution maps of transparent objects of different thicknesses.

TABLE 2: Measurement error analysis of transparent objects.

Number	Nominal thickness (mm)	RMSE (mm)	Relative minimum errors (%)
1	30	0.2586	0.86
2	25	0.3417	1.3668

4. Conclusions

Faced with the problem of detecting distance between surfaces of the transparent material with large area and thickness, we propose a method based on low-cost TOF continuous-wave modulation and depth map patching. We start with the optical expressions inherent in TOF depth sensors. Based on the analysis of the imaging principle of the depth sensor, the encoding and decoding operations combined with the Gray code are used to effectively achieve the distance detection between surfaces of the transparent material. At the same time, given the problem that the depth map generated by the low-cost TOF depth sensor contains many holes that have a huge impact on the detection, a repair method of the deep convolutional neural network is proposed. It effectively improves the performance of the entire detection system.

In addition, although we achieve better detection results, the method in this paper is not appropriate for the case where the refractive index of the transparent material changes. In the future, the relevant theoretical model will be improved and the experimental device will be adjusted to make it suitable for internal uneven transparent material.

Data Availability

No data were used to support this study.

Conflicts of Interest

The authors declare that they have no conflicts of interest.

Acknowledgments

The authors would like to thank the Jiangsu Government Scholarship for Overseas Studied (JS-2019-209) for support.

References

- [1] Y. Dou, J. Qin, and X. Chang, "The study of a capacitance sensor and its system used in measuring ice thickness, sedimentation and water level of a reservoir," in *Proceedings of the International Forum on Information Technology and Applications*, pp. 616–619, IEEE, Chengdu, China, May 2009.
- [2] M. R. Özgü, J. C. Chen, and N. Eberhardt, "A capacitance method for measurement of film thickness in two-phase flow," *Review of Scientific Instruments*, vol. 44, no. 12, pp. 1714–1716, 1973.
- [3] J. F. Klausner, L. Z. Zeng, and D. M. Bernhard, "Development of a film thickness probe using capacitance for asymmetrical two-phase flow with heat addition," *Review of Scientific Instruments*, vol. 63, no. 5, pp. 3147–3152, 1992.
- [4] R. Rantson, C. Stolz, D. Fofi, and F. Meriaudeau, "Optimization of transparent objects digitization from visible fluorescence ultraviolet induced," *Optical Engineering*, vol. 51, no. 3, Article ID 033601, 2012.
- [5] F. Mériaudeau, R. Rantson, D. Fofi, and C. Stolz, "Review and comparison of non-conventional imaging systems for three-dimensional digitization of transparent objects," *Journal of Electronic Imaging*, vol. 21, no. 2, Article ID 021105, 2012.
- [6] F. Meriaudeau, R. Rantson, K. Adal, D. Fofi, and C. Stolz, "Non-conventional imaging systems for 3D digitization of transparent objects: shape from polarization in the IR and shape from visible fluorescence induced UV," *AIP Conference Proceedings*, vol. 1537, pp. 34–40, 2013.

Retraction

Retracted: Empirical Investigation on Compressive Strength of Geopolymer and Conventional Concretes by Nondestructive Method

Advances in Materials Science and Engineering

Received 26 December 2023; Accepted 26 December 2023; Published 29 December 2023

Copyright © 2023 Advances in Materials Science and Engineering. This is an open access article distributed under the Creative Commons Attribution License, which permits unrestricted use, distribution, and reproduction in any medium, provided the original work is properly cited.

This article has been retracted by Hindawi, as publisher, following an investigation undertaken by the publisher [1]. This investigation has uncovered evidence of systematic manipulation of the publication and peer-review process. We cannot, therefore, vouch for the reliability or integrity of this article.

Please note that this notice is intended solely to alert readers that the peer-review process of this article has been compromised.

Wiley and Hindawi regret that the usual quality checks did not identify these issues before publication and have since put additional measures in place to safeguard research integrity.

We wish to credit our Research Integrity and Research Publishing teams and anonymous and named external researchers and research integrity experts for contributing to this investigation.

The corresponding author, as the representative of all authors, has been given the opportunity to register their agreement or disagreement to this retraction. We have kept a record of any response received.

References

- [1] B. Ravali, K. B. G. Krishna, D. R. Kanth, K. J. B. Chari, S. V. Prabhu, and R. Ramesh, "Empirical Investigation on Compressive Strength of Geopolymer and Conventional Concretes by Nondestructive Method," *Advances in Materials Science and Engineering*, vol. 2021, Article ID 9575964, 10 pages, 2021.

Research Article

Empirical Investigation on Compressive Strength of Geopolymer and Conventional Concretes by Nondestructive Method

B. Ravali ¹, **K. Bala Gopi Krishna** ¹, **D. Ravi Kanth** ¹, **K. J. Brahma Chari** ²,
S. Venkatesa Prabhu ³, and **R. Ramesh** ³

¹Department of Civil Engineering, Vignan's Foundation for Science Technology and Research, Vadlamudi Guntur 522212, Andhra Pradesh, India

²Department of Civil Engineering, Koneru Lakshmaiah Educational Foundation, Vaddeswaram Guntur 522212, Andhra Pradesh, India

³Department of Chemical Engineering College of Biological and Chemical Engineering, Addis Ababa Science and Technology University, Addis Ababa, Ethiopia

Correspondence should be addressed to R. Ramesh; ramesh.redrouthu@aastu.edu.et

Received 19 July 2021; Revised 13 September 2021; Accepted 27 September 2021; Published 18 October 2021

Academic Editor: Samson Jerold Samuel Chelladurai

Copyright © 2021 B. Ravali et al. This is an open access article distributed under the Creative Commons Attribution License, which permits unrestricted use, distribution, and reproduction in any medium, provided the original work is properly cited.

Need of construction is increasing due to increase in population growth rate. The geopolymer concrete is eco-friendly than ordinary concrete. Current experimental investigation was conducted on ordinary and geopolymer concrete using nondestructive testing (NDT) tests like ultrasonic pulse velocity (UPV) test and rebound hammer (RH) test. Cube specimens of dimensions 150 mm × 150 mm × 150 mm are used to conduct these tests at 7, 14, and 28 days. Proportions considered for concrete are cement-fly ash-river sand (100-0-100% and 60-40-100%), cement-fly ash-robo sand (100-0-100% and 60-40-100%) whereas geopolymer concrete fly ash-metakaolin is taken in proportions of 100-0%, 60-40%, and 50-50%. Alkaline activators (sodium hydroxide and sodium silicate with molarity 12M) were used in preparing geopolymer concrete. The major objective of the current study is to obtain relation between compressive strength of concrete and UPV values.

1. Introduction

Nondestructive testing (NDT) is an approach for reviewing, testing, or analyzing the elements or components on concrete and concrete members. The major purpose of NDT is to evaluate integrity and quality of concrete members without causing any damage to its functionality and integrity [1]. Acoustic Tap Testing was one of the methods of NDT used earlier to nineteenth century, to detect cracks in railroad wheel [2]. NDT is majorly used to test the structural components of a structure for ensuring safety and serviceability. Certain factors like resolution in both vertical and lateral directions and signal to noise ratio impact NDT [3].

Distinct NDT methods are used in Civil Engineering. NDT surface hardness methods are used to identify the material's strength characteristics. Indentation method and rebound hammer method are the two groupings used to identify concrete surface hardness [4]. Rebound or Schmidt hammer is another nondestructive testing equipment. It is used for finding the concrete or rock strength and elastic property. The rebound number is measured spring-loaded mass. Impacting the hammer on smooth concrete block or rock surface at right angles, the rebound number is obtained.

In the recent past, the use of fly ash offers with cement replacing material gains significant importance for reducing the pollution [5]. It becomes one of the ingredients of concrete. Measurement of strength of concrete through

UPV was introduced in USA in the mid-1940s. UPV is one of the NDT methods useful to test quality, homogeneity, and compressive strength of concrete through regression equation. The UPV test consists of transmission of mechanically generated pulses through electro-acoustic transducers. Applied pulse generates longitudinal waves, whose velocity can be determined by transducers. The velocity of waves determined by UPV is correlated to elastic modulus, strength, and so on.

Rebound or Schmidt Hammer. The RH is another NDT equipment. It is used for finding the concrete or rock strength and elastic property. The rebound number is measured spring-loaded mass. Impacting hammer on smooth concrete block or rock surface at right angles, the rebound number is obtained.

Depending on age of concrete, water-cement ratio, properties, and type of aggregate and cement influence UPV values [6]. In addition to these factors, reinforcement which was embedded in the path of pulse also shows significant effect on UPV values [7]. As there are various NDT methods used by industries of civil and structural engineers, there exists an ample amount of literatures related to NDT. The major intent of this paper is to obtain UPV and rebound values of conventional, geopolymer concretes and to develop the relation between compressive strength and UPV values.

2. Materials and Methods

2.1. Cement. 53 Grade OPC (specific gravity = 3.10) is utilized in this experimental study. Based on the data, IS 8112 : 1989 [8], the chemical composition of cement is represented in Table 1.

2.2. Fly Ash (FA). FA is one of the coal combustion products which consists of fine particles collected from boilers with flue gases. FA was collected from the thermal power plant, Kondapalli, Krishna district, Andhra Pradesh, India. Composition of fly ash is presented in Table 1.

2.3. Fine Aggregate. River Sand. River sand is naturally obtained material from river bank. It is widely used in normal construction works. The fineness modulus of river sand is 2.75 and conforming to zone III according to IS 383 : 1970 [9].

Robo Sand. Robo sand is a waste obtained from crushed aggregates. It is also known as artificial sand. 3.62 is the fineness modulus of robo sand. According to IS 383 : 1970 [9], this robo sand conforms to Zone III. Robo sand properties are represented in Table 2.

2.4. Coarse Aggregate. Coarse aggregate is collected from quarry site. 20 mm and 10 mm aggregates are used in this experiment conforming to Zone III as per IS 10262 : 2009 [10]. In this experiment, 60% of 20 mm and 40% of 10 mm aggregates are used. Table 3 represents properties of coarse aggregates.

TABLE 1: Cement and fly ash chemical composition.

Component	% of cement	% of FA
Loss ignition	1. 8	2.0
SiO ₂	20. 4	60.54
Fe ₂ O ₃	3. 2	5.87
Al ₂ O ₃	3. 9	26.20
CaO	63	1.91
MgO	2. 4	0.38
K ₂ O + Na ₂ O	—	1.02
SO ₃	3	0.23

TABLE 2: River sand and robo sand properties.

Property	River sand	Robo sand
Fineness modulus	2.65	3.56
Specific gravity	2.68	2.7
Silt content	0.8%	—

TABLE 3: Test values for coarse aggregate.

Property	Test value
Specific gravity	2.79
Water absorption	0.45%
Aggregate impact value	21.70
Aggregate crushing value	20.60
Combined flakiness and elongation value	22.10

2.5. Metakaolin. The dehydroxylated variety of clay mineral kaolinite is termed metakaolin. It provides high strength to concrete [11]. The disordered kaolinite and ordered kaolinites are converted into dehydroxylates at temperatures of 530–570°C and 570–630°C. A light pinkish metakaolin was employed here whose specific gravity is 2.45.

2.6. Alkaline Activators. For the preparation of geopolymer concrete, chemicals called sodium hydroxide and sodium silicate were used.

Sodium Hydroxide. Generally, sodium hydroxide (NaOH) is available in flakes and pellets. Sodium hydroxide flakes are used in this experiment.

Sodium Silicate. Generally, it is available in gel state and is known as water/liquid glass.

2.7. Solution Preparation. Solution NaOH was prepared 24–48 hours priorly. Due to its presence in form of flakes, NaOH pellets were dissolved properly in water for preparation of sodium hydroxide solution. Experimental property studies of solutions can provide significant thermodynamic information under various temperature and pressure circumstances. Oxygenated compounds like alkaline and alcohols have become a very important additive in mix binders for liquids and solids [12–16]. In order to prepare one litre of 12M NaOH, 480 grams of NaOH was dissolved in water at room temperature, approximately 28 ± 2°C. The molarity equation can be written as follows:

$$M = \frac{n}{v}, \quad (1)$$

where M is the molarity, n refers the moles of solute, and v is the litre of solution.

Molarity = moles of solute/litre of solution
 $12M = 12$ molarity
 $= 12 \times \text{molecular weight}$
 $= 12 \times 40$
 $= 480 \text{ gm.}$

2.8. Mix Design. IS 456:2000 [12] is used for mixing of conventional OPC concrete. Ratio of water to cement used for concrete mixing is 0.35 which is obtained by designing M25 grade concrete. 2400 Kg/m^3 is the density of concrete which is considered for calculation of quantities of materials. According to 10262:2009 [10], absolute volume of coarse as well as fine aggregates is 70% in density of concrete whereas remaining 30% is of geopolymer binders like ash, meta-kaolin, and alkaline activators. The mix proportions are represented in Tables 4 and 5.

2.9. Mixing and Casting. Mixing and casting of geopolymer concretes are kind of conventional concrete. After mixing, the concrete is cast in $150 \text{ mm} \times 150 \text{ mm} \times 150 \text{ mm}$ moulds. The casting is finished by placing concrete in the three layers. A tamping rod is employed for tamping of each layer (25 times) [9, 17].

2.10. Curing. Ambient curing is the curing method adopted for geopolymer concrete. For ordinary concrete, curing is done by placing cubes into a water bath for 7, 14, and 28 days. After curing period completion, specimens are tested.

2.11. Testing

Ultrasonic Pulse Velocity Test Procedure. Basic principle of the UPV test is measuring pulse of longitudinal vibrations that are passing through concrete. The travel time of UPV wave travelling through the concrete will be measured. Velocity of wave depends on geometry and elastic property of material. BS-4408 part-5, ASTM C 597-71, and BIS 13311 (part 1): 1992 [18–20] provided recommendations for utilization of this method.

The compressive wave velocity for homogeneous concrete is evaluated by using the following equation:

$$V = \sqrt{\frac{kE_d}{\rho}}, \quad (2)$$

where $k = 1 - \gamma / [(1 + \gamma)(1 - 2\gamma)]$, E_d is the dynamic elastic modulus, and ρ is the dynamic Poisson's ratio.

Elastic stiffness and mechanical strength are the two influencing factors of UPV. Variations in mix proportions influence pulse velocity. To assess compressive strength, quality of concrete and calibration charts are to be established.

TABLE 4: Mix proportions for GPC.

Mix no.	Mix proportion
GPC 1	100% + 0%MK
GPC 2	60% + 40%MK
GPC 3	50% + 50%MK

TABLE 5: Mix proportions for OPC.

Mix no.	Mix proportion
1	100% + 0%FA+100%RS
2	60% + 40%FA+100%RS
3	60% + 40%FA+0%RS

According to BIS 13311 (part 1): 1992 [15, 18, 19], quality of concrete can be determined by using velocity of ultrasonic pulse waves. Velocity of waves is determined initially. Based on velocity of wave travelling through the concrete specimen, quality of concrete can be identified and is represented in Table 6.

Rebound Hammer or Schmidt Hammer Test Procedure [9]. The rebound hammer with plunger is considered and impacted against concrete surface. Generally, there are different kinds of rebound hammers which are available depending on applications. The impact energy may vary from 0.07–3 kg-m. Number which is obtained from the rebound index is calibrated to compute compressive strength.

The concrete surface on which this rebound test is conducted should be smooth, clean, and dry. Sand paper or stone can be used to rub rough surfaces present on concrete. From edges and discontinuity shapes, the hammer should be impacted 20 mm long. Concrete surface should be maintained perpendicular to the rebound hammer. For each concrete surface, numbers of observations are to be taken. Average of those observations results in strength of concrete. Test procedure for determining rebound values is as per ASTM C-805-85 [21] and BIS 13311 PART 2 [22].

According to BIS 13311 (part 2): 1992 [22], quality of concrete can be determined by using the rebound number. The rebound number is determined initially by impacting the rebound hammer. Based on the number, quality of concrete can be identified and is represented in Table 7.

3. Results and Discussion

Evaluation tests for finding the concrete strength were conducted with various supplements of cement after completion of curing periods. UPV testing machine and rebound hammer are the equipment used for compressive strength evaluation [15, 20, 22].

3.1. For Ultrasonic Pulse Velocity Test. Table 8 contains UPV values of OPC after curing (7, 14, and 28 days). A graph was plotted by considering concrete mix on abscissa and UPV values as ordinates. And the obtained graph is represented as Figure 1.

TABLE 6: Grading of concrete using pulse velocity [8].

UPV (km/sec)	Quality of concrete
Above 4.5	Excellent (E)
3.5–4.5	Good (G)
3–3.5	Medium (M)
Below 3	Poor (P)

TABLE 7: Grading of concrete using the rebound number [8].

Rebound number	Concrete grading
Above 40	Very good (VG)
30–40	Good (G)
20–30	Fair (F)
Below 20	Poor (P)

TABLE 8: UPV values for OPC.

Concrete mix	UPV (km/s)		
	7 days	14 days	28 days
Mix 1	4.731	4.913	5.245
Mix 2	4.913	5.068	5.372
Mix 3	3.452	3.816	4.275

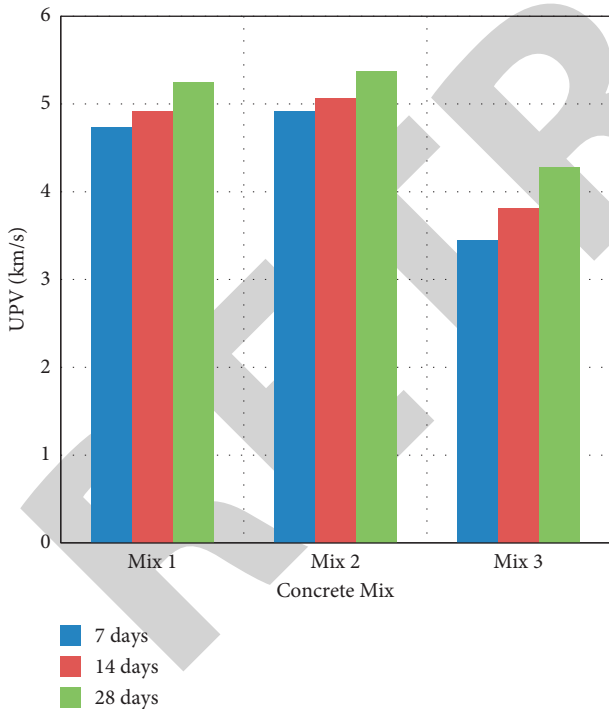


FIGURE 1: UPV values for OPC for different mix proportions.

Figure 1 represents a plot between UPV values for OPC for different concrete mixes. And it was noticed that UPV values are increasing for increasing curing period. UPV values of Mix 3 are decreasing at all ages (7, 14, and 28 days).

Table 9 represents UPV values for GPC concrete of all the three mix proportions after 7, 14, and 28 days of curing.

TABLE 9: UPV values for GPC.

Concrete mix	UPV (km/s)		
	7 days	14 days	28 days
GPC 1	1.534	2.556	3.884
GPC 2	2.523	3.596	4.756
GPC 3	2.573	3.592	4.165

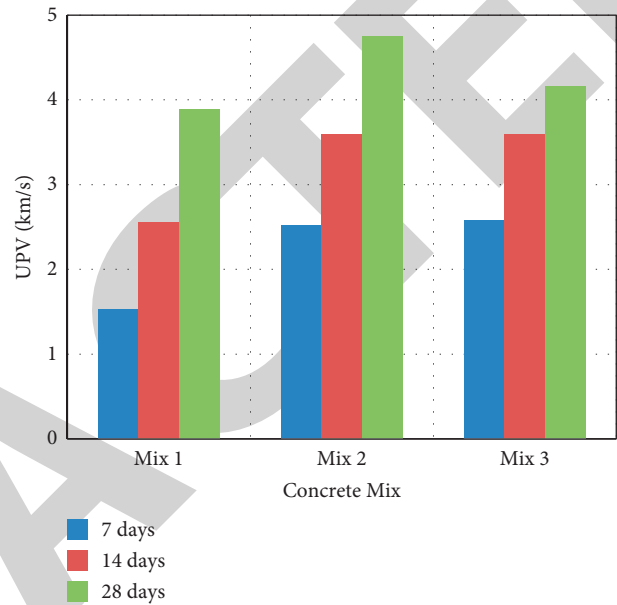


FIGURE 2: UPV value for GPC for different proportions.

TABLE 10: Rebound number for OPC.

Concrete mix	Rebound no.		
	7 days	14 days	28 days
Mix 1	33	25	26
Mix 2	36	28	29
Mix 3	38	31	30

A graph was plotted by considering GPC mix on abscissa and UPV values as ordinates. And the obtained graph is represented as Figure 2.

A plot between UPV values for OPC for different mix proportions is represented in Figure 2. From this figure, it was observed that UPV values increase for increasing curing period. UPV values of Mix 3 are decreasing at all ages (7, 14, and 28 days).

3.2. For Rebound Hammer Test. Table 10 represents the rebound number for different mix proportions of OPC. These values are taken after the curing period (7, 14, and 28 days).

Figure 3 represents a plot between rebound numbers for OPC for different mix proportions. And it is being noticed that rebound values are decreasing with increase in the curing period. A rebound value of Mix 3 is greater when

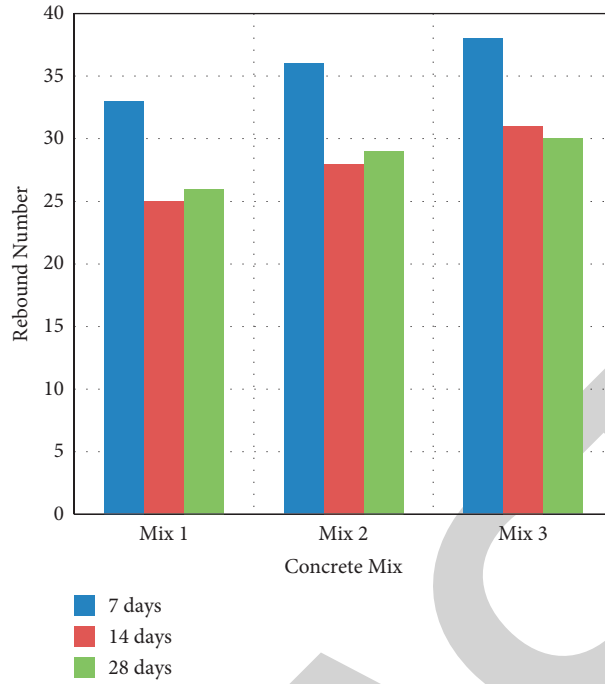


FIGURE 3: Rebound number for different proportions of OPC.

TABLE 11: Rebound number for GPC.

Concrete mix	Rebound no.		
	7 days	14 days	28 days
Mix 1	28	27	26
Mix 2	29	28	28.5
Mix 3	31	31.5	31.25

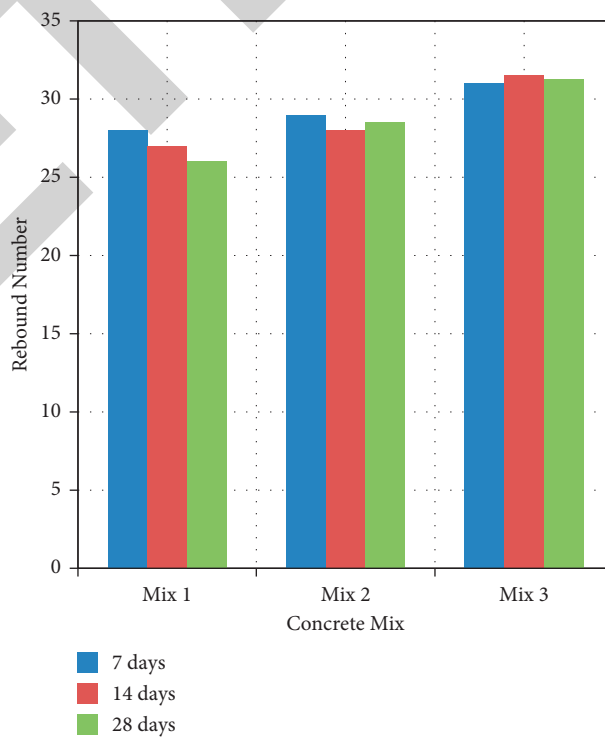


FIGURE 4: Rebound number for different proportions of GPC.

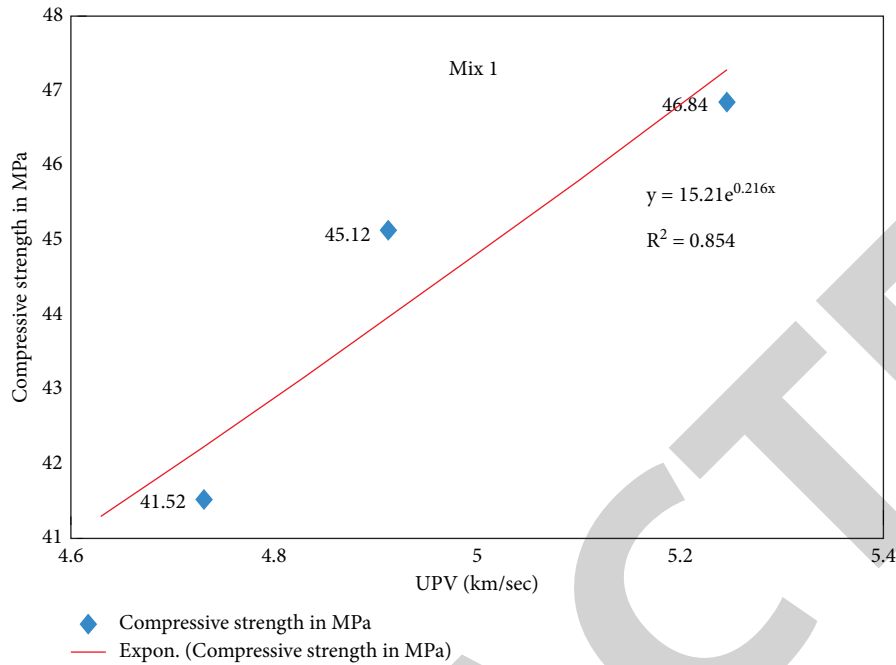


FIGURE 5: Relation between compressive strength and UPV for Mix 1.

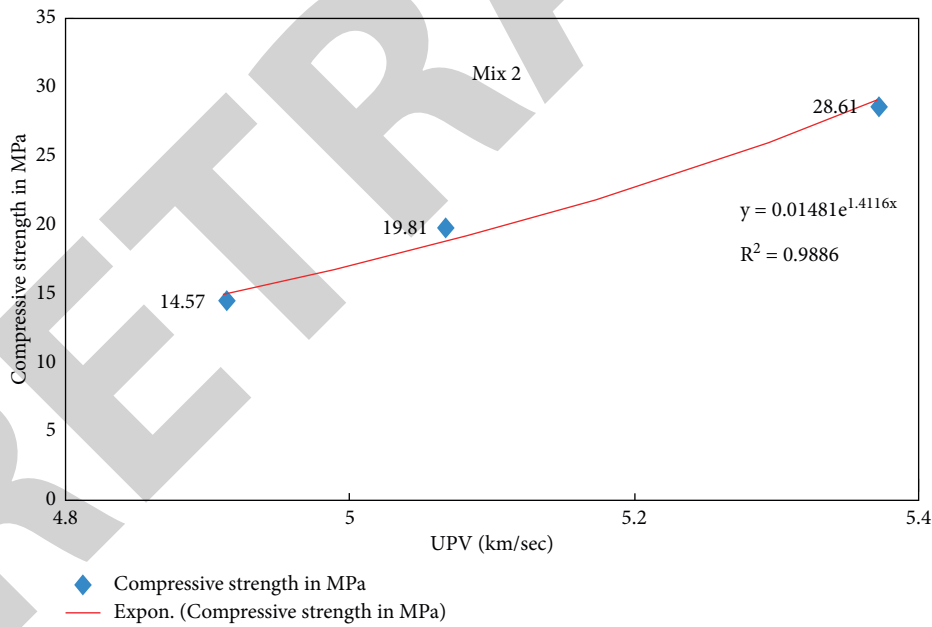


FIGURE 6: Relation between compressive strength and UPV for Mix 2.

compared with other mix proportions at all ages (7, 14, and 28 days).

In Table 11, the rebound number for different mix proportions of GPC is represented. These values are taken after the curing period (7, 14, and 28 days).

Figure 4 represents a plot between rebound numbers for GPC for different mix proportions. And it is being

noticed that, on increasing the curing period, rebound values are also increasing. Rebound value of Mix 3 is greater when compared with other mix proportions at various ages (7, 14, and 28 days). Along with the above results, relations of compressive strength and ultrasonic pulse velocity values were developed and are represented in Figures 5–12.

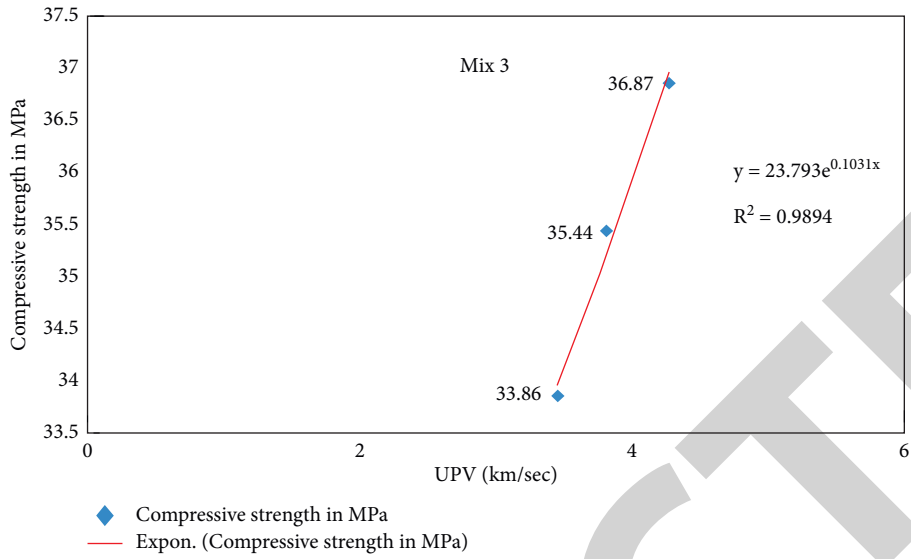


FIGURE 7: Relation between compressive strength and UPV for Mix 3.

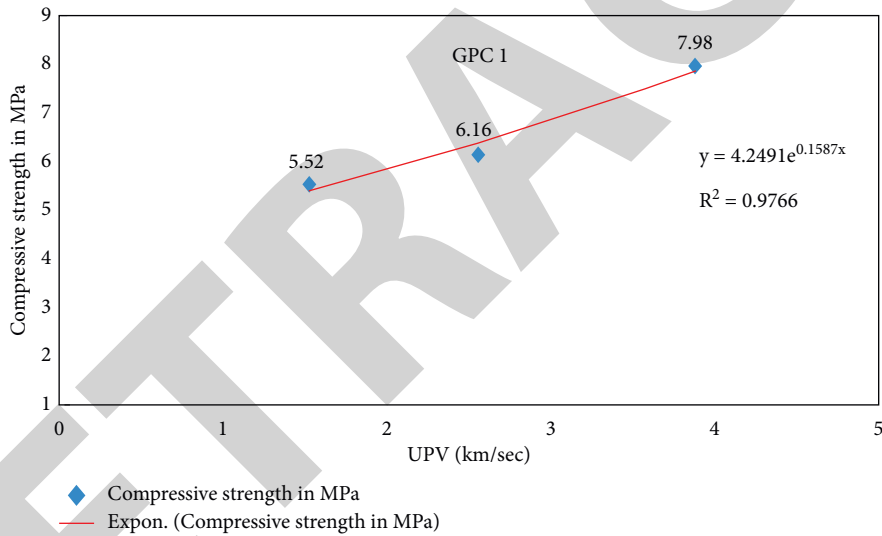


FIGURE 8: Relation between compressive strength and UPV for GPC 1.

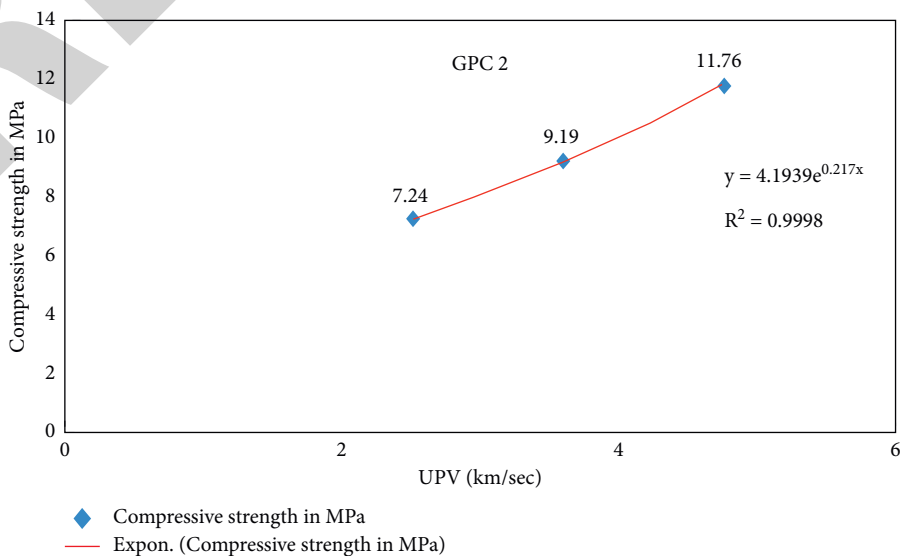


FIGURE 9: Relation between compressive strength and UPV for GPC 2.

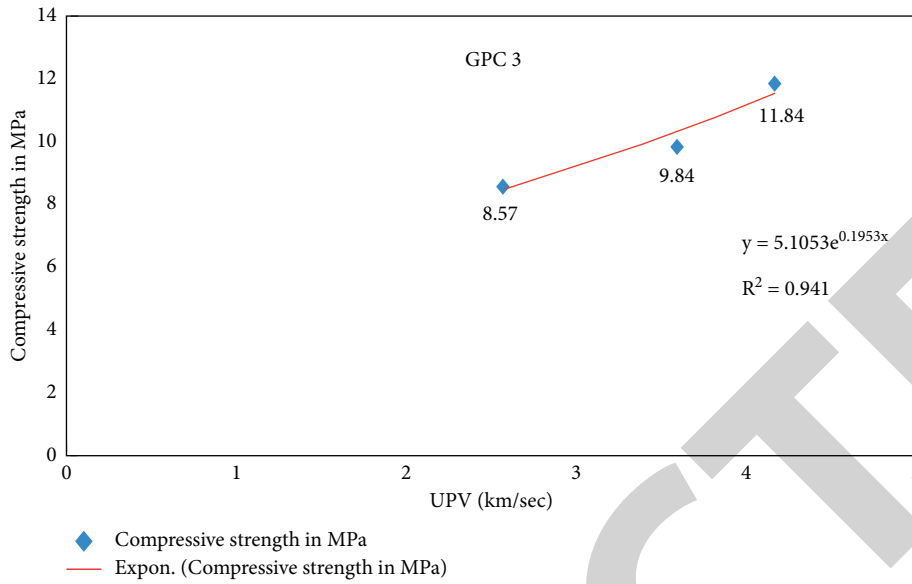


FIGURE 10: Relation between compressive strength and UPV for GPC 3.

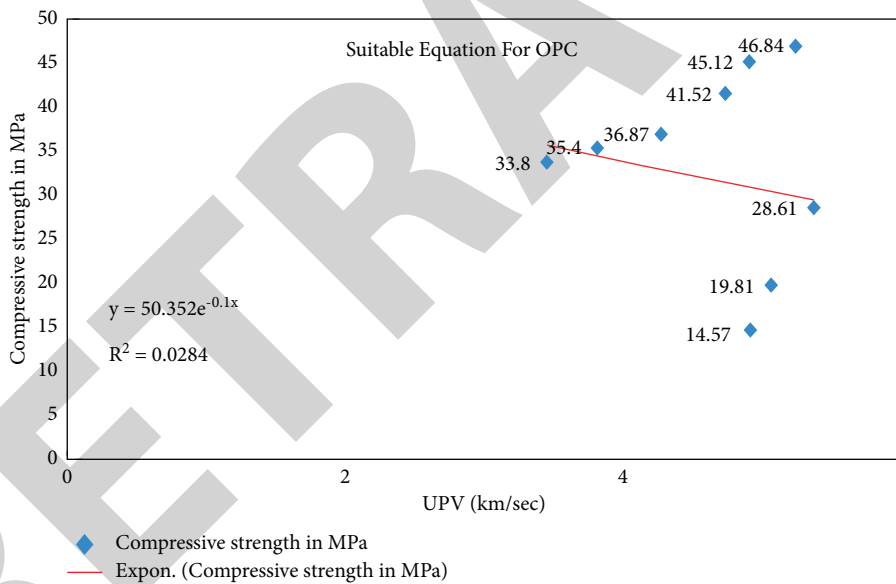


FIGURE 11: Equation obtained for OPC.

There is no specific relation for concrete compressive strength and UPV. From above relations, following equations were determined with respect to mix proportions [16, 20, 23, 24]:

- (1) $y = 15.21e^{0.216x}$ (Mix 1)
- (2) $y = 0.014e^{1.411x}$ (Mix 2)
- (3) $y = 23.79e^{0.103x}$ (Mix 3)

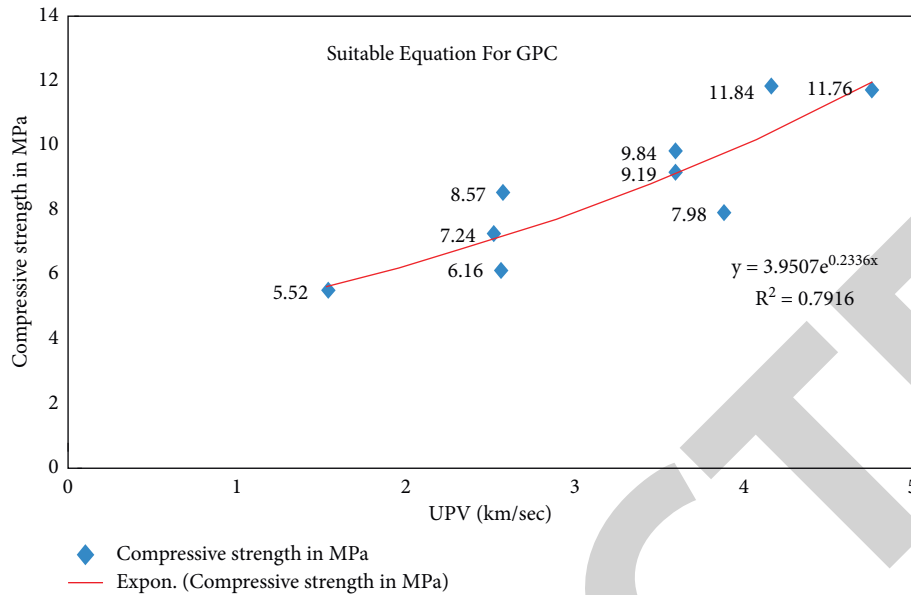


FIGURE 12: Equation obtained for GPC.

$$(4) y = 4.249e^{0.158x} \text{ (GPC 1)}$$

$$(5) y = 4.193e^{0.217x} \text{ (GPC 2)}$$

$$(6) y = 5.105e^{0.195x} \text{ (GPC 3)}$$

where y is the concrete compressive strength and x is the velocity value of concrete.

4. Conclusion

For this present experimental investigation, an equation is determined for comparison of compressive strength and UPV values obtained as follows:

- (i) The UPV and rebound values increase with increase in the curing period.
- (ii) For Mix 2 of OPC concrete, the UPV values increase by 3.8% and 6.42% at 7 to 14 days and 14 to 28 days of curing, respectively. For the same mix proportion, the rebound value increases by 9.1% and 5.5% at 7–14 and 14–28 days of curing, respectively.
- (iii) For Mix 2 of GPC, the UPV values increase with 42.46% and 32.31% at 7–14 days and 14–28 days of curing, respectively. For same mix proportion, the rebound increases by 3.57% and 6.89% at 7–14 and 14–28 days of curing, respectively.
- (iv) With reduction of fly ash content in GPC, the passing time of longitudinal waves is lesser.
- (v) Further investigation of this current study is to develop equations for various mix proportions of both conventional and geopolymer concrete. These are helpful for finding the compressive strength of respective mix proportions.

4.1. Future Scope

Further investigation of this current study is to develop equations for various mix proportions of both

conventional and geopolymer concrete. These are helpful for finding the compressive strength of respective mix proportions.

Many industrial by-product combinations can be used for production of geopolymers.

Structural parameters are investigated using geopolymer.

For utilizing geopolymer concrete in large- and small-scale constructions, experimental investigations can be conducted on structural elements.

Life cycle analysis (LCA) of concrete can also be used to identify the durability of geopolymer concrete.

Data Availability

The data used to support the findings of this study are included in the article and are available from the corresponding author upon request.

Conflicts of Interest

The authors declare that there are no conflicts of interest regarding the publication of this paper.

References

- [1] G. Workman and O. P. Moore, *Nondestructive Testing Handbook 10. Overview*, American Society of Nondestructive Testing, Columbus, OH, USA, 2012.
- [2] R. K. Stanley and P. O. Moore, Eds., *Special Nondestructive Testing Methods*, American Society of Nondestructive Testing, Columbus, OH, USA, 1995.
- [3] D. M. McCann and M. C. Forde, "Review of NDT methods in the assessment of concrete and masonry structures," *NDT & E International*, vol. 34, no. 2, pp. 71–84, 2001.
- [4] J. Helal, M. Sofi, and P. Mendis, "Non-destructive testing of concrete: a review of methods," *Electronic Journal of Structural Engineering*, vol. 14, no. 1, pp. 97–105, 2015.

Retraction

Retracted: Free Vibration Analysis of Thick Rectangular and Elliptical Plates with Concentric Cut-Out

Advances in Materials Science and Engineering

Received 26 December 2023; Accepted 26 December 2023; Published 29 December 2023

Copyright © 2023 Advances in Materials Science and Engineering. This is an open access article distributed under the Creative Commons Attribution License, which permits unrestricted use, distribution, and reproduction in any medium, provided the original work is properly cited.

This article has been retracted by Hindawi, as publisher, following an investigation undertaken by the publisher [1]. This investigation has uncovered evidence of systematic manipulation of the publication and peer-review process. We cannot, therefore, vouch for the reliability or integrity of this article.

Please note that this notice is intended solely to alert readers that the peer-review process of this article has been compromised.

Wiley and Hindawi regret that the usual quality checks did not identify these issues before publication and have since put additional measures in place to safeguard research integrity.

We wish to credit our Research Integrity and Research Publishing teams and anonymous and named external researchers and research integrity experts for contributing to this investigation.

The corresponding author, as the representative of all authors, has been given the opportunity to register their agreement or disagreement to this retraction. We have kept a record of any response received.

References

- [1] A. Merneedi, N. Mohan Rao, L. Natrayan, L. Yuvaraj, and P. Paramasivam, "Free Vibration Analysis of Thick Rectangular and Elliptical Plates with Concentric Cut-Out," *Advances in Materials Science and Engineering*, vol. 2021, Article ID 7212075, 14 pages, 2021.

Research Article

Free Vibration Analysis of Thick Rectangular and Elliptical Plates with Concentric Cut-Out

Anjibabu Merneedi ¹, Nalluri Mohan Rao,² L. Natrayan ³, L. Yuvaraj ⁴,
and Prabhu Paramasivam ⁵

¹Department of Mechanical Engineering, Aditya College of Engineering, Surampalem 533437, Andhra Pradesh, India

²Department of Mechanical Engineering, University College of Engineering, JNTUK, Kakinada 533003, India

³Department of Mechanical Engineering, Saveetha School of Engineering, SIMATS, Chennai 602105, Tamil Nadu, India

⁴Department of Automobile Engineering, Acharya Institute of Technology, Bangalore 560107, Karnataka, India

⁵Department of Mechanical Engineering, College of Engineering and Technology, Mettu University, Metu 318, Ethiopia

Correspondence should be addressed to Anjibabu Merneedi; anjiamiable@gmail.com and L. Natrayan; natrayanphd@gmail.com

Received 24 June 2021; Revised 11 July 2021; Accepted 21 September 2021; Published 16 October 2021

Academic Editor: Samson Jerold Samuel Chelladurai

Copyright © 2021 Anjibabu Merneedi et al. This is an open access article distributed under the Creative Commons Attribution License, which permits unrestricted use, distribution, and reproduction in any medium, provided the original work is properly cited.

This research paper deals with a numerical method which is modified and applied, by the authors to derive an eigenvalue of a thick plate having cut-out in which geometries of plate and cut-outs are different, through a deflection matching condition by including shear deformation and rotary inertia effects, with less computational efforts and high accuracy. The modified Independent Coordinate Coupling Method (ICCM) is validated with FEM package (ANSYS) and applied to know the change in eigenvalues for a plate with cut-out by varying various parameters like aspect ratios, cut-out size, and thickness ratios. Trigonometric functions considered at the boundary level conditions of a simply supported plate should be satisfied. Free vibrational exploration on a thick isotropic plate with various aspect ratios and an elliptical plate with various sizes is carried out through the modified ICCM. Independent coordinates are applied for a plate domain and for a hole domain individually followed by equating the deflection condition of hole and plate, a reduced mass to express with cut-out from which eigenvalues can be obtained. The deflection matching condition facilitates the analysis even though the geometries of plate and cut-outs are different.

1. Introduction

A plate with a cut-out is a commonly existing structure in the domain of aeronautics, civil, marine, and mechanical engineering to accommodate mountings or accessories under the action of various forces. In dealing with such cases, knowledge on dynamics of plates plays a vital role. Plates with cut-outs are subjected to free vibration. Eigenvalues of thin plates may be calculated using classical plate theory and easily obtained, whereas they cannot be applied directly in thick plate analysis due to the effect of rotary inertia. This leads to an overestimation of results. The expression of strain and potential energies of plate must contain the terms of shear and rotary inertia to improve the accuracy of eigenvalues while computing.

From the literature available on the Mindlin plates, Senjanovic et al. [1, 2] derived exact formulas for a plate by reducing a

three-equation system to one equation expressing a potential function in terms of bending deflection. Xiang et al. [3] analyzed Mindlin plates by implementing delta type of kernel wavelet in lateral vibration of plates. Merneedi et al. [4, 5] applied the ICCM method of elliptical and rectangular thin plate by changing the size, position, and number of holes at all possible ways. Aksu [6] applied an energy approach along with a finite difference in a Mindlin's dynamic analysis approach of plate having cut-outs. Rui et al. [7] applied a rational method of superposition in the symplectic space for Mindlin plate's vibration analysis. Xing and Liu [8, 9], implemented a new two-eigenfunction theory to obtain vibrational solutions of a rectangular Mindlin plate, in which amplitude and generalized curvatures are considered as functions.

Liew et al. [10–13] minimized energy function of Mindlin's theory by using the Rayleigh–Ritz method to formulate the

governing eigenvalue equations. Dawe and Roufaeil [14] derived by assuming that plate deflection and rotations are a sequence. The Rayleigh–Ritz approach may be used to compute the natural frequencies of flexural vibrations of a square plate using products of appropriate Timoshenko beam functions. Leissa [15, 16] investigates the free vibrational exploration for twenty-one cases of various rectangular plates through precise analytical techniques. Sayyad and Ghugal [17], proposed a displacement-based theory in which thickness coordinates are used as an exponential function so that transverse shear stress can be obtained directly without any shear correction factor. Kanak and Salil [18] and Merneedi et al. [5] consider the nine-node isoparametric element. The natural frequencies of thin and thick plates with cut-outs were analysed using the first-order shear deformation theory. Prasad et al. [19] utilized the Rayleigh–Ritz approach to apply a three-term deflection function on clamped and simply supported elliptical plates. Leissa [20] calculated the precise fundamental natural frequencies of a simple sup. Maurizi et al. [21], derived fundamental natural frequencies for a vibration of elastic plate using simple static in the presence of a clamped boundary condition. Lam et al. [22] created a computational tool to determine the natural frequencies of circular and elliptical plates; the researchers used the Rayleigh–Ritz method using a set of orthogonal functions called acceptable functions. Shibaoka [23] creates a fundamental normal mode of flexural vibration of an elliptical plate under clamped-clamped boundary conditions. Mcnitt [24] utilized the Galerkin method and an ordinary product solution by ignoring the impact of rotational inertia in the investigation of free vibration of an elliptical plate under clamped boundary conditions using traditional small-deflection theory. Kwak and Han [25] used ICCM to do a free vibrational exploration on a rectangular plate with a hole obtaining energy linked to the hole with plate separately and equated by matching condition of deflection. Hasheminejad et al. [26] formulated the analytical expression for the elliptical plate with an eccentric cut-out. The solution is derived using Helmholtz's decomposition theorem, and this technique is based on Navier's displacement equation of motion. Mathieu functions of translational addition theorems are used to separate the variables.

According to the literature, eigenvalues of a thick rectangular plate with a hole were estimated using several numerical tools such as the Rayleigh–Ritz methodology, FEM, and finite difference techniques and the plate is same. It is identified that if hole and plate are of different geometries, the RRM may lead to complex integrals with tedious numerical computations because of its integral limits [27]. Keeping in view of this, in the present work, the authors proposed a novel modified ICCM to determine the natural frequencies of a structure with cut-out of different shapes by implementing a deflection matching condition along with closed-form integrals to reduce the computational efforts. Shear deformation and rotational inertia effects are among them. Even if the shape of the plate and hole differs, the deflection matching condition simplifies the analysis, which is a key benefit of the ICCM. Using the ICCM, a Mindlin elliptical and rectangular plate's first six natural frequencies with various sizes of cut-outs under simply supported boundary conditions were derived to show the variation of natural frequencies with respect to various hole sizes, and the same is validated through ANSYS software including mode shapes, which was not covered in the literature in view of the authors.

1.1. Free Vibrational Exploration of Rectangle Plate with Cut-Out. Separate energy expressions are formulated for a hole domain and for a plate domain exploration of a plate with hole, and hence deflection matching condition is essential to establish a kinematic relation between these independent coordinate domains. It will also enable us to unify these two independent energies.

1.1.1. Expressions for Rectangular Plate. Consider a thick rectangular plate with a cut-out in $x - y$ plane, having dimensions of $a \times b$ and $a_c \times b_c$, respectively. Expressions for rectangular plate strain energy and kinetic energy from Reference [11] are as follows:

$$V_p = \frac{1}{2} \int_v \left\{ \frac{Eh^2}{1-\mu^2} \left[\left(\frac{\partial \psi_x}{\partial x} + \frac{\partial \psi_y}{\partial y} \right)^2 - 2(1-\mu) \left(\frac{\partial \psi_x}{\partial x} \frac{\partial \psi_y}{\partial y} - \frac{1}{4} \left(\frac{\partial \psi_x}{\partial y} + \frac{\partial \psi_y}{\partial x} \right)^2 \right) \right] + \kappa G \left[\left(\psi_x + \frac{\partial w}{\partial x} \right)^2 + \left(\psi_y + \frac{\partial w}{\partial y} \right)^2 \right] \right\} dv,$$

$$T_p = \frac{1}{2} \omega^2 \int_A \left[\rho h w^2 + \frac{1}{12} \rho h^3 (\psi_x^2 + \psi_y^2) \right] dA,$$
(1)

where h = plate thickness, ρ = mass density, E = modulus of elasticity, w = transverse displacement, G = shear modulus, μ = Poisson's ratio, $\psi_x = -\partial w / \partial x$ = rotation about y direction, $\psi_y = -\partial w / \partial y$ = rotation about x direction, κ = shear correction factor = 5/6, and ω = angular frequency.

Introducing a non-dimensional parameter, thickness to width ratio $\beta = h/b$, aspect ratio $\alpha = a/b$, and non-dimensional variables $\xi = x/a$, $\eta = y/b$, the energy expression of plate is a non-dimensional representation of plate which can be written as follows:

$$V_p = \int_0^1 \int_0^1 \left\{ \left(\frac{1}{\alpha} \frac{\partial \psi_x}{\partial \xi} + \frac{\partial \psi_y}{\partial \eta} \right)^2 - 2(1-\mu) \left[\frac{1}{\alpha} \frac{\partial \psi_x}{\partial \xi} \frac{\partial \psi_y}{\partial \eta} - \frac{1}{4} \left(\frac{\partial \psi_x}{\partial \eta} + \frac{1}{\alpha} \frac{\partial \psi_y}{\partial \xi} \right)^2 \right] \right. \\ \left. + \frac{6(1-\mu)\kappa}{\beta^2} \left[\left(\psi_x + \frac{1}{\alpha} \frac{\partial w}{\partial \xi} \right)^2 + \left(\psi_y + \frac{\partial w}{\partial \eta} \right)^2 \right] \right\} abd\xi d\eta, \quad (2a)$$

$$T_p = \int_0^1 \int_0^1 \left[w^{*2} + \frac{1}{12} \beta^2 (\psi_x^2 + \psi_y^2) \right] abd\xi d\eta, \quad (2b)$$

where $w^* = w/b$.

Admissible functions are considered to expand transverse deflection and the rotations in equations (2a) and (2b) as

$$\begin{aligned} w(\xi, \eta, t) &= \bar{A}_i(\xi, \eta)\Omega(t), \\ \psi_x(\xi, \eta, t) &= \bar{B}_i(\xi, \eta)\Omega(t), \\ \psi_y(\xi, \eta, t) &= \bar{C}_i(\xi, \eta)\Omega(t), \end{aligned} \quad (3)$$

where $\bar{A}_i(\xi, \eta) = [A_1 \ A_2 \ A_3 \ A_4 \ \dots \ A_m]$ is a $(1 \times m)$ matrix and $\Omega_i(\xi, \eta) = [\Omega_1 \ \Omega_2 \ \Omega_3 \ \Omega_4 \ \dots \ \Omega_m]^T$ is $(m \times 1)$ generalized coordinate vector, where “m” denotes admissible functions required for the approximating the deflection curve.

Substituting equation (3) in equations (2a) and (2b) yields

$$T_p = \frac{1}{2} \dot{\Omega}^T M \dot{\Omega}, \quad (4a)$$

$$V_p = \frac{1}{2} \Omega^T K \Omega, \quad (4b)$$

in which

$$M = \rho h b^2 \bar{M}, \quad (5a)$$

$$K = \left(\frac{D}{b^2} \right) \bar{K}, \quad (5b)$$

where

$$\bar{M} = \int_0^1 \int_0^1 \left[(\bar{A}^T \cdot \bar{A}) + \frac{\beta^2}{12} (\bar{B}^T \cdot \bar{B} + \bar{C}^T \cdot \bar{C}) \right] d\xi d\eta, \quad (6a)$$

$$\bar{K} = \int_0^1 \int_0^1 \left\{ \begin{aligned} & \left[\frac{1}{\alpha^2} \frac{\partial \bar{B}^T}{\partial \xi} \cdot \frac{\partial \bar{B}}{\partial \xi} + \frac{\partial \bar{C}^T}{\partial \eta} \cdot \frac{\partial \bar{C}}{\partial \eta} + \frac{1}{\alpha} \left[\frac{\partial \bar{B}^T}{\partial \xi} \cdot \frac{\partial \bar{C}}{\partial \eta} + \frac{\partial \bar{C}^T}{\partial \eta} \cdot \frac{\partial \bar{B}}{\partial \xi} \right] \right] + \\ & (1-\mu) \cdot \left[\frac{1}{\alpha} \left[\frac{\partial \bar{B}^T}{\partial \xi} \cdot \frac{\partial \bar{C}}{\partial \eta} + \frac{\partial \bar{C}^T}{\partial \eta} \cdot \frac{\partial \bar{B}}{\partial \xi} \right] - \frac{1}{2} \left[\left[\frac{\partial \bar{B}^T}{\partial \eta} \cdot \frac{\partial \bar{B}}{\partial \eta} + \frac{1}{\alpha^2} \frac{\partial \bar{C}^T}{\partial \xi} \cdot \frac{\partial \bar{C}}{\partial \xi} \right] + \frac{1}{\alpha} \left[\frac{\partial \bar{B}^T}{\partial \eta} \cdot \frac{\partial \bar{C}}{\partial \xi} + \frac{\partial \bar{C}^T}{\partial \xi} \cdot \frac{\partial \bar{B}}{\partial \eta} \right] \right] \right] + \\ & \left[\frac{6(1-\mu)\kappa}{\beta^2} \left[\left[\bar{B}^T \cdot \bar{B} + \frac{1}{\alpha^2} \frac{\partial \bar{A}^T}{\partial \xi} \cdot \frac{\partial \bar{A}}{\partial \xi} + \frac{1}{\alpha} \left[\bar{B}^T \cdot \frac{\partial \bar{A}}{\partial \xi} + \frac{\partial \bar{A}^T}{\partial \xi} \cdot \bar{B} \right] \right] + \left[\bar{C}^T \cdot \bar{C} + \frac{\partial \bar{A}^T}{\partial \eta} \cdot \frac{\partial \bar{A}}{\partial \eta} + \bar{C}^T \cdot \frac{\partial \bar{A}}{\partial \eta} + \frac{\partial \bar{A}^T}{\partial \eta} \cdot \bar{C} \right] \right] \right] \end{aligned} \right\} d\xi d\eta. \quad (6b)$$

In equations (6a) and (6b), stiffness matrices are represented by \bar{M} , \bar{K} , respectively, along with non-dimensional variables. Equation of motion of plate is obtained by substituting equation (3) in Lagrange’s expression, and its eigenvalue can be computed from

$$[K - \omega^2 M] \Lambda = 0. \quad (7)$$

Using non-dimensional matrices introduced in equations (4a) and (4b), the above eigenvalue problem in non-dimensional form

$$[\bar{K} - \bar{\omega}^2 \bar{M}] \Lambda = 0 \quad (8)$$

will give non-dimensional eigenvalues of a plate, in which “ Λ ” is an eigenvector. In equation (7),

$$\bar{\omega} = \left(\frac{\omega b^2}{\pi^2} \right) \sqrt{\frac{\rho h}{D}} \quad (9)$$

is known as the frequency parameter which represents the flexural rigidity in $D = Eh^3/12(1-\mu^2)$, which is known.

To obtain in terms of admissible function matrices in the X and Y directions, an admissible function matrix from equation (3) has to be changed.

$$\begin{aligned}\bar{A}_i(\xi, \eta) &= A_i(\xi)a_i(\eta), \\ \bar{B}_i(\xi, \eta) &= B_i(\xi)b_i(\eta), \\ \bar{C}_i(\xi, \eta) &= C_i(\xi)c_i(\eta),\end{aligned}\quad (10)$$

where, $i = 1, 2, 3 \dots m$.

1.1.2. Boundary Conditions. A thick simply supported plate is considered and its eigenvalues are derived by considering an individual eigenfunction in each direction for each admissible function.

$$\begin{aligned}A_i(\xi) &= \sqrt{2} \sin(i\pi\xi), \\ a_i(\eta) &= \sqrt{2} \sin(i\pi\eta), \\ B_i(\xi) &= \sqrt{2} \cos(i\pi\xi), \\ b_i(\eta) &= \sqrt{2} \sin(i\pi\eta), \\ C_i(\xi) &= \sqrt{2} \sin(i\pi\xi), \\ c_i(\eta) &= \sqrt{2} \cos(i\pi\eta).\end{aligned}\quad (11)$$

Admissible functions in equation (11) are taken into account in such a way that they meet the assumed boundary conditions of the plate. All geometrical end points of (ξ, η) in equation (3) along with equation (11) will result in a zero deflection.

1.1.3. Energy Expressions for Rectangular Plate with Cut-Out Using ICCM. Kinematic relations are formulated for a plate having cut-out using ICCM; by matching the plate's deflection to the hole's deflection, these relationships may be used to produce updated mass and stiffness matrices as well as distinct plate and hole domains having their own coordinates. Fixing local coordinates to the hole domain is presented for rectangular hole in rectangular plate as illustrated in Figure 1.

Taking non-dimensional coordinates into account, displacement and rotations are expressed as $\xi_h = x_c/a_c$ and $\eta_h = y_c/b_c$.

$$\begin{aligned}w_h(\xi_h, \eta_h, t) &= \bar{A}_{hi}(\xi_h, \eta_h)\Omega(t), \\ \psi_{hx}(\xi_h, \eta_h, t) &= \bar{B}_{hi}(\xi_h, \eta_h)\Omega(t), \\ \psi_{hy}(\xi_h, \eta_h, t) &= \bar{C}_{hi}(\xi_h, \eta_h)\Omega(t),\end{aligned}\quad (12)$$

where $\bar{A}_{hi}(\xi_h, \eta_h) = [A_{h1} \ A_{h2} \ A_{h3} \ \dots \ A_{hm}]$ is an $(1 \times m_h)$ function matrix and $\Omega_h(t) = [\Omega_{h1} \ \Omega_{h2} \ \Omega_{h3} \ \dots \ \Omega_{hm}]^T$ is a $(m_h \times 1)$, here " m_h " is the number of acceptable functions used to approximate deflection in a generalized coordinate vector.

$$\begin{aligned}\bar{A}_{hi}(\xi_h, \eta_h) &= A_{hi}(\xi_h)a_{hi}(\eta_h), \\ \bar{B}_{hi}(\xi_h, \eta_h) &= B_{hi}(\xi_h)b_{hi}(\eta_h), \\ \bar{C}_{hi}(\xi_h, \eta_h) &= C_{hi}(\xi_h)c_{hi}(\eta_h),\end{aligned}\quad (13)$$

where, $i = 1, 2, 3, \dots m_h$.

Equations (12) and (13) represented the potential and kinetic energies.

$$T_H = \frac{1}{2} \dot{\Omega}_h^T M_h \dot{\Omega}_h, \quad (14a)$$

$$V_H = \frac{1}{2} \Omega_h^T K_h \Omega_h. \quad (14b)$$

Hence, total energies of plate with hole are

$$T_{\text{total}} = \frac{1}{2} \dot{\Omega}^T M \dot{\Omega} - \frac{1}{2} \dot{\Omega}_h^T M_h \dot{\Omega}_h, \quad (15a)$$

$$V_{\text{total}} = \frac{1}{2} \Omega^T K \Omega - \frac{1}{2} \Omega_h^T K_h \Omega_h, \quad (15b)$$

where

$$\begin{aligned}M_h &= \rho h b_c^2 \bar{M}_h, \\ K_h &= \left(\frac{D}{b_c^2}\right) \bar{K}_h,\end{aligned}\quad (16)$$

in which

$$\bar{M}_h = \int_0^1 \int_0^1 \left[(\bar{A}_h^T \cdot \bar{A}_h) + \frac{\beta_c^2}{12} (\bar{B}_h^T \cdot \bar{B}_h + \bar{C}_h^T \cdot \bar{C}_h) \right] d\xi_h d\eta_h, \quad (17)$$

$$\bar{K}_h = \int_0^1 \int_0^1 \left\{ \begin{aligned} & \left[\frac{1}{\alpha_c^2} \frac{\partial \bar{B}_h^T}{\partial \xi_h} \cdot \frac{\partial \bar{B}_h}{\partial \xi_h} + \frac{\partial \bar{C}_h^T}{\partial \eta_h} \cdot \frac{\partial \bar{C}_h}{\partial \eta_h} + \frac{1}{\alpha_c} \left[\frac{\partial \bar{B}_h^T}{\partial \xi_h} \cdot \frac{\partial \bar{C}_h}{\partial \eta_h} + \frac{\partial \bar{C}_h^T}{\partial \eta_h} \cdot \frac{\partial \bar{B}_h}{\partial \xi_h} \right] + \right. \\ & (1-\mu) \cdot \left[\frac{1}{\alpha_c} \left[\frac{\partial \bar{B}_h^T}{\partial \xi_h} \cdot \frac{\partial \bar{C}_h}{\partial \eta_h} + \frac{\partial \bar{C}_h^T}{\partial \eta_h} \cdot \frac{\partial \bar{B}_h}{\partial \xi_h} \right] - \frac{1}{2} \left[\left[\frac{\partial \bar{B}_h^T}{\partial \eta_h} \cdot \frac{\partial \bar{B}_h}{\partial \eta_h} + \frac{1}{\alpha_c^2} \frac{\partial \bar{C}_h^T}{\partial \xi_h} \cdot \frac{\partial \bar{C}_h}{\partial \xi_h} \right] + \frac{1}{\alpha_c} \left[\frac{\partial \bar{B}_h^T}{\partial \eta_h} \cdot \frac{\partial \bar{C}_h}{\partial \xi_h} + \frac{\partial \bar{C}_h^T}{\partial \xi_h} \cdot \frac{\partial \bar{B}_h}{\partial \eta_h} \right] \right] \right] + \\ & \left. \frac{6(1-\mu)\kappa}{\beta_c^2} \left[\left[\bar{B}_h^T \cdot \bar{B}_h + \frac{1}{\alpha_c^2} \frac{\partial \bar{A}_h^T}{\partial \xi_h} \cdot \frac{\partial \bar{A}_h}{\partial \xi_h} + \frac{1}{\alpha_c} \left[\bar{B}_h^T \cdot \frac{\partial \bar{A}_h}{\partial \xi_h} + \frac{\partial \bar{A}_h^T}{\partial \xi_h} \cdot \bar{B}_h \right] \right] + \left[\bar{C}_h^T \cdot \bar{C}_h + \frac{\partial \bar{A}_h^T}{\partial \eta_h} \cdot \frac{\partial \bar{A}_h}{\partial \eta_h} + \bar{C}_h^T \cdot \frac{\partial \bar{A}_h}{\partial \eta_h} + \frac{\partial \bar{A}_h^T}{\partial \eta_h} \cdot \bar{C}_h \right] \right] \right\} d\xi_h d\eta_h, \quad (18)$$

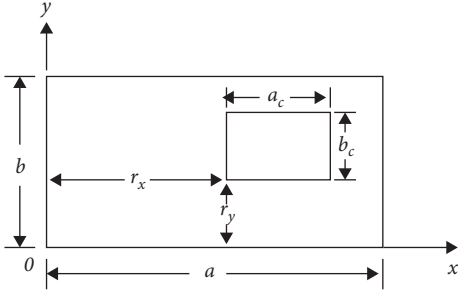


FIGURE 1: Rectangular plate opening with cut-out.

where thickness to width ratio $\beta_c = h/b_c$, aspect ratio $\alpha_c = a_c/b_c$, and non-dimensional variables $\xi_h = x_c/a_c$ and $\eta_h = y_c/b_c$.

Equations (17) and (18) have a distinctive advantage that the integral bounds range from 0 to 1, allowing for a closed-form solution. In terms of plate domain, the displacement

matching requirement of the hole may be represented as follows:

$$\begin{aligned} w_h(\xi_h, \eta_h) &= w(\xi, \eta), \\ \psi_{hx}(\xi_h, \eta_h) &= \psi_x(\xi, \eta), \\ \psi_{hy}(\xi_h, \eta_h) &= \psi_y(\xi, \eta). \end{aligned} \quad (19)$$

The non-dimensional global and local coordinates have the following relationship:

$$\begin{aligned} \xi &= \frac{r_x}{a} + \frac{a_c}{a} \xi_h, \\ \eta &= \frac{r_y}{b} + \frac{b_c}{b} \eta_h. \end{aligned} \quad (20)$$

Considering equations (3), (10), (12), and (13) and by plugging them into equation (19), we can get

$$\begin{aligned} \sum_{i=1}^{m_h} \bar{A}_{hi}(\xi_h, \eta_h) \bar{B}_{hi}(\xi_h, \eta_h) \bar{C}_{hi}(\xi_h, \eta_h) \Omega_{hi}(t) &= \sum_{i=1}^{m_h} A_{hi}(\xi_h) a_{hi}(\eta_h) B_{hi}(\xi_h) b_{hi}(\eta_h) C_{hi}(\xi_h) c_{hi}(\eta_h) \Omega_{hi}(t) \\ &= \sum_{k=1}^m \bar{A}_k(\xi, \eta) \bar{B}_k(\xi, \eta) \bar{C}_k(\xi, \eta) \Omega_k(t) \\ &= \sum_{k=1}^m A_k(\xi) a_k(\eta) B_k(\xi) b_k(\eta) C_k(\xi) c_k(\eta) \Omega_k(t). \end{aligned} \quad (21)$$

Multiplying equation (21) by $A_{hj}(\xi_h) a_{hj}(\eta_h) B_{hj}(\xi_h) b_{hj}(\eta_h) C_{hj}(\xi_h) c_{hj}(\eta_h)$ and performing integration,

$$\begin{aligned} \sum_{i=1}^{m_h} \int_0^1 \int_0^1 A_{hi}(\xi_h) a_{hi}(\eta_h) B_{hi}(\xi_h) b_{hi}(\eta_h) C_{hi}(\xi_h) c_{hi}(\eta_h) A_{hj}(\xi_h) a_{hj}(\eta_h) B_{hj}(\xi_h) b_{hj}(\eta_h) C_{hj}(\xi_h) c_{hj}(\eta_h) d\xi_h d\eta_h \Omega_{hj}(t) \\ = \sum_{k=1}^m \int_0^1 \int_0^1 A_{hi}(\xi_h) a_{hi}(\eta_h) B_{hi}(\xi_h) b_{hi}(\eta_h) C_{hi}(\xi_h) c_{hi}(\eta_h) A_k(\xi) a_k(\eta) B_k(\xi) b_k(\eta) C_k(\xi) c_k(\eta) d\xi_h d\eta_h \Omega_k(t). \end{aligned} \quad (22)$$

Using orthogonal property, equation (22) may be expressed as eigenfunctions of beam

$$\begin{aligned} &= \sum_{k=1}^m \int_0^1 A_{hi}(\xi_h) A_k(\xi) d\xi_h \int_0^1 a_{hi}(\eta_h) a_k(\eta) d\eta_h \int_0^1 B_{hi}(\xi_h) B_k(\xi) d\xi_h \\ &\int_0^1 b_{hi}(\eta_h) b_k(\eta) d\eta_h \int_0^1 C_{hi}(\xi_h) C_k(\xi) d\xi_h \int_0^1 c_{hi}(\eta_h) c_k(\eta) d\eta_h \Omega_k(t) \\ &= \sum_{k=1}^m (T_h)_{ik} \Omega_k(t), \quad i = 1, 2, 3, 4, \dots, m_h. \end{aligned} \quad (23)$$

If we write equation (23) as a matrix, we get

$$\Omega_h = T_{hi} \Omega, \quad (24)$$

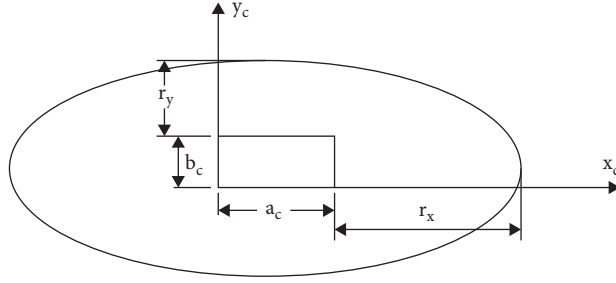


FIGURE 2: Elliptical plate with a rectangular cut-out.

in which T_h is the $m_h \times m$ matrix for transforming coordinates. Inserting equation (24) in to equations (15a) and (15b), we can derive

$$T_{\text{total}} = \frac{1}{2} \dot{\Omega}^T M \dot{\Omega} - \frac{1}{2} \dot{\Omega}^T T_h^T M_h T_h \dot{\Omega} = \frac{1}{2} \dot{\Omega}^T M_r \dot{\Omega}, \quad (25)$$

$$V_{\text{total}} = \frac{1}{2} \Omega^T K \Omega - \frac{1}{2} \Omega_h^T T_h^T K_h T_h \Omega_h = \frac{1}{2} \Omega^T K_r \Omega,$$

where $M_r = M - T_h^T M_h T_h$, $K_r = K - T_h^T K_h T_h$.

In non-dimensional parameters, equations can be stated.

$$M_r = \rho h b^2 \bar{M}_r,$$

$$K_r = \frac{D}{b^2} \bar{K}_r, \quad (26a)$$

$$\text{where } \bar{M}_r = \bar{M} - \left(\frac{b_c^2}{b^2}\right) T_h^T \bar{M}_h T_h,$$

$$\bar{K}_r = \bar{K} - \left(\frac{1}{b_c^2}\right) T_h^T \bar{K}_h T_h, \quad (26b)$$

in which $\bar{b}_{ci} = b_{ci}/b$ $i = 1, 2, 3, \dots, n$.

Hence,

$$[\bar{K}_r - \bar{\omega}^2 \bar{M}_r] \Lambda = 0. \quad (27)$$

From equation (23), ' T_h ' is the transformation matrix because of the integral limits. In equation (25), the eigenvalue of the plate with cut-out can be derived. Equation (26) is used to find the natural frequencies.

1.2. Free Vibrational Exploration of an Elliptical Plate Using ICCM. In the previous section, ICCM was used to evaluate a rectangular plate with a rectangular cut, where the plate and hole geometry were identical. In this section, the natural frequencies of an elliptical plate with a cut-out are computed using ICCM, with the hole and plate geometries modified. An elliptical plate with a hole is assumed in the plane. The semi-major axis " a " and semi-minor axis " b " are considered in direction. The border of an elliptical plate is written as $\xi^2 + \eta^2 = 1$.

The strain energy and kinetic energy of an elliptical plate is

$$V_p = \int_{\xi=0}^1 \int_{\eta=0}^{\sqrt{1-\xi^2}} \left\{ \left(\frac{1}{\alpha} \frac{\partial \psi_x}{\partial \xi} + \frac{\partial \psi_y}{\partial \eta} \right)^2 - 2(1-\mu) \left[\frac{1}{\alpha} \frac{\partial \psi_x}{\partial \xi} \frac{\partial \psi_y}{\partial \eta} - \frac{1}{4} \left(\frac{\partial \psi_x}{\partial \eta} + \frac{\partial \psi_y}{\alpha} \frac{\partial \psi_x}{\partial \xi} \right)^2 \right] \right. \\ \left. + \frac{6(1-\mu)\kappa}{\beta^2} \left[\left(\psi_x + \frac{1}{\alpha} \frac{\partial w}{\partial \xi} \right)^2 + \left(\psi_y + \frac{\partial w}{\partial \eta} \right)^2 \right] \right\} ab d\xi d\eta, \quad (28)$$

$$T_p = \int_{\xi=0}^1 \int_{\eta=0}^{\sqrt{1-\xi^2}} \left[w^{*2} + \frac{1}{12} \beta^2 (\psi_x^2 + \psi_y^2) \right] ab d\xi d\eta.$$

Deflection and rotation terms in the energy expressions (26a) and (26b) of an elliptical plate, to get the non-dimensional parameters, may be written in terms of acceptable functions that are introduced in equation (3) of an elliptical plate. Using relationship between local and global coordinates of hole and plate in equation (20), transformation matrix can be derived by applying an orthogonal property on eigenfunctions. Reduced non-dimensional and elliptical plate with hole stiffness matrices with hole are obtained from equation (25). Equations (26a) and (26b) give the non-

dimensional eigenvalues of the plate with cut-out. Figure 2 shows the elliptical plate with a rectangular cut-out.

Table 1 shows the frequency parameter for a supported elliptical plate $a/b = 2$ and $h/b = 0.2$ of various sizes. Tables 2 and 3 show various sizes of $h/b = 0.4$ and $h/b = 0.6$.

1.3. Numerical Study. The ICCM is validated with the available literature for a rectangular plate with various aspect ratios and a thickness of $h/b = 0.2$ in Table 4. The current

TABLE 1: The frequency parameter, $\bar{\omega} = (\omega b^2/\pi^2)\sqrt{(\rho h/D)}$, for a simply supported elliptical plate $a/b = 2$, $h/b = 0.2$ of various sizes, $a_c/a = b_c/b = 0, 0.1, 0.2, 0.3, 0.4, 0.5, 0.6$.

$\bar{\omega}$	0	0.1	0.2	0.3	0.4	0.5	0.6
$\bar{\omega}_1$	0.3253	0.3129	0.2959	0.2889	0.2949	0.3145	0.3399
$\bar{\omega}_2$	0.5684	0.5662	0.5524	0.5312	0.5229	0.4819	0.4272
$\bar{\omega}_3$	0.8997	0.8927	0.8539	0.6602	0.5459	0.5419	0.5966
$\bar{\omega}_4$	1.0784	1.0427	0.9019	0.8999	0.8395	0.7653	0.7087
$\bar{\omega}_5$	1.3124	1.3003	1.2652	1.2487	1.1474	1.1067	1.1334
$\bar{\omega}_6$	1.4224	1.4026	1.3512	1.2959	1.3654	1.3101	1.2237

TABLE 2: The frequency parameter, $\bar{\omega} = (\omega b^2/\pi^2)\sqrt{(\rho h/D)}$, for a simply supported elliptical plate $a/b = 2$, $h/b = 0.4$ of various sizes, $a_c/a = b_c/b = 0, 0.1, 0.2, 0.3, 0.4, 0.5, 0.6$.

$\bar{\omega}$	0	0.1	0.2	0.3	0.4	0.5	0.6
$\bar{\omega}_1$	0.3043	0.2926	0.2761	0.2674	0.2677	0.2731	0.2636
$\bar{\omega}_2$	0.5096	0.5062	0.4902	0.4679	0.4377	0.3699	0.2972
$\bar{\omega}_3$	0.7724	0.7683	0.6883	0.5339	0.4562	0.4654	0.5002
$\bar{\omega}_4$	0.9099	0.8634	0.7714	0.7505	0.6786	0.6036	0.5544
$\bar{\omega}_5$	1.0776	1.0643	1.0387	1.0138	0.9216	0.8561	0.7968
$\bar{\omega}_6$	1.1531	1.1379	1.0987	1.0647	1.0865	0.9821	0.8469

TABLE 3: The frequency parameter, $\bar{\omega} = (\omega b^2/\pi^2)\sqrt{(\rho h/D)}$, for a simply supported elliptical plate $a/b = 2$, $h/b = 0.6$ of various sizes, $a_c/a = b_c/b = 0, 0.1, 0.2, 0.3, 0.4, 0.5, 0.6$.

$\bar{\omega}$	0	0.1	0.2	0.3	0.4	0.5	0.6
$\bar{\omega}_1$	0.2785	0.2685	0.2531	0.2427	0.2371	0.2296	0.2017
$\bar{\omega}_2$	0.4473	0.4431	0.4269	0.4058	0.3470	0.2823	0.2155
$\bar{\omega}_3$	0.6528	0.6509	0.5541	0.4296	0.3935	0.3964	0.4160
$\bar{\omega}_4$	0.7562	0.7066	0.6495	0.6171	0.5464	0.4831	0.4504
$\bar{\omega}_5$	0.8802	0.8673	0.8499	0.8199	0.7345	0.6549	0.5630
$\bar{\omega}_6$	0.9319	0.9212	0.8909	0.8715	0.8560	0.7395	0.5994

TABLE 4: Frequency parameter $\bar{\omega} = (\omega b^2/\pi^2)\sqrt{(\rho h/D)}$ of various aspect ratios having a plate thickness of $h/b = 0.2$.

Aspect ratio (a/b)	0.4	0.8	1	1.5	2
Present method	5.18318	2.20114	1.768	1.3164	1.15218
Ref. [1, 11]	5.1831	2.2011	1.7679	1.3164	1.1521
% error	—	—	—	—	—

TABLE 5: Frequency parameter $\bar{\omega} = (\omega b^2/\pi^2)\sqrt{(\rho h/D)}$ of a square plate with a cut-out thickness of $h = 0.2$.

	$a_c/a = b_c/b = 0.2$	$a_c/a = b_c/b = 0.4$	$a_c/a = b_c/b = 0.6$	$a/3 \times a/3$
Present method	1.718	1.8355	2.324	5137.428 (rad/sec)
Ref. [18]	1.716	1.8345	2.323	—
Ref. [6]	—	—	—	5136.5 (rad/sec)
% error	0.11%	0.054%	0.043%	0.02%

ICCM results seem to match the available data with a high degree of precision.

The results of a square plate with a cut-out of various sizes are validated with literature in Table 5.

From the Tables 4 and 5, it is clear that the improved ICCM produces correct results when compared to techniques such as RRM, FEM, and FDM, all of which have a

faster convergence time. As a result, the ICCM is used to find the natural frequencies of a thick rectangular plate with different aspect ratios and a cut-out elliptical plate by increasing the size of hole, in foregoing tables. Graphs are plotted in Figures 3 and 5 to show how these natural frequencies are varying with increase in size of cut-out for a rectangular plate and for an elliptical plate, respectively.

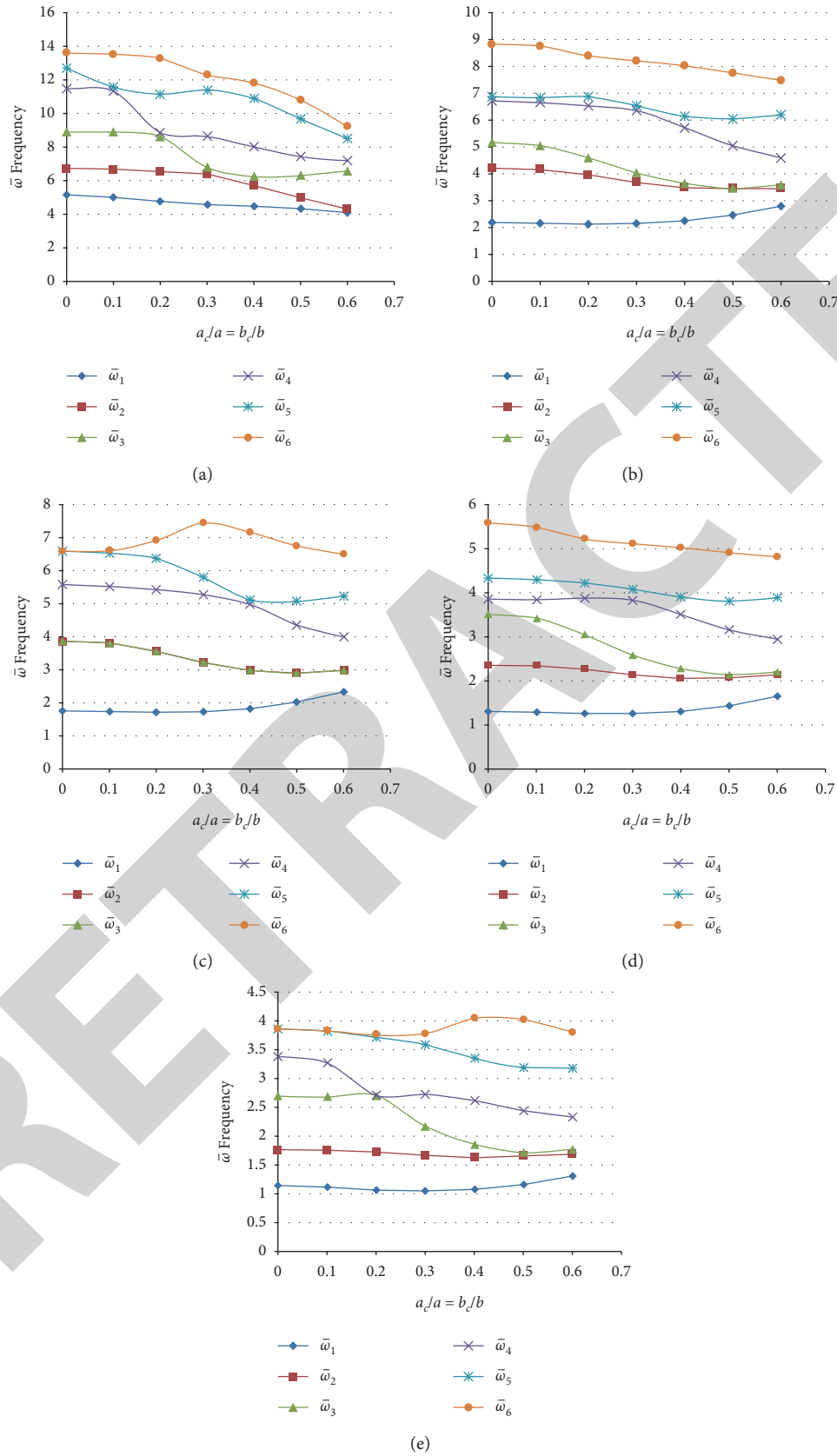
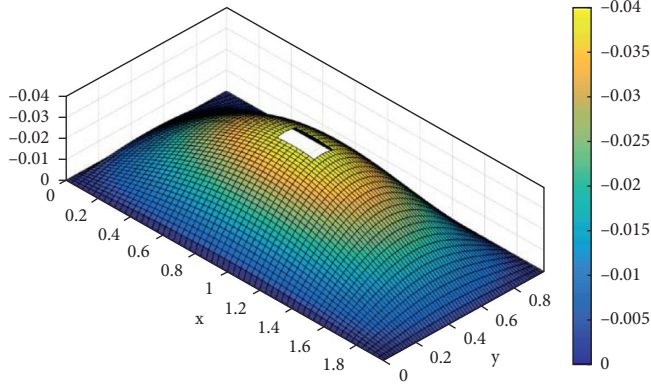
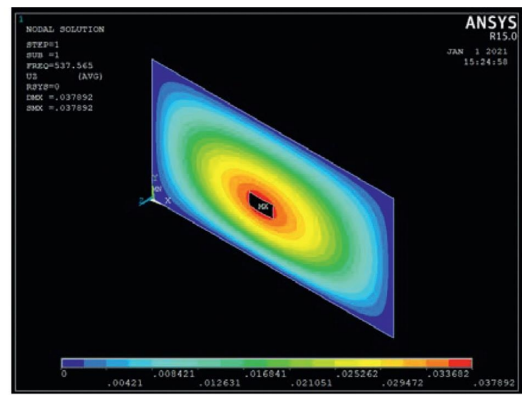


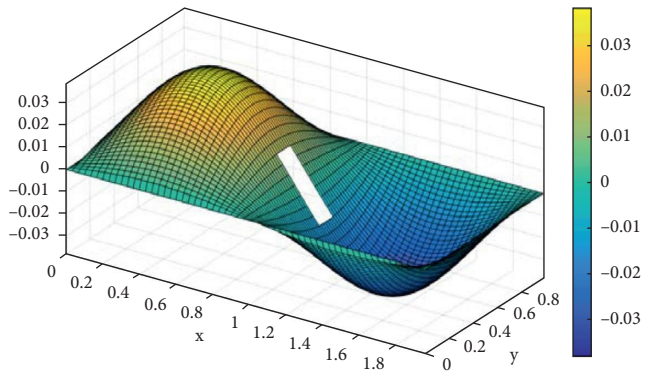
FIGURE 3: Aspect ratio variation of nondimensional eigenvalues. (a) Aspect ratio $a/b=0.4$ and $h/b=0.2$. (b) Aspect ratio $a/b=0.8$ and $h/b=0.2$. (c) Aspect ratio $a/b=1$ and $h/b=0.2$. (d) Aspect ratio $a/b=1.5$ and $h/b=0.2$. (e) Aspect ratio $a/b=2$ and $h/b=0.2$.



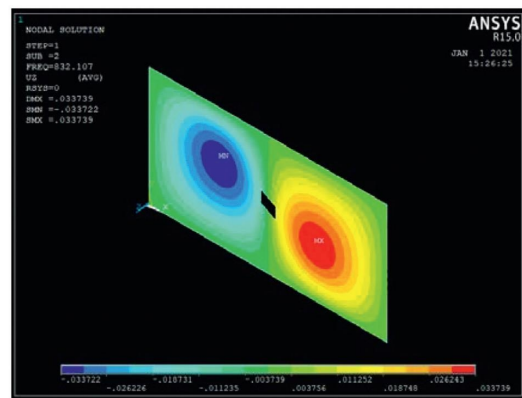
Modeshape 1



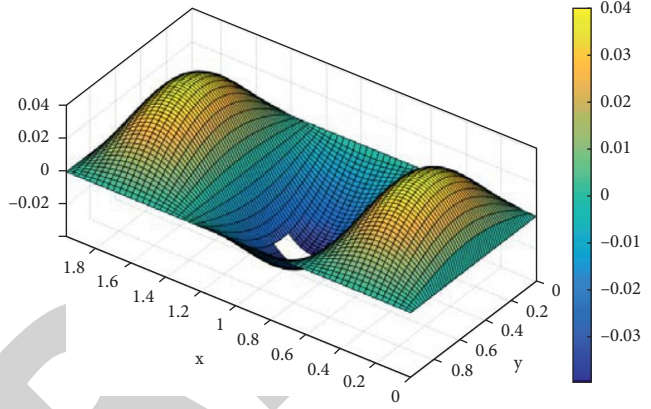
Modeshape 1



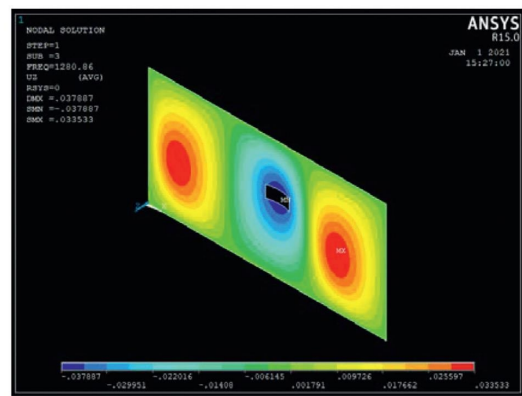
Modeshape 2



Modeshape 2



Modeshape 3



Modeshape 3

(a)

FIGURE 4: Continued.

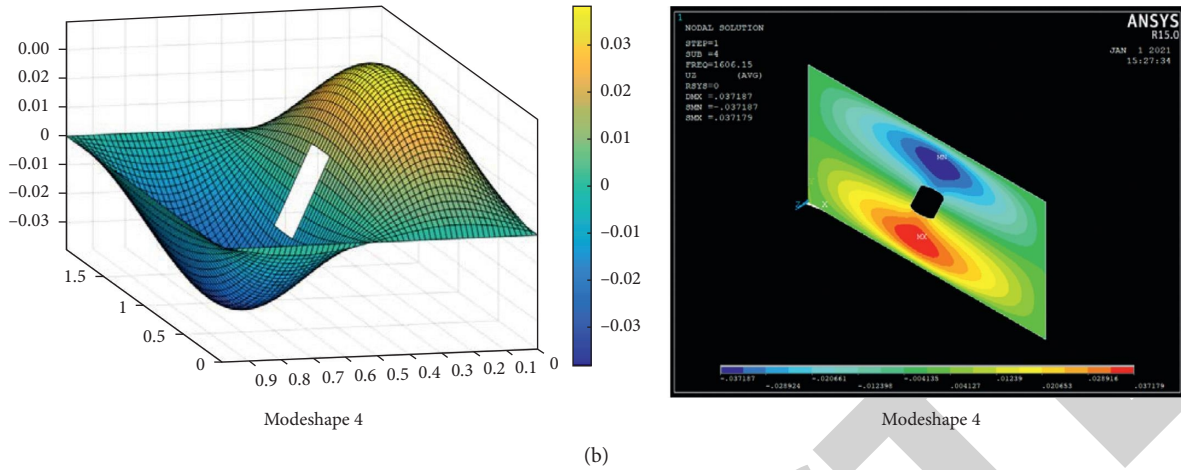


FIGURE 4: Comparison of transverse displacement of various mode shapes of a rectangular plate ($a = 2$, $b = 1$, and $h/b = 0.2$) with a concentric cut-out ($a_c/a = b_c/b = 0.1$) using MATLAB and ANSYS.

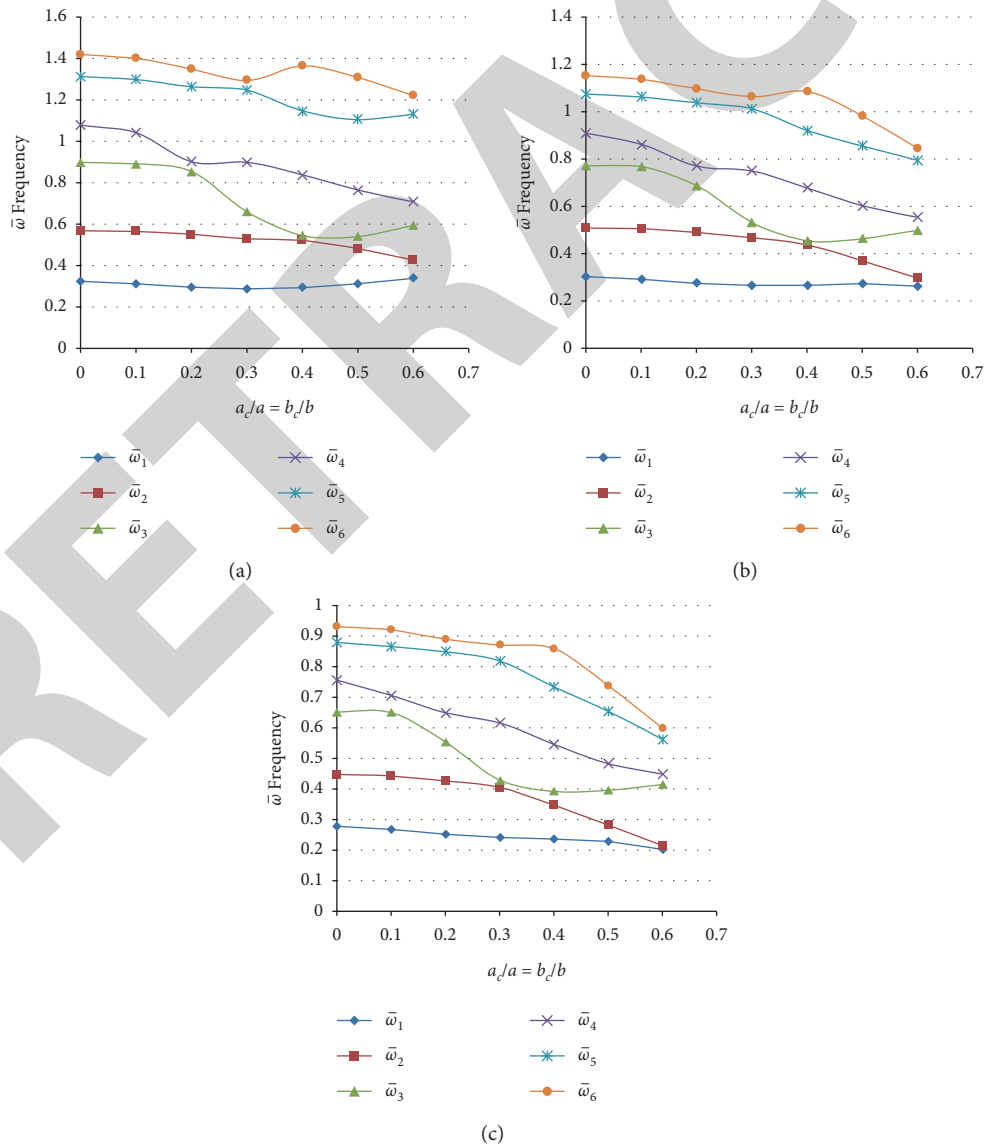


FIGURE 5: Variation of first six natural frequencies of an elliptical plate ($a/b = 2$) with respect to the size of cut-out. (a) Thickness ($h/b = 0.2$). (b) Thickness ($h/b = 0.4$). (c) Thickness ($h/b = 0.6$).

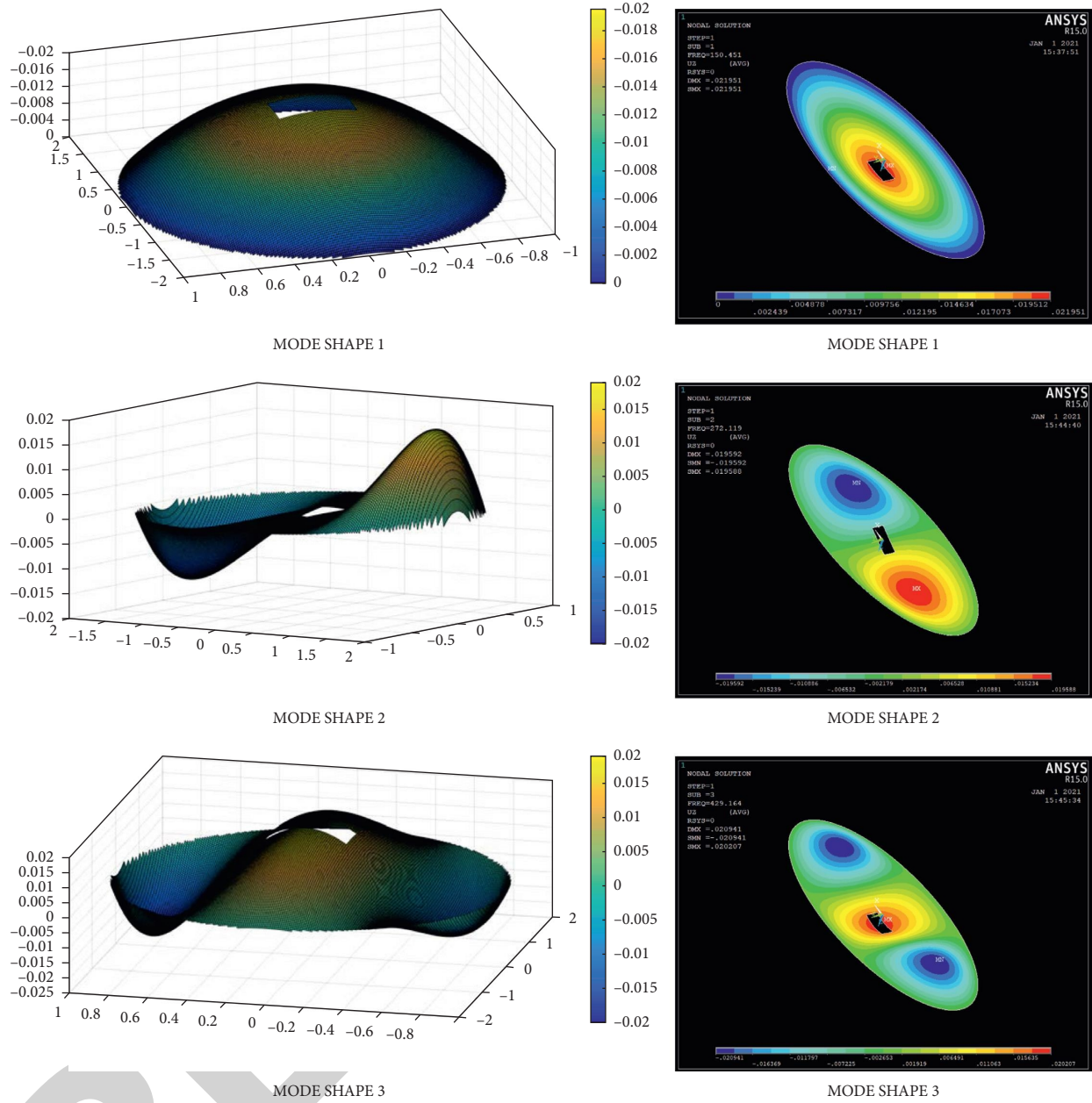


FIGURE 6: Comparison of transverse displacement of various mode shapes of an elliptical plate ($a = 2, b = 1,$ and $h/b = 0.2$) with a concentric cut-out ($a_c/a = b_c/b = 0.1$) using MATLAB and ANSYS.

TABLE 6: The frequency parameter, $\bar{\omega} = (\omega b^2/\pi^2)\sqrt{(\rho h/D)}$, for a simply supported rectangular plate with $a/b = 0.4$ and $h/b = 0.2$ with a concentric cut-out of various sizes, $a_c/a = b_c/b = 0, 0.1, 0.2, 0.3, 0.4, 0.5, 0.6$.

$\bar{\omega}$	0	0.1	0.2	0.3	0.4	0.5	0.6
$\bar{\omega}_1$	5.1831	5.0256	4.7675	4.5761	4.4598	4.3551	4.1113
$\bar{\omega}_2$	6.7212	6.6799	6.5428	6.3699	5.7165	4.9671	4.3116
$\bar{\omega}_3$	8.9138	8.8913	8.6299	6.7994	6.2705	6.3248	6.5839
$\bar{\omega}_4$	11.4875	11.3366	8.8808	8.6475	8.0246	7.4310	7.2052
$\bar{\omega}_5$	12.7040	11.5864	11.1545	11.4103	10.8954	9.6713	8.5177
$\bar{\omega}_6$	13.6145	13.5469	13.2805	12.3054	11.8309	10.799	9.2534

TABLE 7: The frequency parameter, $\bar{\omega} = (\omega b^2/\pi^2)\sqrt{(\rho h/D)}$, for a simply supported rectangular plate with $a/b = 0.8$ and $h/b = 0.2$ with a concentric cut-out of various sizes, $a_c/a = b_c/b = 0, 0.1, 0.2, 0.3, 0.4, 0.5, 0.6$.

$\bar{\omega}$	0	0.1	0.2	0.3	0.4	0.5	0.6
$\bar{\omega}_1$	2.2011	2.1688	2.1314	2.1517	2.2574	2.4669	2.7971
$\bar{\omega}_2$	4.2113	4.1600	3.9625	3.6882	3.4964	3.4614	3.4616
$\bar{\omega}_3$	5.1831	5.0662	4.6087	4.0433	3.6548	3.4749	3.6022
$\bar{\omega}_4$	6.7212	6.6538	6.5398	6.3630	5.7270	5.0472	4.6080
$\bar{\omega}_5$	6.8703	6.8504	6.8794	6.5353	6.1591	6.0669	6.2075
$\bar{\omega}_6$	8.8381	8.7715	8.3998	8.2281	8.0359	7.7668	7.4985

TABLE 8: Frequency parameter for supported elliptical plate with $a/b = 1$ and $h/b = 0.2$.

$\bar{\omega}$	0	0.1	0.2	0.3	0.4	0.5	0.6
$\bar{\omega}_1$	1.7680	1.7446	1.7180	1.7402	1.8355	2.0222	2.3245
$\bar{\omega}_2$	3.8667	3.8089	3.5668	3.2336	2.9938	2.9118	2.9903
$\bar{\omega}_3$	3.8667	3.8093	3.5674	3.2342	2.9941	2.9121	2.9905
$\bar{\omega}_4$	5.5892	5.5317	5.4308	5.2881	4.9846	4.3669	3.9942
$\bar{\omega}_5$	6.6046	6.5418	6.3772	5.8040	5.1319	5.0782	5.2457
$\bar{\omega}_6$	6.6046	6.6107	6.9262	7.4488	7.1699	6.7593	6.5139

TABLE 9: Frequency parameter for supported elliptical plate with $a/b = 1.5$ and $h/b = 0.2$.

$\bar{\omega}$	0	0.1	0.2	0.3	0.4	0.5	0.6
$\bar{\omega}_1$	1.3164	1.2892	1.2549	1.2577	1.3146	1.4388	1.6507
$\bar{\omega}_2$	2.3612	2.3441	2.2673	2.1496	2.0686	2.0764	2.1431
$\bar{\omega}_3$	3.5119	3.4285	3.0505	2.5884	2.2852	2.1470	2.2043
$\bar{\omega}_4$	3.8659	3.8465	3.8823	3.8363	3.5104	3.1620	2.9547
$\bar{\omega}_5$	4.3406	4.2991	4.2203	4.0807	3.9096	3.8168	3.8947
$\bar{\omega}_6$	5.5881	5.4895	5.2256	5.1161	5.0262	4.9138	4.8277

TABLE 10: Frequency parameter for supported elliptical plate with $a/b = 2$ and $h/b = 0.2$.

$\bar{\omega}$	0	0.1	0.2	0.3	0.4	0.5	0.6
$\bar{\omega}_1$	1.1521	1.1167	1.0688	1.0528	1.0810	1.1622	1.3106
$\bar{\omega}_2$	1.7680	1.7606	1.7244	1.6674	1.6338	1.6604	1.6913
$\bar{\omega}_3$	2.7027	2.6848	2.7079	2.1736	1.8632	1.7208	1.7764
$\bar{\omega}_4$	3.3858	3.2700	2.7181	2.7295	2.6171	2.4452	2.3393
$\bar{\omega}_5$	3.8667	3.8222	3.7156	3.5897	3.3512	3.1934	3.1870
$\bar{\omega}_6$	3.8667	3.8378	3.7652	3.7843	4.0480	4.0253	3.8016

TABLE 11: Various aspect ratios of plate.

Aspect ratio a/b	h/b	Cut-out size at which lowest ω is obtained $a_c/a = b_c/b =$	% of ω reduced, when compared with a plate without cut-out
0.4	0.2	0.6	20.6
0.8	0.2	0.2	3.16
1	0.2	0.2	2.82
1.5	0.2	0.2	4.67
2	0.2	0.3	8.61

TABLE 12: Various thickness ratios of plate.

Aspect ratio (a/b)	h/b	Cut-out size at which lowest ω is obtained $a_c/a = b_c/b$	% of ω reduced, when compared with a plate without cut-out
2	0.2	0.3	11.18
2	0.4	0.6	13.37
2	0.6	0.6	27.57

Eigenvectors were also plotted to observe the deflection in Z-direction for each mode of vibration, and it is validated with the mode shape obtained from ANSYS in Figures 4 and 6.

Graphs were plotted for a numerical value in Tables 6–10, as a function of cut-out size.

Case 1. Rectangular plate of different aspect ratios with concentric rectangular hole with increase in its size.

Case 2. An elliptical plate of aspect ratio ($a/b = 2$) of various thickness having a concentric rectangular hole with increase in its size.

2. Results and Discussion

This paper delves at the first six natural frequencies of a thick, rectangular, and elliptical plate. A cut-out is derived using ICCM. Based on the various combinations of aspect ratios and cut-out sizes, the derived numerical results were plotted in Figures 3 and 5. The frequency occurs due to a large hole, and maximum variation was observed compared to a plate without a cut. These observations were tabulated as follows so that the designers can change the natural frequency of a structure up to maximum limit of scope simply by introducing a cut-out. Figure 6 shows the comparison of transverse displacement of various mode shapes of an elliptical plate.

2.1. Rectangular Plate with Cut-Out. The eigenvalue of a rectangular plate with a hole is lower when compared to a rectangular plate without a cut-out, as seen in the images. For an aspect ratio of $a/b = 0.4$ and $h/b = 0.2$, the lowest natural frequency is obtained with a cut-out of size $a_c/a = b_c/b = 0.6$. The cut-out frequency is reduced by 20.6%. Similarly, rectangular plates with cut-out frequency are increased. The combination of aspect ratios and cut-outs are as shown in Table 11.

2.2. Elliptical Plate with Cut-Out. For an aspect ratio of $a/b = 2$ and $h/b = 0.2$, the lowest natural frequency is obtained with a cut-out of size $a_c/a = b_c/b = 0.3$. The frequency is reduced by 11.18% when compared to other combinations of thickness ratios and cut-outs. The lowest natural frequency is obtained as shown in Table 12.

This information is useful to the designers to vary the natural frequency of a structure, up to a maximum limit of scope simply by introducing a cut-out.

3. Conclusions

Numerical results, plotted as curves in Figure 3, reveal that as aspect ratio of the plate is increased, natural frequencies were decreased due to increase in mass without a significant increase in stiffness and the behavior of fundamental natural frequency is consistent with the variation of size of cut-out. It is also observed that in every aspect ratio, 2nd and 3rd mode of frequencies can be made same by including an appropriate size of cut-out. In the same manner, 4th and 5th mode of frequencies can also be made same in every aspect ratio of plate. Aspect ratio $a/b = 0.8$ with $h/b = 0.2$ has a high-frequency range that significantly increased the mass compared to aspect ratio 1. Due to the change in stiffness, the variation of frequencies exists that is smooth in manner. From Figure 5, it is worth noting that increasing the thickness ratio has no discernible influence on the plate's basic natural frequency. In every thickness ratio, mode 3 natural frequency can be made equal to mode 2 natural frequency by introducing a cut-out of size nearer to 0.4, and hence by introducing a cut-out, structure can be made to vibrate in different modes for the same value of natural frequency. From the analysis, for the study of a thick plate with cut-outs, modified ICCM is an excellent numerical tool that converges to the solution faster than other traditional approaches.

Data Availability

The data used to support the findings of this study are included within the article.

Disclosure

This research was performed as a part of the employment of Mettu University, Ethiopia.

Conflicts of Interest

The authors declare that there are no conflicts of interest regarding the publication of this paper.

Acknowledgments

The authors thank Aditya College of Engineering, Andhra Pradesh, University College of Engineering, JNTUK, Kakinada, and Saveetha School of Engineering, SIMATS, Chennai, for the technical assistance. The authors also appreciate the support from Mettu University, Ethiopia.

Retraction

Retracted: Modified Mechanical Structure Electric Bike Design Computation and Prototype Model Implementation

Advances in Materials Science and Engineering

Received 26 December 2023; Accepted 26 December 2023; Published 29 December 2023

Copyright © 2023 Advances in Materials Science and Engineering. This is an open access article distributed under the Creative Commons Attribution License, which permits unrestricted use, distribution, and reproduction in any medium, provided the original work is properly cited.

This article has been retracted by Hindawi, as publisher, following an investigation undertaken by the publisher [1]. This investigation has uncovered evidence of systematic manipulation of the publication and peer-review process. We cannot, therefore, vouch for the reliability or integrity of this article.

Please note that this notice is intended solely to alert readers that the peer-review process of this article has been compromised.

Wiley and Hindawi regret that the usual quality checks did not identify these issues before publication and have since put additional measures in place to safeguard research integrity.

We wish to credit our Research Integrity and Research Publishing teams and anonymous and named external researchers and research integrity experts for contributing to this investigation.

The corresponding author, as the representative of all authors, has been given the opportunity to register their agreement or disagreement to this retraction. We have kept a record of any response received.

References

- [1] K. Ramash Kumar, T. S. Anandhi, B. Vijayakrishna et al., "Modified Mechanical Structure Electric Bike Design Computation and Prototype Model Implementation," *Advances in Materials Science and Engineering*, vol. 2021, Article ID 3673172, 7 pages, 2021.

Research Article

Modified Mechanical Structure Electric Bike Design Computation and Prototype Model Implementation

**K. Ramash Kumar,¹ T. S. Anandhi,² B. Vijayakrishna,³ Monalisa Mohanty,⁴
M. Siva Ramkumar,⁵ H. A. Shivappa,⁶ Belachew Zegale Tizazu ,⁷ B. Kirubakaran,¹
and E. Thinapakar¹**

¹Department of Electrical and Electronics Engineering, Dr. N. G. P. Institute of Technology, Coimbatore 48, Tamilnadu, India

²Department of Electronics and Instrumentation Engineering, Annamalai University, Chidambaram, Tamilnadu, India

³Department of Electrical and Electronics Engineering, Bapatla Engineering College, Bapatla, Andhra Pradesh, India

⁴Department of Electrical and Electronics Engineering, ITER, Siksha 'O' Anusandhan Deemed to be University, India

⁵Department of Electrical and Electronics Engineering, Karpagam Academy of Higher Education, Coimbatore, India

⁶Department of Mechanical Engineering, Dr. Ambedkar Institute of Technology, Bangalore, India

⁷Department of Chemical Engineering, College of Biological and Chemical Engineering, Addis Ababa Science and Technology University, Ethiopia

Correspondence should be addressed to Belachew Zegale Tizazu; belachew.zegale@aastu.edu.et

Received 5 August 2021; Revised 19 August 2021; Accepted 6 October 2021; Published 15 October 2021

Academic Editor: Samson Jerold Samuel Chelladurai

Copyright © 2021 K. Ramash Kumar et al. This is an open access article distributed under the Creative Commons Attribution License, which permits unrestricted use, distribution, and reproduction in any medium, provided the original work is properly cited.

The aim of this paper is to investigate the design computation and prototype model implementation of a Modified Mechanical Structure (MMS) Electric Bike (E-Bike). It is the technology that allows the vehicle to operate with the assistance of electrical energy. All conventional cars will be converted to electric vehicles (EVs) in the future. EVs will be affordable to all types of people, allowing them to fly comfortably and safely. As a result, this paper proposes a design estimate and model implementation of the MMS E-Bike with the smallest number of parts, lowest expense, and lightest weight possible. The most important parts of the designed MMS E-Bike are the battery, MMS, BLDC motor, and electronic commutator with their controller. Because of its adapted mechanical frame nature, the designed E-Bike is low in cost and weight, and it can also go up to 25 kmph. Furthermore, the rider will be able to ride the built MMS E-Bike without any pain to their bodies and should be able to sit comfortably during their journey. In comparison to the Ampere Angel and DMW Electra 20 E-Bikes, the performance of the developed model is tested under various operating conditions, as well as their battery backup.

1. Introduction

With India's growing population, transportation plays an increasingly important role in getting people from one place to another. Traditional-operated vehicles have increased carbon emissions and fuel consumption in the transportation sector on a daily basis. Electric Vehicles (EVs) are a necessary mode of transportation in India to address pollution and the rising demand for nonrenewable energy, and they are equally applicable to all types of citizens [1]. The work in [2] describes the performance of an electric tricycle fitted with solar panels. However, as a result of this report, it

was suggested that electric tricycles be modified to include solar panels in order to improve battery autonomy. In addition, simulations of different topologies are addressed, as well as their computation of solar panel power losses and battery autonomy. Also discussed is a workaround for accumulative battery autonomy. The work in [3] shows a prototype model of a smart E-Bike in detail. However, it has a more complex mechanical structure and is a plug-in EV with two/three wheels. The work in [4] introduces the next generation of E-Bikes. A single mild steel bar is bent into various configurations in this article. Mild steel, a mixture of carbon, nickel, chromium, and iron, is used to build the

mechanical frame because it has higher tensile and compressive capacities than stainless steel and cast iron. The work in [5] discusses a photovoltaic (PV) device that powers a fish-vending women's tricycle. Women, on the other hand, can easily operate the built model to safely transport fish from the landing center to the market. The work in [6] develops and discusses a battery-operated tricycle for a physically disabled individual. However, this model is better for physically disabled people who need to move from one location to another at a higher rate. The work in [7] discusses E-Bike architecture for the fourth generation. From this article, the deep analysis of the E-Bike was carried out based on their requirements applied for it. The work in [8] shows a well-executed expert method for controlling power factor right buck-boost rectifier-fed BLDC motors. However, the speed control of BLDC motor drives and supply side power factor adjustment has been tested under various operating conditions in this article. The work in [9–13] describes various modern DC-DC converters for EVs, as well as their control methods. In the past, the designs of E-Bike companies were compared in all technical respects, as shown in Table 1. Ampere Angel is India's first E-Bike (cycle) manufacturer [14]. The pedal-assist mode and battery operating mode are the two riding modes. It is simple to switch from one mode to another without difficulty in this vehicle. This E-Bike can be operated by people of all ages, including school children, senior citizens, and people of all ages. The comprehensive analysis of the E-Bike at different countries is addressed [16, 17]. The prototype model of this E-Bike is shown in Figure 1, and the rest of the specifications are listed in Table 1. DMW Electra 20 is a single-rider E-Bike manufactured by DMW EVs in India [15]. As shown in Figure 2, it has special wheels with adjustable front suspension for a smooth ride on bumpy roads. This is also a pedal-assist battery-powered electric bike. It is easy to switch from the pedal assist to battery assist mode, and vice versa. Table 1 lists the rest of the information.

The cost, mechanical structure design, operating position, size, and weight of the current E-Bike were all major issues, according to the literature survey and Table 1. As a result, the aim of this article is to create a prototype model of a Modified Mechanical Structure (MMS) E-Bike with low cost/weight and comfortable transportation. ELECLE 1.0 is the name given to it.

2. Proposed E-Bike Block Diagram and Information

The block diagram of the designed E-Bike is discussed in this section (see Figure 3). It is made up of a battery, a BLDC motor drive, and its controller, as well as a throttle valve. The proposed E-Bike uses a lithium ion battery to power the BLDC motor, which has its shaft coupled to a small chain sprocket. Lithium ion batteries are commonly used in EVs due to their high battery efficiency, low maintenance, and high charge power, as shown in Figure 4 [6]. It is powered by a 48 V, 12 AH lithium ion battery.

The next form of motor is the Brushless DC (BLDC) motor, which is also known as an electronically commutated

motor. It is used to transform electrical energy into mechanical energy in this case (Figure 5). It is driven by DC power, which is converted to AC power by an electronic commutator or inverter and used to drive each step. In an E-Bike, the motor controller unit is used to control the power conversion operation. Hall sensors in the BLDC motor recognise the rotor direction angle [6]. These sensors are installed in the motor's rotor and linked to the motor controller as input. Hall sensors needed DC power, which was provided by a motor controller. Three wires supply stages, two wires supply hall sensors, and the remaining three wires receive input from the hall sensors in a BLDC motor [6, 8]. To control the speed of the BLDC motor, a feedback signal from the hall sensors is needed (48 V, 12 A, 500 W, –2800 rpm). This motor is more suitable for EVs because of their

- (i) Better speed versus torque characteristics
- (ii) Noiseless operation
- (iii) High efficiency
- (iv) Long operating life
- (v) High dynamic response
- (vi) Higher speed ranges [8]

In an E-Bike, the throttle supports motor control and propels the bike forward [8]. It helps you to pedal or simply relax and enjoy the trip. The thumb throttle on E-Bikes is controlled by the thumb. A small lever protrudes from the handlebar towards the bike, which controls the throttle. The throttle model is shown in Figure 6.

The motor controller (see Figure 7) is a mechanism that connects the battery to the BLDC motor. It has a current limit of 0.1 A. The EVs' motor controller is configured to drive the BLDC motor in this case. Table 2 lists the specifications of the designed E-Bike.

3. Design Computation of the Proposed E-Bike

The measures for calculating the mechanical structure weight and electrical system of the proposed E-Bike model are as follows [8].

3.1. Speed Calculation (No Load)

Step 1:

Quantity of teeth on smaller sprocket $t_1 = 14$ (see Figure 8)

Quantity of teeth on larger sprocket $t_2 = 37$

Speed on smaller sprocket:

$$N_1 = 2800 \text{ RPM}$$

Taking reduction ratio as 6 [3, 8],

$$N_1 = 2800/6 = 460 \text{ RPM}$$

Step 2:

Via the speed ratio formula

$$N_1 t_1 = N_2 t_2$$

$$\text{Speed of the wheel of EV, } N_2 = 460 \times 14/37 = 174 \text{ RPM}$$

TABLE 1: Comprehensive analysis of existing E-Bike companies.

Model	Ampere Angel [14]	DMW Electra 20 [15]
Battery	36V, 12 AH SLA	36V, 8AH lithium
Wheel size	26 cm	24 cm
Motor	BLDC	BLDC
Cost	Rs. 30,000	Rs. 40,500
Weight	25 kg	27 kg
Location of the battery	Behind to the seat tube	On the down tube
Speed	25 kmph	25 kmph
Limitation	Not applicable for the uphill direction	Not comfortable to sit
Welding points	11	7



FIGURE 1: Prototype model of the Ampere Angel E-cycle [14].



FIGURE 2: Prototype model of the DMW Electra 20 E-cycle [15].

Step 3:

Diameter of the wheel of EV = 56 cm = 560 mm

Circumference of the wheel of EV = $\pi \times D$

= $3.14 \times 560 = 1758$ mm.

Step 4:

Speed of EV = speed of the wheel of EV \times circumference of the wheel of EV

= $174 \times 1758 = 335996$ mm/min

= 25 km/hr

3.2. Computation of Essential Power to Drive the E-Bike

Step 1:

Total load acting on the E-Bike is as follows:

Net vehicle weight = 10 kgs

Average human weight = 80 kgs

Average luggage weight = 5 kgs

Battery + motor weight = 5 kgs

Total weight = 100 kgs = $100 \times 9.81 = 981$ N

Step 2:

To find reaction on each wheel:

The total load which is divided equally on both the wheels of the E-Bike

Force (F_{rw}) = $981/2 = 490.5$ N

Where reaction on rear and front wheel are as follows:

$R_{fw} = 0.2 \times 490.5 = 98.1$ N

Step 3:

To obtain the torque on each wheel of the E-Bike:

Total torque = torque on the front wheel of the E-Bike + torque on the rear wheel of the E-Bike

$T = T_{fw} + T_{rw}$

To determine the torque on the front wheel of the E-Bike:

$T_1 = R_{fw} \times D/2 = 98.1 \times (56 \times 10^{-2})/2$

= 30 Nm

Total torque on wheel = $T_1 + T_2 = 60$ Nm

Step 4:

To compute the power on the BLDC motor of the E-Bike:

= $2 \times \pi \times N_2 \times T_1/60$

= $2 \times 3.14 \times 174 \times 30/60 = 500$ W

Battery capacity calculation: 500 W EV is run for 1 hour, watt-hours = $500 \times 1 = 500$ watt-hours, and the efficiency of the battery is 85%. Watt-hours = $500/0.85 = 588$ watt-hours. Ampere hour (at 48 V) = $588/48 = 12$ AH.

4. MMS of the E-Bike

The proposed E-MMS Bike's frame concept was created using the AutoCAD 2017 software. The top tube, head tube fork, down tube, seat tube, seat stay, and chain stay made up the basic E-Bike structure [4, 8]. This new tube, which will provide support, will connect the head tube fork and seat tube. The Kevlar cable was also added for additional support of the proposed E-Bike. The Kevlar cable is a superdurable material that does not conduct electricity. This cable provides perfect dimension stability and protects the E-Bike from oscillations.

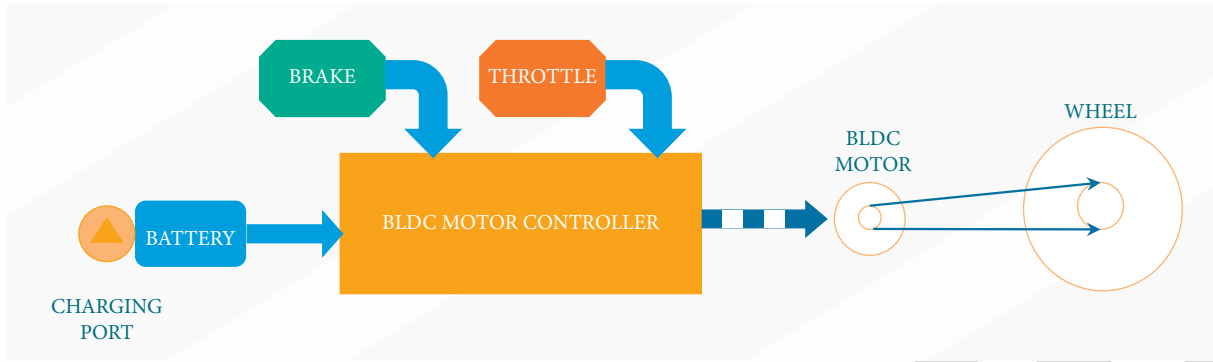


FIGURE 3: Block diagram of the proposed prototype model of ELECLE 1.0.

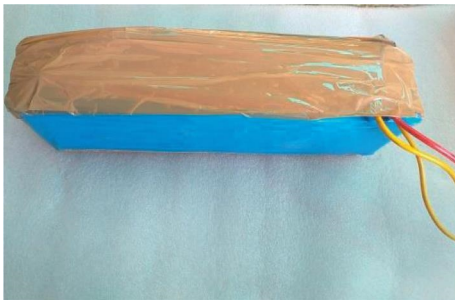


FIGURE 4: Model of the lithium ion battery.



FIGURE 5: Model of the BLDC motor drive.



FIGURE 6: Model of the throttle.



FIGURE 7: Typical model of the motor controller.

In the proposed E-Bike, the Kevlar cable replaces the top tube, down tube, seat stay, and chain stay. As a result of these changes, the weight/cost of the E-Bike was reduced, as was its MMS. Figure 9 depicts the planned E-Bike as well as its MMS dimensions.

5. Prototype Model of the MMS E-Bike and Result Analysis

Mild steel was used to create the E-Bike frame. The frame was created using AutoCAD software and precise mechanical calculations. Welding points for this frame were 4 to 6 points. The rider would not be scared while riding because of the basic frame design. Since the rider's center of gravity is closer to the seat tube, he or she can handle the bike with less effort. The bike's weight was reduced to less than ten kilograms. Mild steel materials are simple to work with when it comes to welding and cutting. These materials are

capable of high loading while remaining low in cost. The electric bike is made of mild steel, which gives it enough power. Figures 9 and 10 represent the final prototype model of the planned E-Bike, as well as its dimensions.

5.1. Proposed E-Bike Dimensions (Figures 9 and 10)

- Distance from the ground to seat = 100 cm
- Distance from the ground to motor = 20 cm
- Seat tube distance = 45 cm
- Distance from the head tube to seat tube = 75 cm
- Front wheel diameter = 56 cm
- Rear wheel diameter = 56 cm
- No. of teeth on the motor sprocket = 14
- No. of teeth on the rear wheel sprocket = 37

Table 3 shows the efficiency of the designed E-Bike. In comparison to the Ampere Angel and the DMW Electra 20, the built E-Bike has superior performance in terms of cost, speed, welding points, weight, and operating position (see Table 1).

TABLE 2: Specifications of the proposed E-Bike.

S. no.	Components	Specifications	Quantity
1	Brushless DC motor	Voltage- 48 V; current- 12 A; power- 500 W; and speed- 2800 RPM	1
2	Mechanical structure (welding)	Mild steel	-
3	Battery	Voltage- 48 V and current- 12 A	1
4	Wheel with disc	28 inches	2



FIGURE 8: Chain sprocket with teeth.

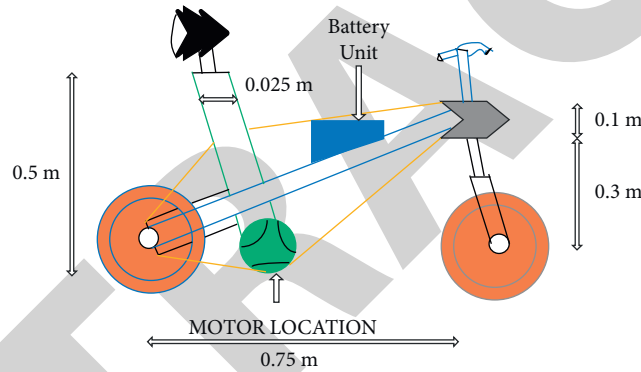


FIGURE 9: MMS E-Bike design using AutoCAD software.



FIGURE 10: Prototype model of the proposed E-Bike.

TABLE 3: Result analysis of the designed E-Bike (ELECLE 1.0).

Model	ELECLE 1.0 (proposed model)
Battery and backup	48 V, 12 AH Li-ion and 1.2 hour
Wheel size	30 cm
Motor	BLDC
Cost	Rs. 20,000
Weight	20 kg
Location of the battery	Between top and down tubes
Speed	25 kmph
Limitation	Vibration and comfort to travel
Welding points	4

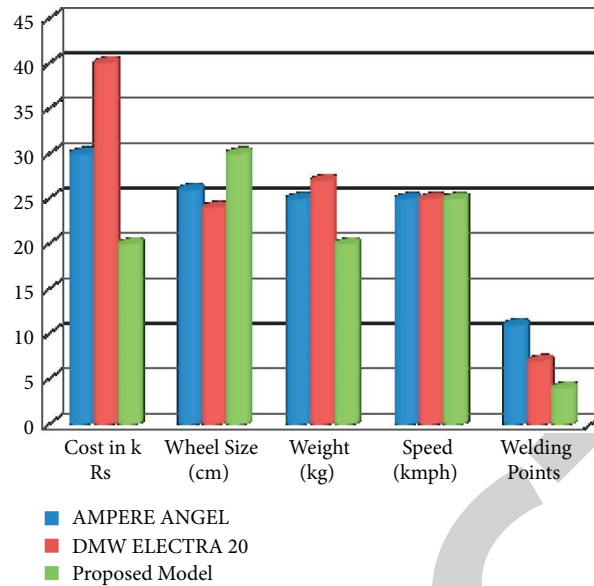


FIGURE 11: Comprehensive graphical analysis of the proposed E-Bike and existing E-Bike model.

Figure 11 shows the graphical analysis of the proposed E-Bike and existing E-Bike models. From this chart, it is evident that the designed model has low cost, less number of joints, and less model weight over the existing model.

6. Conclusions

This article successfully illustrated the concept computation and prototype model implementation of the MMS E-Bike. The computation of the electrical and mechanical systems was specifically discussed. The E-Bike is constructed based on its calculations by assembling and connecting the battery, MMS, BLDC motor, and electronic commutator to their controller mechanically and electrically. The key advantages of the designed E-Bike are its low cost and light weight, which are due to the MMS and materials used in its construction. It could also reach speeds of up to 25 kmph, particularly in hilly areas. Riders should be able to ride the E-Bike without experiencing any pain in their bodies and should be able to sit comfortably when transporting. The built model has been put through its paces with companies including Ampere Angel and DMW Electra 20 E-Bikes. Depending on the weight of the E-Bike, it can be increased to a high power level.

Data Availability

The data used to support the findings of this study are included within the article.

Conflicts of Interest

The authors declare no conflicts of interest.

References

- [1] C. Kiefer and F. Behrendt, "Smart E-bike monitoring system: real-time open source and open hardware gps assistance and sensor data for electrically-assisted bicycles," *IET Intelligent Transport Systems*, vol. 10, pp. 1–10, 2015.
- [2] D. Mohamed, D. Said, and R. Ahmed, "Autonomy analysis of a solar electric tricycle," in *Proceedings of the 2015 3rd International Renewable And Sustainable Energy Conference (IRSEC)*, pp. 1–6, Marrakech, Morocco, December 2015.
- [3] S. Katoch, Rahul, and R. K. Bindal, "Design and implementation of smart electric bike eco-friendly," *International Journal of Innovative Technology and Exploring Engineering*, vol. 8, no. 6S4, 2019.
- [4] N. Pavan Kumar Reddy and K. V. S. S. Vishnu Prasanth, "Next generation electric bike," in *Proceedings of the IEEE International Conference On Power, Control, Signals And Instrumentation Engineering*, pp. 2280–2286, Chennai, India, September 2017.
- [5] G. Gaswin Kastro and V. jain, "Solar powered tricycle for fish vending women," in *Proceedings of the 2017 IEEE Region 10 Conference (TENCON)*, Penang, Malaysia, November 2017.
- [6] K. Ramash Kumar, K. Aswin, S. Hariharan et al., "Design and fabrication of electric vehicle for physically challenged person," *International Journal of Innovative Technology and Exploring Engineering*, vol. 8, no. 10, pp. 4297–4300, 2019.
- [7] R. Meireles, J. Silva, A. Teixeira, and E. Bernardo Ribeiro, "Bike design for the fourth generation bike-sharing services," in *Proceedings of the EVS27 International Battery, Hybrid and Fuel Cell Electric Vehicle Symposium*, Barcelona, Spain, November 2013.
- [8] P. Sivakumar, V. Rajasekaran, and K. Ramash Kumar, "Investigation of intelligent controllers for variable speed PFC buck-boost rectifier fed BLDC motor drive," *Journal of Electrical Engineering*, vol. 17, no. 4, pp. 459–471, 2017.
- [9] K. R. Kumar, N. Arunkumar, N. Arunkumar, and T. S. Sivakumaran, "Implementation of non-linear controller for contemporary DC-DC converter," *International Journal on Electrical Engineering and Informatics*, vol. 11, no. 4, pp. 622–637, 2019.
- [10] S. Chakraborty, M. Mahedi Hasan, H.-N. Hasan, D.-D. Tran, M. E. Baghdadi, and O. Hegazy, "DC-DC converter topologies for electric vehicles, plug-in hybrid electric vehicles and fast

Research Article

Developing an Empirical Relationship to Predict the Wear Characteristics of Ni-Based Hardfaced Deposits on Nuclear Grade 316LN Austenitic Stainless Steel

S. Gnanasekaran ¹, Samson Jerold Samuel Chelladurai ², G. Padmanaban,³
Ramesh Arthanari ⁴, and V. Balasubramanian ³

¹Department of Mechanical Engineering, Sri Shakthi Institute of Engineering and Technology, Chinniyampalayam, Coimbatore, Tamil Nadu, India

²Department of Mechanical Engineering, Sri Krishna College of Engineering and Technology, Coimbatore, Tamilnadu, India

³Centre for Materials Joining & Research (CEMAJOR), Department of Manufacturing Engineering, Annamalai University, Annamalainagar, Tamil Nadu, India

⁴Department of Mechanical Engineering, Chennai Institute of Technology, Tamil Nadu, India

Correspondence should be addressed to Samson Jerold Samuel Chelladurai; samsonjeroldsamuel@skcet.ac.in

Received 4 August 2021; Revised 29 September 2021; Accepted 6 October 2021; Published 14 October 2021

Academic Editor: Alicia E. Ares

Copyright © 2021 S. Gnanasekaran et al. This is an open access article distributed under the Creative Commons Attribution License, which permits unrestricted use, distribution, and reproduction in any medium, provided the original work is properly cited.

Using the nickel-based Colmonoy 5 hardfacing alloy, components made of austenitic stainless steel (ASS) used in nuclear power plants can be hardfaced. Hardfacing is the process of applying complex and wear-resistant materials to substrates that require abrasion resistance. The tribological characteristics of a reactor-grade material NiCr-B hardfaced deposit were studied and reported in this paper. Hence, in this investigation, an effort has been made to develop empirical relationship to predict weight loss of laser hardfaced Ni-based alloy surface incorporating laser parameters using statistical tools such as design of experiments (DoE) and analysis of variance (ANOVA). The developed empirical relationship can be effectively used to trail the weight loss (wear resistance) of laser hardfaced nickel alloy surfaces by altering laser parameters. This method has proven very effective. A power of 1300 W, powder feed rate of 9 g/min, travel speed of 350 mm/min, and defocusing distance of 32 mm were all combined to achieve a minimum weight loss of 0.0164 grams.

1. Introduction

The Indian prototype fast breeder reactor (PFBR) is a pool-type liquid sodium-cooled reactor with two independent sodium circuits (primary and secondary heat exchangers), with the intermediate heat exchanger (IHX) allowing thermal contact between the main pool and the auxiliary circuit. Thermal exchange occurs between the IHX and a steam generator (SG), which powers conventional steam turbines via the use of auxiliary sodium circuits. In PFBR, austenitic stainless steel (AISI 316LN) is the primary structural material (e.g., main vessel, inner vessel, grid plate, and primary pipework, among others), with a nitrogen

content of 0.06–0.08 percent and service temperatures exceeding 800°F [1]. In order to transfer heat between the primary and secondary heat exchangers, liquid sodium is used as a transfer medium. During normal operation, the minimum sodium temperature in the primary pool is 400°C, and the mean above-core temperature is 550°C. The sodium temperatures in the secondary circuit range between 355 and 525°C at their lowest and highest points, respectively. The liquid sodium coolant acts as a decreasing specialist, allowing the self-protective layer that forms on the ASS external surface of the sodium needs to be evacuated and removed. To improve self-welding and galling resistance, a common technique is to face these components with nickel-

or cobalt-based alloys. The induced Co60 radioactive isotopes are generated in nuclear reactor environment [2, 3] was discovered in stellite Co-based alloys, which are used as a hardfacing material in high-temperature applications. Since the Colmonoy grades include substantial quantities of chromium and boron, they may be a strong replacement in terms of adhesive wear resistance for cobalt-based stellite alloys. This is because these elements are highly concentrated in the alloy [4, 5]. Colmonoy alloys have a greater hardness than stellite. The existence of chromium carbide (CrC) and chromium boride (CrB) in the deposit is ascribed to this, as opposed to carbide precipitates exclusively in stellite and chromium borides found in the deposit [6].

A material's wear resistance is a mechanical property that must be present to resist surface damage when moving dynamically across surfaces [3, 7, 8]. During tribology testing, the physical, chemical, physical, and mechanical characteristics of the wear produced cavities vary in response to the changing conditions. The change in the shape of the wear clot may have an impact on the amount of frictional force that is applied immediately. Wear procedures may be divided into four types using steel-based alloys: adhesive wear, abrasive wear, oxidation wear, and plastic extrusion [9–12]. In general, the relationship between a material's hardness and its wear resistance is inverse. This reservoir has a greater wear resistance than stainless steel, resulting in longer service life for FBR components. Hardfacing is a frequently used method for increasing the lifetime of heavy load components that has been widely known technic. However, even though hardfacing alloys have been developed to have the optimal chemistry and microstructure for certain service conditions, dilution with a substrate changes their physical properties over a relatively significant percentage of their whole thickness.

However, despite the fact that this alloy has superior mechanical characteristics, the friction and wear caused by this alloy have not yet been well investigated and understood as a function of sliding distance. The parameters of the hardfacing process affect the quality of the deposits significantly. Only a few research studies were performed to understand better the effect on individual wear characteristics of laser process parameters. In this study, an effort has been made to develop an empirical connection to forecast wear resistance of hardfaced alloy deposits utilizing statistical methods, such as experimental design, variance analysis, and regression analysis, integrating major laser surface characteristics.

2. Experimental Work

2.1. Substrate (Base Metal) and Hardfaced Powder (Colmonoy 5) Properties. It is essential to highlight that in this study, the substrate (316LN stainless steel) is nucleic stainless steel that is widely used for, among other uses, valves, valve cones, and spindles. The chemical composition of the base metal was obtained using a vacuum spectrometer (make: ARL USA; Model3460). Sparks were ignited at various locations of the base metal sample, and their spectrum was analyzed for the estimation of alloying elements. The chemical compositions of the substrate material and hardfaced powder are shown in

Tables 1 and 2, respectively. The austenitic AISI 316LN stainless-steel rolling plates with a thickness of 12 mm served as the foundation for this structure. Heating the substrate to 400 C was done in order to alleviate internal tensions and slow down the cooling rate in order to prevent the development of fractures after the deposition process was completed. The hardfacing tests were performed by using an automated disk laser machine [13, 14].

The formation of a single layer, as shown in Figure 1, was the foundation for the research. Pure argon gas (99.9% purity) was used in the experiment to protect the gas and to feed the powder gas. According to the manufacturer, the deposit had an average thickness of 0.8–2 mm [15, 16]. To determine the realistic range of operations of the laser hardfacing parameters (Table 3), a significant number of trial tests have been conducted, each with different parameters, all of which remaining constant. Table 4 shows the most important components and their relative significance. The experimental design (DoE) method was used in order to reduce the quantity of experimental work. In order to minimize experimental conditions, a central composite rotatable design matrix with four variables and five levels was utilized. We were able to construct four-factor factorial designs with 16 points, eight-star points, and six center points using the design matrix (Table 5), including 30 sets of coded conditions. The upper and lower limits of the parameters are referred to the digits +2 and –2, respectively, in the code. This formula may be used to calculate the intermediate level coded values which are as follows:

$$Xi = 2X - \frac{(X_{\max} + X_{\min})}{(X_{\max} - X_{\min})}, \quad (1)$$

where A variable from X_{\min} to X_{\max} must be coded with X .

The deposits were made in line with the design matrix requirements and were made randomly to avoid systemic error from entering results. Figure 2 displays a sample of the produced deposits. For the metallography study, the deposits were chopped into small pieces while they were hardfaced. The dry slide wear resistance at room temperature was determined using a pin-on-disk setup [17, 18]. Pins are chopped from a thick ASS plate using electric discharge equipment in order to provide the required wear specimens for testing. Rugged test specimens were polished with a 1000 micron SiC sheet and then with Al_2O_3 to achieve the necessary roughness (RA) value of just under 0.25 micron.

Wear rate and coefficient of friction (COF) of the hardfaced surfaces were evaluated using the pin-on-disc wear test as per ASTM G99-05. Specimens were extracted from the hardfaced stainless-steel plate as per stranded dimensions of 10 mm diameter and 20 mm length pin spinning disk slide at 55 mm diameter with a pitch circle of 45 mm diameter and linear speed of 0.1 m/s. The specimens were evaluated at room temperature under normal load conditions with a typical load of 50 N [19, 20]. After each test, the specimen's weight loss was used to determine the specimen's wear resistance. All experiments have been repeated to verify that they are reasonably reproducible. Before and after each trial, the specimen was carefully cleaned in alcohol and gently dried, and the weight loss was quantified to an accuracy of 0.001 mg before and after each test.

TABLE 1: Substrate material chemical composition in wt %.

C	Ni	Cr	Mo	Si	Mn	Cu	Nb	S	P	W	Fe
0.0200	12.550	17.270	2.350	0.290	1.690	0.0470	0.020	0.0270	0.026	0.03	Bal

TABLE 2: Colmonoy 5 hardfaced power chemical composition in wt %.

C	Fe	Cr	Si	B	O	Ni
0.410	3.100	10.440	4.020	2.260	0.030	Balance

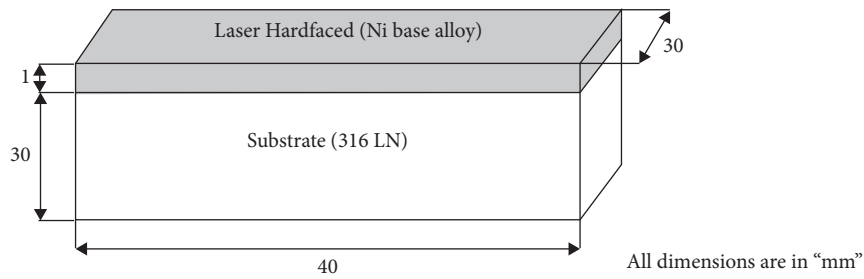


FIGURE 1: Schematic diagram of single-layer hardfacing.

TABLE 3: The variables of the process parameters and their operating range.

S.No	Process parameters	Symbols	Units	Levels				
				-2	-1	0	1	2
1	Laser power	P	Watts	1100	1300	1500	1700	1900
2	Rate of powder feed	F	Gram/min	3	5	7	9	11
3	Travel speed	T	mm/min	300	350	400	450	500
4	Defocusing distance	D	mm	17	22	27	32	37

TABLE 4: Macrostructure investigation to determine the laser hardfacing's operating range.

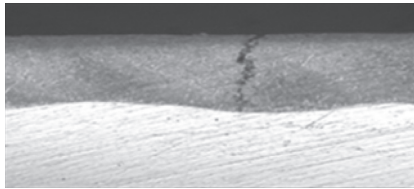



S. no.	Parameters	Working range	Macrographs	Observations	Causes
1	Laser power (P)	$P > 1900$ Watts		Minor crack and high dilution	Excessive heat input
		$P < 1100$ Watts		Powders escaping will cause pores	Inadequate heat input
2	Rate of powder feed (F)	$F > 11$ grams/min		Cracks	Specific energy input is insufficient
		$F < 3$ grams/min		High penetration and dilution depth	Higher specific input of energy

TABLE 4: Continued.

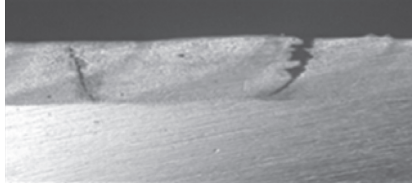
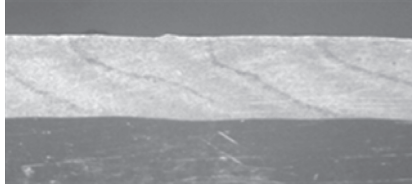
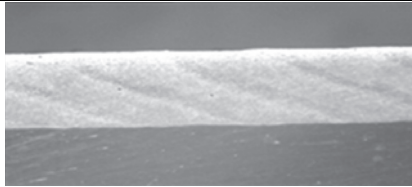
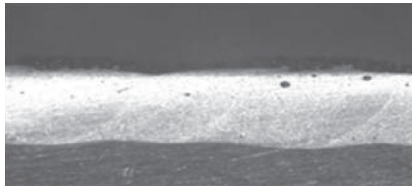
S. no.	Parameters	Working range	Macrographs	Observations	Causes
3	Travel speed (T)	$T > 500$ mm/min		Cracks as a result of the increased travel speed	Lower heat input
		$T < 300$ mm/min		Higher deposition thickness and minor cracks	Increased heat input
4	Defocusing distance (D)	$D > 37$ mm		Inadequate bonding	The energy density per unit is low
		$D < 17$ mm		Pores	The increased energy density per unit of measurement

TABLE 5: Pin-on-disc wear test parameters

Parameter	Values
Pin size (mm)	Diameter = 10, length = 20
Disc size (mm)	Diameter = 120, thickness = 8
Load (N)	50
Velocity range (m/s)	1
Sliding distance (m)	500

3. Developing an Empirical Relationship

In the present work, weight loss is influenced by the laser hardfacing process parameters such as laser power (Q), travel speed (T), rate of powder feed (F), and defocusing distance (D), and it may be stated as follows [9, 21, 22]:

$$\text{weight loss of laser hard faced deposit } (W) = f(P, F, T, D). \tag{2}$$

It is provided by the second-order polynomial regression equation that is used to describe the response surface Y as follows:

$$Y = b_0 + \sum b_i x_i + \sum b_{ij} x_i x_j \tag{3}$$

The following is an example of a polynomial expression:

$$W = b_0 + b_1(P) + b_2(F) + b_3(T) + b_4(D) + b_{12}(PF) + b_{13}(PT) + b_{14}(PD) + b_{23}(FT) + b_{24}(FD) + b_{11}(P^2) + b_{22}(F^2) + b_{33}(T^2) + b_{44}(D^2) + \text{grams}. \tag{4}$$

b_0 represents the mean value of the response, whereas $b_1, b_2, b_3, b_4,$ and b_{44} represent linear relations and square relations of variables, respectively. The coefficient value was estimated with the help of the Design Expert 7 program at a 95% level of confidence. The implication of each coefficient is



FIGURE 2: Fabricated deposits.

determined using the student's t -test and the P values for each coefficient. When the value of "Prob > F " is less than 0.050, it implies that the model terms are statistically significant ($P < 0.05$). The words P, F, T, D, PF, PT, PD, FD, TD, and F2 are the most important in this context. The final

empirical connection was built only based on this coefficient. The last empirical affiliation of Ni-based hardfaced deposits produced after that wear test was carried out to find the wear resistance in weight loss and is shown in Table 6 [23].

$$\text{Weigh loss} = \left[\begin{array}{l} -0.10071 + 1.42307E - 0.04 * (P) - 0.010069 * (F) + 6.00779E - 004 * (T) - 4.22966E - 003 * (D) + \\ 2.67969E - 006 * (P * F) - 4.80313E - 007 * (P * T) + 7.51875E - 007 * (P * D) - 1.39375E - 006 * (F * T) + 1.59062E - 004 * (F * D) + 4.86250E - 006 \\ * (T * D) + 5.54427E - 009 * (P^2) + 1.60677E - 005 * (F^2) + 7.08333E - 010 * (T^2) - 3.42917E - 006 * (D^2) \end{array} \right] \cdot \text{grams}'' R_2 - 0.906'' \quad (5)$$

The appropriateness of the relationship mentioned above is determined via the use of analysis of variance (ANOVA). The results of the ANOVA test are shown in Table 6; the required confidence level was set at 95 percent in this case. It is possible to regard the connection to be satisfactory. The calculated value of the fraction F of both the connection established must not exceed the tabular value of the ratio F for the necessary confidence to be able to evaluate that model sufficiently [24]. Fisher's F test, the probability is extremely low, indicates that the regression model has a very high level of significance. The determination coefficient is used to determine the model's overall goodness of fit (R^2). According to the findings, the determination coefficient in response was calculated at 0.98, showing that 98% of the research values support the compatibility with model predictions [25].

In most of the situations, the signal-to-noise ratio greater than 4 is desirable. During this study, the signal-to-noise ratio was 30.969, which suggests that the signal is sufficient. This model may be utilized to travel through the design space. Figure 3 depicts the correlation graph between the expected and actual hardness of hardfaced Ni deposits. This implies that the gap in both actual and expected weight reduction is minimal. Table 7 shows the difference between the actual and anticipated weight reduction. Figure 4 depicts a single-track deposit with a 50% track overlap on the deposit [26–28].

R^2 should always be between 0 and 1. If a model is statistically sound, it should have an R^2 value close to or greater than 1.0. The phrase with significant terms is then rebuilt using the updated R^2 value. The Adj. $R^2 = 0.961$ value is also outstanding, suggesting that the model is highly relevant. The R^2 score for prediction is 0.906, indicating that the model can account for 90.6% of the variability in predicting outcomes. This is in reasonable accord with the Adj. R^2 of 0.961. The coefficient of variation was determined to be as low as 3.97, suggesting a negligible discrepancy between experimental and predicted values [29, 30].

To construct the joint at 1300 W, a rate of powder feed of nine grams per minute, a travel speed of three hundred and fifty millimetres per minute, and a defocusing distance of thirty millimetres per minute, the following parameters were

used: the specimen's cross section (Figure 5(a)) demonstrates that there are no surface fractures or indications of lack of adhesion in the specimen. When the track was metallographically inspected, it was discovered to have a dendritic structure that was uniformly dispersed across it with a continuous interface (Figure 5(b)) [31, 32]. The solid solution phase of Ni in the form of a dendrite is the microstructural component that dominates the deposit's microstructure. Additionally, microstructure reveals the presence of a large number of precipitate particles, especially chromium-rich carbides, in the sample (Figure 5(b)). Colmonoy 5 coatings are comprised of three major components such as Cr-rich precipitates such as CrB and CrC, Ni solid solution dendrites, and Ni-B-Si binary and ternary eutectic phases such as NiB and NiSi (Figure 6) [13]. Once at the interface (500 HV) with base metal, the hardness values remain constant until near the deposit's top (825 HV) (230 HV). Perhaps the alloys' hardness is linked to the occurrence of hard phases such as Ni₃B and Cr₂₃C₆. The presence of a uniformly distributed mixture of complex carbides and borides precipitates is believed to be responsible for the deposits' enhanced hardness. Table 8 shows the confirmation test results. It shows error in percentage and actual weight loss, and forecast weight loss is also conformed [33, 34].

To evaluate wear resistance, the substrate and deposited surfaces were subjected to a pin-on-disc wear test. The wear test parameters are shown in Table 5. At room temperature, the wear tests were performed in a self-mating setting with no external mating. It is evident that the rate of wear increases rapidly during the first stage of the wear test. The asperities on the specimens' worn surfaces, which result in the actual contact area of the friction pair being smaller than its nominal counterpart, are attributed to the material's increase in frictional resistance. At first, the asperities on the test piece's surface flake off throughout the run, and the wear rate increases as the test continues. After 30 minutes, when the sliding time is extended, the wear rate decreases, and this tendency continues. Wear resistance is enhanced in materials such as chromium borides (2575 VHN) and chrome carbides (1670 VHN) due to the complex phases in the coating serving as protective layers during the wear test [35, 36].

TABLE 6: The design matrix and the experiment findings.

Exp no.	Coded values				Actual values				Weight loss (grams)
	P	F	T	D	P (Watts)	F (gram/min)	T (mm/min)	D (mm)	
1	-1	-1	-1	-1	1300	5	350	22	0.0322
2	1	-1	-1	-1	1700	5	350	22	0.04141
3	-1	1	-1	-1	1300	9	350	22	0.0183
4	1	1	-1	-1	1700	9	350	22	0.0313
5	-1	-1	1	-1	1300	5	450	22	0.039
6	1	-1	1	-1	1700	5	450	22	0.0291
7	-1	1	1	-1	1300	9	450	22	0.028
8	1	1	1	-1	1700	9	450	22	0.01826
9	-1	-1	-1	1	1300	5	350	32	0.0238
10	1	-1	-1	1	1700	5	350	32	0.0328
11	-1	1	-1	1	1300	9	350	32	0.0164
12	1	1	-1	1	1700	9	350	32	0.0322
13	-1	-1	1	1	1300	5	450	32	0.0362
14	1	-1	1	1	1700	5	450	32	0.0279
15	-1	1	1	1	1300	9	450	32	0.0268
16	1	1	1	1	1700	9	450	32	0.0249
17	-2	0	0	0	1100	7	400	27	0.0262
18	2	0	0	0	1900	7	400	27	0.0317
19	0	-2	0	0	1500	3	400	27	0.0368
20	0	2	0	0	1500	11	400	27	0.0198
21	0	0	-2	0	1500	7	300	27	0.0277
22	0	0	2	0	1500	7	500	27	0.0283
23	0	0	0	-2	1500	7	400	17	0.0304
24	0	0	0	2	1500	7	400	37	0.0250
25	0	0	0	0	1500	7	400	27	0.0287
26	0	0	0	0	1500	7	400	27	0.0279
27	0	0	0	0	1500	7	400	27	0.0287
28	0	0	0	0	1500	7	400	27	0.0279
29	0	0	0	0	1500	7	400	27	0.0269
30	0	0	0	0	1500	7	400	27	0.0297

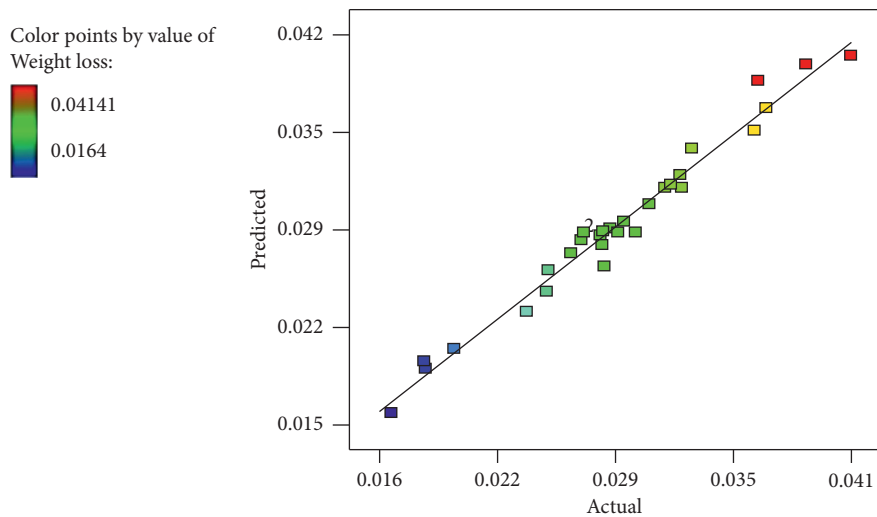


FIGURE 3: Correlation graph.

TABLE 7: ANOVA test results.

Source	Sum of squares	Degree of freedom	Mean square	F value	P value (prob > F)	Whether significant or not
Model	9.662E-4	14	6.901E-5	140.87	<0.0001	Significant
P	4.053E-5	1	4.053E-5	82.74	<0.0001	Significant
F	4.437E-4	1	4.437E-4	905.69	<0.0001	Significant
T	5.042E-10	1	5.042E-10	10.52	0.0048	Not significant
D	2.487E-5	1	2.487E-5	50.76	<0.0001	
PF	2.538E-5	1	2.538E-5	51.80	<0.0001	
PT	3.409E-4	1	3.409E-4	695.82	<0.0001	
PD	5.096E-6	1	5.096E-6	10.40	0.0057	
FT	1.710E-6	1	1.710E-6	3.49	0.0814	
FD	5.059E-5	1	5.059E-5	103.27	<0.0001	
TD	3.150E-5	1	3.150E-5	64.30	<0.0001	
P ²	1.538E-6	1	1.538E-6	3.14	0.0968	
F ²	1.724E-7	1	1.724E-7	0.35	0.0519	
T ²	7.715E-9	1	7.715E-9	0.016	0.9018	
D ²	1.372E-7	1	1.372E-7	0.28	0.6044	
Residual	7.348E-6	15	4.899E-7			
Lack of fit	6.209E-6	10	6.209E-7	2.73	0.1399	Not significant
Pure error	1.139E-6	5	2.277E-7	Pred. R ²	0.9616	
Cor total	9.735E-4	29		Press	3.741E-5	
Std. deviation	6.999E-4			Mean	0.028	
R ²	0.9925			C.V %	2.45	
Adj. R2	0.9854			Adeq. precision	30.969	



FIGURE 4: Pin-on-disc samples extracted from laser hardfaced deposit.

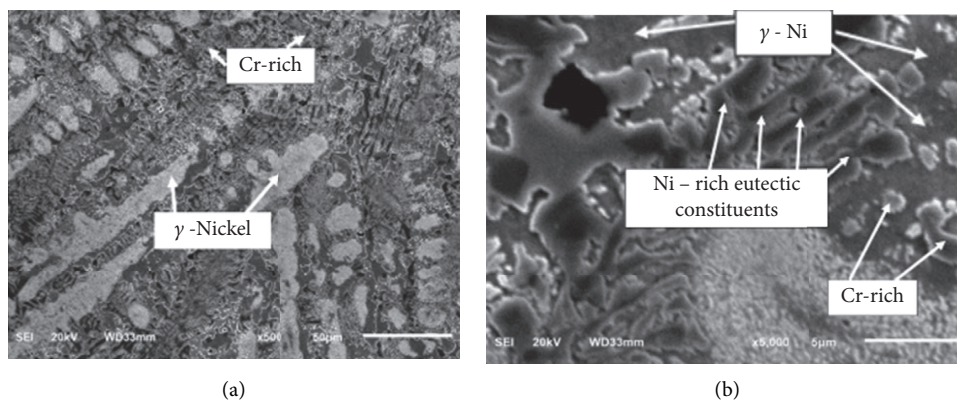
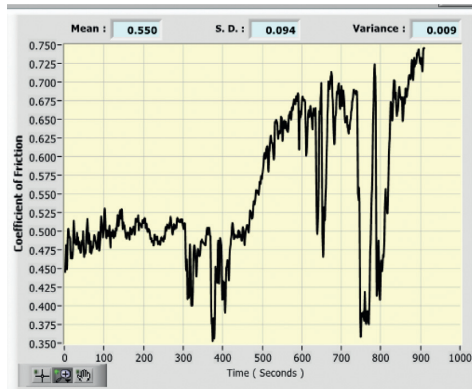


FIGURE 5: Scanning electron micrograph of laser hardfaced deposit.

Top surface
of wear test
specimen

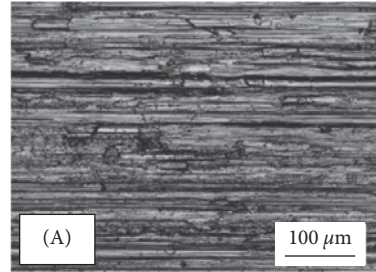


Co-efficient of friction graph

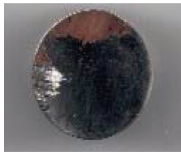


(a)

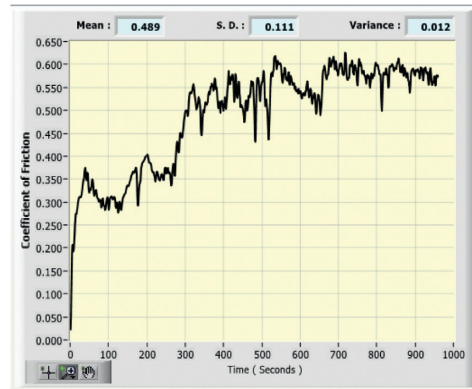
SEM Image



Top surface
of wear test
specimen

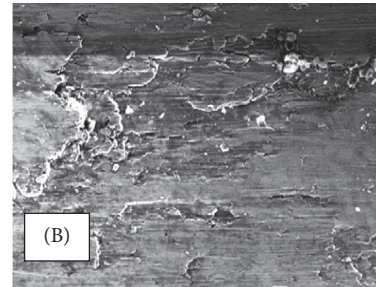


Co-efficient of friction graph



(b)

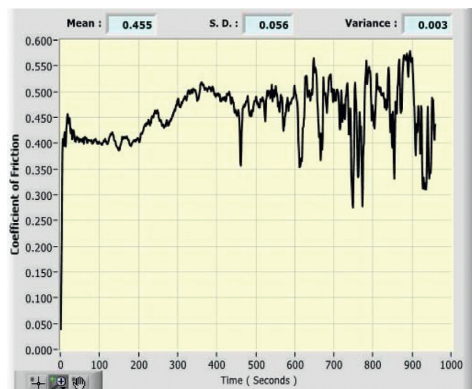
SEM Image



Top surface
of wear test
specimen



Co-efficient of friction graph



(c)

SEM Image

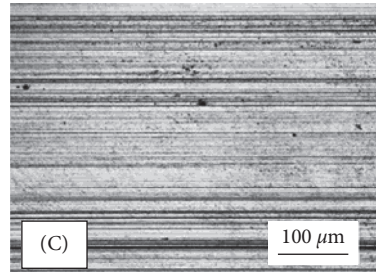


FIGURE 6: Microscope image of worn surface: (a) substrate; (b) Sample 2; (c) Sample 8.

TABLE 8: Confirmation test results.

S. no.	Power (W)	Rate of powder feed (g/min)	Travel speed (mm/min)	Defocusing distance (mm)	Real weight loss in gram	Forecast weight loss in gram	Error in percentage %
01	1100	4	325	20	0.0307	0.0296	3.58
02	1400	6	400	26	0.2728	0.2800	-2.63
03	1800	8	470	30	0.2802	0.2715	3.10

4. Conclusions

- (1) It was possible to predict the hardness of nickel-based hardfaced deposits on 316LN austenitic stainless-steel substrates using an empirical model that took into account laser properties. This relationship was established and tested.
- (2) It was possible to obtain a maximum hardness of 820 HV by employing a power of 1300 W, a powder feed rate of 9 g/min, a travel speed of 350 mm/min, and a defocusing distance of 32 mm, all of which were combined.
- (3) Among the four laser factors examined, the rate of powder feed (as measured by the F value) has the most significant impact on hardness, followed by laser power, defocusing distance, and travel speed, in that order.

Data Availability

The data used to support the findings of this study are included within the article.

Conflicts of Interest

The authors declare that there are no conflicts of interest regarding the publication of this paper.

References

- [1] S. L. Mannan, S. C. B. Chetal, and S. B. Bhoje, *Materials R&D for Prototype Fast Breeder Reactor*, S. L. Mannan and M. D. Mathew, Eds., Indira Gandhi Centre for Atomic Research, Kalpakkam, India, 2003.
- [2] G. Chakraborty, S. K. Albert, and A. K. Bhaduri, "Effect of dilution and cooling rate on microstructure and magnetic properties of Ni base hardfacing alloy deposited on austenitic stainless steel," *Materials Science and Technology*, vol. 28, no. 2, pp. 454–459, 2012.
- [3] A. K. Bhaduri, R. Indira, S. K. Albert, B. P. S. Rao, S. C. Jain, and S. Asokkumar, "Selection of hardfacing material for components of the Indian Prototype Fast breeder reactor," *Journal of Nuclear Materials*, vol. 334, no. 2–3, pp. 109–114, 2004.
- [4] N. Jeyaprakash and C.-H. Yang, "Comparative study of NiCrFeMoNb/FeCrMoVC laser cladding process on nickel-based superalloy," *Materials and Manufacturing Processes*, vol. 35, no. 12, pp. 1383–1391, 2020.
- [5] N. Jeyaprakash, C. H. Yang, M. Duraiselvam, and S. Sivasankaran, "Comparative study of laser melting and pre-placed Ni–20% Cr alloying over nodular iron surface," *Archives Civil and Mechanical Engineering*, vol. 20, p. 20, 2020.
- [6] N. Jeyaprakash, C. H. Yang, and S. Sivasankaran, "formation of FeCrMoVC layers on AA6061 by laser cladding process: microstructure and wear characteristics," *Transactions of the Indian Institute of Metals*, vol. 73, pp. 1611–1617, 2020.
- [7] D. Zhang and X. Zhang, "Laser cladding of stainless steel with Ni-Cr3C2 and Ni-WC for improving erosive-corrosive wear performance," *Surface and Coatings Technology*, vol. 190, no. 2–3, pp. 212–217, 2005.
- [8] L. J. da Silva and A. S. C. M. D'Oliveira, "NiCrSiBC coatings: effect of dilution on microstructure and high temperature tribological behavior," *Wear*, vol. 350–351, pp. 130–140, 2016.
- [9] L. C. Lim, Q. Ming, and Z. D. Chen, "Microstructures of laser-clad nickel-based hardfacing alloys," *Surface and Coatings Technology*, vol. 106, pp. 183–192, 1998.
- [10] S. K. Albert, S. Venkadesan, and S. L. Mannan, "Studies on a nickel base hardfacing alloy deposited on stainless steel," in *Proceedings of the Symposium On Joining of Materials for 2000 AD*, pp. 363–369, Indian Institute of Welding, Tiruchirapalli, India, December 1991.
- [11] D. K. Dwivedi, "Adhesive wear behaviour of cast aluminium– silicon alloys: overview," *Materials and Design*, vol. 31, pp. 2517–2531, 2010.
- [12] B. K. Prasad, "Structure–property related changes in hypoeutectic Al–Si alloys induced by solutionizing," *Materials Transactions, JIM*, vol. 34, pp. 873–881, 1994.
- [13] D. K. Dwivedi, A. Sharma, and T. V. Rajan, "Friction and wear behaviour of hypereutectic Al–Si base alloys at low sliding velocities," *Transactions of the Indian Institute of Metals*, vol. 54, pp. 247–254, 2001.
- [14] R. K. Mahanti, K. Lal, A. N. Sinha, and C. S. Shivaramkrishnan, "A novel technique for hyper eutectic aluminium–silicon alloy melt treatment," *Materials Transactions, JIM*, vol. 34, pp. 1207–1211, 1993.
- [15] K. Gurumoorthy, M. Kamaraj, K. Prasad Rao, A. Samba Siva Rao, and S. Venugopal, "Microstructural aspects of plasma transferred arc surfaced Ni-based hardfacing alloy," *Materials Science and Engineering A*, vol. 456, pp. 11–19, 2007.
- [16] C. Sudha, P. Shankar, R. V. Subba Rao, R. Thirumurugesan, and M. Vijayalakshmi, "Baldev Raj, Microchemical and microstructural studies in a PTA weld overlay of Ni–Cr–Si–B alloy on AISI 304L stainless steel," *Surface and Coatings Technology*, vol. 202, pp. 2103–2112, 2008.
- [17] S. Gnanasekaran, G. Padmanaban, V. Balasubramanian, H. Kumar, and S. K. Albert, "Optimizing the laser parameters to attain maximum hardness in nickel based hardfacing surfaces," *Journal of the Mechanical Behavior of Materials*, vol. 26, no. 2–3, pp. 113–126, 2017.
- [18] S. Gnanasekaran, G. Padmanaban, and V. Balasubramanian, "Effect of laser power on metallurgical, mechanical and tribological characteristics of hardfaced surfaces of nickel-based alloy," *Lasers in Manufacturing and Materials Processing*, vol. 4, no. 4, pp. 178–192, 2017.
- [19] K. Gurumoorthy, M. Kamaraj, K. P. Rao, A. S. Rao, and S. Venugopal, *Materials Science and Engineering A*, vol. 456, pp. 11–19, 2007.
- [20] I. Hemmati, V. Ocelik, and J. T. M. De Hosson, "Dilution effects in laser cladding of Ni–Cr–B–Si–C hardfacing alloys," *Materials Letters*, vol. 84, pp. 69–72, 2012.

- [21] 20.ASTM G 99 – 04, *Standard Test Method for Wear Testing with a Pin-On-Disk Apparatus*, ASTM International, West Conshohocken, PA, USA, 2016.
- [22] I. Hemmati, *Laser-Deposited Metallic Coatings: Processing, Characterization, Alloy Development*, Ph.D Thesis, University of Groningen, Groningen, Netherlands, 2013.
- [23] Q. Ming, L. C. Lim, and Z. D. Chenc, “Laser cladding of nickel-based hardfacing alloys,” *Surface and Coatings Technology*, vol. 106, pp. 174–182, 1998.
- [24] H. Zhang, Y. Shi, M. Kutsuna, and G. J. Xu, “Laser cladding of Colmonoy 6 powder on AISI316L austenitic stainless steel,” *Nuclear Engineering and Design*, vol. 240, no. 10, pp. 2691–2696, 2010.
- [25] D. C. Montgomery, *Design and Analysis of Experiments*, Wiley, Hoboken, NJ, USA, 2004.
- [26] K. Y. Benyounis and A. G. Olabi, “Optimization of different welding processes using statistical and numerical approaches - a reference guide,” *Advances in Engineering Software*, vol. 39, no. 6, pp. 483–496, 2008.
- [27] C. Samson Jerold Samuel, K. Murugan, A. P. Ray, M. Upadhyaya, V. Narasimharaj, and S. Gnanasekaran, “Optimization of process parameters using response surface methodology: a review,” *Materials Today: Proceedings*, vol. 37, no. 2, pp. 1301–1304, 2021.
- [28] S. Gnanasekaran, S. Senthil Kumar, N. raj Venugopal et al., “Effect of laser power on microstructure and tensile properties of pulsed Nd:YAG laser beam welded AISI 301 austenitic stainless steel joints,” *Materials Today: Proceedings*, vol. 37, no. 2, pp. 934–939, 2021.
- [29] M. Qian, L. C. Lim, Z. D. Chen, and W. I. Chen, “Parametric studies of laser cladding processes,” *Journal of Materials Processing Technology*, vol. 63, no. 1–3, pp. 590–593, 1997.
- [30] A. I. Khuri and J. A. Cornell, *Response Surfaces: Designs and Analyses*, Roulledge, Oxford, England, 2nd edition, 1996.
- [31] S. Gnanasekaran, G. Padmanaban, and V. Balasubramanian, “Effect of laser hardfacing process parameters on microstructural characteristics and microhardness of Ni–Cr–B–Si–C deposit on austenitic stainless-steel substrate,” *Journal of Advanced Microscopy Research*, vol. 12, no. 3, pp. 173–181, 2017.
- [32] S. Gnanasekaran, G. Padmanaban, V. Balasubramanian, H. Kumar, and S. K. Albert, “Correlation between travel speed, microstructure, mechanical properties and wear characteristics of Ni-based hardfaced deposits over 316LN austenitic stainless steel,” *High Temperature Materials and Processes*, vol. 38, pp. 16–29, 2019.
- [33] G. S. Padmanaban and V. Balasubramanian, H. Kumar and S.K. Albert, Laser hardfacing of colmonoy-5 (Ni-Cr-Si-B-C) powder onto 316LN austenitic stainless steel: effect of powder feed rate on microstructure,” *Mechanical Properties and Tribological Behavior” Lasers in Engineering*, vol. 42, no. 4-6, pp. 283–302, 2019.
- [34] G. Padmanaban and V. Balasubramanian, “Optimization of laser beam welding process parameters to attain maximum tensile strength in AZ31B magnesium alloy,” *Optics & Laser Technology*, vol. 42, no. 8, pp. 1253–1260, 2010.
- [35] J. D. Majumdar and I. Manna, *Laser-Assisted Fabrication of Materials*, Springer Series in Materials Science, New York, NY, USA, 2012.
- [36] D. Kesavan and M. Kamaraj, “The microstructure and high temperature wear performance of a nickel base hardfaced coating,” *Surface and Coatings Technology*, vol. 204, no. 24, pp. 4034–4043, 2010.

Retraction

Retracted: Effects of Novel Material Field Effect Transistor for Heterogeneous Energy and Traffic-Aware Secure Applications

Advances in Materials Science and Engineering

Received 11 July 2023; Accepted 11 July 2023; Published 12 July 2023

Copyright © 2023 Advances in Materials Science and Engineering. This is an open access article distributed under the Creative Commons Attribution License, which permits unrestricted use, distribution, and reproduction in any medium, provided the original work is properly cited.

This article has been retracted by Hindawi following an investigation undertaken by the publisher [1]. This investigation has uncovered evidence of one or more of the following indicators of systematic manipulation of the publication process:

- (1) Discrepancies in scope
- (2) Discrepancies in the description of the research reported
- (3) Discrepancies between the availability of data and the research described
- (4) Inappropriate citations
- (5) Incoherent, meaningless and/or irrelevant content included in the article
- (6) Peer-review manipulation

The presence of these indicators undermines our confidence in the integrity of the article's content and we cannot, therefore, vouch for its reliability. Please note that this notice is intended solely to alert readers that the content of this article is unreliable. We have not investigated whether authors were aware of or involved in the systematic manipulation of the publication process.

Wiley and Hindawi regrets that the usual quality checks did not identify these issues before publication and have since put additional measures in place to safeguard research integrity.

We wish to credit our own Research Integrity and Research Publishing teams and anonymous and named external researchers and research integrity experts for contributing to this investigation.

The corresponding author, as the representative of all authors, has been given the opportunity to register their agreement or disagreement to this retraction. We have kept a record of any response received.

References

- [1] C. Ambika Bhuvanewari, E. D. Kanmani Ruby, A. Manjunathan, R. Balamurugan, P. Jenopaul, and B. Z. Tizazu, "Effects of Novel Material Field Effect Transistor for Heterogeneous Energy and Traffic-Aware Secure Applications," *Advances in Materials Science and Engineering*, vol. 2021, Article ID 9085854, 9 pages, 2021.

Research Article

Effects of Novel Material Field Effect Transistor for Heterogeneous Energy and Traffic-Aware Secure Applications

C. Ambika Bhuvaneshwari ¹, E. D. Kanmani Ruby ¹, A. Manjunathan ²,
R. Balamurugan ³, P. Jenopaul ⁴, and Belachew Zegale Tizazu ⁵

¹Vel Tech Rangarajan Dr. Sagunthala R & D Institute of Science and Technology, Chennai, Tamil Nadu, India

²K. Ramakrishnan College of Technology, Trichy, Tamil Nadu, India

³K. Ramakrishnan College of Engineering, Trichy, Tamil Nadu, India

⁴Adi Shankara Institute of Engineering and Technology, Kalady, Kerala, India

⁵Department of Chemical Engineering, College of Biological and Chemical Engineering, Addis Ababa Science and Technology University, Addis Ababa, Ethiopia

Correspondence should be addressed to Belachew Zegale Tizazu; belachew.zegale@aastu.edu.et

Received 4 August 2021; Revised 26 August 2021; Accepted 2 September 2021; Published 13 October 2021

Academic Editor: Samson Jerold Samuel Chelladurai

Copyright © 2021 C. Ambika Bhuvaneshwari et al. This is an open access article distributed under the Creative Commons Attribution License, which permits unrestricted use, distribution, and reproduction in any medium, provided the original work is properly cited.

The advent of the automated technological revolution has enabled the Internet of Things to rejuvenate, revolutionize, and redeem the services of sensors. The recent development of microsensor devices is distributed in a real-world terrestrial environment to sense various environmental changes. The energy consumption of the remotely deployed microsystems depends on its utilization efficiency. Improper utilization of sensor nodes' heterogeneity could lead to uneven energy consumption and load imbalance across the network, which will degrade the performance of the network. The proposed heterogeneous energy and traffic aware (HETA) considers the key parameters such as delay, throughput, traffic load, energy consumption, and life span. The residual energy and a minimum distance between the base station and cluster members are taken into consideration for the cluster head selection. The probability of hitting data traffic has been utilized to analyse energy and traffic towards the base station. The role of the sensor node has been realized and priority-based data forwarding are also proposed. As a result, the heterogeneous energy and traffic aware perform well in balancing traffic towards the base station, which is analysed in terms of maximum throughput and increase in a lifetime of heterogeneous energy networks more than 5000 rounds, and the algorithm outperforms 34.5% of nodes are alive with transmissible energy. The proposed research also endorses unequal clustering and minimum energy consumption. We have modeled our proposed research using various p-type junctionless nanowire FET without doping injunctions. The materials used in this analysis were silicon (Si), germanium (Ge), indium phosphide (InP), gallium arsenide (GaAs), and Al(x) Ga(1-x)As. The dimensions of the p-type cylindrical nanowire channel were 25 nm long and 10 nm in diameter.

1. Introduction

The pandemic monster, COVID-19, has become a huge challenge to present-day trauma-free automation technology. Now, the technology is moving in such a mode. So, beyond the specific application, the need for microsystems has been developed. Towards the smart living environment, wireless sensor network with multisourced Internet of things (IoT) has changed in many applications such as monitoring, surveillance, healthcare, automation, entertainment, and

industry. The only major challenge of the world for the last year has been the hazardous increase of COVID-19 positive test cases. The impending doom of the situation is the emergent need of the hour, and it has forced us to undergo basic health monitoring for the nonsymptom cases too. The technology in engineering always concerns with providing solutions to the medical field. Wireless sensor networks, artificial intelligence, robotics, and pervasive computing all as a whole have built an interdisciplinary concept to overcome day-to-day challenges in a smart way.

An environmental sensor such as RFID readers, video cameras, sound, pressure, temperature, humidity, and luminosity are some of the devices that provide information about the people to be monitored. The key problem for planning and managing the network for continuous monitoring will lead to maximum energy consumption. The types of multisources have been classified as link heterogeneity, energy heterogeneity, and computation heterogeneity which progresses the routing algorithm performance, network lifetime, network stability, reliability, etc., [1]. In the previous work, energy heterogeneity has been considered and topology has been designed to manage the energy by a centralized clustering scheme. Together with energy, network traffic is exponentially growing.

The development of micro-electro-mechanical system technology provides sophisticated applications that make the sensors relatively better and complex in technology advancement [2]. The cost of servicing and maintaining the IoT and handling with a larger number of sensors deployment play the major role [3], and replacing batteries in already deployed location is difficult based on the specific application.

This paper aims at balancing the traffic load towards the base station from the dual communication environment. With regards to direct communication and cluster-based communication, more traffic can be experienced in direct communication. The probability of traffic has been analysed concerning the data priority using finite-state mechanism, and from that, the sleep and awake schedule are provided for nonpriority and priority nodes. This would help in preventing the NP-hard problem and enhance the network lifetime with an increase in the number of heterogeneous energy nodes.

This paper is organized as follows. In Section 2, related works and required background are provided. Our proposed system model and algorithm are explained in Section 3. From the evaluation, the simulation results and analysis are discussed in Section 4. Finally, the article is concluded in Section 5.

2. Related Works

In [4], the author has concentrated on the scheduling of clustering through polling technique instead of traditional TDMA and CDMA, in cluster head election and routing algorithm have been developed under ABC and ant colony optimization. Fuzzy C means that clustering is taken for the artificial bee colony algorithm to find the optimal cluster head and to avoid the long-distance intracluster communication and the ant colony optimization has been applied for the best routing technique. The uneven clustering is balanced in [5]; the algorithm divides the network into different sizes such as near the base station clusters are smaller in size and the farther cluster is larger to balance the cost of the network and the increase of life too. Many energy-oriented algorithms are available using the Markov decision process formulated to balance the transmission energy. In [6], a centralized distributed algorithm is proposed to minimize the node's intracluster transmission

energy. The author concludes that using the decision policy, the power of transmission remains constant for the 40-time slots. Another work for centralized energy, proposed for the energy efficiency [7, 8], measured MDP for the transmission power selection, from which the state has been performed based on the fading channel and the reception error. Processing gain of the system is considered in modulation and coding schemes [9]. The simultaneous transmissions from different sensors are on different spreading codes. The interference of the base station concerns the priority frame selection-based CDMA [10]; from that, optimal selection of sensing groups has been given. In [11], the author has proposed the two priority schemes such as energy efficiency and data gathering. It mainly focuses on event-related data to be transmitted in the system. In [12], the matrix geometric method evaluates the performance of each traffic class by dynamic priority adjustment. Advanced zonal selection [13] is a heterogeneous routing protocol. In the middle zone, the nodes make direct communication with the sink node and they follow cluster-based communication at the boundary region. The cluster head selection is based on maximum residual energy and the minimum distance from the sink node. The unbalanced energy consumption due to the dynamic change of the topology is carried out using distance similarity index, and CH load is reduced using dual cluster head [14]. In [15], the author proposes an organized multipath and balanced load algorithm that ensures awareness of energy consumption. In [16], the author discusses the Markov decision process for adaptive intelligent dynamic water resource planning for urban areas to supply water on a sensitivity-driven method. The unequal clustering is addressed using a single path and mobile sink's multipath routing [17] and the HEESR is proposed. In [18–20], the swarm intelligence maximum coverage of the node has been discussed and compared with designed p-type junctionless nanowire FET without doping junctions. In [21–26], sensed heterogeneous data processing is carried out for different applications such as agriculture, weather information, and health monitoring for both live information and stored information. In [27–32], results have represented the feasibility that the sensor could be used to distinguish the different harnesses of the materials. To investigate the electrical transfer studies, various semiconductor materials such as silicon (Si), germanium (Ge), indium phosphide (InP), gallium arsenide (GaAs), and $\text{Al}(x)\text{Ga}(1-x)\text{As}$ are used. Additionally, surface charge and potential analysis are also studied.

3. Proposed Methodology

The HETA proposes a novel priority-based traffic-aware algorithm that the lifetime and stability of the network depends on the residual energy, the distance between the nodes, and the sleep and awake schedule is based on the coverage area-based node selection from the priority table to maintain the stability of the network even during the increase in the number of heterogeneous energy nodes.

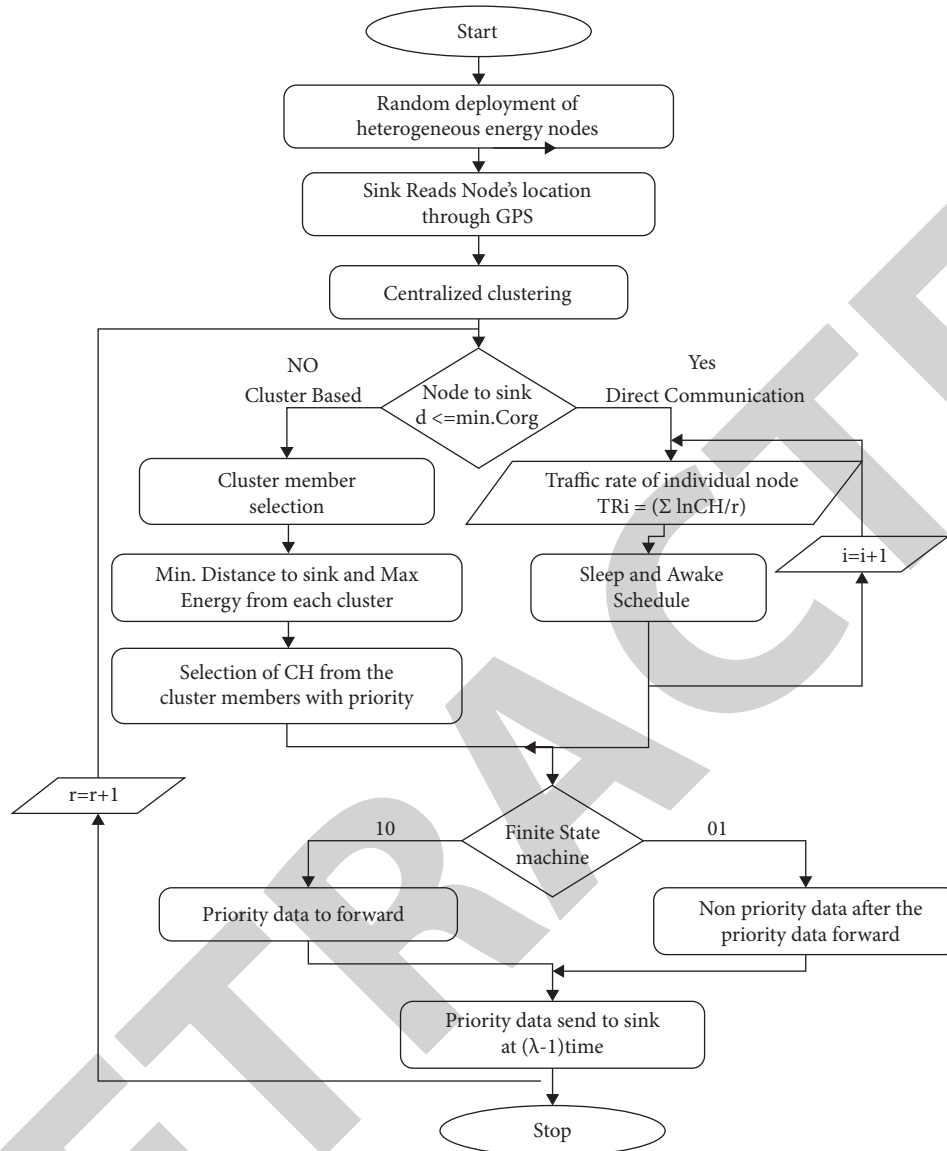


FIGURE 1: Flow diagram of HETA algorithm.

3.1. HETA Method. The proposed research is the priority-based balancing of the load over the network. The energy consumption of each node depends on the total number of packets and distance towards the receiving node. Here, the sink node performs the centralized clustering algorithm as explained in the previous work. The cluster head selection has been carried out in two important parameter considerations. Firstly, in each zone, the nodes which have maximum energy are selected as CH, and while increasing the number of transmission rounds, it should not become less than minimum energy (ETX + EDA). Secondly, the node has a minimum intracluster distance and less threshold distance to the sink to which the cluster member can be added.

The increase in scalable leads to a decrease in throughput. Due to the simultaneous transmission by the different sensors, whose transmission is on different spreading codes, interference could occur at the base station. Hence, the priority-based data processing is carried out

using Moore's finite state machine. Since the state of the node always depends on the present situation and also this data information is controlled by the state, this method has been followed. The prioritized code division multiple access is used for the data transmission between the zone1 active nodes and the CHs from the other zones. Active sensors are classified into different priorities that are controlled by the base station. In Figure 1, HETA is explained via flow diagram to differentiate the low-priority nodes from high-priority nodes, and we preassign the priority level at the system setup. From Figure 2(b), the CH has a high priority, and other active nodes (CM) from zone1 have low priority of the nodes' state diagram. The gate contact work function is achieved by applying gate terminal input potential. The SiO_2 gate has 4.1 eV work function and relative permittivity value of 4.2. On both ends of the wire, perfect ohmic contacts were established. Figure 2(a) shows the structure and electrical connection of the junctionless nanowire FET. Because of

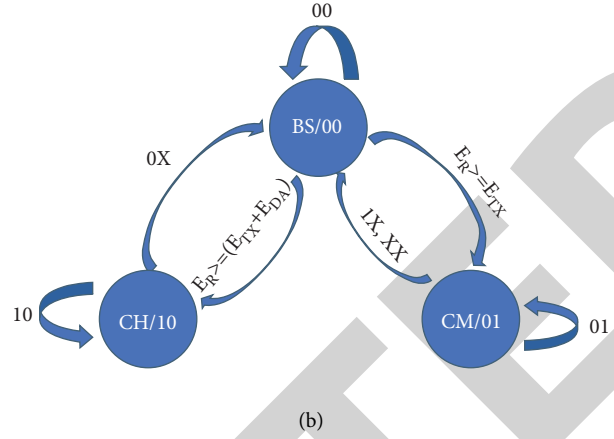
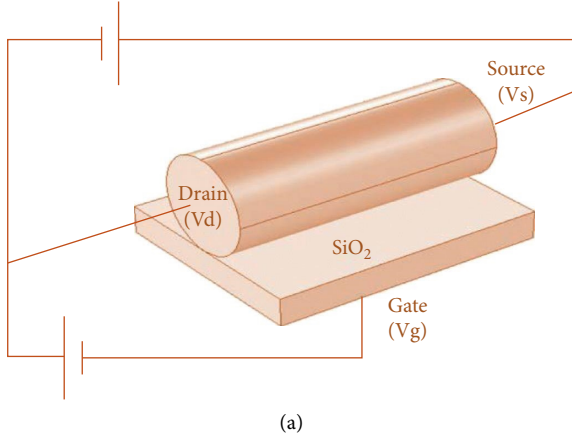


FIGURE 2: (a) Structure and electrical connections of junctionless nanowire FET. (b) Finite state mechanism.

TABLE 1: Simulation parameter consideration.

Parameter	Value
Network size	100 m × 100 m
Number of sensor nodes	100–300
Normal node initial energy	0.5–1.5 J
Eelec	50 nJ per bit
Efs	10 pJ per bit
Emp	0.0013 pJ per bit
Packet length (l)	4000 bits

p-type nanowire FET, the gate signal, which has the negative bias and drain, also has negative bias with respect to the source.

By using the Markov model, the FSM has been realized. The probability of getting priority information is $P(x)$, and the probability of getting nonpriority information is $P(y) = 1 - P(x)$. The data aggregation from different sensing devices based on the TDMA schedule is given by the CH.

The transition probability matrix of the state diagram given in expression expresses the present state i to the next state j transition matrix as

$$P = \begin{pmatrix} P_{11} & \cdots & P_{i1} \\ \vdots & \ddots & \vdots \\ P_{1j} & \cdots & P_{ij} \end{pmatrix}. \quad (1)$$

The probability of data forwarding from state i to state j extends to t -step transitions, given in equation (2); the transmission at t times is expressed in equation (3):

$$P_{ij} = P(X_{t+1} = j | X_t = i), \quad (2)$$

$$P(X_t = j | X_0 = i) = P(X_{n+t} = j | X_n = i) = (Pt)_{ij}. \quad (3)$$

For any n , here, we can consider the CH as the subset of the state space S . The hitting probability of the CH from its cluster members considered the data transmission from the steady-state phase. Equation (4) is the hitting probability:

$$hiCH = (X_t A: t \geq 0 | X_0 = i). \quad (4)$$

In the nonclustering environment, the increase in the number of sensing nodes creates an increase in the data rate. Hence, the traffic towards the BS increases, so the traffic aware of sleep and awake is needed for the network stability. The traffic rate of each node (TR_i) per round is given as

$$TR_i = \frac{\sum_1^{r-1} l_{nCH}}{r}, \quad (5)$$

where l is the data packet of each node noncluster head (nCH) in zone1 and r represents the number of rounds. From that, the HETA algorithm helps in a minimum number of CH allocations based on the increased residual energy and minimum distance to the base station. Since the data forwarding in the direct communication-sensing nodes follow the event driven, the average traffic rate of the network is given as

$$TR_{NW} = \frac{\sum_1^{r-1} l_{nCH} + K_{CH}}{r}. \quad (6)$$

A larger traffic rate of the node increases the average traffic rate of the network. Therefore, an alternate sleep-and-awake schedule is given by the BS concerning the node's position. Each node in the zone1, based on the Euclidian distance neighboring nodes' table, has been updated. In each cycle, one from each segment will endure for data transmission using

$$E_{Z1} = \sum_{i=1}^{nAN} E_{TX} \cdot l. \quad (7)$$

The sum of the transmitting energy of the active nodes (AN) in zone1 ($Z1$) is the total energy of the direct communication of the nodes with priority scheduling. Hence, by using equation (8), the total energy consumption of the network per round is given:

$$ETot = E_{Z1} + \sum_{i=1}^{nCH} (E_{TX} + E_{DA}) \cdot l + \sum_{i=1}^{nCM} E_{TX} \cdot l. \quad (8)$$

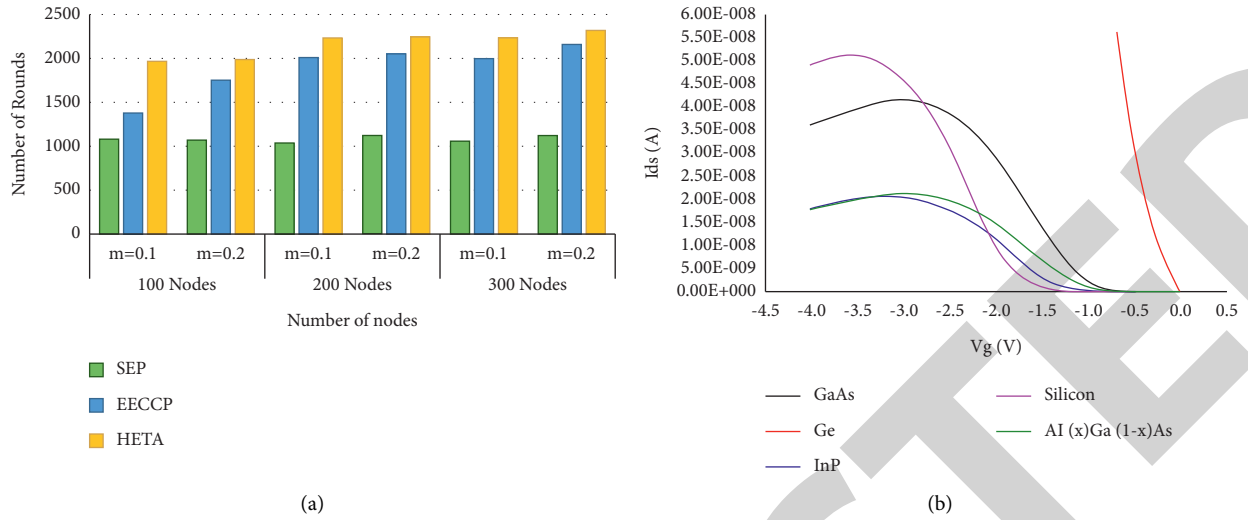


FIGURE 3: (a) Stability of the network with an increase in the number of nodes. (b) Characteristics of drain current with negative gate voltage.

TABLE 2: Stability of the network in various heterogeneous energy.

Stability	100 nodes		200 nodes		300 nodes	
	$m = 0.1$	$m = 0.2$	$m = 0.1$	$m = 0.2$	$m = 0.1$	$m = 0.2$
SEP	1083	1074	1045	1130	1069	1128
EECCP	1389	1759	2014	2057	2008	2164
HETA	1973	1999	2235	2252	2236	2325

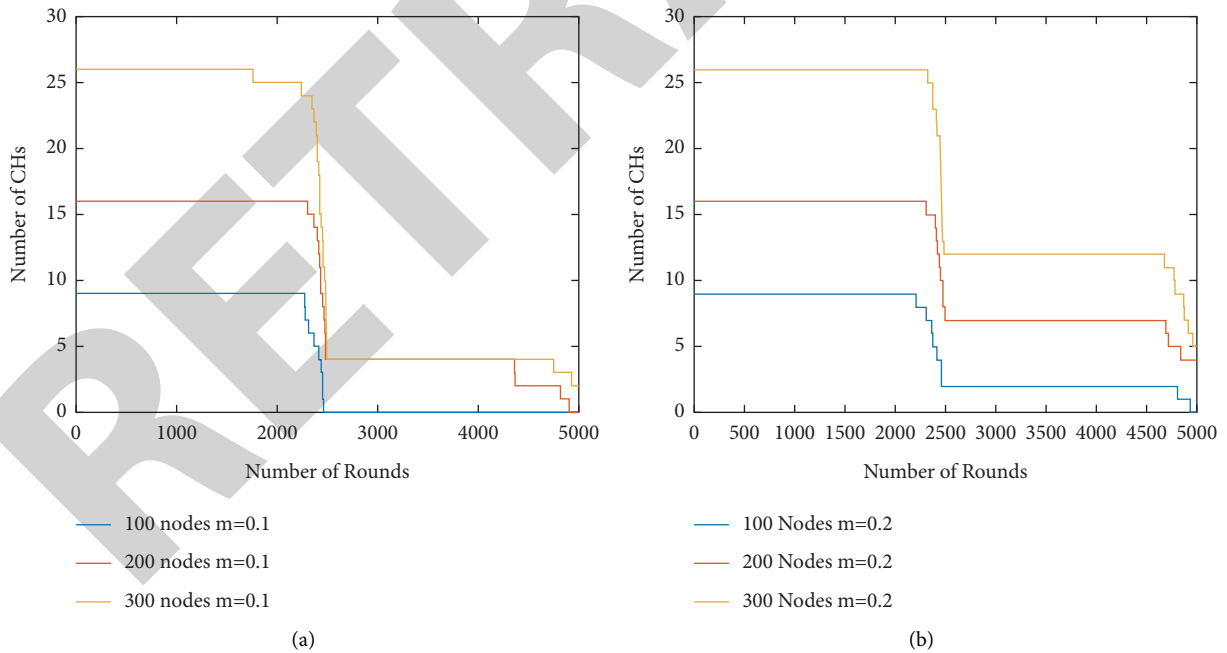


FIGURE 4: The static CH allocation in different nodes. (a) 10% of heterogeneous energy; (b) 20% of heterogeneous energy.

4. Results and Discussion

The proposed HETA algorithm evaluation is based on the simulation in MATLAB, with a $100\text{ m} \times 100\text{ m}$ square region. The nodes are deployed randomly with heterogeneous

energy within the monitoring area. Table 1 lists the simulation initial parameters consideration.

The random deployment of the heterogeneous energy nodes in the monitoring area and the sink node is placed at the center of the network. Nearer nodes of the base station

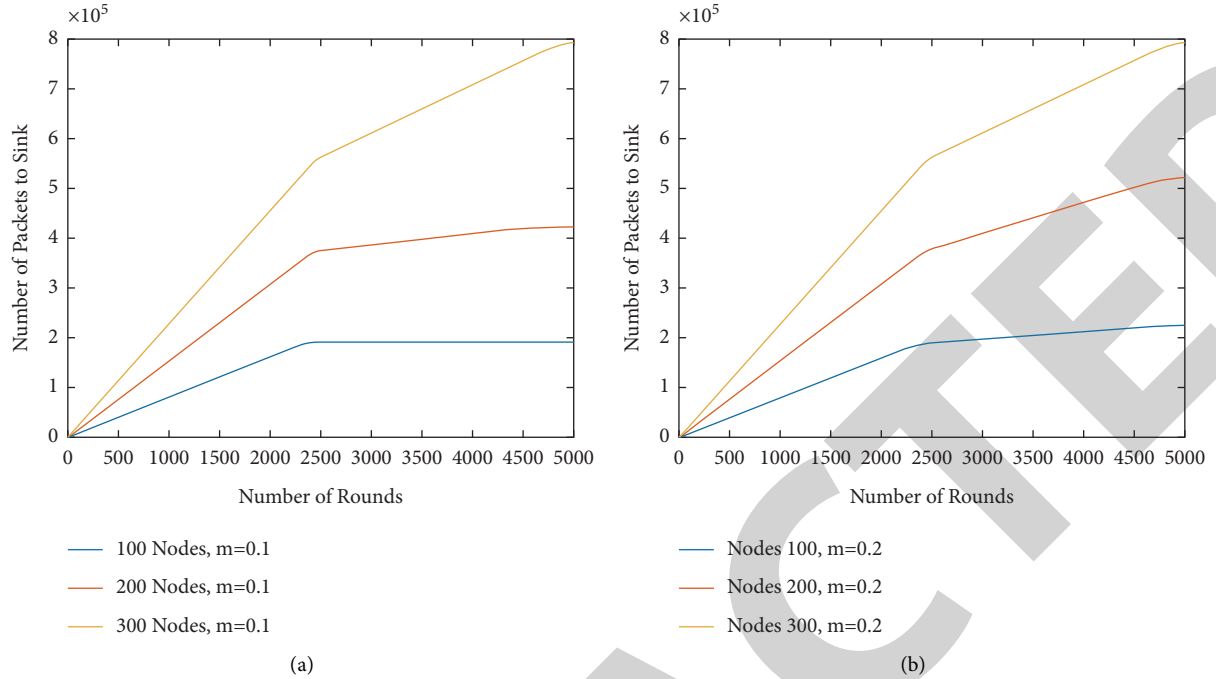


FIGURE 5: Throughput of the network in different scales. (a) 10% of heterogeneous energy; (b) 20% of heterogeneous energy.

TABLE 3: Traffic near to the base station.

S.No	Node ID	Residual energy	Distance (m)	Duty cycle of EECCP	Duty cycle of HETA
1	9	1.4998	10.1	1	1
2	6	1.4998	20.2	1	1
3	1	1.4998	23.5	1	1
4	47	0.4998	9.3	1	2
5	85	0.4998	12.7	1	2
6	87	0.4998	14.4	1	2
7	30	0.4998	21.9	1	2
8	88	0.4998	25.1	1	2
9	5	1.4998	11	1	3
10	51	0.4998	17.5	1	3
11	81	0.4998	26	1	3
12	48	0.4998	27.9	1	3

TABLE 4: Residual energy (in Joules) after 5000 transmission rounds.

HWSN	Initial energy	EECCP	HETA
100 nodes with 10%	64.97	53.38	54.38
100 nodes with 20%	79.97	67.36	67.44
200 nodes with 10%	129.94	117.22	117.98
200 nodes with 20%	159.94	146.28	147.47
300 nodes with 10%	194.92	181.89	182.51
300 nodes with 20%	239.92	226.09	227.49

will carry over the direct communication and farther nodes will undergo cluster-based communication. Figure 3(a) illustrates the stability of the network by understanding the first node dead (FND) with the maximum number of successful rounds with all nodes in the network are active. Our algorithm outperforms well in the various energy level

of nodes up to 300. The time taken by any of the nodes in a network to reach its dead condition defines the stability of the network. Table 2 demonstrates the performance of the proposed algorithms with respect to stability. While considering 10% heterogeneous energy nodes initially starting with 100, 200, and 300 nodes, whereas the FND after 1972

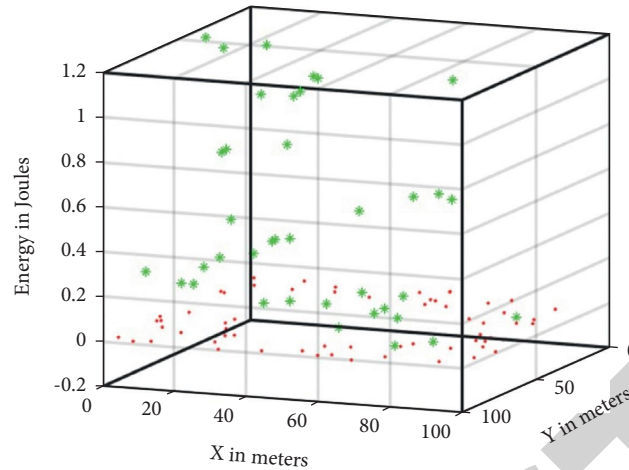


FIGURE 6: The residual energy of the network after 5000 rounds in 20% of heterogeneous energy of 100 nodes.

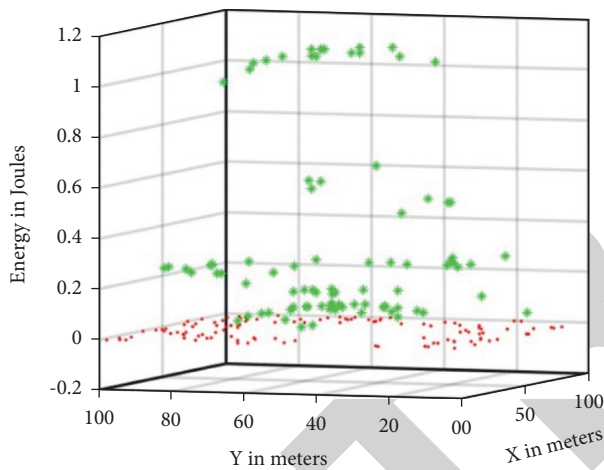


FIGURE 7: The residual energy of the network after 5000 rounds in 20% of heterogeneous energy of 200 nodes.

rounds, 2234 rounds, and 2235 rounds, respectively. Similarly, nodes with 20% of heterogeneous energy from 100, 200, and 300 increase in nodes the stability of the network lifetime achieved from the FND after the 1998 rounds, 2251 rounds, and 3223 rounds, respectively. While comparing the stability with SEP 22% better stability and with EECCP, 7% of better stability has been obtained.

4.1. Effect of Gate Voltage on Drain Current for Heterogeneous Energy. The drain currents were measured by changing the negative gate voltage from zero to 4.0 volts. Variations of drain current with biasing the negative gate voltage from 0 to -4 V is shown in Figure 1. The measured values are taken from the center point of the nanowire. The plot indicates that the values of drain current of indirect band gap materials are higher than the direct bandgap materials and alloy. From Figure 3(b), Ge and Si have higher values of drain current compared with other materials. The $\text{Al}(x)\text{Ga}(1-x)$ As semiconductor alloy has lower drain current changes. The electron mobility behavior attributes the lower current in InP and higher variations in Ge.

From Figures 4(a) and 4(b), the maximum energy consumption part of the network is the number of CH allocation with 10% and 20% of heterogeneous energy nodes, respectively. An increase in CH leads to an increase in energy consumption. From that, the HETA algorithm helps in a minimum number of CH allocations based on the increased residual energy and minimum distance to the base station. The algorithm was performed on centralized clustering technique, with static topology consideration. Hence, the lifetime of the network is increased to more than 5000 rounds.

Figures 5(a) and 5(b) illustrate the throughput of the network in 10% and 20% heterogeneous energy, respectively. HWSN with a different increase in node deployment is also carried out. In both scenarios, the successful packet delivery has been balanced even in the increase in the number of nodes for direct communication. Priority-based sleep and awake schedule provided the excellent load balancing of the network for more than 5000 rounds.

In Table 3, the traffic near the BS of the HETA protocol has been compared with the EECCP protocol [19]. From that, EECCP creates more traffic expressed in the form of all Zone1 nodes and cluster heads hit the BS. However, in HETA algorithm, based on the flow control technique, three segments were formed and the controlled data forwarding has been achieved on a priority basis. The run-time scenario also has been carried out to understand the cluster head allocation with respect to the distance and residual energy.

In Table 4, the energy utilization of HETA has been compared with EECP, 300 nodes of energy efficiency obtained 0.6%, and for 200 nodes, it is 0.7%, and for 100 nodes, it is 1.5% increase. The priority model of high and low has been considered. The classification of the priority of hierarchical approach need to considered.

Figure 6 illustrates the remaining energy of the network having 100 nodes with 20% of heterogeneous energy. On various energy levels, the higher energy level node of either advanced or intermediate nodes are elected as CH and also the cluster members are managed within the threshold distance, so the energy consumption of the normal nodes is well balanced.

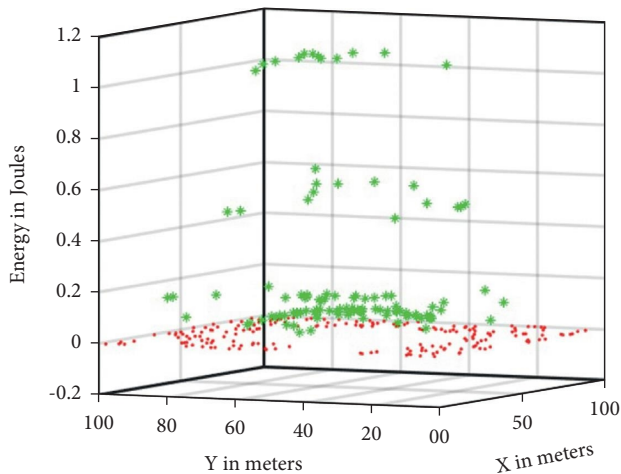


FIGURE 8: The residual energy of the network after 5000 rounds in 20% of the heterogeneous energy of 300 nodes.

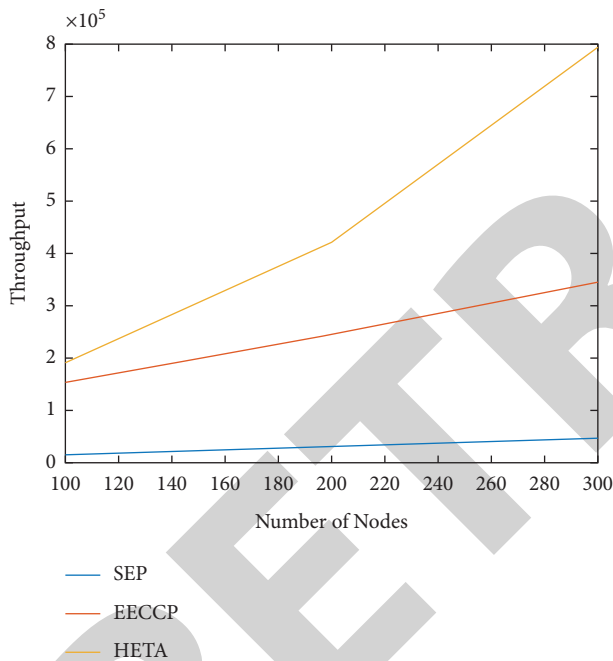


FIGURE 9: Throughput.

Near to the BS, load balancing is achieved based on the traffic-aware sleep-and-awake schedule and the energy consumption that has been reduced; hence, 25% of nodes are still alive after 5000 rounds.

Figure 7 illustrates the remaining energy of the network having 200 nodes with 20% of heterogeneous energy. In 80% of normal nodes, applying the HETA algorithm helps cluster head selection from higher energy nodes such as advanced or intermediate nodes; also, the cluster members are managed within the threshold distance, so the energy consumption of the normal nodes is well balanced. Near the BS, load balancing is achieved based on the traffic-aware sleep-and-awake schedule; the energy consumption has been reduced; 38.5% of nodes are still alive after 5000 rounds even with an increase in the number of nodes.

Similarly, Figure 8 illustrates the remaining energy of the network that has 300 nodes with 20% of heterogeneous energy. In 80% of normal nodes, applying the HETA algorithm moderately helps in increase of the number of nodes, and load balancing achieved comparatively more than 5% from 200 nodes and more than 15% from 100 nodes scenarios. Figure 9 illustrates the throughput, comparing HETA algorithm, performs 92% better than SEP and 40% better than EECCP. In more than 300 nodes, the algorithm results are stable due to the increase in traffic near the base station.

5. Conclusion

The proposed heterogeneous energy and traffic-aware algorithm serves as a better solution for scalable and priority-based packet forwarding. From the quality-of-service analysis, the proposed algorithm outperforms well in network stability. The network stability parameter of FND is compared with SEP, and it provides better stability up to 1097 rounds and 65% more energy efficient in heterogeneous network. Further incorporating the priority-based traffic-aware packet forwarding technique, the designed HETA outperforms the existing in terms of throughput by 40%, ultimately increasing the performance of the network. The proposed method includes an improvement of cluster head selection to reduce the data congestion with minimized energy consumption. To conclude, the designed algorithm gives a better performance for a heterogeneous network, leaving a track of additional delay which will be dealt in the future work. The indirect bandgap materials have higher response over the direct band gap material. InP has the highest surface potential values. This high change of surface potential in nanowire FETs can be used in nanostructured sensor applications.

Data Availability

The data used to support the findings of this study are included within the article.

Conflicts of Interest

The authors declare that they have no conflicts of interest.

References

- [1] S. Tanwar, N. Kumar, and J. J. P. C. Rodrigues, "A systematic review on heterogeneous routing protocols for wireless sensor network," *Journal of Network and Computer Applications*, vol. 53, pp. 39–56, 2015.
- [2] M. Barceló, A. Correa, J. Vicario, and A. Morell, "Multi-tree routing for heterogeneous data traffic in wireless sensor networks," in *Proceedings of the 2013 IEEE International Conference on Communications (ICC)*. IEEE, pp. 1899–1903, Budapest, Hungary, November 2013.
- [3] Y.-K. Chen, "Challenges and opportunities of internet of things," in *Proceedings of the 17th Asia and South Pacific design automation conference*. IEEE, pp. 383–388, Sydney, Australia, January 2012.

Retraction

Retracted: Design and Implementation of SOC-Based Noncontact-Type Level Sensing for Conductive and Nonconductive Liquids

Advances in Materials Science and Engineering

Received 26 December 2023; Accepted 26 December 2023; Published 29 December 2023

Copyright © 2023 Advances in Materials Science and Engineering. This is an open access article distributed under the Creative Commons Attribution License, which permits unrestricted use, distribution, and reproduction in any medium, provided the original work is properly cited.

This article has been retracted by Hindawi, as publisher, following an investigation undertaken by the publisher [1]. This investigation has uncovered evidence of systematic manipulation of the publication and peer-review process. We cannot, therefore, vouch for the reliability or integrity of this article.

Please note that this notice is intended solely to alert readers that the peer-review process of this article has been compromised.

Wiley and Hindawi regret that the usual quality checks did not identify these issues before publication and have since put additional measures in place to safeguard research integrity.

We wish to credit our Research Integrity and Research Publishing teams and anonymous and named external researchers and research integrity experts for contributing to this investigation.

The corresponding author, as the representative of all authors, has been given the opportunity to register their agreement or disagreement to this retraction. We have kept a record of any response received.

References

- [1] J. L. M. Iqbal, M. S. Kishore, Arulkumaran Ganeshan, and G. Narayan, "Design and Implementation of SOC-Based Noncontact-Type Level Sensing for Conductive and Nonconductive Liquids," *Advances in Materials Science and Engineering*, vol. 2021, Article ID 7630008, 12 pages, 2021.

Research Article

Design and Implementation of SOC-Based Noncontact-Type Level Sensing for Conductive and Nonconductive Liquids

J. L. Mazher Iqbal ¹, Munagapati Siva Kishore,¹ Arulkumaran Ganeshan ²,
and G. Narayan³

¹Department of Electronics & Communication Engineering, School of Electrical & Communication, Vel Tech Rangarajan Dr. Sagunthala R&D Institute of Science and Technology, Chennai, India

²Department of Electrical and Computer Engineering, Bule Hora University, Bule Hora, Ethiopia

³School of Electronics Engineering, Vellore Institute of Technology (VIT), Vellore, India

Correspondence should be addressed to J. L. Mazher Iqbal; mazheriq@gmail.com and Arulkumaran Ganeshan; drgrulkumaran@bhu.edu.et

Received 1 August 2021; Revised 16 August 2021; Accepted 19 August 2021; Published 5 October 2021

Academic Editor: Samson Jerold Samuel Chelladurai

Copyright © 2021 J. L. Mazher Iqbal et al. This is an open access article distributed under the Creative Commons Attribution License, which permits unrestricted use, distribution, and reproduction in any medium, provided the original work is properly cited.

In contrast to the existing electromechanical systems, the noncontact-type capacitive measurement allows for a chemically and mechanically isolated, continuous, and inherently wear-free measurement. Integration of the sensor directly into the container's wall offers considerable savings potential because of miniaturization and installation efforts. This paper presents the implementation of noncontact (NC)-type level sensing techniques utilizing the Programmable System on Chip (PSoC). The hardware system developed based on the PSoC microcontroller is interfaced with capacitive-based printed circuit board (PCB) strip. The designer has the choice of placing the sensors directly on the container or close to it. This sensor technology can measure both the conductive and nonconductive liquids with equal accuracy.

1. Introduction

Nowadays, all automotive vehicles are fitted with a fuel-level sensor. It measures the quantity of fuel left in the fuel tank. A fuel-level sensor is present in the fuel tank for a prolonged period and exposed to fuel, fuel additives, corrosive sulphur, methanol, and ethanol. So, manufactures in the automobile industry need novel solutions for the longevity of fuel-level sensors. The novel solutions should also reduce cost, space, and weight and enhance the reliability of fuel sensors. The fuel-level sensor can sense numerous liquid in the automobile industry such as cooling water, windshield cleaning engine oil, and power steering fluid. The noninductive, capacitance-based sensor is capable of estimating the level of conducting as well as nonconducting fluids. The level sensor checks the fluid level in tanks. Level sensors quantify the fluid level at straight and bent states of fuel tanks. Recently, capacitive sensors have been used in many applications such as touch sensing, proximity detection systems, brake fluid

measurement, fuel-level measurement, engine oil measurement, and cooling water level. Capacitive sensor's advantages are higher sensitivity, lower mechanical stress, higher reliability, and lower impact on the temperature coefficients. Several methods are available to convert the capacitance into analog voltages. The popular techniques used in capacitance-to-analog voltage converters are transimpedance amplifier and an alternating current (AC) bridge with voltage amplifier. The limitations of these techniques are low sensitivity and nonidealities of the sensor. The low sensitivity in the interfacing circuit is due to ignoring the minimum change in the capacitance. The nonidealities are temperature, induced frequency, and switch noise. This paper discusses the current in the noncontact-type level measuring technique using System on Chip (SoC)-based approach.

The paper [1] discusses a noncontact fluid level measurement method. The resources used in the level sensor were enameled copper winding wire, acrylic bar, acrylic

pipes, and acrylic sheet. In paper [2], noncontact capacitance-type level sensors for conductive fluids are discussed. The paper [3] discusses the capacitive-based level sensor which is used in ingestion water circulation systems. The aquatic level sensor has been intended by multilayer pipes and is equivalent to a commercially existing ultrasound aquatic level sensor. The limitation is that it is a contact sensor. The paper [4] discusses the water level computation using the capacitive sensor with the printed circuit board (PCB). The paper [5] discusses the capacitive touch systems with styli consisting of the touch sensor, analog frontend integrated circuit, and microcontroller unit. The limitation is the degradation of the signal to noise ratio as the touch sensor is located far from the finger. The paper [6] presents an extensive review of the various types of sensors used in automobiles. The paper [7] discusses the multifunctional parallel-plate capacitor sensor with four electrodes. The level of the fluid is determined by sensing the values of the capacitance. Furthermore, the permittivity and angle of the fluid container are also estimated. The paper [8] presents a liquid-level sensor based on etched fiber Bragg grating (FBG). In this, an edge-emitting light emitting diode (LED) feeds aFBG which is partially in air and partially immersed in the liquid. The difference in the absorption spectra is used to measure the liquid level.

The paper [9] presents a liquid-level measurement system based on a remote grounded capacitive sensor. The sensor comes in direct contact with the liquid whose level is being measured, thus making it prone to degradation. The paper [10] discusses the development of a capacitive sensor for minute liquid droplet detection. It works on the principle of a change in dielectric constant between the plates of a parallel-plate capacitor driven by an AC voltage. However, the intended use of this sensor is in liquid dispensing systems. The paper [11] presents a measurement system that has been developed using a single-tube capacitive sensor to determine the fluid level in vehicular fuel tanks which addresses the effect of fuel sloshing due to vehicle acceleration. In our earlier article [12–16], high-performance reconfigurable architectures were proposed. The architecture discussed does not discuss the concept of SoC computing. The paper [17] discusses the development of a PCB-based capacitive pressure sensing system. The paper [18] presents a fiber optic liquid-level sensor based on a Mach–Zender optical interferometer. A major disadvantage of this system is that it works best at a temperature range of 20–40°C.

The paper [19] discusses the electrical model intended for noncontact capacitance-based liquid sensors to define liquid-level dependence. In paper [20], the authors designed a noncontact uniform circular cylinder-based capacitance-type level sensor for a conducting fluid made of insulating material. An improved linear operational amplifier with adjustable bridge sensitivity measures the variation in capacitance due to variation in the liquid level. The paper [21] discusses the signal conditioning circuit minimum parasitic capacitance for translating capacitance variation into frequency. The limitation of the transformer is that the circuit is not complementary metal-oxide-semiconductor (CMOS) compatible. The paper [22] discusses the method of

computing the error of fluid oxygen level-to-capacitance translation. In paper [23], the authors designed and fabricated a fluid level measurement structure created on a beached tubular capacitive sensor for conductive fluids. The structure is not capable to shield the potential of the extensive computing choice and high linearity. The paper [24] discusses the features of a paired spiral capacitance sensor for the quantity of the fluid theft in flat lubricant-aquatic dual-stage drift. The limitation of the paper is that it does not consider the edge protecting conductors to decrease the current. The paper [25] discusses a method established on a modest linear capacitor array, and it is capable of resolving differences of the solid fraction. The paper [26] presents a modified version of a noncontact capacitance level transducer for a conducting liquid explained in paper [7]. The paper [27] discusses the interfacing of a capacitive sensor with the common microcontroller Arduino. The paper [28] discusses the possibilities of using common off-the-shelf ultrasonic sensors for fuel-level sensing applications.

The paper [29] presents a noninvasive portable capacitive transducer for measuring fuel level of portable engines. Although the sensor itself is not in direct contact with the fuel, the measurement unit consists of three coated copper electrodes which are inside the fuel tank. The paper [30] discusses the optical fiber sensor established on silica spout configuration. The paper [31] discusses the optical fiber sensor for an instantaneous measure of fluid level and temperature. The sensor is designed by incorporating a no-core fiber and fiber Bragg raucous. The paper [32] discusses the capacitive sensor with an array of electrodes resembling to comb structure for fluid level measurement. The paper [33] discusses the Helmholtz resonance process to design a fluid level gauge using liquid hydrogen. The paper [34] discusses the fluid level measurement structure founded on energetic pipe pressure conventional for high-temperature corrosive molten salts. The paper [35] discusses the fluid level structure based on discrete wavelet packet multiresolution proportional integral (PI) controller.

In paper [36], the authors discuss the flexible liquid-level optical fiber sensing to measure the liquid level. In paper [37], the authors discuss the light guide plate-based optical liquid-level sensor. The paper [38] discusses the development of the capacitive fuel measurement sensor. The sensor comprises of two copper plates acting like a parallel-plate capacitor. The system detects a change in fluid level based on the change in capacitance. In paper [39], the authors designed an instrument for determining the liquid level. The instrument uses a multisensory model comprising a capacitive level sensor, ultrasonic level sensor, and capacitance pressure sensor to measure the liquid. The paper [40] discusses a fuel-level measurement model based on a single-tube cross-capacitance sensor. The disadvantage is that it is an immersive-type sensor, making it prone to quicker degradation. From the above literature review, it is evident that the implemented methodologies are predominantly contact-type sensing techniques. The limitations are that the liquid is to be immersed in the tube and a separate structure is needed to know the liquid level.

In this paper, we describe the development of a distant capacitive-type level sensor. The proposed sensor is fabricated using an easily available multilayer PCB. The sensor comprises a PCB configured with two coplanar probes. This paper focuses on the brake fluid level measurement in four-wheelers. The proposed methodology in this paper overcomes the limitation discussed in the literature. The flex PCB structure is to be mounted on the container wall. The capacitive-type fluid level measurement using a capacitive sensor is easy to assemble, costs less, more robust, high repeatability, high resolution, and easy to install. Using this methodology lowers the development cost of the sensor and related interfacing electronic circuits. This paper is organized as follows. Section 2 presents the proposed methodology and design resources. The capacitance modeling and analysis are presented in Section 3. Section 4 presents the design and implementation of capacitance liquid-level sensing. Section 5 presents the results and discussion. Finally, Section 6 presents the conclusion.

2. Proposed Methodology

This section discusses the methodology and hardware-software design resources for noncontact-type level sensing and their feasibility. The capacitor structural sensor is proposed in this paper. Fluid level is a significant parameter in the industrial evolutions. A noticeable substitute in the industrial automation is the capacitive level measurement relative to mechanical structures. Capacitive fluid level sensors are conductive packs or dash pads placed on a nonconductive material such as plastic or glass or PCB. The intrinsic capacitance of the PCB dash pads is the parasitic capacitance (C_p). Once the fluid moves towards the sensor, a small fluid capacitance (C_L) is added to C_p . This is illustrated in Figure 1. Liquid-level sensing implies calculating the increased capacitance while water exists near the sensor.

The Programmable System on Chip (PSoC) 4 CapSense Element given in the PSoC Creator Integrated Development Environment (IDE) processes the capacitance through introducing a current into the sensor through a current Digital to Analog Converter (IDAC). A timer measures how long it takes the IDAC to charge the sensor's voltage to a reference voltage using a comparator.

2.1. Parasitic Capacitance. The parasitic capacitance (C_p) is the undesirable capacitance present between chunks of an electronic circuit purely because they are located close to each other. The CapSense Element processes the total capacitance and addition of parasitic and fluid capacitance ($C_{TOTAL} = C_p + C_L$) restricted by dynamic range. The bigger the C_p , the lesser the fluid slice of the entire signal. It reduces the system sensitivity in the presence of liquid hence increases the total system accuracy. The main components of parasitic capacitance in CapSense designs are sensor capacitance and dash capacitance. The sensor dimensions are increased by increasing the in-dash measurement and reducing the annular gap. However, it leads to more C_p value. The technique that decreases the C_p value and declines the

noise immunity is to broaden the gap between the sensor and the ground.

2.2. Mechanical Variations. Mechanical variations within the system can take many forms to change the sensor's C_p . There are two types of mechanical variations.

- (1) Motionless disparity is usually generated through developed tolerances in the sensor assembly, PCB, and sensor arrangement towards the fluid container. Static variations, if understood and controlled, are compensated during manufacturing with the baseline calibration operation.
- (2) Dynamic variation is caused during operation. These changes often manifest themselves as changes to C_p by changing the sensor's capacitor dimensions. Unlike temperature changes, dynamic variation is difficult to compensate. It is the best to design the system to minimize dynamic-mechanical variation effects on the sensors.

The most common mechanical variation encountered is a change in the distance between capacitor plates, where the first plate is the sensor and the second plate is the liquid surface. It is triggered through air-bubbles present in the adhesive. The adhesive attaches the sensors to the container—the air-bubbles propagate and shrink through air pressure. Another cause is when the sensors are not directly attached to the liquid container allowing a changing air gap between the sensor substrate and the container wall. These effects are reduced by eliminating air-bubbles; hence, the mechanical design is adequate to sustain precise sensor arrangement.

2.3. Temperature Effects. Temperature variations during maneuvers have a substantial effect on performance. Compensation for temperature deviation is addressed through augmented sensor designs. A small isolating air gap should exist between the fluid basin and the sensor substrate.

2.4. Capacitive Level Measurement. Even though capacitive level sensing is a familiar technique, it is not used in automotive applications because of its sensitivity to the conductivity of the fluid and variations in dielectric constant. Contemporary development in capacitive level sensing such as smart capacitive organization with reparation of the side effects and emergent processor power in the sensors makes use in automobile applications.

2.5. Capacitive Sensor Section. The capacitive sensor section consists of the fixed capacitor on a typical PCB intended to measure the fuel level. The design arrangement of the capacitive sensors is distinct. The inclination of the fluid is determined using differential capacitive measurement. PSoC 4200 is used as the target device to implement the non-contact-type level sensing. The PSoC-4 device with CapSense circuitry (CY8CKIT-042) is interfaced with capacitive sensors. It senses the deviation in the capacitance in the

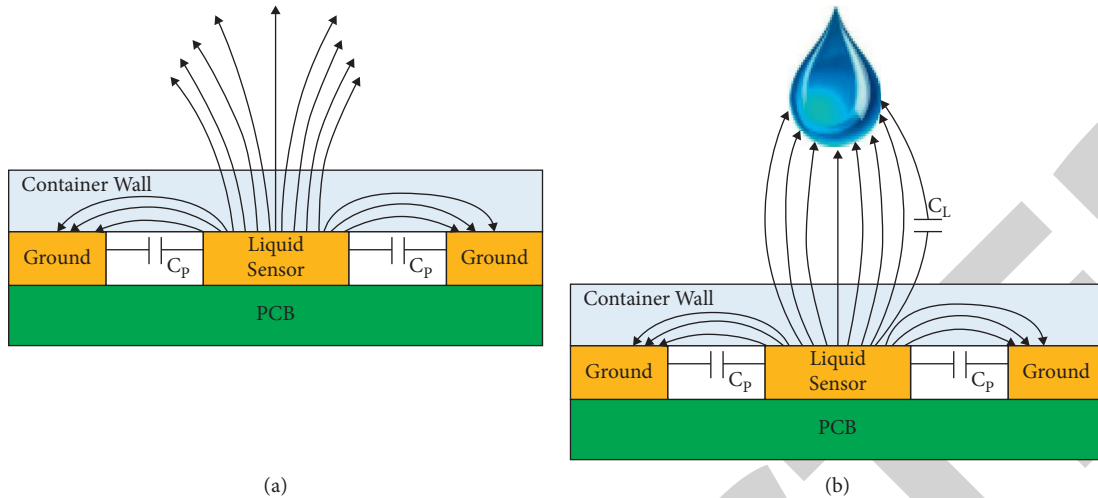


FIGURE 1: (a) Capacitive level sensor. (b) Extra capacitance once fluid approaches the sensor.

container. It also calculates the liquid level based on the capacitance variations of the sensors in the CapSense block shown in Figure 2. Figure 3 shows the system-level diagram.

3. Capacitance Modeling

This section describes the implementation of a five-segment capacitance linear slider. The linear capacitance sensor debugs data and positions the slider on a PC using the CapSense embedded tuner Graphical User Interface (GUI) via I2C communication. The CapSense tuner provides a quick and easy method for monitoring and updating capacitance linear slider parameters.

3.1. CapSense Component. This section demonstrates the functionality of the CapSense component. Figure 4 shows the PSoC top design and pins mapping diagram of the capacitive linear slider. The capacitive linear slider uses CapSense and EZI2C Slave modules.

3.2. Firmware. After building and installing the project in CY8CKIT-042, launch the Tuner Graphical User Interface (GUI) and then right-click the CapSense Component and select launch tuner in the menu to configure it as an analog channel. The analog channel gets the raw count of the capacitance shown in Figure 5. Figures 6 and 7 show the firmware flowchart and the circuit diagram of CapSense block.

The proposed work uses the smart sense (Full Auto-Tune) tuning method to implement a linear slider. The EZI2C slave is used to display the sensor information and slider touch position statistics on a PC using the CapSense tuner in the PSoC Creator IDE via Inter-Integrated Circuit (I2C).

The current through the resistor is measured and converted to equivalent voltage using a current to voltage rectifier. The capacitance of the sensor is incremented when the touch is recognized. The increments in capacitance of the

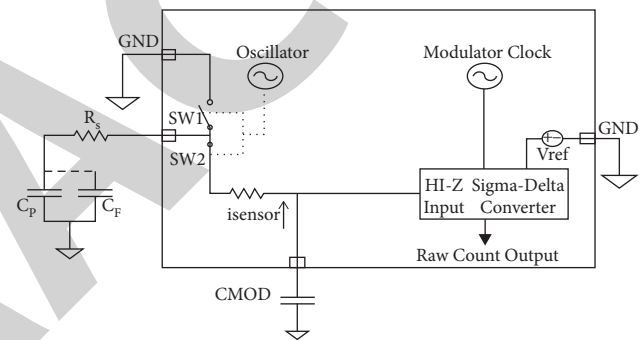


FIGURE 2: CapSense block diagram.

sensor also increment the current through the resistor. The CapSense block adjusts by controlling the modulation and frequency of the oscillator which results in an increase in voltage between the resistors.

4. Design and Implementation

This section presents the design and demonstration of capacitance liquid-level sensing. The linear sensor capacitance debugs and positions the data and liquid using the inbuilt CapSense tuner on a PC as a friendly GUI via universal asynchronous receiver-transmitter (UART) communication. This CapSense tuner GUI gives the observer a predictive method for validating and calibration of capacitance parameters.

4.1. Design. The design spark schematic tool draws the logical design and drives the PCB design. However, the PCB drawing tool is used without importing the layout schematic. The PCB design produces the productional data and the final assembled PCB. Design Spark generates the Gerber files, and generated Gerber files are directly sent to the manufacturer. From this Gerber data, the EMS providers can produce the final physical PCBs. A capacitive sensor built utilizing distinctive materials relies upon the prerequisite and

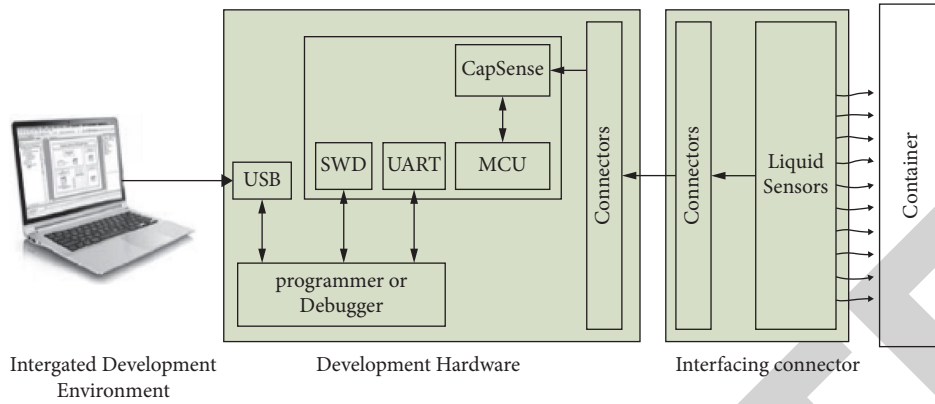


FIGURE 3: System-level diagram.

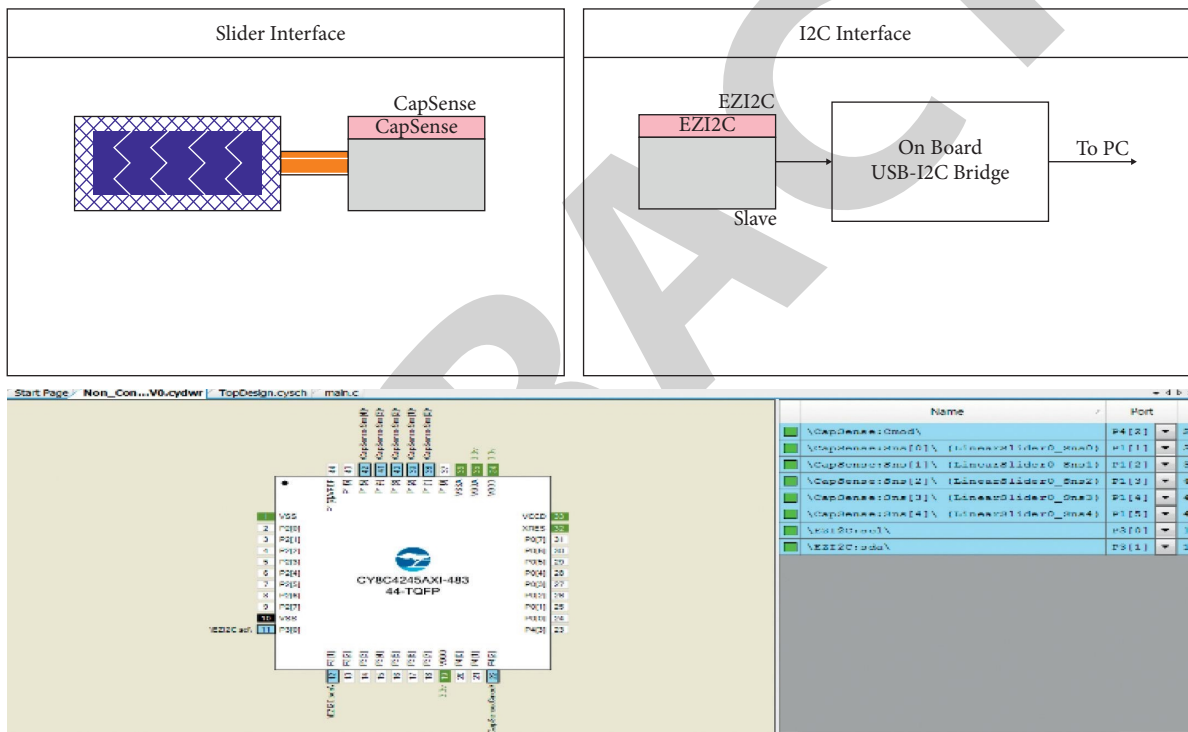


FIGURE 4: Top design and pin mapping.

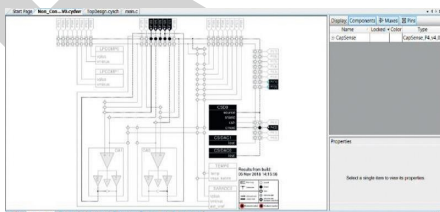


FIGURE 5: Analog channel configuration for CapSense.

application. Capacitive sensor development incorporates a conductive surface which detects that the user touch is associated with the pin of the capacitive controller utilizing a conductive follow or connection. It clarifies that an entire development plan is underneath a nonconductive overlay material. The user has access to approach the top side of the

overlay. The well-known strategy for sensor development is the etching of copper pads and FR4 PCB material.

4.2. *Overlay Parameters.* In a capacitance sensor configuration, overlay material is put over the sensor pad to shield it from the anticipation of direct finger contact and environment parameters. The geometry of a capacitive estimating framework is profoundly complex than a coplanar parallel-plate capacitor. In the parallel-plate capacitance model, C_F is corresponding to ϵ_r . Further, high dielectric steady will result in high sensitivity. Because of the lower dielectric constant of air, any bubbles/air gaps between the sensor cushion and overlay ought to be maintained at a strategic distance for better resolution. Dielectric constants of usually utilized overlay materials for PCB are recorded in

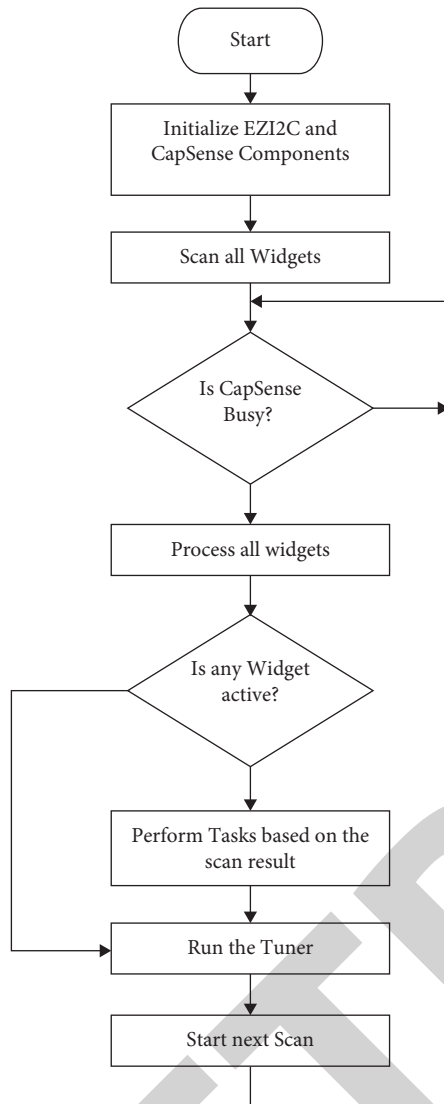


FIGURE 6: Firmware flowchart.

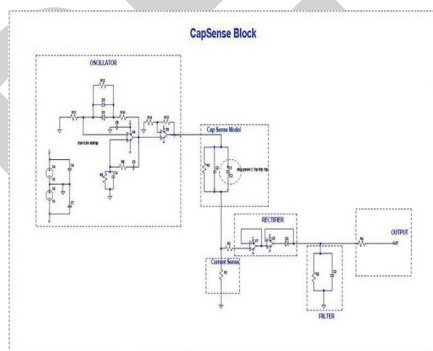


FIGURE 7: Circuit diagram of CapSense block.

Table 1. Materials with dielectric steady somewhere in the range of 2.0 and 8.0 are appropriate for capacitive detecting applications. The conductive material cannot be fit as an overlay substrate due to its impedance. Consequently, we should not utilize paints that contain metal particles in the

TABLE 1: Dielectric constants of insulation materials.

Material	Dielectric constant
Air	1.0
Formica	4.6–4.9
Glass (standard)	7.6–8.0
Glass (ceramic)	6.0
Pet film (mylar)	3.2
Polycarbonate (lexan)	2.9–3.0
Acrylic (plexiglass)	2.8
ABS	2.4–4.1
Wood table	1.2–2.5
Gypsum	2.5–6.0

overlay. Sensitivity is reciprocally dependent on the thickness of overlay material, as illustrated in Figure 8. Overlay materials should have reasonable mechanical contact to the PCB sensor. This can be accomplished utilizing a 3M type nonconductive sort adhesive film. This increases the sensitivity of the system by taking out any air gaps in the middle of the overlay and the sensor pads.

4.3. Sensor PCB Design. The sensor terminals have been planned with geometrical parameters chosen for a sufficient sensitivity. The PCB is structured utilizing Design Spark. Figures 9 and 10 show the sensor PCB and sensor pattern, respectively. The PCB is manufactured by an external vendor, with the parameters shown in Table 2. Figure 11 shows the fabricated PCB. The designed sensor is further fabricated and tested by using the high precision LCR meter. The designed PCBs have a parasitic capacitance of ~ 37 pF (with overlay). The capacitance can change depending on the medium and can go up to ~ 200 pF considering the human hand as a reference to determine the max effective capacitance. Each PCB exhibits different capacitance based on their properties and overlay materials. So, it is required to determine the capacitance thresholds of the designed sensor. Initially, it is measured using a high-resolution LCR meter. The maximum capacitance is determined by having a human hand placed proximity to the sensor. The measurement desk appears in Figure 12. The designed sensor is interfaced to Cypress PSoC4 dev kit using the interfacing card. The interfaced card has the impedance matching resistors of 560 ohms in each sensor lines. The connector pin layout is made that can be easy to interface. Figure 13 shows the connector layout of the sensor. The designed sensor is interfaced with Cypress PSoC 4 dev kit using the interfacing card. The connector pin layout is made that can be easy to interface.

4.4. Measurement and Calibration. The noncontact-type fluid level system arrangement consists of four segments. Figure 14 shows the diagram of a fluid level system. The device under-test (DUT) consists of a sensor, interfacing card, and PSoC 4. The sensor input is directly integrated into the container's wall that offers a considerable savings potential in terms of miniaturization and installation efforts. The output is taken from PSoC 4. The PSoC 4 is a

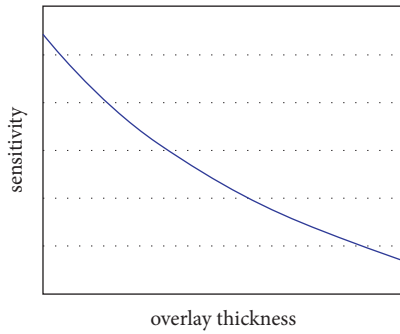


FIGURE 8: Sensitivity vs. overlay thickness.



FIGURE 9: Sensor PCB.

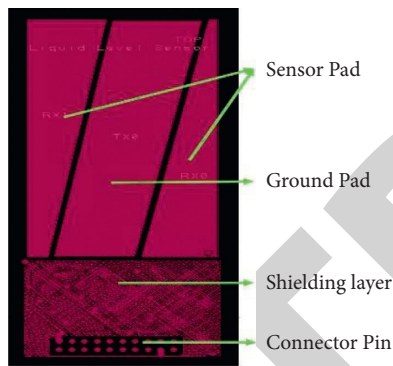


FIGURE 10: Sensor pattern.

TABLE 2: Dielectric constants of insulation materials.

PCB material	FR4
Thickness	0.4 mm
Type of pouring	Copper
Dimensions	100 * 50 mm
Connector type	Berg stick

programmable embedded system on chip, integrating custom analog and digital peripheral functions, memory, and an Arm Cortex-M0 microcontroller on a single chip. Figure 15 demonstrates the usage procedure and estimation. The personal computer (PC) is associated with the PSoC development board, PSoC creator 4.1, and Tera Term Terminal. The PC with the PSoC 4 microcontroller (PSoC 4200M) dev platform uses the PSoC debugger connected to USB interface. The test code is transferred to the microcontroller unit (MCU) by the PSoC Creator 4.1. The information from the MCU is displayed in Tera Term window at serial communication (COM2) port. The sensor is placed on a nonconductive surface in association with the PSoC 4200M

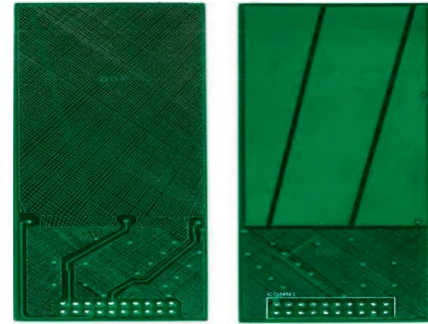


FIGURE 11: Fabricated PCB.

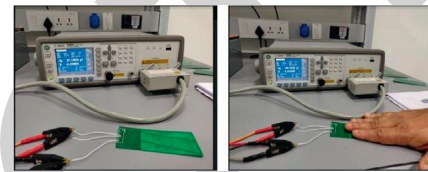


FIGURE 12: Capacitance measurement by the LCR meter.

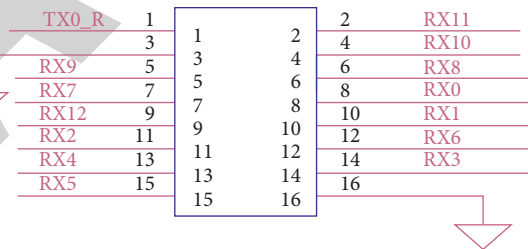


FIGURE 13: Connector layout of sensor.

development board, which utilizes a berg stick connector on another small interfacing board. The estimation results perused at various levels of the Department of Transportation (DOT4) type brake liquid segment from the base: zero levels with the base unfilled, 10 mm (similar tallness of the reflected light (RL) sensor), 15 mm, and 20 mm. The dimension is estimated at most extreme 70 mm.

5. Result and Discussion

The oscillator block provides the reference frequency for capacitance detection. Figures 16 and 17 show the tuner widget view and tuner graph, respectively. A simulation is carried out to sense the capacitance ranging from 10pF to 50 pF in the step size of 10 pF. Figure 18 shows the oscillator frequency. Figures 19–21 show the CapSense-simulation. As the frequency varies with capacitance, the current across the sense resistor also varies. Figure 19 shows the current sense-capacitance variation from 10 pF to 50 pF. The sensed current is fed to the sigma-delta converter of PSoC. The behavior of capacitance vs. current is analyzed implementing a hardware rectifier and filter. It will rectify the frequency output of the current sense to the direct current

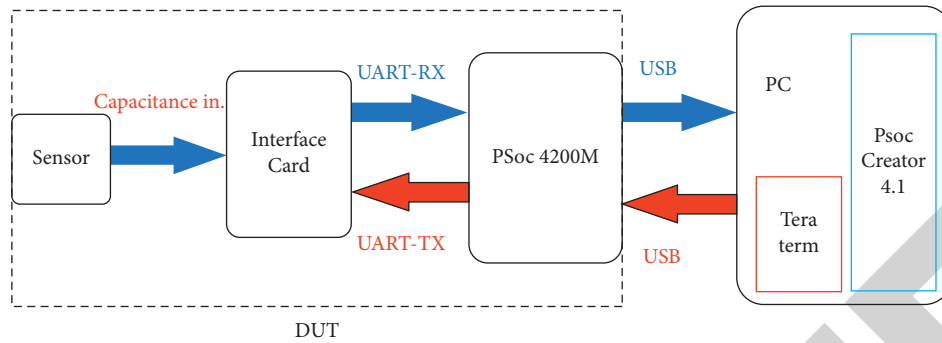


FIGURE 14: Measurement diagram for the fluid level system.

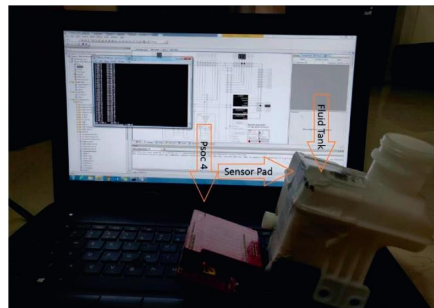


FIGURE 15: Device under-test-measurement setup.

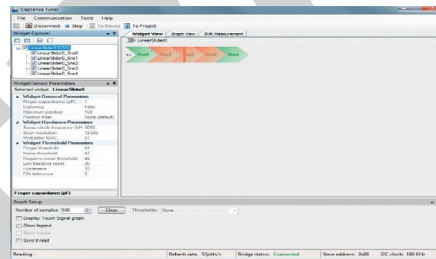


FIGURE 16: Tuner widget view.

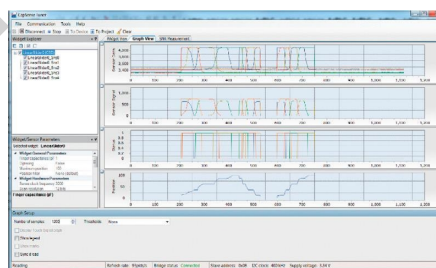


FIGURE 17: Tuner graph view.

(DC) component. Figure 20 shows the output voltage after rectification of the concerned current. This voltage values can be directly fed to any microcontroller using analog-to-digital converters (ADCs) of higher resolution. Figure 21 shows the rectification based on the peak voltage.

The PSoC 4 development board is configured for capacitance measurement. The measured capacitance values are read directly from the PSoC 4 board by using the Tera

Term Terminal. The PSoC development board measures the difference in capacitance between the two sensor pads as raw counts. The change in parasitic capacitance of the sensor is avoided through proper shielding employed on the sensor. Figure 22 shows the linearity of the sensor. The measured capacitance values are read directly from the PSoC 4 board by using Tera Term terminal. The level capacitance is increased with the increase in the fluid level from bottom of the

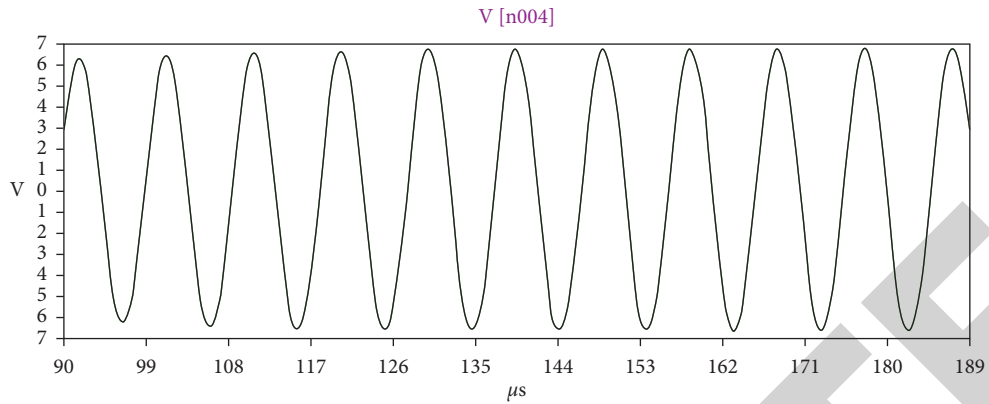


FIGURE 18: Oscillator frequency output-100 kHz.

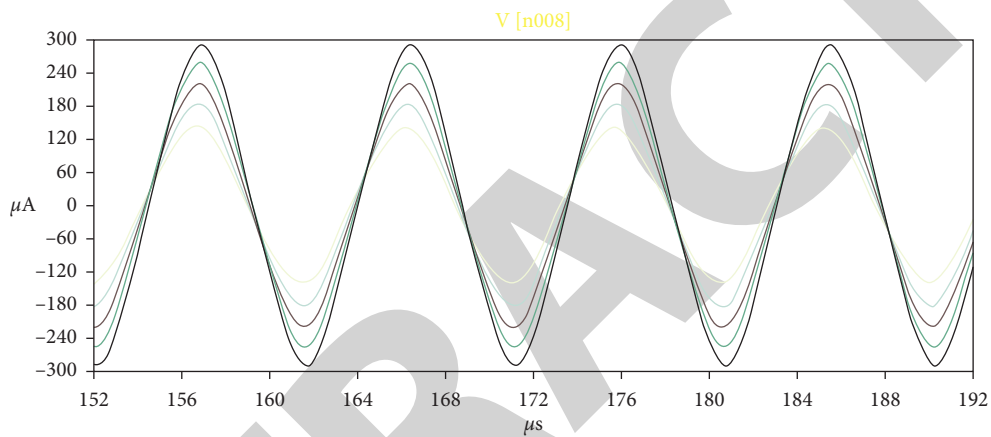


FIGURE 19: Current sense-capacitance varied from 10 pF to 50 pF.

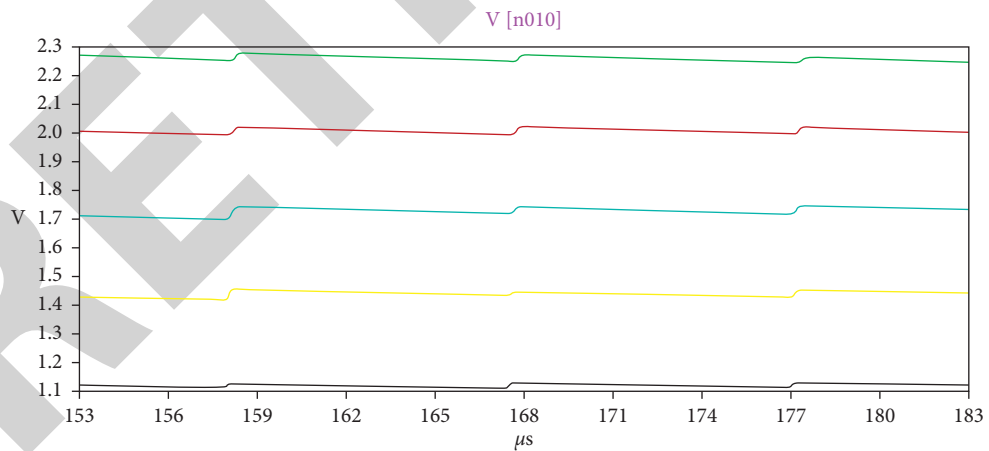


FIGURE 20: Current to rectified voltage output.

tank. The prominent change in parasitic capacitance of the sensor is eliminated by having proper shielding employed on the sensor. The solution for reducing the temperature effects on the capacitance is attained by designing the sensor based on Flexi PCB and maintains minimum connection length as possible. Level sensors are spearheaded in checking the fluid level in tanks and are utilized in numerous applications. The development model of a distant capacitive-type level sensor

is a low cost measurement method and can be deployed with different types of liquids. The model is used for both conductive and nonconductive liquid-level measurement. The model may be used in several applications because of its structure strategy and process approach. The applications are proximity detection, touch buttons, irrigation, bio-medical area, pharmaceutical industry, and automation application. The proposed capacitive sort sensor is

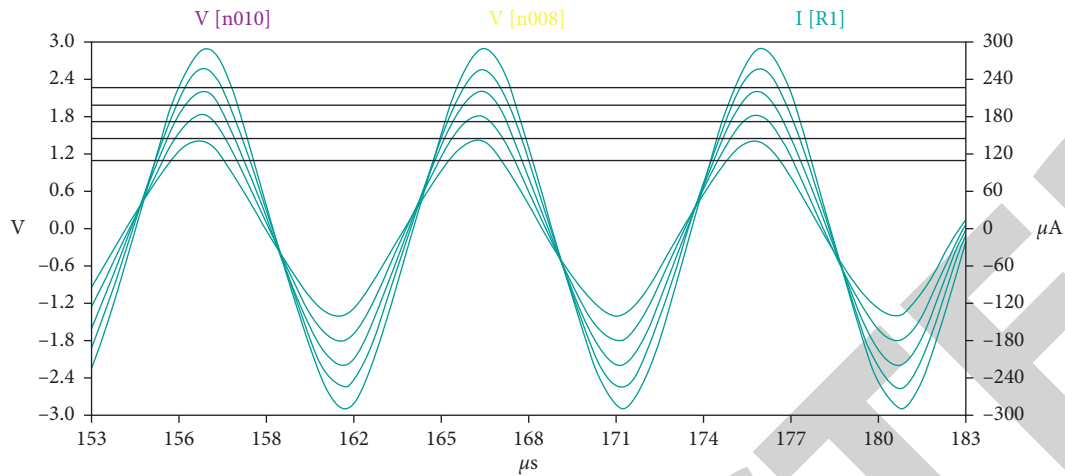


FIGURE 21: Rectification based on the peak voltage.

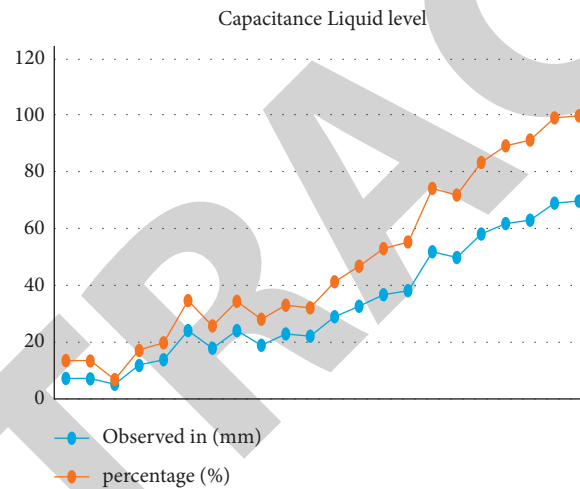


FIGURE 22: Sensor linearity.

TABLE 3: Measurements at various temperatures.

Temperature in degree	Fluid level (brake fluid)			
	Observed (mm) @40 mm	Observed (mm) @50 mm	Observed (mm) @60 mm	Observed (mm) @70 mm
0	0	27.8	27.8	13.9
5	13.7	41.7	55.6	55.6
10	27.8	48.6	62.5	62.5
20	34.7	48.6	62.5	76.4
22.81	34.7	48.6	62.5	76.4
30	34.7	48.6	62.5	76.4

manufactured utilizing generally accessible multilayer PCB. In this manner, the generation cost and the related interfacing electronic circuits are nearly less.

5.1. *Temperature Tests.* One of the main complexities for designing the sensor is to compensate for the temperature and humidity effects. The sensor is made using two coplanar

sensor pads and a ground pad in between and to take the resultant capacitance difference. So, the sensor ability is verified through the temperature tests performed (0°C to 60°C—limitation in temperature due to the development board thresholds), and the results are shown in Table 3. Figure 23 shows the temperature and fluid level. As the temperature increased, the fluid level increased, and above 20°C, the fluid level gets saturated with respect to

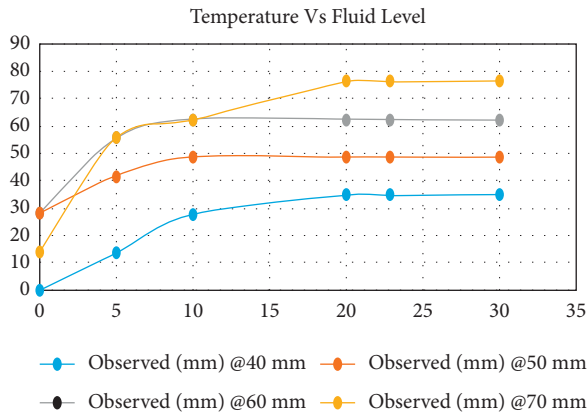


FIGURE 23: Temperature vs. fluid level.

temperature. The solution to reduce the temperature effects on the capacitance is by designing the sensor based on flexi PCB and maintaining minimum connection length as possible.

6. Conclusion

Capacitive-type sensors are essential for monitoring the level of the liquid. In this paper, development of a capacitive-type linear slider and a capacitive-type touch and noncontact sensor has been demonstrated using PSoC development kit which has inbuilt CapSense component for capacitance measurement and EZI2C/UART for communication to PC. The performance of the capacitive sensor design improves the reliability. The reliability is enhanced due to the decrease in corrosion of metallic electrodes due to noncontact with the fluid. The performance of the proposed sensor on the development board for touch and proximity has been experimentally evaluated. The proposed methodology includes liquid-level sensor development, interfacing the sensor to a digital data-acquisition system and testing.

Data Availability

The data used to support the findings of this study are included within the article.

Conflicts of Interest

The authors declare that there are no conflicts of interest.

References

- [1] E. P. Wigner, "Theory of traveling-wave optical laser," *Physical Review*, vol. 134, pp. A635–A646, Dec. 1965.
- [2] H. Kurss and W. Kahn, "A note on reflector arrays," *IEEE Transactions on Antennas and Propagation*, vol. 15, no. 5, pp. 692–693, Sep 1967.
- [3] J. H. Davis and J. R. Cogdell, "Calibration program for the 16-foot Antenna," Elect. Eng. Res. Lab., Univ. Texas, Austin, TX, USA, Tech. Memo. NGL-006-69-3, 1987.
- [4] E. E. Reber, R. L. Michell, and C. J. Carter, "Oxygen absorption in the Earth's atmosphere," pp. 4230–4246, Aerospace Corp, Los Angeles, CA, USA, Tech. Rep. TR-0200, 1988.
- [5] Western Electric Co., *Transmission Systems for Communications*, pp. 44–60, Western Electric Co., Winston-Salem, NC, USA, 3rd edition, 1985.
- [6] W. J. Fleming, "Overview of automotive sensors," *IEEE Sensors Journal*, vol. 1, no. 4, pp. 296–308, 2001.
- [7] S. C. Bera, J. K. Ray, and S. Chattopadhyay, "A Low-Cost Noncontact Capacitance-Type Level Transducer for a Conducting Liquid," *IEEE Transactions on Instrumentation and Measurement*, vol. 55, no. 3, pp. 778–786, 2006.
- [8] B. Yun, N. Chen, and Y. Cui, "Highly Sensitive Liquid-Level Sensor Based on Etched Fiber Bragg Grating," *IEEE Photonics Technology Letters*, vol. 19, no. 21, pp. 1747–1749, 2007.
- [9] F. Reverter, X. Li, and G. C. M. Meijer, "Liquid-level measurement system based on a remote grounded capacitive sensor," *Sensors and Actuators A: Physical*, vol. 138, no. 1, pp. 1–8, 2007.
- [10] A. Ernst, W. Streule, N. Schmitt, R. Zengerle, and P. Koltay, "A capacitive sensor for non-contact nanoliter droplet detection," *Sensors and Actuators A: Physical*, vol. 153, no. 1, pp. 57–63, 2009.
- [11] E. Terzic, R. Nagarajah, and M. Alamgir, "A neural network approach to fluid level measurement in dynamic environments using a single capacitive sensor," *Sensors & Transducers*, vol. 114, no. 3, pp. 41–55, 2010.
- [12] J. L. Mazher Iqbal and S. Varadarajan, "A New Algorithm for FIR Digital Filter Synthesis for a Set of Fixed Coefficients," *European Journal of Scientific Research, EJSR*, vol. 59, no. 1, pp. 104–114, 2011.
- [13] J. L. Mazher Iqbal and S. Varadarajan, "Performance Comparison of Reconfigurable Low Complexity FIR Filter Architectures," in *Communications in Computer and Information Science*, vol. 250, pp. 844–849, Springer-Verlag, Berlin, Germany, 2011.
- [14] J. L. Mazher Iqbal and S. Varadarajan, "High Performance Reconfigurable FIR Filter Architecture Using Optimized Multiplier," *Circuits, Systems, and Signal Processing*, vol. 32, no. 2, pp. 663–682, 2013.
- [15] J. L. Mazher Iqbal and S. Varadarajan, "Memory Based and Memory Less Computation for Low complexity Reconfigurable Digital FIR filter," *WSEAS Transactions on Systems*, vol. 12, no. 3, pp. 142–153, 2013.
- [16] J. L. Mazher Iqbal and T. Manikandan, "FPGA-Based Reconfigurable Architectures for DSP Computations," *Advances in Intelligent Systems and Computing*, vol. 1163, pp. 587–594, August 2020.
- [17] L. Vracar, A. Prijic, D. Vuckovic, and Z. Prijic, "Capacitive Pressure Sensing Based Key in PCB Technology for Industrial Applications," *IEEE Sensors Journal*, vol. 12, no. 5, pp. 1496–1503, 2012.
- [18] X. Zhang, W. Peng, Z. Liu, and Z. Gong, "Fiber Optic Liquid Level Sensor Based on Integration of Lever Principle and Optical Interferometry," *IEEE Photonics Journal*, vol. 6, no. 2, pp. 1–7, April 2014.
- [19] S. C. Bera, H. Mandal, S. Saha, and A. Dutta, "Study of a Modified Capacitance-Type Level Transducer for Any Type of Liquid," *IEEE Transactions on Instrumentation and Measurement*, vol. 63, no. 3, pp. 641–649, 2014.
- [20] K. Chetpattananondh, T. Tapoanoi and P. Phukpattaranont, N. Jindapetch, "A self-calibration water level measurement using an interdigital capacitive sensor," *Sensors and Actuators A: Physical*, vol. 209, pp. 175–182, 2014.

Retraction

Retracted: Development of Novel Nano-Silver-Based Antenna for Green Agriculture

Advances in Materials Science and Engineering

Received 26 December 2023; Accepted 26 December 2023; Published 29 December 2023

Copyright © 2023 Advances in Materials Science and Engineering. This is an open access article distributed under the Creative Commons Attribution License, which permits unrestricted use, distribution, and reproduction in any medium, provided the original work is properly cited.

This article has been retracted by Hindawi, as publisher, following an investigation undertaken by the publisher [1]. This investigation has uncovered evidence of systematic manipulation of the publication and peer-review process. We cannot, therefore, vouch for the reliability or integrity of this article.

Please note that this notice is intended solely to alert readers that the peer-review process of this article has been compromised.

Wiley and Hindawi regret that the usual quality checks did not identify these issues before publication and have since put additional measures in place to safeguard research integrity.

We wish to credit our Research Integrity and Research Publishing teams and anonymous and named external researchers and research integrity experts for contributing to this investigation.

The corresponding author, as the representative of all authors, has been given the opportunity to register their agreement or disagreement to this retraction. We have kept a record of any response received.

References

- [1] S. D., V. R., R. A., B. S., M. A., and K. Sahile, "Development of Novel Nano-Silver-Based Antenna for Green Agriculture," *Advances in Materials Science and Engineering*, vol. 2021, Article ID 9065960, 9 pages, 2021.

Research Article

Development of Novel Nano-Silver-Based Antenna for Green Agriculture

Subitha D. ¹, Vani R. ², Raja A. ³, Balasubramani S. ⁴, Manjunathan A. ⁵,
and Kibebe Sahile ⁶

¹Department of Electronics and Communication Engineering,
Vel Tech Rangarajan Dr. Sagunthala R&D Institute of Science and Technology, Chennai, India

²Department of ECE, SRM Institute of Science and Technology, Ramapuram, Chennai, India

³Department of ECE, Saveetha School of Engineering, SIMATS, Chennai, India

⁴Department of ECE, R. M. D. Engineering College, Chennai, India

⁵Department of ECE, K. Ramakrishnan College of Technology, Trichy, India

⁶Department of Chemical Engineering, College of Biological and Chemical Engineering,
Addis Ababa Science and Technology University, Addis Ababa, Ethiopia

Correspondence should be addressed to Kibebe Sahile; kibebe.sahile@aastu.edu.et

Received 1 July 2021; Accepted 12 August 2021; Published 28 September 2021

Academic Editor: Samson Jerold Samuel Chelladurai

Copyright © 2021 Subitha D. et al. This is an open access article distributed under the Creative Commons Attribution License, which permits unrestricted use, distribution, and reproduction in any medium, provided the original work is properly cited.

The designed antenna is a monopole Z-shaped antenna operating in an unlicensed band of 2.4 GHz fabricated using low cost inkjet printing technology. The proposed inkjet printing technology is eco-friendly since the material used here is an ordinary “paper” that is suitable for the green technology. The conducting patch of silver nanoparticle (AgNP) ink has very high conductivity 35,700,000 S/m and instant curing property which helps in fabrication process without UV curing or oven heating. The printer used also is the cheap home printer HP DJ 2130 rather than the expensive Brother and Epson printers used in previous works. The printed antenna will be helpful in conditions to ascertain its performance in green agriculture in the form of RF-ID sensors, soil pH value sensor, and moisture sensor. The proposed antenna attains the gain of 2.5 dBi at the ISM band of 2.4 GHz with optimal VSWR value between 1 and 2 over the desired frequency band. The directivity and radiation efficiency of the proposed antenna are 2 dBi and 80%, respectively. The overall cost of the proposed antenna is much lesser in the order of 10 times than the recent low cost design.

1. Introduction

Green agriculture is the revolution of Indian agriculture that addresses the problems such as land pollution, biodiversity, and climate change. The land preservation can be done by controlling the addition of pollutants into the soil. Fertilizers, nonbiodegradable waste, and e-waste are the causes of land pollution. The quality and quantity of such pollutants need to be measured for the upgradation of soil property. In our country, for strengthening the high biodiversity areas, the transformation of agricultural systems is highly essential. To catalyze transformation in agricultural sector, more concentration towards the sustainable

landscape management is needed. Land is a vital resource to humankind, like air and water. Land degradation is the deterioration or loss of the productive capacity of the soils for the present and future. This is a global challenge that affects everyone through food insecurity, higher food prices, climate change, environmental hazards, and the loss of biodiversity and ecosystem services. Land pollution is happening at an alarming pace, contributing to a dramatic decline in the productivity of croplands and rangelands worldwide [1–3]. Hence, rapid remedial action is essential for developing green agriculture system in our country. Hence, an array of antennas that acts as a sensor for measuring various on-field parameters of the agricultural

land is required to facilitate the easiness and readiness of farmers before cultivation. The proposed irrigation antenna module serves as a means of supporting the farmers by monitoring soil qualities such as chemical property (pH value, organic content), fertility, moisture, and environmental properties such as rainfall, humidity, temperature, and motion. Irrigation antennas can be deployed with leafs, automatic sprinkler systems, and pumps and in cultivation machines. Wireless sensors need to be deployed over the fields to enable farmers for easy monitoring of the current field status and prediction of the crop status. The deployment of wireless antenna modules which serve as sensors of various environmental and chemical parameters help in eliminating long runs of copper cables around the farms which are unsafe, difficult to implement, and costly [4, 5].

The technology more suitable here for developing the agricultural network antenna is the inkjet printing technology which is highly economic and supports mass production. Inkjet printing is a technology that is used mainly in pattern making. This method is widely accepted for variety of applications as it is highly environment friendly, cheap, and flexible [6–9] with all kinds of substrates such as paper, silicon, and mica sheets. The usual process of antenna fabrication involves masking and etching operations which are both time and cost consuming. But, this printing technology is a direct writing method that jets the conductive ink droplets directly on the substrates using an ordinary office printer. The inkjet printing methodologies for printing a Z-shaped monopole CPW fed antenna is being discussed here.

Inkjet printed Z-shaped CPW monopole antenna is designed at the frequency of 904.5 MHz in [6] using Dimatix DMP-2800 Series printer by jetting silver nanoink on ordinary paper substrate. There are many reasons for choosing paper as the substrate as it is an excellent candidate at low cost for RF-ID and RF applications [10, 11]. In the work of [12], the similar monopole CPW Z-shaped antenna is designed at 1.57 GHz on glossy paper using silver nanoink of viscosity 2.30 mPa s and surface tension of 32 mN/m. The printer used in this work is Fujifilm Dimatix 2800 and offers maximum gain of 1.67 dB. In the above two works, the printed antenna requires postsynthesis annealing for higher conductivity of nanoink. One another drawback of the above works is that the printer used for the designs are very expensive in the order of ₹20,00,000. The recently proposed antenna design in [13, 14], printed on PET substrate at the ISM band of 2.4 GHz, is curing free and also uses much cheaper office printer in comparison with the Dimatix printer used in the earlier works. The previous works on inkjet printed antennas made prints with expensive Brother and Epson printers [15]. These printers are equipped with special, detachable ink tanks of huge storage capacity that requires more ink to be filled that makes the process costlier.

The objective of the proposed work is to design the printable antenna using much cheaper printer preferable to be used with low quantity of ink. The printer used in the proposed design is cheaper than the recent low-cost office

printer used in [16] and also the printer head is thermal, whereas the printer head used in other previous literatures used much expensive piezo-electric head printers. Moreover, the proposed printing design uses nanoink whose conductivity is in the order of 3.57×10^7 S/m that is nearly 4 times higher than the silver NP (nanoparticle) ink used in the recent work [13]. The AgNP used here has the instant curing capacity that avoids the sintering/annealing process. Thus, the curing-free, low-cost AgNP ink suitable for thermal head-based highly inexpensive HP home printer-based design methodology is explained in this paper.

The remainder of this paper is organized as follows: Section 2 discusses on the design of monopole antenna element and its validation in CST-MWS tool, Section 3 focuses the fabrication of this antenna in eco-friendly inkjet printing process, and the scope of this antenna in green agriculture is presented in Section 4.

2. Design of Z-Shaped Monopole Microstrip Patch Antenna

Microstrip patch antenna is the popular printed antenna that plays a significant role in all applications due to its ease of fabrication, low cost, and flexibility with other circuit elements [17]. The compact patch antenna consists of a conductive plate over the substrate of dielectric. This is highly preferred over the other antennas specifically for wireless applications due to its compact planar structure that can be easily fixed over leaf or stem or conformal over the surface of any object. The shape and dimension of the antenna decide the frequency of operation of the antenna.

The performances of the antenna such as wider bandwidth, higher resolution, and better radiation are all enhanced by choosing substrates with low dielectric constant (less than 6) that leads to larger antenna dimension. Hence, another easy way of enhancing the antenna performance is inserting slots to perturb the flow of current. This current perturbation helps to increase the BW in comparison with the conventional patch by diverting the current direction. The following section explains the design steps of the Z-shaped microstrip patch antenna as pointed out in [18]. Figure 1 depicts the configuration of the Z-shaped patch antenna element. The dimensions of the above design are calculated in accordance with the centre of frequency (f_0) and hence the wavelength (λ_0). The patch which is rectangular in shape has the width (W) and length (L) as the major dimensions. This is according to software description. Two slot lengths are approximately equal to width of the patch (w) and placed symmetrically in the XY plane from the patch radiator with slot width L_1 . Initially, the length L and width W of the patch radiator having substrate of dielectric constant ϵ_r and thickness h are calculated as given in the steps below. These steps involve the calculation width (W), effective dielectric constant (ϵ_{reff}), and change in dimension (∇L) due to the fringing effects between the patch and the substrate.

Step 1: calculation of width is done using the following equation:

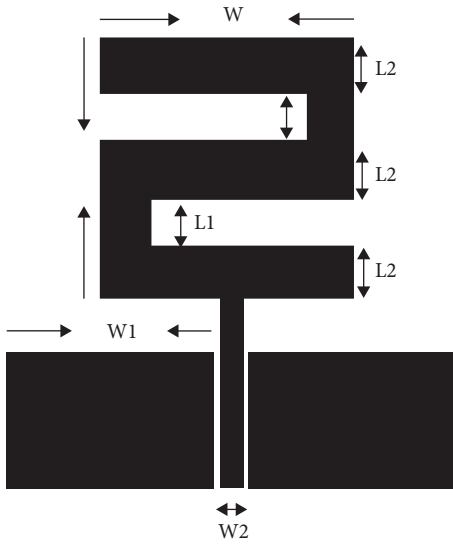


FIGURE 1: Configuration of Z-shaped microstrip patch antenna.

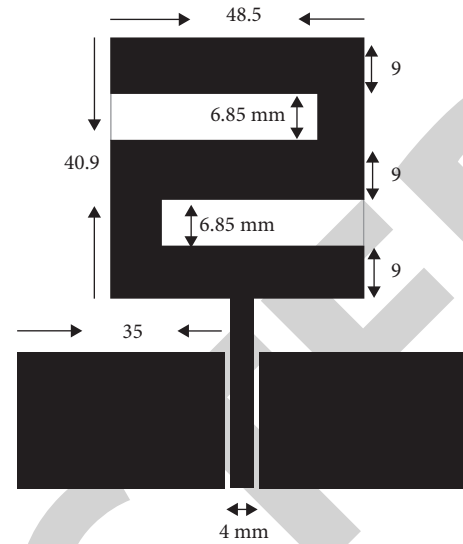


FIGURE 2: CPW monopole element design.

$$W = \frac{c}{2f_0} \left(\sqrt{\frac{2}{1 + \epsilon_r}} \right), \quad (1)$$

where ϵ_r is the dielectric constant of the substrate and c is the velocity of EM wave in free space (3×10^8).

Step 2: calculation of effective dielectric constant is by using the following equation:

$$\epsilon_{\text{reff}} = \frac{1 + \epsilon_r}{2} + \frac{\epsilon_r - 1}{2} \left(1 + 12 \frac{h}{W} \right)^{-(1/2)}. \quad (2)$$

Step 3: calculation of change in dimension is indicated as in the following equation:

$$\nabla L = 0.412h \frac{(\epsilon_{\text{reff}} + 0.3)((W/h) + 0.26)}{(\epsilon_{\text{reff}} - 0.26)((W/h) + 0.8)}. \quad (3)$$

Step 4: calculation of length of the patch is as defined in the following equation:

$$L = \frac{c}{2f_0 \sqrt{\epsilon_{\text{reff}}}} - 2\nabla L. \quad (4)$$

For our proposed antenna element chosen with the ordinary “paper” as the substrate having dielectric constant = 2.31, operating at the frequency of $f_0 = 2.4$ GHz, the dimensions calculated using equations (1)–(4) are given in Figure 2, so as to insert two slotted sections symmetrically with respect to the centre, the thickness of the Z-element is chosen as $L_2 = 9$ mm and $L_1 = 6.85$ mm such that the total length $3L_2 + 2L_1 = L = 40.9$ mm. Figure 3 shows the design of Z-shaped microstrip patch antenna using Ansys HFSS antenna design tool with the theoretical calculations obtained above. Figure 4 shows the reflection coefficient of the proposed design with simulation and experimental results that almost match. The obtained results show that they are well below the required threshold of -10 dB at the operating

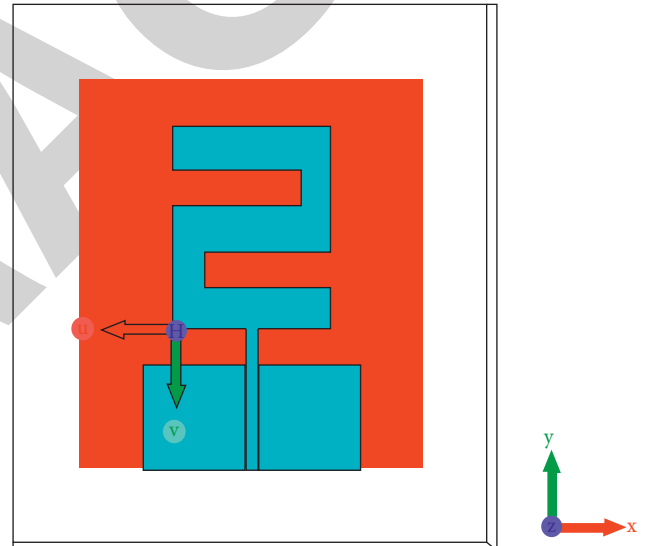


FIGURE 3: Z-shaped monopole element design using Antenna Design tool.

frequency of 2.4 GHz. This is the unlicensed frequency band typically used for the agricultural applications worldwide. Figure 5 shows the VSWR characteristics of the designed antenna and is attaining the optimal value in the band of interest. Figures 6 and 7 show the directivity and gain of 3 D plots that show the gain and directivity of 2 dBi and 2.5 dBi, respectively.

3. Inkjet Printing of Monopole Microstrip Patch Antenna

The inkjet printing is the extremely inexpensive, direct writing method that jets the ink droplets directly on the substrates. The substrate chosen for the antenna must be compatible with the printer and the ink used to fabricate the radiator patch on the chosen substrate must be flow-free

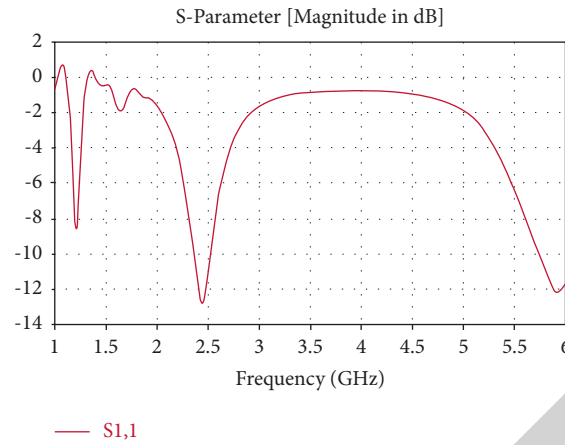


FIGURE 4: Reflection coefficient of the proposed design.

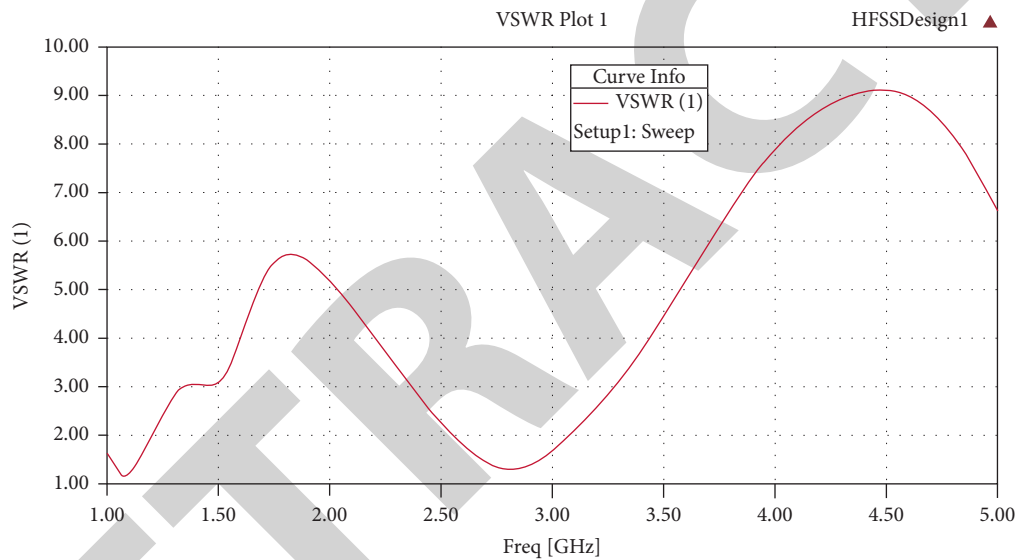


FIGURE 5: VSWR coefficient of the proposed design.

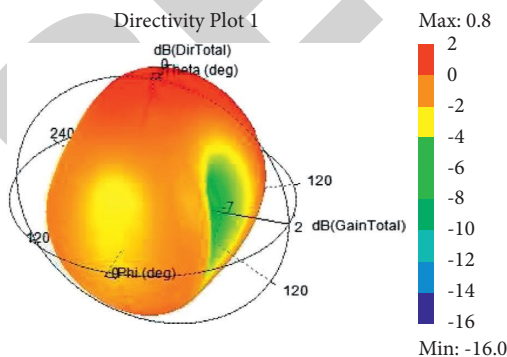


FIGURE 6: Directivity plot of the proposed design.

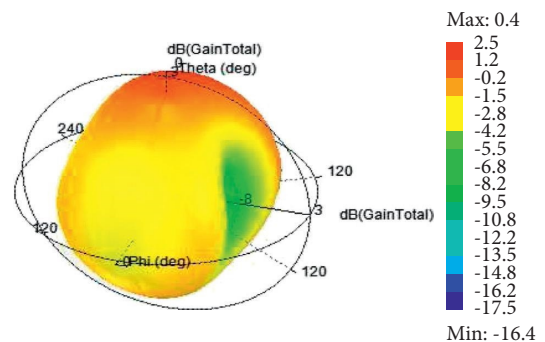


FIGURE 7: Gain plot of the proposed design.

from the printer nozzle. Hence, the selection of printer that suits for the substrate and the ink plays a major role in this inkjet printing technology. The proposed design uses only commercially available desktop inkjet printer that can be operated by refilling the single black and white cartridge.

After taking the printouts, the printed antenna needs to undergo the curing process in order to raise the conductivity of the radiator patch to a specific value. Traditional methods of curing involve oven heating, exposure to UV, etc. But, the ink used in the proposed technique requires no curing since

it supports instant curing which is the additional benefit of this work.

Hence, the principal parameters that decide the quality of fabrication in inkjet printing are the substrate properties such as thickness and dielectric constant, resistivity of conductive ink, printer cost, and challenges in curing process as shown in Table 1. The process of inkjet printing of the designed monopole antenna is briefed in the upcoming Sections 3.1 and 3.2.

3.1. Proposed Low-Cost Inkjet Printing. This section explains the process of the proposed low-cost inkjet printing for the antenna fabrication. The proposed design makes use of relatively inexpensive ordinary “paper” as substrate and curing-free “silver nanoparticle ink” as the conductive ink. In order to take the printouts, initially the cartridge HP 302 shown in Figure 8 is filled with the nanoparticle ink using the syringe. The printer used in the proposed fabrication process is the readily available, extremely low-cost, thermal head-based HP printer.

The work [15] demonstrates various examples of inkjet printed antennas fabricated by using conductive silver ink on photograph paper substrates. The printed antenna design proposed in this paper makes use of curing-free “silver nanoink.” The substrate used is the commercially available, low-cost, ordinary “paper” as the substrate material. The A4 size “paper” of 75 GSM having average thickness of approximately 0.1 mm is preferred. But, the earlier works on inkjet printed antenna used comparatively costlier dielectric materials like mica sheets and glossy papers as the substrates. Hence, the material chosen in the proposed design costs very low of less than ₹0.50 per paper and compatible with all types of printers as the thickness of the paper is also very less (<0.1 mm). The glossy paper can be used in place of “ordinary paper” as substrate to improve the durability of substrate.

The conductive ink used for fabricating the patch radiator is the silver nanoparticle ink NS6130-10-1300-Ag, 99.9%, APS (average particle size) 30–100 nm. The ink is the silver nanoparticle ink of viscosity of 8 Cp and surface tension of minimum 30 dyne/cm that helps to control the ejection of ink droplets from the nozzle. Selection of proper sintering process is the bottleneck of nanoink as mentioned in [17, 19]. One of the main reasons for selecting the nanoparticle-based ink is the possibility of sintering at extremely low temperatures and resistivity against oxidation. Hence, this ink is suitable for printers with thermal heads (HP printers) as they easily melt at low temperature compared to bulk inks. This avoids the use of expensive printers with piezo-electric heads (Brother and Epson printers) which are used in the literatures [10, 20, 21]. Another property of the ink is the resistivity against oxidation that helps to prevent the ink being clogged in the printer heads. Hence, this ink is more suitable for printers with thermal heads (HP printers) as they easily melt at low temperature compared to bulk inks. This ink is also suitable for all types of printers, but the ink used in previous literatures used only printers with piezo-electric heads which are expensive Brother and Epson printers.

TABLE 1: Properties of ink and substrate.

"Ink" properties	
Viscosity	8 Cp
Surface tension	35 mn/m
Conductivity	35,700,000 s/m
Linear formula	Ag
Molecular weight	107.87 g/mol
Storage temperature	2–8°C
Thermal expansion	$18.9 \mu\text{m}\cdot\text{m}^{-1}\cdot\text{k}^{-1}$ (25°C)
Particle size	30–100 nm
Surface tension	30–32 dyne/cm
Density	1.22 g/mL at 25°C
Boiling point	2162°C
Young's modulus	83 GPa
Bulk density	0.312 g/cm ³
Solvent	Water-based or organic
"Substrate" properties	
Relative permittivity	4.01
Loss tangent	0.07
Dielectric constant	2.31
Thickness	0.1 mm



FIGURE 8: HP 302 cartridge filled with nanoparticle ink NS6130-10-1300 using ordinary medical syringe.

The previous works on inkjet printed antennas made prints with expensive Brother and Epson printers. These printers are equipped with special, detachable ink tanks that are refillable using the preferable conductive inks. But, the drawback of this ink tank attached printers are that they need huge quantity of ink to fill the tanks and so large amount of conductive inks are required (minimum of 25 mL in each of the three cartridges). Another drawback of these printers is the difficulty of reusing the ink after some time as the inks get clogged with the printer heads, spoiling the whole printer system. The printer used in the proposed design is the much cheaper, readily available one that uses single BW cartridge that occupies only a minimal ink quantity (less than 10 mL). The printer used for printing is HP DJ 2130 series printer that uses easily refillable cartridges.



FIGURE 9: Printing of Z-shaped monopole antenna on paper using HP DJ 3120 printer.

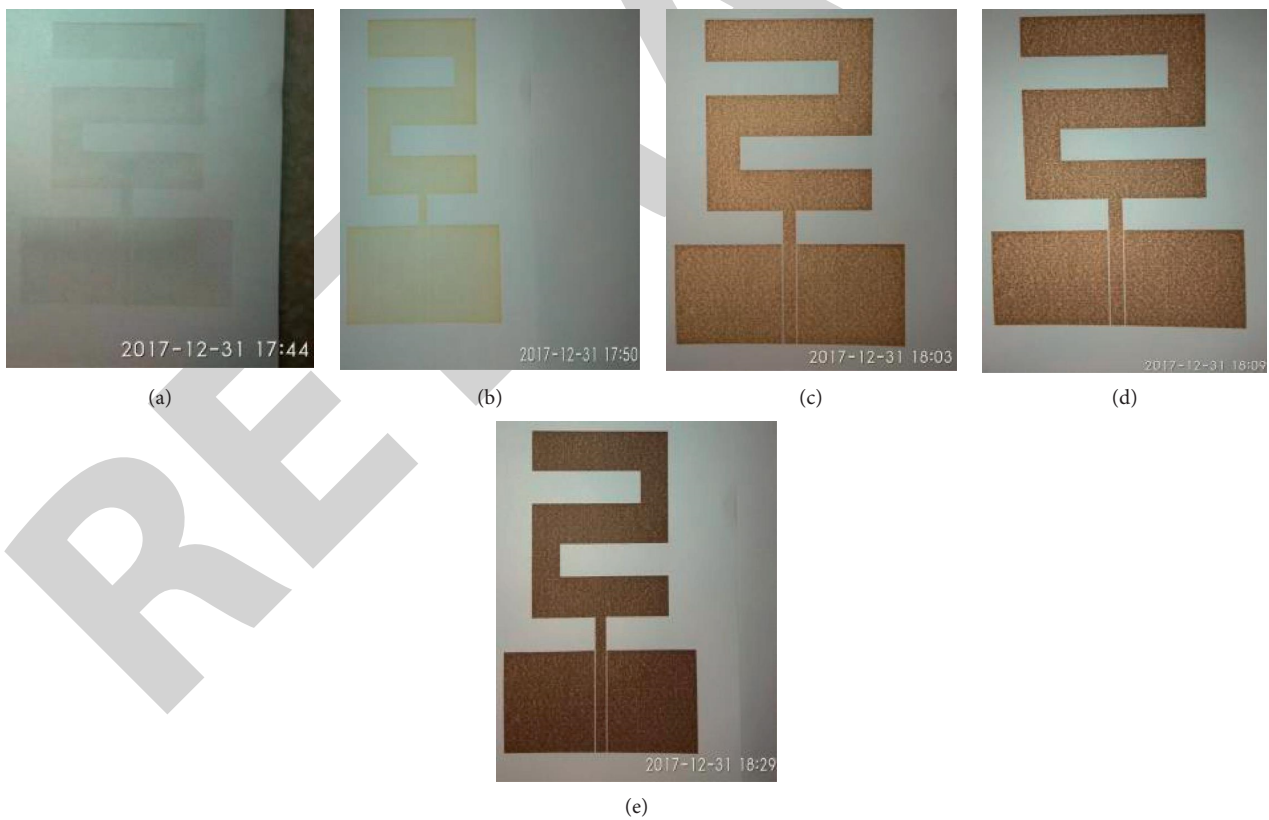


FIGURE 10: Curing of inkjet printing antenna at different time instants: (a) at time 17.44, (b) at time 17.50, (c) at time 18.03, (d) at time 18.09, and (e) at time 18.29.

TABLE 2: Conductivity Vs time of AgNP at room temperature.

Time (msecs)	Resistance (ohms/cm)
0	10 M
5	9
10	5
15	4.2
25	3.9
40	2.1
45	2

TABLE 3: Comparison of the proposed design and the recent works.

Parameters	[6]	[12]	[13]	[15]	Proposed design
Printer used	Dimatix printer 2800 series	Dimatix printer 2800 series	Office printer	Epson C88+	HP DJ 2130 printer
Printer head	Piezo-electric	Piezo-electric	Piezo-electric	Piezo-electric	Thermal head
Cost of the printer	Very expensive ₹20,00,000	Very expensive ₹20,00,000	Cheap ₹42,000	Expensive ₹1,00,000	Very cheap ₹3,000
Resonant frequency	904.5 MHz	1.57 GHz	2.45 GHz	—	2.4 GHz
Conductivity of ink	4×10^6 S/m	1.6×10^6 S/m	1.11×10^7 S/m	—	3.57×10^7 S/m
Substrate used	Normal paper	Glossy paper	PET	Photo paper	Normal paper
Cost of the ink	Expensive >70000	Expensive >70000	Cheap <30000	—	Cheap <3000
Postprocessing	Annealing processes for 10 hrs in an expensive industrial oven heating	Annealing processes for 4 hrs in an expensive industrial oven heating	Not required	Annealing processes for 90 mins in a commercial oven heating	Not required
Preheating	Heating vacuumed platen up to 60°C	Heating vacuumed platen up to 60°C	Not required	Not required	Not required
Annealing temperature	100	180	Not required	160°C–170°C	Not required
Gain	—	1.67 dB	1.44 dBi	—	2 dBi

The cost of this printer is not more than ₹3000 along with the use-and-throw cartridges. Figure 8 shows the ordinary medical syringe used for filling up the single BW cartridge of the HP DJ 2130 printer. The printing process is depicted in Figure 9.

3.2. Design Steps of Antenna Fabrication Using Inkjet Printing.

The fabrication of antenna using a readily available paper, curing-free silver nanoink, and cheap office printer is summarized as follows:

- (i) Antenna design is simulated using CST-MWS tool. The simulated designs are converted to Gerber file format.
- (ii) HP DJ 2130 printer is connected to the computer where the designs are stored in Gerber file format.
- (iii) The HP 302 BW cartridge compatible with the abovementioned printer needs to be empty with no more ink left inside.
- (iv) The syringe is first filled with the silver nanoparticle ink NS6130-10-1300.
- (v) Using the syringe, the cartridge is injected with 10 mL of ink.
- (vi) The JK Copier 75 GSM A4 size paper is fed in the input tray of the printer. In the printer settings, the “paper type” is chosen as “Plain paper.”
- (vii) After taking the prints, the print heads are cleaned with alcoholic wipes to avoid clogging of ink over the print heads. This prevents the cartridges getting damaged due to ink deposition.
- (viii) Once the process is completed, the cartridge is removed and stored in the refrigerators if the ink is left over. If this is not done, the chemical property of the ink may change. This is due to the reaction between the thermal head of the HP printer and the ink.
- (ix) The final step of fabrication is the curing process due to which the resistivity of the patch radiator decreases. The ink chosen here does not require separate curing process and hence by simply keeping the antenna at room temperature of around 28°C obtains the maximum conductivity in 45 minutes.
- (x) This curing process can be accelerated and maximum conductivity is reached in less than 5 minutes time if the printed design is exposed to sunlight (around 30–34°C).

- (xi) The cured antenna samples are connected with SMA connector by simply applying physical pressure and then the characteristics are measured using network analyzer.

3.3. Curing of Inkjet Printing. Curing is the final stage of antenna fabrication in inkjet printing technology. Curing process helps to increase the conductivity of the patch since thermal agitation mobilizes the electrons present in the heated patch radiator. Curing also removes excess solvent and provides uniformity by providing connectivity between the particles. In the process of curing, the uniformity is increased which plays a major role in inkjet printing. Traditional curing method used in the previous literature [15] used commercially available ovens to heat the printed antennas for about 90 minutes.

The resistance of the printed element is in the order of few k Ω s immediately after printing, whereas it reduces to the order of few Ω s after curing. The time and temperature of curing determine the conductivity of the patch. In our proposed design, no such technique is needed for curing. The silver nanoparticle ink used in our design instantly cures while exposing to sunlight (30–34°C). Without sunlight, the conductive traces are allowed to attain the maximum conductivity by keeping the printed traces of design in room temperature (28°C) for about 90 minutes. Figures 10(a)–10(e) show the curing process at different time instants from the time the printout is taken (time stamp is attached in each picture).

From Figures 10(a)–10(e), it is clear that as the time progresses, the darkness of the conducting surface increases which shows that the conductivity increases. This is done without using any additional curing process and allowing to simply resting at room temperature of around 28°C. It is noticed that the maximum time needed for curing is 45 minutes from the time of taking printout at IST 17.43 and the final maximum conductivity at IST 18.29, as shown in Figure 10(e). Table 2 provides the variation in resistivity with respect to time at room temperature measured at 1 cm length of the conductive strip. Table 3 summarises the recent works on inkjet printing of Z-shaped antenna and performance is analysed. The AgNP used here has the instant curing capacity that avoids the sintering/annealing process. Thus, the curing-free, low-cost AgNP ink suitable for thermal head-based highly inexpensive HP home printer-based design methodology is designed and analysed in this work. This can be further modified to be used in other wireless applications as this work achieves higher gain in comparison with other similar works [22].

4. Conclusion

The single Z-shaped monopole element printed using “inkjet” printing technology uses relatively inexpensive desktop inkjet printer and ordinary “paper” as the substrate material. The ink chosen for the patch has the chemical properties which allow instant curing, whereas the ink used in the previous works used the most complex oven heating

or electrical curing. Thus, the proposed antenna design is superior in all aspects. Additionally, there are many types of papers such as porous, hydrophobic, and semitransparent papers. The hydrophilic property is very useful in implementing sensors for rainfall, fog, and humidity measurement on leafs and surface of soils. Hence, the future focus of this work is to design antenna on various materials like this and analysing them in various climatic and soil conditions. In addition to this, implementation of array structures using inkjet printing is the future work to be carried out in near future for high gain applications in the areas where there is huge terrestrial loss.

Data Availability

The data used to support the findings of this study are included within the article.

Conflicts of Interest

The authors declare that they have no conflicts of interest.

References

- [1] V. V. Navarkhele, A. K. Kapre, and A. A. Shaikh, “Dielectric properties of black soil with chemical fertilizers at X-band,” *Environment International*, vol. 29, pp. 437–450, 2003.
- [2] P. J. Bevelacqua, “Antenna types,” 2021, <http://www.antennatheory.com>.
- [3] P. Rajalakshmi and S. Devi Mahalakshmi, “IoT based crop-field monitoring and irrigation automation,” in *Proceedings of the International Conference on Intelligent Systems and Control*, pp. 1–6, Coimbatore, India, January 2016.
- [4] R. N. Rao and B. Sridhar, “IoT based smart crop-field monitoring and automation irrigation system,” in *Proceedings of the Second International Conference on Inventive Systems and Control*, pp. 19–20, Coimbatore, India, January 2018.
- [5] B. S. Saraf and H. Gawali, “IoT based smart irrigation monitoring and controlling system,” in *Proceedings of the International Conference on Recent Trends in Electronics*, pp. 815–819, Information & Communication Technology, Bangalore, India, May 2017.
- [6] A. Rida, Z. Konstas, R. Vyas, K. Katsibas, N. Uzunoglu, and M. M. Tentzeris, “A Novel “Green” Inkjet-Printed Z-Shaped Monopole Antenna for RFID Applications,” in *Proceedings of the 2009 3rd European Conference on Antennas and Propagation*, Berlin, Germany, March 2009.
- [7] L. Zhang, D. Chao, P. Yang et al., “Flexible pseudocapacitive electrochromics via inkjet printing of additive-free tungsten oxide nanocrystal ink,” *Advanced Energy Materials*, vol. 10, no. 17, Article ID 2000142, 2020.
- [8] J. Huang, L. J. Segura, T. Wang, G. Zhao, H. Sun, and C. Zhou, “Unsupervised learning for the droplet evolution prediction and process dynamics understanding in inkjet printing,” *Additive Manufacturing*, vol. 35, Article ID 101197, 2020.
- [9] R. Li, H. Fan, L. Shen et al., “Inkjet printing assisted fabrication of polyphenol-based coating membranes for oil/water separation,” *Chemosphere*, vol. 250, Article ID 126236, 2020.
- [10] L. Yang, A. Rida, R. Vyas, and M. M. Tentzeris, “RFID tag and RF structures on a paper substrate using inkjet-printing technology,” *IEEE Transactions on Microwave Theory and Techniques*, vol. 55, no. 12, pp. 2894–2901, 2007.

Retraction

Retracted: A Comprehensive Examination of Bandgap Semiconductor Switches

Advances in Materials Science and Engineering

Received 26 December 2023; Accepted 26 December 2023; Published 29 December 2023

Copyright © 2023 Advances in Materials Science and Engineering. This is an open access article distributed under the Creative Commons Attribution License, which permits unrestricted use, distribution, and reproduction in any medium, provided the original work is properly cited.

This article has been retracted by Hindawi, as publisher, following an investigation undertaken by the publisher [1]. This investigation has uncovered evidence of systematic manipulation of the publication and peer-review process. We cannot, therefore, vouch for the reliability or integrity of this article.

Please note that this notice is intended solely to alert readers that the peer-review process of this article has been compromised.

Wiley and Hindawi regret that the usual quality checks did not identify these issues before publication and have since put additional measures in place to safeguard research integrity.

We wish to credit our Research Integrity and Research Publishing teams and anonymous and named external researchers and research integrity experts for contributing to this investigation.

The corresponding author, as the representative of all authors, has been given the opportunity to register their agreement or disagreement to this retraction. We have kept a record of any response received.

References

- [1] S. Siva Subramanian, R. Saravanakumar, B. P. Ganthia et al., "A Comprehensive Examination of Bandgap Semiconductor Switches," *Advances in Materials Science and Engineering*, vol. 2021, Article ID 3188506, 8 pages, 2021.

Review Article

A Comprehensive Examination of Bandgap Semiconductor Switches

S. Siva Subramanian ¹, **R. Saravanakumar**,² **Bibhu Prasad Ganthia**,³ **S. Kaliappan** ⁴,
Surafel Mustefa Beyan ⁵, **Maitri Mallick**,⁶ **Monalisa Mohanty**,⁷ and **G. Pavithra**⁸

¹Department of EEE, Karpagam College of Engineering, Coimbatore, India

²Department of Wireless Communication, Institute of Electronics and Communication Engineering, Saveetha School of Engineering, Saveetha Institute of Medical and Technical Sciences, Chennai, Tamilnadu, India

³Electrical Engineering, IGIT Sarang, Dhenkanal, Odisha, India

⁴Department of EEE, Kumaraguru College of Technology, Coimbatore, Tamilnadu, India

⁵School of Chemical Engineering, Jimma Institute of Technology, Jimma University, Jimma, Oromia, Ethiopia

⁶Department of Civil Engineering, KMBB College of Engineering and Technology, Khordha, Odisha, India

⁷Electrical & Electronics Engineering, ITER, Siksha "O" Anusandhan Deemed to be University, Bhubaneswar, Odisha, India

⁸Department of Electronics and Communication Engineering, Dayananda Sagar College of Engineering (DSCE), Bangalore, Karnataka, India

Correspondence should be addressed to S. Siva Subramanian; siva.ace@gmail.com and Surafel Mustefa Beyan; surafel.beyan@ju.edu.et

Received 5 July 2021; Accepted 29 July 2021; Published 25 September 2021

Academic Editor: Samson Jerold Samuel Chelladurai

Copyright © 2021 S. Siva Subramanian et al. This is an open access article distributed under the Creative Commons Attribution License, which permits unrestricted use, distribution, and reproduction in any medium, provided the original work is properly cited.

Improvements in the material characteristics of bandgap semiconductors allow the use of high-temperature, high-voltage, and fast switch rates in power devices. Another good reason for creating new Si power converter devices is that previous models perform poorly. The implementation of novel power electronic converters means high energy efficiency but a more logical use of electricity. At this moment, titanium dioxide and gallium nitride are the most prospective semiconductor materials because of their great features, established technology, and enough supply of raw components. This study is focused on providing an in-depth look at recent developments in manufacturing Si-C- and high-powered electronic components and showcasing the whole scope of the newly developing product generation.

1. Introduction

Using electronic switching devices is the most efficient way to handle electrical energy. As of today, over 40% of global energy is used to generate, store, and distribute electricity, making power electronics a critical part of the process. On power electronic converters, the power semiconductor devices' losses account for a substantial percentage of the energy loss. Si's blocking voltage capabilities as well as the operating temperature and switching frequency have been proven to be limited [1–5]. So far, the maximum commercial breakdown voltage for

Si IGBTs is 6.5 kV, and the device must operate at a restricted switching temperature of 200°C.

Currently used power converters must contend with certain inevitable physical limitations, including costly cooling systems and costly passive components. As a result, we may anticipate a young generation of power converters that use wide bandgap semiconductors. Enhancing the performance of the power transformations will enable better overall utilisation of energy and improved size and durability of power converters [6–10].

According to researchers, silicon carbide (Si-C) or gallium nitride (Ga-N) are considered the most promising

semiconductor material candidates because they have excellent theoretical qualities, lucrative business availability of the starting ingredients, and mature technological processes. WBG semiconductors' prospects as a replacement for Si (Figure 1) emphasise several important material characteristics [11–14].

Therefore, the process technology for WBG semiconductor materials is of higher interest to device manufacturers, which makes these materials attractive for high-power electronics. Ga-N's potential performance advantage is reduced high-frequency and high-voltage requirements [15–18], along with limited high-quality bulk substrates for vertical devices, which means that Si-C has a higher chance of securing high-voltage device sales.

This is a new development in power electronics; while many improvements are still required, this represents a breakthrough. Material benefits, such as reduced manufacturing costs, low maintenance costs, and so on, are only partly realised owing to varying material qualities, technological constraints, unoptimized device designs, and device reliability problems [19–23]. In addition, there will be a significant research effort for the development of modelling and electro thermal characterization techniques for these power devices, as well as for optimal package at elevated performance, controllers, and processors.

This article provides an overview of current and anticipated future advancements in new Si-C- or Ga-N-based electrochemical capacitors as well as current improvements [24–29].

2. Power Devices

Compared to Si-C equivalents, an increase of 10 in blocking voltage is achievable, because of the higher dielectric critical field of Si-C. The major benefit of Si-C's greater thermal conductivity is that it enables operation at higher power density ratings and uses less space for the cooling system, as illustrated in Figures 2 and 3 [30, 31].

In Figure 4, in order to reduce DMOSFET inversion channel resistance, the development of 4H-Si-C DMOSFETs was postponed. A brilliant MOSFET integration and MOS interface research effort have been made in the last few years. One of the most impressive breakthroughs in the field of Si-C MOS consumer electronics was realised by lowering the charge carrier density (D_{it}) and enhancing the surface morphology, resulting in an increase in the MOS channel's performance [32].

IGBTs have gained popularity recently, and blocking voltage capacities exceeding 10 kV have been recorded [33]. An expectation is that Si-C power switches will boost their voltage capabilities to about 20–30 kV in the near future [34–36]. As in development of power MOSFETs, important breakthroughs were made in the quality and large circuit mobility of the MOSFETs. Best-outcome n-channel IGBT structures also require advances in the epilayer growing process. Cree has published details on ultra-high-voltage 4H-Si-C thyristors [37–39]. A 4 h silicon-controlled switch with IGBT chip size of 6.7 mm

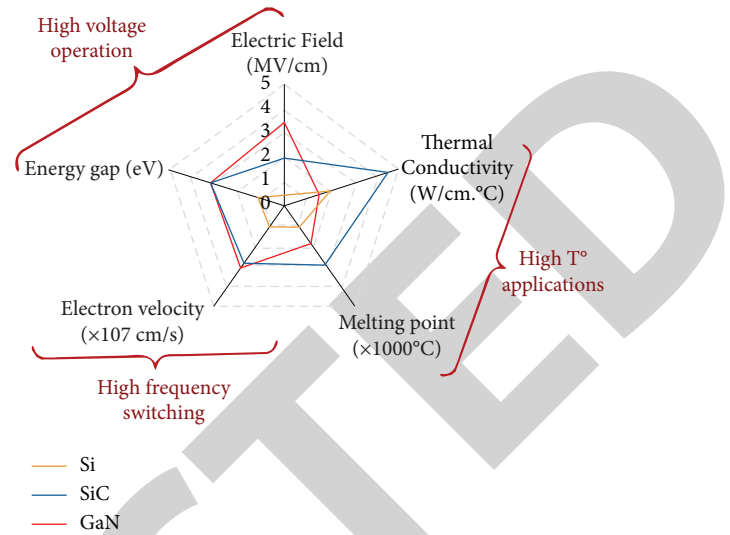


FIGURE 1: An overview showcasing silicon, silicon carbide, and gallium nitride properties.

and an environment influences of 0.16 cm^2 had a 0°C differential specified on to one of $24 \text{ m}\Omega \text{ cm}^2$ with just a gate bias of 20 V.

It is a need of filtering 4.7 kV with just a capacitance of $50 \mu\text{A}$, and turn-on \pm turn-off periods of 168 but rather 106 ns at room temperature. BJTs made from silicon carbide nevertheless exhibit deterioration in both load current and forward voltage drop under forward stress, caused by layering failures in the base-emitter region [40–44].

Conductivity manipulation and the inverse thermal resistance with the forward voltage drop are beneficial for Si-C-GTO structures as well. The Si-CGT (silicon-based gate turn-off thyristor) [45–48] has the cross section illustrated in Figure 5.

3. Ga-N Power Devices

WBG, huge critical magnetic current, high electron mobility, and somewhat good thermal conductivity make Ga-N excellent for high-voltage, high-frequency, and high-temperature applications. Ga-N-based devices are currently marketed in the photonics sector, whereas silicon is in the early stages of power applications. As a result, Ga-N epilayers have mostly been produced on substrates other than commercial high-quality free-standing Ga-N substrates. Gaining top-notch, single-crystalline Ga-N films is critical for power conversion, and thus good worldwide epitaxial relationships are necessary. Compared with the other substrates, Ga-N epilayers produced on Si substrates provide a low cost technique, as well as provide growth on high-strength resins up to 200 mm [49, 50].

Due to the absence of phase change Ga-N substrates, most reported Ga-N semiconducting power diodes are lateral or quasi-vertical devices. A breakdown voltage of 9.7 kV was observed on sapphire substrates [51–53] even if the forward voltage loss is still significant. Sapphire substrate-mounted Ga-N rectifiers are gaining a lot of interest

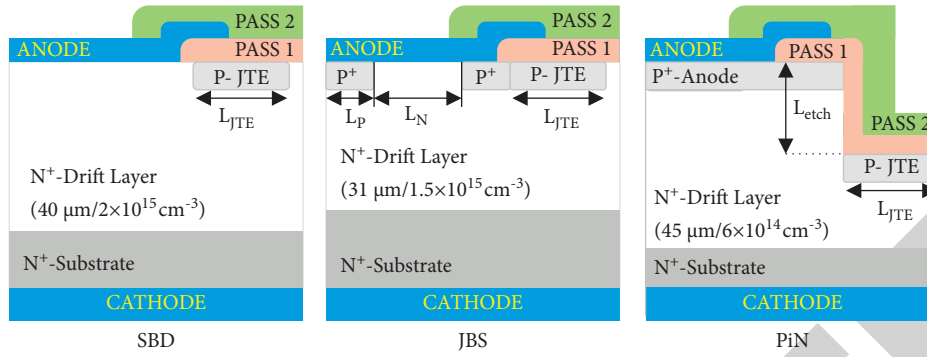


FIGURE 2: Schottky diode.

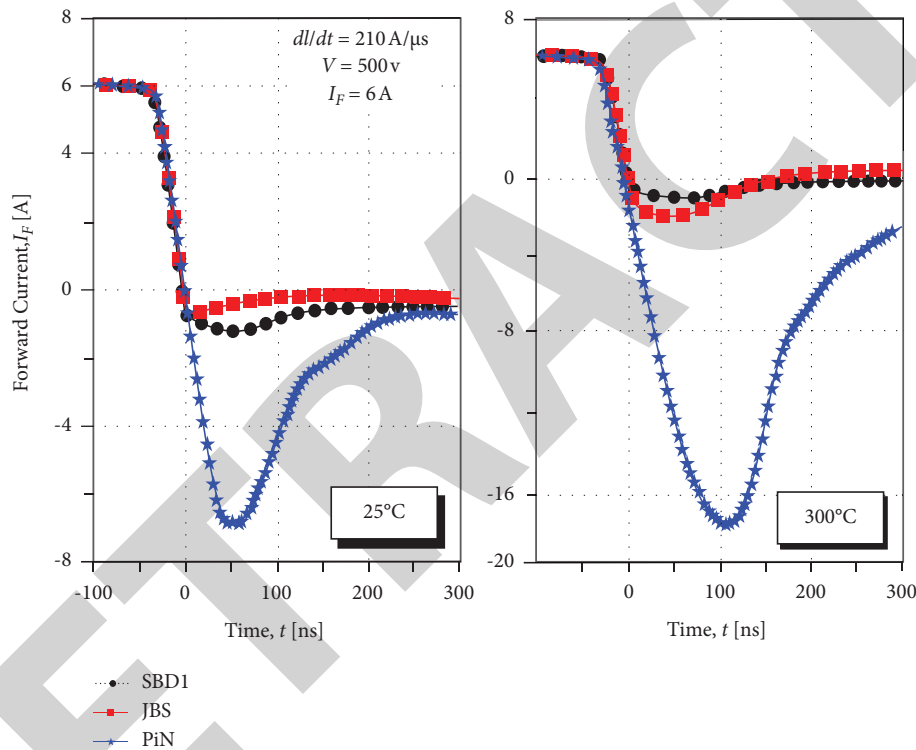


FIGURE 3: Inductive load turn off.

because of their low cost. Recently, 600 V Ga-N ZnO diodes are expected to be introduced in market with Si-C Schottky rectifiers. Additionally, professional Ga-N eukaryotic initiation will now be readily accessible in the market in the 600 V–1.2 kV output voltage. However, on the other hand, Ga-N-based voltage dc-dc converters in the range of 600 V–3.3 kV are also being studied, but improvements in material strength of inserted p-type Ga-N are still required.

AlGa-N/Ga-N heterostructures include a 2-D electron gas (2DEG) because of the significant band edge discontinuity of Ga-N and AlGa-N and also because of the presence of polarisation forces that provide a substantial 2DEG concentration with transistors values (1200–2000 cm²/Vs). Ga-N HMT-S (Figure 6) are inherently normally on semi-conductors since a negative gate bias is required to remove the 2DEG. A significant trade-off has recently been achieved

between breakdown voltage and on-resistance with these devices [54–58].

Significant advancements have been achieved since the Ga-N-based HEMT switch appeared [45]. For instance, HEMT microwave output power output both on diamond and Si-C has increased from 1.1 degree in 1996 to 40 W/mm lately. Additionally, Ga-N HMT-S is approaching 10 kV, and Ga-N-based pv panels have already been demonstrated. The initial HEMT structures' electrical performance may be improved by reducing the dielectric constant collapse and increasing the gate-to-drain breakdown voltage by adjusting the surface morphological trap densities [47]. Three approaches are shown here: surface pay n-Ga-N-cap fabrication, submerged gating with professional plate arrangement, and ferric oxide of surface states through silicon nitride and perhaps other insulating layers [59].

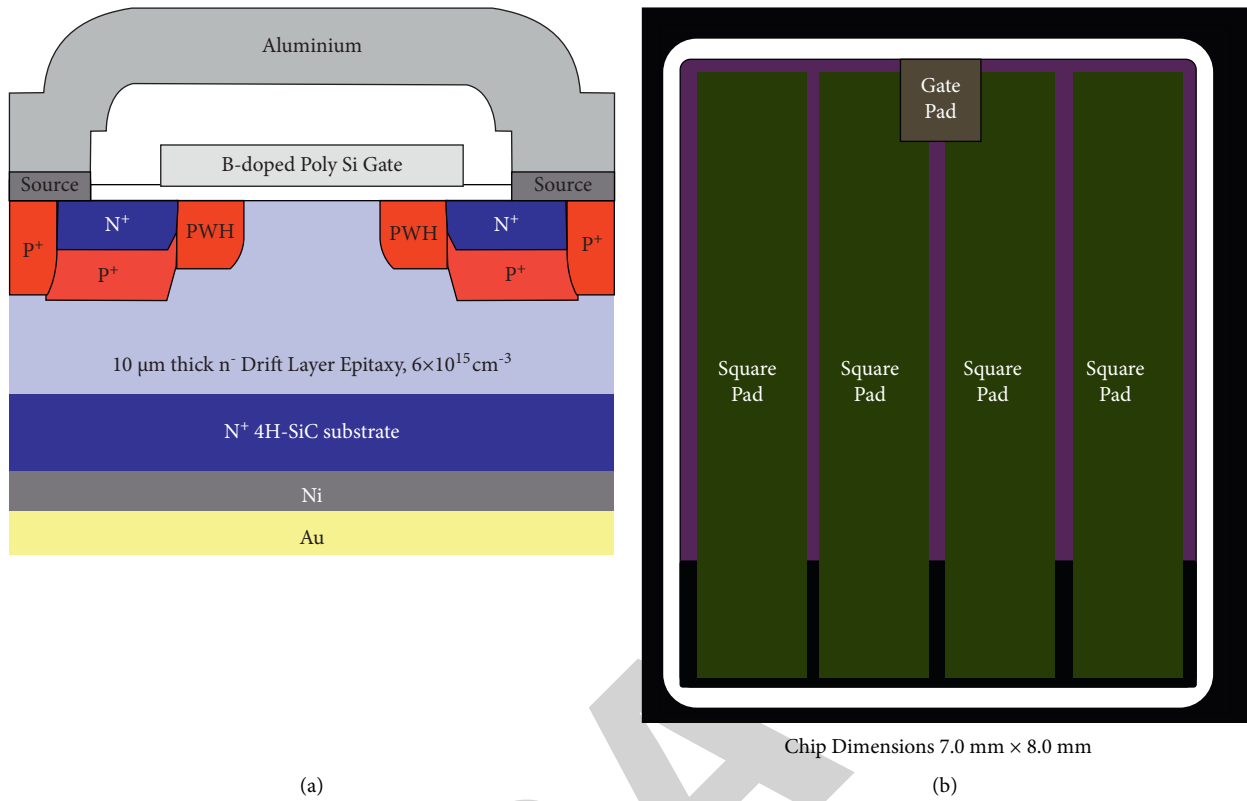


FIGURE 4: Diagram of DMOSFET.

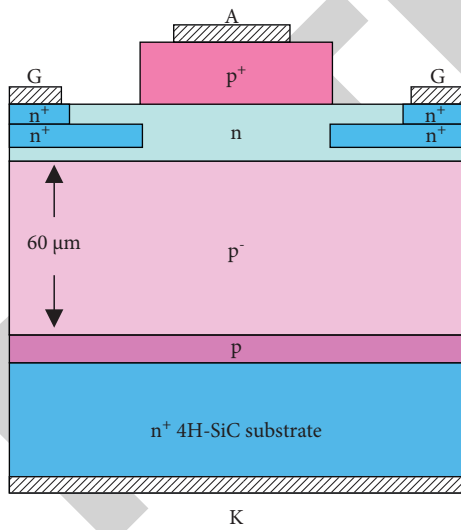


FIGURE 5: Structure of Si-C.

Specifically, 2.2kV HEMT structures produced on silicon utilising a novel Si substrate removal technique have recently been described [60]. In contrast, structures produced on bulk silicon have a blocking voltage capacity of 700 V. Also, Ga-N-based HEMT power switches for kilowatt-level power conversion are manufactured on semi-insulating Si-C substrates, which include field-plated gates [61].

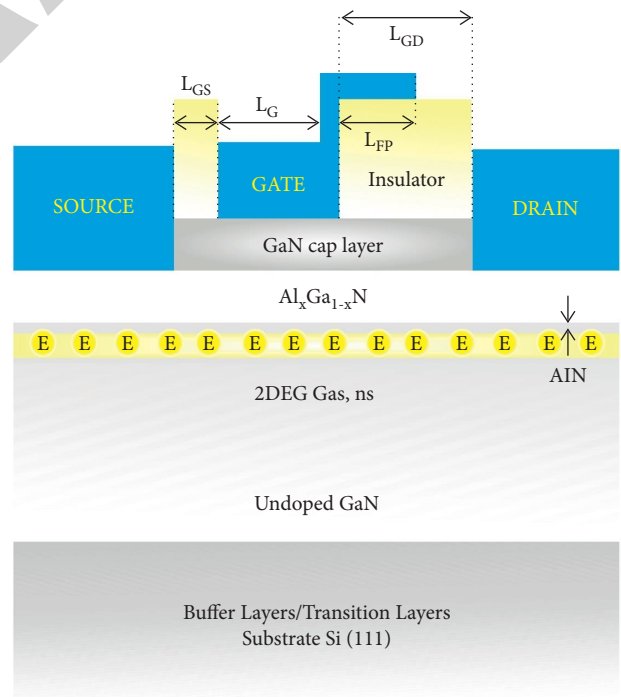


FIGURE 6: Cross section of a normally on Ga-N HEMT.

Ga-N HMT-S are essentially normally off devices, making them challenging to employ in power systems where apparently controls are desired. In light of this, considerable

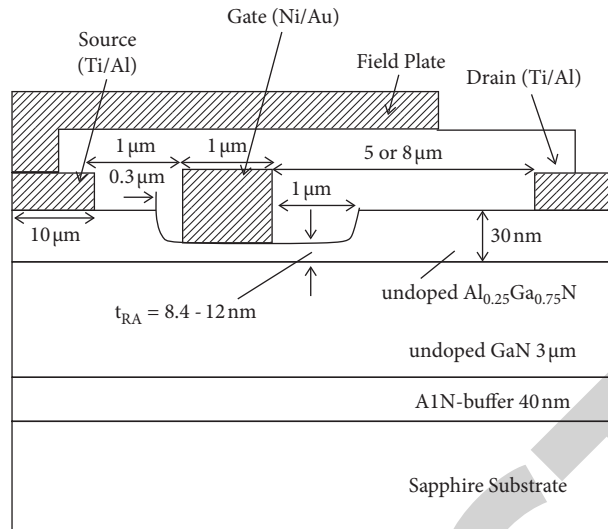


FIGURE 7: Recessed-gate Ga-N HEMT structure.

research has been done in developing Ga-N HEMT devices via many different approaches. A recessed-gate structure (Figure 7) was shown in [62] such that the AlGa-N layer beneath the gate area is too thin to create a 2DEG, which gives rise to a good threshold voltage. One solution for creating a routinely Ga-N HEMT is to use a diethyl ether plasma treatment in the gate area [63] instead of decreasing the AlGa-N thickness. Incorporation of fluoro ions in the AlGa-N barrier results in an increase in threshold voltage shift, which may be eliminated by postgate annealing at a low temperature. AlGa-N/Ga-N HMT-S acquire their high performance when they are combined with a gate recess and a fluorine-based surface treatment. The selective development of a p-n connection gate [58, 64] allows the thinning of the 2DEG barrier below (see Figure 8).

Ga-N-HMT-S are usually available with breakdown voltages in the range of 20–600 V. Breakdown voltages for Ga-N-HMT-S are typically in the 20-600 V range. EPC, for example, offers 600V-170mΩ nitride HMT-S with output impedances ranging from 40 V/33 A to 200 V/12 A, whereas MicroGa-N has 600 V-170 mΩ Ga-N HMT-S with an applied voltage and a 200 kΩ output impedance.

Devices, also called fabricated HMT-S, are layered on a sapphire substrate, and their measured on-resistances and insulating voltages are both higher than 2 kV with estimated on-resistances reaching 24–22 Ω-mm in both directions. Since the introduction of improved Ga-N HEMT process technology, it is also proper to say that the introduction of Ga-N diodes, which can shield the HEMT gate from voltage peaks, allows the combination of Ga-N diodes. Additionally, high-voltage power devices are also being developed for monolithic integration and for use in peripheral structures that include sensing/protection/control capabilities.

Because of the normally off operation and wide conduction band offset of Ga-N lateral MOSFETs, they are less vulnerable to hot electrostatic interaction and other reliability issues, especially issues related to the surface states and present collapse. To enable the incorporation of lateral

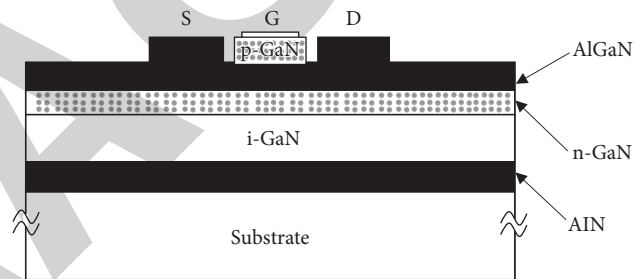


FIGURE 8: Schematic cross section of a p-n gate Ga-N HEMT [57].

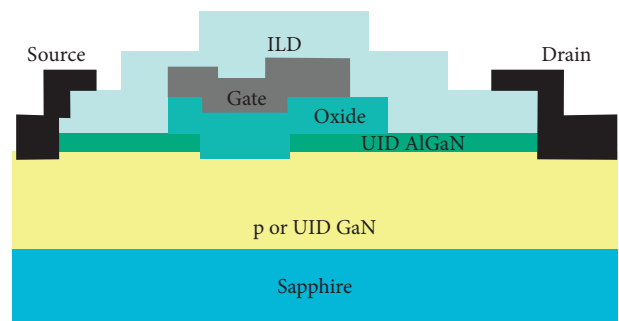


FIGURE 9: Schematic cross-sectional view of a lateral Ga-N hybrid MOS-HFET.

nitride MOSFETs with channel mobility numbers of 170 cm²/Vs and a blocking voltage capacity of 2.5 kV, the high-quality SiO₂/Ga-N interface [63] was used. However, the existence of rare metal and its layer thickness and scattering issues causes an impact on silicon. A heterostructure including AlGa-N/Ga-N may be introduced into the RESURF area of something like the Ga-N MOSFETs in order to overcome this (see Figure 9). This hybrid MOS-HEMT [64] combines the advantages of either the MOS barrier height or the 2DEG Ga-N power switching.

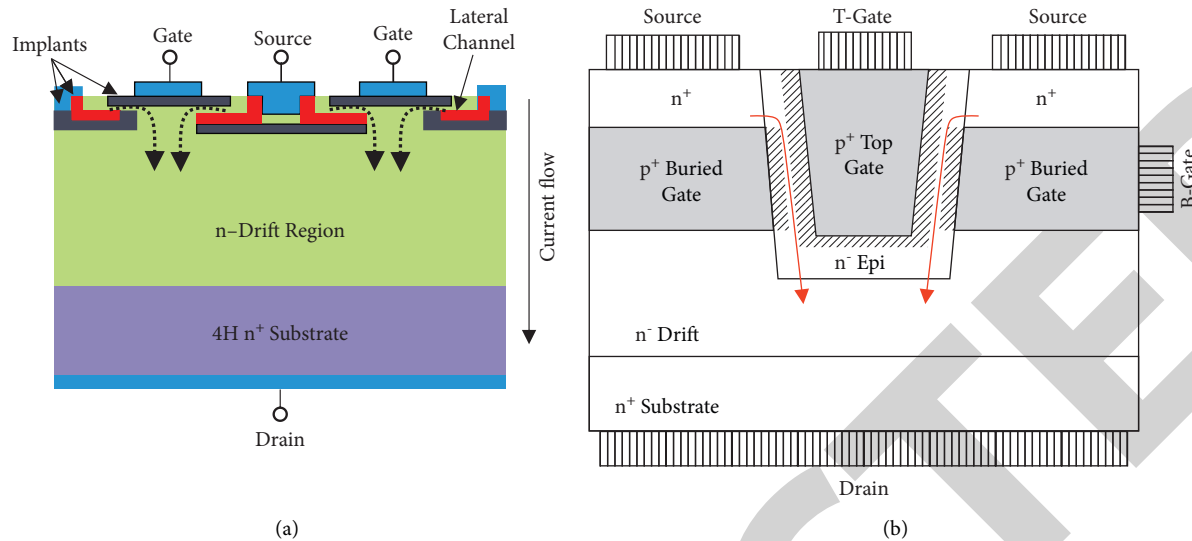


FIGURE 10: Diagram of JFET.

4. Conclusion

This article provides an overview of current advances in power devices, especially WBG semiconductor materials, that are powered by miniature RF motors. It is possible that future generations of more efficient power converters may be realised using WBG characteristics, even in applications that are limited by Si-based systems, including such increased and greater operation. Wafer-based bipolar (WB) semiconductors, such as Si-C and Ga-N, are currently the most appropriate WBG nanomaterials for next-generation power devices because of the excellent quality of wafers and the ready-to-use technical procedure.

Also, commercially available Si-C SBDs and JBS diodes are strong rivals to Si diodes. In Figure 10, Si-C JFETs or MOSFETs would contend alongside Si IGBTs through to collapse values in the area of 5 kV, while Si IGBTs will thereafter compete with Si-C JFETs and MOSFETs beyond breakdown voltages of 5 kV. JFETs will be the first industrial Si-C switches since Si-C MOSFETs cannot be made to work with better gate-contact interfaces. Si-C JFETs and low-voltage Si MOSFETs in series with a normally on JFET are well established for hybrid cascade topologies. Conversely, JFETs with the gate turned off still have large resistive channels that need further enhancement. Over the last few years, 1.2 kV Si-C MOSFETs have already been commercially available. Improving the Si-C MOSFET should lead to improvements in the Si-C IGBT, which may pave the way for IGBTs with breakup voltages exceeding 10 kV.

Most of the Ga-N power devices produced use epitaxial layers of Ga-N on substrates like silicon, sapphire, or silicon carbide. A Ga-N diode of this magnitude has been successfully demonstrated and is expected to be put into general commercial use soon. One last alternative that is being explored for limited, increased Ga-N power switches is hybrid MOS-HEMT architectures.

Data Availability

The data used to support the findings of this study are included within the article.

Conflicts of Interest

The authors declare that they have no conflicts of interest.

References

- [1] M. Berzelius, "XLII. On the mode of obtaining silicium, and on the characters and properties of that substance," *Philosophical Magazine*, vol. 65, no. 324, pp. 254–267, 1825.
- [2] T. Thomson, *A System of Chemistry in Four Volumes*, Baldwin, Cradock, and Joy, vol. 1, p. 252, London, UK, 5th edition, 1817.
- [3] M. Faraday, *Experimental Researches in Electricity*, vol. 1, pp. 122–124, Richard and John Edward Taylor, London, UK, 1839.
- [4] F. Braun, "Über die Stromleitung durch Schwefelmetallic," in *Semiconductor Devices: Pioneering Papers*, S. M. Sze, Ed., vol. 153, no. 4, pp. 556–563, World Scientific Publishing Co., Singapore, 1874.
- [5] J. C. Bose, "Detector for electrical disturbances," 1904, U. S. Patent 755,840, <https://ieeexplore.ieee.org/document/658774>.
- [6] J. E. Lilienfeld, "Method and apparatus for controlling electric currents," 1930, U. S. Patent No. 1,745,175, <https://patentimages.storage.googleapis.com/fa/5d/33/ed2769d48fac4d/US1745175.pdf>.
- [7] A. H. Wilson, "The theory of electronic semi-conductors," *Proceedings of the Royal Society of London - Series A: Containing Papers of a Mathematical and Physical Character*, vol. 133, no. 822, pp. 458–491, 1931.
- [8] A. H. Wilson, "A note on the theory of rectification," *Proceedings of the Royal Society of London - Series A: Containing Papers of a Mathematical and Physical Character*, vol. 136, no. 830, pp. 487–498, 1932.
- [9] B. Davydov, "On the rectification of current at the boundary between two semiconductors," *Compt. Rend. Doklady Acad. Sci., URSS*, vol. 20, p. 279, 1938.

- [10] N. F. Mott, "Note on the contact between a metal and an insulator or semi-conductor," *Mathematical Proceedings of the Cambridge Philosophical Society*, vol. 34, no. 4, pp. 568–572, 1938.
- [11] W. Schottky, "Halbleitertheorie der Sperrschicht," *Naturwissenschaften*, S. M. Sze, Ed., vol. 26, no. 52, p. 843, 1938.
- [12] R. S. Ohl, *Light-Sensitive Electric Device*, 1946, U. S. Patent 2402662, <https://patents.google.com/patent/US2443542A/en>.
- [13] J. H. Scaff and R. S. Ohl, "Development of silicon crystal rectifiers for microwave radar receivers," *Bell System Technical Journal*, vol. 26, no. 1, pp. 1–30, 1947.
- [14] W. Shockley, "The theory of p-n junctions in semiconductors and p-n junction transistors," *Bell System Technical Journal*, vol. 28, no. 3, pp. 435–489, 1949.
- [15] H. C. Theurer, "Method of processing semiconductive materials," U. S. Patent 3,060,123, 1962, <https://patents.google.com/patent/US3060123A/en>.
- [16] J. R. Harris, "WILLIAMSON v THE INSPECTOR--GENERAL OF PENAL ESTABLISHMENTS," Victorian Reports, [1958] VR, pp. 330–334, Bell Laboratories Record, New York, NY, USA, 1958.
- [17] M. Tanenbaum, *Bell Labs Notebook No. 25505*, p. 30, Texas Instruments, Dallas, TX, USA, 1954.
- [18] J. Andrus and W. L. Bond, "Photoengraving in transistor fabrication," in *Transistor Technology*, F. J. Biondi, Ed., vol. III, pp. 151–162, D. Van Nostrand, Princeton, NJ, USA, 1958.
- [19] W. Shockley, "Memorandums, golden west theme book, and record," in *Shockley Papers, Accession Listing 95-153, Box 2B* Department of Special Collections, Stanford University Libraries, Stanford, CA, USA, 1955.
- [20] G. E. Moore, "The role of Fairchild in silicon technology in the early days of Silicon Valley," *Proceedings of the IEEE*, vol. 86, no. 1, pp. 53–62, 1998.
- [21] J. A. Hoerni, "Method of manufacturing semiconductor devices," U. S. Patent 3,025,589, 1962, <https://patents.google.com/patent/US3333324>.
- [22] R. N. Noyce, "Semiconductor Device-And-lead Structure," U. S. Patent 2981877, 1961, <https://ieeexplore.ieee.org/document/4785577>.
- [23] D. Kahng, "Electric field controlled semiconductor device," U. S. Patent No. 3,102,230, 1963, <https://patents.google.com/patent/US3102230A/en>.
- [24] R. Norman, J. Last, and I. Haas, "Solid-state micrologic elements," in *Proceedings of the Solid-State Circuits Conference. Digest of Technical Papers*, vol. 3, pp. 82–83, IEEE International, Philadelphia, PA, USA, February 1960.
- [25] R. L. Fogelson, "The Design of High Speed All Transistor Logic Circuits," *Fairchild Silicon Transistors, Application Data APP-49*, vol. 49, 1962.
- [26] H. W. Rugg and R. H. Beeson, "New Forms of "All Transistor" Logic," in *Proceedings of the 1962 IEEE International Solid-State Circuits Conference. Digest of Technical Papers*, Philadelphia, PA, USA, February 1961.
- [27] R. H. Norman and H. E. Stephenson, "Shift Register Employing Insulated Gate Field Effect Transistors," U. S. Patent 3454785, <https://patents.google.com/patent/US3454785A/en>.
- [28] G. Moore, *The Future of Integrated Electronics*, Fairchild Semiconductor internal publication, Sunnyvale, CA, USA, 1964.
- [29] F. Faggin and T. Klein, "Silicon gate technology," *Solid-State Electronics*, vol. 13, no. 8, pp. 1125–1144, 1970.
- [30] M. P. Forrer, "Survey of circuitry for wristwatches," *Proceedings of the IEEE*, vol. 60, no. 9, pp. 1047–1054, 1972.
- [31] el-cat.com, "Properties of silicon and silicon wafers," <http://www.el-cat.com/silicon-properties.htm>.
- [32] D. K. Schroder, R. N. Thomas, and J. C. Swartz, "Free carrier absorption in silicon," *IEEE Transactions on Electron Devices*, vol. 25, no. 2, pp. 254–261, 1978.
- [33] et-cat.com, "Properties of silicon and silicon wafers," <http://www.el-cat.com/silicon-properties.htm>.
- [34] C. B. Collins, R. O. Carlson, and C. J. Gallagher, "Properties of gold-doped silicon," *Physical Review*, vol. 105, no. 4, pp. 1168–1173, 1957.
- [35] C. B. Collins and R. O. Carlson, "Properties of silicon doped with iron or copper," *Physical Review*, vol. 108, no. 6, pp. 1409–1414, 1957.
- [36] Y. Tokumaru, *Properties of silicon doped with nickel*, Japan Society of Applied Physics, Tokyo, Japan, 1963.
- [37] W. B. Chua and K. Rose, "Electrical properties of high-resistivity nickel-doped silicon," *Journal of Applied Physics*, vol. 41, no. 6, pp. 2644–2647, 1970.
- [38] B. E. Deal and M. Sklar, "Thermal oxidation of heavily doped silicon," *Journal of the Electrochemical Society*, vol. 112, no. 4, pp. 430–435, 1965.
- [39] M. J. Mleczko, C. Zhang, H. R. Lee et al., "HfSe₂ and ZrSe₂: two-dimensional semiconductors with native high- κ oxides," *Science Advances*, vol. 3, no. 8, Article ID e1700481, 2017.
- [40] D. M. Zajac, A. J. Sigillito, M. Russ et al., "Resonantly driven CNOT gate for electron spins," *Science*, vol. 359, no. 6374, pp. 439–442, 2018.
- [41] B. G. Yacobi, *Semiconductor Materials: An Introduction to Basic Principles*, pp. 1–3, Springer, Berlin, Germany, 2003.
- [42] L. Łukasiak and A. Jakubowski, "History of semiconductors," *Journal of Telecommunication and Information Technology*, vol. 3, 2010.
- [43] P. Robin Morris, *A History of the World Semiconductor Industry*, pp. 11–25, IET, London, UK, 1990.
- [44] Y. P. Varshni, "Temperature dependence of the energy gap in semiconductors," *Physica*, vol. 34, no. 1, pp. 149–154, 1967.
- [45] S. M. Sze, *Physics of Semiconductor Devices*, John Wiley & Sons, New York, NY, USA, 2nd edition, 1981.
- [46] K. Chain, J.-h. Huang, J. Duster, P. K. Ko, and C. Hu, "A MOSFET electron mobility model of wide temperature range (77 - 400 K) for IC simulation," *Semiconductor Science and Technology*, vol. 12, no. 4, pp. 355–358, 1997.
- [47] A. G. Sabnis and J. T. Clemens, "Characterization of the electron mobility in the inverter Si surface. Int Electron Devices Mtg 18–21. 69," *American Scientific Research Journal for Engineering, Technology, and Sciences (ASRJETS)*, vol. 7, no. 1, pp. 50–70, 1979.
- [48] K. Chen, H. Clement Wann, J. Dunster, P. K. Ko, C. Hu, and M. Yoshida, "MOSFET carrier mobility model based on gate oxide thickness, threshold and gate voltages," *Solid-State Electronics*, vol. 39, no. 10, pp. 1515–1518, 1996.
- [49] D. S. Jeon and D. E. Burk, "MOSFET electron inversion layer mobilities—a physically based semi-empirical model for a wide temperature range," *IEEE Transactions on Electron Devices*, vol. 36, no. 8, pp. 1456–1463, 1989.
- [50] W. Grabinski, M. Bucher, J. M. Sallese, and F. Krummenacher, "Compact modeling of ultra-deep sub-micron CMOS devices," in *Proceedings of the International Conference on Signals and Electronic Systems, ICSES*, pp. 13–27, Ustron, Poland, October 2000.
- [51] F. F. Fang and A. B. Fowler, "Hot electron effects and saturation velocities in Silicon inversion layers," *Journal of Applied Physics*, vol. 41, no. 4, pp. 1825–1831, 1970.

Retraction

Retracted: Experimental Investigation and Optimization on Friction Stir Welding of Nylon 6A Using Taguchi and ANOVA with Microstructural Analysis

Advances in Materials Science and Engineering

Received 26 December 2023; Accepted 26 December 2023; Published 29 December 2023

Copyright © 2023 Advances in Materials Science and Engineering. This is an open access article distributed under the Creative Commons Attribution License, which permits unrestricted use, distribution, and reproduction in any medium, provided the original work is properly cited.

This article has been retracted by Hindawi, as publisher, following an investigation undertaken by the publisher [1]. This investigation has uncovered evidence of systematic manipulation of the publication and peer-review process. We cannot, therefore, vouch for the reliability or integrity of this article.

Please note that this notice is intended solely to alert readers that the peer-review process of this article has been compromised.

Wiley and Hindawi regret that the usual quality checks did not identify these issues before publication and have since put additional measures in place to safeguard research integrity.

We wish to credit our Research Integrity and Research Publishing teams and anonymous and named external researchers and research integrity experts for contributing to this investigation.






The corresponding author, as the representative of all authors, has been given the opportunity to register their agreement or disagreement to this retraction. We have kept a record of any response received.

References

- [1] G. S. V. Seshu Kumar, A. Kumar, S. Rajesh, R. B. R. Chekuri, and A. G. Adigo, "Experimental Investigation and Optimization on Friction Stir Welding of Nylon 6A Using Taguchi and ANOVA with Microstructural Analysis," *Advances in Materials Science and Engineering*, vol. 2021, Article ID 7483393, 12 pages, 2021.

Research Article

Experimental Investigation and Optimization on Friction Stir Welding of Nylon 6A Using Taguchi and ANOVA with Microstructural Analysis

G. S. V. Seshu Kumar ¹, Anshuman Kumar ¹, S. Rajesh ²,
Rama Bhadri Raju Chekuri ² and Amsalu Gosu Adigo ³

¹Department of Mechanical Engineering, Koneru Lakshmaiah Education Foundation (Deemed to be University), Vaddeswaram, Guntur, Andhra Pradesh, India

²Department of Mechanical Engineering, Sagi Rama Krishnam Raju Engineering College, Bhimavaram, Andhra Pradesh, India

³Department of Chemical Engineering, College of Biological and Chemical Engineering, Addis Ababa Science and Technology University, Addis Ababa, Ethiopia

Correspondence should be addressed to G. S. V. Seshu Kumar; svskgajula@gmail.com and Amsalu Gosu Adigo; amsalu.gosu@aastu.edu.et

Received 31 July 2021; Accepted 2 September 2021; Published 18 September 2021

Academic Editor: Samson Jerold Samuel Chelladurai

Copyright © 2021 G. S. V. Seshu Kumar et al. This is an open access article distributed under the Creative Commons Attribution License, which permits unrestricted use, distribution, and reproduction in any medium, provided the original work is properly cited.

Friction stir welding is an environmentally friendly process of joining due to the nonusage of flux, or any shield gas, and it does not produce any harmful gases when compared to the joining process of fusion. Therefore, this article proposes an experimental investigation and optimization technique for studying the process of FSW on nylon 6A or polycaprolactam polymer composite plates. Specifically, the influence of input operating process parameters such as tool rotational speed (TRS), feed rate, and pitch values on the output response parameters like ultimate tensile strength (UTS) and hardness of welded joints is examined. In addition, L_{27} orthogonal array of Taguchi approach is employed for the optimization of design experiments of FSW parameters. The experimental setup is carried out with various process parameter combinations like 500 rpm, 1000 rpm, and 1500 rpm as TRS, and 30 mm, 40 mm, and 50 mm as feed rate by varying the pitch values as 1 mm, 2 mm, and 3 mm. Further, the analysis of variance (ANOVA) is also employed for finding the significant parameters of input process using the regression analysis equations. Finally, microstructural analysis is used to assess the mixing or dispersing uniformity of composites effectively.

1. Introduction

For improving production efficiency and reducing the costs with lower environmental effect in electronic, automobile, and aerospace devices, the benefits of good corrosion resistance, high specific strength, processing ability, and excellent design freedom have the potential in polymers and polymer matrix composites (PMCs) [1, 2]. The joining technology of welding techniques like adhesive bonding and mechanical fastening is required for the large and complex parts fabrication [3]. At the bonding region, stress concentration appears easily for reducing the joint reliability by manipulating the mechanical fastening that results in the

increasing of lightweight design deterioration. Relatively, adhesive bonding is mature that requires long processing cycle. However, humidity resistance, impact resistance, and fatigue resistance are not enough for reducing joint property. The welding process is the best joining technique that includes different kinds, such as electric resistance welding, linear vibration welding, hot plate welding, FSW, and ultrasonic welding, etc. [3]. Three different processes are included in these welding techniques: (a) a layer of molten material formation to be joined on the surfaces, (b) upsetting forms the bonding, and (c) the stage pressure and molten material cools should be maintained for preventing the forming of voids within the weld zone [4]. Spot welding is

performed mainly by ultrasonic welding but need to spend higher costs on tools and machines and more time is required for preparation. For forming the proper joint at a terribly slow rate, a v -groove requires for extrusion and hot gas welding methods. However, the properties rely on the skill level of operator highly. The flatten face is required for friction welding and the higher costs are included for machine parts. FSW has the potential of overcoming the drawbacks of aforementioned welding techniques due to the fact that it has benefits like high joint quality, severe plastic deformation, low temperature and machine/tool consumable costs, low process time, and no preparation [5]. Figure 1 shows the schematic diagram of FSW. In the rotational tool, a pin and a specially designed shoulder are included during FSW method. At a high rotational velocity, the frictions with the workpieces produce material flow to mix, generate frictional heat to smoothen the materials, and combine the welded materials for welding.

As the polymers include the molecules with various chain lengths and do not include definite melting point instead of melting ranges, FSW is not a solid-state process and its thermoplastic polymers are distinct from metal [6]. Some shorter chains of FSW may reach the melting point while applying FSW/P to polymers, whereas longer chains are in solid state. For thermoplastic polymers, FSW was implemented in 1997 and seldom works report due to the immaturity. Nelson et al. [7] have improved different tools to combine thermoplastic polymers. In 2005, and especially after 2009, the systematical research has started on the FSW of thermoplastic polymers [8]. The joining of PMCs and thermoplastic polymers is realized by FSW. These polymer composites are 20% carbon fiber-reinforced PP composite [9], 30% glasses fiber-reinforced PP composite [10], polyethylene terephthalate (PET) [11], polycaprolactam (nylon 6) [12], polymethyl methacrylate (PMMA) [13], acrylonitrile butadiene styrene (ABS) [14], poly carbonate (PC) [15], poly propylene (PP) [16], and different grades of polyethylene (PE) [17]. Raza et al. used a specific developed tool with a grooved conical pin and a concave shoulder based on high-density polyethylene (HDPE) sheet friction stir welded joints [18]. With and without including the ceramic particulates, the joints were manufactured that included silica, graphite, alumina, and silicon carbide (SiC). In addition, the strain rate impact on the tensile properties of welded joints and base material was also studied. In the applications of high strain rate, the significance could be given to the composite joint of SiC-HDPE providing tool design and optimal parameters for stir welding. Jain et al. [19] discussed that the particles dispersion in metal, polymer matrix, and ceramic composites via conventional routes was very tough due to the poor compatibility properties of particles' clustering or agglomeration. The two-pass friction stir processing is used for dispersing the particles of titanium dioxide on the surface of aluminum matrix uniformly. Huang et al. have studied the FSW of PMCs and thermoplastic polymers, dissimilar metal, and polymer FSW, and multifunctional composites fabrication [20]. Further, the future P -related or FSW scientific research and engineering, thermoplastic polymers, and PMCs with the FSW or P -related scientific research and

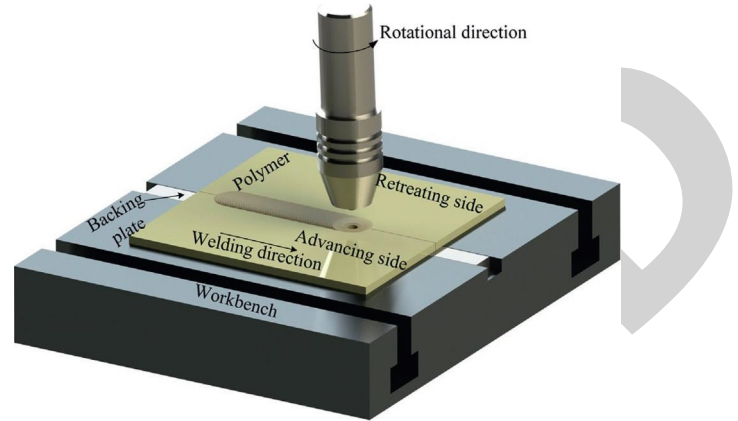


FIGURE 1: Schematic diagram of FSW.

engineering production have also been established. The FSW of nitrile butadiene rubber composite or polyamide 6 with and without an additional heating system was performed in [21]. During the heat assisted FSW, sound joints were obtained based on the heat input and cooling volume regulation. At varying rotational speeds, the tool configuration reliability was analyzed through the mechanical experiments. The creation of defects and improper fusion have been minimized by creating the welds with a heating system that results in substantial development of mechanical properties. They concluded that the maximum tensile strength was 61 MPa with more than 91% of base material mass. Meng et al. [22] have proposed adhesive bonding and multiscale mechanical interlocking for generating the stable hetero junctions between metals and PMCs and improving the mechanical properties. The multiscale mechanical interlocking and adhesive bonding resulted in the overall tensile shear strength of 27 MPa. In [23], authors have studied the Rockwell hardness and impact strength of UHMW polyethylene composites reinforced with nano-hydroxyapatite particles that are FSP-manufactured. Here, the processing metrics were shoulder temperature, strengthening material's volume fraction, tool traverse speed, and spindle speed. It is essential to choose the processing parameters for the variance analysis (ANOVA). The agglomeration of the reinforcing particles and induced voids and channels were caused by the low temperature and higher levels of tool traverse speed and fraction of volume in the microscopic analysis that leads to the reduction of impact strength and the formed composite hardness. The FSW techniques for aluminum alloy sheets for joining different types of thermoplastics with and without fibers are addressed in [24], where an experimental research work is recommended to get insight into the welding parameters' effects on the hybrid joints' efficiency in terms of tensile shear strength. In the instrument geometries investigation, the welding technique and material weldability were considered. For thermoplastic, the FSW is an efficient technique for aluminum joining based on the disclosed findings. Further, microstructural inspection resulted in the strong blending between thermoplastic and aluminum as well as defect-free welds.

The composite sheets of thermoplastic polymer base that include 12% continuous carbon fiber with two advanced speeds of 5/6 and 9 mm/min and two rotational speeds of 355 and 250 rpm in the shape of buttocks were analyzed by Bidgolia et al. [25]. In this low-cost turning system and FSW, a modern tool is used that is made of plain carbon steel st37. In addition, the full relation of materials was shown by the optical microscope images. The development and creation of cavities is contributed by increasing the inlet temperature and they convert into cavities in the tube. Further, the parameters that affect the link efficiency such as the rotational speed and key shoulder diameter were also included. Based on the scanning electron microscopy (SEM), the rotational speed is improved that leads to the continuous carbon fibers grinding and enhanced the tensile strength. Recently, the FSW was applied to glass fiber-reinforced polyamide 6 (PA6) [26]. It is measured in the fiber length distribution and weld strength in the weld seam. The friction stir welded specimen's main effects were investigated based on the tensile strength. According to the higher touch pressures, a tensile strength of 50% of base material strength may be viewed. Additionally, the optical measuring method is implemented and tested for fiber length large-volume measurement. Hajideh et al. used the FSW approach to research the potential of welding of polycarbonate and dissimilar polymethyl methacrylate sheets [27]. The impacts on the process parameters' joints mechanical properties such as heater temperature, rotational, and traverse speeds were analyzed comprehensively. The heater temperatures of 120°C and rotation and traverse speeds of 2100 rpm and 8 mm/min were provided as the optimized mechanical properties of the joint. In the optimal joining state, the welded joint was obtained with a strength equivalent to 98% of polycarbonate and more hardness than the polycarbonate. Authors in [28] have studied the effects on square, threaded, and tapered nylon 6 plates based on three different pin profiles. The method of marker material insert was utilized to analyze the material flow of post-weld specimens visually. The marker material is on the advancing side or retreating side for all pins shown by the uniform vertical stirring with symmetrical pattern. Unlike metals, the pin profile major role was determined in horizontal displacement, where the greatest backward displacement of marker materials was shown by a square pin. Moreover, on any side, the forward flow of all pin profiles was not found. Kumar et al. [29] have studied the feasibility of FSW on the glass-filled nylon 6 composites. Based on an injection molding machine, nylon 6 composites filled with glass were generated and joined with H13 tool steel using a cylindrical pin profile in the FSW process. The factors like tool tilt angle (0°, 1°, and 2°), tool traverse speed (0.2, 0.3, and 0.4 mm/s), and TRS (400, 500, and 600 rpm) with constant standoff distance (0.2 mm) were used in a full factorial experiment design for investigating the morphological and mechanical properties of FSW sections of glass-filled nylon 6 composites. In addition, ANOVA has been employed for estimating the tensile strength significance and percentage elongation process parameters. Practically, the classical metals and unfilled polymers have been replaced using PMCs because of their

superior attributes like low-cost and enhanced toughness with excellent strength/stiffness-to-weight ratio. In addition, for thermoplastic polymers, FSW became one of the important welding methodologies [30].

Thus, this article proposes FSW aspects of PMCs and thermoplastic polymers (new technologies of FSW to eliminate defects, thermomechanical behavior, mechanical properties, and variables of welding process), dissimilar FSW of polymer and metal, and fabrication of multifunctional composites. Therefore, this article proposes an experimental investigation and optimization technique for studying the process of FSW on nylon 6A or polycaprolactam polymer composite plates. Specifically, the influence of input operating process parameters such as TRS, feed rate, and pitch values on the output response parameters like UTS and hardness of welded joints is examined. In addition, L_{27} orthogonal array of Taguchi approach is employed for the optimization of design experiments of FSW parameters. Further, ANOVA is also employed for finding the significant parameters of input process using the regression analysis equations. Finally, microstructural analysis is used to assess the mixing or dispersing uniformity of composites effectively.

2. Materials and Methods

In this work, the nylon 6A is utilized which is a polymer for reproducing the properties of nylon 6,6 with nonviolation of patent on the production. It is relevant to the semicrystalline polyamide. Unlike any other nylons, nylon 6A is not a condensation polymer. But ring-opening polymerization is formed that makes a special case by comparing between addition polymers and condensation. In general, fibers of nylon 6A are tough to deal with because they contain elasticity, high tensile strength, and luster. They are resistant to the chemicals and abrasion highly such as alkalis and acids. Usually, 2.4% of water can be absorbed by the fibers even though it reduces the tensile strength. Moreover, it includes the glass transition temperature of 47°C. Prior to the generation of different color results, nylon 6A can be dyed in a solution path as it is white as a synthetic fiber. The heat protection is up to 150°C, the melting point is at 215°C, the density is 1.14 gm/cc, and the tenacity is between 6 and 8.5 gm/den. 12% of ledeburitic chromium tool steel is included in D3 steel with the great resistance of wears. However, it can be used as cutting tools for shear cutting edges, blanking dies for paper and plastics, sheets up to 4 mm thickness, and rotational shear edges with the thicknesses of sheets up to 2 mm. High chromium 12% tool steel and 2% of high carbon with high wear resistance are the major properties of D3 steel. After making the dies and tools, the hardness is 57 to 58 HRC which is reached using this D3 steel that anneals to easy machining based on its supply condition.

2.1. Tensile Strength Test. For assessing the composites and matrix alloy mechanical behavior, tensile tests are utilized. The matrix alloy and composites were machined to tensile the

specimens with gauge length of 30 mm and a length of 13.5 mm. UTS, often termed as TS, is the maximum stress that a material can withstand while being stretched or pulled before necking, which is when the specimen's cross-section starts to significantly contract. Figure 2 demonstrates the ASTM standard specimen dimensions for UTS.

2.2. Hardness. Practically, the material resistance is measured using shore hardness, where it has several shore hardness scales for determining the hardness of different materials like super soft gels, rigid plates, fibers, rubber, etc. To have the common point of reference for discussing the materials such as super soft gels, rigid plates, fibers, and rubber, the shore hardness scales were discovered to the people. A greater resistance indicates a higher number on the scale to indentation and hence harder materials. Less resistance and thus soft materials are indicated by the lower number of scales.

2.3. Microstructure Analysis. From nylon 6A polymer composite, the samples with metallographic structure were taken that were joined with the method of FSW. In micro and macro size, the structures containing the dynamic recrystallization zone (DCZ), thermomechanically affected zone (TMAZ), heat affected zone (HAZ), and base metal (BM) are investigated. From the welding joints' cross-sectional surfaces, both micro- and macrostructure images have been taken.

2.4. Design of Experiments Using Taguchi Method. This work utilized the Doe method for collecting the data and obtaining the accurate results. Three process parameters like pitch (mm), feed rate (mm/min), and TRS (rpm) were chosen for orthogonal array (L_{27}) and the results are analyzed using MINITAB 19 software. In addition, the HCHCr tool is used to join the work piece and the hardness, and UTS are measured as output responses of FSW joint. Table 1 lists the values of input process parameters with corresponding levels.

2.4.1. Taguchi Method. In the machining processes, the most utilized robust design approach is the Taguchi technique, which was analyzed for finding the controllable parameters with the best characteristics of response in FSW. In the experimental designs, the Taguchi technique is used based on orthogonal array for reducing the uncontrollable components effects while establishing the tests. Owing to the constant distribution of interactions between facts and the input components, Taguchi L_{27} orthogonal array as demonstrated in Table 2 is used for the experiments to minimize the uncontrolled components. The Taguchi design of experiments was evaluated to obtain the data through the conversion it to signal-to-noise (S/N) ratio after completing the trials. In different ways, the standard S/N ratio values are determined and assessed using the intended quality value, with nominal being better, lower being better, and greater being better.

3. Experimental Investigation

This section describes the experimental investigation, which is done to verify the mechanical attributes of FSW on nylon 6A (also known as polycaprolactam material) as shown in Figure 3(a). Here, UTS and hardness are employed as the properties to be investigated before and after the process of FSW. The work is done using an automatic fed vertical milling machine by setting the TRS and feeds accordingly with the taper threaded tool profile consideration as shown in Figure 3(b). Figure 4 illustrates the machining setup of FSW with the following specifications:

- (i) Capacity of motor: 7.5 hp
- (ii) Speed of rotation: 35 to 750 rpm
- (iii) Feed rate: 16 to 800 mm/min
- (iv) Make: HMT
- (v) Length of bed: 1000 × 400 × 450 mm

3.1. The Tool. Tool steel is the mixture of variety of alloy and carbon steels, and they are well-suited for being used as tools due to their suitability, distinctive hardness, ability of holding a cutting edge at elevated temperatures, and resistance to abrasion and deformation. Thus, tool steels can be exploited for shaping of other materials. Tool steels contain six groups such as hot-work, high-speed, shock-resisting, cold-work, water-hardening, and special purpose. Based on the toughness, shock resistance, strength, required surface hardness, working temperature, and cost requirements, the group choice is selected. In this work, HCHCr is considered as tool material and its specifications are given below.

- (i) Tool length: 100 mm
- (ii) Tool tip's diameter: 2 mm
- (iii) The pin length: 4.7 mm
- (iv) Tool shoulder's diameter: 20 mm

3.2. Process. The plates with dimensions are considered as 100 × 50 × 6 mm; then shearing process is used to cut the plates into the required size. Both plates are then clamped to the machine bed as illustrated in Figure 5(a). At the plates joining, a center bit is given the plunge depth and a hole is created to traverse the plates for the tool to be made the FSW, as shown in Figure 5(b). Then, the tool passes on the two plates' intersection after creating the hole when the pressure is applied on the plates using the tool shoulder. Based on the automatic feeds, the tool moves on to the other side of weld. Some time is given for the friction after inserting the tool to develop and the material is heated up to the plates' red-hot condition. However, the time is known as the indentation time and is considered as 5–8 seconds. The plates are considered as the friction stir welded once the tool reaches the other side as demonstrated in Figure 5(c).

4. Results and Discussion

This section describes the results obtained using FSW process of nylon 6A material and HCHCr tool with taper

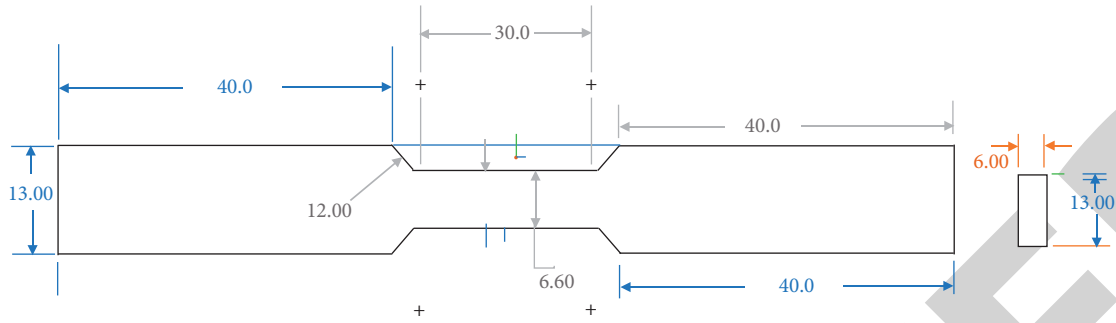


FIGURE 2: ASTM standard specimen dimensions for UTS.

TABLE 1: Input process parameters.

Process parameters	Level 1	Level 2	Level 3
TRS (rpm)	500	1000	1500
Feed rate (mm/min)	30	40	50
Pitch (mm)	1	2	3

threaded tool profile by varying the pitch values. Here, TRS (rpm), feed rate (mm/min), and pitch (mm) are considered as input process parameters while the UTS and hardness are assumed as output parameters, which means the strength of welding is assessed using these UTS, and hardness values. As we need the maximum tensile strength, the input parameters performed the concept of the larger, the better criteria. Table 3 lists the obtained experimental output parameters such as UTS and hardness with the variation in input process parameters like TRS (rpm), feed rate (mm/min), and pitch (mm).

4.1. Analysis of Variance (ANOVA). The ANOVA is employed to measure how the input operating process parameters influence the output response parameters, i.e., mechanical attributes of welded joints, via the association between these two input and output variables, where the

Fisher test is applied to measure the significance degree in these relationships. In this work, the maximum tensile yield stress is analyzed. For each control factor, ANOVA is required to be estimated for accessing the factors impact on response. To investigate which design parameters affect the characteristic significantly, the experimental results are assessed using the method of ANOVA, which can identify the input parameters contributions on UTS and hardness. To detect the process parameters whose variance in the design space impacts the output response metrics, ANOVA is applied while choosing 90% of confidence interval for experimental investigation. If the computed probability (P) value is about 10% or less, the factor significance is considered. After ANOVA, the obtained value of P is demonstrated in Table 4 as well as their significance on output response metrics like UTS and hardness, respectively.

4.2. Regression Analysis. After the process of weld joining, the regression analysis is conducted based on the obtained data results. The linear equations are derived that are relevant to the dependent and independent variables, which is performed using MINITAB software and the regression equations are mentioned as follows:

$$\begin{aligned}
 \text{UTS} &= 123.0 - 0.0225A - 3.90B - 20.2C + 0.000004A^2 \\
 &\quad + 0.0449B^2 + 5.6C^2 + 0.000134AB + 0.0056AC + 0.243BC - 0.00197AC^2 - 0.064BC^2, \\
 \text{HARDNESS} &= 115.2 + 0.0372A - 2.382B - 18.5C - 0.000016A^2 \\
 &\quad + 0.03313B^2 + 4.16C^2 - 0.000080AB + 0.01079AC + 0.010BC - 0.00203AC^2 - 0.008BC^2.
 \end{aligned} \tag{1}$$

Based on the listed values of R^2 , $\text{Adj-}R^2$, and $\text{Pred-}R^2$ in Table 5, the potency of equation (1) can be realized for predicting the variance inside the design space. After employing ANOVA, the derived model equations were used to estimate the variability within the design space for all output responses based on the results analysis.

For detecting the control factors, robustness is measured in Taguchi designs that decrease the product or process variability while minimizing the uncontrollable factors' effects (noise factors). Design parameters are control factors

and controllable parameters are process parameters. During product use or production, noise factors cannot be controlled, but they can be controlled during experimentation. For force variability to occur, the noise factors are calculated in a Taguchi designed method. The settings of optimal control factor are detected to make the process or product resistant or robust towards variation against noise factors. The control factor settings are indicated by higher values of S/N ratio that reduce the noise factors impact. The measurement of how the response is varied regarding the target

TABLE 2: Taguchi L_{27} orthogonal array.

S. No.	TRS (rpm)	Feed rate (mm/min)	Pitch (mm)
1	500	30	1
2	500	30	2
3	500	30	3
4	500	40	1
5	500	40	2
6	500	40	3
7	500	50	1
8	500	50	2
9	500	50	3
10	1000	30	1
11	1000	30	2
12	1000	30	3
13	1000	40	1
14	1000	40	2
15	1000	40	3
16	1000	50	1
17	1000	50	2
18	1000	50	3
19	1500	30	1
20	1500	30	2
21	1500	30	3
22	1500	40	1
23	1500	40	2
24	1500	40	3
25	1500	50	1
26	1500	50	2
27	1500	50	3

or nominal value under various noise conditions is measured using the S/N ratio. Based on the experimental objective, different S/N ratios are chosen, and three quality characteristics are introduced by Taguchi, such as larger is better, nominal is better, and smaller is better.

4.3. Process Parameters Effect on UTS. Table 6 lists the response values for S/N ratios of UTS. Figure 6 depicts the input operating process parameters such as TRS, feed rate, and pitch for S/N ratio on UTS, where the deviation of response line is with respect to the horizontal line, which demonstrates that these operating process parameters highly impact the performance measure, which also led to significant influence on UTS. The speed and pitch are the most significant input operating process parameters of machining for UTS in FSW of nylon 6A material with HCHCr tool while the feed rate is the least significant input operating process parameter.

4.4. Process Parameters Effect on Hardness. Table 7 demonstrates the response for S/N ratios of hardness. Figure 7 depicts the input operating process parameters such as TRS, feed rate, and pitch for S/N ratio on hardness, where the deviation of response line is with respect to the horizontal line, which demonstrates that these operating process parameters highly impact the performance measure, which also led to significant influence on hardness. The TRS, pitch,

and feed rate are the most significant input operating process parameters of machining for UTS in FSW of nylon 6A material with the HCHCr tool.

4.5. Microstructure Analysis. From the polymer composite of nylon 6A, the samples with metallographic structure are considered, which are later integrated with the FSW and then examined in detail. FSW joints include the structures that contain thermomechanically affected zone (TMAZ), base metal (BM), heat affected zone (HAZ), and nugget zone as demonstrated in Figure 8. These structures are studied in both micro and macro size. In addition, from the welding joints' cross-sectional surfaces, micro- and macrostructure-based images are taken, which are illustrated in Figure 9.

Based on the TRS and feed rate, structures have been changed. The wide gaps were observed in the joining zones if the welded sample's microstructure was examined with the TRS of 1500 rpm and a feed rate up to 50 mm/min. The less porosity has occurred at the joining zones if the welded sample's microstructure was tested with the TRS of 500 rpm and a feed rate of 30 mm/min. Then, the material is extruded to join better. In the welding center, the gaps and the zones at the bottom of nugget zone are observed. In the welded joints, the amounts of gaps and size increase by increasing the value of feed rate and TRS. In the defects' size, the increment is predicted with the reducing of temperature in the unit time and area.

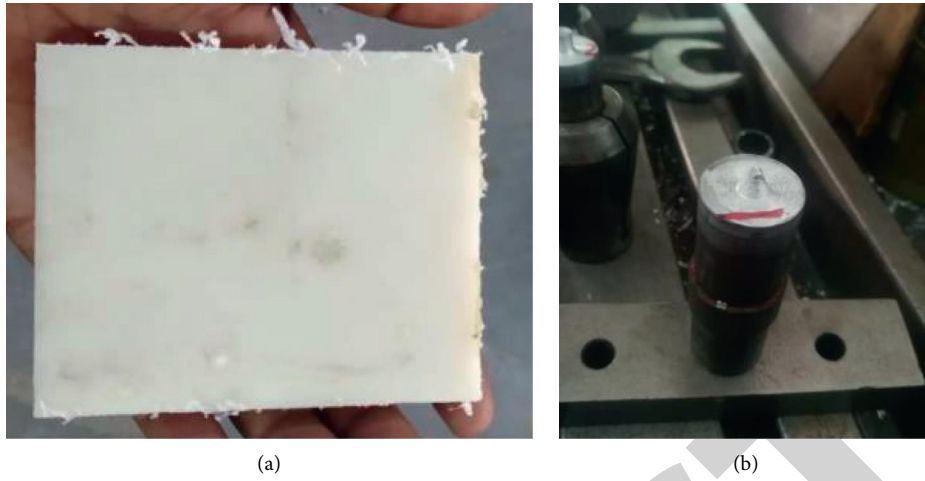


FIGURE 3: (a) Raw material of nylon. (b) Taper threaded tool.



FIGURE 4: Machine used for FSW.

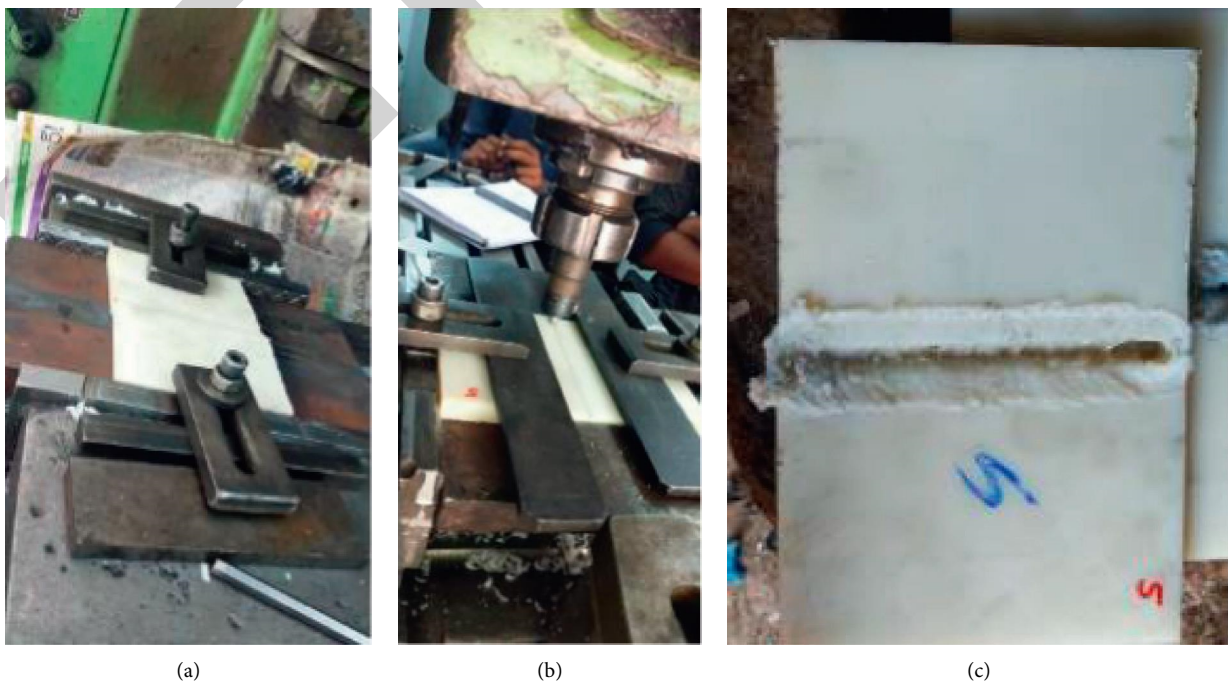


FIGURE 5: (a) Workpiece clamping. (b) FSW process. (c) Final specimen joint.

TABLE 3: Obtained experimental results of UTS and hardness.

S. No.	TRS (rpm)	Feed rate (mm/min)	Pitch (mm)	UTS (N/mm ²)	Hardness
1	500	30	1	32.97	76.00
2	500	30	2	31.34	72.11
3	500	30	3	35.86	73.11
4	500	40	1	17.96	79.33
5	500	40	2	18.95	72.21
6	500	40	3	21.91	75.11
7	500	50	1	32.11	81.33
8	500	50	2	33.32	77.11
9	500	50	3	34.98	78.12
10	1000	30	1	27.92	86.11
11	1000	30	2	21.35	87.12
12	1000	30	3	24.81	88.91
13	1000	40	1	26.52	86.12
14	1000	40	2	23.12	84.13
15	1000	40	3	22.16	85.67
16	1000	50	1	26.17	88.12
17	1000	50	2	22.35	88.90
18	1000	50	3	20.89	89.93
19	1500	30	1	19.34	89.16
20	1500	30	2	20.21	90.45
21	1500	30	3	18.34	92.89
22	1500	40	1	21.78	87.56
23	1500	40	2	22.17	84.13
24	1500	40	3	19.07	87.13
25	1500	50	1	22.67	93.21
26	1500	50	2	21.07	94.22
27	1500	50	3	22.45	95.61

TABLE 4: Major factors and corresponding P values for the process of FSW.

Model Factors	UTS	Hardness
A	0.023	0.001
B	0.076	0.004
C	0.040	0.007
A ²	0.060	0.036
B ²	0.045	0.001
C ²	0.030	0.001
AB	0.098	0.080
AC	0.021	0.004
BC	Insign	0.017
AC ²	Insign	Insign
BC ²	0.075	Insign

TABLE 5: Residuals for all the performance measures.

	UTS	Hardness
R ²	0.9024	0.9554
Adj-R ²	0.8992	0.9115
Pred R ²	0.8324	0.8408

TABLE 6: Response for S/N ratios of UTS.

Level	TRS	Feed rate	Pitch
1	28.92	27.99	27.88
2	27.53	26.60	27.36
3	26.33	28.20	27.54
Delta	2.59	1.60	0.52
Rank	1	2	3

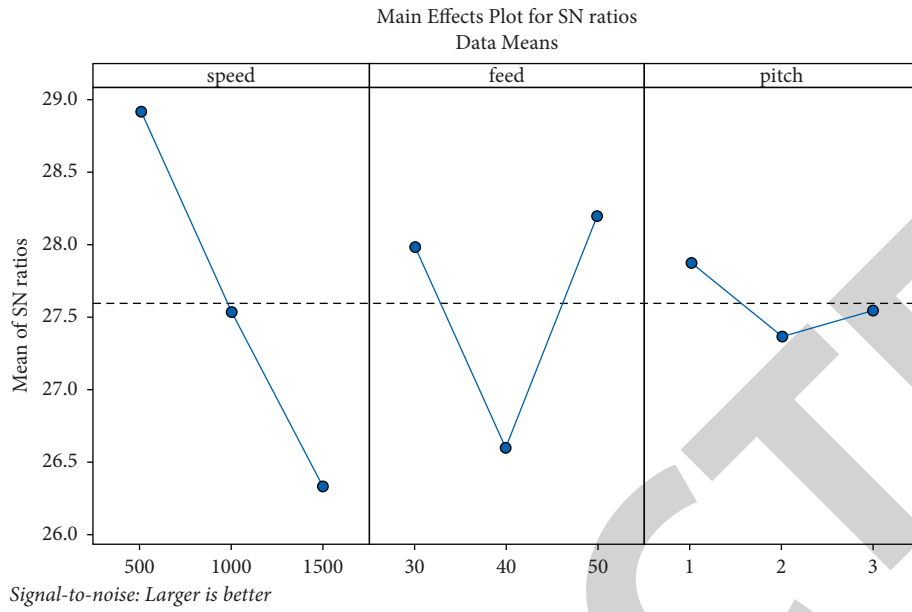


FIGURE 6: Main effect plot for S/N ratio of UTS.

TABLE 7: Response for S/N ratios of hardness.

Level	TRS	Feed rate	Pitch
1	37.61	38.45	38.59
2	38.81	38.30	38.38
3	39.12	38.80	38.57
Delta	1.51	0.51	0.21
Rank	1	2	3

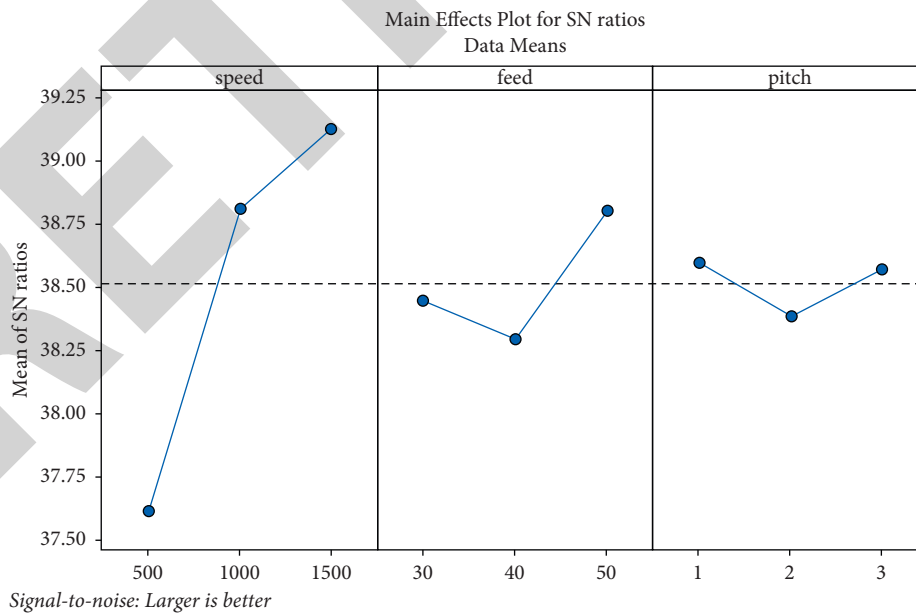


FIGURE 7: Main effect plot for S/N ratio of hardness.

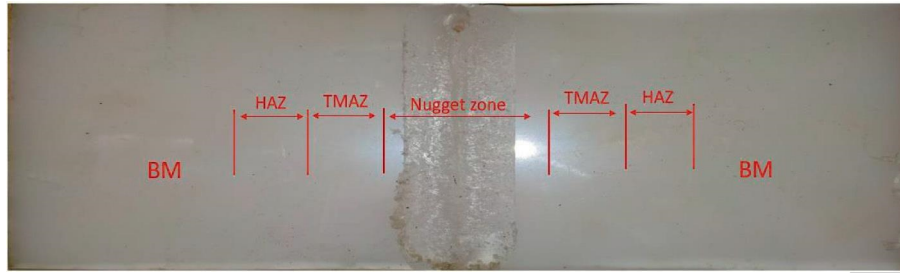


FIGURE 8: Formed zones in the weld cutaway in the FSW method.

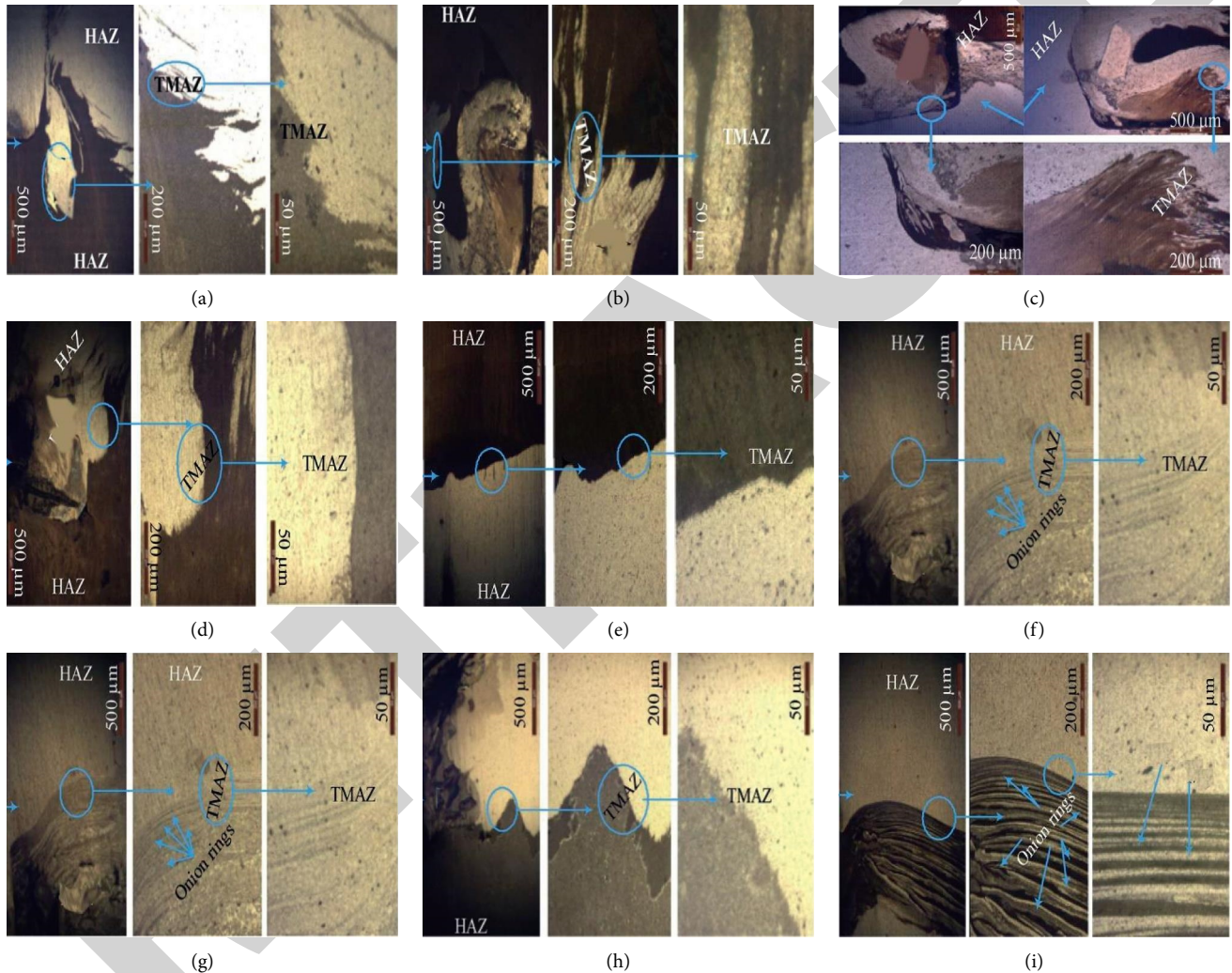


FIGURE 9: Obtained microstructural images with different welding parameters. (a) TRS: 500 rpm, and feed rate: 30 mm/min. (b) TRS: 500 rpm, and feed rate: 40 mm/min. (c) TRS: 500 rpm, and feed rate: 50 mm/min. (d) TRS: 1000 rpm, and feed rate: 30 mm/min. (e) TRS: 1000 rpm, and feed rate: 40 mm/min. (f) TRS: 1000 rpm, and feed rate: 50 mm/min. (g) TRS: 1500 rpm, and feed rate: 30 mm/min. (h) TRS: 1500 rpm, and feed rate: 40 mm/min. (i) TRS: 1500 rpm, and feed rate: 50 mm/min.

5. Conclusion

This article proposed an experimental investigation of FSW process on nylon 6A polymer material using the HCHCr

tool with taper threaded tool profile by varying the pitch values. In addition, optimal process parameters are obtained using Taguchi's L_{27} orthogonal array approach. Further, ANOVA with regression equations is also done to disclose

the effectiveness of input operating process parameters impact on the output responses like UTS and hardness. The final conclusions made from the obtained experimental and optimized results are as follows:

- (i) The results of Taguchi proved that the mathematical models have an ability to forecast the parameters of FSW with the confidence interval of 95%
- (ii) The most significant and the least significant FSW parameters are the tool rotation and feed rate, respectively
- (iii) The parameters like feed and TRS were considered for FSW joints UTS of nylon 6A polymer composite
- (iv) The optimum FSW parameters such as the feed rate of 30 mm/min, tool pitch of 3 mm, and the TRS of 500 rpm obtained the maximum UTS

The FSW technique joined with the micro- and macrostructures of welding joints has shown that the varied welding seams relied on welding parameters, which has impacted the value of hardness. The major difference between hardness values of joints was the differing hardness values with the heat influence although the joints' hardness values were made with both pin geometries. In the experiments, the lowest and highest hardness values have been computed. The maximum and minimum hardness values were obtained for the feed rate of 30 mm/min, TRS of 1500 rpm and the feed rate of 50 mm/min, TRS of 500 rpm, respectively.

Data Availability

The data used to support the findings of this study are included within the article.

Disclosure

This study was performed as a part of the Employment of Addis Ababa Science and Technology University, Addis Ababa, Ethiopia.

Conflicts of Interest

The authors declare that there are no conflicts of interest regarding this study.

References

- [1] S. R. Strand, *Effects of Friction Stir Welding on Polymer Microstructure*, Theses and Dissertations, Brigham Young University, Provo, Utah, 2004.
- [2] M. Barmouz, P. Shahi, and P. Asadi, "Friction stir welding/processing of polymeric materials," *Advances in Friction-Stir Welding and Processing*, Elsevier, Amsterdam, Netherlands, pp. 601–670, 2014.
- [3] A. Pramanik, A. K. Basak, Y. Dong et al., "Joining of carbon fibre reinforced polymer (CFRP) composites and aluminium alloys - a review," *Composites Part A: Applied Science and Manufacturing*, vol. 101, pp. 1–29, 2017.
- [4] A. Mostafapour and F. Taghizad Asad, "Investigations on joining of Nylon 6 plates via novel method of heat assisted friction stir welding to find the optimum process parameters," *Science and Technology of Welding & Joining*, vol. 21, no. 8, pp. 660–669, 2016.
- [5] R. S. Mishra and Z. Y. Ma, "Friction stir welding and processing," *Materials Science and Engineering: R: Reports*, vol. 50, no. 1–2, pp. 1–78, 2005.
- [6] S. Eslami, P. J. Tavares, and P. M. G. P. Moreira, "Friction stir welding tooling for polymers: review and prospects," *International Journal of Advanced Manufacturing Technology*, vol. 89, no. 5–8, pp. 1677–1690, 2017.
- [7] T. W. Nelson, C. D. Sorenson, and C. J. Johns, "Friction stir welding of polymeric materials," US Patent, US01014501, 2001.
- [8] J. Gao, X. Cui, C. Liu, and Y. Shen, "Application and exploration of friction stir welding/processing in plastics industry," *Materials Science and Technology*, vol. 33, no. 10, pp. 1145–1158, 2017.
- [9] H. Ahmadi, N. B. Mostafa Arab, and F. A. Ghasemi, "Optimization of process parameters for friction stir lap welding of carbon fiber reinforced thermoplastic composites by Taguchi method," *Journal of Mechanical Science and Technology*, vol. 28, pp. 278–284, 2014.
- [10] G. H. Payganeh, N. B. Mostafa Arab, Y. Dadgar Asl, F. A. Ghasemi, and M. Saeidi Boroujeni, "Effects of friction stir welding process parameters on appearance and strength of polypropylene composite welds," *International Journal of the Physical Sciences*, vol. 6, no. 19, pp. 4595–4601, 2011.
- [11] Z. Kiss and T. Czigány, "Effect of welding parameters on the heat affected zone and the mechanical properties of friction stir welded poly(ethylene-terephthalate-glycol)," *Journal of Applied Polymer Science*, vol. 125, no. 3, pp. 2231–2238, 2012.
- [12] A. Zafar, M. Awang, S. R. Khan, and S. Emamian, "Investigating friction stir welding on thick Nylon 6 plates," *Welding Journal*, vol. 95, no. 6, pp. 210–218, 2016.
- [13] F. Simões and D. M. Rodrigues, "Material flow and thermo-mechanical conditions during friction stir welding of polymers: literature review, experimental results and empirical analysis," *Materials & Design*, vol. 59, pp. 344–351, 2014.
- [14] N. Sadeghian and M. K. Besharati Givi, "Experimental optimization of the mechanical properties of friction stir welded Acrylonitrile Butadiene Styrene sheets," *Materials & Design*, vol. 67, pp. 145–153, 2015.
- [15] F. Lambiase, A. Paoletti, and A. Di Ilio, "Effect of tool geometry on mechanical behavior of friction stir spot welds of polycarbonate sheets," *International Journal of Advanced Manufacturing Technology*, vol. 88, no. 9–12, pp. 3005–3016, 2016.
- [16] B. Kusharjanta, W. Raharjo, and Triyono, "Temperature comparison of initial, middle and final point of polypropylene friction stir welded," *AIP Conference Proceedings*, vol. 1717, Article ID 040011, 2016.
- [17] S. Saeedy and M. K. B. Givi, "Investigation of the effects of critical process parameters of friction stir welding of polyethylene," *Proceedings of the Institution of Mechanical Engineers - Part B: Journal of Engineering Manufacture*, vol. 225, no. 8, pp. 1305–1310, 2011.
- [18] K. Raza, M. Shamir, M. K. A. Qureshi, A. S. Shaikh, and M. Zain-ul-abdein, "On the friction stir welding, tool design optimization, and strain rate-dependent mechanical properties of HDPE-ceramic composite joints," *Journal of Thermoplastic Composite Materials*, vol. 31, no. 3, pp. 291–310, 2018.
- [19] V. K. S. Jain, J. Varghese, and S. Muthukumaran, "Effect of first and second passes on microstructure and wear properties

Retraction

Retracted: Characterization of Composite RFID Antennas Based on Thermal Properties: A Survey

Advances in Materials Science and Engineering

Received 26 December 2023; Accepted 26 December 2023; Published 29 December 2023

Copyright © 2023 Advances in Materials Science and Engineering. This is an open access article distributed under the Creative Commons Attribution License, which permits unrestricted use, distribution, and reproduction in any medium, provided the original work is properly cited.

This article has been retracted by Hindawi, as publisher, following an investigation undertaken by the publisher [1]. This investigation has uncovered evidence of systematic manipulation of the publication and peer-review process. We cannot, therefore, vouch for the reliability or integrity of this article.

Please note that this notice is intended solely to alert readers that the peer-review process of this article has been compromised.

Wiley and Hindawi regret that the usual quality checks did not identify these issues before publication and have since put additional measures in place to safeguard research integrity.

We wish to credit our Research Integrity and Research Publishing teams and anonymous and named external researchers and research integrity experts for contributing to this investigation.

The corresponding author, as the representative of all authors, has been given the opportunity to register their agreement or disagreement to this retraction. We have kept a record of any response received.

References

- [1] C. Varadhan, F. Ashine Chamatu, and S. Arulsevi, "Characterization of Composite RFID Antennas Based on Thermal Properties: A Survey," *Advances in Materials Science and Engineering*, vol. 2021, Article ID 8905489, 9 pages, 2021.

Review Article

Characterization of Composite RFID Antennas Based on Thermal Properties: A Survey

Chitra Varadhan ¹, Fekadu Ashine Chamatu ² and S. Arulselvi¹

¹Department of ECE, Bharath Institute of Higher Education and Research, Chennai 600 073, Tamilnadu, India

²Department of Chemical Engineering, College of Biological and Chemical Engineering, Addis Ababa Science and Technology University, Addis Ababa 16417, Ethiopia

Correspondence should be addressed to Chitra Varadhan; chitralaya@gmail.com and Fekadu Ashine Chamatu; fekadu.ashine@aastu.edu.et

Received 25 July 2021; Revised 17 August 2021; Accepted 19 August 2021; Published 16 September 2021

Academic Editor: Samson Jerold Samuel Chelladurai

Copyright © 2021 Chitra Varadhan et al. This is an open access article distributed under the Creative Commons Attribution License, which permits unrestricted use, distribution, and reproduction in any medium, provided the original work is properly cited.

In this paper, a comprehensive survey on thermal and geometric design parameters of composite materials utilized in the fabrication of modern RFID systems has been discussed mainly due to its advantages such as lightweight and high strength. Designing of RF antenna setup requires careful consideration of material, geometric and fabrication parameters. Polymer materials were chosen as the substrate and subjected to extensive studies to determine and predict the capability of the miniaturized RFID antenna. The effect of the polymer matrix composite (PMC) material on the antenna parameters such as gain, bandwidth, and return loss is analyzed and realized that improvement in bandwidth and perfection in impedance matching can be further accomplished by employing fractal structure. It is also discovered that the thermal properties affect the impedance and operating frequencies, thus enabling multilayer PMC deploying fractal structured RFID antennas to be used for many applications such as logistics, aerospace, biomedical, and mining.

1. Introduction

Recent trends in the field of composites involve vigorous research in composite materials-based radio frequency identification (RFID) antennas. RFID comprises of two important elements, reader and tag. The radio waves are travelling from the reader, whereas tag has the ability to respond accordingly. The tag/reader is capable for both transmission and receiving the data by means of RF antennas. The major features of RFID technology are primarily the contactless transmission of data and nonline of sight between reader and tag. There tag encounters various environmental challenges such as grime, paint, fog, snow, ice, and bottles with chemicals while in storage. A massive utilization of UHF-RFID tag/readers in the day-to-day life such as item movement tracing, railway rolling stock identification, theft prevention, tracking library books, toll collections, vehicle parking access control, building access control, retail stock managements, proximity cards, and vehicle immobilizer systems.

Electro-civil industries such as aerospace or shipbuilding are widely using carbon-based materials in the fields as they demonstrate superior properties such as higher corrosion resistivity, long life time, and high stability within a wide temperature domain. Due to the extensive properties of carbon-based materials which are highly incorporated in resonators, filters, transmission lines, and high gain antenna designs, Aixin et al. communicated on composite metamaterials, exhibiting abundant properties in the microwave starting from 1 GHz to 100 GHz [1]. RFID system communicating through antenna includes the substrate sandwiched between the patch and ground plane. The substrate of the RFID antenna can be fabricated using a flexible heat sensitive polymer or a rigid heat retardant polymer based on the user application. Designing planar antennas is precisely dependent on the dielectric constant values such as loss tangent ($\tan \delta$) and relative permittivity (ϵ_r). An increase in value of dielectric constant results in decrease of the antenna size yielding a narrow bandwidth, due to capacitive load influenced in RF energy [2]. Similarly, the thermal

conductivity will influence the effects during the usage of antenna, resulting in shift in operating frequency, thus affecting the read range of the antenna. Design of RFID antenna is crucial and RFID engineers must have a broad vision about the temperature range experienced on the substrate during usage such that the selection of composite material should not deteriorate the overall performance of antenna.

Multilayered composite materials comprising of cardboard, gypsum, and natural flaked graphite were considered. The fundamental definite characters of radio-absorbing materials are influenced by the working range of the radiation wavelengths and thickness of the composite material. Composite absorbing materials can be employed in the RFID antenna as substrate, as well as radiating element to decrease the weight of the antenna, to improve the durability and to enhance the thermal expansion. The objective of the utilization of composite material is to enhance the performances such as gain and directivity, meanwhile suppressing interferences among the elements of antenna and performing with excellent transmission features in extensive RFID antenna frequency ranges. Bucky paper (single-walled carbon nanotube) is one of the most extremely conductive materials.

The remainder of the paper is organized as follows. Session 2 initiates with composite materials in RFID as a radiating element and elaborates on antenna substrates. Section 3 showcases the thermal conductivity measurement setup followed by the thermal conductivity in RFID, and conclusion is presented in Section 4.

2. Composite Material in RFIDs as Radiating Element and Substrates

Creation of optically transparent antennas appropriate for RFID systems can be adapted to various forms through the usage of conductive polymers [3,4]. In earlier days, RFID technology applications implemented nonconventional materials such as silver-ink, due to reasonable price. However, they are impractical for flexible RFIDs and are conformal as conductive polymers with the limitation of operation in low frequency applications. Literature surveys are proving that the composite materials used in RFID antenna have equivalent radiation characteristics to that of a traditional metal model. A popular fabrication method suggested in the literature survey is to coat the graphene on a nonplanar surface of the antenna.

Nicholas et al. [4] fabricated the antenna in copper as well as conductive polymer, Clevios PH500 PEDOT-PSS, through description; the selected conductive polymer has conductivity of 300 S/m. To optimize the conductivity, 10% dimethyl sulfoxide (DMSO) is combined with polymer, and to decrease the surface tension, 2% surfactant (Tween-21) is added. On simulation of both the RFID antennas, it was observed that the modified antenna shows conductivity closely equal to 5×10^5 S/m, which is nearer to the conductivity of copper 5.9×10^7 S/m. For the substrate, polyethylene terephthalate (PET) was chosen and the improvised RFID antenna was fabricated on the conductive polymer,

with the dielectric constant of 3.8 and the thickness of 0.5 mm. Since dipole antenna does not require ground plane, the antenna is transparent, easy to design, and flexible in nature. Few properties and its corresponding values of graphene which is used as metal surface in the RFID antenna are listed in Table 1.

Biocomposite materials such as wood plastic composite (WPC) are served as antenna substrate, especially for the frequencies 1–20 GHz. One of the popular selection of WPC is polypropylene (PP) and Leucaena Leucocephala wood filler used as an adhering (laminated) substrate for RFID antenna. The WPC is a desirable material as it is commonly available in nature and cost-effective with thermal resistance up to 180°C of melting point. The hot and cold pressing methods are used to construct the antenna substrate. During the progression, certain gap dispute arises due to the formation of internal blisters due to heat transmission. Measurement of thermal distribution and dielectric properties inside the substrate measurement is difficult to perform. However, the study of temperature and pressure required for hot/cold pressing, material moisture content, venting time, and humidity are essential, since the water absorption leads to the formation of air bubble inside the prototype, therefore resulting in degradation of RF signal. The literature says that the thermal properties of wood are mostly affected by denseness, wood structure, fibre, moisture, and carbon contents. Therefore, wood filler with polypropylene as RFID substrate is laminated to provide tolerance to moisture absorption and also raise the immunity to the thermal conductivity.

In polymer thick film technology, the usage of conductive paste as substrate is due to improved electrical performance of printed RFID antennas even though the conductive paste gives rise to increase in resistance [5]. This technology works well at low temperatures on cost-effective substrates, especially in membrane keyboards and electromagnetic shielding to avoid electromagnetic interferences in the miniaturized electronic devices. Most commonly used conductive pastes are copper oxide and silver oxide. The particle density of the conductive silver paste provides substantial increase in paste properties, as the resistance of copper oxide paste is substantially increased after curing when compared with silver oxide which remains invariable irrespective of change in environmental conditions. The resistivity of conductive paste can be decreased by 70%; reliability improved around 2.4 times and also reduction in area compared to conventional smart labels when particle density is increased. Due to compression process, the conductive silver particles create a contact with substrate material and produce better performance compared to copper engraved smart labels.

The composite materials are associated in injectable RFID antenna; a passive RFID antenna is embedded at the bottom of the skin to transfer the data for monitoring the glucose level and orthopaedic identification. The antenna is printed on plastic sheets as stickers and is fixed subdermally. In traditional methods, the antenna includes conductive inks and paints submerged inside the skin. This results in occurrence of imperfection due to ageing. Recent research on

TABLE 1: Properties of graphene-composite metal antennas [3].

Parameters	Brass	Zoltek Px 35	Aluminium
Tensile strength	450	4137	100
Tensile modulus	100	242	75
Density	8500	1810	2700
Electrical resistivity	6×10^{-8}	15.5×10^{-6}	3×10^{-8}
Temperature of melting (decomposition) of metal (GCM) ($^{\circ}\text{C}$)	900	>650	650
Coefficient of thermal expansion	19.1×10^{-6}	8×10^{-8}	23.8×10^{-6}

polymer engineering development has devised injectable nanocomposite hydrogel material which is solid at body temperature [6–9]. The muscles act as ground plane and the antenna injected on the fat gives accurate results compared to conventional injectable skin antennas. This modified RFID antenna provides sufficient substitution for the future generation work on subdermal RFID antennas.

Mobile antennas can be realized using polymer magneto-dielectric (MD) material and copper coating as radiating element. A schematic representation of polymer-based mobile antenna is shown in Figure 1. Polycarbonate is used as a substrate and the performances are evaluated and compared with conventional FR 4 [10]. It is observed that there is a difference in wavelength between the antenna substrate and human body. This causes a shift in resonant frequency, which is moderated by the usage of MD substrate, resulting in greater efficiency. It was also detected that the regression of performance of the antenna is reduced by implementation of MD material when compared with conventional material. The weight of the magneto-dielectric antenna is 2.88 g, which is slightly more compared with traditional mobile antenna weighing 1.41 g.

In recent years, anisotropic conductive adhesives (ACAs) are very popular in applications of RFID flip chip packaging. The ACAs are having enormous advantages when compared with conventional bonding materials due to minimal cost, less processing steps, and lower processing temperature for large scale RFID tag inlays manufacturing. Majorly there are two types of ACAs, one is anisotropic conductive pastes (ACPs) and another is anisotropic conductive films (ACFs). Fabrication of a flexible RFID antenna with polymer adhesive continues to prove as a struggle. Compared to ACPs, the cost of ACFs is much higher and the stability of RFID tags is low. ACAs are structured by blending micro-sized spherical silver components with possible curing agent into a thermos-set epoxy resin. On aluminium blended with polyethylene terephthalate (PET), the RFID chips were fabricated, silver/PET was printed, and silver/paper antenna was printed through hot-press bonding process. Reliability tests are performed and flip chip on flex association were calculated [11] in which it was discovered that during the hot-press process, the polymer matrix is unstable and nonuniform. Hence, post-curing was suggested to improve the stability of the antenna substrate. The RFID tags adhering to the substances which contain conductive materials result in degradation of radiation properties such as impedance mismatch, shifting in operating frequency, changes in radiation pattern, and reflection in radiating RF energy (S_{11}). These variations

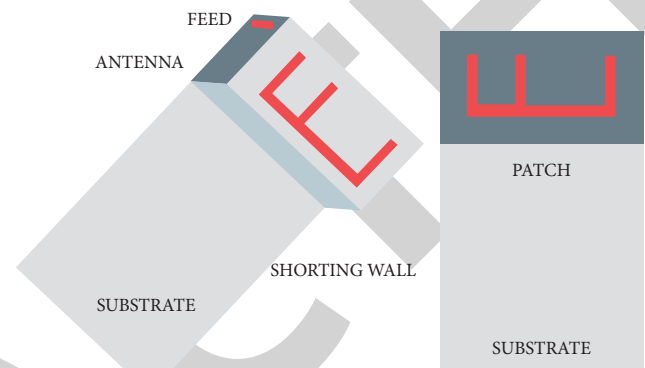


FIGURE 1: Polymer-based mobile antenna on polycarbonate substrate.

depend on the shape, size, and antenna distance from the conductive material [11]. Thus, selection of composite materials is very essential to improve the RFID reader/tag antenna parameters.

3. Thermal Conductivity in RFID

RFID technology depends on common parameters, such as pressure, luminosity, humidity, deformation, and temperature. Due to measurement inaccuracy of the above parameters, the antenna performance is compromised. Accuracy of antenna is of utmost importance in critical applications and increase in temperature induces degradations in performance of RF signals. Temperature is nothing but heat intensity present in any element or body. Therefore, thermal analysis has become mandatory for commercial applications of RFID antennas. As from the literature surveys, parameters like operating frequencies and impedances decline due to increased temperature in metallic parts and substrate of the tag antenna [12, 13]. This results in impedance mismatch between reader and tag; this discrepancy can be avoided by self-tuning circuit in the RFID chip. The self-tuning circuits are used for acquiring values from chip memory bank for acknowledged input temperature values and a RFID tag can be regulated and worked as a temperature sensing element. This method can be adopted only for fixed RFID tags, since the input impedance is a function of received power. Thus, the self-tuning circuit can be activated to accomplish various values of known input power [14]. Table 2 presents association between the thermal expansion coefficient and the thermal coefficient of relative permittivity.

TABLE 2: Input impedance of the three RFID chips as function of temperature [12].

Temperature (°C)	Real part of impedance (Ω)			Imaginary part of impedance (Ω)		
	30	6.85	8.03	7.45	-139	-134
40	7.4	7.34	7.46	-138	-135	-132
50	7.53	8.5	7.81	-138	-133	-131
60	7.69	8.6	8.16	-138	-133	-131
70	7.9	8.66	8.23	-134	-134	-131
80	8.52	8.79	9.34	-138	-133	-131

In the design consideration, RT6010.2LM is used as a substrate ($\epsilon_r = -425$ ppm/°C), which gives high thermal coefficient. The RFID tag is activated with a very low power sensor providing extraordinary read range, accomplished with smaller size. The electrical performance is directly proportional to the reading distance; hence, a low antenna resistance is necessary, especially for long range systems, e.g., airline baggage handling or parcel services. There are 2 methods to decrease the resistance: (1) increasing the track height by repeated print of the coil structure or (2) increasing the particle density within the paste by applying a compression process. Due to its economic and ecological advantages, the second method can be adopted. The thermal modification of substrate contributes overall sensitivity of tag. Konstantinos et al. described that the variation in temperature results in slight increase of input impedance by very little amount on real part while the imaginary part remains unaffected. Due to the presence of self-tuning circuit, the imaginary part remains almost constant in the UHF-RFID chips. Some properties of commonly used substrate are listed in Table 3. The substrates and its corresponding coefficient of thermal expansion and temperature coefficient of relative permittivity are tabulated.

A UHF passive RFID temperature sensor tag antenna is designed and simulated using EM software. A cavity backed slot antenna is proposed in this design as a RFID tag antenna. Polytetrafluoroethylene (PTFE) material is realized as temperature sensing material due to its high thermal expansion around 140 ppm/°C. In the centre of the slot antenna, a copper-layered PTFE pole is employed and is vicinity to the cavity ceiling. Thus, between cavity ceiling and PTFE surface, a loaded capacitor is induced. When temperature increases, PTFE approaches cavity ceiling, thus there is a change in frequency of slot antenna due to the thermal expansion. The expansion results in a frequency deviation of 30 MHz/10°C and of 10.5 m read range with the calculated value. Figure 2 shows the linear relationship between thermal displacement vs temperature variations [15–19]. Generally, the thermal expansion can be realized at moderate temperatures. The effects of thermal expansion can also be experimented in metallic nanostructures through 5 nm-wide RFID slot antenna by providing additional degree of freedom in the nanostructure results in improved functionality in thermal modulation. The effects of thermal variation are established by comparing the features of air-filled slot antenna and spacer-filled slot antennas.

The EM software and coupled mode method (CMM) were used to simulate and measure the modulation in resonant frequency at different temperature. The temperature deformation of slot antenna is embedded on glass substrate. During the increase of heat gradually from 25°C to 190°C, it is observed that the width of slot antennas is diminished from 5 nm to 2 nm due to thermal expansion. During heating, the slot antenna thickness increases linearly. Thus, variation in frequency of operation can be reduced by impregnating the nanostructures with active materials, for example, vanadium dioxide-based nanostructures.

3.1. Thermal Monitoring Measurement Setup. The thermal properties were measured using thermal property analyser. The antenna under test (AUT) is experimented by perfectly insulating the small antennas in the Fresnel region and the temperature is monitored [20–24]. The cold temperature measurement setup which is maintained under -100 °C can be extended to full cold-hot temperature spectrum. The liquid nitrogen is filled in the bottom part to cool the AUT; the heat conduction mechanism is designed without affecting the performance reduction build up on the surface of AUT in a laboratory setup with a material under test (MUT). MATLAB was used to develop the model and the flowchart of thermal prognostic cycle is shown in Figure 3.

At room temperature, it attains -105 °C and the resonant frequency is measured with the help of RF cable. The temperature is monitored by the thermistors and data logger. Multiprobe system is used to measure the RF changes with respect to the variation in the temperature. Thus, it determines the RF dependency with respect to changes in temperature within the same setup. This testing method leads to a very efficient and cost-effective thermal testing. It is focused on three important parameters, volume heat capacity, thermal diffusivity, and thermal conductivity with respect to the temperature. SVR algorithm is used to find the probable temperatures; using this algorithm, a prognostic model is established. Irregularities in temperature along with the joints of RF power cables are compared with the output temperature. Thus, the degradation can be analyzed and corrected.

3.2. Performance Evaluation of Thermal Sensitivity between Composite and Traditional Materials. For the performance evaluation of RFID reader/tag antennas, monitoring the thermal sensitivity is a very essential parameter. Yang et al. [25] identified two important sensing approaches for thermal monitoring which are electrical and thermal properties of sensing materials. The temperature-dependent electrical properties are sensed with water and high density polyethylene-Ba_{0.3}Sr_{0.7}TiO₃ (HDPE-BST). The thermal expansion properties are measured with mercury and polytetrafluoroethylene (PTFE). In antennas, the patch is constructed for electrical properties, due to narrow bandwidth characteristics, favourable for sensing operations. To determine electrical sensing properties, initially water is embedded as substrate of patch antenna to reconfigure the antenna resonant frequency with temperature ($\Delta f/\Delta T$);

TABLE 3: Properties of frequently used substrate [12].

Substrate	Coefficient of thermal expansion ($x/y/z$ axis)	Thermal coefficient of relative permittivity (ϵ_r)
RT6010.21.M	24/24/27 ppm/ $^{\circ}$ C	-425 ppm/ $^{\circ}$ C
RT6006	47/34/117 ppm/ $^{\circ}$ C	-410 ppm/ $^{\circ}$ C
RO4350 B	10/12/32 ppm/ $^{\circ}$ C	+50 ppm/ $^{\circ}$ C
RO4003 C	11/14/46 ppm/ $^{\circ}$ C	+40 ppm/ $^{\circ}$ C
RT5870	22/28/173 ppm/ $^{\circ}$ C	-115 ppm/ $^{\circ}$ C
RT5880	31/48/237 ppm/ $^{\circ}$ C	-125 ppm/ $^{\circ}$ C

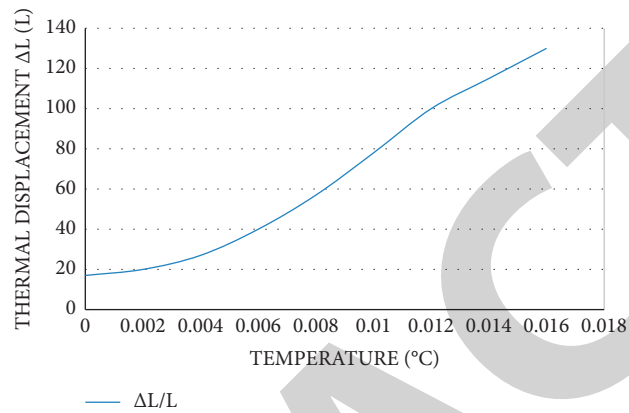


FIGURE 2: Comparison between thermal displacement and temperature.

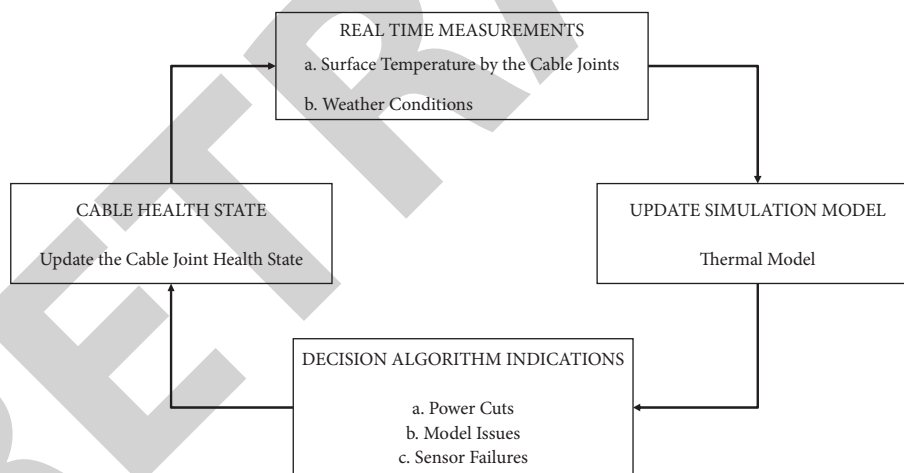


FIGURE 3: Thermal monitoring flowchart.

permittivity of water reduces from 80 at 20° C to 67 at 60° C. To find the sensitivity of the antenna, the parameters such as frequency shift/temperature, gain realization, and bandwidth are calculated [26–32]. Thus, the observed result is 3.2 dB realized gain with 4.33% bandwidth and 4 MHz/ 10° C frequency shift.

Since water inside the substrate is difficult to control and low reliability of the design, a novel composite material HDPE-BST was proposed to integrate with the patch as a substrate. The measurement of the antenna material parameters such as loss tangent and relative permittivity was studied under different temperatures. Due to small observed gain, it was noted that there is a significant decrease of read range to 4.2 m at 16° C.

The read range is calculated by using Friis transmission equation. The designed antenna is simulated using HFSS software and the results are compatible with the calculated results. The design is fabricated and the prototype is measured in the anechoic chamber. In Figure 4, structure of slot antenna HDPE-BST sensing antenna is depicted.

For identifying thermal properties, cavity backed slot antennas are created to integrate mercury as sensing material inside the cavity. For temperature monitoring, the large coefficient of thermal expansion of mercury (180 ppm/ $^{\circ}$ C) is appropriate. Tunable cavity resonators can be used to change the tuning gap between cavity ceiling and the metal post in cavity effectively. This results in small variation (Approx.

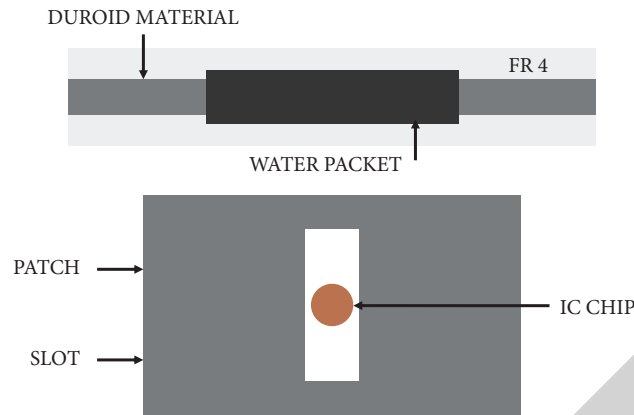


FIGURE 4: Structure of the HDPE-BST sensing antenna.

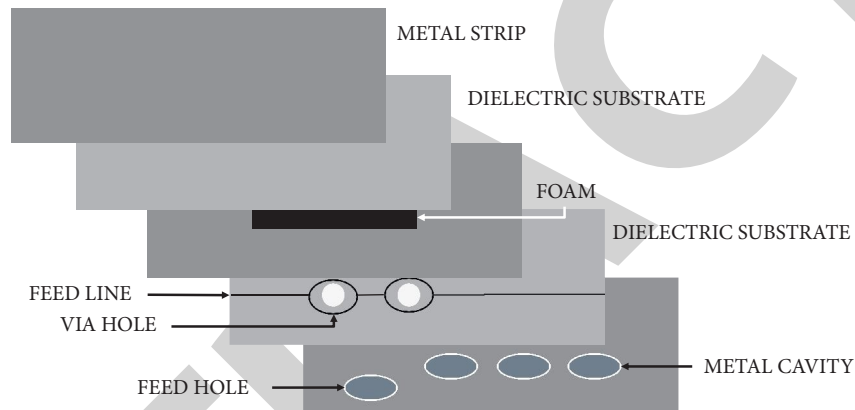


FIGURE 5: Capacitive loaded cavity backed RFID slot antenna structure.

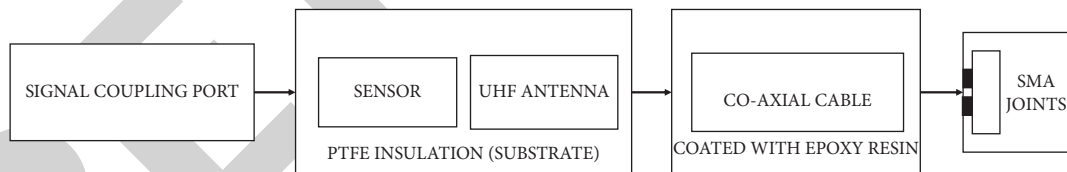


FIGURE 6: Structure of PTFE sensing antenna.

13 MHz/10 °C) in the order of μm , which effectively causes changes in frequency transformation in MHz. The sensing material forms a huge capacitive loaded with cavity backed in the slot antenna. According to the change in temperature, a change in gap thickness is created, which produces change in resonant frequency of the RFID slot antenna, as shown in Figure 5.

Since integration of mercury as liquid is difficult inside the cavity, an alternative sensing element based on PTFE was proposed. Due to the solid state of PTFE, higher sensitivity was achieved by close proximity to the ceiling of the cavity [33–38]. The prototype antenna, fabricated with PTFE, observed 40 MHz/10°C with read range of 14 m, which is the best option for sensing elements compared to the other

proposed designs, thus making composites to be highly desirable as sensing antennas in practical applications [39–43]. For a constant temperature, the read range follows a normal distribution with a sharp peak at the resonant frequency. However, as the temperature increases, the graph is skewed with the same normal distribution with slightly lesser read range values [44–54]. General structure of PTFE sensing antenna is depicted in Figure 6.

4. Conclusion

In this communication, the properties of composite materials used in modern RFID system have been discussed and studied due to its appreciable properties such as lightweight

and high strength. Thermal properties and structural design specifications of the substrate materials have been reviewed and discovered that the thermal properties affect the impedance and operating frequencies. Designing of RF passives antenna requires consideration of material, structure, fabrication parameters, and other uncertainties. The effects of composite material have been studied in detail and the performance of the compact multiband RFID antenna was forecasted using the models. By extending this approach, investigation of the behavior of complete setup can be calculated, containing other prime parameters, such as RFID antenna size, structure, and losses in material, and thermal variation with frequency. Based on the parameters, the gain of the antenna, bandwidth, and reflection coefficients can be inferred. For further improvement, miniaturization can be attained by deploying suitable fractal geometry RFID antennas with composite material. The composite material-based antennas can be used for many applications such as biomedical, satellite, and mining applications.

Data Availability

The data used to support the findings of this study are included within the article.

Conflicts of Interest

Chitra Varadhan received her Bachelor degree in Electronics and Communication Engineering from Regional Engineering College (NIT, affiliated with Bharathidasan University, Trichy, Tamil Nadu, India) in 1996 and completed Master of Engineering in College of Engineering, Anna University, Guindy, Chennai, in 2008. Currently, she is pursuing PhD in Design of Fractal RFID Antennas in BIHER (Bharath Institute of Higher Education and Research, Chennai, Tamil Nadu, India). Arulselvi is working as an associate professor in BIHER (Bharath Institute of Higher Education and Research, Chennai, Tamil Nadu, India). Her areas of specialization include networking and communications. Currently, she is guiding Chitra Varadhan in the area of Fractal RFID Antennas. The authors declare that they have no conflicts of interest.

References

- [1] L. Martin, D. Staiculescu, H. Li, S. L. Ooi, C. P. Wong, and M. M. Tentzeris, "Investigation of the impact of magnetic permeability and loss of magnetic composite materials on RFID and RF passives miniaturization," in *Proceedings of the 2007 Workshop on Computational Electromagnetics in Time-Domain*, pp. 1–4, Perugia, Italy, October 2007.
- [2] N. Dugin, T. Zaboronkova, and E. Myasnikov, "Using carbon-based composite materials for manufacturing C-range antenna devices," *Latvian Journal of Physics and Technical Sciences*, vol. 53, no. 5, pp. 17–23, 2016.
- [3] N. J. Kirsch, N. A. Vacirca, E. E. Plowman, T. P. Kurzweg, A. K. Fontecchio, and K. R. Dandekar, "Optically transparent conductive polymer RFID meandering dipole antenna," in *Proceedings of the 2009 IEEE International Conference on RFID*, pp. 278–282, Orlando, FL, USA, April 2009.
- [4] M. Luniak, M. Roellig, and K. J. Wolter, "A technology enabling improved properties of polymer conductive pastes," in *Proceedings of the 26th International Spring Seminar on Electronics Technology*, pp. 104–107, High Tatras, Slovakia, May 2003.
- [5] A. M. Chrysler, C. M. Furse, K. L. Hall, and Y. Chung, "Effect of material properties on a subdermal UHF RFID antenna," *IEEE Journal of Radio Frequency Identification*, vol. 1, no. 4, pp. 260–266, 2017.
- [6] S. Amendola, R. Lodato, S. Manzari, C. Occhiuzzi, and G. Marrocco, "RFID technology for IoT-based personal healthcare in smart spaces," *IEEE Internet of Things Journal*, vol. 1, no. 2, pp. 144–152, 2014.
- [7] Z. Xiao, X. Tan, X. Chen et al., "An implantable RFID sensor tag toward continuous glucose monitoring," *IEEE Journal Biomedical Health Information*, vol. 19, no. 3, pp. 910–919, 2015.
- [8] S. Milici, S. Amendola, A. Bianco, and G. Marrocco, "Epidermal RFID passive sensor for body temperature measurements," in *Proceedings of the IEEE RFID Technology Application Conference (RFID TA)*, pp. 140–144, Tampere, Finland, September 2014.
- [9] J. Jungyub Lee, J. Juhyang Lee, K. Yonghun Cheon, and Y. Cheon, "Miniaturized antennas with reduced hand effects in mobile phones using magneto-dielectric material," *IEEE Antennas and Wireless Propagation Letters*, vol. 13, pp. 935–938, 2014.
- [10] X.-H. Cai, B. An, Y.-P. Wu, F.-S. Wu, and X.-W. Lai, "Research on the contact resistance and reliability of flexible RFID tag inlays packaged by anisotropic conductive paste," in *Proceedings of the 2008 International Conference on Electronic Packaging Technology & High Density Packaging*, pp. 1–5, Shanghai, China, July 2008.
- [11] K. Zannas, H. El Matbouly, Y. Duroc, and S. Tedjini, "Self-tuning RFID tag: a new approach for temperature sensing," *IEEE Transactions on Microwave Theory and Techniques*, vol. 66, no. 12, pp. 5885–5893, 2018.
- [12] M. C. Caccami and G. Marrocco, "Electromagnetic modeling of self-tuning RFID sensor antennas in linear and nonlinear regimes," *IEEE Transactions on Antennas and Propagation*, vol. 66, no. 6, pp. 2779–2787, 2018.
- [13] M. C. Caccami and G. Marrocco, "Electromagnetic characterisation of self-tuning UHF RFID tags for sensing application," in *Proceedings of the 2016 IEEE International Symposium on Antennas and Propagation (APSURSI)*, pp. 1273–1274, Fajardo, PR, USA, June 2016.
- [14] F. Amato, C. Miozzi, S. Nappi, and G. Marrocco, "Self-tuning UHF epidermal antennas," in *Proceedings of the 2019 IEEE International Conference on RFID Technology and Applications (RFID-TA)*, pp. 380–383, Pisa, Italy, September 2019.
- [15] Q. Qiao, L. Zhang, F. Yang, Z. Yue, and A. Z. Elsherbeni, "A high sensitivity capacitively-loaded UHF RFID temperature sensor tag using PTFE material," in *Proceedings of the 2014 IEEE Antennas and Propagation Society International Symposium (APSURSI)*, pp. 1310–1311, Memphis, TN, USA, July 2014.
- [16] M. Dhaouadi, M. Mabrouk, T. P. Vuong, A. C. de Souza, and A. Ghazel, "A capacitively-loaded loop antenna for UHF near-field RFID reader applications," in *Proceedings of the 2015 IEEE Radio and Wireless Symposium (RWS)*, pp. 193–195, San Diego, CA, USA, January 2015.
- [17] Q. Liu, Y. Yu, and S. He, "Capacitively loaded, inductively coupled fed loop antenna with an omnidirectional radiation

- pattern for UHF RFID tags,” *IEEE Antennas and Wireless Propagation Letters*, vol. 12, pp. 1161–1164, 2013.
- [18] Y.-K. Jung and B. Bomson Lee, “Capacitively loaded loop antenna fed by wideband metamaterial balun,” in *Proceedings of the 2009 IEEE Antennas and Propagation Society International Symposium*, pp. 1–4, North Charleston, SC, USA, June 2009.
- [19] P. Cheong, S. N. Lam, Y. Q. Qui, W. W. Choi, and K. W. Tam, “A tunable antenna-filter module for simultaneous UHF RFID-based power facility monitoring and partial discharge measurement,” in *Proceedings of the 2010 International Conference on Applications of Electromagnetism and Student Innovation Competition Awards (AEM2C)*, pp. 182–186, Taipei, Taiwan, August 2010.
- [20] A. Giacomini, R. Morbidini, L. J. Foged et al., “Thermal testing of small antennas in multi-probe spherical near-field systems,” in *Proceedings of the 2017 Antenna Measurement Techniques Association Symposium (AMTA)*, pp. 1–6, Atlanta, GA, USA, October 2017.
- [21] L. J. Foged, A. Giacomini, and R. Morbidini, “Thermal testing of small antennas in spherical near field system,” in *Proceedings of the 2011 IEEE International Conference on Microwaves, Communications, Antennas and Electronic Systems (COMCAS 2011)*, pp. 1–7, Atlanta, GA, USA, October 2011.
- [22] C. Bencivenni, M. Gustafsson, A. Haddadi, A. U. Zaman, and T. Emanuelsson, “5G mmwave beam steering antenna development and testing,” in *Proceedings of the 2019 13th European Conference on Antennas and Propagation (EuCAP)*, pp. 1–4, Krakow, Poland, March 2019.
- [23] C.-Y. Tsai, H. E. Chen, I. Hu, D.-L. Chen, D. Tarnq, and C. P. Hung, “System thermal analysis of RF SiP module in smartphone,” in *Proceedings of the 2020 15th International Microsystems, Packaging, Assembly and Circuits Technology Conference (IMPACT)*, pp. 165–167, Taipei, Taiwan, October 2020.
- [24] D. Sato, N. Yamada, and K. Tanaka, “Thermal characterization of hybrid photovoltaic module for the conversion of sunlight into microwave in solar power satellite,” in *Proceedings of the 2015 IEEE 42nd Photovoltaic Specialist Conference (PVSC)*, pp. 1–4, New Orleans, LA, USA, June 2015.
- [25] F. Yang, Q. Qiao, L. Zhang, Z. Yue, and A. Z. Elsherbeni, “High-sensitivity RFID sensing antennas: from sensing mechanism selections to antennas structure designs,” in *Proceedings of the 2014 XXXIth URSI General Assembly and Scientific Symposium (URSI GASS)*, pp. 1–4, Beijing, China, August 2014.
- [26] K. Chang, Y.-h. Kim, Y.-j. Kim, and Y. Yoon, “Patch antenna using synthesized polyimide for RFID sensing,” in *Proceedings of the 2006 European Conference on Wireless Technology*, pp. 83–86, Manchester, UK, September 2006.
- [27] S. Manzari, A. Catini, C. Di Natale, and G. Marrocco, “Ambient sensing by chemical-loaded UHF-RFIDs,” in *Proceedings of the 2013 7th European Conference on Antennas and Propagation (EuCAP)*, pp. 1718–1720, Gothenburg, Sweden, April 2013.
- [28] X. Song, G. Wang, and Y. He, “Design of the high-sensitivity RFID sensor tag with MOEA/D-DE,” in *Proceedings of the 2016 International Symposium on Antennas and Propagation (ISAP)*, pp. 950–951, Okinawa, Japan, October 2016.
- [29] M. Wagih and J. Shi, “Wireless ice detection and monitoring using flexible UHF RFID tags,” *IEEE Sensors Journal*, 2021.
- [30] B. Wang, M.-K. Law, J. Yi, C.-Y. Tsui, and A. Bermak, “A –12.3 dBm UHF passive RFID sense tag for grid thermal monitoring,” *IEEE Transactions on Industrial Electronics*, vol. 66, no. 11, pp. 8811–8820, 2019.
- [31] K. Pan, L. Teng, L. Ting, X. Zhou, A. A. Stokes, and Z. Hu, “Soft wireless battery-free UHF RFID stretchable sensor based on microfluidic technology,” *IEEE Journal of Radio Frequency Identification*, vol. 3, no. 4, pp. 252–258, 2019.
- [32] A. A. Aziz, A. Mursyidi, R. Tahir, and A. Rahman Nurul, “Measurement of dielectric and thermal properties of Leucaena Leucocephala bio composite substrate with different composition mixture,” *Journal of Engineering and Science Research VL*, vol. 2, 2018.
- [33] C. Pelvillain, P. Cussac, S. Diahm, Z. Valdez-Nava, M.-L. Locatelli, and T. Lebey, “Dielectric and thermal properties of parylene N and D films for power electronic surface insulation,” in *Proceedings of the 2015 IEEE 11th International Conference on the Properties and Applications of Dielectric Materials (ICPADM)*, pp. 508–511, Sydney, Australia, July 2015.
- [34] X. Huang, P. Peng, W. Peng, J. Yu, F. Liu, and P. Jiang, “Thermal conductivity and dielectric properties of epoxy composites with hyperbranched polymer modified boron nitride nanoplatelets,” in *Proceedings of the 2012 IEEE International Conference on Condition Monitoring and Diagnosis*, pp. 1089–1092, Bali, Indonesia, September 2012.
- [35] Suwarno and F. Salim, “Effects of electric arc on the dielectric properties of liquid dielectrics,” in *Proceedings of the 2006 IEEE 8th International Conference on Properties & applications of Dielectric Materials*, pp. 482–485, Bali, Indonesia, June 2006.
- [36] N. Rahman, S. Chen, K. A. Korolev, M. N. Afsar, R. Cheung, and M. Aghion, “Millimeter wave complex permittivity measurements of high dielectric strength thermoplastics,” in *Proceedings of the 2008 IEEE Instrumentation and Measurement Technology Conference*, pp. 2146–2149, Victoria, Canada, May 2008.
- [37] H. S. Yun, J. Jeong, D. Kim, and D.-S. Kim, “Active thermal control of 5 nm gap terahertz antennas,” in *Proceedings of the 2018 43rd International Conference on Infrared, Millimeter, and Terahertz Waves (IRMMW-THz)*, pp. 1–2, Nagoya, Japan, September 2018.
- [38] J. Castellon, H. Yahyaoui, O. Guille, E. David, M. Guo, and M. Fréchette, “Dielectric properties of POSS/LDPE and MgO/LDPE nanocomposites compounded by different techniques,” in *Proceedings of the 2017 IEEE Conference on Electrical Insulation and Dielectric Phenomenon (CEIDP)*, pp. 457–460, Fort Worth, TX, USA, October 2017.
- [39] X. Chen, J. Liu, J. Zheng et al., “Insulation property analysis of cross-linked polyethylene based on density functional theory,” in *Proceedings of the 2018 12th International Conference on the Properties and Applications of Dielectric Materials (ICPADM)*, pp. 347–350, Xi’an, China, May 2018.
- [40] K. Wu, Y. Wang, X. Wang, M. Fu, and S. Hou, “Effect of space charge in the aging law of cross-linked polyethylene materials for high voltage DC cables,” *IEEE Electrical Insulation Magazine*, vol. 33, no. 4, pp. 53–59, 2017.
- [41] H. Ren, L. Zhong, W. Zhao et al., “Influence of crosslinking byproducts on DC conductivity of HVDC XLPE cable insulation,” in *Proceedings of the 2018 IEEE Conference on Electrical Insulation and Dielectric Phenomena (CEIDP)*, pp. 90–93, Cancun, Mexico, October 2018.
- [42] A. Hedir, O. Jbara, M. Moudoud, F. Slimani, S. Rondot, and F. Bellabas, “Behaviour of cross-linked polyethylene used as high voltage power cables insulation due to environmental constraints,” in *Proceedings of the 2018 International*

Retraction

Retracted: Structural Classification of Basalt FRP at High Temperatures

Advances in Materials Science and Engineering

Received 26 December 2023; Accepted 26 December 2023; Published 29 December 2023

Copyright © 2023 Advances in Materials Science and Engineering. This is an open access article distributed under the Creative Commons Attribution License, which permits unrestricted use, distribution, and reproduction in any medium, provided the original work is properly cited.

This article has been retracted by Hindawi, as publisher, following an investigation undertaken by the publisher [1]. This investigation has uncovered evidence of systematic manipulation of the publication and peer-review process. We cannot, therefore, vouch for the reliability or integrity of this article.

Please note that this notice is intended solely to alert readers that the peer-review process of this article has been compromised.

Wiley and Hindawi regret that the usual quality checks did not identify these issues before publication and have since put additional measures in place to safeguard research integrity.

We wish to credit our Research Integrity and Research Publishing teams and anonymous and named external researchers and research integrity experts for contributing to this investigation.

The corresponding author, as the representative of all authors, has been given the opportunity to register their agreement or disagreement to this retraction. We have kept a record of any response received.

References

- [1] S. Vummadisetti, S. R. Pasalapudi, S. K. Gottapu, K. K. Goriparthi, and A. Batu, "Structural Classification of Basalt FRP at High Temperatures," *Advances in Materials Science and Engineering*, vol. 2021, Article ID 6917471, 9 pages, 2021.

Research Article

Structural Classification of Basalt FRP at High Temperatures

Sudhir Vummadiseti ¹, Sesa Ratnam Pasalapudi ², Santosh Kumar Gottapu ³,
Kranthi Kumar Goriparthi ³ and Areda Batu ⁴

¹Department of Civil Engineering, Vignan's Institute of Information Technology (A), Duvvada, Visakhapatnam 530049, India

²Department of Civil Engineering, Gayatri Vidya Parishad, Rushikonda, Visakhapatnam 530045, India

³Department of Civil Engineering, Gayatri Vidya Parishad College of Engineering (A), Madhurawada, Visakhapatnam 530048, India

⁴Department of Chemical Engineering, College of Biological and Chemical Engineering, Addis Ababa Science and Technology University, Addis Ababa, Ethiopia

Correspondence should be addressed to Areda Batu; areda.batu@aastu.edu.et

Received 6 August 2021; Revised 23 August 2021; Accepted 27 August 2021; Published 13 September 2021

Academic Editor: Samson Jerold Samuel Chelladurai

Copyright © 2021 Sudhir Vummadiseti et al. This is an open access article distributed under the Creative Commons Attribution License, which permits unrestricted use, distribution, and reproduction in any medium, provided the original work is properly cited.

In this study, two different temperatures are considered to verify the mechanical response of basalt fiber-reinforced polymer specimens. Initially, fibers are subjected to 300°C temperature for 4 hours and 600°C temperature for 2 hours in an electrical muffle furnace effectively. Later, laminates were prepared with these fibers and machined into test strips to verify their mechanical properties by conducting tensile and flexural tests. These laminates were compared with specimens prepared with normal fibers, i.e., fibers without temperature treatment. Moreover, the ductility and elastic behavior of the basalt fiber-laminated specimens are studied to figure out the possible structural applications. The residual stress of specimens subjected to 300°C temperature under tensile loading is about 84%, whereas for 600°C temperature, it is only 13% of maximum stress. A similar trend has been observed for specimens tested under flexural loading condition. Hence, it is concluded that the basalt fiber-reinforced polymer laminate can withstand and depict satisfactory results up to 300°C elevated temperature irrespective of time.

1. Introduction

Ductility is the capacity of a structural member to undertake large inelastic deformations without notable loss of strength or stiffness. Due to ductility, structures or materials can absorb energy by deforming into an inelastic range under the application of force. In other words, it is the ability to withstand plastic deformation before fracture which can be defined as the ratio of the ultimate deformation at an assumed collapse point to the yield deformation. For resistance to earthquake forces, the structure, elements, and connections shall be designed to have ductile failure to avoid sudden collapse. However, ductility is hard to achieve in many structural members such as deep beams, pile caps, and corbels. Since such members tend to fail mostly in the shear mode, the assumptions of the linear-elastic flexural theory and pure bending theory are not valid. These members require special considerations for design and

detailing. Therefore, in order to achieve ductility, many design methodologies like Strut-and-Tie model and materials such as admixtures, plasticizers, and fibers are adopted. Moreover, with the increase in fire-related disasters around the world, the importance of fire-resistant construction is escalating.

In recent decades, many researchers [1–11] have studied the properties and applicability of basalt fiber in structural members due to its high temperature resistance, high durability, high elastic strength, sustainability, etc. It has been found that satisfactory mechanical and thermal-resistant properties of structural members can be achieved using chopped basalt fibers, basalt fiber-reinforced polymer (BFRP) bars, BFRP sheets, laminates, etc. However, contradictory findings are also available in the literature regarding the residual mechanical strength of basalt fibers subjected to elevated temperature conditions. Therefore, in this work, an attempt has been made to study the mechanical

properties of basalt fibers subjected to various temperature conditions. The chopped fibers could not be tested directly due to the smaller lengths, for which laminates are prepared to test the mechanical properties as per ASTM standards. The basalt fiber samples were elevated to different temperatures, and then, through mechanical testing, the residual stress of fibers was evaluated and compared. Therefore, in recent times, the basalt fibers are of importance in research because of its high mechanical properties, thermal resistance, durability, sustainability, low production cost, etc. Basalt filaments are formed by melting the basalt rock which passes through orifices and pullers over a roller [12]. The economic advantage, lower environmental impact, and higher mechanical strength are achieved because no additives are required to produce these fibers from high-strength basalt rocks. The authors of [12, 13] found that volcanic magma crystallizes to basalt with very low water content at the time of crystallization. Basalt rocks are the partial melting products of primitive rocks such as garnet peridotite. Basalt consists of minerals such as plagioclase and clinopyroxene along with olivine, nepheline, melilite, hypersthene, quartz, etc. Based on the original rock used, the produced fibers may exhibit different mechanical and chemical properties. Soares et al. [14] stated that acidic basalt which contains more than 46% of SiO_2 is suitable for production of basalt fiber because in order to develop glass network, high silica content is necessary. As stated earlier, basalt fibers are available with different chemical compositions containing 51.56–57.5% SiO_2 , 16.9–18.2% Al_2O_3 , 5.2–7.8% CaO , 1.3–3.7% MgO , 2.5–6.4% Na_2O , 0.8–4.5% K_2O , 4.0–9.5% Fe_2O_3 , etc.

Investigation was performed on temperature resistance of basalt fibers which generally has an operational temperature range from -200°C to 800°C [15]. Basalt fibers perform much better than glass fibers as the temperature range of basalt fibers is -269°C to 700°C as compared to glass fibers whose temperature range is from -60°C to 500°C [16]. Most of the studies show that basalt fibers perform very efficiently at high temperatures. However, contradictory results are found in different literature studies regarding the residual mechanical strength of basalt fibers subjected to elevated temperature conditions. The authors of [16] found that with the increase of time of exposure and elevated temperature up to 300°C , the strength of basalt fibers increased up to 19.1%. Also, 32.8% reduction of strength is observed in similar testing conditions [17]. Zollo et al. [16] explained that the reformation of fiber structure around the nucleating agents led to the thermal stability of the fibers. However, Arvo Ivar and Bjorklund [17] described from SEM and XRD analysis that the short-order structure of basalt fibers decreased in size which led to reduction in tensile strength. A lot of research was performed on functionally graded hybrid composite materials, and parametric study has also been performed on these novel layups [18–22]. This layup can be applied in case of basalt fibers also. Therefore, it is necessary to analyze residual mechanical strength of the basalt fiber specimens subjected to elevated temperatures because such variations occur due to the change in the

crystalline structure of the fiber which is mainly governed by the presence of iron oxides.

2. Experimental Methods

2.1. Procedure

2.1.1. Tensile Properties of BFRP Specimens. The in-plane tensile properties of polymer matrix composite materials reinforced with high-modulus fibers can be determined as per ASTM D 3039/D3039M [23]. Monotonically tensile load is applied on the flat strip of the material with a constant rectangular cross section which is mounted in the grips as shown in Figure 1.

The maximum load carried before failure is the ultimate failure strength of the material. Moreover, if the strain or displacement is monitored, then stress-strain response can be obtained. The speed of test should be controlled at a constant head displacement rate of 2 mm/min or a standard strain rate of 0.01 min^{-1} .

2.1.2. Flexure Properties of BFRP Specimens. Basalt fiber-reinforced polymer (BFRP) specimens were subjected to flexural load under the three-point bending system as shown in Figure 2. Both rigid and semirigid materials in the shape of rectangular bars moulded directly or machined from plates, sheets, or moulded shapes can be tested within the 5% strain limit of the test methods [1].

As shown in Figure 2, a bar of rectangular cross section resting on two supports is loaded at midway where the radius of the support is of minimum 3.2 mm to maximum 1.6 times the specimen depth, whereas the maximum radius of the loading nose is limited to 4 times the specimen depth. The support span-to-depth ratio of 16:1 should be maintained at a strain rate of 0.01 mm/mm/min. The failure occurs at a maximum strain of 5%. The rate of crosshead motion is determined using the following equation:

$$R = \frac{ZL^2}{6D} \quad (1)$$

The flexural strength, chord, secant, or tangent modulus of elasticity and the total work can be measured by calculating the area under the load-deflection curve. If “ r ” is the strain in mm/mm, the mid-span deflection (D) can be calculated using the following equation:

$$D = \frac{rL^2}{6d} \quad (2)$$

2.2. Material Properties

2.2.1. Basalt Fibers. Basalt fibers were acquired from Go Green Products, Chennai, which were of 24 mm length and diameter more than 5 microns (Go Green Products 2018). As per the supplier, the density was 2.6 g/cm^3 , melting point was 1450°C , and they constituted odorless golden shine fibers (Figure 3). Their chemical composition is shown in Table 1.



FIGURE 1: Tensile test of the BFRP specimen with a universal testing machine.

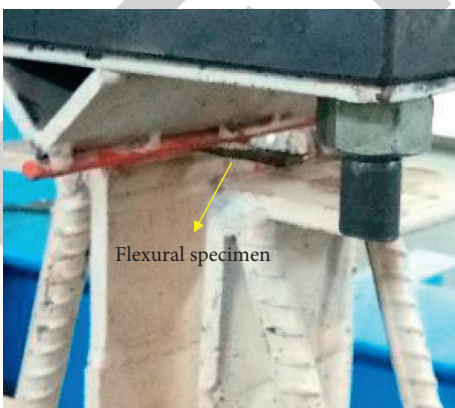


FIGURE 2: Three-point loading for testing of BFRP flexure specimens.

2.2.2. Epoxy and Hardener. An epoxy resin of grade “Resin 691” and a hardener of grade “Reactive Polyamide 140” have been used. The ratio of the resin to hardener is maintained at 9:1 by weight [24]. The mechanical properties of the resin are given in Table 2.



FIGURE 3: Chopped basalt fibers.

TABLE 1: Chemical composition of basalt fibers as provided by the supplier.

Chemical name	Percent
SiO ₂	51.6%–59.3
Al ₂ O ₃	14.6%–18.3
CaO	5.9%–9.4
MgO	3.0%–5.2
Na ₂ O + K ₂ O	3.6%–5.3
TiO ₂	0.8%–2.25
Fe ₂ O ₃ + FeO	9.0%–14.0
Others	0.09%–0.13

TABLE 2: Mechanical properties of Resin 691.

Property	Value
Density (g/cm ³)	2.6
Poisson's ratio	0.32
Tensile strength (MPa)	71
Tensile stiffness (GPa)	3.6
Tensile failure strain (%)	4.0
Glass transition temperature (°C)	91.23
Decomposition temperature (°C)	230

TABLE 3: Thermal properties of the basalt fiber.

Property	Value
Work temperature, °C	–269 to 700°C
Blind temperature, °C	1050°C
Thermal conductivity coefficient (w/m° K)	0.03 to 0.038
Maximum service temperature, °C	650°C
Melting temperature, °C	1350°C
Fire blocker	Upto 1200°C
Coefficient of thermal expansion	$1.4 \times 10^{-6}/^{\circ}$
Specific heat capacity	0.86 J/g.K

The thermal properties of the basalt fiber are significant in the current study. Hence, the properties are depicted in Table 3.



FIGURE 4: Basalt fibers subjected to temperature heating: (a) muffle furnace; (b) fibers removed from muffle furnace after heating.



FIGURE 5: Aluminum sheets used for curing for smooth finishing.



FIGURE 6: Dimensioning and cutting of specimens from the laminates with a DoAll machine.

3. Specimen Preparation

As per ASTM D3039/D3039M [3], five basalt fiber-reinforced (BFRP) specimens of uniform geometry should be prepared. The geometry depends on fiber orientation, gage length, grip type and length, use of tab, etc. At three places in the gage section, width (w) and thickness (h) are calculated to find the average cross-section area (A) from the following equation:

$$A = w \times h. \quad (3)$$

The laminates of size $310 \times 310 \times 2.5 \pm (0.15)$ mm (length \times width \times thickness) are prepared in the mould developed at Advanced Composites Laboratory, BITS, Pilani. The mechanical properties of basalt fibers are characterized

by subjecting them to elevated temperatures of 300°C and 600°C . Initially, the fibers are kept in an electric muffle furnace as shown in Figure 4(a), and the fibers are removed after heating, as shown in Figure 4(b).

The mould of heavy flat metal base plates is used to apply uniform pressure to prepare the laminates, flat aluminum sheets are used for smooth surface finishing, and the outer rectangular blockboard ring is used to maintain the dimension of the laminates, as shown in Figure 5. The matrix consists of the epoxy resin of grade "Resin 691" along with the hardener "Reactive Polyamide 140" at the ratio of 9:1 by weight. The ratio of the fiber to matrix is maintained as 0.6. Since the glass transition temperature of the resin is 91.23°C and decomposition temperature is 230°C only, the laminates are not tested at

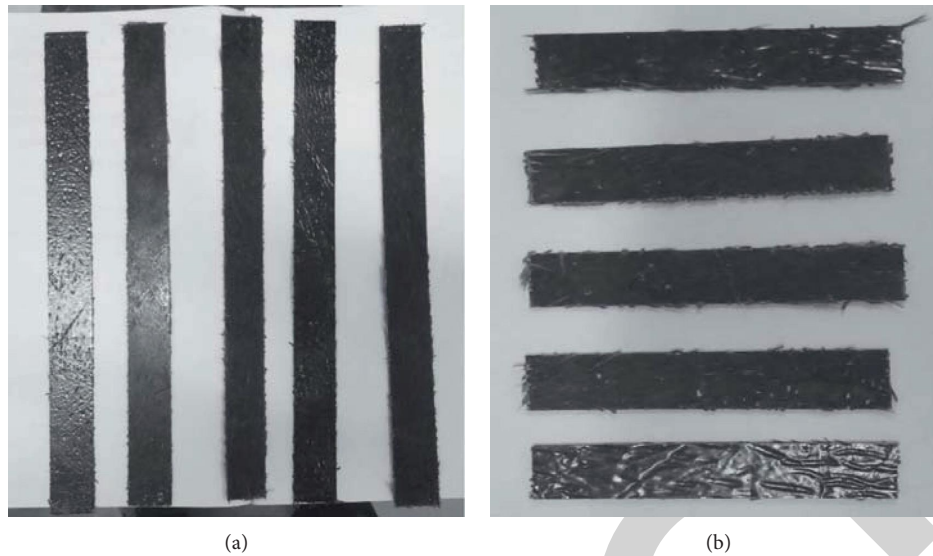


FIGURE 7: Test specimens: (a) tensile and (b) flexural specimens.



FIGURE 8: Failure of the BFRP specimen under tensile loading.

elevated temperatures but only the residual stress of fibers are calculated by preparing the laminates using the resin and hardener. Even though many attempts were made to prepare linearly oriented fiber-reinforced composite plates, due to the smaller length of the fiber and dispersion of epoxy resin, the orientation of fibers in the laminates was considered as randomly distributed. After mixing the fibers with the matrix, the

plates are tightened using screws and kept for minimum 40 hours of conditioning.

After proper conditioning of the laminates, specimens are prepared by cutting using a DoAll cutting machine at Mechanical Workshop, BITS, Pilani, as shown in Figure 6. The tensile specimens of size $250 \times 25 \times 2.5$ mm (length \times width \times thickness) are considered as per Table 2 of ASTM D 3039/D 3039M, and flexure specimens of size 12.7×2.5 mm (width \times thickness) with varying lengths are used to accommodate at least 10% overhanging after maintaining 16 : 1 span-to-depth ratio conforming to ASTM D790 [25].

Three types of specimens have been prepared in this study. One with fibers without any temperature treatment, other with fibers subjected to 300°C elevated temperature, and the last with fibers subjected to 600°C elevated temperature. These three specimens are named as BFRP-I, BFRP-II, and BFRP-III, respectively. Laminates are machined, and all the 5 specimens (both for tensile and flexural tests) are depicted in Figure 7.

The coefficient of variation of the tensile and flexural stress of the specimens tested has been calculated using equation (4) to maintain the quality of work done. The coefficient of variation for all the specimens is not greater than 10% which is considerable:

$$\bar{x} = \sum \frac{x_i}{n} \quad (4)$$

4. Results and Discussion

The BFRP specimens are tested, and the results are discussed as follows.

4.1. Tensile Behavior. The failure of the BFRP specimen tested in a universal testing machine is shown in Figure 8. The type of failure observed was lateral gage middle (LGM)

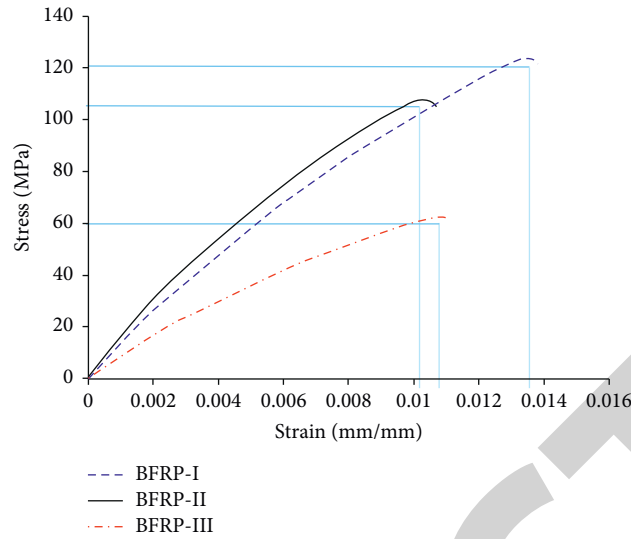


FIGURE 9: Stress-strain response of tensile BFRP specimens.

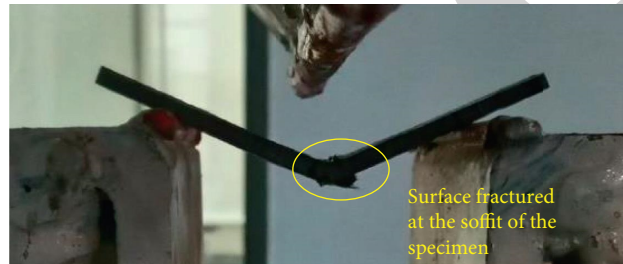


FIGURE 10: Three-point bending test conducted on the BFRP specimen.

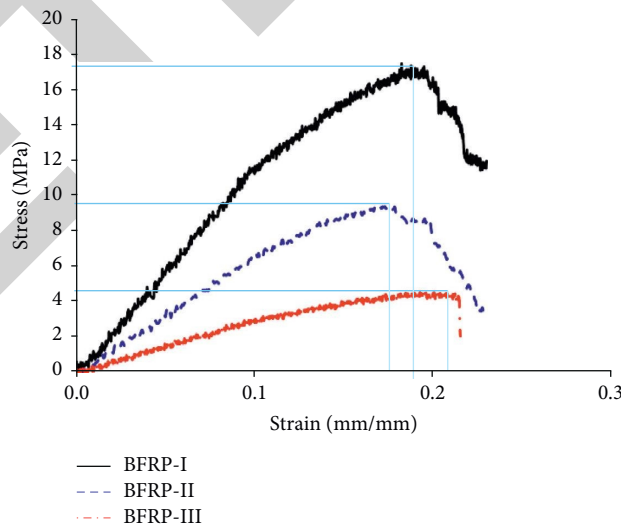


FIGURE 11: Stress-strain response of flexural BFRP specimens tested at room temperature and elevated temperature.

failure since the crack appeared laterally at the mid-position of the specimen. A similar type of failure was observed in all the specimens tested under tensile load.

The stress-strain graphs of BFRP-I, BFRP-II, and BFRP-III are depicted in Figure 9, and the bar charts representing

the maximum stress obtained and the maximum strain obtained at peak stress are also shown in Figure 12.

BFRP-I has obtained the highest tensile stress among other specimens subjected to elevated temperature. It is worth noting that specimens elevated at 600°C have the least tensile stress.

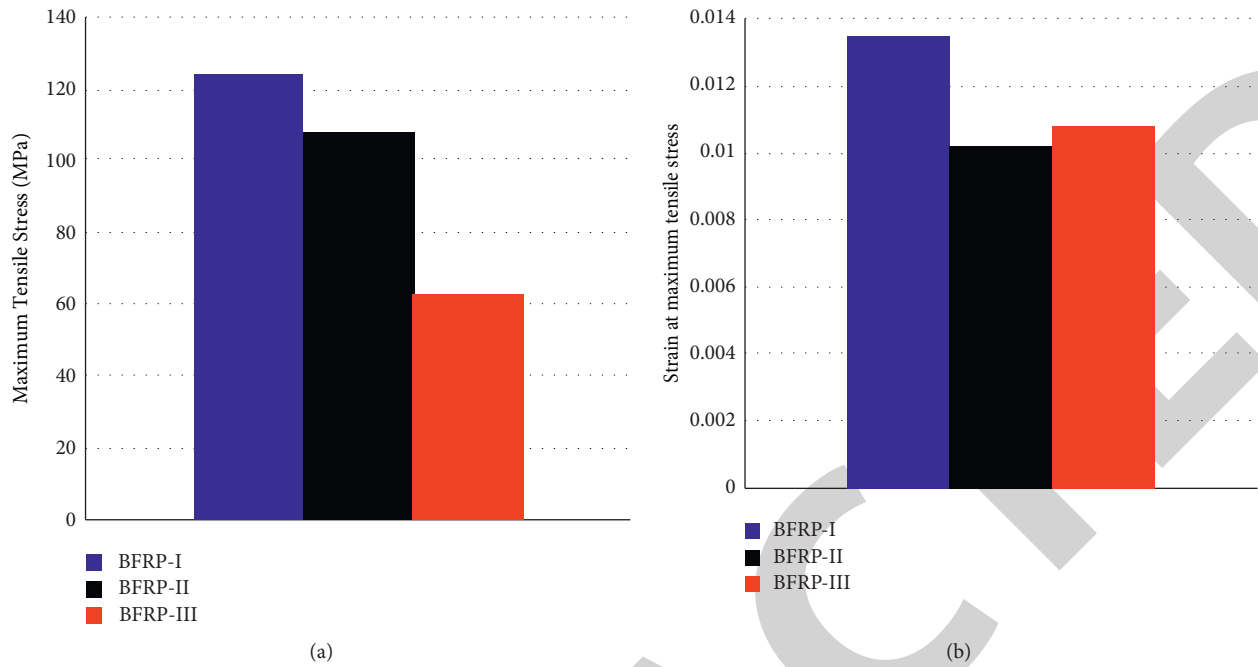


FIGURE 12: Tensile bar charts: (a) maximum stress with respect to specimen; (b) strain at maximum stress obtained.

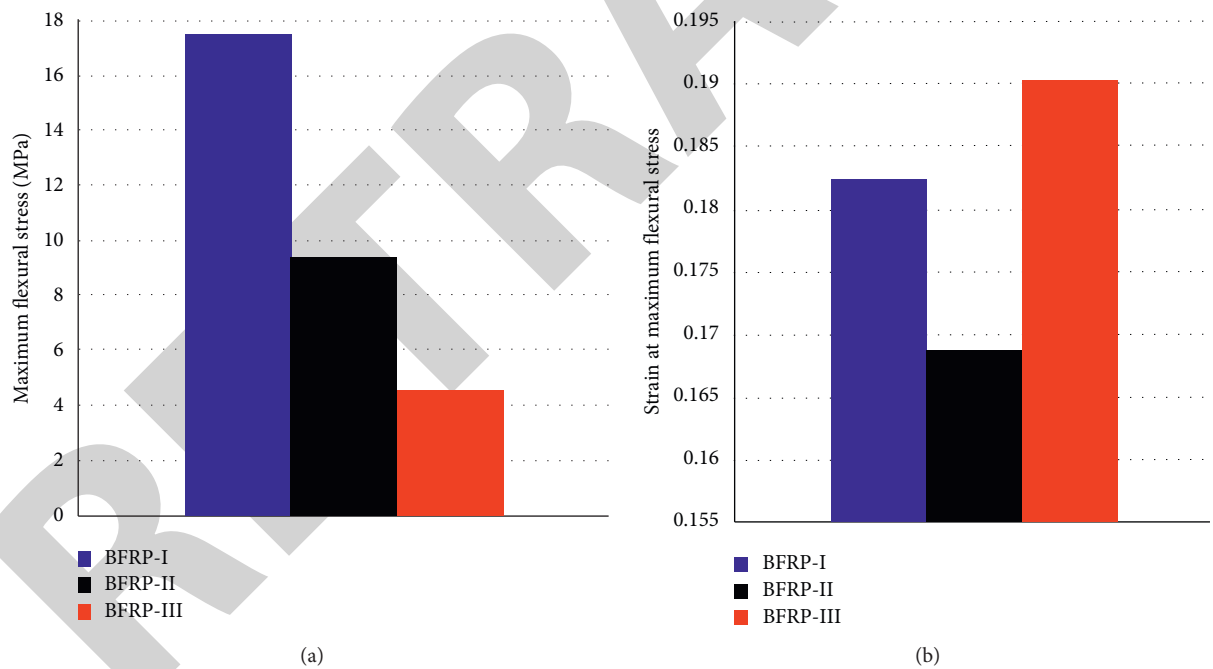


FIGURE 13: Flexure bar charts: (a) maximum stress with respect to specimen; (b) strain at maximum stress obtained.

Hence, it is observed that increase in tensile stress is observed until 300°C temperature. Further increase in temperature leads to decrease in tensile stress. Although the stress is low, temperature-elevated specimens exhibit ductile nature; i.e., the failure of the specimens is not catastrophic.

4.2. Flexural Behavior. The specimens are tested under a three-point bending apparatus as shown in Figure 10. The

soffit of the specimen was fractured upon the application of load at the middle as shown in Figure 10.

The flexural stress-strain graphs are plotted in Figure 11. It is observed that BFRP-I, i.e., the specimen without temperature curing, obtained the highest flexural stress among other specimens. The BFRP-II specimen has higher flexural stress than the BFRP-III specimen. A similar trend has been observed in the case of tensile specimens.

As shown in Figures 12 and 13, the residual tensile stress of basalt fibers elevated to 300°C is around 84%, whereas for 600°C, it is around 13% of maximum stress. However, the strain at maximum stress shows that ductile behavior of the specimen is maintained even at 600°C which signifies that even at higher temperature, the fibers perform quite well in case of serviceability. The reduction of stress due to higher temperature may not be due to change in the crystalline structure of the fibers but also due to poor interlaminar shear strength. The specimens are ductile in nature since none of the specimens collapsed suddenly (see Figures 9 and 11).

Particularly, in comparison with the tensile results, it was discovered that the residual stress of flexure basalt fibers elevated at 300°C is approximately 54% of the maximum stress, while it is approximately 10% of the maximum stress in the case of fibers elevated at 600°C.

The current study's structural applications are diverse. The laminates made of basalt fiber can be used as a direct material or as a retrofitting material. Roof panels, pultruded beams, load bearing I-sections, partition members, pedestrian bridges, railway sleepers, and other structural members made of basalt fibers can be used directly. The basalt fibers can be utilized for column wrapping and slab strengthening by connecting the fiber sheet at the soffit and as near surface mounted members in the case of retrofitting technique. The following are some of the applications for basalt fiber-reinforced polymer laminates. The added benefit of this material, in particular, is that it is thermally resistant.

5. Conclusions

The following conclusions are made from this study:

- (1) Basalt fiber has high tensile strength and modulus of elasticity, making it suitable for use in reinforced composites.
- (2) The electrical insulation of basalt fiber is greater than that of glass fiber.
- (3) The electromagnetic wave has excellent permeability; if a basalt fiber cloth is added to the building's wall, it can produce good shielding for all types of electromagnetic waves.
- (4) The residual stress of basalt fiber decreases, as the temperature increases in case of both tensile and flexural specimens irrespective of time.
- (5) The experiment shows the sustainability and reusability of basalt fiber since at higher temperature, the ductile behavior is maintained and residual stress up to 300°C is still satisfactory.
- (6) With the use of high-temperature-resistant epoxy resin, basalt fibers can be used in fire-resisting constructions very effectively.
- (7) Excellent compatibility with metal, plastic, carbon fiber, and other materials is found. Also, the composite of basalt continuous fiber and various types of resin has a stronger bonding strength than of glass fiber and carbon fiber. In terms of strength,

composites made of continuous basalt fiber are equivalent to E-glass fiber, but elastic modulus has obvious advantages in all types of fibers.

Abbreviations

- A: Area of cross section of the specimen (mm²)
 R: Crosshead motion (mm)
 Z: Rate of straining (mm/mm/min)
 L: Support span (mm)
 d: Depth of the beam (mm)
 r: Strain (mm)
 D: Mid-span deflection (mm)
 w: Width of the specimen (mm)
 h: Thickness of the specimen (mm)
 \bar{x} : Average value of samples
 n: Number of specimens.

Data Availability

The data used to support the findings of this study are included within the article.

Disclosure

This study was performed as part of the employment at Addis Ababa Science and Technology University, Addis Ababa, Ethiopia.

Conflicts of Interest

The authors declare that there are no conflicts of interest.

References

- [1] J. Sim and C. Park, "Characteristics of basalt fiber as a strengthening material for concrete structures," *Composites Part B: Engineering*, vol. 36, no. 6-7, pp. 504-512, 2005.
- [2] S. Carmignato, I. M. De Rosa, F. Sarasini, and M. Valente, "Characterization of basalt fibre reinforced vinylpolyester composite: an overview," in *Proceedings of the 2nd International Conference on Innovative Natural Fiber Composites for Industrial Applications*, Rome, April 2009.
- [3] A. N. Lisakovski, Y. L. Tsybulya, and A. A. Medvedyev, "Yarns of basalt continuous fibers," in *Proceedings of the Fiber Society Spring 2001 Meeting*, pp. 23-25, Raleigh, NC, May 2001.
- [4] J.-M. Park, W.-G. Shin, and D.-J. Yoon, "A study of interfacial aspects of epoxy-based composites reinforced with dual basalt and SiC fibres by means of the fragmentation and acoustic emission techniques," *Composites Science and Technology*, vol. 59, no. 3, pp. 355-370, 1999.
- [5] S. Matkó, P. Anna, G. Marosi et al., "Use of reactive surfactants in basalt fiber reinforced polypropylene composites," *Macromolecular Symposia*, vol. 202, no. 1, pp. 255-268, 2003.
- [6] T. Czigány, "Basalt fiber reinforced hybrid polymer composites," *Materials Science Forum*, vol. 473-474, pp. 59-66, 2005.
- [7] P. I. Bashantnik, V. G. Ovcharenko, and Y. A. Boot, "Effect of combined extrusion parameters on mechanical properties of basalt fiber-reinforced plastics based on polypropylene," *Mechanics of Composite Materials*, vol. 33, no. 6, pp. 600-603, 1997.

Retraction

Retracted: Multiobjective Optimization of Mechanical Properties on Sisal-Glass Fiber-Reinforced Hybrid Composites Using Response Surface Methodology and LINGO Analysis

Advances in Materials Science and Engineering

Received 26 December 2023; Accepted 26 December 2023; Published 29 December 2023

Copyright © 2023 Advances in Materials Science and Engineering. This is an open access article distributed under the Creative Commons Attribution License, which permits unrestricted use, distribution, and reproduction in any medium, provided the original work is properly cited.

This article has been retracted by Hindawi, as publisher, following an investigation undertaken by the publisher [1]. This investigation has uncovered evidence of systematic manipulation of the publication and peer-review process. We cannot, therefore, vouch for the reliability or integrity of this article.

Please note that this notice is intended solely to alert readers that the peer-review process of this article has been compromised.

Wiley and Hindawi regret that the usual quality checks did not identify these issues before publication and have since put additional measures in place to safeguard research integrity.

We wish to credit our Research Integrity and Research Publishing teams and anonymous and named external researchers and research integrity experts for contributing to this investigation.

The corresponding author, as the representative of all authors, has been given the opportunity to register their agreement or disagreement to this retraction. We have kept a record of any response received.

References

- [1] S. Rangunath, A. N. Shankar, K. Meena et al., "Multiobjective Optimization of Mechanical Properties on Sisal-Glass Fiber-Reinforced Hybrid Composites Using Response Surface Methodology and LINGO Analysis," *Advances in Materials Science and Engineering*, vol. 2021, Article ID 2376148, 10 pages, 2021.

Research Article

Multiobjective Optimization of Mechanical Properties on Sisal-Glass Fiber-Reinforced Hybrid Composites Using Response Surface Methodology and LINGO Analysis

S. Ragnath ¹, A. N. Shankar ², K. Meena ³, B. Guruprasad ⁴, S. Madhu ⁵,
N. Rakesh ⁶, M. Hariprabhu ⁷, S. Balamuralitharan ⁸, and Nahom Daniel ⁹

¹Mechanical Engineering, SVS College of Engineering, Coimbatore 642109, Tamilnadu, India

²Department of HSE & Civil Engineering, University of Petroleum & Energy Studies, Dehradun, India

³Department of Computer Science and Engineering,

Vel Tech Rangarajan Dr. Sagunthala R&D Institute of Science and Technology, Avadi, Chennai, Tamilnadu 600054, India

⁴Department of Mechanical Engineering, Alagappa Chettiar Government College of Engineering and Technology, Karaikudi, Tamilnadu, India

⁵Department of Automobile Engineering, Saveetha School of Engineering, Saveetha Institute of Medical and Technical Sciences, Chennai, Tamilnadu, India

⁶Department of Mechanical and Industrial Engineering, University of Technology and Applied Sciences, Nizwa, Oman

⁷Department of Electrical and Electronics Engineering, M. Kumarasamy College of Engineering, Karur, Tamilnadu, India

⁸Department of Mathematics, College of Engineering and Technology, SRM Institute of Science and Technology, Kattankulathur, Chengalpattu, Tamilnadu, India

⁹Department of Chemical Engineering, College of Biological and Chemical Engineering, Addis Ababa Science and Technology University, Addis Ababa, Ethiopia

Correspondence should be addressed to Nahom Daniel; nahom.daniel@aastu.edu.et

Received 19 July 2021; Accepted 16 August 2021; Published 8 September 2021

Academic Editor: Samson Jerold Samuel Chelladurai

Copyright © 2021 S. Ragnath et al. This is an open access article distributed under the Creative Commons Attribution License, which permits unrestricted use, distribution, and reproduction in any medium, provided the original work is properly cited.

The aim of this research work was to develop the optimal mechanical properties, namely, tensile strength, flexural strength, and impact strength of sisal and glass fiber-reinforced polymer hybrid composites. The sisal, in the form of short fiber, is randomly used as reinforcements for composite materials, which is rich in cellulose, economical, and easily available as well as glass fibers have low cost and have good mechanical properties. In addition, epoxy resin and hardener were for the fabrication of composites by compression molding. The selected materials are fabricated by compression molding in various concentrations on volume basics. The combination of material compositions is obtained from the design of experiments and optimum parameters determined by the Response Surface Methodology (RSM). From the investigation of mechanical properties, the sisal is the most significant factor and verified by ANOVA techniques. The multiobjective optimal levels of factors are obtained by LINGO analysis.

1. Introduction

The natural fiber is one of the most growing materials in the field of composite materials, which is available as a natural resource and has properties; there is a demand for high-performance composite materials in applications such as automotive, aircraft, and space. Natural fibers such as banana, hemp sisal, jute, flax, and coconut were used as

reinforced materials on fiber composite fabrications. The wide availability of natural fibers has encouraged the progress of natural fiber components on developed composites. Hence, it should have more benefits than synthetic fiber; for example, it has a biodegradable, considerable cost, low density, and most adequate properties [1–5]. There is a relationship between the epoxy resin and carbon fiber in their mechanical properties. The effects of fiber orientations

are 0, 35, 45, and 90, and the number of laminates and the type of resigning are taken as variables, but results were mainly dependent on the fiber orientation. The matrix materials such as thermoset polymer (epoxy resin) have the highest mechanical properties, and they are concluded that parameters that are taken into account are fiber orientation > number of laminates > resin type [1–9].

The experimental investigation was done on bananas and sisal hybrid composites to constrain the fiber load in the range of 0.20 to 0.50 volume fraction on fabrication. The materials are in the form of short fibers. They are randomly oriented to get increments on mechanical properties while increasing load [10]. Synthesis and mechanical properties of *Hibiscus sabdariffa* fiber with urea-formaldehyde (UF) were analyzed, and fibers that were taken into account are particle sizes, short fibers, and long fibers, and they found that UF resin has been more effective than the short fiber reinforcement [11]. The alkali-treated hollow epoxy particles were produced by water-based emulsion method along with polyester matrix composite. They examined tensile strength, tensile modulus, and flexural strength properties of the composites. Due to the interlocking of the polyester matrix into the pore regions of hollow epoxy particles, there is an increase in the mechanical, water absorption, and diffusion coefficient properties of the polyester composite [12].

The variation in the composition of epoxy resin had increasing mechanical properties of developed composites. The bio-based epoxy resin concluded that the physico-mechanical and thermal properties were increased and used for manufacturing high-performance automotive and aerospace products [13]. The unidirectional orientation of developed composites had better results than random orientation sisal fiber epoxy resin for tensile and flexural properties of sisal fiber-reinforced epoxy composites [14]. The mechanical behaviors of surface-modified sisal fiber epoxy composites were analyzed, and the optimum mechanical properties were obtained at 18% NaOH-treated sisal fibers and 110% enhancement in the tensile strength. they concluded that NaOH-treated sisal-epoxy composites varied linearly with fiber fractions reaching different percentages [15].

The mechanical and water absorption properties of jute/banana fibers were investigated through layering sequence and hybridization on fabrication and concluded that tensile and flexural strength of developed composites were higher than those of distinct composites. But the layering patterns have more significant effects than the other effects on tensile, flexural, and impact properties of the composite using the ANOVA[16]. The mechanical properties of glass and jute fiber composites were analyzed, and the results showed that the optimal addition of jute fibers produces more strength on developed composites. For the evaluation of experimental results, the FEM base numerical studies were followed, and finally, they predict that incorporation of natural and synthetic fibers was improved by the strength of mechanical properties [17]. Physicomechanical properties on banana fiber-reinforced polypropylene composites were studied, and these composites are prepared by compression molding with UV-treated banana fibers being used and its

mechanical properties increased significantly compared to untreated specimens. The optimum properties are obtained on 75 UV passes [18]. The alkali-treated sisal fibers with polypropylene composites were examined, and the results concluded that the treated fiber composites were improved because of their adhesion nature between the fibers and matrix; at the same time, treated fibers were damaged during the process [19].

MAPP treatment fibers were used to improve fire resistance and thermal properties of kenaf and sisal fiber-reinforced polypropylene composites. However, the impact strength of composites decreased with the addition of MAPP to the fiber because the interfacial bond strength between fiber and matrix decreased [20]. There is an effect of fiber twist on the mechanical properties of prepared composites on both unimpregnated and resin-impregnated sisal yarns. A critical fiber twist level for unimpregnated and impregnated sisal yarns was found as the tensile strengths were decreased and increased with increasing levels of fiber twists, respectively. It concluded that lower twist levels led to higher mechanical properties of composites. The experimental results are proved analytically by using Rao's model [21]. The mechanical and fracture behavior of banana fiber composites with maleic anhydride (MA) as a compatibilizer and glycerol triacetate ester (GTA) on the properties of PLA/BF composites was studied by Majhi et al.. Compatibilized biocomposites exhibited improved tensile modulus to the tune of 62% and GTA plasticized composites showed improvement in impact strength by 143% [22].

From the exhaustive literature survey, the present work is planned to be carried out by developing hybrid fiber-reinforced polymer composites with the combination of sisal fiber and epoxy matrix materials. The developed composites were investigated on mechanical properties, namely, tensile strength, flexural strength, and impact strength according to ASTM standard. The empirical models were developed through RSM for predicting the experimental value. The aim of the present work is to predict optimum levels of process parameters for tensile, flexural, and impact strength. In addition, LINGO analysis was used to determine the suitable compositions of selected materials for obtaining a quality composite specimen.

2. Experimental Setup

2.1. Materials. In experimental research work, the sisal and glass fiber were taken as reinforcement materials in the form of short and mate woven type fibers, respectively, to increase the mechanical properties of linear and lateral dimensions of the fabricated specimen and to increase the performance of flexural and impact strength. The epoxy resin is used as a matrix to obtain the desired composite specimens which are procured by local dealers [23]. Hence, to improve the bonding strength of the composite, the natural fibers have undergone 5% of NaOH alkali treatment for half an hour; finally, fibers are cleaned by water and dried at an environmental temperature for a couple of days. To increase the impact and flexural strength properties, reinforcement of sisal fibers is applied randomly between the mate-type glass

fibers which are taken as constant [24]. In addition, for better adhesive properties, LY556 Epoxy Resin and Hardener Hy951 are used to mix in the ratio of 10:1 to speed up the curing stage in the fabrication process. Table 1 shows the designed level of factors for fabricating sample specimens [25].

2.2. Fabrication. The number of experiments and mixing compositions of a specified range of materials is obtained from the design of experiments, and it is tabulated in Table 2. The DOE is used to minimize the number of experiments through which the materials, cost, and time were reduced, and also, it produces results without any deviation.

From the above-designed experiments, different combination samples were fabricated by compression molding machine by volume fraction method. During the molding process, the setup is kept at 500 psi at 95°C for 60 minutes. The fabrication work was completed at the Kumaraguru College of Technology, Coimbatore, India.

2.3. Testing Standards. The developed composite specimens were examined according to ASTM standards. The tensile strength test was carried out on UTM in accordance with ASTM D3039 with a constant strain rate of 1.25 mm/min. At the same time, flexural moduli were determined by ASTM D790 standards as the size of specimens was taken as $125 \times 13 \times 9 \text{ mm}^3$ and the test was conducted by Lloyd instrument LR 100 kN. In addition, the impact strength of composite materials was analyzed by the impact Izod testing machine as per the ASTM D256 [24, 26]. During the result summarized and the evaluation result, the average values of each tested sample are considered to obtain a precision value.

3. Results and Discussion

The mechanical properties, namely, tensile, flexural, and impact strength of tested sample results are summarized in Table 3 and to be analyzed in the following manner.

For tensile strength, Figure 1 shows that experiment 2 has a slightly high strength (31.89 MPa) as compared to the other experiments, and the maximum strength is found in the order of $2 > 8 > 1 > 3 > 4 > 9 > 5 > 6 > 7$. The greatest tensile strength of the composite was formed in the volume % of the mean level composition of the specified range. By increasing the volume of sisal content, the same volume of epoxy resin strength of the composite drops out. (In addition, sisal content in the same volume of epoxy resin composite drops the strength.) However, the lowest strength was obtained in a high level of sisal and epoxy resin content in fabricated specimens. It is noted that volume fraction is increased in both factors endowed with very less strength (21.98 MPa) as compared to other experiments because of the variation in binding between the reinforcement with matrix materials [27, 28].

Figure 2 shows the variation of flexural strength of tested samples. It is clearly understood that the maximum and minimum strengths of flexural properties are also followed

in the same trend of tensile strength and the strength order $2 > 1 > 3 > 8 > 4 > 5 > 9 > 6 > 7$. However, the variation of the maximum strength of the first two values has a high range of deviation (161.34 MPa and 134.65 MPa), and it is observed that both levels of sisal fibers were decreased. It shows that the addition of materials led to a decrease in flexural strength rapidly and the deviation is 60 MPa [29].

The mechanical properties of impact strength of examined sample results are plotted as a graph in Figure 3; while reviewing the results, the maximum range occurred in the low-level mixing composition experiment only. Hence, the consequences of impact strength entirely differ from the other tested properties and the maximum to a minimum order of experiments as $6 > 1 > 5 > 3 > 8 > 2 > 4 > 7 > 9$ [30].

3.1. ANOVA. The statistical analysis ANOVA was carried out, and it is reported in Tables 4–6. From the ANOVA, the obtained P value is less than 0.05. From the ANOVA techniques, it can be concluded that the P value is lesser than the F value; the null hypothesis can be rejected, accepting alternative hypothesis which says that there is a significant effect on layering sequence on the mechanical strength of the composite [16].

From Table 4, the model is significant for the output response of tensile strength. The epoxy resin is the most significant factor (<0.05) and sisal fiber is not much more significant factor (>0.05), and it is already observed in the experimental data, the optimum range of tensile strength is obtained (15% and 25% of sisal and epoxy resin) at the same level of sisal fiber, and tensile strength is reduced which changes the level of epoxy resin. Hence, the experimental result and ANOVA calculation are almost the same.

It can be observed from ANOVA, the model is significant for the output response of flexural strength shown in Table 5. The sisal fiber is the most significant factor (<0.05) and epoxy resin is not much more significant factor (>0.05), and it is most suitable for experimental data because the maximum flexural strength is obtained (15% and 25% of sisal and epoxy resin) at the same level of epoxy resin, and flexural strength is reduced which changes the sisal fiber content. However, sisal fiber is the most significant factor in the test.

The impact strength of the experiment proves that sisal fiber is a more significant factor when compared to epoxy resin described in Table 6. The objective of this investigation is to predict the most influencing level of factors, which affects the strength of mechanical parameters. The desirability of the experiment is 99.5% obtained from DOE as shown in Figure 4.

3.2. Development of Regression Model. The simplest and efficient mathematical model for the tensile, flexural, and impact strength test was developed by a Response Surface Methodology considering four independent process parameters with desired levels. The regression equations were used to predict the circularity and cylindricity of hybrid composite, and selected parameters are efficiently correlated with experimental results [31].

TABLE 1: Factors and level of experiments.

Factors	Unit	Notation	Factor level		
			-1	0	+1
Vol.% of sisal fiber	Vol.%	X_1	10	15	20
Vol.% of epoxy resin	Vol.%	X_2	20	25	30

TABLE 2: Experiment design matrix for the fabrication of specimen.

Description	Exp. 1	Exp. 2	Exp. 3	Exp. 4	Exp. 5	Exp. 6	Exp. 7	Exp. 8	Exp. 9
Std. order	4	9	7	5	6	1	8	2	3
Run order	1	2	3	4	5	6	7	8	9
Vol.% of sisal X_1	-1	0	0	+1	-1	-1	+1	0	+1
Vol.% of epoxy resin X_2	0	0	+1	0	+1	-1	+1	-1	-1

TABLE 3: Design matrix and average results of mechanical properties.

Run order	Std. order	Vol.% of sisal X_1	Vol.% of epoxy resin X_2	Tensile strength (MPa)	Flexural strength (MPa)	Impact strength (J)
1	4	-1	0	27.62	134.65	4.20
2	9	0	0	31.89	161.34	3.40
3	7	0	+1	27.59	133.84	3.51
4	5	+1	0	27.09	127.91	2.75
5	6	-1	+1	23.92	111.06	4.00
6	1	-1	-1	23.78	103.21	4.30
7	8	+1	+1	21.98	100.83	2.75
8	2	0	-1	28.50	131.19	3.50
9	3	+1	-1	25.06	104.59	2.58

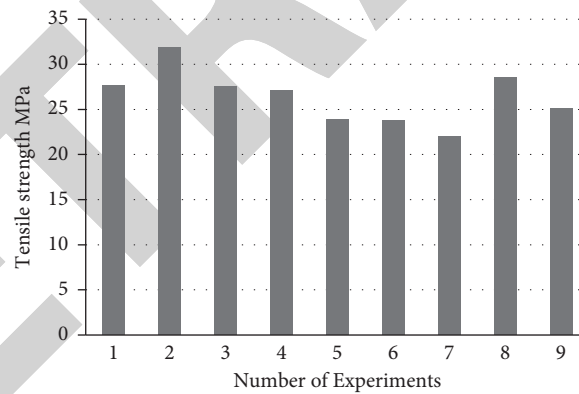


FIGURE 1: Tensile properties of designed composites.

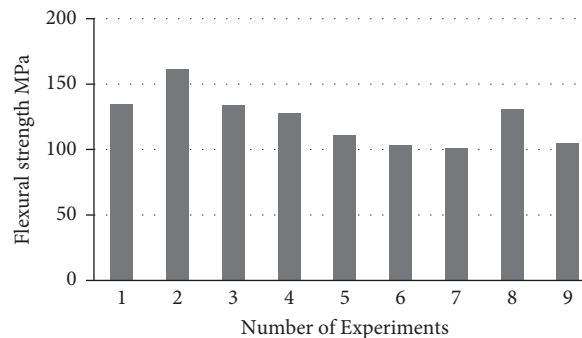


FIGURE 2: Flexural properties of designed composites.

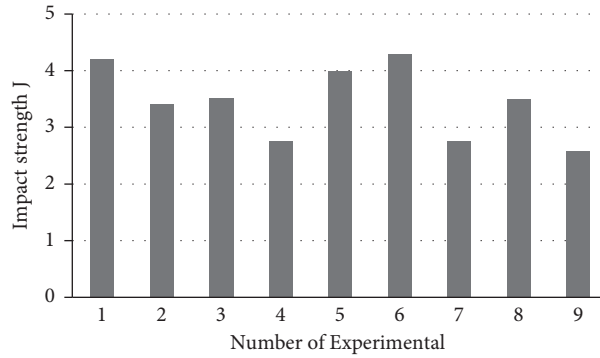


FIGURE 3: Impact properties of designed composites.

TABLE 4: ANOVA for the tensile strength test.

Source	SS	DF	MS	F value	P value Prob > F	Status
Model	72.13	5	14.43	326.66	0.0003	Significant
A-sisal	0.24	1	0.24	5.39	0.1030	
B-epoxy	2.48	1	2.48	56.11	0.0049	
AB	2.59	1	2.59	58.55	0.0046	
A ²	39.07	1	39.07	884.83	<0.0001	
B ²	27.75	1	27.75	628.40	0.0001	
Residual	0.13	3	0.044			
Cor total	72.26	8				

TABLE 5: ANOVA for the flexural strength test.

Source	SS	DF	MS	F value	P value Prob > F	Status
Model	3174.22	5	634.84	414.75	0.0002	Significant
A-sisal	40.49	1	40.49	26.45	0.0142	
B-epoxy	7.60	1	7.60	4.97	0.1122	
AB	33.77	1	33.77	22.06	0.0182	
A ²	1614.98	1	1614.98	1055.09	<0.0001	
B ²	1477.38	1	1477.38	965.19	<0.0001	
Residual	4.59	3	1.53			
Cor total	3178.81	8				

TABLE 6: ANOVA for the impact strength test.

Source	SS	DF	MS	F value	P value Prob > F	Status
Model	3.31	3	1.10	320.26	<0.0001	Significant
A-sisal	3.26	1	3.26	943.94	<0.0001	
B-epoxy	2.817E-003	1	2.817E-003	0.82	0.4076	
AB	0.055	1	0.055	16.01	0.0103	
Residual	0.017	5	3.449E-003			
Cor total	3.33	8				

for tensile strength = $-109.3015 + 0.53413A + 0.39961B - 1.45009E^{-04} * AB - 1.37077E^{-03} * A^2 - 3.9071E^{-04} * B^2$,

flexural strength = $-816.16785 + 3.21139A + 2.88435B - 5.24079E^{-04} * AB - 8.81253E^{-03} * A^2 - 2.85086E^{-03} * B^2$,

impact strength = $7.52142 - 0.023319A - 3.83062E^{-03} * B + 2.11922E^{-05} * AB$.

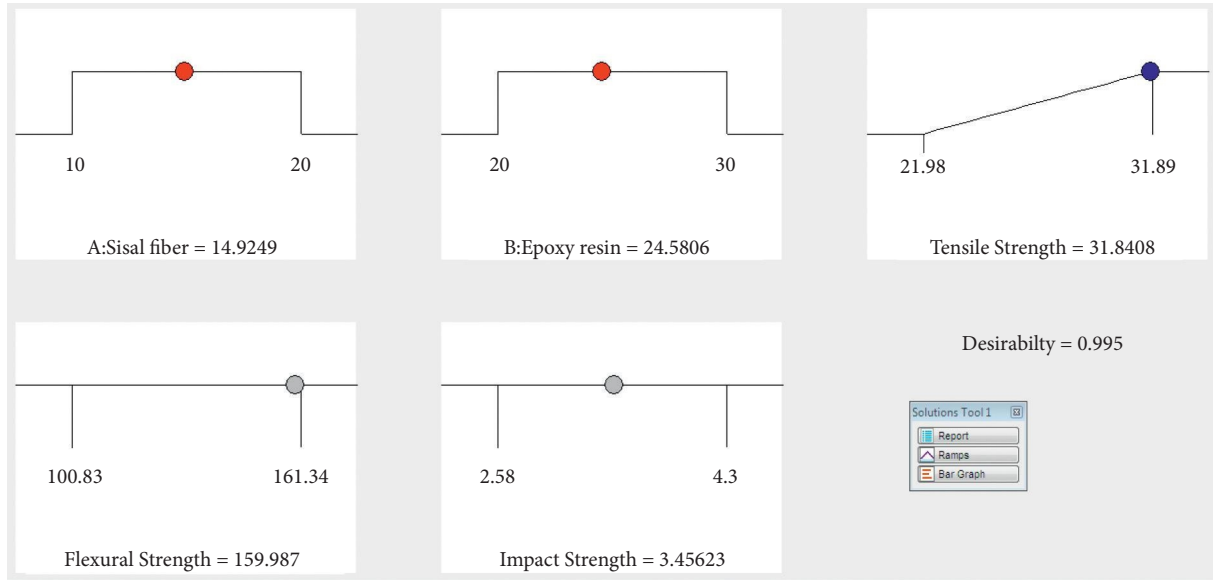


FIGURE 4: Desirability of tested composite sample result.

TABLE 7: Comparison of experimental and predicted values of response variables.

Exp.	Tensile strength (MPa)			Flexural strength (MPa)			Impact strength (J)		
	Exp. value	Predict. value	Error (%)	Exp. value	Predict. value	Error (%)	Exp. value	Predict. value	Error value
1	27.62	27.49	+0.47	134.65	134.88	-0.17	4.20	4.17	+0.71
2	31.89	31.59	+0.94	161.34	160.86	+0.29	3.40	3.44	-1.16
3	27.59	27.22	+1.35	133.84	134.96	-0.82	3.51	3.42	+2.63
4	27.09	26.85	+0.89	127.91	130.01	-1.61	2.75	2.70	+1.85
5	23.92	23.95	-0.12	111.06	111.87	-0.72	4.00	4.04	-0.99
6	23.78	23.6	+0.76	103.21	103.56	-0.33	4.30	4.31	-0.23
7	21.98	21.64	+1.57	100.83	101.24	-0.40	2.75	2.80	-1.78
8	28.50	28.53	-0.10	131.19	132.41	-0.92	3.50	3.46	+1.15
9	25.06	24.62	+1.78	104.59	104.45	+0.13	2.58	2.61	-1.14

The evaluated results of tensile, flexural, and impact strength are compared with a predicted value, which is obtained from the design of experiments. The percentage of error is calculated as follows:

$$\% \text{ of error} = \left(\frac{\text{experimental value} - \text{predicted value}}{\text{predicted value}} \right) * 100. \tag{2}$$

The % of error value of mechanical properties is listed in Table 7. The most response variables of all the experiments can be observed when a maximum and minimum percentage of error lies at $\pm 2\%$. The scatter diagram of the tensile, flexural, and impact strength test shows the experimental value and predicted values of response variables. It can be observed that the predicted value of all response variables is fairly close to the corresponding experimental values shown in Figures 5(a)–5(c). There is a three-dimensional response surface plot of a combined effect of independent variables on tensile, flexural, and impact strength tests. It was clearly understood by viewing

Figures 5(d)–5(f) that the tensile and flexural results are obtained in the form of the quadratic curve but linear model formed for impact strength result. It is used to analyze the critical level of factors.

3.3. LINGO Optimization. LINGO is one of the optimization tools to obtain the best result with the minimum number of experiments and reduced cost and time [32]. The optimum values of tensile, flexural, and impact strength of mechanical properties on developed composites specimen are shown in Table 8.

The optimum values of individual response and corresponding factor levels are obtained as shown in Figures 6(a)–6(c). The combo strength of tensile and flexural properties of different applications with different ranges of importance (1 : 1,3 : 1,1 : 3) are evaluated before starting the experiment. During the deformation of the test, the fibers are pulling out. Hence, the tensile strength is less as compared to the flexural strength. Due to the mat form, glass fiber is used to increase the flexural strength and it is used in the outer surface of the specimen.

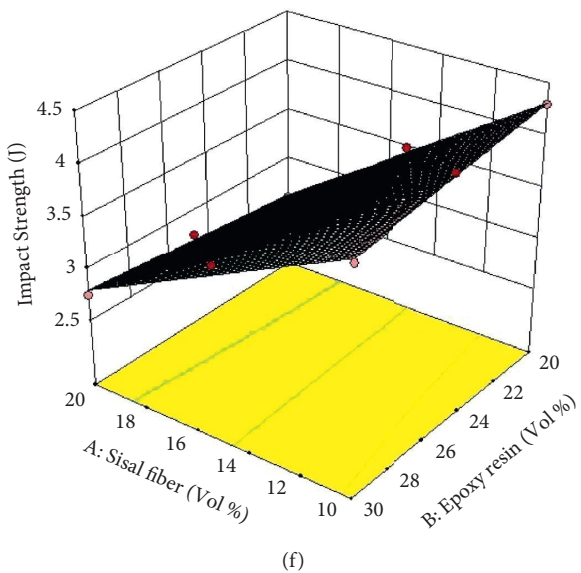
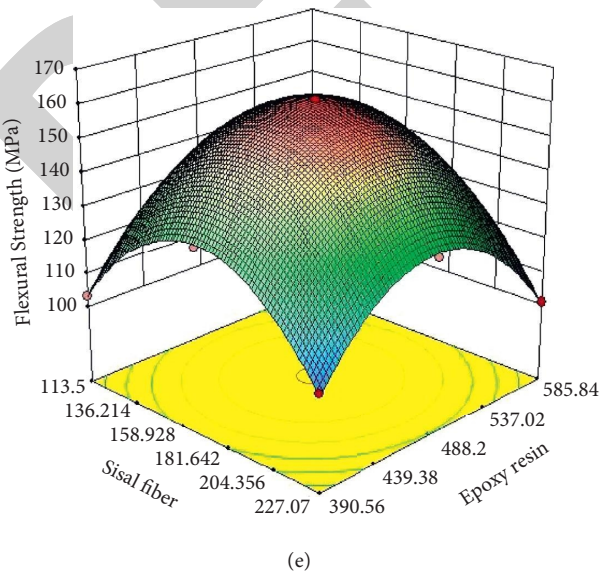
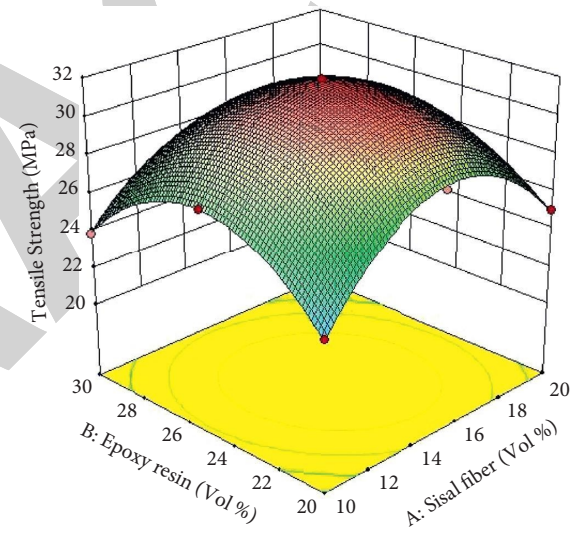
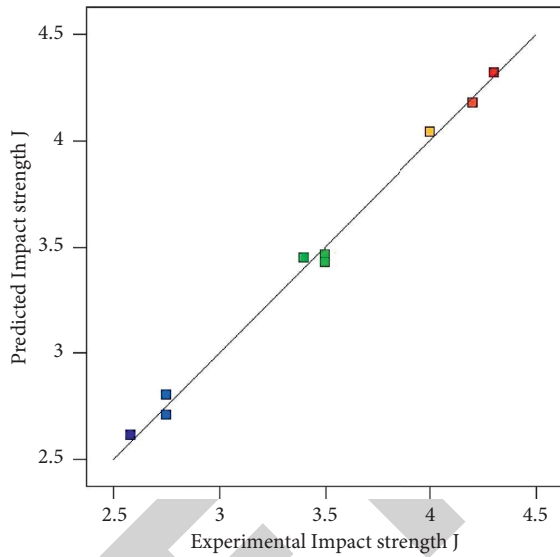
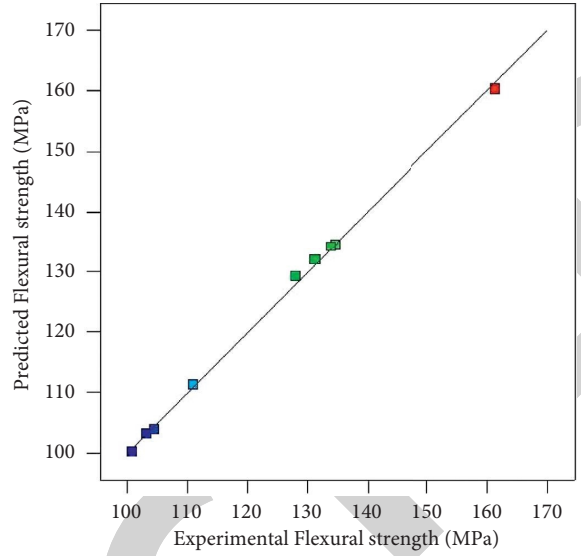
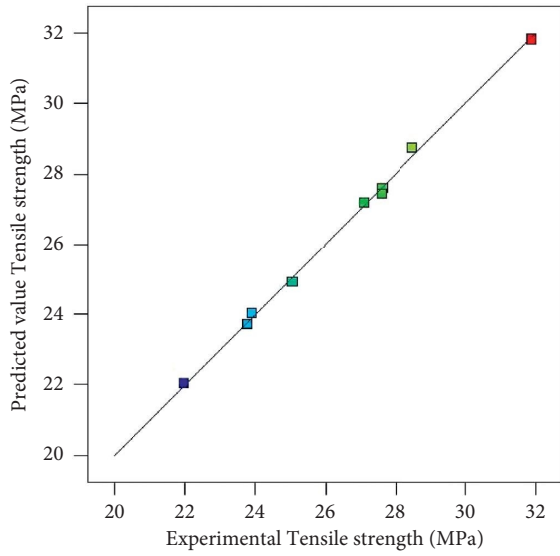


FIGURE 5: (a–c) Scatter diagrams and (d–f) 3D response surface plots for the tensile, flexural, and impact strength.

TABLE 8: Various optimum levels of response.

Response	Optimum value	Optimum level of factors	
	Strength	Sisal fiber (grms)	Glass fiber (grms)
Tensile strength	31.84626 MPa	169.4426	479.9459
Flexural strength	160.3204 MPa	167.6219	490.4665
Impact strength	4.318260 J	113.5000	390.5800
Tensile and flexural strength (1 : 1)	96.06351 MPa	167.8331	489.2174
Tensile and flexural strength (3 : 1)	63.94075 MPa	168.1365	487.4384
Tensile and flexural strength (1 : 3)	136.1428	167.7684	489.5994

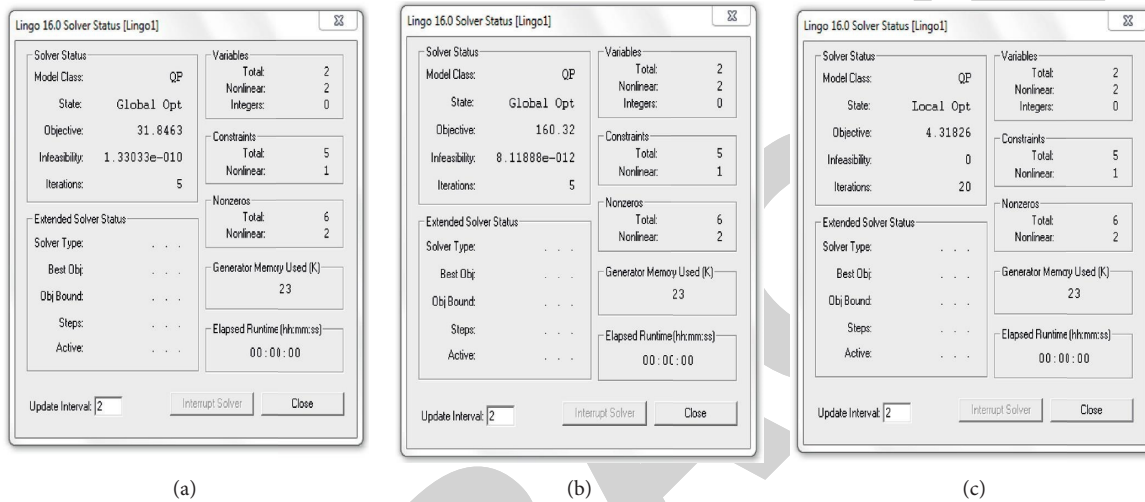


FIGURE 6: (a–c) LINGO optimization of tensile, flexural, and impact strength.

TABLE 9: Confirmation of tested sample results for output response variables.

Factors	Sisal fiber	Epoxy resin	
Selected level of factors (Vol.%)	12	23	
Mechanical properties	Predicted value	Experimental value	Error (%)
Tensile strength (MPa)	29.67	30	+1.08
Flexural strength (MPa)	146.65	146.75	-0.61
Impact strength (J)	3.92	3.88	-1.04

3.4. *Confirmation Test.* Confirmation tests were conducted using the same experimental procedure to confirm the results of experiments; by using the regression model equation, the predicted values are compared to the experimental values and the deviation is obtained within the range of error % as shown in Table 9.

4. Conclusion

The optimization of mechanical properties which are tensile, flexural, and impact strength of sisal/glass-fiber-reinforced hybrid composites was analyzed, and the conclusion is as follows:

- (i) It is observed that the sisal is the most significant factor for tensile and impact strength properties of designed composites and not much more significant on flexural test
- (ii) The experimental results of tensile, flexural, and impact strength are fairly close to the predicted

value, which is obtained by RSM, and the error percentage lies at $\pm 2\%$

- (iii) The desirability was obtained as 98.8% of tested composites. From the above investigation, it can be found that the most significant levels of factors are determined and used for specified mechanical applications
- (iv) LINGO optimization tool is used to determine the optimum strength of combined response such as tensile and flexural properties and corresponding level of factors
- (v) Confirmation tests are done to confirm the results of RSM and ANOVA and error % lies at $\pm 1.5\%$ for predicted and experimental values

Data Availability

The data used to support the findings of this study are included within the article.

Disclosure

This study was performed as a part of the employment of Ambo University, Ethiopia.

Conflicts of Interest

The authors declare that there are no conflicts of interest to publish this article.

References

- [1] A. S. Luyt and M. E. Malunka, "Composites of low-density polyethylene and short sisal fibers: the effect of wax addition and peroxide treatment on thermal properties," *Thermochimica Acta*, vol. 426, no. 1-2, pp. 101-107, 2005.
- [2] C. Velmurugan, V. Muthukumar, K. Ragupathy, and S. Ragunath, "Modeling volume loss of heat treated Al 6061 composites using an artificial neural network," *Procedia Materials Science*, vol. 5, pp. 31-40, 2014.
- [3] F. M. Sapuan and S. M. A. Oqla, "Natural fiber reinforced polymer composites in industrial applications: feasibility of date palm fibers for sustainable automotive industry," *Journal of Cleaner Production*, vol. 66, pp. 347-354, 2014.
- [4] Y. Li, Y. W. Mai, and L. Ye, "Sisal fiber and its composites: a review of recent developments," *Composites Science and Technology*, vol. 60, no. 11, pp. 2037-2055, 2000.
- [5] T. Brocks, M. O. H. Cioffi, and H. J. C. Voorwald, "Effect of fiber surface on flexural strength in carbon fabric reinforced epoxy composites," *Applied Surface Science*, vol. 274, pp. 210-216, 2013.
- [6] H. Rahmani, S. H. M. Najafi, and A. Ashori, "Mechanical performance of epoxy/carbon fiber laminated composites," *Journal of Reinforced Plastics and Composites*, vol. 33, no. 8, pp. 733-740, 2014.
- [7] Y. Karaduman, M. M. A. Sayeed, L. Onal, and A. Rawal, "Viscoelastic properties of surface modified jute fiber/polypropylene nonwoven composites," *Composites Part B: Engineering*, vol. 67, pp. 111-118, 2014.
- [8] B. R. Vijaya, S. K. Junaid, R. Niranjan et al., "Evaluation of mechanical properties of abaca-jute-glass fiber reinforced epoxy composite," *Materials & Design*, vol. 51, pp. 357-366, 2013.
- [9] M. Cai, H. Takagi, A. N. Nakagaito, Y. Li, and G. I. N. Waterhouse, "Effect of alkali treatment on interfacial bonding in abaca fiber-reinforced composites," *Composites Part A: Applied Science and Manufacturing*, vol. 90, pp. 589-597, 2016.
- [10] M. Idicula, K. Joseph, and S. Thomas, "Mechanical performance of short banana/sisal hybrid fiber reinforced polyester composites," *Journal of Reinforced Plastics and Composites*, vol. 29, no. 1, pp. 12-29, 2010.
- [11] A. S. Singha and V. K. Thakur, "Mechanical properties of natural fiber reinforced polymer composites," *Bull Matr Sci*, vol. 31, pp. 791-799, 2010.
- [12] N. Saba, M. Jawaid, O. Y. Allothman, M. Paridah, and A. Hassan, "Recent advances in epoxy resin, natural fiber-reinforced epoxy composites and their applications," *Journal of Reinforced Plastics and Composites*, vol. 35, no. 6, pp. 447-470, 2015.
- [13] M. K. Gupta and R. K. Srivastava, "Tensile and flexural properties of sisal fibre reinforced epoxy composite: a comparison between unidirectional and mat form of fibres," *Procedia Materials Science*, vol. 5, pp. 2434-2439, 2014.
- [14] Y. Chen, Y. Li, Y. You, J. Xiao, and Q. Song, "Research on mechanical properties of epoxy/glass fiber composites cured by microwave radiation," *Journal of Reinforced Plastics and Composites*, vol. 33, no. 15, pp. 1441-1451, 2014.
- [15] T. Padmavathi, S. V. Naidu, and R. Rao, "Studies on mechanical behavior of surface modified sisal fibre - epoxy composites," *Journal of Reinforced Plastics and Composites*, vol. 31, no. 8, pp. 519-532, 2012.
- [16] N. Venkateshwaran and A. ElayaPerumal, "Mechanical and water absorption properties of woven jute/banana hybrid composites," *Fibers and Polymers*, vol. 13, no. 7, pp. 907-914, 2012.
- [17] M. Rafiqzaman, M. Islam, H. Rahman, S. Talukdar, and N. Hasan, "Mechanical property evaluation of glass-jute fiber reinforced polymer composites," *Polymers for Advanced Technologies*, vol. 27, no. 10, pp. 1308-1316, 2016.
- [18] H. U. Zaman, M. A. Khan, and R. A. Khan, "Banana fiber-reinforced polypropylene composites: a study of the physico-mechanical properties," *Fibers and Polymers*, vol. 14, no. 1, pp. 121-126, 2013.
- [19] C. Wu, S. Jia, R. Chen et al., "Composites of sisal fiber/polypropylene based on novel vane extruder: effect of interface and damage on mechanical properties," *Journal of Reinforced Plastics and Composites*, vol. 32, no. 24, pp. 1907-1915, 2013.
- [20] G. Phiri, M. Khoathane, and E. Sadiku, "Effect of fiber loading on mechanical and thermal properties of sisal and kenaf fiber-reinforced injection moulded composites," *Journal of Reinforced Plastics and Composites*, vol. 33, no. 3, pp. 283-293, 2014.
- [21] H. Ma, Y. Li, and D. Wang, "Investigations of fiber twist on the mechanical properties of sisal fiber yarns and their composites," *Journal of Reinforced Plastics and Composites*, vol. 33, no. 7, pp. 687-696, 2014.
- [22] S. K. Majhi, S. K. Nayak, S. Mohanty, and L. Unnikrishnan, "Mechanical and fracture behavior of banana fiber reinforced Poly(lactic acid) biocomposites," *Int J Plast Technol*, vol. 14, pp. S57-S75, 2010.
- [23] S. Ragunath, C. Velmurugan, and T. Kannan, "Optimization of tribological behavior of nano clay particle with sisal/jute/glass/epoxy polymer hybrid composites using RSM," *Polymers for Advanced Technologies*, vol. 28, no. 12, pp. 1813-1822, 2017.
- [24] S. Ragunath, C. Velmurugan, T. Kannan, and S. Thirumurugan, "Evaluation of tensile, flexural and impact properties on sisal/glass fiber reinforced polymer hybrid composites," *Indian Journal of Engineering and Materials Sciences*, vol. 25, pp. 425-431, 2018.
- [25] P. K. Bajpai and I. Singh, "Drilling behavior of sisal fiber-reinforced polypropylene composite laminates," *Journal of Reinforced Plastics and Composites*, vol. 32, no. 20, pp. 1569-1576, 2013.
- [26] K. L. Pickering, M. G. A. Efendy, and T. M. Le, "A review of recent developments in natural fiber composites and their mechanical performance," *Composites Part A: Applied Science and Manufacturing*, vol. 83, pp. 98-112, 2016.
- [27] R. Rahman, M. Hasan, M. Huque, and N. Islam, "Physico-mechanical properties of maleic acid post treated jute fiber reinforced polypropylene composites," *Journal of Thermoplastic Composite Materials*, vol. 22, no. 4, pp. 365-381, 2009.
- [28] M. S. Jamil, I. Ahmad, and I. Abdullah, "Effects of rice husk filler on the mechanical and thermal properties of liquid natural rubber compatibilized high-density polyethylene/

Retraction

Retracted: Experimental and Thermal Investigation on Powder Mixed EDM Using FEM and Artificial Neural Networks

Advances in Materials Science and Engineering

Received 26 December 2023; Accepted 26 December 2023; Published 29 December 2023

Copyright © 2023 Advances in Materials Science and Engineering. This is an open access article distributed under the Creative Commons Attribution License, which permits unrestricted use, distribution, and reproduction in any medium, provided the original work is properly cited.

This article has been retracted by Hindawi, as publisher, following an investigation undertaken by the publisher [1]. This investigation has uncovered evidence of systematic manipulation of the publication and peer-review process. We cannot, therefore, vouch for the reliability or integrity of this article.

Please note that this notice is intended solely to alert readers that the peer-review process of this article has been compromised.

Wiley and Hindawi regret that the usual quality checks did not identify these issues before publication and have since put additional measures in place to safeguard research integrity.

We wish to credit our Research Integrity and Research Publishing teams and anonymous and named external researchers and research integrity experts for contributing to this investigation.

The corresponding author, as the representative of all authors, has been given the opportunity to register their agreement or disagreement to this retraction. We have kept a record of any response received.

References

- [1] V. N. R. Jampana, P. S. V. Ramana Rao, and A. Sampathkumar, "Experimental and Thermal Investigation on Powder Mixed EDM Using FEM and Artificial Neural Networks," *Advances in Materials Science and Engineering*, vol. 2021, Article ID 8138294, 12 pages, 2021.

Research Article

Experimental and Thermal Investigation on Powder Mixed EDM Using FEM and Artificial Neural Networks

Venkata N. Raju Jampana ¹, P. S. V. Ramana Rao ¹ and A. Sampathkumar ²

¹Centurion University of Technology and Management, Visakhapatnam, Andhra Pradesh, India

²Dambi Dollo University, Dembi Dolo, Ethiopia

Correspondence should be addressed to A. Sampathkumar; dr.sampathkumar@dadu.edu.et

Received 14 July 2021; Revised 14 August 2021; Accepted 19 August 2021; Published 6 September 2021

Academic Editor: Samson Jerold Samuel Chelladurai

Copyright © 2021 Venkata N. Raju Jampana et al. This is an open access article distributed under the Creative Commons Attribution License, which permits unrestricted use, distribution, and reproduction in any medium, provided the original work is properly cited.

Electric discharge machining (EDM) process is one of the earliest and most extensively used unconventional machining processes. It is a noncontact machining process that uses a series of electric discharges to remove material from an electrically conductive workpiece. This article is aimed to do a comprehensive experimental and thermal investigation of the EDM, which can predict the machining characteristic and then optimize the output parameters with a newly integrated neural network-based methodology for modelling and optimal selection of process variables involved in powder mixed EDM (PMEDM) process. To compare and investigate the effects caused by powder of differently thermo physical properties on the EDM process performance with each other as well as the pure case, a series of experiments were conducted on a specially designed experimental setup developed in the laboratory. Peak current, pulse period, and source voltage are selected as the independent input parameters to evaluate the process performance in terms of material removal rate (MRR) and surface roughness (Ra). In addition, finite element method (FEM) is utilized for thermal analysis on EDM of stainless-steel 630 (SS630) grade. Further, back propagated neural network (BPNN) with feed forward architecture with analysis of variance (ANOVA) is used to find the best fit and approximate solutions to optimization and search problems. Finally, confirmation test results of experimental MRR are compared using the values of MRR obtained using FEM and ANN. Similarly, the test results of experimental Ra also compared with obtained Ra using ANN.

1. Introduction

The process of PMEDM is known as the appropriate abrasive material mixing with the powder formatted metallic material into the dielectric fluid, where the powder particles (i.e., electrically conductive) are amalgamated in the dielectric fluid that mitigates the insulating strength of particles and enhances the distance of spark gap between the workpiece and tool for uniform distribution of electric discharge in all the directions. This is also referred as new advancement to get better innovations and enhancement in the potentialities of EDM process [1]. This process is more static, i.e., highly stable, and results in enhanced MRR and smoothed surface [2, 3]. In addition, EDM process is also called as thermal erosion procedure [4]. During the process of machining, there will be a change in the machining surface layer

physical properties due to the instantaneous rise in the temperature, which also results in the residual stress presence. This is the main factor that influences the surface quality of machining and its functional performance. In addition, the properties of component are also influenced by thermal residual stresses with higher magnitude, which are formed on the surface of workpiece upper layer because of speedy curing of EDM process [5, 6]. Usually, utilization of components in EDM occurs at certain circumstances such as higher temperature, stress, and fatigue-load, which results in significant mitigation in component's fatigue life. Hence, it is required to utilize powder mixing methods, which do not need any posttreatment procedure to find the optimized machining parameters of EDM, which also suppress the cracks formation in the recast layer for maximum life even under various fatigue-loads. The dilation of enough powder

particles to the dielectric in EDM results in enhanced quality in the surface finishing with maximum speed of machining compared to the classical EDM process (without powder mixing). Standard dielectric circulation device employed in PMEDM is illustrated in Figure 1, which is installed in the setup of traditional EDM operational tank. It also comprises with a micropump or stirrer, which is used to prevent the settling of powder particles at the dielectric reservoir bottom, and it also assists to keep the powder particles on the workpiece surface from stagnating. There are some permanent magnets (shown in blue color) distributed by the filtering device to insulate the debris from the particles of powder.

1.1. Powder-Based Parameters

1.1.1. Type of Powder. Generally, MRR and surface durability improves, and instrument wear rate reduces by adding the dielectric powder. Further, the efficiency of processes has impacted distinctly by these sorts of powders. Some of the effected parameters are nonmagnetic characteristics, thermal conductivity, suspension capabilities, and electric conductivity. Inorganic oxide powders are not considered as the better output characteristics due to the even distribution of dielectric powder.

1.1.2. Powder Size. In machined surface quality, an influential parameter is additive particle size [7]. The higher interelectrode gap is resulted for larger particles based on the analyzation of experimental results. It leads to the lower deionization between tool and workpiece and greater contamination. The gap increases by the larger powder size, but MRR is reduced, and Ra is increased [8].

1.1.3. Powder Conductivity. The discharge gap increases by adding the conductive fine powder electrically in dielectric that enhances spark frequency and improves debris flushing [7]. From the interelectrode gap, heat with large amount is confiscated by forming the shallow crates on the surface of workpiece due to the higher thermal conductivity of these particles [9, 10].

1.1.4. Powder Concentration. Due to the enhancement of number of discharges by powder concentration, which improves MRR [11], surface roughness is decreased while lowering the energy per spark [12]. An optimum powder concentration is needed with the consistent increment in concentration which improves the amount of powder particles in the discharge gap. The discharge energy transfer impedes to the workpiece and arching and short-circuiting while reducing the surface and quality of MRR [13].

1.1.5. Powder Density. The surface forces affect the powder particle density that has allowed the particle distribution in the dielectric uniformly. These forces could balance by the lower density and requirement of powder quantity is

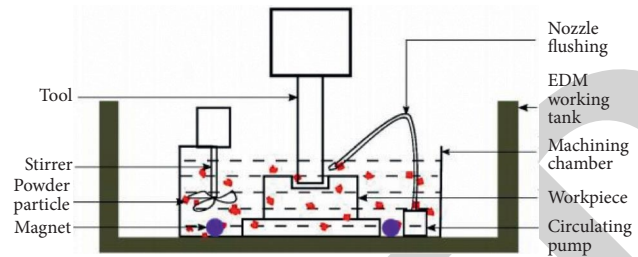


FIGURE 1: PMEDM setup.

reduced due to the reduction of settling down of powder amount at the tank bottom [14].

2. Related Work

Surekha et al. [15] have studied aluminium powder added EDM for EN-19 alloy steel machining based on a brass electrode and disclosed that peak current (I_p) and gap voltage (V_G) parameters have impacted the values of MRR. In [16], Tahsin et al. have examined Ti6Al4V ELI material PMEDM for analysing the effect of powder concentration of SiC on the surface topography, subsurface structures, and particle deposition. The material transfer mechanism improves the suspended particle concentration and lowers the pulse currents. Because of secondary discharges scarcity, the depletion of current material transfer mechanism has performed at higher pulse rate. Selvarajan et al. [17] reviewed EDM with different industrial demanded composite materials and demonstrated various parameters that effect on the performance. Choudhury et al. [18] have focused on investigation on the hybrid PMEDM using the powders of multiwalled carbon nanotube (CNT) and aluminium that mixed in kerosene for machining the EN-19 alloy steel with brass electrode. Kumar et al. [19] have tested the machinability of Inconel 825 with addition of graphene nanopowder to the die sinking EDM dielectric fluid. For creating the conditions of optimum process, the methodology of response surface (RSM) is exploited. The impact of input process parameters such as I_p , pulse on time (T_{ON}), and V_G on output response features like MRR, Ra, and TWR was also examined. Later, the Inconel-800 machinability using PMEDM has been investigated [20], where the experimental designs and optimization have performed using desirability approach and RSM. The most effected metrics for MRR included tool material, T_{ON} , and I_p while powder materials, tool material, T_{ON} , and I_p for TWR. Mishra and Routaray [21] have focused on achieving the objective of correlating the thermally induced hardness of workpiece impact with EDM performances and the modified property establishes that is responsive for the deviation change in the output responses behaviour in sinking the process of electrical discharge machining. Based on four controllable input parameters such as V_G , pulse of time (T_{OFF}), T_{ON} , and I_p , the RSM has implemented using central composite design approach for experimental comparative study. Here, the desired response variables were chosen as the energy density, TWR, and MRR. The changes in output responses such as energy density, TWR, and MRR have affected

predominantly through the observation of hardness change based on the process of base alloy induction thermal hardening. Sidhu and Yazdani [22] have evaluated for predicting the optimal machining conditions in the particular-reinforced metal matrix composites (30 vol%SiC/A359) EDM. In [23], the authors have investigated the chromium powder effect that mixed with EDM surface features of alloy tool steel SKD11. The chromium content increases on machined surface if chromium powder concentration is high and discharge current is low. Ekmekci et al. [24] have proposed a substitute realistic technique to generate the coating or biocompatible interfaces for medical applications. While processing the Ti6Al4V EDM, combination of deionized water and hydroxyapatite (HA) powder has been used as a dielectric fluid. Khazraji et al. [25] studied the impact of parameters on copper and graphite electrodes when PMEDM is processed using RSM. For graphite and copper electrodes, the total percentage of heat has increased by adding micropowders of SiC into dielectric fluid. However, the generated heat is higher compared to the used kerosene dielectric. The improvement of 110% and 124% has been achieved with the use of same kerosene dielectric and electrodes in WLT, respectively. In [26], the authors have tested the input variable effect on TWR, MRR, and overcut size during PMEDM of AISI 1045, H11 die steel, and HCHCr. Kerosene and commercial EDM oil have been used as dielectric fluids with three powders such as tungsten, graphite, and silicon and brass, graphite, and tungsten as electrodes. Based on the results, TWR reduced and MRR and overcut size increased with powder concentration. Kuriachen et al. [27] have studied the SiC microparticle effect that mixed to dielectric media on Ti6Al4V machining with tungsten carbide electrode. The statistical design of RSM-Box Behnken has been proposed and the process variables effect was tested such as powder concentration, capacitance, and voltage over machining features such as TWR and MRR using variance analysis. At minimum levels of powder concentration and middle levels of voltage and capacitance, maximum MRR has been obtained and minimum TWR attained at minimum levels of voltage, capacitance, and powder concentration. Baseri et al. [28] have studied the effect of TiO₂ nanopowder on EDM rotary tool of H13. The input parameters of tool rotation speed, spark energy, and powder concentration percentage influence on the responses such as Ra, TWR, and MRR. Based on the integration of rotational tool and nanopowder, the EDM efficiency has been improved. S. Tripathy and D. K. Tripathy [29] studied the parameters such as I_p , V_G , powder concentration, T_{ON} , and duty cycle and their impact on machining characteristics such as TWR, EWR, MRR, and Ra with the addition of chromium powder to the dielectric fluid in EDM. The adaption of Taguchi method integrated with this technique also demonstrated for preference order as similar as ideal solution. For PMEDM of H11 die steel, optimization of multiple performance characteristics has been discussed using the copper electrode. The optimum process conditions have been obtained and the reduced Ra was observed on improving the chromium powder concentration. Recently, the impact on molybdenum disulphide powder that is mixed

to dielectric medium during micro-EDM of Inconel 718 is studied [30]. The results have shown that the MRR has maximized at powder optimum size, i.e., 50 nm. In [31], SS630 grade of EDM process is investigated and optimized using Taguchi approach, where flushing pressure, T_{ON} , T_{OFF} , and I_p are assumed as input process variables. The output performance has been measured with MRR and Ra. Further, optimization was also done using Taguchi approach by assuming L_{16} orthogonal array with Minitab software. However, it is important to make a note that SS630 content based on PMEDM has not been analysed in the literature. The stainless-steel substance SS630 is extremely hard to do machining due to the factors such as high corrosive resistance, high build-up edge propensity, and poor thermal conductivity. However, the product applications in different industries such as pharmaceutical industries, pump production, and other device prototypes and, in addition, several recent works focused on optimization of process parameters using fuzzy networks [32] and artificial neural networks [33–35]. Therefore, this article proposes an experimental and thermal investigation with process parameter optimization using BPNN with feed forward architecture on PMEDM for SS630 using SiC powder as dielectric fluid. In addition, copper tungsten (CuW) is selected as the tool electrode owing to the copper which is a high conductive element electrically. Instead of kerosene, EDM oil is used as a dielectric substance due to the unfortunate environmental and other external conditions.

2.1. Proposed Methodology. In the current experimental study, EDM is considered to carry out the experiments with CuW cylinder tool electrode, which has a diameter of 10 mm, and we tested the dielectric flow system that was modified for suspended dielectric medium of SiC powder circulation in small quantities for preventing the whole dielectric fluid contamination. SS630 is chosen as a workpiece with the size of $70 \times 40 \times 8$ mm. The input parameters are selected as concentration of SiC powder, servo voltage, I_p , and T_{ON} using 18 experiments with three factors and three levels of factorial design experiments.

3. Materials and Methods

The SS630 material is chosen for workpiece that has thickness of 8 mm and rectangular dimensions of 70×40 mm. At lower temperatures, a single ageing treatment can harden to reduce the risk of distortion using this SS630 as workpiece. In addition, if corrosion and high strength are required, then grade 630 is an ideal selection for the experimental analysis. A mixture of tungsten and copper is used for electrode material of CuW, where the distinct particles of one metal have included material that dispersed in a matrix of the other one as tungsten and copper are not soluble mutually. It has a length of 21.5 mm and a diameter of 12.5 mm. Tables 1 and 2 show the chemical composition and material properties for both workpiece and electrodes, respectively.

TABLE 1: Chemical composition of SS630 material.

Element	Weight (%)
Carbon (C)	0.036–0.44 Max
Manganese (Mn)	0.60–1.00 Max
Silicon (Si)	0.40 Max
Chromium (Cr)	16.00–18.00
Nickel (Ni)	10.00–14.00
Molybdenum (Mo)	2.00–3.00
Phosphorus (P)	0.05 Max
Sulphur (S)	0.030 Max
Nitrogen (N)	0.10 Max
Iron (Fe)	Balance

SiC powder has a set of unique physical-chemical properties such as large bandwidth, high resistance to oxidation and corrosion, low coefficient of thermal expansion, excellent thermal conductivity, high hardness, and mechanical stability at higher temperatures. The chemical composition of SiC is demonstrated in Table 3.

3.1. Performance Measurements. This section describes the performance measurements utilized in PMEDM process of SS630, where both MRR and SR have been used as an output performance validation. Here, the mean absolute deviation is measured from the average surface level to obtain the value of Ra (in μm) based on a computer-controlled Ra tester. By using the removed volume of material per unit time, MRR is computed because it is a crucial parameter that shows effect on the productivity and processing time of EDM machining. The definition of MRR is described as the ratio between pre- and postmachining weight difference of workpiece and the multiplication of workpiece density and machining time, which is formulated as follows:

$$\text{MRR} = \frac{W_b - W_a}{\rho_w \times t} \times 1000 \text{ mm}^3/\text{min}, \quad (1)$$

where W_b and W_a (in gm) denote the weight of workpiece before and after machining process, respectively; ρ_w denoted as the workpiece material density which is 7750 kg/m^3 for SS630 grade; and t is the processing time of machining, i.e., 5 mins.

3.2. Modelling and Simulation of the Heat Flux Using FEM. For all EDM and PMEDM models, the feasibility of problem is obtained by considering the following assumptions to overcome the issues of EDM such as random, uncertainty, and high complexity nature:

- (1) Workpiece and tool material properties are relied on temperature
- (2) Transient type of temperature analysis is considered
- (3) Heat source is assumed as the heat flux Gaussian distribution on the workpiece material surface during T
- (4) The channel of EDM discharge spark is considered as a uniform shape of cylindrical column

- (5) Not effecting the element shape and density
- (6) Isotropic and homogeneous characteristics of workpiece materials
- (7) Considering an axisymmetric model
- (8) Heat flux incident magnitude on the electrodes is not depending on the affected surface profile
- (9) The diameter of a channel would be between $10 \mu\text{m}$ and $100 \mu\text{m}$ and the electrode can be considered as a semiinfinite body

3.3. ANN Model. For modelling complex nonlinear relationships between variables, ANNs are used as an intelligent tool that mimics the work process as a nervous system. It contains a network of artificial neurons that can learn the complicated relationship between input variables such as T_{ON} , machining time, I , and source voltage (V_s) and output variables such as MRR and Ra. First, we designed a set of experiments and fed to relevant ANN model that can model the interrelation between input and output variables. The outcome of the settled dataset machining parameter that provided to ANN model is predicted using this model and it is categorized into two sets known as testing and training datasets. For neural network training, the dataset of training is used while the prediction of model accuracy is verified using the testing dataset.

4. Experimental Setup

This section describes the experimental setup process that carried out the analysis on effects of one or more factors of parameters on the machined surface finish by focusing on determining the effect of input process parameters such as T_{ON} , T_{OFF} , I , and V_s . Performance evaluation of all the experiments has been done using the die sinking EDM machine of FORMATICS 50 model equipped with ELEC-TRONICA PRS 20, as shown in Figure 2. Before the process of machining, the electrode surfaces and workpieces are polished and cleaned. Tables 4 and 5 are listed with the selected input factors and their corresponding levels and selected experimental conditions, respectively. On the machined surfaces, the Ra is computed based on the tester of Talysurf surface roughness, which is computed transversely with the consideration of cut-off length as 0.8 mm and the process is repeated for three times for estimating the average values.

4.1. Thermal Investigation Using FEM. For estimating both molten material deformations by plasma pressure and temperature distribution, the commercial finite element code ANSYS is incorporated for EDM in the single discharge analysis procedure. To determine solutions for engineering problem, finite element code is used by ANSYS. The complex interaction of various physical phenomena is involved in EDM which is a complicated thermal process. Thus, FEM is employed for simulating the stress and temperature distributions into the workpiece, where a powerful software like ANSYS is needed for improving the FEM-based EDM model

TABLE 2: Typical properties of commonly used copper tungsten compositions.

Composition	Density (g/cm ³)	Hardness (kgf/mm ²)	Resistivity (μΩ·cm)
W50/Cu50	11.85	115	3.2

TABLE 3: Chemical composition of SiC.

SiC	Silicon carbide
Density	3.21 g/cm ³
Molecular weight/molar mass	40.11 g/mol
Melting point	2,730°C
Thermal conductivity	3 W m-k
Specific heat	1800 j/kg-k

TABLE 5: Experimental conditions.

Working condition	Description
Workpiece	SS630 grade (70 × 40 × 8 mm)
Electrode	CuW (diameter 12.5 mm and length 21.5 mm)
Dielectric	SiC powder
Polarity	Normal
Gap voltage	70 V
Machining time	5 mins



FIGURE 2: Machining process of PMEDM.

TABLE 4: Input process parameters and their levels.

Parameter	Level 1	Level 2	Level 3
C_p (%)	0	3	5
T_{ON} (μs)	8	12	16
T_{OFF} (μs)	15	22	30
I_p (Amps)	6	10	14
V_s (Volts)	3	4	5

with the consideration of all complicated aspects of process. It can be used with different models and analyses any complicated geometry that includes different capabilities of FEM ranging from a linear, simple, and static analysis to a nonlinear, complex, and transient dynamic analysis in the structural mechanics, electromagnetic and thermal systems, and fluid mechanics.

Here, ANSYS 14.5 software has been utilized to simulate the results for PMEDM modelling by creating the work geometry through the appropriate boundary constraints and applying different types of loads. The mapped meshing technique is used for meshing the workpiece domain. As mentioned earlier, SS630 and CuW are utilized as specimens for a single discharge set. Figure 3 depicts the temperature

distribution obtained for $I_p = 14$ A with $T = 750$ μs, where the distribution of temperature is maximum at the end of workpiece and minimum at the middle of workpiece, i.e., 100°C and 22.001°C, respectively. After the distribution of temperature, the heat flux is computed and plotted, as shown in Figure 4, where the maximum heat flux is 1.7577 W/mm² at the workpiece end region and the minimum heat flux is 0.1553 W/mm² at the middle region of workpiece. The structural error is disclosed in Figure 5, with the maximum and minimum MRR of 0.01209 mJ and 0.0013343 mJ at the end region and middle region of workpiece, respectively.

5. Results and Discussion

5.1. Calculation of Analytical MRR (A-MRR). To estimate the removed material amount from specimen, temperature profile is used that has been obtained from FEM and to form circular parabolic geometry, crater is formed owing to each discharge. The paraboloid geometry is used to define the theoretical crater volume as formulated below:

$$V_c = \frac{1}{2} \times \pi \times S \times R_c^2, \quad (2)$$

where S represents the depth; R_c is the crater radius; V_c (FEM) is the volume, and 3D points contained in V_c represent the points over liquid temperature; and S and R_c values are obtained by estimating the temperature distributions over depth and radius directions of workpiece.

5.2. Calculation of Experimental MRR (E-MRR). MRR is described as the quotient value of division of pre- and postmachining weight difference and density and time of workpiece machining. It is defined as follows:

$$\text{MRR} = \frac{W_b - W_a}{\rho_w \times t} \times 1000 \text{ mm}^3/\text{min}, \quad (3)$$

where ρ_w indicates the density of workpiece; t is the machining processing time; and W_b and W_a represent the before and after machining workpiece weight. Table 6 is listed with the obtained values of A-MRR, T-MRR, and Ra with varying the input process variables using FEM and

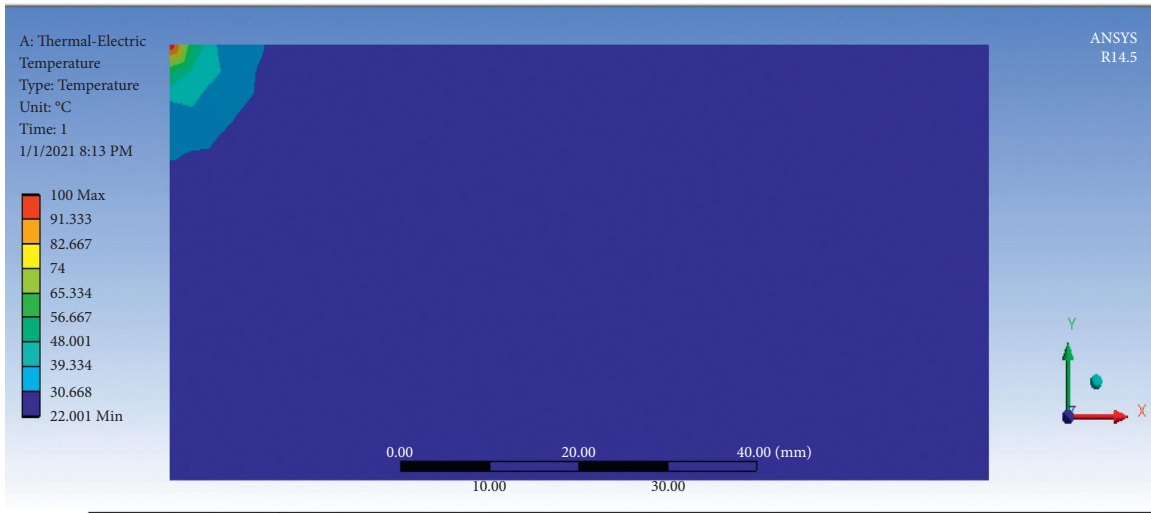


FIGURE 3: Temperature distribution obtained for a current intensity value of 14 A and pulse duration 750 μ s.

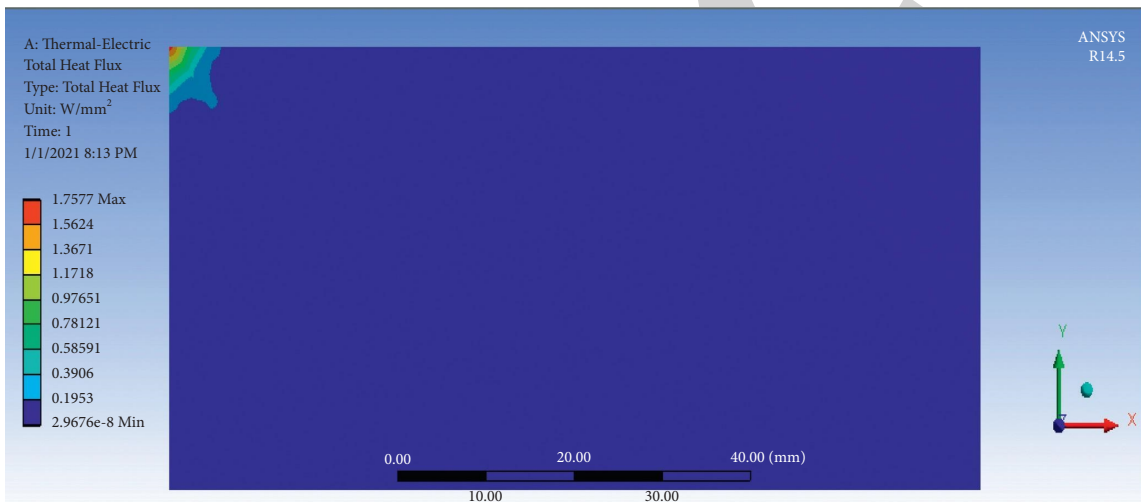


FIGURE 4: Volume of material removed for current intensity value of 14 A and pulse duration 750 μ s.

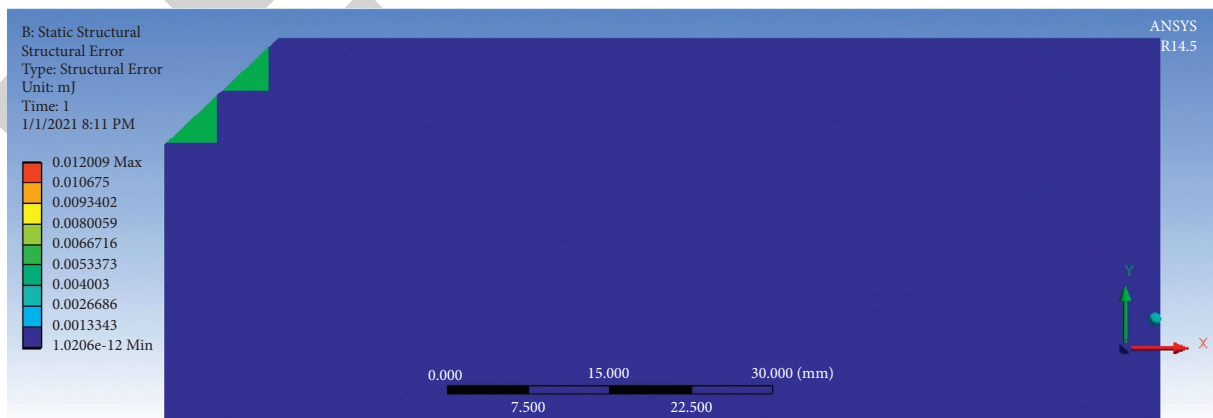


FIGURE 5: Structural error.

experimentally for the PMEDM process of SS630. In addition, the performance comparison graph of A-MRR and E-MRR is demonstrated in Figure 6.

5.3. *Reasons for Deviation in Values of A-MRR and E-MRR.* Practically, some deviations are noticed in the values of A-MRR compared to the E-MRR, which is due to some

TABLE 6: Obtained values of A-MRR, E-MRR, and Ra.

S. No.	C_p	T_{ON}	T_{OFF}	I_p	V_s	A-MRR (mm ³ /min)	E-MRR (mm ³ /min)	Ra (μ m)
1	0	8	15	6	3	1.914	2.145	2.932
2	0	12	22	10	4	2.562	2.986	2.381
3	0	16	30	14	5	5.142	5.008	5.142
4	3	8	15	10	4	2.154	2.256	2.461
5	3	12	22	14	5	4.521	4.469	2.594
6	3	16	30	6	3	3.941	3.997	5.173
7	5	8	15	6	5	3.842	4.120	2.196
8	5	12	22	10	3	4.641	4.976	3.868
9	5	16	30	14	4	5.814	5.896	3.790
10	7	8	15	14	4	3.910	4.139	2.542
11	7	12	22	6	5	3.143	3.245	3.481
12	7	16	30	10	3	4.963	4.897	2.896
13	9	8	15	14	3	4.144	4.245	2.760
14	9	12	22	6	4	3.794	3.986	2.749
15	9	16	30	10	5	5.903	6.113	1.695
16	12	8	15	10	5	3.943	3.876	3.521
17	12	12	22	14	3	5.304	5.436	3.987
18	12	16	30	6	4	3.949	4.103	2.612

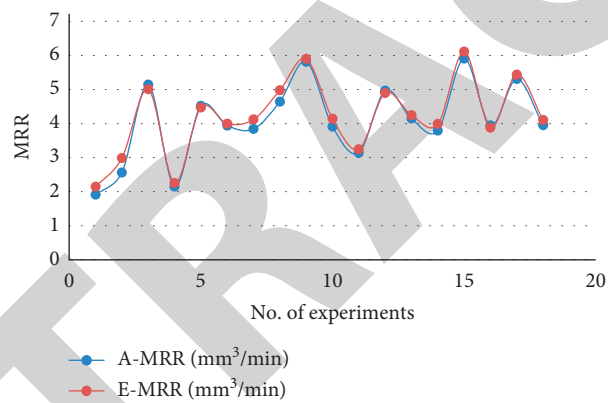


FIGURE 6: Performance comparison graph of A-MRR and E-MRR.

simplifying assumptions such as no ignition delays while machining, hundred percent material flushing efficiency, and not depositing the recast layer in the workpiece after machining. The flushing of melted workpiece materials is not done fully from the crater and a considerable number of melted materials is solidified in the crater again and formed the recast layer. The realization of ideal machining conditions is not done because of improper debris flushing those results in arching into the interelectrode gap while processing the machining of high energy discharges and reduced the actual value of MRR. Due to the parameters such as spark gap, sensitivity, dielectric fluid, and lift medium, the MRR is affected. In addition, an important role is played by dielectric fluid medium as it comes into picture for convection only, but it is essential to consider during machining process. By vaporizing and melting the material, the material removal is caused from the workpiece mainly. The dielectric material is taken away by the molten metal, but the molten metal is under heavy pressure owing to the plasma channel. Moreover, the material removal problem arises from workpiece due to the adhesive property of molten metal.

However, it is a tough task to design the model with the inclusion of all practical effects to the analytical model.

5.4. ANOVA. For each control factor, ANOVA is required to be estimated for accessing the factors impact on response. To investigate which design parameters effect the characteristic significantly, the experimental results have been assessed using the method of ANOVA, which can identify the input parameter contributions on Ra and MRR. To detect the process parameters whose variance in the design space impacts the output response metrics, ANOVA is applied while choosing 90% of confidence interval for experimental investigation. If the computed probability (p) value is about 10% or less, the factor significance is considered. After ANOVA, the obtained value of p is demonstrated in Table 7 and their significance on output response metrics such as Ra and MRR, respectively.

5.5. Regression Analysis. After the process of PMEDM, the regression analysis is conducted based on the obtained data

TABLE 7: Major factors and corresponding p values for PMEDM process.

Model Factor	p value	
	Ra	MRR
A	0.086	0.062
B	0.072	0.007
C	0.079	0.097
D	0.048	0.054
E	0.022	"Insig"
AB	0.075	0.030
AC	0.015	"Insig"
AD	0.063	"Insig"
AE	"Insig"	0.010
BC	"Insig"	0.056
DE	0.062	0.029
ABC	0.047	0.096
ADE	"Insig"	"Insig"

results and the linear equations are derived that are relevant to the dependent and independent variables, which is

performed using Minitab software and the regression equations are as follows:

$$Ra = 12.39 + 7.02A + 2.08B + 0.978C - 3.23D - 8.96E - 0.016AB + 0.0146AC - 0.311AD - 0.81AE - 0.0751BC + 0.802DE - 0.0088ABC + 0.0383ADE, \quad (4)$$

$$E - MRR = -5.18 - 7.22A - 1.06B - 0.66C + 1.83D + 5.31E + 0.027AB + 0.0129AC + 0.431AD + 1.04AE + 0.0560BC - 0.445DE + 0.0045ABC - 0.0768ADE. \quad (5)$$

Based on the listed values of R^2 , $Adj-R^2$, and $Pred-R^2$ in Table 8, the potency of equations (4) and (5) can be realized for predicting the variance inside the design space. After employing ANOVA, the derived model equations have been found out for estimating the variability within the design space for all output responses based on the results analyzation.

5.6. Modelling of Proposed Feed Forward BPNN. Figure 7 shows the block diagram of the proposed scalable conjugate gradient-based feed forward BPNN, where the input process variables such as C_p , I , V_S , T_{ON} , and T_{OFF} are given as input to the proposed 5-10-2 architecture of feed forward BPNN, as shown in Figure 8, which consists of single input layer, hidden layer, and output layer. The input layer contains 5 nodes that represent C_p , I , V_S , T_{ON} , and T_{OFF} as input nodes. The hidden layer consists of 10 nodes that are denoted as hidden nodes and the output layer consists of two nodes, i.e., MRR and Ra as output nodes. Two stages are involved in the proposed PMEDM process modelling, i.e., testing and training of network using experimental machining data. The values for T_{ON} , T_{OFF} , I , V_S , C_p , Ra, and MRR have been included in the training dataset. Such types of 96 datasets have been used, out of which 82 were randomly chosen and utilized for training purpose in case of SiC powder added EDM while remaining 14 datasets presented for training the network as new application data to test and validate the network model predictive accuracy. Hence, the data which had not been used for training are used to evaluate the network. The predicted MRR and Ra are compared with the

target values of MRR and Ra, i.e., E-MRR and E-Ra. Final optimized values of P-MRR and P-Ra will be computed based on the weight's adjustment, which reduces the error values.

5.6.1. Data Preprocessing. It is essential to perform the experimental data into patterns before the training of NN and mapping learnt. An input condition vector P_i is used to create the training and test pattern vectors where it contains C_p , T , I , and V_S and the corresponding target vector T_i , which consists of MRR and Ra. It is an important thing to consider the input and output data scale specifically in case of different operating ranges for process parameters. Without any skewing variable results, the ANN will be trained effectively by ensuring the scaling or normalizing. In the training, all input parameters are equally important, and each term is mapped to a value between -1 and 1 based on the following formula of linear mapping:

$$N = \frac{(R - R_{\min}) \times (N_{\max} - N_{\min})}{(R_{\max} - R_{\min})} + N_{\min}, \quad (6)$$

where N is the normalized value of the real variable; N_{\max} and N_{\min} refer to the normalization minimum and maximum values, respectively; and R_{\min} and R_{\max} are the minimum and maximum values of real variable while R is the real variable. Table 9 demonstrates the comparison of obtained output responses such as MRR and Ra using experimentation and prediction which are denoted as P-MRR and P-Ra. The performance comparison graph of obtained

TABLE 8: Residuals for all performance parameters.

	Ra	MRR
R^2	0.9124	0.9154
Adj- R^2	0.8962	0.9015
Pred- R^2	0.8824	0.8408

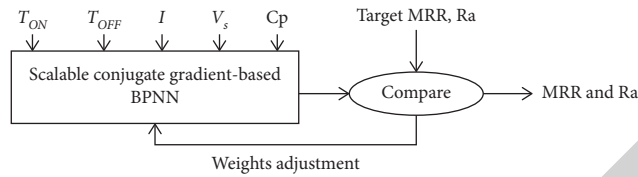


FIGURE 7: Proposed block diagram of scalable conjugate gradient-based feed forward BPNN.

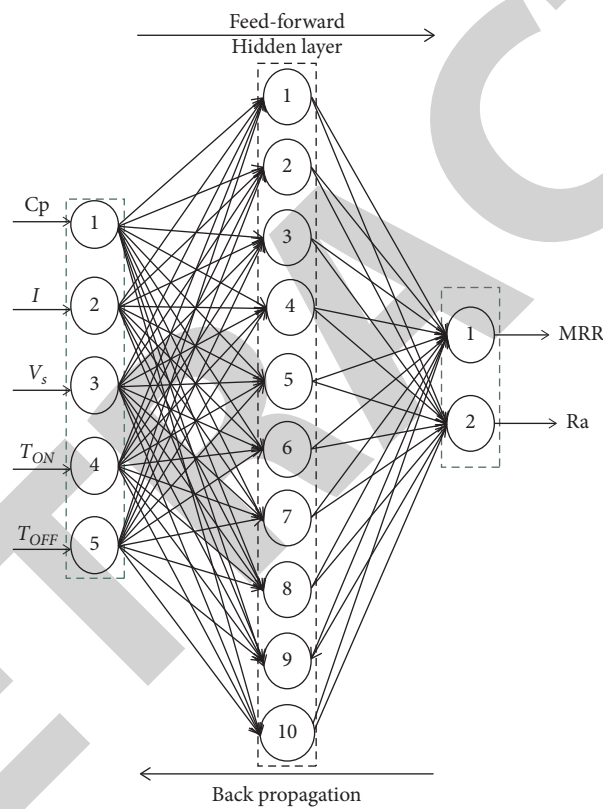


FIGURE 8: Proposed 5-10-2 architecture of feed forward BPNN.

TABLE 9: Comparison of E-MRR and E-Ra with optimized values predicted using ANN model, i.e., P-MRR and P-Ra.

S. No.	C_p	T_{ON}	T_{OFF}	I_p	V_s	E-MRR (mm ³ /min)	P-MRR (mm ³ /min)	E-Ra (μ m)	P-Ra (μ m)
1	0	8	15	6	3	2.145	2.301	2.932	2.910
2	0	12	22	10	4	2.986	2.820	2.381	2.112
3	0	16	30	14	5	5.113	5.092	5.142	5.231
4	3	8	15	10	4	2.256	2.457	2.461	2.568
5	3	12	22	14	5	4.469	4.134	2.594	2.448
6	3	16	30	6	3	3.997	3.896	5.173	5.198
7	5	8	15	6	5	4.120	4.110	2.196	2.019
8	5	12	22	10	3	4.976	4.954	3.868	3.782
9	5	16	30	14	4	5.896	5.784	3.790	3.793

TABLE 9: Continued.

S. No.	C_p	T_{ON}	T_{OFF}	I_p	V_s	E-MRR (mm^3/min)	P-MRR (mm^3/min)	E-Ra (μm)	P-Ra (μm)
10	7	8	15	14	4	4.139	4.124	2.542	2.547
11	7	12	22	6	5	3.245	3.214	3.481	3.442
12	7	16	30	10	3	4.897	4.891	2.896	2.895
13	9	8	15	14	3	4.245	4.321	2.760	2.667
14	9	12	22	6	4	3.986	3.997	2.749	2.789
15	9	16	30	10	5	6.113	6.192	1.695	1.731
16	12	8	15	10	5	3.876	3.897	3.521	3.567
17	12	12	22	14	3	5.436	5.332	3.987	3.980
18	12	16	30	6	4	4.103	3.985	2.612	2.423

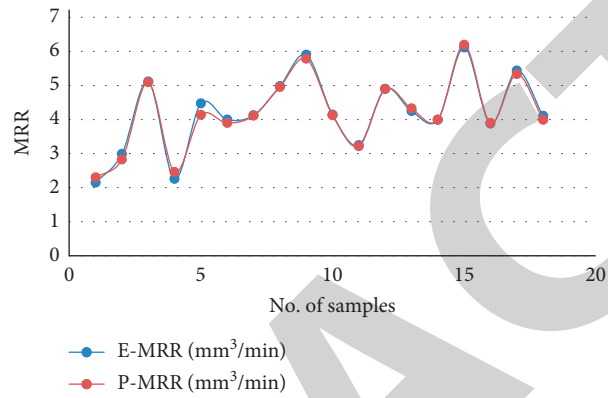


FIGURE 9: Performance comparison of obtained values of E-MRR and P-MRR for number of samples.

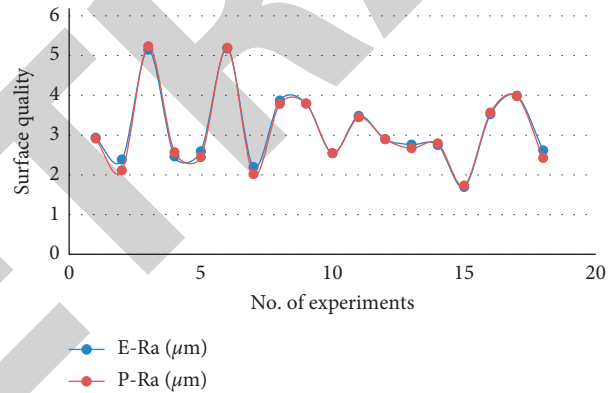


FIGURE 10: Performance comparison of obtained values of E-Ra and P-Ra for number of samples.

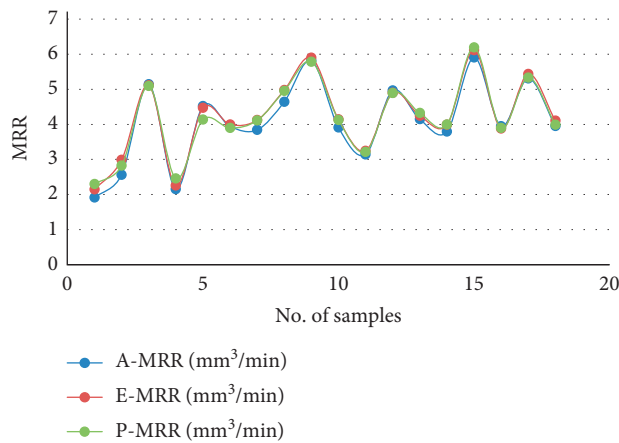


FIGURE 11: Performance comparison graph of MRR using FEM and experimental and feed forward BPNN models.

TABLE 10: Final optimization results of PMEDM process in different machining regimes.

Setting level	Optimal Ra and MRR parameters				
	A-MRR	E-MRR	P-MRR	E-Ra	P-Ra
C_p 9%, T_{ON} 16 μ s, T_{OFF} 30 μ s, I_p 10 A, and V_S 5 V	5.903	6.113	6.192	1.695	1.735
Relative error (%)	3.43		1.29		2.35

values of E-MRR, P-MRR and E-Ra, and P-Ra are illustrated in Figures 9 and 10, respectively.

Figure 11 demonstrates the performance comparison of the obtained MRR values using FEM and experimental and proposed scalable conjugate-based feed forward BPNN models. It shows the values of A-MRR, E-MRR, and P-MRR are quite similar with lesser error values. Final confirmation test results are demonstrated in Table 10, where the values of A-MRR and E-MRR are compared with the obtained P-MRR using ANN model at an optimal combination of input process parameters with C_p 9%, T_{ON} 16 μ s, T_{OFF} 30 μ s, I_p 10 A, and V_S 5 V. Similarly, Ra was also compared at same combination of input process variables. In addition, relative error also computed for disclosing the significance of FEM analysis and ANN model with lesser than 4% of error.

6. Conclusion

This article addressed an investigation on PMEDM process of SS630 grade using SiC that has been carried out to analyse its performance with the additives of favourable effects of mixing powder into dielectric fluid, where four input process variables such as C_p , I_p , V_S , and T are considered with two output response measures, i.e., E-MRR and E-Ra. In addition, FEM analysis is employed for finding the distribution of temperature, heat flux, and statistical error. Then, A-MRR is computed based on the values of temperature distribution on SS630 workpiece material. Further, BPNN model with feed-forward architecture is utilized for finding the optimal process parameter combination of input variables such as C_p , I_p , V_S , and T and measured the output responses as P-MRR and P-Ra. Finally, confirmation test results are presented in terms of MRR as A-MRR, E-MRR, and P-MRR and surface quality as E-Ra and P-Ra. It is found that the relative error is below 4%.

The following conclusions are derived using the simulation and validation results:

- (1) In the process of PMEDM, ANN model effectiveness has been proved in predicting the values of both Ra and MRR.
- (2) The optimal input conditions can synthesize using the ANOVA model appropriately in addition to the ANN for PMEDM.
- (3) The MRR is maximized, and Ra is minimized by the optimal input settings subjecting to necessary process constraints.

Data Availability

The data used to support the findings of this study are included within the article.

Disclosure

This study was performed as a part of the employment of Dambi Dollo University, Ethiopia.

Conflicts of Interest

Authors declare that there are no conflicts of interest in publication.

References

- [1] R. Atefi, N. Javam, A. Razmavar, and F. Teimoori, "The influence of EDM parameters in finishing stage on surface quality, MRR and EWR," *Research Journal of Applied Sciences, Engineering and Technology*, vol. 4, no. 10, pp. 1287–1294, 2012.
- [2] S. Prabhu and B. K. Vinayagam, "Analysis of surface characteristics of AISI D2 tool steel material using Electric Discharge Machining process with Single wall carbon nano tubes," *International Journal of Engineering and Technology*, vol. 2, pp. 35–41, 2010.
- [3] N. S. Khundrakpam, H. Singh, S. Kumar, and G. S. Brar, "Investigation and modeling of silicon powder mixed EDM using response surface method," *Int. J. Curr. Eng. Technol.* vol. 4, no. 2, pp. 1022–1026, 2014.
- [4] B. Reddy, G. N. Kumar, and K. Chandrashekar, "Experimental investigation on process performance of powder mixed electric discharge machining of AISI D3 steel and EN-31 steel," *Int. J. Curr. Eng. Technol.* vol. 4, no. 3, pp. 1218–1222, 2014.
- [5] H. Singh, "Experimental study of distribution of energy during EDM process for utilization in thermal models," *International Journal of Heat and Mass Transfer*, vol. 55, pp. 5053–5064, 2012.
- [6] B. Izquierdo, J. A. Sanchez, S. Plaza, I. Pombo, and N. Ortega, "A numerical model of the EDM process considering the effect of multiple discharges," *International Journal of Machine Tools and Manufacture*, vol. 49, no. 3-4, pp. 220–229, 2009.
- [7] T. Yih-fong and C. Fu-chen, "Investigation into some surface characteristics of electrical discharge machined SKD-11 using powder-suspension dielectric oil," *Journal of Materials Processing Technology*, vol. 170, pp. 385–391, 2005.
- [8] A. Bhattacharya, A. Batish, and N. Kumar, "Surface characterization and material migration during surface modification of die steels with silicon, graphite and tungsten powder in EDM process," *Journal of Mechanical Science and Technology*, vol. 27, no. 1, pp. 133–140, 2013.
- [9] B. Jabbaripour, M. H. Sadeghi, and M. R. Shabgard, "Investigating surface roughness, material removal rate and corrosion resistance in PMEDM of r-TiAl intermetallic," *Journal of Manufacturing Processes*, vol. 15, no. 1, pp. 158–166, 2013.

Retraction

Retracted: Investigation on V₂O₅ Thin Films for Field Effect Transistor Applications

Advances in Materials Science and Engineering

Received 26 December 2023; Accepted 26 December 2023; Published 29 December 2023

Copyright © 2023 Advances in Materials Science and Engineering. This is an open access article distributed under the Creative Commons Attribution License, which permits unrestricted use, distribution, and reproduction in any medium, provided the original work is properly cited.

This article has been retracted by Hindawi, as publisher, following an investigation undertaken by the publisher [1]. This investigation has uncovered evidence of systematic manipulation of the publication and peer-review process. We cannot, therefore, vouch for the reliability or integrity of this article.

Please note that this notice is intended solely to alert readers that the peer-review process of this article has been compromised.

Wiley and Hindawi regret that the usual quality checks did not identify these issues before publication and have since put additional measures in place to safeguard research integrity.

We wish to credit our Research Integrity and Research Publishing teams and anonymous and named external researchers and research integrity experts for contributing to this investigation.

The corresponding author, as the representative of all authors, has been given the opportunity to register their agreement or disagreement to this retraction. We have kept a record of any response received.

References

- [1] S. K. Suresh Babu, D. Jackuline Moni, D. Gracia, and A. G. Adigo, "Investigation on V₂O₅ Thin Films for Field Effect Transistor Applications," *Advances in Materials Science and Engineering*, vol. 2021, Article ID 2414589, 7 pages, 2021.

Research Article

Investigation on V_2O_5 Thin Films for Field Effect Transistor Applications

S. K. Suresh Babu ¹, D. Jackuline Moni ², D. Gracia ³ and Amsalu Gosu Adigo ⁴

¹Centre for Nanoscience and Genomics, Karunya Institute of Technology and Sciences, Coimbatore, India

²Department of Electronics and Communication Engineering, Karunya Institute of Technology and Sciences, Coimbatore, India

³Department of Electronics and Communication Engineering, Sri Ramakrishna Engineering College, Coimbatore, India

⁴Department of Chemical Engineering, College of Biological and Chemical Engineering, Addis Ababa Science and Technology University, Addis Ababa, Ethiopia

Correspondence should be addressed to S. K. Suresh Babu; sksureshababu@karunya.edu and Amsalu Gosu Adigo; amsalu.gosu@aastu.edu.et

Received 28 July 2021; Accepted 19 August 2021; Published 6 September 2021

Academic Editor: Samson Jerold Samuel Chelladurai

Copyright © 2021 S. K. Suresh Babu et al. This is an open access article distributed under the Creative Commons Attribution License, which permits unrestricted use, distribution, and reproduction in any medium, provided the original work is properly cited.

V_2O_5 thin films are analyzed for the substitution of SiO_2 to reduce the leakage current in devices when SiO_2 becomes ultrathin in submicron technology. Vanadium pentoxide (V_2O_5) has a high-k dielectric constant of 25 and can be replaced as a gate oxide in the field-effect transistor. V_2O_5 is deposited using pulsed laser deposition (PLD) in the oxygen (O_2) environment at room temperature and characterized. The films surface morphology has been examined by scanning electron microscopy. The capacitance, dielectric constant, and dielectric loss are analyzed for fabricated metal oxide semiconductor (MOS) structure using Solartron SI-1260 impedance analyzer. The transfer characteristic of the fabricated device is analyzed using National Instruments NI-PXI 4110. The I_{ON}/I_{OFF} ratio of 10^6 and threshold voltage (V_{TH}) of 0.6 V is obtained.

1. Introduction

Thin film technology has a vital role in electronic industries. The active thin film transistor (TFT) is a part of thin film technology which is a composition of various thin layers to form the MOSFET. These layers can be formed by a device either over silicon or a glass substrate. The replacement of silicon dioxide (SiO_2) with other materials is becoming a great challenge in the community. Many developments have occurred with SiO_2 , but still the current leakage in a device has not been controlled in the transistor. This current leakage leads a battery to drain in minutes in the gadgets and also reduces the efficiency by producing an enormous amount of heat. So, in order to solve this problem, material with high dielectric constant (k) of more than 3.9 has to be used [1]. Pulsed laser deposition techniques have been reported to fabricate V_2O_5 thin films [2–7]. The paper deals with the preparation of V_2O_5 using pulsed laser deposition,

and its performance as a gate dielectric in MOSFET. V_2O_5 is reported as the best rare Earth materials in terms of good thermodynamic stability and high quality interface with silicon. Hence, these materials are studied for silicon FET.

2. Experimental

Many deposition techniques are available in the literature for coating the thin films. Pulsed laser deposition (PLD) technique is used for its uniform and stoichiometry deposition [8–12]. Nd-YAG laser at 355 nm is used to deposit a thin film onto the substrate, and the deposition is carried out in a chamber at oxygen (O_2) atmosphere [13–20]. The base pressure maintained during deposition is about 3.8×10^{-6} torr. The V_2O_5 (Sigma-Aldrich, 99.999%) target is placed in a sample holder which will rotate at a rate of 10 rotations per minute (rpm) during deposition. V_2O_5 thin films are deposited on the glass and silicon substrate in room

temperature [21–25]. The confirmation of V_2O_5 phase angle is done using XRD. The thin films' surface morphology is studied by scanning electron microscope (JEOL model JSM-6390), and amorphous nature of V_2O_5 films is found using X-ray diffractometer (Shimadzu model XRD-6000). The optical properties of the thin films were studied using ultraviolet spectroscopy (Shimadzu UV-240) and photoluminescence spectroscopy. The electrical properties were studied using an impedance analyzer (Solartron SI-1260) by varying the frequency. The transfer I–V characteristics of fabricated MOSFET were carried out with National Instrument PXI 4110.

3. Results and Discussion

V_2O_5 film (at R.T.) is deposited using PLD for gate dielectric.

V_2O_5 thin films are deposited at room temperature and 400°C using PLD, as shown in Figure 1. These deposited films are analyzed for the selection of the best film for the gate dielectric of FET.

3.1. Structural Analysis. The structural characterization, done by interpreting the XRD peak data, gives an insight about the crystallinity and phase changing behavior of the film when annealed at different temperatures. From the XRD plot, as in Figure 2, it is clearly shown that, as the temperature increases, the amorphous nature of the film is revealed. Deposition of the film is carried out at 400°C and subjected to vacuum annealing and then annealed at 400°C , wherein an increase in its crystalline nature is observed. The peak is observed at 17 (2theta value) for 400°C , and its (hkl Miller indices) values correspond to (002), and the system observed is orthorhombic in structure. The small peak is observed at 32.8 (2theta value) for the silicon substrate and verified from the JCPDS (78–0250), and its values corresponds to (111).

Grain size can be determined, with the Scherrer formula as

$$D = \frac{\lambda * 0.94}{\beta \cos \theta}, \quad (1)$$

where λ is the wavelength, θ is the Bragg angle, and β as the line broadening (Table 1).

The XRD pattern of V_2O_5 at room temperature, shown in Figure 2, reveals that the amorphous nature and the same film is annealed at 400°C and obtained at 2θ at 17° . Also, the more amorphous nature of the thin film ensures a high-k dielectric value which marks its application in the fabrication of FET devices as gate dielectric.

The energy dispersive X-ray spectrum is shown in Figure 3. The observation of peaks further confirms the presence of vanadium dioxide in the deposited thin film.

3.2. Surface Topography Analysis. Figure 4 gives the SEM image of V_2O_5 at room temperature and illustrates a granular nature. The porosity increases the diffusion barrier



FIGURE 1: V_2O_5 thin film deposition using PLD.

properties and will have a high-resistance effect on the layer, which can be more suitable for the gate dielectric layer.

3.3. Film Morphology Analysis Using AFM. AFM image (Figure 5) shows the small step layer deposition at maximum peak difference as 833 nm over z -axis of the deposited film. It is observed for the $20\ \mu\text{m} \times 20\ \mu\text{m}$ size of the placed sample. From the histogram graph, as shown in Figure 6, it is clearly observed that very few points are noted at higher peaks and all other points are almost uniformly deposited.

Observations carried out from the AFM characterization are given in Table 2. The root mean square roughness is about 125 nm and maximum peak is observed at 832 nm may be due to the ion implantation in the silicon substrate. The roughness average is noted as 96 nm which shows the smooth deposition obtained using PLD and is more suitable for the thin film transistor. The average height is 329 nm and proves the smooth deposition of the V_2O_5 thin film.

3.4. Capacitance, Dielectric Constant, and Dielectric Loss Analysis. Solartron SI-1260 is used for the analysis of capacitance, dielectric constant, and dielectric loss of V_2O_5 deposited at room temperature. Metal oxide semiconductor (MOS) structure is deposited over the N-Type silicon using the PLD technique, as shown in Figure 7. Gold is coated over the deposited film as terminals for electrodes. From equation (2), the capacitance of the MOS structure is calculated and plotted in Figure 8:

$$C = \frac{k \cdot \epsilon \cdot A}{d}. \quad (2)$$

From Figure 8, it is observed that the capacitance (in microfarad) of the MOS gradually decreases with the increase in the frequency; the amorphous state of the film has a good charging value till kilo Hz. This configured film can be more suitable for the low-frequency applications:

From equation (3) and (4), the obtain dielectric loss is

$$\tan \delta = \frac{\epsilon''}{\epsilon'}, \quad (5)$$

where t is thickness of the film, ω is angular frequency, Z' is the real part of impedance, Z'' is the imaginary part of impedance, ϵ_0 is permittivity of free space, and A is the area of the film.

The dielectric constant for the deposited film is observed high at low frequency and decreases with increase

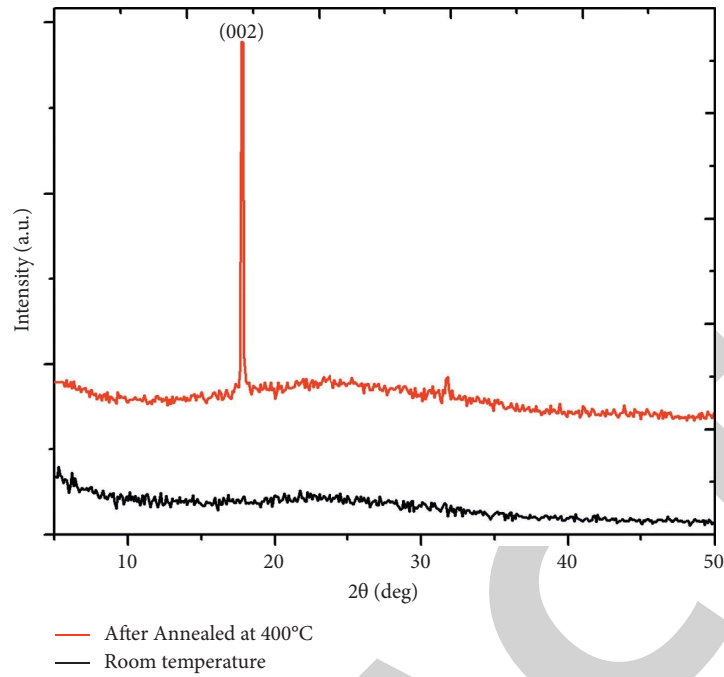


FIGURE 2: XRD plot of V_2O_5 at room temperature.

TABLE 1: The grain size of the thin films.

Sample	D (nm)
As deposited	134
400°C	185

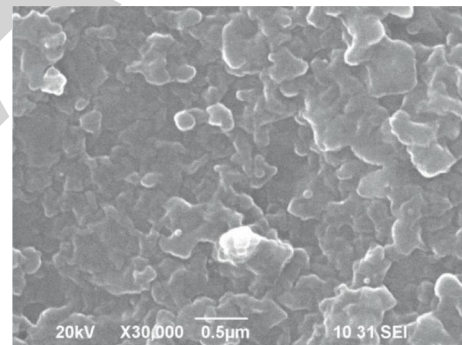


FIGURE 4: V_2O_5 SEM image of at room temperature.

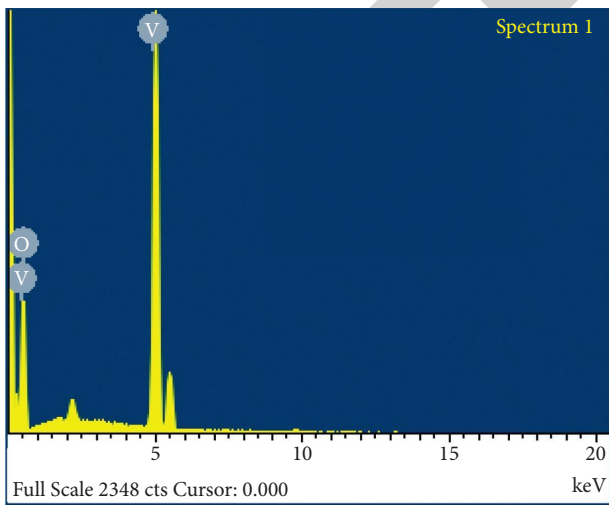


FIGURE 3: V_2O_5 EDAX spectra.

in frequency, as shown in Figure 9. These changes happen because of larger grain boundaries of amorphous film at the applied electric filed [23].

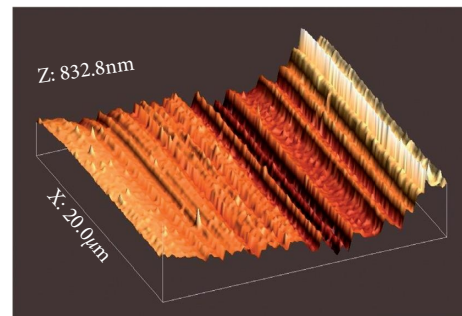
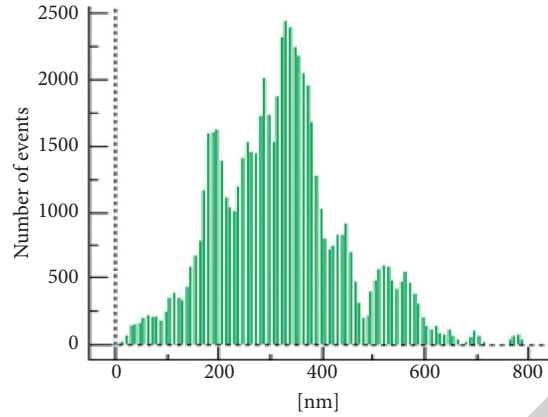
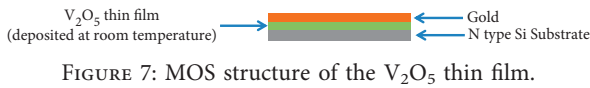
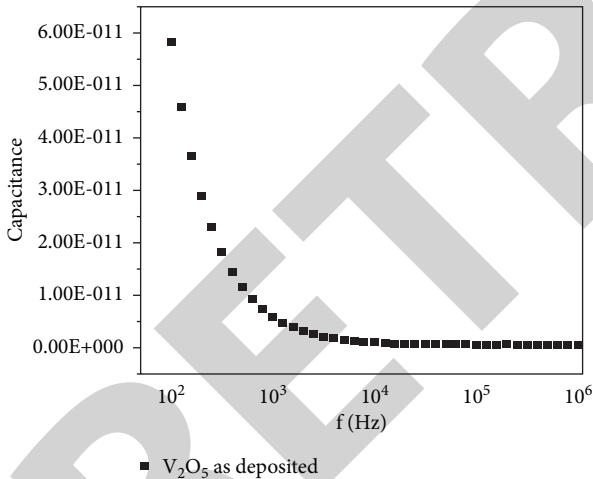


FIGURE 5: V_2O_5 AFM image at room temperature.

FIGURE 6: Histogram graph of the AFM image of V_2O_5 .TABLE 2: V_2O_5 parameter analysis using AFM.

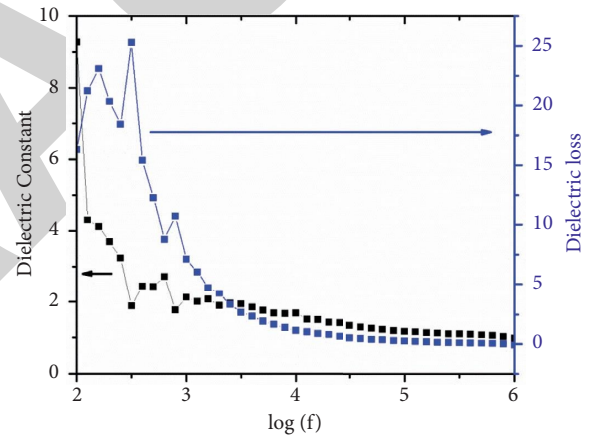
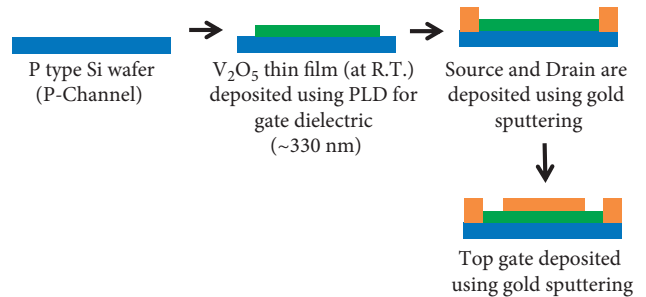
RMS roughness (nm)	Maximum value (nm)	Average roughness (nm)	Average height (nm)
125	832	96	329

FIGURE 7: MOS structure of the V_2O_5 thin film.FIGURE 8: Capacitance vs. frequency analysis of the V_2O_5 thin film prepared at room temperature.

$$\epsilon' = \frac{t}{\omega A \epsilon_0} \cdot \frac{Z''}{Z'^2 + Z''^2}, \quad (3)$$

$$\epsilon'' = \frac{t}{\omega A \epsilon_0} \cdot \frac{Z'}{Z'^2 + Z''^2}. \quad (4)$$

With these capacitance, dielectric constant, and dielectric loss results, the V_2O_5 thin film deposited at room temperature is more stable at low frequency and can be a better gate dielectric layer in the replacement of conventional SiO_2 in MOSFET.

FIGURE 9: Dielectric constant and dielectric loss vs. log frequency of the V_2O_5 thin film prepared at room temperature.FIGURE 10: Fabrication steps involved in the V_2O_5 film gate dielectric-based Si-MOSFET.

4. MOSFET Fabrication

Figure 10 shows the fabrication steps of V_2O_5 thin film gate dielectric-based Si-MOSFET. In this device, P-type silicon is used as the channel and also as a base layer for the proposed

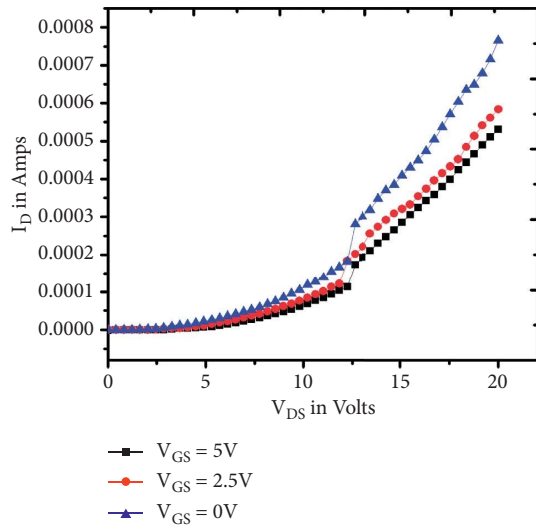


FIGURE 11: Output characteristics of V_2O_5 thin film gate dielectric of Si-MOSFET.

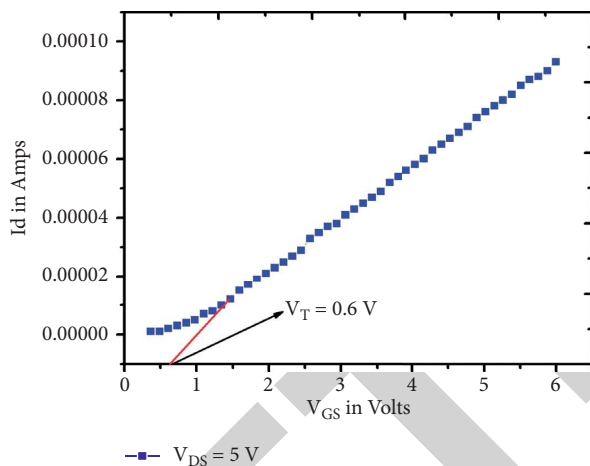


FIGURE 12: Transfer characteristics of V_2O_5 thin film gate dielectric of Si-MOSFET (square root of drain current vs. V_{GS}).

device. It is well cleaned and processed for the device fabrication. Inside the PLD chamber, the prepared V_2O_5 pellet is fixed as the target. With prepared stainless steel (SS) mask, the V_2O_5 thin film is deposited at 330 nm at room temperature as a gate dielectric layer. The thickness is measured using AFM. By using sputtering as the source, drain and gate are deposited with gold (Au) with the designed SS-mask.

The electrical characterization of fabricated MOSFET is carried out using National Instruments NI-4100. With the designed LabVIEW platform, the output and transfer characteristics are analyzed. Figure 11 shows the output characteristics of V_2O_5 gate dielectric-based Si-MOSFET.

In output characteristics, V_{DS} is varied between 0 and 20 Volts with various constant gate voltage (0, 2.5 V, and 5 V), and the corresponding drain current I_D is noted. Kink in the I-V characteristics is because of the sudden rise in the applied voltage (randomly set by the program), which causes this effect.

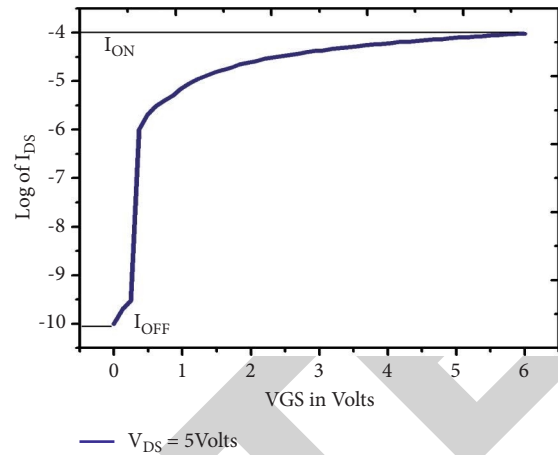


FIGURE 13: Transfer characteristics of V_2O_5 thin film gate dielectric of Si-MOSFET (log. of drain current vs. V_{GS}).

From Figure 12, the threshold voltage V_{TH} is found to be 0.6 V [26–29]. The I_{ON}/I_{OFF} ratio of fabricated MOSFET is calculated from the transfer characteristics results which are shown in Figure 13. The I_{ON}/I_{OFF} current ratio can be calculated by plotting the obtained drain current in the log scale; by measuring the maximum point in graph to minimum point of drain current gives the value of the I_{ON}/I_{OFF} current ratio as 10^6 .

The results show that the fabricated MOSFET has less leakage current from the observed I_{ON}/I_{OFF} current and V_2O_5 thin film is more suitable for the gate dielectric of MOSFET.

5. Conclusion

The various characteristics of V_2O_5 is analyzed and reported. The replacement of SiO_2 dielectric in MOSFET is due to its large leakage current in submicron technology; the MOS structure of the V_2O_5 thin film is studied, and its capacitance, dielectric constant, and dielectric loss at low frequency are analyzed. The results revealed that the V_2O_5 thin film deposited at room temperature can be used as the gate dielectric of MOSFET. The Si-MOSFET is fabricated with V_2O_5 thin film as the gate dielectric by using PLD. It is also observed that the good I_{ON}/I_{OFF} current ratio is 10^6 and threshold voltage (V_{TH}) is 0.6 V. This I_{ON}/I_{OFF} ratio shows less leakage current with stable threshold voltage, and henceforth, the V_2O_5 thin film can be a good replacement of SiO_2 in MOSFET [30–36].

Data Availability

The data used to support the findings of this study are included within the article.

Disclosure

This study was performed as a part of the Employment of Addis Ababa Science and Technology University, Ethiopia.

Conflicts of Interest

The authors declare that they have no conflicts of interest.

References

- [1] H. Chakraborty and D. Durga Misra, "Characterization of high-k gate dielectrics using MOS capacitors," *International Journal of Scientific and Research Publications*, vol. 3, no. 12, 2013.
- [2] J. Scarminio, A. Talledo, A. A. Andersson, S. Passerini, and F. Decker, "Stress and electrochromism induced by Li insertion in crystalline and amorphous V_2O_5 thin film electrodes," *Electrochimica Acta*, vol. 38, no. 12, pp. 1637–1642, 1993.
- [3] R. Enjalbert and J. Galy, "A refinement of the structure of V_2O_5 ," *Acta Crystallographica Section C Crystal Structure Communications*, vol. 42, no. 11, pp. 1467–1469, 1986.
- [4] C. Sanchez, J. Livage, and G. Lucazeau, "Infrared and Raman study of amorphous V_2O_5 ," *Journal of Raman Spectroscopy*, vol. 12, no. 1, pp. 68–72, 1982.
- [5] R. Baddour-Hadjean, J. P. Pereira-Ramos, C. Navone, and M. Smirnov, "Raman study of electrochemical lithium intercalation into sputtered crystalline V_2O_5 thin films," *Chemistry of Materials*, vol. 20, no. 5, pp. 1916–1923, 2008.
- [6] S. Senapati and S. Panda, "Effect of aging of V_2O_5 sol on properties of nanoscale films," *Thin Solid Films*, vol. 599, pp. 42–48, 2016.
- [7] D. O. Scanlon and A. Walsh, B. J. Morgan and G. W. Watson, "An ab initio study of reduction of V_2O_5 through the formation of oxygen vacancies and Li intercalation," *Journal of Physical Chemistry C*, vol. 112, no. 26, pp. 9903–9911, 2008.
- [8] M. Benmoussa, A. Outzourhit, A. Bennouna, and E. L. Ameziane, "Electrochromism in sputtered V_2O_5 thin films: structural and optical studies," *Thin Solid Films*, vol. 405, no. 1-2, pp. 11–16, 2002.
- [9] A. Kumar, P. Singh, N. Kulkarni, and D. Kaur, "Structural and optical studies of nanocrystalline V_2O_5 thin films," *Thin Solid Films*, vol. 516, no. 6, pp. 912–918, 2008.
- [10] J. Huotari, R. Bjorklund, J. Lappalainen, and A. Lloyd Spetz, "Pulsed laser deposited nanostructured vanadium pentoxide thin films characterized as ammonia sensors," *Sensors and Actuators B*, vol. 217, pp. 22–29, 2015.
- [11] D. Q. Liu, W. W. Zheng, H. F. Cheng, and H. T. Liu, "Thermochromic VO_2 thin film prepared by post annealing treatment of V_2O_5 thin film," *Advanced Materials Research*, vol. 79–82, pp. 747–750, 2009.
- [12] A. Mauger and C. M. Julien, " V_2O_5 thin films for energy storage and conversion," *AIMS Materials Science*, vol. 5, no. 3, p. 349, 2018.
- [13] C. Julien, E. Haro-Poniatowski, M. A. Camacho-López, L. Escobar-Alarcón, and J. Jiménez-Jarquín, "Growth of V_2O_5 thin films by pulsed laser deposition and their applications in lithium microbatteries," *Materials Science and Engineering: B*, vol. 65, no. 3, pp. 170–176, 1999.
- [14] L. Amorin, H. Cardozo, L. D. S. Martins, and A. Urbano, "Commitment between roughness and crystallite size in the vanadium oxide thin film opto-electrochemical properties," *Materials Research*, vol. 22, 2018.
- [15] Y. Zhang, J. Zheng, Y. Zhao, T. Hu, Z. Gao, and C. Meng, "Fabrication of V_2O_5 with various morphologies for high-performance electrochemical capacitor," *Applied Surface Science*, vol. 377, pp. 385–393, 2016.
- [16] K. Shibuya and A. Sawa, "Optimization of conditions for growth of vanadium dioxide thin films on silicon by pulsed-laser deposition," *AIP Advances*, vol. 5, no. 10, Article ID 107118, 2015.
- [17] C. V. Ramana, O. M. Hussain, R. Pinto, and C. M. Julien, "Microstructural features of pulsed-laser deposited V_2O_5 thin films," *Applied Surface Science*, vol. 207, no. 1–4, pp. 135–138, 2003.
- [18] S. Majid, D. K. Shukla, F. Rahman, K. Gautam, V. G. Sathe, and R. J. Phase, D. M. Phas, "Characterization of pulsed laser deposition grown V_2O_5 converted VO_2 ," *Journal of Physics: Conference Series*, vol. 755, Article ID 012027, 2016.
- [19] A. L. S. Hassen-Bey, T. Hakim, S. Lafane, and A. Z. Ait Djafer, "Substrate effect on electrical properties of vanadium pentoxide thin film for memristive device applications," in *Proceedings of the IEEE-Icse2016*, Kuala Lumpur, Malaysia, August 2016.
- [20] M. Jeanne, J.-G. Zhang, J. Turner, and D. Ginley, *Lithium Charging Capacities of Vanadium Pentoxide Thin Films Grown by Pulsed Laser Deposition for Rechargeable Li Battery Applications*, National Renewable Energy Laboratory, Golden, CO, USA, 1617.
- [21] G. A. Niklasson, S.-Y. Li, and C. G. Granqvist, "Thermochromic vanadium oxide thin films: electronic and optical properties," *Journal of Physics: Conference Series*, vol. 559, Article ID 012001, 2014.
- [22] N. B. Atan, I. B. Ahmad, and B. B. Yeop Majlis, "Effects of high-k dielectrics with metal gate for electrical characteristics of 18nm nmos device," in *Proceedings of the IEEE-ICSE 2014*, Kuala Lumpur, Malaysia, August 2014.
- [23] R. Fajgar, J. Kupcik, S. Jan, and N. Filip, "Characterization and properties of titanium-vanadium pentoxide thin films prepared by arf laser ablation," in *Proceedings of the NANOCON 2010. International Conference*, Olomouc, Czech Republic, October 2010.
- [24] X.-F. Zhang, K.-X. Wang, X. Wei, and J.-S. Chen, "Carbon-coated V_2O_5 as high performance cathode material for lithium ion batteries," *Chemistry of Materials*, vol. 23, no. 24, pp. 5290–5292, 2011.
- [25] N. M. Abd-Alghafour, N. M. Ahmed, Z. Hassan, and S. M. Mohammad, "Influence of solution deposition rate on properties of V_2O_5 thin films deposited by spray pyrolysis technique," *AIP Conference Proceedings*, vol. 1756, no. 1, Article ID 090010, 2016.
- [26] K.-J. Baeg, G.-T. Bae, and Y.-Y. Noh, "Efficient charge injection in p-type polymer field-effect transistors with low-cost molybdenum electrodes through V_2O_5 i," *ACS Applied Materials & Interfaces*, vol. 5, no. 12, pp. 5804–5810, 2013.
- [27] V. K. Kaushik, C. Mukherjee, T. Ganguli, and P. K. Sen, "Electrical and optical characteristics of aerosol assisted CVD grown ZnO based thin film diode and transistor," *Journal of Alloys and Compounds*, vol. 696, pp. 727–735, 2017.
- [28] S. Zhao, J. K. Sin, B. Xu, M. Zhao, Z. Peng, and H. Cai, "A high performance ethanol sensor based on field-effect transistor using a $LaFeO_3$ nano-crystalline thin-film as a gate electrode," *Sensors and Actuators B: Chemical*, vol. 64, no. 1-3, pp. 83–87, 2000.
- [29] Y. Shimizu, K. Nagase, N. Miura, and N. Yamazoe, "New preparation process of V_2O_5 Thin film based on spin-coating from organic vanadium solution," *Japanese Journal of Applied Physics*, vol. 29, no. 9, pp. L1708–L1711, 1990.
- [30] E. C. Elizabeth, "Optical properties of vanadium dioxide and vanadium pentoxide thin films," *Applied Optics*, vol. 30, no. 19, 1991.
- [31] R. André, F. Natálio, M. Humanes et al., " V_2O_5 nipla," *Advanced Functional Materials*, vol. 21, no. 3, pp. 501–509, 2011.
- [32] Y. Yue and H. Liang, "Micro- and nano-structured vanadium pentoxide (V_2O_5) for electrodes of lithium-ion batteries," *Advanced Energy Materials*, vol. 7, no. 17, 17 pages, Article ID 1602545, 2017.
- [33] S. Deng, Z. Yuan, Z. Tie, C. Wang, L. Song, and Z. Niu, "Electrochemically induced metal-organic-derived amorphous V_2O_5 for superior rate aqueous zinc-ion batteries,"

Retraction

Retracted: Continuous Sorption of Remazol Brilliant Orange 3R Using *Caulerpa scalpelliformis* Biochar

Advances in Materials Science and Engineering

Received 26 December 2023; Accepted 26 December 2023; Published 29 December 2023

Copyright © 2023 Advances in Materials Science and Engineering. This is an open access article distributed under the Creative Commons Attribution License, which permits unrestricted use, distribution, and reproduction in any medium, provided the original work is properly cited.

This article has been retracted by Hindawi, as publisher, following an investigation undertaken by the publisher [1]. This investigation has uncovered evidence of systematic manipulation of the publication and peer-review process. We cannot, therefore, vouch for the reliability or integrity of this article.

Please note that this notice is intended solely to alert readers that the peer-review process of this article has been compromised.

Wiley and Hindawi regret that the usual quality checks did not identify these issues before publication and have since put additional measures in place to safeguard research integrity.

We wish to credit our Research Integrity and Research Publishing teams and anonymous and named external researchers and research integrity experts for contributing to this investigation.

The corresponding author, as the representative of all authors, has been given the opportunity to register their agreement or disagreement to this retraction. We have kept a record of any response received.

References

- [1] G. Ravindiran, P. Sugumar, and G. Elias, "Continuous Sorption of Remazol Brilliant Orange 3R Using *Caulerpa scalpelliformis* Biochar," *Advances in Materials Science and Engineering*, vol. 2021, Article ID 6397137, 7 pages, 2021.

Research Article

Continuous Sorption of Remazol Brilliant Orange 3R Using *Caulerpa scalpelliformis* Biochar

Gokulan Ravindiran ¹, Pradeepkumar Sugumar ² and Elias G ³

¹Department of Civil Engineering, GMR Institute of Technology, Rajam, Andhra Pradesh 532127, India

²Department of Civil Engineering, VNR Vignana Jyothi Institute of Engineering and Technology, Hyderabad 500090, India

³Department of Mechanical Engineering, College of Electrical and Mechanical Engineering, Addis Ababa Science and Technology University, Addis Ababa, Ethiopia

Correspondence should be addressed to Gokulan Ravindiran; gokulravi4455@gmail.com and Elias G; elias.gmichael@aastu.edu.et

Received 26 July 2021; Accepted 20 August 2021; Published 3 September 2021

Academic Editor: Samson Jerold Samuel Chelladurai

Copyright © 2021 Gokulan Ravindiran et al. This is an open access article distributed under the Creative Commons Attribution License, which permits unrestricted use, distribution, and reproduction in any medium, provided the original work is properly cited.

An ever increase in the utilization of water for domestic and industrial activities resulted in the depletion of fresh water. Water is being used in huge quantities for manufacturing and other activities. The toxic pollutants used in the industries get mixed with water and result in the degradation of water quality. Textile industries are considered as one of the major industries that release a huge quantity of wastewater. The dye used in the textile industries is not completely utilized in the dyeing process and gets mixed with water and reaches the environment. *Caulerpa scalpelliformis*, a novel sorbent, was used for the preparation of biochar and successive removal of dyes in a continuous operation. The operating conditions, namely, biochar bed depth, dye flow rate, and initial dye concentration, were investigated, and the experimental result was validated with the mathematical models.

1. Introduction

Globally, emerging pollutants from industries had become the major challenge in recent years that cause an impact on the environment, human health, and aquatic fauna life. The major pollutants that are used in huge quantities are dyes [1]. Due to their complex nature and nonbiodegradable properties, they are difficult to remove once they are mixed with water [2]. Hence, wastewater has to be treated before discharging into water bodies [3]. If 1 mg/L of dyes is mixed in water, it acts as a thin trap on the surface of the water bodies [4, 5]. This will block the sunlight diffusion deep into the water bodies that affects photosynthesis activity. This results in the degradation of much aquatic life [6–8].

The most commonly adopted methods are precipitation, membrane filtration, oxidation, ion exchange, and adsorption process [9, 10]. Adsorption using activated carbon was considered as one of the prominent treatment methods [11]. Many adsorbents, namely, zeolite, silicate, lime, and activated carbon, were used. Among different adsorbents, activated

carbon is the most commonly used due to enhanced characteristics toward pollutant removal efficiency. However, due to its expensive nature and difficulties in regeneration, recent studies have focused on biosorption using waste materials [12]. Many biosorbents were successfully produced from agricultural waste, seaweeds, waste biomass, plant leaves, and fruit seeds. Several microorganisms, namely, bacteria, yeast, fungi, algae, and cyanobacteria, were also used in biosorption techniques, but using the live microorganism for biosorption has several disadvantages. Under moist conditions, proteinous materials of microbes will putrefy; maintaining and discarding microbes will result in additional cost. So, the development of alternate novel adsorbents for toxic pollutants' removal is emerging research.

Biochar is a carbonaceous material formed in the oxygen-limited environment under the thermal breakdown process. This biochar is rich in carbon, functional groups, and active binding sites, and several pores are present due to the pyrolysis process [13]. Many researchers proved that biochar produced from rice husk, coconut shell, peanut

shell, marine seaweeds, orange peel, date seeds, palm seeds, etc., can be successfully utilized for pollutant removal [14]. Energy from waste is considered one of the tools for reducing greenhouse gases in the atmosphere. The emerging techniques, namely, gasification, torrefaction, and pyrolysis, are used for converting waste into energy [15]. Among these methods, slow pyrolysis is considered as one of the promising techniques for converting waste into energy, resulting in solid residue called biochar, bio-oil, and synthetic gas [16].

Nearly 45% of textile dyes used worldwide are found to be reactive dyes [17] that are toxic and carcinogenic [18]. The presence of aromatic rings in the structural composition of dyes indicates nonbiodegradable properties. The reactive dyes will form covalent bonds between the fabric surface and the dye ions, resulting in strong binding. So, reactive dyes are a major challenge, and many batch studies were conducted. However, not many studies have demonstrated the remediation of reactive dyes in a continuous study. The present study focusses on the utilization of biochar produced from *Caulerpa scalpelliformis* for the decolorization of Remazol Brilliant Orange 3R (RBO3R).

2. Materials and Methods

2.1. Biosorbent Preparation. *Caulerpa scalpelliformis* is a marine seaweed that is available naturally in the seashore of South India. The required amount of seaweeds was collected and washed with deionized water. The washed seaweeds were sun-dried for 7 days to remove the moisture content naturally. The seaweeds were shredded into 7.5 mm and maintained in a hot air oven for 24 h at 103°C. Finally, the seaweeds were kept in the muffle furnace for 15 minutes at a temperature of 350°C. Remazol Brilliant Orange 3R (RBO3R) was obtained from Sigma-Aldrich, India.

2.2. Batch Study. The batch study was conducted in a controlled environment in an orbital shaker. 100 ml of the required initial dye concentration was used to investigate the sorption process. 150 rpm was maintained in the shaker for 6 h. After the required equilibrium time, 3 ml of the sample was taken and centrifuged at 3000 rpm for 5 min. The clear solution is taken for the measurement of the final dye concentration using a spectrophotometer at 490 nm. The partition coefficient is calculated to determine the optimum initial dye concentration for the sorption using biochar.

2.3. Continuous Study. Figure 1 illustrates the experimental setup used for the investigation of the sorption process. A peristaltic pump is used to give the feed from the bottom of the column at varying flow rates. An adjustable plunger is provided at the top of the column to vary the biochar bed depth. Glass beads are provided at the bottom of the column to maintain a steady flow inside the column. The sample received at the outlet port is taken to a spectrophotometer for analysis at 490 nm. The column data analysis, namely, overall sorption zone (Δt), breakthrough time (t_b), exhaustion time (t_e), the total amount of dye sorbed (m_{total}), the volume of wastewater treated (V_{eff}), removal efficiency

(%), and sorption capacity (mmol/g), was calculated [6]. Furthermore, mathematical modeling, namely, modified dose-response (MDR) model and Yoon-Nelson (YN), was studied. As suggested by Sujatha et al. 2021 [19], the error analysis was calculated to find the accuracy of the models.

3. Results and Discussion

3.1. Batch Study. The batch adsorption study concluded that a maximum removal efficiency of 76.2% was obtained with 0.1905 mmol/g as uptake capacity. Furthermore, biochar was investigated for reusability potential. The result concluded that sodium hydroxide with an S/L ratio of 5 and desorption efficiency of 99.2% was obtained. Figure 2 illustrates the partition coefficient of biochar at different initial RBO3R concentrations. From Figure 2, it is concluded that the partition coefficient was decreasing with a surge in initial RBO3R concentration. For instance, the partition coefficient of 3.92, 3.18, 1.6, 0.6, and 0.37 L/g was observed for 0.1, 0.25, 0.5, 0.75, and 1 mmol/L, respectively. This indicates that biochar is having good potential at lower concentrations rather than at higher concentrations [20].

3.2. Continuous Study. Generally, the dye removal process was studied in batch operation, and this will not create a solution for a real-time wastewater treatment system. Since most of the treatment plants are operating continuously, a treatment method that favors the continuous removal of the toxic pollutants will be practically exploring a possible solution [19]. Figure 3 illustrates the overall performance of the column in RBO3R removal. The biochar bed depth (25, 20, and 15 cm), flow rate (0.6, 0.48, and 0.3 L/hr), and initial RBO3R concentration (0.1, 0.2, and 0.25 mmol/L) were studied.

3.3. Biochar Depth on RBO3R Sorption. Figure 4 illustrates the performance of the packed bed column by varying biochar bed depth. Table 1 summarizes the overall column parameters during sorption of RBO3R. It is observed that a surge in bed depth enhanced the volume of wastewater treated. For instance, at a biochar depth of 25 cm, the total volume of wastewater treated was 3.3 L, and the overall sorption zone reported was 11 hours. The removal efficiency of 74.53 and 72.69% was obtained for 20 and 25 cm bed depths. The sorption capacity of 0.084 and 0.087 mmol/g was obtained for 20 and 25 cm. Based on the sorption capacity, removal efficiency, and volume of effluent treated, a biochar depth of 25 cm was selected as the best condition for the maximum performance of the column. Table 2 summarizes the model constants for MDR and YN models. A correlation coefficient of 0.961 was observed for the MDR model. Tables 3 and 4 brief different error analyses. From Tables 3 and 4, it is concluded that the MDR model is superior to the YN model since the error was very less.

3.4. Flow Rate on RBO3R Sorption. Figure 5 illustrates the removal efficiency of RBO3R at varying flow rates. For instance, at a flow rate of 0.3, 0.48, and 0.6 L/hr, the sorption

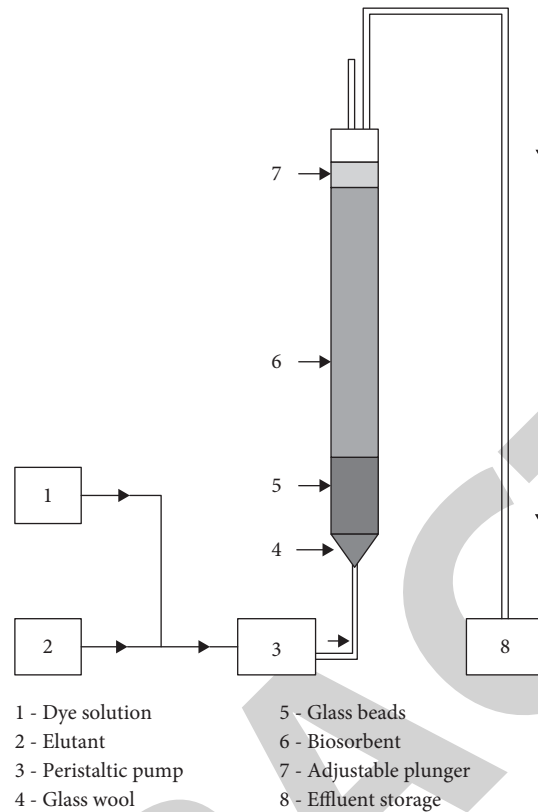


FIGURE 1: Experimental setup for continuous removal of RBO3R [4].

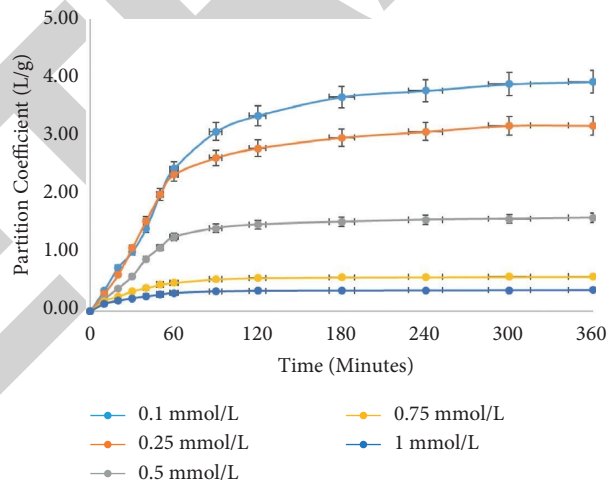


FIGURE 2: Partition coefficient for sorption of RBO3R.

capacity of 0.087, 0.081, and 0.073 mmol/g was obtained. The removal efficiency of 72.69% was observed at a flow rate of 0.3 L/hr. The improved efficiency and sorption capacity at decreased flow rate were due to the increased overall sorption zone. For instance, the overall sorption zone for 0.3, 0.48, and 0.6 L/hr was attained as 11, 7.25, and 5.26 h, respectively. It is obvious that, at decreased flow rate, the time for biochar to interact with dye molecules will be high [21, 22]. This may result in increased interaction between the dye and biochar and resulted in increased binding capacity

of biochar [23, 24], whereas at the increased flow rate, the dye molecules will get washed out since the time for binding will be very less [25, 26]. So, it is concluded that a flow rate of 0.3 L/hr is optimum for RBO3R sorption.

3.5. Initial Concentration on RBO3R Sorption. From Figure 6, it was clear that removal efficiency was higher at a lower RBO3R concentration. For instance, the removal efficiency of 79.56% was obtained at 0.1 mmol/L, whereas at

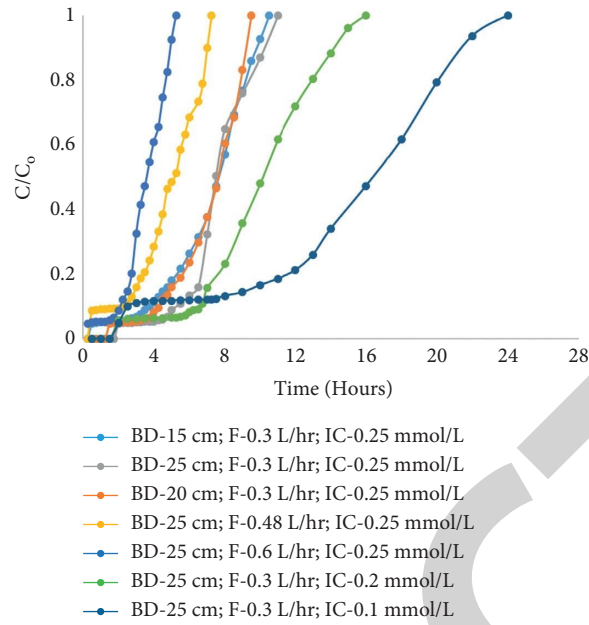


FIGURE 3: Overall sorption of RBO3R.

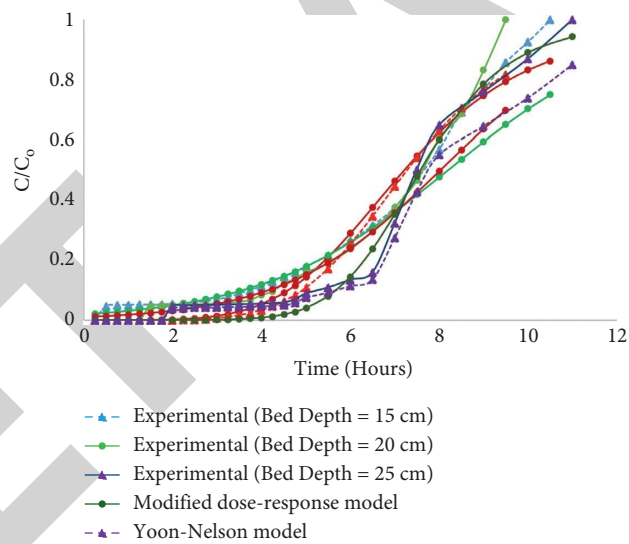


FIGURE 4: Sorption of RBO3R by varying bed depth with mathematical modeling.

TABLE 1: Column parameters at varying conditions.

Initial RBO3R concentration (mmol/L)	Flow rate (L/hr)	Bed height (cm)	Sorption capacity (mg/g)	t_b (h)	t_e (h)	Δt (h)	V_{eff} (L)	Removal efficiency (%)
0.25	0.3	15	0.093	0.5	10	10.5	3.15	67.37
0.25	0.3	20	0.084	1.75	7.75	9.5	2.85	74.53
0.25	0.3	25	0.087	2	9	11	3.3	72.69
0.25	0.48	25	0.081	0.5	6.75	7.25	3.48	58.53
0.25	0.6	25	0.073	0.25	5.01	5.26	3.15	64.64
0.2	0.3	25	0.088	2	14	16	4.8	63.64
0.1	0.3	25	0.055	5.5	18.5	24	4.8	79.56

TABLE 2: Mathematical model constants for RBO3R sorption.

Initial RBO3R concentration (mmol/L)	Flow rate (L/hr)	Bed height (cm)	MDR model			YN model		
			a_{mdr}	b_{mdr}	R^2	t	k_{YN}	R^2
0.25	0.3	15	4.890	2.162	0.973	8.188	0.477	0.986
0.25	0.3	20	5.615	2.182	0.965	8.025	0.571	0.983
0.25	0.3	25	7.584	2.275	0.987	10.129	0.456	0.879
0.25	0.48	25	4.026	2.354	0.967	5.116	0.742	0.984
0.25	0.6	25	5.026	2.122	0.984	3.611	1.402	0.989
0.2	0.3	25	5.301	2.973	0.992	10.190	0.538	0.992
0.1	0.3	25	5.899	3.219	0.961	12.667	0.327	0.882

TABLE 3: Statistical error analysis for the MDR model.

Initial RBO3R concentration	Flow rate	Bed depth (cm)	MDR model						
			AARE	HYBRID	ARE	MPSED	RMSE	Adj R^2	R^2
0.25	0.3	15	0.004	0.463	0.409	2.397	0.023	0.969	0.973
0.25	0.3	20	0.004	0.366	0.441	2.505	0.024	0.969	0.965
0.25	0.3	25	0.004	0.274	0.402	2.287	0.022	0.969	0.987
0.25	0.48	25	0.003	0.271	0.301	1.684	0.016	0.961	0.967
0.25	0.6	25	0.003	0.155	0.291	1.439	0.013	0.980	0.984
0.2	0.3	25	0.003	0.178	0.285	1.568	0.015	0.991	0.992
0.1	0.3	25	0.005	0.421	0.456	2.555	0.024	0.954	0.961

TABLE 4: Statistical error analysis for the YN model.

Initial RBO3R concentration	Flow rate	Bed depth (cm)	YN model						
			AARE	HYBRID	ARE	MPSED	RMSE	Adj R^2	R^2
0.25	0.3	15	0.005	0.642	0.482	2.823	0.027	0.984	0.986
0.25	0.3	20	0.005	0.394	0.457	2.600	0.025	0.980	0.983
0.25	0.3	25	0.005	0.454	0.517	2.942	0.028	0.859	0.879
0.25	0.48	25	0.002	0.081	0.164	0.920	0.009	0.981	0.984
0.25	0.6	25	0.001	0.029	0.126	0.622	0.006	0.986	0.989
0.2	0.3	25	0.001	0.019	0.093	0.510	0.005	0.991	0.992
0.1	0.3	25	0.006	0.773	0.618	3.461	0.033	0.861	0.882

AARE: absolute average relative error; HYBRID: hybrid fractional error function; ARE: average relative error; MPSED: Marquardt's percent standard error deviation (MPSED); RMSE: root mean square error; Adj R^2 : adjusted R^2 .

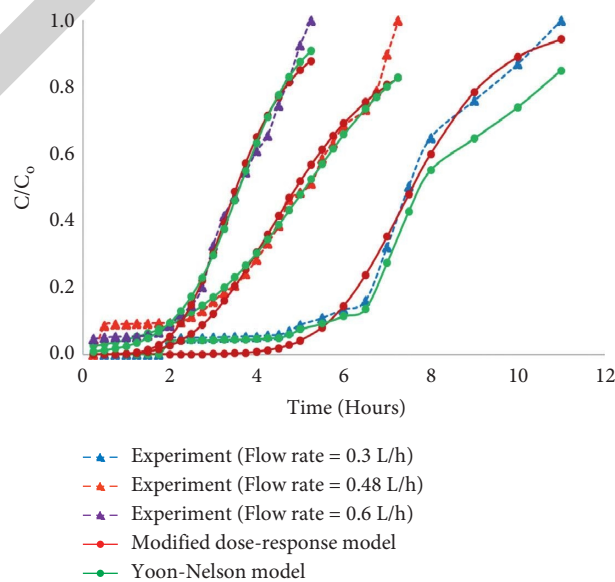


FIGURE 5: Sorption of RBO3R by varying flow rate with mathematical modeling.

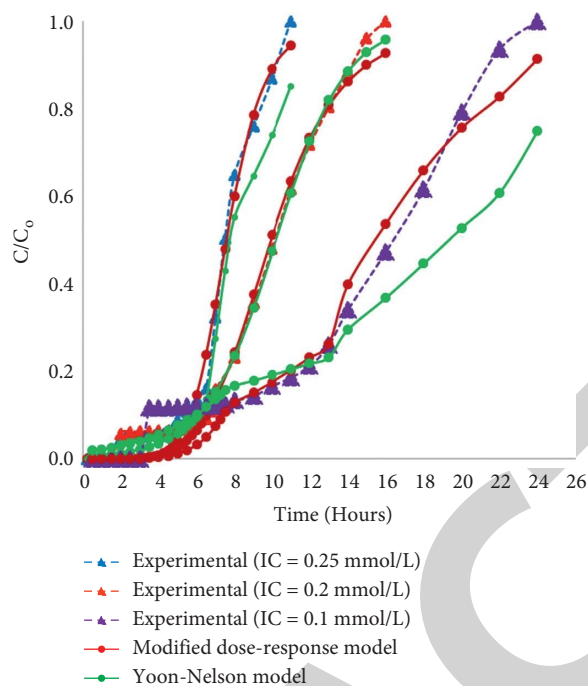


FIGURE 6: Sorption of RBO3R by varying initial concentration with mathematical modeling.

0.25 mmol/L, 72.69% was attained. The increased efficiency at reduced initial RBO3R concentration may have occurred because of the availability of abundant binding sites toward very few dye molecules [27, 28]. This may result in maximum sorption, whereas at higher concentration, the availability of the dye molecules was very high, and this may result in decreased removal efficiency [29, 30]. The overall sorption zone time was increased with a reduction in initial RBO3R concentration. For instance, a sorption zone of 11, 16, and 24 h was obtained for 0.25, 0.2, and 0.1 mmol/L. The overall sorption zone was found to be less for a practical application. Based on the overall column performance, 0.25 mmol/L was selected as an optimum initial RBO3R concentration for RBO3R sorption.

4. Conclusion

Biochar synthesized from *Caulerpa scalpelliformis* can be effectively used in continuous operation. The maximum removal efficiency of 72.69% and sorption capacity of 0.087 mmol/g were obtained at a biochar depth of 25 cm, a flow rate of 0.3 L/hr, and an initial RBO3R concentration of 0.25 mmol/L. The mathematical model study concluded that the MDR model was superior. Future research can be explored on assessing the potential of biochar by investing in regeneration studies. Possible assessments need to be conducted to suggest the solution to overcome the secondary pollutants to the environment.

Data Availability

The data used to support the findings of this study are included within the article.

Disclosure

This study was performed as a part of the employment of Addis Ababa Science and Technology University, Ethiopia.

Conflicts of Interest

The authors declare that they have no conflicts of interest regarding the publication of this paper.

Acknowledgments

The authors appreciate the support from Addis Ababa Science and Technology University, Ethiopia. They thank the GMR Institute of Technology, Rajam, Andhra Pradesh, and VNR Vignana Jyothi Institute of Engineering and Technology, Hyderabad, for the technical assistance to complete this experimental work.

References

- [1] A. Abdolali, W. S. Guo, H. H. Ngo et al., "Typical lignocellulosic wastes and by-products for biosorption process in water and wastewater treatment: a critical review," *Bioresource Technology*, vol. 160, pp. 57–66, 2014.
- [2] M. M. Felista, W. C. Wanyonyi, and G. Ongera, "Adsorption of anionic dye (Reactive black 5) using macadamia seed Husks: kinetics and equilibrium studies," *Scientific African*, vol. 7, e00283 pages, 2020.
- [3] P. M. Miladinova, R. K. Vaseva, and V. R. Lukanova, "Synthesis and investigation of some acid azo dyes for wool," *Journal of Chemical Technology and Metallurgy*, vol. 22, pp. 49–54, 2015.
- [4] A. Fegousse, A. El Gaidoumi, and Y. Miyah, "Pineapple bark performance in dyes adsorption: optimization by the central

Retraction

Retracted: Experimental Analysis of Mechanical Properties and Durability of Cement-Based Composite with Carbon Nanotube

Advances in Materials Science and Engineering

Received 26 December 2023; Accepted 26 December 2023; Published 29 December 2023

Copyright © 2023 Advances in Materials Science and Engineering. This is an open access article distributed under the Creative Commons Attribution License, which permits unrestricted use, distribution, and reproduction in any medium, provided the original work is properly cited.

This article has been retracted by Hindawi, as publisher, following an investigation undertaken by the publisher [1]. This investigation has uncovered evidence of systematic manipulation of the publication and peer-review process. We cannot, therefore, vouch for the reliability or integrity of this article.

Please note that this notice is intended solely to alert readers that the peer-review process of this article has been compromised.

Wiley and Hindawi regret that the usual quality checks did not identify these issues before publication and have since put additional measures in place to safeguard research integrity.

We wish to credit our Research Integrity and Research Publishing teams and anonymous and named external researchers and research integrity experts for contributing to this investigation.

The corresponding author, as the representative of all authors, has been given the opportunity to register their agreement or disagreement to this retraction. We have kept a record of any response received.

References

- [1] Y. Du, P. Gao, J. Yang, F. Shi, and M. Shabaz, "Experimental Analysis of Mechanical Properties and Durability of Cement-Based Composite with Carbon Nanotube," *Advances in Materials Science and Engineering*, vol. 2021, Article ID 8777613, 12 pages, 2021.

Research Article

Experimental Analysis of Mechanical Properties and Durability of Cement-Based Composite with Carbon Nanotube

Yubing Du ^{1,2,3}, Peiwei Gao ¹, Jianming Yang ^{2,3}, Feiting Shi ²,
and Mohammad Shabaz ^{4,5}

¹Department of Civil and Airport Engineering College of Civil Aviation/College of Flight,
Nanjing University of Aeronautics and Astronautics, Nanjing 210016, China

²College of Civil Engineering, Yancheng Institute of Technology, Yancheng 224051, China

³Jiangsu Collaborative Innovation Center for Ecological Building Materials and Environmental Protection,
Yancheng Institute of Technology, Yancheng 224051, China

⁴Arba Minch University, Arba Minch, Ethiopia

⁵Chitkara University Institute of Engineering and Technology, Chitkara University, Punjab, India

Correspondence should be addressed to Mohammad Shabaz; mohammad.shabaz@amu.edu.et

Received 18 May 2021; Accepted 21 August 2021; Published 1 September 2021

Academic Editor: Samson Jerold Samuel Chelladurai

Copyright © 2021 Yubing Du et al. This is an open access article distributed under the Creative Commons Attribution License, which permits unrestricted use, distribution, and reproduction in any medium, provided the original work is properly cited.

In order to study the mechanical properties and durability of cement-based composite with carbon nanotube, the test and analysis experiments are designed. Raw materials and related pharmaceutical instruments are prepared, to obtain cement-based composite with carbon nanotube samples by catalytic pyrolysis according to different proportions. The prepared sample is taken as the experimental object, and different bearing capacities are applied on different positions of the sample, to observe the change of the sample, and then, the experimental results of the mechanical properties of composite materials are obtained. The durability test results are obtained by combining the impermeability and frost resistance of the test object. The average compressive strength is 84.09 MPa, the average flexural strength is 16.9 MPa, and the crack resistance index is 22.5. In addition, the structure and diffusion coefficient of the sample also change in different degrees after the solution immersion and freeze-thaw treatment. Through longitudinal comparison, the more the carbon nanotubes are added into cement-based composite, the better its mechanical properties and durability are.

1. Introduction

Carbon nanotubes are one-dimensional quantum materials with special structure. When various nanoparticles are incorporated into the matrix, nanocomposites are created that outperform conventional materials in terms of performance. The major cause for the nanocomposites' enhanced features and qualities is the nanoparticles' modest loading into the base matrix, since nanoparticles have a superior dispersion in the parent matrix. [1–3]. Carbon nanotubes are mainly composed of hexagonal carbon atoms, which form several to dozens of concentric tubes. The distance between layers is about 0.34 nm, and the diameter is generally 2–20 nm. According to the different orientation of the carbon hexagon along the axial direction, it can be divided into three types: zigzag, armchair,

and spiral. Among them, helical CNTs have chirality, while zigzag and armchair CNTs have no chirality. As one-dimensional nanomaterials, carbon nanotubes are light in weight, perfectly connected in hexagonal structure, and have many unusual mechanical, electrical, and chemical properties. In recent years, with the in-depth study of carbon nanotubes and nanomaterials, their broad application prospects are also constantly emerging [4, 5]. Carbon nanotubes can be regarded as curled graphene sheets. Therefore, according to the number of graphene sheets, they can be divided into single-walled carbon nanotubes and MWCNTs. According to the conductive properties of carbon nanotubes, they can be divided into metal type carbon nanotubes and semiconductor type carbon nanotubes. According to whether there are tube wall defects, they can be divided into perfect carbon nanotubes and

defective carbon nanotubes. According to the shape, it can be divided into straight tube type, carbon nanotube bundle, Y type, snake type, and so on. As a raw material, carbon nanotubes are widely used in many fields because of their excellent mechanical, electrical, heat transfer, and optical properties.

Cement-based composite is a kind of composite material based on Portland cement, which is composed of alkali resistant glass fiber, general synthetic fiber, various ceramic fiber, carbon and aramid fiber, metal wire, natural plant fiber and mineral fiber as reinforcement, adding fillers, chemical additives, and water through composite process. It is better than ordinary concrete. Taking the short cut alkali resistant glass fiber composite with content of about 3%–10% as an example, its density is 1600–2500 kg/m³, impact strength is 8.0–24.5 N·mm/mm², compression strength is 48–83 MPa, and thermal expansion coefficient is $(11-16) \times 10^{-6} \text{K}^{-1}$ [6]. The properties vary with the raw materials, ratio, process, and curing conditions used. Cement-based composite materials are basically used to manufacture building components, such as interior and exterior wall panels and ceilings. In 1994, foreign researchers used chemical cutting method to introduce active functional groups to the surface of carbon nanotubes, at the same time, combined with ultrasonic treatment method to get well dispersed carbon nanotubes aqueous solution, and studied the mechanism of different types of anionic surfactants on the dispersion of carbon nanotubes, to obtain cement-based composite with carbon nanotubes.

Gillani et al. [7] found that the uniform dispersion of the multiwall carbon nanotubes (MWCNTs) in the composite matrix holds the key for the mechanical properties of the resulting composite. Foldyna et al. [8] proposed a novel technique of CNTs dispersing using acoustic generator of pulsating jets. Saralch et al. [9] have found that the dispersion of nanoclay in the polypropylene matrix plays a significant role in the preparation of nanocomposites. Their study of stress-strain behaviour during the tensile testing of nanocomposite along with critical examining using field emission scanning electron microscope (FESEM) of the fracture surface has evolved that part per hundred of resin (phr) value around five provides maximum strength.

Carbon nanotube composites have been studied at home and abroad. However, unlike other matrix materials, there are few reports on cement-based composite with carbon nanotubes. In recent years, some scholars have made a preliminary exploration on the mechanical and electrical properties of cement-based composite with carbon nanotubes. Foreign researchers have studied the mechanical properties of cement-based composites with nanocarbon fiber. In order to improve the dispersibility of carbon nanofibers in cement matrix, dispersant and ultrasonic are used to make treatment. First, the dispersed carbon nanofiber aqueous solution is prepared. The best dispersing suspension can be obtained when the ratio of dispersant and carbon nanofiber is the same. In the cement-based composite materials, the analysis shows that the nanocarbon fiber controls the growth of nanoscale microcracks, while the bending strength, elastic modulus, and hardness of the

composite materials are greatly enhanced. In recent two years, Harbin University of Technology, Tongji University, Dalian University of Technology, and other universities have begun to explore the carbon nanotube reinforced cement-based materials and made some basic breakthroughs. Through uniaxial compression test and fatigue crack test, the basic mechanical properties of ordinary concrete and self-compacting concrete mixed with three types of nanocarbon fiber are tested, and the optimum mixing amount is discussed. It is found that nanocarbon fiber with proper mixing amount and good dispersion can improve the compressive strength and splitting tensile strength of concrete and has a good reinforcement effect on concrete materials.

Carbon nanotubes have excellent physical and chemical properties and have a very wide application prospect in cement-based composite materials. However, at present, researchers all over the world are faced with the following common problems: the large-scale preparation of carbon nanotubes is still a bottleneck, which greatly limits the application of development and research of carbon nanotubes; the mechanical properties of carbon nanotubes and its reinforcement mechanism are not clear; the durability of cement-based composite materials is almost not studied. To solve these common problems, we need to strengthen the cooperation between material researchers and experts and scholars in the field of chemistry. On the one hand, we need to break through the key technology, further research and develop new technology with low cost and suitable for large-scale production of carbon nanotubes, and continue to study its mechanical properties. On the other hand, through modeling and simulation to strengthen the research of growth phenomenon and mechanism, the experimental analysis results on the durability of composite materials are obtained, so as to truly realize its application in the field of cement concrete.

2. Preparation of Cement-Based Composite with Carbon Nanotube

Based on the analysis of the research situation of cement-based composite with carbon nanotube at home and abroad, the research content of this experiment is proposed, which mainly includes four aspects: the first is to study the preparation results and characterization of carbon nanotube by different types of water reducing agents; the second is to study the macro-mechanical properties of modified cement-based materials with carbon nanotube and the mechanism of carbon nanotube reinforced cement; the third is to study the method and technology of carbon fiber orientation arrangement in cement and the mechanical properties of cement-based materials modified by carbon fiber orientation arrangement; the fourth is to study the durability of the cement-based composite with carbon nanotube [10]. Therefore, first, the mechanical properties and durability of cement-based composite with carbon nanotube are prepared as the research samples.

2.1. Preparation of Raw Materials. The composition of raw materials is closely related to their macroproperties. The properties and types of raw materials have a crucial influence

on the experimental results. Therefore, the selection and application of raw materials should meet the requirements of the experiment, which is the key link to ensure the smooth progress of the experiment. The raw materials used in this preparation will be introduced in detail in the following content.

2.1.1. Carbon Nanotubes. The carbon nanotubes used in the experiment include common multiwall carbon nanotubes (IMC6) and common carboxyl MWCNTs (IMC6—CH), which are produced by Beijing Boyu Hi-Tech New Material Technology Co., Ltd. [11]. IMC6—CH is a modified carboxylated derivative of IMC6 treated by chemical oxidation in liquid phase. The surface of IMC6 is inert and lack of active functional groups. There are a large number of COOH functional groups on the surface of IMC6—CH, which makes it easier for the MWCNTs with carboxyl group to bond with cement matrix and bridging agent. The physical parameters of MWCNTs are shown in Table 1.

It can be seen from Table 1 that the size of carbon nanotubes is very small, the length diameter ratio is large, the purity is high, and the specific surface is large.

2.1.2. Dispersant. Arabic gum is selected as the water dispersing agent of carbon nanotubes. Arabic gum can improve the hydrophilicity and dispersibility of MWCNTs by its long chain coating. Polyvinyl alcohol has good chemical cross-linking with cement matrix, and the hydroxyl group in polyvinyl alcohol may be connected with carboxyl group. Polyacrylamide is used to improve mortar performance with other fibers at the same time and shows good compatibility with fibers, so polyvinyl alcohol and polyacrylamide are selected as two bridging agents. The defoamer is tributyl phosphate.

2.1.3. Cement. As the most important cementitious material in construction engineering, the physical and chemical properties of cement have a great influence on the properties of cement products. The cement used is the benchmark cement produced by the Institute of Cement Science and New Building Materials Science of China Academy of Building Materials Science according to the National Standard of the People's Republic of China GB 8076-2008. Its chemical composition is shown in Table 2.

In addition, the physical parameters of P-O42.5 cement need to be analyzed, and the analysis results are shown in Table 3.

2.1.4. Water Reducing Agent. Water reducing agent is the key to improve the working performance of carbon fiber composite cement slurry. The water reducing agent molecules adsorb on the particles of cementitious materials in the fresh cement slurry to play a repulsive role and release water and form a layer of solvated film to play a lubricating role, so as to play a water reducing effect in the mixture [12, 13]. The water reducer used is the Bsaf powder water reducer MELFLUX[®] 2651F, which is a modified polycarboxylic ether

made by spray drying process. The bulk density parameter of the water reducer is 30–60/100 cm³, the drying loss is 2%, the pH value is 6.5–8.5, and the addition amount is 0.05%–1.5%.

2.2. Connection of the Preparation Instrument. Corresponding instruments are prepared according to the preparation method of cement-based composite with carbon nanotube, including QM - 3SP2 planetary ball mill, cement mortar mixer, cement mortar test body forming vibrating platform, 40 mm × 40 mm × 160 mm cement mortar test mold, analytical balance, weighing paper, and so on [14], in addition, the type of ultrasonic instrument produced by Shanghai Shenganalytical Ultrasonic Instrument Co., Ltd., the type of microcomputer controlled full-automatic pressure testing machine produced by Shanghai Hualong Testing Instrument Co., Ltd., the type of microcomputer controlled electronic universal testing machine produced by Jinan Sida Testing Technology Co., Ltd., and the type of electrohydraulic servouniversal testing machine produced by the American System Company. The prepared preparation instruments are connected according to the preparation principle, and the resulting preparation experimental device is shown in Figure 1.

2.3. Smoke and Dust Emission Real-Time Monitoring Subsystem. According to the mechanical properties of the amount of carbon nanotubes to lead sulphate cement paste, the mechanical properties change of lead sulphate cement pastes with different water cement ratio and same amount of carbon nanotubes, and the effect of age on the mechanical properties of cement, based on the reference mix proportion of high-performance cement-based composite materials, the preparation mix proportion of cement-based composite materials with carbon nanotube as shown in Table 4 is designed.

2.4. Execution of Preparation Process. As one of the most potential materials in nanomaterials, the preparation of carbon nanotubes has been widely concerned. At present, the preparation methods of carbon nanotubes mainly include arc discharge method, laser evaporation method, and catalytic pyrolysis method, among which catalytic pyrolysis method is widely used in the preparation of carbon nanotubes due to its advantages of easy control of reaction process, strong applicability, simple preparation method, and high product purity [15]. The raw materials are added into the experimental device according to the designed mix proportion, and then, magnetic stirring and ultrasonic treatment are carried out. Then, the samples of cement-based composite with carbon nanotube are obtained by catalytic pyrolysis. The process of catalytic pyrolysis is as follows: dissolve a certain amount of analytical pure Co(NO₃)₂ in deionized water, add a certain amount of silica gel with a certain size, stir it evenly, and then, stand it; take the precipitate and put it into a porcelain boat, put it in a quartz tube, and get the nanometal particles attached to the silica gel through drying, burning, and high-purity hydrogen

TABLE 1: Physical parameters of MWCNTs.

Type	IMC6—CH	MWCNTs-OH
Diameter (nm)	20–40	>50
Length (μ m)	10–30	10–20
-Oh/-CH content (wt%)	0.71	0.71
Purity (wt%)	>95	>95
Bulk density (g/cm^3)	0.18	0.18
Specific surface (m^2/g)	>80	>60

TABLE 2: Chemical composition of reference cement.

P-O42.5 cement		Fly ash	
Chemical composition	Content	Chemical composition	Content
SiO ₂	20.93	SiO ₂	58.31
Al ₂ O ₃	4.89	Al ₂ O ₃	29.63
Fe ₂ O ₃	2.89	Fe ₂ O ₃	3.65
CaO	60.42	CaO	1.80
MgO	3.56	MgO	0.43
K ₂ O	0.56	K ₂ O	0.11
SO ₃	2.27	SO ₃	0.67
Loss	3.60	f-CaO	0.93
—	—	Cl-	0.011
—	—	Loss	4.53

TABLE 3: Physical parameters of P-O42.5 cement.

Parameter	Parameter value
Specific surface area ($\text{m}^2 \cdot \text{kg}^{-1}$)	330
Loss on ignition (%)	3.65
Setting time (min)	Initial coagulation
	Final coagulation
Flexural strength (MPa)	3D
	28d
Compressive strength (MPa)	3D
	28d

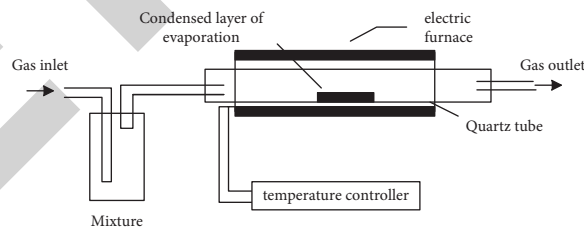
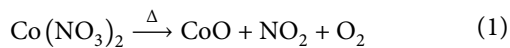
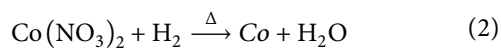


FIGURE 1: Preparation of experimental device.

reduction. This is the catalyst for thermal cracking of hydrocarbons [16]. The expression of the reaction process is shown as follows:



At the same time, the following reaction occurs:



The reaction process of pyrolysis of hydrocarbons is to mix C_2H_2 with a certain proportion of nitrogen as a compressed gas to pass through a quartz tube, which has

been drained of oxygen. At high temperature, C_2H_2 decomposes carbon and grows carbon nanotubes under the catalysis of metal particles. The reaction is as follows:



After the experiment, the sediment in the porcelain boat is taken for analysis, and the preparation results are shown in Figure 2.

2.5. Specimen Forming. The suspended carbon nanotubes are added to the cement-based material to form composite test

TABLE 4: Mix proportion of cement-based composite with carbon nanotube.

Sample no.	R-0	S-5	S-8	S-10	S-20	S-30	D-10
Water cement ratio	0.30	0.30	0.30	0.30	0.30	0.30	0.30
Cement content	0	0.05	0.08	0.10	0.15	0.20	0.30
Types of carbon nanotubes	IMC6	IMC6	IMC6	IMC6	IMC6-CH	IMC6-CH	IMC6-CH
Content of carbon nanotubes	0.04	0.08	0.12	0.16	0.20	0.04	0.08
Deionized water (g)	236	236	236	236	236	236	236
Cement (g)	629	629	629	629	629	629	629
Dispersant (g)	0	0.2	0.32	0.40	0.58	0.80	0.80
Water reducing agent (g)	0.3	0.3	0.3	0.3	0.3	0.3	0.3
Fly ash (g)	157	157	157	157	157	157	157
Sand (g)	1218	1218	1218	1218	1218	1218	1218
PVP content	0	0.015	0.024	0.030	0.045	0.060	0.090
PMA content	0	0.015	0.024	0.030	0.045	0.060	0.090

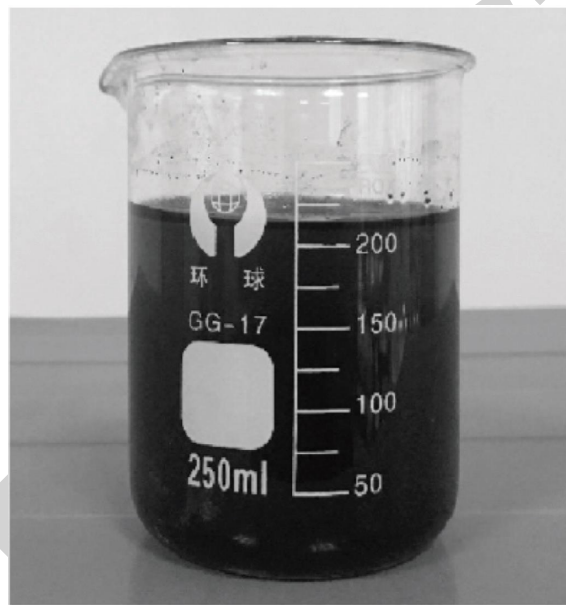


FIGURE 2: Configured carbon nanotube suspension.

pieces. The size of composite test pieces is $40\text{ mm} \times 40\text{ mm} \times 160\text{ mm}$. The relationship between the modulus of carbon nanotubes and its diameter and length is obtained. The modulus of carbon nanotubes increases with the increase of diameter but finally tends to converge. The modulus of carbon nanotubes decreases with the increase of length and also tends to converge [17]. In this way, there are certain requirements on the length and diameter of the molecular structure mechanics model in terms of the size. The carbon nanotubes with the diameter of about and over the length are taken for analysis. Carbon nanotubes (10, 10) are selected for analysis, and the outer diameter and thickness structure of the specimen cost are shown in Figure 3.

3. Mechanical Properties of Cement-Based Composite with Carbon Nanotube

According to GB/t17617-1999 Test Method for Strength of Cement Mortar, DKZ - 5000 type bending strength tester is used to test the impact of MWCNTs on the

bending strength of cement-based composite, and WHY type microcomputer controlled automatic press is used to test the impact of MWCNTs on the compressive strength of cement-based composite [18]. The fracture morphology of cement-based composite with MWCNTs is characterized by means of SU-70 SEM, and the interaction mechanism between carbon nanotubes and cement is explored. Combined with the results of mechanical analysis of cement-based composite materials with carbon nanotube, specific tests are carried out for different mechanical properties, and corresponding mechanical properties experimental results are obtained.

3.1. Theoretical Analysis of Mechanical Properties. In the mechanical property test of carbon fiber cement nanocomposites, WDW-50 microcomputer controlled electronic universal testing machine is used to carry out three-point bending test, with a span of 100 mm, uniformly loaded at a rate of 0.20 mm/min until breaking. The compressive strength is tested by the WHY-300 microcomputer controlled automatic

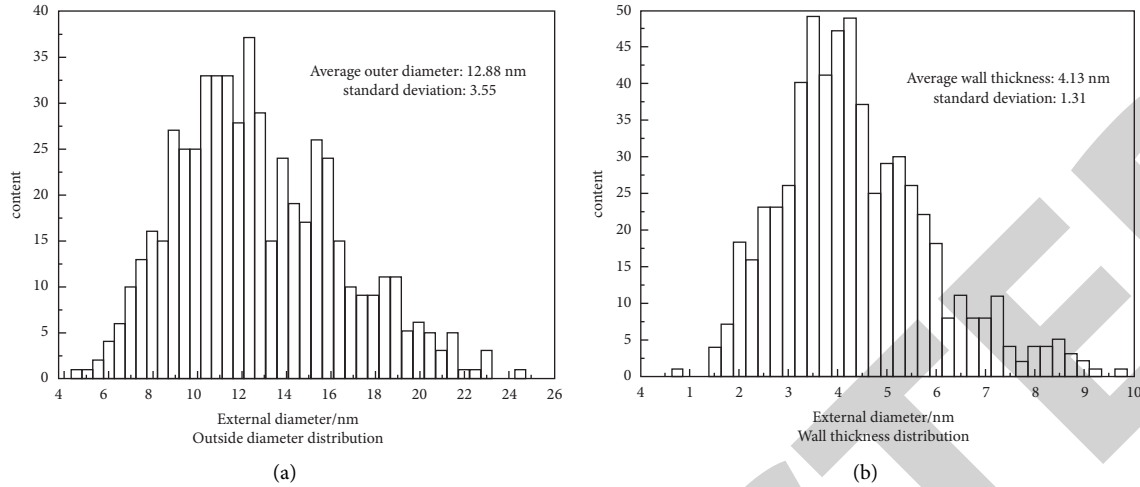


FIGURE 3: Outer diameter and thickness distribution of MWCNTs.

pressure testing machine and is loaded at the rate of 2400 N/s until the specimen is damaged [19]. WDW-50 microcomputer controlled electronic universal testing machine is used to test the tensile strength of fatigue crack, and the loading rate is 0.20 mm/min. The bending properties of the specimens are tested by MTS318 universal electrohydraulic servotesting machine at the loading rate of 0.10 mm/min. Finally, the mechanical properties of cement-based composite with carbon nanotube are obtained by synthesizing several mechanical properties.

Assuming that the diameter and length of the cement-based composite with carbon nanotube are D and L , the mechanical properties of the cylindrical solid can be determined by making its strain energy equal to the strain energy of the molecular structure mechanical model. The cement-based composite samples with carbon nanotubes are transversely isotropic materials, so they should have five elastic constants. In this way, combined with the intuitive geometric characteristics of molecular mechanics test and molecular structure mechanics, it can be based on the fact that carbon nanotubes are transversely isotropic, that is to say, they are symmetrical with respect to the cross-section, so that the equivalent continuum is also transversely isotropic [20]. According to the theory of composite mechanics, there is a stress-strain relationship. First, according to the generalized Hooke's law, the stress-strain relationship of different linear elastomers can be expressed as follows:

$$\begin{bmatrix} \sigma_1 \\ \sigma_2 \\ \sigma_3 \\ \sigma_4 \\ \sigma_5 \end{bmatrix} = \begin{bmatrix} C_{11} & C_{12} & C_{13} & C_{14} & C_{15} \\ C_{21} & C_{22} & C_{23} & C_{24} & C_{25} \\ C_{31} & C_{32} & C_{33} & C_{34} & C_{35} \\ C_{41} & C_{42} & C_{43} & C_{44} & C_{45} \\ C_{51} & C_{52} & C_{53} & C_{54} & C_{55} \end{bmatrix} \begin{bmatrix} \varepsilon_1 \\ \varepsilon_2 \\ \varepsilon_3 \\ \varepsilon_4 \\ \varepsilon_5 \end{bmatrix}. \quad (4)$$

In (4), C_{ij} is the stiffness coefficient, ε_i is the elastic strain coefficient, and σ_i is the stress coefficient. Through the transformation of matrix in (4), five independent stress moduli C_{11} , C_{12} , C_{23} , C_{22} , and C_{44} are obtained. The stress moduli obtained are the macroscopic constants of equivalent continuum model corresponding to cement-

based composite with carbon nanotube [21]. The elastic stiffness coefficient of cement-based composite with carbon nanotube is defined as C_{11} , C_{12} , C_{23} , C_{22} , and C_{44} , the transverse shear modulus is G_{23} , the transverse bulk modulus is K_{23} , the axial shear modulus is G_{13} , and the axial style modulus is E_1 . Then, the stress elastic stiffness coefficient of cement-based composite with carbon nanotube can be expressed as follows:

$$\begin{cases} G_{23} = \frac{C_{22} - C_{23}}{2} \\ G_{13} = C_{44} \\ K_{23} = \frac{C_{22} + C_{23}}{2} \\ E_1 = C_{11} - \frac{2C_{12}^2}{C_{22} + C_{23}} \end{cases} \quad (5)$$

From the previously mentioned description and the theory, it can be seen that the stress-strain relationship of the continuum can be obtained only by determining the elastic constant through the test method.

3.2. Setting of Mechanical Property Test Index. Under the support of the previously mentioned mechanical property theory of cement-based composite with carbon nanotube, the test index of mechanical property is set up. The flexural strength index of cement-based composite with carbon nanotube is calculated as follows:

$$R_f = \frac{3F_{\max} \cdot L}{2b^3}. \quad (6)$$

In (6), the parameter R_f is the flexural strength, F_{\max} represents the load force when the cement-based composite with carbon nanotube specimen breaks, and L and b

represent the side length of the span and the direct contact surface of the experimental specimen, respectively [22]. Similarly, the calculation formula of compressive strength index in mechanical properties can be obtained as follows:

$$R_c = \frac{F_c}{A_y}, \quad (7)$$

where R_c is the compressive strength, F_c is the maximum load force when the specimen is damaged, and A_y is the area of the compression surface. In addition, the calculation formula of splitting tensile strength index is as follows:

$$R_t = \frac{2F_{\max}}{\pi A_p}, \quad (8)$$

where R_t and A_p , respectively, represent the splitting tensile strength and splitting surface area of the test piece [23]. The final mechanical property test index is the bending toughness index of cement-based composite with carbon nanotube. The corresponding fracture energy formula is as follows:

$$G_F = \frac{mg\delta_0 + W_0}{th} = \frac{mg\delta_0 + \int_0^{\delta_0} P(\delta)d\delta}{th}. \quad (9)$$

In (9), G_F is the fracture energy of the prepared specimen, W_0 is the area enclosed under the load deflection curve, m and g represent the mass and acceleration of gravity of the prepared specimen, δ_0 represents the displacement after the final fracture of the cement-based composite with carbon nanotube specimen, $P(\delta)$ represents the load deflection curve, and t and h are the height and thickness of the specimen respectively.

3.3. Mechanical Property Test and Result Analysis. The prepared cement-based composite with carbon nanotube samples are divided into several groups on average and are put into different experimental environments to test different mechanical properties.

3.3.1. Flexural Strength Test. Under the same water cement ratio, the flexural strength of different carbon nanotubes on the carbon nanotubes cement-based composite specimens is tested. The prepared specimens are placed in a horizontal position, the force application equipment is used to apply on both ends of the specimens, respectively, the force application value is recorded, and the surface change of the composite is observed [24]. When 0 N, 50 N, 100 N, and 200 N are applied, the change of composite is shown in Figure 4.

The loading force applied on the cement-based composite with carbon nanotube and the state of the experimental material are integrated. All the data are substituted into (6), and the flexural strength test results are obtained.

The results in Table 5 shows that the flexural strength of cement-based composite with carbon nanotube is 6.9 MPa at 1d, 14.1 MPa and 16.8 MPa at 3d and 28d, and 16.9 MPa at 56d, respectively [25].

3.3.2. Compressive Strength Test. When any of the six compressive strengths exceeds the average value, the average value shall be taken as the compressive strength result after it is eliminated. The compressive strength test process is shown in Figure 5.

Through the recording and calculation of compressive loading data, the experimental results of compressive strength of composite materials are shown in Table 6.

According to Table 6, at the same water-to-cement ratio, the addition of cement-based composite with carbon nanotube does not significantly improve the compressive strength of the cement pack. Under four different water cement ratios, the compressive strength of cement-based composite with carbon nanotube is close to that of blank sample or partially enhances its compressive strength [26]. The average compressive strength of cement-based composite with carbon nanotube is 84.09 MPa.

3.3.3. Test of Crack Resistance Index. Table 7 shows the test results of crack resistance index of cement-based composite with different carbon nanotubes.

In Table 7, l_i and d are the length and thickness of cement-based composite with carbon nanotube specimens, respectively. Finally, the crack resistance index test result of the composite is 22.5.

4. Durability Experiment of Cement-Based Composite with Carbon Nanotube

The durability of cement-based composites with carbon nanotube is the ability of materials to resist the long-term damage caused by both their own and natural environment. That is to ensure its durability. The better the durability is, the longer the service life of the material is. Taking the composite as the research object, the durability experiments of the composite are carried out from two aspects of impermeability and frost resistance.

Permeability refers to the transport and movement process of solution in some media under pressure gradient. For concrete, its permeability generally refers to whether the air, water, and salt ions in the water solution in the external environment are easy to invade into the internal characteristics of concrete and is expressed by permeability coefficient. The durability of cement-based materials has a direct impact on the safety and service time of the building structure, and the impermeability is one of its most important durability. The impermeability of cement-based materials is also related to the durability of other aspects, such as the penetration of water, air, and chloride ions into the reinforced concrete; the penetration of sulphate into the concrete is also due to the penetration of water and chloride ions into the concrete, the freeze-thaw damage, alkali aggregate reaction, and so on, which are closely related to the permeability. If the permeability of cement-based materials is good, all kinds of aggressive ions, water, and air are not easy to enter into the concrete, thus ensuring the durability of the concrete structure. The samples are saturated in saturated solution of Korean chloride for one hour and then soaked for 24 hours. Before the installation of the test piece, the ultrasonic bath shall be conducted for three minutes to ensure that the surface of the test piece is clean, free of oil, dust, and water drops. After fixing

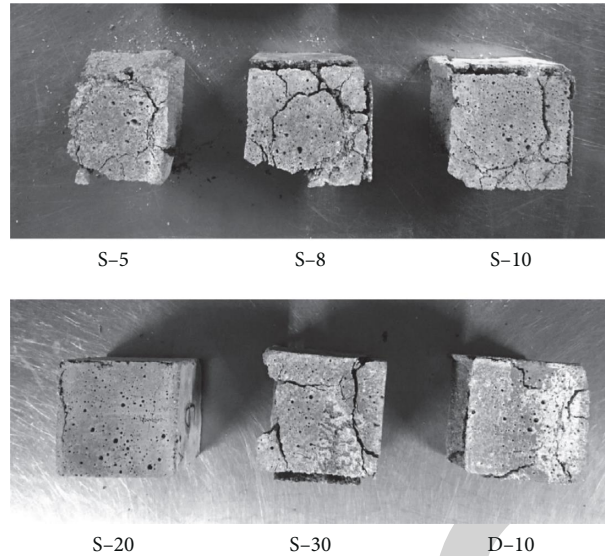


FIGURE 4: Cross-section picture of composite sample after bending test.

TABLE 5: Flexural strength of cement-based composite with carbon nanotube.

Sample	1D	3D	28d	56d
R-0	6.3 MPa	10.2 MPa	13.4 MPa	13.9 MPa
S-5	6.5 MPa	16.1 MPa	18.4 MPa	18.6 MPa
S-8	7.7 MPa	18.6 MPa	21.3 MPa	23.2 MPa
S-10	7.9 MPa	16.9 MPa	20.9 MPa	20.1 MPa
S-20	7.8 MPa	15.3 MPa	17.8 MPa	18.4 MPa
S-30	6.8 MPa	12.6 MPa	15.5 MPa	11.1 MPa
D-10	5.3 MPa	9.5 MPa	10.5 MPa	13.1 MPa

the test piece with a clamp, about 300 ml, 0.3 mol/l NaOH solution (or KOH solution) is injected into the cylinder of the test piece on the anode surface, and about 12 L sodium chloride solution with a mass concentration of 10% is put into the test container on the cathode surface. The test host is connected for power on test. According to the initial temperature, the instrument will automatically determine the test time, and the test data will be automatically recorded and saved. The permeability resistance of the cement-based composite with carbon nanotube is determined by observing the microstructure of the composite. The microstructure observation results of the composite at different soaking stages are shown in Figure 6. It is found that the reuniting of carbon nanotubes takes place, and then, the bridging was also observed. The scanning electron microcopy (SEM) image for sample A3 shows that the bridged tubes have growth/deposition of hydration products on them.

According to the statistics and comparison of relevant data, the chloride diffusion coefficient of cement-based composite with different carbon nanotube content at the age of 28 days is obtained, as shown in Figure 7.

The frost resistance refers to the property that the material resists multiple "freeze-thaw cycles" without fatigue, breakage, or damage. The test shall be conducted according to the relevant requirements of the quick-freezing method in the specification. Four days before the start of the freeze-thaw test, the carbon

nanotube sample shall be taken out of the standard curing box for visual inspection, and then, it shall be immersed in an aqueous solution of $20 \pm 2^\circ\text{C}$, and the water level shall be more than 20 mm above the top surface of the sample outer surface. After four days, the sample is taken out from the water and the surface water is dried, to start the quality test and dynamic elastic modulus test of the sample after the sample label. Each group of samples is put into the sample box, and then, the sample box is put into the sample frame in the freeze-thaw box. During the test, it needs to ensure that the height of the water surface in the box is 5 mm higher than the top surface of the sample. The freeze-thaw solution is added into the freeze-thaw box until the liquid level of the freeze-thaw solution exceeds the liquid level in the box. In the center of the freeze-thaw box, a sample box with a temperature measuring sample is placed, and a temperature measuring sensor is inserted into the freeze-thaw liquid around. After multiple freeze-thaw treatments, the surface changes of cement-based composite with carbon nanotube are shown in Figure 8.

In Figure 8, the images 1–4 show the surface morphology of the test piece as the number of freeze-thaw cycles increases gradually. The pore quantification results of cement-based composite materials with different carbon nanotubes after freeze-thaw cycles are shown in Figure 9.

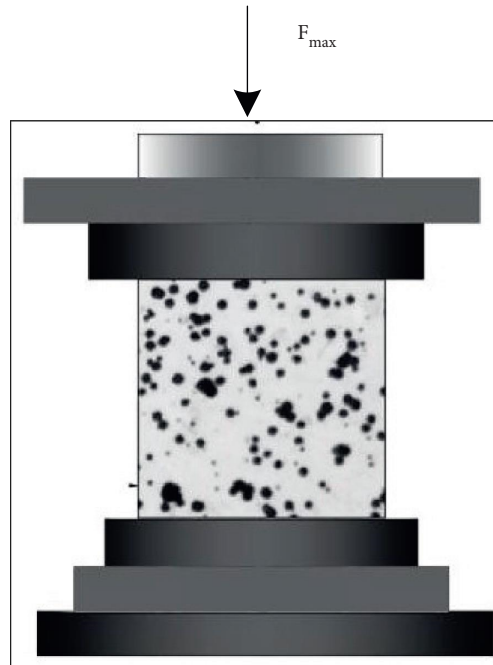


FIGURE 5: Diagram of compression loading.

TABLE 6: Compressive strength of cement-based composite with carbon nanotube.

Sample	Water-to-cement ratio (w/C)	Content of carbon nanotubes	Compressive strength (MPa)		
S-5	0.25	0	77.6	84.8	89.9
S-8	0.25	0.05	76.8	87.4	91.0
S-10	0.25	0.075	76.6	85.8	88.8
S-20	0.25	0.1	77.9	85.2	91.5
S-30	0.25	0.125	78.1	85.1	90.2
S-30	0.25	0.15	79.0	76.2	91.8

TABLE 7: Crack resistance of cement-based composite with carbon nanotube.

Sample	/mm	d (mm)	A_p	$A_p * l_i$ (mm)	R_t
S-5	20	0.40	0.25	5	
S-8	10	0.35	0.25	2.5	
S-10	10	0.27	0.25	2.5	22.5
S-20	30	0.25	0.25	7.5	
S-30	20	0.33	0.25	5	

From Figure 9, it can be seen that the cement-based composite with high content of carbon nanotubes has smaller pores and fewer pores, which proves that the composite with high content of carbon nanotubes has higher frost resistance. Based on the test results of the

frost resistance and permeability resistance of the cement-based composite with carbon nanotubes, it can be concluded that the more the carbon nanotubes are added into the cement-based composite, the better the durability of the corresponding material is.

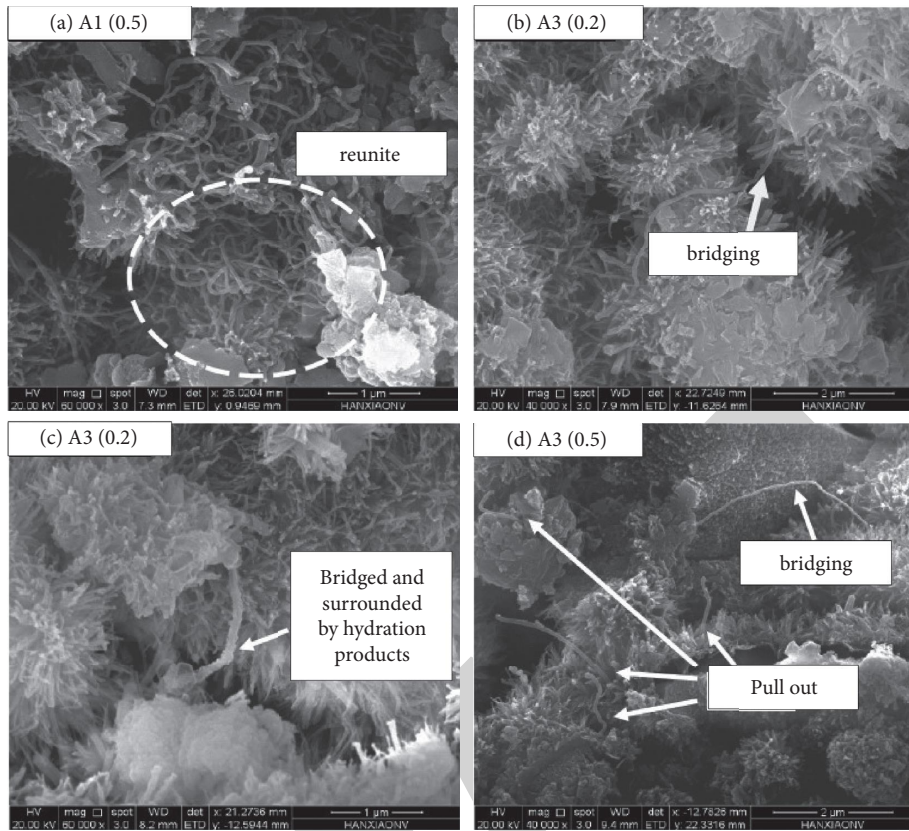


FIGURE 6: SEM of cement-based composite with carbon nanotube.

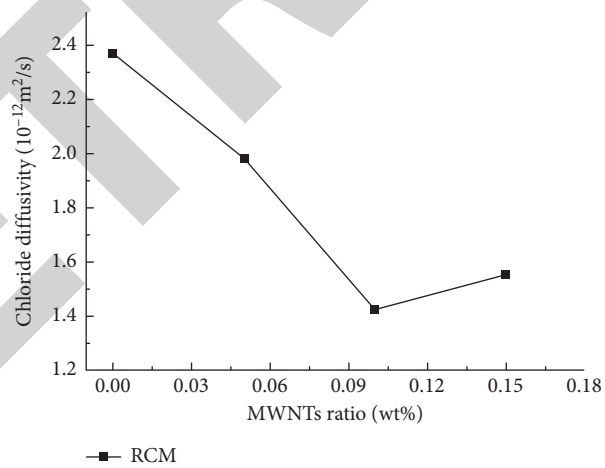


FIGURE 7: Chloride diffusion coefficient of cement-based composite with different carbon nanotubes content.

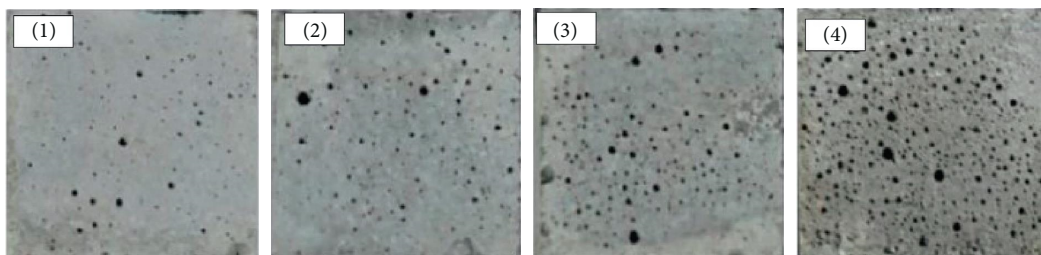


FIGURE 8: Test piece of cement-based composite with carbon nanotube after freeze-thaw cycle.

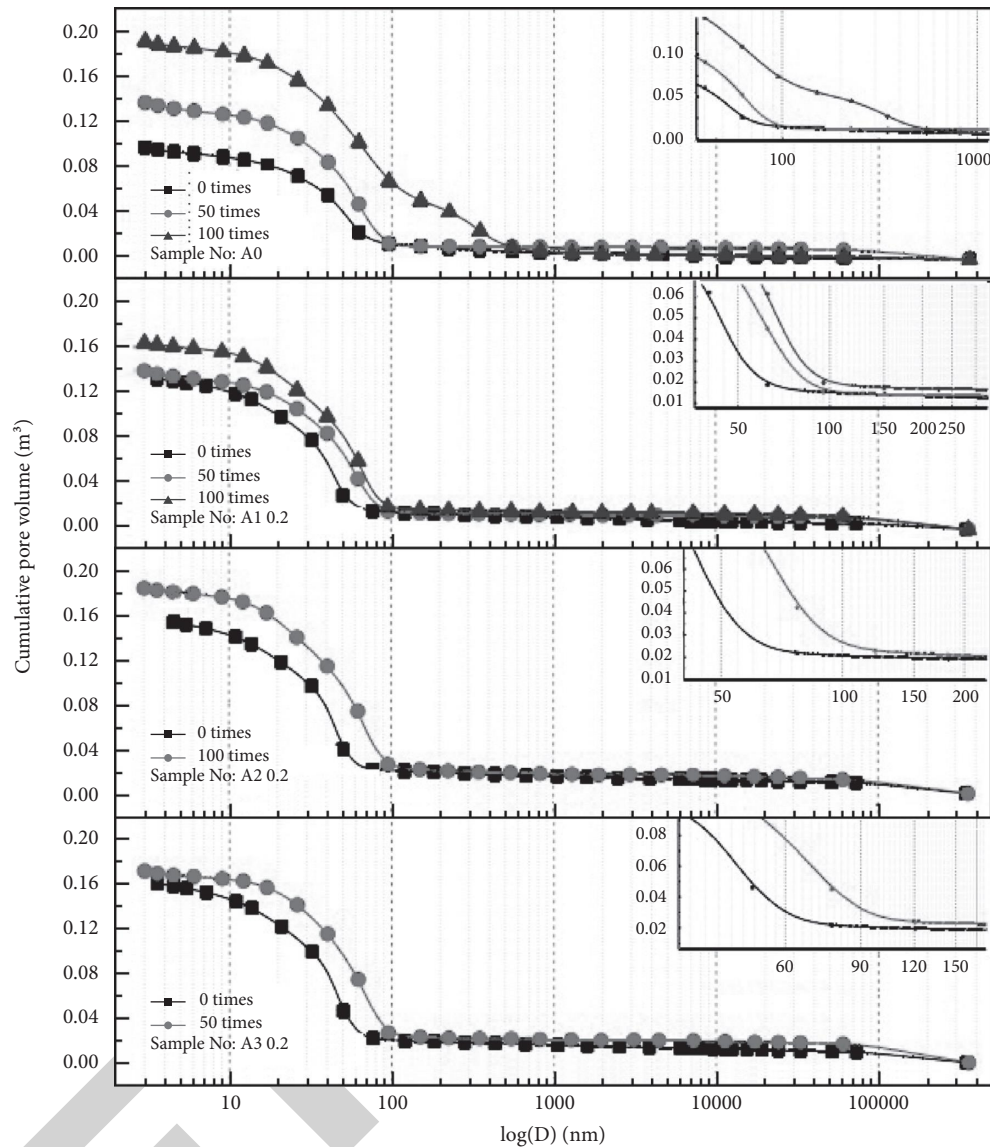


FIGURE 9: Pore volume and pore diameter curve under freeze-thaw cycle.

5. Conclusion

At present, the research of carbon nanotubes has become a global hotspot and has been applied in the fields of field emission, nanoelectronic devices, nanomachinery, composite materials, and so on. With the increasingly mature technology of preparation and synthesis and purification of carbon nanotubes, low-cost mass production of carbon nanotubes has become possible. However, the current high-tech concrete is still brittle, in terms of compressive strength. At present, the high-tech concrete has been very strong, comparable to the metal materials, but the tensile strength is far from the metal materials, so the key to study the high-tech concrete is to toughen, and the emergence of carbon nanotubes provides the possibility to solve this problem. Therefore, it has become an urgent task to explore and study the application of carbon nanotubes in cement concrete. It was found by the present study that the average compressive

strength of cement-based composite with carbon nanotube is 84.09 MPa. Flexural strength of cement-based composite with carbon nanotube is 6.9 MPa at 1d, 14.1 MPa and 16.8 MPa at 3d and 28d, and 16.9 MPa at 56d, respectively. Once the production, preparation, and application of carbon nanotubes make an important breakthrough, it will certainly drive the development of the whole nanotechnology. At the same time, it will also drive the rise of a series of related high-tech industries, lead to a new technological revolution, and bring great benefits to the whole society.

Data Availability

The data used in this article are available upon request.

Conflicts of Interest

The authors declare no conflicts of interest.

Retraction

Retracted: Comparative Analysis of Natural Fibre Reinforced Composite Material Using ANSYS

Advances in Materials Science and Engineering

Received 26 December 2023; Accepted 26 December 2023; Published 29 December 2023

Copyright © 2023 Advances in Materials Science and Engineering. This is an open access article distributed under the Creative Commons Attribution License, which permits unrestricted use, distribution, and reproduction in any medium, provided the original work is properly cited.

This article has been retracted by Hindawi, as publisher, following an investigation undertaken by the publisher [1]. This investigation has uncovered evidence of systematic manipulation of the publication and peer-review process. We cannot, therefore, vouch for the reliability or integrity of this article.

Please note that this notice is intended solely to alert readers that the peer-review process of this article has been compromised.

Wiley and Hindawi regret that the usual quality checks did not identify these issues before publication and have since put additional measures in place to safeguard research integrity.

We wish to credit our Research Integrity and Research Publishing teams and anonymous and named external researchers and research integrity experts for contributing to this investigation.

The corresponding author, as the representative of all authors, has been given the opportunity to register their agreement or disagreement to this retraction. We have kept a record of any response received.

References

- [1] K. G. Saravanan, R. Prabu, A. Sivapragasam, and N. Daniel, "Comparative Analysis of Natural Fibre Reinforced Composite Material Using ANSYS," *Advances in Materials Science and Engineering*, vol. 2021, Article ID 9391237, 17 pages, 2021.

Research Article

Comparative Analysis of Natural Fibre Reinforced Composite Material Using ANSYS

K. G. Saravanan ¹, R. Prabu ², A. Sivapragasam ¹ and Nahom Daniel ³

¹Department of Mechanical Engineering, Sona College of Technology, Salem, Tamil Nadu, India

²Department of Mechanical Engineering, Mahendra Engineering College, Namakkal, Tamil Nadu, India

³Department of Chemical Engineering, College of Biological and Chemical Engineering, Addis Ababa Science and Technology University, Addis Ababa, Ethiopia

Correspondence should be addressed to K. G. Saravanan; kgsmechanical@gmail.com and Nahom Daniel; nahom.daniel@aastu.edu.et

Received 20 July 2021; Revised 31 July 2021; Accepted 17 August 2021; Published 31 August 2021

Academic Editor: Samson Jerold Samuel Chelladurai

Copyright © 2021 K. G. Saravanan et al. This is an open access article distributed under the Creative Commons Attribution License, which permits unrestricted use, distribution, and reproduction in any medium, provided the original work is properly cited.

The regulations of legislative bodies regarding the recycling and reuse of automotive materials has caused a great deal of obligation among automotive manufacturers to use natural fibres or green composites. Green composites or more commonly known as bio-composites are made up of natural fibres. Natural fibres are used by humankind since prehistoric times. The natural fibre is obtained from plants as well as animals. Since the natural fibre is obtained from natural as well as biological resources, it is biodegradable and recyclable. This paper presents the study and analysis conducted to address the suitability of natural fibre in the automotive industry. This paper discusses the finite element analysis of four different natural fibre composites used for making car door panel, i.e., flax, jute, sisal, and leather are taken for the material study. This paper helps to find the effectiveness of each of the four natural fibre composites that have already been used in the automotive sector. This paper includes the analysis of four different natural fibres with and without the addition of the aluminium as the reinforcement material. This project revolves around the design of the composite fibre sheet and analysis of the mechanical parameters such as equivalent stress, shear stress, strain, deformation, and so on. The studies and observations of the analysis showed that the natural fibre with the aluminium reinforcement proved to be much stronger than that without the reinforcement. The results of finite element analysis showcased lowest total deformation and equivalent strain in the flax as 1.026 mm and 0.017 mm/mm, respectively. However, sisal showed the lowest equivalent stress and shear stress which were 68.09 and 38.178 MPa, respectively. Additionally, leather showed the highest amount of stress, strain, and deformation, and hence leather was deemed to have undesirable properties regarding the usage in car door panels. All the materials except leather were found to be safe under the loading conditions. Hence, the flax fibre is recommended by the project to have superior properties compared to the other materials.

1. Introduction

The ever-increasing demand and popularity of the environment-friendly natural resources have caused a major movement in the automotive industry [1]. The usage of natural fibre bio-composite has been increasing in the automotive industry for a long time. The high-strength fibres having high tensile strength such as Kevlar, glass fibre, carbon, and so on are difficult to recycle and are very costly to manufacture. Hence, the environmental impact of synthetic material and the rising prices of the such artificially

developed materials are also the causes of the growing demand of the natural fibre composite materials [2–4]. The industry research found out that the industrial use of natural fibre reinforced polymer composite was nearly 2.1 billion USD in 2010 [5, 6]. This market size is currently on the growing trend and is predicted to grow to 6.50 billion USD in 2021. Around 80000–160000 tons of natural fibres are used every year in the automotive industry across the globe [7]. Natural fibres or green fibres are obtained from plants and animals. They are hence readily available throughout the world. Some of the natural fibres that have been in use are

flax, sisal, coconut, bamboo, coir, jute, feather, leather, wool, etc [8, 9]. Natural fibre polymer composites are made by using natural fibres with various polymer matrices or resins. The polymers or resins can be thermoplastic or thermoset [5, 10]. The thermoplastic matrix becomes softer material when the heat is applied to the surface of the material. Reshaping of thermoplastic resin can be done with the application of heat and pressure. Some of the examples of the thermoplastics are polyethylene, PVC, PP, etc [5, 10]. Thermosets, on the other hand, cannot be moulded and melted into the final shape. They can become soft under the application of heat and have superior mechanical properties compared to the thermoplastics. This is why they are very difficult to be easily recycled and reused [1, 11]. But few of the research studies show that recycling and reusing of thermosets are possible. Thermosets are in low melting solids and liquids for and are difficult to cure. Some of the thermoset polymers include polyester, acrylics, epoxies, phenolic resins, vinyl esters, polyurethanes, etc [10, 12].

Composite materials most commonly have a continuous bulk phase, called a matrix, and one scattered, contiguous phase, which is considered a tougher and stronger refurbishment. Strengthening content may contain fibres, fragments, or flakes. The principle of composites is that in the bulk process, the load is borne on a broad surface and moved to the reinforcement, which, being more solid, increases composite strength [13, 14]. The interface bonding of the natural fibre and the polymer matrix dictates the physical properties of the natural fibre reinforced polymer composites. The interface bonding tests such as single fibre compression, pull out, and compression tests are commonly used to test the bonding effectiveness in the fibre reinforced composites [3].

The effectiveness of the natural fibre composites is dependent upon the number of the fibre strands, shapes, and lengths as well as the fibre orientation and adhesion quality of the matrix [1, 13]. The properties of natural fibres can vary due to some factors such as maturity, size, and processing methods. Fibre reinforced composites have woven and non-woven arrangements where the woven fabric has the characteristics of the interlacing of the yarns which are perpendicularly interlocked fibres. The twist angle of the yarn also plays a role in the fibre cohesion and woven strength. However, the twist angle can be effective up to certain limit after which it is shown to have reduction in the bonding strength of fibre and polymer resins [1, 15]. The natural fibres, when embedded with the resin matrix, can impart high strength, less density, high stiffness, and better damping characteristics onto the NFRP composites [5, 10]. Even though natural fibres have bit lesser strength compared to glass fibres, they are twice as light compared to glass fibres and have similar stiffness, which is a great advantage. The utilization of the natural fibre composites provides 20% of cost reduction and 30% of reduction of the weight of automotive parts [10, 11]. The natural fibre materials are also shown to have better cost-effectiveness and better energy recovery compared to glass and carbon fibres [8].

Though natural fibres offer a lot of advantages, they also have many more shortcomings on their own. The natural

fibres are found to be hydrophilic because of the polarity of hydroxyl groups present in the lignin and cellulose material. Hydrogen bonding of hydroxyl groups helps to retain water in the natural fibres, and this is the reason why the humidity sensitizes the composite materials and can cause swelling of the natural fibres and resins [8, 16]. Also, the plant fibres have bigger oscillations due to the growth of the plant fibres [7]. The binding of the fibre and polymer composites can be difficult to execute because of variations of fibre and matrix chemical structures [5, 17]. From the research, it is determined that the natural fibre modulus can reduce with the increase in its diameter [18, 19]. Hence, the bonding capability of the fibre and resin can be greatly improved by the surface modification processes of fibres such as plasma treatment, chemical treatment, and biological treatment methods [17]. Fahim et al. carried out the tensile behavior study of dried plant and animal fibre composites, and they found out that the rice straw showed the downward trend with the increase in fibre loading volume proportion till 40% of rice straw volume and increased further on fibre loading at 50%. The tensile strength of hybrid fibre (i.e., combination of chicken feather and rice straw) was found to be higher than rice straw and chicken feather at 50% fibre loading. Fibre length can also impact the bonding of matrix and fibre, causing clamping [3].

Natural fibre composites are in growing use in the automotive industry since the 1990s [10, 20]. Since the popularity of natural fibre, Germany has been the leader in using natural fibre composite materials. The first and significant attempt for utilization of natural fibres in the automotive industry was made by German manufacturer Mercedes-Benz. In 1996, Mercedes-Benz made use of epoxy matrix along with jute fibre in the E-class cars. In 1999, they manufactured the inner door panel by utilizing 35% of semirigid elastomer and 65% of blend mixture of hemp, flax, and sisal fibres. Along with Mercedes-Benz, other automobile manufacturers such as BMW, Volkswagen, and Audi have used natural fibre composites for interior and exterior applications [7, 20]. Audi also attracted considerable attention after they manufactured the door trim panels of A2 midrange car by using a mixture of flax/sisal along with the polyurethane matrix. Volvo used soya bean foam linings for the seats in V70 and C70 models. They also employed the cellulose-based floor tray for noise reduction purpose. In the United Kingdom, Ford Mondeo utilized the kenaf fibre and propylene polymer for its door panel which has reduced the mass of the door by 5–10% [7, 21]. In the recent times, various automotive manufacturers have started to adopt NFRPC in the interior and exterior parts of the vehicle such as door panels, trunk liners, seat backs, spare tyre lining, boot lining, door trim panels, windshield, back cushions, spare wheel compartment cover, and so on [20, 22–24].

2. Material Selection

As stated earlier, several natural fibres are used by automotive industries since the 90s. The prospect of the usage of NFPC in the automotive sector is great and hopeful. Modern auto manufacturers have employed the natural fibre

composites for the car panels, seats, floors, etc. Hence, this project is also involved in finding out appropriate natural fibre materials for the door panels. Materials such as flax, jute, sisal, and leather are selected for review and analysis. Along with them, the bonding agent epoxy resin and another reinforcement metal Al-3003 are also discussed in this paper. The description of the aforementioned materials is presented below.

2.1. Flax. Flax is a member of the genus *Lignum* of the limacine family and also known as common flax or linseed. This is a grain and fibre crop grown in colder areas of the country. The term “flax” refers to the spun fibres of the flax plant in addition to referring to the plant itself. Flax is cultivated for its seeds which can be ground into a meal or converted into linseed oil, a component found in many wood-finishing products as a dietary substitute and as an ingredient. Flax has already been used as a replacement to glass fibres and carbon fibre materials in the automotive industry. A conference paper published by Christiano et al. presented a study of ECOSHELL frame in which the manufacturing processes and mechanical properties of the various flax reinforcement structures were presented. Flax reinforcements, namely, non-woven mat, balanced fabric or woven fabric, and unidirectional fabric, were bonded with the epoxy resin and their mechanical properties were tested. The tests showed that the unidirectional fabric yielded the highest ultimate tensile strength and woven fabric induced a higher rate of shear stress with the corresponding increase in the shear strain. However, the woven fabric absorbed the highest energy during the drop weight impact test [6, 10]. Before rinsing and drying in the field, flax is replenished with dew or cold/warm water. Flax dressing is used to take the fibres out of the head, consisting of kicking, shaking, and pounding. Before making a bonding of flax fibre with the resin matrix, the fibres are dried properly. Flax fibres are very susceptible to the water and moisture absorption and will lead to poor adhesion between the resin and fibres [10]. Flax fibres have variation in their properties depending on the treatment methods and extraction procedures. In this project, we have taken a normal dried out flax fibre. The properties of the natural fibres are presented in the Table 1 [25, 26].

2.2. Jute. Jute is a thick, gentle, and brilliant fibre that can stretch into coarse, strong threads. It is derived from the *Corchorus* family, which belonged to the *Tiliaceae* families. “Jute” is the name of the plant or of the fabric used in producing burlap, hessian, or gunny cloth. Jute plant is harvested in the subtropical climate regions such as Bangladesh, Nepal, India, Brazil, China, Thailand, and so on. The production of jute fibres has been steadily increasing and the production has increased from 1 million ton per year in 1900 to 3292 million tonnes in 2004.

Jute is one of the most widely available and cheaper natural fibers with variety of applications produced in cotton. The primary constituents of the jute fibres are cellulose as well as the lignin plant materials. They have

TABLE 1: Properties of flax fibre.

Properties	Values
Density (kg/m ³)	1400
Young's modulus (MPa)	60000
Poisson's ratio	0.41
Tensile strength (MPa)	343
Elongation at break (%)	2.1

irregular cross sections, and they have varying diameters ranging from 0.01 mm to 0.04 mm.

A design conducted by Cristiano et al. on the jute fibre composites determined that the vibration observed in the wet jute fibre was lesser than that of the treated jute fibres. However, the dried jute fibres were more susceptible to moisture due to the removal of the protective layer of wax and oils. The treatment in the jute fibres prompted the increase of the stiffness and reduction of strain in the composites [10]. Some of the properties of the jute fibres are listed in Table 2 [27, 28].

2.3. Sisal. Sisal is a plant species of *Agave* which is prevalently harvested in Southern Mexico but nowadays cultivated and naturalized in various countries. It is also known as *Agave sisalana*. It generates a steep fibre used in the manufacture of various goods.

The lightweight sisal fabric is hand- or machine-scraped from the fibres. The fibres are drained and the remaining dirt is removed by the brushes, which renders them clean. Sisal produces durable and sturdy fabrics, which are highly moist and heat resistant. Natural fibres are viewed in their properties and compared to their properties. Regarding natural fibres, one must be mindful that due to natural conditions, there are wide differences in properties. Sisal cultivation can be done in short times, and it is having high tensile strength, tenacity, abrasion resistance, acid, saltwater, and alkali resistance. Which makes it very suitable in automotive applications [1]. Sisal fibres are used in the window panels and seats of the vehicle. The properties of the sisal fibre are shown in Table 3 [29, 30].

2.4. Leather. Leather is a fibre material which is obtained from animal skin. A variety of skins including the skin of birds, cattle, and wild animals are used for manufacturing leather. The animal skin is first subjected to a salt bath which decreases the bacterial growth. Then, the skin is subjected to a water bath. After that, the leather is subjected to the tanning process. After several processes, the leather is dyed and the final product is obtained. Leather and animal skins were used for preservation purpose, and it has been used for clothes, boots, handbags, furniture, and tools. Leather has a variety of mechanical properties depending upon the nature of skin and choice in the manufacturing processes. Additionally, properties of leather also vary accordingly to the water content and temperature. The striking feature of the leather is that it can withstand repeated flexure with sustaining failure [16]. The properties of leather are shown in Table 4.

TABLE 2: Properties of jute fibre.

Properties	Values
Density (kg/m ³)	1400
Young's modulus (MPa)	25000
Poisson's ratio	0.361
Tensile strength (MPa)	200
Elongation at break (%)	1.16

TABLE 3: Properties of the sisal fibre.

Properties	Values
Density (kg/m ³)	1330
Young's modulus (MPa)	38000
Poisson's ratio	0.4
Tensile strength (MPa)	468
Elongation at break (%)	1.9

TABLE 4: Properties of leather.

Properties	Values
Density (kg/m ³)	860
Young's modulus (MPa)	220
Poisson's ratio	0.4

2.5. Epoxy Resin. Epoxy resins are thermosetting resins that are converted into hard cured material under the application of curing methods. They are normally in the liquid form or soft solid. After curing, they remain solid even under the application of heat and degrade only after a certain temperature limit is reached. There are pure epoxy resins, vinyl-ester resins, and thermoset polyester resins [10]. In this project, pure epoxy resins are used in the fibre composite sheet for bonding the fibres. There are two ingredients in the pure epoxy resins: a resin and a hardener having equal or proportionate ratio. They are normally used in the structural applications such as in building and constructive applications. They are also used in manufacturing adhesives, paints, coatings, fabrics, floors, and other items. The properties of epoxy resin are shown in Table 5.

2.6. Aluminium-3003 (Al-3003). Aluminium-3003 is a type of non-heat-treatable alloy which can be obtained in the forms of flat-rolled coil, plate, and sheet. This alloy is the most widely used aluminium alloy and has excellent mechanical properties. Al-3003 has excellent corrosion resistance but cannot be hardened by the heat-treatment process. It can be slightly hardened by cold working and soft annealing processes [31]. It has fairly moderate tensile strength and has high ductility. This aluminium alloy is used as pipes in the automotive industry. Since these alloys are available in sheets, this project has contemplated the proposition of using Al-3003 in conjunction with the aforementioned natural fibres. The properties of aluminium-3003 are shown in Table 6.

TABLE 5: Properties of epoxy resin.

Properties	Values
Density (kg/m ³)	1280
Young's modulus (MPa)	35000
Poisson's ratio	0.35

TABLE 6: Properties of aluminium-3003 (adapted from [32]).

Properties	Values
Density (kg/m ³)	2730
Young's modulus (MPa)	73000
Poisson's ratio	0.33
Thermal conductivity (W/mK)	190
Tensile strength (MPa)	130
Elongation at break (%)	10
Fatigue strength (MPa)	55

3. Research Consideration

The procedure employed for the selection of the most efficient natural fibre involves few of the assumptions. The natural fibres which are to be analysed are supposed to be dried out and unwoven. The leather is considered to be tanned and is considered to be obtained from cattle. The project is not concerned about the examination of moisture effect on the natural fibres. The project considers the equal use of epoxy resin and hardener for bonding purpose. Along with the aforementioned considerations, the fibre composites are analysed upon following assumptions.

- (1) Porosity is absent in the fibres.
- (2) The fibres are considered to be isotropic and uniform.
- (3) The fibres have uniform properties along their length.
- (4) The bonding between the resin and fibres is supposed to be perfect without the presence of air bubbles and slippage.
- (5) Fibre alignment is considered to be perfect and without non-uniformity.
- (6) Voids and gaps in the composite material are absent.

4. Modelling

The modelling procedure is started by considering the dimensions of the natural fibre sheet that will be used for further analysis. The composite material which will be used for the further analysis is designed as a 10 mm thick sheet having bonding between the epoxy resin and natural fibres. The composite sheet is the constituent of the door panel of the car in which several of these sheets are supposed to be joined to achieve required dimensions of the door panel. There are supposed to be 6 fibre strands in the 10 mm thick panel sheet in which there is a 2 mm thick layer of the epoxy between the natural fibre strands. Hence, the epoxy resin is sandwiched between the alternative layers of the natural

fibres. The natural fibre sheet is supposed to be made from 300 mm long fibre strands having 0.33 mm of diameter. The width of the sheet is designed to be 50 mm where 2 mm of the epoxy resin is sandwiched alternatively. There are two models to be designed for further analysis. The first model will be designed from natural fibre and matrix resin in the alternative fashion, whereas the second model is assumed to have aluminium reinforcement in the middle portion of the composite sheet. It will have fibres and resin matrix alternately, but aluminium is supposed to be placed centrally. After considering every dimension of the natural fibre sheet panel, the design is carried out using SolidWorks software. The 2D and 3D models of the design are presented in Figures 1 and 2.

4.1. *Model 1 (Fully Natural Fibre)*. Composite fibre with fully natural fibre and resin is shown in Figure 1.

4.2. *Model 2 (Natural Fibre with Al-3003)*. The features used for 3D modelling are Solidworks extrude and cut extrude options. The 3D models and 2D models are shown in Figures 3 and 4.

5. Analysis

The analysis of the composite fibre model is conducted using ANSYS. The analysis of the natural fibre is divided into two sections: natural fibre with epoxy composite and natural fibre with aluminium reinforcement. The analysis is done for the forced load condition where the composite sheet is subjected to 2500 N load. The results obtained by the analysis of the various natural fibres will help to find out the most suitable material for the window panel of the car. The procedure for the analysis is described below.

5.1. *Engineering Data*. For performing the analysis on the natural fibre composite sheet, the engineering data regarding the materials and their properties must be known. In this project, all the data regarding the analysis of the composite sheet are noted as mentioned before. After inputting the engineering data, meshing is carried out.

5.2. *Meshing*. The meshing of the composite sheet model is to discretize the model into small elements. After the design is completed using SolidWorks software, the model is imported to ANSYS. The meshing nodes and elements are edited to make the entire analysis process as accurate as possible. This composite model has 4080 elements and 30575 nodes. The mesh of the composite fibre is shown in Figure 5, and the details of mesh are shown in Figure 6.

5.3. *Boundary Value Conditions*. Horizontal load of 2500 N is applied to the top middle section of the fibre composite sheet. Fixed support is applied at the left end of the composite sheet. Same load condition is applied for model 2 as well. After setting up the boundary conditions, the data are processed and the results are obtained in terms of elastic or

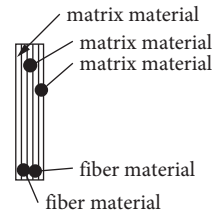


FIGURE 1: Composite fibre with fully natural fibre and resin.

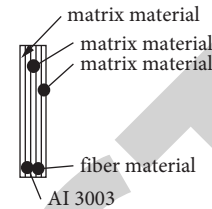


FIGURE 2: Composite fibre with aluminium reinforcement.

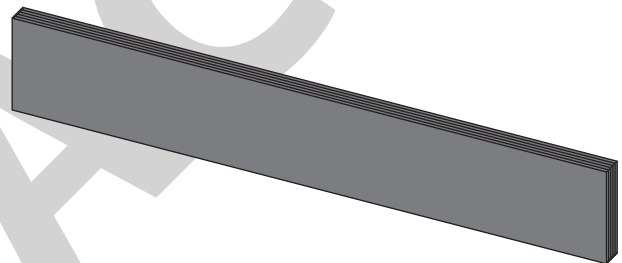


FIGURE 3: 3D model of the composite fibre sheet.

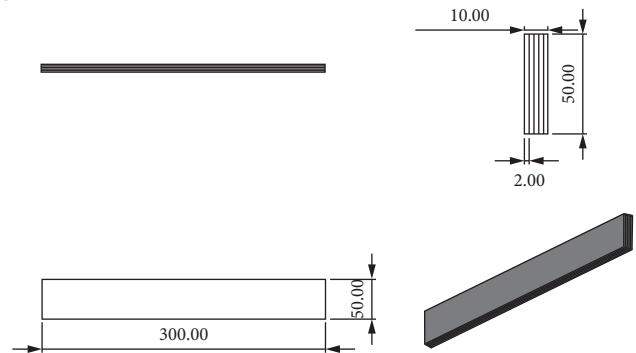


FIGURE 4: Detailed view of the composite fibre sheet.

equivalent strain, deformation, equivalent stress, and shear stress. The boundary condition of the analysis for the forced load condition is shown in Figure 7.

6. Results

The boundary conditions are followed by the results in the form of different parameters. The engineering data used for the analysis of the project are mentioned in the previous sections. The variables are obtained in the form of results which are deformation, stress, and strain, respectively. The analysis for model 1 will predict the behavior of every selected natural fibre under the application of impact force.

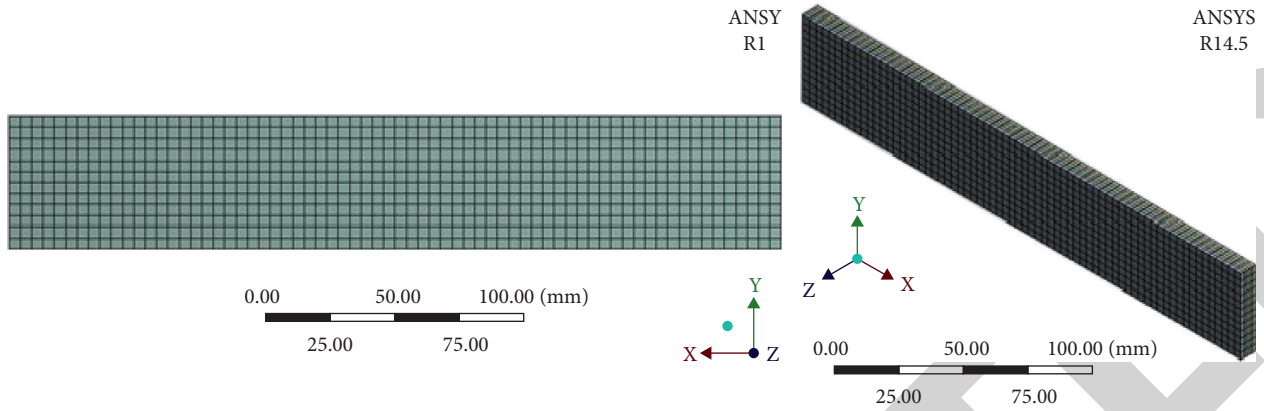


FIGURE 5: Mesh of the composite sheet.

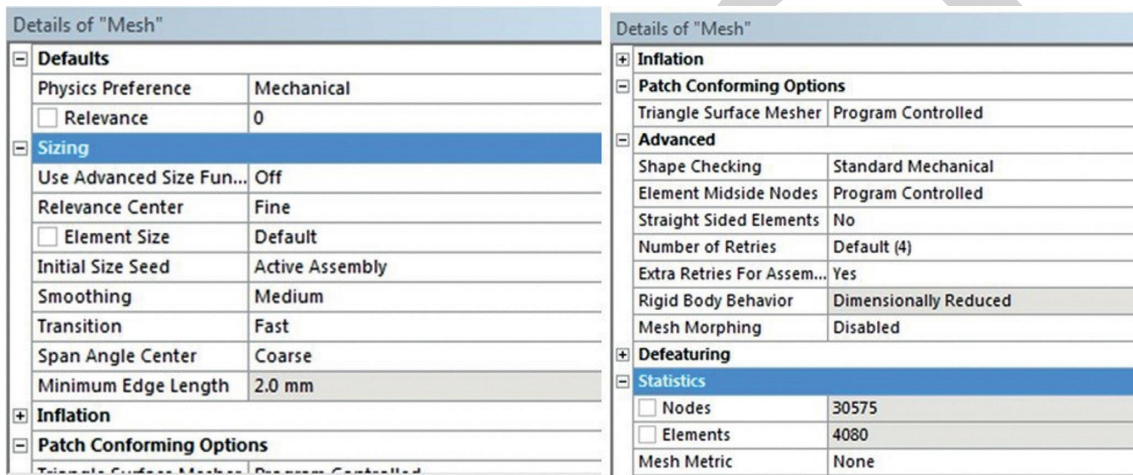


FIGURE 6: Details of the mesh.

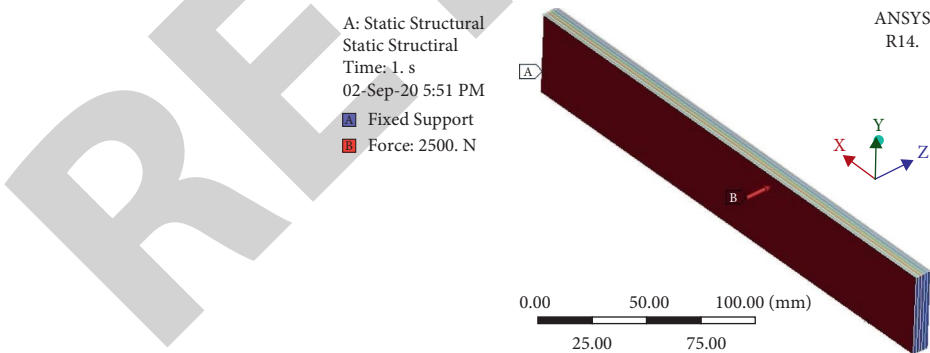


FIGURE 7: Boundary condition for forced load.

The analysis of model 2 will help to determine the behavior of aluminium and natural fibre due to the application of force.

6.1. Model 1 (Fully Natural Fibre). The findings from ANSYS for model 1 are presented in Figures 8–23.

6.2. Model 2 (Natural Fibre with Al-3003). The findings from ANSYS for model 2 are presented in Figures 24–39.

The analysis made on flax, jute, sisal, and leather is shown in the images above. All the parameters, namely, total deformation, equivalent stress, equivalent strain, and shear stress, are identified for every material. The pattern of variable results is identical for model 1 and model 2.

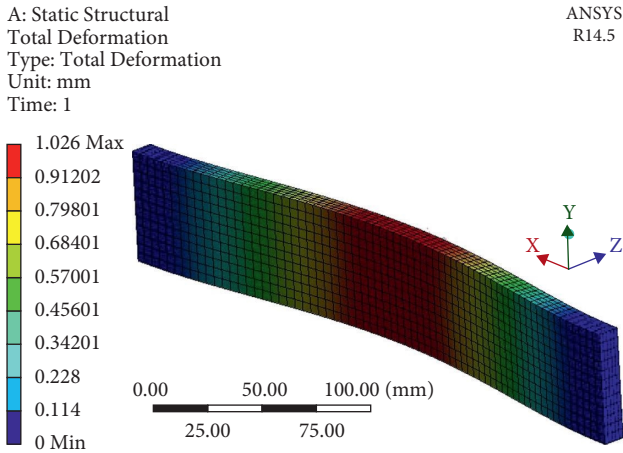


FIGURE 8: Total deformation—flax (model 1).

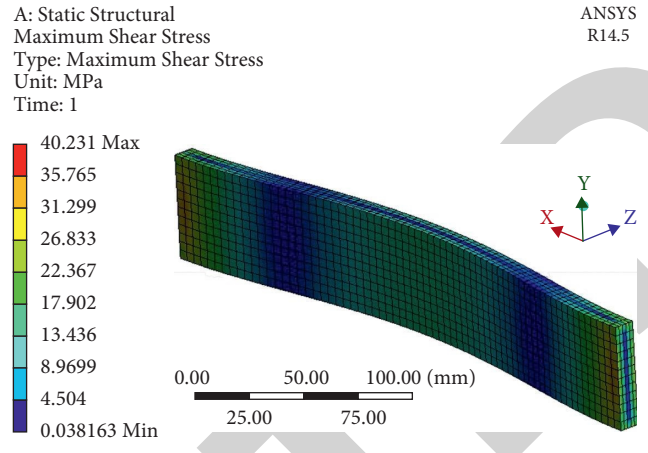


FIGURE 11: Max shear stress—flax (model 1).

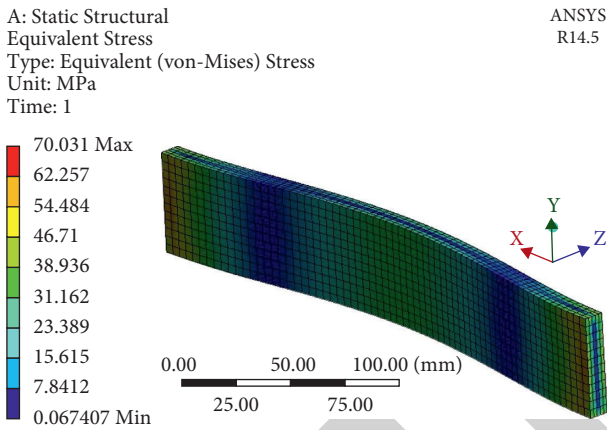


FIGURE 9: Equivalent stress—flax (model 1).

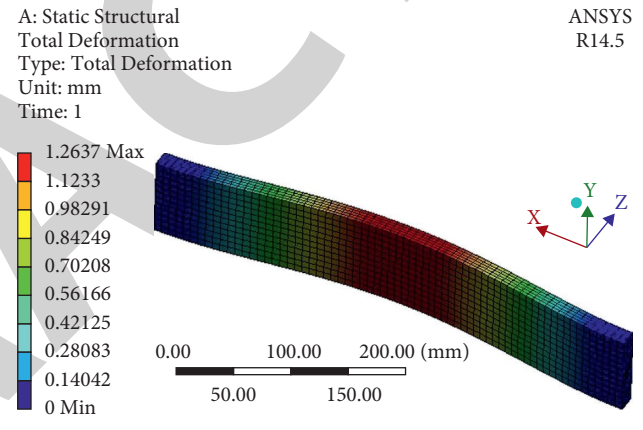


FIGURE 12: Total deformation—jute (model 1).

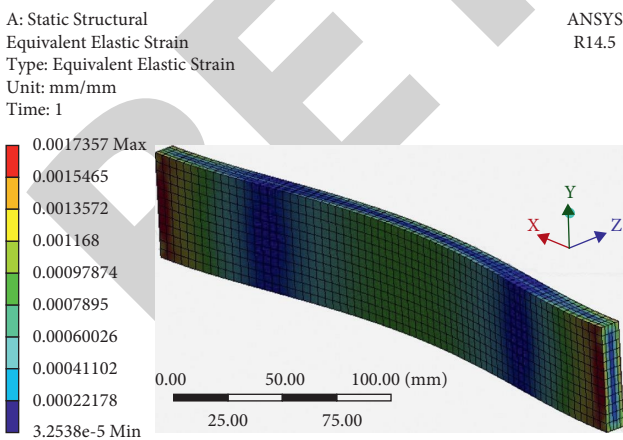


FIGURE 10: Equivalent strain—flax (model 1).

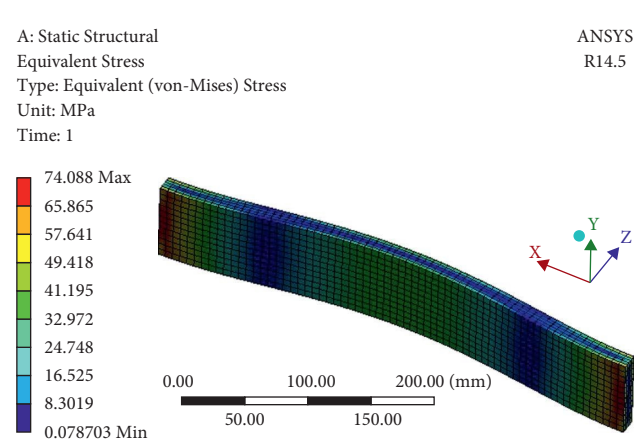


FIGURE 13: Equivalent stress—jute (model 1).

However, the values for both models vary due to difference in additional reinforcement. Having aluminium-3003 as the central reinforcement has helped to reduce the deformation, stress, and strain, respectively. Using aluminium as the central reinforcement was more effective compared to the

fully natural fibre reinforcement. The deformation of the composite sheet shows the highest displacement of the material in the middle section and decreases gradually towards the ends of the sheet. Equivalent stress, however, is higher at the ends and middle portion of the sheet. Also, the

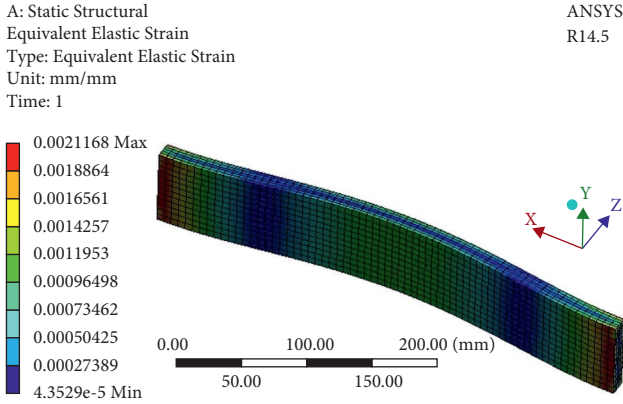


FIGURE 14: Equivalent strain—jute (model 1).

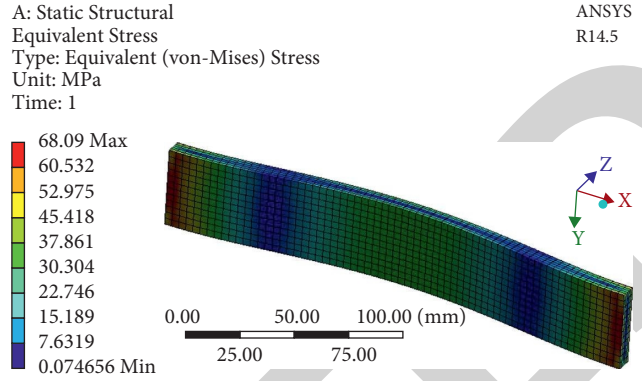


FIGURE 17: Equivalent stress—sisal (model 1).

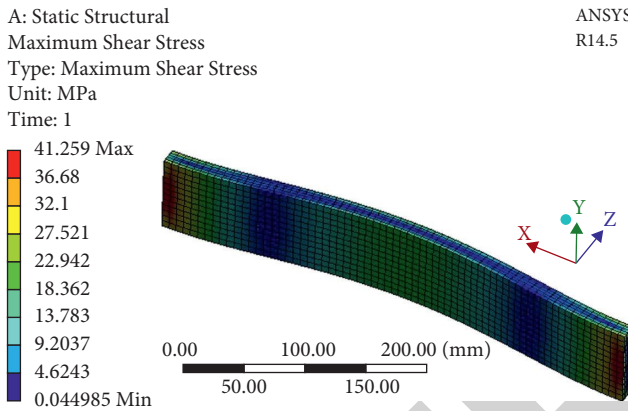


FIGURE 15: Max shear stress—jute (model 1).

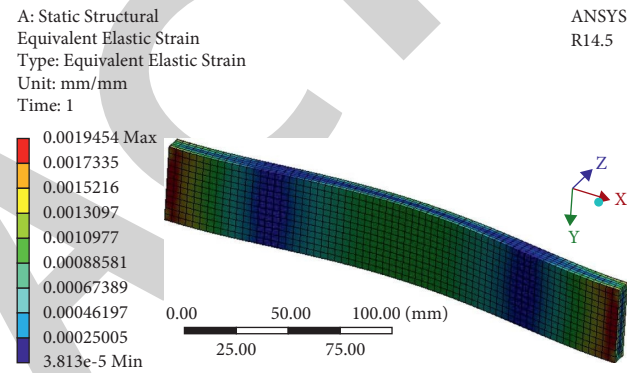


FIGURE 18: Equivalent strain—sisal (model 1).

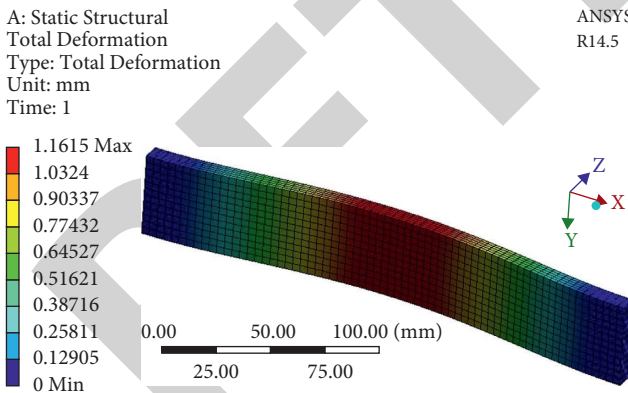


FIGURE 16: Total deformation—sisal (model 1).

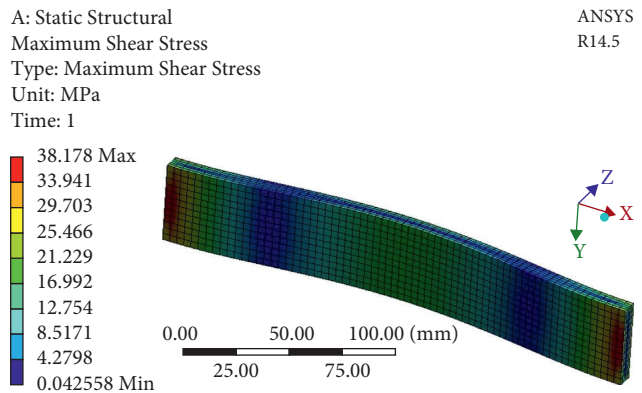


FIGURE 19: Max shear stress—sisal (model 1).

equivalent strain follows the same pattern as the equivalent stress. Max shear stress is observed in the middle and at the ends. From the results, it is evident that the leather showed the highest value for deformation, strain, and stresses. Flax and sisal had moderate to low values of deformation, strain, and stress, which is desirable in the construction of window panel.

The cumulative vector number of the displaced physical structures refers to the total deformation resulting from

ANSYS. The elastic strain is the ratio of material distortion to the original shape. Shear stress is the stress caused by equal and opposite tangential forces within the material section. The von Mises equivalent stress is applied to find out if the ductile material having isotropic nature will yield when it is loaded. The results of variables for model 1 and model 2 are presented in Tables 7 and 8.

Figures 40 and 41 show the graphical representation of the results for model 1 and model 2.

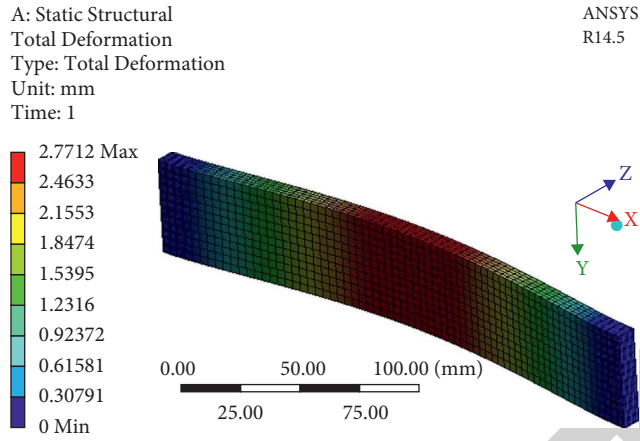


FIGURE 20: Total deformation—leather (model 1).

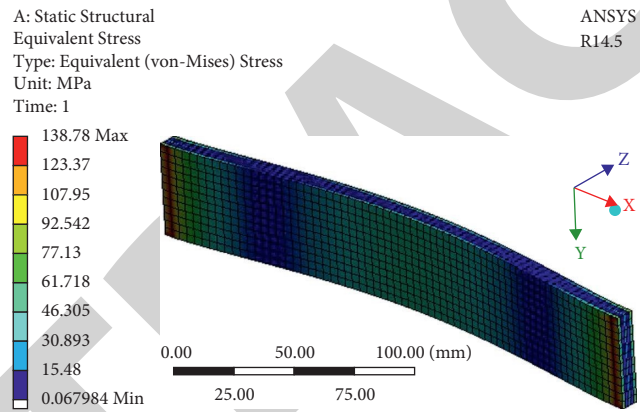


FIGURE 21: Equivalent stress—leather (model 1).

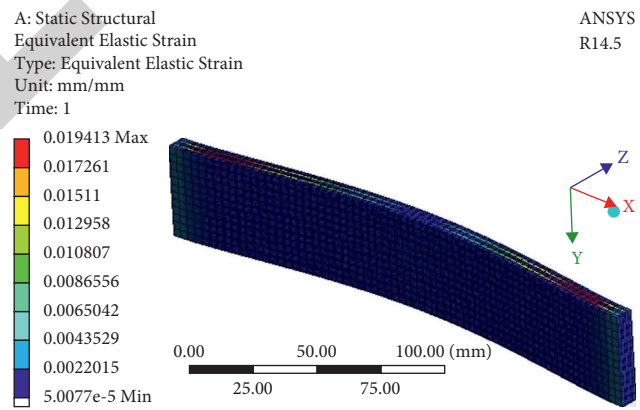


FIGURE 22: Equivalent strain—leather (model 1).

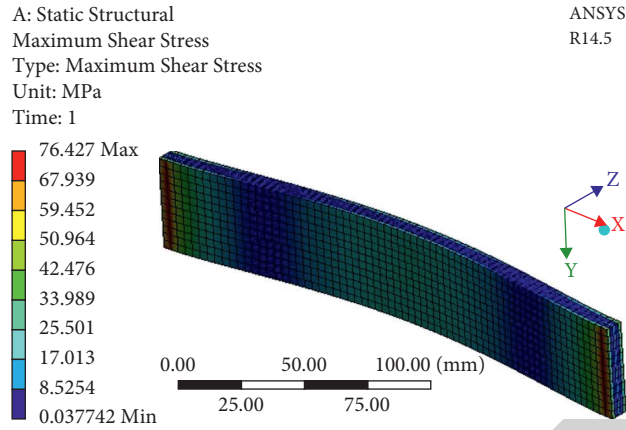


FIGURE 23: Max shear stress—leather (model 1).

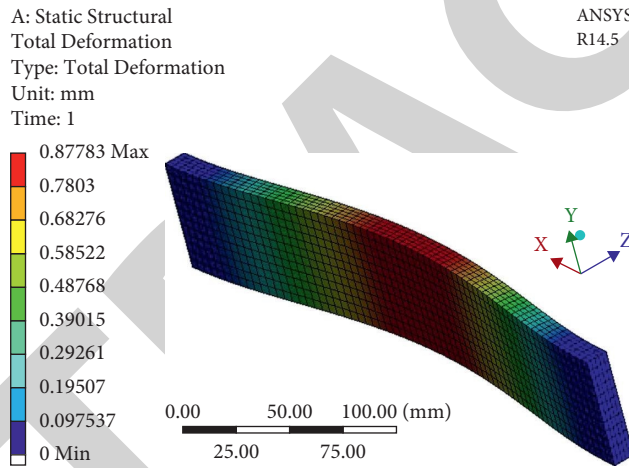


FIGURE 24: Total deformation—flax (model 2).

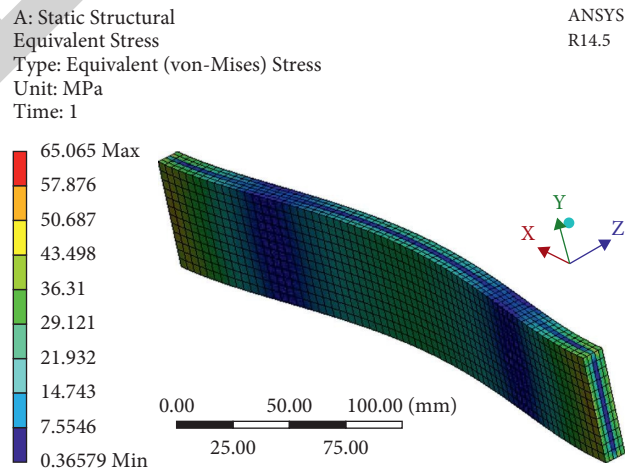


FIGURE 25: Equivalent stress—flax (model 2).

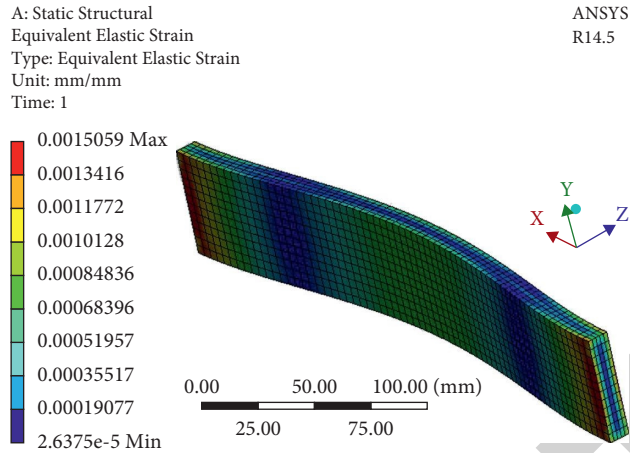


FIGURE 26: Equivalent strain—flax (model 2).

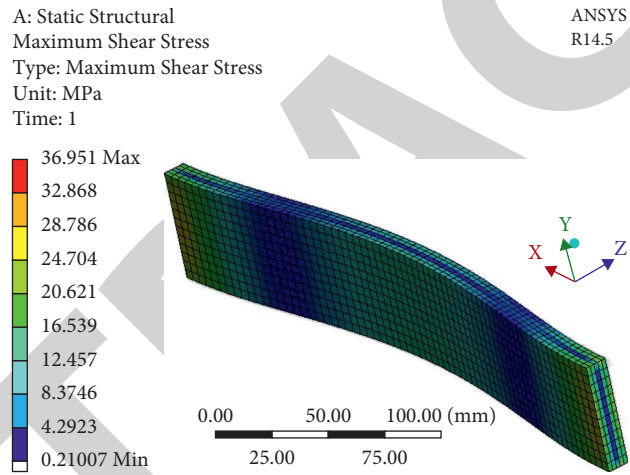


FIGURE 27: Max shear stress—flax (model 2).

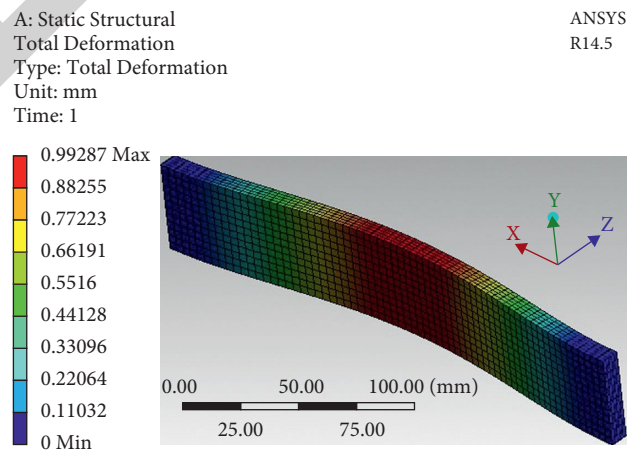


FIGURE 28: Total deformation—jute (model 2).

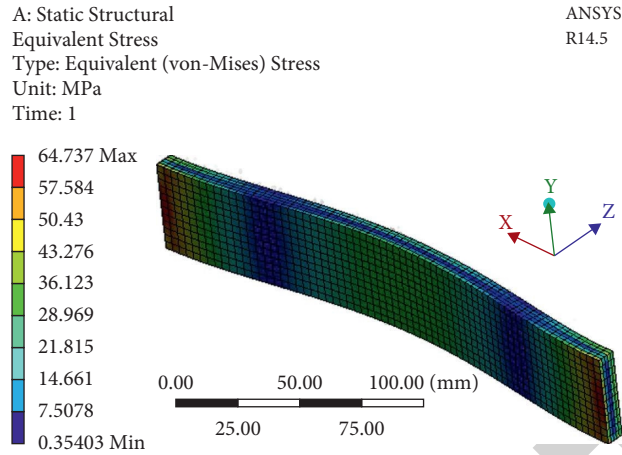


FIGURE 29: Equivalent stress—jute (model 2).

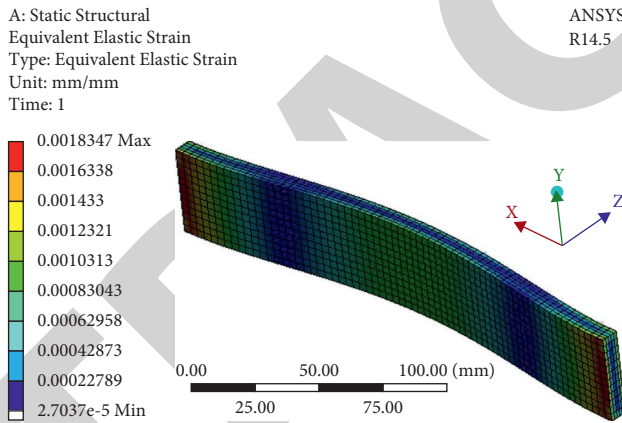


FIGURE 30: Equivalent strain—jute (model 2).

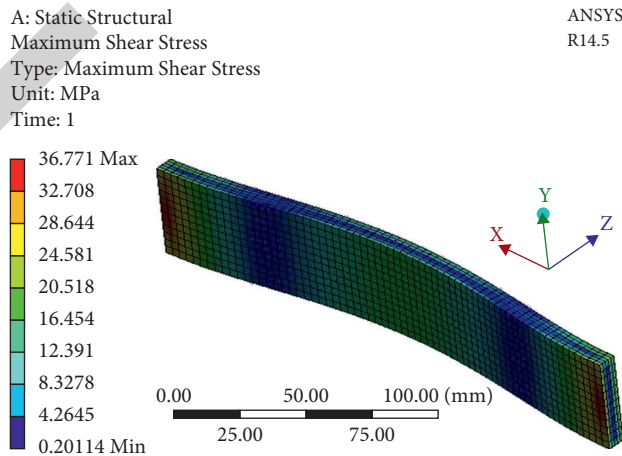


FIGURE 31: Max shear stress—jute (model 2).

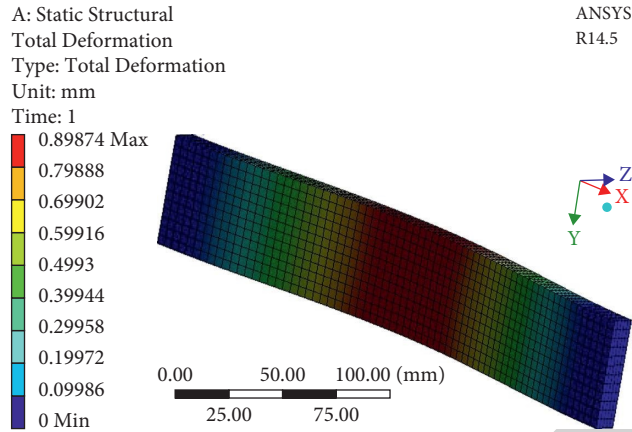


FIGURE 32: Total deformation—sisal (model 2).

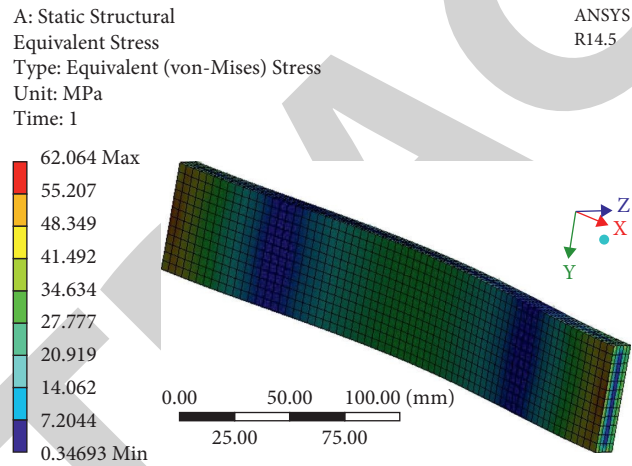


FIGURE 33: Equivalent stress—sisal (model 2).

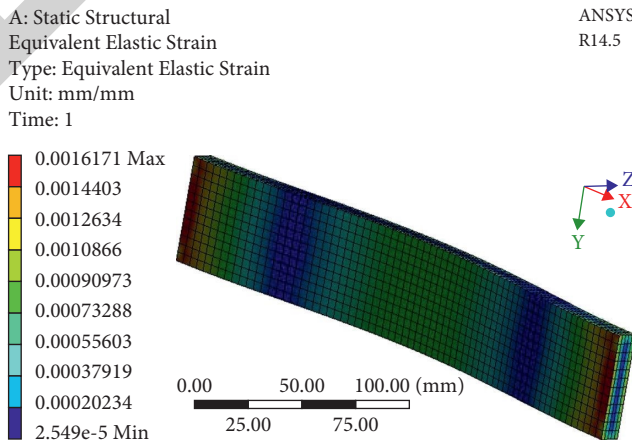


FIGURE 34: Equivalent strain—sisal (model 2).

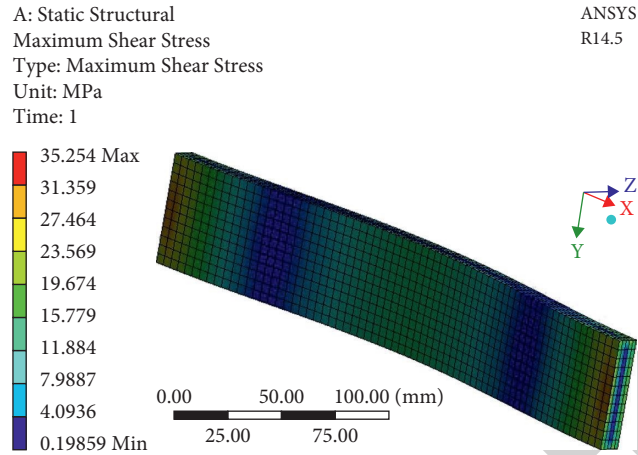


FIGURE 35: Max shear stress—sisal (model 2).

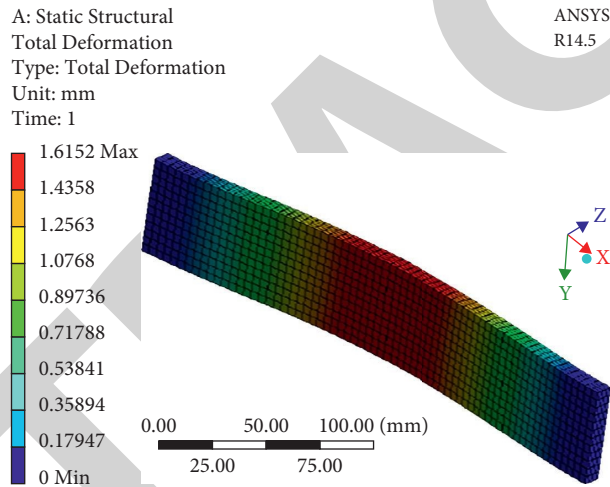


FIGURE 36: Total deformation—leather (model 2).

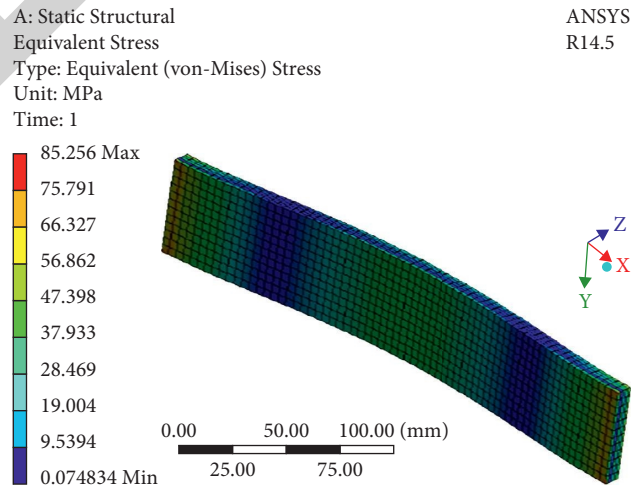


FIGURE 37: Equivalent stress—leather (model 2).

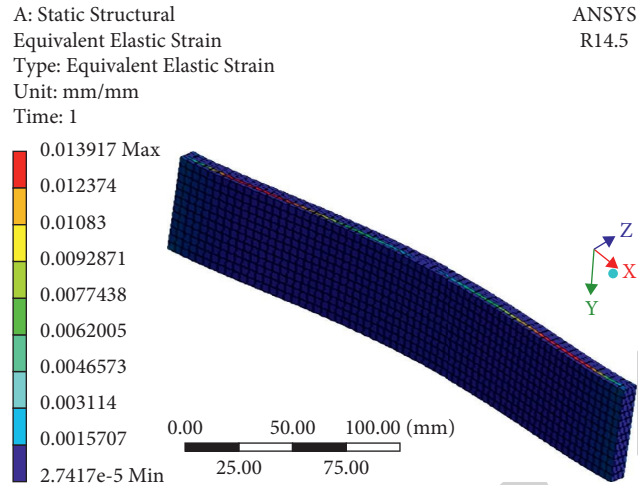


FIGURE 38: Equivalent strain—leather (model 2).

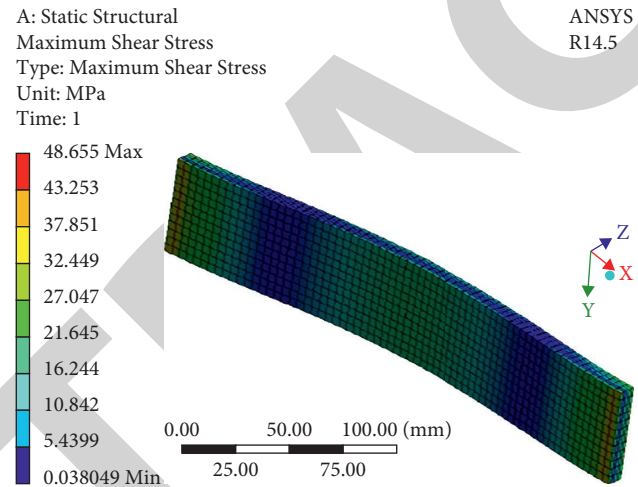


FIGURE 39: Max shear stress—leather (model 2).

TABLE 7: Model 1.

No.	Material	Total deformation (mm)	Equivalent elastic strain (mm/mm)	Equivalent stress (MPa)	Shear stress (MPa)
1	Flax	1.026	0.001735	70.03	40.231
2	Jute	1.2637	0.002116	74.088	41.259
3	Sisal	1.1615	0.001945	68.09	38.178
4	Leather	2.7712	0.01941	138.78	76.427

TABLE 8: Model 2.

No.	Material	Total deformation (mm)	Equivalent elastic strain (mm/mm)	Equivalent stress (MPa)	Shear stress (MPa)
1	Flax	0.87783	0.00150	65.065	36.951
2	Jute	0.99287	0.0018347	64.747	36.771
3	Sisal	0.89874	0.0016171	62.064	35.254
4	Leather	1.6152	0.01391	85.256	48.655

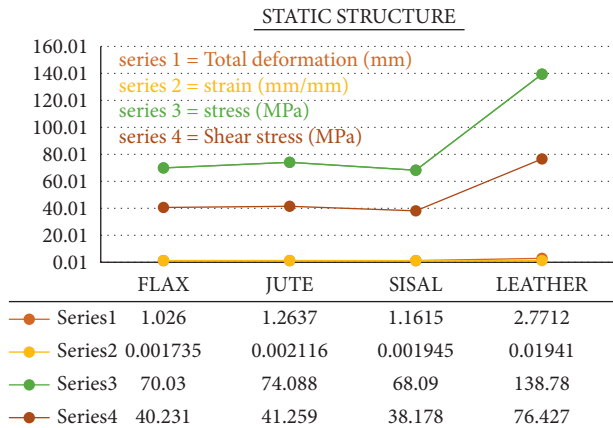


FIGURE 40: Graphical representation of model 1 results.

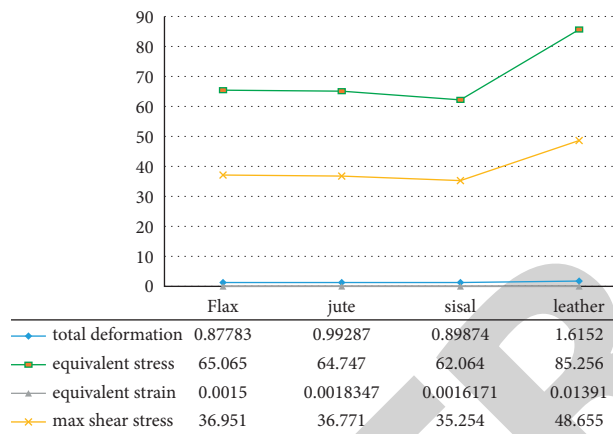


FIGURE 41: Graphical representation of model 2 results.

7. Conclusion

The results from the analysis are obtained in terms of deformation, tension, and strain for the composite beam. The tests are compared, and the most suitable fibre with the best overall characteristics is found. The ANSYS results show that flax and sisal have better mechanical properties compared to jute and leather. Leather is deemed to be unsuitable for door panels because of its high deformation and induced stresses. Based on the characteristics of deformation, flax is the best material, but sisal, on the other hand, has the lowest stresses. Hence, flax can be used for the production of door panels of the automobile.

This project is successful in the execution of design and analysis of natural fibres. The material study and analysis dictate the suitability of natural fibres in the automotive sector. The analysis results show that natural fibres can be used as an alternative to other high-strength synthetic fibre materials. The natural fibres are found to be safe and suitable for use in the automotive industry.

The natural fibre composite industry is a promising field whose continuous growth is inevitable. With the regulations made by the EU for the emission and recycling of waste, the natural fibre used in the automotive industry is picking up

the pace. With the growing concerns over the environmental protection and sustainable development, natural fibres are promising resources which can be utilized in a variety of industries to promote environmental awareness.

There is a significant lack of research on the field of natural fibre composite materials. Properties of various types of natural fibre having different types of alignments are difficult to predict, and hence research studies are needed to find out the behavior of various natural fibres. There is a need to accurately address the moisture and porosity present in natural fibres. Research studies can be carried out to determine the effect of moisture on natural fibre materials [33–35].

Data Availability

The data used to support the findings of this study are included within the article.

Conflicts of Interest

The authors declare that they have no conflicts of interest.

References

- [1] P. Pecas, V. H. Carvalho, H. Salman, and M. Leite, "Natural fibre composites and their applications: a review," *Journal of Composites Science*, vol. 2, 2018.
- [2] W. Sutopo, M. Fauzan, and Y. Yuniaristanto, "A comparative analysis of natural fiber reinforced for an interior electric car," *Jurnal Mekanikal*, vol. 39, 2016.
- [3] I. S. Fahim, S. M. Elhaggar, and H. Elayat, "Experimental investigation of natural fiber reinforced polymers," *Materials Sciences and Applications*, vol. 03, no. 02, pp. 59–66, 2012.
- [4] L. Drzal, S. Selke, B. Harte, and G. Hinrichsen, *Natural Fibers, Biopolymers, and Biocomposites*, CRC Press, Boca Raton, FL, USA, 2005.
- [5] L. M. Adb Ali, M. N. M. Ansari, G. Pua, M. Jawaid, and M. S. Islam, "A review on natural fiber reinforced polymer composite and its applications," *International Journal of Polymer Science*, vol. 15, 2015.
- [6] K. L. Pickering, M. G. A. Efendy, and T. M. Le, "A review of recent developments in natural fibre composites and their mechanical performance," *Composites Part A: Applied Science and Manufacturing*, vol. 83, pp. 98–112, 2016.
- [7] N. Ramli, N. Mazalan, Y. Ando et al., "Natural fiber for green technology in automotive industry: a brief review," in *Proceeding of the IOP Conference Series: Materials Science and Engineering*, Kerala India, June 2012.
- [8] E. Jayamani, S. Hamdan, M. D. RezaurRahman, and M. K. BinBakria, "Comparative study of dielectric properties of hybrid natural fiber composites," in *Proceedings of the 12th Global Congress on Manufacturing and Management GCCM*, Vellore, India, December 2014.
- [9] S. Erden and K. Ho, *Fiber reinforced composite in Fiber Technology for Fiber-Reinforced Composites*, Elsevier, Amsterdam, Netherlands, 2017.
- [10] A. Cristiano, S. Arlindo, L. Reis, P. Ferr, and M. J. Fereitas, "Sustainable design of automotive components through jute fiber composites: an integrated approach," *New Trends and Developments in Automotive Industry*, vol. 14, pp. 223–254, 2011.

Retraction

Retracted: Impact of Different Electrolytes on the Machining Rate in ECM Process

Advances in Materials Science and Engineering

Received 26 December 2023; Accepted 26 December 2023; Published 29 December 2023

Copyright © 2023 Advances in Materials Science and Engineering. This is an open access article distributed under the Creative Commons Attribution License, which permits unrestricted use, distribution, and reproduction in any medium, provided the original work is properly cited.

This article has been retracted by Hindawi, as publisher, following an investigation undertaken by the publisher [1]. This investigation has uncovered evidence of systematic manipulation of the publication and peer-review process. We cannot, therefore, vouch for the reliability or integrity of this article.

Please note that this notice is intended solely to alert readers that the peer-review process of this article has been compromised.

Wiley and Hindawi regret that the usual quality checks did not identify these issues before publication and have since put additional measures in place to safeguard research integrity.

We wish to credit our Research Integrity and Research Publishing teams and anonymous and named external researchers and research integrity experts for contributing to this investigation.

The corresponding author, as the representative of all authors, has been given the opportunity to register their agreement or disagreement to this retraction. We have kept a record of any response received.

References

- [1] K. G. Saravanan, R. Prabu, A. R. Venkataramanan, and E. T. Beyessa, "Impact of Different Electrolytes on the Machining Rate in ECM Process," *Advances in Materials Science and Engineering*, vol. 2021, Article ID 1432300, 6 pages, 2021.

Review Article

Impact of Different Electrolytes on the Machining Rate in ECM Process

K. G. Saravanan ¹, R. Prabu ², A. R. Venkataramanan ¹ and Eden Tekle Beyessa ³

¹Department of Mechanical Engineering, Sona College of Technology, Salem, Tamil Nadu, India

²Department of Mechanical Engineering, Mahendra Engineering College, Namakkal, Tamil Nadu, India

³School of Biomedical Engineering, Jimma Institute of Technology, Jimma University, Jimma, Oromia, Ethiopia

Correspondence should be addressed to K. G. Saravanan; kgsmechanical@gmail.com and Eden Tekle Beyessa; eden.tekle@ju.edu.et

Received 2 August 2021; Revised 10 August 2021; Accepted 13 August 2021; Published 30 August 2021

Academic Editor: Samson Jerold Samuel Chelladurai

Copyright © 2021 K. G. Saravanan et al. This is an open access article distributed under the Creative Commons Attribution License, which permits unrestricted use, distribution, and reproduction in any medium, provided the original work is properly cited.

Electrochemical machining is a nonconventional machining process in which the metal removal is achieved by the electricity and chemical solution known as an electrolyte. It is the reverse electrolysis process where the application of electricity facilitates the current travel in between anode and cathode. The mechanism of the ion movement is similar to the electrolysis process. Electrochemical machining (ECM) is a type of advanced machining process which employs electricity to perform the machining process on the workpiece. It is also known as a reverse electroplating process where metal removal is achieved instead of metal deposition on the metal surface. There are various parameters that affect the metal removal process in the ECM process, such as electrolyte, power supply, workpiece material, and tool material. The electrolyte is one of the key factors impacting the machining rate, surface finish, and reliability of the produced parts. In this project, a brief study is carried out regarding the electrochemical process and the electrolytes where the properties, functions, merits, and demerits are evaluated. The impact of the various electrolytes and their suitability for machining of various metals is also discussed. The findings of the effect produced by using the mixture of the electrolyte in the electrochemical machining process are discussed in this project. The effects of the complexing agents on the electrolyte and the electrochemical process as a whole are also reviewed.

1. Introduction

Electrochemical machining is a nonconventional machining process in which the metal removal is achieved by the electricity and chemical solution known as an electrolyte. Electrochemical machining is a modern and advanced metal removal technique that can produce metalworking for complex materials [1]. It is a very accurate machining process that can perform machining for any type of conductive workpiece. ECM finds its use in aerospace, construction, microsystems, medical equipment, and power supply systems [1, 2]. The electrochemical process is the noncontact metal removal process where no heat is applied, due to which the problems related to the conventional machining process are eliminated [2]. There is no tool wear due to which no defective layers are produced due to the tool on the workpiece [3], as shown in Figure 1.

1.1. Mechanism of ECM Process. ECM process is the reverse electrolysis process where the application of electricity facilitates the current travel in between anode and cathode. The mechanism of the ion movement is similar to the electrolysis process [2, 3]. For example, in the electrolysis of copper metal, the electrolysis process is conducted where the impure copper metal is kept to the anode material, and pure copper is kept as the cathode in the electrolyte of CuSO_4 solution. Copper atoms in the impure anode material are dissolved and travel to the cathode terminal via the electrolyte solution. The traveling is facilitated by a diffusion mechanism, and ions always travel from higher concentration regions to lower concentration regions to achieve chemical equilibrium. The concentration of the copper ion is high at the anode terminal, due to which they travel to the cathode terminal after getting attracted. Along with diffusion, the migration and convection also facilitate the

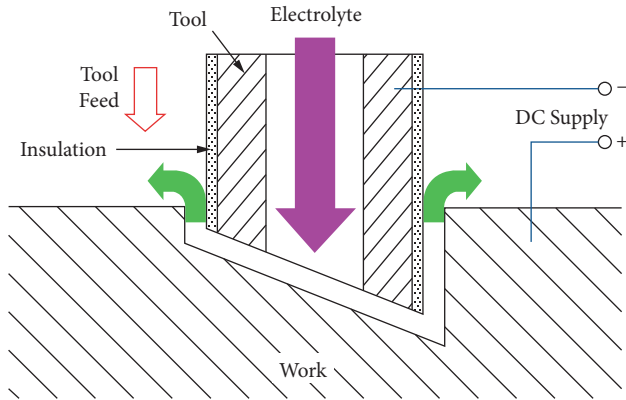


FIGURE 1: Electrochemical machine process.

complete electrolysis process. The migration mechanism is caused due to the potential field between the electrodes and the electrolyte. The third mechanism existing in the electrolysis and electrochemical process is convection which is caused due to the externally produced mechanical forces by stirring and bubbles in the solution [3]. The mechanism of copper purification is presented in Figure 2.

In the ECM process, the workpiece is connected to the positive terminal, known as the anode, and the tool is connected to the negative terminal known as a cathode [2]. The gap is always maintained between the tool and the workpiece. ECM process works in the principle of Faraday's law of electricity and Ohm's law. In the ECM process, the electrical conductivity of chemical electrolytes across the gap is considered to be constant. The electrical potential of the circuit is also assumed to be constant at all machining periods [4]. The cathode terminal of the ECM setup transmits electrons and releases the hydroxide (OH^-) ions, whereas the anode terminal releases electrons and they eventually become the metal ions, as shown in Figure 3.

2. Electrolyte

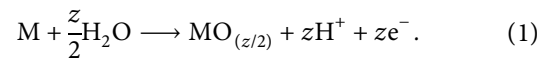
The electrolyte is the primary component of the electrochemical machining process. It has a significant role in material removal as well as tool wear. It has mainly three functions in the ECM process, carrying the current between workpiece and tool and removing the products of reactions from the interelectrode gap (IEG) [3].

The performance of the chemical machining process depends upon the selection of the electrolyte [5]. The electrolytes in the ECM process must have low corrosive nature and toxicity, high conductivity, and high electrochemical and chemical stability. The important properties of the electrolyte can be identified using the Polarization curve. Polarization curve is the graphical plot of the voltage or power density vs. current or current density of electrolyte cellular stack [6]. In the ECM machining process, the electrolyte is selected in such a way that no deposition of the material exists on the cathode. The deposition, if present, can deform the tool shape, and it can also impact the surface finishing of the workpiece. Moreover, the electrolyte also

should be able to take away the excess heat generated during the ECM process.

3. Mechanism of the Layer Formation

Depending upon the nature of the electrolyte and its selection process, the nature of the chemical reaction between the anode and cathode terminal can also be varied. The electrolyte can be categorized into two types, passivating electrolyte and nonpassivating electrolyte [3]. Passivating electrolyte facilitates passive layer development on the workpiece surface. This layer is composed of hydroxides and oxides, and it is formed after the current is passed between the workpiece and tool electrode terminals. Passive films can be electrically insulated and thus can hamper the chemical etching and dissolution process. But these films help in improving the machining resolution [7]. Nonpassivating electrolytes do not allow the film to be formed on the workpiece since the aggressive ions present in the electrolyte make the film unstable [3]. Nonpassivating electrolytes have a higher machining rate compared to the passivating electrolytes; however, the surface finish quality can be affected [8]. Passive layers on the workpiece are developed by workpiece metal itself along with the reaction from the surroundings. The water molecules are dissolved in the electrolytic solution and perform the following reaction forming the oxide layer as given below [9]:



Passive films can be insulators or noninsulators. The insulating film on the workpiece is self-subdued. The result is in the form of a thick and dense layer on the surface in a homogenous manner. However, the passive film can be cracked and distorted by the uneven electric field. The film can also be impacted by the addition of different functional ions [10].

4. Selection of Electrolyte

Electrolytes can be classified into four main categories depending upon their nature and physical form. They are neutral aqueous salts, aqueous acids, aqueous alkalis, and nonaqueous electrolytes, respectively. Neutral aqueous salts are mostly used electrolytes since they are relatively cheaper and are generally harmless to the working tool and machinery. The chlorides and phosphates of the metals such as Sodium, Potassium, Magnesium, calcium, etc., are some of the neutral electrolytes. Acidic electrolytes are used when the dissolution is not effective and possible by using other electrolytes. Some of the acidic electrolytes are sulfuric acid, hydrochloric acid, nitric acid, perchloric acid, etc. The interelectrode gap can be reduced to a great extent since the ions and other reaction products are firmly dissolved in the electrolytic solution. This also eliminates the problem of clogging. This is the reason why electrochemical micro-machining prefers acidic electrolytes [11]. According to the experimental investigation conducted by Yong et al. decided that the acidic electrolyte can produce very high machining

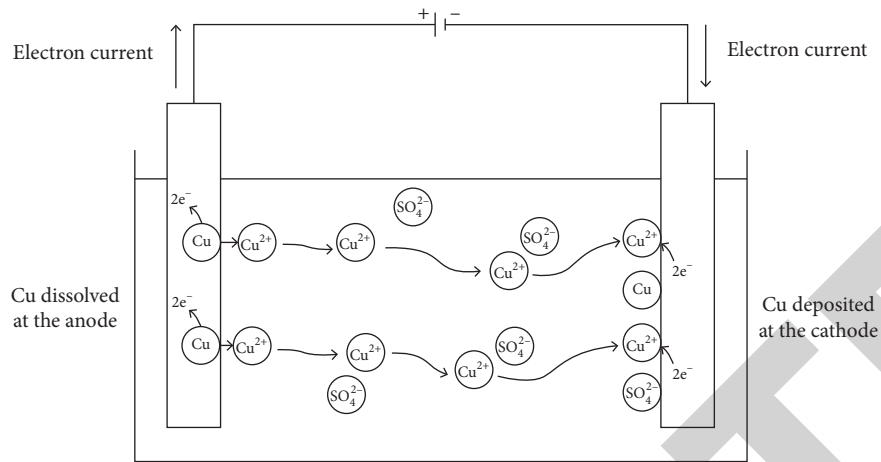


FIGURE 2: Diffusion of copper in copper sulphate and purification of copper.

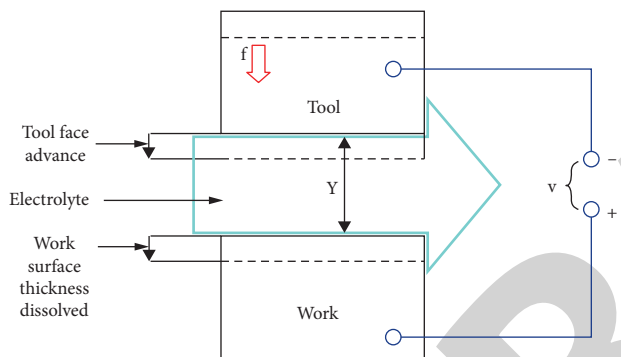


FIGURE 3: Mechanism of ECM process.

efficiency along with better surface quality [12]. Alkalis, including sodium hydroxide generally, are not recommended as electrolytes since they tend to promote the formation of the passive film. Due to the precipitation caused by the hydroxide ions, the IEG needs to be larger to accommodate the film thickness. The alkali electrolytes also tend to have the problem of clogging due to the precipitates. But some of the metal systems, such as tungsten carbide, are preferably soluble in the alkali electrolytes such as potassium hydroxide and can be used for particular metal systems only.

Nonaqueous electrolytes are nonpassivating electrolytes since they do not allow the oxygen molecules necessary for forming the passive oxide films. They are beneficial for the metals forming the metal oxides, but these electrolytes have the problem of dissolving the metal ions resulting in lower conductivities of the solution [3]. Some of the nonaqueous electrolytes are gel electrolytes, dry polymer electrolytes, ceramic electrolytes, ionic plastic crystals, etc. [13–15]. They can also operate at the small IEG since the gases and precipitation products are not produced. Solid electrolytes are already used in machining metal workpieces. Sjöström and Su have performed rapid micropatterning on the titanium using ethylene glycol electrolyte [16]. They also observed that there was no emission of gas and precipitation.

One of the most common electrolytes used in the ECM process is concentrated sodium chloride (NaCl). It is used

for machining stainless steel when a very shiny surface is required. Sodium chloride does not produce the layer on the stainless steel metal, and this allows the workpiece to be machined easily and quickly. Another electrolyte named sodium nitrate is normally used for machining the steel in case a very close replication of the tool is required. Sodium nitrate prevents stray corrosion, which helps to obtain a highly precise replica of the tool [3, 17]. The extent of current density also impacts the ECM process. For instance, in the case of sodium nitrate electrolyte, high current density leads to anodic dissolution, whereas the low current density increases passivation of the electrolyte [3].

ECM process is improved by employing the oxygen-rich electrolyte. Murugan and Jain investigated the effect of the cathode on the distribution of temperature in the ECM machining process. They made use of sodium chloride along with the enrichment of oxygen. From the experimentation, they determined that the material removal rate got increased with the addition of oxygen to the mixture [18]. Trimmer and others have used 0.05 M of hydrochloric acid for creating submicron nanoresolution structures. It is obtained on the substrate of the nickel surface [19]. Research studies have determined that the more concentrated electrolyte in conjunction with an increase in current density increases machining, and tool performs overcutting of the workpiece [20]. Rathod et al. have found out that, with the increase in the concentration of electrolyte, the resolution of the machining process gets reduced. This was because, with the increase in the electrolyte conductivity, the ions available for the reaction would be in increasing number [21]. It has also been identified that the resolution of the ECM process can be easily improved by adding the electrolyte resistance across the solution [22].

Fan et al. noticed that the mixture of the sodium chloride along with the HCl acid brought an increase in the electrolyte concentration, which lead to the machining overcut [23]. This indicates that the positive correlation of the mixed electrolyte with the concentration of the electrolyte helps to increase the machining rate. Hence, the varying concentration of the electrolyte has its advantages and disadvantages. With the lower concentration electrolyte, chemical

etching is particularly lower compared to the highly concentrated electrolyte. This is particularly beneficial in the machining of micro-sized particles [24]. Moreover, the electrolyte concentration is found to have an impact on the current density, ultimately leading to the change in machining resolution. The lower concentration of electrolyte can therefore produce higher machining resolution [25]; on the other hand, the increase in concentration has its advantages. Ayyappan and Sivakumar concluded that the higher concentration of the electrolyte helped to increase the surface finish of the machined workpiece [26]. Zohoor et al. have researched the effect of electrolytes and their nature on the ECM process of 304 Steel [2]. They compared the working of electrolytes such as sodium nitrate, sodium chloride, and potassium chloride at different currents. From the research, they found out that the material removal rate (MRR) is higher for NaCl and KCl compared to the NaNO₃ at the same working conditions. Side gap was found to be highest for KCl, with NaNO₃ having the least side gap. Surface roughness was observed to be increasing with the current for sodium nitrate, but it was the opposite for sodium chloride and potassium chloride.

Researches show that when a particular amount of acid is mixed with the natural salt electrolytes, it tends to increase the side gap and material removal rate in comparison with the pure natural electrolytes. Moreover, the surface roughness is also found to be in decreasing trend with the mixed electrolytes [2]. But in the case of the alkali or oxidant electrolytes such as sodium bromate (NaBrO₃), the production of oxide passive layer negatively impacts the machining rate along with the dimensional and geometrical accuracy [27]. In the case of alkaline electrolytes, the mixing of two electrolytes can improve the machining accuracy of the ECM process. Sabahi and Razfar have investigated the effect of mixing of sodium hydroxide and potassium hydroxide on the machining efficiency of the electrochemical discharge machining (ECDM) process. They found out that the mixing of two alkaline electrolytes increased electrical conductivity. The mixing also helped to increase the microchannel depth and limited the stray erosion of the workpiece. They also noticed that the increased concentration was achieved due to mixing, and the surface finish was also observed to be better when the alkaline electrolytes were mixed [28].

5. The Solubility of Electrolyte with Complexing Agents

Complexing agents are mainly used for dissolving the electrolyte with the metallic ions in the ECM process. Complexing agents are highly soluble in water and have high complexing ability and low viscosity, which makes them suitable to be used in the ECM process. They have a ligand structure that gets attached to metallic and hydroxide ions. Some of the ligand structures are calcimines, complexone groups, polyhydroxy acid groups, etc. In the ECM process, the workpiece placed in the anode terminal gets oxidized into metallic ions. In case of reaction with neutral electrolyte, the workpiece forms the layer of hydroxide precipitate with

the electrolyte. When the complexing agent is added to the electrolytic solution, the ligand of the complexing agent gets intermixed with the hydroxide ions and oxygen molecule with the metal ion to produce the clathrate. This product, known as clathrate, is soluble in water. The complexing ability of the agent determines the stability of the clathrate product. Hence, in this way, the insoluble products in the ECM process get dissolved with the help of the complexing agents [29].

The addition of the complexing agents can drastically improve the metal removal rate of the ECM process. The experimentation was conducted by Yong et al. on various composite electrolytes along with some of the natural electrolytes such as NaCl, NaNO₃, and NaClO₄. They observed that the metal removal rates of natural electrolytes, including NaNO₃ and NaClO₄, were identical. They added complexing agents and additives to the natural electrolytes and observed the metal removal rates of the ECM process. They found out that the MRR of natural electrolytes having the EDTANa₂ and tea as additives or complexing agents got improved by 22% and 10%, respectively. Moreover, the addition of complexing agents, namely sodium citrate, sodium gluconate, and sodium tartrate in the electrolytes increased the MRR by 35%, 43%, and 34%, respectively [12].

The electrolyte also plays an important role in the removal of excess heat from the reaction zone. Excess heat originated during the reaction can severely affect the tool and electrolyte. Excessive heat during the reaction also produces bubbles across the IEG and can cause boiling of the electrolyte [3, 23]. Electrolyte heat dissipation is necessary because the high amount of heat during the ECM reaction also leads to the poor surface quality of the machined workpiece. Research conducted by Bannard also indicates that the temperature of the electrolyte above 40 degree Celsius produced a gradually poorer surface quality of the workpiece [30]. Hence, it is very important to avoid the boiling of electrolytes. For prevention of boiling, the temperature of the electrolyte must be lesser than the boiling point of the electrolyte. N. K. Jain and V. K. Jain [31] have presented the equation for the temperature constraint of the electrolyte in the ECM process, which is given as follows:

$$T_b - T_{in} + \frac{1.0}{\alpha_K} \left[1.0 - \left(1.0 + \frac{S_k}{(1.0 - \alpha_{vo})^n} \frac{f^2}{U} \right)^{0.5} \right] \geq 0.0, \quad (2)$$

where T_b = boiling temperature of the electrolyte, T_{in} = electrolyte temperature at the inlet, α_K = temperature coefficient of electrolyte, f = tool feed rate, and U = electrolyte flow velocity.

6. Conclusion

According to this research study, it is presented that different reviews and experiments in electrochemical machining are already conducted. The electrochemical process, including the importance of electrolytes in the machining process, is reviewed. The most important component of the ECM process, known as the electrolyte, is also discussed in detail

and the importance of the mixing of electrolytes is also reviewed. The chemical properties and function of different electrolytes and the impact of passive films on the machining process are also discussed.

While it is very difficult to select the particular type of electrolyte for general use in the ECM process due to the variation of properties of different electrolytes and workpieces, it is possible to find out more suitable electrolytes for certain applications. Acidic electrolytes such as HCl and H₂SO₄ are preferred in electrochemical micromachining due to higher machining efficiency and accuracy of surface finish. Natural electrolytes such as NaCl and NaNO₃ are nontoxic and do not cause any harm to the tool and workpiece. They also ensure that the passive film on the workpiece does not exist. Solid electrolytes such as gel, polymer, and ceramic electrolytes are used when the passive film is highly undesirable, and IEG is small.

Mixed electrolytes formed by intermixing of electrolytes with the complexing substances are highly efficient compared to the traditional electrolytes. Mixed electrolytes are found to be better in terms of machining rate, surface finish quality, electrolyte solubility, etc. Other mixed electrolytes formed by mixing two electrolytes are also found to be higher in concentration compared to the individual electrolytes. The electrolyte concentration also is found to be positively correlated with the machining rate and surface finish quality.

From the study, it is evident that the intermixing of different electrolytes can improve the various process parameters of the ECM process. Further research regarding the complexing agents and their impact on the solubility of various electrolytes are also necessary.

Data Availability

The data used to support the findings of this study are included within the article.

Conflicts of Interest

The authors declare that they have no conflicts of interest.

References

- [1] Z. Pandilov, "Application of electrochemical machining for materials used in extreme conditions," *IOP Publishing*, vol. 329, Article ID 012014, 2018.
- [2] M. Zohoor, S. Jalili, A. Alipour, and R. Mosallanejad, "Effect of electrolyte type on electrochemical machining of 304 steel," *International Journal of Applied Engineering Research*, vol. 12, no. III, pp. 20–39, 2016.
- [3] R. J. Leese and A. Ivanov, "Electrochemical micromachining: an introduction," *Advances in Mechanical Engineering*, vol. 8, no. I, pp. 1–13, 2016.
- [4] S. K. Mukherjee, S. Kumar, and P. K. Srivastava, "Effect of electrolyte on the current-carrying process in electrochemical machining," *Journal of Mechanical Engineering Science*, vol. 221, pp. 1415–1419, 2007.
- [5] S. S. H. Lijo Paul, "Improvement in Machining Rate with Mixed Electrolyte in ECDM Process," *Procedia Technology*, vol. 25, pp. 1250–1256, 2016.
- [6] M. Thomas, P. Alberto, T. Georgios, and D. M. Giancarlo, "EU harmonised polarisation curve test method for low-temperature water electrolysis," *Joint Research Centre*, vol. 330, pp. 1–29, 2018.
- [7] Z. Zeng, Y. Wang, Z. Wang, D. Shan, and X. He, "A study of micro-EDM and micro-ECM combined milling for 3D metallic microstructures," *Precision Engineering*, vol. 36, no. 3, pp. 500–509, 2012.
- [8] M. Datta, "Anodic Dissolution of metals at high rates," *IBM Journal of Research and Development*, vol. 37, no. 2, pp. 207–226, 1993.
- [9] J. W. Schultze and M. M. Lohrengel, "Stability, reactivity and breakdown of passive films. Problems of recent and future research," *Electrochimica Acta*, vol. 45, pp. 2499–2513, 2000.
- [10] A. Ghosh, "Electrochemical machining," *Encyclopedia of Nanotechnology, Bharat Bhushan*, vol. 29182, pp. 684–688, 2012.
- [11] B. Bhattacharya, J. Munda, and M. Malapati, "Advancement in electrochemical micromachining," *International Journal of Machine Tools and Manufacture*, vol. 44, pp. 1577–1589, 2004.
- [12] L. Yong, Z. Di, Z. Yongbin, H. Shaofu, and Y. Hongbing, "Experimental investigation on complex structures machining by electrochemical micromachining technology," *Chinese Journal of Aeronautics*, vol. 23, no. 5, pp. 578–584, 2010.
- [13] K. Perzyna, R. Borkowska, J. Syzdek, A. Zalewska, and W. Wieczorek, "The effect of additive of Lewis acid type on lithium-gel electrolyte characteristics," *Electrochimica Acta*, vol. 57, pp. 58–65, 2011.
- [14] J. Syzdek, R. Borkowska, K. Perzyna, J. M. Tarascon, and W. Wieczorek, "Novel composite polymeric electrolytes with surface-modified inorganic fillers," *Journal of Power Sources*, vol. 173, no. 2, pp. 712–720, 2007.
- [15] J. Luo, O. Conrad, and I. F. J. Vankelecom, "Imidazolium methanesulfonate as a high temperature proton conductor," *Journal of Materials Chemistry*, vol. 1, no. 6, pp. 2238–2247, 2013.
- [16] T. Sjöström and B. Su, "Micropatterning of titanium surfaces using electrochemical micromachining with an ethylene glycol electrolyte," *Materials Letters*, vol. 65, pp. 3489–3492, 2011.
- [17] A. Lesch, G. Wittstock, C. Burger, B. Walther, and J. Hackenberg, "External control of anodic dissolution mechanism of 100Cr6 in nitrate/chloride mixed electrolytes," *Journal of Electrochemical Science and Engineering*, vol. 1, no. 1, pp. 39–54, 2011.
- [18] V. K. Jain and S. Murugan, "Investigations into the effect of cathode material on temperature distribution during electrochemical machining," *International Journal of Production Research*, vol. 24, no. 2, pp. 439–450, 1986.
- [19] A. L. Trimmer, J. L. Hudson, M. Kock, and R. Schuster, "Single-step electrochemical machining of complex nanostructures," *Applied Physics Letters*, vol. 82, no. 19, pp. 3327–3329, 2003.
- [20] B. Bhattacharyya and J. Munda, "Experimental Investigation on the influence of electrochemical machining parameters on machining rate and accuracy in Micro-machining domain," *International Journal of Machine Tools and Manufacture*, vol. 43, no. 13, pp. 1301–1310, 2003.
- [21] V. Rathod, B. Doloi, and B. Bhattacharyya, "Experimental investigation into machining accuracy and surface roughness of microgrooves fabricated by the electrochemical micro-machining," *Journal of Engineering Manufacture*, vol. 229, no. 10, pp. 1781–1802, 2014.

Retraction

Retracted: Utilization of Red Mud-Fly Ash Reinforced with Cement in Road Construction Applications

Advances in Materials Science and Engineering

Received 26 December 2023; Accepted 26 December 2023; Published 29 December 2023

Copyright © 2023 Advances in Materials Science and Engineering. This is an open access article distributed under the Creative Commons Attribution License, which permits unrestricted use, distribution, and reproduction in any medium, provided the original work is properly cited.

This article has been retracted by Hindawi, as publisher, following an investigation undertaken by the publisher [1]. This investigation has uncovered evidence of systematic manipulation of the publication and peer-review process. We cannot, therefore, vouch for the reliability or integrity of this article.

Please note that this notice is intended solely to alert readers that the peer-review process of this article has been compromised.

Wiley and Hindawi regret that the usual quality checks did not identify these issues before publication and have since put additional measures in place to safeguard research integrity.

We wish to credit our Research Integrity and Research Publishing teams and anonymous and named external researchers and research integrity experts for contributing to this investigation.

The corresponding author, as the representative of all authors, has been given the opportunity to register their agreement or disagreement to this retraction. We have kept a record of any response received.

References

- [1] S. C. K, K. S, and K. Sahile, "Utilization of Red Mud-Fly Ash Reinforced with Cement in Road Construction Applications," *Advances in Materials Science and Engineering*, vol. 2021, Article ID 3728652, 8 pages, 2021.

Research Article

Utilization of Red Mud-Fly Ash Reinforced with Cement in Road Construction Applications

Sarath Chandra K,¹ Krishnaiah S,¹ and Kibebe Sahile²

¹Department of Civil Engineering, Jawaharlal Nehru Technological University (JNTU), Anantapur, Andhra Pradesh, India

²Department of Chemical Engineering, College of Chemical and Biological Engineering, Addis Ababa Science and Technology University, Addis Ababa, Ethiopia

Correspondence should be addressed to Kibebe Sahile; kibebe.sahile@aastu.edu.et

Received 12 July 2021; Accepted 17 August 2021; Published 26 August 2021

Academic Editor: Samson Jerold Samuel Chelladurai

Copyright © 2021 Sarath Chandra K et al. This is an open access article distributed under the Creative Commons Attribution License, which permits unrestricted use, distribution, and reproduction in any medium, provided the original work is properly cited.

Industrialization is the key to the growth of any country's economy. However, on the other hand, the production of industrial waste is increasing enormously, which adversely impacts the environment and natural resources. Red mud is also a widespread industrial waste produced during aluminium extraction from bauxite ore in Bayer's process. Red mud is a highly alkaline material that creates a massive environmental threat in nature. To reduce the impact of this solid waste material, the ideal method is to use it in construction works with appropriate stabilization. This study envisages the strength properties of red mud with fly ash and cement to use it as a road construction material in the subgrade. The influence of fly ash and cement on improving the strength properties of red mud was studied in detail by replacing red mud with 10%, 20%, and 30% with fly ash and 1%, 3%, and 5% of cement to its dry weight. The CBR (California bearing ratio) value was increased from 1.58% to 11.6% by stabilizing red mud with fly ash and cement, which can be used as a road construction material. The UCS (unconfined compressive strength) of red mud was increased from 825 kPa to 2340 kPa upon curing for 28 days with the right mix of fly ash and cement. Along with the strength properties, the chemical analysis of leachate for the best suitable mix was performed according to the TCLP method to understand the hazardous materials present in the red mud when it is injected as ground material. Both strength properties and the leachate characteristics prove that the red mud with suitable fly ash and cement is an excellent material in road constructions.

1. Introduction

The cost for construction of rigid and flexible pavements with subgrade of low California bearing ratio (CBR) values is exceptionally higher because of the high thickness of the pavement required. Expulsion and substitution of low CBR soils is one of the methods to increase the CBR of the subgrade. The subgrade soil having low CBR values is expelled and placed with the soil of high CBR values, in the event that it is accessible in the adjacent zones monetarily. But, every time, it is not practicable to discover soils of high CBR values to be utilized as subgrade over low CBR soil. Also, taking the soil from a region where the soil is utilized for agricultural purpose will decrease the yield. Also, it will make many depressions in the ground which may result in

land degradation. The disposal of tremendous amounts of solid wastes like red mud and flyash which comes from manufacturing industries makes a number of geo-environmental issues such as groundwater contamination and surface water and neighborhood air contamination, other than loss of profitable land close to the plant site. These solid wastes can be combined to deliver a composite material of high CBR values and good compressive strength which can be utilized as subgrade instead of soils of low values.

Red mud (RM) is an industrial waste produced from Bayer's technique of extracting aluminium from bauxite ore. It is also known as bauxite residue. The quantity of RM generated varies between 60 and 70% of the prepared metals, depending on the purity and immaculateness of the bauxite minerals [1]. More than 150 million tonnes of RM are

produced worldwide, with India contributing 9 million tonnes each year [2]. Every tonne of alumina produced produces 0.8–1.6 tonnes of RM [3]. When RM is dumped directly into the land surface, its high alkalinity (pH: 11–13) poses an environmental concern. The total annual production of red mud from various countries was estimated and presented in Figure 1.

Figure 2 depicts the production of aluminium, the generation of RM, and its use in India, revealing a significant discrepancy between production and utilization of RM. In most countries, the most prevalent way of RM disposal is to dump it into specially prepared landfills adjacent to plants, which produces air pollution from very fine particles and groundwater pollution if leaching occurs. In 2010, an aluminium sludge discharge occurred near Ajka in Hungary. Another spillover incident in January 2018 in Belem has served as a reminder to everyone that storing large quantities of RM can result in unanticipated property and human loss [6, 7]. Using RM in the construction sector is the most effective way to lessen its impact [8]. For the past 20 years, bricks manufactured using RM, as well as other waste materials and stabilizers, have been in use [9]. Even still, as seen in Figure 2, there is a significant disparity between output and use. If RM is used to make subgrade or subbase in roads, a large proportion of it can be employed, which can assist to prevent the conservation of virgin materials and resources on the one hand and the utilization of waste materials on the other hand [10].

Many research studies have been conducted on the utilization of red mud and proved that the RM alone will not give the desired strength for any construction and it should be treated with any of the neutralizing methods to reduce the impact of it on environment [11]. In order to this, RM is mixed with the another industry waste material called fly ash (FA) which gives a pozzolonic nature to the virgin RM. Fly ash is a byproduct of coal combustion that can be obtained from coal-fired power plants and other coal-burning facilities. The availability of FA in India is expected to be between 80 and 100 million tonnes per year. Every thermal power station that generates 1000 MW of power produces 3500 tonnes of FA per day on average [12]. On average 28,000 ha of land has been used to dump the fly ash near the industries and the presence of fine particles will result a destruction to plant and human life directly by creating air pollution [13]. RM is rich in iron and FA is good at silica and aluminium which helps to develop and good strength when both are used in a right combination.

The FA used in this work is a class F fly ash which is low in pozzolonic reaction. So, an attempt was made to add another geotechnical stabilizer called cement to improve the strength properties of RM-FA in a very minimum amount [14]. A Portland cement is generally used for the purpose of stabilization [15]. Here, a small amount of cement was used to get better strength values to RM-FA and recommend it as a competitive subgrade material in road constructions. A thorough laboratory investigation was made on various combinations of RM-FA with cement and determined the strength properties of all the combinations by using UCS and CBR as the parameters. Upon finding the strength

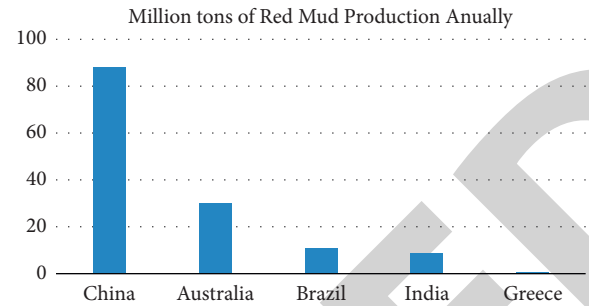


FIGURE 1: Annual production of red mud from various countries [4].

properties, the most suitable combination was used to collect the leachate and performed the chemical analysis of it to understand the presence of hazardous materials in it. Comparison of these hazardous chemicals with the WHO standards was made to use the RM-FA reinforced with cement effective in environmental perspective also.

2. Materials

2.1. Red Mud. The Hindalco Aluminium Industry in Belgaum, Karnataka, India, provided a solid RM waste. The collected RM is allowed to air-dry before starting the laboratory testings in order to remove the moisture which is present in it. According to ASTM-D422-63, gradation of bare RM sample is performed to understand the percentage of various geotech materials [16]. The majority of the RM is silt (75%) that passes through a 75 μ m sieve, with the remaining fractions of 10% clay and 15% sand. As per Unified Soil Classification System (USCS), RM has the most silt, which is classed as silt of low plasticity (ML). The specific gravity of RM has been determined to be 2.85. Compaction tests are performed by using modified proctor compaction tests, as per ASTM D 1557-12 [17]. The maximum dry density (MDD) and optimum moisture content (OMC) of bare RM were 31.39 % and 16 kN/m³, respectively. The pH of the RM which was used in this research study was 11.05 which shows the nature of highly alkaline material. The CBR values of unsoaked and soaked RM were 5.76% and 1.58%, respectively. UCS samples were prepared based on the OMC and MDD of the RM, and the results show that the UCS of RM is 815 kPa for the 28 days curing.

Scanning electron microscopy (SEM), X-ray fluorescence (XRF), and X-ray diffraction method (XRD) were performed on the bare RM to have a better understanding of the material. SEM and XRD of RM are presented in Figure 3. The SEM image depicts the loose structure of the RM, and the same was presented in Figure 3(a). The XRD pattern of the RM waste presented in Figure 3(b) reveals chalcite ($\text{Na}_5\text{Al}_3\text{CSi}_3\text{O}_{15}$), gibbsite ($\text{Al}(\text{OH})_3$), muscovite ($\text{KAl}_2(\text{FOH})$), calcite (CaCO_3), and hematite (Fe_2O_3) as the primary mineral phases. It identifies the minerals in the RM with pinpoint accuracy. The chemical composition of RM is measured by the XRF analyzer. Fe_2O_3 , Al_2O_3 , SiO_2 , CaO , Na_2O , TiO_2 , K_2O , and MgO are the primary chemical components of RM. The percentage of these

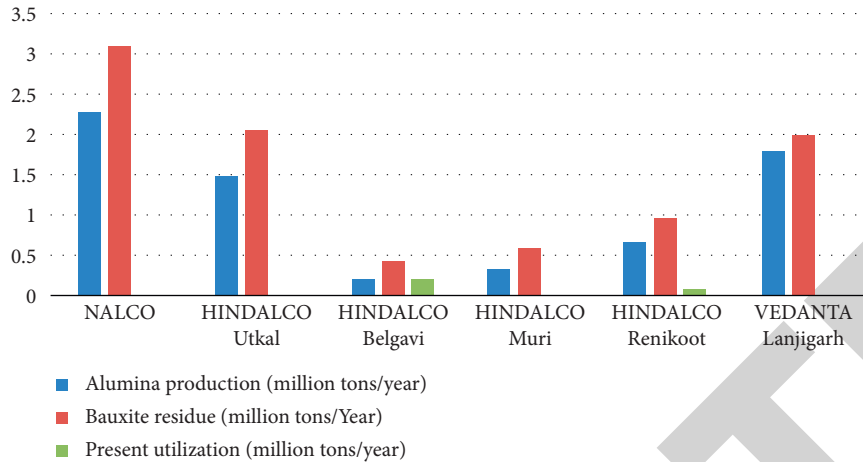


FIGURE 2: Production of aluminium and red mud and its utilization annually [5].

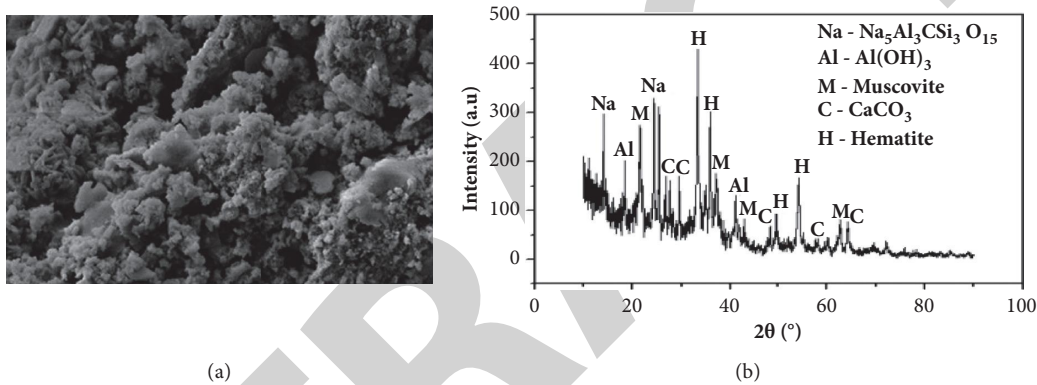


FIGURE 3: (a) SEM of red mud and (b) XRD of red mud.

chemical elements in bauxite will vary based on the procedure, property, and phase of the bauxite and will alter over time.

2.2. Fly Ash. Raichur Thermal Power Plant in Shakthinagar, Raichur District, Karnataka, India, provided the FA. The Karnataka Power Corporation Limited (KPCL) operates a coal-fired electric power station that produces 1.5 million tonnes of FA every year [18]. The principal chemical composition of the FA employed in this study is 46.2% SiO_2 , 19.54% Al_2O_3 , 13.46% Fe_2O_3 , and 7.61% CaO which are obtained by performing an XRF analysis. FA was classed as class F according to ASTM C618-12 [19] because the total chemical composition of SiO_2 , Al_2O_3 , Fe_2O_3 , and CaO was greater than 70% and CaO was less than 10%. FA has the specific gravity of 2.51. The SEM and XRD images of FA are presented in Figure 4. The SEM image depicted in Figure 4(a) shows that the shape of the particles are sphere, whereas the shape of particles in RM are angular, which directly proves a better combination to use both of them in construction works. The XRD of the FA is shown in Figure 4(b), with peak values for the principal amorphous phases: quartz, calcite, mullite, hematite, and calcium sulphate.

2.3. Cement. Portland cement of 53 grade was used for the purpose of stabilization of various combinations of RM-FA. Induction of cement in the RM-FA combination helps to increase the strength parameters of RM and its various combinations. Cement is used as a good stabilizer in many construction works and highly acceptable material in the stabilization of soils in subgrade and subbase construction of roads. Cement stabilization significantly enhances soil stiffness and strength to the point that it aids pavement and building foundations structurally. The specific gravity of cement is very high which is of 3.11 g/cc. The chemical composition of cement was determined by XRF analyzer and identified CaO , SiO_2 , Al_2O_3 , and Fe_2O_3 are the major proportions of it.

3. Methodology

Geotechnical properties of bare RM were studied initially in detail to analyze the usage of the material as a subgrade material in road construction. Then, RM is replaced with FA by 10%, 20%, and 30% to its dry weight. Same combinations were again stabilized with 1%, 3%, and 5% of cement to determine the strength properties of RM-FA. The list of combinations and their nomenclature is presented in Table 1. Modified proctor compaction test was

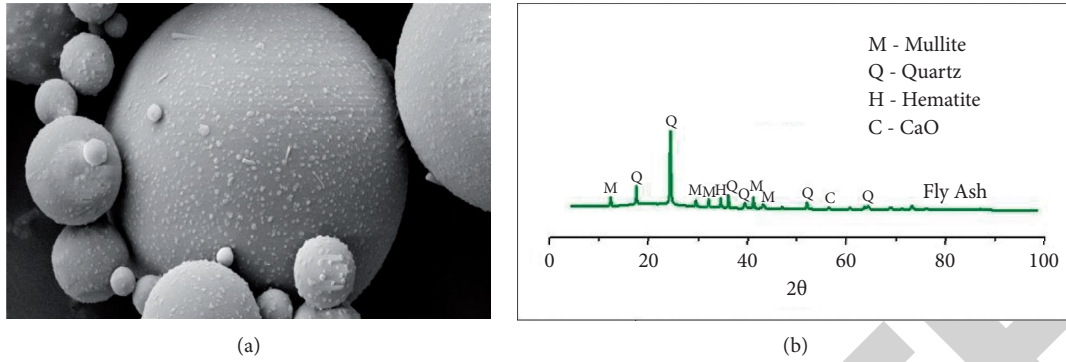


FIGURE 4: (a) SEM of fly ash and (b) XRD of fly ash.

TABLE 1: Combinations of RM-FA and cement with nomenclatures.

S. no.	Sample combination (%)	Nomenclature
1	100RM + 0FA + 0CM	RFC1
2	90RM + 10FA + 0CM	RFC2
3	90RM + 10FA + 1CM	RFC3
4	90RM + 10FA + 3CM	RFC4
5	90RM + 10FA + 5CM	RFC5
6	80RM + 20FA + 0CM	RFC6
7	80RM + 20FA + 1CM	RFC7
8	80RM + 20FA + 3CM	RFC8
9	80RM + 20FA + 5CM	RFC9
10	70RM + 30FA + 0CM	RFC10
11	70RM + 30FA + 1CM	RFC11
12	70RM + 30FA + 3CM	RFC12
13	70RM + 30FA + 5CM	RFC13

used to determine the compaction characteristics such as OMC and MDD for all the combinations. Unsoaked CBR and soaked CBR of 4 days were conducted on all the combinations by compacting with the OMC obtained from the compaction test. UCS of all the samples were determined for 1 day, 7 days, and 28 days of curing period by making the samples with the OMC of respective combination. UCS samples were prepared as per the UCS test procedure and covered in a polythene cover to allow the curing for 1 day, 7 days, and 28 days. All the samples were tested for compressive strength using unconfined compressive strength testing machine, and the reading was noted. Upon conducting all the geotechnical tests, the best combination was used to perform the TCLP (Toxicity Characteristics Leaching Procedure) test was performed, and the leachate was collected from the sample. The hazardous chemicals present in the leachate were studied and compared with the various water quality standards for the safe utilization of RM-FA in subgrade of roads.

4. Results and Discussion

4.1. Modified Proctor Compaction Test. All combinations were subjected to a modified proctor compaction test to determine the compaction characteristics, and the results are reported in Table 2. The OMC and MDD values are presented in Table 2, in percentage and kN/m^3 for various

trials of RM and FA without and with cement reinforcement, respectively. OMC of RM was reduced with the increase of FA and MDD was increased upto a substitution of 20%. The 30% substitution of FA to RM does not show any effect on the MDD, but the OMC was decreased further. The trend of increasing the MDD and reduction of OMC was even continued with the addition of cement also but the change was very minimum compared with and without cement. The nonplastic character of FA resulted in a decrease in OMC, but the particle size of FA, which acts as a padding material up to a point, resulted in an increase in MDD.

According to IRC SP: 20-2002, the minimum MDD value should be 14.4 kN/m^3 and OMC should not be more than 20% to select any material as a subgrade. In the present study, all the samples satisfy the IRC specifications with respect to MDD though water content is not in the limits. Though the OMC is higher than the specified values, the RM-FA with cement can be confidently used as a subgrade material because of the satisfying values of dry density. MDD of RM-FA has increased from 16 kN/m^3 to 17.1 kN/m^3 with the 20% replacement of FA and 5% of cement, which is a sample combination of RFC9. OMC was reduced to 27.55% from 31.39% with the replacement of 20% FA and 5% cement. It proves that the addition of FA and cement increases the compaction and strength of RM with the right proportion of water.

TABLE 2: OMC and MDD of various trails of RM-FA with and without cement.

S. no.	Sample name	OMC (%)	MDD (kN/m ³)
1	RFC1	31.39	16.00
2	RFC2	30.11	16.10
3	RFC3	30.12	16.15
4	RFC4	30.00	16.20
5	RFC5	29.66	16.30
6	RFC6	29.88	16.35
7	RFC7	28.45	16.85
8	RFC8	27.99	16.91
9	RFC9	27.55	17.10
10	RFC10	26.99	16.80
11	RFC11	26.03	16.80
12	RFC12	25.66	16.79
13	RFC13	25.01	16.70

4.2. California Bearing Ratio. The CBR test was administered on all the samples by mixing with the water based on OMC obtained for the respective combination. All the samples were soaked in water for 4 days by keeping a surcharge weight of 5 kg as per the standard procedure. 50 kN proving ring was used to determine the CBR value of all the combinations. The soaked CBR values of various combinations of RM-FA with cement are presented in Figure 5. The minimum CBR required to use any material as a subgrade material is 8% as per the guidelines of IRC 2012 specifications. RM with 20% replacement of FA showed the CBR value of more than 8% for with and without cement combinations. The presence of cement further increased the strength by creating the pozzolonic reaction among the RM-FA samples. RFC9 shows the highest CBR value of 11.6% which is highly accepted for the construction of subgrades in the road construction. The effect of cement reinforcement is well distinguished in the CBR properties of RM-FA samples. The soaked CBR values of RM with 30% replacement of FA were reduced because of higher absorption of water which results in the loss of bearing capacity of the material upon soaking. The results present in Figure 5, indicate that the RM-FA reinforced with cement can be a subgrade.

4.3. Unconfined Compressive Strength. Figure 6 shows the UCS values of various combinations of RM-FA with cement. UCS samples were produced using the combinations listed in Table 1 and the OMC, MDD combinations listed in Table 2, in accordance with the standard UCS validation process. All the samples were cured for 1 day, 7 days, and 28 days of curing period at a room temperature of 27°C. Three curing times were chosen to see how the strength of various combinations increased over time. C-S-H gel is produced with the increase of time in silica-based materials, and this gel helps to impart the strength in the combinations by densifying the materials. Cured samples were tested by using the UCS testing machine, and the values are presented in Figure 6. UCS values of RM-FA without cement are presented in Figure 6(a). With better curing time and temperature, high strength can be attained [20]. It is observed that the UCS values are increased with the increase of fly ash upto 20%, and at 30% replacement, it is observed that the reduction in strength

because of higher consumption of water, even the same trend, was observed with the cement stabilization.

According to IRC: 37-2012 specifications [21], the compressive strength value should be between 800 and 3000 kPa for low volume to high volume road subgrades. It is observed that the combination of RFC9 with 80%RM, 20%FA, and 5% cement shows the maximum strength value of 2340 kPa, which is highly acceptable for the construction of mid to high volume traffic roads as a subgrade material. It is observed that the strength improvement in RFC9 was approximately three times more than the virgin RM. These results confirm that the RM-FA with 5% of cement will surely satisfy the IRC specifications of road subgrade constructions. Higher amount of cement stabilization can be made but limited the work to only 5% addition by taking low-cost stabilization method as the key factor.

4.4. Geoenvironmental Study. The pH of RM is very high, and it is observed as alkaline in nature. This indicates that the RM may impose the environmental threat by polluting the ground water with the seepage. Addition of FA to RM helps to neutralize the RM and reduces the effect of its hazardous content in leachate. Utilization of any waste material may pose ground water pollution without proper liners and protective measure. In this study, the best combination is RFC9, which shows the better values of CBR, and UCS is used to collect the leachate from the TCLP procedure. The TCLP test includes extracting pollutants from a 100 gram sample of waste material using a suitable extraction fluid. A liquid to solid ratio of 20 : 1 is used, and the mixture is rotated at 30 rpm for 18 ± 2 hours by using an apparatus called rotary agitation device. The extraction fluid utilized for TCLP test is based on the level of alkaline nature of the waste material. High alkaline waste materials are leached with a set quantity of acetic acid at $\text{pH } 2.88 \pm 0.05$, whereas other waste materials are leached using acetic acid buffered with 1-N NaOH at $\text{pH } 4.93 \pm 0.05$. The ultimate pH of the mixture is determined after spinning, and it is filtered, then the leachate was collected from the sample, and the hazardous chemicals present in it were presented by performing the chemical analysis of it. Selected list of hazardous chemicals is used to understand the concentration of each hazardous chemicals, and the same are presented in Table 3. The results were compared with the

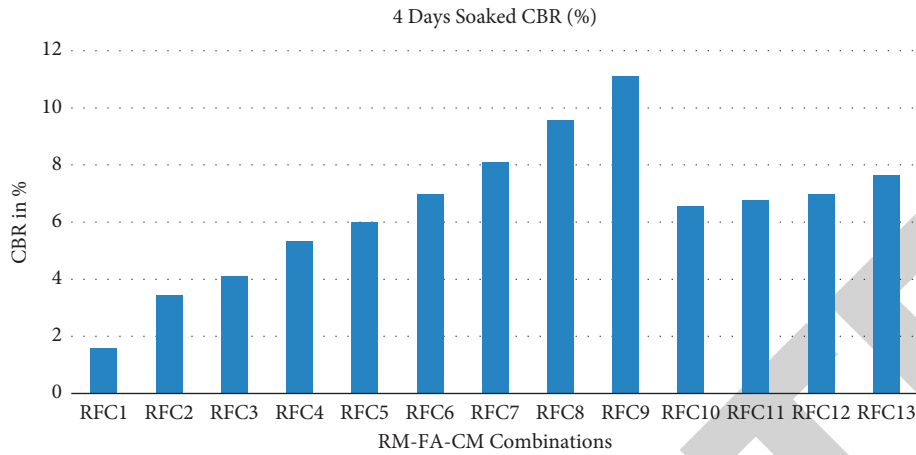
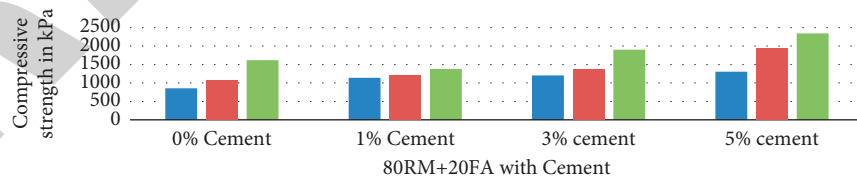
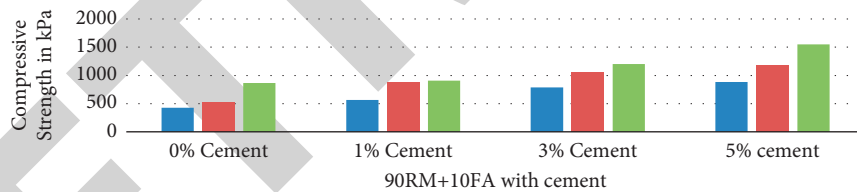
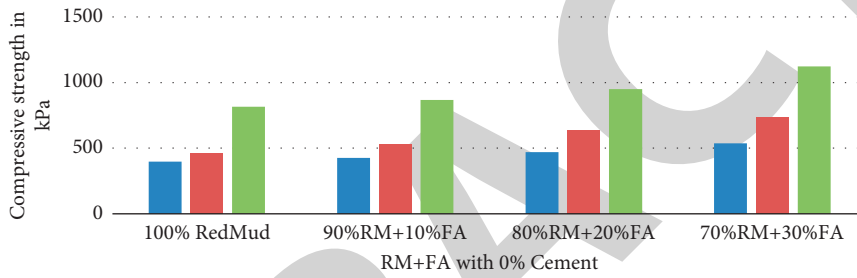


FIGURE 5: CBR values of RM-FA reinforced with cement.



(c)
FIGURE 6: Continued.

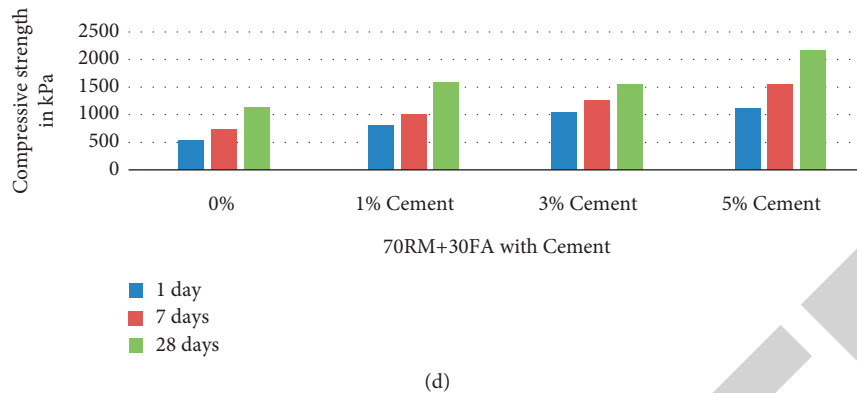


FIGURE 6: UCS of RM-FA reinforced with cement.

TABLE 3: Chemical analysis of leachate of RM and RFC9 in comparison with the various standards.

Analytes	Results obtained (mg/l)		Drinking water standards (mg/l)	TCLP limits (mg/l)	WHO standards of drinking water (mg/l)
	RM	RFC9			
Arsenic (As)	0.001	0.160	0.05	5.0	0.01
Cadmium (Cd)	0.04	0.23	0.005	1.0	0.003
Chromium (Cr)	0.76	1.16	0.1	5.0	0.05
Lead (Pb)	0.70	1.98	0.015	5.0	0.01
Mercury (Hg)	0.001	0.02	0.002	0.2	0.001
Sodium (Na)	4.12	6.76	20	40	20
Calcium (Ca)	216.8	234	20–208	—	20–208
Silica (SiO ₂)	116.9	145.77	100	200	100

TCLP standards and WHO standards. The results show that the hazardous chemicals are within the permissible limits of TCLP standards. This confirms that the RM-FA with cement reinforcement can be highly recommended to use as a subgrade material in construction of roads with respect to geotechnical and geoenvironmental studies.

5. Conclusions

The strength development of the red mud and fly ash as a sustainable material for subgrade application with varied ratios of cement to its dry weight was evaluated in this work through a series of experiments. FA replacement to RM showcased the improvement in strength of RM by resulting very good values of CBR and UCS. The addition of FA to RM reduces the OMC and increases the MDD, and the same trend was continued with the addition of cement. The addition of cement in this work was limited to only 5% to develop a low-cost sustainable material from the industrial solid wastes. The CBR value of all the combinations of RM with 20% FA shows more than 8%, which shows that the RM-FA combinations are accepted to use as a subgrade material. The UCS values of 28 days cured samples of RM with 20% FA and 5% cement show the highest values among all the combinations and will fall in the limits given by the IRC in relation to strength parameters. Geoenvironmental study shows that the RFC9 sample has all the toxic metals are within the allowable limits and concludes

that the RM-FA with cement will be a very good sustainable material.

Data Availability

The data used to support findings of this study are included within the article.

Conflicts of Interest

The authors declare that they have no conflicts of interest regarding the publication of this paper.

Acknowledgments

The authors thank the Department of Civil Engineering, School of Engineering and Technology, Christ University, Bangalore, for providing the laboratory facilities to conduct all the experiments.

References

- [1] R. K. Paramguru, P. C. Rath, and V. N. Misra, "Trends in red mud utilization—a review," *Mineral Processing and Extractive Metallurgy*, vol. 26, pp. 1–29, 2005.
- [2] K. Evans, "The history, challenges, and new developments in the management and use of bauxite residue," *Journal of Sustainable Metallurgy*, vol. 2, no. 4, pp. 316–331, 2016.

Retraction

Retracted: Effect of the Reinforcement Phase on Indentation Resistance and Damage Characterization of Glass/Epoxy Laminates Using Acoustic Emission Monitoring

Advances in Materials Science and Engineering

Received 26 December 2023; Accepted 26 December 2023; Published 29 December 2023

Copyright © 2023 Advances in Materials Science and Engineering. This is an open access article distributed under the Creative Commons Attribution License, which permits unrestricted use, distribution, and reproduction in any medium, provided the original work is properly cited.

This article has been retracted by Hindawi, as publisher, following an investigation undertaken by the publisher [1]. This investigation has uncovered evidence of systematic manipulation of the publication and peer-review process. We cannot, therefore, vouch for the reliability or integrity of this article.

Please note that this notice is intended solely to alert readers that the peer-review process of this article has been compromised.

Wiley and Hindawi regret that the usual quality checks did not identify these issues before publication and have since put additional measures in place to safeguard research integrity.

We wish to credit our Research Integrity and Research Publishing teams and anonymous and named external researchers and research integrity experts for contributing to this investigation.

The corresponding author, as the representative of all authors, has been given the opportunity to register their agreement or disagreement to this retraction. We have kept a record of any response received.

References

- [1] C. S. Kumar, K. Saravanakumar, P. Prathap et al., "Effect of the Reinforcement Phase on Indentation Resistance and Damage Characterization of Glass/Epoxy Laminates Using Acoustic Emission Monitoring," *Advances in Materials Science and Engineering*, vol. 2021, Article ID 5768730, 11 pages, 2021.

Research Article

Effect of the Reinforcement Phase on Indentation Resistance and Damage Characterization of Glass/Epoxy Laminates Using Acoustic Emission Monitoring

C. Suresh Kumar,¹ K. Saravanakumar,² P. Prathap,³ M. Prince,³ G. Bharathiraja,⁴
S. Kannan,⁵ S. Madhu,⁶ and P. Kumaran⁷ 

¹Department of Aeronautical Engineering, Bharath Institute of Higher Education and Research, Selaiyur, Chennai, India

²Department of Aerospace Engineering, SRM Institute of Science & Technology, Kattankulathur, Chennai, Tamil Nadu, India

³Department of Mechanical Engineering, Sri Krishna College of Technology, Coimbatore, Tamil Nadu, India

⁴Department of Mechanical Engineering, Saveetha School of Engineering, Saveetha Institute of Medical and Technical Sciences, Chennai, Tamil Nadu, India

⁵Department of Mechanical Engineering, Hindusthan College of Engineering and Technology, Coimbatore, Tamil Nadu, India

⁶Department of Automobile Engineering, Saveetha School of Engineering, Saveetha Institute of Medical and Technical Sciences, Chennai, Tamil Nadu, India

⁷Department of Mechanical Engineering, Wolaita Sodo University, Wolaita Sodo, Ethiopia

Correspondence should be addressed to P. Kumaran; pkumaran2003et@gmail.com

Received 22 June 2021; Revised 15 July 2021; Accepted 10 August 2021; Published 24 August 2021

Academic Editor: Samson Jerold Samuel Chelladurai

Copyright © 2021 C. Suresh Kumar et al. This is an open access article distributed under the Creative Commons Attribution License, which permits unrestricted use, distribution, and reproduction in any medium, provided the original work is properly cited.

The effect of reinforcement phases on indentation resistance and damage behavior of glass/epoxy laminates was investigated in this research work. Woven glass fiber mat and nonwoven chopped glass fiber mat were used as fiber reinforcement phases for fabricating the laminates. Low-velocity impact and quasi-static indentation tests were performed on both laminates to investigate the contact behavior and energy-absorbing capability. Moreover, the acoustic emission (AE) technique was employed to monitor the indentation damage resistance. AE parameters including normalized cumulative counts (NCC), normalized cumulative energy (NCE), rise angle (RA), and felicity ratio (FR) were analyzed. The bidirectional laminates showed premature load drops and drastic changes in the normalized cumulative counts/energy profile in the beginning of loading cycles, indicating the development of macrodamage such as debonding/delamination. AE sentry function results of bidirectional laminates show longer P_{II} function at the earlier stages, associated with minor P_{III} function and greater P_{IV} function, indicating the continuous degradation and progression of damage. In contrast, the chopped laminates exhibited superior postimpact performance than the bidirectional laminates. The presence of randomly oriented fibres prevents the delamination crack propagation during compression loading, which was attributed with the increased residual compressive strength.

1. Introduction

Due to their unique properties, such as high specific strength and modulus, better temperature resistance, corrosion resistance, tailorability, and stability, fiber-reinforced polymer composite materials have been widely used in engineering applications such as aerospace, automobile, marine, and wind turbine industries. However,

impact/indentation-induced damage in laminated composite structures can result in a significant reduction of structural strength [1]. Many researchers have attempted the prediction of impact-induced damage in polymer matrix composites (PMCs). In most studies, the effect of impact velocity, incident energy, impact geometry [2], and fiber architecture [3, 4] has been investigated. Nevertheless, the low-velocity impact (LVI) is the most destructive for

PMC because the internal damage may not be seen during visual inspection, and also, it can cause significant reduction in strength. Furthermore, the damage caused by LVI is identical to that caused by quasi-static indentation (QSI) loading, which was experimentally proved by Kumar et al. [5] and Xiao et al. [6]. They concluded that loading speed had little effect on penetration energy. As a result, the method for calculating penetration energy may also be used in static testing [7].

Under LVI and QSI tests, several parameters such as peak force, incident energy, elastic energy, absorbed energy, and dent depth were used to evaluate impact- and indentation-induced damage. Due to better control of the maximum transverse force and more accurate direct measurement of out-of-plane displacement, the QSI test was successfully employed to replace LVI [8]. They concluded that the morphology of the damage and the absorbed energy were identical in both experiments. In the characterization of composite laminates, damage initiation and propagation are important factors to consider. ASTM D6264-12 standard [9] governs the QSI test of composite laminates, whereas the ASTM D7136-15 standard directs the LVI test of composite laminates [10]. However, further investigation is needed to fully understand the evolution of indentation-induced damage in composite laminates.

The effect of the reinforcement phase on indentation resistance and damage characterization is investigated by using online AE monitoring in this research work. For evaluating damage resistance in laminated composite materials, acoustic emission (AE) is a useful nondestructive testing (NDT) approach. When a material deforms or fractures, transient elastic strain waves are produced inside the material, causing AE [11, 12]. As a result, this approach may identify damage initiation and progression in composite laminates under loading in real time [13–16]. AE energy, amplitude, counts, rising angle (RA), duration, and peak frequency were utilized by Kumar et al. [17] to characterize damage mechanisms in glass/carbon/epoxy composite laminates. Only a few studies have used QSI loading with AE monitoring to simulate LVI behavior and evaluate damage initiation and progression [18].

AE parametric analysis was used to assess the resistance to indentation-induced damage in hybridized patch repaired glass/epoxy laminates [19]. However, based on the combination of mechanical strain energy stored in the materials and acoustic energy propagated by fracture events, the sentry function (SF) was computed for analyzing the amount of induced damage in laminated composites [20, 21]. This function was employed to investigate the damage development and estimate the residual strength of laminated composites subjected to out-of-plane loading. However, due to anisotropic behavior of composite laminates, it is a critical task to determine the damage progression and residual performance in glass/epoxy laminates with various reinforcing phases under out-of-plane and in-plane loading. The goal of this study is to employ an efficient AE-based comprehensive damage characterization technique to evaluate indentation-induced damage and

residual compressive strength in chopped and bidirectional GFRP composite laminates. However, acoustic emission (AE) parameters such as normalized cumulative counts (NCC), normalized cumulative energy (NCE), rising angle (RA), and felicity ratio were used to assess indentation damage resistance (FR). Furthermore, the relationship between mechanical strain energy and AE energy was employed to better understand the damage progression and residual compressive strength.

2. Experimental Procedure

2.1. Materials and Sample Preparation. Bidirectional E-glass fiber mats of 200 g/m^2 and nonwoven chopped E-glass fiber mats of 300 g/m^2 were employed as fiber reinforcements. The matrix material for both laminates was epoxy resin (LY556) with hardener (HY951) at a 10:1 ratio. The glass fibres were layered together, and rollers were used to better impregnate the fiber reinforcement with resin. In a 30 kN compression moulding machine, the laminates were allowed to cure for 24 hrs at room temperature under a pressure of 50 kg/cm^2 . A nominal thickness of $4.5 (\pm 0.25)$ mm was achieved with a stacking sequence of 16 layers of composite laminates. A water jet cutting machine was used to cut samples of size 150 mm long and 100 mm wide for the ASTM D6264-98(04) standard indentation test, ASTM D7136M-05 standard low-velocity impact test, and ASTM D7137M-12 standard compression after impact or indentation (CAI) test.

2.2. Drop Weight Impact (LVI) Testing. The laminates were impacted at a velocity of 3 m/s and nominal impact energy of 9.45 Joules using a Fractovis drop weight impact tester. Five samples were impacted for both configurations. The cross-head mass of the impacting plunger was 1.92 kg, and the hemispherical indenter had a diameter of 12.7 mm and a clamping force of 1000 N. The photograph of the falling weight impact tower used for testing is shown in Figure 1. The impactor was dropped at the center of the laminates. During the impact testing, parameters such as impact force, deformation, and impact energy were recorded.

2.3. Quasi-Static Indentation (QSI) Testing. Tinius Olsen UTM was used to perform quasi-static indentation (QSI) testing in accordance with the ASTM D6264-98(04) standard. The four corners of the rectangular samples were tightly secured on the fixtures, and then an indentation test was performed directly above at the center of the laminate as shown in Figure 2. With an aim of comparing the behavior of indented and impacted laminates, a series of indentation experiments were performed at a speed of 1 mm/minute. The identical hemispherical indenter was used for investigating indentation-induced damage resistance. Cyclic indentation tests were used to assess the progressive damage resistance of five different types of laminates. These experiments were carried out until three predetermined displacements were reached, namely, 5 mm, 6 mm, and 7 mm, respectively. During cyclic indentation,



FIGURE 1: (a) Fractovis instrumented impact tester. (b) Impact striker with the load cell. (c) Specimen holder, clamped during impact.

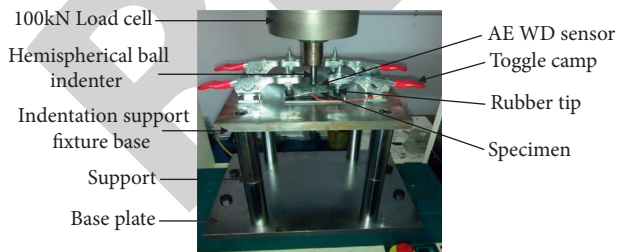


FIGURE 2: Quasi-static indentation (QSI) testing setup.

the parameters of peak contact force and indentation displacement were recorded. The incident energy, elastic energy, and absorbed energy parameters were derived from the received data. Five specimens were evaluated in each category, and the average of the results was used to interpret the data.

3. Compression after Impact and Indented (CAI) Testing

CAI testing was performed with a 100 kN Tinius Olsen UTM in accordance with ASTM D7137M-12 for determining residual compressive strength. For arresting the global buckling, the CAI specimens were clamped precisely on the fixture by adjusting four supporting plates. Stroke control was used to apply a compressive load at a displacement rate of 0.5 mm/minute. A data acquisition system recorded the force versus displacement history during the CAI test. The force-displacement curve was used to calculate the maximum failure load. CAI strength of the samples was calculated from the maximum failure load [22].

3.1. Acoustic Emission (AE) Monitoring. In this study, an eight-channel AE system (supplied by Physical Acoustic Corporation) with a sampling rate of 3 MHz and a 40 dB

preamplification was used. A 45 dB threshold was used to filter the ambient noise. AE measurements were made utilising two wideband (WD) sensors in a linear setup during QSI experiments. The nominal longitudinal distance between the two AE sensors was set at 100 mm. Three wideband (WD) sensors in a 2D planar location covering the indentation and impacted region were used in the CAI test with AE monitoring. These three sensors were arranged to make a 60 mm wide equilateral triangle. As a couplant, high-vacuum silicone grease was employed between the sensors and the sample. To determine the wave behavior and calibration of sensors, a standard pencil-lead break test was performed. The average wave velocity for bidirectional and chopped glass/epoxy was calculated to be 3228 m/s and 2830 m/s, respectively, using this method. The peak definition time (PDT) for bidirectional and chopped glass/epoxy in QSI tests was found to be 31 μ s and 35 μ s, respectively. The peak definition time (PDT) for bidirectional and chopped glass/epoxy in the CAI test was found to be 18 μ s and 21 μ s, respectively. The hit definition time (HDT) and hit lockout time (HLT) were set to 150 μ s and 300 μ s, respectively.

4. Results and Discussion

4.1. Load-Displacement Response. The typical force-displacement response of bidirectional and chopped glass/epoxy laminates subjected to out-of-plane loading is shown in Figures 3(a) and 3(b). Both glass/epoxy laminates were subjected to 5 mm indentation depth during quasi-static indentation loading and an impact velocity of 3 m/s during impact loading. In both out-of-plane loading conditions, the chopped glass/epoxy laminates exhibited significantly higher peak contact loads compared to the bidirectional glass/epoxy laminates. The plastic deformation (permanent dent) of chopped glass/epoxy laminates was about 0.49 to 1.3 mm, which was less than bidirectional glass/epoxy laminates. Similar trends were observed in the peak contact force and residual deformation for bidirectional and chopped laminates under both loading conditions (shown in Figure 3). This result evidences that the local bending resistance of laminates is significantly influenced by the fiber reinforcement phases [23, 24].

Similarly, the linear stiffness shows the laminates' capacity to sustain a central point load without local bending at the indentation location (due to the fiber reinforcements). The slope of the force-deformation curve before the initial load drop was used to calculate the linear stiffness of chopped and bidirectional glass/epoxy laminates. As indicated in Figures 3 and 4, the linear stiffness response of chopped glass/epoxy laminates was marginally higher than that of bidirectional glass/epoxy laminates.

4.2. Cyclic Indentation Loading. Cyclic indentation was performed on the chopped and bidirectional glass/epoxy laminates for predefined displacements of 5, 6, and 7 mm, respectively. The load-displacement behavior of chopped and bidirectional glass/epoxy laminates subjected to cyclic indentation is depicted in Figure 5. The rigidity of the

laminates was found to be quite high when they were transversely loaded with a steel ball indenter in cycle-1 (C-1) up to 5 mm. There was a considerable drop in stiffness when the laminates were subjected to cycle-2 (C-2) up to 6 mm. Furthermore, during cycle-3, there was a significant reduction in stiffness (C-3).

The peak load exhibited by bidirectional laminates was observed to decrease significantly with cyclic loading. In contrast, the chopped laminates exhibited similar peak load (1700 N \pm 100 N) for all the cycles attributing to the superior load-bearing performance. The residual deformation, on the contrary, was shown to significantly increase after cyclic indentation. The damage induced inside the laminates was intensified during cyclic indentation, causing severe damage accumulation/progression. The primary damage observed was matrix cracking, followed by delamination between the layers and fiber breakage due to bending at the nonimpacted side of the laminates. Ultimately, the laminates fail through local bending and penetration on the bottom surface. The effect of reinforcement phases on peak force and absorbed energy is depicted in Figure 6.

The increase in absorbed energy indicates the damage experienced by the composite laminates during cyclic indentation. The amount of energy absorbed is determined by the fiber reinforcement phase (architecture). As shown in Figure 6, chopped glass/epoxy laminates had a lower percentage of absorbed energy than bidirectional glass/epoxy laminates. This is due to the presence of randomly oriented chopped glass fiber reinforced in different orientations in the polymer matrix, which acted as a barrier to damage progression. The bidirectional laminates, on the contrary, show a significant increase in absorbed energy, indicating the buildup of severe delamination damage during cyclic indentation (shown in Figure 7).

5. Evaluation of Damage Propagation Using AE Activities

As shown in Figure 8, the indentation damage resistance of composite laminates was investigated using AE parameters including normalized cumulative counts (NCC), normalized cumulative energy (NCE), and rise angle (RA) during cyclic indentation loading and unloading. Three different slopes of NCC and NCE have been identified for measuring the damage progression based on the evaluation of indentation damage resistance. Stage A: the lowest slope with a low RA value (<17 ms/V) indicated microdamage but had no significant effect on the material stiffness. Stage B: macrodamage was discovered to have the steepest slope, with a medium value of RA (45 ms/V), resulting in material stiffness loss. Stage C: the steepest slope with the highest RA value (>45 ms/V) indicated the buildup of macrodamages, indicating catastrophic failure of the material.

When compared to the chopped laminates, the bidirectional laminates showed an early load drop (initial). This result shows that the onset of stiffness loss (damage initiation) was premature in bidirectional laminates. Figure 8 depicts the increasing trend of the RA value from the beginning of the loading to the greatest peak force achieved

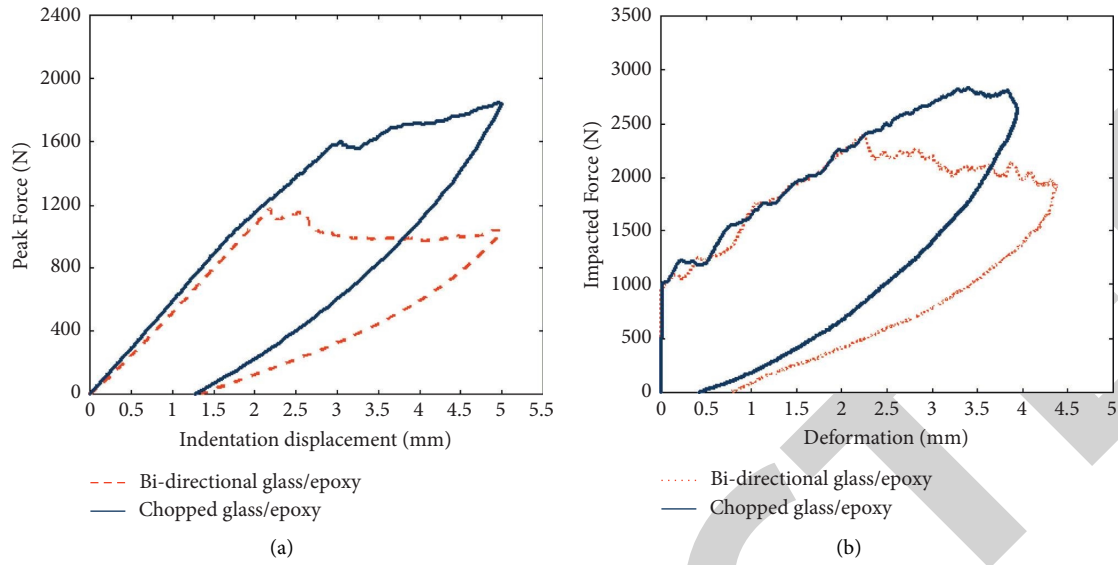


FIGURE 3: Force-displacement response of bidirectional and chopped glass/epoxy laminates: (a) QSI and (b) LVI loading.

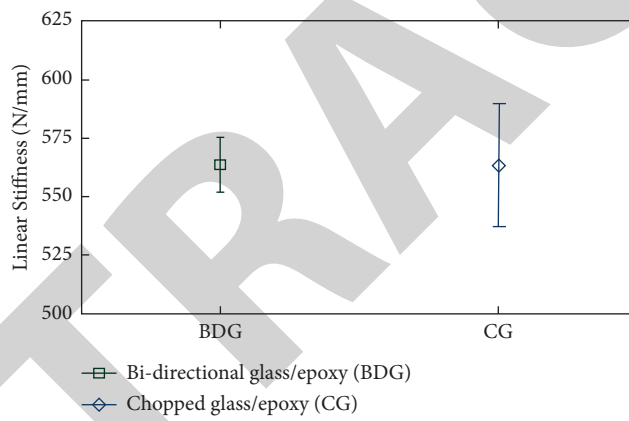


FIGURE 4: Linear stiffness for bidirectional and chopped laminates.

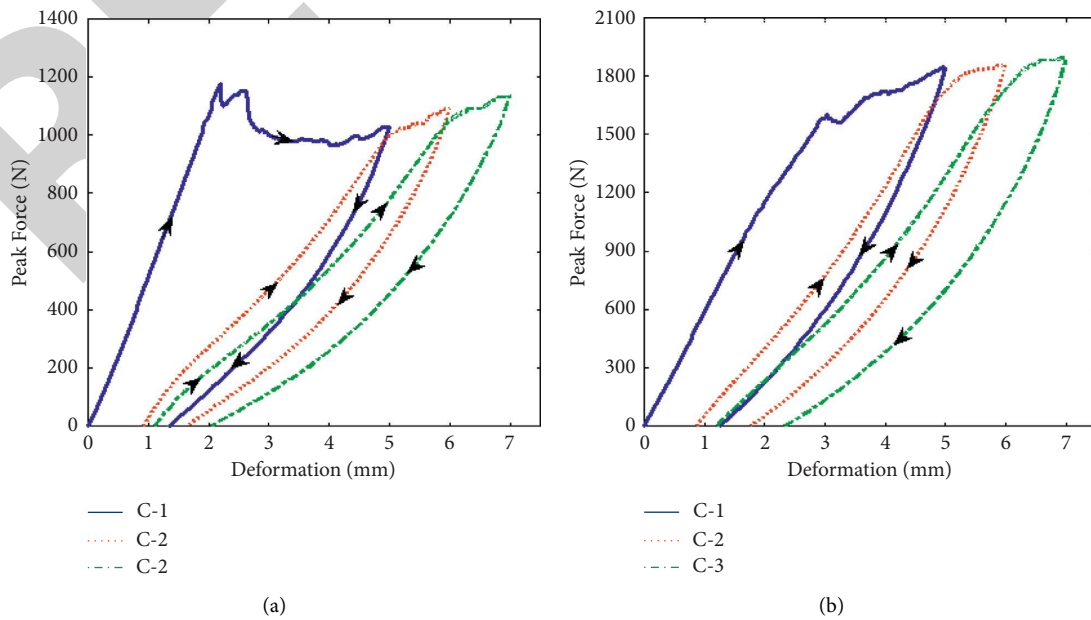


FIGURE 5: Effect of phases of reinforcement under cyclic indentation: (a) bidirectional glass/epoxy and (b) chopped glass/epoxy.

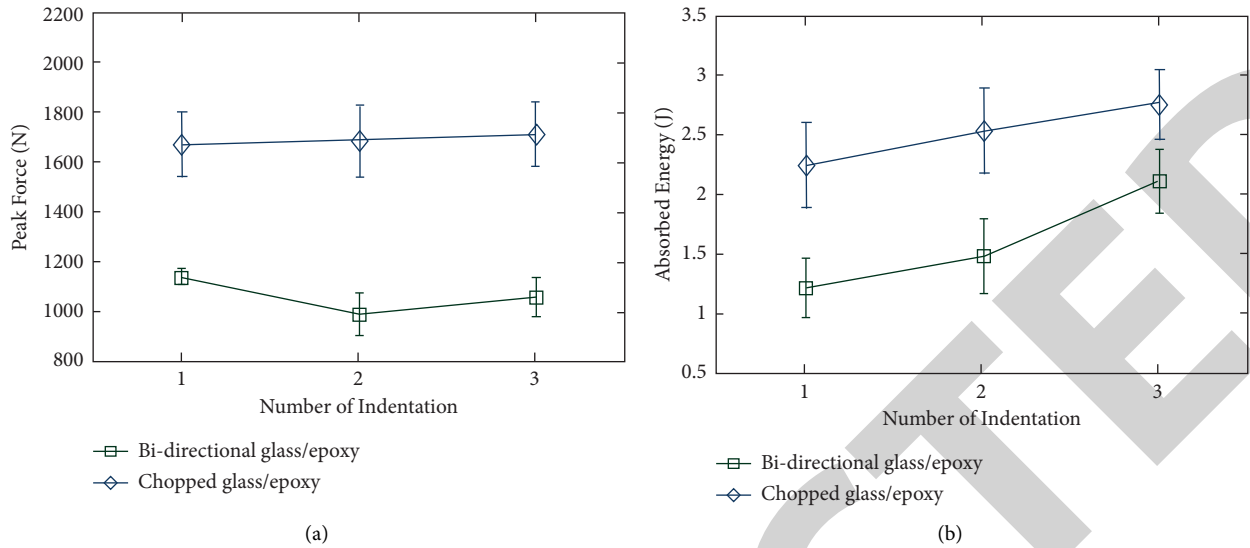


FIGURE 6: (a) Number of indentations vs. peak force and (b) number of indentations vs. absorbed energy for the phases of glass fiber reinforcement.

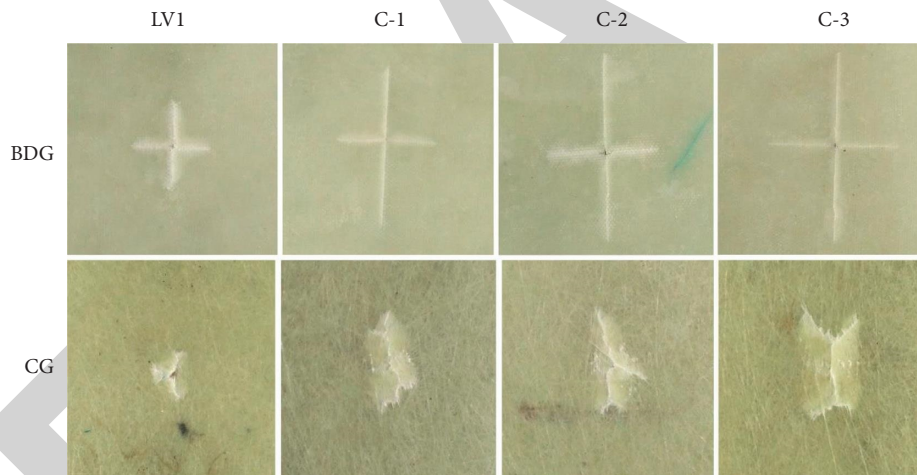


FIGURE 7: Damage pattern of bidirectional and chopped laminates subjected to low-velocity impact (LVI) and cyclic indentation.

during cyclic indentation. AE cumulative counts and energy, on the contrary, emerged at a faster rate, with RA values exceeding 45 ms/V (stage C) and a considerable drop in laminate stiffness during cyclic indentation. The profile of normalized cumulative counts (NCC) and normalized cumulative energy (NCE) for the chopped laminates shows similar trends. The bidirectional laminates, on the contrary, showed a dramatic change in the NCC/NCE profile, indicating the onset of macrodamage such as debonding/delamination at an early stage of loading cycles. In bidirectional laminates, the AE signals acquired during cyclic indentation were intense, severe damage initiation and accumulation.

For bidirectional laminates, the rise angle (RA) was observed to emerge from an earlier stage of loading. Also, the RA signals associated to stage B and stage C were found to be

severe, especially when attaining peak force. In contrast, the intensity of RA signals corresponding to stage A and stage B was dominant in chopped laminates attributing to the matrix cracking/debonding of randomly oriented fibres. This result revealed that, under cyclic out-of-plane loading, the resistance to indentation damage progression in randomly oriented chopped glass/epoxy laminates was higher than bidirectional glass/epoxy laminates.

6. Determination of Materials' Degradation

Felicity ratio (FR) is a tool for analyzing the degradation of materials under cyclic loads. The felicity ratio is the ratio of the load at which AE first appears within a cycle to the prior cycle's highest load (FR). For each cycle, a clear onset of the AE activity should be targeted in order to quantify FR [1, 5].

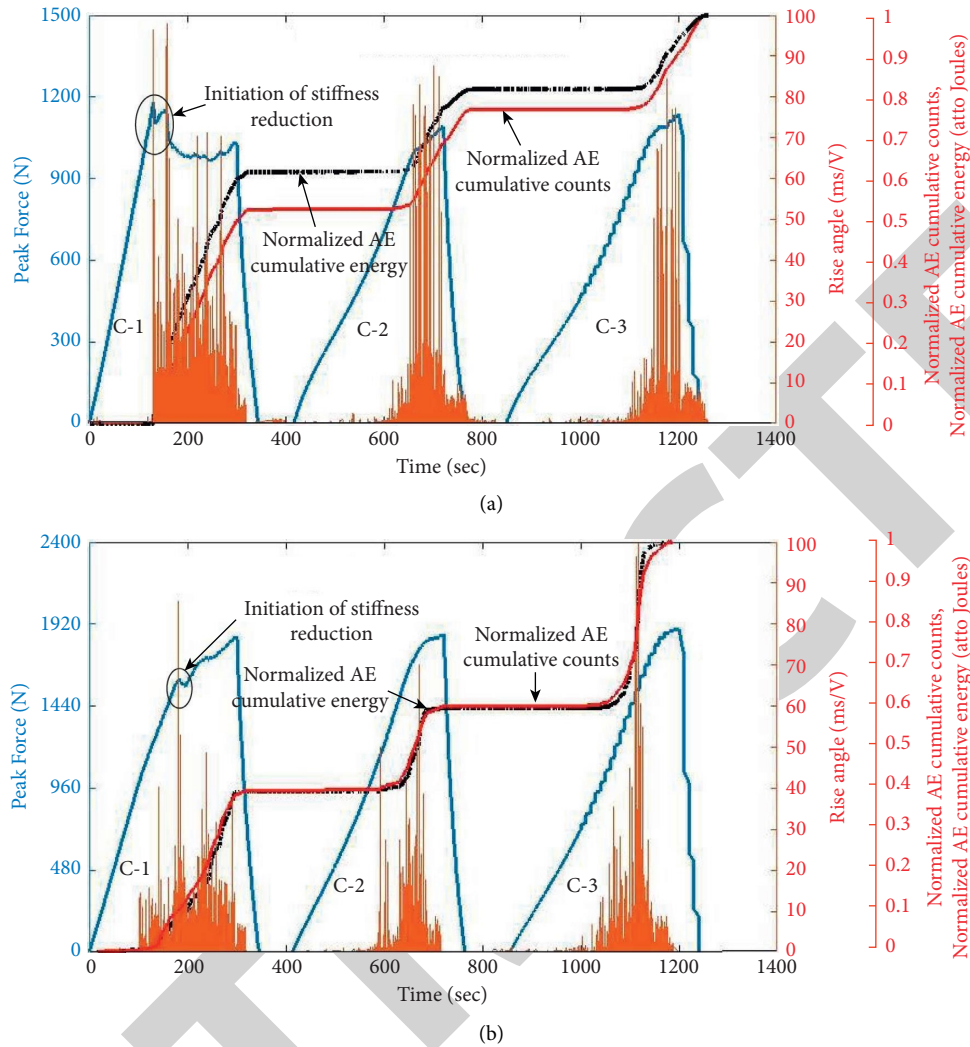


FIGURE 8: Representation of AE activity with damage progression during cyclic indentation: (a) bidirectional glass/epoxy and (b) chopped glass/epoxy laminates.

The loading point where there was considerable AE activity during reloading operations was carefully examined during cyclic indentation. Figure 8 shows the cumulative counts and energy of AE, as well as the loading history for a specific cycle.

The felicity ratio (above unity) indicates that the laminates are in good condition. As seen in Figure 9, the FR decreases from the undamaged state to the damage progression state. For chopped and bidirectional glass/epoxy laminates, FR decreased to 0.71 and 0.80 during the first-cycle indentation, respectively. For chopped and bidirectional glass/epoxy laminates, FR values were 0.59 and 0.41 at the second-cycle indentation, respectively. This significant decrease in FR with each subsequent cycle suggests that the laminates have deteriorated from their initial undamaged state. Under cyclic loading, the results show that chopped glass/epoxy laminates have a higher

FR. Another interesting result in the phases of reinforced laminates, the crack propagation, has been critically resisted by randomly oriented chopped glass fiber laminates as shown in Figure 9.

7. Damage Evaluation Using Mechanical and AE Energy

By combining mechanical and AE data, a thorough damage evaluation in composite laminates can be obtained. The sentry function (SF) can be evaluated as follows:

$$f(x) = \text{Ln} \left[\frac{E_s(x)}{E_a(x)} \right], \quad (1)$$

$$\text{Int}(f) = \int_{\Omega_{\text{AE}}} f(x) dx,$$

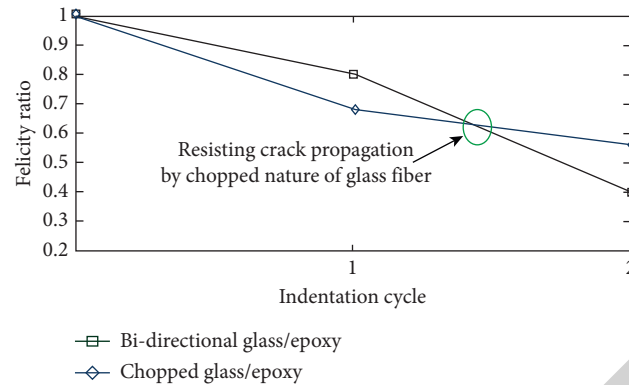


FIGURE 9: Measurement of damage resistance in the phase of reinforcement under cyclic indentation.

where E_S denotes the mechanical strain energy, E_a denotes the acoustic energy, and Ω_{AE} is the time interval between AE signals. Sentry function (SF) is represented by the four distinct behaviors (P_I , P_{II} , P_{III} , and P_{IV}). The growing phase (P_I) is linked to the storing of strain energy. The sudden drop phase (P_{II}) is defined as an abrupt release of accumulated strain energy as a result of severe damage occurrences. P_{III} is the constant phase, which is linked to progressive strain energy storage as a result of material degradation. The P_{IV} phase implies that the strain energy storing ability of the material is lower than the AE activity.

Figure 10 shows the sentry function behavior and load-displacement response of chopped and bidirectional glass/epoxy laminates. During indentation, the laminate's load resistance increases, followed by slope changes and sequential load drops, all of which contribute to significant delamination/fiber breakage damage mechanisms. In the laminates, the small P_{II} -type function indicates the occurrence of microdamage, while the large decrease of the P_{II} -type function denotes the beginning of macrodamage. This is because the initiation of macrodamage resulted in an instantaneous release of stored energy, resulting in an AE signal with high energy content. Different trends in the SF curve were observed after the initial loss of stiffness (onset of macrodamage). With the P_I -type function coupled with the minor P_{II} -type function, the chopped laminates had a higher slope.

However, at an early level of loading, the bidirectional laminates showed a dominant and longer P_{II} -type function. On further loading, bidirectional laminates show minor P_{III} function with increased P_{IV} function, signifying the continuous damage progression. These results indicated that the chopped laminates have higher indentation-induced damage resistance than bidirectional laminates. Bidirectional laminates were found to have a longer big fall than chopped laminates. This indicates that macrofailure in bidirectional laminates occurs rapidly, and the AE method is more sensitive in evaluating indentation damage resistance in these cases. The damage pattern and progression are clearly visible in the photographs of the laminates shown in Figure 7.

8. Estimation of Residual Compressive Strength

During service conditions, the laminated structures are frequently subjected to impact loading events. Low-energy impact usually causes local indentation, matrix cracking, fiber-matrix debonding, and delamination, while high impact energies cause dominant delamination/fiber breakage. The presence of such damages in a composite structure reduces mechanical properties dramatically, particularly residual compressive strength. Hence, it is essential to assess the postimpact performance of the composite laminates by conducting compression after the impact/indentation test according to ASTM D7137M-12 standards [13, 22]. Figure 11 depicts that, as the number of indentation events increases, the residual compressive strength decreases. Furthermore, postimpacted (LVI) laminates had a greater residual compressive strength than indented (QSI) laminates. In comparison to QSI samples, LVI samples showed less delamination and significantly more intralaminar fracture [1, 5].

Based on the consideration of different phases of reinforcement, chopped laminates offered greater residual compressive strength than bidirectional laminates. The randomly oriented glass fibres in the laminate hindered the delamination crack propagation under compression loading, which resulted in improved strength. However, as depicted in Figure 12, bidirectional laminates possess a higher percentage drop in residual compressive strength. When woven laminates are subjected to impact loading exceeding the threshold energy, severe delamination occurs, and the in-plane fibres in the warp/weft direction are significantly ruptured. During compression loading, the failure begins prematurely at this impact damage region, followed by unstable crack propagation over the sample width, and finally, fiber microbuckling causes ultimate rupture.

The extent of indentation-induced damage for chopped laminates was less than bidirectional laminates as depicted in Figure 7. Through interfacial debonding, the presence of chopped fibres in various directions

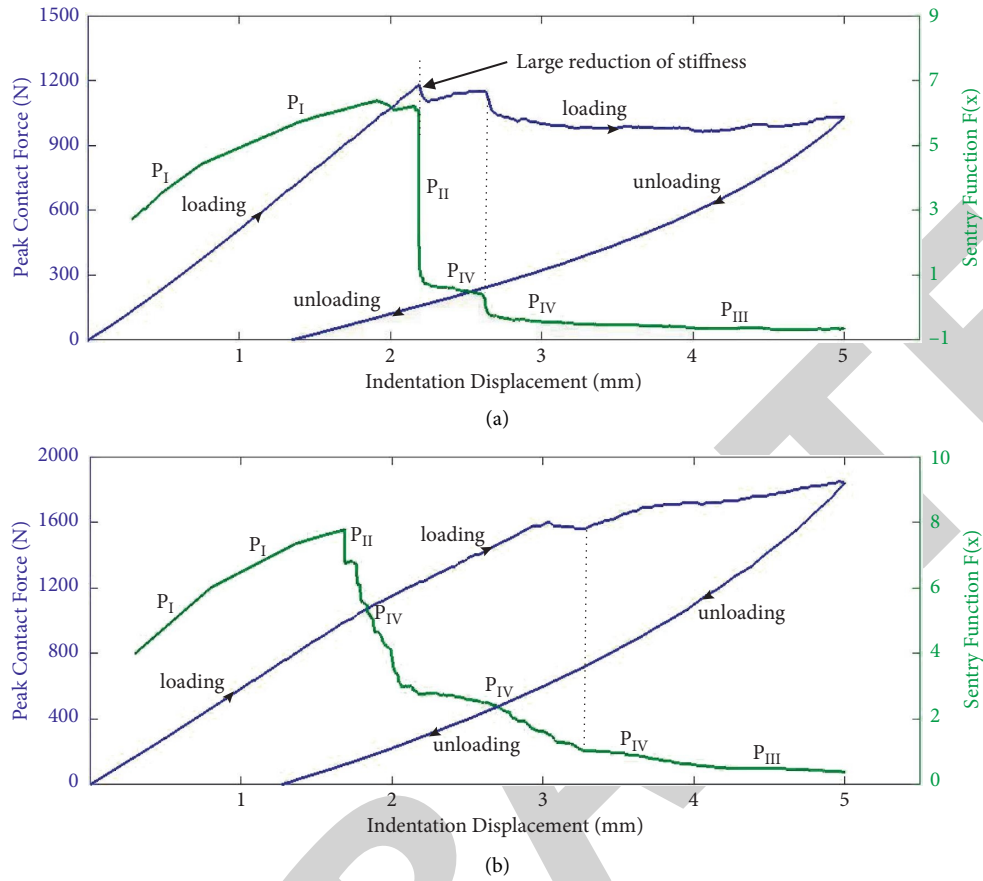


FIGURE 10: Load-displacement response and sentry function: (a) bidirectional glass/epoxy and (b) chopped glass/epoxy laminates.

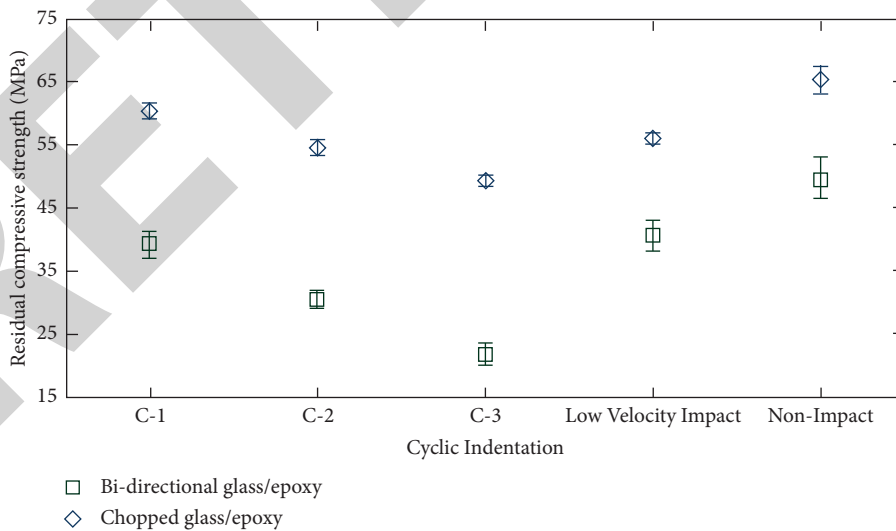


FIGURE 11: Residual compressive strength of bidirectional and chopped laminates.

enhances crack nucleation and crack propagation, resulting in steady damage progression. The randomly oriented chopped fibres in the polymer matrix possess

high intralaminar fracture toughness which attributes to the enhanced postimpact residual compressive strength.

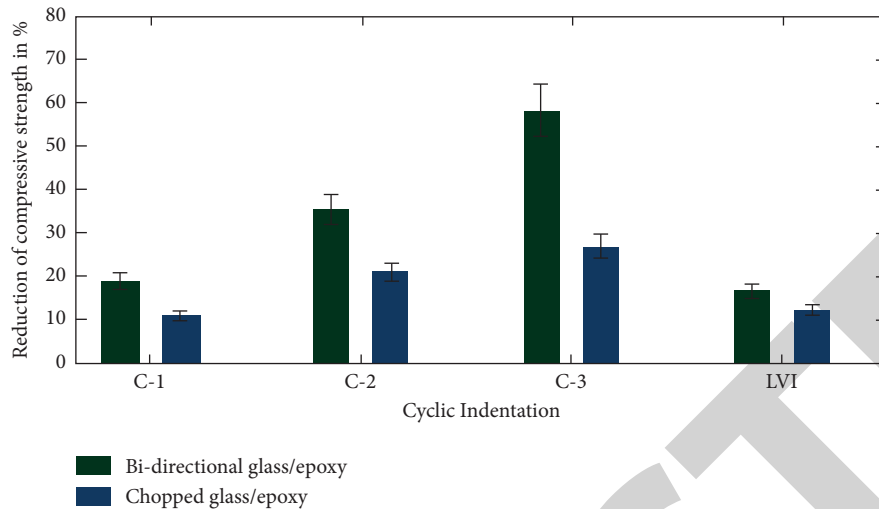


FIGURE 12: Percentage reduction of compressive strength of bidirectional and chopped laminates.

9. Conclusion

The effect of reinforcement phases on low-velocity impact response and quasi-static indentation behavior of laminates was investigated in this research work. Two phases of fiber reinforcements, one bidirectional E-glass fiber mat and the other nonwoven chopped E-glass fiber mat, were used for fabricating the glass/epoxy laminates. Low-velocity impact and quasi-static indentation tests were performed on both laminates to investigate the contact behavior and energy-absorbing capability. The goal of this study is to use AE monitoring to assess indentation damage resistance and quantify the extent of damage induced under transverse loading. The conclusions were drawn as follows:

- (i) The local indentation resistance of the chopped glass/epoxy laminates is significantly higher than that of the bidirectional glass/epoxy laminates.
- (ii) During cyclic indentation, dominant reduction in contact stiffness and increase in permanent dent evidence severe damage accumulation/progression. At the earlier stage of loading cycles, the bidirectional laminate showed premature load drops and steep change in the normalized cumulative counts/energy profile, attributing to macrodamage initiation, such as debonding and delamination.
- (iii) AE sentry function results of bidirectional laminates show longer P_{II} function at the earlier stages, associated with minor P_{III} function and greater P_{IV} function, indicating the continuous degradation and progression of damage. Therefore, AE techniques confirmed to be an effective tool for determining the progression of damage in composite structures.
- (iv) In all the cases, chopped glass/epoxy laminates exhibited higher residual compressive strength compared to bidirectional laminates. The

inclusion of randomly oriented glass fibres, which prevent delamination fracture propagation under compression loading, was attributed with this improvement.

Data Availability

The data used to support the findings of this study are included within the article. Should further data or information be required, these are available from the corresponding author upon request.

Disclosure

This research was performed as a part of the employment of Wolaita Sodo University, Wolaita Sodo, Ethiopia.

Conflicts of Interest

The authors declare that there are no conflicts of interest regarding the publication of this paper.

Acknowledgments

The authors thank the Department of Aerospace Engineering, Madras Institute of Technology (MIT), Chennai, India, for providing experimental facilities to complete this research work. Also, they appreciate the support from Wolaita Sodo University, Ethiopia.

References

- [1] C. S. Kumar, V. Arumugam, and C. Santulli, "Characterization of indentation damage resistance of hybrid composite laminates using acoustic emission monitoring," *Composites Part B: Engineering*, vol. 111, pp. 165–178, 2017.
- [2] C. Atas and D. Liu, "Impact response of woven composites with small weaving angles," *International Journal of Impact Engineering*, vol. 35, pp. 80–97, 2008.

Retraction

Retracted: Development of Smart Sensing Technology Approaches in Structural Health Monitoring of Bridge Structures

Advances in Materials Science and Engineering

Received 26 December 2023; Accepted 26 December 2023; Published 29 December 2023

Copyright © 2023 Advances in Materials Science and Engineering. This is an open access article distributed under the Creative Commons Attribution License, which permits unrestricted use, distribution, and reproduction in any medium, provided the original work is properly cited.

This article has been retracted by Hindawi, as publisher, following an investigation undertaken by the publisher [1]. This investigation has uncovered evidence of systematic manipulation of the publication and peer-review process. We cannot, therefore, vouch for the reliability or integrity of this article.

Please note that this notice is intended solely to alert readers that the peer-review process of this article has been compromised.

Wiley and Hindawi regret that the usual quality checks did not identify these issues before publication and have since put additional measures in place to safeguard research integrity.

We wish to credit our Research Integrity and Research Publishing teams and anonymous and named external researchers and research integrity experts for contributing to this investigation.

The corresponding author, as the representative of all authors, has been given the opportunity to register their agreement or disagreement to this retraction. We have kept a record of any response received.

References

- [1] A. Sivasuriyan, D. S. Vijayan, A. LeemaRose et al., "Development of Smart Sensing Technology Approaches in Structural Health Monitoring of Bridge Structures," *Advances in Materials Science and Engineering*, vol. 2021, Article ID 2615029, 14 pages, 2021.

Research Article

Development of Smart Sensing Technology Approaches in Structural Health Monitoring of Bridge Structures

Arvindan Sivasuriyan ^{1,2}, D. S. Vijayan ³, A. LeemaRose ⁴, J. Revathy ⁵,
S. Gayathri Monicka ⁶, U. R. Adithya ⁷, and J. Jebasingh Daniel ⁸

¹AarupadaiVeedu Institute of Technology, Vinayaka Missions Research Foundation, Paiyanoor, Chennai 603104, India

²Anand School of Architecture, Chennai 603103, India

³Civil Engineering, AarupadaiVeedu Institute of Technology, Vinayaka Missions Research Foundation, Paiyanoor, Chennai 603104, India

⁴SRM Valliammai Engineering College, Chennai, Tamil Nadu, India

⁵Civil Engineering, B.S. Abdur Rahman Crescent Institute of Science and Technology, Chennai, Tamil Nadu, India

⁶EEE, SRMIST Ramapuram, Chennai, Tamil Nadu, India

⁷KTH Royal Institute of Technology, Stockholm, Sweden

⁸Department of Civil Engineering, Hawassa University, Hawassa, Ethiopia

Correspondence should be addressed to D. S. Vijayan; vijayan@avit.ac.in

Received 14 July 2021; Revised 26 July 2021; Accepted 30 July 2021; Published 20 August 2021

Academic Editor: Samson Jerold Samuel Chelladurai

Copyright © 2021 Arvindan Sivasuriyan et al. This is an open access article distributed under the Creative Commons Attribution License, which permits unrestricted use, distribution, and reproduction in any medium, provided the original work is properly cited.

In recent years, immense development in Structural Health Monitoring (SHM) of bridges helps address the life span and reliability of bridge structure at contrasting phases of their service life. This article provides a detailed understanding of bridge monitoring, and it focuses on sensors utilized and all kinds of damage detection (strain, displacement, acceleration, and temperature) according to bridge nature (scour, suspender failure, disconnection of bolt and cables, etc.) and environmental degradation under static and dynamic loading. This paper presents information about various methods, approaches, case studies, advanced technologies, real-time experiments, stimulated models, data acquisition, and predictive analysis. Future scope and research also discussed the implementation of SHM in bridges. The main aim of this research is to assist researchers in better understanding the monitoring mechanism in bridges.

1. Introduction

Civil engineering structures include buildings, bridges, and dams that are beginning to fail from original quality once constructed, and the usage of buildings and infrastructures is unavoidable to the whole world. Therefore, it is necessary to know about the functioning of structures in terms of their life span and usage level. Excess dynamic forces such as earthquakes, heavy wind, environmental changes, and heavy goods-vehicle must track the structural integrity and detect the damage and frequently referred to as structural health monitoring [1]. The main motive of structural health monitoring (SHM) is to evaluate the performance and identify the bridge's physical state and other structures [2].

SHM of the bridge structure is an essential topic among researchers concerning the bridge structure, and the most contemporary studies contain monitoring of dynamic behavior, strain, displacement, acceleration, temperature, and loads. SHM is purely dependent on sensors and their applications. Bridge structures consist of wired and wireless sensor networks, which help monitor the structure and provide data accurately. The placement of sensors in bridge structure will deliberately depend on previous practice. The SHM of the bridge structure is necessary to improve and deserve development in research and development.

This article outlines the proposed policy and plan in SHM of bridge structure and provides valid information about current techniques and technologies in bridge

structures. The applicable bridge structure properties, parameters, loading, and conditions are conferred and discussed. Monitoring of bridge structure has some operational strategies, including selecting sensors, deploying, tools and automated technology, storage, and transmission. SHM in the bridge is highly dependent on automated strategies that are more advanced and easier to use. Therefore, those techniques have been discussed. However, techniques that are related to visual inspection are not examined. This article also addresses feature extraction and advanced data processing in SHM. Structure prediction will assist in anticipating damage to any structure at an early stage. For example, depending on the commutation of automobiles and loads on the bridge, the lifespan of a bridge with loads based on day-to-day traffic may be projected. Similarly, using predictive analysis, the load sustained by any structure over time may be used to determine the building's life span. Sensors installed at various locations (joints) of the structures may be used to monitor the structures.

The sensor receives information from the structure that will be monitored for health. The sensor will be selected based on the database's requirements. The information will instead be conditioned by amplification and filtering. The analog signal data will be transformed into digital form for computational processing in the next stage of data acquisition (DAQ). The processed data is then saved or sent to the appropriate access point.

2. Process of Structural Health Monitoring

In recent years, SHM of civil structures has been a critical topic for research. SHM helps to detect the damage of a structure, and it also provides early caution of a structure that is not in a safe condition for usage. Civil infrastructure like bridges gets damaged with time, and the reason for the damage is heavy vehicles, loading environmental changes, and dynamic forces such as seismic. These types of changes mainly occur at existing structures constructed long ago, and various methods will detect that damage. The strategy of SHM involves observing the structure for a certain period to notice the condition of the structure and the periodic measurements of data will be collected, and the features of data will be extracted from these computation results, and the process of analysis can be done with the help of a featured data to find out the present-day health of the structure. The information collected from the process can be updated periodically to monitor the structure and based on the data collected through monitoring a structure, and the structure can be strengthened and repaired, and rehabilitation and maintenance can be completed [3].

The nondestructive test will be the primary motive for SHM to evaluate the state and conditions of the structure in its lifetime, and the vital role of the SHM is the ability of the system to predict the health status of the structure [4]. SHM can be applicable for few factors in bridge structure to detect the quality of the problem at the right time, bearing capacity of the bridge structure to be checked and technical procedures to be followed to improve bearing capacity; reinforcement and risk factors should be considered based on

test results [5]. Structural problems may occur due to the low-quality execution during construction, lack of inspection and maintenance, and poor design, making the structure functionally low compared to its required strength [6]. To find the natural frequency and corresponding mode shapes of a structure, the global dynamic technique is used, and this technique will display the correct information about the position and sharpness of the damage [7]. The position and severity of cracks will be predicted using baseline data in the model properties [8]. Vibration based SHM technique plays a vital role in both static and dynamic response of a structure, and this technique will indicate the physical properties of a structure such as cracks, loosening and stiffness reduction, and magnitude estimation [9]. SHM of structure purely depends on sensor operations and Principal Component Analysis (PCA) [10]. Stiffness reduction in structure is also verified by using a finite element model with the help of measured static and dynamic responses [11]. The analysis process can be done using finite element modeling (FEM) software, which is very powerful and shows accurate damage prediction results [12]. Overview of the SHM process is portrayed in Figure 1.

3. Damage Analysis and Prediction

Developing and developed countries should come up with modern structures using modern technologies. SHM plays a vital role among the recent technologies in civil engineering, and it plays an essential role in detecting damage.

There are four stages of damage prediction:

- Stage 1: identification of damage present in the structure
- Stage 2: geometric location of the damage should be analyzed
- Stage 3: critical condition of the damage should be analyzed
- Stage 4: predicting the remaining life span of the structure [13]

4. Needs for SHM

- (1) Structural damage can be detected on time using SHM that leads to immediate action
- (2) Design parameters should be confirmed without flaws because SHM is based on parameters affected by statistical variation and uncertainty
- (3) Monitoring the design validation, stress, and external loads and understanding the structural behavior can be simplified by SHM [14]
- (4) SHM is an effective way to know about the actual behavior of the structure, and it helps to enhance the future design of the structure
- (5) SHM helps to predict the quality standard of the structure due to continuous monitoring
- (6) Early prediction of damages helps to save many people's lives and give a possible solution to control the damages

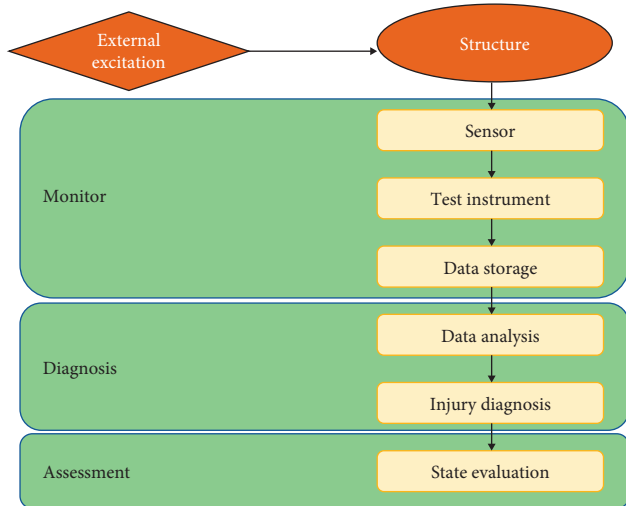


FIGURE 1: Overview of SHM.

- (7) SHM plays a vital role in studying hidden information
- (8) Usage of the SHM technique will avoid catastrophic failure and allow maximum use of structure
- (9) The structure can be maintained well for both long terms and short terms
- (10) SHM plays an integral part in reducing human error and improving the reliability and safety of a structure
- (11) SHM is cost consumption comparing to general manual maintenance [15]

To spot the external sign of damage in structures, some techniques such as ultrasonic, radiography, acoustic, eddy currents, thermal magnetic field, or electromagnetic impedance can be used to predict the intensity of the damage. If needed, test samples may be collected and tested in the laboratory. However, critical parts of the structure may not be approached in this technique, and it is also hard and cost-effective, and it largely depends on the visual inspector with a high level of experience.

Many kinds of research have been discussed in the past decades to automate the visual inspection to predict the damage of the structure quicker and as an alternative is SHM methods which have intelligent materials such as piezoelectric, fiber optic, and shape memory alloys to work innovative according to environmental changes:

- (1) Global dynamic techniques in SHM
- (2) Electromechanical impedance (EMI) Technique in SHM

5. Global Dynamic Technique

According to this technique, the structure will be tested under the low-frequency stimulation, and this results in some vibrations responses such as velocities, acceleration, and displacements which are noted, and then few modes shapes and corresponding natural frequency have been

determined. The health of the structure can be predicted by comparing baseline parameters and current parameters. The disadvantage of this technique is its low sensitivity to elemental damage.

6. Electromechanical Impedance (EMI) Technique in SHM

In this technique, the structure is embedded with a piezoelectric (PZT) sensors patch for monitoring purposes, and the sensor patch is the high-frequency range that forms the standard for monitoring the health of the structure [16].

7. Sensors Used in SHM

SHM technique purely depends on the sensors to monitor the structure, so different sensors can be used. There are many types of sensors used by the industry for structural health monitoring. Few are discussed in the following:

- (1) Piezoelectric sensors (PZT)
- (2) Fiber optic sensors (FOS)
- (3) Microelectromechanical systems (MEMS)
- (4) Acceleration sensors
- (5) Displacement sensors
- (6) Strain sensors
- (7) Temperature sensors

These sensors have been used according to the requirement. Sensors are used for quick evaluation for health monitoring of structure when damage occurs. Figure 2 shows a few critical sensors usage in SHM and its operating principle and applications.

Venugopal et al. adopted a PZT sensor for monitoring the concrete cube size $150\text{ mm} \times 150\text{ mm} \times 150\text{ mm}$ and PZT patch of size $10\text{ mm} \times 10\text{ mm} \times 10\text{ mm}$ to predict the deviations and damage in the concrete structure [17]. Jeong-Tae et al. adopted PZT and acceleration sensors to record the wind speed and vibration responses in a cable stayed bridge under two consecutive typhoons. With the help of vibration monitoring, tension force has been estimated and wireless monitoring system is described [18]. Kim et al. conducted another experiment with piezoelectric sensor-embedded smart skin to analyze the structure's health status using the wireless technique to estimate tension force and vibration using temperature effects [19]. Huynh et al. have observed through their experimental process that PZT size should be maximum to have a flexible section, and it helps to identify the geometric size of the task for detecting damage [20]. Figure 3 depicts five levels of damage in the degree of complexity and SHM performance.

Mujica et al. employed different method to perform statistical analysis by using baseline PCA model in order to collect the sensor information stored in the structure to compare with monitoring outcome [21]. Park et al. used PZT patch for outlier analysis framework to anticipate bolt loosening in multistory building [22]. Annamdas and Soh adopted a PZT transducer, and electromagnetic interference

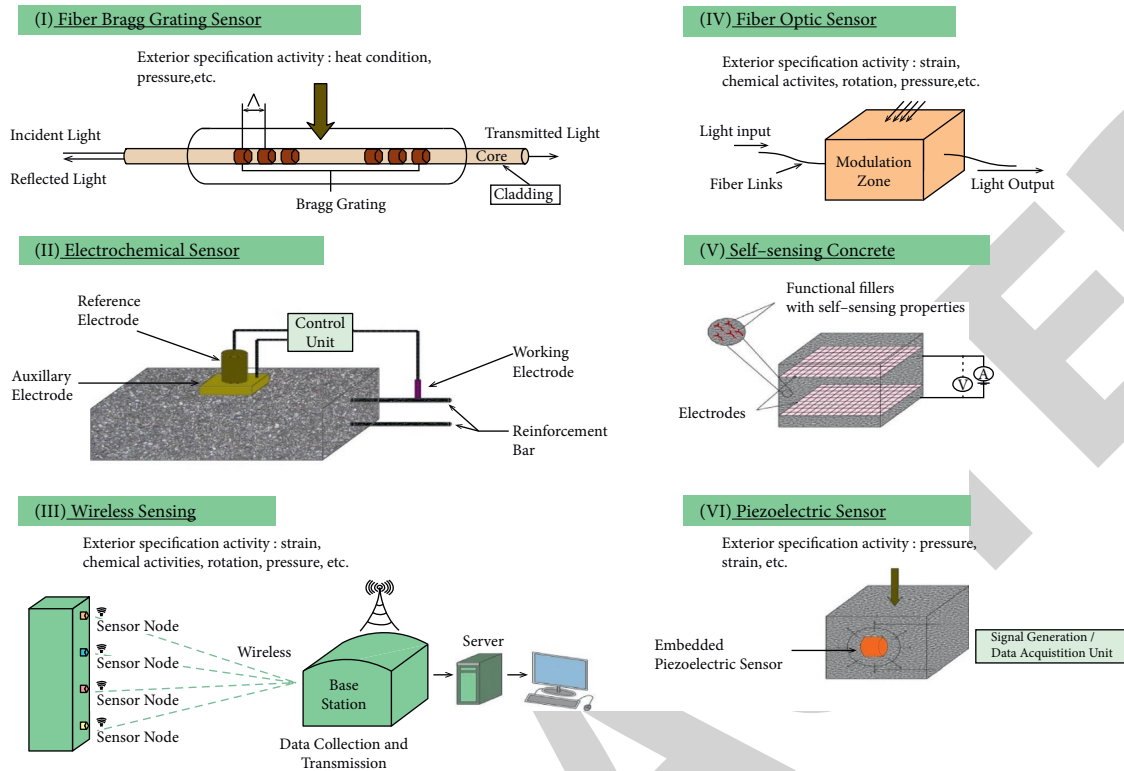


FIGURE 2: Some of the critical sensors used in structural health monitoring of a civil structure.

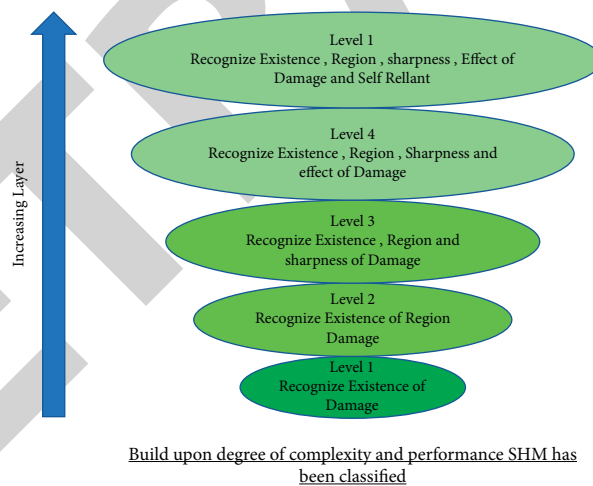


FIGURE 3: Levels of detecting damage in SHM.

(EMI) techniques have been used to monitor the structures. EMI models help analyze the structure, and the author reviewed the engineering structure that SHM techniques have done for the past two decades [23].

Park and Inman used advanced impedance-based SHM techniques to predict the damage, and variation in impedance will result in variation in structure. An autoregressive with Exogenous Variables (ARX) model has been constructed by measuring impedance data to analyze the structural damage with confidence [24]. Nguyen et al. carried out vibration and impedance tests for wind towers and developed a hybrid damage detection for wind towers to

monitor bolt loosening due to vibration [25]. Figure 4 shows phases of power supply for piezoelectric sensors. Figure 5 represents the setup for piezoelectric sensors.

Park et al. conducted an advanced experimental study on railway track damage detection by using a two-step support vector machine (SVM) method using piezoelectric sensors, and the study successfully established the optimal separable hyperplanes [26]. Thanh-Canh et al. also implemented an impedance-based damage detection method for civil structures. It applies a high-frequency impedance response and senses the temperature effect, severity of damage, and durability [27]. Radhika and Annamdas used EMI and

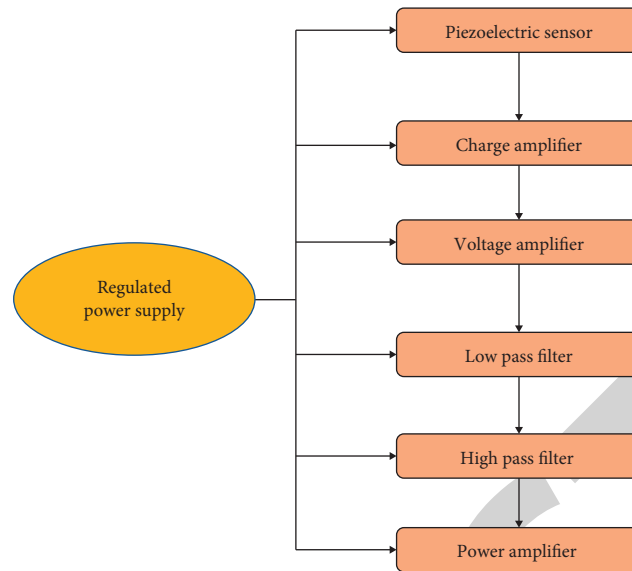


FIGURE 4: Power supply for piezoelectric sensors.

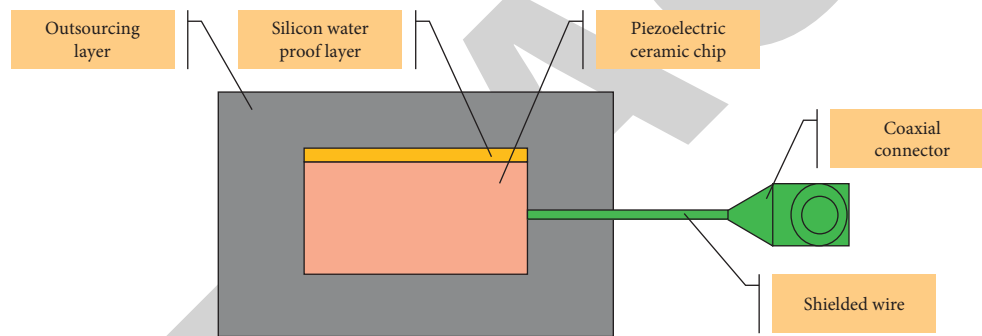


FIGURE 5: Piezoelectric sensors setup in SHM.

electrical impedance to monitor axial compression loading, fatigue cycling loading, and axial buckling in civil structures [28]. Yang et al. used both FBG and PZT sensors for SHM of tunnel structure. Both sensors can give an accurate response in the monitoring of a tunnel structure. It exposes thermal expansion or temperature variation and vibration monitoring [29].

Annamdas and Radhika have applied electromechanical impedance technique based SHM and also used two sensors such as PZT and macrofiber composite (MFC) for concrete structure, timber structure, and concrete specimen [30]. Annamdas et al. adopted the EMI technique to check the level of stress and damage occurrence possibility in concrete and aluminum specimens in SHM [31]. Annamdas and Soh used the EMI technique with PZT sensors to predict the damage of structure using 3D model and root means square deviation (RMSD) methods for experimental investigation [32]. Suresh et al. used the EMI technique for SHM and nondestructive evaluation techniques applies two PZT sensors sizes, $10\text{ mm} \times 10\text{ mm} \times 0.15\text{ mm}^3$ and $10\text{ mm} \times 10\text{ mm} \times 0.15\text{ mm}^3$, which were used to pledge to the exterior portion of the two aluminum blocks sizes $48\text{ mm} \times 48\text{ mm} \times 10\text{ mm}^3$ for monitoring [33]. Cunha and

Caetano used piezoelectric sensors to identify the damage in civil engineering structure, and experimental model analysis techniques have been obtained [34]. Figure 4 shows phases of power supply for piezoelectric sensors.

Suresh et al. employed cost-intensive impedance analyzers (LCR) meters for practicing EMI techniques with some low-cost equipment such as a digital multimeter and function generator. LCR measurements provide more accuracy compared to results, and excellent reports have been generated [35]. Huynh et al. proposed an EMI for monitoring prestressed tendon anchorages, and temperature effect has good accuracy using PCA based algorithm [36].

Bado et al. presented multiple sensing points as an ideal method to detect deformation and strain by using Distributed Optical Fiber Sensors (DOFS), and the experimental investigation has been carried out in real time by applying load in seven parallel S500 steel reinforcements at 20 mm diameter of rebar [37]. Jayawickrema et al. conducted an experiment using concrete beam dimension of $100\text{ mm} \times 250\text{ mm} \times 1400\text{ mm}$ which was casted using M20 grade of concrete reinforced with 6 mm and 8 mm rebar for top and bottom reinforcement, respectively. The concrete beam was embedded with fiber Bragg grating sensors (FBG)

during casting, later examined under flexural loading up to 20 kN on a three-point bending position without a decrease in the structural strength. The FBG sensors are required to analyze the strain transfer. A finite element model was created by using FEA software ABAQUS, and the outcome of the analysis will be compared with experimental results [38].

Li et al. have presented a review of SHM of primary civil structures such as pile, buildings, pipelines, tunnels, dams, and bridges using fiber optic sensors and pointed out past obstacles. Auspicious investigation with collected information has been discussed. Fiber grating sensors are used to measure the strain displacements and cracks. The process of concrete deformation, shrinkage, period, and thermal swelling period has been monitored consistently and concluded that SHM using fiber optic sensors show remarkable results. It seems to offer an outstanding improvement in the future [39].

Minutolo et al. have carried out an actual time experiment on concrete beam dimension 1800 mm in length and 200 mm in breadth. The primary and distribution reinforcement consists of 12 mm dia and 8 mm dia, respectively, to measure the tensile and compressive axial strain using Brillouin Optical Time Domain Analysis (BOTDA). The variation in strain within the beam's cross section will be measured using four sensing fibers positioned along with the beam. BOTDA sensors hold a constant report of the structure during load time history with proper reading. It concludes that bending moment and neutral axis are proper, and BOTDA is considered a suitable sensor to monitor the beam's structural behavior [40].

Lopez-Higuera proposed a review article on fiber optics sensors in SHM. Sensors should validate by it because it is necessary to make sure the data provided by sensors will act as an actual behavior of the structure. Optical fiber sensors (OFS) techniques will be used for heavy structures such as bridge girder, tunnel, and pipeline. Acoustic sensing can also be predicted by OFS technology in industrial structures [41]. Ko and Ni discussed SHM systems for large-scale bridges to examine the damage and collapse. Optimal maintenance of structure has been discussed. Significant issues such as recent technological improvement in the bridges, data acquisition, and innovative sensing have been carried out. It also demonstrated the communications signal processing and sensing systems in bridge monitoring. The valuable information has been collected, and it will be helpful to predict the damage and improve the reliability, durability, and integrity of the bridge structure [42].

Barrias et al. presented a review exclusively in SHM using distributed optical fiber sensors (DOFS) for civil structure and examined all the data which has been discussed with accurate results [43]. Taheri presented a review article on five critical sensors in DOFS. Significant advantages and disadvantages of the five critical sensors were discussed, and it was pointed out that fiber optics and Bragg gratings sensors are widely used for SHM [44]. Shu has used piezoelectric ceramic sensors with cement paste to monitor the RCC structure and found that sensors work fine with a concrete structure and point out

that sensitivity varies according to the size and shape of the sensors [45]. Figure 6 represents various types in fiber optic sensors.

8. Analysis and Characteristics of SHM in Bridges

Zhang et al. have presented an overview of SHM for masonry arch bridges using penetrating radar (GPR) and interferometric synthetic aperture radar (InSAR) technologies. GPR contributes structural detailing, and InSAR helps to compute displacements in structure. InSAR research took nearly 21 months to predict the behavior of the bridge structure under both static and dynamic conditions [46]. Alamdari et al. have carried out real-time monitoring on the Sydney Harbor Bridge in Australia with 800 Jack arches and help predict the irregular responses using the *K*-means clustering algorithm [47]. Saleh et al. carried out real time with 135 laboratory experiments and in situ studies from 2000 to 2019 by using Noncontact Testing (NCT) technologies to monitor the structure easy and quick compared to general methods:

- (1) Environmental conditions and materials properties should be considered for GPR analysis
- (2) Terrestrial laser scanner (TLS) methods should be used for different environmental conditions for live traffic
- (3) For photogrammetric control, close-range photogrammetry (CRP) methods are used
- (4) Infrared thermograph (IRT) techniques are used to produce automated data processing algorithms [6]

Roy et al. have used a multihopped wireless sensor network (WSN) for SHM in Kando Bridge, Japan, to predict damage and its location [48]. Eshghi et al. have used Mahalanobis distance (MD) techniques to predict the damage by using piezoelectric sensors network. A surrogate model has been developed to determine the performance of the structure [49].

Rodrigues et al. carried out real-time monitoring in Leziria Bridge, a concrete bridge embedded with vertical displacement transducer and strain transducer based on FBG sensor category to identify cracks, displacement, and damage creep and shrinkage [50]. Chae et al. employed five types of 45 sensors wireless in suspension bridges using ZigBee and code division multiple access (CMDA) approaches for long-distance wireless communications. The monitoring process happened around three months from April 2007 to June 2007 in Yeongjong Grand Bridge [51].

Wan et al. adopted fiber optic sensors for three-span bridge monitored under both static and dynamic loading conditions and pointed out that accuracy level is higher to predict the shape of displacement [2]. Li et al. experimented using OFG sensors embedded with glass fiber reinforced polymer (GFRP-OFBGS) in Ebian bridge to identify the fatigue damage and dynamic response [52].

Chakraborty et al. have carried out a real-time experiment in a natural bridge located in Gliwice (Poland) using various embedded sensors combined for long-term

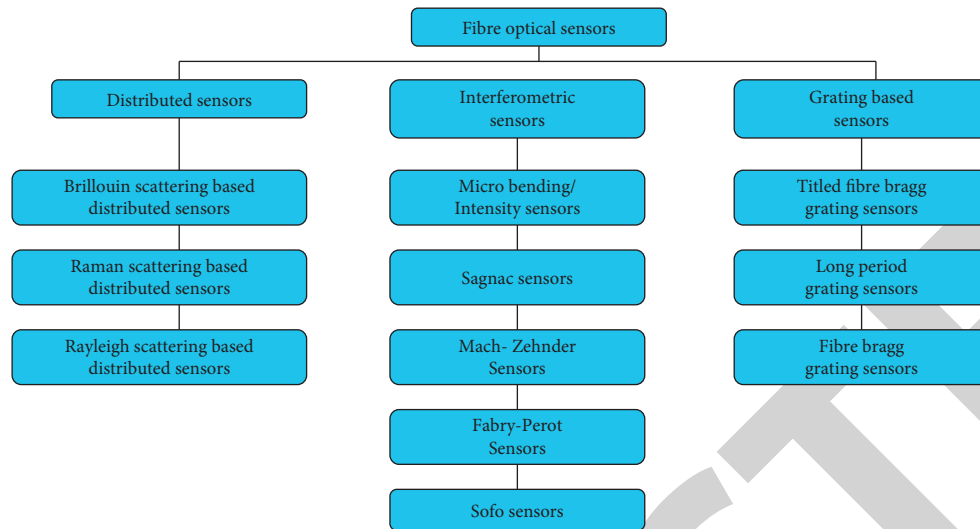


FIGURE 6: Fiber optic sensors in SHM.

monitoring of concrete structure to identify damage in fatigue assessment and strain measurements [53].

Mustaphaa et al. conducted an experiment using FBG sensors and Fiber Optic Sensors (FOSs) to predict loading data and severity of damage by using Convolution Neural Network (CNN) and support vector machine (SVM) techniques in small-scaled test bridge [54]. Pachón et al. carried out a real-time experiment in Historical Bridge of Posadas (Cordoba, Spain) by using optimal sensor placement approach to predict the damage. At the same time, genetic optimization techniques were used to find the dynamic responses and 3D models created for a better understanding of structural behavior [55]. Rodrigues et al. have monitored steel bridges to determine strain using FBG and experiment carried out in Eiffel Bridge, Portugal, and monitored for structural rehabilitation [56].

Chan et al. have used FBG sensors to monitor the Tsing Ma bridge in Hongkong, that is, 1378-meter-long suspension bridge, and it has been provided with 40 FBG sensors to monitor the structural health of a bridge [57]. Bremer et al. have used fiber optic crack sensors and fiber optic moisture sensors to detect crack and moisture and also a chemical reaction in concrete structure [58]. Iqbal and Khan et al. employed piezoelectric sensors in the wireless network to monitor hybrid bridge energy harvester (HBEH) to predict vibrations and damage [59]. Mei et al. have suggested two approaches, such as Mel-frequency cepstral coefficients (MFCCs) and PCA, and also dealt with vehicle bridge interaction (VBI) techniques by fixing sensors for detecting damage in both laboratory and numerical models that have been examined [60].

Wang et al. have carried out in real time in long-span cable-stayed bridge to record the dynamic behavior, acceleration, displacement, and variation in amplitude. Three modes have been considered to determine wind speed, and high frequency should be checked to determine the variation in acceleration [61]. Zheng et al. examined fatigue test and cyclic test in both loading and unloading conditions using

FBG sensors to monitor steel wire in bridge cable force [62]. Abruzzese et al. adopted embedded remotely handled Internet of Things (IoT) sensors to determine the accelerations and stresses in both laboratory and in situ experiments that have been carried out for current and future structures [63].

9. Necessity for SHM in Bridges

The functional supervision of bridges in real time is important for detailed risk assessment and taking measures. Damage surveillance is the sensor's primary input, while damage assessment and then use of information are the sensor's output data. These sensor data will be exploited to verify and determine the health of the structures. The output of this procedure is updated on a regular basis based on the structure's potential, and damage may be effectively treated. Dos Reis et al. employed local strain sensors to measure the strain data in suspension bridges by adopting a heuristic segmentation algorithm, and the statistical control of monitoring shows better results in the daytime. It would not disclose much during the night [64]. Shoukry et al. have carried out real-time monitoring in Star City Bridge in Morantown, WV. The measurement took around 306 meters over spans with 700 sensors for a long time monitoring lightweight bridge decks. The bridge performance has been monitored for 4 years to measure the stress, strain, and expansion joint using the LRFD approach [65]. Oskoui et al. carried out real-time monitoring on a five-span continuous precast posttensioned box girder bridge that is 332 meters long using Brillouin Scattering based on an optical sensor spot the microcracks appear in bridge [66].

Megid et al. used the acoustic emission (AE) technique using multiple sensors to detect dynamic behavior, fatigue, and the severity of cracks of steel bridge which are to be monitored [67]. Kister et al. carried out real-time monitoring on west mill bridge by using OFBG sensors. The bridge has been monitored for three years to detect the damage, and sensors survived successfully. The finite

element model is also used to predict the behavior of the structure [68]. Chilamkuri and Kone have experimented on varadhi road bridge to determine the displacement and vibration using accelerometers [69].

Whelan et al. have carried out real-time vibration monitoring on a long-term bridge using wireless sensors network (MEMS) to predict the vibration and other dynamic activities under traffic loads. Model analysis was also performed using a numerical simulation model [70]. Fujino et al. have carried out real-time monitoring on a bridge in Japan to determine the vibration, seismic isolation, checking of structural components, structural valuation, and damage disclosure by using advanced sensing technology and concluded that the technique serves several benefits to monitor a structure [71].

Moreu et al. used smart wireless sensors (WSS) to measure bridge response. Both field and finite element models have been discussed, and it managed to monitor the traffic load, strain, and vibration, and an experimental setup was made for a double track steel bridge located at the southern part of Chicago [72]. Lee et al. studied different approaches for damage detection called continuous relative wavelet entropy- (CRWE-) based DSI. The experiment has been conducted in truss bridge structure, and the approach is found as effective to identify the levels of damage [73].

10. Detection of Damage in Bridges

Damage detection in SHM is the process of observing and predicting the structures through time utilizing irregular distributed assessments. Numerical analysis of the damage sensitive choices extracted from the measured values, information on the current condition, and subsequent interpretation of the system health is delivered. Çelebi et al. examined the behavior of suspension bridges in Carquinez, CA, by using accelerometers to measure the damage. Dynamic behavior such as frequencies, damping, and modal analysis is examined. The frequencies were taken into account, showing 0.46 Hz and 0.98 Hz for modes and 0.39 translational frequencies. The torsion and longitudinal motions were also discussed [74]. Khoa et al. presented a case study by applying the SHM technique in Sydney Harbor Bridge using modern sensor technology to analyze data. Support Vector Machine (SVM) approach has been proposed for supervised and unsupervised learning to detect damage. Other methods such as Random projection (RP), PCA, piecewise aggregate approximation (PAA) were also used for SHM and concluded that RP with SVM methods works 200 times faster than other methods to detect damage accurately [75].

Li et al. discussed a Nonlinear Principal Component Analysis (NLPCA) approach in cable stayed bridge to determine the depth of the bridge scour by comparing both in-situ and FEM system it helps to determine the damage and dynamic behavior of a bridge structure. The SHM system was carried out at Hangzhou Bay Bridge [76]. Deng et al. experimented with long-span bridges to predict the damage and measuring deflection by adopting multi-sensors. MRLP

and Generalized Pareto Distribution (GDP) methods were compared to determine the vertical deflection [77].

Oshima et al. has conducted a damage detection experiment in a real bridge using a piezoelectric actuator to monitor fatigue, the variant in vibration, and severity and location of the damage. The experiment happened on steel bridge Hokkaido, Japan, using the Power spectrum density (PSD) approach [78]. Li et al. demonstrated a benchmark problem coordinated by the center of structural monitoring and control at the Harbin institute of technology. This method applies to both numerical models and site monitoring of long-span cable-stayed bridges. The main motive of this approach is damage detection of bridge girders, identifying cable stresses, fatigue, and cracks [79].

Dorvash and Pakzad has conducted a laboratory experiment for Golden Gate Bridge by adopting WSN to predict the damage [80]. Furinghetti et al. have discussed cloud computing techniques for data acquisition to detect the damage in structure to be recorded and this approach has been discussed in both software and hardware perspective, which refined at EUCENTRE foundation in Italy [81]. Perry et al. demonstrated a new approach by collecting the images of bridge quality, the severity of the damage, expansion of damage, and a spot of the damage has been monitored using the Unmanned Aerial Vehicles (UAVs) method that is a more convenient approach to access the health of the bridge [82].

Van Le and Nishio has studied Global Positioning System (GPS) monitoring to determine thermal damage of the long-span cable-stayed bridge. Finite element models were created to predict the damage and Autoregressive Integrated Moving Average (ARIMA) coefficient to collect the recorded response of the structure [83]. Neves et al. has applied Artificial Neural Network (ANN) with unsupervised learning access to detect the damage of bridge structure. Optimization in placing a sensor and strategy of detecting damage are considered [84]. List et al. carried out real-time monitoring of Tamar Bridge in UK. It is a suspension bridge 335 meters long, and in the year 2001, extra stay cables and cantilever decks have been provided. The bridge was monitored for around four years to measure damage, dynamic behavior, temperature effect, wind force, and displacement [85].

Fujino and Siringoringo presented an overview SHM of bridges in Japan by converting the monitoring process into three sectors. (i) Reduction of risk and vulnerability possibility has been discussed (ii) sensor technology and practicing techniques are studied (iii) prediction of damage, natural threat and climatic situations are monitored [86].

11. Predictive Analysis in Bridges

Predictive analysis plays a vital role in SHM of bridges, which helps predict the damage and evaluate the bridge's health condition. The predictive analysis approach helps to determine both static and dynamic characteristics of the bridges and also helps to predict the future problems of the bridges.

Xia et al. have carried out both in-situ test and laboratory experiment on two structures in the Tsing Ma Suspension Bridge that has a span of 1377 meters and Guangzhou new television tower is 600 meters height to predict the deviations in vibration and variations in thermal conditions [87]. Thomson et al. studied the economic crisis and maintenance of bridges in the USA by using predictive analysis in SHM and found that around 70000 bridges seem unsatisfactory in structural health and concluded that proper maintenance and rehabilitation are needed [88]. Keenahan et al. studied another method to predict the dynamic behavior of bridge structure by using accelerometers in a truck-trailer vehicle system approach to predict the vibration occurs due to vehicles and used numerical models with both Rayleigh damping hysteresis damping techniques and also concluded that both values are pretty similar [89]. Walia et al. studied damage prediction in a 100-year-old steel bridge with a deck using accelerometers. Time frequency and typical frequency methods have been approached [90]. The following conclusion has been made:

- (1) Power Spectral Density (PSD) diagrams are used to predict the amplitude and frequency
- (2) The first mode deviation in PSD helps to predict the priority in bridge retrofiting
- (3) Prediction of the damage and structural frequency of the bridge STFT approach is considered
- (4) Wavelet packet transform (WPT) methods were adopted to predict the flexibility in the modal response
- (5) However, WPT will not identify damage spot before retrofiting [90]

Van Le and Nishio has carried out SHM in a cable-stayed bridge in Vietnam by using (ARIMA) model, and data provided by GPS were used to predict the static responses and global deformation [91]. Nishio et al. have used a finite element model to predict the dynamic characteristics of the structure and the possibility of repairing bridges using data acquisition, model parameters, and the possibility of failure and damage prediction [92]. de Almeida Cardoso et al. carried out an unsupervised learning approach of predictive analysis using the wireless technique. Convictional sensors technology and other possible gadgets provide data to predict the irregular behavior of the structure in real time [93].

Nejad et al. adopted WSN to predict the structural response of the bridge piers from a seismic damage perspective. This study only has the prototype numerical model analysis with two receivers and six transmitters with a proposed model of six piers [94]. Sun et al. have carried out real-time monitoring on the long-span bridge in China and proposed three levels of prediction through case study (i) GPS measurement has been considered to predict the bridge health status (ii) with the help of cumulative displacement by viscous damper helps to determine expansion joints of the suspension bridge (iii) wind and vibration are predicted by installing mass dampers [95]. Adriaenssens et al. have carried out a case study in Strecker bridge to demonstrate a

piece of adequate information and data from a monitored bridge, and it helps to predict the damage and other health issues of a bridge structure [96].

Górski et al. presented a case study on highway cable-stayed Maxau Rhine Bridge to predict the dynamic behavior, mode shapes, natural frequency, accelerations in the bridge deck, and vibration [97]. Das et al. developed the ARMA model to predict the structure's response and compared under different parameters of the dynamic behavior of structure those study has been applied on real-time practice [98]. Tan et al. approached the "drive bridge inspection" concept to predict dynamic behavior and natural frequency using Fast Fourier Transform (FFT) and Vehicle Bridge Interaction (VBI) algorithm. Predicting of damage and acceleration also monitored using wavelet analysis techniques [99].

Diez et al. researched real-time in Sydney Harbor Bridge using supervised learning KNN based outlier detection methods to monitor bridge damage and detect damage [100]. Biswajit et al. have discussed some case studies on bridges and other structures. Control algorithm and reduction of dimension approaches have been investigated to predict the damage, vibration, damping, and other structural related problems, and, finally, piezoelectricity has been evaluated [101]. Santos et al. have used real-time data of Z-24 Bridge (Switzerland) and Tamar Bridge (UK) by using the Expectation-Maximization (EM) algorithm and Memetic Algorithm (MA) to detect the damages which increase the quality of the structure [102].

Miyamoto et al. have discussed a new method called "State Representation Methodology" (SRM) to monitor a bridge based on the previous data using the SVM approach to predict the dynamic characteristic of the bridge structure [103]. Yu et al. have performed both laboratory and numerical model analysis to monitor the bridge scour. Scour monitoring is essential in SHM, so the sensor's scour sensor and the sensors are easier to handle. This setup helps to predict the severity and depth of the scour [104]. Li et al. examined the deformity of wire breakage in bridge cable using AE techniques, and through waveguide, AE signal should be analyzed to identify the breakage of wire before it happened [105].

Fisher et al. carried out numerical model and lab experiment to predict the scour in the bridges, and the latest sensors are applied to measure the water and soil sedimentation level in the bridges [106]. Praksh et al. have carried out in real-time monitoring by using laboratory data to detect the damage of the structural components by using two-phase modeling and estimation framework approach. The main motive of the experiment is predicting the deflection so that the model of the parameters should be considered using the Bayesian approach [107]. Ballio et al. have carried out bridge management to Borgoforte bridge to monitor the complete response of the bridge such as wind, water, debris flow, loads due to traffic, possibility of scour at the pier, and other damage possibilities [108]. The predictive analysis supports businesses and suppliers in enhancing the performance and resistance of buildings to dynamic loads.

These dynamic loads will be based on current events, natural catastrophes, and disasters. SHM predictive analysis aids in determining the service life of reinforced concrete, which may contribute to a country's infrastructure projects based on existing structures [109].

12. Data Acquisition in Bridges

Data acquisition plays a vital role in converting the sensor data from bridge monitoring into digital presentation. It is an automated technique that helps collect the information from in situ experiment, and that information has been considered input data. It has been converted by using analog-to-digital converter (ADC), and finally using received information health status of the bridge structure has been evaluated.

Lorenzoni et al. adopted DAQ to analysis in the five different types of existing bridges such as Reinforced Cement Concrete Arch Bridge, Masonry Bridge, Multigirder RCC Bridge, Steel Box Bridge, and Steel Trusses Bridge have been monitored for one year to predict the model analysis, natural frequency and mode shapes to safeguard the bridge from structural failures [110]. Neves et al. applied data optimization techniques using Bayesian theorem to practice wise decision-making to ensure the safety of the bridge structure [111].

13. Future Scope of Research and Trends

SHM of bridges is an essential and more convenient technique compared to direct inspection, in particular for bridges, because most of the bridges around the world are almost 40 to 100 years old, and many of them are considered as a heritage structure, so bridge maintenance is considered as a principal requirement across the globe. Therefore, SHM is the most suited and consistent technique to detect all the variety of damages under static and dynamic loading. Here, some of the future scopes of research and trends have been discussed:

- (1) Advancement in sensor technologies is mandatory to increase the sensing capability and innovating sensing for long-term monitoring.
- (2) Damage should be identified according to the environmental changes, so the bridge monitoring should be appropriately abstracted and even more advanced concerning environmental changes.
- (3) Local and global level diagnostics are demonstrated in SHM to contribute the outstanding results along with local level NDE techniques help to identify spot and harshness of the damage, whereas global level techniques produce screening.
- (4) Robust optimization algorithm was adopted to measure the static and dynamic response of the structure.
- (5) It is essential to monitor creep and shrinkage behavior in bridge structure, but there is a lack and

imperfection due to the flaws in existing code, so it needs to be updated.

- (6) Advanced DAQ technique is needed to track the entire monitoring of data without any error.
- (7) Positives and negatives should be adequately communicated using the same technical terms worldwide to avoid mistakes.
- (8) Developing low-cost dense sensor arrays and innovative methods to powering the sensing system using energy were harvested from the structure's operational environment.
- (9) Digital information time-series, prediction modeling strategies can forecast future loads from the present condition of the system.

14. Conclusion

This article provides detailed information about the SHM of bridges and the application of SHM in different bridge structures, and various works reported have been discussed. Based on the detailed discussion, the following points have been specified:

- (1) Application and practices of key sensors such as FOS, MEMS, PZT, acceleration sensors, displacement sensors, strain sensors, and temperature sensors are studied. Fiber optic sensors and piezoelectric sensors are widely used sensors for the last two decades for both global and local monitoring, and the various possibilities of predicting damages have been discussed.
- (2) Bridge maintenance and rehabilitation according to current trends have been discussed concerning SHM techniques.
- (3) Bridges only acquire long-term monitoring processes so that sensors should have surviving capability under all kinds of environmental changes.
- (4) A wide range of technical knowledge is necessary to adopt SHM to understand the data and information provided by sensors.
- (5) Skilled human resources must install the sensor and another setup in situ to receive the data without any errors and obstacles.
- (6) Damage detection has been addressed in this proposed review article, and it is nothing more than a change in the boundary condition and system connection that would have an impact on the system's present or future performance. Damage may build up over time, resulting in fatigue or corrosion buildup in the system. These will change the stiffness, mass, or energy dissipation of a system, potentially altering the system's dynamic response.
- (7) The method of predictive analysis has been addressed, and it will be selected based on the structure, environment, operational limitations, and practicality of using the technique. The dynamic

reaction of a structure will be examined in relation to environmental changes.

This article provides a clear vision towards SHM of bridges with its recent technological developments based on the real-time in situ experiments, laboratory studies, and numerical model practices, and it also discussed DAQ and predictive analysis approach to detect the damages on bridge structure to provide the safety and reliability by adopting structural health monitoring technique.

Data Availability

The data used to support the findings of this study are available upon request.

Consent

No human subjects or animals were used for the research in this article. Hence, no consent to participate was required.

Conflicts of Interest

The authors declare that they have no known conflicts of interest or personal relationships that could have appeared to influence the work reported in this article.

Authors' Contributions

Conceptualization was performed by Arvindan Sivasuriyan, D. S. Vijayan, A. LeemaRose, and J. Revathy. Methodology was developed by Arvindan Sivasuriyan and S. Vijayan. Validation was performed by J. Revathy. Formal analysis was done by S. Gayathri Monicka and U. R. Adithya. Investigation was done by Arvindan Sivasuriyan and D. S. Vijayan. Data curation was performed by Arvindan Sivasuriyan, D. S. Vijayan, S. Gayathri Monicka, and J. Revathy. Original draft was written by Arvindan Sivasuriyan. Reviewing and editing were performed by D. S. Vijayan, J. Revathy, and S. Gayathri Monicka. Validation was done by Arvindan Sivasuriyan and D. S. Vijayan. Supervision was done by D. S. Vijayan, J. Revathy, S. Gayathri Monicka, and Jebasingh Daniel Joseph. All authors have read and agreed to the published version of the manuscript.

Acknowledgments

Research outcomes of the manuscript were supported by Aarupadai Veedu Institute of Technology, Chennai. We would also like to extend our thanks to the authors from Aarupadai Veedu Institute of Technology, Chennai, for providing the needed technical support.

References

- [1] P. C. Chang, A. Flatau, and S. C. Liu, "Review paper: health monitoring of civil infrastructure," *Structural Health Monitoring*, vol. 2, no. 3, pp. 257–267, 2003.
- [2] W. Hong, Z. Lv, X. Zhang, and X. Hu, "Displacement shape measurement of continuous beam bridges based on long-gauge fiber optic sensing," *Optical Fiber Technology*, vol. 56, Article ID 102178, 2020.
- [3] M. A.-B. Abdo, *Structural Health Monitoring History, Applications and Future*, Open Science, Manikonda Jagir, India, 2015.
- [4] J. Li and H. Hao, "Health monitoring of joint conditions in steel truss bridges with relative displacement sensors," *Measurement*, vol. 88, pp. 360–371, 2016.
- [5] C. Zhou, Y. Wu, G. Cui et al., "Comprehensive measurement techniques and multi-index correlative evaluation approach for structural health monitoring of highway bridges," *Measurement Journal International Measurement Confederation*, vol. 152, Article ID 107360, 2020.
- [6] S. Abu Dabous and S. Feroz, "Condition monitoring of bridges with non-contact testing technologies," *Automation in Construction*, vol. 116, Article ID 103224, 2020.
- [7] S. Bhalla and C. Soh, *Electro-Mechanical Impedance Technique for Structural Health Monitoring and Non-destructive Evaluation*, Indian Institute of Technology, Delhi, India, 2008.
- [8] M. I. Friswell and J. E. T. Penny, "Crack modeling for structural health monitoring," *Structural Health Monitoring*, vol. 1, no. 2, pp. 139–148, 2002.
- [9] F. P. Kopsaftopoulos and S. D. Fassois, "Vibration based health monitoring for a lightweight truss structure: experimental assessment of several statistical time series methods," *Mechanical Systems and Signal Processing*, vol. 24, no. 7, pp. 1977–1997, 2010.
- [10] H. Bin Huang, T. H. Yi, and H. N. Li, "Sensor fault diagnosis for structural health monitoring based on statistical hypothesis test and missing variable approach," *Journal of Aerospace Engineering*, vol. 30, no. 2, pp. 1–14, 2017.
- [11] S. Schommer, V. H. Nguyen, S. Maas, and A. Zürbes, "Model updating for structural health monitoring using static and dynamic measurements," *Procedia Eng.*, vol. 199, pp. 2146–2153, 2017.
- [12] Y. Yang, Y. Y. Lim, and C. K. Soh, "Practical issues related to the application of the electromechanical impedance technique in the structural health monitoring of civil structures: II. Numerical verification," *Smart Materials and Structures*, vol. 17, no. 3, 2008.
- [13] Rytter, *Aalborg Universitet Vibrational Based Inspection of Civil Engineering Structures Rytter*, Aalborg Universitet, Aalborg, Denmark, 1993.
- [14] T. Visalakshi, N. Kaur, S. K. Dhawan et al., "Recent advances in structural health monitoring based on EMI technique," in *Proceedings of the International Conference on Trends and Challenges in Concrete Structures*, vol. 11501, pp. 1–10, Ghaziabad, India, December 2013.
- [15] M. Singh, "Structural health monitoring using smart material and smart system," *Concrete*, vol. 3, no. 4, pp. 277–290, 2016.
- [16] R. Shanker, "An integrated approach for structural health monitoring rama shanker," vol. 196, Dr. thesis, Indian Institute of Technology, Delhi, India, 2009.
- [17] V. G. M. Annamdas, Y. Yang, and C. K. Soh, "Impedance based concrete monitoring using embedded PZT sensors," *International Journal for Computational Civil and Structural Engineering*, vol. 1, no. 3, pp. 414–424, 2010.
- [18] J. T. Kim, T. C. Huynh, and S. Y. Lee, "Wireless structural health monitoring of stay cables under two consecutive typhoons," *Structural Monitoring and Maintenance*, vol. 1, no. 1, pp. 47–67, 2014.
- [19] J. T. Kim, K. D. Nguyen, and T. C. Huynh, "Wireless health monitoring of stay cable using piezoelectric strain response

- and smart skin technique,” *Smart Structures and Systems*, vol. 12, no. 3-4, pp. 381–397, 2013.
- [20] T. C. Huynh, D. D. Ho, N. L. Dang, and J. T. Kim, “Sensitivity of piezoelectric-based smart interfaces to structural damage in bolted connections,” *Sensors*, vol. 19, p. 17, 2019.
- [21] L. E. Mujica, M. Ruiz, F. Pozo, J. Rodellar, and A. Güemes, “A structural damage detection indicator based on principal component analysis and statistical hypothesis testing,” *Smart Materials and Structures*, vol. 23, no. 2, 2014.
- [22] G. Park, A. C. Rutherford, H. Sohn, and C. R. Farrar, “An outlier analysis framework for impedance-based structural health monitoring,” *Journal of Sound and Vibration*, vol. 286, no. 1–2, pp. 229–250, 2004.
- [23] V. G. M. Annamdas and C. K. Soh, “Application of electromechanical impedance technique for engineering structures: review and future issues,” *Journal of Intelligent Material Systems and Structures*, vol. 21, no. 1, pp. 41–59, 2010.
- [24] G. Park and D. J. Inman, “Structural health monitoring using piezoelectric impedance measurements,” *Philosophical Transactions of the Royal Society A Mathematical Physical Engineering Science*, vol. 365, no. 1851, pp. 373–392, 2006.
- [25] T.-C. Nguyen, T.-C. Huynh, J.-H. Yi, and J.-T. Kim, “Hybrid bolt-loosening detection in wind turbine tower structures by vibration and impedance responses,” *Wind and Structures*, vol. 24, no. 4, pp. 385–403, 2017.
- [26] S. Park, D. J. Inman, J. J. Lee, and C. B. Yun, “Piezoelectric sensor-based health monitoring of railroad tracks using a two-step support vector machine classifier,” *Journal of Infrastructure Systems*, vol. 14, no. 1, pp. 80–88, 2008.
- [27] T. C. Huynh, N. L. Dang, and J. T. Kim, “Advances and challenges in impedance-based structural health monitoring,” *Structural Monitoring Maintenance*, vol. 4, no. 4, pp. 301–329, 2017.
- [28] M. A. Radhika and V. G. M. Annamdas, “Experimental studies on structural load monitoring using piezoelectric transducer based electromechanical impedance method,” *Journal of Review Article*, vol. 2, pp. 1–14, 2013.
- [29] Y. Yang, V. G. M. Annamdas, C. Wang, and Y. Zhou, “Application of multiplexed FBG and PZT impedance sensors for health monitoring of rocks,” *Sensors*, vol. 8, no. 1, pp. 271–289, 2008.
- [30] V. G. M. Annamdas and M. A. Radhika, “Electromechanical impedance of piezoelectric transducers for monitoring metallic and non-metallic structures: a review of wired, wireless and energy-harvesting methods,” *Journal of Intelligent Material Systems and Structures*, vol. 24, no. 9, pp. 1021–1042, 2013.
- [31] V. G. M. Annamdas, Y. Yang, and C. K. Soh, “Influence of loading on the electromechanical admittance of piezoceramic transducers,” *Smart Materials and Structures*, vol. 16, no. 5, pp. 1888–1897, 2007.
- [32] V. G. M. Annamdas and C. K. Soh, “Three dimensional electromechanical impedance model ii: damage analysis and pzt characterization,” *Journal of Aerospace Engineering*, vol. 20, pp. 63–71, 2007.
- [33] S. Bhalla and C. K. Soh, “Electromechanical impedance modeling for adhesively bonded piezo-transducers,” *Journal of Intelligent Material Systems and Structures*, vol. 15, no. 12, pp. 955–972, 2004.
- [34] A. Cunha and E. Caetano, “Experimental modal analysis of civil engineering structures,” *Sound and Vibration*, vol. 40, no. 6, pp. 12–20, 2006.
- [35] S. Bhalla, A. Gupta, S. Bansal, and T. Garg, “Ultra low-cost adaptations of electro-mechanical impedance technique for structural health monitoring,” *Journal of Intelligent Material Systems and Structures*, vol. 20, no. 8, pp. 991–999, 2009.
- [36] T. C. Huynh, N. L. Dang, and J. T. Kim, “PCA-based filtering of temperature effect on impedance monitoring in prestressed tendon anchorage,” *Smart Structures and Systems*, vol. 22, no. 1, pp. 57–70, 2018.
- [37] M. F. Bado, J. R. Casas, and A. Barrias, “Performance of Rayleigh-based distributed optical fiber sensors bonded to reinforcing bars in bending,” *Sensors*, vol. 18, no. 9, 2018.
- [38] H. M. Jayawickrema, J. A. Epaarachchi, N. K. Hettiarachchi, and L. H. J. Jeewantha, “Monitoring structural performances of concrete beams using fibre bragg grating (FBG) sensors,” in *Proceedings of the 10th International Conference on Structural Engineering and Construction Management*, Kandy, Sri Lanka, December 2019.
- [39] H. N. Li, D. S. Li, and G. B. Song, “Recent applications of fiber optic sensors to health monitoring in civil engineering,” *Engineering Structures*, vol. 26, no. 11, pp. 1647–1657, 2004.
- [40] V. Minutolo, L. Esposito, P. Ferla, S. Palladino, and R. Zona, “Non linear strain measures on concrete structures by means of embedded optical fiber sensors,” *International Journal of Civil Engineering & Technology*, vol. 10, no. 12, pp. 10–12, 2019.
- [41] J. M. López-Higuera, “Fiber optics in structural health monitoring,” in *Proceedings of the 2010 Conference Optical Fiber Communication Collocated National Fiber Optic Engineers Conference OFC/NFOEC*, vol. 7853, pp. 1–9, San Diego, CA, USA, 2010.
- [42] J. M. Ko and Y. Q. Ni, “Technology developments in structural health monitoring of large-scale bridges,” *Engineering Structures*, vol. 27, no. 12, pp. 1715–1725, 2005.
- [43] A. Barrias, J. R. Casas, and S. Villalba, “A review of distributed optical fiber sensors for civil engineering applications,” *Sensors*, vol. 16, no. 5, 2016.
- [44] S. Taheri, “A review on five key sensors for monitoring of concrete structures,” *Construction and Building Materials*, vol. 204, pp. 492–509, 2019.
- [45] Z. Shu, “Application of piezoelectric materials in structural health monitoring of civil engineering structure,” *Chemical Engineering Transactions*, vol. 59, pp. 523–528, 2017.
- [46] L. Zhang, G. Wu, and X. Cheng, “A rapid output-only damage detection method for highway bridges under a moving vehicle using long-gauge strain sensing and the fractal dimension,” *Measurement Journal International Measurement Confederation*, vol. 158, Article ID 107711, 2020.
- [47] M. M. Alamdari, T. Rakotoarivelo, and N. L. D. Khoa, “A spectral-based clustering for structural health monitoring of the Sydney Harbour Bridge,” *Mechanical Systems and Signal Processing*, vol. 87, pp. 384–400, 2017.
- [48] K. Roy, H. Ogai, B. Bhattacharya, S. Ray-Chaudhuri, and J. Qin, “Damage detection of bridge using wireless sensors,” *IFAC*, vol. 45, no. 23, 2012.
- [49] A. T. Eshghi, S. Lee, H. J. Jung, and P. Wang, “Design of structural monitoring sensor network using surrogate modeling of stochastic sensor signal,” *Mechanical Systems and Signal Processing*, vol. 133, Article ID 106280, 2019.
- [50] C. Rodrigues, C. Félix, A. Lage, and J. Figueiras, “Development of a long-term monitoring system based on FBG sensors applied to concrete bridges,” *Engineering Structures*, vol. 32, no. 8, pp. 1993–2002, 2010.

- [51] M. J. Chae, H. S. Yoo, J. Y. Kim, and M. Y. Cho, "Development of a wireless sensor network system for suspension bridge health monitoring," *Automation in Construction*, vol. 21, no. 1, pp. 237–252, 2012.
- [52] D. Li, Z. Zhou, and J. Ou, "Dynamic behavior monitoring and damage evaluation for arch bridge suspender using GFRP optical fiber Bragg grating sensors," *Optics & Laser Technology*, vol. 44, no. 4, pp. 1031–1038, 2012.
- [53] J. Chakraborty, A. Katunin, P. Klikowicz, and M. Salamak, "Embedded ultrasonic transmission sensors and signal processing techniques for structural change detection in the Gliwice bridge," *Procedia Structural Integrity*, vol. 17, pp. 387–394, 2019.
- [54] S. Mustapha, A. Kassir, K. Hassoun, Z. Dawy, and H. Abi-Rached, "Estimation of crowd flow and load on pedestrian bridges using machine learning with sensor fusion," *Automation in Construction*, vol. 112, Article ID 103092, 2020.
- [55] P. Pachón, R. Castro, E. García-Macías, V. Compan, E. Puertas, and "E. Torroja's bridge," "Tailored experimental setup for SHM of a historical bridge with a reduced number of sensors," *Engineering Structures*, vol. 162, pp. 11–21, 2018.
- [56] C. Rodrigues, F. Cavadas, C. Félix, and J. Figueiras, "FBG based strain monitoring in the rehabilitation of a centenary metallic bridge," *Engineering Structures*, vol. 44, pp. 281–290, 2012.
- [57] T. H. T. Chan, L. Yu, H. Y. Tam et al., "Fiber Bragg grating sensors for structural health monitoring of Tsing Ma bridge: background and experimental observation," *Engineering Structures*, vol. 28, no. 5, pp. 648–659, 2006.
- [58] K. Bremer, M. Wollweber, F. Weigand et al., "Fibre optic sensors for the structural health monitoring of building structures," *Procedia Technology*, vol. 26, pp. 524–529, 2016.
- [59] M. Iqbal and F. U. Khan, "Hybrid vibration and wind energy harvesting using combined piezoelectric and electromagnetic conversion for bridge health monitoring applications," *Energy Conversion and Management*, vol. 172, pp. 611–618, 2018.
- [60] Q. Mei, M. Gül, and M. Boay, "Indirect health monitoring of bridges using mel-frequency cepstral coefficients and principal component analysis," *Mechanical Systems and Signal Processing*, vol. 119, pp. 523–546, 2019.
- [61] H. Wang, J. X. Mao, and Z. D. Xu, "Investigation of dynamic properties of a long-span cable-stayed bridge during typhoon events based on structural health monitoring," *Journal of Wind Engineering and Industrial Aerodynamics*, vol. 201, Article ID 104172, 2020.
- [62] R. Zheng, L. Liu, X. Zhao, Z. Chen, C. Zhang, and X. Hua, "Investigation of measurability and reliability of adhesive-bonded built-in fiber Bragg grating sensors on steel wire for bridge cable force monitoring," *Measurement Journal International Measurement Confederation*, vol. 129, pp. 349–357, 2018.
- [63] D. Abruzzese, A. MiCheletti, A. Tiero et al., "IoT sensors for modern structural health monitoring," *A new frontier, Procedia Structural Integrity*, vol. 25, pp. 378–385, 2019.
- [64] J. dos Reis, C. Oliveira Costa, and J. Sá da Costa, "Local validation of structural health monitoring strain measurements," *Measurement Journal International Measurement Confederation*, vol. 136, pp. 143–153, 2019.
- [65] S. N. Shoukry, M. Y. Riad, and G. W. William, "Longterm sensor-based monitoring of an LRFD designed steel girder bridge," *Engineering Structures*, vol. 31, no. 12, pp. 2954–2965, 2009.
- [66] E. A. Oskoui, T. Taylor, and F. Ansari, "Method and monitoring approach for distributed detection of damage in multi-span continuous bridges," *Engineering Structures*, vol. 189, pp. 385–395, 2018.
- [67] W. A. Megid, M. A. Chainey, P. Lebrun, and D. Robert Hay, "Monitoring fatigue cracks on eyebars of steel bridges using acoustic emission: a case study," *Engineering Fracture Mechanics*, vol. 211, pp. 198–208, 2019.
- [68] G. Kister, R. Badcock, Y. M. Gebremichael et al., "Monitoring of an all-composite bridge using Bragg grating sensors," *Construction and Building Materials*, vol. 21, no. 7, pp. 1599–1604, 2007.
- [69] K. Chilamkuri and V. Kone, "Monitoring of varadhi road bridge using accelerometer sensor," *Materials Today Proceedings*, vol. 33, 2020.
- [70] M. J. Whelan, M. V. Gangone, K. D. Janoyan, and R. Jha, "Real-time wireless vibration monitoring for operational modal analysis of an integral abutment highway bridge," *Engineering Structures*, vol. 31, no. 10, pp. 2224–2235, 2009.
- [71] Y. Fujino, D. M. Siringoringo, Y. Ikeda, T. Nagayama, and T. Mizutani, "Research and implementations of structural monitoring for bridges and buildings in Japan," *Engineering*, vol. 5, no. 6, pp. 1093–1119, 2019.
- [72] F. Moreu, R. E. Kim, and B. F. Spencer, "Railroad bridge monitoring using wireless smart sensors," *Structural Control and Health Monitoring*, vol. 24, no. 2, 2017.
- [73] S. G. Lee, G. J. Yun, and S. Shang, "Reference-free damage detection for truss bridge structures by continuous relative wavelet entropy method," *Structural Health Monitoring*, vol. 13, no. 3, pp. 307–320, 2014.
- [74] M. Çelebi, S. F. Ghahari, and E. Taciroglu, "Responses of the odd couple Carquinez, CA, suspension bridge during the Mw6.0 south Napa earthquake of August 24, 2014," *Journal Civil Structure Health Monitoring*, vol. 9, no. 5, pp. 719–739, 2019.
- [75] N. L. D. Khoa, B. Zhang, Y. Wang, F. Chen, and S. Mustapha, "Robust dimensionality reduction and damage detection approaches in structural health monitoring," *Structural Health Monitoring*, vol. 13, no. 4, pp. 406–417, 2014.
- [76] S. Li, S. He, H. Li, and Y. Jin, "Scour depth determination of bridge piers based on time-varying modal parameters: application to Hangzhou Bay bridge," *Journal of Bridge Engineering*, vol. 22, no. 12, pp. 1–13, 2017.
- [77] Y. Deng, A. Li, S. Chen, and D. Feng, "Serviceability assessment for long-span suspension bridge based on deflection measurements," *Structural Control and Health Monitoring*, vol. 25, no. 11, pp. 1–23, 2018.
- [78] T. Oshima, Y. Miyamori, S. Mikami, T. Yamazaki, S. Beskhyroun, and M. F. Kopacz, "Small damage detection of real steel bridge by using local excitation method," *Journal Civil Structure Health Monitoring*, vol. 3, no. 4, pp. 307–315, 2013.
- [79] S. Li, H. Li, C. Lan, and Y. Liu, "SMC structural health monitoring benchmark problem using monitored data from an actual cable-stayed bridge," *Structural Control and Health Monitoring*, vol. 17, 2013.
- [80] S. Dorvash and S. N. Pakzad, "Stochastic iterative modal identification algorithm and application in wireless sensor networks," *Structural Control and Health Monitoring*, vol. 17, 2013.
- [81] M. Furinghetti, A. Pavese, F. Lunghi, and D. Silvestri, "Strategies of structural health monitoring for bridges based on cloud computing," *Journal Civil Structure Health Monitoring*, vol. 9, no. 5, pp. 607–616, 2019.
- [82] B. J. Perry, Y. Guo, R. Atadero, and J. W. van de Lindt, "Streamlined bridge inspection system utilizing unmanned

Retraction

Retracted: Flexural Behaviour of Chicken Mesh Ferrocement Laminates with Partial Replacement of Fine Aggregate by Steel Slag

Advances in Materials Science and Engineering

Received 26 December 2023; Accepted 26 December 2023; Published 29 December 2023

Copyright © 2023 Advances in Materials Science and Engineering. This is an open access article distributed under the Creative Commons Attribution License, which permits unrestricted use, distribution, and reproduction in any medium, provided the original work is properly cited.

This article has been retracted by Hindawi, as publisher, following an investigation undertaken by the publisher [1]. This investigation has uncovered evidence of systematic manipulation of the publication and peer-review process. We cannot, therefore, vouch for the reliability or integrity of this article.

Please note that this notice is intended solely to alert readers that the peer-review process of this article has been compromised.

Wiley and Hindawi regret that the usual quality checks did not identify these issues before publication and have since put additional measures in place to safeguard research integrity.

We wish to credit our Research Integrity and Research Publishing teams and anonymous and named external researchers and research integrity experts for contributing to this investigation.

The corresponding author, as the representative of all authors, has been given the opportunity to register their agreement or disagreement to this retraction. We have kept a record of any response received.

References

- [1] S. Jayaprakash, J. Dhanapal, V. Deivasigamani, and E. G., "Flexural Behaviour of Chicken Mesh Ferrocement Laminates with Partial Replacement of Fine Aggregate by Steel Slag," *Advances in Materials Science and Engineering*, vol. 2021, Article ID 7307493, 9 pages, 2021.

Research Article

Flexural Behaviour of Chicken Mesh Ferrocement Laminates with Partial Replacement of Fine Aggregate by Steel Slag

Sridhar Jayaprakash ¹, Jegatheeswaran Dhanapal ², Vivek Deivasigamani ³,
and Elias G ⁴

¹Department of Civil Engineering, GMR Institute of Technology, Rajam, Srikakulam, Andhra Pradesh, India

²Department of Civil Engineering, Sona College of Technology, SonaNagar, Salem, Tamil Nadu, India

³Department of Civil Engineering, KPR Institute of Engineering and Technology, Coimbatore, Tamil Nadu, India

⁴Department of Mechanical Engineering, College of Electrical and Mechanical Engineering, Addis Ababa Science and Technology University, Addis Ababa, Ethiopia

Correspondence should be addressed to Elias G; elias.gmichael@aastu.edu.et

Received 23 July 2021; Revised 31 July 2021; Accepted 6 August 2021; Published 17 August 2021

Academic Editor: Samson Jerold Samuel Chelladurai

Copyright © 2021 Sridhar Jayaprakash et al. This is an open access article distributed under the Creative Commons Attribution License, which permits unrestricted use, distribution, and reproduction in any medium, provided the original work is properly cited.

Bending tests were conducted on ferrocement laminates containing chicken mesh and steel slag. The fundamental goal of the examination was to investigate the effects of partial substitution of fine aggregate by steel slag in cement mortar combining chicken mesh of different volume fractions as reinforcement in thin ferrocement laminates. The following variables were investigated: (a) volume fraction of chicken mesh as 0.94%, 1.88%, 2.82%, and 3.77% and (b) level of steel slag substitution from 0% to 50% by weight fine aggregate. Results show that ferrocement laminates with chicken mesh of volume fractions of 3.77% and 30% substitution of fine aggregate with steel slag display better performance in terms of load deflection behaviour, first crack load, ultimate load, energy absorption, and ductility ratio when related with other specimens. An analytical model has been proposed to predict the ultimate moment carrying capacity of ferrocement laminates under flexure to validate the experimental results.

1. Introduction

Ferrocement is a special form of reinforced concrete construction where real composite action exists between the cement matrix and mesh [1]. The ferrocement may be reinforced with mesh made of metal or other materials. The fineness of mortar matrix and its composition should be in agreement with the mesh and the framework system it is meant to encapsulate. The mortar may contain discontinuous fibres [2]. The uniform spreading and high superficial area to volume ratio of its reinforcement result in better crack arrest mechanism. Volume fraction plays a vital role in ultimate strength carrying capacity. It is very popular as the raw material is readily available and can be prepared in any shape and it is fire resistant [3]. The properties of ferrocement are highly reliant on the type, amount, alignment, and strength properties of mesh and reinforcing rods [4]. Ferrocement laminates with chicken mesh, weld mesh, and

well-designed mortar can be an alternative and cost-effective technique in strengthening and repair of structural elements for improving load carrying capacity and ductility [5].

Ferrocement laminates under flexure and compression show higher performance with galvanised iron mesh when compared with ferrocement with polypropylene mesh. But laminates with polypropylene mesh exhibited improved ductility properties as compared to GI mesh panels. Increase in thickness of laminate and number of layers results in higher load carrying capacity [6]. Bamboo based ferrocement slab with 40 mm and 50 mm under flexure shows similar first crack load and ultimate load. The ultimate load has been found to be twice that of the first crack loads. Large ductility was observed before final failure under flexure [7]. Ferrocement with expanded metal mesh has higher energy captivation when compared with ferrocement with welded wire mesh or fiber glass mesh. Increase in number of layers increases energy absorption for beams made of Autoclaved Aerated Lightweight Brick Core

(AAC) [8]. Flexural performance of ferrocement increases when wire mesh is used with epoxy. With increase in number of layers of wire mesh flexural strength, cracking behaviour and energy absorption increase. Wire mesh-epoxy composites are more efficient than carbon fibres in flexural strength and ductility [9].

Ferrocement beams with welded wire mesh exhibit increase in shear capacity and less number of crack patterns compared with reference and expanded wire mesh [10]. Ferrocement slab with 10% rubber powder as replacement of cement was found to change the brittle failure to ductile failure with a small reduction in ultimate flexural strength [11]. Aerated slurry-infiltrated chicken mesh ferrocement exhibits ductile failure which can be used as a building construction material. Theoretical model developed confirms the experimental results [12]. Ferrocement containing perlite light weight aggregate (LWA) indicates flexural behaviour of light weight ferrocement increases with number of expanded rib lath layers [13]. Incorporation of 10% LECA in ferrocement leads to the increase of energy absorption by 48%, ductility index by 26%, and crack width by 106% [14]. Ferrocement with 4% of high calcium wood ash by weight of cement exhibited better structural performance when compared to control ferrocement without high calcium wood ash. Addition of HCWA in mortar increases the engineering performance and also contributes as potential binding material [15]. Cementitious matrices containing silica fume and fly ash in ferrocement have high strength, increased load carrying capacity, lateral confinement, and ductility [16]. Flexural strength of welded square mesh ferrocement of U shaped channel section mesh is higher than ferrocement channel section with woven square mesh. With increase in number of layers of mesh from 2 to 4, flexural strength and load carrying capacity increase [17].

U-shaped ferrocement with 98 expanded steel mesh exhibits higher first crack load, ultimate load, and serviceability load when compared with beams reinforced with EX156 expanded steel mesh and then specimens reinforced with woven mesh [18]. The beams with lightweight brick have higher first crack load and ultimate load when compared with conventional beams with welded wire mesh. Similarly, use of light weight brick resulted in reduction of serviceability load and energy absorption [19]. This paper presents the experimental results of ferrocement laminates under flexure with chicken mesh and partial replacement of fine aggregate by steel slag and proposes an analytical model to determine the ultimate moment carrying capacity of ferrocement laminates under flexure.

2. Properties of Materials Used

2.1. Cement. Ordinary Portland cement of 53 grades was used in this investigation and its physical properties were tested in accordance with Indian standards [20]. Specific gravity was 3.15 and initial and final setting time was 35 minutes and 10 hours, respectively. The test results comply with the requirements as per Indian Codal Provisions [21].

2.2. Fine Aggregate

2.2.1. Sand. Fine aggregate passing through 2.36 mm sieve having specific gravity 2.68 under Zone II as per the

recommendations of IS 383, 1970, ACI 549 1R-93, 1999, and Ferrocement Model Code (FMC) 2001 was used [22–24].

2.2.2. Steel Slag. Steel slag is a byproduct acquired in basic oxygen furnace (BOF) during change of iron to steel or in electric arc furnace (EAF) during softening of scrap to make steel. Steel slag is defined as a nonmetallic item, comprising basically of calcium silicates and ferrites joined with intertwined oxides of iron, aluminum, manganese, and calcium that are grown at the same time with steel in essential oxygen, electric curve, or open hearth heaters [25]. Steel slag could be used as substitute material for normal sand in mortar either mostly or completely [26]. Steel slag with specific gravity 2.95 with a division going through 2.36 mm sieve was utilized for cement mortar for fabrication of ferrocement laminates. The chemical composition of steel slag is usually expressed in terms of simple oxides calculated from elemental analysis determined by Le Chatelier method [27]. Table 1 arrays the chemical composition of steel slag from a typical base oxygen furnace [25].

2.3. Water. Water fit for drinking is generally fit for casting ferrocement laminate and water used is free of acids, oils, alkalis, and other organic impurities and its pH value is 7 ± 1 .

2.4. Reinforcement for Ferrocement Laminate. The properties of chicken mesh are on par with the steel reinforcing bars used in reinforced concrete [2]. Chicken mesh with diameter 0.5 mm and yield strength of 312 N/mm^2 as per the manufacturer data was used.

3. Experimental Investigations on Ferrocement Laminates

The mortar mix proportion was taken as 1 : 2, w/c ratio 0.40 [28]. Steel slag replacement from 0% to 50% by weight of fine aggregate in increments of 10% was adopted for experimental investigation of ferrocement laminate under flexural loading.

3.1. Flexural Behaviour of Ferrocement Laminates. The experimental work involves casting and testing of ferrocement laminates [23] of size $150 \text{ mm} \times 25 \text{ mm} \times 500 \text{ mm}$ with partial replacement of fine aggregate by steel slag from 0% to 50% by weight of fine aggregate in increments of 10% in mortar matrix under flexure by closed mould method of bundling of chicken meshes.

For the study, a total number of 72 specimens were cast of size $150 \text{ mm} \times 25 \text{ mm} \times 500 \text{ mm}$, and volume fractions of 0.94%, 1.88%, 2.82%, and 2.377% for 1 layer, 2 layers, 3 layers, and 4 layers were used. The cross section of the specimen is shown in Figure 1. The details of the specimen with chicken mesh are arrayed in Table 2. The designation refers to the number of layers of mesh reinforcement, ferrocement, type of mesh, and percentage of replacement of steel slag for fine aggregate. For example, 1FCC0 refers to 1

TABLE 1: Chemical composition of steel slag.

Constituent	Composition (%)	Composition (%) as per ACI 233 R-03
CaO	32.5	32 to 45
SiO ₂	34	32 to 42
Fe ₂ O ₃	0.3	0.1 to 0.5
MgO	9	5 to 15
Al ₂ O ₃	22	7 to 16
P ₂ O ₅	0.56	—
SO ₃	0.7	—

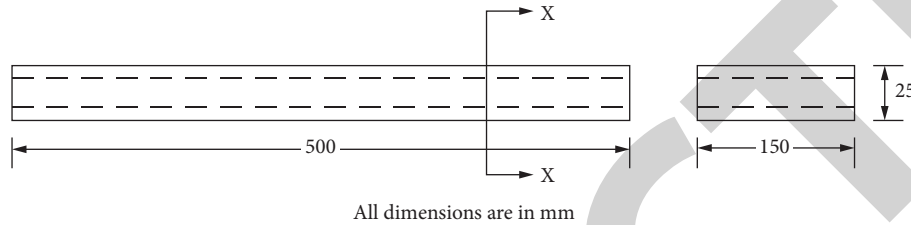


FIGURE 1: Cross section of the ferrocement laminates.

TABLE 2: Details of test specimen with chicken mesh for flexure test.

Type of mesh	Designation	No. of layers	Volume fraction V_r (%)	Steel slag (%)	No. of specimens
Chicken mesh	1FCC0	1	0.94	0	3
	1FCC10			10	3
	1FCC20			20	3
	1FCC30			30	3
	1FCC40			40	3
	1FCC50	50	3		
	2FCC0	2	1.88	0	3
	2FCC10			10	3
	2FCC20			20	3
	2FCC30			30	3
	2FCC40			40	3
	2FCC50	50	3		
	3FCC0	3	2.82	0	3
	3FCC10			10	3
	3FCC20			20	3
	3FCC30			30	3
	3FCC40			40	3
	3FCC50	50	3		
	4FCC0	4	3.77	0	3
	4FCC10			10	3
4FCC20	20			3	
4FCC30	30			3	
4FCC40	40			3	
4FCC50	50	3			

layer of mesh reinforcement in ferrocement with weld mesh and 0% steel slag replacement for fine aggregate.

The ferrocement laminates were subjected to flexure test under the simply supported span of 400 mm with loads at one third points. In the present investigation, deflection at the midpoint for each 0.5 kN load was noted with the help of dial gauge of the least count of 0.01 mm/divisions. During testing, observations were made for (a) deflection at the midpoint for each 0.5 kN increment of loading, (b) load at first crack, (c) ultimate load, and (d) mode of failure of all specimens.

4. Analytical Investigation on Ferrocement Laminates

4.1. Prediction of Ultimate Moment for Ferrocement Laminates. An analytical model for determining ultimate moment carrying capacity of ferrocement using plastic moment approach is presented. The proposed stress strain block for ferrocement laminate is shown in Figure 2.

In this investigation, the following assumptions were made:

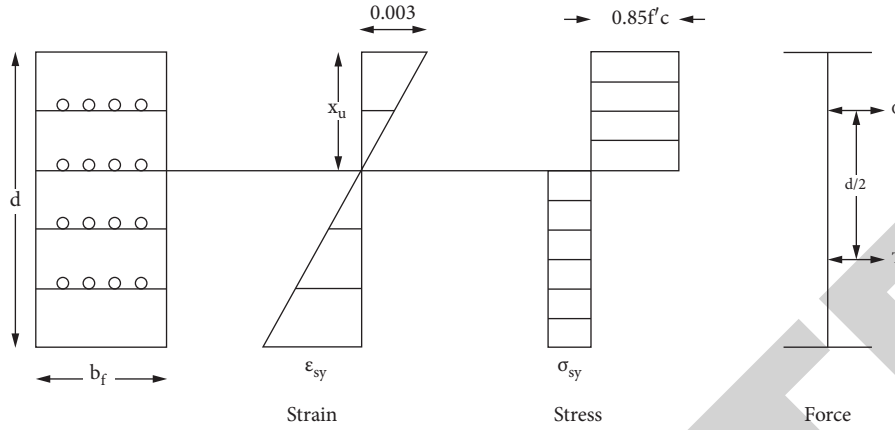


FIGURE 2: Stress strain block for ferrocement laminate.

- (1) The compressive stress in mortar was represented by a rectangular stress block with stress intensity of $0.85f'_c$ and depth equal to neutral axis depth
- (2) Perfect bond existed between the steel mesh and mortar
- (3) The material was considered as a homogenous material
- (4) Plane section remained plane even after bending
- (5) The maximum usable compressive strain in mortar was 0.003
- (6) The properties in tension were predicted by assuming all steel layers are in the plastic range
- (7) The depth of plastic neutral axis was determined by equating compressive force equal to tensile force
- (8) The distribution of reinforcement was uniform throughout the section

The behaviour of laminate was assumed similar to that of RC beams [29]. Therefore, the total force due to compression is equal to total force due to tension. From the stress strain block in Figure 2, the equations for compressive and tensile forces were obtained as

$$\begin{aligned} C &= 0.85f'_c b_f x_u, \\ T &= \sigma_{cy} b_f (d - x_u). \end{aligned} \quad (1)$$

The tensile strength of the composite σ_{cy} was obtained from assuming all the steel layers in the plastic range:

$$\begin{aligned} \sigma_{cy} &= \eta V_r \sigma_{ry} \\ &= X. \end{aligned} \quad (2)$$

Moment due to compressive force is

$$M_c = 0.425f'_c \cdot b_f d^2 \frac{X}{0.85f'_c + X}. \quad (3)$$

Moment due to tensile force is

$$M_T = 0.5b_f \cdot d^2 \times \left(1 - \frac{X}{0.85f'_c + X}\right). \quad (4)$$

Final moment is

$$M = M_c \text{ or } M_T, \quad (5)$$

where x_u is the depth of neutral axis, V_r is the volume fraction of mesh reinforcement, M_c is the moment due to compressive force, M_T is the moment due to tensile force, f'_c is the compressive strength of mortar (N/mm^2), b_f and d are the breadth and thickness of the ferrocement laminate (mm), σ_{ry} is the yield strength of mesh reinforcement (N/mm^2), σ_{cy} is the tensile strength of composite, and η is the efficiency factor for reinforcement.

5. Results and Discussion

5.1. First Crack Load and Ultimate Load. In the case of ferrocement laminates with chicken mesh, the first crack load is shown in Figure 3; for specimens 1FCC30 with volume fraction 0.94% and 2FCC30 with volume fraction 1.88%, the first crack load is enhanced about 40% and 25%, respectively, when compared to 1FCC0 and 2FCC0. For the specimens 3FCC30 reinforced with volume fraction 2.82% and 4FCC30 reinforced with volume fraction 3.77%, first crack load increased by 29% and 77%, respectively, when compared to 3FCC0 and 4FCC0.

From Figure 4 for specimens 1FCC30 and 2FCC30, the ultimate load increased about 91% and 63%, respectively, when compared to 1FCC0 and 2FCC0. In regard to the specimens 3FCC30 and 4FCC30, the ultimate load enhanced about 22% and 36%, respectively, when compared to 3FCC0 and 4FCC0.

It is clear that, for ferrocement laminates, first crack load and ultimate load gradually increased from 0% to 30% replacement of steel slag by weight of fine aggregate and decreased for 40% and 50% replacement irrespective of the volume fraction and type of mesh reinforcement. This is due to the good bonding characteristics of mesh reinforcements with 30% replacement of steel slag by weight of fine aggregate (optimised % replacement). There are only marginal variations in first crack load for all the specimens with different volume fractions and different replacement levels. The first crack load and ultimate load achieved by the specimens with chicken mesh of volume fraction 1.88% with 30% steel slag replacement are higher than those of the

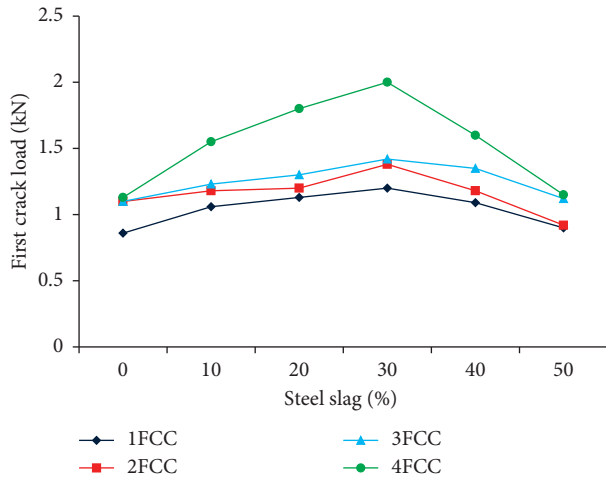


FIGURE 3: First crack load for different levels of steel slag replacement and volume fractions of chicken mesh ferrocement laminates.

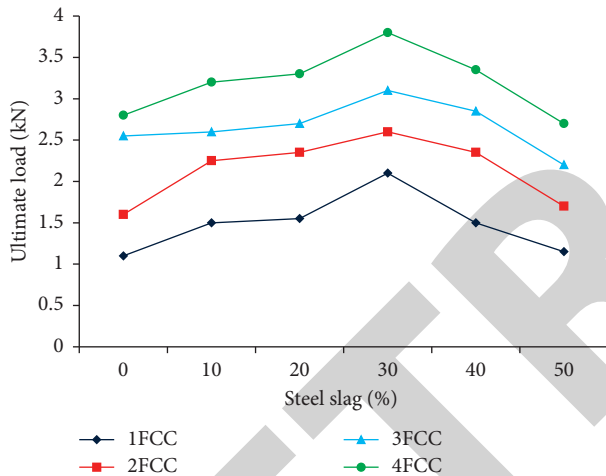


FIGURE 4: Ultimate load for different levels of steel slag replacement and volume fractions of chicken mesh ferrocement laminates.

specimens with chicken mesh of volume fraction 3.77% without replacement. It shows that the addition of steel slag has considerable effect on increasing the load carrying capacity.

Moreover, first crack load and ultimate load were maximum for ferrocement laminates with volume fraction of 3.77% because of increased moment arm due to increase in the depth of mesh layers from the neutral axis of the section [30].

5.2. Load-Deflection Characteristics. An experimental load-deflection curve of ferrocement with their transition points (i.e., cracking, yielding, and ultimate) is discussed using Figures 5–8. It is observed that the ferrocement laminates exhibit linear elastic behaviour up to the first crack load. Figures 5 and 6 depict the load deflection behaviour of specimens with chicken mesh reinforced with volume fractions 0.94% and 1.88%. The specimen started to yield

when the load was 0.86 kN, 1.2 kN, 1.1 kN, and 1.38 kN for the specimens 1FCC0, 1FCC30, 2FCC0, and 2FCC30, respectively. On further increment of load, the specimens reach an ultimate load of 1.1 kN, 2.1 kN, 1.6 kN, and 2.6 kN for specimens 1FCC0, 1FCC30, 2FCC0, and 2FCC30, respectively.

Figures 7 and 8 show the load-deflection behaviour of specimens with chicken mesh with volume fractions 2.82% and 3.77%. Initially, as the load is increased, the transition point of cracking is obtained for specimens 3FCC0, 3FCC30, 4FCC0, and 4FCC30 when the load is at 1.1 kN, 1.42 kN, 1.13 kN, and 2 kN, respectively. When the static load is further increased, the yielding of mesh reinforcement occurs and specimens reach the ultimate load of 2.55 kN, 3.1 kN, 2.8 kN, and 3.8 kN, respectively. The ultimate load of 4FCC30 was found to be 49% higher than the control specimen.

5.3. Energy Absorption Capacity. Energy absorption is the area under the load-deflection curve. The energy absorption capacity of specimens with chicken mesh is manifested in Figure 9.

Figure 9 shows that, for the specimens with chicken mesh reinforced with volume fraction 0.94%, 1.88% maximum energy absorption was obtained for the specimens 1FCC30 and 2FCC30 which was about 67% and 51% higher than 1FCC0 and 2FCC0. For the specimen 3FCC30 reinforced with volume fraction 2.82%, the energy absorption increased about 21% when compared to control specimen. Energy absorption of the specimen 4FCC30 reinforced with volume fraction 3.77% increased about 79% compared to control specimen.

5.4. Ductility Ratio. Ductility ratio is the ratio of deflection at ultimate load to that at the onset of yielding. The ductility ratio shown in Figure 10 increased about 46% for the specimen 1FCC30 which is reinforced with the volume fraction 0.94%. The specimens 2FCC30 and 3FCC30 increased about 27% and 9%, respectively, when compared to control specimen. The specimen 4FCC30 increased about 19% when compared with control specimen. It is clear that a specimen with optimum percentage of replacement of steel slag (i.e., 30 percent) by weight of fine aggregate has produced higher ductility strength.

5.5. Effect of Mortar Matrix. From the test results, it is clear that the addition of steel slag in the mortar matrix, which was used for ferrocement laminates, has considerably reduced the deflection. The mortar matrix with 30% steel slag by weight of fine aggregate has influenced the initial strength as well as long-term strength in ferrocement laminates which in turn increases the first crack load and ultimate load. The specimens with 30% steel slag by weight of fine aggregate gave sufficient warning before failure. So this, in turn, represents that 30% replacement of steel slag by weight of fine aggregate is the optimum percentage of replacement for fine aggregate.

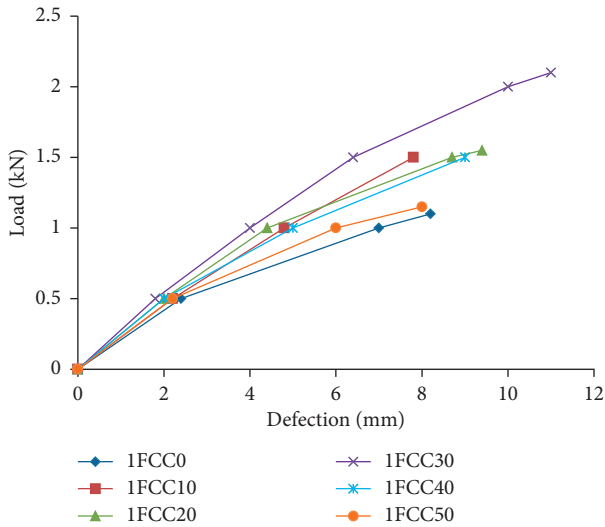


FIGURE 5: Load vs. deflection for ferrocement laminates with volume fraction 0.94%.

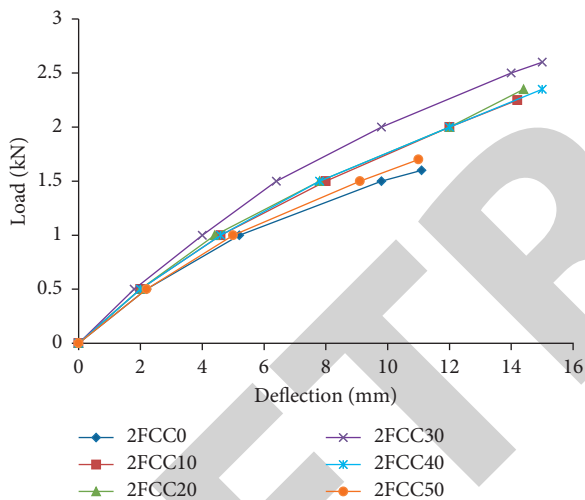


FIGURE 6: Load vs. deflection for ferrocement laminates with volume fraction 1.88%.

5.6. Effect of Number of Wire Mesh Layers. It is evident from the graphs that the strength increases with an increase in the number of layers of mesh. The number of layers is attributed to the increase in passive confining pressure which in turn is dependent on the volume fraction of transverse wires [31]. Therefore, the chicken mesh with 0.5 mm diameter and the mesh opening have direct influence on the increase in strength of the specimen. The specimens with 3 layers and 4 layers are equally spaced and distributed within the depth. The transverse wires in meshes provided a better anchorage for a bond with cement matrix and a better restraint against lateral expansion of the matrix in the compression zone [31]. The chicken mesh with higher volume fraction of mesh reinforcement provided better crack control mechanism by the formation of a large number of well distributed cracks.

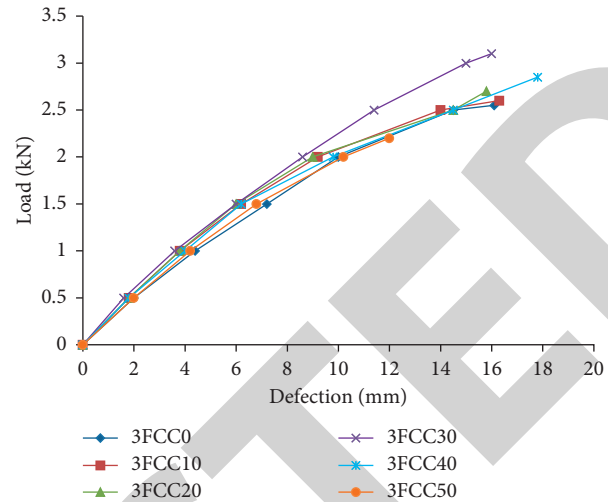


FIGURE 7: Load vs. deflection for ferrocement laminates with volume fraction 2.82%.

5.7. Mode of Failure. Flexural pattern failure was observed for all specimens. Most of the cracks were generated near the centre on increase in loads. The crack pattern for various specimens is displayed in Figure 11.

The specimens with volume fraction 0.943% showed a single major crack at the middle of the specimen. Due to the increase in the cover of mesh reinforcement, the ferrocement laminates failed suddenly after reaching the ultimate load. The specimens reinforced with chicken mesh of volume fraction 1.880% showed a formation of cracks not far from loading points of the specimen. For the specimens reinforced with volume fraction 2.82%, the parallel cracks were well distributed at the middle of the specimen. For the specimens with volume fraction 3.77%, the cracks were well distributed at the centre and it was observed that no separation of specimen occurred even after failure, but it was attached by mesh.

5.8. Analytical Investigation on Ferrocement Laminates

5.8.1. Correlation of Analytical and Experimental Ultimate Moment. The analytical model developed to determine the ultimate moment capacity of ferrocement laminates is discussed. The ultimate moment capacity of every specimen was experimentally calculated by testing the laminates under loads at one third points. The experimentally calculated ultimate moment values were compared with that of predicted analytical moment values determined using equations (3) or (4). From the comparison of results, it was clearly established that the proposed analytical equation for the calculation of ultimate moment capacity of ferrocement laminates with partial and without substitution of fine aggregate by steel slag goes hand in hand with experimental values. The variation in analytical and experimental moment value is checked for $\pm 20\%$ accuracy.

The correlation of analytical and experimental moments is shown in Figure 12. All the specimens reinforced with volume fractions 1.88%, 2.82%, and 3.77% fall within the

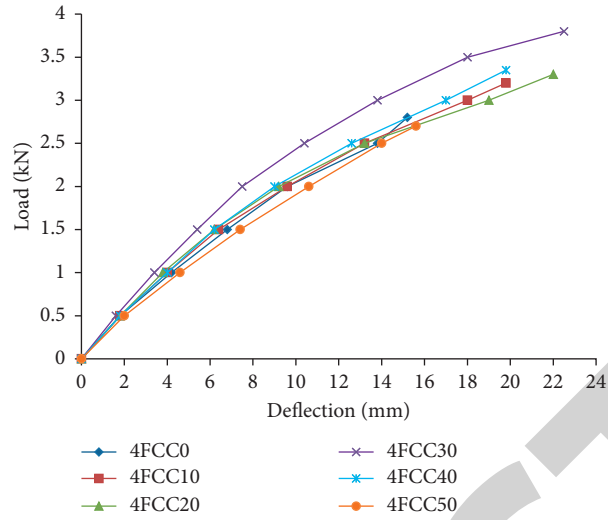


FIGURE 8: Load vs. deflection for ferrocement laminates with volume fraction 3.77%.

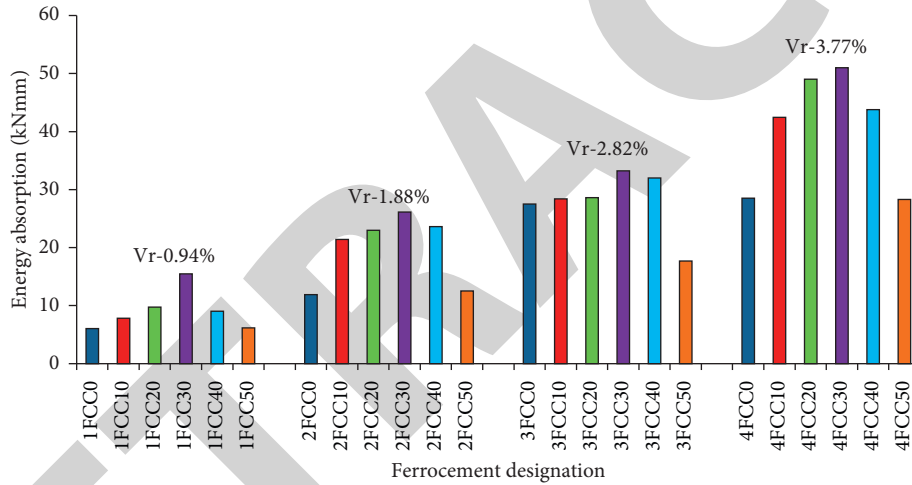


FIGURE 9: Energy absorption for different levels of steel slag replacement and volume fractions of chicken mesh ferrocement laminates.

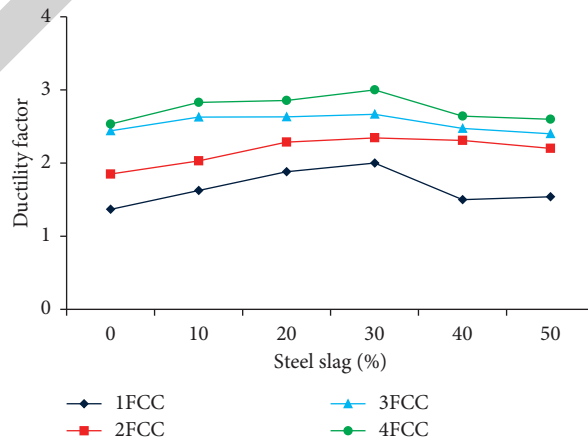


FIGURE 10: Ductility ratio for different levels of steel slag replacement and volume fractions of chicken mesh ferrocement laminates.

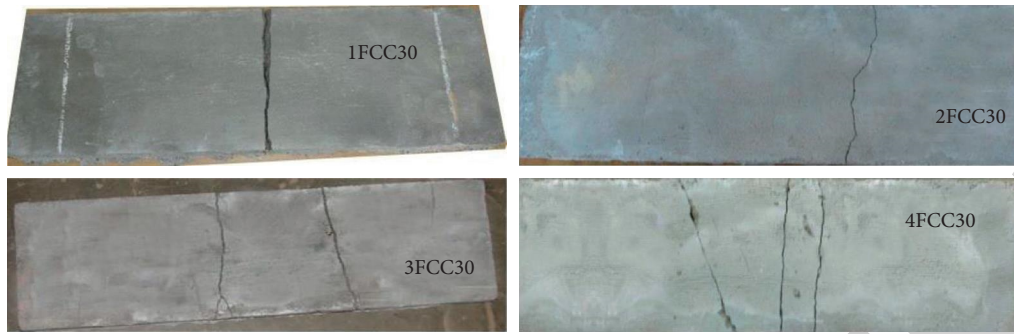


FIGURE 11: Crack pattern of ferrocement laminates under flexure.

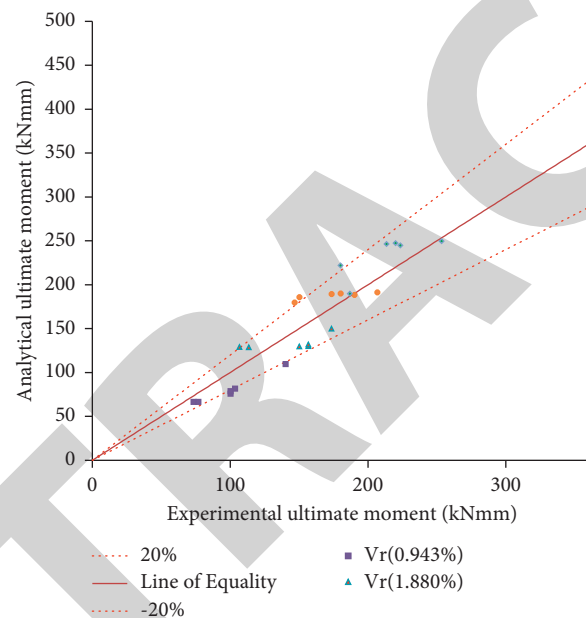


FIGURE 12: Correlation between analytical moment and experimental moment for ferrocement laminates.

$\pm 20\%$ accuracy whereas the specimens reinforced with volume fraction 0.94% had variation in the specimens with 10%, 20%, 30%, and 40% substitution of steel slag by weight of fine aggregate.

6. Conclusions

The following conclusions can be drawn from experimental and analytical investigations:

- (1) The first crack load and ultimate load were found to be maximum for specimens with volume fraction 3.77%, i.e., 4 layers, and 30% replacement of steel slag by weight of fine aggregate
- (2) Addition of steel slag of 30% and chicken mesh of volume fraction 3.77% in ferrocement laminates has reduced the deflection when compared to other specimens

(3) From an overall assessment, i.e., the maximum first crack load, ultimate load, deflection, and energy absorption, optimum results were obtained for ferrocement laminates with a volume fraction of 3.77% and steel slag replacement of 30%

(4) The ultimate moment capacity of ferrocement laminates obtained from the proposed analytical model was found to be in good agreement with the experimental values and accuracy fell within $\pm 20\%$

Data Availability

The data used to support the findings of this study are included within the article.

Conflicts of Interest

The authors declare that they have no conflicts of interest.

Retraction

Retracted: Optimization of CNC End Milling Process Parameters of Low-Carbon Mold Steel Using Response Surface Methodology and Grey Relational Analysis

Advances in Materials Science and Engineering

Received 26 December 2023; Accepted 26 December 2023; Published 29 December 2023

Copyright © 2023 Advances in Materials Science and Engineering. This is an open access article distributed under the Creative Commons Attribution License, which permits unrestricted use, distribution, and reproduction in any medium, provided the original work is properly cited.

This article has been retracted by Hindawi, as publisher, following an investigation undertaken by the publisher [1]. This investigation has uncovered evidence of systematic manipulation of the publication and peer-review process. We cannot, therefore, vouch for the reliability or integrity of this article.

Please note that this notice is intended solely to alert readers that the peer-review process of this article has been compromised.

Wiley and Hindawi regret that the usual quality checks did not identify these issues before publication and have since put additional measures in place to safeguard research integrity.

We wish to credit our Research Integrity and Research Publishing teams and anonymous and named external researchers and research integrity experts for contributing to this investigation.









The corresponding author, as the representative of all authors, has been given the opportunity to register their agreement or disagreement to this retraction. We have kept a record of any response received.

References

- [1] R. Suresh Kumar, S. Senthil Kumar, K. Murugan et al., "Optimization of CNC End Milling Process Parameters of Low-Carbon Mold Steel Using Response Surface Methodology and Grey Relational Analysis," *Advances in Materials Science and Engineering*, vol. 2021, Article ID 4005728, 11 pages, 2021.

Research Article

Optimization of CNC End Milling Process Parameters of Low-Carbon Mold Steel Using Response Surface Methodology and Grey Relational Analysis

R. Suresh Kumar ¹, S. Senthil Kumar ², K. Murugan,³ B. Guruprasad ⁴,
Sreekanth Manavalla ⁵, S. Madhu ⁶, M. Hariprabhu ⁷, S. Balamuralitharan ⁸,
and S. Venkatesa Prabhu ⁹

¹Department of Mechanical Engineering, Sri Eshwar College of Engineering, Coimbatore, India

²Department of Mechanical Engineering, RMK College of Engineering and Technology, Pudukottai, Tamil Nadu, India

³Government Polytechnic College, Valangaiman, Tamil Nadu, India

⁴Department of Mechanical Engineering, Alagappa Chettiar Government College of Engineering and Technology, Karaikudi, Tamil Nadu, India

⁵School of Mechanical Engineering & Electric Vehicles Incubation, Testing and Research Centre, Vellore Institute of Technology, Chennai, Tamil Nadu, India

⁶Department of Automobile Engineering, Saveetha School of Engineering, Saveetha Institute of Medical and Technical Sciences, Chennai, Tamil Nadu, India

⁷Department of Electrical and Electronics Engineering, M. Kumarasamy College of Engineering, Karur, Tamil Nadu, India

⁸Department of Mathematics, College of Engineering and Technology, SRM Institute of Science and Technology, Kattankulathur, Chengalpattu, Tamil Nadu, India

⁹Department of Chemical Engineering, College of Biological and Chemical Engineering, Addis Ababa Science and Technology University, Addis Ababa, Ethiopia

Correspondence should be addressed to R. Suresh Kumar; rsk777mech@gmail.com and S. Venkatesa Prabhu; venkatesa.prabhu@aastu.edu.et

Received 15 June 2021; Revised 29 June 2021; Accepted 3 August 2021; Published 16 August 2021

Academic Editor: Antonio Gloria

Copyright © 2021 R. Suresh Kumar et al. This is an open access article distributed under the Creative Commons Attribution License, which permits unrestricted use, distribution, and reproduction in any medium, provided the original work is properly cited.

The manufacturing sectors are consistently striving to figure out ways to minimize the consumption of natural resources through rational utilization. This is achieved by a proper understanding of every minute influence of parameters on the entire process. Understanding the influencing parameters in determining the machining process efficacy is inevitable. Technological advancement has drastically improved the machining process through various means by providing better quality products with minimum machining cost and energy consumption. Specifically, the machining factors such as cutting speed, spindle speed, depth of cut, rate of feed, and coolant flow rate are found to be the governing factors in determining the economy of the machining process. This study is focused on improving the machining economy by enhancing the surface integrity and tool life with minimum resources. The study is carried out on low-carbon mold steel (UNS T51620) using Box–Behnken design and grey regression analysis. The optimized multiobjective solution for surface roughness (R_a), material removal rate (MRR), and power consumed (P_c) and tool life is determined and validated through the confirmatory run. The optimized set of parameters in Box–Behnken design and grey regression analysis with that of confirmatory runs shows a 10% deviation that proves the reliability of the optimization techniques employed.

1. Introduction

In the past decades, CNC machining has gained an irreplaceable stand in offering higher reliability, accuracy, and productivity. Moreover, CNC milling provides higher flexibility in choosing the machining parameters levels when compared to a conventional milling process. In industries, different types of milling processes are employed such as plain milling, end milling, side milling, and gang milling. Out of these, in automobile, aerospace, and metal processing industries, the CNC end milling process is inevitable due to its high precision accuracy and reliability. Being a versatile process, end milling has already conquered unrivalled place in the manufacturing sector fulfilling the requirements. In any machining process, numerous parameters are involved that govern the process. These parameters are classified as controllable and noncontrollable parameters. Controllable parameters are those which can be tuned according to the needs such as spindle rotation, cutting wheel speed, rake angle, feed rate, and depth of cut. Noncontrollable parameters are those which cannot be directly controlled rather can be governed indirectly through controllable parameters. Tool wear, surface roughness, and chip formation vibrations are few to name.

An experimental study was carried on Al2014-T6 by Ming-Yung and Chang [1] on surface integrity. Trial runs were conducted by slot end milling. The study revealed that vibrations during machining and the rate of feed are the key factors governing the surface roughness. Palanisamy et al. [2] explored the machining consequences for CNC end milling and arrived at an optimized set of machining parameters. The study included application of a genetic algorithm, and the result revealed a higher influential contribution by feed and depth of cut on surface roughness. A detailed study on the implementation of adaptive control in CNC machining was carried out by Suresh Kumar et al. [3]. In this study, the research progress in maintaining the accuracy and reliability of machining parameters was discussed elaborately. The article summed up the techniques developed so far in improving the efficacy of CNC machining. A theoretical approach was proposed for forecasting surface integrity by Martellotti [4] and Quintana et al. [5]. The study was restricted to a single-objective function where the possible effects of other responses were not considered. An analytical model was developed by Mansour and Abdalla [6]. A comparison study was presented by Suresh Kumar et al. [7], which focused on deviation recorded between genetic algorithm (GA) and artificial neural networks (ANN) in achieving optimum machining factors for CNC milling.

Alauddin et al. [8] investigated controllable factors affecting the roughness and life of the tool used for machining. Cutting speed, rate of feed, and depth of axial cut are taken as the governing parameters. Chang et al. [9] and Coker and Shin [10] conceded the optimization exploration using DOE on face roughness. In another research, DOE was used by Gologlu and Sakarya [11] and Dhokia et al. [12] to predict the optimum level of surface roughness. Suresh Kumar et al. [13] optimized CNC end milling of BSL168 using Box-Behnken design. The material considered was an

aluminium composite used for aeronautical applications. The work included optimization of contradictory responses, namely surface integrity and MRR by controlling the machining constraints namely spindle speed, rate of feed, and depth of cut.

The literature survey also provides an insight into the application of advanced optimization techniques such as GA, ANN, and fuzzy [14–19] to arrive at an optimized set of parameters for machining. Kumar et al. [20] investigated the influencing parameters in the machining of AMS 4205. The experiment involved a multiobjective approach towards providing a solution for achieving optimum results for roughness and MRR. The study included Taguchi robust design and Box-Behnken design for arriving at the optimized level of parameters. A detailed literature survey was carried out by Zain et al. [21] on genetic algorithm and their application towards the optimization of cutting parameters in CNC milling. Suresh Kumar et al. [22] optimized the surface integrity using CNC milling. The material considered was A91060 and HSS tools used. The study included the application of response surface methodology to derive the governing mathematical model for finding the optimum solution through genetic algorithms.

A detailed report on the machining effect between the work material and tool used was carried out by Brezocnik and Kovacic [23]. Ganesh Kumar et al. [24] carried out a detailed review on cutting tool measurement in the turning process using cloud computing systems. The study involved the application of a genetic algorithm limited to a single objective function. Oktem et al. [25] applied a genetic algorithm in arriving at the optimized parameter to achieve minimum surface roughness. A multiobjective approach for optimization of cyclone separator was carried out by Venkatesh et al. [26] using Taguchi robust design and validated using numerical simulation. Ganesh Kumar et al. [27] suggested optimum tool stress in CNC turning of EN8 steel using a numerical approach.

From the above-detailed study, one can witness extensive research in the field of machining processes using higher-order optimization tools. At the same time, it is noteworthy to state that most of the work executed is limited to single-objective functions. In reality, any machining process is always associated with more than one response of contradictory nature. Therefore, it becomes obligatory to cram the consequences of accompanying responses to fix the preeminent machining parameters.

This study addresses a multiobjective function where an attempt is made to arrive at optimizing contradictory responses namely roughness (R_a), MRR, and power consumption (P_c). The work material is a low-carbon mold steel (UNS T51620), which is hard to machine.

2. Experimental Outline

The sequential approach of the study is given as follows:

- (1) Assigning of levels for each parameter
- (2) Execution of experimental run based on Box-Behnken design

- (3) Measurement of the roughness, MRR, and tool life in terms of P_c
- (4) Development of mathematical model for the prediction of R_a , MRR, and P_c . It is also subjected to adequacy check using ANOVA
- (5) Application of grey regression analysis (GRA) for optimization
- (6) Confirmatory runs to validate the results attained

3. Methodology and Implementation

3.1. Material and Tool. Low-carbon mold steels contain chromium and nickel as the main alloying elements and are classified in group P steels. These steels are usually nitrided or carburized to attain the desirable qualities. These steels are good in machinability as they can be easily machined into complex and large molds and dies. They are mostly used in injection molds and die casting. Due to its wide range of applications, prehardened UNS T51620 steel is taken as the work material. The material hardness ranges between 30 and 40 HRC. Rectangular work material of dimensions 75 mm × 30 mm × 12 mm is taken for machining. The elemental composition of the material is shown in Table 1. The material is found to have extensive applications in electronic equipment, car accessories, and home appliances.

The work material is hard in nature due to the presence of manganese and nickel in higher percentages followed by carbon content as stated in Table 1. Based on the literature survey, TiCN is taken as the cutting tool material having a Rockwell hardness of 88.

3.2. Controllable and Noncontrollable Parameters. A machining operation is highly influenced by parameters such as speed of spindle, feed, depth of cut, tool rake angle, coolant flow rate, roughness, and tool life. Out of these, certain parameters can be governed before the execution of machining, and they are known as controllable parameters, whereas certain parameters vary based on the influence of so-called uncontrollable parameters. Such dependent parameters are known as noncontrollable factors. In this study, the controllable factors are speed of the spindle (A), depth of cut (B), feed (C), and flow rate of coolant (D). The noncontrollable factors or responses are taken as surface roughness (R_a), material removal rate (MRR), and power consumed (P_c). The levels of the selected controllable parameters are finalized based on the manufacturer's specifications and researches carried out so far.

The controllable parameters identified are feed (mm/min), spindle speed (rpm), depth of cut (mm), and flow rate of coolant (l/min). Figure 1 shows the trial runs conducted in a 3-axis vertical milling centre. A surface tester (Mitutoyo) is employed for measuring the roughness of the machined. Figure 2 shows the experimental runs conducted on the work material. The surface tester has a resolution varying from 0.01 microns to 0.3 microns. The average roughness value (R_a) is considered for the analysis.

TABLE 1: Chemical composition.

Mn	Cr	Ni	C	Si	Mo	S
0.86	0.033	0.8	0.36	0.44	0.9	0.35



FIGURE 1: Trial runs conducted.



FIGURE 2: Measurement of roughness.

3.3. Design Matrix. Experimental iterations were based on Box-Behnken model. The controllable parameters are assigned with three levels, and two responses are considered as detailed in Table 2. The sequence of experimental runs and responses are shown in Table 3.

4. Results and Discussions

The parametric effects on the responses are discussed individually in the following sections. For each response, optimized level of machining parameters based on desirability function. The competency of the desirability function is validated by analysis of variance (ANOVA).

4.1. Response Surface Model for the Prediction of Surface Roughness. The ANOVA analysis for roughness (R_a) is given in Table 4.

" F -value" of 636600 with " P value" below 0.0001 confirms the significance of the desirability function. The function is said to be insignificant if the values are greater than 0.10. In other words, a 0.01% chance is there that an

TABLE 2: Machining parameters and their levels.

Parameters	Unit	Level 1	Level 2	Level 3
Spindle speed (<i>A</i>)	rpm	1200	1850	2500
Depth of cut (<i>B</i>)	mm	0.2	0.4	0.6
Feed rate (<i>C</i>)	mm/min	1000	1500	2000
Coolant flow rate (<i>D</i>)	l/min	4	6	8

TABLE 3: Experimental runs and responses.

<i>A</i> (rpm)	<i>B</i> (mm)	<i>C</i> (mm/min)	<i>D</i> (l/min)	R_a (microns)	MRR (mm ³ /min)	P_c (HP)
1850	0.2	1000	6	4.217	0.2361	0.207
1850	0.6	2000	6	2.650	1.2931	1.408
1200	0.4	1000	6	4.797	0.7826	0.751
2500	0.4	2000	6	2.070	0.7466	0.865
2500	0.4	1500	4	2.746	0.6249	0.635
1200	0.4	2000	6	4.550	0.8636	1.026
1850	0.4	1500	6	3.434	0.7646	0.808
1850	0.2	1500	4	4.646	0.1954	0.253
1850	0.4	1500	6	3.434	0.7646	0.808
1850	0.4	1500	6	3.434	0.7646	0.808
1200	0.2	1500	6	5.334	0.3351	0.425
2500	0.4	1500	8	1.642	0.7873	0.819
1850	0.2	1500	8	3.542	0.3578	0.437
2500	0.6	1500	6	1.534	1.1941	1.190
1200	0.4	1500	8	4.122	0.9043	0.981
1850	0.6	1000	6	2.897	1.2121	1.133
1850	0.4	1000	4	4.109	0.6429	0.578
1850	0.4	2000	8	2.758	0.8863	1.037
1850	0.4	1000	8	3.005	0.8053	0.762
1200	0.6	1500	6	4.014	1.3111	1.351
1200	0.4	1500	4	5.226	0.7419	0.796
2500	0.2	1500	6	2.854	0.2181	0.264
1850	0.6	1500	8	2.222	1.3338	1.363
1850	0.2	2000	6	3.970	0.3171	0.482
1850	0.4	1500	6	3.434	0.7646	0.808
1850	0.6	1500	4	3.326	1.1714	1.179
1850	0.4	1500	6	3.434	0.7646	0.808
1850	0.4	2000	4	3.862	0.7239	0.853
2500	0.4	1000	6	2.317	0.6656	0.590

TABLE 4: Roughness (R_a)—analysis of variance.

Response surface linear model						
Analysis of variance						
Source	Sum of squares	df	Mean square	<i>F</i> -value	<i>P</i> value	
Model	27.52382748	4	6.88095687	636600.00	<0.0001	Significant
<i>A</i>	18.45715248	1	18.45715248	628620.00	<0.0001	
<i>B</i>	5.2272	1	5.2272	68590	<0.0001	
<i>C</i>	0.183027	1	0.183027	5998618.94	<0.0001	
<i>D</i>	3.656448	1	3.656448	1834573.15	<0.0001	
Residual error	1.58333	24	0			
Lack of fit	0	20	0			
Pure error	0	4	0			
Cor total	27.52382748	28				
Standard deviation	0.000397911		R^2	0.999998975		
Mean	0.54264		Adj R^2	0.99999754		
CV (%)	0.073328765		Pred R^2	NA		
PRESS	NA		Adequate precision	3152.502951		

insignificant effect may arise due to noise. Moreover, R^2 , Adj R^2 , and Pred R^2 values indicate a positive approach towards its higher efficacy, and the values are close to 1. The surface interaction plots shown below provide a lucid view on the interaction between machining parameters and the response R_a .

4.1.1. Parameter Interaction Effects. The interaction graph for parameters A and B on response R_a is shown in Figure 3. Minimum roughness is achieved when spindle speed is at its maximum level of 2500 rpm with feed rate maintained at its intermediate level of 1500 mm/min. Any deviation from the above-mentioned level resulted in an adverse effect on response R_a . It is noteworthy to observe that parameter B provides a flexible range between 0.4 mm and 0.6 mm. The interaction graph for D and C on response R_a is depicted in Figure 4. The effect of parameter D is found to have the least contribution on R_a when measured with supplementary parameters considered.

Figure 5 shows the interaction graph of parameters A and D on R_a . When the level of parameter D is maintained between 4 l/min to 8 l/min, it resulted in achieving minimum surface roughness but is found to be associated with the influence of spindle speed. Better results are attained when parameter A is increased gradually along with parameter D.

The effect of parameters C and D is depicted in Figure 6. On careful analysis, one can find that parameter C dominates over parameter B influencing the response R_a . From experimental runs 3 and 6, one can find that increasing the level of feed rate minimizes the roughness. At the same time, experimental run 28 exhibits the influence of parameter A on surface roughness when the other parameters are kept at the same level as stated in runs 3 and 6. This provides a lucid view on the influencing parameters affecting the response R_a . In this case, the order of prominent parameters influencing the response R_a is in the order of parameters A and C followed by parameters B and D.

4.1.2. Predicted Optimum Parameters for R_a . Table 5 shows the optimized level of machining parameters.

4.2. Response Surface Model for the Prediction of MRR. The ANOVA analysis for the response MRR is highlighted in Table 6. “F-value” of 668091 with “P-value” below 0.0001 shows the significance of the developed model. The function is said to be insignificant if the values are greater than 0.10. In other words, a 0.01% chance is there that an insignificant effect may arise due to noise. Moreover, R^2 , Adj R^2 , and Pred R^2 values indicates a positive approach towards its higher efficacy as the values are close to 1. The surface interaction plots shown below provide a lucid view on the interaction between machining parameters and the response MRR.

4.2.1. Parameter Interaction Effects. The following interaction graph depicts the effect of the parameters on MRR. Figure 7 reflects the interaction effect of parameters A and B on MRR. Experimental runs 1, 16, and 17 show a gradual

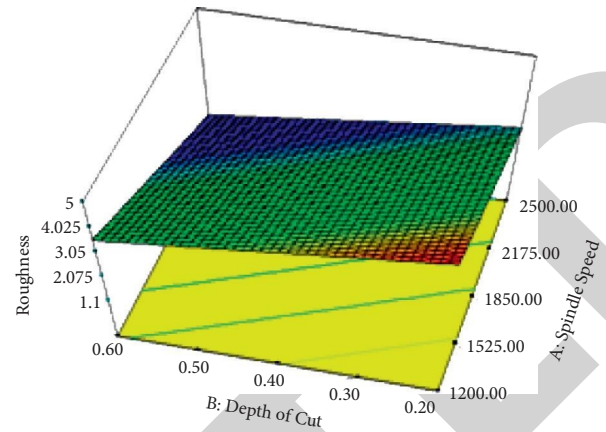


FIGURE 3: Interaction graph of A and B on R_a .

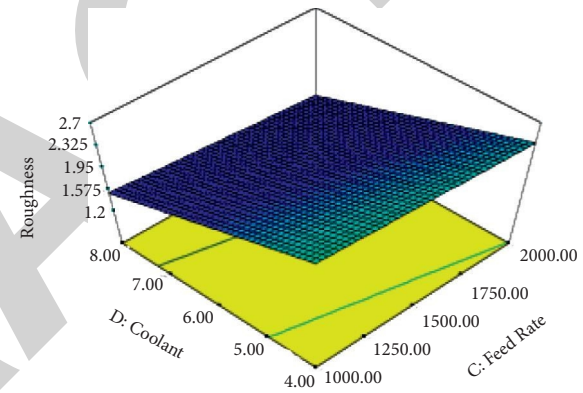


FIGURE 4: Interaction graph of C and D on R_a .

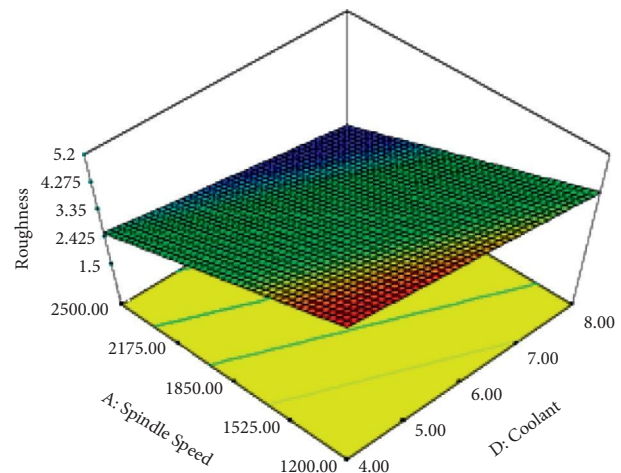


FIGURE 5: Interaction graph of A and D on R_a .

increase in MRR when parameters A and C are kept at level 1 and parameter C is gradually increased. On the other hand, in experimental runs 5, 11, and 13, the level of parameter A is changed, and other parameters are assigned at level 1. It is observed that though there is an increase in MRR, the rate of

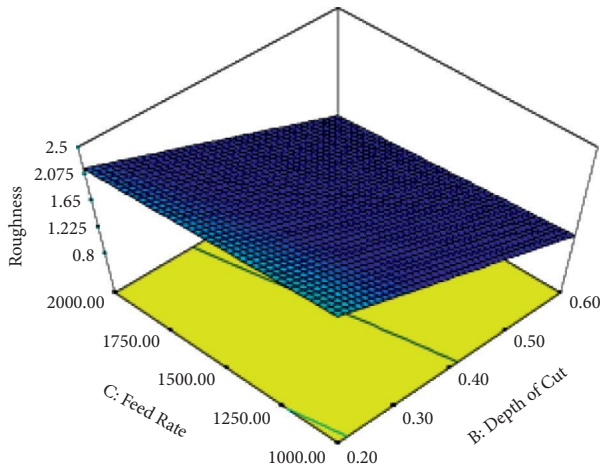


FIGURE 6: Interaction graph of C and D on R_a .

TABLE 5: Optimized level of parameters for roughness.

A (rpm)	B (mm)	C (mm/min)	D (l/min)	R_a (microns)
2495.75	0.47	1000.01	8	1.5439

increase seen is much lower than in the former case. This evidence established firmly that parameter C plays a very prominent role compared to parameter A.

The machining effect of parameters C and B on MRR is shown in Figure 8. Experimental runs 4, 5, and 29 show a gradual increase in MRR when parameters A and B are maintained at 2500 rpm, 0.4 mm, respectively, and parameter C is gradually increased. Whereas, in experimental runs 8, 9, and 26, the level of parameters A and C are kept constant (1850 rpm and 1500 mm/min), and parameter B is varied. It is observed that there is a drastic increase in MRR when compared with that of parameter C. This evidence established firmly that parameter B plays a very prominent role compared to parameter C.

Figure 9 describes the machining effect of parameters D and C on MRR. Experimental runs 8 and 13, 18 and 28, and 23 and 26 clearly depict the effect of parameter D when other parameters are kept constant. In the above-stated experimental runs, a pattern of increase in MRR can be observed. The applied coolant enhances the quantity of material removed by washing off the removed materials and heat generated while machining. On the other hand, in experimental runs 3 and 6 and runs 17 and 28, the level of parameter C is alone changed and found that the application of coolant enhances MRR compared to parameter C but depends on parameters B and A.

The machining effect of parameters A and D on MRR is shown in Figure 10. Experimental runs 8 and 13, 18 and 28, and 23 and 26 clearly depict the effect of coolant flow rate when other parameters are kept constant. In the above-stated experimental runs, an increase in the MRR is observed. On the other hand, experimental runs 11 and 22, 3 and 29, and 14 and 20 show an increase in MRR when spindle speed is varied keeping all other parameters constant.

4.2.2. Predicted Optimized Set of Machining Parameters for MRR. Table 7 shows the optimized level of machining parameters.

4.3. Response Surface Model for the Prediction of Power Consumed (P_c). Table 8 reflects the ANOVA analysis for the response, P_c . “F-value” of 534600.00 with “P-value” below 0.0001 highlights the significance of the developed function. The function is said to be insignificant if the values are greater than 0.10. In other words, a 0.01% chance is there that an insignificant effect may arise due to noise. Moreover, R^2 , Adj R^2 , and Pred R^2 values indicate a positive approach towards its higher efficacy as the values are close to 1. The interaction graphs shown below provide a lucid view on the interaction between machining parameters and the response P_c .

4.3.1. Parameter Interaction Effects. Figures 11 and 12 interpret the interaction effect of machining parameters on power consumption (P_c). Figure 11 reflects the machining effect of parameters A and B on P_c . Experimental runs 8 and 9, 12 and 22, and 11 and 15 show a rapid increase in power consumption when feed rate is increased, while other parameters are taken as constant. This shows that an increased parameter B increases the force of cutting, thereby consuming more power. On the other hand, in experimental runs 12, 15, and 17 when the level of parameter A is changed and other parameters are kept constant, an increase in power consumption is observed as parameter A increases. But the impact on power consumption is a little lower when compared to parameter B.

Figure 12 reflects the effect of parameters B and C on power consumption. Experimental runs 4, 5, and 29 show a rapid increase in power consumption when parameter C is increased while other parameters are taken as constant. This indicates that an increase in parameter C considerably increases power consumption due to drastic variations in cutting forces. On the other hand, in experimental runs 8, 9, and 26 parameter A is changed, and other parameters are assigned as constant. From the experimental runs, it is observed that though parameter A affects power consumption directly, it is highly influenced parameter B followed by C.

In Figure 13, the machining behaviour of parameters D and C on P_c is shown. Experimental runs 8 and 13, 18 and 28, and 23 and 26 clearly depict the effect of parameter D when other parameters are kept constant. In the above-stated experimental runs, an increase in power consumption is observed in the above-mentioned runs. This proves that coolant contributes negligibly in addressing power consumption. On the other hand, in experimental runs 3 and 6 and runs 17 and 28, the level of parameter C is alone changed and is observed that an increase in parameter C on P_c .

Figure 14 represents the machining effect of parameters A and D and coolant on P_c . Experimental runs 8 and 13, 18 and 28, and 23 and 26 clearly depict the effect of parameter D when other parameters are kept constant. In the above-stated experimental runs, it is observed that coolant

TABLE 6: Material removal rate (MRR)—analysis of variance.

Response surface linear model						
Analysis of variance table						
Source	Sum of squares	df	Mean square	F-value	P value	
Model	2.99759928	4	0.74939982	668091.1902	<0.0001	Significant
A	0.041067	1	0.041067	1034328.952	<0.0001	
B	2.857728	1	2.857728	749879.2755	<0.0001	
C	0.019683	1	0.019683	430180.4257	<0.0001	
D	0.07912128	1	0.07912128	636600.00	<0.0001	
Residual error	1.87633	24	0			
Lack of fit	0	20	0			
Pure error	0	4	0			
Cor total	2.99759928	28				
Standard deviation	0.000697911		R^2	0.98768975		
Mean	0.54264		Adj R^2	0.98524754		
CV (%)	0.073328765		Pred R^2	NA		
PRESS	NA		Adequate precision	2152.502951		

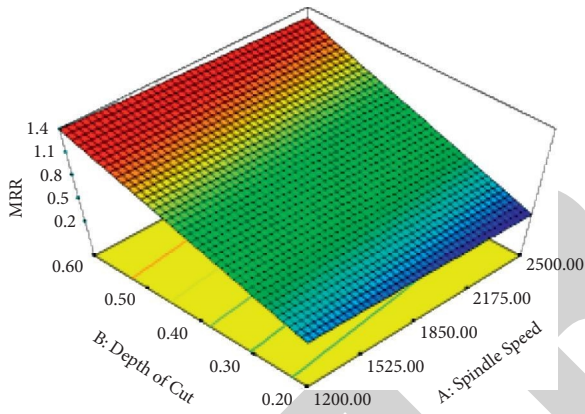


FIGURE 7: Interaction graph of B and A on MRR.

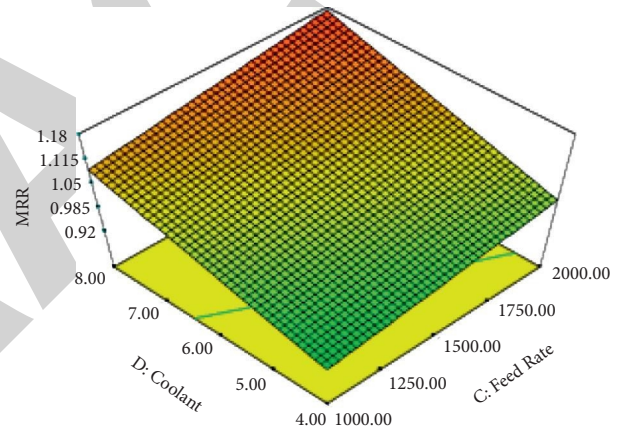


FIGURE 9: Interaction graph of D and C on MRR.

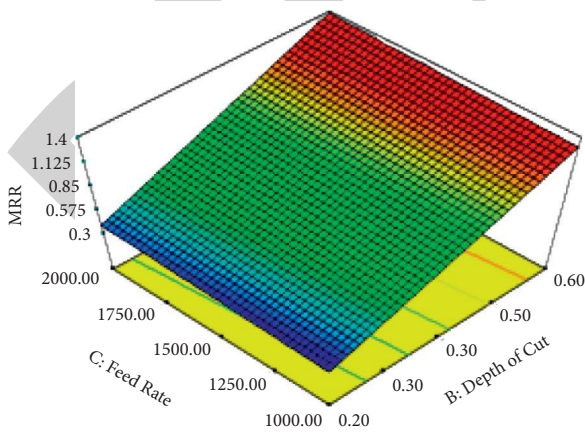


FIGURE 8: Interaction graph of C and B on MRR.

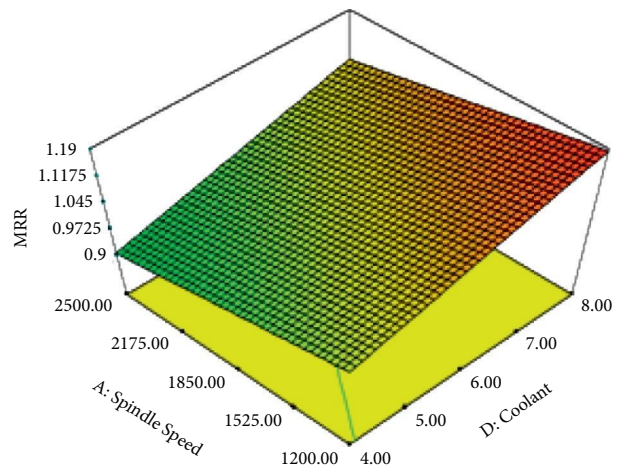


FIGURE 10: Interaction graph of A and D on MRR.

behaviour varies depending upon the combination of other parameters. On the other hand, experimental runs 11 and 22, 3 and 29, and 14 and 20 show a decrease in P_c when parameter A is increased.

4.3.2. Predicted Optimized Set of Machining Parameters for P_c . Table 9 shows the optimized level of machining parameters.

TABLE 7: Optimized level of parameters for MRR.

A (rpm)	B (mm)	C (mm/min)	D (l/min)	MRR (IPM)
2495.75	0.47	1000.01	8	0.916658

TABLE 8: Power consumed (P_c)—ANOVA.

Source	Sum of squares	df	Analysis of variance			P value	Significant
			Mean square	F-value			
Model	2.9792694	4	0.74481735	534600.00	<0.0001		
A	0.07795632	1	0.07795632	512366.00	<0.0001		
B	2.572428	1	2.572428	636600.00	<0.0001		
C	0.226875	1	0.226875	506366.00	<0.0001		
D	0.10201008	1	0.10201008	47690.00	<0.0001		
Residual error	3.87633	24	0				
Lack of fit	0	20	0				
Pure error	0	4	0				
Cor total	2.9792694	28					
Standard deviation	0.000786511		R^2	0.98557689			
Mean	0.57264		Adj R^2	0.95952475			
CV (%)	0.083328765		Pred R^2	NA			
PRESS	NA		Adequate precision	3152.502951			

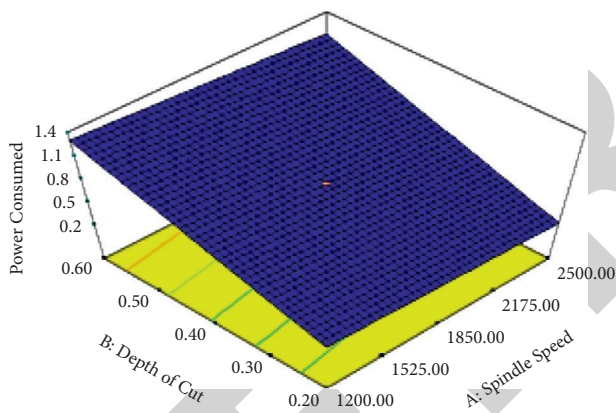


FIGURE 11: Interaction graph of A and C on P_c .

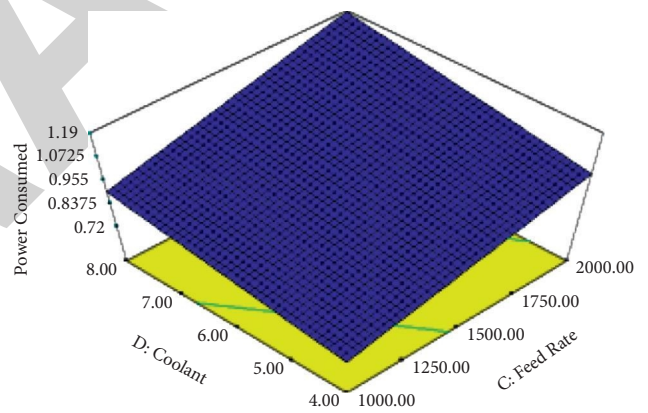


FIGURE 13: Interaction graph of D and C on P_c .

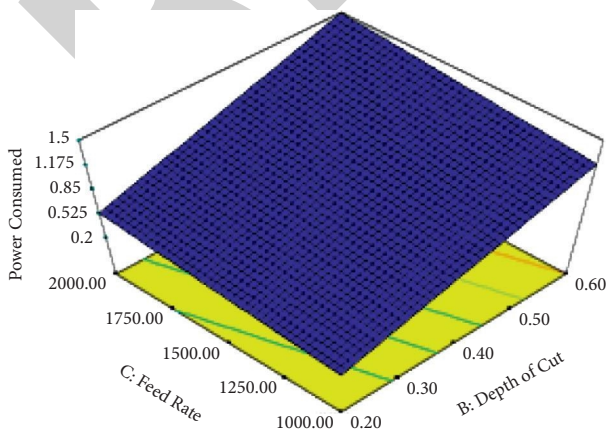


FIGURE 12: Interaction graph of C and B on P_c .

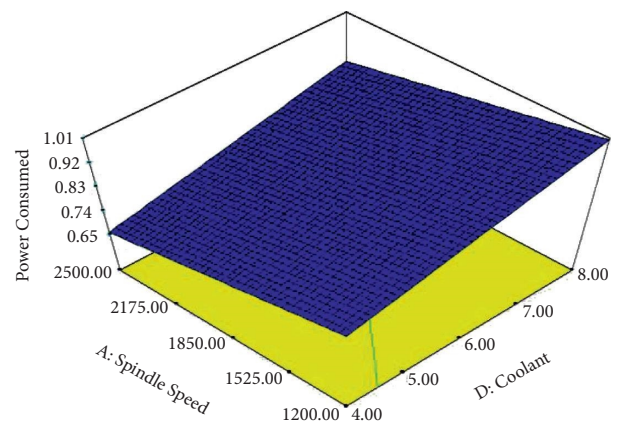


FIGURE 14: Interaction graph of A and D on P_c .

TABLE 9: Optimized level of parameters for power consumption (P_c).

A (rpm)	B (mm)	C (mm/min)	D (l/min)	P_c (HP)
2495.75	0.47	1000.01	8	0.843122

TABLE 10: Grey regression analysis.

Normalized values			Deviation sequence			Grey relation coefficients			Grey relational grade	Rank
R_a	P_c	MRR	R_a	P_c	MRR	R_a	P_c	MRR		
0.294	1.000	0.976	0.706	0.000	0.024	0.415	1.000	0.954	0.790	2
0.706	0.000	0.096	0.294	1.000	0.904	0.630	0.333	0.356	0.440	26
0.141	0.547	0.521	0.859	0.453	0.479	0.368	0.525	0.511	0.468	22
0.859	0.453	0.551	0.141	0.547	0.449	0.780	0.477	0.527	0.595	10
0.681	0.644	0.652	0.319	0.356	0.348	0.611	0.584	0.590	0.595	9
0.206	0.318	0.453	0.794	0.682	0.547	0.386	0.423	0.478	0.429	27
0.500	0.500	0.536	0.500	0.500	0.464	0.500	0.500	0.519	0.506	14
0.181	0.962	1.010	0.819	0.038	-0.010	0.379	0.930	1.020	0.776	3
0.500	0.500	0.536	0.500	0.500	0.464	0.500	0.500	0.519	0.506	14
0.500	0.500	0.536	0.500	0.500	0.464	0.500	0.500	0.519	0.506	14
0.000	0.818	0.894	1.000	0.182	0.106	0.333	0.734	0.824	0.630	7
0.972	0.490	0.517	0.028	0.510	0.483	0.946	0.495	0.509	0.650	6
0.472	0.809	0.875	0.528	0.191	0.125	0.486	0.723	0.799	0.670	4
1.000	0.182	0.178	0.000	0.818	0.822	1.000	0.379	0.378	0.586	11
0.319	0.356	0.420	0.681	0.644	0.580	0.423	0.437	0.463	0.441	25
0.641	0.229	0.163	0.359	0.771	0.837	0.582	0.393	0.374	0.450	24
0.322	0.691	0.637	0.678	0.309	0.363	0.425	0.618	0.580	0.541	12
0.678	0.309	0.435	0.322	0.691	0.565	0.608	0.420	0.469	0.499	19
0.613	0.538	0.502	0.387	0.462	0.498	0.564	0.520	0.501	0.528	13
0.347	0.047	0.081	0.653	0.953	0.919	0.434	0.344	0.352	0.377	29
0.028	0.510	0.555	0.972	0.490	0.445	0.340	0.505	0.529	0.458	23
0.653	0.953	0.991	0.347	0.047	0.009	0.590	0.913	0.982	0.829	1
0.819	0.038	0.062	0.181	0.962	0.938	0.734	0.342	0.348	0.475	21
0.359	0.771	0.908	0.641	0.229	0.092	0.438	0.686	0.845	0.656	5
0.500	0.500	0.536	0.500	0.500	0.464	0.500	0.500	0.519	0.506	14
0.528	0.191	0.197	0.472	0.809	0.803	0.515	0.382	0.384	0.427	28
0.500	0.500	0.536	0.500	0.500	0.464	0.500	0.500	0.519	0.506	14
0.387	0.462	0.570	0.613	0.538	0.430	0.449	0.482	0.538	0.490	20
0.794	0.682	0.618	0.206	0.318	0.382	0.708	0.611	0.567	0.629	8

5. Optimization of Parameters by Grey Regression Analysis

The following steps are followed to arrive at the optimal solutions:

- (1) Normalization of responses: in this step, preprocessing of data is performed based on the objective function defined. If the normalization or data preprocessing is based on the “larger the better” function, then it is computed based on equation (1). If the normalization or data preprocessing is based on “smaller the better” function, then it is computed based on equation (2). Normalization is a method to arrive at a comparable data set from the original set of data reducing the percentage of variation for ease of analysis.

$$Xi(k) = \frac{xi(k) - \min xi(k)}{\max xi(k) - \min xi(k)}, \tag{1}$$

$$Xi(k) = \frac{\max xi(k) - xi(k)}{\max xi(k) - \min xi(k)}, \tag{2}$$

where $i = 1, \dots, m, k = 1, \dots, n, m$ is the number of experimental data, and n is the number of responses. $Xi(k)$ represents the value after data preprocessing; $xi(k)$ represents the original sequence data; $\max xi(k)$ is the largest value of $xi(k)$; and $\min xi(k)$ is the minimal value.

- (2) Computation of deviation sequence: based on responses, “smaller the better” option is applied for R_a and P_c whereas for MRR, the “larger the better” option is applied. In this step, the deviation is calculated for normalized values. In this, for each response, the deviation in each case is recorded with respect to the higher normalized value attained.
- (3) Computation of grey relational coefficients: the grey regression coefficients are calculated using the relation shown in equation (3): Here, $\xi_i(k)$ is the grey relational coefficient. Δ_{\min} and Δ_{\max} are the minimum and maximum values of absolute differences. And, ψ is 0.5, which is the distinguishing or identification coefficient that usually ranges from 0 to 1:

TABLE 11: Optimized parameter by GRA.

A (rpm)	B (mm)	C (mm/min)	D (l/min)
2500	0.2	1500	6

TABLE 12: Confirmatory runs.

Optimization tool	A (rpm)	B (mm)	C (mm/min)	D (l/min)	R_a (microns)	MRR (IPM)	P_c (HP)
Box-Behnken	2495.75	0.47	1000.01	8	1.543	0.916658	0.843122
GRA	2500	0.2	1500	6	1.398	0.8296	0.7961
Deviation					0.154	0.087	0.047
% deviation					10	9	6

$$\xi_i(k) = \frac{\Delta \min + \psi \Delta \max}{\Delta o_i(k) + \psi \Delta \max} \quad (3)$$

- (4) Computation of grey relational grade: the grey relational grade (γ) represents the correlation level between the reference and comparability sequences. In this stage, a multiobjective function is converted into a single-objective function. The following equation is the governing equation for arriving at grey relational grade:

$$\gamma^i = \frac{1}{n} \sum_{k=1}^n \xi_i(k). \quad (4)$$

- (5) Optimal parameters: in this step, rank is identified for each set of values. Based on the rank attained, the optimized level is easily figured out which provides the optimum solution by considering all responses together.

Table 10 shows the grey regression analysis performed on the experimental values.

5.1. Optimized Set of Parameters Using Grey Regression Analysis (GRA). From Table 10, the highest rank is contributed by the 22nd experimental run, which includes the following combination of parameters (Table 11).

6. Confirmatory Runs

To validate the above, confirmatory runs were conducted, and Table 12 shows the results attained.

7. Conclusions

The machining parameter optimization is performed on the low-carbon mold steel in CNC end milling. The responses roughness, MRR, power consumption, and tool life were optimized. The optimization process includes responses that have contradictory effect on each other. For example, the objective function needs to be minimum for optimizing roughness and power to arrive at minimum machining cost. At the same time, the production time taken must also be

minimum where the material removal rate comes into play. The objective function for material removal rate is always maximum, which is opposite to the previous one. Therefore, the process becomes complex, and to arrive at the optimal solution, one has to approach a multiobjective function. In this experimental analysis, the following observations are found to be notable:

- (1) Minimum surface roughness attained in the combination of 2500 rpm, 0.6 mm, 1500 mm/min, and 6 l/min
- (2) Minimum power consumption attained in the combination of 1850 rpm, 0.2 mm, 1000 mm/min, and 6 l/min
- (3) Maximum material removal attained in the combination of 1850 rpm, 0.6 mm, 1500 mm/min, and 8 l/min
- (4) All the above cases stand valid till they are treated as single responses.
- (5) In multiobjective optimization, the optimum level is achieved at 2495.75 rpm, 0.47 mm, 1000 mm/min, and 8 l/min using Box-Behnken design
- (6) In GRA, better results are attained at 2500 rpm, 0.2 mm, 1500 mm/min, and 6 l/min
- (7) Since the percentage deviation is within 10% both optimization techniques can be considered for machining of the investigated material.

Data Availability

The data used to support the findings of this study are included within the article.

Disclosure

This study was performed as a part of the employment of Addis Ababa Science and Technology University, Ethiopia.

Conflicts of Interest

The authors declare that there are no conflicts of interest regarding the publication of this article.

Retraction

Retracted: Process Development for Edible Film Preparation Using Avocado Seed Starch: Response Surface Modeling and Analysis for Water-Vapor Permeability

Advances in Materials Science and Engineering

Received 26 December 2023; Accepted 26 December 2023; Published 29 December 2023

Copyright © 2023 Advances in Materials Science and Engineering. This is an open access article distributed under the Creative Commons Attribution License, which permits unrestricted use, distribution, and reproduction in any medium, provided the original work is properly cited.

This article has been retracted by Hindawi, as publisher, following an investigation undertaken by the publisher [1]. This investigation has uncovered evidence of systematic manipulation of the publication and peer-review process. We cannot, therefore, vouch for the reliability or integrity of this article.

Please note that this notice is intended solely to alert readers that the peer-review process of this article has been compromised.

Wiley and Hindawi regret that the usual quality checks did not identify these issues before publication and have since put additional measures in place to safeguard research integrity.

We wish to credit our Research Integrity and Research Publishing teams and anonymous and named external researchers and research integrity experts for contributing to this investigation.

The corresponding author, as the representative of all authors, has been given the opportunity to register their agreement or disagreement to this retraction. We have kept a record of any response received.

References

- [1] R. Ramesh, H. Palanivel, S. Venkatesa Prabhu, B. Z. Tizazu, and A. A. Woldesemayat, "Process Development for Edible Film Preparation Using Avocado Seed Starch: Response Surface Modeling and Analysis for Water-Vapor Permeability," *Advances in Materials Science and Engineering*, vol. 2021, Article ID 7859658, 7 pages, 2021.

Research Article

Process Development for Edible Film Preparation Using Avocado Seed Starch: Response Surface Modeling and Analysis for Water-Vapor Permeability

R. Ramesh ¹, Hemalatha Palanivel ², S. Venkatesa Prabhu ¹,
Belachew Zegale Tizazu ¹ and Adugna Abdi Woldeamayot ²

¹Department of Chemical Engineering, College of Biological and Chemical Engineering, Addis Ababa Science and Technology University, Addis Ababa, Ethiopia

²Department of Biotechnology, College of Biological and Chemical Engineering, Addis Ababa Science and Technology University, Addis Ababa, Ethiopia

Correspondence should be addressed to Hemalatha Palanivel; hemalatha.palanivel@aastu.edu.et

Received 24 June 2021; Accepted 2 August 2021; Published 12 August 2021

Academic Editor: Samson Jerold Samuel Chelladurai

Copyright © 2021 R. Ramesh et al. This is an open access article distributed under the Creative Commons Attribution License, which permits unrestricted use, distribution, and reproduction in any medium, provided the original work is properly cited.

Starch-based edible films are gaining huge interest in food packaging industries. In the present work, avocado seed starch (ASS) was extracted and used to develop an edible film. The influence of four important process factors, starch, agar, sorbitol, and Tween-20, was studied on one of the important barrier properties, water-vapor permeability (WP), of developed edible film. The three-level RSM design with Box–Behnken approach was carried out to investigate the film property, WP. ASS-based edible films were prepared by the casting method. The results revealed that the increment in the contents of Tween-20 and sorbitol reduces the WP of the film. Using the response surface analysis, the effect of the aforementioned factors was analyzed; they showed significant impact on WP. To predict the influence of the selected process parameters, a second-order polynomial equation was constructed. Additionally, Pareto analysis of variance was employed over the obtained results to investigate the significance of the developed process model.

1. Introduction

Petroleum-based non-biodegradable polymeric wastes are significantly increasing the ecological impacts and creating huge global concern. Hence, there is an imperative requirement to develop eco-friendly bio-based materials to alternate the nonrenewable plastic materials [1, 2]. Cellulose derivatives, proteins, gums, lipids, and starch are well-known biopolymers that are commonly used as raw material for biodegradable films. Specifically, for packaging processed or fresh foods, these biopolymers offer significant contribution of preparing thin edible films [3]. One of the abundant, nontoxic, and renewable resources is starch that has the potential capability of forming continuous matrix [4–6]. Starch has the potential advantage of being comparatively low cost. It is able to form films that have a similar

characteristic to synthetic polymers such as being odorless, transparent, and tasteless and having oxygen permeability resistance. However, the films prepared using starch generally require the amalgamation of plasticizer for reducing their brittleness. Another important ingredient for preparing eco-friendly packaging films is agar, which is a biodegradable polysaccharide [7–9]. It is used as a cohesive mediator in the polymeric chain and provides better improvisation in properties related to mechanical and barrier possessions [10, 11]. During the preparation of edible films, hydrophobic constituents (surfactants) are added to decrease the hygroscopicity of the films that can provide appreciable desirability [12]. Different studies have reported about the investigation of behavior of water-vapor permeability (WP) on edible film with respect to different factors [13]. The combined effect of starch extracted from avocado

seed, agar, Tween-80, and sorbitol has not been described elsewhere. Keeping this view, it is important to study about the barrier properties with respect to different proportions of process variables to gain appropriate knowledge about the possibilities of applications for food packing materials. Hence, this investigation was aimed to investigate the effect of selected process factors, namely, avocado seed starch, agar, Tween-20, and sorbitol, on the important barrier property, WP, of an edible film. The combination of the aforementioned parameters was designed using the three-level Box–Behnken method; further, the WP of the film developed from each combination was determined and analyzed by response surface approach.

2. Materials and Methods

2.1. Materials. Avocado seeds were collected from the fruit market of Addis Ababa, Ethiopia (Figure 1). Tween-20 (food grade with 99% purity) and sorbitol (food grade with 98% purity) were obtained from Hi-Media Chemicals, Addis Ababa. Agar was procured from Merck Chemicals, Addis Ababa.

2.2. Extraction of Avocado Seed Starch (ASS). Avocado seeds were grounded well using the laboratory mixer-grinder. The powder was well saturated by soaking with large amounts of distilled water. Prior to this process, sodium metabisulphite was dissolved (0.075% (w/v)) with the distilled water. Further, the soaked content of material was kept to settle for 4 h at room temperature, approximately, $28 \pm 2^\circ\text{C}$. Then, the clear supernatant liquid was carefully transferred to a clean beaker. The sedimented starch was washed repeatedly using sodium metabisulphite solution till the clear suspension was observed. In order to remove the cell debris, the obtained sediment was further filtered using a fine muslin cloth. From the resultant filtration, the clear suspension was collected. Again, it was filtered using $224 \mu\text{m}$ fine sieve. Subsequently, it was subjected to keep deposit. The starch was sedimented and then it was repeatedly washed using distilled water until the wash water was observed to be free of impurities and clear. As a result, the starch was isolated, then sieved, and dried in air at room temperature. In the extracted starch, the amylopectin and amylose concentrations were determined using the method explained by Nogueira et al. [14]. Presence of moisture in the starch was determined by the AOAC procedure [15].

2.3. Preparation of Edible Films. The formulation solutions to prepare the film were formulated with different combinations of agar (0.5–1.0 g), sorbitol (0.5–1.0 ml), Tween-20 (0.1–0.5 ml), and ASS (1–3 g). Casting is one of the well-recognized methods for edible film preparation. This method was adopted to develop the films by following the method specified by Sundramurthy et al. [16]. The developed clear films were carefully detached from the Petri dishes; further, they were equilibrated at 25°C with 57% relative humidity for 3 days before the experimental investigations.



FIGURE 1: Avocado (*Persea americana*) seed.

2.4. Determination of Water-Vapor Permeability (WP). For food packaging purpose, one of the important barrier properties, water-vapor permeability, is a huge concern for edible films. WP of the developed film was assessed using the method defined by Mali et al. [17]. As per the standard, ASTM D6701, WP was considered. The film thickness was assessed using an appropriate digital micrometer. WP (g/m s Pa) was detected using

$$\text{WP} = \frac{\text{WVTR}}{K(P_1 - P_2)l}, \quad (1)$$

where l refers to the thickness of the film (m), K refers to the saturation vapor pressure of water (Pa) at the test temperature (25°C), P_1 refers to relative humidity of the desiccator, and P_2 refers to the relative humidity in the permeation cell. The average value of triplicate experiments was recorded as response.

2.5. Experimental Design and Statistical Analysis. In this investigation, the effect of selected factors (ASS content (F1), 1–3 g; sorbitol concentration (F2), 0.5–1.0 ml; concentration of agar (F3), 0.5–1.0 g; and Tween-20 (F4) contentment, 0.1–0.5 ml) on the WP of the edible films was studied. The Box–Behnken design (BBD) can be more effective than other design approaches. Moreover, it also needs fewer runs compared to other response surface designs. Hence, the BBD design was considered for carrying out the combination of different concentrations of selected factors. Using a

nonlinear regression technique, a second-order polynomial equation was constructed using the experimental results. This model can be used to analyze the true functional relationship between WP and chosen independent factors. This equation can be written as follows:

$$WP = \beta_0 + \sum_{j=1}^k \beta_j F_j + \sum_{j=1}^k \beta_{jj} F_j^2 + \sum_i \sum_{<j=2}^k \beta_{ji} F_i F_j + e_i, \quad (2)$$

where WP is water-vapor permeability (in the present study, as response); F_i and F_j are process factors (i and j range from 1 to k); β_0 implies model intercept coefficient; β_j , β_{jj} , and β_{ij} are refer to interaction coefficients; k refers to the number of selected independent factors (where k is 4 in this work); and e_i is the error function [18]. Results from experimentations were subjected to be analyzed by a statistical software application, Design-Expert 12.0.7.1 (Stat-Ease Inc., USA). To determine the coefficients, the multiple regression investigation was executed. These coefficients can be taken to determine the response (WP). In order to examine the compatibility of the different models constructed to the experimental results, the model summary statistics and sequential model sum of squares were tested. Pareto analysis of variance was carried out to assess the attained experimental results. Different statistical analyses such as F value, p value, sum of squares, degrees of freedom, determination of coefficient, coefficient of variation, predicted determination of coefficient, and adjusted determination of coefficient were employed to obtain the significance of the statistical status of the developed model. Further, the model was used to generate 3D plots for response surfaces to correlate the pure relation between WP and selected four independent factors.

3. Results and Discussion

3.1. Chemical Composition of ASS. Figures 2(a) and 2(b) show the starch extracted from the avocado seed and edible film prepared using ASS, respectively. As per the standard procedure, the chemical composition of the ASS was determined. The results showed that the presence of the isolated starch was observed to be $97.32 \pm 0.51\%$. Furthermore, the presence of moisture content of $10.45 \pm 0.54\%$ and ash content of $0.23 \pm 0.02\%$ was also observed. It was found that the content of amylopectin and amylose in the ASS was determined to be 71% and 29%, respectively. Generally,

edible film is formed by the involvement of two different process, namely, retrogradation and gelatinization. In retrogradation, solubility of dissolved starch was decreased. During the gelatinization process, leaching of amylose present in the starch, disruption, and swelling are involved. Hence, amylose is a significant liability during edible film preparation using starch because of its capability to establish the continuous viscous mass on the film forming solutions. Additionally, amylose shows an appreciable rate in the retrogradation progression. In this study, a substantial content of the amylose was found in the ASS as reported by Bastarrachea et al. [19].

3.2. Experimental Design Analysis. Different combinations of process variable according to the Box-Behnken experimental design with obtained responses are presented in Table 1. Each edible film prepared from the BBD design combination was subjected to examine WP. These data were examined. Different models, namely, cubic, quadratic, interactive (2FI), and linear models, were used to get regression correlation equation. Based on the tests, namely, model summary statistics and the sequential model sum of squares, the appropriateness of equation among various models to express the effect of chosen process factors over the WP was carried out, and it is presented in Table 2.

From the results of the model adequacy test, it was observed that interactive (2FI) and linear models have comparatively lower value of R^2 , predicted R^2 , and adjusted R^2 . It was found that the cubic model can be aliased. Thus, the quadratic model for including linear, interactive, and quadratic terms was selected to express the effect of process factors on the WP of ASS-based bio-films. Additionally, adequacy of obtained quadratic model was investigated by Pareto analysis of variance.

3.3. Model Development and Statistical Analysis. The mathematical model of second-order polynomial equation (equation (3)) can be used to fit the experimental results to generate the empirical models. This equation of the model can exhibit the true correlation between WP and the selected independent factors. The obtained empirical model of quadratic form in terms of actual parameters is presented as follows:

$$\begin{aligned} WP = & 1.00588 - 0.300167 \text{ Starch} - 1.30517 \text{ Sorbitol} \\ & + 0.107833 \text{ Agar} + 0.370833 \text{ Tween 20} + 0.127000 \text{ Starch} * \text{ Sorbitol} \\ & + 0.034000 \text{ Starch} * \text{ Agar} - 0.015000 \text{ Starch} * \text{ Tween 20} + 0.068000 \text{ Sorbitol} * \text{ Agar} \\ & - 0.135000 \text{ Sorbitol} * \text{ Tween 20} - 0.445000 \text{ Agar} * \text{ Tween 20} + 0.047708 (\text{Starch}^2) \\ & + 0.579333 (\text{Sorbitol}^2) + 0.025333 (\text{Agar}^2) - 0.266667 (\text{Tween 20}^2). \end{aligned} \quad (3)$$

Fisher's F -test was used to examine the statistical significance of the obtained polynomial model using ANOVA analysis. From the analysis, it was observed that the

predicted model was very good in being statistically significant (Table 3). The model F -value was found to be higher ($F_{\text{Model}} = 4102.45$), and acceptable low probability value



FIGURE 2: The starch extracted from ASS (a) and the developed edible film prepared from ASS (b).

TABLE 1: Design combination of process variables and obtained responses (WP).

Run no.	ASS content (g)	Sorbitol (ml)	Agar (g)	Tween-20 (ml)	WP of film (g/m ² ·s·Pa) ×10 ⁻¹⁰
1	3	1	0.75	0.3	0.345
2	2	0.75	0.75	0.3	0.266
3	2	0.75	0.5	0.1	0.252
4	2	1	1	0.3	0.297
5	2	0.75	1	0.1	0.363
6	2	0.75	0.75	0.3	0.266
7	3	0.75	0.75	0.5	0.255
8	2	0.75	1	0.5	0.217
9	2	0.5	0.5	0.3	0.319
10	1	1	0.75	0.3	0.269
11	2	1	0.5	0.3	0.225
12	3	0.5	0.75	0.3	0.367
13	1	0.75	0.75	0.5	0.249
14	2	1	0.75	0.5	0.191
15	2	0.5	1	0.3	0.374
16	2	0.75	0.75	0.3	0.266
17	2	0.75	0.5	0.5	0.195
18	1	0.75	1	0.3	0.332
19	2	1	0.75	0.1	0.306
20	1	0.5	0.75	0.3	0.418
21	2	0.75	0.75	0.3	0.266
22	3	0.75	1	0.3	0.366
23	2	0.75	0.75	0.3	0.266
24	2	0.5	0.75	0.1	0.379
25	3	0.75	0.5	0.3	0.282
26	1	0.75	0.75	0.1	0.345
27	3	0.75	0.75	0.1	0.363
28	1	0.75	0.5	0.3	0.282
29	2	0.5	0.75	0.5	0.291

($p < 0.0001$) showed that the predicted model was statistically significant to express WP of the films. The high value of R^2 (0.9998) specified that correlation between experimental and predicted values was found to be high. The values of predicted R^2 (0.9986) and the adjusted R^2 (0.9995) were found to be very close to the value of R^2 which is in good agreement.

3.4. Response Surface Analysis for Water-Vapor Permeability. BBD coupled with RSM was used to assess the effect of four selected independent factors such as ASS (1–3 g), Tween-20 (0.1–0.5 ml), agar (0.5–1.0 g), and sorbitol (0.5–1.0 ml) on WP of the ASS-based edible films. Using a generated mathematical equation (equation (2)), plots for 3D response surface were drawn as a function of two independent factors, while

TABLE 2: Adequacy of tested models for WP as response.

Source	Std. dev	R^2	Adjusted R^2	Predicted R^2	PRESS	
Linear	0.0358	0.6836	0.6309	0.5285	0.0460	
2FI	0.0367	0.7512	0.6130	0.2847	0.0697	
Quadratic	0.0013	0.9998	0.9995	0.9986	0.0001	Suggested
Cubic	0.0003	1.000	1.000	0.9991	0.0001	Aliased

PRESS: predicted residual error sum of squares.

TABLE 3: ANOVA analysis for predicted second-order polynomial equation.

Source	Sum of squares	df	Mean square	F value	p value	
Model	0.0974	14	0.0070	4102.45	<0.0001	Significant
A-starch	0.0006	1	0.0006	338.41	<0.0001	
B-sorbitol	0.0221	1	0.0221	13028.60	<0.0001	
C-agar	0.0129	1	0.0129	7625.63	<0.0001	
D-Tween-20	0.0310	1	0.0310	18278.60	<0.0001	
AB	0.0040	1	0.0040	2376.91	<0.0001	
AC	0.0003	1	0.0003	170.36	<0.0001	
AD	0.0000	1	0.0000	21.22	0.0004	
BC	0.0001	1	0.0001	42.59	<0.0001	
BD	0.0002	1	0.0002	107.43	<0.0001	
CD	0.0020	1	0.0020	1167.31	<0.0001	
A ²	0.0148	1	0.0148	8702.87	<0.0001	
B ²	0.0085	1	0.0085	5012.92	<0.0001	
C ²	0.0000	1	0.0000	9.59	0.0079	
D ²	0.0007	1	0.0007	435.04	<0.0001	
Residual	0.0000	14	1.696E-06			
Lack of fit	0.0000	10	2.375E-06			Not significant
Pure error	0.0000	4	0.0000			
Cor total	0.0975	28				

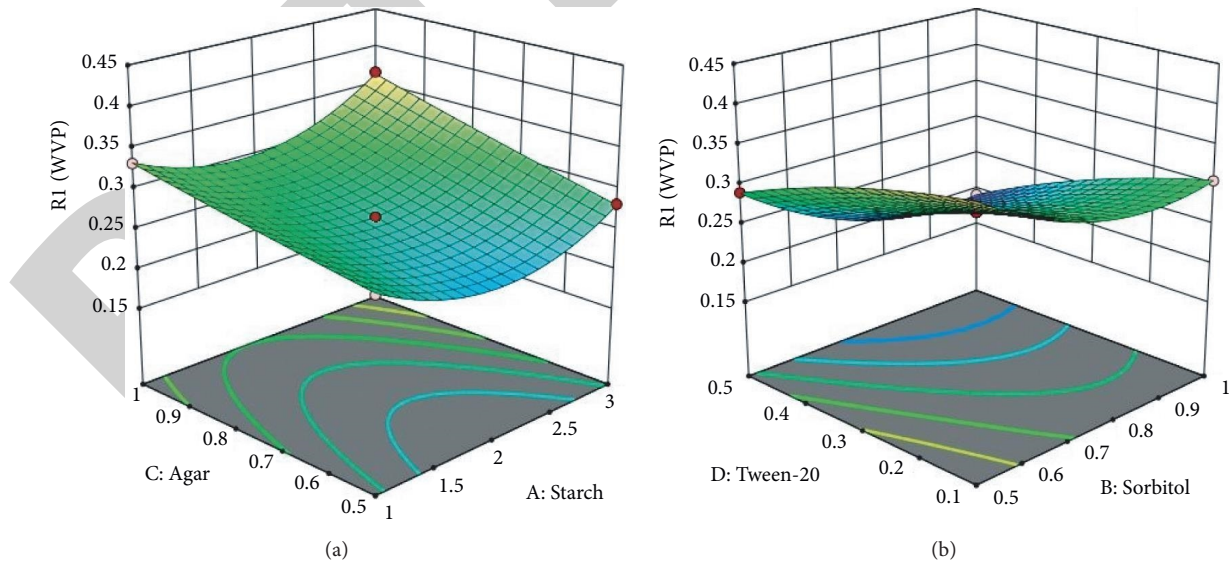


FIGURE 3: Continued.

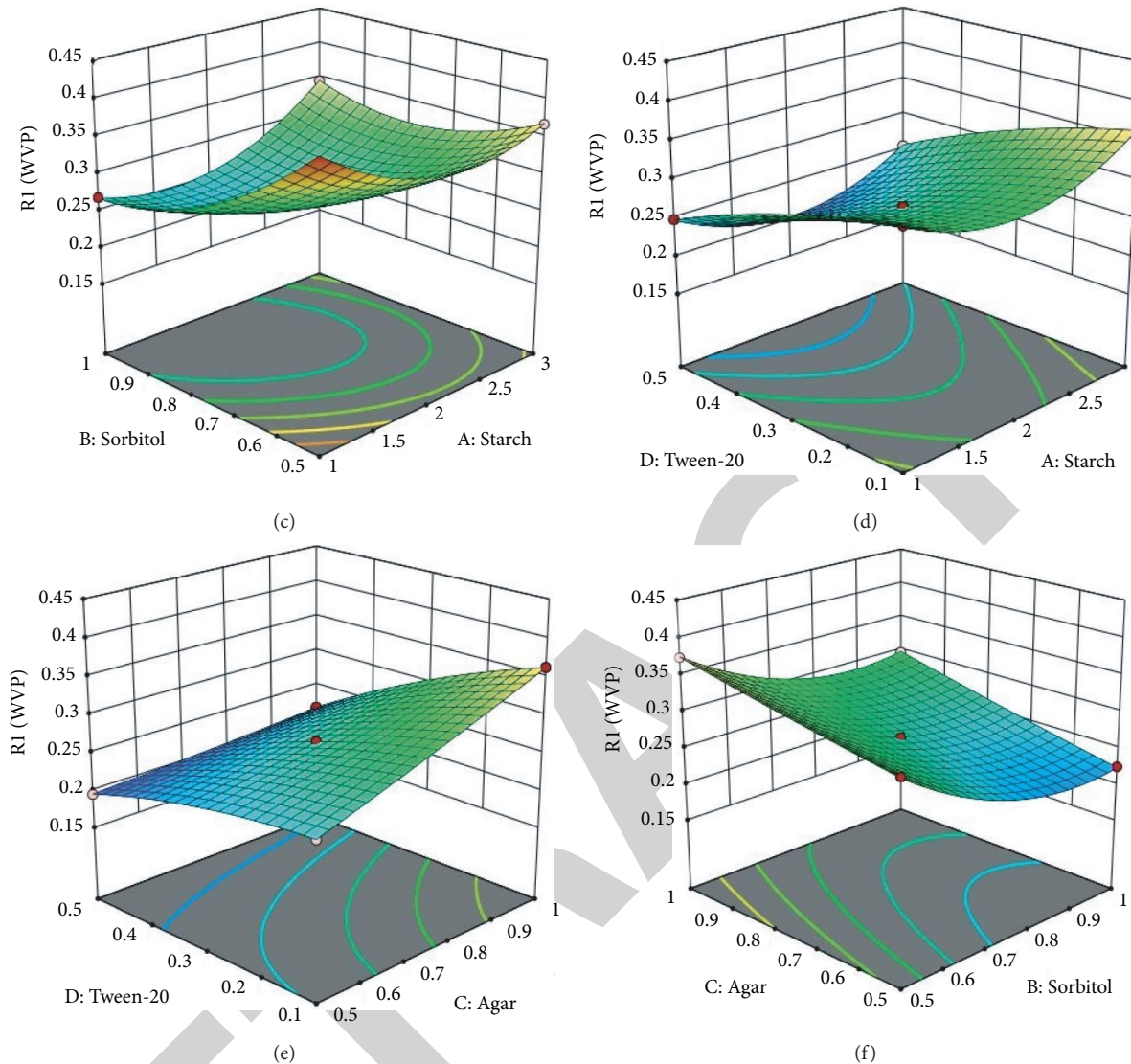


FIGURE 3: 3D surface showing the interaction impacts of process variables on WP.

the other two parameters were kept at constant. Experimental results revealed that the increase in concentration of starch and agar led to the increase in WP (Figure 3(a)).

This is because of intermolecular connections becoming high between starch and agar at high concentrations. In addition, high concentrations of starch and agar increase the free space that led to extending the intermolecular distance. Normally, increment in plasticizer concentration reduces the intermolecular bonds among the polymer chains [20]. But in this case, WP of ASS films was slowly decremented with sorbitol concentration increment (Figure 3(b)). This happened due to the ineffectiveness in reducing intermolecular hydrogen bonding between amylopectin and amylose [21–23]. Additional increment in Tween-20 concentration reduces the affinity water and available number of polar groups. Hence, WP of the films were getting decremented (Figure 3(b)). From the developed model, it was observed that the concentration of starch and sorbitol had the negative effect on WP. Since the WP needs to be minimized, these factors are

considered as most effective factors. Steric-hindrance structure of the Tween-20 is also responsible for the hydrophilic/lipophilic balance (HLB) ratio and hydrophobicity [24–26].

4. Conclusion

The edible film was developed using the starch extracted from avocado seeds (ASS). The combinations of different concentrations of ASS (1-3g), Tween-20 (0.1-0.5ml), agar (0.5-1.0g), and sorbitol (0.5-1.0ml) were examined for the WP. The effect of the four important process factors on the water-vapor permeability (WP) of the developed films was investigated using the three-level Box–Behnken design coupled with RSM. The developed edible films seemed to be homogenous and transparent. From the experimental results, it was found that WP of the ASS-based films decreased with increment in Tween-20 and sorbitol. It is apparent that WP is well controlled by surfactant and plasticizer

Retraction

Retracted: XRD Peak Profile Analysis of SiC Reinforced Al₂O₃ Ceramic Composite Synthesized by Electrical Resistance Heating and Microwave Sintering: A Comparison

Advances in Materials Science and Engineering

Received 26 December 2023; Accepted 26 December 2023; Published 29 December 2023

Copyright © 2023 Advances in Materials Science and Engineering. This is an open access article distributed under the Creative Commons Attribution License, which permits unrestricted use, distribution, and reproduction in any medium, provided the original work is properly cited.

This article has been retracted by Hindawi, as publisher, following an investigation undertaken by the publisher [1]. This investigation has uncovered evidence of systematic manipulation of the publication and peer-review process. We cannot, therefore, vouch for the reliability or integrity of this article.

Please note that this notice is intended solely to alert readers that the peer-review process of this article has been compromised.

Wiley and Hindawi regret that the usual quality checks did not identify these issues before publication and have since put additional measures in place to safeguard research integrity.

We wish to credit our Research Integrity and Research Publishing teams and anonymous and named external researchers and research integrity experts for contributing to this investigation.








The corresponding author, as the representative of all authors, has been given the opportunity to register their agreement or disagreement to this retraction. We have kept a record of any response received.

References

- [1] M. Mohankumar, S. Praveen Kumar, B. Guruprasad et al., "XRD Peak Profile Analysis of SiC Reinforced Al₂O₃ Ceramic Composite Synthesized by Electrical Resistance Heating and Microwave Sintering: A Comparison," *Advances in Materials Science and Engineering*, vol. 2021, Article ID 8341924, 7 pages, 2021.

Research Article

XRD Peak Profile Analysis of SiC Reinforced Al₂O₃ Ceramic Composite Synthesized by Electrical Resistance Heating and Microwave Sintering: A Comparison

Madhan Mohankumar ¹, **S. Praveen Kumar**,² **B. Guruprasad** ³, **Sreekanth Manavalla** ⁴,
Joshua Stephen Chellakumar Isaac JoshuaRamesh Lalvani ⁵, **P. L. Somasundaram** ⁶,
P. Tamilarasu ⁷ and **Prakash Singh Tanwar** ⁸

¹Department of Mechanical Engineering, Velammal Engineering College, Chennai, Tamil Nadu, India

²Faculty of Mechanical and Production Engineering, Arba Minch Institute of Technology, Arba Minch University, Arba Minch, Ethiopia

³Department of Mechanical Engineering, Alagappa Chettiar Government College of Engineering and Technology, Karaikudi, Tamilnadu, India

⁴School of Mechanical Engineering & Electric Vehicles Incubation, Testing and Research Centre, Vellore Institute of Technology Chennai, Vellore, Tamilnadu, India

⁵Faculty of Mechanical and Production Engineering, Arba Minch Institute of Technology, Arba Minch University, Arba Minch, Ethiopia

⁶Department of Electrical and Electronics Engineering, M.Kumarasamy College of Engineering, Karur, Tamil Nadu, India

⁷Department of Electrical and Electronics Engineering, Kongu Engineering College, Perundurai, Tamil Nadu, India

⁸Department of Computer Science and Engineering, Lovely Professional University, Phagwara, Punjab, India

Correspondence should be addressed to Madhan Mohankumar; madhanesecme08@gmail.com and Joshua Stephen Chellakumar Isaac JoshuaRamesh Lalvani; isaac.jrl@amu.edu.et

Received 17 July 2021; Accepted 28 July 2021; Published 4 August 2021

Academic Editor: Samson Jerold Samuel Chelladurai

Copyright © 2021 Madhan Mohankumar et al. This is an open access article distributed under the Creative Commons Attribution License, which permits unrestricted use, distribution, and reproduction in any medium, provided the original work is properly cited.

Al₂O₃ with 10 wt.% of SiC ceramic composite is synthesized at 1500°C by electrical resistance heating sintering with a holding time of 5 hours and microwave sintering methods with a holding time of 15 minutes. The samples generated by the two methods are characterized using powder X-ray diffraction and field emission scanning electron microscopy (FESEM). Experiments with both samples showed that the existence of the α -Al₂O₃ and β -SiC phases in both samples was verified by the findings of XRD pattern on both samples. Microstructure study illustrates that the Al₂O₃ matrix particles have spherical-like shape and their average matrix particle size is 67 ± 5 nm for electrical resistance heating sintered sample and 38 ± 5 nm for microwave sintered sample. The lattice strain and crystallite size of Al₂O₃ matrix were measured using Williamson–Hall (W-H) methods, which were achieved via the use of XRD peak broadening, based on a diffraction pattern. Three modified W-H models were used to compute other parameters, including strain (ϵ) and stress (σ), as well as energy density (u). These models were the uniform deformation model (UDM), the uniform deformation energy density model (UDEM), and the uniform deformation stress model (UDSM). The average crystallite sizes of α -Al₂O₃ attained from these three models of Williamson–Hall (W-H) methods and FESEM analysis are correlated and found very close to each other. In all three models of the W-H technique, X-ray diffraction peak profile examination of electrical resistance heating-sintered and microwave-sintered Al₂O₃/10 wt. % SiC ceramic composite reveals that the microwave-sintered sample has finer crystallite size with less strain.

1. Introduction

Among all the ceramics, alumina (Al_2O_3) are extensively used in engineering applications owing to its thermal and chemical inertness, comparably high strength, and electrical and thermal insulators together with the availability and bounteousness [1–8]. In spite of the abovementioned advantages, brittleness and low fracture toughness of Al_2O_3 create restrictions of its applications. One of the methods to overcome this limitation is the synthesis of fibre or particulate reinforced Al_2O_3 ceramic composites. In this, reinforcement can be a polymer, metal, or ceramics. A ceramic material, silicon carbide (SiC), perchance, is one of the options for the secondary phase which bring about the enhancement of Al_2O_3 matrix [9–14]. Nihara stated that inclusion of SiC particles in little amount to the Al_2O_3 matrix can enhance the mechanical properties of $\text{Al}_2\text{O}_3/\text{SiC}$ structural ceramic composite substantially in comparison with monolithic Al_2O_3 [15–19]. They found that the addition of 5 wt.% SiC as a secondary phase improved the strength and fracture toughness of the material from 350 to 1520 MPa and 3.5 to 4.8 MPam^{1/2}, respectively, by increasing the amount of SiC in the material [15]. There are various ways to sinter this structural ceramic composite such as standard pressureless sintering, hot isostatic pressing, spark plasma sintering, and microwave sintering. Among these, microwave sintering is one of the effective and energy-saving methods which also enhances the mechanical and microstructure of $\text{Al}_2\text{O}_3/\text{SiC}$ ceramic composites [16, 17].

Crystallite size and morphology play vital parts in several applications of the ceramic composites, which have induced the researchers to concentrate on the fabrication methods, type of composites, and sintering methods. XRD peaks' profile investigation has become a very compelling tool for microstructural characterization of ceramics either in bulk or in powder form. It was widely accepted that the Debye–Scherrer technique and the Williamson–Hall method were both appropriate for calculating the lattice strain (ϵ) and the crystallite size (D) from the broadening of XRD peaks, respectively [18–24]. No material has a perfect crystal structure because of their finite size which leads to an anomaly from ideal crystallinity which produces the X-ray diffraction peak broadening [24, 25]. The information from the pattern obtained from diffractometer apparently gives about the expansion of X-ray diffraction peaks and can be directly quantified. However, it is essential to become aware of that broadening of diffraction peaks arises primarily as a result of the following two factors, namely, crystallite size and lattice strain [26]. It is a common practice to use peak profile analysis of diffraction pattern to estimate microstructural characteristics such as lattice strain and crystallite size, and the findings are compared with the observable attributes of the material [27]. Both the microstructural quantities mentioned above influence the intensity and width of the Bragg peak and produce a 2θ peak position shift.

$\text{Al}_2\text{O}_3/10$ wt.% SiC ceramic composite is developed in this study using both electrical resistance heating sintering and microwave sintering techniques. To estimate the following microstructural properties, the authors perform an

XRD peak profile analysis utilising the Debye–Scherrer and modified Williamson–Hall (W–H) techniques. There are three properties of α - Al_2O_3 that have been determined: crystallite size (D), lattice stress (σ), and lattice stiffness (S). In order to compute the above properties, modified W–H plots were utilised. According to the literature review, a thorough and comparative study of X-ray diffraction peak profile analysis using these modified W–H models on electrical resistance heating sintered and microwave sintered $\text{Al}_2\text{O}_3/10$ wt.% SiC ceramic composite has not been published.

2. Experimental Procedure

The ceramic composite $\text{Al}_2\text{O}_3/10$ wt.% SiC was synthesized at 1500°C using electrical resistance heating sintering and microwave sintering techniques. The appropriate weight percentage of Al_2O_3 (Sigma Aldrich Chemicals Pvt Ltd, 99.5%) and SiC (Sigma Aldrich Chemicals Pvt Ltd, 99%) was milled at a speed of 350 rpm for 6 hours with isopropyl alcohol in a planetary ball mill (VB Ceramics, Chennai, India) using tungsten carbide (WC) lined vial and tungsten carbide (WC) ball. After milling, the homogeneous mixture was dried and sieved. With a dwell period of 30 seconds and a pressure of 60 MPa, the homogeneous mixture was compacted into pellets of circular cross section with 5 mm radius and 3 mm thickness using a cold uniaxial press. An initial batch of pellets was sintered at 1500°C for 5 hours in an electrical resistance heating furnace with molybdenum disilicide (MoSi_2) as the heating element, and an additional batch of pellets was sintered at the same temperature with a minimum holding time of 15 minutes in a microwave furnace equipped with a magnetron that produces microwaves at 2.45 GHz and a susceptor that served as the axillary heating element. In both the sintering methods, 10°C per minute heating was used. In both the electrical resistance heating furnace and the microwave furnace, the specimens were furnace cooled after they had been sintering. X-ray diffractogram of the synthesized specimens were reported using XRD-Smart Lab (9 kW), Japan, diffractometer with $\text{CuK}\alpha$ radiation ($\lambda = 1.54060 \text{ \AA}$) utilising 45 kV and 30 mA as operating conditions. 4° per minute, 0.02° per step, and a scan range of 10° to 90° were the scan speeds, steps angles, and scan ranges, respectively. An FESEM (Supra 55-Carl Zeiss, Germany) was used to examine the morphology of the powders in the sintered sample and estimate their composition. Using ImageJ software, the particle size was calculated using the line interpolation technique.

3. Results and Discussion

3.1. X-Ray Diffraction Analysis. Figure 1 exemplifies the diffractogram of microwave-sintered and electrical resistance heating-sintered $\text{Al}_2\text{O}_3/10$ wt.% SiC ceramic composite sample, recorded between 10° and 90° of Bragg angle (2θ). All the observed peaks of X-ray diffraction pattern can be indexed with the rhombohedral system of α - Al_2O_3 and β -SiC, referenced in the JCPD's file no. 71–1123 with space group R3c and 89–4793 with space group R3m, respectively.

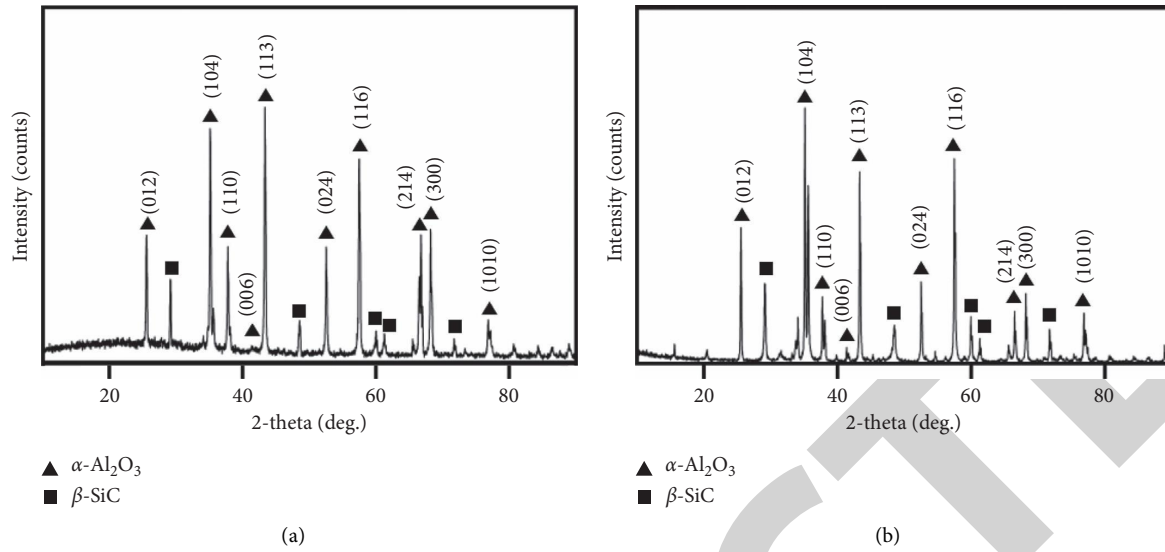


FIGURE 1: XRD pattern of $\text{Al}_2\text{O}_3/10$ wt.% SiC: (a) microwave sintered and (b) electrical resistance heating sintered.

The R3c space group has both hexagonal and rhombohedral unit cells. The fundamental structure is made up of hexagonal oxygen planes interspersed with aluminium planes. The R3m space group of β -SiC indicates the rhombohedral polymorphs, which have zigzag atomic position of Si and C.

The lattice parameter of α - Al_2O_3 matrix phase determined from the X-ray diffraction pattern of electrical resistance heating sintered sample were $a = b = 4.758 \text{ \AA}$ and $c = 12.998 \text{ \AA}$ and microwave sintered samples were $a = b = 4.759 \text{ \AA}$ and $c = 12.995 \text{ \AA}$ and those relatively close when equated with the lattice parameter of α - Al_2O_3 unit cell were $a = b = 4.761 \text{ \AA}$ and $c = 12.99 \text{ \AA}$ from the JCPD's file no. 71-1123. In both microwave-sintered and electrical resistance heating-sintered sample, strong and sharp peaks of stable α - Al_2O_3 phase were present and indicate that the samples have crystalline phase, and no other phases of Al_2O_3 were found because the starting powder used was stable α - Al_2O_3 . In the X-ray diffraction analysis, it was found that the microwave-sintered sample peaks were more intense than those of the electrical resistance heating-sintered sample, indicating that the microwave-sintered sample exhibits higher levels of crystallinity than the electrical resistance heating sample.

3.2. Crystallite Size and Strain Determination

3.2.1. Debye-Scherrer Method. In general, the increase in peak width in the X-ray diffractogram and in the peak profile analysis as a result of dislocation growth is by reason of an increase in lattice strain, crystallite size, and instrumental magnification as a result of dislocation growth [28]. The peak broadening caused by instrumental magnification must be taken into consideration while conducting a systematic examination for lattice strain and crystallite size effects. The X-ray diffractogram of a standard Al_2O_3 was obtained in order to isolate the instrumental peak widening from the sample. The corrected peak broadening corresponding to the

various peaks of α - Al_2O_3 was calculated using the following equation [29]:

$$\beta_{hkl} = \left[(\beta_{hkl})_{\text{measured}}^2 - (\beta_{hkl})_{\text{instrumental}}^2 \right]^{1/2} \quad (1)$$

Equation (2) shows how to determine the size of a crystallite using the Scherrer formula, which is given below:

$$D = \frac{k\lambda}{\beta_{hkl} \cos \theta} \Rightarrow \beta_{hkl} = \frac{k\lambda}{D \cos \theta} \quad (2)$$

where k is the shape factor (0.9), D is the crystallite size in nm, λ is the wavelength of X-ray (Cu $K\alpha = 0.15406 \text{ nm}$), and β_{hkl} is the full width at half maxima (FWHM) of an individual peak at 2θ . Table 1 shows the α - Al_2O_3 average crystallite size of electrical resistance heating-sintered and microwave-sintered $\text{Al}_2\text{O}_3/10$ wt.% SiC composite.

3.2.2. Williamson-Hall Method

(1) *Uniform Deformation Model (UDM).* In addition to the strain, the crystallite size and defects in the crystallite lattice may cause X-ray diffraction peaks to be generated in a variety of other situations. By examining the full width half maximum of the peak as a function of Bragg's angle (2θ), Williamson-Hall analysis clearly separates the peak deformation caused by the crystallite size and the lattice strain [30]. Equation (3) was used to calculate the amount of crystal defect and distortion that produces strain in the powders which results in peak broadening:

$$\varepsilon = \frac{\beta_{hkl}}{4 \tan \theta} \quad (3)$$

It has been shown that the crystallite size-induced peak width changes as $1/\cos \theta$ and that the lattice strain varies as $\tan \theta$ using equations (2) and (3), respectively. The total peak widening, which is the sum of the peak broadening caused by both lattice strain and crystallite size, is given by [31]

TABLE 1: Results of Debye–Scherrer, WH plots and SEM image

Method	Debye–Scherer		UDM		W-H methods				SEM D in nm		
	D in nm	D in nm	Strain	D in nm	Strain	Stress σ in MPa	D in nm	Strain		Stress σ in MPa	u in kJm^{-3}
Electrical resistance heating sintering	67.15	61.41	4.1E-0.5	70.67	4.3E-0.5	389.81	74.95	4.5E-0.5	394.65	183.34	67 ± 5
Microwave sintering	37.71	37.05	4.7E-0.6	39.63	4.6E-0.6	388.77	40.36	4.6E-0.6	392.43	189.67	38 ± 5

$$\beta_{hkl} = \beta_D + \beta_\varepsilon, \quad (4)$$

where β_D is the peak broadening on account of crystallite size, β_ε is the peak broadening as a result of lattice strain, and β_{hkl} is the instrumentally adjusted full width half-maximum intensity of the peak broadening. The value of the instrumentally adjusted full width half-maximum intensity of each peak is calculated using equation (1). Given the assumption of self-reliant contributions of lattice strain and crystallite size to peak broadening, the broadening of the peak is equal to the sum of equations (2) and (3), which is denoted by [32]

$$\beta_{hkl} = \frac{k\lambda}{D \cos \theta} + 4\varepsilon \tan \theta. \quad (5)$$

We may get by rearranging equation (5) the following:

$$\beta_{hkl} \cos \theta = \frac{k\lambda}{D} + 4\varepsilon \sin \theta. \quad (6)$$

Based on the assumption that strain is even in all crystallographic directions, as shown in equation (6), the Williamson–Hall equation, also known as the uniform deformation model (UDM), may be used to predict crystallographic direction in a variety of situations. UDM models assume that crystal nature is isotropic, with the assumption that the material's characteristics are not affected by the direction of measurement in the crystallographic direction, as the case with conventional models. With $\beta_{hkl} \cos \theta$ on the y -axis and $4\varepsilon \sin \theta$ on the x -axis, a graph was created and a linear fit was performed. The y -intercepts of the graph represent the crystallite size (D) of the matrix and the slope

represents the amount of strain (ε) in the α - Al_2O_3 matrix. While the UDM plots for electrical resistance heating-sintered sample and microwave-sintered sample are shown in Figures 2(a) and 2(b), respectively, and the average crystallite size and lattice strain are shown in Table 1.

(2) *Uniform Stress Deformation Model (USD M)*. In numerous scenarios, the concepts of homogeneity and isotropies are not met. In order to overcome this and assimilate more practical condition, an approach of anisotropic is implemented. Consequently, anisotropic strain (ε) is used to improve the W-H equation. The stress owing to lattice distortion is assumed to be even across all directions of crystallography in the uniform stress deformation model (USD M), presuming particles have only a small microstrain. In uniform stress deformation model (USD M), stress and strain have linear relationship based on Hook's law:

$$\sigma = \varepsilon Y_{hkl} \Rightarrow \varepsilon = \frac{\sigma}{Y_{hkl}}, \quad (7)$$

where σ is the crystal stress, Y_{hkl} is the modulus of elasticity, and ε is the anisotropic microstrain. The Williamson–Hall technique is modified in the USD M method by replacing equation (7) for equation (6) [32]:

$$\beta_{hkl} \cos \theta = \frac{k\lambda}{D} + \frac{4\sigma \sin \theta}{Y_{hkl}}. \quad (8)$$

Equation (9) gives Young's modulus for hexagonal crystal structures [33]:

$$Y_{hkl} = \frac{[h^2 + (h + 2k)^2/3 + (al/c)^2]^2}{S_{11}(h^2 + (h + 2k)^2/3)^2 + S_{33}(al/c)^4 + (2S_{13} + S_{44})(h^2 + (h + 2k)^2/3)(al/c)^2}, \quad (9)$$

where S_{11} , S_{13} , S_{33} , and S_{44} are the elastic compliances of Al_2O_3 with values 2.3×10^{-12} , 0.4×10^{-12} , 2.2×10^{-12} , and $-6.8 \times 10^{-12} \text{ m}^2\text{N}^{-1}$ respectively; “ a ” and “ c ” are lattice parameters [34]. By plotting, $\beta_{hkl} \cos \theta$ along the y -axis and $4 \sin \theta / Y_{hkl}$ along the x -axis, the slope of the linear fit provides the uniform stress (σ) and the y -intercept provides the crystallite size (D). The USD M plots for electrical resistance heating-sintered and microwave-sintered $\text{Al}_2\text{O}_3/10 \text{ wt. \% SiC}$ samples are shown in Figures 3(a) and 3(b), respectively, and the values of

uniform deformation stress (σ) and crystallite size (D) are included in Table 1.

(3) *Uniform Deformation Energy Density Model (UDED M)*. The crystal energy density of the sample was calculated using the UDED M model. Crystals were formerly thought to follow a homogeneous and isotropic model, according to traditional view. Nevertheless, the assumption of homogeneity and isotropy is false in a large number of cases. Furthermore, when examining the deformation energy

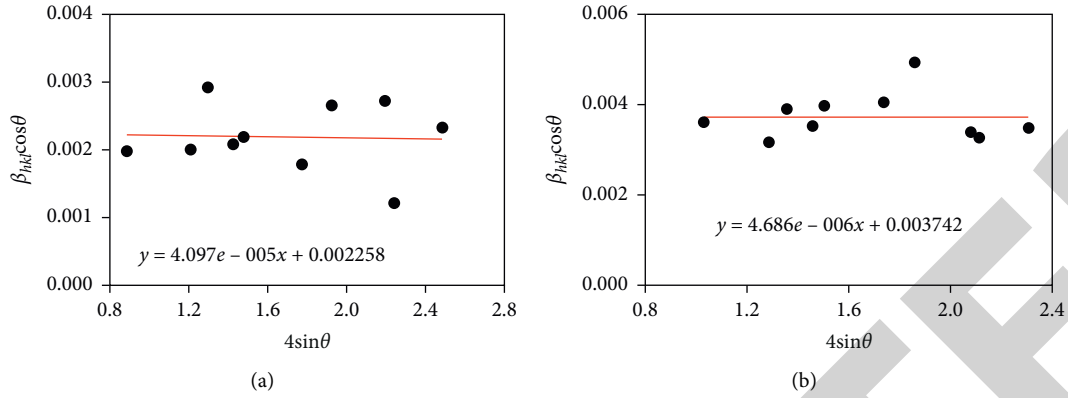


FIGURE 2: UDM plot for $\text{Al}_2\text{O}_3/10\text{wt. \% SiC}$ sample: (a) electrical resistance heating sintering and (b) microwave sintering.

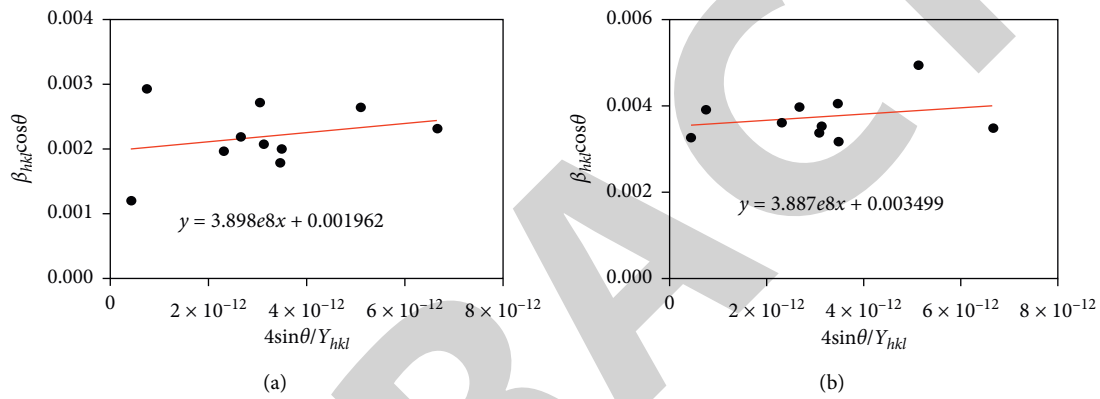


FIGURE 3: USDM plot for $\text{Al}_2\text{O}_3/10\text{wt. \% SiC}$: (a) electrical resistance heating sintering; (b) microwave sintering.

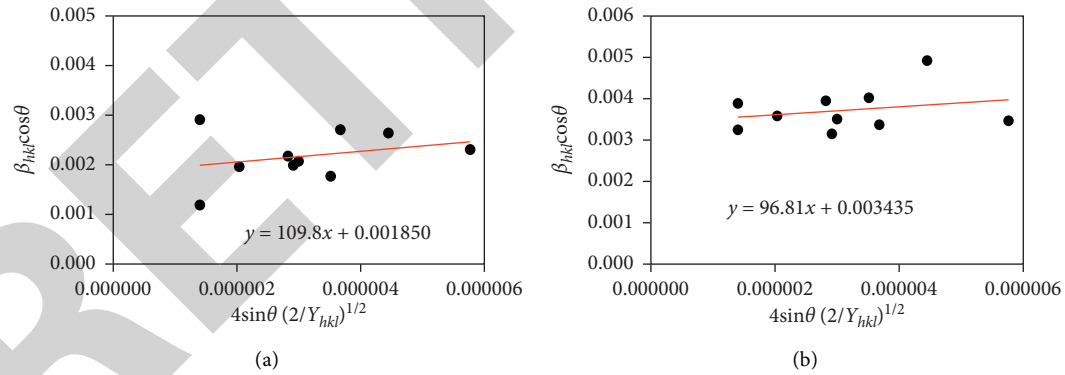


FIGURE 4: UEDDM plot for $\text{Al}_2\text{O}_3/10\text{wt. \% SiC}$: (a) electrical resistance heating sintering; (b) microwave sintering.

density, the strain-stress connection is not independent. Hooke's law used for an elastic system shows that $u = \epsilon^2 Y_{hkl}/2$ is used to calculate the density of deformation energy. As a result, equation (9) may be changed as follows based on the energy and strain relationship:

$$\beta_{hkl} \cos \theta = \left(\frac{k\lambda}{D} \right) + \left(4 \sin \theta \left(\frac{2u}{Y_{hkl}} \right)^{1/2} \right). \quad (10)$$

The UEDDM plots for electrical resistance heating-sintered and microwave-sintered $\text{Al}_2\text{O}_3/10 \text{ wt. \%}$ are shown

in Figures 4(a) and 4(b). The values of anisotropic energy density (u) and average crystallite size (D), which are given in Table 1, are calculated using the slope and Y -intercept.

3.3. Morphological Study. Figure 5 shows the average matrix particle size and morphology of $\text{Al}_2\text{O}_3/10 \text{ wt. \% SiC}$ -sintered powder as analysed using a field emission scanning electron microscope picture. It can be clearly confirmed that the attained sintered sample powders are spherical in shape with agglomeration of particles. The average matrix particle size

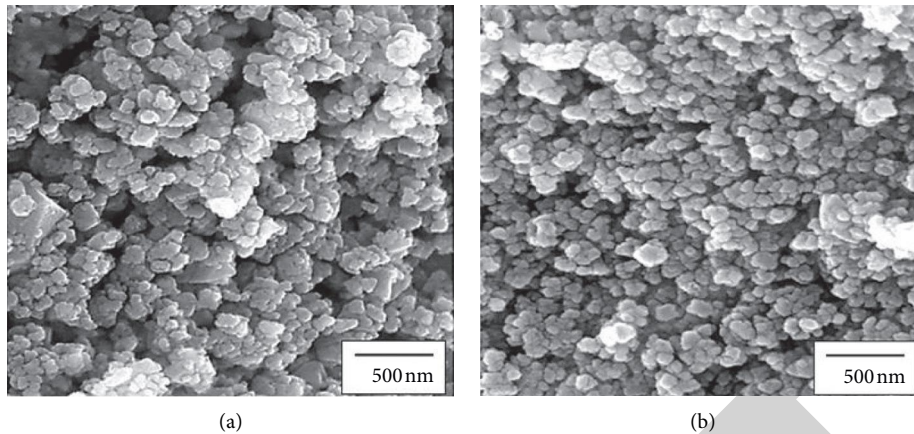


FIGURE 5: SEM image of sintered powder: (a) electrical resistance heating sintered; (b) microwave sintered.

can be seen as 67 ± 5 nm for electrical resistance heating-sintered $\text{Al}_2\text{O}_3/10$ wt.% SiC and 38 ± 5 nm for microwave-sintered $\text{Al}_2\text{O}_3/10$ wt.% SiC, and the results are very close to the values obtained by Debye-Scherrer and W-H plot. The reason behind the reduction of average matrix particle size of microwave-sintered sample is volumetric heating and less dwell time than electrical resistance heating sintering. The longer dwell time in electrical resistance heating sintering results in grain growth and forms coarse matrix particle, and it was evident in the previous studies [19].

4. Conclusion

$\text{Al}_2\text{O}_3/10$ wt. % SiC ceramic composite is successfully synthesized at 1500°C by electrical resistance heating sintering and microwave sintering methods. The electrical resistance heating sintering method has a longer holding time of 5 hours, and microwave sintering has a shorter holding time of 15 minutes. Powder XRD and FESEM are used to characterise the samples from both techniques. The XRD study reveals the existence of α - Al_2O_3 and β -SiC phases in the samples synthesized using both methods, but the intensity of the peaks is higher in the sample synthesized by microwave sintering than in the sample synthesized by electrical resistance heating sintering, indicating that the microwave sintered sample is more densely packed. The lattice parameter of α - Al_2O_3 matrix phase determined from the X-ray diffraction pattern of electrical resistance heating-sintered sample were $a = b = 4.758 \text{ \AA}$ and $c = 12.998 \text{ \AA}$ and microwave-sintered samples were $a = b = 4.759 \text{ \AA}$ and $c = 12.995 \text{ \AA}$. X-ray diffraction peak broadening was evaluated using three models of W-H techniques: the UDM, UDSM, and UDEDM. There was an acceptable degree of accuracy in estimating the values of various physical parameters such as energy density, stress, and strain using these three W-H analysis models; thus, these three W-H plot models are highly sought after for describing crystal perfection. When compared to electrical resistance heating-sintered sample, microwave-sintered sample shows fine crystallite size with less strain. When compared to the W-H techniques, the SEM findings were in close agreement with each other.

Data Availability

The data used to support the findings of this study are included within the article.

Conflicts of Interest

The authors declare that they have no conflicts of interest.

Acknowledgments

This research was performed as a part of the Employment of Arba Minch Institute of Technology, Arba Minch University, Ethiopia.

References

- [1] J. Bai, X. Yang, S. Xu, Y. Shi, and J. Yang, "Fabrication of highly dense Al_2O_3 ceramics," *Scripta Materialia*, vol. 68, no. 6, pp. 393–395, 2013.
- [2] Y.-H. Choa, A. Nakahira, and K. Niihara, "Microstructure and mechanical properties of SiC platelet reinforced $\text{Al}_2\text{O}_3/\text{SiC}$ -particle hybrid composites," *Journal of Materials Science*, vol. 35, no. 12, pp. 3143–3149, 2000.
- [3] Z. B. Yin, C. Z. Huang, B. Zou, H. L. Liu, H. T. Zhu, and J. Wang, "Study of the mechanical properties, strengthening and toughening mechanisms of $\text{Al}_2\text{O}_3/\text{TiC}$ micro-nanocomposite ceramic tool materials," *Materials Science and Engineering A*, vol. 77, pp. 9–15, 2013.
- [4] D. Sciti, J. Vicens, and A. Bellosi, "Microstructure and mechanical properties of Alumina-SiC nanocomposite prepared from ultrafine powders," *Journal of Materials Science*, vol. 37, no. 17, pp. 3747–3758, 2002.
- [5] Y.-W. Kim and J.-G. Lee, "Pressureless sintering of alumina-titanium carbide composites," *Journal of the American Ceramic Society*, vol. 72, no. 8, pp. 1333–1337, 1989.
- [6] S. Yoshioka, L. Boatema, S. v. d. Zwaag, W. Nakao, and W. G. Sloof, "On the use of TiC as high-temperature healing particles in alumina based composites," *Journal of the European Ceramic Society*, vol. 36, no. 16, pp. 4155–4162, 2016.
- [7] D. Żymelka, S. Saunier, D. Goeuriot, and G. Molimard, "Densification and thermal gradient evolution of alumina during microwave sintering at 2.45 GHz," *Ceramics International*, vol. 39, pp. 3269–3277, 2013.

Retraction

Retracted: Optimization of Reinforced Aluminium Scraps from the Automobile Bumpers with Nickel and Magnesium Oxide in Stir Casting

Advances in Materials Science and Engineering

Received 26 December 2023; Accepted 26 December 2023; Published 29 December 2023

Copyright © 2023 Advances in Materials Science and Engineering. This is an open access article distributed under the Creative Commons Attribution License, which permits unrestricted use, distribution, and reproduction in any medium, provided the original work is properly cited.

This article has been retracted by Hindawi, as publisher, following an investigation undertaken by the publisher [1]. This investigation has uncovered evidence of systematic manipulation of the publication and peer-review process. We cannot, therefore, vouch for the reliability or integrity of this article.

Please note that this notice is intended solely to alert readers that the peer-review process of this article has been compromised.

Wiley and Hindawi regret that the usual quality checks did not identify these issues before publication and have since put additional measures in place to safeguard research integrity.

We wish to credit our Research Integrity and Research Publishing teams and anonymous and named external researchers and research integrity experts for contributing to this investigation.

The corresponding author, as the representative of all authors, has been given the opportunity to register their agreement or disagreement to this retraction. We have kept a record of any response received.

References

- [1] V. Vijayan, A. Parthiban, T. Sathish et al., "Optimization of Reinforced Aluminium Scraps from the Automobile Bumpers with Nickel and Magnesium Oxide in Stir Casting," *Advances in Materials Science and Engineering*, vol. 2021, Article ID 3735438, 10 pages, 2021.

Research Article

Optimization of Reinforced Aluminium Scraps from the Automobile Bumpers with Nickel and Magnesium Oxide in Stir Casting

V. Vijayan,¹ A. Parthiban,² T. Sathish ,³ L. Ponraj Sankar,⁴ S. Dinesh Kumar,⁵ S. Saravanakumar,⁶ and Dawit Tafesse ⁷

¹Department of Mechanical Engineering, K. Ramakrishnan College of Technology (Autonomous), Samayapuram, Trichy 621 112, Tamil Nadu, India

²Department of Mechanical Engineering, Vels Institute of Science, Technology & Advanced Studies, Pallavaram, Chennai 600 117, Tamil Nadu, India

³Department of Mechanical Engineering, Saveetha School of Engineering, SIMATS, Chennai 602 105, Tamil Nadu, India

⁴Department of Civil Engineering, CMR Institute of Technology, Hyderabad, India

⁵Department of Mechanical Engineering, St. Peter's Institute of Higher Education and Research, Avadi, Chennai 600 054, Tamil Nadu, India

⁶Department of Mechanical Engineering, M.Kumarasamy College of Engineering, Karur, Tamil Nadu, India

⁷Department of Mechanical Engineering, Faculty of Manufacturing, Institute of Technology, Hawassa University, Hawassa, Ethiopia

Correspondence should be addressed to Dawit Tafesse; dawitt@hu.edu.et

Received 25 June 2021; Accepted 16 July 2021; Published 31 July 2021

Academic Editor: Samson Jerold Samuel Chelladurai

Copyright © 2021 V. Vijayan et al. This is an open access article distributed under the Creative Commons Attribution License, which permits unrestricted use, distribution, and reproduction in any medium, provided the original work is properly cited.

Here, the investigation is spotlighted on the aluminium alloy from the waste materials of the automobile bumpers which is a reinforced metal matrix composite created with 5 percentage of nickel and 5 percentage of magnesium oxide through the stir casting method. The stir casting process inputs parameters such as pressure of squeezing, time of squeezing, and speed of stirrer which were optimized based on the two mechanical properties' outcome such as the tensile strength (TS) and Rockwell hardness. There are nine different experiments which were conducted based on the L9 array. The Taguchi method is used to identify the optimum input values for the greatest result of the processing condition by Minitab software. The responses-based parameters were ordered based on the rank identified through the investigational effects. Finally, the optimized input consideration values and the linear equations are recommended for both the considered outputs as conclusions.

1. Introduction

Around the world, scraps of the automobiles are increased day by day, so the effective utilization of the wastes of automobiles, such as accidental bodies, damaged bodies, and replaced bodies, can be reusable after recycling. Here, especially the automobile bumpers which are made up of aluminium were chosen for this investigation. Christy et al. [1] completely explained about optimization techniques used for the input parameters of the squeeze and stir casting

with the help of the Taguchi technique. They also explained with the various microstructure diagrams and comparison plots. They used the four input parameters for the four output responses. The basic things of the optimization techniques for the various machining processes of composites such as various proportions of aluminium with zirconium carbide composite [2], several combinations of aluminium with silicon carbide [3], and numerous combinations of aluminium with nanomaterials [4] in the same way machining such as parameters of the laser welding

process [5], electrochemical machining process [6], A-GTAW welding [7], diffusion bonding process [8], turning process on the Lathe machine [9]. Krishnan et al. [10] discussed fully about the metal matrix composites which are produced from the aluminium scrap and materials from the wastes. They give the justification and implementation idea about the various techniques used for the production from those wastes and the scraps. They also defended based on the microstructures and also with characteristics of the composite material with the preliminary materials. Gesing et al. [11] clearly discussed regarding the light metals recycling through the used vehicles and life-ended vehicles' parts and scraps. These recommendations provide confidence to create this type of the research work. Similarly, Gupta et al. [12] reviewed through various research articles and explained about the process of solidification of metal matrix composites. In this investigation mainly focused with the used or damaged or scraped aluminium automobile bumpers recycling with the reinforcement then the optimization undergo with the basic mechanical properties like tensile strength and hardness based input parameters. Alaneme et al. [13] successfully explained regarding the creation in addition age-hardening accomplishment of aluminium composite through silicon carbide for the formation of composite through stir casting method.

Mohan et al. [14] explained the mechanical properties-based optimization of the parameters on the aluminium composites. Pawar et al. [15] professionally investigated about spur gear-based composite of aluminium reinforcement with silicon carbide. They fully expressed the different application with perfect experimental discussion with different figures. Evangelia Georgantzia et al. [16] exclusively clarified concerning AA6XXX series numerous applications with regard to more than a few sizes of physical components in dissimilar forms, process of welding, and equipment through bolted places of equipment. Weiwei et al. [17] investigated about the wheel hub of aluminium alloy failure-based analysis with various simulations. They mentioned the importance of the bumpers as follows: it is accomplished of enduring influences at 2 mph through complete breadth and 1 mph on bends. The bumper must be adept of tolerating influences to prevent 5 mph crashes of the automobiles. Vousden [18] mentioned about the Ferrari about its bumper shape made up of aluminium which is stress-free fiber of carbon composites with neglectable weight. Zhang et al. [19] investigated about the aluminium alloy of 7003 based on the stress corrosion with respect to the automobile vehicles. They also focused on the bumpers made up of aluminium with merits and demerits. These aluminium bumpers were less in weight and more strong when compared to steel. Weiwei et al. [17] discussed about automobile parts-based examination such as breakage of the wheel made up of the aluminium alloy with the various simulations and recommendations of the recycling of the used and damaged automobile parts. Vijay Kumar et al. [20] entirely examined various magnesium-based research articles and they provided the maximum information about the composites of biodegradable magnesium. They also gave the importance for the attention with properties and their availability, usages

on the environment. The biodegradable magnesium composites had the advanced strength to wear ratio in addition to furthermore articulated microstructure of the composite by means of various SEM pictures.

Abhijit et al. [21] completely reviewed by means of more than sixty research articles regarding the composite of the magnesium with various combinations of alloys. They concluded that the magnesium is used to strengthen the engineering materials with numerous fabrication methods and also they gave details about the reinforcement influence on the magnesium with additional materials such as silicon carbide, aluminium oxide, boron carbide, titanium carbide, fibers, and carbon nanotubes. This investigation predominantly focused to find the appropriate parameters used to produce the recycling of the scraps or wastes from the automobile bumpers by the way of composite formation with nickel and magnesium oxide in stir casting process. The suitable parameters were considered based on the experimental consequence of furthest desirable mechanical properties such as tensile strength and hardness of the composite produced by the way of stir casting process.

1.1. Experimental Setup. The waste aluminium bumpers were collected from various mechanic shops and different automobile service centers. Then, some pieces of the entire waste bumper were taken for this investigation and were cleaned and converted into small pieces which are also converted into powder form by pulverizing. It contains 1.1 to 1.7 percentage of silicon, 0.7 to 1.3 percentage of magnesium, 0.8 to 1.18 percentage of copper, 0.7 to 1.2 percentage of manganese, and 0.5 percentage of chromium in the total composition. Then, the cleaned aluminium majorly used then the five percentage of nickel and five percentage of magnesium oxide reinforce in the total volume of the composite metal.

The stir casting setup used for this experimental trail is bottom pouring method. It contains the control panel, electrical furnace, runway preheater, die, reinforcement preheating chamber, and hydraulic sequence pressure ram. Initially, the pieces of the automobile bumpers and the nickel and magnesium were placed in the stir casting place, as shown in Figure 1. As shown in Table 1, there are nine experimental trails which created hydraulic squeeze pressures considered as 80 MPa, 100 MPa, and 120 MPa. The sintering speed varies from 400 rpm, 500 rpm, and 600 rpm. The time of the squeeze varied as 20 sec, 40 sec, and 60 sec. The holding pressure was maintained as 300°C throughout all experiments.

As shown in Table 1, the specimens were formed as per the size of 30 mm × 30 mm × 120 mm as width, length, and height by bottom pouring on the mold. There are nine specimens prepared with pressure, time, and speed variations for the specimens. Then, the specimens were used to take the tensile strength as per the traditional method in the universal testing machine as per the standards. Then, the tensile strength was noted for each specimen. Similarly, the Rockwell hardness machine with the diamond indenter cone is used to identify the hardness of each specimen and the corresponding values were noted.



FIGURE 1: The friction stir machine setup used.

TABLE 1: Experimental trails of design.

Experimental trail No.	Pressure (P) (MPa)	Time (t) (s)	Speed (N) (rpm)
ET 1	80	20	400
ET 2	80	40	500
ET 3	80	60	600
ET 4	100	20	500
ET 5	100	40	600
ET 6	100	60	400
ET 7	120	20	600
ET 8	120	40	400
ET 9	120	60	500

2. Results and Discussion

The measured values of the tensile strength and the hardness values are clearly mentioned in Table 2 for all the experimental trails. Here, the Taguchi technique was implemented for both tensile strength and hardness separately and jointly. For all these three conditions, larger is better condition which is used for the processing in the Minitab-18 software.

Individual plots and combination plots were utilized to identify the real impact on the experimental results.

Figure 2 shows the tensile strength foremost result diagram for ratio of SN and Figure 3 shows the tensile strength foremost result diagram for ratio of means clearly. From these two diagrams, the maximum output is obtained in the range for pressure of squeezing is 120 MPa, time of squeezing is 60 sec, and speed of stirrer is 400 rpm. Table 3

TABLE 2: Results of the experiments.

Experimental trail No.	Pressure (P) (MPa)	Time (t) (s)	Speed (N) (rpm)	Tensile strength (MPa)	Hardness (HRB)
ET 1	80	20	400	128.48	49.82
ET 2	80	40	500	133.98	51.26
ET 3	80	60	600	139.48	52.7
ET 4	100	20	500	121.2	46.1
ET 5	100	40	600	126.7	47.54
ET 6	100	60	400	169.7	62.66
ET 7	120	20	600	113.92	42.38
ET 8	120	40	400	156.92	57.5
ET 9	120	60	500	162.42	58.94

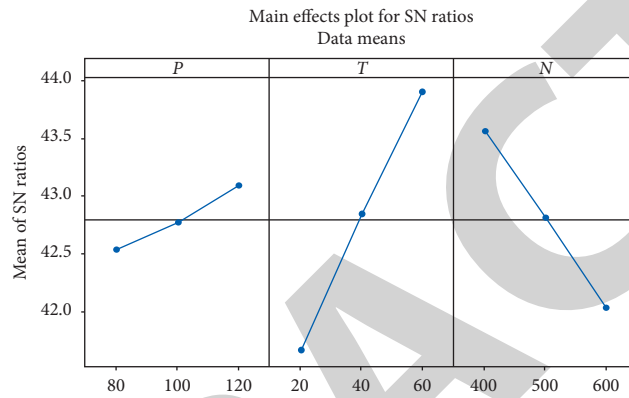


FIGURE 2: Tensile strength: foremost result diagram for ratio of SN (in X axis, P is the pressure in MPa, T is the time in s, and N is the speed in rpm).

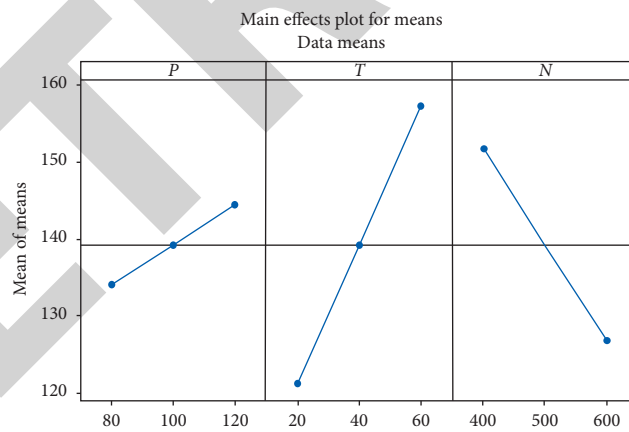


FIGURE 3: Tensile strength: foremost result diagram for ratio of means (in X axis, P is the pressure in MPa, T is the time in s, and N is the speed in rpm).

details about the responses for SN ratio and means for the tensile strength; from that response table, the most impacted factor is time of squeezing; secondly, it is speed of stirrer, and the last parameter is pressure of squeezing. Table 4 shows variance analysis provided that the minimum “ P ” values which express the reliability of the experiments and parameters are considered.

Figure 4 shows the three different plots of contour diagram in a single plot. It contains the contour diagrams of the time verses pressure, speed verses pressure, and then

speed verses time. The variations were represented as the color variations which are clearly represented in the right side of the diagram; each range has a different color for the representations. Figure 5 represents the histogram diagram for the tensile strength with respect to the frequencies which have the mean as 139.2 MPa and standard deviation of 19.51.

The probability plot is shown in Figure 6 with respect to the tensile strength which is represented in X axis and percent is mentioned in the Y axis. In this diagram, entire values were near to the mean line of the plot nearly four to

TABLE 3: Tensile strength response table.

Level	Response for SN ratio			Response for means		
	P (MPa)	t (s)	N (rpm)	P (MPa)	t (s)	N (rpm)
1	42.54	41.66	43.56	134.0	121.2	151.7
2	42.77	42.84	42.81	139.2	139.2	139.2
3	43.09	43.90	42.03	144.4	157.2	126.7
Delta	0.55	2.24	1.54	10.4	36.0	25.0
Rank	3	1	2	3	1	2

TABLE 4: Tensile strength variance analysis for SN ratios.

Source	DF	Seq SS	Adj SS	Adj MS	F	P value
P (MPa)	2	0.4570	0.45696	0.22848	54.29	0.018
t (s)	2	7.5283	7.52829	3.76415	894.43	0.001
N (rpm)	2	3.5365	3.53650	1.76825	420.17	0.002
Residual error	2	0.0084	0.00842	0.00421		
Total	8	11.5302				

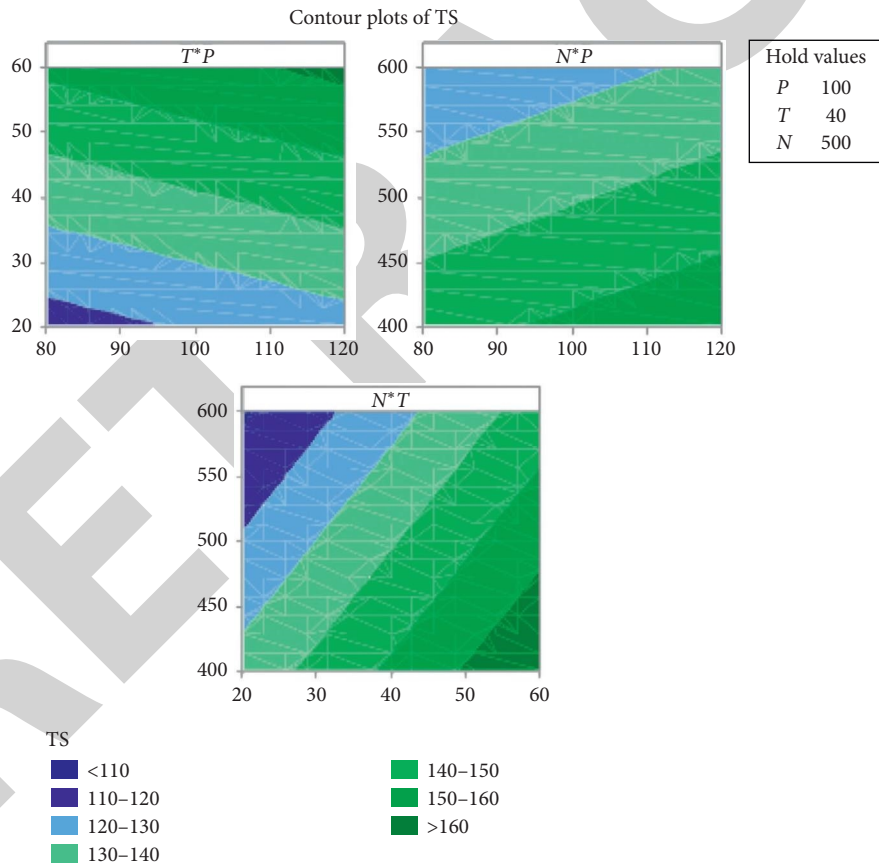


FIGURE 4: Contour diagrams for tensile strength (P , pressure in MPa; T , time in s; N , speed in rpm).

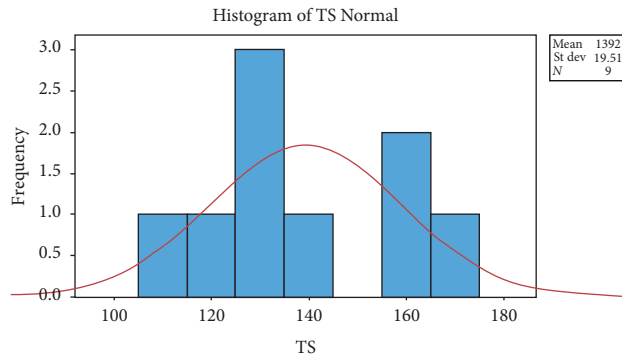


FIGURE 5: Tensile strength responses as histogram (X axis: TS in MPa and Y axis: frequency in Hz).

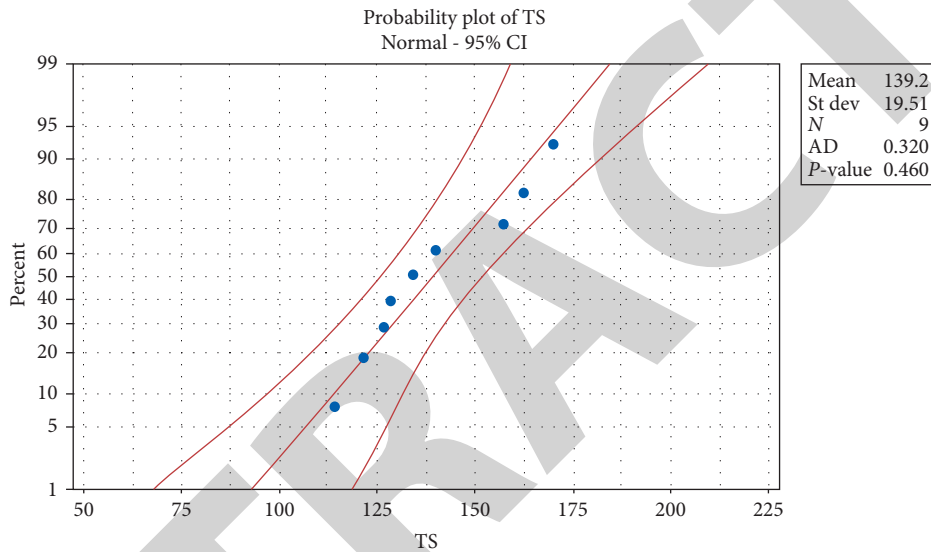


FIGURE 6: Tensile strength responses as probability plot (X axis: TS in MPa and Y axis: %).

five points' lies on the mean line. By using the regression, the following equation is formed for the tensile strength with respect to the contribution considerations:

$$\text{regression equation for tensile strength} = TS = 139.6 + 0.2610P + 0.9000T - 0.1250N. \tag{1}$$

The experimental results of the hardness-based foremost result diagram for ratio of SN and means of date are plotted in Figures 7 and 8, respectively; in the same order, these experiments analysed based on the condition of larger is better. The optimum input parameters for the upper most results of the harness were 120 MPa of the pressure of squeezing, 60 sec time of squeezing, and 400 rpm speed of stirrer. These values were also confirmed by both the SN ratio-based diagram and means-based diagram.

The corresponding response table based on the SN ratio and means is shown as Table 5 with the condition of larger is better. For both the conditions, time reached the rank one, speed of stir reached the second rank, and the holding pressure reached the last rank among these three parameters based on the experimental results of the hardness. Similarly, Table 6 lists the variation of the analysis for the hardness results based on the SN ratio. The *P* value is less than 0.2 for all the parameters, especially time and speed have very low value of the *P* value in Table 6.

$$\text{Regression equation for hardness (HRB)} = 58.70 + 0.04200P + 0.3000T - 0.04560N. \tag{2}$$

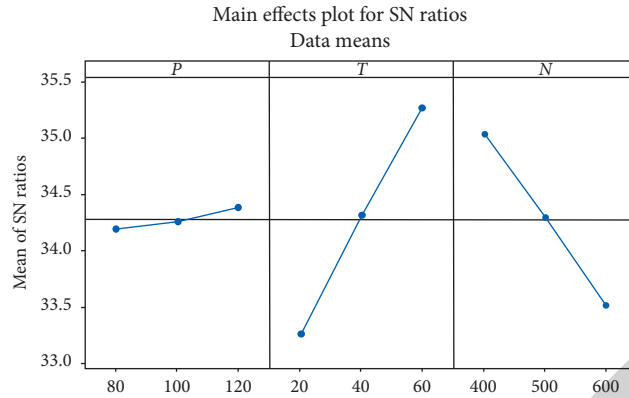


FIGURE 7: Hardness: foremost result diagram for ratio of SN (in X axis, P is the pressure in MPa, T is the time in s, and N is the speed in rpm).

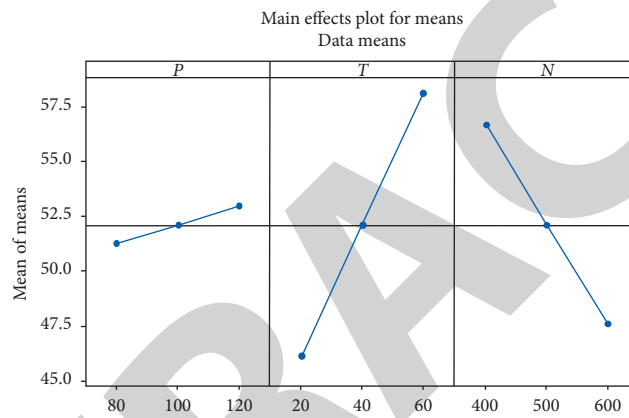


FIGURE 8: Hardness: foremost result diagram for means (in X axis, P is the pressure in MPa, T is the time in s, and N is the speed in rpm).

TABLE 5: Hardness response table with ranks.

Level	Response for SN ratio			Response for means		
	P (MPa)	t (s)	N (rpm)	P (MPa)	t (s)	N (rpm)
1	34.19	33.26	35.03	51.26	46.10	56.66
2	34.25	34.31	34.29	52.10	52.10	52.10
3	34.38	35.26	33.51	52.94	58.10	47.54
Delta	0.19	2.01	1.52	1.68	12.00	9.12
Rank	3	1	2	3	1	2

TABLE 6: Analysis of variance of hardness for ratios of SN.

Source	DF	Seq SS	Adj SS	Adj MS	F	P value
P (MPa)	2	0.05575	0.05575	0.02787	5.09	0.164
t (s)	2	6.04324	6.04324	3.02162	551.85	0.002
N (rpm)	2	3.46786	3.46786	1.73393	316.67	0.003
Residual error	2	0.01095	0.01095	0.00548		
Total	8	9.57780				

Figure 9 provides the details of the experimental results of the hardness as the contour plot depends on the parameter variations in a single diagram with the color variations for the identification of the range variation on the results. Similarly, the histogram view of the experimental outcomes of the hardness values is clearly plotted in

Figure 10 with linear relation curve. There is no gap in between the columns available on the histogram diagram. The probability chart for the harness results is plotted in Figure 11. All the experimental values nearly closer the median line on the chat. Nearly six to seven points were nearly close to the median line.

In Table 7, the confirmation test is created with the combination of the both tensile and harness strength based foremost result diagram for ratio of SN is shown in Figure 12, and the foremost result diagram for data means is shown in Figure 13; similarly, response table with ranks based on SN ratios is shown as Table 6. As shown in Figures 12 and 13, the maximum output of both the mechanical properties reached higher values at the pressure of squeezing 120 MPa, time of squeezing 60sec, and speed of stirrer

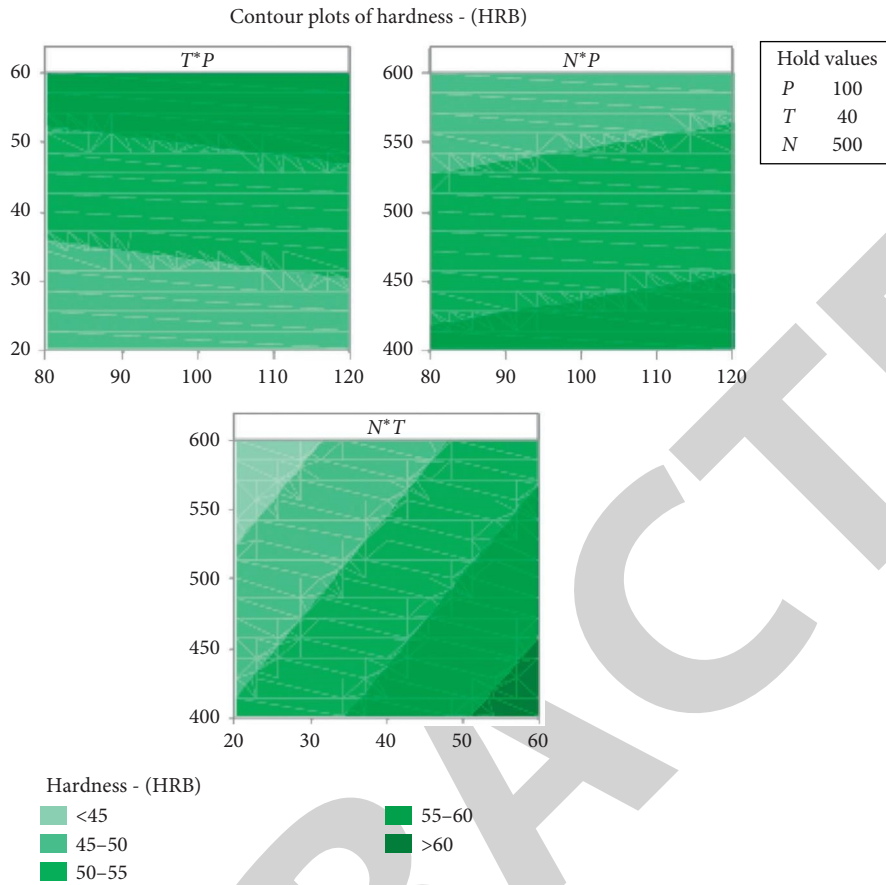


FIGURE 9: Hardness-contour plot depends on the parameters variations (P , pressure in MPa; T , time in s; N , speed in rpm).

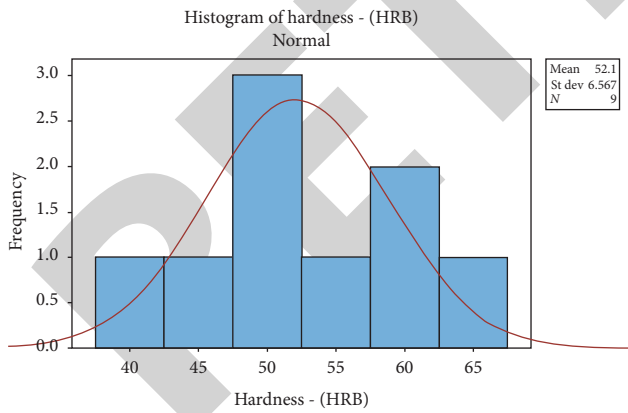


FIGURE 10: Hardness: histogram diagram (X axis: TS in MPa and Y axis: frequency in Hz).

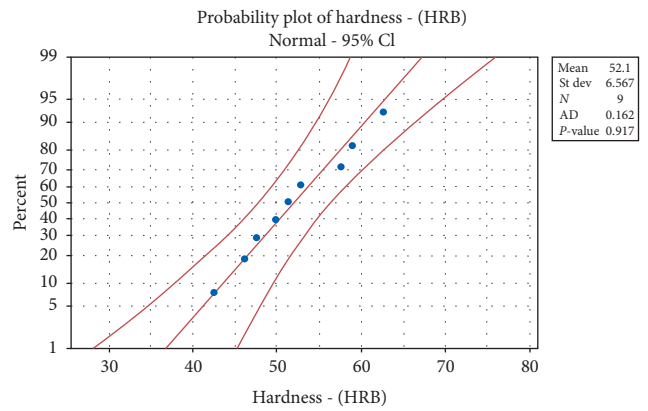


FIGURE 11: Hardness: probability plot (X axis: TS in MPa and Y axis: %).

TABLE 7: Tensile strength and harness-based response table with ranks based on SN ratios.

Level	P (MPa)	t (s)	N (rpm)
1	36.61	35.68	37.47
2	36.69	36.75	36.73
3	36.84	37.71	35.95
Delta	0.23	2.04	1.52
Rank	3	1	2

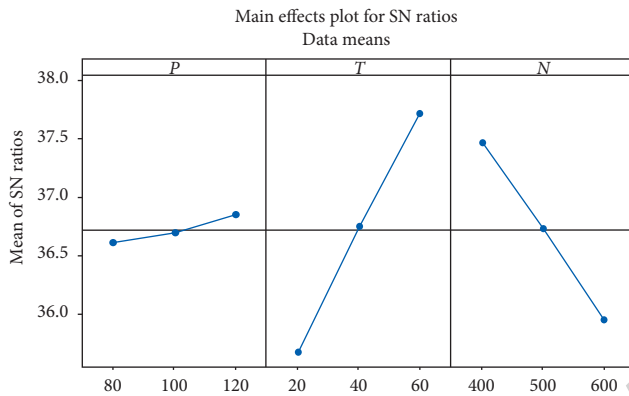


FIGURE 12: Both tensile strength and harness-based foremost result diagram for ratio of SN (In X axis, P is the pressure in MPa, T is the time in s, and N is the speed in rpm).

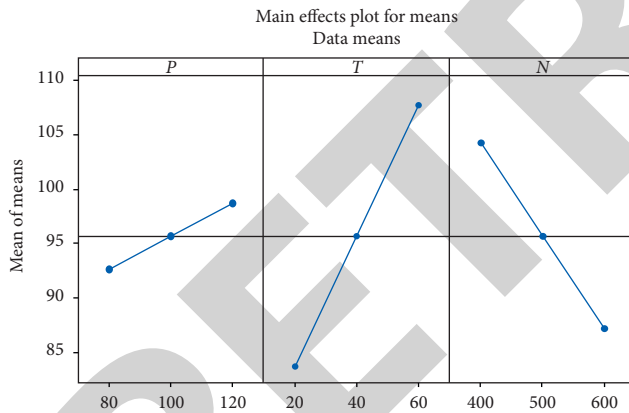


FIGURE 13: Both tensile strength and harness-based foremost result diagram for data means (In X axis, P is the pressure in MPa, T is the time in s, and N is the speed in rpm).

400 rpm. The corresponding ranking is obtained in the order of time, speed, and pressure as first, second, and third.

3. Conclusions

This optimization study of reinforced aluminium scraps from the automobile bumpers with nickel and magnesium oxide in stir casting gave the following results as conclusions:

- (i) The recycling of the aluminium automobile bumpers into the reinforced composite is possible.
- (ii) For the experimental results of the tensile strength, hardness and both combination conditions

response table gave the first rank for time of squeezing, the second rank for speed of stirrer, and the third rank for holding pressure.

- (iii) The regression equations (1) and (2) were created for tensile strength and hardness with respect to the same conditions, respectively.
- (iv) Both the enhanced mechanical properties were obtained at the input parameters such as pressure of squeezing 120 MPa, time of squeezing 60 sec, and speed of stirrer 400 rpm.
- (v) The optimized contribution concern values and the linear equations are recommended for tensile strength and hardness.
- (vi) Further scope of this work was extended to conduct the impact test for the same material with increase of the reinforcement for preventing the impact of accident to the vehicle.

Data Availability

The data used to support the findings of this study are included within the article. Further data or information is available from the corresponding author upon request.

Disclosure

This study was performed as part of employment in Hawassa University, Ethiopia.

Conflicts of Interest

The authors declare that there are no conflicts of interest regarding the publication of this paper.

Acknowledgments

The authors appreciate the supports from Hawassa University, Ethiopia. The authors thank Saveetha School of Engineering, Chennai, for the technical assistance to complete this experimental work.

References

- [1] J. V. Christy, R. Arunachalam, A.-H. I. Mourad, P. K. Krishnan, S. Piya, and M. Al-Maharbi, "Processing, properties, and microstructure of recycled aluminum alloy composites produced through an optimized stir and squeeze casting processes," *Journal of Manufacturing Processes*, vol. 59, pp. 287–301, 2020.
- [2] T. Sathish and N. Sabarirajan, "Synthesis and optimization of AA 7175 - Zirconium Carbide (ZrC) composites machining parameters," *Journal of New Materials for Electrochemical Systems*, vol. 24, no. 1, pp. 34–37, 2021.
- [3] T. Sathish, N. Sabarirajan, and S. Karthick, *Materials Today Proceedings*, Elsevier Publisher, Netherlands, Accepted, 2019.
- [4] T. Sathish, K. Muthukumar, R. Saravanan, and V. Dhinakaran, "Study on temperature difference of aluminium nitride nanofluid used in solar flat plate collector over normal water," *AIP Conference Proceedings*, vol. 2283, no. 1, AIP Publishing LLC, Article ID 020126, 2020.

Retraction

Retracted: Mechanical Strength and Fatigue Fracture Analysis on Al-Zn-Mg Alloy with the Influence of Creep Aging Process

Advances in Materials Science and Engineering

Received 11 July 2023; Accepted 11 July 2023; Published 12 July 2023

Copyright © 2023 Advances in Materials Science and Engineering. This is an open access article distributed under the Creative Commons Attribution License, which permits unrestricted use, distribution, and reproduction in any medium, provided the original work is properly cited.

This article has been retracted by Hindawi following an investigation undertaken by the publisher [1]. This investigation has uncovered evidence of one or more of the following indicators of systematic manipulation of the publication process:

- (1) Discrepancies in scope
- (2) Discrepancies in the description of the research reported
- (3) Discrepancies between the availability of data and the research described
- (4) Inappropriate citations
- (5) Incoherent, meaningless and/or irrelevant content included in the article
- (6) Peer-review manipulation

The presence of these indicators undermines our confidence in the integrity of the article's content and we cannot, therefore, vouch for its reliability. Please note that this notice is intended solely to alert readers that the content of this article is unreliable. We have not investigated whether authors were aware of or involved in the systematic manipulation of the publication process.

Wiley and Hindawi regrets that the usual quality checks did not identify these issues before publication and have since put additional measures in place to safeguard research integrity.

We wish to credit our own Research Integrity and Research Publishing teams and anonymous and named external researchers and research integrity experts for contributing to this investigation.





The corresponding author, as the representative of all authors, has been given the opportunity to register their agreement or disagreement to this retraction. We have kept a record of any response received.

References

- [1] M. Ponnusamy, B. P. Pulla, T. Sathish et al., "Mechanical Strength and Fatigue Fracture Analysis on Al-Zn-Mg Alloy with the Influence of Creep Aging Process," *Advances in Materials Science and Engineering*, vol. 2021, Article ID 1899128, 5 pages, 2021.

Research Article

Mechanical Strength and Fatigue Fracture Analysis on Al-Zn-Mg Alloy with the Influence of Creep Aging Process

Muruganatham Ponnusamy ¹, Bhanu Pratap Pulla,² T. Sathish ³,
Sivakumar Karthikeyan ⁴, S. Ravindran,⁵ Balachandra Pattanaik ⁶, and Ram Subbiah⁷

¹Deputy Registrar IIIT, Kalyani, West Bengal, India

²Department of Mechanical Engineering, Addis Ababa Science and Technology University, Addis Ababa, Ethiopia

³Department of Mechanical Engineering, Saveetha School of Engineering SIMATS, Chennai 602105, Tamil Nadu, India

⁴Department of Mechanical Engineering, SRM Valliammai Engineering College, Kattankulathur SRM Nagar 603203, Chennai, Tamil Nadu, India

⁵Department of Mechanical Engineering, Sri Sairam Engineering College, West Tambaram, Chennai 600044, Tamil Nadu, India

⁶Department of Electrical and Computer Engineering, Wollega University, Nekemte, Ethiopia

⁷Department of Mechanical Engineering, Gokaraju Rangaraju Institute of Engineering and Technology, Nizampet, Hyderabad, India

Correspondence should be addressed to Balachandra Pattanaik; balachandrapattanaik14251425@gmail.com

Received 23 June 2021; Revised 5 July 2021; Accepted 14 July 2021; Published 31 July 2021

Academic Editor: Samson Jerold Samuel Chelladurai

Copyright © 2021 Muruganatham Ponnusamy et al. This is an open access article distributed under the Creative Commons Attribution License, which permits unrestricted use, distribution, and reproduction in any medium, provided the original work is properly cited.

The Al-Zn-Mg alloy comes under the aluminium alloy; it possesses good capability of age hardening and superior strength in contrast to other alloys. The numbers of creep aging experiments are conducted with the support of different temperature levels such as 180, 200, and 2000°C. The effects of tests are reflected on the tensile test and fatigue tests; the temperature and stress directly affects the creep characteristics, mechanical strength, and fatigue performance of the Al-Zn-Mg alloy. The time period of the creep test is maintained as 15 hrs with constant load of 200 MPa and 220 MPa. The increasing temperature increases the tensile strength and fatigue life of the Al-Zn-Mg alloy under initial condition; furthermore, continuous increment reduces the strength and fatigue existence. In the fatigue test, the fatigue span of the Al-Zn-Mg is extremely enhanced by the application of creep aging at a particular temperature. The 3D profilometry image visibly shows the influence of temperature in forming a fracture in fatigue analysis through microstructure analysis.

1. Introduction

Creep aging is one class of forming process with merger of creep deformation and aging of material, both improve the material properties and life time of working. This creep aging process concentrated on fabrication of aircraft panels and more integral parts [1–3]. Creep aging is a precision forming, used to reduce the fracture while the material is processed. Most of the research conducted creep aging process to analyse and improve the microstructures and mechanical properties. Creep aging process is a method of heat treatment in the forming process with creep action; the material

for creep aging is loaded in elastic nature in a gripper. The loaded elastic material is kept in a temperature set for a predetermined time period [4, 5]. The constant load and under in thermal exposure of the material elements of the metal are undergone to impulsive and change of microstructure and the mechanical properties of the Al-Zn-Mg alloy. From the creep aging process, the change of the material properties and the spring back effects of the materials are easy to control [6]. The materials containing aluminium alloys and combination of elements such as copper, magnesium, and zinc are used in the industry. These alloys are developed by heat treatments; furthermore, these

alloys are used as special purpose alloys or high-effective performance alloys [7, 8]. In heat treatment, the atoms huddle and slide within the aluminium matrix, for these atomic changes improve the mechanical strength as well as hardness of the alloys. In this work, we carry out creep aging process on the Al-Zn-Mg alloy with different thermal exposures and different creep loads to evaluate the tensile strength of the material and the fatigue fracture [9–11].

2. Materials and Properties

The aluminium alloys include more zinc compared to magnesium; few of the alloys have less than one zinc and magnesium. The casings and wrought components are formed by the Al-Zn-Mg alloys; these alloys have less castability character. The zinc and magnesium are the major constituent elements of the Al-Zn-Mg alloys; with the increasing ratio of the zinc, the magnesium ratio offered superior strength and flexible for heat treatment process [12, 13]. The low contribution ratios introduce excellent weldability. The chemical composition of each element is tabulated in Table 1.

2.1. Experimental Procedure. The specimens are prepared for the creep test, as shown in Figure 1, and the specimens are sized from the plate as per the standards (ASTM E139) using wire cut EDM machine [14].

Initially, the specimens are tested in the tensile testing machine and the tensile value is found; conducting the initial test, the plot of stress-strain curve is obtained, as illustrated in Figure 2. The initial tested samples offered the tensile values: tensile strength is 430 MPa and the yield strength is 325 MPa; the test was conducted by using nine samples.

2.2. Creep Aging Process. The creep aging was conducted on the selected specimens with applied of the constant stress values are 0 MPa, 200 MPa, and 220 MPa, respectively; the selected temperature levels are 180°C, 200°C, and 220°C, respectively. The aging time period maintained for all specimens is 15 hours. Each specimen is tested before it is cleaned well and the wet nature removed. The specimen before entering the testing chamber can be weighted to identify the creep behaviour after the creep aging process is finished. The specimen is mounted in between upper and lower hook rigidity with the aid of mounts; the lower end is connected to constant load. The hanging position of the sample is surrounded by the selected temperature level for the purpose of heat treatment process, and the entire arrangement is kept at a selected time period such as 15 hours [15]. The creep aging setup is clearly illustrated in Figure 3.

2.3. Tensile Testing and Fatigue Testing. After creep aging, the specimens were tested using the tensile testing machine, the model of VENUS Tech Pvt, and the capacity of testing machine was 40 ton with computerized operation. The fatigue test was conducted by using the sine-wave loading arrange model machine effectively; all the specimens

TABLE 1: Chemical composition range of Al-Zn-Mg alloys.

Material	Wt.% of composition
Zn	2–8
Mg	0.5–4
Cu	0–3
Fe	0.1–0.8
Si	0.05–0.3
Cr	0.0–0.5
Mn	0.0–1.5
Ti	0.0–0.5
B	0.0–0.05
Zr	0.0–0.25
Ag	0.0–1.0
Be	0.0–0.10
Other elements	<0.05 each



FIGURE 1: Typical creep aging sample.

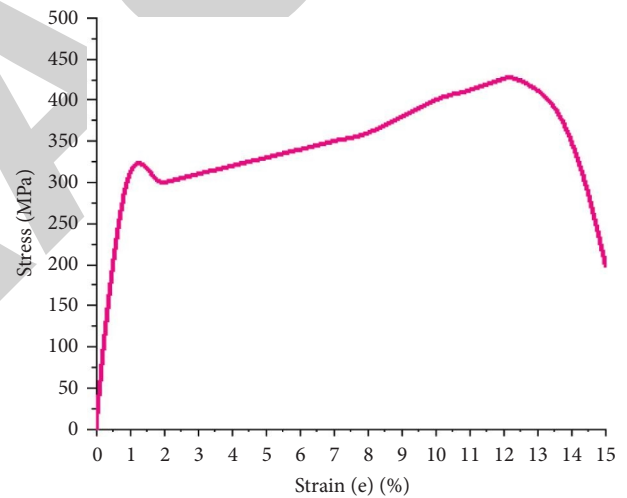


FIGURE 2: Stress-strain curve of the initial sample.

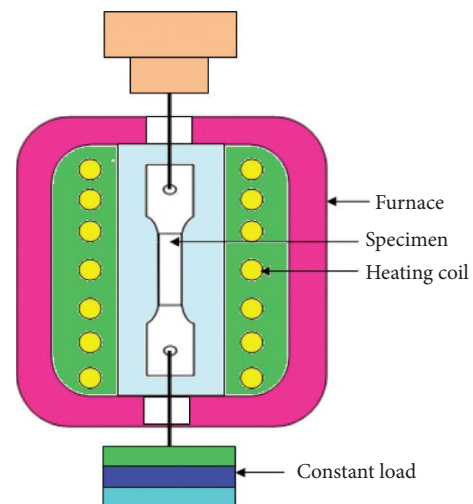


FIGURE 3: Creep aging arrangement.

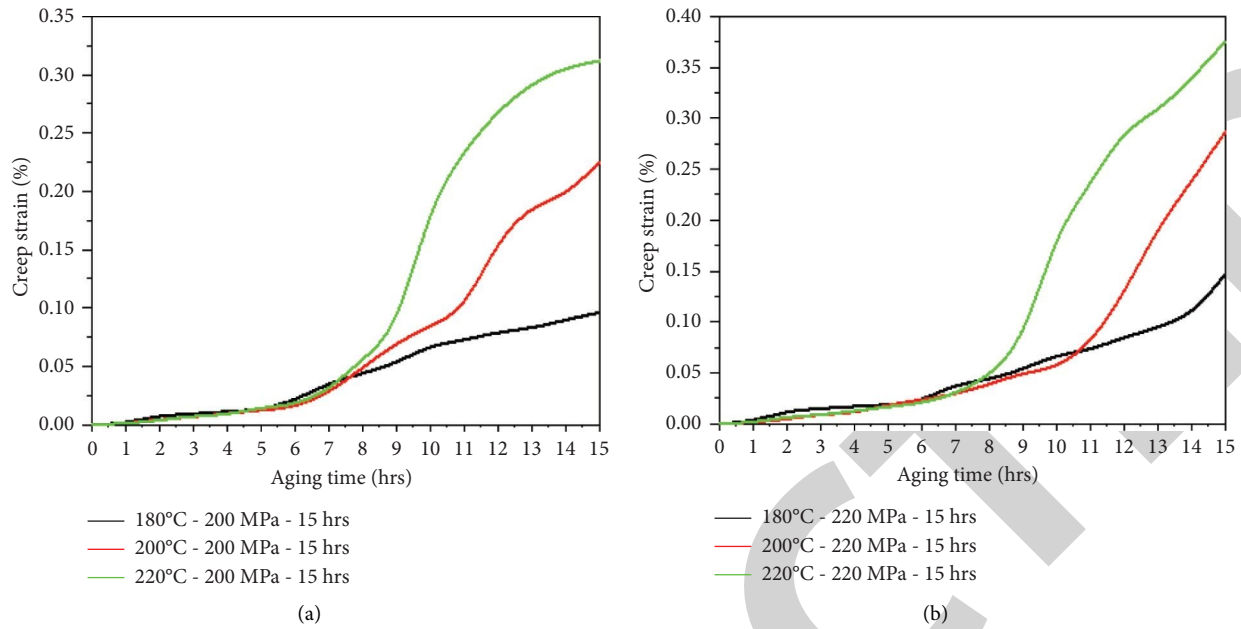


FIGURE 4: (a) Creep aging graph, aging time vs. creep strain (200 MPa). (b) Creep aging graph, aging time vs. creep strain (220 MPa).

underwent the fatigue test with a range of the stress ratio value as 0.1 (40/400 MPa). The fatigue test loading frequency was selected as 15 Hz using a fatigue testing machine at room temperature.

3. Results and Discussion

3.1. Creep Analysis of Alloy. Figure 4(a) shows the aging time with the creep strain graph visibly; the Al-Zn-Mg alloy was tested at different levels of temperature with 200 MPa; stress concentration was measured. The aging time was continually increased and stopped at 15 hours; under such a condition the creep curve shows a steady state. Figure 4(b) illustrates the aging time with the creep strain graph applying 220 MPa, and both the graphs shows an increase of temperature the creep strain steadily increased.

Table 2 presents the creep strain of the Al-Zn-Mg with a variety of temperature levels and stress levels. With the increase in temperature, 180°C, under the applied stress of 200 MPa, the creep strain rate was increased as 0.096% at the same temperature stress which varied as 220 MPa; the creep strain obtained was 0.146%. With the influence of temperature, 200°C, with applied stress of 200 MPa, the creep strain was attained as 0.225%; with the same temperature but with increase of stress, 220 MPa, the creep strain was attained as 0.288. With the increase of temperature from 180°C to 220°C, the stress was maintained at 200 MPa and the creep strain was acquired as 0.312; furthermore, with the increase of the stress value, 220 MPa, but with the same temperature, the creep strain was increased to 0.375.

3.2. Mechanical Strength of Al-Zn-Mg Alloy. Applying orthogonal test in the Al-Zn-Mg alloy after creep aging, the mechanical strength was analysed and presented in Table 3, clearly. Table 3 effectively illustrates that the aging

TABLE 2: Creep strain with a variety of aging temperature and stress values.

Temperature (°C)	Stress (MPa)	Creep strain in %
180	200	0.096
	220	0.146
200	200	0.225
	220	0.288
220	200	0.312
	220	0.375

temperature was highly influenced to change the mechanical properties. With the temperature level from 180°C to 200°C, the tensile strength and the yield strength increased; further increase of temperature at the level of 220°C, decreased tensile strength and yield strength continually.

3.3. Influencing of Aging Temperature on Fatigue Analysis of the Al-Zn-Mg Alloy. Figure 5 plainly shows the fatigue analysis of the alloy with constant stress, 200 MPa, after creep aging with 15 hrs time period. This graph shows the constant stress level at 180°C aging temperature; the moderate value, such as 56,347 cycles, is obtained; furthermore, with increase in temperature, 200°C, and with constant stress, the high fatigue cycles were attained as 81,358. With high temperature, 220°C, and with constant stress, the fatigue cycles were decreased to 32,562.

3.4. Influence of Stress on Fatigue Analysis of the Al-Zn-Mg Alloy. Figure 6 shows the fatigue analysis of alloy with different stress levels after creep aging of 15 hrs at constant temperature of 200°C. For not applied of stress, the fatigue level of the alloy is 25,682 cycles for 15 hrs of aging; furthermore, increasing the stress level to 200 MPa, increases

TABLE 3: Mechanical strength of Al-Zn-Mg alloy after creep aging.

Temperature (°C)	Stress (MPa)	Tensile strength (MPa)	Yield strength (MPa)	Elongation %
180	0	442.76	312.75	18.23
	200	468.48	340.21	20.12
	220	465.38	331.49	20.34
200	0	463.19	390.68	11.75
	200	490.63	410.23	11.37
	220	487.34	408.39	12.02
220	0	423.15	356.42	9.34
	200	432.89	386.81	9.64
	220	438.67	391.59	9.82

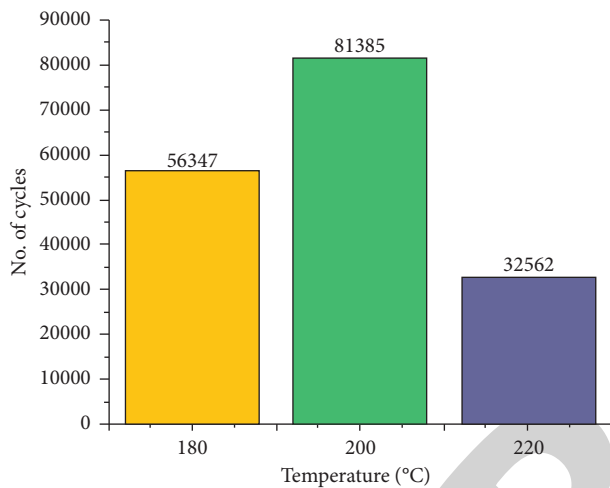


FIGURE 5: Fatigue analysis of the alloy with constant load after creep aging of 15 hrs.

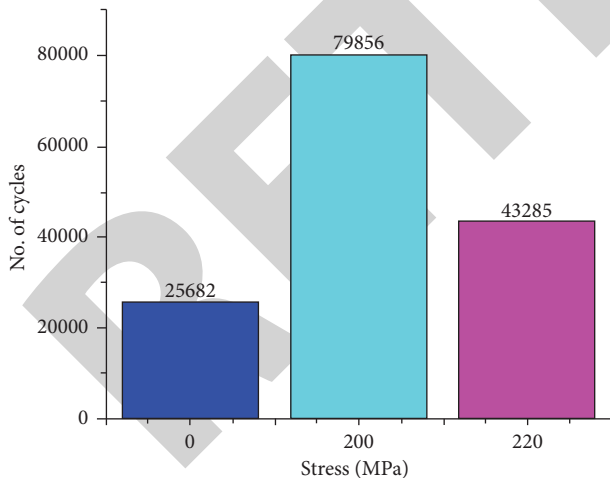


FIGURE 6: Fatigue analysis of alloy with different stress levels after creep aging of 15 hrs.

the fatigue life to 79,656 cycles. The highest stress 220 MPa applied the fatigue life was decreased.

4. Conclusion

The Al-Zn-Mg alloy was fabricated, and the creep aging was carried out successfully through the heat treatment process.

Applying constant stress and implementing varying temperature effectively, the tensile strength and fatigue analysis was carried out, and the result was clearly pointed out as follows:

- (i) the increase of temperature, 180°C, under the applied stress of 200 MPa, the creep strain rate increased was 0.096% at the same temperature stress which varied as 220 MPa; the creep strain obtained was 0.146%. With the influence of temperature, 200°C, with applied stress of 200 MPa, the creep strain was attained as 0.225%. With the increase of temperature at 180°C to 220°C, the stress was maintained as 200 MPa; the creep strain was acquired as 0.312; furthermore, the stress value increased as 220 MPa, but in the same temperature, the creep strain increased as 0.375.
- (ii) The temperature level increases from 180°C to 200°C; the tensile strength and the yield strength were increased, but further increasing temperature to 220°C, tensile strength and yield strength were decreased continually.
- (iii) From the 180°C of aging temperature, the moderate value such as 56,347 cycles was obtained; furthermore, with increase of temperature, 200°C, with constant stress, the high fatigue cycles were attained as 81,358. When temperature is 220°C with constant stress, the fatigue cycles decreased as 32,562.
- (iv) Fatigue analysis of alloy with different stress levels after creep aging of 15 hrs at constant temperature of 200°C is carried out. For not applied of stress, the fatigue level of the alloy is 25,682 cycles for 15 hrs of aging; furthermore, increasing the stress level to 200 MPa, the fatigue life was increased as 79,656 cycles. When the highest stress 220 MPa is applied, the fatigue life is decreased.
- (v) Future scope of this study is extended to increase the strength of the alloys by applying reinforcements and is further planned to conduct the wear and corrosion test.

Data Availability

The data used to support the findings of this study are included within the article. Further data or information are available from the corresponding author upon request.

Retraction

Retracted: Mechanical Behavior of Silica Fume Concrete Filled with Steel Tubular Composite Column

Advances in Materials Science and Engineering

Received 26 December 2023; Accepted 26 December 2023; Published 29 December 2023

Copyright © 2023 Advances in Materials Science and Engineering. This is an open access article distributed under the Creative Commons Attribution License, which permits unrestricted use, distribution, and reproduction in any medium, provided the original work is properly cited.

This article has been retracted by Hindawi, as publisher, following an investigation undertaken by the publisher [1]. This investigation has uncovered evidence of systematic manipulation of the publication and peer-review process. We cannot, therefore, vouch for the reliability or integrity of this article.

Please note that this notice is intended solely to alert readers that the peer-review process of this article has been compromised.

Wiley and Hindawi regret that the usual quality checks did not identify these issues before publication and have since put additional measures in place to safeguard research integrity.

We wish to credit our Research Integrity and Research Publishing teams and anonymous and named external researchers and research integrity experts for contributing to this investigation.

The corresponding author, as the representative of all authors, has been given the opportunity to register their agreement or disagreement to this retraction. We have kept a record of any response received.

References

- [1] M. Sandeep Kauthsa Sharma, S. Umadevi, Y. Sai Sampath et al., "Mechanical Behavior of Silica Fume Concrete Filled with Steel Tubular Composite Column," *Advances in Materials Science and Engineering*, vol. 2021, Article ID 3632991, 9 pages, 2021.

Research Article

Mechanical Behavior of Silica Fume Concrete Filled with Steel Tubular Composite Column

Maganti Sandeep Kauthsa Sharma,¹ S. Umadevi,² Yerra Sai Sampath ,³ K. Vasugi,¹ K. J. N. Sai Nitesh,⁴ V. Swamy Nadh ,⁵ and L. Natrayan ⁶

¹School of Civil Engineering, VIT University, Chennai 600 127, Tamilnadu, India

²Centre for Nanoelectronics and VLSI Design, SENSE, VIT University, Chennai 600 127, Tamilnadu, India

³Department of Civil Engineering, Arba Minch University, Arba Minch, Ethiopia

⁴Department of Civil Engineering, Anurag University, Hyderabad 500088, Telangana, India

⁵Civil Engineering Department, Aditya College of Engineering, Surampallem 533437, Andhra Pradesh, India

⁶Department of Mechanical Engineering, Saveetha School of Engineering, SIMATS, Chennai 602105, Tamil Nadu, India

Correspondence should be addressed to Yerra Sai Sampath; yerra.sai@amu.edu.et and V. Swamy Nadh; swamynadh09@gmail.com

Received 24 June 2021; Revised 11 July 2021; Accepted 22 July 2021; Published 31 July 2021

Academic Editor: Samson Jerold Samuel Chelladurai

Copyright © 2021 Maganti Sandeep Kauthsa Sharma et al. This is an open access article distributed under the Creative Commons Attribution License, which permits unrestricted use, distribution, and reproduction in any medium, provided the original work is properly cited.

Recycling or utilization of industrial waste is becoming more popular as people become more environmentally conscious. Silica fume is a by-product of the smelting process in the silicon and ferrosilicon industries. This study examines the mechanical behavior of steel tubular composite column filled with conventional concrete and silica fume concrete experimentally under axial compressive loading. For the study, variability in steel tube thickness and column height with a constant diameter are considered. To explore the influence of silica fume in concrete, microstructural analyses are carried out by SEM, XRD, and FTIR. The experimental results reveal that the use of silica fume as a replacement of cement is feasible; the silica fume concrete-filled steel tubular (SCFST) column has marginal enhancement strength capacity compared to CFST column as thickness increases.

1. Introduction

The concrete-filled steel tubular (CFST) composite columns are been used in the modern engineering systems. Detailed experimental and computational studies have been carried out in the past [1–3]. Main advantages of CFST columns are no reinforced cage and no formwork as the steel tube can extremely be used as formwork and they are fire resistant. Based on the various research works carried out, it can be said that circular columns should be preferred over square-shaped CFSTs [4, 5], in order to further enhance structural performance and meet various design requirements, the focus of tubular columns [6, 7], concrete-filled double-skin tubular columns [8], stub columns with carbon fiber reinforcement polymer (CFRP) wrap material [9–12], and concrete-filled aluminium columns [13, 14]. Such

experiments were mainly aimed at using new alloys or modifying standard CFST column configurations to enhance the structural efficiency of composite columns. Yogeshwaran et al. [15] investigated 42 concretes with varying diameter-thickness ratio and three different concrete strengths. The strength, load-axial shortening, load-axial strain, and failure patterns of columns were studied and compared with American and Australian/New Zealand design approaches. Ren et al. [16] conducted an experimental and analytical study on 44 specimens with different shapes. The results of distinct CFST columns performed the ductile manner. Outward buckling is observed at the middle of the member.

Infilled concrete makes a significant role in CFST columns; many researchers have attempted to build composite columns using different types of concrete other than traditional one. Wang et al. [17] had conducted an

experimental investigation on twenty composite columns filled with the reactive powder concrete (RPC) under axial compression. Paranthaman et al. [18] had investigated RAC with filled in stainless steel composite specimens with square and circular shapes, with a replacement ratio of 0, 25%, 50%, and 75%. Also, results were compared with six different codes. Geng et al. [19] studied the time-depended behavior recycled aggregate concrete by 0, 50, and 100% compared with the numerical model.

To examine the performance infilled concrete in the CFST stub column under axial compressive loading, various research works carried out the experiment with different mixes with a constant cement content or with industrial by-products and w/c ratio, which were mixed with industrial by-products such as steel slag, fly ash, silica fume, and lightweight aggregate [20–24]. They are examined with the FE model and Euro code 4. The results explain that despite the use of various types of aggregates, all CFST columns behavior was reasonably well. Zhu et al. [25] investigated the analytical investigation on three different larger diameter concrete-filled higher strength steel stub columns (CFHSST) under compression and compared with Euro code 4 predictions. It is found that load-displacement graphs of three concrete infilled stub columns were like one another. Load-strain curves and failure patterns are observed. Abed et al. [26] studied member stiffness. Abed et al. [26] conducted a test on the 20 concrete-filled steel tubular (CFST) stub columns with dune sand and 4 hollow columns under the axial compression. Results showed that the CFST stub columns with dune sand, identical to traditional CFST stub columns, acted in exhibited a high compressive strength outward buckling failure pattern. The use of waste materials/by-products in building products has been increasingly emphasized in the latest years. The use of by-products in concrete can bring important financial and environmental advantage in concrete making. In this study, for a sustainable ecofriendly environment, silica fume partially replaced with cement in conventional concrete as a core material and hollow steel pipe with a constant diameter, height variation, and thickness variation are the two constituents used.

2. Materials

2.1. Infill Material. In this experimental program, a nominal strength of 25 MPa with 0.4 water cement ratio was employed with various concrete combinations. To determine the compressive strength, cube specimens were prepared as per Indian Standards IS: 10086-1982. Silica fume was substituted by 0, 5, 10, and 15% with cement, manufacturing sand is completely replaced with fine aggregate in each mix, and superplasticizers up to 2% of the binder is used. A machine mixer was employed to prepare the mixes. Three specimens were tested to failure under the compressive testing machine of axial capacity 2000 kN. The optimum percent replacement of the silica fume is carried out for 7 and 28 days of curing of cube specimen. Mix proportions for each mix are given in Table 1. Figure 1 shows the materials used for the concrete mix. The average compressive strength concrete cubes are given in Table 2.

3. Experimental Procedure

3.1. Steel Tubular Columns. In this test program, all the hollow steel tubes (HSS) of circular cross-section with a constant diameter of 75 mm are provided from the local supplier with a thickness of 1.5 mm and 2 mm, with heights of 300 mm and 500 mm. The experimental test setup for composite column under loading is shown in Figure 2. The SCFST columns are for determination of physical properties of HSS section, the coupon test is followed according to the American Standard Testing Materials (ASTM), the hollow section of the both thickness (2 specimens for each thickness) should be cut accordingly, and it should be inserted into the tensile compressive testing machine.

3.2. Infilled Composite Column. Totally, 24 infilled circular composite columns are cast with two different heights 300 mm and 500 mm and with a constant diameter of 75 mm were tested, which includes both the thickness of 1.5 mm and 2 mm. Conventional concrete mix and silica fume concrete matrix mix were used as the infilled material. The specimens were chosen based on height and thickness; concrete was placed in the corresponding hollow steel tubular columns in three layers, where the one end is closed with a thin film sheet placed on the flat base plate and the other end is open. Figure 3 shows the experimental test setup with two dial gauges to observe the lateral deflection of the specimen. Mix proportions for infilled concrete column values are given in Table 3.

4. Results and Discussion

4.1. Microstructural Studies. The material's mechanical properties depend only on its microstructure, which is observed using scanning electron microscopy (SEM). SEM analyses are used to determine the material's surface area. Scanning electron microscopy not only provides topographical but also the compositional study of the material. The raw powder of silica fume, harden conventional concrete powder, and silica fume concrete powder are viewed after 28 days under SEM analysis. Figure 4 shows the SEM microstructural images of the silica fume powder sample in various magnifications such as 50 μm , 20 μm , 10 μm , 5 μm , and 2 μm . The silica fume particles observed are spheroid shapes, and the particle sizes are too small that varies from 0.18 μm to 0.26 μm as shown in Figure 4. Also, noticed that in the SEM images, the raw material of silica fume is closely packed with no pores [22]. Figure 5 shows SEM images of conventional concrete after 28 days of curing in various magnifications such as 50 μm , 20 μm , 10 μm , 5 μm , and 2 μm . From the images, the formation of denser concrete was observed. This shows the formation of calcium silicate hydrate (CHS), portlandite (CH), and pores found. Particle sizes for conventional concrete vary from 0.19 μm to 0.26 μm . Formation a highly dense microstructure of CSH-formed concrete with a small amount of CH and less porous spaces are observed for silica fume concrete after 28 days of

TABLE 1: Mix proportions for cube specimens.

Mix	Cement (kg/m ³)	Silica fume (kg/m ³)	Water (kg/m ³)	Coarse aggregate (kg/m ³)	Manufacturing sand (kg/m ³)
1	350	0	140	1140	896
2	365.75	19.25	140	1117.04	877.68
3	346.5	38.5	140	1112.44	874.06
4	327.25	57.75	140	1109	871.64



FIGURE 1: Concrete constituents (cement, sand, silica fume, fly ash, aggregate, and superplasticizer).

TABLE 2: Compressive strength behavior of cubes.

Mix	Percentage replacement of silica fume (%)	7 days strength (MPa)	28 days strength (MPa)
1	0	24.12	33.28
2	5	25.48	35.14
3	10	26.89	37.61
4	15	25.08	35.87

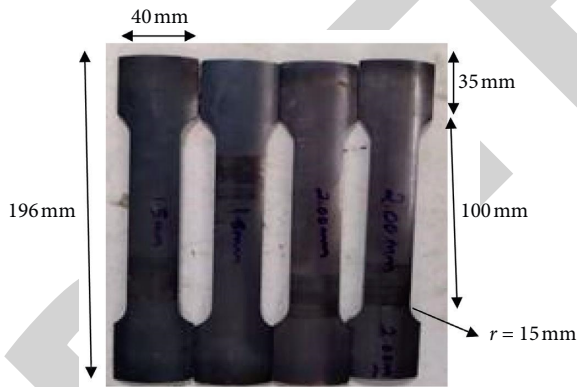


FIGURE 2: Coupon test specimen dimensions as per ASTM.

curing as shown in Figure 6, a much denser and more compacted material compared to conventional concrete. The scale of particles varies from 0.18 to 0.32 μm , noticed that the influence of silica fume rises in compressive strength [27].

4.2. XRD Analysis. The qualitative materials are analyzed using X-ray diffraction (XRD). Mostly, this method is used to define the crystalline material structure. The graph is drawn between intensity and a frequency of 2θ . The raw powder of silica fume, harden conventional concrete powder, and silica fume concrete powder after 28 days of curing are tested under XRD analysis. The silica fume powder XRD



FIGURE 3: Test setup for the composite column.

pattern is illustrated in Figure 7. It observed the quartz presence from silica fume powder XRD graph. The first point is $2\theta = 21.02$, the second peak is $2\theta = 26.5$, and the third peak is $2\theta = 28.14$.

TABLE 3: Mix proportions for infilled concrete column.

Mix	Cement (kg/m ³)	Silica fume (kg/m ³)	Water (kg/m ³)	Coarse aggregate (kg/m ³)	Manufacturing sand (kg/m ³)	Superplasticizer (kg/m ³)
1	391.35	0	156.54	808.23	1140.02	7.82
2	352.22	39.13	156.54	802	1135.18	7.82

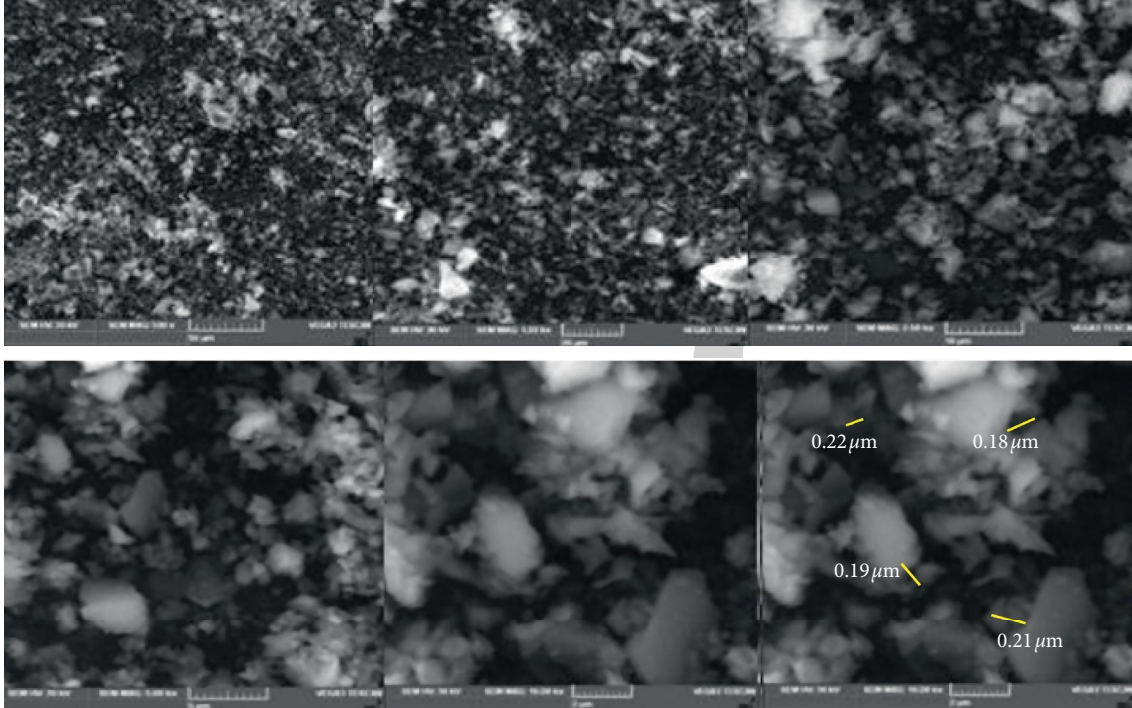


FIGURE 4: SEM microstructure of the silica fume powder sample.

XRD results for the conventional concrete after 28 days of curing are shown in Figure 7. The result shows the presence of quartz (Q), silicate calcium hydrate (CSH), silicate calcium (CS), calcite (C), and portlandite (P) peaks. The first peak is measured at $2\theta = 21^\circ$, the presence of a quartz compound, the second peak at $2\theta = 24^\circ$, the presence of a calcite compound, and the peaks are at 2θ between 26° and 27.5° , indicating the presence of quartz compound reveals that crystalline phases in concrete. Figure 8 shows the XRD analysis of the sample of silica fume concrete. It shows the formation of calcite component significantly increased in silica fume concrete when the peak angle $2\theta = 25^\circ$ to 27° compared to plain concrete. This reflects the presence of amorphous material in compounds called calcite (C), quartz (Q), and calcium silicate (CS). It also reflects calcium silicate hydrate (CSH) formation at an angle $2\theta = 42.92^\circ$ [27].

4.3. FTIR Analysis. Figure 9 shows the FTIR graph of the conventional concrete after 28 days of the curing period. The primary characteristic peaks of C-S-H may be found between 1081 cm^{-1} and 981 cm^{-1} (Si-O asymmetric stretching vibration). The peaks below 3500 cm^{-1} are caused by stretching vibrations of free molecular water or adsorbed water on the surface of the control concrete. The presence of portlandite (CH) is easily recognized by FTIR spectroscopy,

which is well detected by a strong distinct peak at 3640 cm^{-1} . The S-O stretching vibration of $(\text{SO}_4)^{2-}$ is also identified at $1150\text{--}1100\text{ cm}^{-1}$ [28].

Figure 10 shows the silica fume powder picture from FTIR. The strong bands at 681 cm^{-1} , 724 cm^{-1} , 871 cm^{-1} , 981 cm^{-1} , 1081 cm^{-1} , 1100 cm^{-1} , and 1200 cm^{-1} attribute the basic Si-O vibrations. They are identical in terms of silica modifications. The peaks between 1130 cm^{-1} and 1200 cm^{-1} are characteristics of Si-O-Si bonds (symmetric and asymmetric stretch). The presence of sodium alginate bands ranging from 800 cm^{-1} to 470 cm^{-1} are Si-O vibration absorption bands. The OH stretching in silanol occurs generally as peaks above 3500 cm^{-1} . The peak bands between 3441 cm^{-1} and 3647 cm^{-1} indicate the presence of silica, while monohydrogen bond occurs between the bandwidths 3600 cm^{-1} and -3400 cm^{-1} . The closeness of these peaks generally results in spectra that are heavily overlapped. The peak 981 cm^{-1} indicates the occurrence on calcium silicate hydrate [29, 30].

4.4. Composite Column Test. The measured axial load capacity for the 24 concrete composite columns of both lengths and both thicknesses with a constant diameter are presented in Table 4, as an average of 3 specimens for each mix. From the experimental results, it was clear that the replacement of

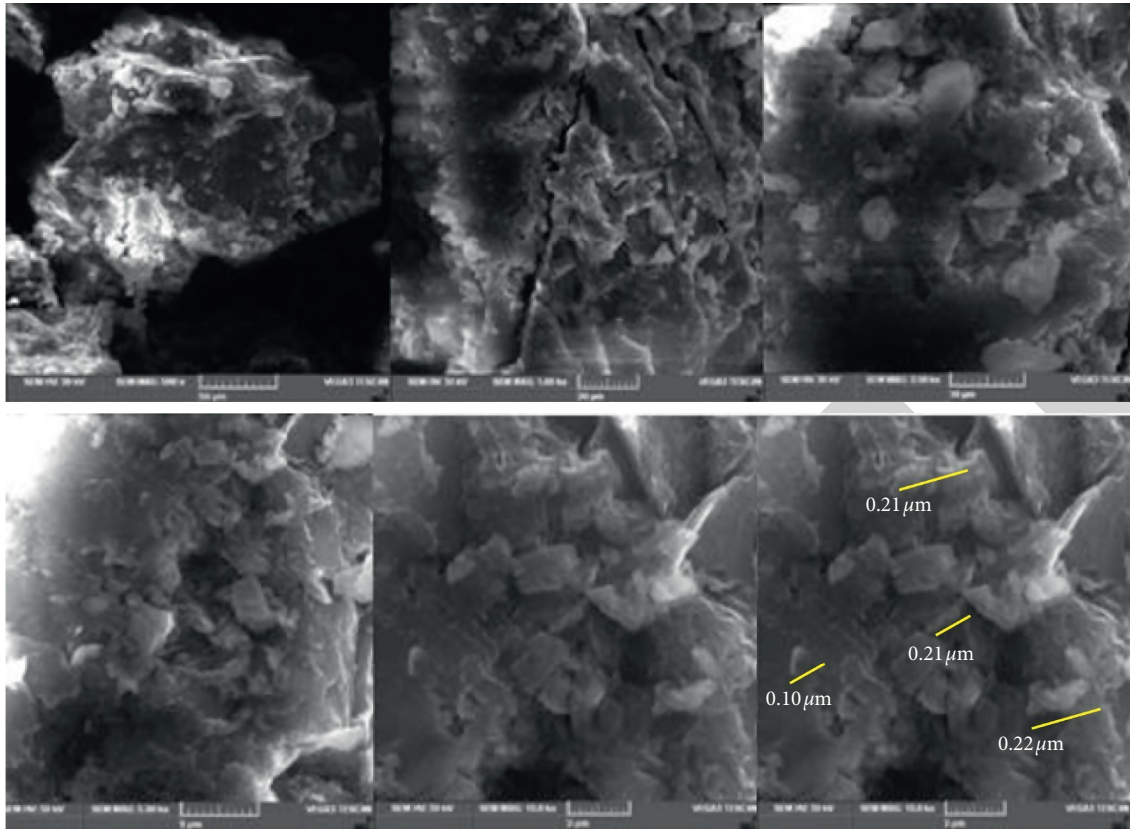


FIGURE 5: SEM microstructure images of the conventional concrete.

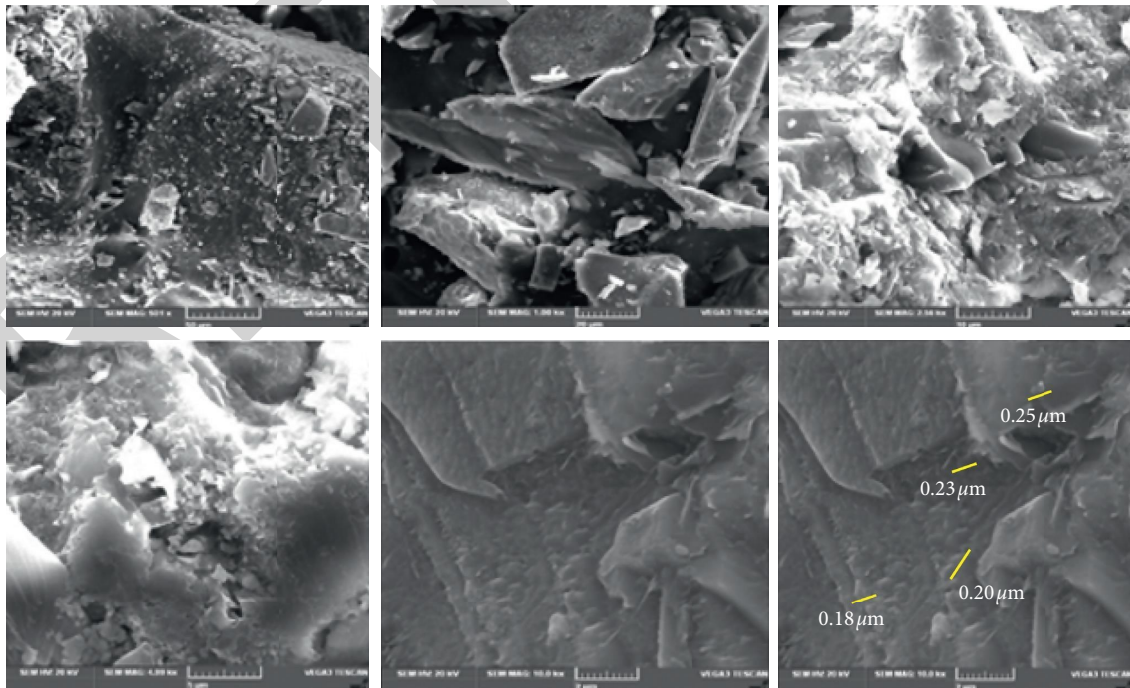


FIGURE 6: SEM microstructure images of the silica fume concrete.

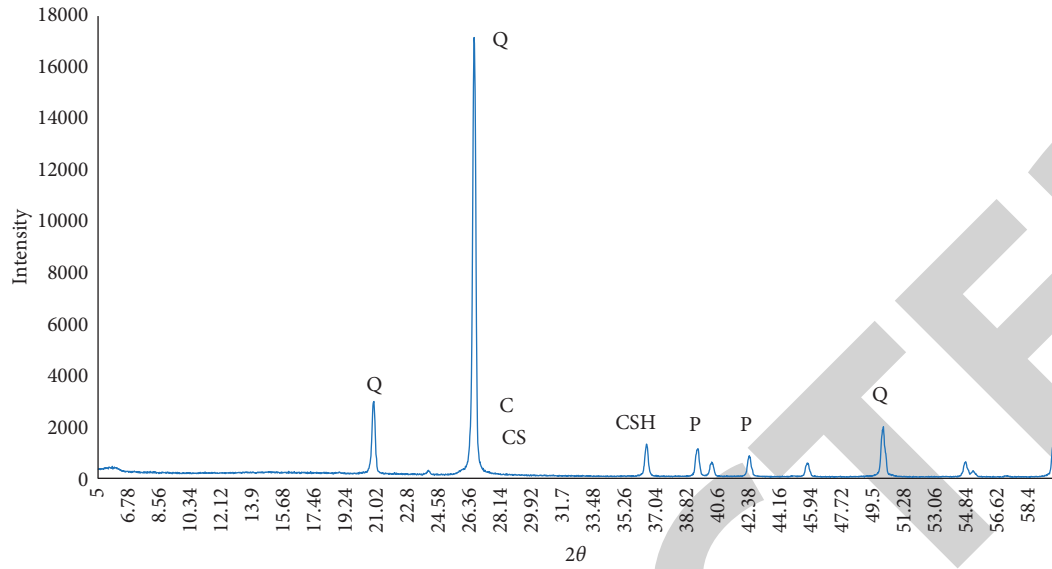


FIGURE 7: XRD image of conventional concrete after 28 days of curing.

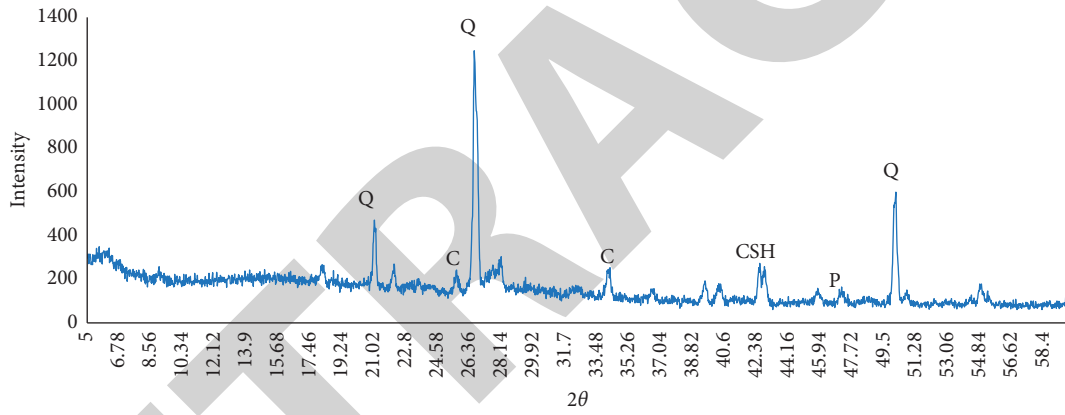


FIGURE 8: XRD image of silica fume concrete after 28 days of curing.



FIGURE 9: FTIR analysis graph of conventional concrete after 28 days of curing.

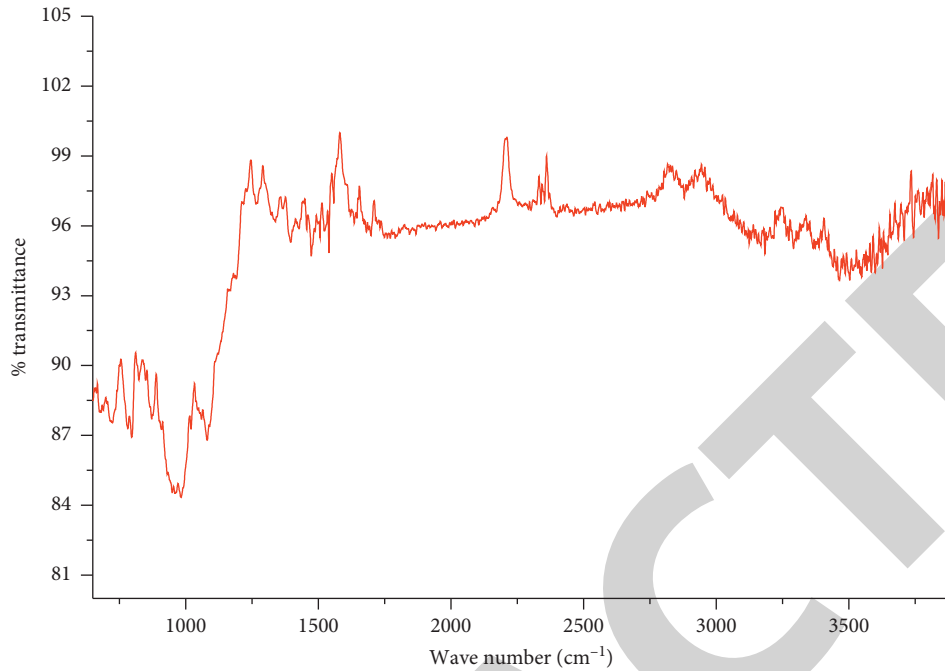


FIGURE 10: FTIR analysis graph of silica fume concrete after 28 days of curing.

TABLE 4: Composite column specimens and test results.

S. no	Percentage replacement of silica fume (%)	Thickness (mm)	Height (mm)	Diameter (mm)	Load carrying capacity (kN)
1	0	1.5	300	75	335.5
2	10	1.5	300	75	360.38
3	0	1.5	500	75	301.55
4	10	1.5	500	75	332.42
5	0	2	300	75	386.25
6	10	2	300	75	416
7	0	2	500	75	382.66
8	10	2	500	75	403.18



(a)



(b)

FIGURE 11: Mode of failure for coupon specimens 1.5 mm and 2 mm thick.

silica fume with cement in concrete enhances the strength of concrete specimen after 28 days water curing. It was that the axial loading capacity increases with an increase in the thickness.

4.5. *Mode of Failure.* Figure 11 shows the mode of failure for the coupon specimens after the tensile test; it was observed that failure occurred at the web portion of the specimen. Also, it was observed that there was a change in the area of



FIGURE 12: Mode of failure for composite columns of 1.5 mm and 2 mm steel tube thickness.

the specimen after the test. Figure 12 shows the failure of the composite columns of 1.5 mm thickness and failure of the composite columns of 2 mm thickness. In both the cases, it observed the outward buckling at the middle portion of the column for 300 mm height specimens (both thicknesses). As the height of the column increases, it observed a shear failure at top and bottom with outward buckling at middle for 1.5 mm thick columns. The thickness increases the shear failure at the one end of the column.

5. Conclusions

- (i) Optimum partial replacement is 10%. Compressive strength varies by 11.51% from normal mix to silica fume that replaced concrete after 28 days curing.
- (ii) XRD results confirm the presence of quartz compound which helps in strengthening of concrete mix and forms a crystalline phase.
- (iii) SEM analysis, it was observed that the microstructure gives the disintegration of Si and Al compounds. FTIR confirms strengthening of concrete mix.
- (iv) Peak load of the normal concrete infilled column and silica fume concrete column with height 300 mm and 500 mm varies with 17.88% and 34.77%, respectively.
- (v) Peak load of the hollow steel column with height 300 mm, 1.5 mm thickness, and 2 mm thickness varies with 8.04% and hollow steel column with height 500 mm, 1.5 mm thickness, and 2 mm thickness varies with 29.58%, respectively.
- (vi) SCFST column strength capacity of 1.5 mm thick, 300 mm height varies with CFST column by 7.5%. For 1.5 mm thick, 500 mm height SCFST column varies with the CFST column by 9.3%. The strength capacity is 2 mm thick, and 300 mm height SCFST column varies with CFST column by 7.15%. For 2 mm thick, 500 mm height SCFST column varies with the CFST column by 5%.
- (vii) Shear failure and outward buckling mode of failures are observed for long and short composite columns, respectively.

Data Availability

The data used to support the findings of this study are included in the article and are available from the corresponding author upon request.

Disclosure

It was performed as a part of the employment of Arba Minch University, Ethiopia.

Conflicts of Interest

The authors declare that there are no conflicts of interest.

Acknowledgments

The authors appreciate the supports from Arba Minch University, Ethiopia. The authors thank Vellore Institute of Technology, Chennai, for the technical assistance for carrying out the experiments.

References

- [1] L.-H. Han, W. Li, and R. Bjorhovde, "Developments and advanced applications of concrete-filled steel tubular (CFST) structures: members," *Journal of Constructional Steel Research*, vol. 100, pp. 211–228, 2014.
- [2] S. Güler, F. Korkut, N. Yaltay, and D. Yavuz, "Axial behaviour of concrete filled steel tube stub columns: a review," *Journal of Bio- and Tribo-Corrosion*, vol. 5, no. 3, p. 77, 2019.
- [3] S. Morino, "Recent developments on concrete-filled steel tube members in Japan," in *Composite Construction in Steel and Concrete*, vol. 4, pp. 644–655, Elsevier, Amsterdam, Netherlands, 2002.
- [4] S. Yogeshwaran, L. Natrayan, S. Rajaraman, S. Parthasarathi, and S. Nestro, "Experimental investigation on mechanical properties of epoxy/graphene/fish scale and fermented spinach hybrid bio composite by hand lay-up technique," *Materials Today: Proceedings*, vol. 37, no. 2, pp. 1578–1583, 2021.
- [5] D. Hernández-Figueirido and A. Piquer, "Behavior of steel-reinforced concrete-filled square steel tubular stub columns under axial loading," *Journal of Constructional Steel Research*, vol. 104, pp. 211–230, 2015.

Retraction

Retracted: Optimization of Remazol Black B Removal Using Biochar Produced from *Caulerpa scalpelliformis* Using Response Surface Methodology

Advances in Materials Science and Engineering

Received 26 December 2023; Accepted 26 December 2023; Published 29 December 2023

Copyright © 2023 Advances in Materials Science and Engineering. This is an open access article distributed under the Creative Commons Attribution License, which permits unrestricted use, distribution, and reproduction in any medium, provided the original work is properly cited.

This article has been retracted by Hindawi, as publisher, following an investigation undertaken by the publisher [1]. This investigation has uncovered evidence of systematic manipulation of the publication and peer-review process. We cannot, therefore, vouch for the reliability or integrity of this article.

Please note that this notice is intended solely to alert readers that the peer-review process of this article has been compromised.

Wiley and Hindawi regret that the usual quality checks did not identify these issues before publication and have since put additional measures in place to safeguard research integrity.

We wish to credit our Research Integrity and Research Publishing teams and anonymous and named external researchers and research integrity experts for contributing to this investigation.

The corresponding author, as the representative of all authors, has been given the opportunity to register their agreement or disagreement to this retraction. We have kept a record of any response received.

References

- [1] R. Gokulan, S. Balaji, and P. Sivaprakasam, "Optimization of Remazol Black B Removal Using Biochar Produced from *Caulerpa scalpelliformis* Using Response Surface Methodology," *Advances in Materials Science and Engineering*, vol. 2021, Article ID 1535823, 8 pages, 2021.

Research Article

Optimization of Remazol Black B Removal Using Biochar Produced from *Caulerpa scalpelliformis* Using Response Surface Methodology

R. Gokulan ¹, S. Balaji ², and P. Sivaprakasam ³

¹Department of Civil Engineering, GMR Institute of Technology, Rajam, Srikakulam 532 127, Andhra Pradesh, India

²Department of Civil Engineering, Kongu Engineering College, Perundurai, Erode 638 060, Tamilnadu, India

³Department of Mechanical Engineering, College of Electrical and Mechanical Engineering, Center of Excellence-Nanotechnology, Addis Ababa Science and Technology University, Addis Ababa, Ethiopia

Correspondence should be addressed to P. Sivaprakasam; shiva@aastu.edu.et

Received 5 July 2021; Revised 17 July 2021; Accepted 22 July 2021; Published 31 July 2021

Academic Editor: Samson Jerold Samuel Chelladurai

Copyright © 2021 R. Gokulan et al. This is an open access article distributed under the Creative Commons Attribution License, which permits unrestricted use, distribution, and reproduction in any medium, provided the original work is properly cited.

Optimization of process conditions for the removal of Remazol Black B was investigated using response surface methodology (Box-Behnken design). The biodecolorization of dye was studied using biochar produced from waste biomass of *Caulerpa scalpelliformis* (marine seaweeds). The reactions were optimized by varying sorbent dosage, solution pH, temperature, and initial dye concentration. The results indicated that dye removal efficiency of 80.30% was attained at an operating condition of 4 g/L (sorbent dosage), 2.0 (solution pH), 35°C (temperature), and 0.25 mmol/L (initial dye concentration). The regression coefficient of the developed model was calculated to be 97% which shows good fit of the model.

1. Introduction

Wastewater generation has become one of the most important pollutants. All types of industrial wastewater and dye-bearing wastewater need effective treatment. Every year approximately 7 lakh metric tonnes of dyes are utilized. It is also predicted that 5% to 10% of these dyes are not utilized and are directly released into the water bodies [1, 2]. The use of dyes has increased in the textile and industrial sectors due to their convenience and natural coloring [3]. Dyes are commonly complex structures that are more stable, and it is difficult to remove them from the wastewater completely [4]. If these dyes without proper treatment are discharged into the nearby streams or rivers, they will affect the aquatic life [4]. Dyes will change the color of water bodies and reduce the photosynthesis process [4]. Dyes when mixed with drinking water will cause serious health issues; since dyes are toxic and poisonous in nature, they may cause many side effects to human health [5].

The removal of dyes can be achieved by treating with physical, chemical, or biological methods. These methods include coagulation with sedimentation and flocculation [6], photochemical oxidation [7], adsorption [8], ozonation [9], and electrochemical oxidation [10]. However, there are several limitations related to these methods [11]. The important disadvantage is cost associated with the treatments and generation of huge quantity of secondary pollutants to the environment [11]. In recent times, many researchers investigated biosorption of dye molecules using low cost adsorbents that are produced from naturally available waste materials. Some of the commonly used biomass materials are bagasse [12], rice husk [12], coffee bean husk [12], vine shoots [13], pecan shell [12], corn cob [12], walnut shell [12], coconut shell [14–16], and seaweeds [17, 18]. These naturally available materials are considered as wastes that are generated in huge quantity every year. Hence, utilizing waste biomass for the removal of toxic pollutants will result in the conversion of waste to energy [19]. Seaweed-based biochar is a recent eco-friendly tool that can be used as adsorbent, and

it can be easily regenerated [20]. It is also reported that biochar is used for the soil enrichment [21, 22].

Biochar is produced in a limited oxygen environment at a temperature greater than 300°C. Feedstock used for the production of the biochar plays a very important role in deciding the characteristics of the biochar. Dry feedstocks (moisture content less than 30%) have more advantages than wet feedstocks (moisture content more than 30%). The main objective of the present research is to utilize green marine seaweed that is naturally available in the seashores as a sorbent for the remediation of the dye molecule. The cost associated with this adsorbent is very low. Nowadays, the statistical program developed by many researchers helped in carrying out many experiments in a shorter period of time in finding the optimum process conditions for the best outcome [23]. Response surface methodology (RSM) is a statistical tool used to study the interaction between different parameters at different levels [24–26]. The main objective of the present research is to utilize *Caulerpa scalpelliformis* for the remediation of the Remazol Black B molecule. *Caulerpa scalpelliformis* is a seaweed that is naturally overgrown in the coastal region of south Tamil Nadu. These seaweeds are well known for their antimicrobial activity, and their application in biosorption is less reported. The cost associated with this adsorbent is very low. Very limited research has been conducted using *Caulerpa scalpelliformis* for toxic pollutant removal, and production of biochar from this seaweed is not reported. So, the current research will provide a sustainable solution for the toxic pollutant removal.

2. Materials and Methods

2.1. Biochar and Dye. *Caulerpa scalpelliformis* marine seaweeds were obtained from seashores of Mandapam region (Tamil Nadu, India). The biomass was cleaned and sun-dried for 7 days. The dried biomass is used for the biochar production [27]. Different temperature ranges between 300 and 500°C are used for the pyrolysis to obtain maximum biochar yield. The maximum biochar yield of 47.5% was obtained at 350°C. Remazol Black B (RBB) used in the study was procured from Sigma-Aldrich. Remazol Black B has the following empirical formula: $C_{26}H_{21}N_5Na_4O_{19}S_6$, having color index of 20505, molecular weight of 991.82 mmol/g, and λ_{max} of 597. Figure 1 illustrates the structural composition of Remazol Black B.

2.2. Batch Studies. The batch studies were investigated in controlled environment using rotary shaker for 8 hours at 160 rpm. After the completion of the batch studies, the sample was centrifuged at 3000 rpm for 5 min to separate pellet. 5 ml of the clear solution was taken for the measurement of the final dye concentration using a spectrophotometer. The experiments were conducted under different conditions by varying sorbent dose (2, 4, and 6 g/L), pH (2, 3, and 4), temperature (25, 35, and 45 °C), and initial dye concentration (0.25, 0.5, and 1 mmol/L). Equations (1) and (2) are used to calculate the dye sorption and dye removal efficiency.

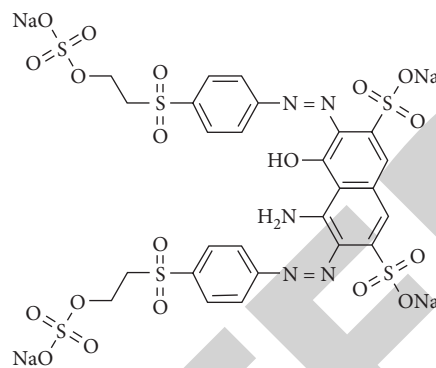


FIGURE 1: The structural composition of Remazol Black B (RBB).

$$Q = \frac{V(C_0 - C_e)}{W}, \quad (1)$$

$$\text{removal efficiency} = \frac{(C_0 - C_e)}{C_0} \times 100. \quad (2)$$

2.3. Experimental Design (RSM). The Box–Behnken design (BBD) was used to find the interaction of different parameters. Analysis of variance (ANOVA), residual plots, surface plot, and response optimizer were used to understand the interaction among different variables that will result in maximum removal efficiency. Table 1 summarizes the different levels of all independent variables. Equation (3) is used to analyze the BBD:

$$Y = \beta_0 + \sum_{i=1}^k \beta_i x_i + \sum_{i=1}^K \beta_{ii} x_i^2 + \sum_{i=1}^0 \sum_{j=i+1} (\beta_{ij} x_i x_j + \varepsilon), \quad (3)$$

where Y denotes the response (% removal), β is the regression coefficient, x_i and x_j are independent variables, and ε represents the error.

3. Results and Discussion

3.1. Predictive Model. Equation (4) shows the model developed by the BBD using the input variables, and the response can be calculated.

$$Y = 65.42 - 1.6A + 7.87B - 1.63C + 0.52D + 0.08A^2 - 1.99B^2 - 20.66C^2 - 0.006D^2 + 3AC. \quad (4)$$

The R^2 value decides the quality of the developed model. The R^2 value for the developed model is 0.9717, which is very close to unity and relatively high. This shows that 97% of the removal efficiency is based on the independent variable and only 3% of the total deviations are not correlated with the developed model. The high value of R^2 shows that the good fit of the developed model. The P value exceeding 0.05 is considered not to be significant and less than 0.05 is considered to be significant. From Table 2, the results show that equilibrium pH and initial dye concentration are significant. Table 2 summarizes the different factors of ANOVA. F value of 29.48 shows the significance of the model. The values of R^2 and R^2_{adj} were found to be 0.9717 and 0.9388, respectively.

TABLE 1: BBD input variables with levels.

	Levels		Variables	Variable code
1	0	-1		
2	4	6	Biochar dose (g/L)	A
2	3	4	Equilibrium pH	B
0.25	0.50	1.0	Initial dye concentration (mmol/L)	C
25	35	45	Temperature (°C)	D

These values showed that the developed model is good and the values of the independent variables are accurate with very less error. Thus, the developed model can predict the RBB removal using biochar derived from *Caulerpa scalliformis*. The developed model has good agreement with experimental results using four independent variables [28].

3.2. Optimization of Dye Removal. Table 3 summarizes the removal efficiency for 27 experimental trails. Optimization of the process variable is carried out using the quadratic model created with different levels of different variables. The RBB dye removal efficiency of 79.97% is achieved at a biochar dosage 4 g/L, equilibrium pH of 2, initial dye concentration of 0.25 mmol/L, and temperature of 35°C. The corresponding RBB dye removal efficiency with respect to the experiment is found to be 80.30%. The residual error of 0.333 was obtained between experimental and predicted values of the best trail. Thus, the result confirmed that the RSM is a reliable optimization tool for the RBB dye removal using biochar derived from *Caulerpa scalliformis*.

3.3. Residual Plots for Response Yield. From Figure 2, one can clearly understand the response of each experiment by studying the normal probability plot, fitted values, histogram, and observational orders. The normal probability plot and fitted values clearly show that all the experimental data are in accordance with the predicted values of the RSM. But only two observations deviate with a residual error of more than -1 and 2. From the histogram, frequency is grouped into five ranges. 8 frequencies are in the range of -0.25 to +0.25 residual errors, and 8 frequencies are in the range of -0.25 to -0.75. 9 frequencies are between 0.25 and 0.75, 1 frequency is in the range of -1.25 to -1.75, and 1 frequency is in the range of 1.75 to 2.25. From Figure 1, it can be clearly seen that all the values are found to be close to the predicted value of RSM, and a maximum residual error of -1.33 and 2.00 is observed in the plot for observations 13 and 14.

3.4. Influence of Process Parameters on Dye Removal. The dependent variable and the independent variable that influence the % dye removal can be studied by three-dimensional response surface plot. By fixing the other two variables at fixed levels, the dependent variable can be used to understand the mechanism. It can give a clear understanding of the main variables and interaction effects that influence the % dye removal.

3.5. Influence of Initial Dye Concentration and Biochar Dosage. Figure 3 shows the influence of initial dye concentration and biochar dosage on % dye removal for fixed pH of 3 and temperature of 35°C. Biochar dosage is a crucial parameter which decides the economy of the treatment. Figure 3 clearly shows that when the concentration is increased, % removal of dye decreases. As reported by Vijayaraghavan and Yun [29], the surge in dye concentration will reduce % removal of dye, and this is because at higher concentration, the uptake capacity becomes saturated, and further sorption will not take place and affects the % dye removal. It is also observed from Figure 3 that % removal of dye increases with the surge in the biochar dosage. % removal of dye gradually increases from a dosage of 2 g/L to 6 g/L. A similar type of work was carried out by Gokulan et al. [18] who reported that increase in dosage increases the % removal of dye. It is also reported that % removal of dye depends not only on the mass of sorbent but also on the uptake capacity of the biochar. Higher biochar dosages will have sufficient exchangeable active binding sites on the sorbent matrix [30].

3.6. Influence of Initial Dye Concentration and pH. Figure 4 illustrates the influence of initial dye concentration and pH at fixed biochar dosage of 4 g/L and temperature of 35°C. Figure 4 shows that surge in pH from 2 to 3 reduced the removal efficiency. This clearly shows that if pH is not maintained properly, it will decrease the % removal of dye. Due to the presence of lignocellulosic constituents that comprise carboxyl, sulfate, and amine groups, the removal efficiency will increase with a decrease in pH. Presence of these compounds will increase the interactions between biochar and the dyes which will increase % removal of dye.

3.7. Influence of Initial Dye Concentration and Temperature. From Figure 5, it is obvious that the rise in temperature improved % removal of dye from the solute. Gokulan et al. [18] in his work reported that increase in temperature strongly influences % dye removal and also increases the sorption capacity of the sorbent that is used for dye removal. But from the economic point of view, cost will be high if the temperature is maintained at 45°C, and the difference in % dye removal between 35°C and 45°C is only around 2 to 3%. Since 35°C is the room temperature, it may be considered as optimum for the dye removal.

3.8. RSM Optimizer. RSM optimizer is employed to visualize the percentage increase in removal efficiency of the dye by considering process conditions. From Figure 6, it is

TABLE 2: Analysis of variance for the removal of Remazol Black B.

Source	Degree of freedom	Seq SS	Adj MS	F	P
Regression	14	343.969	24.5692	29.48	<0.0001
Linear	4	302.918	2.4373	2.92	0.067
A	1	15.413	1.0898	1.31	0.275
B	1	199.267	5.2132	6.26	0.028
C	1	79.568	0.0177	0.02	0.886
D	1	8.670	1.9743	2.37	0.150
Square	4	32.051	8.0127	9.62	<0.001
A ²	1	8.263	0.5926	0.71	0.416
B ²	1	14.681	21.1559	25.39	<0.001
C ²	1	7.078	8.8981	10.68	0.007
D ²	1	2.028	2.0281	2.43	0.145
Interaction	6	9.000	1.5000	1.80	0.182
AC	1	9.000	9.0000	10.80	0.007
Residual error	12	10.000	0.8333	*	*
Lack of fit	10	10.000	1.0000		
Pure error	2	0.000	0.0000		
Total	26	353.969			

$R^2 = 0.9717$; $R^2_{adj} = 0.9388$.

TABLE 3: Experimental and predicted responses of BBD with residual error.

Run order	A	B	C	D	Yield (%)		Residuals
	Biochar dosage (g/L)	Equilibrium pH	Initial dye concentration (mmol/L)	Temperature (°C)	Experiment	RSM	
1	4	2	0.25	35	80.30	79.97	0.333
2	4	2	0.75	35	74.15	74.82	-0.667
3	2	3	0.75	35	71.10	70.43	0.667
4	4	3	0.50	35	76.60	76.60	0.000
5	6	3	0.50	45	77.80	78.30	-0.500
6	4	4	0.50	45	71.10	70.77	0.333
7	4	3	0.25	25	76.75	76.42	0.333
8	4	2	0.50	45	79.25	78.92	0.333
9	2	4	0.50	35	69.90	69.73	0.167
10	4	4	0.50	25	69.40	69.07	0.333
11	4	3	0.50	35	76.60	76.60	0.000
12	2	2	0.50	35	78.05	77.88	0.167
13	2	3	0.25	35	77.25	78.58	-1.333
14	6	3	0.75	35	77.70	75.70	2.000
15	4	3	0.75	45	72.30	72.97	-0.667
16	4	3	0.25	45	78.45	78.12	0.333
17	4	3	0.50	35	76.60	76.60	0.000
18	2	3	0.50	25	74.50	74.33	0.167
19	4	4	0.75	35	66.00	66.67	-0.667
20	2	3	0.50	45	76.20	76.03	0.167
21	6	2	0.50	35	79.65	80.15	-0.500
22	4	4	0.25	35	72.15	71.82	0.333
23	6	3	0.25	35	77.85	77.85	0.000
24	4	2	0.50	25	77.55	77.22	0.333
25	6	4	0.50	35	71.50	72.00	-0.500
26	6	3	0.50	25	76.10	76.60	-0.500
27	4	3	0.75	25	70.60	71.27	-0.667

apparent that removal efficiency of 80.95% is achieved at a biochar dose of 2 g/L, equilibrium pH of 2.0, initial dye concentration of 0.25 mmol/L, and temperature of 41.96°C ($\approx 42^\circ\text{C}$). It is also predicted that the composite desirability of 0.9973 is achieved for these process conditions, which shows that the predicted values are accurate. Batch studies

were conducted with these predicted process conditions. Three batch trials were conducted, and the removal efficiency obtained was 81.10%, 81.05%, and 80.98%, respectively. So, the average removal efficiency obtained from the batch study is 81.04%. The obtained values agree with the predicted value. From the results, it is concluded

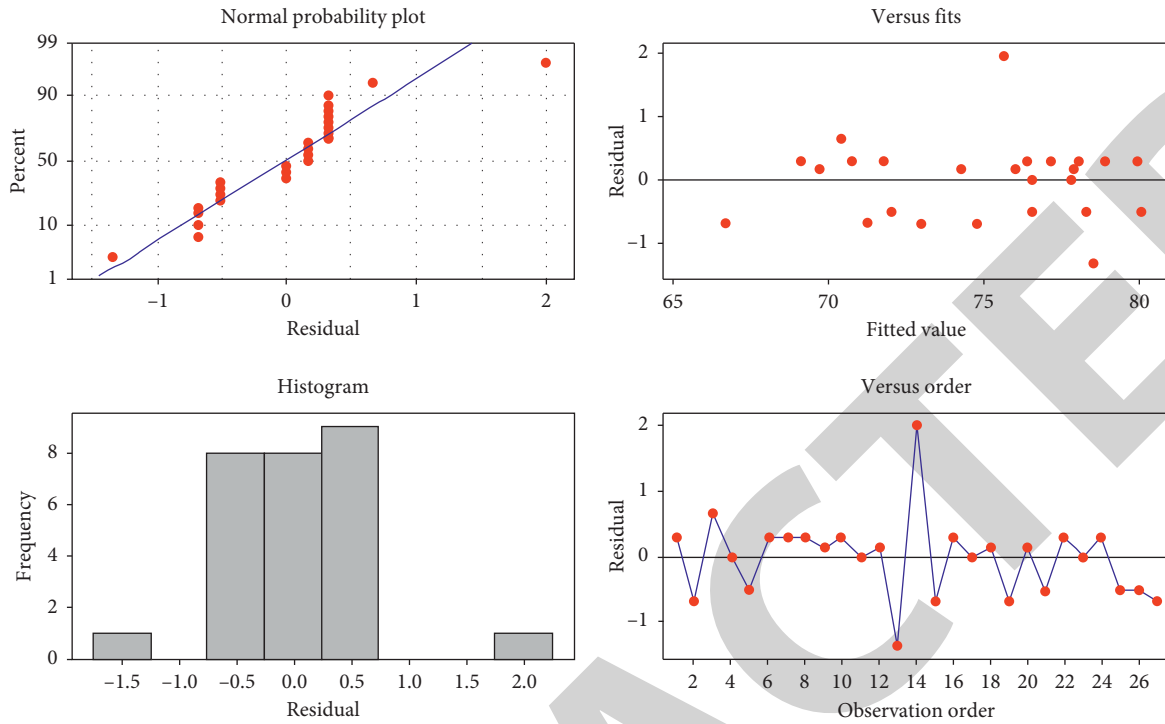


FIGURE 2: Residual plots for response yield.

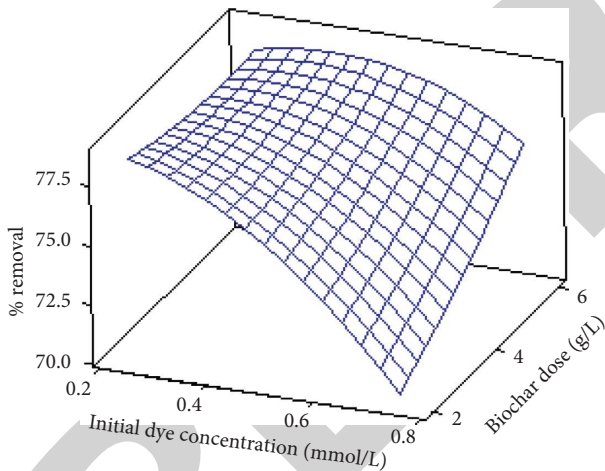


FIGURE 3: Effect of initial dye concentration (mmol/L) and biochar dosage (g/L).

that RSM optimizer increased the removal efficiency from 79.97% to 80.95%, i.e., increase of 0.98% ($\approx 1\%$). The batch studies revealed that the removal efficiency increased from 80.30% to 81.04%, i.e., increase of 0.74%.

3.9. Sorption Isotherm and Kinetic Studies. To understand the mechanism of adsorption, batch study was carried out at different initial dye concentrations varying from 0.1 to 1 mmol/L at constant pH, temperature, and biochar dosage. Kinetic study is also carried at varying time intervals from 5 to 360 minutes to determine the removal efficiency with respect to time. From isotherm studies, it is

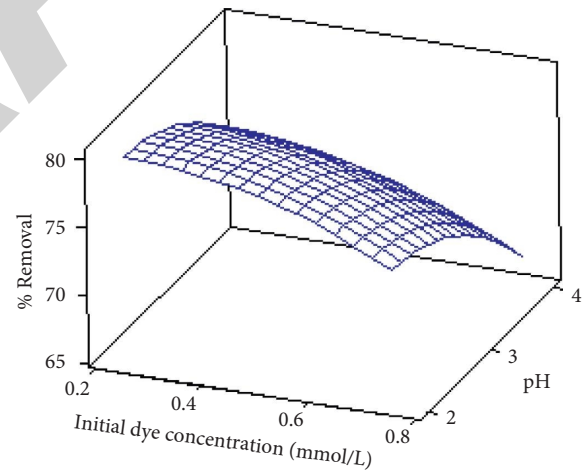


FIGURE 4: Effect of initial dye concentration (mmol/L) and pH.

concluded that the highest uptake of 0.161 mmol/g is attained in the Toth model. Langmuir, Freundlich, Sips, and Toth models were used, and the Toth model is found to have a highest regression coefficient of 0.9999 and % error of 0.6042. From the isotherm studies, it is also concluded that the increase in initial dye concentration decreased removal efficiency. For instance, at an initial dye concentration of 0.05 mmol/L, the removal efficiency is found to be 81.2%, whereas at 1 mmol/L, the removal efficiency is found to be 32.1%. So, at low concentration, biochar is capable of acting as an effective adsorbent. The kinetic study results showed that adsorption was maximum in the first 90 minutes. At a time interval of 120 minutes, almost 90% of the dyes are adsorbed, and a

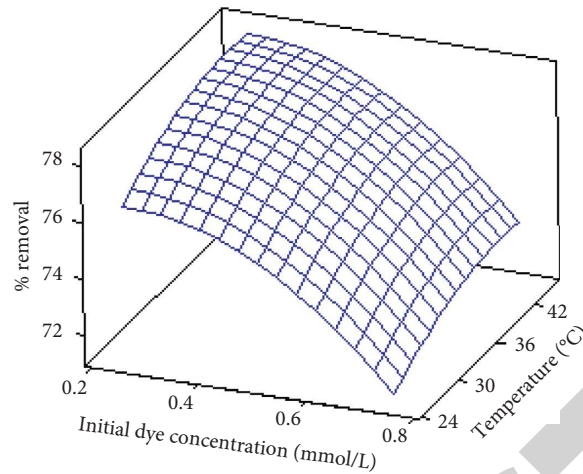


FIGURE 5: Effect of initial dye concentration (mmol/L) and temperature (°C).

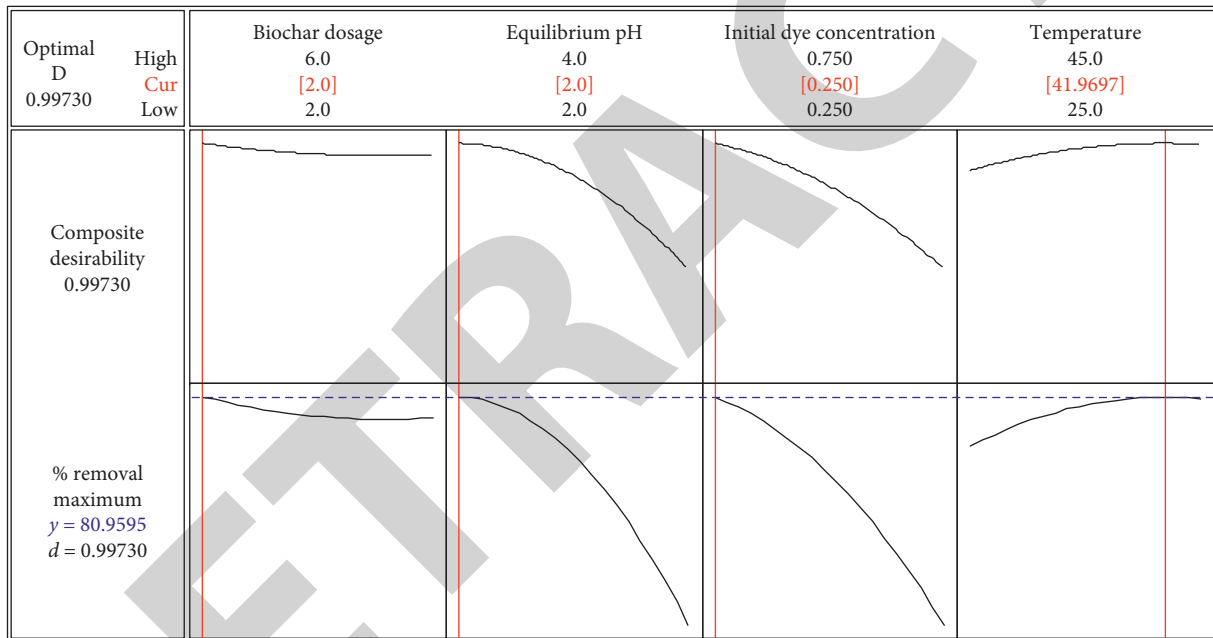


FIGURE 6: RSM optimizer for enhanced dye removal efficiency.

further increase in time resulted in very less adsorption. Kinetic study results show that a contact time of 120 minutes gives optimum values. Pseudo-first-order and pseudo-second-order models were used to predict the uptake capacity of the adsorbent, and the pseudo-first-order model was found to have highest regression coefficient of 0.99 under all conditions.

4. Conclusion

From the study, it is concluded that *Caulerpa scalpelliformis*-derived biochar can be effectively used for the removal of RBB. The RSM-based BBD matrix for an independent variable is developed, and the results showed that the predicted value and experimental value are close to each other. RBB dye removal efficiency of 79.97% is achieved at a biochar dosage of 4 g/L, equilibrium pH of 2, initial dye

concentration of 0.25 mmol/L, and temperature of 35°C, whereas for the same conditions, the removal efficiency of 80.30% is obtained in experimental studies, which is very close to the predicted value of the RSM with a residual error of 0.333. Thus, the RSM model successfully determined the removal efficiency of RBB dye using biochar derived from *Caulerpa scalpelliformis*.

Data Availability

The data used to support findings of this study are included within the article.

Conflicts of Interest

The authors declare that they have no conflicts of interest regarding the publication of this paper.

Acknowledgments

The authors appreciate the support from Addis Ababa Science and Technology University, Ethiopia. The authors also thank GMR Institute of Technology, Rajam, Andhra Pradesh, and Kongu Engineering College, Erode, Tamil Nadu, for providing technical assistance to complete this experimental work.

References

- [1] H. Zollinger, *Color Chemistry—Synthesis, Properties and Applications of Organic Dyes and Pigments*, VCH, Vancouver, Canada, 1987.
- [2] S. Padmavathy, S. Sandhya, K. Swaminathan, Y. V. Subrahmanyam, T. Chakrabarti, and S. N. Kaul, "Aerobic decolorization of reactive azo dyes in presence of various cosubstrates," *Chemical and Biochemical Engineering*, vol. 17, pp. 147–151, 2003.
- [3] S. Sivarethinamohan, G. Ravindiran, J. R. Hanumanthu, K. Gaddam, P. Saravanan, and S. K. Muniyasamy, "Effective removal of remazol brilliant orange 3R using a biochar derived from *Ulva reticulata*," *Energy Sources, Part A: Recovery, Utilization, and Environmental Effects*, pp. 1–14, 2021.
- [4] J. R. Hanumanthu, G. Ravindiran, R. Subramanian, and P. Saravanan, "Optimization of process conditions using RSM and ANFIS for the removal of remazol brilliant orange 3R in a packed bed column," *Journal of the Indian Chemical Society*, vol. 98, no. 6, Article ID 100086, 2021.
- [5] R. M. Jayaraju, K. Gaddam, G. Ravindiran et al., "Biochar from waste biomass as a biocatalyst for biodiesel production: an overview," *Applied Nanoscience*, 2021.
- [6] R. Gokulan, A. V. Kumar, V. Rajeshkumar, and S. Praveen, "Remazol effluent treatment in batch and packed bed column using biochar derived from marine seaweeds," *Nature Environment and Pollution Technology*, vol. 19, no. 5, pp. 1931–1936, 2020.
- [7] Y. Yang and D. T. Wyatt, "Decolorization of textile dye-stuffs using UV/H₂O₂ photochemical oxidation technology," *Textile Chemist and Colorist*, vol. 30, no. 4, pp. 27–35, 1998.
- [8] K. K. H. Choy, G. McKay, and J. F. Porter, "Sorption of acid dyes from effluents using activated carbon," *Resources, Conservation and Recycling*, vol. 27, no. 1–2, pp. 57–71, 1999.
- [9] Y. Xu, R. E. Lebrun, P.-J. Gallo, and P. Blond, "Treatment of textile dye plant effluent by nanofiltration membrane," *Separation Science and Technology*, vol. 34, no. 13, pp. 2501–2519, 1999.
- [10] R. Pelegrini, P. Peralta-Zamora, A. R. De Andrade, J. Reyes, and N. Durán, "Electrochemically assisted photocatalytic degradation of reactive dyes," *Applied Catalysis B: Environmental*, vol. 22, no. 2, pp. 83–90, 1999.
- [11] A. Stolz, "Basic and applied aspects in the microbial degradation of azo dyes," *Applied Microbiology and Biotechnology*, vol. 56, no. 1–2, pp. 69–80, 2001.
- [12] J. M. Dias, M. C. M. Alvim-Ferraz, M. F. Almeida, J. Rivera-Utrilla, and M. Sánchez-Polo, "Waste materials for activated carbon preparation and its use in aqueous-phase treatment: a review," *Journal of Environmental Management*, vol. 85, no. 4, pp. 833–846, 2007.
- [13] B. Corcho-Corral, M. Olivares-Marín, C. Fernández-González, V. Gómez-Serrano, and A. Macías-García, "Preparation and textural characterisation of activated carbon from vine shoots (*Vitis vinifera*) by H₃PO₄-Chemical activation," *Applied Surface Science*, vol. 252, no. 17, pp. 5961–5966, 2006.
- [14] W. Li, K. Yang, J. Peng, L. Zhang, S. Guo, and H. Xia, "Effects of carbonization temperatures on characteristics of porosity in coconut shell chars and activated carbons derived from carbonized coconut shell chars," *Industrial Crops and Products*, vol. 28, no. 2, pp. 190–198, 2008.
- [15] I. A. W. Tan, A. L. Ahmad, and B. H. Hameed, "Adsorption of basic dye on high-surface-area activated carbon prepared from coconut husk: equilibrium, kinetic and thermodynamic studies," *Journal of Hazardous Materials*, vol. 154, no. 1–3, pp. 337–346, 2008.
- [16] F. S. Vieira, A. R. Cestari, I. F. Gimenez, N. L. V. Carreño, and L. S. Barreto, "Kinetic and calorimetric study of the adsorption of dyes on mesoporous activated carbon prepared from coconut coir dust," *Journal of Colloid and Interface Science*, vol. 298, pp. 515–522, 2006.
- [17] R. Gokulan, G. Ganesh Prabhu, and J. Jegan, "A novel sorbent *Ulva lactuca* -derived biochar for remediation of remazol brilliant orange 3R in packed column," *Water Environment Research*, vol. 91, no. 7, pp. 642–649, 2019.
- [18] R. Gokulan, G. G. Prabhu, and J. Jegan, "Remediation of complex remazol effluent using biochar derived from green seaweed biomass," *International Journal of Phytoremediation*, vol. 21, no. 12, pp. 1179–1189, 2019.
- [19] L. Li, D. Zou, Z. Xiao et al., "Biochar as a sorbent for emerging contaminants enables improvements in waste management and sustainable resource use," *Journal of Cleaner Production*, vol. 210, pp. 1324–1342, 2019.
- [20] J. Jegan, S. Praveen, T. B. Pushpa, and R. Gokulan, "Biodecolorization of basic violet 03 using biochar derived from agricultural wastes: isotherm and kinetics," *Journal of Biobased Materials and Bioenergy*, vol. 14, no. 3, pp. 316–326, 2020.
- [21] D. D. Warnock, J. Lehmann, T. W. Kuyper, and M. C. Rillig, "Mycorrhizal responses to biochar in soil - concepts and mechanisms," *Plant and Soil*, vol. 300, no. 1–2, pp. 9–20, 2007.
- [22] C. J. Atkinson, J. D. Fitzgerald, and N. A. Hipps, "Potential mechanisms for achieving agricultural benefits from biochar application to temperate soils: a review," *Plant and Soil*, vol. 337, no. 1–2, pp. 1–18, 2010.
- [23] G. Torgut, M. Tanyol, F. Biryán, G. Pihtili, and K. Demirelli, "Application of response surface methodology for optimization of remazol brilliant blue r removal onto a novel polymeric adsorbent," *Journal of the Taiwan Institute of Chemical Engineers*, vol. 80, pp. 1–9, 2017.
- [24] Z.-Y. Zhong, Q. Yang, X.-M. Li, K. Luo, Y. Liu, and G.-M. Zeng, "Preparation of peanut hull-based activated carbon by microwave-induced phosphoric acid activation and its application in remazol brilliant blue r adsorption," *Industrial Crops and Products*, vol. 37, no. 1, pp. 178–185, 2012.
- [25] F. Karacan, U. Ozden, and S. Karacan, "Optimization of manufacturing conditions for activated carbon from Turkish lignite by chemical activation using response surface methodology," *Applied Thermal Engineering*, vol. 27, no. 7, pp. 1212–1218, 2007.
- [26] P. Sivaprakasam and P. Hariharan, "Modeling the machining parameters of micro wire electrical discharge machining of AL 2024 T351," *Applied Mechanics and Materials*, vol. 367, pp. 466–470, 2013.
- [27] Z. Mahdi, A. E. Hanandeh, and Q. Yu, "Influence of pyrolysis conditions on surface characteristics and methylene blue adsorption of biochar derived from date seed biomass," *Waste and Biomass Valorization*, vol. 8, no. 6, pp. 2061–2073, 2017.

Retraction

Retracted: Improvement on Mechanical Properties of Submerged Friction Stir Joining of Dissimilar Tailor Welded Aluminum Blanks

Advances in Materials Science and Engineering

Received 26 December 2023; Accepted 26 December 2023; Published 29 December 2023

Copyright © 2023 Advances in Materials Science and Engineering. This is an open access article distributed under the Creative Commons Attribution License, which permits unrestricted use, distribution, and reproduction in any medium, provided the original work is properly cited.

This article has been retracted by Hindawi, as publisher, following an investigation undertaken by the publisher [1]. This investigation has uncovered evidence of systematic manipulation of the publication and peer-review process. We cannot, therefore, vouch for the reliability or integrity of this article.

Please note that this notice is intended solely to alert readers that the peer-review process of this article has been compromised.

Wiley and Hindawi regret that the usual quality checks did not identify these issues before publication and have since put additional measures in place to safeguard research integrity.

We wish to credit our Research Integrity and Research Publishing teams and anonymous and named external researchers and research integrity experts for contributing to this investigation.

The corresponding author, as the representative of all authors, has been given the opportunity to register their agreement or disagreement to this retraction. We have kept a record of any response received.

References

- [1] R. Suryanarayanan, V. G. Sridhar, L. Natrayan et al., "Improvement on Mechanical Properties of Submerged Friction Stir Joining of Dissimilar Tailor Welded Aluminum Blanks," *Advances in Materials Science and Engineering*, vol. 2021, Article ID 3355692, 6 pages, 2021.

Research Article

Improvement on Mechanical Properties of Submerged Friction Stir Joining of Dissimilar Tailor Welded Aluminum Blanks

R. Suryanarayanan ¹, V. G. Sridhar,¹ L. Natrayan ², S. Kaliappan ³,
Anjibabu Merneedi ⁴, T. Sathish ², and Alazar Yeshitla ⁵

¹School of Mechanical Engineering, Vellore Institute of Technology, Chennai 600127, Tamil Nadu, India

²Department of Mechanical Engineering, Saveetha School of Engineering, SIMATS, Chennai 602105, Tamil Nadu, India

³Department of Mechanical Engineering, Velammal Institute of Technology, Chennai 601204, Tamil Nadu, India

⁴Department of Mechanical Engineering, Aditya College of Engineering, Surampalem 533437, Andhra Pradesh, India

⁵Department of Biotechnology, College of Biological and Chemical Engineering, Addis Ababa Science and Technology University, Addis Ababa, Ethiopia

Correspondence should be addressed to R. Suryanarayanan; suryan237@gmail.com and Alazar Yeshitla; alazar.yeshi@aastu.edu.et

Received 27 June 2021; Revised 13 July 2021; Accepted 21 July 2021; Published 28 July 2021

Academic Editor: Samson Jerold Samuel Chelladurai

Copyright © 2021 R. Suryanarayanan et al. This is an open access article distributed under the Creative Commons Attribution License, which permits unrestricted use, distribution, and reproduction in any medium, provided the original work is properly cited.

Friction stir welding is a solid-state welding method that produces joints with superior mechanical and metallurgical properties. However, the negative effects of the thermal cycle during welding dent the mechanical performance of the weld joint. Hence, in this research study, the joining of aluminum tailor welded blanks by friction stir welding is carried out in underwater conditions by varying the welding parameters. The tensile tests revealed that the underwater welded samples showed better results when compared to the air welded samples. Maximum tensile strength of 229.83 MPa was obtained at 1000 rpm, 36 mm/min. The improved tensile strength of the underwater welded samples was credited to the suppression of the precipitation of the secondary precipitates due to the cooling action provided by the water. The lowest hardness of 72 HV was obtained at the edge of the stir zone which indicated the weakest region in the weld zone.

1. Introduction

Friction stir welding (FSW), a solid welding technique, is employed to produce weldments with superior joint properties when compared to conventional welding methods. Developed in the year 1991 by The Welding Institute, UK, the FSW process has seen a rapid growth in transportation industry especially in high-speed rails, high-speed ferries, aircrafts, and automobiles [1, 2]. The application of tailor welded blanks in automobiles has enhanced the productivity at reduced costs and has a great potential in marine applications [3]. Aluminum alloys such as Al 5083 and Al 6082, marine grade alloys, are used in ship hull and superstructure and extruded stiffeners [4, 5]. Zadpoor et al. [6] studied the mechanical and microstructural characteristics of the tailor welded blanks. Leitão et al. [7] studied the formability of

friction stir welded similar and dissimilar tailor welded blanks of Al 5182-H111 and 6016-T4. Gungor et al. [4] joined Al 5083 H111 and Al 6082-T6 alloys in similar and dissimilar configurations and studied the tensile and fatigue strength of the welded joints. Dragatogiannis et al. [5] achieved superior properties in Al 5083-Al 6082 joint by FSW by incorporating TiC nanoparticles in the weld zone. Peel et al. [8] observed better mechanical properties by placing Al 5083 on the advancing side as it enhanced sufficient material mixing at the stir zone. Anil et al. [9] obtained superior properties in dissimilar joint configuration when compared to similar joint configuration in FSW of Al 5083 and Al 6082. Svensson et al. [10] joined Al 5083 and Al 6082 by FSW and observed precipitates in the weld zone which was the reason of low microhardness. Donatus et al. [11] studied the material flow in dissimilar FSW of Al 5083-

O and Al 6082-T6 and concluded that tool shoulder and pin played a vital role in material transportation and microstructural evolution. Liu et al. [12] observed increased tensile strength in underwater FSW of Al 2219 samples when compared with that of air welded samples.

Yogeshwaran et al. found that welding speed played a significant role in determining the failure zone of the weld joint as the increase in welding speed resulted in narrowing of the softening region [13]. Rui et al. [14] studied the influence of water temperature on mechanical properties of submerged friction stir welded Al 7050 alloys. Mofid et al. [15] observed that rapid cooling action provided by the submerged medium (liquid nitrogen and water) dented the growth of intermetallic compound formation in submerged friction stir welding of Al and Mg alloys. Kokila et al. [16] also observed similar phenomena in underwater FSW of Al and Mg alloys. Rathinasuriyan and Senthilkumar [17] studied the effects of water head on mechanical properties of the underwater FSW of Al 6061 and optimized it along with other process parameters by response surface methodology. Sabari et al. [18] studied the effects of pin profile on mechanical and microstructural properties in submerged friction stir welding of Al 2519-T87 alloy. Rouzbehani et al. [19] observed that water cooling reduced the width of the HAZ layer in the weld zone in submerged friction stir welding of Al 7075 alloys. Wahid et al. [20] concluded that low peak temperatures obtained in submerged friction stir welding due to water cooling resulted in denting of grain growth and dissolution of precipitates that enhanced the strength of the weld joint. Since most of the literatures have reported the joining of Al 5083 and Al 6082 in air conditions, the underwater welding of these two alloys have not been reported in any of the literatures available; hence, an attempt is done to study the tensile properties and microhardness of the underwater friction stir welded samples.

2. Materials and Methods

Aluminum alloys Al 5083 and Al 6082 were cut to required size of $150 \times 80 \times 6$ mm and $150 \times 80 \times 5$ mm using power axe-saw machine and cleaned with acetone to remove dust and oil. The chemical composition and mechanical properties of the alloys are given in Tables 1 and 2, respectively.

The FSW machine, R. V. Machine Tools, 11 kW was employed to join Al 5083 and Al 6082 which were placed on the advancing side (AS) and retreating side (RS), respectively, Figure 1.

A square pin (Figure 2) of H-13 tool steel with tool dimensions of 25 mm shoulder diameter and pin length of 4.7 mm is used to join the blanks based on the results obtained from previous research studies. The square pin tool was selected for the joining the dissimilar Al alloy, as this tool induces sufficient plasticization of the Al alloys due to the increased probe area and also due to the pulsating action of the tool [21].

Six samples were welded under water condition at 29°C and 25 mm water head. The FSW process parameters and the test results are given in Table 3. The weldments were cut to the dimensions of 100×25 mm tensile test specimen

TABLE 1: Chemical composition of aluminum alloys.

Element	Al 5083	Cu	Fe	Mg	Mn	Si	Cr	Al
Wt%		0.1	0.4	4.2	0.4	0.25	0.2	Balance
Element	Al 6082	Si	Fe	Cu	Mn	Cr	Zn	Al
Wt%		0.7	0.4	0.1	0.6	0.2	0.18	Balance

according to ASTM E8M-02 standard and tested at cross-head speed of 1 mm. The hardness test was conducted using ASTM E-92 standard at loading conditions of 200 g for 15 s.

3. Results and Discussion

The mechanical properties of underwater welded samples at different tool rotational speeds are compared. The underwater welded samples possessed high strength than the air welded samples. The samples welded at a constant weld speed of 24 mm/min were observed with tunnel defects. The tunnel defects are formed due to insufficient plasticization and poor material mixing by the tool profile at the specific welding speed [22]. However, the samples welded underwater at 36 mm/min showed better mechanical properties, as shown in Figure 3. The rapid cooling action provided by water resulted in denting the grain growth and formation of fine grains that might have enhanced the mechanical strength. Moreover, the welding temperature during the underwater FSW would have been $<250^\circ\text{C}$, which dented the coarsening of the strengthening precipitate Mg_2Si to enhance the weld strengths of underwater welded samples compared to the air welded samples [23, 24]. The tensile test samples of failed at the weld zone indicating the nugget zone is not in contact with the submerged medium during FSW which resulted in formation of a weaker zone at the nugget region [12]. The tensile strength of the underwater tensile welded samples tends to decrease with increase in tool rotational speed that increases the temperature at the weld zone which resulted in grain growth in the weld zone; hence, the drop in tensile strength is observed [25, 26].

According to Zadapoor et al. [6] the tensile strength of the tailor welded blank is impacted by the change in the stress concentration factor at the nugget zone, which depends on the thickness of the alloy. Since the blanks of two different thicknesses are being welded, the thickness at the weld zone (nugget) is slightly higher than the thickness of Al 6082; therefore, gradual change in thickness of the nugget zone may improve the mechanical properties of the welded sample. Moreover, the joints during tensile testing show heterogeneous plasticization due to their differences in thicknesses. The plastic deformation in the tailor welded samples during the monotonic loading during the tensile test is determined by the following equation.

$$\frac{YS}{UTS} = \frac{T1}{T2} \quad (1)$$

where T1 and T2 are the thickness of the blanks, mm.

According to this criterion, when the ratio of yield strength to ultimate tensile strength is lesser than the ratio of thicknesses, the plastic deformation is said to be concentrated in both the alloys, whereas when the ratio of strengths

TABLE 2: Mechanical properties of aluminum alloys.

Density (kg/cm ³)	Yield strength (MPa)	Ultimate tensile strength (MPa)	Elongation (%)	Alloy
2.66	288	341	23	Al 5083
2.70	143	295	11	Al 6082

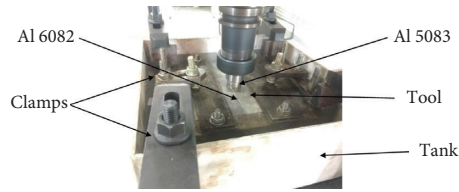


FIGURE 1: Submerged FSW set-up.

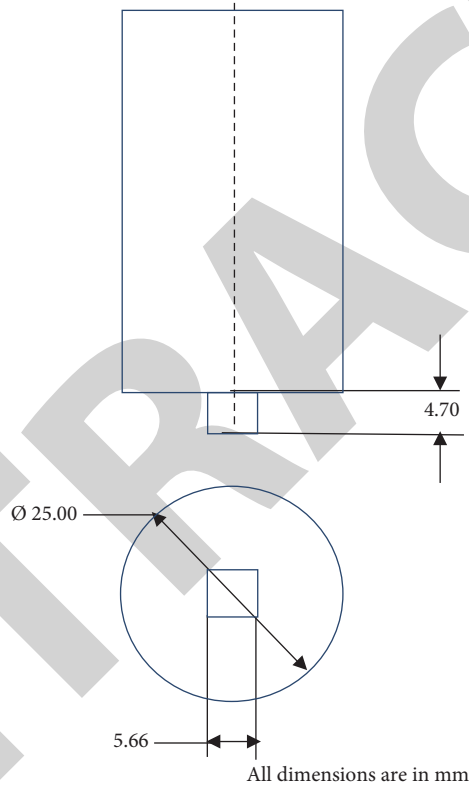


FIGURE 2: Square probe FSW tool.

TABLE 3: Welding parameters for air and underwater FSW with results.

Sample no.	Rotational speed (rpm)	Welding speed, mm (s)	Air welded, yield strength (MPa)	Air welded, ultimate tensile strength (MPa)	Underwater welded, yield strength (MPa)	Underwater welded, ultimate tensile strength (MPa)
1	1000	24	78.99	87	129.68	140.68
2	1200	24	82.25	114.7	134.19	138.28
3	1400	24	87.99	91.82	136.47	148.78
4	1000	36	120	122.18	159.28	229.89
5	1200	36	128	138.78	177.715	182.44
6	1400	36	150.64	154.13	165.626	208.48

is greater than the thickness ratio, then the thinner alloy Al 6082 is plastically deformed. The samples 4 and 5 welded at 36 mm/min agree with the first condition as given in Table 4.

3.1. *Microhardness and Microstructure analysis.* Figure 4 shows the microhardness results; the study was carried out for the sample 4 by application of 200 g load for 15 s. The

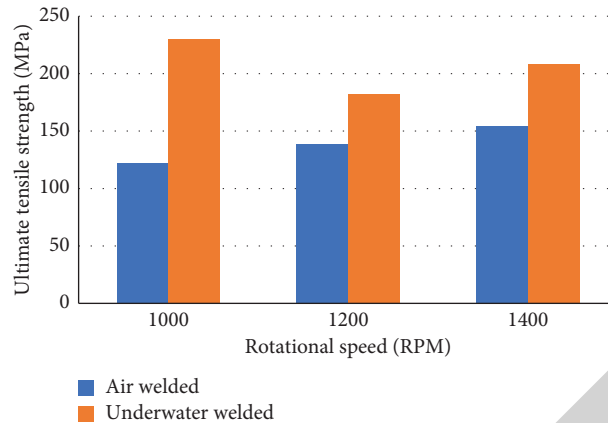


FIGURE 3: Comparison of tensile strength for air welded and underwater welded FSW samples at 36 mm/min.

TABLE 4: Limiting stress ratio criterion.

Sample no.	YS (MPa)	UTS (MPa)	YS/UTS	T ₁ /T ₂
4	159.28	229.89	0.69	0.83
5	165.62	208.48	0.79	0.83
6	177.71	182.44	0.97	0.83

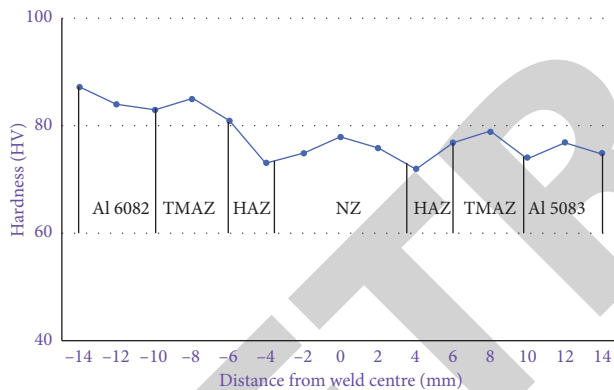


FIGURE 4: Microhardness survey for sample 4, underwater welded specimen joined at 1000 rpm, 36 mm/min.

lowest hardness of 72 HV was observed at the edge of the stir zone (SZ) which indicated the region of failure at the weld zone. The hardness increased at SZ and TMAZ to show that these regions have been strengthened by the water cooling effect.

The microstructure analysis was performed by polishing the sample with different grades of emery sheets and velvet cloth polishing with diamond solution, followed by etching the sample with Keller's reagent. The macrostructure (Figure 5) revealed the mixed flow between the two alloys at the stir zone. The mixed flow indicated that Al 5083 and Al 6082 were able to undergo severe plastic deformation induced by the square tool; however, the complete mixing of the alloys was not achieved [21].

The optical microstructure (Figure 6) revealed the formation of the kissing bond or oxide line with severe plastic deformation (OJLwSPD), which was caused due to the breakdown of the surface oxides. The formation of such a

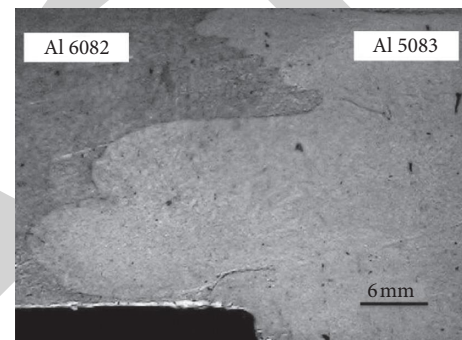


FIGURE 5: Macrostructure of sample 4, underwater welded specimen joined at 1000 rpm, 36 mm/min.

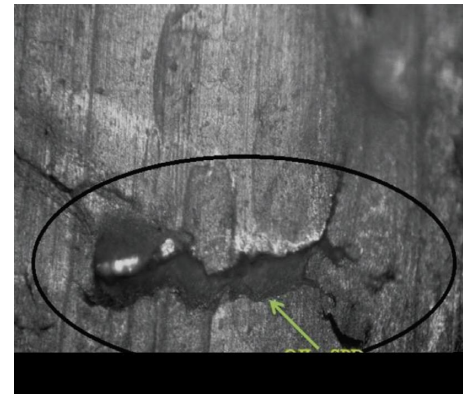


FIGURE 6: Microstructure of sample 4, underwater welded specimen joined at 1000 rpm, 36 mm/min.

defect was due to the insufficient plasticization due to poor stirring of Al 5083 and Al 6082 in underwater conditions.

4. Conclusions

The underwater welded samples perform better mechanically when compared to air welded samples. Maximum tensile strength of 229.83 MPa was obtained at 1000 rpm, 36 mm/min. The rapid cooling action provided by the water resulted in enhancement of the mechanical strength when

compared to air welded samples. The tensile strength of the weld joint decreased with the increase in tool rotational speed that increased the heat input during the welding process that resulted in grain growth at the stir zone. All the six joints welded underwater failed at the weld zone. The lowest hardness of 72 HV obtained for water welded samples was observed at the stir zone indicating the failure zone of tensile-tested joint.

Data Availability

The data used to support the findings of this study are included within the article and are available from the corresponding author upon request.

Disclosure

It was performed as a part of the Employment of College of Biological and Chemical Engineering, Addis Ababa Science and Technology University, Ethiopia.

Conflicts of Interest

The authors declare that there are no conflicts of interest.

Acknowledgments

The authors thank to Vellore Institute of Technology, Chennai, and Saveetha School of Engineering, SIMATS, Chennai, for providing characterization supports to complete this research work.

References

- [1] R. Nandan, T. Debroy, and H. Bhadeshia, "Recent advances in friction-stir welding - process, weldment structure and properties," *Progress in Materials Science*, vol. 53, no. 6, pp. 980–1023, 2008.
- [2] V. Paranthaman, K. S. Sundaram, and L. Natrayan, "Effect of silica content on mechanical and microstructure behaviour of resistance spot welded advanced automotive trip steels," *Silicon*, pp. 1–10, 2021.
- [3] E. E. Feistauer, L. A. Bergmann, L. S. Barreto, and J. F. Dos Santos, "Mechanical behaviour of dissimilar friction stir welded tailor welded blanks in Al-Mg alloys for Marine applications," *Materials & Design*, vol. 59, pp. 323–332, 2014.
- [4] B. Gungor, E. Kaluc, E. Taban, and A. Sik, "Mechanical, fatigue and microstructural properties of friction stir welded 5083-H111 and 6082-T651 aluminum alloys," *Materials and Design*, vol. 56, pp. 84–90, 2014.
- [5] D. A. Dragatogiannis, E. P. Koumoulos, I. A. Kartsonakis, D. I. Pantelis, P. N. Karakizis, and C. A. Charitidis, "Dissimilar friction stir welding between 5083 and 6082 Al alloys reinforced with TiC nanoparticles," *Materials and Manufacturing Processes*, vol. 31, no. 16, pp. 2101–2114, 2016.
- [6] A. A. Zadpoor, J. Sinke, R. Benedictus et al., "Mechanical properties and microstructure of friction stir welded tailor-made blanks," *Materials Science and Engineering: A*, vol. 494, no. 1–2, pp. 281–290, 2008.
- [7] C. Leitao, R. M. Leal, D. M. Rodrigues, A. Loureiro, and P. Vilaça, "Mechanical behaviour of similar and dissimilar AA5182-H111 and AA6016-T4 thin friction stir welds," *Materials & Design*, vol. 30, no. 1, pp. 101–108, 2009.
- [8] M. J. Peel, A. Steuwer, P. J. Withers, T. Dickerson, Q. Shi, and H. Shercliff, "Dissimilar friction stir welds in AA5083-AA6082. Part I: process parameter effects on thermal history and weld properties," *Metallurgical and Materials Transactions A*, vol. 37, no. 7, pp. 2183–2193, 2006.
- [9] K. K. S. Anil, S. M. Murigendrappa, and H. Kumar, "A bottom-up optimization approach for friction stir welding parameters of dissimilar AA2024-T351 and AA7075-T651 alloys," *Journal of Materials Engineering and Performance*, vol. 26, no. 7, pp. 3347–3367, 2017.
- [10] L. E. Svensson, L. Karlsson, H. Larsson, B. Karlsson, M. Fazzini, and J. Karlsson, "Microstructure and mechanical properties of friction stir welded aluminium alloys with special reference to AA 5083 and AA 6082," *Science and Technology of Welding and Joining*, vol. 5, no. 5, pp. 285–296, 2000.
- [11] U. Donatus, G. E. Thompson, X. Zhou, J. Wang, and K. Beamish, "Flow patterns in friction stir welds of AA5083 and AA6082 alloys," *Materials & Design*, vol. 83, pp. 203–213, 2015.
- [12] H. J. Liu, H. J. Zhang, Y. X. Huang, and L. Yu, "Mechanical properties of underwater friction stir welded 2219 aluminum alloy," *Transactions of Nonferrous Metals Society of China*, vol. 20, no. 8, pp. 1387–1391, 2010.
- [13] S. Yogeshwaran, L. Natrayan, G. Udhayakumar, G. Godwin, and L. Yuvaraj, "Effect of waste tyre particles reinforcement on mechanical properties of jute and abaca fiber- epoxy hybrid composites with pre-treatment," *Materials Today: Proceedings*, vol. 37, no. 2, pp. 1377–1380, 2021.
- [14] D. F. Rui, Q. S. Zeng, C. S. Rui, L. Ying, J. L. Hui, and L. Lei, "Improvement of weld temperature distribution and mechanical properties of 7050 aluminum alloy butt joints by submerged friction stir welding," *Materials & Design*, vol. 32, no. 10, pp. 4825–4831, 2011.
- [15] M. A. Mofid, A. Abdollah-Zadeh, F. M. Ghaini, and C. H. Gür, "Submerged friction-stir welding (SFSW) underwater and under liquid nitrogen: an improved method to join Al alloys to Mg alloys," *Metallurgical and Materials Transactions A*, vol. 43, no. 13, pp. 5106–5114, 2012.
- [16] R. V. Kokila, S. R. Radhamohan, L. Natrayan, D. Usha, and V. R. Niveditha, "Guided container selection for data streaming through neural learning in cloud," *Int. J. Syst. Assur. Eng. Manag.*, pp. 1–7, 2021.
- [17] C. Rathinasuriyan and V. S. Senthil, "Modelling and optimization of submerged friction stir welding parameters for AA6061-T6 alloy using RSM," *Metallic Materials*, vol. 54, no. 04, pp. 297–304, 2016.
- [18] S. S. Sree, S. Malarvizhi, and V. Balasubramanian, "Characteristics of FSW and UWFSW joints of AA2519-T87 aluminium alloy: effect of tool rotation speed," *Journal of Manufacturing Processes*, vol. 22, pp. 278–289, 2016.
- [19] R. Rouzbehani, A. H. Kokabi, H. Sabet, M. Paidar, and O. O. Ojo, "Metallurgical and mechanical properties of underwater friction stir welds of Al7075 aluminum alloy," *Journal of Materials Processing Technology*, vol. 262, pp. 239–256, 2018.
- [20] M. A. Wahid, Z. A. Khan, A. N. Siddiquee, R. Shandley, and N. Sharma, "Analysis of process parameters effects on underwater friction stir welding of aluminum alloy 6082-T6," *Proceedings of the Institution of Mechanical Engineers - Part B: Journal of Engineering Manufacture*, vol. 233, no. 6, pp. 1700–1710, 2019.

Retraction

Retracted: Effects of the FR 4 Substrate Realized in a Circularly Polarized UHF-RFID Reader Antenna with Fractal Geometry for Enhancing Parameters

Advances in Materials Science and Engineering

Received 26 December 2023; Accepted 26 December 2023; Published 29 December 2023

Copyright © 2023 Advances in Materials Science and Engineering. This is an open access article distributed under the Creative Commons Attribution License, which permits unrestricted use, distribution, and reproduction in any medium, provided the original work is properly cited.

This article has been retracted by Hindawi, as publisher, following an investigation undertaken by the publisher [1]. This investigation has uncovered evidence of systematic manipulation of the publication and peer-review process. We cannot, therefore, vouch for the reliability or integrity of this article.

Please note that this notice is intended solely to alert readers that the peer-review process of this article has been compromised.

Wiley and Hindawi regret that the usual quality checks did not identify these issues before publication and have since put additional measures in place to safeguard research integrity.

We wish to credit our Research Integrity and Research Publishing teams and anonymous and named external researchers and research integrity experts for contributing to this investigation.



The corresponding author, as the representative of all authors, has been given the opportunity to register their agreement or disagreement to this retraction. We have kept a record of any response received.

References

- [1] C. Varadhan, S. Arulsevi, and F. Ashine Chamatu, "Effects of the FR 4 Substrate Realized in a Circularly Polarized UHF-RFID Reader Antenna with Fractal Geometry for Enhancing Parameters," *Advances in Materials Science and Engineering*, vol. 2021, Article ID 8475621, 7 pages, 2021.

Research Article

Effects of the FR 4 Substrate Realized in a Circularly Polarized UHF-RFID Reader Antenna with Fractal Geometry for Enhancing Parameters

Chitra Varadhan ¹, S. Arulselvi,¹ and Fekadu Ashine Chamatu ²

¹Department of ECE, Bharath Institute of Higher Education and Research, Chennai 600 073, Tamilnadu, India

²Department of Chemical Engineering, College of Biological and Chemical Engineering, Addis Ababa Science and Technology University, Addis Ababa 16417, Ethiopia

Correspondence should be addressed to Fekadu Ashine Chamatu; fekadu.ashine@aastu.edu.et

Received 26 June 2021; Revised 9 July 2021; Accepted 17 July 2021; Published 28 July 2021

Academic Editor: Samson Jerold Samuel Chelladurai

Copyright © 2021 Chitra Varadhan et al. This is an open access article distributed under the Creative Commons Attribution License, which permits unrestricted use, distribution, and reproduction in any medium, provided the original work is properly cited.

The proposed RFID reader antenna progressed with perfect electric conductor (PEC) as the radiating element and FR 4 as the substrate to achieve circular polarization, enhancement in bandwidth, and read range. The design presents a CPW feed RFID antenna for near-field reading applications, between the range of 903 MHz to 929 MHz. The operating frequency of the proposed design is 900 MHz, axial ratio of the model is less than 3 dB, impedance bandwidth is 256 MHz, and axial bandwidth is 36 MHz, proving to be adequate for near-field RFID reader applications such as item-level tagging and smart shelf. The proposed antenna model is realized with fractal structure to achieve miniaturization. The developed antenna is optimized using EM software for numerical analysis. The designed antenna is fabricated, and the prototype is characterized in terms of dielectric constant and loss tangent. The obtained results indicate high correlation with simulation results.

1. Introduction

Monopole RFID antennas are widely applicable in the field of mobile applications and military, biomedical, and aerospace industries. The important property of monopole antenna selection is broad-band achievement. The performance of the antenna greatly depends upon the substrate parameters such as uniformity, dielectric constant, and loss tangent [1]. Extensive literature surveys were performed regarding the parameters stating that certain substrates produce an improvement in bandwidth performance [2–8]. Another survey reported that the material contains less values of loss tangent and dielectric constants and produces better result compared to higher values [9].

In modern wireless communication industry, the RFID system plays major role in accessing data. RFID uses two components to exchange information, namely, a

reader and tag. The product information is transmitted by the tag, and the stored data can be retrieved by the reader. RFIDs are operated within various microwave frequency bands; among these, UHF-RFIDs provide specific significance in wireless technology. In the RFID domain, reader construction in the UHF band is widely used due to the long read range (1 m–10 m), and this is mostly applicable in container tracking, pallet tracking, parking lot access, and electronic toll fee collection [10–16]. The construction and design of RFID antennas comprise challenges such as size, read range, and bandwidth coverage. In general, high frequencies and microwave frequency scale are reserved for UHF-RFID system applications. Every nation adopts its own ranges similar to 840.5–844.5 MHz in China, 865–867 MHz in India, and 902–928 MHz in USA and Argentina. Considering all these bands, the experiment selected an RFID range from 840 to 928 MHz.

FR 4 glass fiber-reinforced and epoxy-based substrate fabricated by high-pressure thermoplastic lamination is very popular and resourceful as it exhibits good strength-to-weight ratios. The FR 4 substrate is generally used as an electrical insulator in applications such as semiconductive dielectric, with significant mechanical properties, solvent-resistant properties, and also water absorption rate taken as approximately zero (0.125 in <0.10%). The importance of the FR 4 substrate is it can maintain the most important property of electrical insulation and mechanical specification in both wet or dry conditions. In the proposed RFID reader antenna, FR 4 is used as a substrate as it exhibits better performance [17–23].

Perfect electric conductor (PEC) is used as the radiating element as well as ground plane in the design of an antenna. The patch and ground planes are superimposed on the same plane. PEC demonstrates one of the most unique characteristics, that is, zero resistivity. By freezing the magnetic plasma to zero or if the flux value of initial condition is zero, it maintains zero value constantly. Zero flux is allowed, but not required to perform. With the help of this unique property, the antenna is coated with PEC to provide the maximum power transfer throughout the radiating plane at that instant, explained in detail in the result section. From the literature, the coplanar waveguide (CPW) circularly polarized (CP) RFID reader antenna can access the tag data without any degradation from its polarization and is not sensitive to orientation of the receiver and transmitter. But, the CP-RFID antenna producing smaller amount reading capability is the major challenge in this domain [24, 25]. Basically, the CP can be achieved either by using diagonal feed, dual feed, or by allocating asymmetry in antenna structures. To achieve circular polarization in the antenna, various methods such as dual feed exciting by the orthogonal mode, truncated edge, and slotted types are prominently used [26–31].

In the proposed design, highlight of the antenna achieving, a modified monopole CPW fractal structure is incorporated to provide higher bandwidth at 900 MHz. The bandwidth is increased by 4–5% compared with the normal patch antenna employed, due to the usage of the FR 4 substrate and 20% improvement with the CPW monopole structure [32–34]. The fractal concept is included in the antenna design to reduce the size along with circular polarization. The communication is detailed as follows: Section 2 gives the design concepts, the result and discussions are detailed in Section 3, and calculations and tabulated results are provided in Section 4.

2. Design of the RFID Reader Antenna

The proposed CPW-UHF-RFID reader antenna implemented with FR 4 as the substrate with an optimum thickness of 1.6 mm and medium dielectric constant of 4.3 to achieve circular polarization with good bandwidth performance at 900 MHz resonance frequency. PEC is considered in the antenna design as the radiating element and ground plane in same surface on the rectangular FR 4 glassy substrate, thus reducing the cost of fabrication. The thickness

selection of perfect electric conductor is 0.036 mm. A common microstrip coplanar waveguide monopole antenna structure is displayed in Figure 1(a). The abovementioned parameters incorporated flawlessly result in an omnidirectional radiation pattern but reduction in antenna directivity. The directivity of the antenna is enhanced by implanting additional planes in the design. The bandwidth of the antenna is also improved by means of introducing fractal design in the radiating pole. Implementing fractal structure accomplishes greater bandwidth as well as circular polarization. The fractal geometry creates several operating frequencies, but the fundamental mode is obtained by increasing the total electrical length. Increment in length results in issues in compactness. The basic structures can be a line or surface or even a volume, which are used in the design. Selecting a suitable fractal geometry design to acquire high directivity, smaller size, and multiband behaviour are the electrical challenges. The design of proposed fractal antenna is illustrated in Figure 1(b).

In the proposed design, the contribution of substrate FR 4 plays an important role in increasing the bandwidth of the antenna. The structure and shape of the substrate in the design of the antenna is the main parameter such as the dielectric constant and loss tangent. Initially, the glass epoxy matrix is reinforced with woven glass cloth and cured in 130°C to remove the surplus components. The configuration of FR 4 varies with thickness results in shift of the operating frequency. It is also direction dependent; that is, the composite material varies with length and width and the bandwidth changes accordingly. Thus, the selection of dimension of the FR 4 substrate raises a crucial flag in the design of the RFID reader antenna. Even the thickness of PEC selected between 0.033 mm to 0.0356 mm results in not obtrusive degradation at lower frequencies but reflects substantial deprivation and nonlinearities at high frequencies. Thus selection of material, fractal design structure, and dimension of antenna is a challenge in the design of RFIDs.

Numerous ways are there in practice to bring out the circular polarization in antenna design. In this manuscript, the 1st-order simple fractal design is applied to create circular polarization. The overall dimension of the antenna is 90 mm × 105 mm, and FR 4 material with $\epsilon_0 = 4.3$ and loss tangent = 0.025 is considered as a substrate of the antenna with the thickness $t = 1.6$ mm. The design also involves $\lambda/4$ CPW feed and ground plane. In the zeroth iteration, a single monopole having a length of $\lambda/8$ and by projecting slant 45° plane initiates axial ratio in the design as illustrated in Figure 2(a). As described in Figure 2(b), the first iteration introduces an inverted L shape with perimeter $3\lambda/16$. The successive complete corresponding iterations are shown in Figures 2(c) and 2(d). The perimeter of the conductive material PEC is increased by implementing fractal dimensions such that the designed antenna resonates at 900 MHz. The inverted L shape maintains a diagonally opposite relation at each and every iteration, and this introduces circular polarization in the proposed RFID reader antenna. The impedance 50 Ohm is realized, and axial ratio is improved by selecting the stub length of the ground plane as $L = 30$ mm, width 3 mm is overhanging from ground plane. The

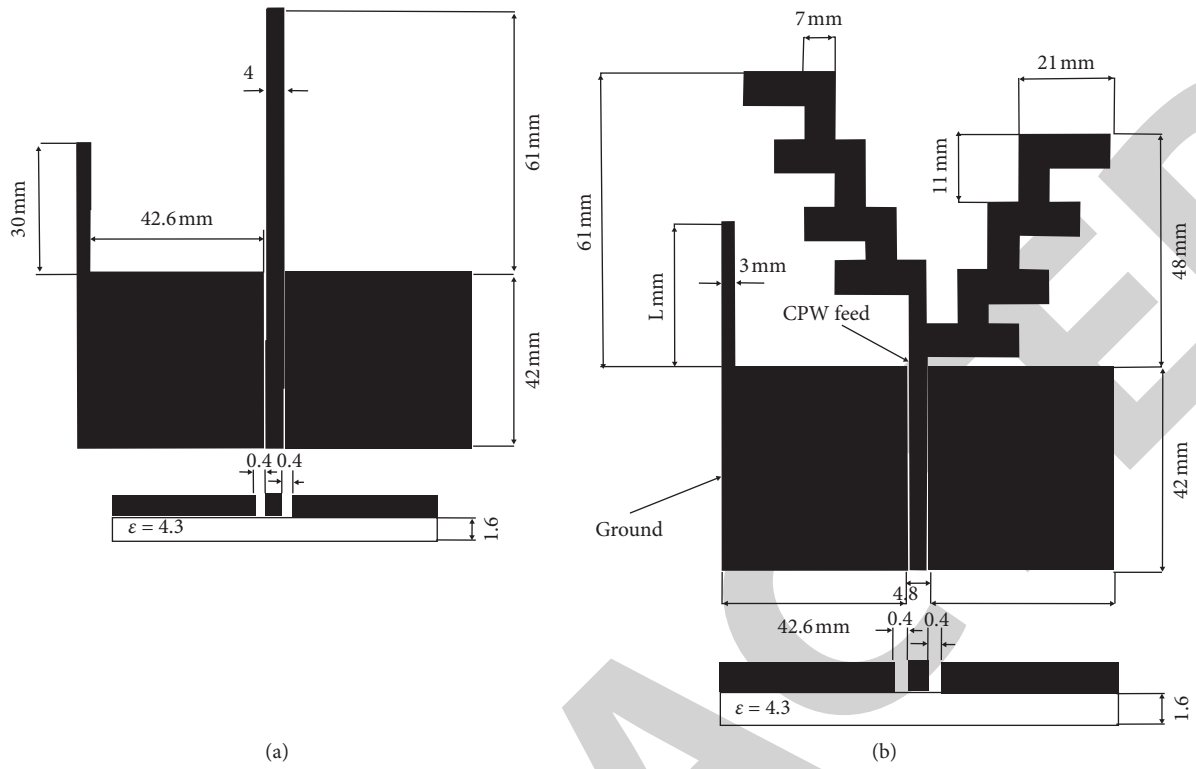


FIGURE 1: (a) Monopole CPW antenna without the fractal structure with the FR 4 substrate. (b) Monopole CPW proposed fractal antenna with the FR 4 substrate.

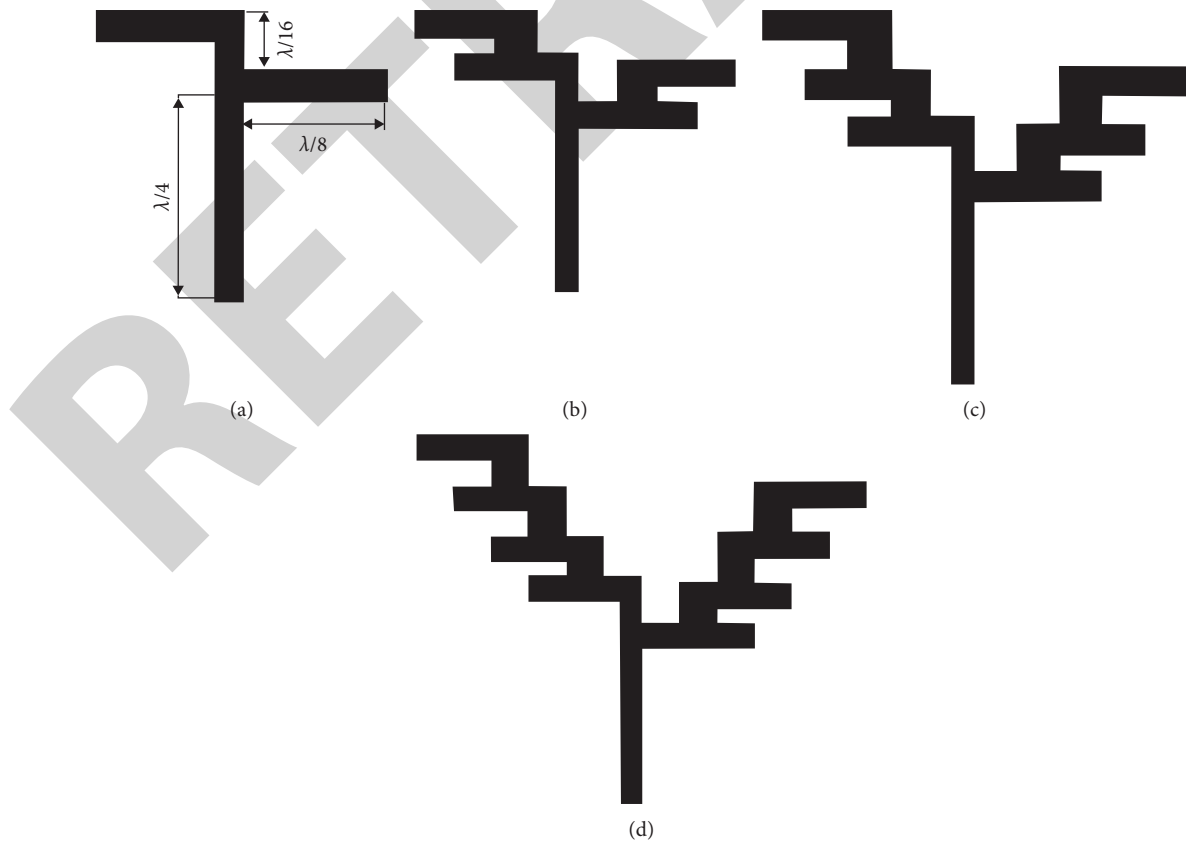


FIGURE 2: (a) L-shaped monopole; (b), (c), (d) iterations of the inverted L-shaped fractal structure, $\lambda = 160$ mm.

proposed RFID reader fractal antenna structure using PEC creates infinity conductivity and generates right-hand polarization while the flipped arms generate left-hand polarization accordingly. Also, it exhibits the fractal structure supporting the generation of RHCP surface current distribution all over the RFID reader antenna.

Table 1 lists the substrate parameters and PEC thickness of the design specifications of the proposed RFID reader antenna. Table 2 enumerates various materials with corresponding dielectric constants and loss tangents. Lower value of dielectric constant and less loss tangent offer wider bandwidth and directivity. Thereby, FR 4 is selected for the proposed antenna. The corresponding relative permittivity and loss tangents are summarized in Table 2.

3. Result and Measurement

The proposed antenna is simulated using EM software; the obtained S_{11} results are verified with a typical monopole structure and are illustrated in Figure 3. The result indicates that the bandwidth is expanded significantly due to deployment of the composite materials along with the fractal structure in the design antenna. The calculated parameters incorporated in the design and simulation result in increased bandwidth compared to the monopole antenna around 325 MHz (35.7%) with a frequency of operation of 910 MHz and impedance bandwidth of 28.5% for 900 MHz. Thus, the simulated results indicate that the proposed antenna is suitable for item-level tagging and smart shelf applications in manufacturing industries.

Figure 4 is composed of the axial ratio that compares the multiple iterations exclusively to describe its gradual progress and the axial ratio that declines to approximately 0 dB along with respect to the main lobe direction. The simulated result shows various proposals taken and an optimum length of PEC is considered in the design and had attained perfect resonating frequency with an appreciable axial ratio. This fidelity can be achieved by the uniform surface current distribution due to zero resistivity of the PEC.

The calculation of axial ratio is verified by both frequency-domain and time-domain solvers. The observed results of AR are approximately in 3 dB bandwidth of 36 MHz (14%) of impedance bandwidth, width = 3 mm and a stub length = 30 mm is protruded outside from the CPW plane, thus diminishing the axial ratio down from 3 dB to 0 dB. Similarly, various lengths of stub are taken and simulated. Variation of length of PEC offers various axial ratios with respect to frequency. Optimum length of PEC is considered in the design of RFID reader application and equipped in the fabrication; the effects and optimized result of the proposed antenna are spotlighted in Figure 5.

4. Prototype Fabrication and Measurement of Results

The read range parameter is used for measurement of the efficiency of the designed antenna. The efficiency can be deviated by the operating frequency in terms of the wavelength λ if the thickness selection of substrate varies. The

TABLE 1: Substrate and PEC design specification of the proposed RFID reader antenna.

FR 4 substrate and PEC design specifications	
Dielectric constant (ϵ_r)	4.3
Thickness of the substrate	1.6 mm
Loss tangent (δ)	0.019~0.02
Conductor thickness (perfect electric conductor)	0.035 mm

TABLE 2: Various dielectric materials with dielectric constants and loss tangent comparison.

Dielectric material	Dielectric constant (ϵ_r)	Loss tangent (δ)
Alumina (95%)	9.75	0.0003
Beryllia	6.5	0.0004
CEM	4.5	0.025
Gallium arsenide	13	0.006
Roger 5870	2.33	0.0012
Roger 5880	2.2	0.0004
Silicon	11.9	0.004
Teflon	2.08	0.0004
Vaseline	2.16	0.001
FR 4 (proposed antenna)	4.3	0.02

assumed transmitted power (P_t) is 4 Watt; similarly, the approximated received power (P_r) is 1 mW. The minimum detectable power P_d of 1 mW and the reader gain (1.35 dBi) are maintained. The read range can be calculated by means of the Friis transmission equation.

Power density can be calculated from

$$p = \frac{P_T}{4\pi R^2} \quad (1)$$

Considering the transmit antenna gain G_t , the power density becomes

$$p = \frac{P_T}{4\pi R^2} G_t \quad (2)$$

Assuming the effective aperture of the antenna, the received power becomes

$$P_R = \frac{P_T G_t G_r \lambda^2}{(4\pi R)^2} \quad (3)$$

Thereby, the read range is calculated by the above-mentioned Friis transmission equation. The optimum read range is taken, and the length and width of the antenna are theoretically calculated before the design of the antenna. The theoretical and simulated results are verified, and the results are optimized. Then, the design of the RFID reader antenna is fabricated as presented in Figure 6.

The fabricated antenna is compared with the existing products in terms of operating frequency, gain of the antenna, read range, and the size of the antenna, as shown in Table 3. The first two antennas attain circular polarization with larger gain, but the size of the antenna is very large, as these kinds of antennas use stacked layers of composite substrates, which are commercially available. The third

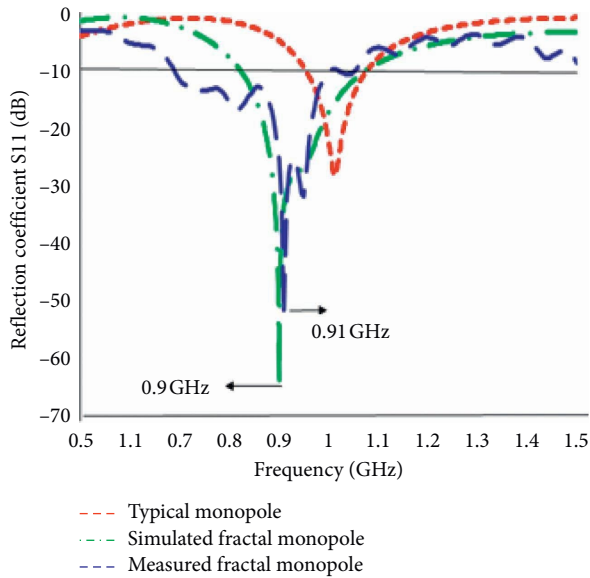


FIGURE 3: Simulation and measured characteristics of the reflection coefficient vs. frequency of the proposed antenna.

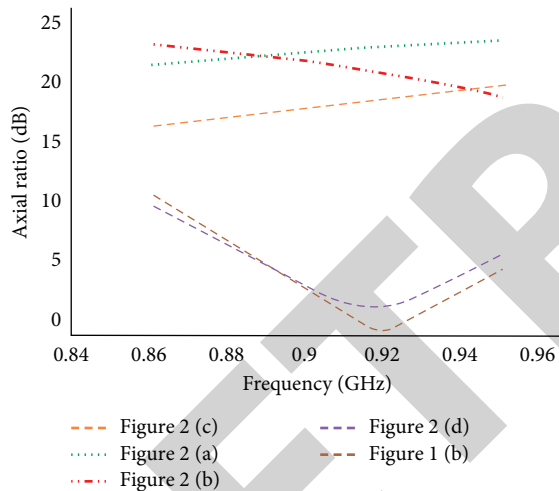


FIGURE 4: Simulated result: AR setup along the direction of the main lobe.

antenna generates circular polarization with four different slots with a square patch with FR 4 suggested as the substrate of the RFID antenna (45° plane). Though the antenna uses the FR 4 substrate, it produces very low gain due to the deformities present on the patch surface; also, the bandwidth of the antenna is very less.

From Table 4, it can be seen that the proposed RFID reader antenna bandwidth is possibly upgraded from 3% to 20% compared to various substrate materials. It is proven that the fabricated RFID reader antenna uses FR 4 as the substrate to achieve cost reduction and also produces

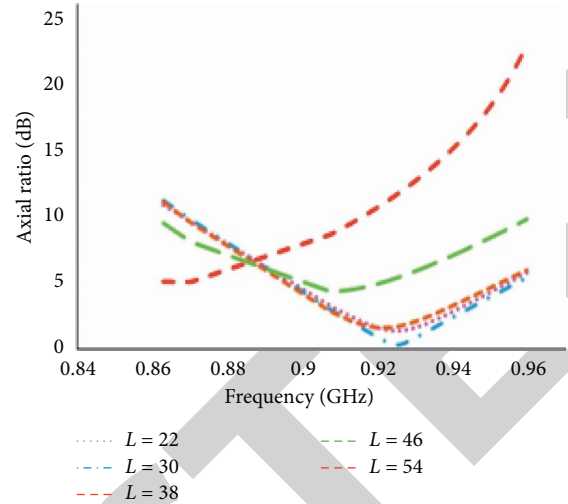


FIGURE 5: Microstrip stub length variation results in AR.

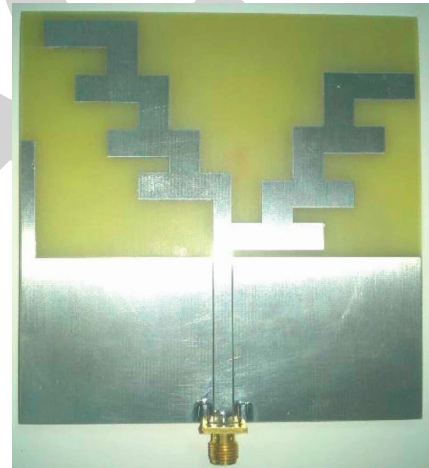


FIGURE 6: Fabricated prototype of the RFID reader antenna.

appreciable return loss. Many different materials and their corresponding return loss and bandwidth are compared with the proposed antenna. It is observed that the designed antenna gives extraordinary return loss and bandwidth (%). The reason behind the uncertainty is due to frequency dependence of relative permittivity and loss tangent. Normally, the relative permittivity is not constant for a material; rather, it falls down with increasing operating frequency. The proposed fractal structure operates well between 902–928 MHz bandwidth, accomplishing circular polarization, the CPW feed provides wider bandwidth with a considerable gain of 1.35 dBi, thus owing to be highly suitable for near field applications, and the fractal structure is used in size reduction of the antenna when compared to other commercial types.

TABLE 3: Proposed antenna vs. existing product parameters.

Product/ID	Frequency range (MHz)	Max gain (dBi)	Read range (m)	Antenna dimension ($L \times W \times H$ mm ³)
Laird/S9025PR	902–928	5.5	3.85	133 × 133 × 18
Motorola/AN720	902–928	6.5	4.19	133 × 133 × 18
ACSSMP antenna/FR 4	918–929	0.5	1.16	90 × 90 × 4.8
Proposed antenna	902–928	1.35	1.9	105 × 90 × 1.6

TABLE 4: Parameter comparison with the proposed antenna.

Substrate	Thickness (inches)	Return loss (dB)	Bandwidth (%)
Duroid 5880	0.050	−20.4237	6.25
Duroid 5870	0.062	−17.1080	12.76
RO 3003	0.06	−10.3912	4.34
RO 3006	0.050	−6.6731	3.26
TMM–10i	0.050	−18.5130	20.83
Duroid 6010	0.025	−26.0205	7.60
GIL MC 5	0.030	−27.6043	10.86
FR 4 (proposed antenna)	0.0014	−51.37	14

5. Conclusions

The proposed UHF-RFID reader antenna is realized using FR 4 as the substrate with optimum thickness, and perfect electric conductor (PEC) is equipped as the radiating stub and accomplishes circular polarization with an operating frequency of 900 MHz. The selected material FR 4 is covalently tethered with PEC, thus forming a strong network structure. It is very much compact due to implementation of the fractal structure, and an acceptable gain of 1.35 dBi and 1.9 m read range are achieved. It attains circular polarization (<3 dB) from 903 to 929 MHz of 4% with the central frequency, the impedance bandwidth of 256 MHz, and axial bandwidth of 36 MHz. The iteration sequence results in inverted fractal L shapes giving rise to attain circular polarization, which is very much suitable for the RFID near-field reader antenna applications such as item-level tagging and smart shelf.

Data Availability

The data used to support the findings of this study are included within the article.

Conflicts of Interest

Mrs. Chitra Varadhan, received her bachelor's degree in Electronics and Communication Engineering from Regional Engineering College (NIT-affiliated with Bharathidhasan University), Trichy, Tamil Nadu, India, in 1996, and completed Master of Engineering in College of Engineering, Anna University, Guindy, Chennai, in 2008. She is currently pursuing PhD in design of fractal RFID antennas in BIHER (Bharath Institute of Higher Education and Research), Chennai, Tamil Nadu, India. Dr. S. Arulselvi is working as an associate professor in BIHER (Bharath Institute of Higher Education and Research), Chennai, Tamil Nadu, India. Areas of specialization include networking and communications. She is currently guiding Mrs. Chitra Varadhan in the area of fractal RFID antennas.

References

- [1] Y. X. Liu, E. T. Kang, K. G. Neoh, J. F. Zhang, C. Q. Cui, and T. B. Thiam Beng Lim, "Surface graft copolymerization enhanced adhesion of an epoxy-based printed circuit board substrate (FR-4) to copper," *IEEE Transactions on Advanced Packaging*, vol. 22, no. 2, pp. 214–220, May 1999.
- [2] S. Fatima Farida, P. M. Hadalgi, P. V. Hunagund, and S. Rafath Ara, "Effect of substrate thickness and permittivity on the characteristics of rectangular microstrip antenna," in *Proceedings of the 1998 Conference on Precision Electromagnetic Measurements Digest (Cat. No.98CH36254)*, pp. 598–599, Washington, DC, USA, July 1998.
- [3] A. A. Qureshi, M. U. Afzal, T. Tauqeer, and M. A. Tarar, "Performance analysis of FR-4 substrate for high frequency microstrip antennas," in *Proceedings of the 2011 China-Japan Joint Microwave Conference*, pp. 1–4, Hangzhou, China, April 2011.
- [4] D. Mittal, A. Nag, A. Kaur, and E. Sidhu, "High directivity FR4 substrate slotted defected ground microstrip patch antenna for X-band applications," in *Proceedings of the 2016 International Conference on Global Trends in Signal Processing, Information Computing and Communication (ICGTSPIC)*, pp. 344–347, Jalgaon, India, December 2016.
- [5] D. H. Schaubert, D. M. Pozar, and A. Adrian, "Effect of microstrip antenna substrate thickness and permittivity: comparison of theories with experiment," *IEEE Transactions on Antennas and Propagation*, vol. 37, no. 6, pp. 677–682, 1989.
- [6] M. C. Zaretsky, P. Li, and J. R. Melcher, "Estimation of thickness, complex bulk permittivity and surface conductivity using interdigital dielectrometry," in *Proceedings of the Conference Record of the 1988 IEEE International Symposium on Electrical Insulation*, pp. 162–166, Cambridge, MA, USA, June 1988.
- [7] V. Rathi, S. Rawat, and H. S. Pokhariya, "Study the effect of substrate thickness and permittivity on patch antenna," in *Proceedings of the 2011 IEEE International Conference on Signal Processing, Communications and Computing (ICSPCC)*, pp. 1–4, Xi'an, China, September 2011.
- [8] C.-W. Hong and M.-C. Lee, "A novel FR-4 material for embedded substrate," in *Proceedings of the 2011 6th International Microsystems, Packaging, Assembly and Circuits*

Retraction

Retracted: Evaluation of Microstructure, Hardness, and Tensile Properties: A Comparative Study of Stir Cast and Extruded Al7005/Glass-/Fly-Ash-Reinforced Hybrid MMCs

Advances in Materials Science and Engineering

Received 26 December 2023; Accepted 26 December 2023; Published 29 December 2023

Copyright © 2023 Advances in Materials Science and Engineering. This is an open access article distributed under the Creative Commons Attribution License, which permits unrestricted use, distribution, and reproduction in any medium, provided the original work is properly cited.

This article has been retracted by Hindawi, as publisher, following an investigation undertaken by the publisher [1]. This investigation has uncovered evidence of systematic manipulation of the publication and peer-review process. We cannot, therefore, vouch for the reliability or integrity of this article.

Please note that this notice is intended solely to alert readers that the peer-review process of this article has been compromised.

Wiley and Hindawi regret that the usual quality checks did not identify these issues before publication and have since put additional measures in place to safeguard research integrity.

We wish to credit our Research Integrity and Research Publishing teams and anonymous and named external researchers and research integrity experts for contributing to this investigation.

The corresponding author, as the representative of all authors, has been given the opportunity to register their agreement or disagreement to this retraction. We have kept a record of any response received.

References

- [1] P. K. Swamy, S. Mylraiah, and D. Basheer, "Evaluation of Microstructure, Hardness, and Tensile Properties: A Comparative Study of Stir Cast and Extruded Al7005/Glass-/Fly-Ash-Reinforced Hybrid MMCs," *Advances in Materials Science and Engineering*, vol. 2021, Article ID 8601484, 7 pages, 2021.

Research Article

Evaluation of Microstructure, Hardness, and Tensile Properties: A Comparative Study of Stir Cast and Extruded Al7005/Glass-/Fly-Ash-Reinforced Hybrid MMCs

Praveen Kumar Swamy ¹, Shantharaja Mylaraiah,¹ and Dadapeer Basheer ²

¹Department of Mechanical Engineering, University Visvesvaraya College of Engineering, Bangalore University, Bengaluru, Karnataka, India

²Department of Mechanical Engineering, Haramaya Institute of Technology, Haramaya University, Dire Dawa, Ethiopia

Correspondence should be addressed to Dadapeer Basheer; dadapeerb@yahoo.com

Received 25 June 2021; Revised 11 July 2021; Accepted 19 July 2021; Published 28 July 2021

Academic Editor: Samson Jerold Samuel Chelladurai

Copyright © 2021 Praveen Kumar Swamy et al. This is an open access article distributed under the Creative Commons Attribution License, which permits unrestricted use, distribution, and reproduction in any medium, provided the original work is properly cited.

The effect of extrusion ratio and addition of glass and fly ash on microstructural, mechanical properties, and fracture behavior of Al composites is examined. Both the composites and hybrid composites are prepared by the liquid metallurgical technique. Microstructure, extrusion effect on hardness, tensile properties, and fracture are studied using an optical micrograph, hardness tester, Universal Testing Machine, and scanning electron microscope, respectively. Experimental results show that increasing the extrusion ratio leads to a significant enhancement in mechanical properties such as tensile, compression, and yield strength and Young's modulus, but results in a small reduction of ductility. It has been revealed that the presence of glass and fly ash improve the mechanical properties significantly with a slight reduction in ductility compared to the Al alloy. Fracture behaviour of the base alloy and composites show intergranular ductile and brittle cleavage mode failure as observed by SEM.

1. Introduction

Due to numerous advantages such as castability, high toughness, and corrosion resistance, aluminium alloy and its MMCs have a wide range of applications in various engineering sectors such as automotive, aerospace, and marine industries, among others [1–3]. Much research has been carried out on developing MMCs using various reinforcements such as SiC, Al₂O₃, CNTs, and graphene [4–8]. Industrial waste such as fly ash and cenospheres are also used to develop MMCs [9]. MMCs' properties are more susceptible to microstructure, reinforcement type and size, and fabrication processes [10]. Many uncontrolled parameters involved in the metal matrix composite (MMC) fabrication process lead to deleterious defects such as porosity and uneven distribution of particles in the final

product [11–13]. Many researchers [14–16] claim that the quality of casting is improved by secondary processes such as rolling or forging or extrusion by means of reduction of porosity and uniform distribution of particles in the matrix alloy. The extrusion process not only reduces the casting defects but also refines the grain boundaries in the composites [17]. Kumar et al. [18] claimed that Al grains were elongated, which break into subgrains during the deformation stage. Many researchers claim that the average particle size reduces due to the extrusion process because of particle fragmentation leading to the improvement in mechanical properties such as ultimate tensile strength, hardness, and even ductility to some extent. The fragmented particles (nano or micro) significantly modify the microstructure of composites by inducing higher dislocation density induced in the matrix alloy.

The induced dislocation density is one of the important parameters which enhance the properties of composites. Extruded alloy composite microstructures show that the coarse grains of the matrix alloy are refined to a considerable extent which results in the improvement of hardness, tensile strength, and wear resistance of the composite material. The smaller quantity and size of precipitation formed due to direct hot extrusion along with finer and uniform microstructure significantly increase the mechanical properties. But, most of the work reported in the literature is focused on micro and single type of reinforcement. Although the addition of reinforcement and extrusion is achieved in single-type reinforcement Al composites, no research work so far has focused on the extrusion process to produce hybrid composites (one shorter fiber and particles). The objective of this work is to investigate the effect of extrusion on the mechanical properties of Al/glass, Al/fly ash, and Al/glass/fly ash composites.

2. Experimental Studies

In order to develop hybrid composites, the materials Al7005 alloy and reinforcements (short S-glass and fly ash) are chosen as the matrix and reinforcements, respectively. The chemical composition results are presented in Table 1.

The Al7005/hybrid MMCs were fabricated using a popular liquid metallurgy route, i.e., by the stir casting technique. In a reactance heater, Al7005 alloy was melted using a graphite furnace and saturated to 800°C. C₂Cl₆ (10 gm/1 kg of Al) tablets were used to degas the smelted metal. Stirring was carried out using a Cr-steel stirrer coated with ZrO₂ at a rate of 500 rpm. Later, preweighted glass fibres (diameter: 5–10 μm) and fly ash (particle size of 25–30 μm) reinforcements were added into the smelted metal. Stirring was then persisted for almost 15 min to mitigate reinforcement agglomeration. The smelted composite was then dispensed into the cast iron die (preheated) at a soaking temperature of ≈730°C. The die was warmed to room temperature. The Al alloy with and without reinforcements were hot extruded at 500°C using a mechanical extrusion machine at an extrusion rate of 0.5 mm/s at two different ratios of 2.66:1 and 5.32:1. The graphite lubricant was used during the extrusion process.

The dispersal of reinforcements within the Al7005 matrix alloy is examined using an optical microscope. After tensile testing, the fracture surfaces are examined by scanning electron microscopy (Hitachi SEM). The hardness test is performed using a Brinell hardness tester (Blue Star) in accordance with the ASTM E384 standard. Tensile testing is carried out by using a Shimadzu Universal Testing Machine in accordance with the ASTM E8M-15a standard.

3. Results and Discussion

3.1. Optical Microscopic Studies. Figure 1 (A1–A4 and E1–E4) shows the optical micrographs of Al7005, Al/5% glass, Al/6% fly ash, and Al/5% glass/6% fly ash composites

TABLE 1: Chemical composition of Al7005 alloy [19].

Chemical composition of Al 7005 alloy (wt.%)							
Cr	Cu	Fe	Mg	Mn	Si	Zn	Al
0.10	0.01	0.11	1.38	0.54	0.03	4.44	Balance

for both the as cast and extruded specimens. For comparison purposes, both are arranged in the same row as cast material corresponding to their respective compositions. Figure 1 (A2 and E2) shows the microstructures of Al/5wt.% glass short fiber, in which a quite random distribution is observed, which limits the dendrite formation and growth. Figure 1 (A3 and E3) reveals that the fly ash is randomly dispersed with uneven size, but with regular shape in the form of clusters. Fly ash is found to be rich in silica particles, contributing to impurity elements. The microstructure of the Al/5% glass/6% fly ash composite after the extrusion process is presented in Figure 1 (A4 and E4). It shows a good bonding between the reinforcement and matrix material without forming any porosity after the extrusion process.

3.2. Hardness. The test for change of properties at two extrusion ratios is conducted at a similar weight fraction for comparison. Mechanical properties depend on the type of reinforcement, and it is evidenced by comparing the data obtained in the case of Al, Al/5% glass, Al/6% fly ash, and Al/5% glass/6% fly ash. Figure 2 represents the hardness (BHN) of Al7005, Al/5% glass, Al/6% fly ash, and Al/5% glass and 6% fly ash composite which showed an improvement in hardness of 114 BHN, 106 BHN, and 118 BHN, respectively. The hardness of glass fiber (3000 MPa) is much higher than that of Al7005 alloy (350 MPa) and fly ash (23 MPa); hence, the glass-fiber-reinforced composites show higher hardness compared to others.

The increased hardness is not only due to the presence of the reinforcement but also derived from the grain refinement during solidification and the extrusion process. During the extrusion process, the reinforcement was crushed resulting in finer particles. The finer particles enhance a finer grain size, which leads to higher hardness. Another reason for the increased hardness of the extruded specimens is the matrix-to-reinforcement particle size ratio (PSR). The higher hardness values for the lower PSR at the same volume fraction improve bonding between the matrix and reinforcements [20].

3.3. Ultimate Tensile Strength. Figure 3 shows the ultimate tensile strength of both the as cast and extruded samples of all four types of materials under similar conditions. Both reinforcements show improvement in UTS, but glass fiber shows higher strength than fly ash composites. Even though fly ash exhibits a lower strength, its composites show higher tensile strength due to grain modification by the addition of fly ash. Hence, the tensile strength is higher than that of pure matrix alloy. On the other hand, the hybrid Al/glass/fly ash composites exhibited maximum strength around 315 to

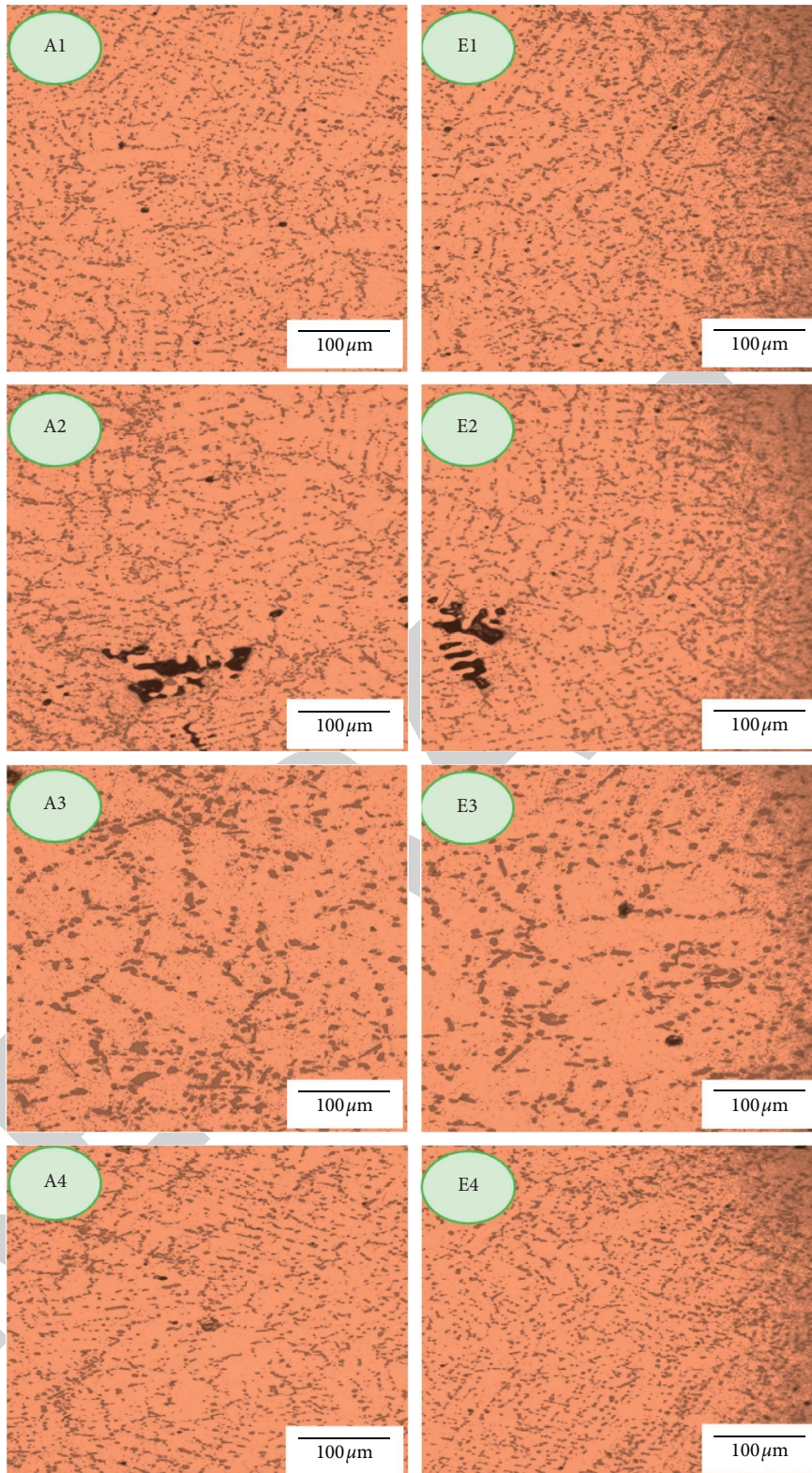


FIGURE 1: Microstructure morphology of as cast (A) extruded ratio of 5.32 : 1 (E) for (1) Al7005 alloy, (2) 5% glass-fiber-reinforced, (3) 6% fly-ash-reinforced, and (4) 5% glass- and 6% fly-ash-reinforced composites.

386 MPa. A tremendous enhancement in the UTS was achieved in the case of Al/glass/fly ash hybrid composites. The addition of glass fiber in the Al/fly ash composites

enhances the UTS. This may be due to the compatibility among glass and fly ash reinforcements, ultimately developing good bonding with Al 7005 [20].

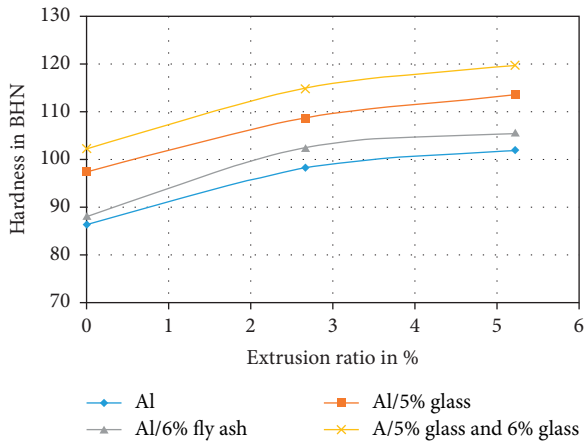


FIGURE 2: Effect of extrusion on the hardness of Al, Al/glass, Al/fly ash, and Al/glass/fly ash composites.

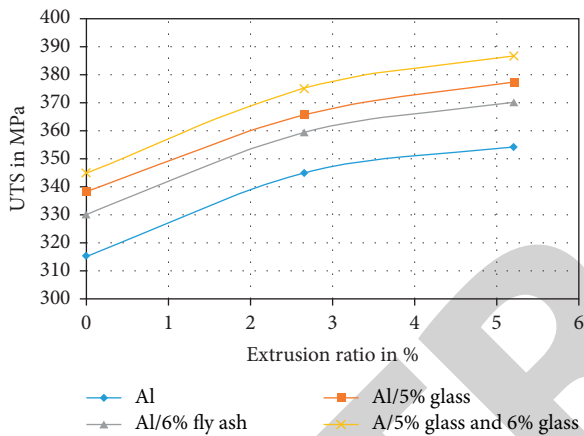


FIGURE 3: Effect of extrusion on the UTS of Al, Al/glass, Al/fly ash, and Al/glass/fly ash composites.

3.4. Yield Strength. The yield strength of the as cast and extruded Al, Al/glass, Al/fly ash, and Al/glass/fly ash composites is shown in Figure 4. Compared with Al and Al/6% fly ash composites, other two combinations such as Al/5% glass and Al/5% glass/6% fly ash composites show remarkable enhancement in the yield strength (7% and 8.5%, respectively). With increasing extrusion ratio, the yield strength of these composites is improved. Compared with the 2.66:1 composites, tensile properties increased by 5.33% and 7.3%, respectively, for both Al/5% glass and Al/5% glass/6% fly ash composites. It clearly indicates that extrusion significantly strengthened the interfacial bonding strength between glass and Al matrix which leads to the elongation of matrix materials [21].

3.5. Compression Strength. Figure 5 represents the compressive strength of all the four specimens as a function of extrusion ratio. The glass- and fly-ash-reinforced composites exhibit higher compressive strengths, compared to the other three specimens irrespective of extrusion ratio. The improvement in compression strength is due to an increase in the dislocation density at the interface of reinforcement and

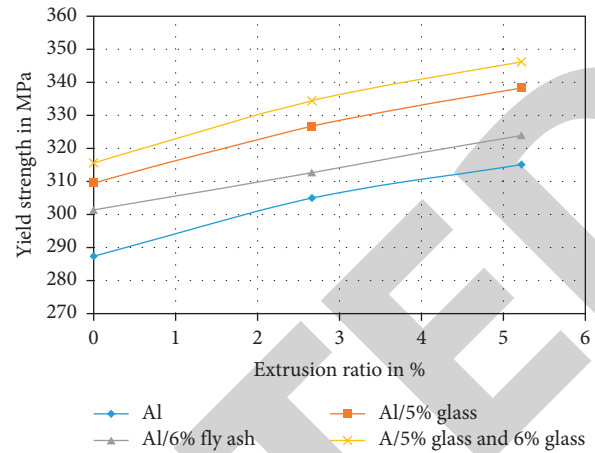


FIGURE 4: Effect of extrusion on the yield strength of Al, Al/glass, Al/fly ash, and Al/glass/fly ash composites.

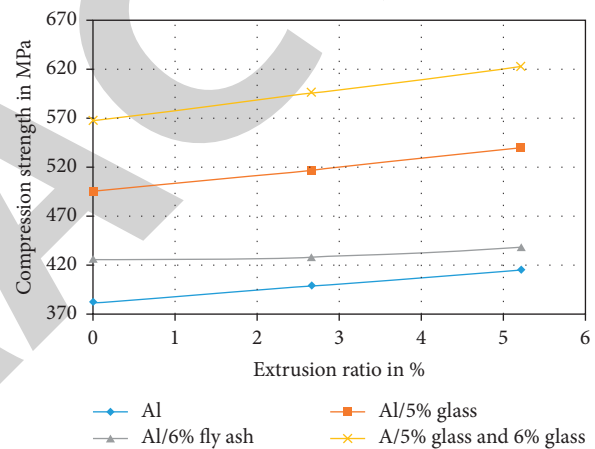


FIGURE 5: Effect of extrusion on the ultimate compressive strength of Al, Al/glass, Al/fly ash, and Al/glass/fly ash composites.

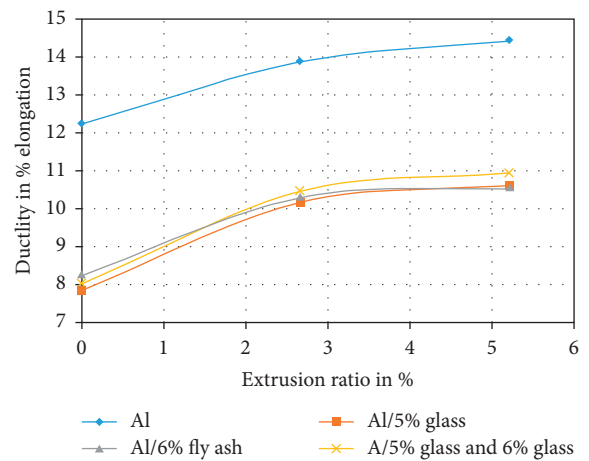


FIGURE 6: Effect of extrusion on the ductility of Al, Al/glass, Al/fly ash, and Al/glass/fly ash composites.

the matrix alloy property mismatch. The higher dislocation leads to a barrier for plastic deformation. Extrusion improves the homogeneity and reduction in particle size or

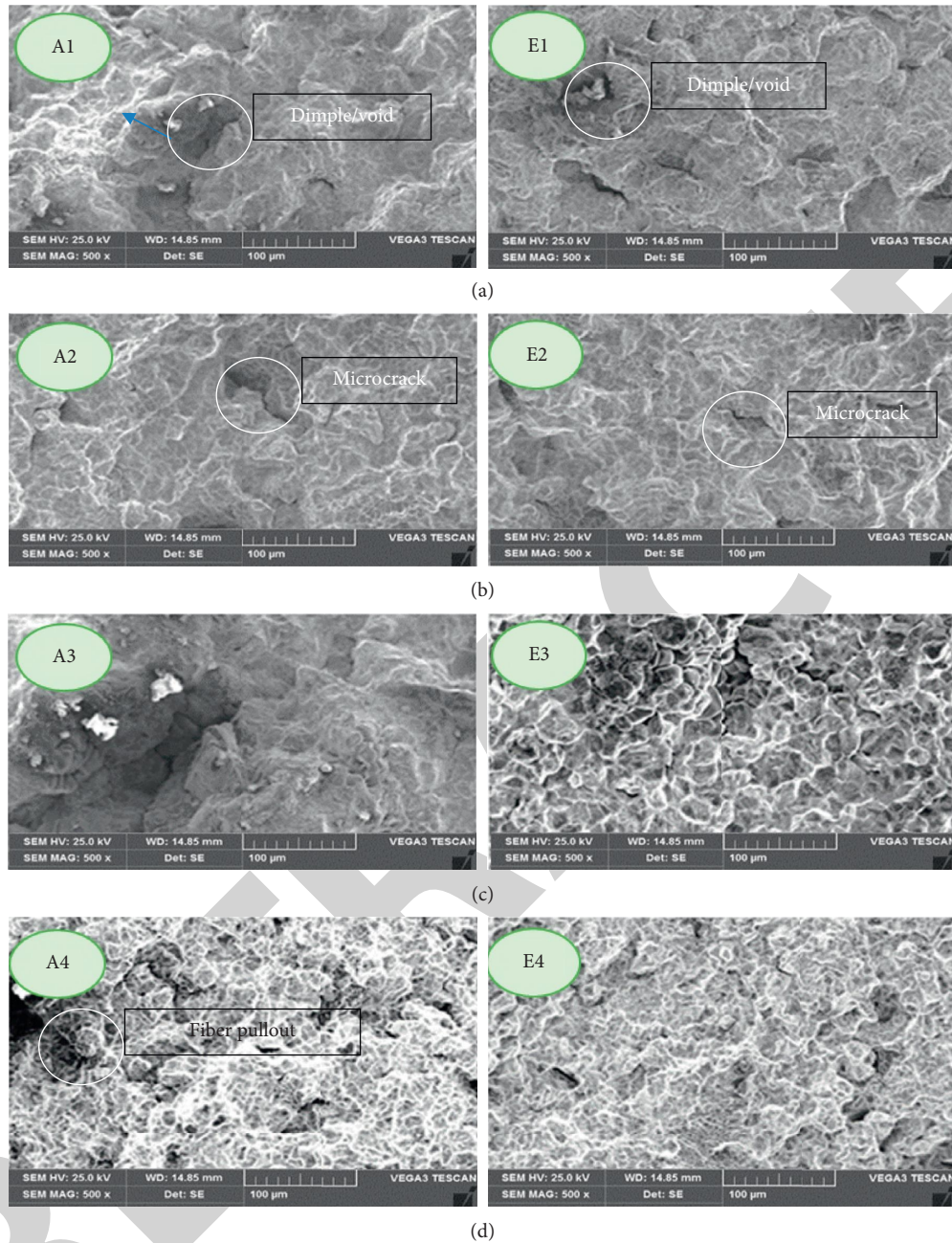


FIGURE 7: Fracture surfaces of as cast (A) extruded ratio of 5.32:1 (E) for (a) Al7005 alloy, (b) 6% fly-ash-reinforced, (c) 5% glass-fiber-reinforced, and (d) 5% glass- and 6% fly-ash-reinforced composites.

fiber length which leads to improvement in mechanical properties [22].

3.6. Ductility. Figure 6 shows the variations of ductility in the case of both the as cast and extruded specimens of different compositions. Addition of either the fly ash or glass to composites drastically reduces the ductility. However, the ductility increases with the extrusion process, due to the dynamic process of recovery, recrystallization and closer packing of the reinforcement, and a smaller interparticle spacing in the matrix. The tensile properties such as elastic

modulus, UTS, and yield strength did not increase significantly with the extrusion ratio; however, the ductility significantly increased with the extrusion ratio. The same is true for all the specimens of both the as cast and composites. The mechanical strength of Al/fly was found to be lower compared to other two composites. As the fly ash spheres increase (840 kg/m^3 density more than three times less than that of Al alloy; it becomes 18 volume fraction), dispersion of particles in the matrix alloy becomes very difficult leading to agglomeration of the fly ash. It reduces the relative density of Al/fly ash composites, which provides a site for initiation of the crack from the agglomeration. In other words, the

interdistance among fly ash particles is larger due to agglomeration, which causes a decrease in strength. The agglomeration increases the brittleness along the grain boundaries, diminishing grain boundary pinning which eventually decreases the strength of fly-ash-reinforced Al composites [23].

3.7. Fracture Studies. Figure 7(a)–7(d) show the fractured surface of Al, Al/fly ash, Al/glass, and Al/glass/fly ash composites, respectively, in the as cast and extruded conditions. It clearly showed that the extruded specimen fracture surfaces appear to be smooth and there exists good bonding between matrix and reinforcement. The bonding between reinforcement and matrix alloy changed which became closer gradually. The Al/glass extruded specimen (Figure 7(c)) and Al/glass/fly ash in both the as cast and extruded specimen (Figure 7(d)) are dominated by brittle fracture. But, in other directions, Al (Figure 7(a)) and Al/fly ash (Figure 7(b)) composites in both the cast and extruded form showed ductile failure; however, they exhibit dimple structure. The ductile-fracture surface has multiple finer dimples and microvoids triggered by the preliminary loading condition, which results in microcracks that proliferate and ultimately fracture in a ductile manner. The only transgranular grain boundary resides in composite specimens that failed due to brittle fracture and surface [24].

4. Conclusions

Experimental studies on the behavior of mechanical and microstructure of Al 7005 composites with and without extrusion conditions were conducted as per ASTM standards. The following important conclusions are drawn:

- (i) The extrusion process and its ratio have a high influence on the reinforcement, porosity, and breakage of the fiber in the matrix alloy. These two factors promote reduction in grain boundary resulting in better distribution of reinforcement thereby increasing the mechanical strength of the extruded specimens.
- (ii) The glass- and fly-ash-reinforced composites and hybrid composites exhibit higher values of hardness and tensile strength than the matrix alloy due to grain refinement during solidification.
- (iii) The optical micrographs of the composite specimens revealed a uniform distribution of glass fiber and fly ash in the matrix alloy along with grain refinement, due to the addition of reinforcements.
- (iv) The tensile strength of 5% glass-reinforced Al composites, 6% fly-ash-reinforced Al composites, and 5% glass-/6% fly-ash-reinforced Al hybrid composites is 370 MPa, 378 MPa, and 388 MPa compared to matrix alloy of 353 MPa.
- (v) All hybrid matrix composites exhibit better tensile, hardness, and yield strengths than the matrix alloy but low ductility.

- (vi) All the composites materials show brittle failure, and the base metal shows failure of ductility due to the limited amount of material displacement, observed as per the fractography.

Data Availability

Data are available on request.

Conflicts of Interest

The authors declare no conflicts of interest.

References

- [1] A. Lakshmikanthan, S. Bontha, M. Krishna, P. G. Koppad, and T. Ramprabhu, "Microstructure, mechanical and wear properties of the A357 composites reinforced with dual sized SiC particles," *Journal of Alloys and Compounds*, vol. 786, no. 25, pp. 570–580, 2019.
- [2] L. Avinash, H. Kumar, A. Parthasarathy, K. N. K. Varun, and B. Sajjan, "The effect of ceramic reinforcement on the microstructure, mechanical properties and tribological behavior of al-7.5%si-0.5%mg alloy," *Applied Mechanics and Materials*, vol. 867, 2017.
- [3] A. Lakshmikanthan, R. T. Prabhu, S. B. Udayagiri, P. G. Koppad, M. Gupta, and M. Krishna, S. Bontha, "The effect of heat treatment on the mechanical and tribological properties of dual size SiC reinforced A357 matrix composites," *Journal of Materials Research and Technology*, vol. 9, no. 3, pp. 6434–6452, 2020.
- [4] A. Parthasarathy, L. Avinash, K. N. K. Varun, B. Sajjan, and S. Varun, "Fabrication and characterization of Al-0.4%Si-0.5%Mg - SiCp using," *Permanent Mould Casting Technique* *Applied Mechanics and Materials*, vol. 867, pp. 34–40, 2017.
- [5] B. Sajjan, L. Avinash, S. Varun, K. N. Varun Kumar, and A. Parthasarathy, "Investigation of mechanical properties and dry sliding wear behaviour of graphite reinforced Al7068 alloy," *Applied Mechanics and Materials*, vol. 867, pp. 10–18, 2017.
- [6] L. Avinash, T. P. Ram, A. Parthasarathy, K. N. V. Kumar, and B. Sajjan, "Wear and mechanical behaviour of Hypo-eutectic Al-7%Si-0.5%Mg alloy (A357) reinforced with Al₂O₃ particles," *Applied Mechanics and Materials*, vol. 829, pp. 66–72, 2016.
- [7] M. Naik, L. H. Manjunath, V. Koti, A. Lakshmikanthan, P. Koppad, and S. Kumaran, "Al/Graphene/CNT hybrid composites: hardness and sliding wear studies," *FME Transactions*, vol. 49, no. 2, pp. 414–421, 2021.
- [8] H. R. M. Naik, L. H. Manjunath, V. Malik, G. M. Patel, K. K. Saxena, and A. Lakshmikanthan, "Effect of microstructure, mechanical and wear on Al-CNTs/graphene hybrid MMC'S," *Advances in Materials and Processing Technologies*, , pp. 1–14, Taylor & Francis, 2021.
- [9] N. Vinayaka, A. Lakshmikanthan, G. M. Patel, and C. P. Selvan, V. K. Jain, S. A. Srinivasan and H. Harsha, "Mechanical, microstructure and wear properties of Al 6113 fly ash reinforced composites: comparison of as-cast and heat-treated conditions," *Advances in Materials and Processing Technologies*, , pp. 1–16, Taylor & Francis, 2021.
- [10] L. Avinash, T. Ramprabhu, and S. Bontha, "The effect on the dry sliding wear behavior of gravity cast A357 reinforced with dual size silicon carbide particles," *Applied Mechanics and Materials*, vol. 829, pp. 83–89, 2016.

Retraction

Retracted: Effect of Tool Profile Influence in Dissimilar Friction Stir Welding of Aluminium Alloys (AA5083 and AA7068)

Advances in Materials Science and Engineering

Received 26 December 2023; Accepted 26 December 2023; Published 29 December 2023

Copyright © 2023 Advances in Materials Science and Engineering. This is an open access article distributed under the Creative Commons Attribution License, which permits unrestricted use, distribution, and reproduction in any medium, provided the original work is properly cited.

This article has been retracted by Hindawi, as publisher, following an investigation undertaken by the publisher [1]. This investigation has uncovered evidence of systematic manipulation of the publication and peer-review process. We cannot, therefore, vouch for the reliability or integrity of this article.

Please note that this notice is intended solely to alert readers that the peer-review process of this article has been compromised.

Wiley and Hindawi regret that the usual quality checks did not identify these issues before publication and have since put additional measures in place to safeguard research integrity.

We wish to credit our Research Integrity and Research Publishing teams and anonymous and named external researchers and research integrity experts for contributing to this investigation.

The corresponding author, as the representative of all authors, has been given the opportunity to register their agreement or disagreement to this retraction. We have kept a record of any response received.

References

- [1] S. Jayaprakash, S. Siva Chandran, T. Sathish et al., "Effect of Tool Profile Influence in Dissimilar Friction Stir Welding of Aluminium Alloys (AA5083 and AA7068)," *Advances in Materials Science and Engineering*, vol. 2021, Article ID 7387296, 7 pages, 2021.

Research Article

Effect of Tool Profile Influence in Dissimilar Friction Stir Welding of Aluminium Alloys (AA5083 and AA7068)

S. Jayaprakash ¹, S. Siva Chandran,² T. Sathish ³, Bhiksha Gugulothu ⁴, R. Ramesh ⁵,
M. Sudhakar,² and Ram Subbiah⁶

¹Department of Electrical and Electronics Engineering, Sathyabama Institute of Science and Technology, Chennai, Tamil Nadu, India

²Department of Mechanical Engineering, Sri Sairam Engineering College, Sai Leo Nagar, West Tambaram, Chennai 44, Tamil Nadu, India

³Department of Mechanical Engineering, Saveetha School of Engineering, SIMATS, Chennai 602 105, Tamil Nadu, India

⁴Department of Mechanical Engineering, Bule Hora University, Addis Ababa, Bule Hora, Ethiopia

⁵Department of Chemical Engineering, Addis Ababa Science and Technology University, Addis Ababa, Ethiopia

⁶Department of Mechanical Engineering, Gokaraju Rangaraju Institute of Engineering and Technology, Nizampet, Hyderabad, India

Correspondence should be addressed to Bhiksha Gugulothu; bhikshagugulothu14251425@gmail.com

Received 23 June 2021; Revised 5 July 2021; Accepted 14 July 2021; Published 22 July 2021

Academic Editor: Samson Jerold Samuel Chelladurai

Copyright © 2021 S. Jayaprakash et al. This is an open access article distributed under the Creative Commons Attribution License, which permits unrestricted use, distribution, and reproduction in any medium, provided the original work is properly cited.

Friction stir welding is an innovative welding process for similar and dissimilar joining of the materials effectively. FSW simply modified the grain structure and also improved the strength of the joints for any type of alloying elements. This experimental study planned to carry out the joining process for dissimilar materials such as aluminium alloys 5083 and 7068. Three different types of tools are involved to find the ultimate tensile strength and Vickers hardness. The tool types are straight cylindrical tool, taper cylindrical tool, and triangular tool. The process factors for this investigation are a rotational speed of 800, 1000, 1200, and 1400 rpm, welding speed of 30, 40, 50, and 60 mm/min, axial force of 3, 4, 5, and 6 kN, and plate thickness of 5, 6, 7, and 8 mm. The hardness value and the ultimate tensile strength were increased in the welding zone, which proves the effects of tool profiles are efficiently utilized.

1. Introduction

The aluminium alloy is one of the effective materials used worldwide in all field applications, and due to the excellent strength of the aluminium alloy, it is used for all structural work in the construction field [1]. The aluminium alloy is adaptable for all types of welding process and possesses good corrosion resistance in the marine environment. The aluminium alloys with reinforcement improve the wear properties in the sliding friction method. The friction stir welding method is used to weld a minimum-thickness plate without damaging the specimen, and the FSW process

eliminates the bending of the work part after welding [2–4]. Different tool pin profiles are used to join the samples with extraordinary strength and good surface modification. The main advantage of the FSW is a nonconsumable tool is used since the cost of electrode for the welding process is avoided [5]. The tool rotational speed and welding speed are directly influenced in the welding strength of the components, and it reflects on the mechanical test. All sheets and plates are welded effectively; nowadays, the circular specimen is also welded through the FSW process in the pipe joint and solid round bar joint successfully [6]. The shoulder area of the tool pressing and levelling of the intermixing materials without

wastage during the welding process, based on the tool selection single pass ride and multipass ride, was used to obtain rigid welding. The tilt angle of the tool position gives uniform mixing and reduces the defects of the materials after welding, and the wear of the tool was avoided by selecting proper tool material for work and the suitable parameters [7–9]. The FSW process was introduced by Wayne Thomas at TWI Ltd. in 1991. The tool rotational speed changes the microstructure of the material by the way of utilizing stirring action. The lot of researchers used the FSW process effectively, and this investigation planned to conduct the dissimilar weld joint using the material of AA5083 and AA7068 successfully. The different parameters influenced are rotational speed, welding speed, axial force, and plate thickness [10].

2. Selection of Materials

Consideration of the application and material selection is one of the major roles in the investigation.

The dissimilar FSW joint material is selected on the basis of application and mechanical strength characters. The AA7068 aluminium alloy has provided the superior mechanical strength and corrosion resistance [11]. This AA7068 alloy is commonly applied for fuel pump manufacturing, rocker arm assembly fabrication, high-speed engine, valve body construction, and gears. AA7068 has provided maximum tensile strength and hardness, and this alloy is used in the fabrication of container and tipper truck bodies. The chemical composition of AA5083 and AA7068 is illustrated in Table 1.

2.1. Experimental Procedure. The FSW process considers the process factors, and all the factors and their values are presented in Table 2.

The friction stir welding process was carried out in the CNC vertical milling machine, and the specimens taken for this work were 100 * 50 * 4 mm for both plates [12]. The tool pin for the FSW was considered as a straight cylindrical shape, taper cylindrical, and triangular profile pin for each experimental trials, as shown in Figure 1 [13]. The tool material of the process was high-speed steel (HSS). The specimens are mounted on the table with the help of fixture, and the tool rotates and plunges the work material with selected parameters. The high penetration produced the uniform mixture and the permanent joints. After welding, the specimen was prepared as per the standard dimensions for conducting the tensile test, and the Universal Testing Machine was used to carry out the tensile test with 40 Ton capacity [14]. The all samples were tested effectively, the readings were noted, and the maximum tensile strength was identified. The microhardness of the specimens was tested in the Vickers hardness testing machine for each sample. The maximum hardness value of the sample was classified from other samples efficiently.

TABLE 1: Chemical composition of AA7079 and AA8050.

Material	% of composition of AA5083	% of composition of AA7068
Cr	0.2	0.050
Cu	0.10	2.5
Fe	0.3	0.14
Mg	4.5	2.9
Mn	0.5	0.1
Si	0.2	0.12
Zn	0.1	7.8
Ti	0.15	0.08
Zr	—	0.16
Ni	—	0.040
Al	Remaining	Remaining

TABLE 2: Friction stir welding process and its value.

Notation	Factors	Level	Level	Level	Level
		1	2	3	4
P	Rotational speed (rpm)	800	1000	1200	1400
Q	Welding speed (mm/min)	30	40	50	60
R	Axial force (kN)	3	4	5	6
S	Plate thickness (mm)	5	6	7	8

3. Result and Discussion

The process factors of the investigation and the output value of tensile strength are presented in Table 3.

From Table 3, the maximum tensile strength was obtained as 290 MPa, and the factors of influence are a rotational speed of 1400 rpm, welding speed of 40 mm/min, axial force of 5 kN, and plate thickness of 5 mm [15]. The analysis of variance result is summarized in Table 3. From the ANOVA in the linear model, the rotational speed has high contribution such as 15.16%, and in the square model, plate thickness (mm) * plate thickness (mm) was contributed as 14.09%. In the 2-way interaction model, the welding speed (mm/min) * plate thickness (mm) was contributed as 33.24%. The rotational speed was the most influencing factor of this investigation, and the second factor of influence was welding speed, Table 4.

3.1. Regression Equation. $UTS \text{ (MPa)} = -826 + 1.008 \text{ Rotational speed (rpm)} - 2.26 \text{ Welding speed (mm/min)} + 83.6 \text{ Axial force (kN)} + 119.1 \text{ Plate thickness (mm)}$.

$- 0.000029 \text{ Rotational speed (rpm)} * \text{Rotational speed (rpm)}$.

$+ 0.1094 \text{ Welding speed (mm/min)} * \text{Welding speed (mm/min)} + 0.83 \text{ Axial force (kN)} * \text{Axial force (kN)} + 3.83 \text{ Plate thickness (mm)} * \text{Plate thickness (mm)}$.

$+ 0.00122 \text{ Rotational speed (rpm)} * \text{Welding speed (mm/min)}$.

$- 0.0767 \text{ Rotational speed (rpm)} * \text{Axial force (kN)}$.

$- 0.1039 \text{ Rotational speed (rpm)} * \text{Plate thickness (mm)}$.

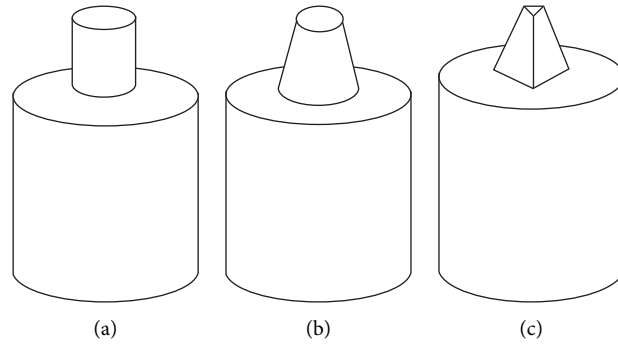


FIGURE 1: FSW tool. (a) Cylindrical tool, (b) Taper tool, and (c) Triangular tool.

TABLE 3: FSW factors' contribution and the output of tensile strength.

Exp. no.	Rotational speed (rpm)	Welding speed (mm/min)	Axial force (kN)	Plate thickness (mm)	Tensile strength (MPa)
1	800	30	3	5	210
2	800	40	4	6	250
3	800	50	5	7	180
4	800	60	6	8	160
5	1000	30	4	7	240
6	1000	40	3	8	270
7	1000	50	6	5	285
8	1000	60	5	6	245
9	1200	30	5	8	262
10	1200	40	6	7	190
11	1200	50	3	6	185
12	1200	60	4	5	240
13	1400	30	6	6	257
14	1400	40	5	5	292
15	1400	50	4	8	275
16	1400	60	3	7	212

TABLE 4: Analysis of variance result.

Source	DF	Seq SS	Contribution (%)	Adj SS	Adj MS	F value	P value
Model	13	23106.8	94.36	23106.8	1777.44	2.57	0.314
Linear	4	6937.3	28.33	9341.1	2335.27	3.38	0.241
Rotational speed (rpm)	1	3712.8	15.16	8831.8	8831.78	12.79	0.07
Welding speed (mm/min)	1	2132.1	8.71	173.6	173.55	0.25	0.666
Axial force (kN)	1	4.5	0.02	24	23.97	0.03	0.869
Plate thickness (mm)	1	1087.8	4.44	482.4	482.44	0.7	0.491
Square	4	7388.2	30.17	10407.1	2601.76	3.77	0.221
Rotational speed (rpm) * Rotational speed (rpm)	1	410.1	1.67	7691.4	7691.38	11.14	0.079
Welding speed (mm/min) * Welding speed (mm/min)	1	637.6	2.60	637.6	637.56	0.92	0.438
Axial force (kN) * Axial force (kN)	1	2889.1	11.80	6029.5	6029.52	8.73	0.098
Plate thickness (mm) * Plate thickness (mm)	1	3451.6	14.09	5363.3	5363.28	7.77	0.108
2-way interaction	5	8781.3	35.86	8781.3	1756.25	2.54	0.306
Rotational speed (rpm) * Welding speed (mm/min)	1	2.9	0.01	127.6	127.96	0.18	0.709
Rotational speed (rpm) * Axial force (kN)	1	192.2	0.79	56	5816.96	0.86	0.803
Rotational speed (rpm) * Plate thickness (mm)	1	435.8	1.78	435.8	1435.75	0.63	0.51
Welding speed (mm/min) * Axial force (kN)	1	10.2	0.04	7705	7705	11.16	0.079
Welding speed (mm/min) * Plate thickness (mm)	1	8140.2	33.24	8140.2	8140.17	11.79	0.075
Error	2	1381.2	5.64	1381.2	690.59		
Total	15	24487.9	100.00				

– 0.056 Welding speed (mm/min) * Axial force (kN).
 – 1.356 Welding speed (mm/min) * Plate thickness (mm).

– 0.00 Axial force (kN) * Plate thickness (mm).

Table 5 presents the different tool profiles involved to produce the ultimate tensile strength effectively. Using a

TABLE 5: Summary of the different tool profiles with ultimate tensile strength.

S. no.	Tool profile	Rotational speed (rpm)	Ultimate tensile strength (MPa)			
			30 mm/min- 3 kN	40 mm/min- 4 kN	50 mm/min- 5 kN	60 mm/min- 6 kN
1.	Cylindrical taper tool	800	235	228	215	220
2.		1000	246	237	226	236
3.		1200	267	253	242	238
4.		1400	192	180	187	192
5.	Triangular tool	800	234	225	210	215
6.		1000	247	242	247	240
7.		1200	286	265	254	259
8.	1400	210	194	186	205	
9.	Straight cylindrical tool	800	246	234	226	232
10.		1000	256	243	246	246
11.		1200	275	260	267	262
12.		1400	210	215	206	208

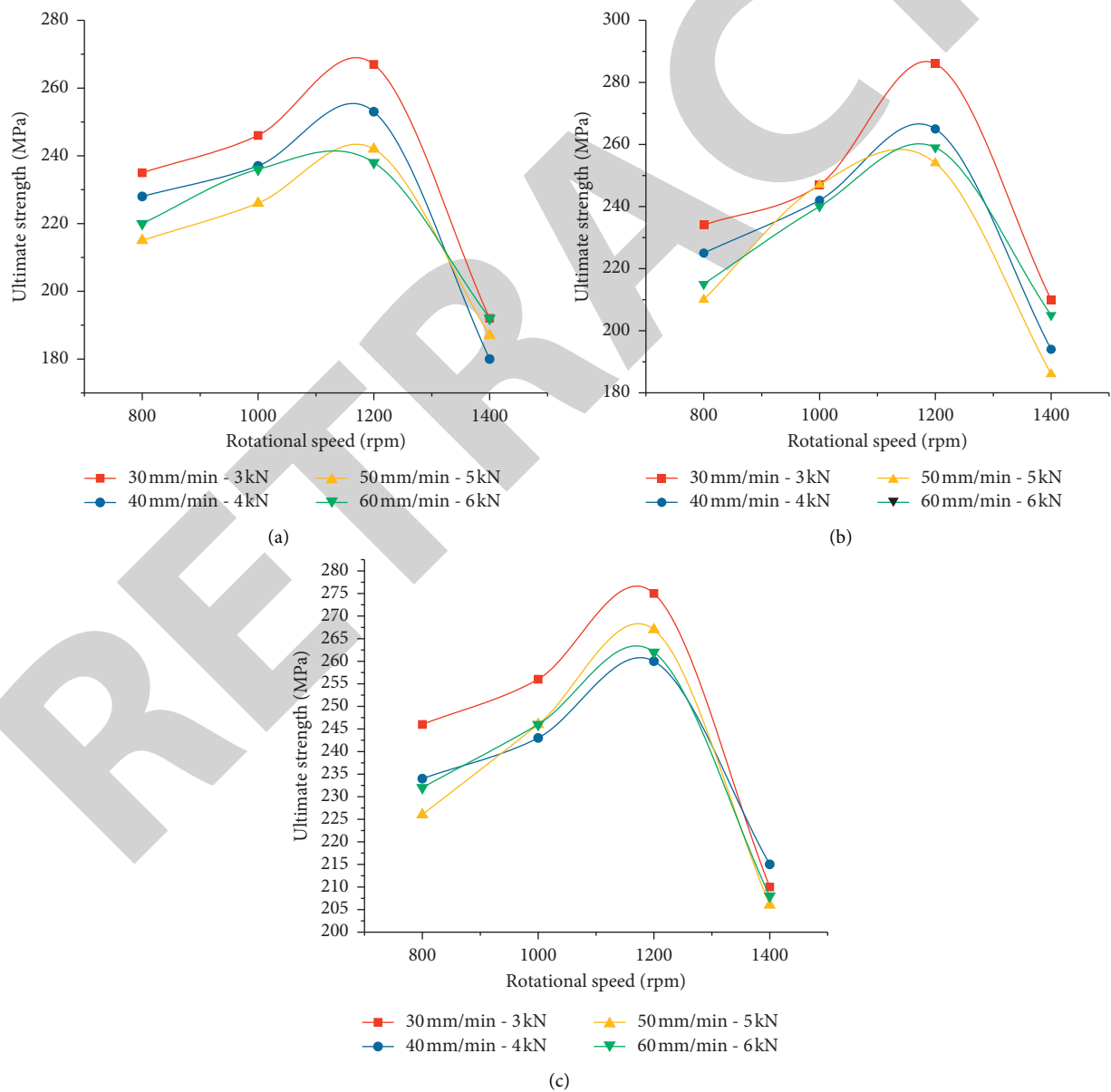


FIGURE 2: (a) Rotational speed vs. ultimate tensile strength (cylindrical taper tool), (b) Rotational speed vs. ultimate tensile strength (triangular tool), and (c) Rotational speed vs. ultimate tensile strength (straight cylindrical tool).

TABLE 6: Summary of different tool profiles with microhardness.

S. no.	Tool profile	Rotational speed (rpm)	Microhardness (HV)			
			30 mm/min- 3 kN	40 mm/min- 4 kN	50 mm/min- 5 kN	60 mm/min- 6 kN
1.	Cylindrical taper tool	800	45	50	48	46
2.		1000	62	66	68	58
3.		1200	75	70	72	66
4.		1400	56	52	42	50
5.	Triangular tool	800	55	48	55	52
6.		1000	68	60	75	66
7.		1200	86	75	68	78
8.	1400	62	65	54	54	
9.	Straight cylindrical tool	800	46	50	52	48
10.		1000	64	66	68	60
11.		1200	82	80	74	72
12.		1400	58	48	52	50

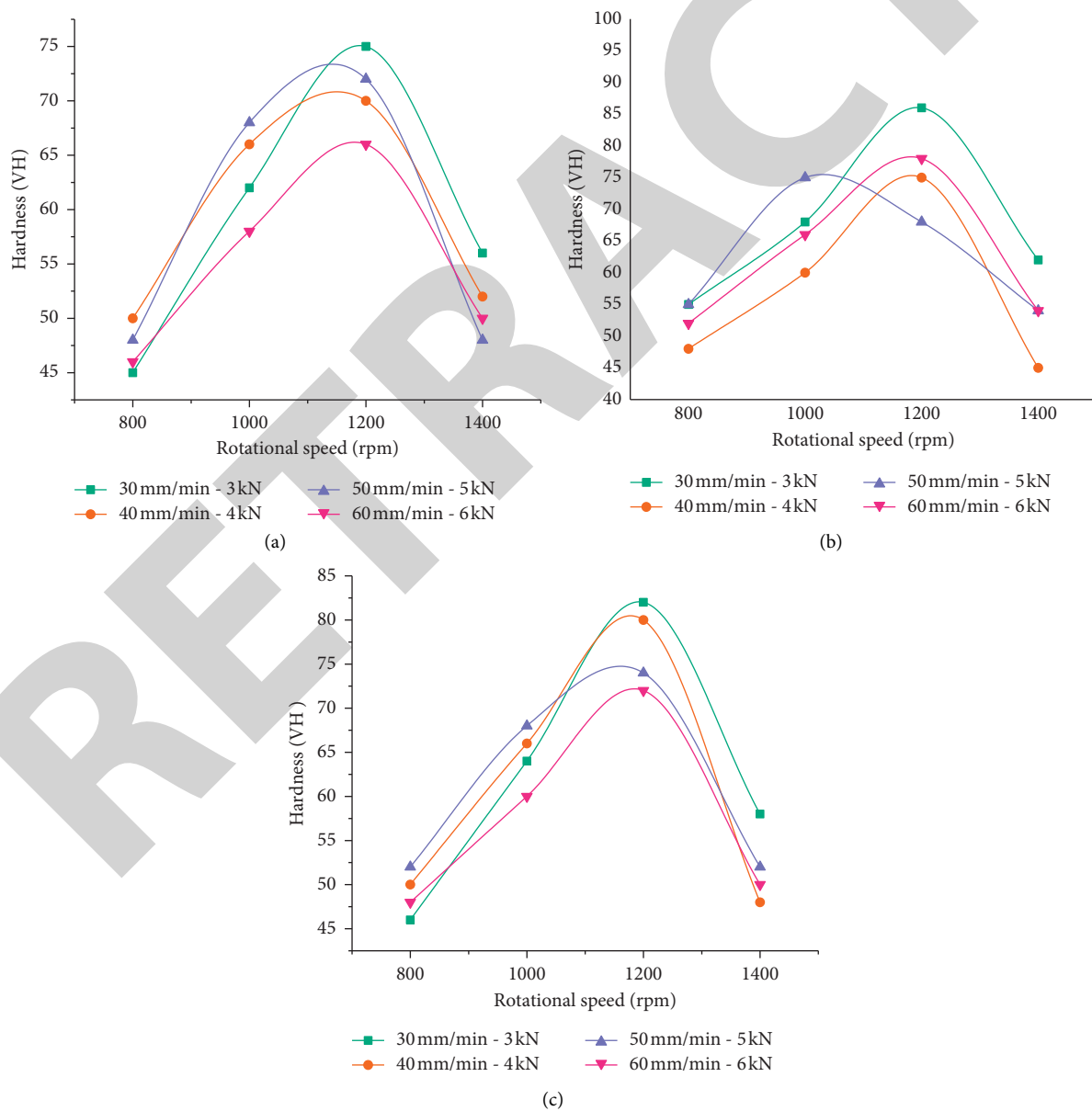


FIGURE 3: (a) Rotational speed vs. hardness (cylindrical taper tool), (b) Rotational speed vs. hardness (triangular tool), and (c) Rotational speed vs. hardness (straight cylindrical tool).

cylindrical taper tool, the minimum tensile strength obtained was 180 MPa with the rotational speed of 1400 rpm, welding speed of 40 mm/min, and axial force of 4 kN. The maximum tensile strength attained was 267 MPa, involving of a rotational speed of 1200 rpm, welding speed of 30 mm/min, and axial force of 3 kN. Using a triangular tool, the maximum tensile strength was 286 MPa offered by the influence of a rotational speed of 1200 rpm, welding speed of 30 mm/min, and axial force of 3 kN. Using a straight cylindrical tool, the maximum tensile strength of 275 MPa was attained as by the way of a rotational speed of 1200 rpm, welding speed of 30 mm/min, and axial force of 3 kN. From this analysis, it can be seen that all the tools provided the maximum tensile strength with consideration of a rotational speed of 1200 rpm, welding speed of 30 mm/min, and axial force of 3 kN.

3.2. Effects of Tool Profiles with Tool Speed in Ultimate Tensile Strength. Figures 2(a)–2(c) show the different rotational speeds versus ultimate tensile strengths by the influence of different tool pin profiles. From the entire graph, it can be seen that the increase of rotational speed increases the tensile strength, and the maximum tensile strength was obtained in the influence of 1200 rpm, a welding speed of 30 mm/min, and an axial force of 3 kN. With further increase of rotational speed, the tensile strength rapidly fell down; it proves the rotational speed effects in the tensile strength. The triangular tool was given the maximum tensile strength of 286 MPa.

3.3. Effects of Tool Profiles with Tool Speed in Microhardness. Table 6 presents the microhardness of the weld joint with the influence of different tool profiles. Using a cylindrical taper tool, the minimum and maximum microhardness were obtained as 42 HV and 75 HV. With the involvement of a triangular tool, the minimum and maximum microhardness were obtained as 48 HV and 86 HV. With the application of a straight cylindrical tool, the minimum and maximum microhardness were attained as 46 HV and 82 HV. The triangular tool was given the maximum microhardness value of 86 HV.

The rotational speed versus microhardness graph is illustrated in Figure 3(a), and the graph shows the minimum rotational speed provided the minimum hardness values. The increasing trends of rotational speed, welding speed, and the axial force provided the maximum hardness value. At a rotational speed of 1200 rpm, the maximum hardness was obtained, and with further increase of rotational speed from 1200 rpm to 1400 rpm, the hardness value decreased constantly. The maximum hardness value obtained by using a cylindrical tool was 75 HV with the support of a welding speed of 30 mm/min and axial force of 3 kN.

Figure 3(b) visibly shows the maximum hardness obtained by using a triangular tool was 86 HV with the influence of a rotational speed of 1200 rpm, welding speed of 30 mm/min, and axial force of 3 kN. As in Figure 3(c), the maximum

hardness value acquired was 82 HV by using a straight cylindrical tool with the rotational speed of 1200 rpm, welding speed of 30 mm/min, and axial force of 3 kN.

4. Conclusions

The joining material of AA5083 and AA7068 aluminium alloy was joined by friction stir welding with different process variables. The maximum ultimate tensile strength and microhardness were successfully conducted, and the results are pointed out as follows:

From the ANOVA test, using a cylindrical taper tool, the maximum ultimate tensile strength was attained as 267 MPa. Using a triangular tool, the maximum ultimate tensile strength obtained was 286 MPa. Using a straight cylindrical tool, the maximum ultimate tensile strength of 275 MPa was attained. From this analysis, it can be seen that all the tools provided the maximum tensile strength with consideration of a rotational speed of 1200 rpm, welding speed of 30 mm/min, and axial force of 3 kN. With the increase of rotational speed from 1200 rpm to 1400, the tensile strength rapidly decreased.

By using a cylindrical taper tool, the minimum and maximum microhardness were obtained as 42 HV and 75 HV. The implementation of a triangular tool provided the minimum and maximum microhardness of 48 HV and 86 HV. The application of a straight cylindrical tool provided the minimum and maximum microhardness of 46 HV and 82 HV. The triangular tool offered the maximum tensile strength and microhardness of the investigation.

In future, the present study will analyse the wear performance and corrosion behaviour of the dissimilar materials and it is also planned to conduct the fatigue test for failure analysis.

Data Availability

The data used to support the findings of this study are included in the article. Further data or information is available from the corresponding author upon request.

Conflicts of Interest

This study was performed as a part of the employment at Bule Hora University, Ethiopia.

Acknowledgments

The authors appreciate the support from Bule Hora University, Ethiopia. The authors thank Saveetha School of Engineering, Chennai, for the technical assistance to complete this experimental work.

Retraction

Retracted: Industrial Waste Water Recycling Using Nanographene Oxide Filters

Advances in Materials Science and Engineering

Received 26 December 2023; Accepted 26 December 2023; Published 29 December 2023

Copyright © 2023 Advances in Materials Science and Engineering. This is an open access article distributed under the Creative Commons Attribution License, which permits unrestricted use, distribution, and reproduction in any medium, provided the original work is properly cited.

This article has been retracted by Hindawi, as publisher, following an investigation undertaken by the publisher [1]. This investigation has uncovered evidence of systematic manipulation of the publication and peer-review process. We cannot, therefore, vouch for the reliability or integrity of this article.

Please note that this notice is intended solely to alert readers that the peer-review process of this article has been compromised.

Wiley and Hindawi regret that the usual quality checks did not identify these issues before publication and have since put additional measures in place to safeguard research integrity.

We wish to credit our Research Integrity and Research Publishing teams and anonymous and named external researchers and research integrity experts for contributing to this investigation.







The corresponding author, as the representative of all authors, has been given the opportunity to register their agreement or disagreement to this retraction. We have kept a record of any response received.

References

- [1] P. Yuvarani, S. Vijayachitra, V. Ranganayaki et al., "Industrial Waste Water Recycling Using Nanographene Oxide Filters," *Advances in Materials Science and Engineering*, vol. 2021, Article ID 4528949, 7 pages, 2021.

Research Article

Industrial Waste Water Recycling Using Nanographene Oxide Filters

P. Yuvarani ¹, **S. Vijayachitra** ², **V. Ranganayaki**,³ **S. Sathish Kumar** ⁴,
K. Srujan Raju ⁵, **M. Sivachitra** ⁶, and **Ishwarya Komalnu Raghavan** ⁷

¹Department of EIE, M. Kumarasamy College of Engineering, Karur, Tamilnadu, India

²Department of EIE, Kongu Engineering College, Perundurai, Erode, Tamilnadu 638052, India

³Department of EEE, Dr.NGP Institute of Technology, Coimbatore, Tamilnadu, India

⁴Department of EEE, M. Kumarasamy College of Engineering, Karur, Tamilnadu, India

⁵Department of Computer Science and Engineering, CMR Technical Campus, Hyderabad, Telangana, India

⁶Department of EEE, Kongu Engineering College, Perundurai, Erode, Tamilnadu 638052, India

⁷Department of Electromechanical Engineering, Faculty of Manufacturing, Institute of Technology, Hawassa University, Hawassa, Ethiopia

Correspondence should be addressed to Ishwarya Komalnu Raghavan; ishwarya138@hu.edu.et

Received 9 June 2021; Accepted 10 July 2021; Published 19 July 2021

Academic Editor: Samson Jerold Samuel Chelladurai

Copyright © 2021 P. Yuvarani et al. This is an open access article distributed under the Creative Commons Attribution License, which permits unrestricted use, distribution, and reproduction in any medium, provided the original work is properly cited.

Nanomaterials play a vital role in healthcare, electronics, manufacturing industries, biotechnology, and security systems. One such material is graphene and its oxides are specifically used for recycling industrial waste water. Graphene, a single layer in honeycomb cross section, provides excellent attention because of its significant optical, mechanical, and physical properties. GO was utilized to decrease the acidic or essential centralization of the mechanical wastewater into reusable water for the modern reason utilizing graphene channels. In this paper, sample solution (waste water) is taken from paper industry. Graphene channels can be created from the pencil graphite. Graphene has the high goals of separating capacity, and graphene is considered as “a definitive RO film” in light of its stronger, thinner, and more chemically safe nature than the polymer layers. Graphene oxide layers are likewise to be used in the desalination plant in place of the RO membrane.

1. Introduction

Nowadays, waste water coming from industries produces major problem to surroundings as well as creates pollution to the environment. Public and government forced the industries to recycle or reduce the waste coming out to stringent standards. Water is one of the primary sources for the process industries such as chemical industry, paper industry, food processing, and cement industry, as well as some other industries which used as coolants' boiler feed water. So, the water used should be free from toxic substances, scale-forming solutes, corrosive substances, and pathogens. Improper treatment will cause contaminations and reduction in processes and may result in poor performance, product deterioration, and sometimes overall

process failure. So, various factors need to be considered before designing the plant such as quality and quantity of water resources, water recycle, and discharge standards. So, appropriate water treatment facility should be planned earlier. Another important aspect in water treatment is that it should be fully investigated in order to analyse the nature of the constituents in the waste water because it may contain some microorganisms, other relative hazards, and metal ions. So, waste water treatment may be done in several levels. So, many industries are looking forward to implement better and portable treatment technologies. Graphene is obtained from pencils, and then, the oxidation process is carried out in order to scatter the carbon layers with oxygen molecules; then, carbon layers are completely separated into single or multilayer by means of reduction

[1]. Graphene not only possesses extremely strong bond mechanically but also has high electromigration [2–8]. As well as, it cannot be dispersed in water or any other organic solvent [9]; other admirable properties are the improvement of a reasonable, biodegradable, and mass GO production, which would be highly significant [10, 11]. GO-silicon bilayer structure is experimented for humidity-sensing detection which exhibited outstanding humidity sensitivity [12]. Graphene has extended potential research applications in solar cells, corrosion prevention, fuel cells' display panels, circuit boards, detection of diseases [13–15], and flexible films [16]. The mechanical properties of polyurethane/graphene oxide/multilayer-graphene (PU/GO-MG) composites exhibit excellent chemical bonding [17]. Chemically reduced graphene oxide (RGO) revealed high sensitivity to NO_2 at the room temperature of 200°C [18]. Polypyrrole/graphene oxide (PPy/GO) indicates enhanced electrochemical performances because of its flexibility and electrochemical activity [19]. Liquid crystallinity nature of the graphene oxide has been well demonstrated [11]. Graphene oxide (GO) membranes are clearly exhibited as an excellent membrane for gas separation process, and it blocks everything except water vapour [20]. Graphene oxide (GO) derived chemically has been used as humidity sensitive coating deposited over quartz crystal microbalances (QCMs) to detect various relative humidity at room temperature [21, 22]. The capacity for graphene oxide to direct electrons relies upon the measure of oxidation in the compound, just as the strategy for amalgamation. It is the oxidization in the arrangement that aggravates electrical conductivity [23, 24], while profoundly oxidized graphene oxide would be an extremely poor channel of power, regardless of whether graphene oxide is to be vigorously decreased. However, it would potentially have the capacity to lead power, and it would in any case not be executed just as high-quality graphene monolayers as far as electron versatility is concerned. In any case, there are techniques that can be used to check this circumstance, and those are by a procedure frequently alluded as functionalization, which intends to artificially change a substance in request to build up its properties to suit a particular application. The properties include dispersibility, toxicity, hygroscopicity, and filtering ability. The subsequent artificially adjusted graphene could then conceivably turn out to be much increasingly versatile for practically boundless applications. Functionalization of graphene oxide can be done by numerous techniques.

2. Materials and Methods

Several methods were used for synthesis of GO such as Hummer's method, modified Hummers method, graphite oxide reduction method, graphite intercalation method, electrochemical method, organic synthesis method, carbon nanotubes conversion method, liquid stripping method, solvent thermal method, and arc-discharge method shown in Figure 1. One of the most commonly used methods was Hummer's method [25].

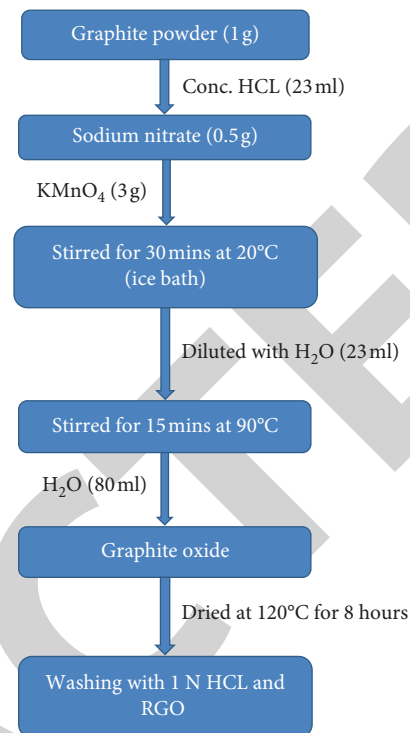


FIGURE 1: Process flowchart of graphene synthesis [25].

In this paper, the reduced graphene oxide is obtained through chemical synthesis. This method was highly recommended because the GO yield is high and the cost is also low compared with other methods.

2.1. Chemicals Required. Graphite powder, concentrated HCL (hydrochloric acid), sodium nitrate, potassium permanganate, distilled water, sulphuric acid, and hydrogen peroxide.

2.2. Hummer's Method of Synthesis. Graphene oxide is synthesized by Hummer's method through oxidation of graphite [25, 26]. The stepwise procedure is mentioned in Figure 2.

- (1) Graphite powder (1 g) and conc. HCL (23 mL) are taken in a beaker and kept in an ice bath at temperature $0\text{--}5^\circ\text{C}$, as shown in Figure 3
- (2) Sodium nitrate (0.5 g) is added in a beaker and stirred for 30 minutes at 20°C and KMnO_4 (3 g) is added into the beaker
- (3) After 30 minutes, it is diluted with H_2O (23 mL) and stirred for 15 minutes at 90°C ; after some time, H_2O (80 mL) is added to the solution
- (4) After stirring some time, graphite oxide is synthesized and then washed with 1N HCL (hydrochloric acid) several times
- (5) The washed graphite oxide is dried at 120°C for 8 hours, as shown in Figure 4, centrifuged, as shown in Figure 5, and dried, as shown in Figure 6, and, finally, reduced graphene oxide (rGO) is obtained

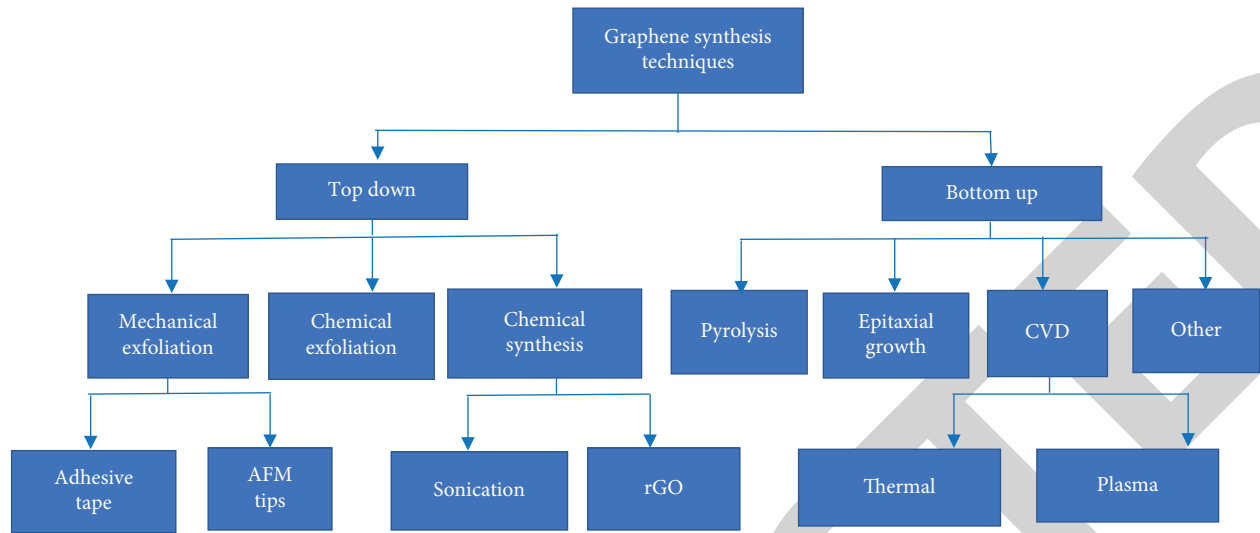


FIGURE 2: Flowchart of Hummer's method [27].



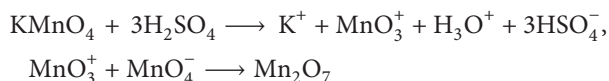
FIGURE 3: Mixture in ice bath below 2°C for about 1 hour.



FIGURE 4: Nanoparticles settled down after 8 hours.

- (6) The obtained graphene oxide may have some other chemical impurities; after centrifugation and further drying process, the final graphene oxide acts as nanofilters

The reaction between potassium permanganate and sulphuric acid will be represented by the following equation [26]:



(1)

GO was analysed using the FTIR analysis for atomic characteristics. The FTIR analysis proved that the sample was converted into a graphene oxide compound. The water samples from the industries and other impure water samples were taken, and it was analysed and filtered using graphene oxide nanoparticles. Graphene oxide allows only the water molecules and filters out various other chemical particles and impurities in the water sample. Graphene possessed the ability to filter out the various microorganisms, dissolved salts, and types of impurities in the water or industrial wastewater.



FIGURE 5: Centrifugation at 1500 rpm for 20 minutes.

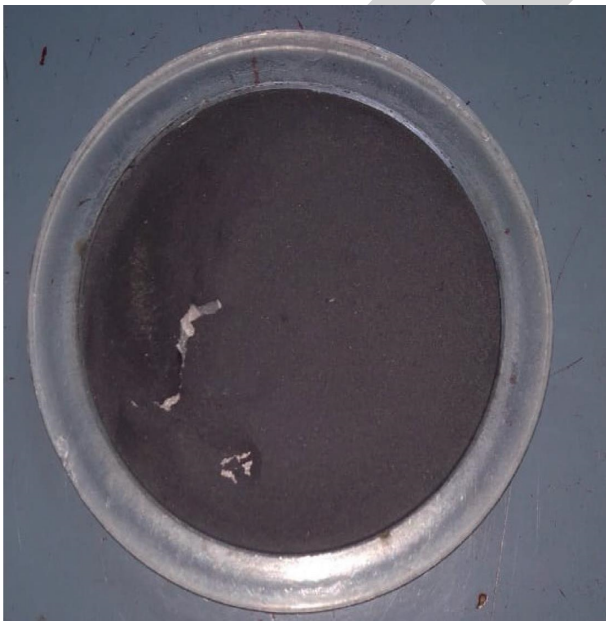


FIGURE 6: Dried at 120°C for 8 hours.

2.3. *Industrial Wastewater Analysis and Treatment.* pH indicates the percentage of hydrogen ions present in the solution. It is necessary to analyse the acidity, alkalinity, and salinity of the water coming out from the industry. Figure 7

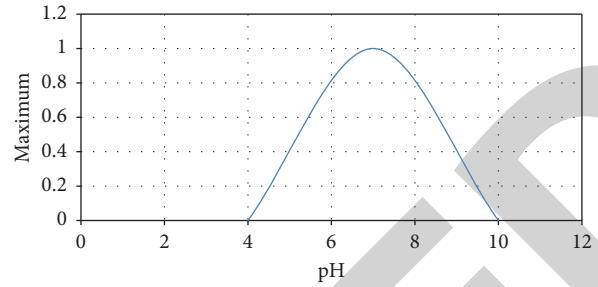


FIGURE 7: A plot for the growth of aquatic organisms as a function of pH.

shows the range of pH for the living organisms. The pH range is between 4 and 10 for the organisms alive.

In paper industries, the measurement of pH is most important due to various reasons:

- (1) Monitor the effluent from SO_2 plants from cooling towers in order to check the right operation of the process equipment
- (2) To prevent from corrosion
- (3) To maintain appropriate chemical equations
- (4) To help the operators to maintain the paper machines under good operating conditions
- (5) To adjust the alkaline or acid conditions for wastewater treatment

Earlier colour changing technique was used, but nowadays, it is replaced by standard pH indicating measurement and control. When neutral compounds are mixed with water, it breaks into more particles. The disassociation of this particle is called ions. When hydrochloric acid breaks, $\text{HCl} \rightarrow \text{H}^+ + \text{Cl}^-$; and it will become a strong acid. Likewise acetic acid breaks up, $\text{HAC} \rightarrow \text{H}^+ + \text{AC}^-$; it will become weak acid. The pH value of neutral solution (pure water) is 7. The definition to represent the pH will be given by the equation as $\text{pH} = -\log[\text{H}^+]$, i.e., negative logarithm of hydrogen ion concentration or $\text{pH} = \log 1/[\text{H}^+]$ log of reciprocal of hydrogen ion concentration.

Figure 8 shows the various levels of wastewater treatment. Majorly, it has been categorized into four types. In the preliminary treatment, all the nonfavourable wastes are eliminated or reduced. Suspended solids and other organic matters have been removed in primary treatment. In secondary treatment, soluble and colloidal organics was removed. Significant amount of phosphorous, heavy metals, viruses, bacteria, and biodegradable organics are removed in tertiary or advanced wastewater treatment.

3. Results and Discussion

The incorporated graphene oxide (GO) was prepared by Hummer's method, and the result was revealed by FTIR.

3.1. *Fourier Transform Infrared Spectrum Analysis.* Fourier transform infrared spectroscopy is used to examine the bonding structure. It is a framework grasped to get an

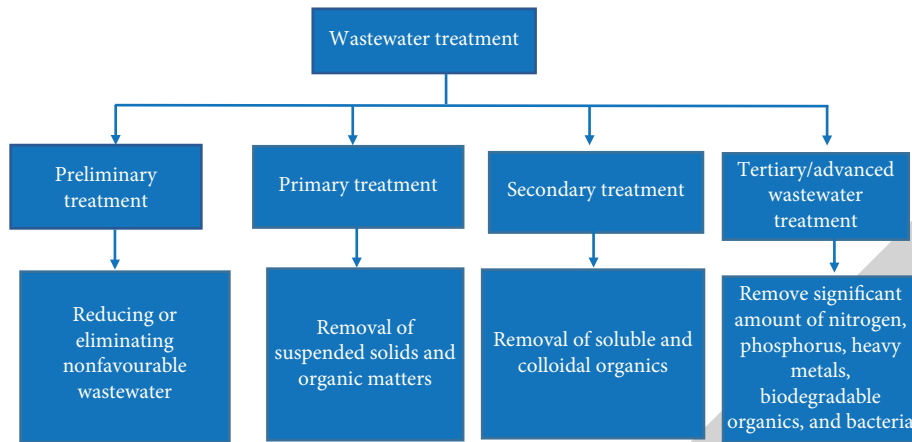


FIGURE 8: Various levels of wastewater treatment.

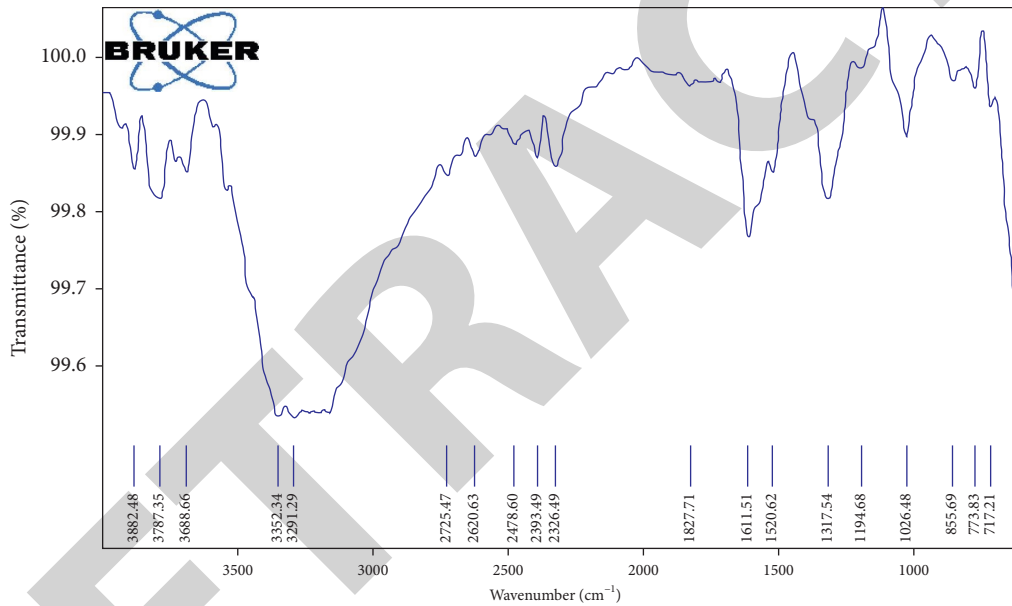


FIGURE 9: Fourier transform infrared spectra of GO.

infrared scope of maintenance, transmission, and photo-conductivity of a solid, gas, or liquid. It expects the powers of the pinnacles which are specifically identified with the sum of test present [28]. The incorporated GO has a crest at 1081 cm⁻¹ which is described to the C-O bond, affirming the nearness of oxide useful gatherings after the oxidation procedure. The crests in the scope of 1630 cm⁻¹ to 1650 cm⁻¹ demonstrate that the C=C security still stayed previously, furthermore, after the oxidation procedure shown in Figure 9. Water absorbed by GO was revealed by wide peak at 2885 cm⁻¹ to 3715 cm⁻¹, contributed by the O-H stretch of H₂O particles. The size of the nanoparticles is around 27–28 nm [26].

3.2. pH Analysis. The sample solution in Figure 10 containing some impurities and acidic content is first analysed and pH of that sample solution is measured. Then, synthesized GO nanoparticles are placed over the filter paper, and the sample solution is tested by pouring over the filter paper, as shown in Figure 11.

Table 1 shows the pH value of the sample solution at different levels. Before filtration, the sample indicates the pH value of 6.47. After first filtration, the pH value of the sample is 6.82, as shown in Figure 12. After the second filtration, the pH value is 6.91, as shown in Figure 13, which is around the neutral.



FIGURE 10: Sample solution pH value.



FIGURE 12: pH value after first filtration.



FIGURE 11: Filter using GO nanoparticles.

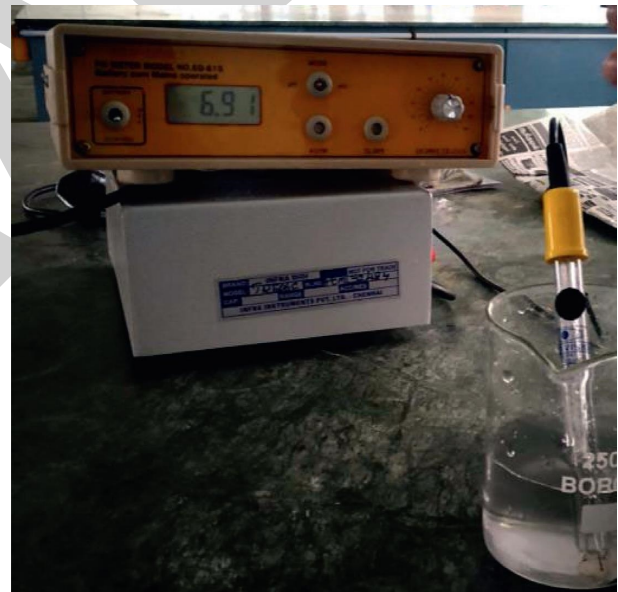


FIGURE 13: pH value after second filtration.

TABLE 1: pH value at different stages.

Nature of the sample	pH value
Sample before filtering	6.47
Sample after first filtration	6.82
Sample after second filtration	6.91

GO was produced from pencil graphite, so it may have some impurities, and it reduces the pH level. On further filtration with the purified GO nanoparticles' layer or paper, it will give better reduction in the pH value to around the neutral level.

4. Conclusion

Nanographene oxide filter paper was obtained by the Hummers method. Fourier transform infrared spectrum revealed the presence of C–O and C=C bonds. The graphene oxide nanofilters are able to filter out the impurities and also ability to reduce the pH level of the industrial waste water into a reusable form. Analysis provides the pH value as neutral around 7. Apart from this filtering ability, graphene oxide is used for gas sensing, energy storing, and to analyse current and voltage characteristics. Thus, graphene is one of the important and future of electronics, electrical, and various other important technologies around the world.

Retraction

Retracted: Parameters Optimization of Dissimilar Friction Stir Welding for AA7079 and AA8050 through RSM

Advances in Materials Science and Engineering

Received 26 December 2023; Accepted 26 December 2023; Published 29 December 2023

Copyright © 2023 Advances in Materials Science and Engineering. This is an open access article distributed under the Creative Commons Attribution License, which permits unrestricted use, distribution, and reproduction in any medium, provided the original work is properly cited.

This article has been retracted by Hindawi, as publisher, following an investigation undertaken by the publisher [1]. This investigation has uncovered evidence of systematic manipulation of the publication and peer-review process. We cannot, therefore, vouch for the reliability or integrity of this article.

Please note that this notice is intended solely to alert readers that the peer-review process of this article has been compromised.

Wiley and Hindawi regret that the usual quality checks did not identify these issues before publication and have since put additional measures in place to safeguard research integrity.

We wish to credit our Research Integrity and Research Publishing teams and anonymous and named external researchers and research integrity experts for contributing to this investigation.




The corresponding author, as the representative of all authors, has been given the opportunity to register their agreement or disagreement to this retraction. We have kept a record of any response received.

References

- [1] M. Kavitha, V. M. Manickavasagam, T. Sathish et al., "Parameters Optimization of Dissimilar Friction Stir Welding for AA7079 and AA8050 through RSM," *Advances in Materials Science and Engineering*, vol. 2021, Article ID 9723699, 8 pages, 2021.

Research Article

Parameters Optimization of Dissimilar Friction Stir Welding for AA7079 and AA8050 through RSM

M. Kavitha,¹ V. M. Manickavasagam,² T. Sathish ,³ Bhiksha Gugulothu ,⁴
A. Sathish Kumar,⁵ Sivakumar Karthikeyan ,⁶ and Ram Subbiah⁷

¹Department of Electrical and Electronics Engineering, Sathyabama Institute of Science and Technology, Rajiv Gandhi Salai, Chennai, Tamil Nadu, India

²Department of Mechanical Engineering, Sri Sairam Engineering College, Sai Leo Nagar West Tambaram, Chennai 44, Tamil Nadu, India

³Department of Mechanical Engineering, Saveetha School of Engineering, SIMATS, Chennai 602 105, Tamil Nadu, India

⁴Department of Mechanical Engineering, Bule Hora University, P.O. Box 144, Addis Ababa, Bule Hora, Ethiopia

⁵Department of Electrical and Electronics Engineering, Holy Mary Institute of Technology and Science, Keesara-Bogaram-Ghatkesar Rd, Kondapur, Telangana 501301, India

⁶Department of Mechanical Engineering, SRM Valliammai Engineering College, Kattankulathur SRM Nagar, Chennai 603203, Tamil Nadu, India

⁷Department of Mechanical Engineering, Gokaraju Rangaraju Institute of Engineering and Technology, Nizampet, Hyderabad, India

Correspondence should be addressed to Bhiksha Gugulothu; bhikshagugulothu14251425@gmail.com

Received 23 June 2021; Accepted 12 July 2021; Published 17 July 2021

Academic Editor: Samson Jerold Samuel Chelladurai

Copyright © 2021 M. Kavitha et al. This is an open access article distributed under the Creative Commons Attribution License, which permits unrestricted use, distribution, and reproduction in any medium, provided the original work is properly cited.

Aluminium alloy is widely used in engineering application, and it can be classified based on the constituent elements or alloying elements. Aluminium alloy is preferred for the nature of its tensile strength, ductility, and corrosion resistance in this research to make a dissimilar friction stir welding joint of aluminium alloys 7079 and 8050 materials. The tensile strength of the weld joint is estimated by the influence of the response surface methodology approach. The welding is carried out by preferred process parameters with a tool speed of 1000–2500 rpm, tool pin diameter of 2–6 mm, welding speed of 50–300 mm/min, and tool shoulder diameter of 10–20 mm. The ANOVA analysis and the prediction of tensile strength were conducted efficiently. From the RSM analysis, the tool pin diameter mostly modified the output of the result.

1. Introduction

The novel technique joins the material permanently by using the friction stir welding process, and the nonconsumable tool is applied to carry the welding process. One best advantage of the FSW process is, without melting the work samples during welding, heat is introduced between tool rotation and specimens [1–3]. The welding is carried out along the straight line in a longitudinal manner of tool movement to join the samples. The homogeneous mixture is achieved applying the pressure in the joint area (soft region) of the specimens. The FSW process effectively joins all alloys

such as aluminium alloys, titanium alloys, copper alloys, magnesium alloys, and steel material by a similar or dissimilar mode. This welding is now fruitfully used in joining polymers, and the FSW process is carried out by Wayne Thomas at TWI Ltd. in 1991 [4–6]. Most of the aluminium alloy is used in the ship building, automotive segment, and aerospace sectors. The different tool profiles are used in friction stir welding as cylindrical, square triangular, and threaded, and the tool rotates and passes through a straight line mode [7]. The shoulder diameter is big in size compared to tool pin diameter, and the pin of the tool plunges into work pieces effectively [8]. The pin rotates at high speed with

intercombination of materials carried out efficiently. The microstructure changed by means of stirring action; it causes the swap of particles from one material to another one remarkably. The strength of the joint is increased, and to form a rigid structure, the study of different zones in the welded area is very important in the friction stir welding process. In arc welding, gas welding and other types of the welding process formed lot of defects, but this FSW process eliminates or minimizes the welding defects if using any material with various parameters [9]. The FSW process is mainly used to make butt joint, even though lap joints are also carried in the FSW process. For the past research, the dissimilar friction stir welding of AA7079 and AA8050 is through response surface methodology. The influence of different process parameters is to evaluate the tensile strength of the weld joint successfully. RSM is a statistical technique to find the optimal parameters and the maximum range of the output value [10–12].

2. Materials

The friction stir welding process planned to make dissimilar aluminium alloy materials such as AA7079 and AA8050. The chemical composition of both the materials is tabulated with their weight percentage in Table 1.

The aluminium alloy 7079 has a wrought alloy with a heat treatable mode, and it has extraordinary strength. It possesses good machinability and workability characters; this alloy is mainly used in the high stressed parts. In the air wings parts, this alloy played a major role in hydraulic function units. The AA8050 aluminium alloy has good strength easy to modify any shape; it has high corrosion resistance behaviour. This alloy can be used in the body building industries.

3. Experimental Procedure

The FSW process considers the process parameters, and all the factors and their values are given in Table 2.

The factors are tool speed (1000–2500 rpm), tool pin diameter (2–6 mm), welding speed (50–300), and shoulder diameter (10–20). The friction stir welding process specimens prepared under the dimensions are 100*50*5 mm for each plate [13]. The straight cylindrical profile tool and the material of HSS tool is used to weld the specimen effectively (Figure 1). The CNC vertical milling machine was used to weld the samples under the various parameters [14]. The specimens are rigidly fixed on the fixture with the proper clamp, the tool rotated above the top surface of the specimens, and the axial force is applied to the tool. The tool rotated clockwise direction, moved, and penetrated the samples in longitudinal direction, and the weld joint was produced accurately. The tensile test was conducted by the influence of UTM machine.

TABLE 1: Chemical composition of AA7079 and AA8050.

Material	% of composition of AA7079	% of composition of AA8050
Cr	0.2	0.05
Cu	0.6	0.05
Fe	0.2	1.2
Mg	3.5	0.05
Mn	0.25	0.85
Si	0.25	0.03
Zn	4.0	0.1
Ti	0.7	—
Al	Remaining	Remaining

TABLE 2: FSW factors and its values.

Notation	Factors	Low	High
A	Tool speed (rpm)	1000	2500
B	Tool pin diameter (mm)	2	6
C	Welding speed (mm/min)	50	300
D	Shoulder diameter (mm)	10	20

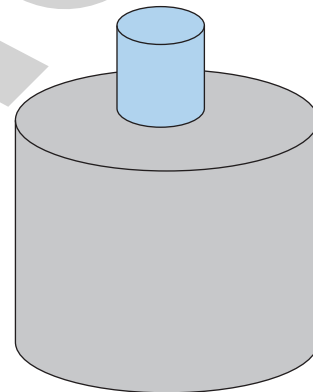


FIGURE 1: FSW cylindrical tool.

4. Result and Discussion

The code value of the experiment, the process factors contribution, and the result of the tensile strength are given in Table 3.

In Table 4, the ANOVA linear model produced the major contribution of tool pin diameter as 6.38% [15]. In the square model, the tool pin diameter * tool pin diameter has contributed at 26.33%, and in the 2-way interaction model, the tool speed (rpm) * tool pin diameter (mm) has the higher percentage contribution such as 6.13%

Figure 2 shows the maximum tensile strength 212 MPa obtained by the influence of tool speed of 1750 rpm, tool pin diameter of 4 mm, welding speed of 300 mm, and shoulder diameter of 20 mm.

TABLE 3: FSW factors contribution and the result of tensile strength.

Experiment no.	A	B	C	D	Tool speed (rpm)	Tool pin diameter (mm)	Welding speed (mm/min)	Shoulder diameter (mm)	Tensile strength (MPa)
1	0	0	0	0	1750	4	175	15	162
2	1	0	0	-1	2500	4	175	10	150
3	1	0	0	1	2500	4	175	20	190
4	0	1	0	-1	1750	6	175	10	92
5	0	-1	0	1	1750	2	175	20	110
6	1	1	0	0	2500	6	175	15	196
7	-1	0	-1	0	1000	4	50	15	208
8	0	-1	-1	0	1750	2	50	15	79
9	0	-1	1	0	1750	2	300	15	125
10	-1	0	0	1	1000	4	175	20	184
11	-1	1	0	0	1000	6	175	15	124
12	1	0	-1	0	2500	4	50	15	157
13	0	0	1	1	1750	4	300	20	212
14	-1	-1	0	0	1000	2	175	15	130
15	1	-1	0	0	2500	2	175	15	90
16	0	1	0	1	1750	6	175	20	186
17	0	-1	0	-1	1750	2	175	10	85
18	0	0	-1	-1	1750	4	50	10	176
19	-1	0	1	0	1000	4	300	15	146
20	0	0	0	0	1750	4	175	15	85
21	0	0	-1	1	1750	4	50	20	192
22	0	0	0	0	1750	4	175	15	156
23	0	1	-1	0	1750	6	50	15	137
24	0	1	1	0	1750	6	300	15	82
25	1	0	1	0	2500	4	300	15	97
26	0	0	1	-1	1750	4	300	10	211
27	-1	0	0	-1	1000	4	175	10	173

TABLE 4: Analysis of variance summary.

Source	DF	Seq SS	Contribution (%)	Adj SS	Adj MS	F value	P value
Model	14	34385.4	67.19	34385.4	2456.10	1.76	0.167
Linear	4	7264.5	14.19	7264.5	1816.12	1.30	0.325
Tool speed (rpm)	1	602.1	1.18	602.1	602.08	0.43	0.524
Tool pin diameter (mm)	1	3267.0	6.38	3267.0	3267.00	2.33	0.152
Welding speed (mm/min)	1	481.3	0.94	481.3	481.33	0.34	0.568
Shoulder diameter (mm)	1	2914.1	5.69	2914.1	2914.08	2.08	0.175
Square	4	19976.9	39.03	19976.9	4994.23	3.57	0.039
Tool speed (rpm)*tool speed (rpm)		1385.6	2.71	1415.6	1415.56	1.01	0.334
Tool pin diameter (mm)*tool pin diameter (mm)		13475.0	26.33	6471.3	6471.26	4.62	0.053
Welding speed (mm/min)*welding speed (mm/min)	1	59.6	0.12	960.0	960.04	0.69	0.424
Shoulder diameter (mm)*shoulder diameter (mm)	1	5056.7	9.88	5056.7	5056.68	3.61	0.082
2-way interaction	6	7144.0	13.96	7144.0	1190.67	0.85	0.556
Tool speed (rpm)*tool pin diameter (mm)		3136.0	6.13	3136.0	3136.00	2.24	0.160
Tool speed (rpm)*welding speed (mm/min)	1	1.0	0.00	1.0	1.00	0.00	0.979
Tool speed (rpm)*shoulder diameter (mm)	1	210.2	0.41	210.3	210.25	0.15	0.705
Tool pin diameter (mm)*welding speed (mm/min)	1	2550.2	4.98	2550.2	2550.25	1.82	0.202
Tool pin diameter (mm)*shoulder diameter (mm)	1	1190.2	2.33	1190.3	1190.25	0.85	0.375
Welding speed (mm/min)*shoulder diameter (mm)	1	56.2	0.11	56.2	56.25	0.04	0.844
Error	12	16793.8	32.81	16793.8	1399.48		
Lack of fit	10	13125.1	25.65	13125.1	1312.51	0.72	0.708
Pure error	2	3668.7	7.17	3668.7	1834.33		
Total	26	51179.2	100.00				

5. Prediction for Tensile Strength (MPa)

The regression equation in uncoded units is given as follows.
 Tensile strength (MPa) = 533 - 0.215 tool speed (rpm) + 37.1 tool pin diameter (mm) + 0.133 welding speed (mm/min) -

43.1 shoulder diameter (mm) + 0.000029 tool speed (rpm) * tool speed (rpm) - 8.71 tool pin diameter (mm) * tool pin diameter (mm) + 0.00086 welding speed (mm/min) * welding speed (mm/min) + 1.232 shoulder diameter (mm) * shoulder diameter (mm) + 0.0187 tool speed (rpm) * tool

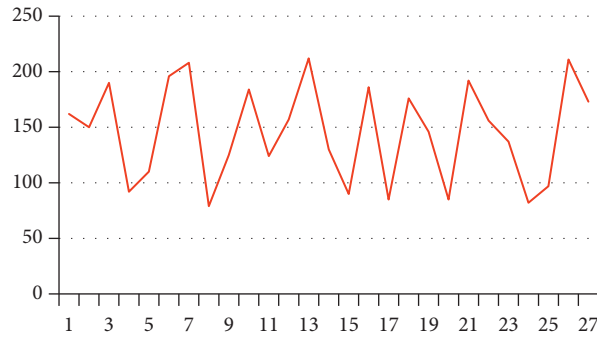


FIGURE 2: Number of specimens vs. tensile strength.

TABLE 5: Response optimization parameters and values setting.

Response optimization	Tensile strength (MPa)
Parameters	Tool speed (1000 rpm) Tool pin diameter (2 mm) Welding speed (50 mm/min) Shoulder diameter (10 mm)
Goal	Tensile strength (MPa) maximum Lower 79
Response importance tensile strength (MPa)	Target 212 Upper 1 Weight 1

TABLE 6: Response optimization.

Tool speed (rpm)	Tool pin diameter (mm)	Welding speed (mm/min)	Shoulder diameter (mm)	Tool strength (MPa)
1000	2.344	300	10	211.428

TABLE 7: Prediction for tensile strength (MPa).

Multiple response prediction				
Variable setting				
Tool speed (rpm)	1000 rpm			
Tool pin diameter (mm)	2.44440 mm			
Welding speed (mm/min)	300 mm/min			
Shoulder diameter (mm)	10 mm			
Response	Fit	SE fit	95% CI	95% PI
Tensile strength (MPa)	211.4	51.1	(100.0, 322.9)	(73.4, 349.5)

pin diameter (mm) + 0.000005 tool speed (rpm) * welding speed (mm/min) + 0.00193 tool speed (rpm) * shoulder diameter (mm) - 0.1010 tool pin diameter (mm) * welding speed (mm/min) + 1.72 tool pin diameter (mm) * shoulder diameter (mm) - 0.0060 welding speed (mm/min) * shoulder diameter (mm).

6. Solution

Tables 5 and 6 illustrate the response optimization parameters and values setting and response optimization of tensile strength, respectively, and there are four factors involved for this experiment. Table 7 presents the prediction for tensile strength (MPa) and the values.

The numerical response optimizer used to create an optimal set of factors involving to offer the maximum tensile strength is shown in Figure 3. In this study, the main target of the result is to maximize the tensile strength. From the graph, it involves predicting tensile strength as the optimum factor of tool speed of 1000 rpm, tool pin diameter of 2.4 mm, welding speed of 300 mm/min, and shoulder diameter of 10 mm, offering the maximum tensile strength of 211.48 MPa.

Figure 4 shows the maximum tensile strength obtained by interaction of pin diameter, the tool speed has fixed as 1700 rpm, the tool pin has 4 mm diameter, and the maximum tensile strength was obtained as 170 MPa. In this experiment, Figure 5 illustrates the maximum tensile

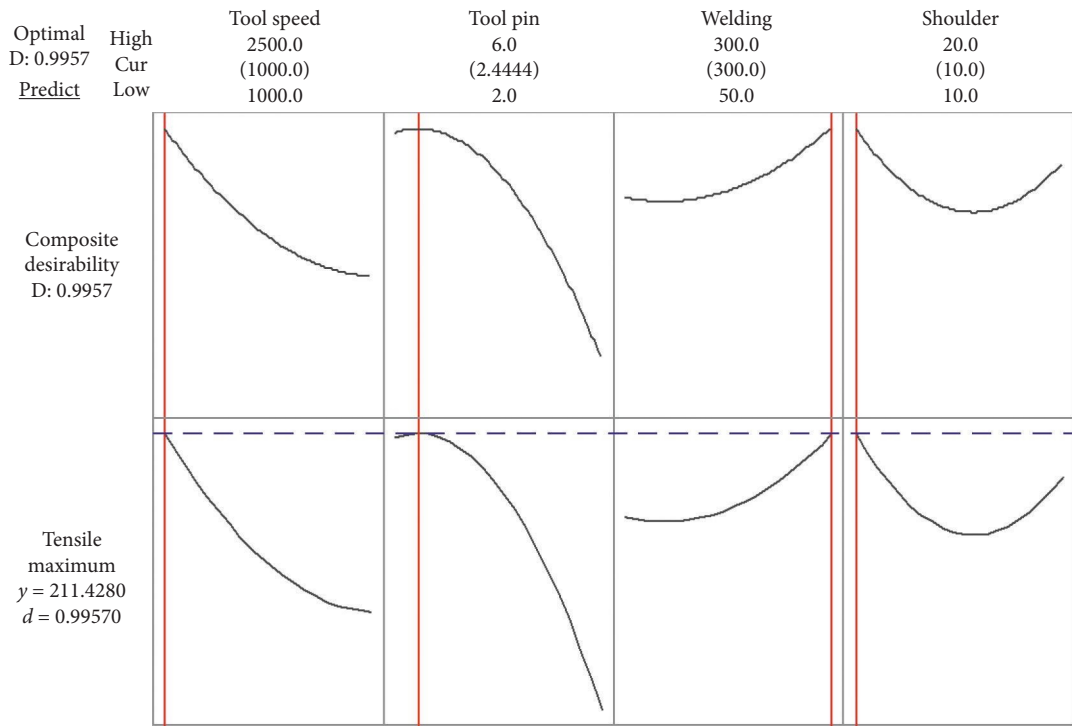


FIGURE 3: Numerical response optimizer graph.

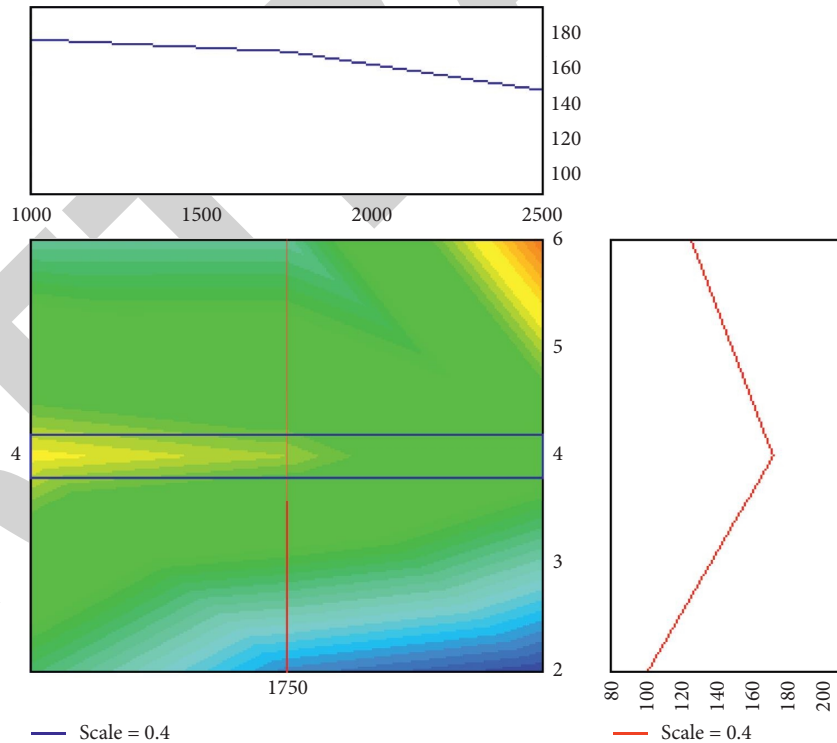


FIGURE 4: Tool speed graph, tool pin diameter vs. tensile strength.

strength offered by the welding speed interaction, the tool pin diameter is fixed as 4 mm, welding speed is 175 mm/min, and the maximum tensile strength obtained is 160 MPa. The welding speed graph in Figure 6 shows that the welding

speed has fixed as 175 mm/min, the maximum tensile strength produced by shoulder diameter interaction. The shoulder diameter of 15 mm influenced to produce the maximum tensile strength as 138 MPa.

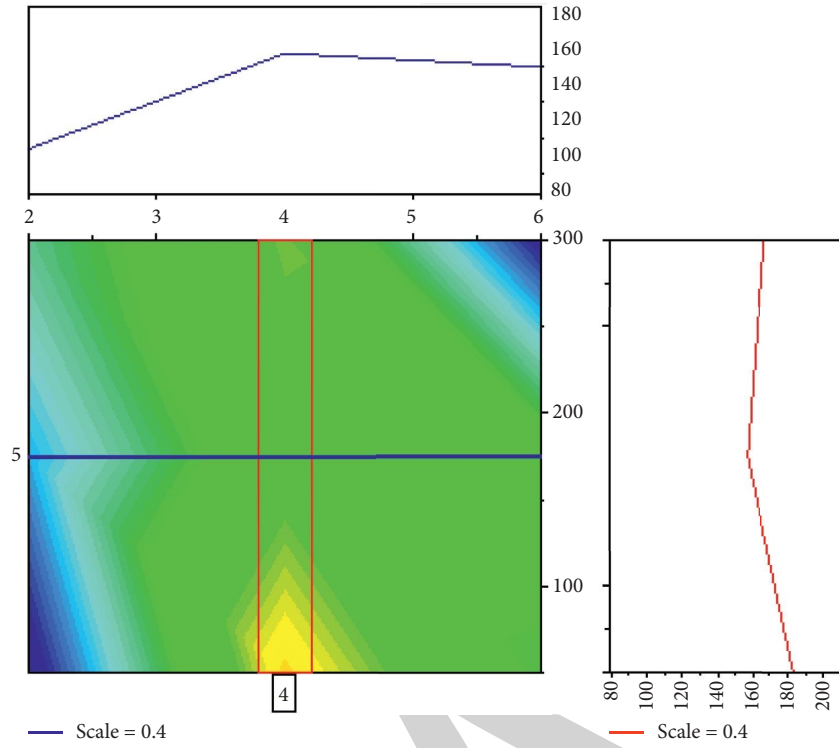


FIGURE 5: Tool pin graph, welding speed vs. tensile strength.

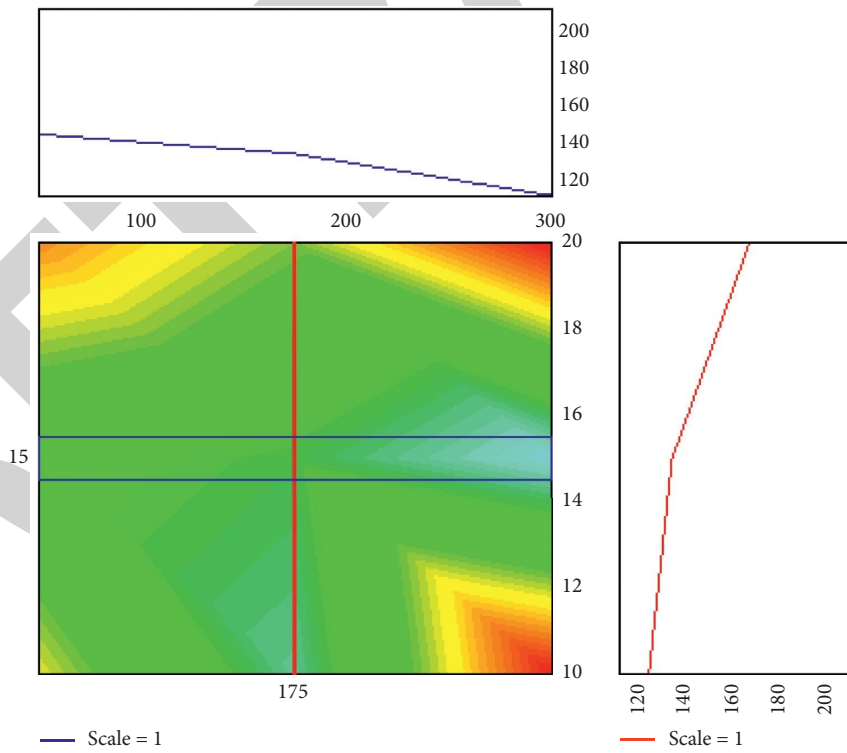


FIGURE 6: Welding speed graph, shoulder diameter vs. tensile strength.

7. Conclusion

The dissimilar friction stir welding of AA7079 and AA8050 aluminium alloy jointed efficiently applying straight cylindrical tool. The response surface methodology was implemented to find the maximum tensile strength and the optimal parameters. The output of this experiment is drawn as follows:

- (1) From the analysis of variance, in the liner model, the major contribution of tool pin diameter was 6.38%, in the square model, the tool pin diameter * tool pin diameter has contributed at 26.33%, and in the 2-way interaction model, the tool speed (rpm) * tool pin diameter (mm) has the higher percentage contribution such as 6.13%
- (2) The maximum tensile strength 212 MPa was obtained by the influence of tool speed of 1750 rpm, tool pin diameter of 4 mm, welding speed of 300 mm, and shoulder diameter of 20 mm
- (3) For the predicted analysis, the optimum factor of tool speed of 1000 rpm, tool pin diameter of 2.4 mm, welding speed of 300 mm/min, and shoulder diameter of 10 mm offered the maximum tensile strength of 211.48 MPa. The predicted tensile strength and the response optimized tensile strength values are near, since the four factors and the values of this evaluation were good.
- (4) Further scope of this study was extended to conduct friction stir processing (FSP) to modify the surface structure of the dissimilar materials

Data Availability

The data used to support the findings of this study are included within the article, and further data or information required is available from the corresponding author upon request.

Disclosure

It was performed as a part of the employment of Bule Hora University, Ethiopia.

Conflicts of Interest

The authors declare that there are no conflicts of interest.

Acknowledgments

The authors appreciate the supports from Bule Hora University, Ethiopia, and thank Saveetha School of Engineering, Chennai, for the technical assistance to complete this experimental work.

References

- [1] M. Ghaffarpour, B. M. Dariani, A. H. Kokabi, and N. A. Razani, "Friction stir welding parameters optimization of heterogeneous tailored welded blank sheets of aluminium alloys 6061 and 5083 using response surface methodology," *Proceedings of the Institution of Mechanical Engineers-Part B: Journal of Engineering Manufacture*, vol. 226, no. 12, pp. 2013–2022, 2012.
- [2] M. Koilraj, V. Sundareswaran, S. Vijayan, and S. R. Koteswara Rao, "Friction stir welding of dissimilar aluminum alloys AA2219 to AA5083-optimization of process parameters using Taguchi technique," *Materials & Design*, vol. 42, pp. 1–7, 2012.
- [3] K. Jagathesh, M. P. Jenarathanan, P. D. Babu, and C. Chanakyan, "Analysis of factors influencing tensile strength in dissimilar welds of AA2024 and AA6061 produced by friction stir welding (FSW)," *Australian Journal of Mechanical Engineering*, vol. 15, no. 1, pp. 19–26, 2017.
- [4] T. Sathish, P. Sevvel, P. Sudharsan, and V. Vijayan, "Investigation and optimization of laser welding process parameters for AA7068 aluminium alloy butt joint," *Materials Today: Proceedings*, vol. 37, pp. 1672–1677, 2021.
- [5] R. Palanivel, R. Laubscher, S. Vigneshwaran, and I. Dinaharan, "Prediction and optimization of the mechanical properties of dissimilar friction stir welding of aluminum alloys using design of experiments," *Proceedings of the Institution of Mechanical Engineers-Part B: Journal of Engineering Manufacture*, vol. 232, no. 8, pp. 1384–1394, 2018.
- [6] N. M. Daniolos and D. I. Pantelis, "Microstructural and mechanical properties of dissimilar friction stir welds between AA6082-T6 and AA7075-T651," *International Journal of Advanced Manufacturing Technology*, vol. 88, no. 9-12, pp. 2497–2505, 2017.
- [7] T. Sathish, S. Rangarajan, A. Muthuram, and R. P. Kumar, "Analysis and modelling of dissimilar materials welding based on K-nearest neighbour predictor," *Materials Today: Proceedings*, vol. 21, pp. 108–112, 2020.
- [8] S. Verma, M. Gupta, and J. P. Misra, "Optimization of process parameters in friction stir welding of armor-marine grade aluminium alloy using desirability approach," *Materials Research Express*, vol. 6, no. 2, Article ID 026505, 2018.
- [9] R. I. Rodriguez, J. B. Jordon, P. G. Allison, T. Rushing, and L. Garcia, "Microstructure and mechanical properties of dissimilar friction stir welding of 6061-to-7050 aluminum alloys," *Materials & Design*, vol. 83, pp. 60–65, 2015.
- [10] R. Kadaganchi, M. R. Gankidi, and H. Gokhale, "Optimization of process parameters of aluminum alloy AA 2014-T6 friction stir welds by response surface methodology," *Defence Technology*, vol. 11, no. 3, pp. 209–219, 2015.
- [11] M. M. Z. Ahmed, S. Ataya, M. M. El-Sayed Seleman, H. R. Ammar, and E. Ahmed, "Friction stir welding of similar and dissimilar AA7075 and AA5083," *Journal of Materials Processing Technology*, vol. 242, pp. 77–91, 2017.
- [12] S. Gholivand, O. Lasekan, C. P. Tan, F. Abas, and L. S. Wei, "Optimization of enzymatic esterification of dihydrocaffeic acid with hexanol in ionic liquid using response surface methodology," *Chemistry Central Journal*, vol. 11, no. 1, pp. 44–10, 2017.

Research Article

Study of Complex Helical Drill with a “S” Type Chisel Edge Tip Orient to Carbon Fiber Reinforced Plastics

Yu He ¹, Xiaolong Zhou ^{2,3}, Ping Zou,³ and Kun Liu⁴

¹School of Urban Rail Transportation, Shanghai University of Engineering Science, Shanghai 201620, China

²Beijing Jingdiao Group, Beijing 102308, China

³School of Mechanical Engineering and Automation, Northeastern University, Shenyang 110819, China

⁴School of Mechanical Engineering, Shanghai Jiao Tong University, Shanghai 200240, China

Correspondence should be addressed to Xiaolong Zhou; 1310054@stu.neu.edu.cn

Received 18 May 2021; Revised 31 May 2021; Accepted 28 June 2021; Published 14 July 2021

Academic Editor: João Paulo Davim

Copyright © 2021 Yu He et al. This is an open access article distributed under the Creative Commons Attribution License, which permits unrestricted use, distribution, and reproduction in any medium, provided the original work is properly cited.

In this paper, a complex helicoids' drill tip of “S” type chisel edge grinded with a three-parallel universal CNC grinding machine tool is carefully studied to obtain the optimum drill bit tip geometry parameters. The effects of experimental parameters, such as apex angle, chisel edge incline angle, and structure circumference rear angle, on the quality of the drilling hole and the machining force were studied from the orthogonal experiment compared with the ordinary drill bit. The range of technological parameters are confirmed which should be used during the drilling process of carbon fiber reinforced plastics (CFRP) in order to realize the reduction of cutting defects such as cutting force and spurs. The effect of spindle speed and feed on the drilling behaviour of the experiment using optimum complex helicoids' drill tip is also analyzed. It is found that the feed has a great influence on the drilling axial force and the spindle speed has little influence on axial force, but great influence on torque.

1. Introduction

Carbon fiber reinforced plastics (CFRP) are characterized by lightweight, stiffness-to-weight ratios, high fracture toughness, and good heat resistance [1]. They have been widely used in airplanes, chemical machinery, communication, transportation, sport equipment, and textweave. However, there are many questions in drilling CFRP because of the most frequent defects, including delamination, fiber pull-out, interlaminar cracks, and thermal degradation after the drilling process. Drilling is the most commonly applied method in conventional machining, accounting for as much as 40% of all material removal processes. So drilling of CFRP has been taken as an important subject in the research field of machining. Due to heterogeneity and anisotropy of CFRP, the drilling principle is different from that in metal drilling. The drilling process of metal materials is mainly dominant by elastic-plastic deformation. The continuous drilling chip in metal materials' machining cannot be formed in the CFRP process. König et al. [2] carried out experimental research on

CFRP drilling in 1985 and concluded that excessively high feed rate during drilling would lead to defects such as delamination tearing at the drilling outlet. Chambers and Bishop [3] studied the drilling parameters of carbon fiber composites in 1995 and concluded that the drilling quality during CFRP drilling was mainly related to the properties of the matrix and the overall performance of the PCD tool. Chen [4] in 1997, by adopting different apex angles, chisel edge angles, and spiral angles of the drill point, conducted the drilling experiment of carbon fiber composite materials. They analyzed the effect of different drill tip geometry parameters on the drilling force and tear. Xu et al. [5] studied the CFRP material machining in terms of wear behavior and machining responses. Rawal et al. [6] detected the milling defects on CFRP structures using the sensor-based online quality monitoring system. Kumar and Verma [7] optimized the multiple response in machining (milling) of graphene oxide-doped EPOXY/CFRP composite using COCOSO-PCA. Furuki et al. [8] developed CBN electroplated end-mill combined cutting and grinding for precision machining of

CFRP. Piquet et al. [9] analyzed the drilling damage in the thin carbon/epoxy laminate using special drills. Yuan et al. [10] investigated the grinding of carbon/epoxy composites using the electroplated CBN wheel with controlled abrasive clusters. Lin and Chen [11] explored the drilling process of the carbon fiber reinforced composite material at high speed. Wang et al. [12, 13] conducted the right-angle free cutting experiment of the one-way type and multiway type CFRP. The relation between the shear force and cutting force of the carbon fiber and resin matrix is obtained when the cutting speed direction and carbon fiber direction angle are in a certain range. Arola et al. [14, 15] used a CCD camera to observe the cutting process of CFRP and FRP composites, and the final observation results showed that the angle between the rake angle of the main cutting edge of the drill tip and the fiber direction had a great influence on the chip formation process during the cutting of fiber reinforced composites. Mihai and Paul [16] analyzed the drilling process of fiber reinforced composites. Vijayan analyzed the high-speed drilling CFRP sheet using the carbide drill bit, by changing the spindle speed and feed [17]. The factor of the influence of drilling parameters on the quality of the hole was determined by using the variance analysis method, and the optimum drilling parameters were obtained. Wei and Feng [18] studied the parameterized geometric design for the complex helical drill point.

Considering that the machinability of CFRP is relatively poor, in this work, a complex helicoids' drill tip of "S" type chisel edge grinded with a three-parallel universal CNC grinding machine tool is carefully studied to obtain the optimum drill bit tip geometry parameters in order to realize the reduction of cutting defects such as cutting force and spurs in the CFRP plate drilling and realize the high-quality drilling. The effect of spindle speed and feed on the drilling behaviour of the experiment using the optimum complex helicoids' drill tip is also analyzed. It is found that the feed has a great influence on the drilling axial force and the spindle speed has little influence on axial force, but great influence on torque.

2. Drilling of CFRP

Due to the inhomogeneity and anisotropy, the chip formation during drilling of CFRP is different from metal materials. The drilling force of twist drill in the drilling process is shown in Figure 1.

According to the structure of twist drill, the rake angle of the main cutting edge of twist drill attains the largest at the turning point of the outer edge, and the closer to the center, the smaller the rake angle is. When it is close to the center, the rake angle becomes negative gradually. The negative value reaches the largest at the chisel edge. In the drilling process, the main cutting effect is from the positive rake angle of the main cutting edge, which leads to that the CFRP is cut off to the fragmented chip. The cutting force in the cutting process of the main cutting edge mainly contains two parts: one is tangential force F_{v1} along the direction of the cutting speed which cuts off the carbon fiber during the drilling process, and the other is the upward axial force F_{z1}

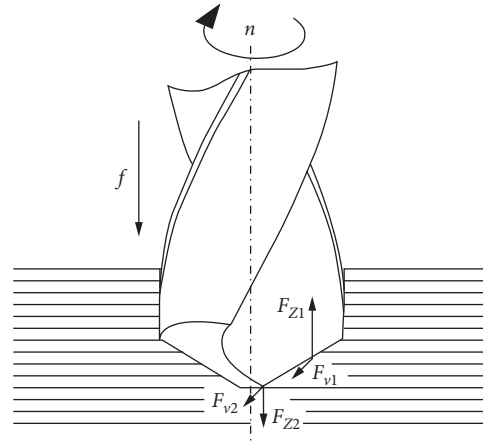


FIGURE 1: Schematic of drill thrust.

increased by the joint action of the cutting edge and twist drill rake face, which has the effect of stripping the fiber layer upward during drilling CFRP. The effect on the inlet side of the drilled hole is particularly obvious, and the tear at the inlet side is mainly caused by F_{z1} . In the main cutting edge of the negative rake angle and chisel edge area, the cutting situation is worse, especially in the chisel edge; in this part, the linear velocity is low, the role of which is to roll up and smash the carbon fiber to chip, and the effect of this part of the structure on the CFRP in the drilling process mainly contains two parts of force, one is tangential force F_{v2} along the tangent direction and the other is downward vertical axial force F_{z2} ; these force components in the process of drilling accounted for 50%~60% of total axial force [19], to which both delamination and outlet tearing during drilling CFRP are directly related.

The base material of the CFRP laminates used in the experiment is epoxy resin, and the reinforcing material is carbon fiber, which is made of multidirectional braided prepreg cloth laid in layers. The specific conditions of the CFRP laminates are shown in Table 1.

The CFRP is a braided composite material, which is composed of multilayer $0^\circ/90^\circ$ interwoven prepreg cloth laid layer by layer. The tool adopted is an ordinary high-speed steel drill bit produced by Haliang Cutting Tool Factory (China); the complex helical surface grinding method is used to grind the drill tip. The drill tip grinding machine is a three-parallel universal joint CNC grinding machine independently developed by Northeastern University (China). It is equipped with control system PCI-1234U, as shown in Figure 2. This machine tool can theoretically grind the complex helicoid drilling point of any parameter.

The drilling experimental platform is composed of a drilling test bed and a drilling force measurement system. The drilling test bench (Figure 3) is a Z3040 radial drilling machine, whose maximum speed is 2000 r/min and feed is 0.04~3.2 mm/r. The drilling force measuring system is composed of SDC series precision drilling force measuring instrument (Figure 3), FS-21/4A (four-channel) DC strain amplifier, analog/digital conversion board, special cable, data acquisition card, data processing software FAS-4D-3, and computer. The main purpose of this study is to find the

TABLE 1: The properties of CFRP.

Reinforcing material	Carbon fiber
Base material	Epoxy
Layer form	0°/90° weaving prepreg cloth
Fiber volume fraction (%)	60
Thickness (mm)	5
Length (mm)	400
Width (mm)	400

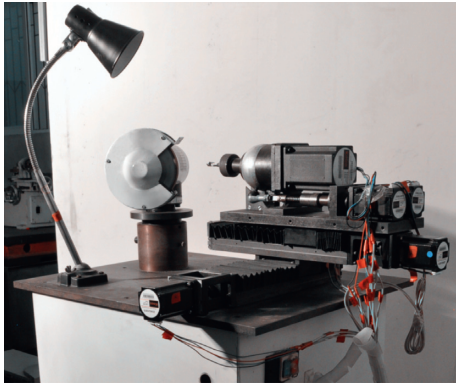


FIGURE 2: Three-parallel CNC grinding machine.



FIGURE 3: Z3040 radial drilling machine.

best drill bit geometric parameters to drill CFRP laminated plates.

3. Experimental Results and Analysis of Drill Tip Geometric Parameters

Under the process parameters of speed $n = 800$ r/min and feed $f = 0.04$ mm/r, drill tips with different geometrical parameters were used to carry out single-factor drilling comparison experiments.

3.1. Influence of Drill Apex Angle on Drilling Force and Tear. With the standard twist drill apex angle 118° as the reference, 100° , 110° , 115° , 120° , 125° , 130° , 140° , and 150° were selected as the apex angle value, respectively, the rear angle value is

10° , and the chisel edge incline angle value for grinding is 60° . The grinding drill bit shape is shown in Figure 4.

The apex angle of the drill tip is mainly determined by the angle between the grinding wheel axis and the drill tip axis. Under the condition that the process parameters are the spindle speed of 800 r/min and the feed rate of 0.04 mm/r, eight drill bits with different vertices are used for drilling, respectively. Figure 5 shows the pictures of the hole inlet and outlet after drilling with several bits.

From Figure 6, it can be seen that the change of the size of the apex angle has a significant influence on the tearing at the inlet and outlet. On the inlet side, the tear defects are relatively small, and the tear factor decreases first and then increases with the increase of the apex angle, and the minimum is near the apex angle 130° . The main reason is that, with the increment of the apex angle, drilling axial force also increase, which, thus, would enhance the extrusion of the fiber layer. However, at the same time, the rake angle of the drill bit main cutting edge also increases; then, the cutting edge becomes sharper, and the carbon fiber can be instantaneously cut off, which can reduce the inlet tear. On the outlet side, it can be clearly seen that the tear defect is larger than that in the inlet side, and the influence of the apex angle on the outlet side is also greater than that on the inlet side. However, the change behavior of the total defect is similar to that on the inlet side. The tear factor also decreases first, then increases with the increase of the apex angle, and reaches the minimum near the apex angle 125° . This is because that, with the decrease of the apex angle, the axial force is reduced. The rake angle of the main cutting edge is correspondingly decreased, and the drilling cutting edge is not sharp. Consequently, the carbon fiber cannot be instantaneously cut off. With the increase of the apex angle, although the main cutting edge rake angle increased, the cutting edges became sharper. And, the cutting edge of concave shape would cut off the carbon fiber easily, but the increase of the apex angle makes drilling axial force increase. The push effect of the drill tip to the outlet of the raw fiber layer is very severe, which causes the fierce outlet side tear. Figure 7 shows the behaviour of the influence of the apex angle of the drill tip on the drilling axial force and torque in the case of the structure's circumferential rear angle $\alpha_{fc} = 10^\circ$ and chisel edge incline angle $\psi = 60^\circ$. As can be seen from the above relationship graph, when the drill point structural circumferential rear angle and chisel edge bevel angle are constant, with the increase of the drill apex angle, axial force has been increased in the approximately linear form; the main reason is that, with the increment of the apex angle, the rake angle and rear angle of the drill tip chisel edge are less, while drilling axial force is mainly concentrated on the chisel edge; as both the chisel edge bevel angles decrease, the scraping extrusion effect of the drilling chisel edge on the material becomes more severe, which will lead to the increase of axial force.

It also can be seen that, with the increment of the apex angle, the torque is decreased. The reason is that, with the increment of the apex angle, the length of the main cutting edge decreases; under the same processing parameters, the material to be cut by the drill bit per processing round is

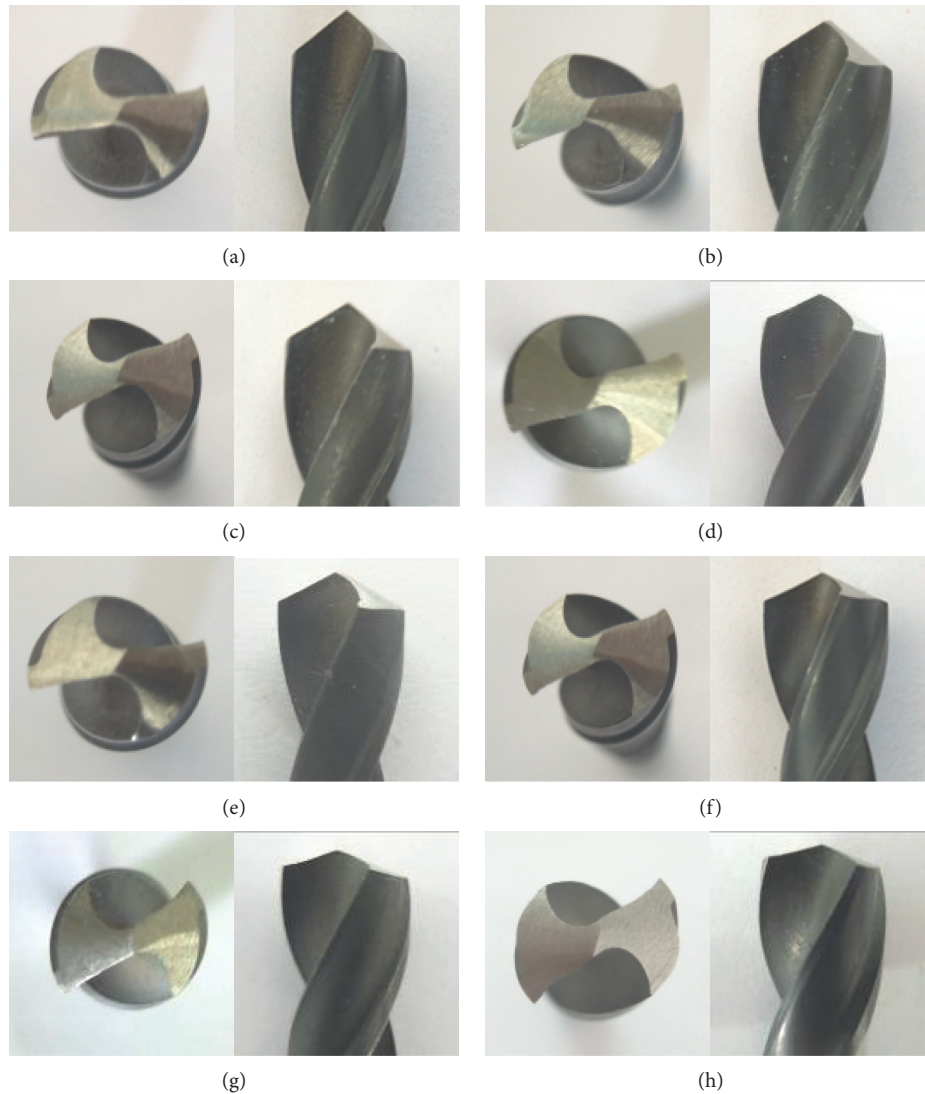


FIGURE 4: The shape of blade-grinded drills. (a) $2\phi = 100^\circ$. (b) $2\phi = 110^\circ$. (c) $2\phi = 115^\circ$. (d) $2\phi = 120^\circ$. (e) $2\phi = 125^\circ$. (f) $2\phi = 130^\circ$. (g) $2\phi = 140^\circ$. (h) $2\phi = 150^\circ$.

reduced; at the same time, along with the rising of the apex angle, the main cutting edge of the rake angle increases; the cutting edges is sharper, which reduces the drilling torque. By analyzing the apex angle on the inlet and outlet, the influence of drilling force, considering the effect of the inlet tear, is significantly less than the tear of outlet, so it is needed to consider the quality of the outlet when choosing the best apex angle; at the same time, considering the strength of the drill tip, on the premise of guaranteeing the quality of drilling, the larger apex angle is chosen; this drill bit is of high intensity and longer life. The best apex angle value is chosen as 125° .

3.2. Influence of Chisel Edge Bevel Angle of Drill Tip on Drilling Force and Tear. The chisel edge bevel angle is a geometric parameter that is sensitive to the grinding parameters. 50° , 60° , 70° , and 80° are, respectively, taken as the chisel edge bevel angle; 125° is selected as the apex angle value, and 10° is

selected as the structure circumferential rear angle for grinding. The grinding drill bit shape is shown in Figure 8.

Figure 9 shows some pictures of the hole inlets and outlets after the drill bits have been drilled.

Figure 10 shows the curve of the influence of the chisel edge angle of the drill tip on the tear factor at the outlet and inlet in the case of the apex angle $2\phi = 125^\circ$ and the structure circumference rear angle $a_{fc} = 10^\circ$. Clearly, with the increase of the chisel edge angle, the outlet and inlet of tear factor increase with the decrease firstly and then increase; the main reason is that, with the increase of the chisel edge angle, the horizontal angle of cutting edge and chisel edge angle are also increased, which makes the chisel edge sharper; the extrusion effect of the chisel edge to the processed materials is reduced, but the horizontal blade angle is too small, which will cause the chisel edge too long; then, the drilling axial force increases, which is not helpful for the drilling of CFRP. Figure 11 is the curve of the influence of the chisel edge incline angle of the drill tip on the drilling axial force and

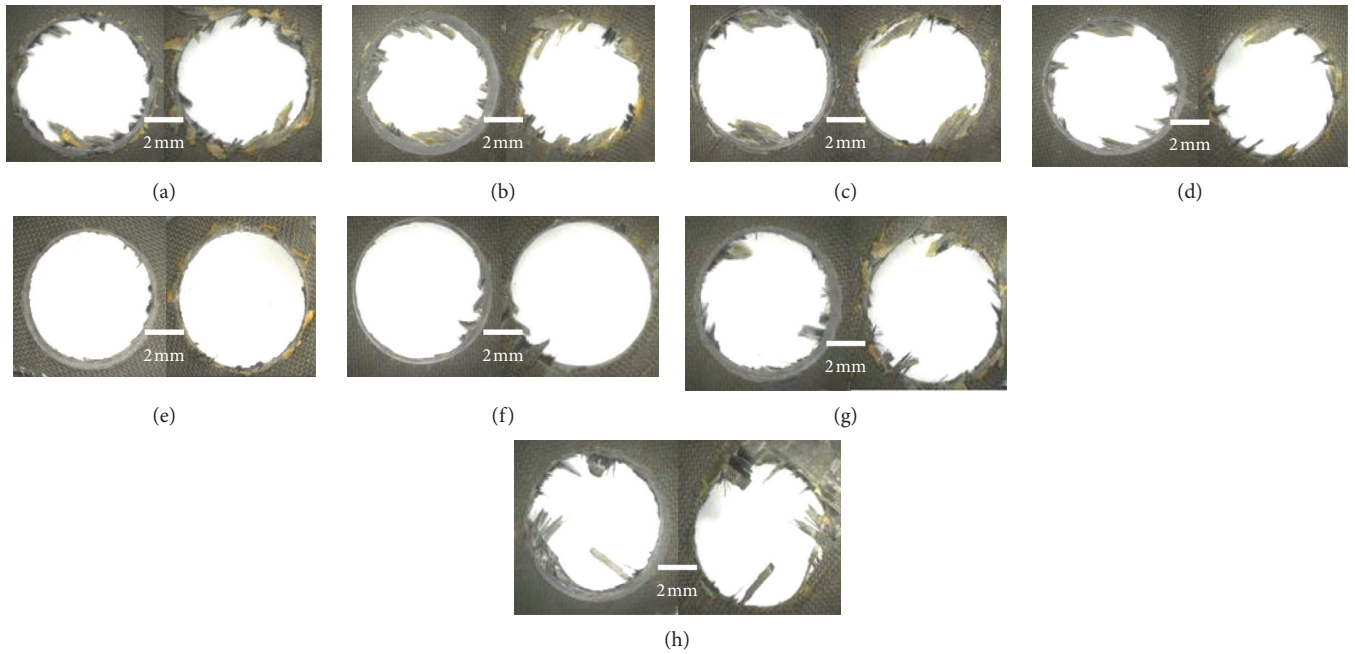


FIGURE 5: The photos of holes drilled by each drill. (a) $2\phi = 100^\circ$. (b) $2\phi = 110^\circ$. (c) $2\phi = 115^\circ$. (d) $2\phi = 120^\circ$. (e) $2\phi = 125^\circ$. (f) $2\phi = 130^\circ$. (g) $2\phi = 140^\circ$. (h) $2\phi = 150^\circ$.

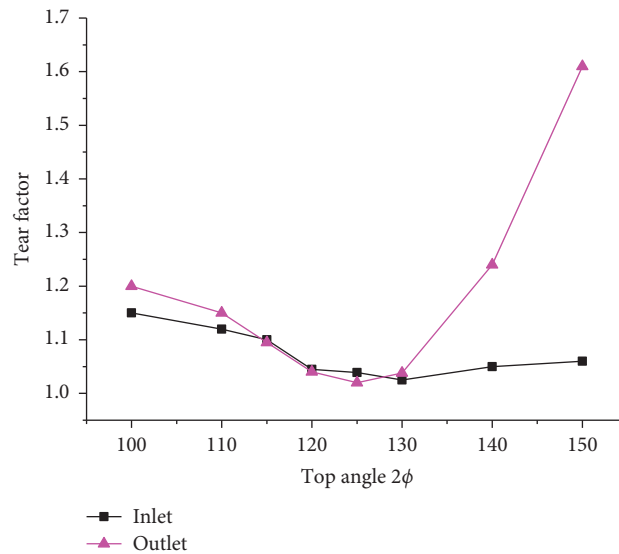


FIGURE 6: Delamination factor F_d at varying point angles.

torque in the case of the apex angle $2\phi = 125^\circ$ and the structural circumferential rear angle $a_{fc} = 10^\circ$. As can be seen from the above relationship graph, under the condition that the drill structural circumferential rear angle and chisel edge angle are constant, with the increase of the drilling chisel edge angle, drilling axial force increases gradually; this is mainly because that, with the increase of the chisel edge angle, the rake angle and rear angle of the chisel edge are reduced; when the chisel edge wedges into the workpiece, it does not become sharp; although the chisel edge at the same time gets shorter, but it would not make influence as big as the former one, so the tendency of the axial force increases.

For torque, it can be seen that, with the increase of the chisel edge angle, drilling torque is gradually reduced; this is mainly because with the increase of the chisel edge angle, the chisel edge gets shorter; although the chisel edge is less sharper than it was when the chisel edge incline angle was smaller, the scraping extrusion effect on the material during the drilling process would increase, so the torque would present a decreasing trend, but because the chisel edge is very short, the corresponding torque is small, so there is less influence to the overall torque of the drill tip. By analyzing the influence of different chisel edge incline angles on the hole inlet, outlet, and drilling force and comprehensively

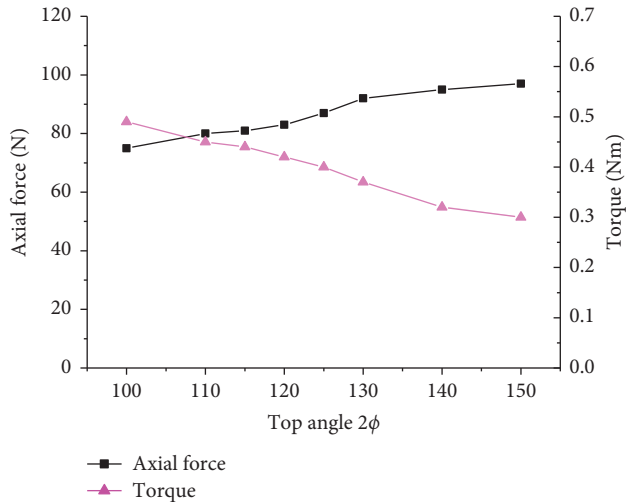


FIGURE 7: Delamination factor F_d at varying point angles.

considering the influence of the chisel edge bevel angle on the axial force and the hole inlet and outlet, the optimal chisel edge bevel angle is determined to be 60° .

3.3. Influence of the Circumferential Rear Angle of the Drill Tip Structure on Drilling Force and Tearing. 5° , 10° , and 15° were selected as the structure circumferential rear angle, 125° as the apex angle value, and 60° as the chisel edge bevel angle value for grinding, and the grinding parameters and the shape of the grinding drill bit are shown in Figure 12.

Figure 13 is a picture of the hole inlet and outlet after several drill bits have been drilled.

Figure 14 shows the influence curve of the size of the circumferential rear angle of the drilling tip structure on the tear factor at the inlet in the case of apex angle $2\phi = 125^\circ$ and chisel edge bevel angle $\psi = 60^\circ$. Due to the drill tip structure circumference rear angle, the apex angle and chisel edge bevel angle are different; their change will only affect the sharp degree of the cutting edges and will not impact other parameters of the drill tip; therefore, it can be seen from the diagram, along with the rising of the drill point structural circumferential rear angle, the tear factor of inlet and outlet has been reduced; this is mainly because the main cutting edge becomes more sharp, and the cutting off effect of carbon fiber is enhanced. However, at the structure's circumference rear angle, the tearing at the outlet appeared abnormal, which was mainly due to the fact that the drill material used in the experiment was high-speed steel, and the main cutting edge wore too fast when drilling CFRP, and the main cutting edge of the drill tip became blunt before a hole was finished. Figure 15 shows the curve of the influence of the size of the circumferential rear angle of the drilling tip structure on the drilling force in the case of apex angle $2\phi = 125^\circ$ and chisel edge bevel angle $\psi = 60^\circ$. It can be seen clearly from the figure that along with the increasing of the drill point structural circumferential rear angle, the drilling torque and axial force are reduced; this is mainly because of the increase of the structure circumferential rear angle which leads to the main cutting edge becoming more sharp; in the

drilling of carbon fiber, the cut off effect is enhanced. The drilling torque is mainly focused on the main cutting edge, and axial force is mainly concentrated on the chisel edge, so the effect of the structure circumferential rear angle on torque is greater than the chisel edge angle. Through the above analysis, it is found that, with the increase of the circumference rear angle of the structure, both the tearing and drilling force at the inlet and outlet of the drilling hole are decreased. Therefore, the circumference rear angle of the structure should be larger, but this will lead to the wear of the main cutting edge of the drilling tip too fast. After comprehensive consideration, the optimal structure circumference rear angle is set as 10° .

3.4. Comparison between the Best Geometric Parameters of Grinding Drill Tips with Ordinary Drill Tips. According to the best geometrical parameters determined in the above sections, the edge grinding bit with apex angle $2\phi_0 = 125^\circ$, rear angle $a_{fc} = 10^\circ$, and chisel edge bevel angle $\psi = 60^\circ$ is used to conduct the drilling experiment on comparison with the standard high-speed steel twist drill. Under the condition of the spindle speed of 800 r/min and the feed of 0.04 mm/r, two tools were used to drill, and the axial force and machining quality were compared.

It can be seen from Table 2 that, under the same process parameters, the axial force of the complex helicoidal drill tip with the best geometric parameters is 28% lower than that of the ordinary twist drill. Figure 16 shows the inlet and outlet of the hole drilled using a complex helicoidal drill point with the best geometry and an ordinary drill bit.

It can be clearly seen from the above figure that, under the same process parameters, the drilling quality of the drill bit sharpened by the helicoid drill tip sharpening method is significantly better than that of the ordinary drill bit during the drilling processing of CFRP.

3.5. Improvement of Drill Tip Structure. The best drill bit tip geometry parameters of the complex helicoid drill bit to machining CFRP is obtained through the above experiment. With the optimal geometric parameters of the complex helical drill bit in drilling CFRP laminated plates, good effect can be achieved, but a closer examination at the hole outlet reveals that there is a slight tear. Therefore, the drill tip is partially improved. In the process of drill grinding, the complex helicoidal drill tips are double-edge sharpened according to the characteristics of Bickford drill tips [20]. The sharpened drill tips are shown in Figure 17.

The effect comparison after drilling is shown in Figure 18.

It can be seen from Figure 18 that the drilling effect of the double edge drill bit at the outlet is better than the drill tip of the single edge. This is because there is a relatively sharp angle at the connecting area between the main cutting edges; therefore, it is easy to squeeze out scraps with burr generated. However, the drill tip of the double edge angle is shaped through secondary grinding, which makes the connecting angle between the main cutting edge and edge area become bigger, which can effectively reduce the burr at the export; at the same time, due

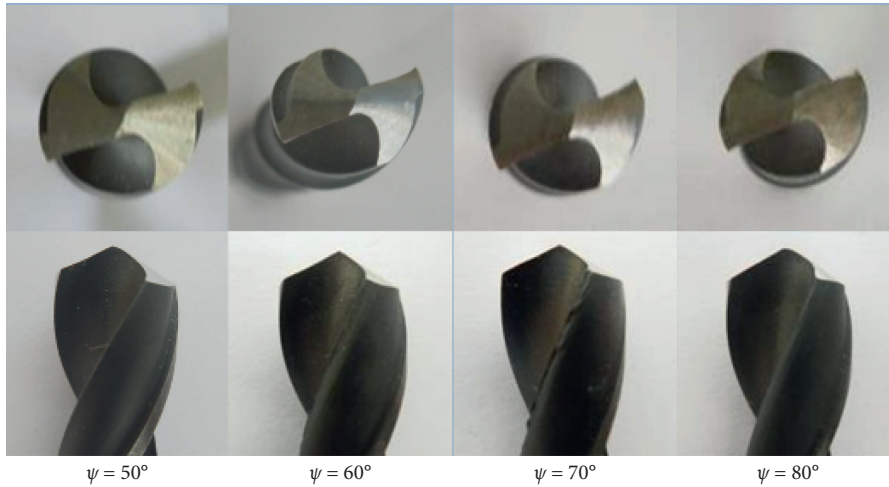


FIGURE 8: The shape of blade-grinded drills.

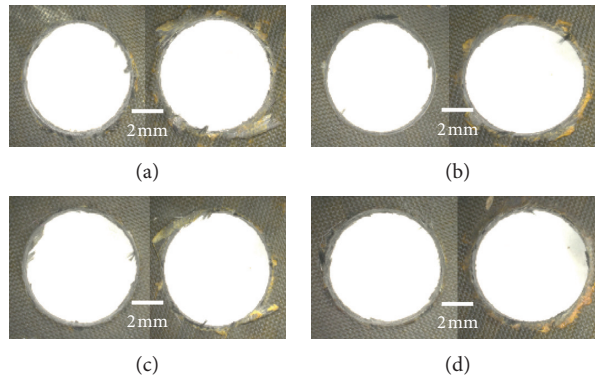


FIGURE 9: The photos of holes drilled by each drill. (a) $\psi = 50^\circ$. (b) $\psi = 60^\circ$. (c) $\psi = 70^\circ$. (d) $\psi = 80^\circ$.

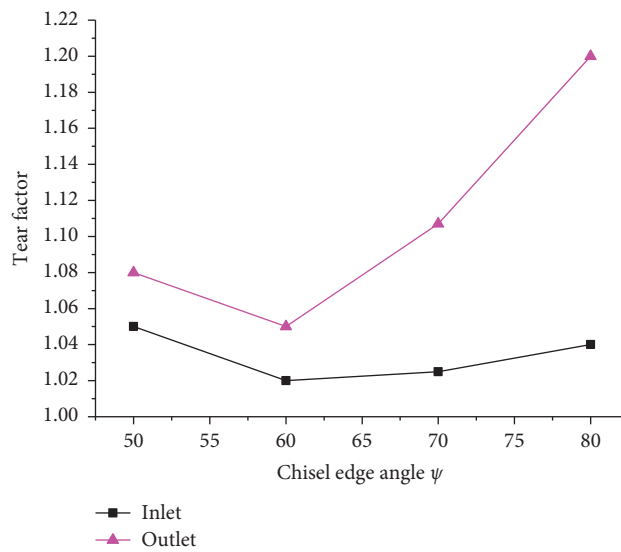


FIGURE 10: Delamination factor F_d at varying ψ .

to the main cutting edge of the double edge angle of the drill tip becoming longer, the load on unit cutting length in the case of the double edge angle tool tip is smaller than that of the single

edge angle tool tip. This is because the main cutting edge of the double edge tool tip becomes longer. In addition, drilling heat is less which is helpful for drill tip cooling.

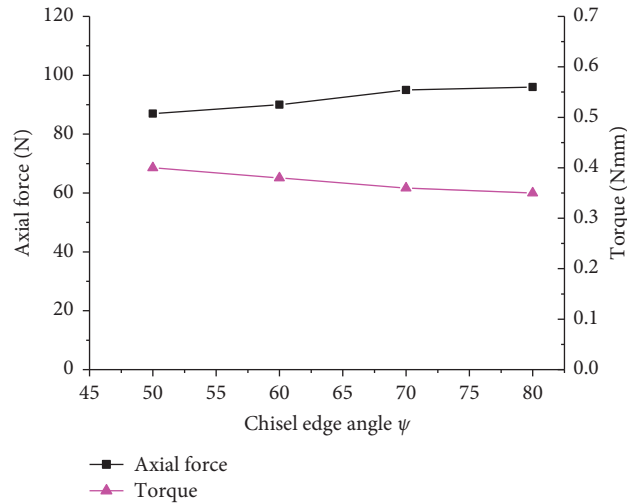
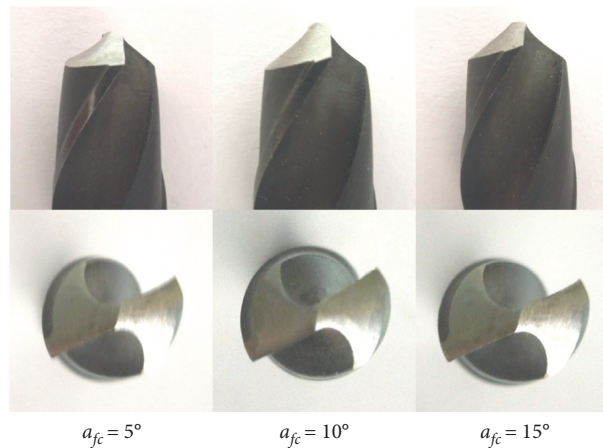


FIGURE 11: Drilling force at varying ψ .



$a_{fc} = 5^\circ$ $a_{fc} = 10^\circ$ $a_{fc} = 15^\circ$

FIGURE 12: The shape of blade-grinded drills.

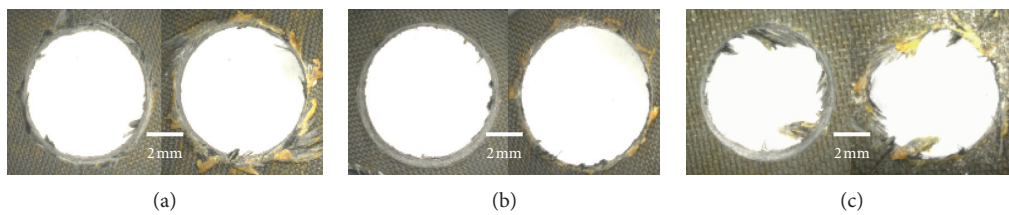


FIGURE 13: The photos of holes drilled by each drill. (a) $a_{fc} = 5^\circ$. (b) $a_{fc} = 10^\circ$. (c) $a_{fc} = 15^\circ$.

Because the chisel edge rake angle of the complex helical surface drill tip grinded by the flat grinding wheel is still small, basically it is the same as the normal drill tip, the shaped grinding wheel of the circular arc angle edge is adopted to grind the drill tip in order to reduce the chisel edge angle of the drill tip and increase the rake angle. This would make the chisel edge more sharp during the drilling process. In addition, the extrusion of the chisel edge to the CFRP is decreased; therefore, the tear generated by the chisel edge is decreased. The sharpened drill tip is shown in Figure 19, and Figure 20 is the comparison of the effect after drilling.

The effect comparison after drilling is shown in Figure 20.

4. Experimental Study on Drilling Process Parameters

Both the geometric parameters of the drill tip and the experimental parameters during drilling have a great influence on the quality of the CFRP hole. It is of great significance to select the appropriate experimental parameters for the quality of the hole and the life of the tool. Hereby, the

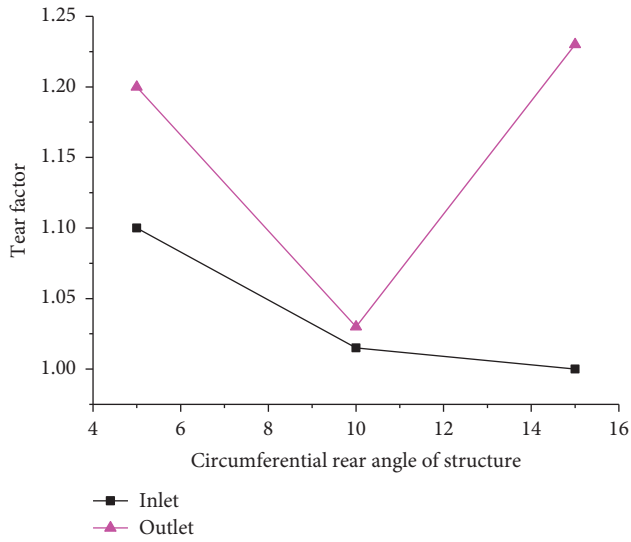


FIGURE 14: Tear factor F_d at varying a_{fc} .

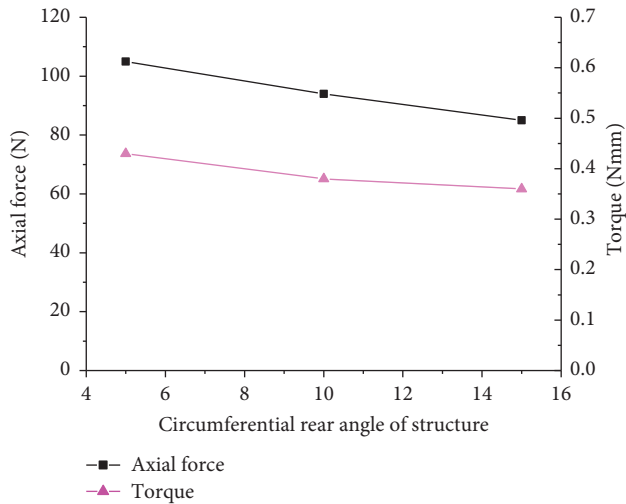


FIGURE 15: Drilling force at varying a_{fc} .

TABLE 2: Comparison of axis force of the two drills.

Tool	Drilling axial force (N)
Sharpening drill	86.53
Standard carbide twist drill	120.26

experimental process and results are introduced and analyzed, and the influence of process parameters on drilling force and drilling quality is obtained. On this basis, the regression analysis of drilling force and the observation of drilling surface quality are carried out. The material used in the experiment is CFRP. The experiment tool adopts the carbide twist drill with diameter $\phi 6$, and other experimental equipment is the same as the equipment used aforementioned.

The main purpose of this experiment is to study the effect of drilling process parameters on CFRP drilling quality and

determine the process range that should be taken in processing CFRP laminates by analyzing the influence of drilling process parameters on hole quality. In the drilling process, the parameters affecting the drilling quality are the spindle speed and feed per rotation [21]. The influence of feed per rotation is bigger than that of the spindle speed. In the selection of the experimental parameters, the spindle speed range is wider. The feed per rotation is set relatively small. So it can comprehensively reflect the effect of spindle rotation and feed per rotation on drilling force and machining quality. The number of experimental groups was designed according to the orthogonal experimental table $L_{16}(4^2 \times 2^9)$, and a total of 16 groups of experiments were carried out. The spindle speed was selected as 500 r/min, 800 r/min, 1250 r/min, and 2000 r/min. The feed per revolution during drilling was selected as 0.04 mm/r, 0.06 mm/r, 0.1 mm/r, and 0.13 mm/r. The experimental parameters are shown in Table 3.

The grinding edge parameters of the cemented carbide twist drill are the optimal geometric parameters (apex angle $2\phi_0 = 125^\circ$, structure circumferential rear angle $a_{fc} = 10^\circ$, and chisel edge incline angle $\psi = 60^\circ$) obtained in the previous part. The data collection is still taken the average value when the drilling process reaches a steady state. The average value of two drilling holes drilled under each process parameter and the orthogonal experimental results are shown in Table 4.

It can be clearly seen from the results in the table that axial force and torque vary greatly under different process parameters, and it is found that the increase of feed and the decrease of rotation speed will increase the axial force and torque.

4.1. Analysis of Drilling Force. Drilling force is one of the most important phenomena produced in the process of drilling, and drilling force can be used as an important evaluation parameter of drilling parameters. The influence of process parameters on drilling force is analyzed, which is helpful to the selection of process parameters. Figures 21 and 22 show the change curves of drilling force corresponding to different feed rates when drilling CFRP with twist drill. It is easy to see that both axial force and torque increase with the increase of the feed rate when drilling CFRP. This is because the greater the feed, the greater the area of the fiber layer cut by the drill tip and the greater the axial force and torque. On the contrary, the larger the area of the fiber layer cut by the drill tip, the smaller the deformation of the fiber layer, which will reduce the drilling force to some extent, but this is only an indirect effect. From the general trend, the axial force and torque increase with the increase of the feed.

It can be seen from Figures 21 and 22 that, with the increase of rotational speed, cutting force has a tendency of decreasing; this is mainly due to the fact that, with the increase of rotational speed, the extrusion deformation of the carbon fiber layer will decrease. The carbon fiber can cut off in an instant, and it will reduce drilling force. However, the influence of the rotational speed on drilling

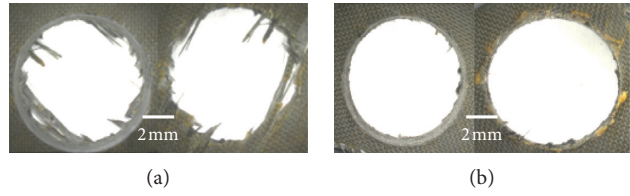


FIGURE 16: Comparison of two drills. (a) By ordinary drill tip. (b) By complex helicoidal drill.

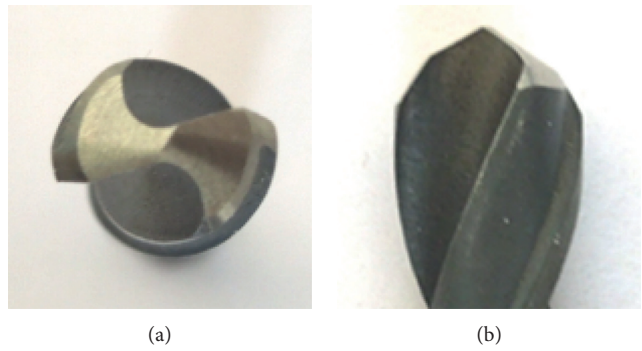


FIGURE 17: Double point angle drill.

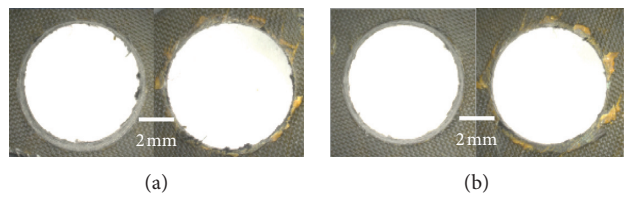


FIGURE 18: Outlet quality comparison. (a) Original sets. (b) Improved sets.

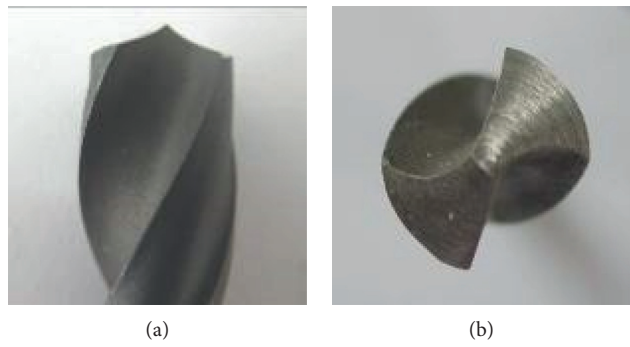


FIGURE 19: The improved drill.

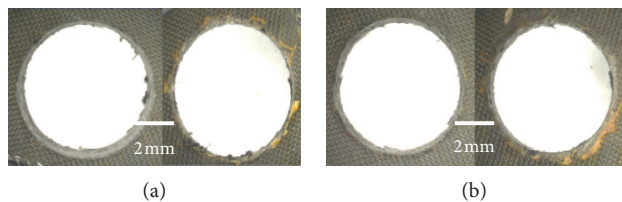


FIGURE 20: Comparison of two holes. (a) Original sets. (b) Improved sets.

TABLE 3: The parameter of the orthogonal array.

	1	2	3	4	5	6	7	8	9	10	11	12	13	14	15	16
n (r/min)	500	800	1250	2000	500	800	1250	2000	500	800	1250	2000	500	800	1250	2000
F (mm/r)	0.04	0.04	0.04	0.04	0.06	0.06	0.06	0.06	0.1	0.1	0.1	0.1	0.13	0.13	0.13	0.13

TABLE 4: The measurement data of the orthogonal experiment.

Feed rate (mm/r)	Spindle speed (r/min)	Axial force F_z (N)	Torque M (N·m)
0.04	500	52.83	0.15
0.04	500	60.52	0.13
0.04	500	66.63	0.11
0.04	500	72.43	0.10
0.06	800	94.82	0.20
0.06	800	111.01	0.17
0.06	800	120.11	0.15
0.06	800	129.63	0.13
0.1	1250	114.21	0.26
0.1	1250	130.23	0.23
0.1	1250	144.35	0.20
0.1	1250	156.09	0.18
0.13	2000	125.41	0.35
0.13	2000	144.12	0.31
0.13	2000	157.81	0.28
0.13	2000	171.19	0.24

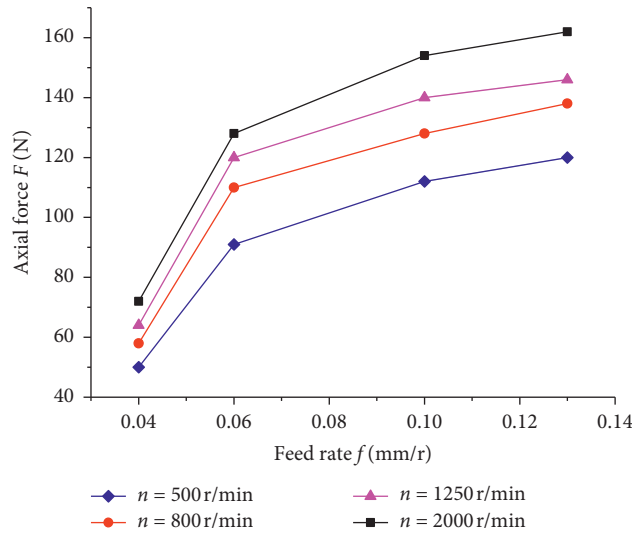


FIGURE 21: Axial force at the varying experimental parameter.

force is small, much smaller than the influence of feeding. It can be seen by force curves, in the process parameters, the effect of feed per rotation on the axial force is relatively significant, which is almost proportional. The effect of the spindle speed on the torque is large. The method of regression analysis was adopted to fit the experience formula of the axial force and torque. According to the commonly used experience formula [22] for drilling axial force and torque, the fitting of the exponential form was carried out. Firstly, the original form of the drilling axial force and torque equation is set as

$$\begin{aligned}
 F &= C_F \cdot n^{X_F} \cdot f^{Y_F}, \\
 M &= C_M \cdot n^{X_M} \cdot f^{Y_M},
 \end{aligned} \tag{1}$$

where F is the axial force, M is the torque, n represents the spindle speed, f_r represents feed per rotation, C_F and C_M are the parameters relative to the nature of the processed material itself and drilling conditions, and X_F , X_M , Y_F , and Y_M are the feed and the index of the rotation speed, respectively. It should be emphasized that, since drill bits of the same diameter were used in this experiment, the influence of

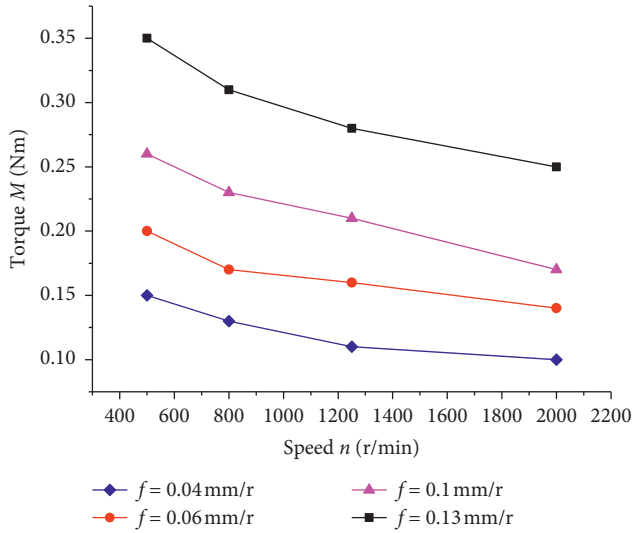


FIGURE 22: Torque at the varying experimental parameter.

the drill bit diameter on axial force and torque was not considered in the calculation of the empirical formula. The fitting results are shown in Table 5.

In order to verify the empirical formula obtained, the formula is tested using the F method, which is to test the significance of the equation directly from the empirical formula results according to the square sum decomposition formula. After analysis, it can be obtained as follows: $F_{\text{speed-axialforce}} = 0.013$, $F_{\text{feed-axialforce}} = 21.553$, $F_{\text{speed-torque}} = 4.645$, and $F_{\text{feed-torque}} = 0.418$. After looking up the F distribution table, it can be obtained as follows: $F_{0.1}(3, 15) = 21.553$, $F_{0.05}(3, 15) = 3.29$, and $F_{0.01}(3, 15) = 5.42$. Then, $F_{\text{feed-axialforce}} > F_{0.1}(3, 15)$ and $F_{0.05}(3, 15) < F_{\text{speed-torque}} < F_{0.01}(3, 15)$. It is found that the feed has a highly significant influence on the axial force, while the axial force change caused by the spindle speed is very small. Spindle speed has a significant effect on the torque, and the change of torque caused by the feed is small.

4.2. Influence of Process Parameters on Hole Inlet/Outlet Tearing. Figure 23 shows the influence curve of rotating speed and feed rate on the tear factor at the drilling hole inlet when drilling CFRP with complex helicoidal drill tips. As can be seen from the change of the curve in the figure, when the speed n is constant, the tear factor at the hole inlet increases with the increase of the feed f ; when the feed f is constant, the tear factor at the hole inlet tends to decrease with the increase of the speed n , but the influence of the speed n on the tear at the inlet is significantly smaller than that of the feed f . It can be concluded that the small feed or high speed can ensure the quality of the drilling hole inlet. Figure 24 shows the influence curve of rotating speed and feed rate on the tear factor at the outlet of the drill hole when drilling CFRP with complex helicoidal drill tips. It can be seen clearly that the influence of speed and feed on the hole outlet tear is bigger than that on the inlet, when the rotational speed n is constant; with the increase of feeding f , the tear factors at the outlet also increase with a fast growing

TABLE 5: The fitting results of axial force and torque.

Fitting variable	Value	Correlation coefficient	Error (%)
C_F	190.331	—	
X_F	0.022	85.1	3.2
Y_F	0.398	100	
C_M	7.693	—	
X_M	0.465	100	16.3
Y_M	0.261	99.7	

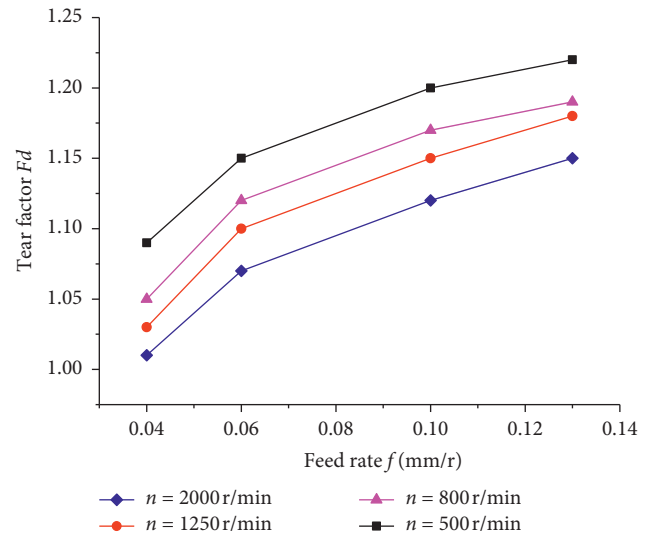


FIGURE 23: Tear factor Fd at the varying experimental parameter (inlet).

speed. This is mainly due to the fact that the increase of feed has caused the rapid increase of axial force, leading to tear at the outlet. When the feed rate is constant, with the increase of speed n , the outlet tear is decreasing, but the decreasing trend is not obvious, which is far less than the effect of the feed rate on the tear. Through the above analysis, it is concluded that when drilling CFRP, it is necessary to ensure a small feed and a high speed in order to get a high-quality drill hole.

4.3. Fiber Fracture Morphology and Microstructure of Cutting Surface. After the CFRP hole was processed, the surface of the CFRP hole was observed by a variable focus optical microscope, and the microstructure of the hole surface, the fracture morphology, and the failure mechanism of carbon fiber were analyzed. Considering that this test material is a bidirectional woven carbon fiber laminate, the two sides of the holes are symmetrical, so only one quarter of the hole surface is observed to obtain a complete picture of the entire hole surface. Because the adjustable range of lens of the microscope is limited, in order to conveniently and efficiently observe the specimen hole wall surface, the size of the sample must be limited in a certain range, so before observation, the drilling hole is cut into small pieces, which needs to be cleaned before observation. Figure 25 shows the observed samples.

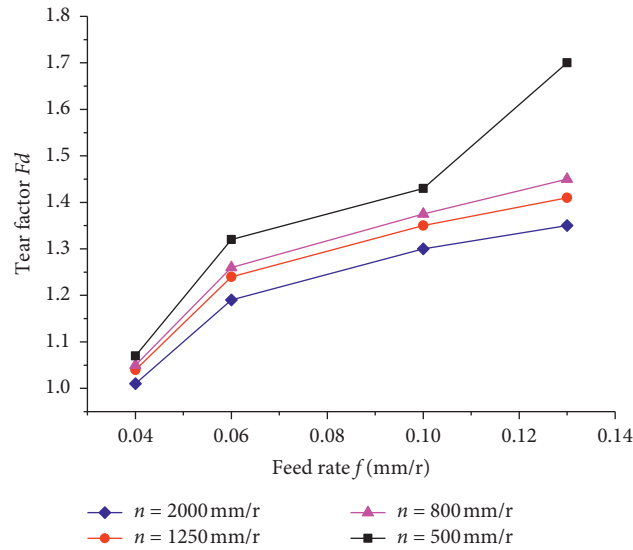


FIGURE 24: Tear factor F_d at the varying experimental parameter (outlet).

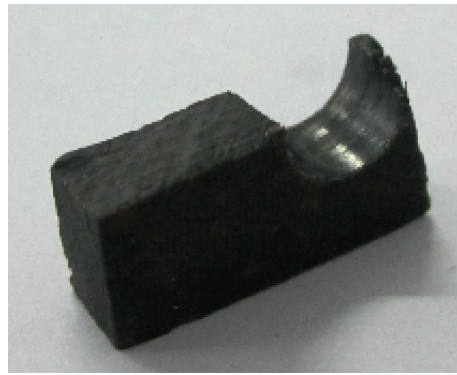


FIGURE 25: Observation sample of the hole wall.

Figure 26 shows the morphology of the inner wall of the hole observed by the microscope. In this case, the process parameters are the rotational speed $n = 2000$ r/min and the feed speed $f = 0.04$ mm/r. Due to the high-speed rotation of the drill bit, the resin matrix of the cutting part was daubed on the machined surface. The resin-coated part of the hole wall looks very smooth due to the fact that the fiber fracture was wrapped, while the part without being resin-coated looks rough because its surface composition is fiber fracture and resin matrix of the fiber layer. The outlet and inlet of the hole are relatively less resin coated, so the rough part is more. It can be also found from the observation of the hole wall surface that the roughness in different location holes is also not identical. The main reason is that the fiber fracture forms are different.

Figure 27 shows the hole wall morphology at several typical angles under high magnification, in which Figure 27(a) shows the hole wall morphology when the angle between the fiber direction and the cutting direction is 0° and 90° , Figure 27(b) shows the hole wall morphology when the angle between the fiber direction and the cutting direction is

45° , and Figure 27(c) shows the hole wall morphology when the angle between the fiber direction and the cutting direction is 135° . When the intersection angle is 0° , because the separation deformation between layers occurs here, most fibers are not cut off, and the hole wall is very smooth. When the intersection angle is 90° , the fibers are all cut off from the root by the cutting edge, and the exposed part of the fracture is very little, which looks smooth in the overall topography. When the intersection angle is 45° , the fracture part is longer than that of the direction of 90° , but the fracture is neat, and the quality is good in the overall topography. However, when the intersection angle is 135° , because the cutting form here is bending shear, the exposed part of the fracture is uneven and looks very rough on the hole wall. This also reveals that when the angle between the fiber direction and the cutting direction is between 0° and 90° , the cutting mode belongs to “straight cutting,” and the surface quality after drilling is smooth. When the fiber direction is between 90° and 180° , the cutting mode belongs to “inverse cutting,” and the surface quality after drilling is rough [23].



FIGURE 26: The whole morphology of the hole.

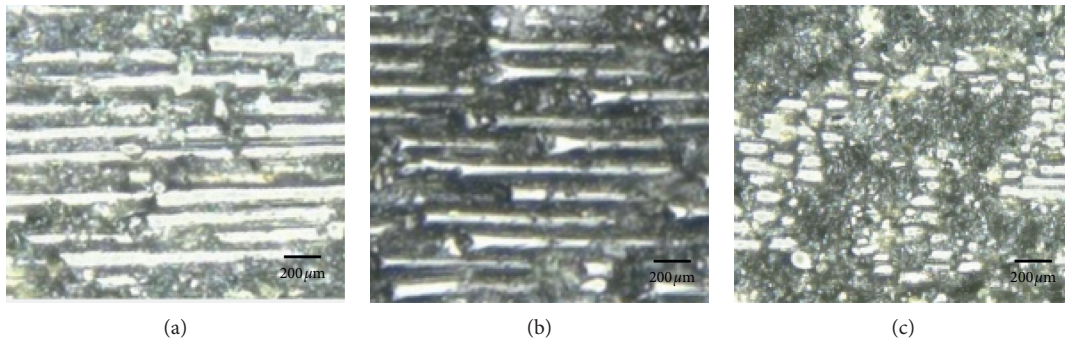


FIGURE 27: The feature of the hole wall at different angles.

5. Conclusion

This work mainly focuses on the drilling experiment of CFRP using the complex helicoid drill tip. The preliminary conclusions can be drawn as follows:

- (1) Under the same process parameters, the best geometrical parameters of the complex helical surface drill tip for CFRP laminates are the apex angle $2\phi = 125^\circ$, chisel edge bevel angle $\psi = 60^\circ$, and circumferential rear angle $\psi = 60^\circ$. The complex helical surface drill tip with the best geometrical parameters can achieve a good effect during the drilling process of CFRP laminates compared with the ordinary drill bit.
- (2) By using the same geometrical parameters of the drill tip at different speeds and feeds, it is found that the feed has a great influence on the drilling axial force, and the drilling of CFRP has a great influence on the tearing at the outlet. The spindle speed has little influence on the axial force, but great influence on torque.
- (3) The drilling hole wall of CFRP is mainly composed of the resin matrix coating part and the fiber fracture part, and the hole wall surface in the “procut” area is smooth, while the hole wall surface in the “anticut” area is rough.

Data Availability

The data used to support the findings of this study are included within the article.

Conflicts of Interest

The authors declare that there are no conflicts of interest regarding the publication of this article.

References

- [1] D. H. Wang, M. Ramulu, and D. Arola, “Orthogonal cutting mechanisms of graphite/epoxy composite. Part 1: unidirectional laminate,” *International Journal of Machine Tools and Manufacture*, vol. 35, no. 12, pp. 1623–1638, 1995.
- [2] W. König, C. Wulf, P. Graß, and H. Willerscheid, “Machining of fiber reinforced plastics,” *CIRP Annals*, vol. 34, no. 2, pp. 537–48, 1985.
- [3] W. Chambers and G. Bishop, “The drilling of carbon fibre polymer matrix composites,” *Processing and Manufacturing*, vol. 3, pp. 565–72, 1995.
- [4] W.-C. Chen, “Some experimental investigations in the drilling of carbon fiber-reinforced plastic (CFRP) composite laminates,” *International Journal of Machine Tools and Manufacture*, vol. 37, no. 8, pp. 1097–1108, 1997.
- [5] J. Xu, T. Lin, J. P. Davim, M. Chen, and M. E. Mansori, “Wear behavior of special tools in the drilling of CFRP composite laminates,” *Wear*, vol. 2021, Article ID 203738, 2021.
- [6] P. Rawal, C. Brillinger, C. Böhlmann, and W. Hintze, “Sensor based online quality monitoring system for detection of milling defects on CFRP structures,” *CEAS Aeronautical Journal*, vol. 11, no. 2, pp. 565–574, 2019.
- [7] J. Kumar and R. K. Verma, “Multiple response optimization in machining (milling) of graphene oxide doped EPOXY/CFRP composite using COCOSO-PCA: a novel hybridization approach,” *Journal of Advanced Manufacturing Systems*, vol. 20, pp. 423–446, 2021.

- [8] T. Furuki, Y. Kabaya, T. Hirogaki, E. Aoyama, K. Inaba, and K. Fujiwara, "Development of cBN electroplated end-mill combined cutting and grinding for precision machining of CFRP," *International Journal of Abrasive Technology*, vol. 8, no. 3, 2018.
- [9] R. Piquet, B. Ferret, F. Lachaud, and P. Swider, "Experimental analysis of drilling damage in thin carbon/epoxy plate using special drills," *Composites Part A: Applied Science and Manufacturing*, vol. 31, no. 10, pp. 1107–1115, 2000.
- [10] H. P. Yuan, H. Gao, Y. J. Bao, and Y. Wu, "Grinding of carbon/epoxy composites using electroplated CBN wheel with controlled abrasive clusters," *Key Engineering Materials*, vol. 389-390, pp. 24–29, 2009.
- [11] S. Lin and K. Chen, "Drilling of carbon fiber-reinforced composite material at high speed," *Wear*, vol. 194, no. 1-2, pp. 156–162, 1996.
- [12] D. H. Wang, M. Ramulu, and D. Arola, "Orthogonal cutting mechanisms of graphite/epoxy composite. Part 2: multi-directional laminate," *International Journal of Machine Tools and Manufacture*, vol. 35, no. 12, pp. 1639–1648, 1995.
- [13] W.-L. Zhu, Z. Zhu, P. Guo, and B.-F. Ju, "A novel hybrid actuation mechanism based XY nanopositioning stage with totally decoupled kinematics," *Mechanical Systems and Signal Processing*, vol. 99, no. 15, pp. 747–759, 2018.
- [14] D. Arola, M. Ramulu, and D. H. Wang, "Chip formation in orthogonal trimming of graphite/epoxy composite," *Composites Part A: Applied Science and Manufacturing*, vol. 27, no. 2, pp. 121–133, 1996.
- [15] W. L. Zhu and A. Beaucamp, "Compliant grinding and polishing: a review," *International Journal of Machine Tools and Manufacture*, vol. 158, Article ID 103634, 2020.
- [16] B. Mihai and X. Paul, "Experimental analysis of drilling fiber reinforced composites," *International Journal of Machine Tools & Manufacture*, vol. 51, pp. 937–946, 2011.
- [17] K. Vijayan, "Optimization of machining parameters at high speed drilling of carbon fiber reinforced plastic (CFRP) laminates," *Composites*, vol. 43, pp. 1791–1799, 2012.
- [18] Z. Wei and H. Feng, "Parameterized geometric design for complex helical drill point," *Journal of Manufacturing Science and Engineering*, vol. 3, pp. 319–324, 2005.
- [19] Y. He, L. Ren, P. Zou, and S. Wang, "Experimental study of a novel ultrasonic vibration-assisted structure for radial milling," *Shock and Vibration*, vol. 2021, Article ID 5590560, 13 pages, 2021.
- [20] K. F. Ehmann, "Grinding wheel profile definition for the manufacture of drill flute," *Annals of the CIRP*, vol. 39, no. 1, pp. 19–24, 1990.
- [21] M. Y. Friedman and M. Bolselavski, "The profile of a helical slot machined by a disk-type cutter with an infinitesimal width, considering undercutting," in *Proceedings of the 13th International Machine Tool Design and Research Conference*, Birmingham, UK, 1972.
- [22] Y. He, Z. Zhou, P. Zou, X. Gao, and K. F. Ehmann, "Study of ultrasonic vibration-assisted thread turning of inconel 718 superalloy," *Advances in Mechanical Engineering*, vol. 11, no. 10, p. 168, 2019.
- [23] H. Zhang and R. Fan, "Studies on cutting force in high speed drilling of CFRP," *Progress of Cutting and Grinding (ICPCJ-98)*, vol. 1998, no. 98, 1998.

Retraction

Retracted: Experimental Study of Thermal and Mechanical Behaviour of Graphite-Filled UJF Composite

Advances in Materials Science and Engineering

Received 26 December 2023; Accepted 26 December 2023; Published 29 December 2023

Copyright © 2023 Advances in Materials Science and Engineering. This is an open access article distributed under the Creative Commons Attribution License, which permits unrestricted use, distribution, and reproduction in any medium, provided the original work is properly cited.

This article has been retracted by Hindawi, as publisher, following an investigation undertaken by the publisher [1]. This investigation has uncovered evidence of systematic manipulation of the publication and peer-review process. We cannot, therefore, vouch for the reliability or integrity of this article.

Please note that this notice is intended solely to alert readers that the peer-review process of this article has been compromised.

Wiley and Hindawi regret that the usual quality checks did not identify these issues before publication and have since put additional measures in place to safeguard research integrity.

We wish to credit our Research Integrity and Research Publishing teams and anonymous and named external researchers and research integrity experts for contributing to this investigation.

The corresponding author, as the representative of all authors, has been given the opportunity to register their agreement or disagreement to this retraction. We have kept a record of any response received.

References

- [1] K. M. Reddy, D. H. Vardhan, Y. S. K. Reddy, G. Raghavendra, and R. Rudrapati, "Experimental Study of Thermal and Mechanical Behaviour of Graphite-Filled UJF Composite," *Advances in Materials Science and Engineering*, vol. 2021, Article ID 3739573, 7 pages, 2021.

Research Article

Experimental Study of Thermal and Mechanical Behaviour of Graphite-Filled UJF Composite

K. Manohar Reddy ¹, **D. Harsha Vardhan** ¹, **Y. Santhosh Kumar Reddy**,¹
Gujjala Raghavendra ² and **Ramesh Rudrapati** ³

¹Department of Mechanical Engineering, PVKK Institute of Technology, Ananthapuramu, Andhrapradesh, India

²Department of Mechanical Engineering, National Institute of Technology, Warngal, Tealanganana, India

³Department of Industrial Engineering, Bule Hora University, Bule Hora, Ethiopia

Correspondence should be addressed to Ramesh Rudrapati; rameshrudrapati@gmail.com

Received 8 June 2021; Revised 28 June 2021; Accepted 5 July 2021; Published 13 July 2021

Academic Editor: Samson Jerold Samuel Chelladurai

Copyright © 2021 K. Manohar Reddy et al. This is an open access article distributed under the Creative Commons Attribution License, which permits unrestricted use, distribution, and reproduction in any medium, provided the original work is properly cited.

The advancement of composites mixed with natural fibers and with fillers has become the most supportable alternative material for engineering applications, especially in industries such as automotive and aerospace. Natural fibers are renewable, cheap, biodegradable, and ecological materials. In the present work, already used woven jute fibers, which are extracted from gunny bags with the same grams per square meter (GSM), were used, and then, woven jute fibers were chemically treated to improve their characteristics. Graphite powder-filled used jute fiber reinforced epoxy composite (UJF) are prepared by using the hand-layup technique. Tests such as tensile, flexure, impact, and thermo-gravimetric analysis (TGA) were conducted. These tests were according to ASTM standards to evaluate the effect of graphite filler content on hybrid epoxy jute composites. The composite material is prepared by changing the content by weight of the filler by 3%, 6%, 9%, and 12%. The experimental results reveal that 6% of the graphite composites showed the maximum tensile strength and modulus. With the increase in the filler content, there is a decrease in the flexural properties. The impact resistance increases slightly up to 6% of the filler content. The study of thermal decomposition showed that the lowest mass loss was found at 9% by weight of the filler content. Morphological analysis performed by FE-SEM showed that the addition of filler content improved the binding of the fiber and matrix up to 6% by weight of the filler content. It should be noted that these hybrid composites are a promising material at low cost for lightweight structural applications.

1. Introduction

The usage of naturally produced plant fibers to reinforce polymeric composites for the production of inexpensive engineering materials has attracted considerable interest in recent years [1]. The latest environmental regulations, as well as market demand, have led the manufacturing sectors (in particular, the automotive [2, 3], construction [4], and packaging [5]) to seek alternative products that can be replaced by existing nonrenewable reinforcing materials such as synthetic fibers [6]. The natural properties provided by the natural fibers help in great thermal and acoustic insulation such as lowering density and giving a traditional

cell structure [7–9]. Scientists across the world started to work on finding out an alternative energy in the scenario of a growing crisis of energy. The fibers traditionally used were carbon, glass, and others. The plastics reinforced with sisal [10, 11], jute [12, 13], bamboo [14], and porcelain fibers [15], amongst the natural fibers, have attracted attention for their low cost compared to man-made fibers [16, 17]. Graphite is a pure carbon in crystalline form, very similar to mica sheets formed tightly by bound atoms [18, 19]. However, at normal temperatures, graphite behaves like perfect dry lubricant due to its porosity [20]. This consists of a structure where the carbon atoms are linked. This link is created by covalent bonds with the other carbons in the same plane by the Van

Der Waals force acting between sequential layers [19]. For the effective use of graphite as stuffing in a polymeric composite, the layers should be detached and spread in the polymeric matrix [21], jute fibers were extracted from the jute substrate, which has a bidirectional orientation [22] and the flexibility to improve the properties of natural fibrous composites by modifying the graphite filler matrix [23]. TGA is a heating method that is widely used to describe both inorganic and organic materials, including polymers (e.g., cellulose). It offers quantitative data on the weight loss of a material as a function of temperature [24]. In our previous work for the optimization of the chemical treatment carried out, KmnO_4 was obtained with a concentration of 30% and a treatment time of 40 minutes, and the same methodology has been adopted in the present work.

In that perspective attempt, the influence of micro-graphite filler on the thermal and mechanical properties of used jute natural fiber composite fabricated through hand-layup technique is studied. The FE-SEM analysis was used to analyse the fractured surface. The results were compared with nontreated used jute fiber composite and treated used jute fiber composites. The results revealed that the graphite filler has a significant impact on the material characteristics.

2. Materials and Methods

2.1. Matrix and Fibers. The Araldite LY 556 (Epoxy) and HY951 (Hardener) in 10:1 ratio is used as a matrix [25]. Used jute woven fiber has been extracted from gunny bags, as shown in Figure 1, and woven jute fibers of 350 ± 10 gram per square meter (GSM) was taken for the study.

2.2. Filler. Graphite filler powder of 10–20 microns is used in the present work. The filler content is varied by weight percentage in the matrix by 3 wt.% to 12 wt.% in the 3 wt.% step sizes. The powder is having a density of 1980 kg per cubic meter and a molecular weight of 12.011 g/mol.

2.3. Chemical Treatment. Initially, the fibers were soaked in methanol and Benzene in a 1 : 1 ratio for 24 hours to remove wax, paint, and foreign contaminants. From the weight loss of jute (fabrics) by the NAOH treatment, it was observed that considerable hemicelluloses content was dissolved. To strengthen the fiber, further treatment was done using alkaline, benzyl chloride, and permanganate solutions, respectively. The optimal chemical treatment for used jute fiber is treating with 30% concentration for 40 minutes and post-treating with KmnO_4 [23], for treated composites named in the present work as 30N40K composites, i.e., 30, for 30%, N for NaoH, 40 for 40 minute treatment time, and K for KmnO_4 . For the composite, adding filler after treatment was named as 30N40K + percentage of filler.

2.4. Preparation of Composite. In the development of hybrid composites, the hand-layup technique was used. Varying proportions of a weighted amount of graphite powder and epoxy resin were mixed and later the hardener (HY-951) was



FIGURE 1: Used jute fiber (UJF).

mixed to begin the reaction. With diverse weight fractions of graphite filler (3%, 6%, 9%, and 12%) in the matrix, specimens were prepared. Filler volume was restricted to 12% in the matrix because of the increase in the filler concentration up to 12%, and the mixture became dense losing its fluidity as of the occurrence of gelation. A mould has been prepared for preparing the composites. Moreover, a spray release the mould has been used to ease the cast plate release. With the help of a mechanical jig-saw cutting machine, the dimensions required were marked and sized using the plate. Composites were prepared and tested as per the ASTM standards.

2.5. Testing. Mechanical testing such as tensile, flexural, and impact testing were carried out as per ASTM Standards of D638, D790, and D256. Tensile and flexural tests were carried out using computerised universal testing machine made by Instron. Test is conducted at a cross head speed of 2.5 mm/min. The impact test was carried out with an impact hammer striking at the rate of 3.2 m/s of mass 1.3 kg.

3. Results and Discussion

3.1. Tensile Strength. Figure 2 shows the differences in the strength of the tensile of the laminated composites with graphite filler and without graphite filler. The tensile test was done on the used jute fiber composite and graphite-filled jute fiber composite samples. This was done so to understand the tensile strength. In addition, to know the contribution made by the fillers, the addition of filler influences the variations in the tensile strength of the laminated composites, and this is due to the good dispersion of the filler in the matrix obtained by mechanical stirring.

Figure 3 shows that the failure of treated jute epoxy is due to fiber pull-out, and it is very clear that there is weak bonding between the matrix and the fiber due to which fibers slipped from the matrix and the scars are observed on the matrix. The untreated used jute epoxy composite has tensile strength of 68 MPa; after chemical treatment, it has enhanced by 34% and reached to 96.28 MPa. The tensile strength of graphite-filled jute fiber composites is higher when compared to that of unfilled composites. This might be because of the restriction of the movement and matrix deformability with the introduction of mechanical restraint and the filler particle size.

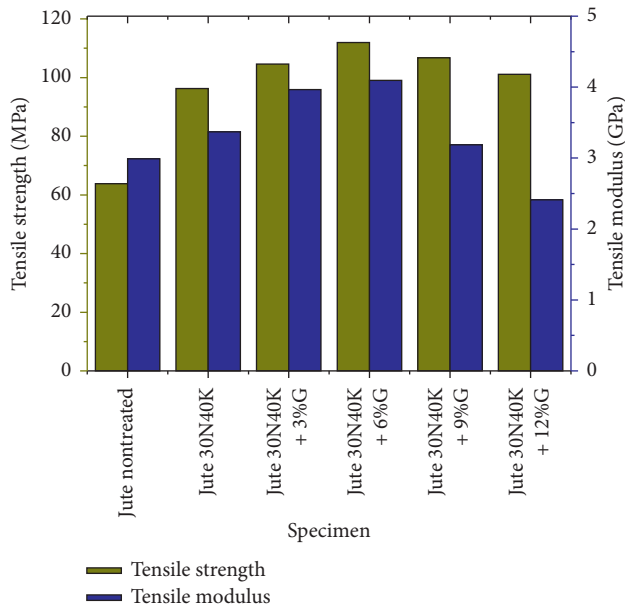


FIGURE 2: Tensile strength of UJE polymer composites.

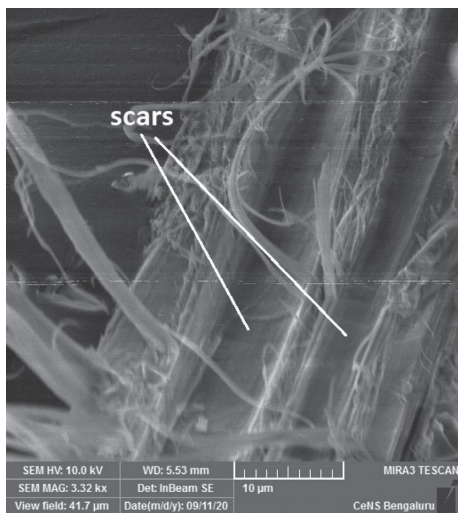


FIGURE 3: SEM of treated used jute epoxy composite specimen.

From Figure 2, the results show that 6 wt.% graphite added epoxy composite with jute fiber as reinforcement yielded the maximum tensile strength value of 111.98 MPa. From Figure 4, it is very clear that, for 6 wt.% filler content, there is strong bonding between the fiber and the matrix. The morphology result shows the splitting of fibers and initiation of matrix cracks. Initially, the matrix fails; then, fiber failure occurs at this percentage. Due to the doping of filler and matrix first failure, the specimen, modulus of composite is reduced, but the strength is enhanced.

Subsequently, it is noticed that because of the increase of filler from 9% to 12%, it is observed that the gradual decrease of the tensile strength and tensile modulus shows slopes down. At 12 wt.% of graphite, tensile strength is observed as 101.14 MPa and modulus is as 2.41 GPa. From Figure 5, it is evident that failure of the composite is due to the slipping of

fibers from the matrix. This phenomenon is due to more amount of filler in the matrix that allows the fiber to slip over the graphite as it is a solid lubricant.

It is obvious that the adding of graphite after a certain amount worsens the tensile strength and the elastic modulus of the composite. It is interesting to note that the increase content of the filler alone and/or 3 wt.% graphite to the fiber shows an enhancement in the vital Longitudinal tensile load-bearing capacity, i.e., tensile strength and the elastic modulus of the epoxy composites [20].

3.2. Flexural Strength. Additionally, the study demonstrates that when graphite content is increased to 9 wt. percent of filler, and the flexural strength increases from 162 MPa to 212 MPa, as shown in Figure 6. This may be due to better adherence of fillers between the matrix and the fiber and also with enriched internal bonding load bearing capability enhanced. Furthermore, flexural strength decreases with the increase of graphite filler due to the agglomeration of graphite filler in the composite. This is due to the high hardness of the filler material [26]. The flexural modulus decreases with an increase in filler content, i.e., graphite percentage decreases.

3.3. Impact Strength. Impact test is conducted to analyse the impact capability of the diverse specimens. Based on the reading obtained from the Charpy impact machine, the energy loss is identified. The impact toughness (strength) is identified by the energy loss of the pendulum, or it can be identified by accurately measuring the height loss in the pendulum's swing. The changes in impact toughness for jute/epoxy laminated composites according to the filling percentage were shown in Figure 7. The percentage of filling is effective on the impact behaviour of jute/epoxy composite material. Among various filling percentages of jute/epoxy composite which was reinforced with 6% filling percentage of graphite, filler had the highest improvement in impact toughness. Graphite filling into jute epoxy up to 6% increased the impact toughness of the material. After 6% filled percentage, these values decreased. This is because the strength in impact loading reduced with the increasing filler density. This occurs as a result of the material's decreased elasticity and the inclusion of fillers, limiting the matrix's deformability and ability to absorb deformation energy. The chemical treatment has greater effect on impact resistance. The filler percentage does not show much effect on impact resistance; however, after 6 wt.%, there is slight reduction in resistance. The more the material's impact energy, the greater its toughness, and vice versa [27].

3.4. Thermal Properties. The thermo-gravimetric analysis (TGA) results of used jute epoxy composite at various filler content are shown in Figure 8. The results revealed that the mass loss was initiated at 100°C and continued up to 410°C. Majority of the mass loss was observed between the temperature range 350–410°C. Up to 100°C, the moisture present in the sample will be evaporated, and then, the matrix

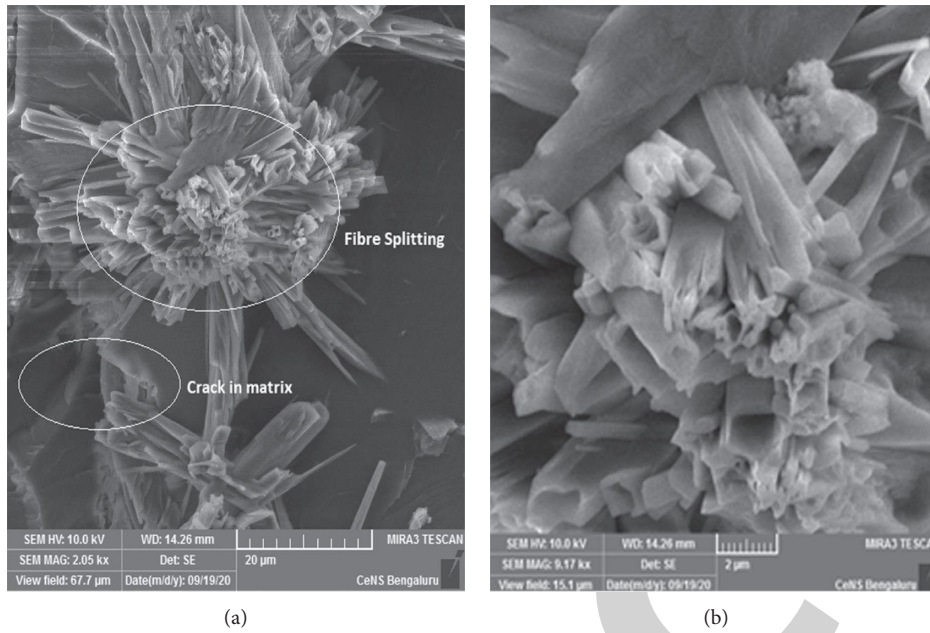


FIGURE 4: SEM of used jute epoxy composite with 6 wt.% of graphite filler in the matrix.

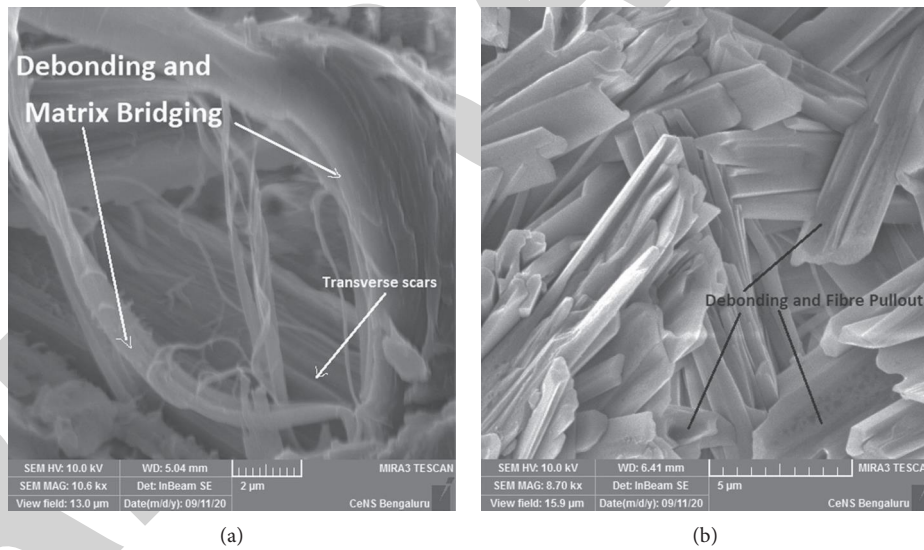


FIGURE 5: SEM of used jute epoxy composite with 12 wt.% of graphite filler in the matrix.

thermal erosion started. From results, it is very clear that the composite specimen without filler initiated mass loss after 100°C, but adding the filler to matrix graphite filler enhanced the stability to resist high temperatures. The matrix degradation was continued up to 350°C.

After 350°C with complete combustion of the matrix, the fibers were exposed and caused by rapid mass loss in

temperature range of 50°C. Natural fiber has less temperature resistance capability. After 400°C, the mass loss was minimum. Almost 70 percent of the composite was completely burnt. The remaining residue slowly degraded with the increase in temperature. After 500°C, there is no observable change in the mass. The residual was very less without filler composite specimen. The residual was

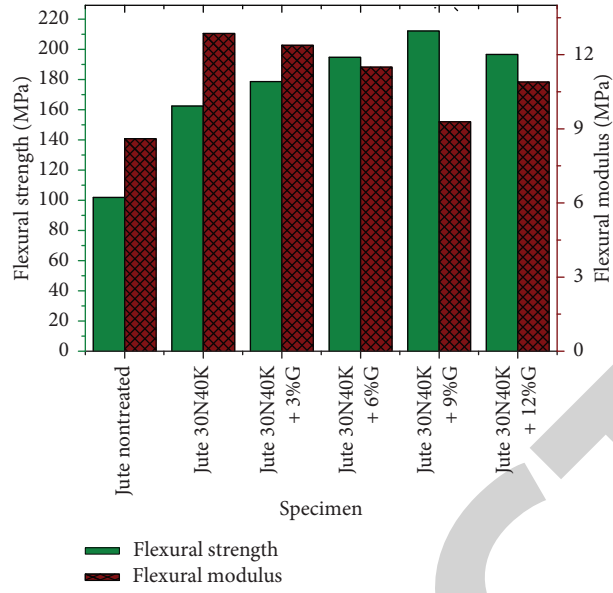


FIGURE 6: Flexural strength of UJE polymer composites.

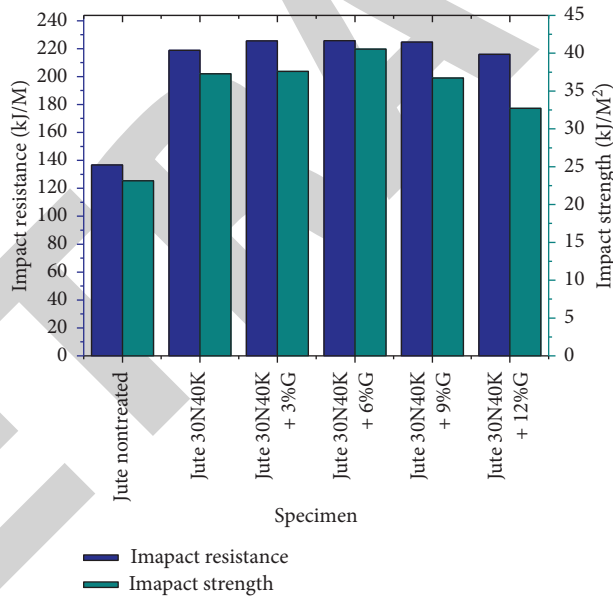


FIGURE 7: Impact strength of UJE polymer composites.

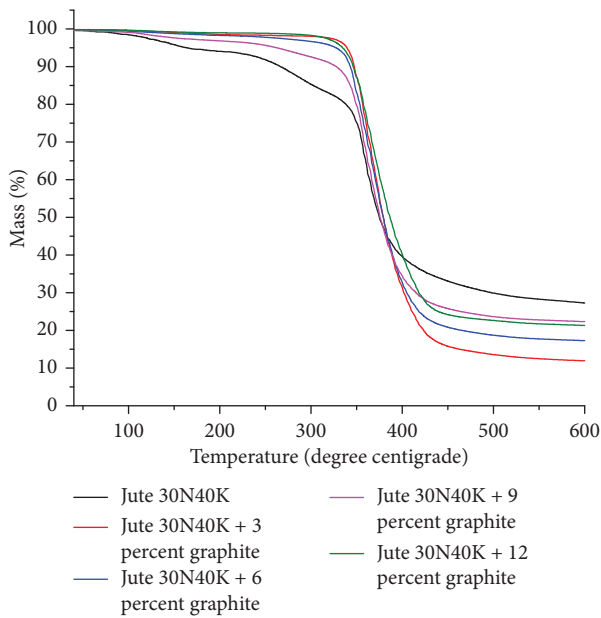


FIGURE 8: TGA curves of chemically treated used jute fiber with different weight ratios of graphite filler.

increasing with the increase in filler content, as the melting point of graphite filler was very high. The residual will increase with an increase in filler content. At the bottom line, the graphite filler enhanced the thermal stability of the composite material and residual.

4. Conclusions

In the present research, by using hand-layup technique, a variety of hybrid composites were developed through the used jute and graphite fillers, which were strengthened with the epoxy thermoset matrix. Evaluation was done on thermal and mechanical properties. The following conclusions were made by this study:

- (1) The results show that 6 wt.% graphite-added epoxy composite with used jute fiber as reinforcement yielded the maximum tensile strength values of 111.98 MPa. The addition of filler influences the variations in the tensile strength of the laminated composites and this is due to the good dispersion of the filler in the matrix attained by mechanical stirring.
- (2) The 9 wt.% graphite added epoxy composite with used jute fiber as reinforcement yielded the maximum flexural strength value of 212 MPa.
- (3) The 6 wt.% of graphite filler composite had the highest improvement in impact toughness. Graphite filling in used jute epoxy up to 6% increased the impact toughness of the material.
- (4) The TGA curve indicated that the graphite filler with 3 wt.% composite shown better thermal stability than the chemically treated used jute fiber composite.

- (5) Graphite filler enhances the mechanical property, creating a mechanical lock between the fiber and the matrix up to 6 wt.% of filler; beyond that, due to the domination of filler content in the matrix, the graphite filler exhibits its natural solid lubricant behaviour, leading to fragile composite.

Data Availability

The data used to support the findings of this study are included within the article.

Disclosure

It was performed as a part of the employment of Bule Hora University.

Conflicts of Interest

The authors declare that there are no conflicts of interest regarding the publication of this paper.

References

- [1] G. Raghavendra, S. Ojha, S. Acharya, and S. Pal, "Jute fiber reinforced epoxy composites and comparison with the glass and neat epoxy composites," *Journal of Composite Materials*, vol. 48, no. 20, pp. 2537–2547, 2014.
- [2] E. G. Koricho, A. Khomenko, M. Haq, L. T. Drzal, G. Belingardi, and B. Martorana, "Effect of hybrid (micro- and nano-) fillers on impact response of GFRP composite," *Composite Structures*, vol. 134, pp. 789–798, 2015.
- [3] N. Saba, M. T. Paridah, and M. Jawaid, "Mechanical properties of kenaf fibre reinforced polymer composite: a review," *Construction and Building Materials*, vol. 76, pp. 87–96, 2015.
- [4] H. O. Öztürk and Y. Kahraman, "Effects of glass fiber reinforcement to tensile strength in epoxy matrix granular composite materials," *Sakarya University Journal of Science*, vol. 23, no. 44066, p. 1, 2019.
- [5] K. Srinivas, A. Lakshumu Naidu, and M. V. A. Raju Bahubalendruni, "A review on chemical and mechanical properties of natural fiber reinforced polymer composites," *International Journal of Performability Engineering*, vol. 13, no. 2, pp. 189–200, 2017.
- [6] R. V. Silva, E. M. F. Aquino, L. P. S. Rodrigues, and A. R. F. Barros, "Curaua/glass hybrid composite: the effect of water aging on the mechanical properties," *Journal of Reinforced Plastics and Composites*, vol. 28, no. 15, pp. 1857–1868, 2009.
- [7] P. K. Bajpai, I. Singh, and J. Madaan, "Comparative studies of mechanical and morphological properties of polylactic acid and polypropylene based natural fiber composites," *Journal of Reinforced Plastics and Composites*, vol. 31, no. 24, pp. 1712–1724, 2012.
- [8] S. Biswas, A. Satapathy, and A. Patnaik, "Effect of ceramic fillers on mechanical properties of bamboo fiber reinforced epoxy composites: a comparative study," *Advanced Materials Research*, vol. 123–125, pp. 1031–1034, 2010.
- [9] S. Biswas, Q. Ahsan, A. Cenna, M. Hasan, and A. Hassan, "Physical and mechanical properties of jute, bamboo and coir

Retraction

Retracted: Strength Enhancement Study on Composites of AA6066 Aluminium Alloy with Magnesium Oxide and Coal Ash

Advances in Materials Science and Engineering

Received 26 December 2023; Accepted 26 December 2023; Published 29 December 2023

Copyright © 2023 Advances in Materials Science and Engineering. This is an open access article distributed under the Creative Commons Attribution License, which permits unrestricted use, distribution, and reproduction in any medium, provided the original work is properly cited.

This article has been retracted by Hindawi, as publisher, following an investigation undertaken by the publisher [1]. This investigation has uncovered evidence of systematic manipulation of the publication and peer-review process. We cannot, therefore, vouch for the reliability or integrity of this article.

Please note that this notice is intended solely to alert readers that the peer-review process of this article has been compromised.

Wiley and Hindawi regret that the usual quality checks did not identify these issues before publication and have since put additional measures in place to safeguard research integrity.

We wish to credit our Research Integrity and Research Publishing teams and anonymous and named external researchers and research integrity experts for contributing to this investigation.

The corresponding author, as the representative of all authors, has been given the opportunity to register their agreement or disagreement to this retraction. We have kept a record of any response received.

References

- [1] L. Ponraj Sankar, G. Aruna, T. Sathish et al., "Strength Enhancement Study on Composites of AA6066 Aluminium Alloy with Magnesium Oxide and Coal Ash," *Advances in Materials Science and Engineering*, vol. 2021, Article ID 2810106, 8 pages, 2021.

Review Article

Strength Enhancement Study on Composites of AA6066 Aluminium Alloy with Magnesium Oxide and Coal Ash

L. Ponraj Sankar,¹ G. Aruna,¹ T. Sathish ,² A. Parthiban,³ V. Vijayan,⁴ S. Dinesh Kumar,⁵ S. Rajkumar ,⁶ Addisalem Mekonnen,⁶ and Mebratu Tufa⁶

¹Department of Civil Engineering, CMR Institute of Technology, Hyderabad, India

²Department of Mechanical Engineering, Saveetha School of Engineering, SIMATS, Chennai 602105, Tamil Nadu, India

³Department of Mechanical Engineering, Vels Institute of Science Technology & Advanced Studies, Pallavaram, Chennai 600117, Tamil Nadu, India

⁴Department of Mechanical Engineering, K. Ramakrishnan College of Technology (Autonomous), Samayapuram, Trichy 621112, Tamil Nadu, India

⁵Department of Mechanical Engineering, St. Peter's Institute of Higher Education and Research, Avadi, Chennai 600054, Tamil Nadu, India

⁶Department of Mechanical Engineering, Faculty of Manufacturing, Institute of Technology, Hawassa University, Hawassa, Ethiopia

Correspondence should be addressed to S. Rajkumar; rajkumar@hu.edu.et

Received 6 June 2021; Accepted 2 July 2021; Published 13 July 2021

Academic Editor: Samson Jerold Samuel Chelladurai

Copyright © 2021 L. Ponraj Sankar et al. This is an open access article distributed under the Creative Commons Attribution License, which permits unrestricted use, distribution, and reproduction in any medium, provided the original work is properly cited.

Aluminium alloy is the most favourable material based on the various properties and economic factors. Always there are so many researches going on based on the enhancement of the material properties with various combinations and the various materials mixing rate depending upon the availability. These researches were focused on the augmentations of the properties, and then the corresponding properties can be used in the various applications depending upon the results. In this study, the AA6066 aluminium alloy composites were created with the magnesium oxide and coal ash with a variety of grouping. The specimens were named as AAMgOCA 1 to AAMgOCA 6 with respect to the volume concentration composition. Then, the composites were tested to identify the impact on various strengths such as yield strength, ultimate tensile strength, shear strength, and flexural strength. These strengths were compared with the two conditions of the composites such as annealed and heat-treated conditions. AAMgOCA 3 has the greatest results in heat-treated condition when compared with the annealed condition.

1. Introduction

There are number of researchers who were encouraged to conduct research to identify the new things and alteration of the existing things which are applicable for engineering materials especially in aluminium alloy due to its wide usage among all the places. Georgantzia et al. [1] explained the various uses of aluminium alloys in different structure-based applications with various recognizable buildings in UK, USA, UAE, Russia, etc. They also reviewed various researchers' point of view and gave idea about the different

grades of aluminium alloys. Davis JR [2] provided the outline of fundamental values and explanations for produced alloys and the equivalent subdivisions. He gave the method of annealed conditions for ductility, toughness, etc.

Zhu et al. [3] discussed the heat treatment conditions and methods of the various aluminium alloys with eight tests. They also followed the design code standards for preparation of the specimens. The various methods can be identified with the basic methods. Mukhopadhyay [4] individually reviewed the aluminium alloy 6XXX series with respect to designing and handing out through nearly

seventy-five references. He completely gave a variety of specifications, heat treatment methods, characteristics, and also the application point of view for the 6XXX series. AA6066 alloy has the percentage composition of 1.3% of magnesium, 1.6% of silicon, 1.15% of copper, 0.38% of chromium, and 1.05% of manganese, and the remaining is aluminium alloy in the total composition [4].

Tiryakioğlu et al. [5] talked about the harness strength in the aluminium alloy with some mathematical relations as well as the various SEM images in the different approaches. The considered material's pulverized powders are shown in Figure 1. Palani et al. [6] mentioned that the annealed casting specimens have higher dimensional stability and ductility when compared with the tempered specimens and similarly explained the hardened products which also have obtainable ductility in front of the elevated temperatures.

Imran et al. [7] investigated the composite specimen of Al7075 aluminium alloy with various combinations of the graphite and bagasse ash for testing of mechanical properties such as the ultimate tensile strength, hardness, percentage of elongation, and yield strength comparison. They also individually plotted and compared the various percentage variations with optimization technique. They concluded that the hybrid composites provided the greatest enhancement in their properties when compared with the individual alloy specimen.

Kumar et al. [8] focused only about the wear and tensile strength of the aluminium-based composite with silicon and titanium. From this investigation, microstructures were clearly identified and porosity can be controlled by the design parameters of the mold. Uthayakumar et al. [9] explained the hybrid composites of boron carbide- and silicon carbide-used aluminium alloy with various sliding circumstance for performance of the wear rate. Kumar and Dhiman [10] investigated and explained the response surface methodology-based hybrid and normal alloy of Al7075 aluminium alloy.

Senapati et al. [11] clearly explained the fly ash participation in the production of matrix composite of the aluminium alloy in the successive way. Mohammed Razzaq et al. [12] explained the reinforcement of the aluminium alloy with the fly ash composites. They clearly explained the basic properties and microstructure with XRD images and SEM images. The bulk density, porosity formation, impact strength, hardness, and brittleness of the reinforced composites were directly proportional to the fly ash content in the total proportions.

Sivaprasad et al. [13] studied the aluminium composite with titanium diboride reinforcement and studied the mechanical properties and mentioned the various applications. Wang et al. [14] investigated the reinforcement of aluminium alloy with the metallic glass fiber with the help of the microstructures and various characteristics. They concluded that the adhesive strength is the prior quality for the composites of the metal matrix. Efsan et al. [15] clearly explained fly ash-based aluminium composites along with applications with respect to the mechanical and physical behaviours.

Singh and Chauhan [16] reviewed the hybrid composites of the aluminium alloy with a number of research articles and they concluded that the properties of the composites were increased with increasing the percentage concentration on the composites. Sun et al. [17] clearly explained the aluminium alloy, titanium oxide, and magnesium oxide-based composite in heat treatment condition with the help of SEM images and XRD images. Tong et al. [18] also investigated the alumina and magnesium oxide composite-based mechanical properties enhancement by heat treatment.

Manikandan et al. [19] discussed magnesium oxide with aluminium alloy composite by reinforcement. The mechanical properties like compression strength, hardness, and wear behaviour were analysed with various SEM images. They concluded that the wear rate can be increased with the increase of the percentage of the magnesium oxide in total volume percentage. Kheder et al. [20] discussed and compared the composite combination of the aluminium alloy with various percentages of aluminium oxide, silicon carbide, and magnesium oxide separately. Increase of these metals in aluminium alloy provides enhancement in the mechanical properties; also, they mentioned that the magnesium oxide with aluminium alloy composite can be used in the structural components in the construction field related applications with high strength. The combined effect of the aluminium alloy at any series with the hard reinforced particles induced the high strength of the composites even at any type of composite preparation process [21, 22]. The mechanical properties also increased gradually by addition of reinforcement particles into the aluminium alloy [23].

In this study, the aluminium alloy composite reinforcement is involved with magnesium oxide and the coal ash with various percentage. Then the composites were forced for annealed and heat-treated conditions. The corresponding mechanical properties for these composites with two conditions were compared to identify the greater results among the composites.

2. Experimental Procedure

For this approach, aluminium alloy AA6066 composites are created using magnesium oxide and coal ash as per the combination of volume percentage variation in the complete volume in Table 1. All the materials were available in the market which are collected and used for the experiments. The coal ash is collected from the thermal power stations outcome which is cleaned and filtered from the various dust particles. The entire composite contains eighty percent of aluminium alloy AA6066 as a major component. The remaining twenty percent of the composite is filled with magnesium oxide and coal ash. Magnesium oxide proportion decreased from twenty percent to zero percent with four percent decrement for each specimen.

Similarly, coal ash percentage is increased from zero contribution to twenty percent with decrement of four percent. There are six combinations of the specimens prepared. The name of composite created was as per the mixing material's notations AAMgOCA (AA means aluminium alloy, MgO means magnesium oxide, and CA means coal

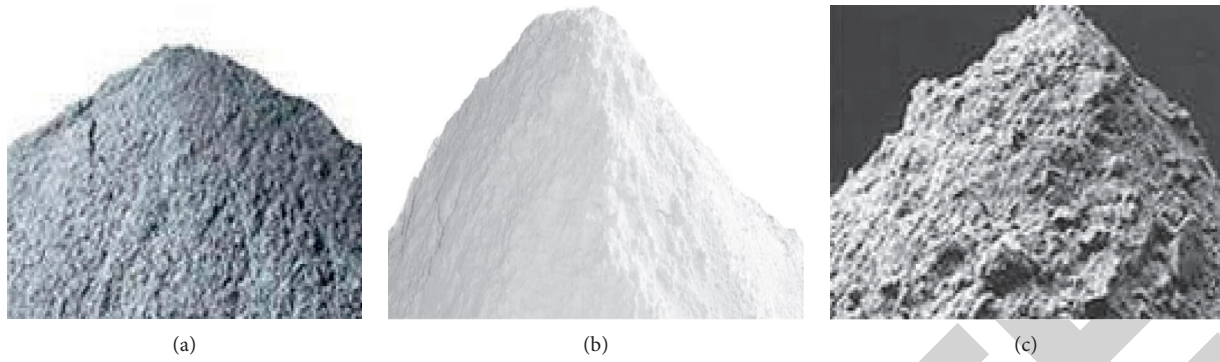


FIGURE 1: Powdered form of the materials. (a) AA6066. (b) MgO. (c) Coal ash.

TABLE 1: Percentage details of the composites for the experimental purpose.

Composite name	Volume percentage of the total composite (%)		
	AA6066	MgO	Coal ash
AAMgOCA 1	80	20	0
AAMgOCA 2		16	4
AAMgOCA 3		12	8
AAMgOCA 4		8	12
AAMgOCA 5		4	16
AAMgOCA 6		0	20

ash) with number from 1 to 6 for the various combinations of metals.

The individual specimens were prepared by the sand molding method. Sand molding process was created by tightly packing of sand with the addition of clay binder and correct level of water in the molding boxes. The mold cavity was formed by the way of pattern. The metal pattern was used for this experimental work; it formed the required shape of the samples after casting. The molten metal was poured into the mold cavity through the gate way; after filling the mold cavity, the molten material was allowed to cool. After solidification process, the casting part was removed from the sand mold; finally, the unwanted projection was removed by the fettling process. The metals used for this investigation were taken in the form of powder with the dimension from 30 microns to 70 microns. Here, the specimen was prepared with the dimension of 40 mm diameter and 200 mm length in three numbers for each combination. Then, the prepared rod specimens were carried for the two conditions such as annealed (900 K) condition and the heat-treated (1100 K) condition and then cooled artificially. Each specimen should maintain these two conditions.

In this place, there are four different mechanical strength tests conducted for the strength comparison on each combination in two conditions. The strengths considered for this experimental investigation were followed such as yield strength (YS), ultimate tensile strength (UTS), shear strength (SS), and flexural strength (FS). All these tests were conducted with the help of the universal testing machine mentioned in Figure 2. ASI brand universal testing machine was used to conduct the tensile test; the universal testing machine had a



FIGURE 2: UTM for the testing.

capacity of 60 tones. The model of the UTM was named UTE-60; this machine was functioning hydraulically. The bending test was also termed flexural test; it was conducted by universal testing machine with three-point bend fixture; normally, 3-point bend fixture was used. Then the created specimens were prepared as per the testing standards of the individual testing conditions with respect to the universal testing machine. In this experimental work ASTM E8 standard procedure was used to conduct the tensile test.

Ultimate tensile strength and the yield strength can be measured in single specimen with the single attempt of the testing. But the shear strength and flexural strength need separate specimens and separate arrangement change in the UTM. Then the corresponding arrangements were created with respect to the testing and Figure 3 shows the arrangement and testing method for the flexural strength. Finally, the experimental results from the individual tests were taken for both annealed condition and heat treatment conditions.

3. Result and Discussion

The complete experimental results of yield strength (YS), ultimate tensile strength (UTS), shear strength (SS), and

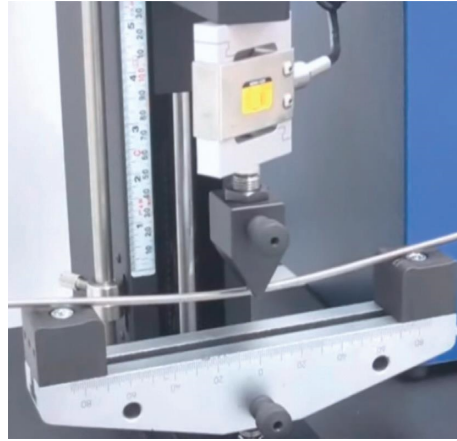


FIGURE 3: Flexural testing.

flexural strength (FS) obtained from the various testing conducted with annealed conditions and heat-treated conditions for the each specimens are clearly pointed out in Tables 2 and 3 correspondingly in the unit of MPa for all the strengths.

Figure 3 represents the yield strength comparison in the form of three-dimensional surface plot for both annealed and heat-treated specimens. Annealed specimens have less yield strength when compared with heat-treated specimens' results. For heat-treated condition, the maximum yield strength (415 MPa) is reached for the specimen AAMgOCA 3 and the minimum yield strength (395.59 MPa) is achieved for the specimen AAMgOCA 1. For the greatest result the annealed specimens were very low when compared with lowest heat-treated specimen.

The experimental outcomes of the ultimate tensile strength comparison for the annealed and heat-treated conditions are explained in Figure 4 as a three-dimensional surface plot. From this plot, ultimate tensile strength of heat-treated specimens' results was greater than the annealed specimens with higher difference. The supreme ultimate tensile strength of 452.76 MPa has been obtained for the specimen AAMgOCA 3 for heat-treated specimens. Similarly, the greatest ultimate tensile strength value for annealed condition can be achieved for the same specimen as 172.98 MPa which is very low.

The measured experimental results of shear strength for heat-treated specimens and annealed specimens were clearly mentioned as the three-dimensional surface plot in Figure 5. The highest and lowest shear strength for the annealed specimens were 109.12 MPa (AAMgOCA 3) and 103.87 MPa (AAMgOCA 1), respectively. Similarly, the greatest and smallest shear strength values for the heat-treated specimens were 265.85 MPa (AAMgOCA 3) and 253.04 MPa (AAMgOCA 1). Among these values, the lowest values of the heat-treated specimen were also higher than the highest shear strength value of the annealed specimens.

In Figure 6, the three-dimensional surface plot was plotted for the comparison on the flexural strength results from the experiments for heat-treated specimens comparison with the annealed specimens. The maximum and

TABLE 2: Experimental outcome of the specimens in annealed conditions.

Specimen name	Annealed specimens (MPa)			
	YS	UTS	SS	FS
AAMgOCA 1	91.2	164.645	103.87	78.455
AAMgOCA 2	93.48	168.761	106.466	80.416
AAMgOCA 3	95.817	172.98	109.128	82.426
AAMgOCA 4	94.619	170.817	107.764	81.396
AAMgOCA 5	93.436	168.682	106.417	80.378
AAMgOCA 6	92.268	166.574	105.087	79.374

TABLE 3: Experimental outcome of the specimens in heat-treated conditions.

Specimen name	Heat-treated specimens (MPa)			
	YS	UTS	SS	FS
AAMgOCA 1	395.59	430.95	253.045	130.39
AAMgOCA 2	405.479	441.723	259.371	133.649
AAMgOCA 3	415.616	452.766	265.855	136.99
AAMgOCA 4	410.421	447.107	262.532	135.278
AAMgOCA 5	405.291	441.518	259.250	133.587
AAMgOCA 6	400.225	435.999	256.009	131.917

minimum flexural strength for the heat-treated specimens were 136.99 MPa (AAMgOCA 3) and 130.89 MPa (AAMgOCA 1), respectively. Similarly, the supreme and least flexural strength values for the annealed specimens were 82.42 MPa (AAMgOCA 3) and 78.45 MPa (AAMgOCA 1). Among these values, the lowest flexural strength (136.99 MPa) of the heat-treated specimen was also higher than the highest flexural strength (82.42 MPa) of the annealed specimens.

The comparisons of the all experimental results based on the strength for the specimens in both heat-treated and annealed condition were clearly mentioned as a bar chart in Figure 7. These composites have the highest ultimate tensile strength and lower flexural strength among these strengths. The annealed specimens have the lower results when compared with heat-treated specimens for all specimens'

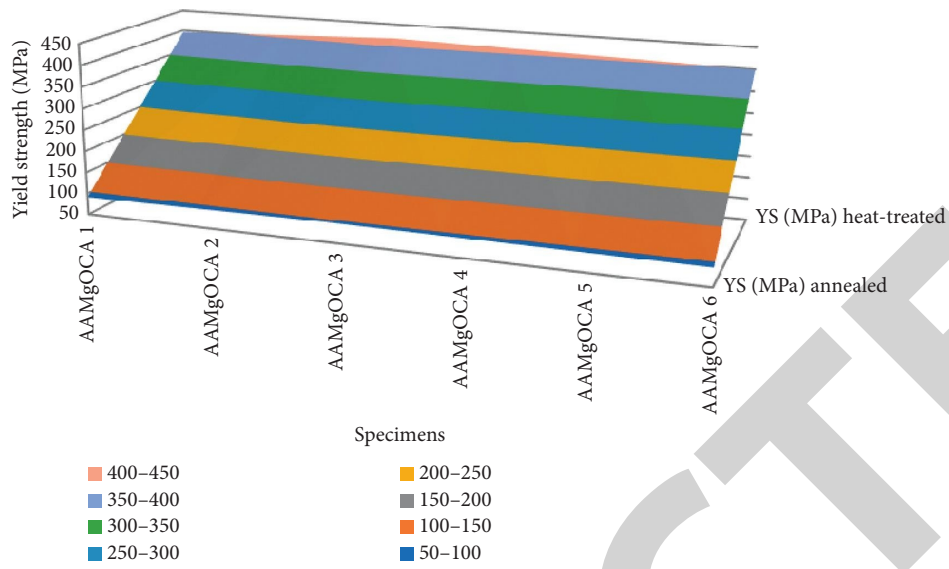


FIGURE 4: Three-dimensional surface plot comparison on yield strength.

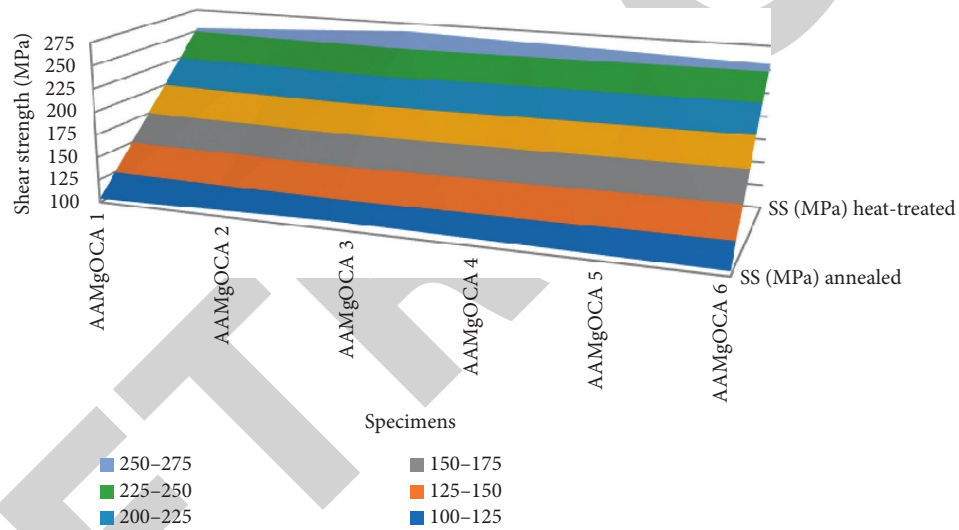


FIGURE 5: Three-dimensional surface plot comparison on shear strength.

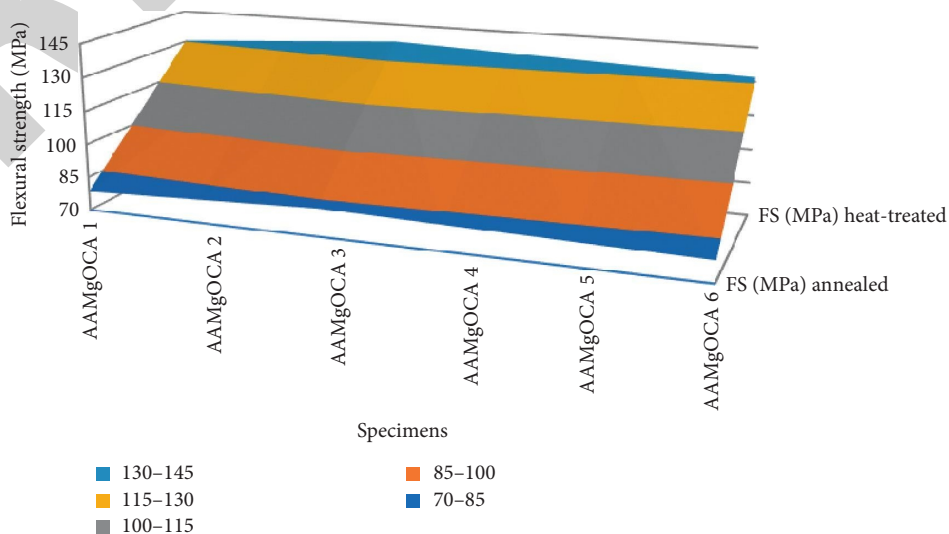


FIGURE 6: Three-dimensional surface plot comparison on flexural strength.

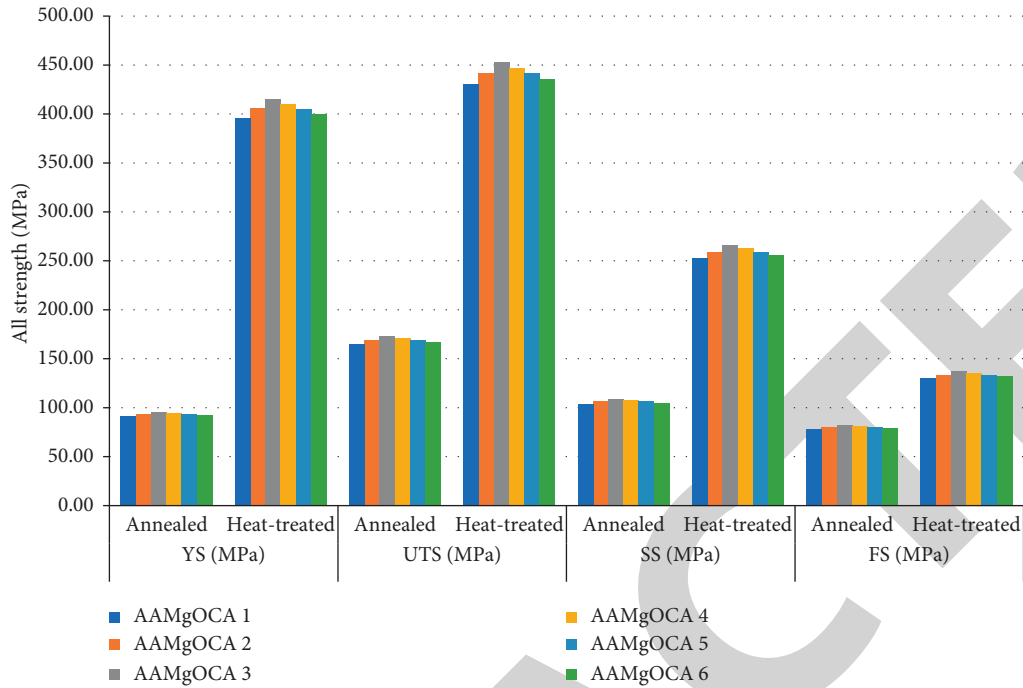


FIGURE 7: Comparison of all specimen results based on strength.

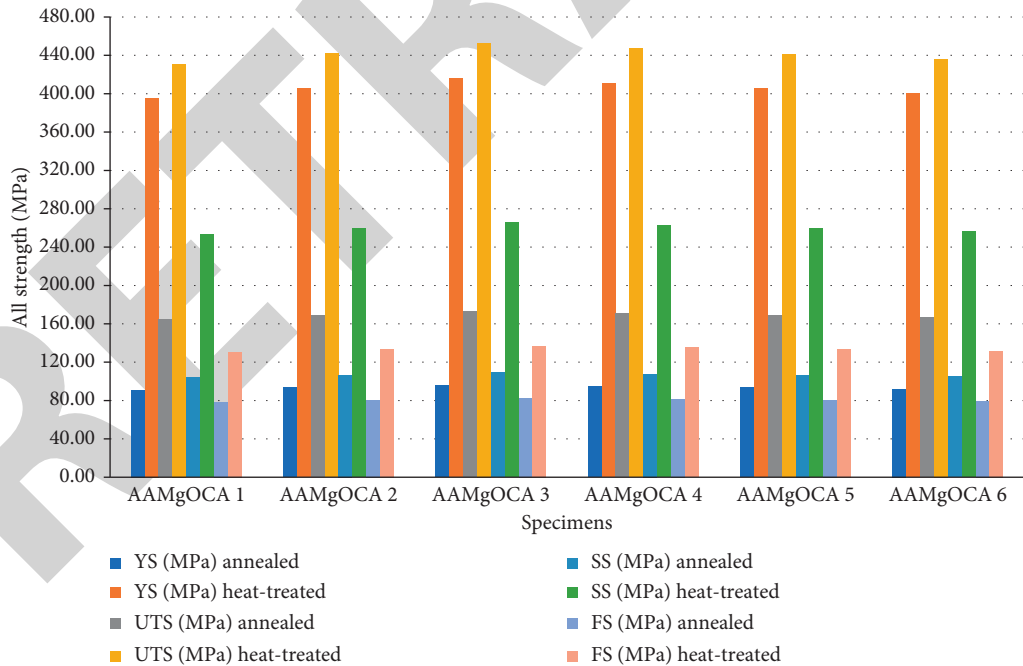


FIGURE 8: Comparison of all experimental results based on specimens.

yield strength (YS), ultimate tensile strength (UTS), shear strength (SS), and flexural strength (FS). The values of all strengths were increased up to the AAMgOCA 3, and then, the strengths were decreased up to AAMgOCA 6.

Similarly, Figure 8 gives the details of experimental results of all strengths for both heat-treated and annealed condition with respect to the individual specimens. Among these six specimens AAMgOCA 3 had the greatest results of

TABLE 4: Maximum experimental results.

Specimen name	YS (MPa)		UTS (MPa)		SS (MPa)		FS (MPa)	
	Annealed	Heat-treated	Annealed	Heat-treated	Annealed	Heat-treated	Annealed	Heat-treated
AAMgOCA 3	95.82	415.62	172.98	452.77	109.13	265.86	82.43	136.99

all strengths when compared with other specimens for both heat-treated and annealed condition. Similarly, AAMgOCA 1 specimen had the minimum values of all tested results in the investigation for both annealing and heat-treated condition. The maximum strength values are mentioned in Table 4 for specimen AAMgOCA 3.

4. Conclusion

The mechanical strength enhancement study on composite of AA6066 aluminium alloy with magnesium oxide and coal ash through various experimental results produced the following as conclusions:

- (i) The composite of the AA6066 aluminium alloy with magnesium oxide and coal ash with different combinations based on Table 1 is possible.
- (ii) In all the experimental results, annealed specimens have the lower results in strength value
- (iii) Similarly, for all the experimental results, heat-treated specimens have the higher results in strength value
- (iv) From the comparison, the specimen "AAMgOCA 3" has reached the highest experimental results for both conditions (Table 4)
- (v) The strength values get increased up to the specimen AAMgOCA 3, and then the results start to decrease simultaneously
- (vi) So, the coal ash participation less than MgO produced the good result when compared with the higher coal ash concentration specimens' results
- (vii) Therefore minimizing the coal ash content and maximizing the MgO participations provide the greatest result in strength
- (viii) At last, 80% of AA6066 aluminium alloy with 12% of MgO and 8% of coal ash reached the maximum yield strength, ultimate tensile strength, shear strength, and flexural strength when compared with the remaining composite specimens

Data Availability

The data used to support the findings of this study are included in the article. Further data or information are available from the corresponding author upon request.

Disclosure

This work was performed as a part of the Employment of College of Engineering and Technology, Hawassa University, Hawassa, Ethiopia.

Conflicts of Interest

The authors declare that there are no conflicts of interest regarding the publication of this paper.

Acknowledgments

The authors appreciate the support from Hawassa University, Ethiopia. The authors thank Saveetha School of Engineering, Chennai, for the technical assistance to complete this experimental work.

References

- [1] E. Georgantzia, M. Gkantou, and G. S. Kamaris, "Aluminium alloys as structural material: a review of research," *Engineering Structures*, vol. 227, Article ID 111372, 2021.
- [2] J. R. Davis, *Alloying: Understanding the Basics*, ASM international, Geauga County, Ohio, 2001.
- [3] J. Zhu, P. Wang, and T. Liu, "Numerical simulation and design of aluminum compression members with plain and lipped channel sections," *Journal of Building Structures*, vol. 31, pp. 163–168, 2010.
- [4] P. Mukhopadhyay, "Alloy designation, processing, and use of AA6XXX series aluminium alloys," *International Scholarly Research Notices*, vol. 2012, 2012.
- [5] M. Tiryakioğlu, J. S. Robinson, M. A. Salazar-Guapuriche, Y. Y. Zhao, and P. D. Eason, "Hardness–strength relationships in the aluminum alloy 7010," *Materials Science and Engineering*, vol. 631, pp. 196–200, 2015.
- [6] Y. Palani, C. Devarajan, D. Manickam, and S. Thanikodi, "Performance and emission characteristics of biodiesel-blend in diesel engine: a review," *Environmental Engineering Research, Korean society of Environmental Engineers*, vol. 27, no. 1, pp. 1–12, 2022.
- [7] M. Imran, S. M. Khan, A. R. A. Khan, S. Megeri, and S. Sadik, "Study of hardness and tensile strength of Aluminium-7075 percentage varying reinforced with graphite and bagasse-ash composites," *Resource-Efficient Technologies*, vol. 2, no. 2, pp. 81–88, 2016.
- [8] S. Kumar, M. Chakraborty, V. SubramanyaSarma, and B. S. Murty, "Tensile and wear behaviour of in situ Al-7Si/TiB₂ particulate composites," *Wear*, vol. 265, no. 1–2, pp. 134–142, 2008.
- [9] M. Uthayakumar, S. Aravindan, and K. Rajkumar, "Wear performance of Al-SiC-B₄C hybrid composites under dry sliding conditions," *Materials & Design*, vol. 47, pp. 456–464, 2013.
- [10] R. Kumar and S. Dhiman, "A study of sliding wear behaviors of Al-7075 alloy and Al-7075 hybrid composite by response surface methodology analysis," *Materials & Design*, vol. 50, pp. 351–359, 2013.
- [11] A. K. Senapati, P. C. Mishra, and B. C. Routara, "Use of waste flyash in fabrication of aluminium alloy matrix composite," *International Journal of Engineering and Technology*, vol. 6, no. no. 2, pp. 905–912, 2014.

Retraction

Retracted: Effect of Grey and White Portland Cement Fillers on Flexural and Shear Strength of GFRP Composite Material

Advances in Materials Science and Engineering

Received 26 December 2023; Accepted 26 December 2023; Published 29 December 2023

Copyright © 2023 Advances in Materials Science and Engineering. This is an open access article distributed under the Creative Commons Attribution License, which permits unrestricted use, distribution, and reproduction in any medium, provided the original work is properly cited.

This article has been retracted by Hindawi, as publisher, following an investigation undertaken by the publisher [1]. This investigation has uncovered evidence of systematic manipulation of the publication and peer-review process. We cannot, therefore, vouch for the reliability or integrity of this article.

Please note that this notice is intended solely to alert readers that the peer-review process of this article has been compromised.

Wiley and Hindawi regret that the usual quality checks did not identify these issues before publication and have since put additional measures in place to safeguard research integrity.

We wish to credit our Research Integrity and Research Publishing teams and anonymous and named external researchers and research integrity experts for contributing to this investigation.

The corresponding author, as the representative of all authors, has been given the opportunity to register their agreement or disagreement to this retraction. We have kept a record of any response received.

References

- [1] D. H. Vardhan, D. Sai Chaithanya Kishore, Y. Santhosh Kumar Reddy, K. Manohar Reddy, G. Raghavendra, and R. Rudrapati, "Effect of Grey and White Portland Cement Fillers on Flexural and Shear Strength of GFRP Composite Material," *Advances in Materials Science and Engineering*, vol. 2021, Article ID 9586474, 7 pages, 2021.

Research Article

Effect of Grey and White Portland Cement Fillers on Flexural and Shear Strength of GFRP Composite Material

D. Harsha Vardhan ¹, **D. Sai Chaithanya Kishore**,² **Y. Santhosh Kumar Reddy**,¹
K. Manohar Reddy,¹ **Gujjala Raghavendra**,³ and **Ramesh Rudrapati** ⁴

¹Department of Mechanical Engineering, PVKK Institute of Technology, Ananthapuramu, Andhra Pradesh 515001, India

²Department of Mechanical Engineering, Srinivasa Ramanujan Institute of Technology, Ananthapuramu, Andhra Pradesh 515701, India

³Department of Mechanical Engineering, National Institute of Technology, Warangal 506004, Telangana, India

⁴Department of Industrial Engineering, Bule Hora University, Bule Hora 144, Ethiopia

Correspondence should be addressed to Ramesh Rudrapati; rameshrudrapati@gmail.com

Received 8 June 2021; Revised 21 June 2021; Accepted 2 July 2021; Published 9 July 2021

Academic Editor: Samson Jerold Samuel Chelladurai

Copyright © 2021 D. Harsha Vardhan et al. This is an open access article distributed under the Creative Commons Attribution License, which permits unrestricted use, distribution, and reproduction in any medium, provided the original work is properly cited.

The mechanical behaviour of glass fiber reinforced polymer (GFRP) composite depends on the type of matrix, filler, and fiber architecture. In order to develop high-strength polymer matrix composites, the composites containing 5%, 10%, and 15% each of Portland grey and white cement filler are prepared by uniformly mixing the epoxy and filler materials, followed by casting by hand layup technique. The flexural and shear test is performed in accordance with ASTM 790 and ASTM D5379, respectively. It has been found that the values of shear strength, flexural strength, and modulus of elasticity vary with the increasing amount of cement component in the polymer. In addition, for a given percentage of the components of the cementitious filler, the values of the mechanical strength of the composites that contain white cement are higher than those of the composites that contain grey cement filler. Damage to composites has been found to involve fiber breakage and delamination primarily.

1. Introduction

The exploration of polymer matrix composites is more on demand, because of their tailorable properties [1–3]. Many researchers are contributing to satisfy the market needs. Among the available polymer composites, the glass fiber reinforced composites are used for exploring more applications because of their incredible mechanical characteristics at low cost [4]. But most of the glass fiber composite failure occurs at matrix fiber interface [5]. In order to make composites stronger, the filler material is introduced into the matrix in micro- and nanoranges. The filler materials show great impact on the mechanical characteristics and failure mechanism, as well as on the fiber matrix bonding [6–9]. From the literature, the researchers have used various kinds of fillers to investigate the effect of the filler material on the characteristics of the composite material. The study is carried out with natural fillers like clay [10]; coconut shell

particles [8]; rice husk, wheat husk, and coconut coir [11]; and oil palm shell (OPS) powder [12]. Extensive research was done more with ceramic fillers and man-made fillers such as MWCNT [12], graphite [13], TiO₂, Sic [14], and Al₂O₃ [15]. The size and the shape of the filler also influence the composite characteristics, and the behaviour composite changes with the factors [16].

A very less amount of research was carried out on the use of compound fillers such as cement into the composite materials as a filler material and the studies reveal that the cement fillers help in the improvisation of the mechanical properties. [17–20]. Cement is a composition of various elements such as limestone or calcium oxide (CaO), silicon dioxide (SiO₂), aluminum oxide (Al₂O₃), iron oxide (Fe₂O₃), magnesium oxide (MgO), and sulphur trioxide (SO₃) and other insignificant elements for the formation of compounds. Basically, there are two categories of grey cement and white cement [18, 19]. Grey cement comprises a larger

amount of iron oxide and manganese oxide compared to white cement. The average granular size of white cement is smaller than that of grey cement. As cement is the combination of fillers commonly using polymer composite, the compound of all those fillers may enhance the mechanical behaviour. This particular aspect has created interest in carrying out this work. To analyse the impact of constituent element combinations, two varieties of Portland cement are considered for the study. It is proved that the glass fiber and cement have a good affinity and they have been used in construction industry as concrete/cement matrix with glass fiber [21–23].

The main objective of the present study was to investigate the effect of cement as a filler in GFRP composites' flexural and shear strengths. Grey and white commercial cement were chosen to be used as a filler. The results of the study show that the cement fillers exhibit significant impact on material characteristics.

2. Materials and Methods

Woven-Twill glass fiber ($0^\circ/90^\circ$) was used in the preparation of GFRP composites. Composite samples are prepared by hand layup. Specific percentages by weight of grey and white cement have been added as 5%, 10%, and 15% by weight of the matrix. First of all, the necessary amount of epoxy (Araldite LY556) is taken in a glass beaker and predefined amount of filler is taken in it. The mixture was manually stirred to create an evenly distributed solution. Upon combining the epoxy and the cement properly, a hardener (Araldite HY951) is introduced at a ratio of 1 : 10 by weight of epoxy and the mixture is remixed. As the mixture is ready, in the hand layup method, a portion of epoxy mixture is poured into mould and distributed uniformly. Next a layer of fibers is placed into the mould, and then remaining mixture is poured and distributed uniformly. Composite is exposed to uniform pressure on top surface to boost the penetration of matrix with fiber so that it does not accumulate epoxy or dry fiber spots. The composite can be treated in a compressed state for approximately 24 hours. Upon diagnosis, the composite is cut in order to prepare samples for different mechanical tests [17].

The fabricated samples are cut into samples to perform flexural and shear tests. Samples are coded as C1 for GFRP, C2 to C4 for grey cement fillers in GFRP, and C5 to C7 for white cement fillers as shown in Table 1. The flexural samples are cut into 126 mm \times 13 mm according to ASTM D790, as shown in Figure 1. Shear test samples are cut into 76 mm \times 19 mm with a middle double V-notch with 90° internal angles and 3.8 mm depth, as per the ASTM D5379 (Iosipescu). Shear test of the composite is as shown in Figure 2. Tests are carried out on computer-aided universal testing machine at a relative humidity of $50 \pm 5\%$ and on an environment temperature of $23 \pm 2^\circ\text{C}$ with a crosshead speed of 5 mm/min. The flexural modulus is an index of flexibility in bending, in other words, the amount of force consumed per unit area per unit of elongation. In order to analyse the rigidity of the samples, the elongation must be kept constant. In this connection, flexural modulus at 1% of strain is measured in the present work.

TABLE 1: Coding of samples.

S. no.	Specimen code	Sample
1	C1	GFRP
2	C2	GFRP with 5 wt.% weight of grey cement filler
3	C3	GFRP with 10 wt.% weight of grey cement filler
4	C4	GFRP with 15 wt.% weight of grey cement filler
5	C5	GFRP with 5 wt.% weight of white cement filler
6	C6	GFRP with 10 wt.% weight of white cement filler
7	C7	GFRP with 15 wt.% weight of white cement filler

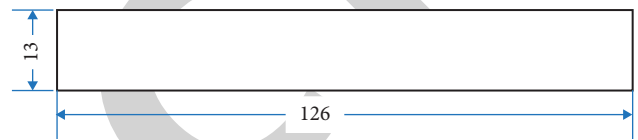


FIGURE 1: Flexural test specimen dimensions as per ASTM D790.

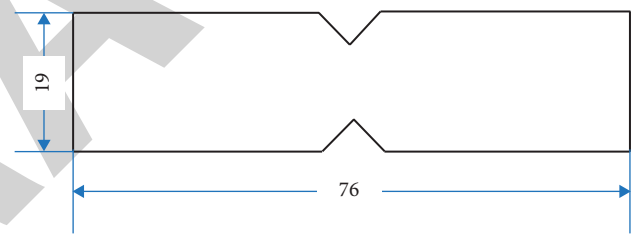


FIGURE 2: Dimensions of the shear (Iosipescu) test of composite as per ASTM D5379.

3. Results and Discussion

Three-point bending test is carried out on the plain glass fiber reinforced polymer (GFRP) composites, GFRP composite with grey Portland cement, and white cement filler composites. For each test case, five samples were tested; mean of three samples were taken by eliminating highest and lowest values; the same is presented in Table 2. The failure point of each composite is analysed under three-point bending. The maximum failure bending force, deflection, and then the strengths were carefully examined and discussed. For precise comparison of elasticity of the material under bending, flexural modulus at 1% strain is evaluated and analysed.

Figure 3 shows the scattering of the maximum force that can be bared by the sample under flexural versus maximum deflection exhibited by the sample; for better analysis, the points are joined to root node, with a straight line. The plain GFRP composite has more deflection than any other sample filler doped samples. The maximum deflection is observed as 5.13 mm.

It is also observed that, by the addition of grey cement fillers, the material becomes rigid, and its deflection reduced to a great extent during the addition of 5% of the Portland

TABLE 2: Flexural test results.

S. no.	Specimen code	Maximum force (N)	Maximum deflection (mm)	Flexural strength (MPa)	Flexural modulus at 1% strain (GPa)
1	C1	179.51	5.130	168.29	5.91
2	C2	198.81	2.434	165.66	6.40
3	C3	239.39	4.070	196.21	6.87
4	C4	235.66	2.753	232.19	8.70
5	C5	191.99	2.015	172.55	5.44
6	C6	210.13	3.650	215.26	8.65
7	C7	186.09	3.693	181.67	7.44

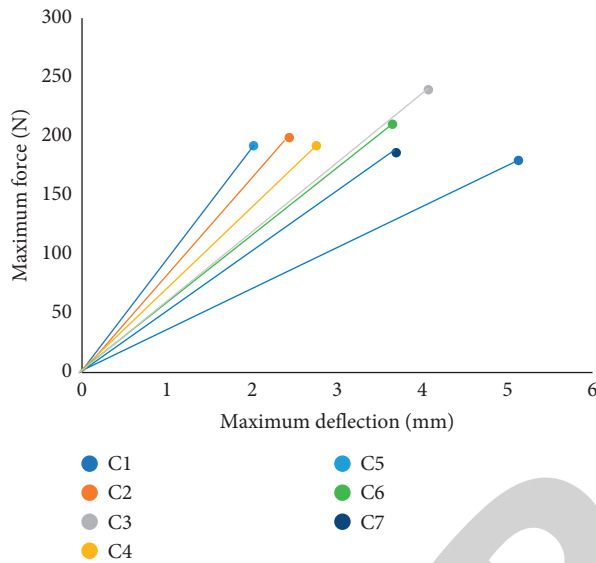


FIGURE 3: Load versus deflection under flexural loading.

cement, and the value is only 2.434 mm. With the increase in the filler content to 10 wt.%, the deflection is increased to 4.070 mm. Then the value is again decreased to 2.753 mm for a further increment of 15 wt.% of grey cement in the GFRP. This phenomenon may be due to the addition of grey cement to epoxy, with the matrix becoming hard and brittle. But when it increased to 10 wt.%, there were more particles in the matrix, creating a strong bond between the matrix and fiber interface, and there was no crack observed on the surface and the failure has occurred only due to fiber peeling. With further increase in filler content, the matrix material becomes more rigid, taking much load for each unit of extension compared to other samples. Figure 4 clearly shows this phenomenon; the scanning electron microscopic image obtained at the fractured surface of a sample with 15% grey cement filler shows the fiber pull-out and clear surface without cracks.

With the addition of the white cement fillers to the composite in 5 wt.%, the deflection of the material is reduced from 5.130 mm to 2.015 mm. The samples have become more rigid as the matrix has become stiffer with the addition of the filler content. Further, with the addition of the filler content of the white cement, the material has reduced its stiffness, showing an increase in the deflection. This is maybe due to the fine particle size of the white cement compared to the grey cement, which allows them to add some flexibility to the composite after binding. At the bottom line, the addition of

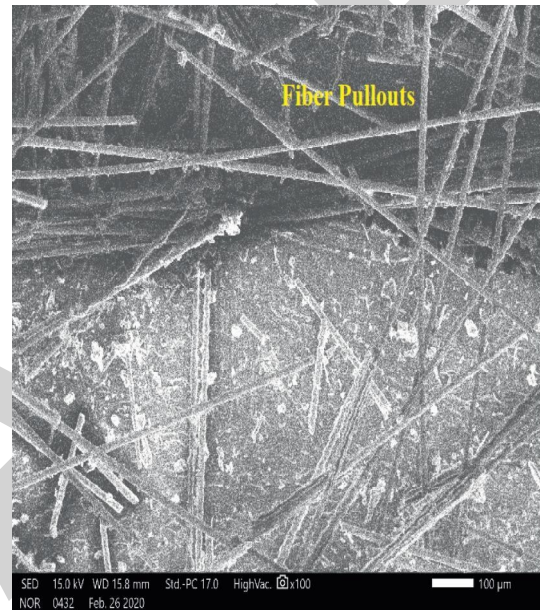


FIGURE 4: Scanning electron microscopy image of flexural test specimen with grey cement filler of 15 wt.%.

cement fillers to composite makes the composite become rigid, reducing its deflection.

Figure 5 represents the variation of the flexural strength of the samples with the addition of the grey and white Portland cement, with weight percentages of 5 wt.%, 10 wt.%, and 15 wt.% for each case. The flexural strength of the plain-woven rowed GFRP is noted as the 168.29 MPa. Meanwhile, by the addition of the grey cement filler with 5 wt.%, the strength is reduced very slightly from 168.29 MPa to 165.66 MPa. In this case, from Table 2 and Figure 3, it is observed that the deflection is also reduced. The material becomes hard and brittle. With the addition of 10 wt.% of the filler content to the composite, the strength of the composite has increased, and, with the further addition of the cement filler to the composite, the strength tends to increase—the more amount of the cement filler there is in the epoxy, the more strength it obtains. As there is a good affinity between glass fiber and cement fillers, the constituent elements are more or less similar, such as SiO_2 , CaO , Al_2O_3 , magnesium, and ferrous oxide. More rigorous chemical studies are to be carried out in this domain to explore the affinity between glass fiber and cement. The maximum strength of the composite observed at 15 wt.% of grey cement filler content is 232.19 MPa. The white cement filler has increased the

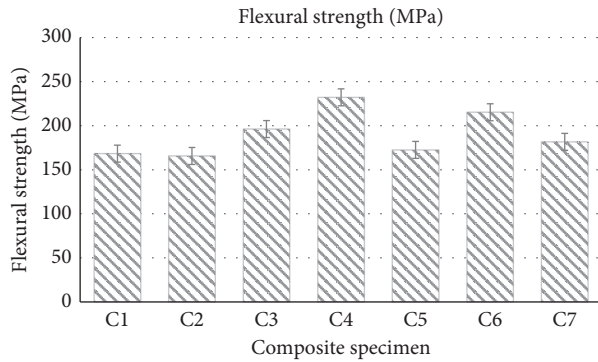


FIGURE 5: Flexural strength of hybrid and nonhybrid composites.

strength of the composite with the addition of filler up to 10 wt.%. The maximum strength obtained is 215.26 MPa. Then its value is decreased to 181.67 MPa for 15 wt.% in comparison up to 10 wt.% the white cement filler exhibiting better strength than the grey cement.

Figure 6 shows the flexural modulus of the GFRP composite and hybrid composite samples with the addition of the grey and white Portland cement, with weight percentages of 5 wt.%, 10 wt.%, and 15 wt.% for each case. The results revealed that, at 1% strain, the white cement filler with 5 wt.% exhibited lower modulus than the plain GFRP. The grey cement with 15 wt.% of cement is having more rigid nature, that is, modulus at 1% strain. The modulus increases with an increase in filler percentage compared to the GFRP. As the cement has more bonding nature, due its natural behaviour, particles bond together and exhibit more modulus or rigidity in bending. In the case of white cement for 1% strain, the value of modulus decreased for 5 wt.% followed by plain woven GFRP and then increased for 10 wt.% and then reduced again with the further addition of the white cement filler up to 15 wt.%.

Figure 7 shows the scattering of the maximum force that can be bared by the sample under shear versus maximum elongation exhibited by the sample; for better analysis, the points are joined to root node, with a straight line. The plain GFRP composite has more deflection than any other filler doped samples. The maximum deflection observed is 3.04 mm. It is also observed that, by the addition of grey cement fillers, the material becomes rigid, and its deflection is reduced to a great extent with the addition of 5% of the Portland cement, and the value is only 1.308 mm. With the increase in the filler content to 10 wt.%, the deflection is decreased to 1.31 mm. Then the value is again decreased to 0.81 mm with the further increment of 15 wt.% of grey cement in the GFRP. We may assume that this phenomenon is due to the addition of grey cement to epoxy and the matrix becomes hard and brittle. But when it is increased to 15 wt.%, there are more particles in the matrix, creating a strong bond between the matrix and fiber interface, and no crack is observed on the surface and the failure has occurred only due to fiber peeling. With further increase in filler content, the matrix material becomes more rigid, taking much load for each unit of extension compared to other samples.

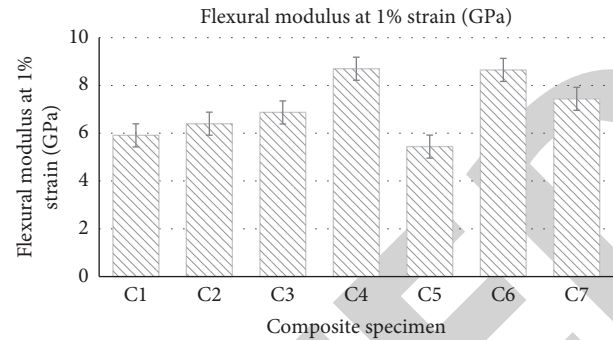


FIGURE 6: Flexural modulus of hybrid and nonhybrid composites at 1% strain.

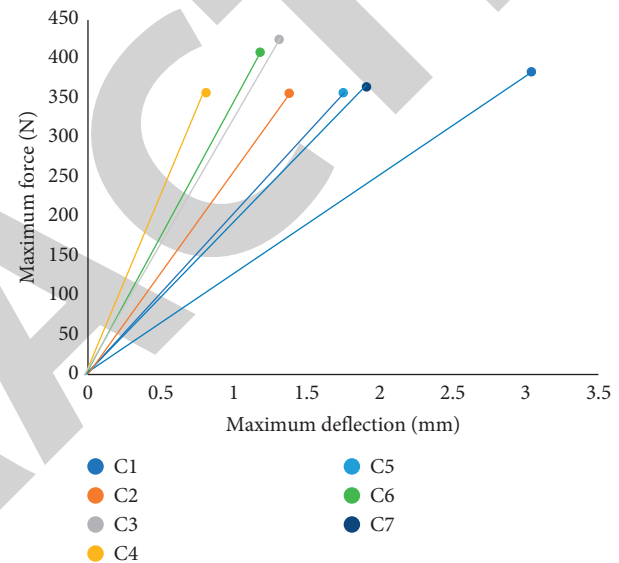


FIGURE 7: Load versus deflection under shear loading.

With the addition of the white cement fillers to the composite in 5 wt.%, the deflection of the material reduced from 3.04 mm to 1.75 mm. The samples have become more rigid with the matrix attaining more stiffness with the addition of the filler content. Further, with the addition of the filler content, the deflection is reduced to 10 wt.% of the filler. The material reduced its stiffness and has shown an increase in the deflection, with the increase of the filler content of white cement. To conclude, the addition of cement fillers to the composite makes the composite rigid reduce its deflection.

Figure 8 shows the variation of the shear strength of the samples with the addition of the grey and white Portland cement, with weight percentages of 5 wt.%, 10 wt.%, and 15 wt.% for each case. The shear strength of the woven GFRP is noted to be 12.02 MPa. Meanwhile, by the addition of the grey cement filler with 5 wt.%, the strength is increased from 12.02 MPa to 16.54 MPa. From Table 3 and Figure 7, it is observed that the deflection is reduced and the material exhibited more strength with the addition of 10 wt.% of the filler content to the composite. With the further addition of the cement filler to the composite, the strength started

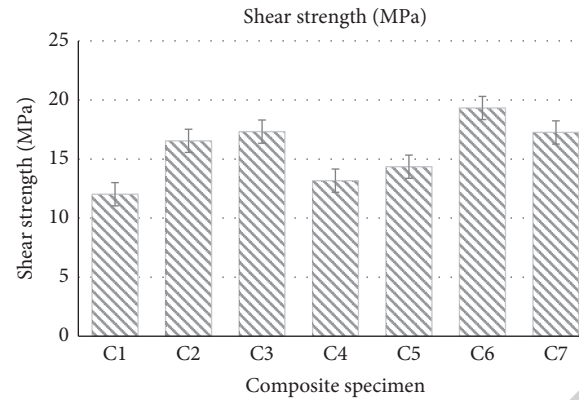


FIGURE 8: Shear strength of hybrid and nonhybrid GFRP composites with cement fillers.

TABLE 3: Shear test results.

S. no.	Specimen code	Break force (N)	Break elongation (mm)	Shear strength (MPa)
1	C1	384.41	3.04	12.02
2	C2	357.06	1.38	16.54
3	C3	425.49	1.31	17.32
4	C4	455.20	0.81	13.17
5	C5	357.70	1.75	14.35
6	C6	409.16	1.18	19.32
7	C7	365.11	1.91	17.25

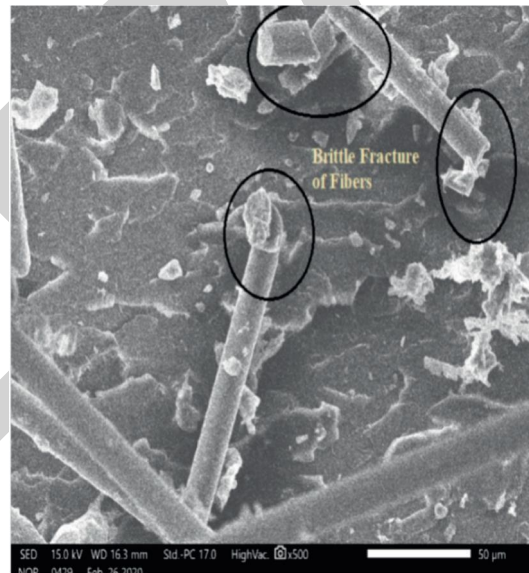


FIGURE 9: Scanning electron microscopy image of shear test specimen with white cement filler of 10 wt.%.

decreasing. At 10 wt.% of the cement filler in the epoxy, more strength is acquired. As there is a good affinity between glass fiber and cement fillers, in both glass fiber and cement fillers, the constituent elements are more or less similar, such as SiO_2 , CaO , Al_2O_3 , magnesium, and ferrous oxide. But, for 15 wt.% of grey cement filler, the content is reduced to 13.17 MPa. The white cement filler has increased its strength of the composite with the addition of filler up to 10 wt.%. The maximum strength obtained is 19.32 MPa. The scanning electron microscopy image of this sample is

shown in Figure 9, a brittle fracture of the matrix and fiber is apparent. There is more bonding between fiber and matrix, many fibers are broken at the root, and it is observed that there is no noticeable peeling or pull-out of fibers under transverse loading.

Therefore the white cement filler exhibits better strength than the grey cement. In the strength point of view of the composite, white cement filler dominates at all other compositions except at 5 wt.%. At the bottom line, we can say that the grey cement-filled composites were

weaker in shear loading compared to the white cement-filled composites.

4. Conclusions

In this study, the effects of grey and white Portland cementitious filler reinforcement on the flexural and shear behaviour of GFRP woven fabric compounds were investigated. Based on the results, the following was concluded:

- (i) Material deflection decreases with the addition of cement fillers for both flexural and shear loading, and load-bearing capacity increases.
- (ii) The flexural strength of the hybrid GFRP composite with grey cement filler increases with the addition of the filler. Flexural strength of the white cement filler hybrid GFRP composite increases up to 10 wt.%, and then it has reduced with further addition.
- (iii) Flexural modulus at 1% strain shows a similar trend to that of the flexural strength of samples.
- (iv) Shear strength of both filler composites increases up to 10 wt.% filler content, and then it has reduced.
- (v) The white cement filler had more strength than the grey cement filler up to 10 wt.% of filler content in flexural loading. In shear loading, the white cement filler exhibited better strength for 10 wt.% and 15 wt.% composites.

Data Availability

The data used to support the findings of this study are included within the article.

Disclosure

This study was performed as a part of the employment of Bule Hora University.

Conflicts of Interest

The authors declare that there are no conflicts of interest regarding the publication of this paper.

References

- [1] G. Raghavendra, S. Ojha, S. K. Acharya, and S. K. Pal, "A comparative analysis of woven jute/glass hybrid polymer composite with and without reinforcing of fly ash particles," *Polymer Composites*, vol. 37, no. 3, pp. 658–665, 2016.
- [2] G. Raghavendra, S. Ojha, S. Acharya, S. Pal, and I. Ramu, "Evaluation of mechanical behaviour of nanometer and micrometer fly ash particle-filled woven bidirectional jute/glass hybrid nanocomposites," *Journal of Industrial Textiles*, vol. 45, no. 6, pp. 1268–1287, 2016.
- [3] R. Ramprasath and S. Jayabal, "Particle swarm and simulated annealing based intuitive search optimization of flexural behaviors in bioparticles impregnated coir fiber-vinyl ester composites," *Polymer Composites*, vol. 37, no. 6, pp. 1765–1774, 2016.
- [4] D. Harsha Vardhan, A. Ramesh, and B. Chandra Mohan Reddy, "A review on materials used for marine propellers," *Materials Today: Proceedings*, vol. 18, no. 7, pp. 4482–4490, 2019.
- [5] P. Choudhury, S. Halder, N. I. Khan, J. Wang, and K. M. Pandey, "Enhanced crack suppression ability of hybrid glass fiber reinforced laminated composites fabricated using GNP/epoxy system by optimized UDM parameters," *Ultrasonics Sonochemistry*, vol. 39, pp. 174–187, 2017.
- [6] R. Satheesh Raja, K. Manisekar, and V. Manikandan, "Study on mechanical properties of fly ash impregnated glass fiber reinforced polymer composites using mixture design analysis," *Materials & Design*, vol. 55, pp. 499–508, 2014.
- [7] M. Hussain, A. Nakahira, and K. Niihara, "Mechanical property improvement of carbon fiber reinforced epoxy composites by Al₂O₃ filler dispersion," *Materials Letters*, vol. 26, no. 3, pp. 185–191, 1996.
- [8] S. M. Sapuan, M. Harimiand, and M. A. Maleque, "Mechanical properties of epoxy/coconut shell filler particle composites," *Arabian Journal for Science and Engineering*, vol. 28, no. 2, pp. 171–181, 2003.
- [9] E. G. Koricho, A. Khomenko, M. Haq, L. T. Drzal, G. Belingardi, and B. Martorana, "Effect of hybrid (micro- and nano-) fillers on impact response of GFRP composite," *Composite Structures*, vol. 134, pp. 789–798, 2015.
- [10] T. Lan, P. D. Kaviratna, and T. J. Pinnavaia, "On the nature of polyimide-clay hybrid composites," *Chemistry of Materials*, vol. 6, no. 5, pp. 573–575, 1994.
- [11] K. Debnath, V. Dhawan, I. Singh, and A. Dvivedi, "Effect of natural fillers on wear behavior of glass-fiber-reinforced epoxy composites," in *Proceedings of the International Conference on Research and Innovations in Mechanical Engineering*, 2014.
- [12] O. Nabinejad, D. Sujan, M. E. Rahman, W. Y. H. Liew, and I. J. Davies, "Hybrid composite using natural filler and multi-walled carbon nanotubes (MWCNTs)," *Applied Composite Materials*, vol. 25, no. 6, pp. 1323–1337, 2018.
- [13] S. Das, S. Halder, N. I. Khan, B. Paul, and M. S. Goyat, "Assessing damage mitigation by silanized milled graphite nanoparticles in hybrid GFRP laminated composites," *Composites Part A: Applied Science and Manufacturing*, vol. 132, Article ID 105784, 2020.
- [14] S.-r. Lu, J. Hongyu, H.-l. Zhang, and X.-y. Wang, "Wear and mechanical properties of epoxy/SiO₂-TiO₂ composites," *Journal of Materials Science*, vol. 40, no. 11, pp. 2815–2821, 2005.
- [15] M. R. Petersen, A. Chen, M. Roll, S. J. Jung, and M. Yossef, "Mechanical properties of fire-retardant glass fiber-reinforced polymer materials with alumina tri-hydrate filler," *Composites Part B: Engineering*, vol. 78, pp. 109–121, 2015.
- [16] S. Samal, "Effect of shape and size of filler particle on the aggregation and sedimentation behavior of the polymer composite," *Powder Technology*, vol. 366, pp. 43–51, 2020.
- [17] U. S. Rai and R. K. Singh, "Synthesis and mechanical characterization of polymer-matrix composites containing calcium carbonate/white cement filler," *Materials Letters*, vol. 58, no. 1–2, pp. 235–240, 2004.
- [18] H. Yang, B. C. Ng, H. C. Yu, H. H. Liang, C. C. Kwok, and F. W. Lai, "Mechanical properties study on sandwich hybrid metal/(carbon, glass) fiber reinforcement plastic composite sheet," *Advanced Composites and Hybrid Materials*, vol. 4, pp. 1–8, 2021.
- [19] N. Pavan Kumar, D. Harsha Vardhan, and B. Anjineyulu, "Fabrication and experimental study of mechanical properties

Retraction

Retracted: Optimization on Operation Parameters in Reinforced Metal Matrix of AA6066 Composite with HSS and Cu

Advances in Materials Science and Engineering

Received 26 December 2023; Accepted 26 December 2023; Published 29 December 2023

Copyright © 2023 Advances in Materials Science and Engineering. This is an open access article distributed under the Creative Commons Attribution License, which permits unrestricted use, distribution, and reproduction in any medium, provided the original work is properly cited.

This article has been retracted by Hindawi, as publisher, following an investigation undertaken by the publisher [1]. This investigation has uncovered evidence of systematic manipulation of the publication and peer-review process. We cannot, therefore, vouch for the reliability or integrity of this article.

Please note that this notice is intended solely to alert readers that the peer-review process of this article has been compromised.

Wiley and Hindawi regret that the usual quality checks did not identify these issues before publication and have since put additional measures in place to safeguard research integrity.

We wish to credit our Research Integrity and Research Publishing teams and anonymous and named external researchers and research integrity experts for contributing to this investigation.

The corresponding author, as the representative of all authors, has been given the opportunity to register their agreement or disagreement to this retraction. We have kept a record of any response received.

References

- [1] Y. Sesharao, T. Sathish, K. Palani et al., "Optimization on Operation Parameters in Reinforced Metal Matrix of AA6066 Composite with HSS and Cu," *Advances in Materials Science and Engineering*, vol. 2021, Article ID 1609769, 12 pages, 2021.

Research Article

Optimization on Operation Parameters in Reinforced Metal Matrix of AA6066 Composite with HSS and Cu

Y. Sesharao,¹ T. Sathish ,² Kumaran Palani ,³ Anjibabu Merneedi,⁴ Natrayan L ,² Melvin Victor De Poures ,² and T. Maridurai²

¹Department of Mechanical Engineering, QIS College of Engineering and Technology, Ongole 523272, Andhra Pradesh, India

²Department of Mechanical Engineering, Saveetha School of Engineering, SIMATS, Chennai 600 125, Tamil Nadu, India

³Department of Mechanical Engineering, Wolaita Sodo University, Wolaita Sodo Post Box- 138, Ethiopia

⁴Department of Mechanical Engineering, Aditya College of Engineering, Surampalem 533437, Andhra Pradesh, India

Correspondence should be addressed to Kumaran Palani; pkumaran2003et@gmail.com

Received 30 May 2021; Revised 16 June 2021; Accepted 22 June 2021; Published 2 July 2021

Academic Editor: Samson Jerold Samuel Chelladurai

Copyright © 2021 Y. Sesharao et al. This is an open access article distributed under the Creative Commons Attribution License, which permits unrestricted use, distribution, and reproduction in any medium, provided the original work is properly cited.

This optimization investigation focused on the reinforced metal matrix composite of aluminium alloy. Novel of this work is to fabricate the AA6066 composite with HSS and Cu, continually conduct machining tests, and evaluate the tool wear, surface roughness, and thrust force of the stir-casted specimens. The aluminium composite has 90 percentage of AA6066 alloy reinforcement with six percentage of high-speed steel and four percentage of copper alloy made by the casting method. The fabricated composites' turning parameters were optimized through the Taguchi method. The turning operation can be done with the help of the normal lathe with the CBN insert tool. The operation parameters such as feed, depth of cut, and steam pressure of the cutting fluid were considered with three different equal intervals in each parameter. In this investigation, the L9 orthogonal array method is used to identify the optimum values of the turning parameters among the considered machining parameters concerning the response such as wear on the turning tool and thrust forces created on machining. The outcome based on the parameters was identified and mentioned as the rank order for individual and combination of all responses with different conditions. Then, the separate and combined optimized input parameters were provided as the conclusion.

1. Introduction

Every operation needed various input parameters with respect to the different operating conditions. These parameters maybe less or more; it depends on the process and output. Among the various parameters, specifically, some of them create more impact on the desirable output on the machining. These parameters' optimization helps to enhance the machining or processing of the materials. So, the optimization of the various inputs of an experiment is needed to identify the most appropriate and preferable output in the accessible available resources. Sathish et al. [1] experimentally explained about the optimization on the machining constraints of the zirconium carbide (ZrC) reinforced aluminium alloy of AA7155 aluminium alloy composites.

Sabarirajan et al. [2] obviously discussed about the AA6063 aluminium alloy reinforcement with the silicon carbide machining parameter optimization by using the Taguchi method with different specific diagrams related to the experimental outcomes. Sevel et al. [3] gave details regarding optimizing of the parameters of the method of laser welding on the butt joints of the AA7068 aluminium alloys with clear diagrammatic representations of the main effect plots with priority order of the considered parameters. Sathish [4] individually investigated the parameters of the electro chemical process by the Taguchi method and explained the clear method of the optimization technique with respect to the reactions of experimental results.

Dinesh Kumar et al. [5] completely explained about the progression parameters of A-GTAW welding process based on the contribution parameters of the joining process by

means of the help of the different plots of the foremost effects. Saravanan et al. [6] entirely explained about the optimization method for the solar flat plate collector with nanofluids of aluminium nitride-based temperature differences through the help of the Minitab software by using the Taguchi method. Muthukumar et al. [7] entirely discussed the step-by-step procedure for the optimization methods with various contour plots by different colour representations on the various ranges of experimental results.

Palaniappan et al. [8] effusively discussed about the turning process parameter-based optimization methods with three different responses to identify the optimum input parameters. They also explained with different plots and tables for the clear vision to identify the parameters. Rajesh et al. [9] completely focused the surface roughness in machining participation for the metal matrix composites of aluminium alloy of AA5083 composite created with the combination of the boron carbide materials. Gurusami et al. [10] obviously explained roughly the optimization in the stir casting process inputs for the rate of corrosion encouragement on the composite materials of the boron carbide reinforcement of the aluminium alloy AA7068.

In the same way, Shetty et al. [11] absolutely discussed about the metal matrix composite-related optimization of the nearly five inputs for the nearly five outputs in turning operation by using the specified tool. The standard lathe machine is practiced at this juncture for the investigation. They also considered the cutting fluid parameters such as steam pressure and diameter of the nozzle. Correspondingly, various forces involved were considered in the turning operation. Natrayan et al. [12] investigated Al-SiC and Al-Al₂O₃ with the help of the powder metallurgy technique. The author completely explained about the various characteristics, compositions of chemicals, and processing methods of the Al-SiC and Al-Al₂O₃ composites.

Georgantzia et al. [13] entirely explained about the various applications of the AA6XXX series in structural elements with various sizes and different shapes, welding process on different places, and bolted equipment design application, and more than that, they were clearly mentioned with the help of various research articles. Davim [14] clearly explained about the turning process cutting parameter-based optimization with the orthogonal arrays in the machining by the normal lathe machine. The considered input parameters were feed, speed, depth of cut, input range, force on the tool, thrust force applied, input voltage, and motor specifications.

Ramnath et al. [15] absolutely reviewed by means of various research articles and explained about the aluminium matrix composites. They explained the various basic experiments and parameter-based optimization of aluminium matrix composites individually reinforced with silicon carbide, aluminium oxide, boron carbide, fiber, zircon, and fly ash. They also summarized the individual special qualities of the abovementioned combination reinforced composites. Shukla et al. [16] identified the separate individual activities of reinforcement composites of silicon carbide used in aluminium which were studied with respect to the consequences of the mechanical properties of the composites such as microstructure effect, toughness, hardness, and tensile

strength. They also explained the various casting techniques used to produce the metal matrix composites.

Verma et al. [17] explained about the influence of difference of silicon and copper contents in aluminium composite alloy produced by the stir casting method. They castoff the copper content from 0.015% to 5.97% and silicon carbide content from 2.02% to 8.6% in the remaining aluminium alloy for the casting process. They correspondingly mentioned that the greatest mechanical properties were formed with increased copper content in the composites. Singla et al. [18] successfully explained about the improvement aluminium reinforcement with silicon carbide-based metal matrix for the optimization process based on the experimental results of the hardness; the maximum percentage of the silicon involvement proved the enhancement on the hardness on the composite material microstructures. Standard high-pressure hydrogen storage vessel, hydraulic valves, high-stressed components used in the machineries, air wings' part, and mobile industry apparatus were fabricated by AA6066 alloy.

Alaneme and Aluko [19] effectively discussed about the fabrication besides age-hardening actions of the composite of aluminium with the silicon carbide for the creation of the aluminium magnesium and silicon composite through the technique of stir casting. Pawar et al. [20] efficiently conversed regarding the aluminium-reinforced composite of the silicon carbide with the application on the spur gear. They also provided various applications of the same composite materials. Natrayan et al. [21] entirely studied about the mechanical property-based input impact of the aluminium composite materials. They only focused the tensile strength of the composite material which concludes that the increase of the silicon carbide is directly proportional to the increase in the tensile strength of the composites. Merneedi et al. applied the ICCM method to investigate the variation of nondimensional natural frequencies of an elliptical and rectangular thin plate by changing the position, size, and number of cut outs in all the possible ways to investigate their effects on the natural frequency of the plate; the same method can also be implemented for the analysis of composite plates [22].

In this work, based on the optimization of the machining parameter such as feed rate, depth of cut with the cutting fluid pressure for the reinforced composite of AA6066 aluminium alloy with high-speed steel and copper is created by way of casting. These contribution considerations of the machining optimization are based on the experimental consequences of the tool wear in addition to the thrust force created at the time of machining with the help of the Taguchi method L9 orthogonal array. These two consequences were optimized separately and in a together manner.

2. Experimental Setup

This experimental investigation is mainly focused on the turning parameters of the reinforced metal matrix composites. Initially, the metal-reinforced specimens were prepared by the casting method [23]. The composition of the AA6066 aluminium alloy is mentioned in Table 1, and the remaining percentage is occupied by the pure aluminium

TABLE 1: Chemical opus of aluminium alloy (AA6066).

Composition	Silicon (%)	Magnesium (%)	Copper (%)	Manganese (%)	Chromium (%)
Percentage	1.80	1.40	1.20	1.10	0.40

alloy. The main contribution as 90 percentage of AA6066 alloy is reinforced with 6% of high-speed steel and 4% of copper alloy in the total percentage of the volume of the weight in the composite formation. All the materials were collected in the powder form from the online purchase. Then, the mixed materials were poured into the combustion chambers with 50,000 C and 500 kW capacity for one hour beyond the molten metal temperature.

Then, the molten metal has the mixture of all powder materials which are poured into the mould cavities for casting. The mould cavities were created as per the requirement of the specimen sizes. As per Figure 1(a), 30 mm diameter and 120 mm length cylindrical specimens were created from the casting method. Then, casted specimens were cleaned and inspected visually, such as size, cracks, and damage, for the second stage of the experiments. The normal traditional lathe machine is chosen for this investigation mentioned in Figure 1(b). It has the following specification: 5 kW motor, screw-guided automatic feed from 0.05 to 2 mm, and tool post and tail stock can be easily movable. Three Jaw chuck job holder is used in this experiment. The tool involved here is the inserts of cubic boron nitride (CBN). In this machining, the cutting fluid is steam with adjustable pressure from 1 bar to 15 bar with the nozzle arrangement in the end of the fluid flow [24].

There are 20 specimens that were created for the experiment, but nine clear defectless specimens are enough to conduct these experiments. Before conducting the experiment, the environment of the machine should be clean, and the cutting fluid should be ready to produce the steam using the electric heater. The CBN tool is fixed in the tool post as per the turning operation. The prepared specimen is fixed in the three-jaw chuck which is tightly fixed by the tools. The center of the specimen is checked properly. The turning distance as per Figure 1(b) is measured by the vernier scale and marked by the black marker. The motor is worked in the counterclockwise direction for this operation. The feed and depth of cut can be fixed by the rotating screw arrangement, and also, the pressure of the cutting fluid is controlled by the controller and monitored by the pressure gauge.

There are three inputs that were taken for the consideration of optimization with respect to the three desired outputs. The considered inputs were pressure of the cutting fluid (P_r), feed in mm per revolution (F), and cutting depth in millimetre (D) as per Table 2. These values were measured with the help of one pressure sensor on the feed tube, one contact sensor on the feed rotating threaded shaft, and a noncontact sensor in the machining place; these all are individually connected to the machine.

The desired outputs were rate of wear on the tool (TW), roughness on the surface (SR) of the machined specimens, and applied force of thrust (TF). Similarly, these all are also measured with the help of the sensors and dynamometer of

the lathe tool. There are 9 combinations, as per Table 2, that were created one by one with respect to the input parameters, and the corresponding values of the outputs were also measured for the clear identification. Each specimen is named as per Table 1 such as SN 1 to SN 9. The initial specimens before machining have the diameter of 30 mm and length of 120 mm, which are turned up to 80 mm length with diameter of 14 mm as per Figure 1(a). All the specimens have been machined in the same dimensions to recognize comparison on the results from each specimen for the considered conditions.

3. Results and Discussion

The wear on the tool on the end of the machining, machined surface roughness, and applied thrust forces of the individual specimens such as SN 1, SN 2, SN 3, SN 4, SN 5, SN 6, SN 7, SN 8, and SN 9 are measured and tabulated in Table 3 in a clear manner. L9 orthogonal array used the Taguchi method here to identify the maximum suitable inputs for the machining. All these three outputs come under the category of smaller is better condition. Because of the user expecting the minimum wear, minimum roughness and lowest thrust force were applied. The individual outputs and combinations of all the output were considered. Taguchi method results by using the Minitab 18 were discussed one by one in the sequence order.

3.1. Tool Wear. Initially, wear on the tool while performing the turning process on the concerned reinforced metal matrix of the aluminium alloy response ranks is tabulated in Table 4 under the condition that the minimum is the suitable.

The corresponding important effect diagram in Figure 2 expresses that the minimum wear rate was reached at 3 bar pressure of the cutting fluid with 0.15 mm per revolution of feed and 0.6 mm of cutting depth; similarly, the maximum wear rate can be obtained on 9 bar of cutting fluid pressure with the 0.10 mm per revolution of feed and 0.9 mm of cutting depth. This is also confirmed by the important effect diagram for the means of the wear rate measured in all the specimens in Figure 3.

There are four diagram representations that are available in a single diagram in Figure 4. It explained the percent with residuals which all are nearly closer to the normal probability line. This gives the reliability of the experiment results. Fitted values with residual relations clearly mentioned the diversion of the point of the results. There is a linear shape only formed in the frequency and residual comparison. Also, there are more than half number of crosses that were available in the versus order plot; it supports the experiment results of wear.

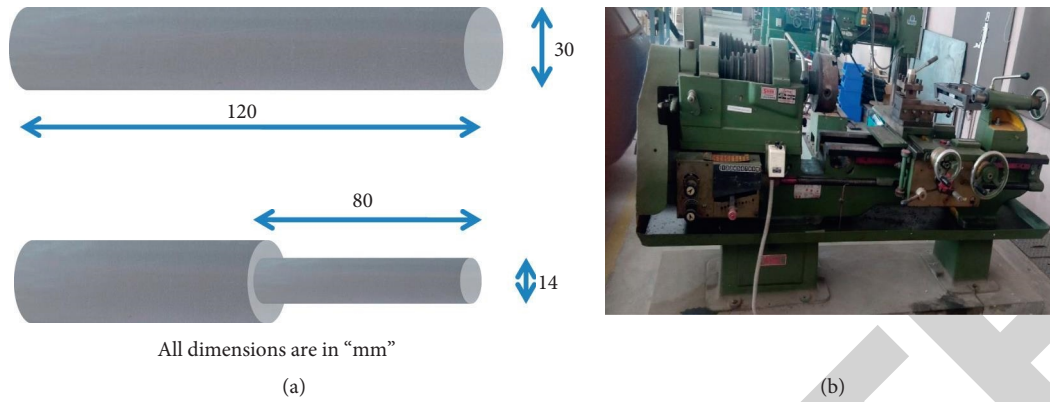


FIGURE 1: (a) Machining dimensions of the specimens. (b) Lathe machine used for this investigation.

TABLE 2: Input parameters variation as per the L9 method.

Specimen's number	Pressure of cutting fluid, P_r (bar)	Feed, F (mm/rev)	Depth of cut, D (mm)
SN 1	3	0.1	0.3
SN 2	3	0.15	0.6
SN 3	3	0.2	0.9
SN 4	6	0.1	0.6
SN 5	6	0.15	0.9
SN 6	6	0.2	0.3
SN 7	9	0.1	0.9
SN 8	9	0.15	0.3
SN 9	9	0.2	0.6

TABLE 3: Stir casting process parameters and its levels.

Specimen's number	TW (mm)	SR (μm)	TF (N)
SN 1	1.003	3.89	50.335
SN 2	0.493	2.85	15.385
SN 3	1.543	4.95	59.998
SN 4	0.893	2.27	17.51
SN 5	1.545	3.61	52.483
SN 6	0.653	2.45	21.15
SN 7	1.445	4.77	71.814
SN 8	0.823	2.39	40.563
SN 9	1.248	4.66	85.407

TABLE 4: Tool wear response ratios of signal to noise.

Level	Pressure of cutting fluid, P_r (bar)	Feed, F (mm/rev)	Depth of cut, D (mm)
1	0.7832	-0.7468	1.7892
2	0.3020	1.3522	1.7339
3	-1.1432	-0.6633	-3.5811
Delta	1.9265	2.0990	5.3703
Rank	3	2	1

3.2. *Surface Roughness.* Table 5 provides the surface roughness response for ratios of signal to noise with the ranks. Figure 5 provides the important effect diagram based on the roughness on the machined surface. The least amount surface roughness on the machined surface was obtained at the cutting fluid pressure of 6 bar with 0.15 mm per

revolution of feed and 0.3 mm of cutting depth; similarly, highest roughness on the machined surface can be obtained on 9 bar of cutting fluid pressure with 0.20 mm per revolution of feed and 0.9 mm of cutting depth. All these values were confirmed with the help of the mean-based important diagram in Figure 6 for roughness on the machined surface.

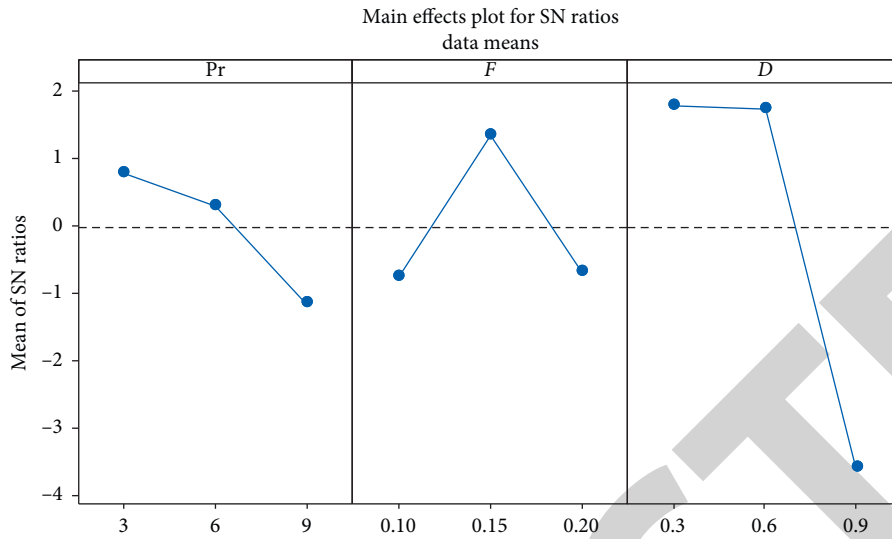


FIGURE 2: SN ratio-based important effect plot for wear on the tool; in the X-axis, Pr denotes pressure of cutting fluid (bar), F denotes feed (mm/rev), and D denotes depth of cut (mm).

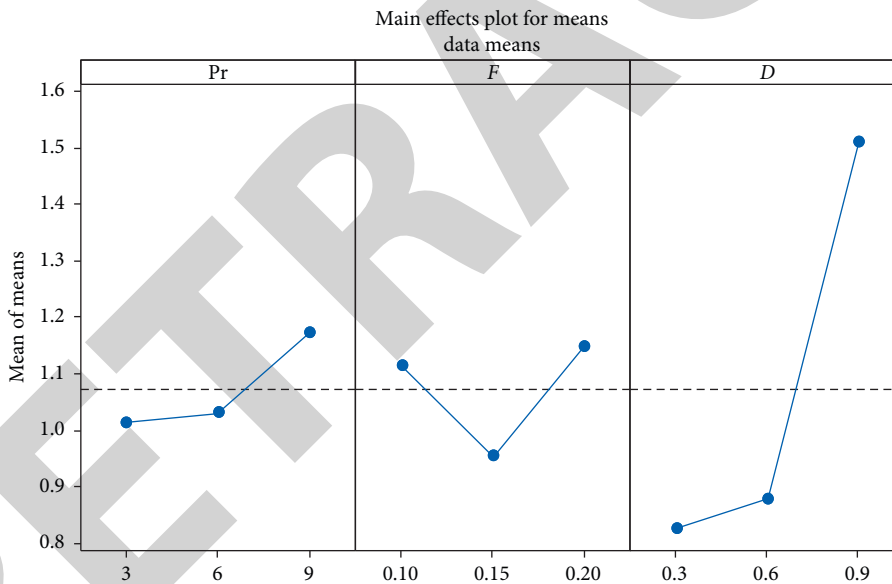


FIGURE 3: Mean-based important effect diagram for wear on the tool; in the X-axis, Pr denotes pressure of cutting fluid (bar), F denotes feed (mm/rev), and D denotes depth of cut (mm).

Figure 7 gives explanation about the four variation plots in the single diagram. It contains the points almost closer to the normal probability line in percent with residuals' variations. This provides the experiment outcomes reliability. Then, the fitted values with residual relations are mentioned. In the frequency and residual comparison, a linear shape is created. Also, there are less than half number of crosses that were obtained in the versus order plot.

3.3. Thrust Force. Table 6 mentions the thrust force-based response for ratios of signal to noise with the ranks. Figure 8 provides the important effect diagram based on the thrust force. The lowest amount thrust force is enough at the cutting fluid pressure of 6 bar with 0.15 mm per revolution of feed and 0.6 mm of cutting depth; similarly, greatest thrust force is needed at 9 bar of cutting fluid pressure with 0.20 mm per revolution of feed and 0.9 mm of cutting depth.

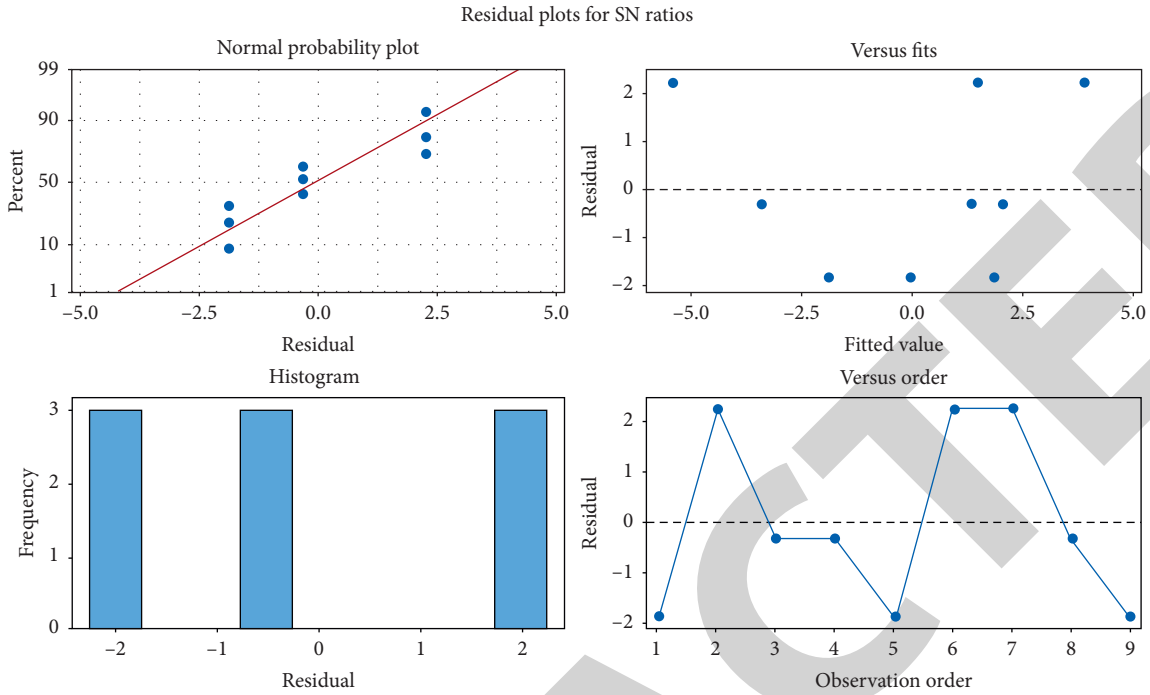


FIGURE 4: Tool wear’s residual plot of percent, frequency, fitted values, and observation order.

TABLE 5: Surface roughness on the machined surface response ratios of signal to noise.

Level	Pressure of cutting fluid, P_r (bar)	Feed, F (mm/rev)	Depth of cut, D (mm)
1	-11.596	-10.830	-9.050
2	-8.685	-9.272	-9.862
3	-11.502	-11.681	-12.871
Delta	2.911	2.409	3.821
Rank	2	3	1

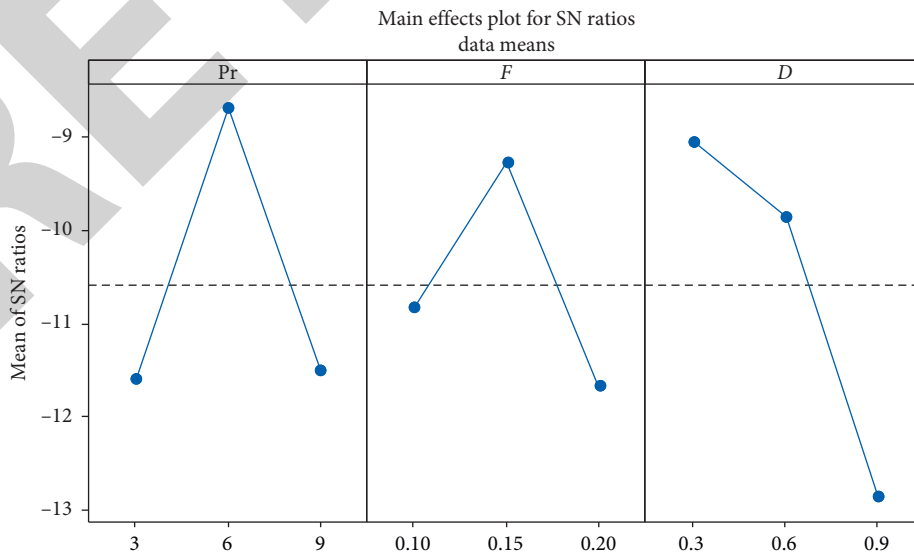


FIGURE 5: SN ratio-based important effect plot for the roughness on the machined surface; in the X-axis, P_r denotes pressure of cutting fluid (bar), F denotes feed (mm/rev), and D denotes depth of cut (mm).

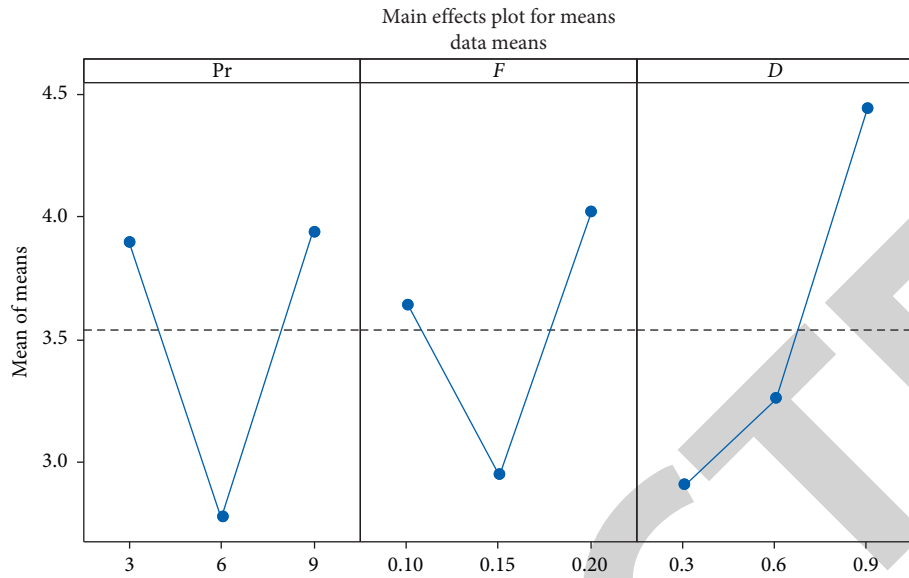


FIGURE 6: Mean-based important effect diagram for the roughness on the machined surface; in the X-axis, Pr denotes pressure (bar), F denotes feed (mm/rev), and D denotes depth of cut (mm).

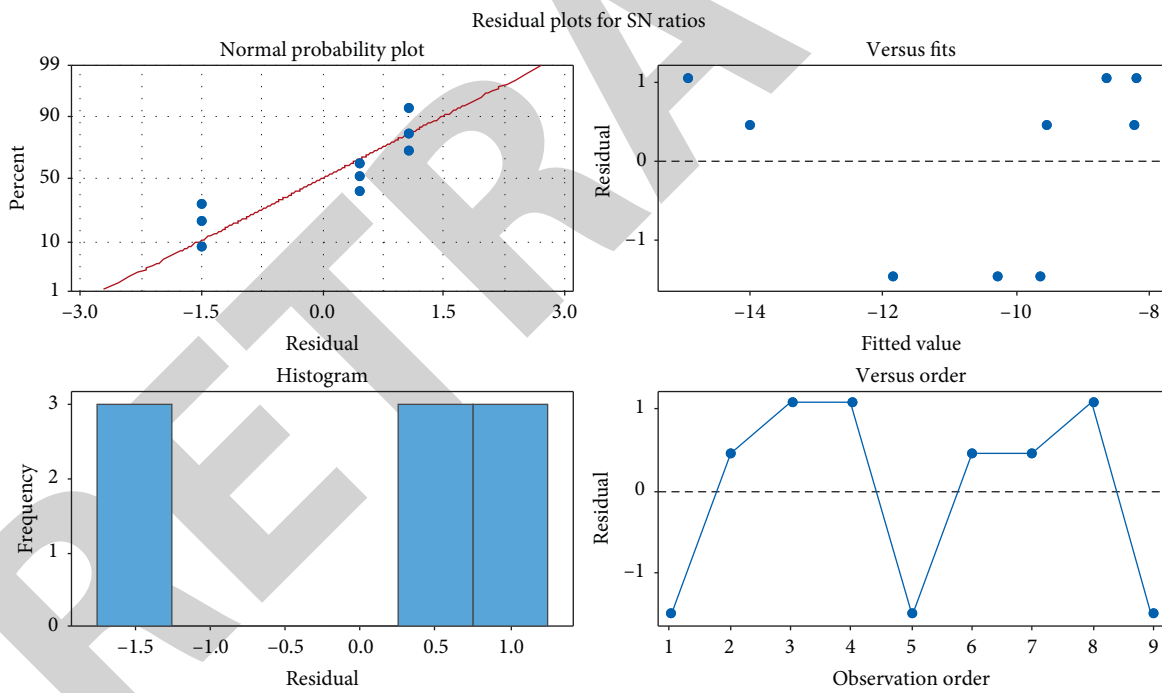


FIGURE 7: Surface roughness on machined surface residual plot of percent, frequency, fitted values, and versus order.

Figure 9 also corroborates the same results' confirmation based on the mean values of the thrust force applied on the specimens during the process of machining. Figure 10 mentions the explanation about various four plots in one diagram. These residuals-based percent and fitted values' plot gives the reliabilities of the experimental results. Then, the frequencies give the linear shape with gaps in the residuals.

Then, versus order gives more than half experiment results crossing the mean line. So, the results have the good quality.

3.4. *Combination of Response.* The three-response-based important diagram is clearly shown in Figure 11. The smaller amount of all these responses was reached at the parameters

TABLE 6: Thrust force-based response ratios of signal to noise.

Level	Pressure of cutting fluid, Pr (bar)	Feed, F (mm/rev)	Depth of cut, D (mm)
1	-31.11	-32.01	-30.90
2	-28.59	-30.10	-29.08
3	-35.97	-33.57	-35.70
Delta	7.38	3.46	6.62
Rank	1	3	2

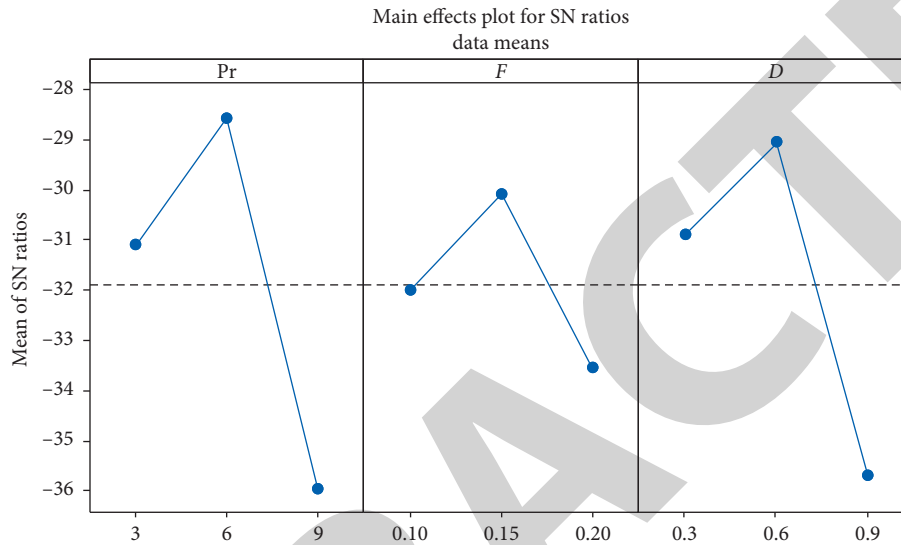


FIGURE 8: Thrust force-based important diagram based on the ratio of SN; in the X-axis, Pr denotes pressure of cutting fluid (bar), F denotes feed (mm/rev), and D denotes depth of cut (mm).

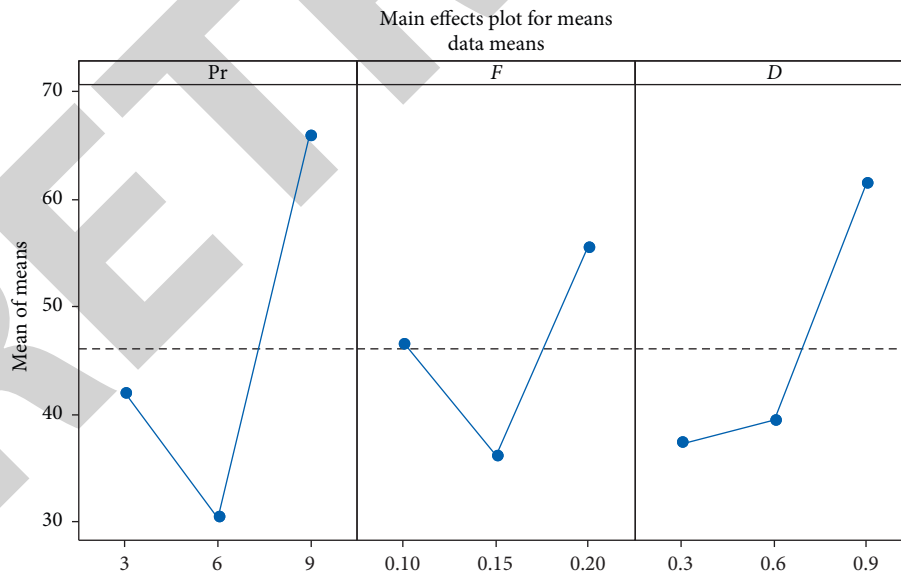


FIGURE 9: Thrust force-based important diagram based on the means; in the X-axis, Pr denotes pressure of cutting fluid (bar), F denotes feed (mm/rev), and D denotes depth of cut (mm).

for the cutting fluid pressure of 6 bar with 0.15 mm per revolution of feed and 0.6 mm of cutting depth; in the same way, highest thrust force was reached at 9 bar of cutting fluid pressure with 0.20 mm per revolution of feed and 0.9 mm of cutting depth; these all are confirmed by Figure 12 based on

the mean values of the process parameters. Tool wear, surface roughness, and thrust force-based signal-to-noise response are mentioned in Table 7 with the ranks.

Residual diagrams based on SN ratios for tool wear, surface roughness, and thrust force-related plot are shown in

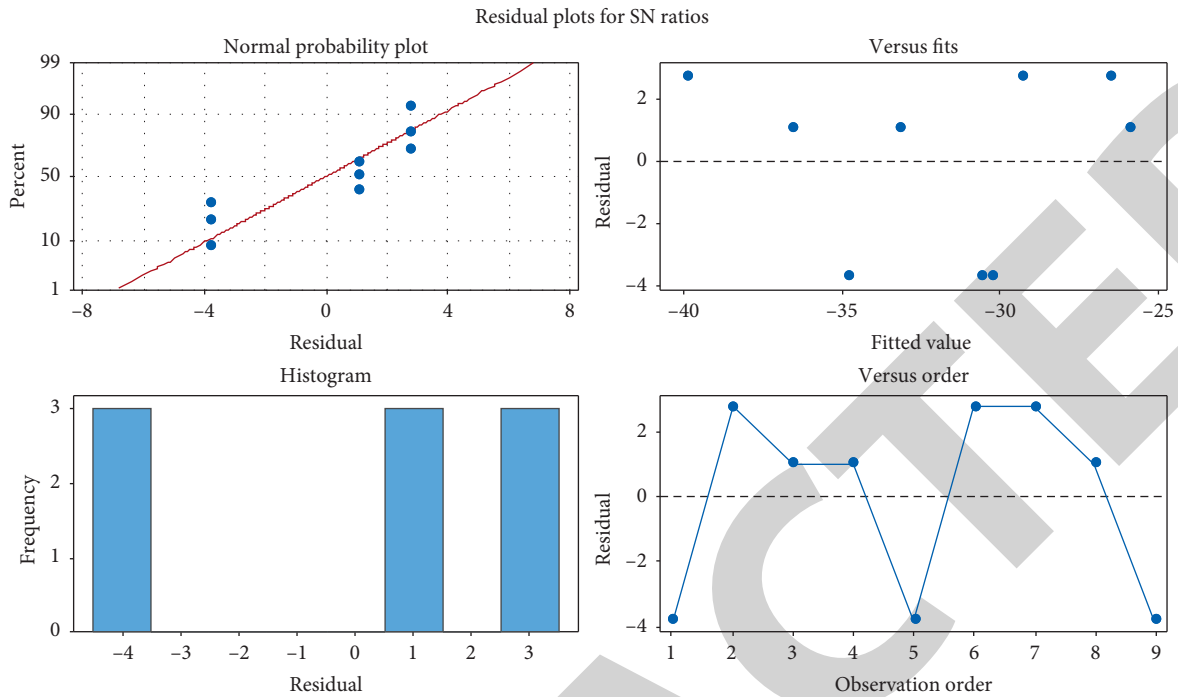


FIGURE 10: Thrust force-based residual plot of percent, frequency, fitted values, and versus order.

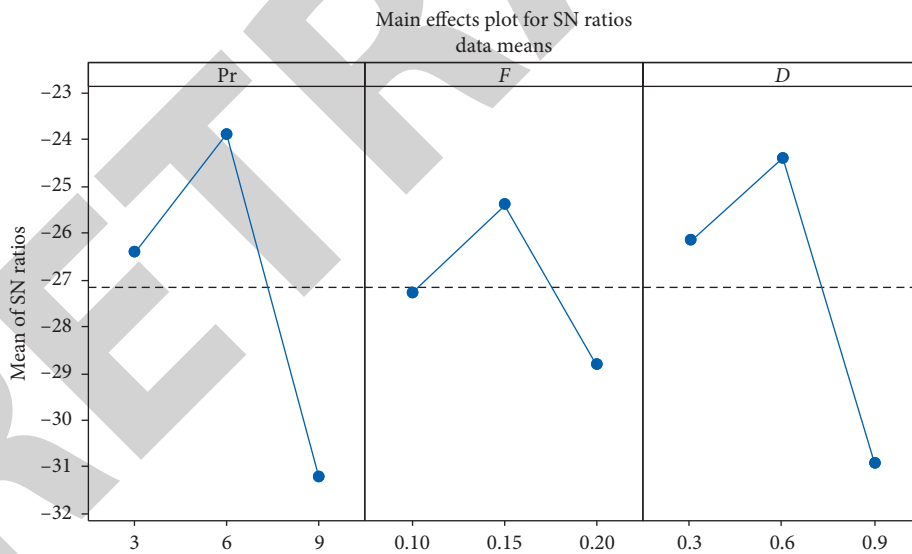


FIGURE 11: Tool wear, surface roughness, and thrust force focused the important diagram-based on the ratio of SN; in the X-axis, pressure of cutting fluid, Pr (bar), feed, F (mm/rev), and depth of cut, D (mm).

Figure 13. The normal probability plot provides the closeness of the point to the median line; similarly, versus fits mentioned the distraction of the points away from the center. The histogram has the gapped vertical columns' shape with

frequencies. The versus order plot gives the reliability of the experiment results with more than half of the experiment counts. Then, Table 8 provides the SN ratio and mean-based outcomes in each trail of the four combinations.

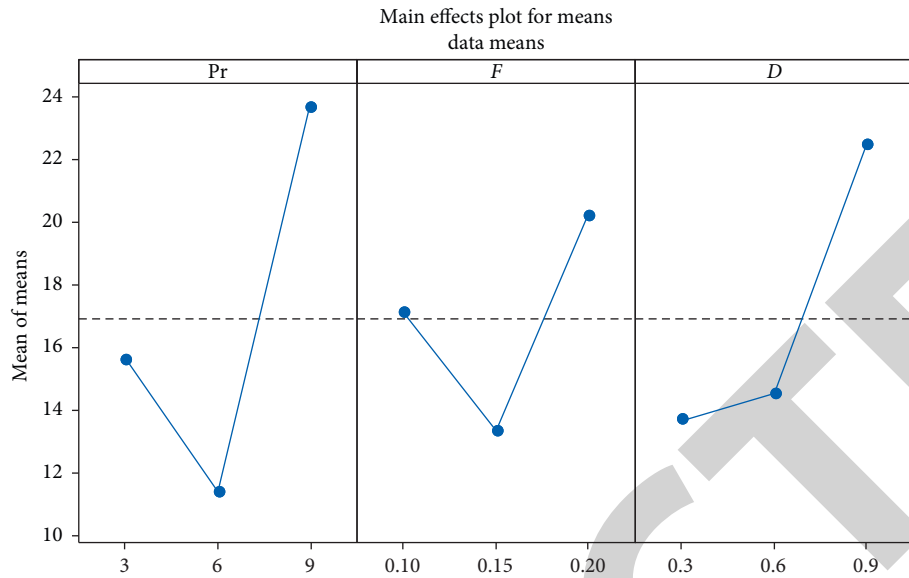


FIGURE 12: Tool wear, surface roughness, and thrust force focused on the important diagram based on the means; in the X-axis, Pr denotes pressure of cutting fluid (bar), F denotes feed (mm/rev), and D denotes depth of cut (mm).

TABLE 7: Tool wear, surface roughness, and thrust force-based response ratios of signal to noise.

Level	Pressure of cutting fluid, Pr (bar)	Feed, F (mm/rev)	Depth of cut, D (mm)
1	-26.41	-27.28	-26.17
2	-23.88	-25.39	-24.39
3	-31.22	-28.83	-30.95
Delta	7.34	3.44	6.56
Rank	1	3	2

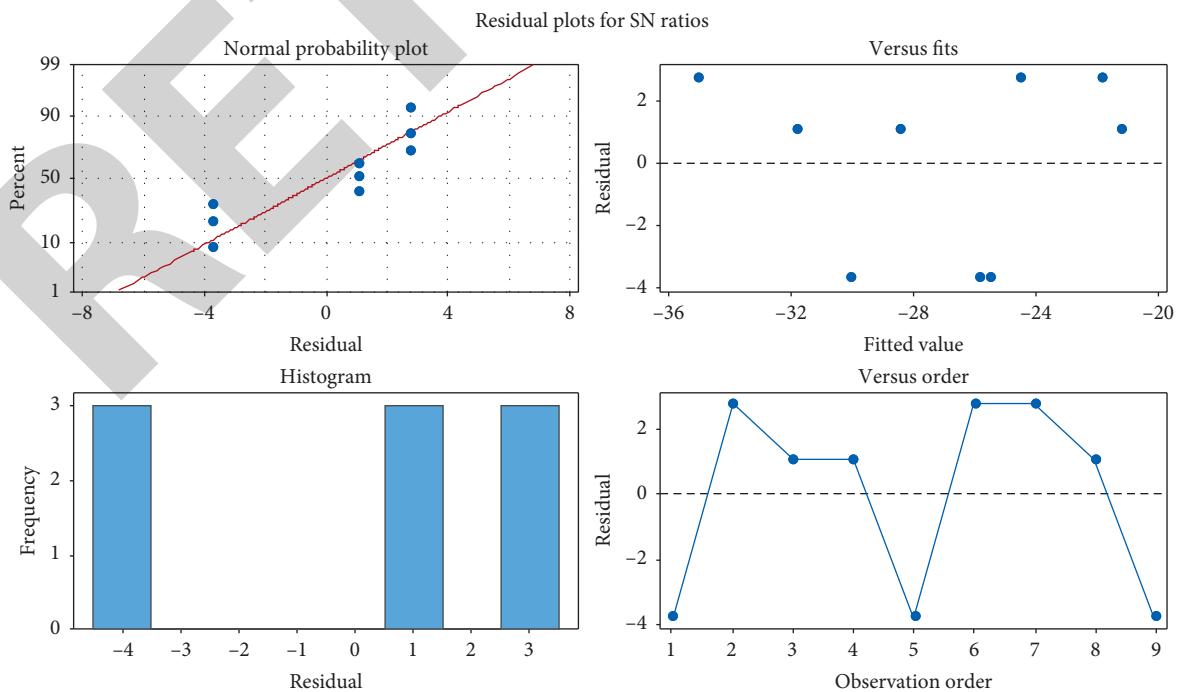


FIGURE 13: Tool wear, surface roughness, and thrust force-focused residual plot of percent, frequency, fitted values, and versus order.

TABLE 8: Cumulative outcome based on the signal-to-noise ratio and means in each trails' comparison.

No.	TW		SR		TF		TW, SR, and TF	
	SNRA 1	Mean 1	SNRA 2	Mean 2	SNRA 3	Mean 3	SNRA 4	Mean 4
1	-0.026	1.003	-11.799	3.890	-34.037	50.335	-29.294	18.409
2	6.143	0.493	-9.097	2.850	-23.742	15.385	-19.122	6.243
3	-3.767	1.543	-13.892	4.950	-35.563	59.998	-30.824	22.164
4	0.983	0.893	-7.121	2.270	-24.866	17.510	-20.178	6.891
5	-3.779	1.545	-11.150	3.610	-34.400	52.483	-29.653	19.213
6	3.702	0.653	-7.783	2.450	-26.506	21.150	-21.797	8.084
7	-3.197	1.445	-13.570	4.770	-37.124	71.814	-32.374	26.010
8	1.692	0.823	-7.568	2.390	-32.163	40.563	-27.408	14.592
9	-1.924	1.248	-13.368	4.660	-38.630	85.407	-33.872	30.438

4. Conclusion

This experimental study on optimization on operation parameters in the reinforced metal matrix of the AA6066 composite with HSS and Cu provided the following as the conclusions:

- (i) The machining can be possible for these conditions followed in the study
- (ii) Tool wear has cutting depth and feed as the most and least priority parameters, respectively
- (iii) Similarly, surface roughness has cutting depth and cutting fluid pressure as the greatest and smallest priority parameters correspondingly
- (iv) For the thrust force, cutting fluid pressure and cutting depth are the highest and lowest priority parameters
- (v) For all the response combinations, the pressure of the cutting fluid has the highest priority, and the feed has the least priority than the remaining input parameters
- (vi) The experimental results such as tool wear, surface roughness, and thrust force were reached at the parameters for the cutting fluid pressure of 6 bar with 0.15 mm per revolution of feed and 0.6 mm of cutting depth

Data Availability

The data used to support the findings of this study are included within the article and are also available from the corresponding author upon request.

Disclosure

This study was performed as a part of the Employment of Wolaita Sodo University, Wolaita Sodo, Ethiopia.

Conflicts of Interest

The authors declare that there are no conflicts of interest regarding the publication of this paper.

Acknowledgments

The authors thank Saveetha School of Engineering, Chennai, for the technical assistance to complete this experimental

work and appreciate the support from Wolaita Sodo University, Ethiopia.

References

- [1] T. Sathish and N. Sabarirajan, "Synthesis and optimization of AA 7175 - zirconium carbide (ZrC) composites machining parameters," *Journal of New Materials for Electrochemical Systems*, vol. 24, no. 1, pp. 34–37, 2021.
- [2] N. Sabarirajan, T. Sathish, and S. Karthick, "Machining parameters optimization of aluminium alloy 6063 with reinforcement of sic composites," *Materials Today: Proceeding*, vol. 33, no. 7, pp. 2559–2563, 2020.
- [3] P. Sevvell, T. Sathish, P. Sudharshan, and V. Vijayan, "Investigation and optimization of laser welding process parameters for AA7068 aluminium alloy butt joint," *Materials Today: Proceeding*, vol. 37, no. 2, pp. 1672–1677, 2021.
- [4] T. Sathish, "Experimental investigation of machined hole and optimization of machining parameters using electrochemical machining," *Journal of Materials Research and Technology*, vol. 8, no. 5, pp. 4354–4363, 2019.
- [5] S. Dinesh Kumar, T. Sathish, K. Muthukumar, and S. Karthick, "Natural inspiration technique for the parameter optimization of A-GTAW welding of naval steel," *Materials Today: Proceeding*, vol. 21, no. 1, pp. 843–846, 2020.
- [6] R. Saravanan, T. Sathish, K. Muthukumar, and V. Dhinakaran, "Study on temperature difference of aluminium nitride nanofluid used in solar flat plate collector over normal water," *AIP Conference Proceedings*, vol. 2283, no. 1, Article ID 020126, 2020.
- [7] K. Muthukumar, T. Sathish, S. Dinesh Kumar, and S. Karthick, "Temperature distribution analysis on diffusion bonded joints of Ti-6Al-4V with AISI 4140 medium carbon steel," *Materials Today: Proceeding*, vol. 21, no. 1, pp. 847–856, 2020.
- [8] S. P. Palaniappan, K. Muthukumar, R. V. Sabariraj, S. Dinesh Kumar, and T. Sathish, "CNC Turning process parameters optimization on Aluminium 6082 alloy by using Taguchi and ANOVA," *Materials Today: Proceeding*, vol. 21, no. 1, pp. 1013–1021, 2020.
- [9] S. Rajesh, D. Chandramohan, and T. Sathish, "Machining parameters optimization of surface roughness analysis for AA5083-Boron Carbide (B₄C) composites," *Materials Today: Proceeding*, vol. 33, no. 7, pp. 4642–4645, 2020.
- [10] K. Gurusami and T. Shalini Sand Sathish, "Optimization of stir casting parameters for corrosion rate analysis of AA7068-Boron carbide composites," *Materials Today: Proceeding*, vol. 33, no. 7, pp. 4650–4655, 2020.

Retraction

Retracted: Improving the Mechanical Properties of Natural Fiber Composites of Hemp Fiber with Ramie and Banana Fiber through Compression Molding Method

Advances in Materials Science and Engineering

Received 26 December 2023; Accepted 26 December 2023; Published 29 December 2023

Copyright © 2023 Advances in Materials Science and Engineering. This is an open access article distributed under the Creative Commons Attribution License, which permits unrestricted use, distribution, and reproduction in any medium, provided the original work is properly cited.

This article has been retracted by Hindawi, as publisher, following an investigation undertaken by the publisher [1]. This investigation has uncovered evidence of systematic manipulation of the publication and peer-review process. We cannot, therefore, vouch for the reliability or integrity of this article.

Please note that this notice is intended solely to alert readers that the peer-review process of this article has been compromised.

Wiley and Hindawi regret that the usual quality checks did not identify these issues before publication and have since put additional measures in place to safeguard research integrity.

We wish to credit our Research Integrity and Research Publishing teams and anonymous and named external researchers and research integrity experts for contributing to this investigation.

The corresponding author, as the representative of all authors, has been given the opportunity to register their agreement or disagreement to this retraction. We have kept a record of any response received.

References

- [1] S. Dinesh Kumar, L. Ponraj Sankar, T. Sathish et al., "Improving the Mechanical Properties of Natural Fiber Composites of Hemp Fiber with Ramie and Banana Fiber through Compression Molding Method," *Advances in Materials Science and Engineering*, vol. 2021, Article ID 7813634, 8 pages, 2021.

Research Article

Improving the Mechanical Properties of Natural Fiber Composites of Hemp Fiber with Ramie and Banana Fiber through Compression Molding Method

S. Dinesh Kumar ¹, **L. Ponraj Sankar** ², **T. Sathish** ³, **V. Vijayan** ⁴, **A. Parthiban** ⁵,
R. Kamalakannan ⁶ and **S. Rajkumar** ⁷

¹Department of Mechanical Engineering, St. Peter's Institute of Higher Education and Research, Avadi, Chennai 600 054, Tamil Nadu, India

²Department of Civil Engineering, CMR Institute of Technology, Hyderabad, India

³Department of Mechanical Engineering, Saveetha School of Engineering, SIMATS, Chennai 602 105, Tamil Nadu, India

⁴Department of Mechanical Engineering, K. Ramakrishnan College of Technology (Autonomous) Samayapuram, Trichy 621 112, Tamil Nadu, India

⁵Department of Mechanical Engineering, Vels Institute of Science Technology & Advanced Studies, Pallavaram, Chennai 600 117, Tamil Nadu, India

⁶Department of Mechanical Engineering, M. Kumarasamy College of Engineering, Karur, India

⁷Department of Mechanical Engineering, Faculty of Manufacturing, Institute of Technology, Hawassa University, Hawassa, Ethiopia

Correspondence should be addressed to S. Rajkumar; rajkumar@hu.edu.et

Received 6 June 2021; Revised 15 June 2021; Accepted 23 June 2021; Published 2 July 2021

Academic Editor: Samson Jerold Samuel Chelladurai

Copyright © 2021 S. Dinesh Kumar et al. This is an open access article distributed under the Creative Commons Attribution License, which permits unrestricted use, distribution, and reproduction in any medium, provided the original work is properly cited.

Natural fiber composite is the most preferable research area in the modern situation due to its availability, applications, and ecofriendly quality. This paper deals with the influence of hemp fiber with the various compositions of the ramie fiber and some basic mechanical properties of banana fiber composites. The hemp fiber is maintained as 20 percentage of total volume. Then, the remaining volume percentage is shared with the ramie fiber and banana fiber with various combinations. Eleven specimens were prepared to identify the some basic mechanical properties. The chemical compositions were mentioned as a pie chart, and then experimental results were plotted as graphical representations like line diagram and radar diagram for clear identification that the composite with higher ramie fiber concentration provided the greater results in the mechanical behaviors. The suitable composite combinations were recommended based on their superior properties as conclusions.

1. Introduction

Composite materials created the revolution of the materials in the world especially the natural fiber composite has the most influence on it based on their physical properties, availability, and economic supports when compared with the metals. This investigation is based on sources of the fiber plant and is shown in Figure 1. Dipen Kumar et al. [1] clearly reviewed about the fiber reinforcement composites with

various industrialized methods, and they identified the characteristics with usage. They also discussed about the synthetic and natural fibers with the help of various images and evidences from the research articles. Asim [2] clearly discussed regarding physical properties and mechanical properties of the hemp fiber with the help of different articles. He also proved the SEM images of bundle fiber and loose fiber also. The hemp fiber chemical compositions are clearly shown in Figure 2.

Seena et al. [4] clearly explained about the glass and banana fibers reinforcement with phenol formaldehyde, and they compared the characteristics individually with the help of various testing methods. They also provided various details and history of the banana fiber from the beginning. Sreekumar et al. [5] focused on the banana fiber reinforced composite with polyester which can be created through RTM, and they gave more attention to the mechanical properties and the water sorption investigations in a clear way. The chemical compositions of the banana are clearly mentioned in Figure 3.

Thonangi et al. [6] explained fully about the natural fiber reinforcement techniques with reliable diagrams, and they also compared the natural fiber with the glass fiber. They mentioned that the availability of the ramie fiber among the world with the help of the various articles and pointed out the chemical compositions and various mechanical properties of the ramie fiber with some list of fibers. The chemical compositions of the ramie fiber are clearly shown in Figure 4.

Layth et al. [3] reviewed with more than hundred research papers regarding the application of the reinforced natural fiber composites. They concluded that the main appreciable properties of the natural fibers when compared with synthetic fibers are less density, low solidity, and good economic characteristics. Mainly these natural fiber composites were used in the construction field, industries of automobiles, decoration field, and so on. They also mentioned that the reinforcement produced the greatest results in characteristics of the composites.

Sathish et al. [7] discussed about the basic properties of the hemp fiber based on the spectroscopy and microscopy. They mentioned that the most important factor of the reinforced natural fiber composite is bonding strength. Michael et al. [8] investigated about the hemp fiber compositions and arrangements with different chemical methods. They treated the hemp fiber with various chemicals such as sodium hydroxide, calcium chloride, calcium hydroxide, and various acids and tested with various thermal methods.

Le Troedec et al. [9] mentioned that the hemp fiber has higher brittleness property than jute fiber composites. Paul et al. [10] mentioned the applications of the hemp fiber as electrical components, products of building, cloths, wrapping materials, and pipes manufacturing. Tara and Reddy [11] discussed about the ramie fiber and modification based on different reaction of hydroxyl groups with isocyanate used chemical treatments. He et al. [12] mentioned the applications of kitchen and home-based furniture, fisher web, screen cloths, and so on.

Chandramohan et al. [13] explained about the ramie fiber. They concluded that the volume fraction of the fiber concentration leads to the augmentation of the properties of the composites but thirty percentage of volume fraction of ramie fiber has the supreme storage modulus amongst the comparison of the other volume fractions. In the same way, Mwaikambo [14] and Zulkifli et al. [15, 16] recommended the thirty percentage volume fraction of the ramie fiber for the greatest results in the mechanical characteristics.

Eko et al. [17] obviously investigated about the epoxy resin used banana composite with surface treatment

influence on the characteristics. They clearly mentioned the basic properties and compositions of the banana fibers. They used the different concentrations of the sodium hydroxide alkali treatment with the banana composite. They concluded that the one percentage of the sodium hydroxide used treatment reaches the greater consequences in the characteristics of the composites when associated with supplementary percentage of concentrations.

Eko et al. [18] completely explained about the reinforced banana fiber composite with different methods especially volume fraction has the most important influence in the mechanical behaviors. Venkateshwaran et al. [19] focused the thermal and mechanical characteristics natural fiber composites of the banana. They are provided the significant improvement and recommendations for the natural fibers which can be executed with the intention of augmentation of the characteristics. Ramesh et al. [20] explained about the banana fiber and pandanus reinforcement composites. They concluded that composites of woven banana fibers have the lesser water absorption when compared with the composite of woven pandanus [21]. From all these investigations, following research gaps are identified.

The hemp, banana, and ramie fibers were separated; combination of these two or other fibers based composites was only studied. However, this investigational research article is noticeably focused on natural fiber composites of constant twenty percentage of hemp fiber with banana and ramie fiber in different combinations of volume fractions and on the basic mechanical behavior (tensile strength, Young's modulus, percentage of elongation and density) based appropriate volume fraction of fiber composites [22].

2. Experimental Procedure

This experiment is conducted with fibers of hemp, banana, and ramie with the resin of polylactic acid by the compression molding method. This experiment is done with the compression molding machine with capacity of five tones, 50 kW powers [23]. It contains upper part of die and lower part of the die with guide pins. Lower part of the die has the heating and cooling facilities with molding cavity. The fiber combinations (as per Table 1) and resin were taken into the mold cavity of specimen size of 250 mm length, 200 mm width, and 12 mm thickness [24]. Then, the upper and lower parts of the die are closed. Then, the pressure of 150 kg/cm² to 600 kg/cm² was applied, and the heat is also applied to the mold place in the range of 70°C to 80°C for the preheating purpose. After curing, the specimens were collected with the help of the extraction pin.

Eleven specimens were prepared as per the variations mentioned in Table 1. All the specimens have 20 percentage of the hemp fiber due to its higher mechanical properties. Then, the banana fiber and the ramie fiber have the remaining 80 percentage with the various combinations to produce the specimens for the testing [25]. The specimens were named *P1* which means piece number 1; similarly, others also named as *P2*, *P3*, . . . , *P11*. The concentration of the banana fiber of volume percentage in the total volume percentage get reduced from eighty percentage to zero

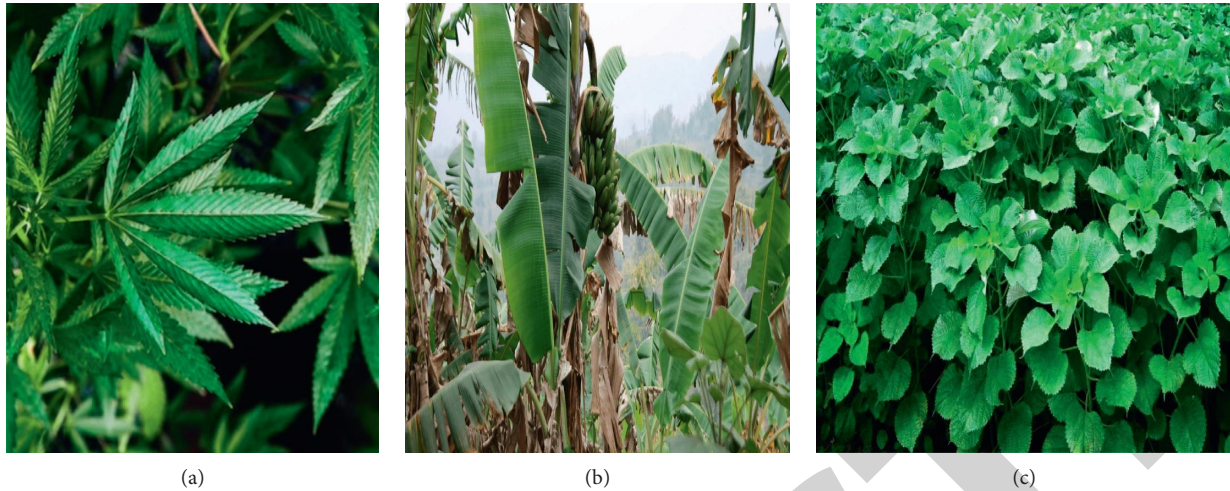


FIGURE 1: Natural fiber plants of (a) hemp; (b) banana; (c) ramie.

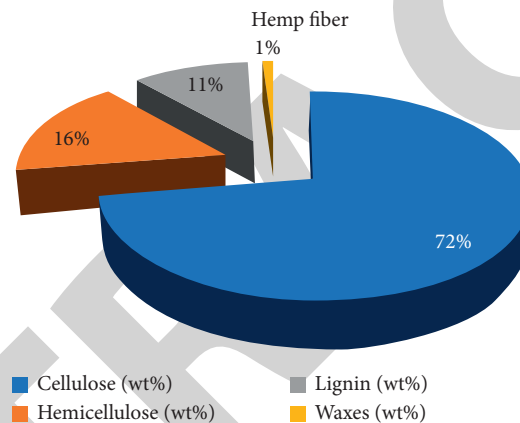


FIGURE 2: Chemical compositions of the hemp fiber [3].

percentage with the decrement of eight percentage of the volume fraction in each specimen from $P1$ to $P11$.

Similarly, ramie fiber volume percentage increased from zero percentage to eighty percentage with eight percentage of volume concentration in the specimens from $P1$ to $P11$, respectively. Then, the individual specimens were prepared as per the ASTM E8 standard methods for the universal testing machine [26]. Here, tensile strength and percentage of elongation were identified with the same testing machine mentioned in Figure 5. However, Young's modulus of the samples can be found based on Hook's law relation such as stress strain relations. The density values of the specimens were measured with the help of the weighing machine. Then, the density is calculated with the ratio of mass to the unit volume calculations.

3. Results and Discussion

The radar diagram really helps to identify the separation of the results with one or more in the sequence level and the interaction between the outcomes of the experimental results. So, in this investigation, radar diagrams especially filled radar diagrams (created by Microsoft Excel

software) were used to realize the results in the clear identification. The experimental results of the tensile strength are plotted in Figure 6(a) as a radar diagram and Figure 6(b) as a line diagram. The tensile strength has enhancement from lower to higher with respect to increasing ramie fiber contribution among the composites. The highest tensile strength is achieved at specimen $P11$; similarly, the lowest tensile strength is achieved at $P1$. From the radar diagram, it is mentioned that $P8$ to $P11$ specimens have the greatest value region from 650 MPa to 740 MPa as experimental results when compared with others.

Similarly, experimental results of Young's modulus in GPa are plotted as radar diagram and line diagram in Figures 7(a) and 7(b), respectively. Here, also Young's modulus gets increased in each specimen with increase in ramie fiber contribution in the specimens. The maximum Young's modulus is reached at the $P11$ composite specimen, and the minimum Young's modulus is reached at specimen $P1$. From the radar diagram, maximum Young's modulus range is identified between 50 GPa and 55 GPa, and among all specimens, $P7$ to $P11$ have reached the maximum values as per the radar diagram.

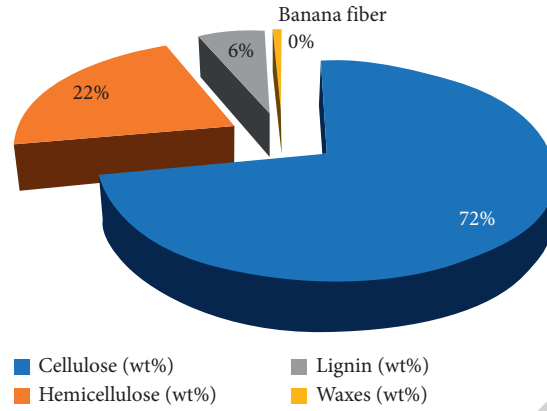


FIGURE 3: Chemical compositions of the banana fiber [3].

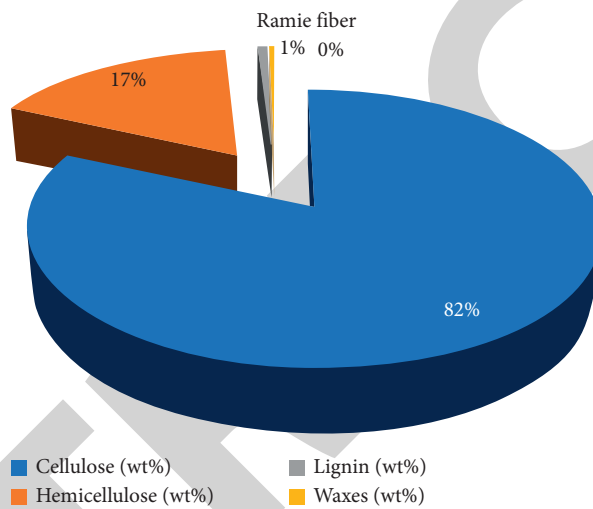


FIGURE 4: Chemical compositions of the ramie fiber [3].

TABLE 1: Natural fiber contribution details in composite specimens.

Specimen piece name	Percentage of fiber used in total volume		
	Hemp	Banana	Ramie
P1		80	0
P2		72	8
P3		64	16
P4		56	24
P5		48	32
P6	20	40	40
P7		32	48
P8		24	56
P9		16	64
P10		8	72
P11		0	80

Figures 8(a) and 8(b) point out the radar diagram and line diagram correspondingly for the experimental outcome of the percentage of elongation which will get decremented with respect to the decrement of the banana fiber composite concentrations. Maximum percentage elongation reached

for specimen P1 is 48%, and the lowest percentage elongation is obtained at specimen P11. From the radar diagram, the maximum percentage of elongation range is between 38% and 48% for the specimens from P1 to P3; similarly, the lowest percentage elongation region is 3% to 12% for



FIGURE 5: Testing machine for the investigation.

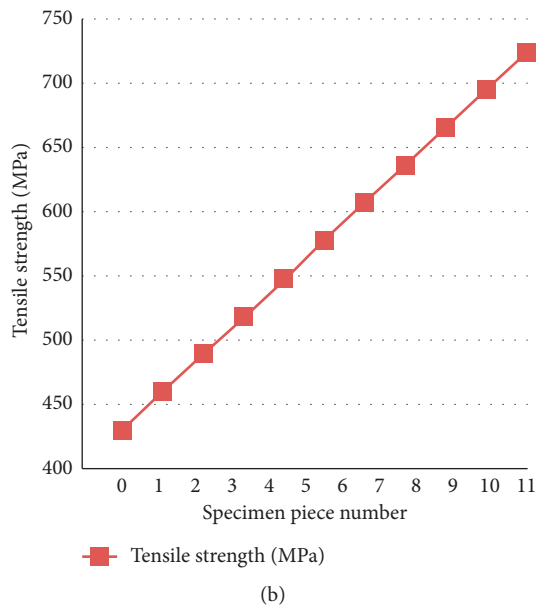
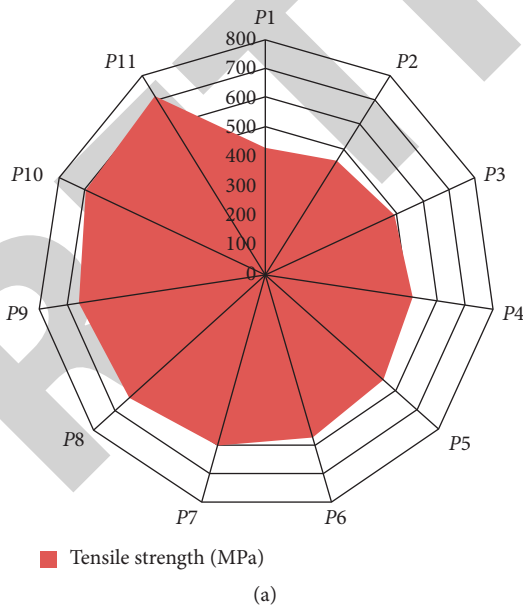


FIGURE 6: Experimental results of the tensile strength in MPa: (a) radar diagram; (b) line diagram.

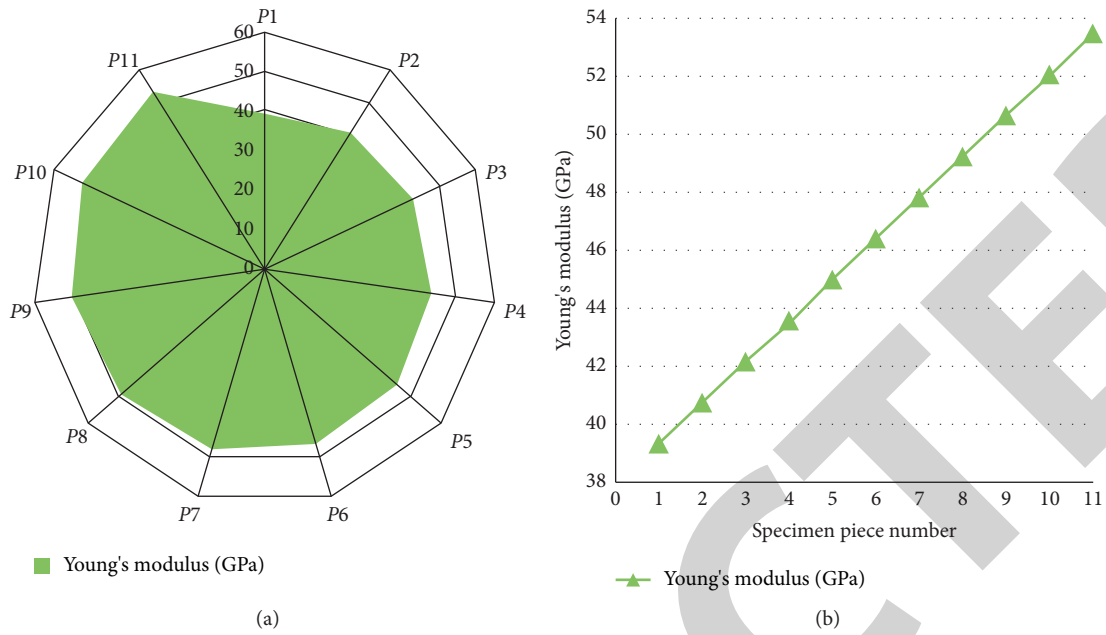


FIGURE 7: Experimental results of Young's modulus in GPa: (a) radar diagram; (b) line diagram.

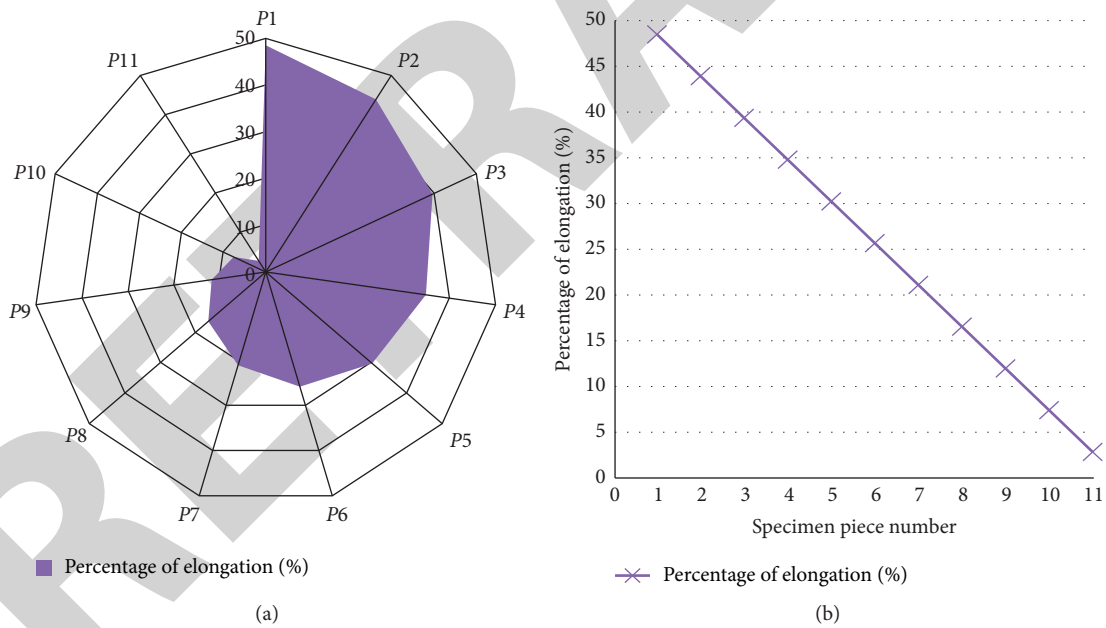


FIGURE 8: Experimental results of the percentage of elongation: (a) radar diagram; (b) line diagram.

specimens P9, P10, and P11. P11 specimens have the maximum contribution of the ramie fiber, so they have the lowest elongation.

In the same way, Figures 9(a) and 9(b) show the radar diagram and line diagram of the experimental results of the density which get augmented results relating to increase in

the concentration of the ramie fiber. From the line diagram, the maximum density of 1.49 g/cm^3 is obtained for specimen P11 and the minimum density of 1.41 g/cm^3 is reached for specimen P1. From the radar diagram, maximum density range is between 1.47 g/cm^3 and 1.49 g/cm^3 of specimens P9 to P11.

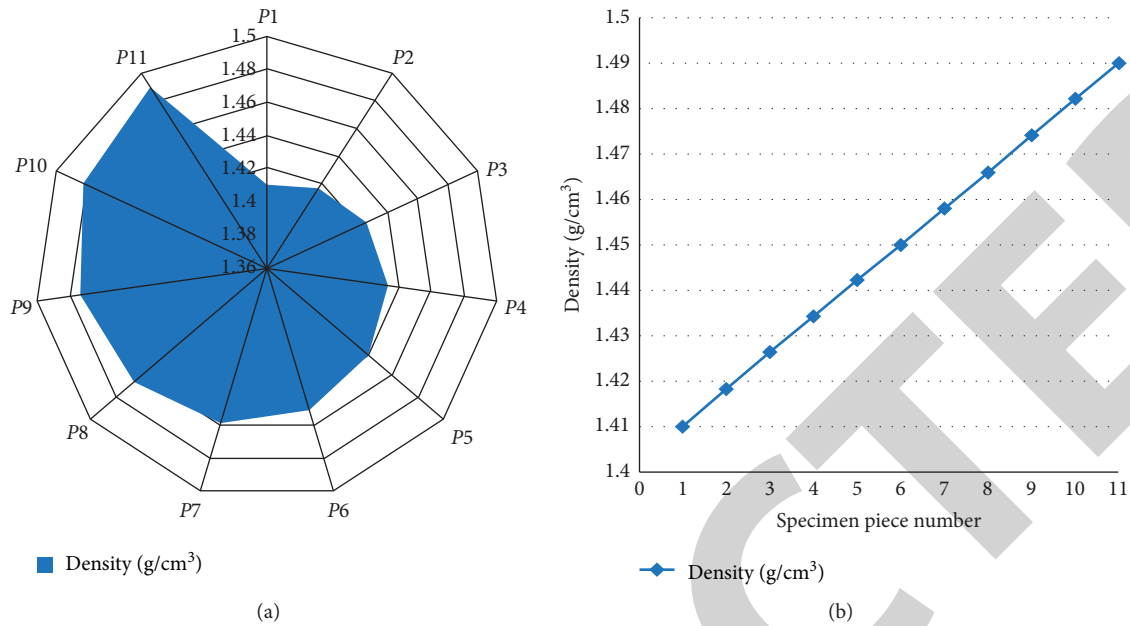


FIGURE 9: Experimental results of the density in g/cm^3 : (a) radar diagram; (b) line diagram.

4. Conclusions

In this experimental study, based on the influence of hemp fiber in the basic mechanical properties of ramie and banana fiber composites, the following results are produced as conclusions:

- (i) Hemp fiber produced the enhancement in each property with respect to the 20 percentage involvement in the total volume percentage in composite fiber
- (ii) With the increment of the ramie fiber, volume percentage produced the incremental values in tensile strength, Young's modulus, and density
- (iii) However, the percentages of elongation get decreased with the influence of ramie fiber concentration
- (iv) Composite specimens P8 to P11 were suitable for greatest tensile strength
- (v) Composite specimens P7 to P11 were suitable for furthestmost Young's modulus
- (vi) Composite specimens P1 to P3 were suitable for maximum percentage elongation
- (vii) Composite specimens P9 to P11 were suitable for supreme density.
- (viii) So, specimens P9 to P11 reached the highest tensile strength, Young's modulus, and density with lower percentage of elongation

Data Availability

The data used to support the findings of this study are included within the article. Additional data or information is available from the corresponding author upon request.

Disclosure

It was performed as a part of the Employment of College of Engineering and Technology, Hawassa University, Hawassa, Ethiopia.

Conflicts of Interest

The authors declare that there are no conflicts of interest regarding the publication of this paper.

Acknowledgments

The authors appreciate the supports from Hawassa University, Ethiopia. The authors thank Saveetha School of Engineering, Chennai, for the technical assistance to complete this experimental work.

References

- [1] R. Dipen Kumar, D. D. Pagar, P. L. Menezes, and E. Linul, "Fiber-reinforced polymer composites: manufacturing, properties, and applications," *Polymers*, vol. 11, no. 10, Article ID 1667, 2019.
- [2] S. Asim, "A study in physical and mechanical properties of hemp fibres," *Advances in Materials Science and Engineering*, vol. 8, Article ID 325085, 2013.
- [3] M. Layth, M. N. M. Ansari, G. Pua, M. Jawaid, and M. Saiful Islam, "A review on natural fiber reinforced polymer composite and its applications," *International Journal of Polymer Science*, vol. 2015, Article ID 243947, 2015.
- [4] J. Seena, M. S. Sreekala, Z. Oommen, P. Koshy, and S. Thomas, "A comparison of the mechanical properties of phenol formaldehyde composites reinforced with banana fibres and glass fibres," *Composites Science and Technology*, vol. 62, no. 14, pp. 1857–1868, 2002.

Retraction

Retracted: Analysis on Emissions and Performance of Ceramic Coated Diesel Engine Fueled with Novel Blends Using Artificial Intelligence

Advances in Materials Science and Engineering

Received 26 December 2023; Accepted 26 December 2023; Published 29 December 2023

Copyright © 2023 Advances in Materials Science and Engineering. This is an open access article distributed under the Creative Commons Attribution License, which permits unrestricted use, distribution, and reproduction in any medium, provided the original work is properly cited.

This article has been retracted by Hindawi, as publisher, following an investigation undertaken by the publisher [1]. This investigation has uncovered evidence of systematic manipulation of the publication and peer-review process. We cannot, therefore, vouch for the reliability or integrity of this article.

Please note that this notice is intended solely to alert readers that the peer-review process of this article has been compromised.

Wiley and Hindawi regret that the usual quality checks did not identify these issues before publication and have since put additional measures in place to safeguard research integrity.

We wish to credit our Research Integrity and Research Publishing teams and anonymous and named external researchers and research integrity experts for contributing to this investigation.

The corresponding author, as the representative of all authors, has been given the opportunity to register their agreement or disagreement to this retraction. We have kept a record of any response received.

References

- [1] T. K. Kotteda, R. B. R. Chekuri, B. Naga Raju, P. R. Kantheti, and S. Balakumar, "Analysis on Emissions and Performance of Ceramic Coated Diesel Engine Fueled with Novel Blends Using Artificial Intelligence," *Advances in Materials Science and Engineering*, vol. 2021, Article ID 7954488, 13 pages, 2021.

Research Article

Analysis on Emissions and Performance of Ceramic Coated Diesel Engine Fueled with Novel Blends Using Artificial Intelligence

Tarun Kumar Kotteda ¹, Rama Bhadri Raju Chekuri ¹, B. Naga Raju ²,
Prasada Raju Kantheti ¹ and S. Balakumar ³

¹Department of Mechanical Engineering, Sagi Rama Krishnam Raju Engineering College, Bhimavaram, Andhra Pradesh, India

²Department of Mechanical Engineering, Anil Neerukonda Institute of Technology and Sciences, Visakhapatnam, Andhra Pradesh, India

³Arba Minch University, Arbaminch, Ethiopia

Correspondence should be addressed to S. Balakumar; sbk25dec@gmail.com

Received 1 June 2021; Revised 16 June 2021; Accepted 22 June 2021; Published 1 July 2021

Academic Editor: Samson Jerold Samuel Chelladurai

Copyright © 2021 Tarun Kumar Kotteda et al. This is an open access article distributed under the Creative Commons Attribution License, which permits unrestricted use, distribution, and reproduction in any medium, provided the original work is properly cited.

The exhaustive nature of petroleum products triggers the obstacles of scarcity, economic imbalance, and environmental depletion. It is difficult to avoid their usage all of a sudden and switch to clean electric prime movers. Under all these circumstances, the researchers may initiate their investigations on alternative fuels for preeminent solution. The present study covers the performance and emissions of a single cylinder, four-stroke, diesel engine fueled with *Pongamia pinnata* and *Calophyllum inophyllum* biodiesels added with *n*-butanol additive at various proportions. In this investigation, the piston has been coated with ceramic material with a thickness of 200 μm topcoat. The blends have been tested at 1500 rpm speed and rated compression ratio of 17.5 : 1 at various operating loads. A comparative result analysis has been made on the engine parameters operated by diesel and showed that mechanical efficiency gradually increases with a percentile increment of *n*-butanol in the blend. Moreover, emissions such as CO, CO₂, NO_x, and opacity were found to be reduced for the samples having high amount of *n*-butanol, whereas HC emissions slightly increased. In addition, all the exhaust gases have been predicted by using second-order polynomial equations generated and artificial Intelligence technique, and the comparative analysis has been made. It has been identified that ANN showed an average accuracy of prediction superior than regression analysis.

1. Introduction

The enormous outrush of overseas trade-off, on the one hand, and enlarging emissions forefront towards environmental depletion, on the other hand, have triggered attentiveness towards replacement for diesel oil and petrol. Fuel oils furnish energy about 90% of shipment and transportation, and the demand is gradually increasing, specifically in swiftly developing countries such as India and China. The domiciliary stock of petroleum oil in our country met quarter of the percentage out of the full demand, whereas the remaining needs are to be satisfied with the help of petroleum by-products imported from foreign countries. Hence, necessary steps have been followed to overcome the foreign

dependency on imports of crude oil. Biodiesel blends are renewable, which are extracted by the chemical treatment of vegetable oils, animal fats, and biomass using transesterification process and are called fatty acid methyl esters [1]. Predominant research has been done on various engines fueled with biofuels blended in diesel and observed appreciable improvement in emissions and performance concern [2, 3]. Karmee and Chadha [4] identified fuel characterization of *Pongamia pinnata* methyl esters relevant to ASTM standards. Suresh Kumar et al. [5] stated that, supervising a single cylinder, diesel engine fueled with PPME blends, the heating value of biodiesel dropped down with an increment of volume % of PPME. In addition, an increase in BSFC and a decrease in NO_x and HC were

noticed at high loads. Significant improvement in CO and NO_x was identified with 20% of *Pongamia pinnata* biodiesel while testing a water-cooled type, single cylinder CI engine, whereas BTE and volumetric efficiency also increase [6].

Rakopoulos et al. [7] triggered research on *n*-butanol blended with diesel and noticed the drop of emissions except HC emissions, and this reduction is higher in percentile increment of butyl alcohol. Nanthagopal et al. [8] studied the effect of pentanol and butanol added with *Calophyllum inophyllum* biodiesel tested on the diesel engine and revealed that BTE was gradually decreased, whereas BSFC increased. On the other hand, CO, NO_x, HC, and opacity emissions were rapidly decreased. This reduction rate is increased with higher % of alcohol content in the blend. Moreover, nitrogen oxides were significantly decreasing due to the cooling effect of alcohol in the blend and high latent heat of vaporization. Ramakrishnan et al. [9] assessed the influence of *n*-pentanol added (10, 15, and 20%) with *Calophyllum inophyllum* diesel blend of 20% on VCR engine and suggested that 20% *n*-pentanol added blend is the feasible one for better performance and combustion, whereas NO and CO emissions are slightly increasing due to effective combustion. Imtenan et al. [10] done their studies on a high speed, four-cylinder diesel engine tested with *Calophyllum inophyllum* blends added with *n*-butanol additive and revealed that the blends with high concentration of additive give promising BSFC and BTE, whereas, on the other hand, nitric oxides and CO emissions are dropped with respect to diesel outcomes.

In recent times, researchers used various optimization techniques, like ANN and RSM; thereby, they can easily predict performance, combustion, and emission parameters relevant to their work. As per their assessment, it is easy to understand the influence of blends thoroughly; thereby, R&D cost may reduce [11–13]. However, so many complications may arise while doing the experimental work on IC engine to analyze its performance and emissions. It is not amazingly effective in the view of economic and time factors. By considering all these consequences, predicting the performance, combustion, and exhaust gas emissions of an engine using various optimization techniques has received notable recognition recently. In this study, various parameters like load acts on an engine, speed of the engine, blend ratio, injection advance, etc. [14]. The computer-interface training techniques are among the precious methods to estimate the engine performance and emission characteristics [15]. ANN and RSM have been selected by innumerable investigators to reduce the number of trails. Because of the accuracy and the potentiality to examine indiscriminate problems that will not have a chance of being solved by statistical and traditional techniques, ANN has become desirable for estimating various engine outcomes [16].

Safieddin Ardebili et al. [17] studied various engine parameters using RSM as an optimization strategy. In this approach, gasoline and fusel fuel have been tested at various ratios ranging from 25 to 75% with an interval of 25% in terms of volume basis. Prediction responses showed 4% of maximum evaluated error compared with that of

experimental outcomes. Subsequently, it can be proved that the RSM models are fitted suitably for predicting performance and emissions of the test rig. In another study, Safieddin Ardebili et al. [18] employed a study of multi-objective optimization with RSM technique. Feasible operating conditions have been examined for various blends of fusel oil mixed with nanobiochar additive. In this investigation, speed of the engine varies from 1800 to 2600 rpm with an interval of 200 rpm, whereas the fusel oil blended with diesel fuel ranges from 5 to 20% with an interval of 5%, and the additive is added at various rates (25, 50, 75, 100, and 125 ppm). Speed of the engine, concentration of fuel oil, and additive have been considered as input responses for prediction analysis, whereas power, BSFC, torque, and various emissions were examined as output responses. At last, comparative analysis has been made in between prediction responses and experimental outcomes. The results depict that the feasible operating conditions for the additive (nanobiochar) were found at 2300 rpm speed and the engine fueled with 10% of fusel oil blended in 90% of diesel and 100 ppm biochar. Prediction analysis using RSM reveals the estimated error below 5%. Despite the fact that various approaches have been progressed to escalate the prediction accuracy of ANN model, the algorithm named feed forward back propagation is the notable one in this area [19]. Mainly, it consists of 3 layers (minimum) as input, hidden, and output layers. Each and every individual layer may include various nodes. Among all, both input and output layers require the particulars from the experimental statistics to create the network architecture and simulation of the system. Levenberg–Marquardt (Trainlm) training function has been practiced for error-free evaluation, in which mean square error decides the dereliction consequence of the network [20]. Most of the experimental investigations have been carried out on various engines with the application of ANN for optimizing the outcomes [21–25]. As time passes on, researchers may use various ceramic coatings to the combustion chamber, piston, etc., in order to improve the performance and reduce the emission with the enhancement of heat transfer rate in combustion reaction [26–30].

There have been innumerable investigations on internal combustion engines powered with *Pongamia pinnata*/*Calophyllum inophyllum* diesel blends. Moreover, no significant studies have been found from the literature related to predicting the engine outcomes using optimization techniques. Therefore, in the present study, ANN and regression models have been employed for optimizing and predicting the emission characteristics of a CI engine fueled with *Pongamia pinnata* and *Calophyllum inophyllum* oils. The originality of the current study is to compare the performance and emission parameters of CI engine with ceramic coated piston tested with novel blends with respect to the diesel outcomes. In addition, comparative analysis has been made in between two optimization models to predict the feasible (emission) responses with best working conditions of a CI engine; thereby, the % of average accuracy has been estimated.

2. Materials and Methods

In this study, Transesterification has been adopted as a filtration technique to prepare the pure biodiesel that has to be followed by esterification technique, as *Pongamia pinnata* and *Calophyllum inophyllum* oils are having high content of free fatty acids. Here, transesterification has been done by heating, followed by stirring of crude sample with an addition of NaOH as base catalyst and methanol. Gravitational technique has followed traditionally, in order to estrange glycerol content from biodiesel using distilled water after the chemical reaction and water wash isolation. Then, the methyl esters of *Pongamia pinnata* and *Calophyllum inophyllum* have been prepared as depicted in Figure 1.

These methyl esters have been blended with neat diesel under various proportions in terms of volume (P10, P20, C10, and C20) with magnetic stirrer setup. Again, these samples are added with an additive (butyl alcohol) in different probabilities varying from 6 to 12% in terms of volume with an interval of 6%. In the current study, *n*-butanol has been used as an additive (oxygenated), and it can easily react with diesel due to its high burning velocities. So, it seems to support the combustion possessed with sufficient amount of oxygen [7, 8, 10]. The nomenclature of the fuels was tested for analyzing the performance and emissions of engine expressed in Table 1. Initially, the properties of all blends are measured with various equipments before testing on an engine and are mentioned in Table 2.

3. Steady State Thermal Analysis

In the current study, statistical analysis has been done on a single cylinder, water cooled type, four-stroke, Kirloskar-TV1, and eddy current dynamometer CI engine with its piston made up of aluminum alloy using ANSYS workbench. This engine has power of 5.2 kW at a configured speed of 1500 rpm. Here, the geometric compression ratio is 17.5 : 1. FEA approach has been implemented on traditional, ceramic glazed piston coated with a thickness of 200 μm topcoat. The particulars to the geometry configuration have been specified at modal section of the segment. The configuration has levant affix contiguity connecting topcoat-bond coats, piston rings-rings groove, and bond coat-membrane. In this manner, geometric modeling of piston has been done, followed by generating a fine meshing with default features considered in workbench settings as shown in Figure 2. The configured model consists of around 45,227 nodes with 27,174 elements.

The study of heat transfer in compression ignition engines is consistently treated as a prejudiced research domain because of complexity. In this study, convective heat transfer has been chosen as the main mechanism for examining the engine performance. Because of the following factors, it is difficult to study the heat transfer in CI engines:

- (1) Uninterrupted variation of gaseous temperatures has been found inside the cylinder
- (2) It is extremely difficult to identify the precise temperature levels and heat transfer coefficient

- (3) Piston operating inside the cylinder is liable for combustion, as it has been exposed to high pressures and temperatures along with heat transfer coefficient

3.1. *Uncoated Piston.* Temperature distribution has been found for both coated and uncoated pistons using the FEA approach, as depicted in Figures 3 and 4.

3.2. *Coated Piston.* To simulate the model for temperature distribution, ANSYS, a mechanical finite element analysis computer software, has been chosen for thermal analysis at steady state. The range of temperatures found for an uncoated piston (without modification) has been found to be of a maximum of 350°C and minimum of 313.96°C, respectively. For a modified piston (ceramic coated at top surface), the temperatures were found to be of a maximum of 355°C and minimum of 323.85°C. Similarly, heat flux of uncoated and coated pistons is disclosed in Figures 5, and 6, respectively.

From the above steady state thermal analysis, plasma spray method has been chosen as a thermal spray coating method to apply the ceramic coating on piston with a thickness of 200 μm topcoat. The coated medium has been transformed into molten phase by means of heat, affects the membrane surface, and swiftly cools down to form coating [26–30]. For decreasing the vital aggregate of gas contamination discharged from engine, this study implies a piston coated with ceramic material for testing the biodiesels.

4. Experimental Engine Test Setup

In this study, the investigations are carried out on a single cylinder, water cooled type, four-stroke, direct injection CI engine with a ceramic coated piston equipped with a dynamometer of eddy current type to apply the load. Alumina has been used as a ceramic material for coating the piston with 200 μm thickness of top coat. A Compression Ignition (CI) engine with its piston coated with any ceramic material attains less heat loss, and it can be named as low heat rejection engine. In view of fuel price hikes and environmental depletion, this modified engine has gaining massive significance in the contemporary world, as it releases fewer emissions [26–30]. It was very well equipped, including combustion pressure and crank angle measurement. There is a provision to measure the flow of air and fuel, temperatures, etc. Here, calorimeter water flow and cooling water are measured by using Rotameters equipped. The engine test rig allows the elucidation of performance characteristics. The schematic representation of engine test bed is depicted in Figure 7. Engine soft package has been attached to assess the computerized performance. There is a provision for measuring injection pressure of fuel at the nozzle with computerized mode. The detailed specifications of engine test bed are described in Table 3. The gaseous emissions are recorded by AVL DI GAS 444N analyzer, and smoke density has been measured with AVL 437C Smoke Meter.

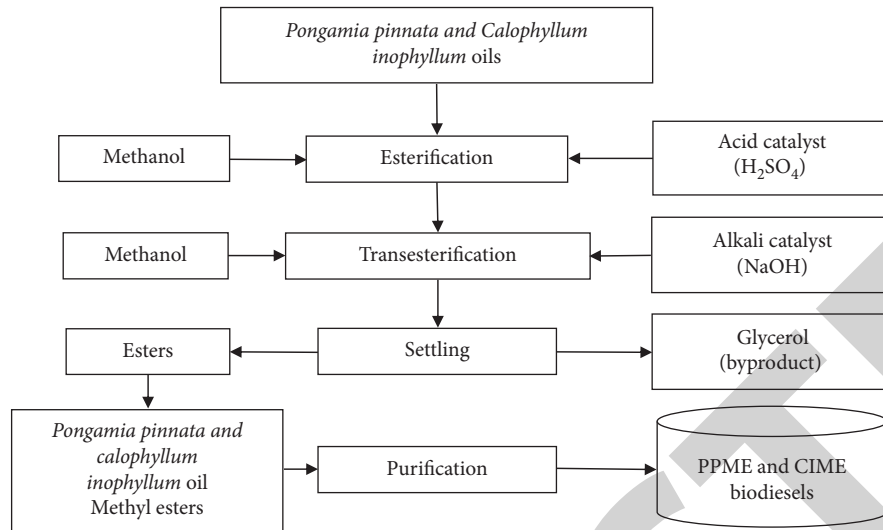


FIGURE 1: Process of preparation for biodiesels.

TABLE 1: Fuel Nomenclature of the tested blends.

Sample	Composition
D100	100% diesel
P10B6	94% (10% PPME + 90% diesel) + 6% <i>n</i> -butanol
P10B12	88% (10% PPME + 90% diesel) + 12% <i>n</i> -butanol
P20B6	94% (20% PPME + 80% diesel) + 6% <i>n</i> -butanol
P20B12	88% (20% PPME + 80% diesel) + 12% <i>n</i> -butanol
C10B6	94% (10% CIME + 90% diesel) + 6% <i>n</i> -butanol
C10B12	88% (10% CIME + 90% diesel) + 12% <i>n</i> -butanol
C20B6	94% (20% CIME + 80% diesel) + 6% <i>n</i> -butanol
C20B12	88% (20% CIME + 80% diesel) + 12% <i>n</i> -butanol

All the blends have been tested by varying the load (0%, 50%, and 100%) at a fixed speed of 1500 rpm with a rated compression ratio (17.5:1). Emissions and performance analysis are carried out on an engine once achieving the stable state. Prediction analysis has been done by considering the experimental data using mathematical modeling and ANN. Finally, a comparative analysis has been done in between the experimental outcomes and soft computing responses.

5. Results and Discussion

5.1. Exhaust Emission Parameters. The ever-increasing demand of petroleum refined products and the unpredictability in their availability may be a reason for the matter of global concern [1–3]. At present, global transformation from ignition engines to electric propulsion mainly depends on emissions. Emissions of diesel engines are inferior to gasoline; however, decreasing the emissions is essential, and the green initiative is necessary.

5.1.1. Nitrogen Oxides (NO_x) Emission. NO_x emission is considered as a major pollutant that requires rigorous diminution. These emissions may depend on in-cylinder temperature, air/fuel ratio, and reaction rate of oxygen in the

blend. Generally, oxygenated additives produce high range of NO_x emissions; it is happened only due to the fact that the amount of nitrogen in the air/fuel mixture reacted with the surplus amount of oxygen in the combustion chamber. Thereby, NO_x emissions are developed in subsequent mechanism called Zeldovich mechanism [9]. But, here, as per the trend statistics of our study, it was clear that the blends of PPME and CIME were added with *n*-butanol additive forms comparatively lower than NO_x with respect to conventional diesel. Irrespective of loads deployed, P10B12, C10B12, and C20B12 blends give lower emissions as illustrated in Figures 8(a) and 8(b). The researchers [7, 8, 10] revealed that this phenomenal reduction was possible with higher amount of *n*-butanol in the blend. It has occurred due to the consequence of lowering the temperature of *n*-butanol. Moreover, the aspects such as rise of dissipated heat and low heating value impact this nature and are superior at odds with their incompatible effects laid due to their lower cetane number compared with diesel [9].

5.1.2. Carbon Monoxide (CO) Emission. In general, CO emissions are developed if adequate quantity of oxygen is not intricate in an enzymatic reaction of combustion process, which may be due to low temperature and lack of oxygen. This resembles what was considered as a byproduct

TABLE 2: Fuel properties of the tested samples.

Sample	Density (kg/m ³)	Flash point (°C)	Fire point (°C)	Viscosity (cSt)	Calorific value (kJ/kg)
D100	830	56	65	3.21	42500
P100	898.7	165	180	2.46	35668
C100	896.8	156	166	2.85	35085
P10B6	851	59	69	3.10	41251
P10B12	854	60	71	3.14	40698
P20B6	856	62	73	3.19	40615
P20B12	858	65	75	3.21	40097
C10B6	849	56	67	3.01	41013
C10B12	850	58	68	3.10	40423
C20B6	852	60	71	3.12	40132
C20B12	854	63	72	3.17	39716

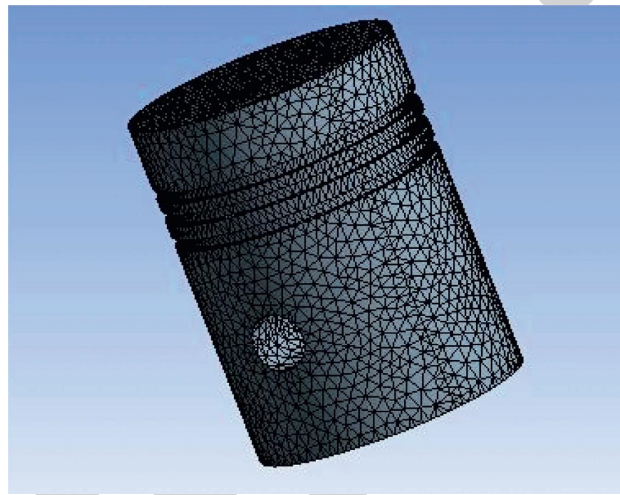


FIGURE 2: Meshed model.

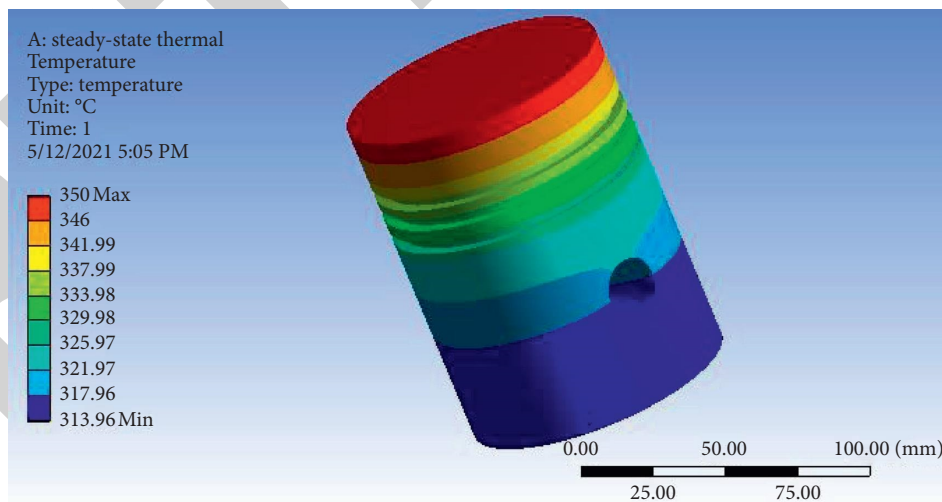


FIGURE 3: Temperature distribution of uncoated piston.

of deficient combustion of carbon. As depicted in Figures 9(a) and 9(b), the PPME and CIME related *n*-butanol blends exhibit lower CO emissions compared with diesel. Irrespective of loads applied, this reduction of CO emissions has been identified as an increase in the ratio of *n*-butanol in

the blend [7, 8, 10]. The density of *n*-butanol is lesser than that of conventional diesel, which evaporates inside the cylinder; thereby, the length of spray atomization is decreased [9]. It results in reduction of CO emissions for *n*-butanol added blends. Moreover, the samples P10B12 and

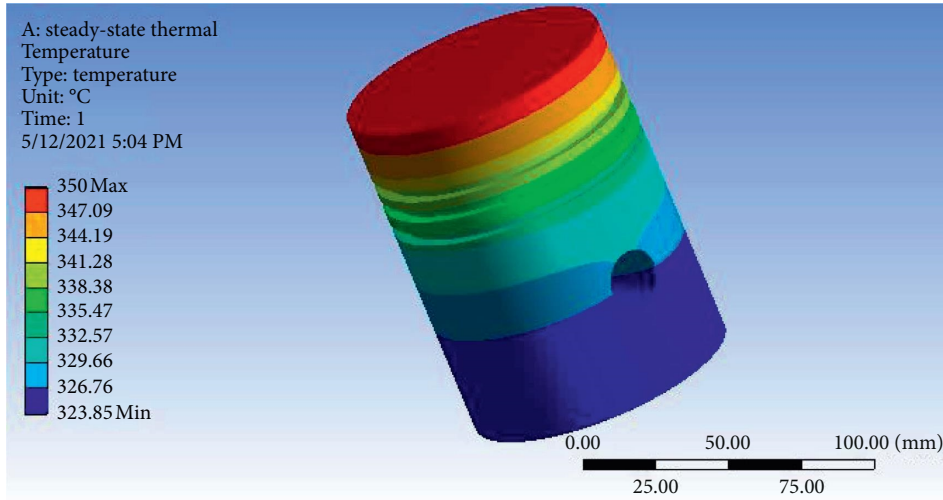


FIGURE 4: Temperature distribution of coated piston.

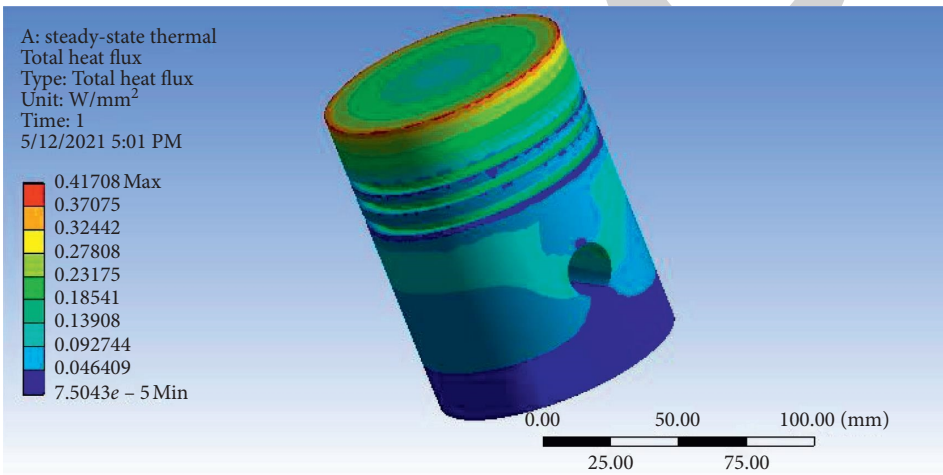


FIGURE 5: Heat flux of uncoated piston.

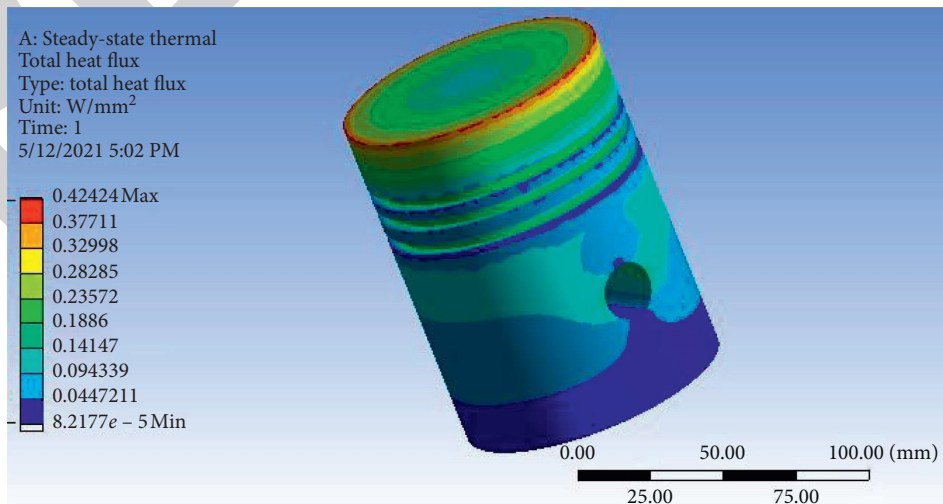


FIGURE 6: Heat flux of coated piston.

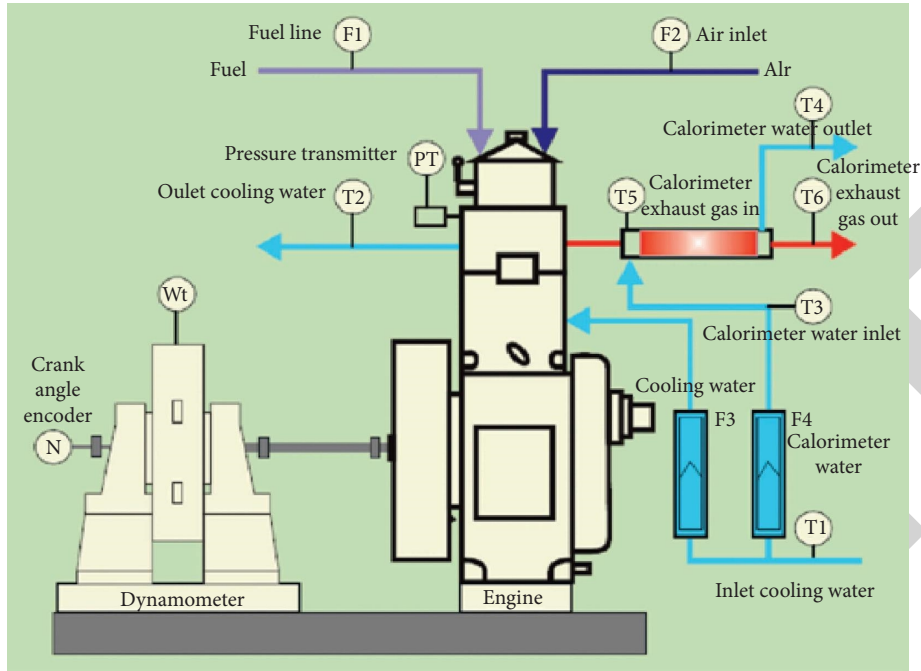


FIGURE 7: Schematic arrangement of the engine testing setup.

TABLE 3: Detailed specifications of the engine test bed.

Parameter	Detailed specification
Make	Kirloskar-TV1
Number of cylinders	Single cylinder (four-stroke)
Type of ignition	Compression ignition
Dynamometer	Eddy current type
Injection type	Direct injection
Cooling type	Water cooled
Rated power	5.2 kW
Rated speed	1500 rpm
Stroke	110 mm
Bore	87.5 mm
Compression ratio	17.5:1
Swept volume	661 cc
Overall dimensions	W 2000 × D 2500 × H 1500 mm
Optional	Computerized diesel injection pressure measurement

C10B12 exhibit lesser CO emissions among all, and compared with, diesel outcomes.

5.1.3. Carbon Dioxide (CO₂) Emission. Figures 10(a) and 10(b) exhibit the variation of CO₂ emissions with respect to load deployed on the engine fueled with various blends. Generally, the emissions such as CO and CO₂ exhibit trade-off effects with each other. This seems to represent that CO₂ gets reduced when CO increases. It should happen; if appropriate oxygen is accessible in the blend, CO₂ will appear due to oxidization of CO [9]. But, here, in our study, no significant variations are observed. Moreover, as per trend statistics, the samples P10B12 and C10B12 possess marginal decrease in CO₂ emissions.

5.1.4. Hydrocarbon (HC) Emission. Figures 11(a) and 11(b) represent statistics of unburned hydrocarbon emissions (HC) with respect to load deployed on an engine fueled with various blends. As per the literature in various research articles, it was evident that phenomenal rise of HC emissions for the blends is concentrated with high percentage of *n*-butanol [7, 8, 10]. In compression ignition engines, HC emissions evolved due to unburned fuel that is confined inside the combustion chamber. In addition, the fuel sprayed inside the combustion chamber reaches the cold cylinder walls that can be settled as unburned hydrocarbons [9]. In our study, HC emissions are gradually increasing with the increase in the amount of *n*-butanol in the blend. This may be because of the slow and poor-air fuel mixing, because of the rise of the evaporated heat levels of *n*-butanol,

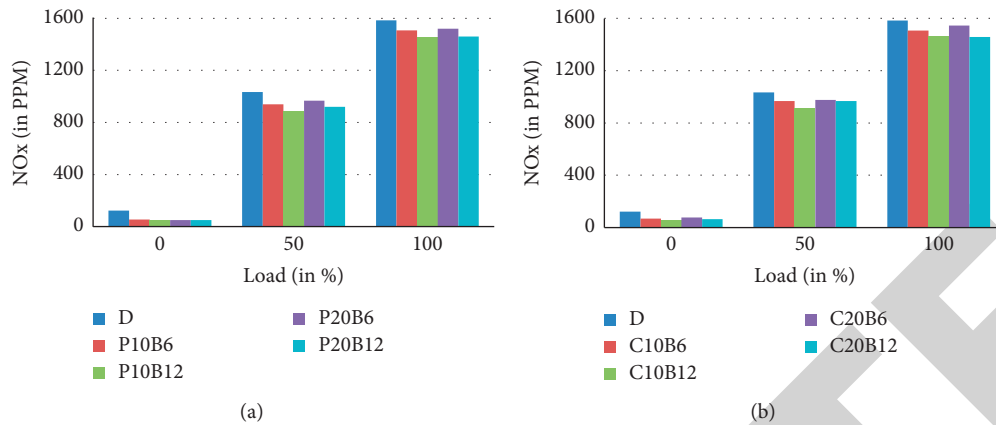


FIGURE 8: (a). NO_x vs load for PPME samples. (b). NO_x vs load for CIME samples.

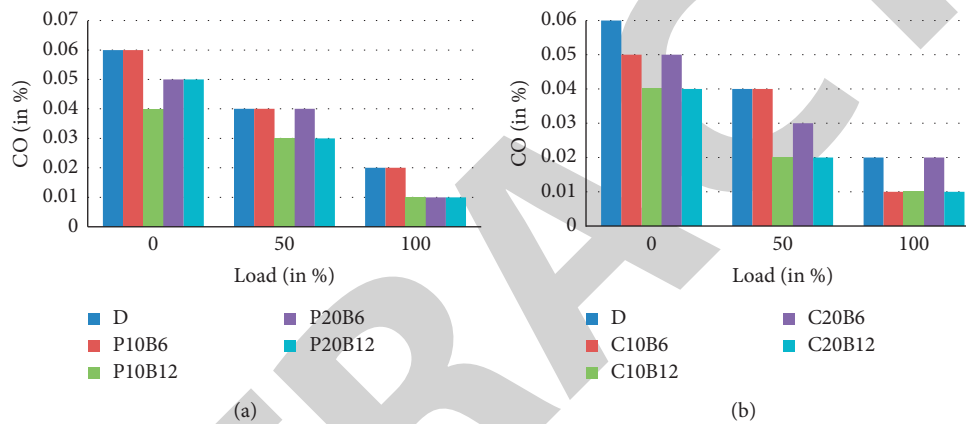


FIGURE 9: (a). CO vs load for PPME samples (b). CO vs load for CIME samples.

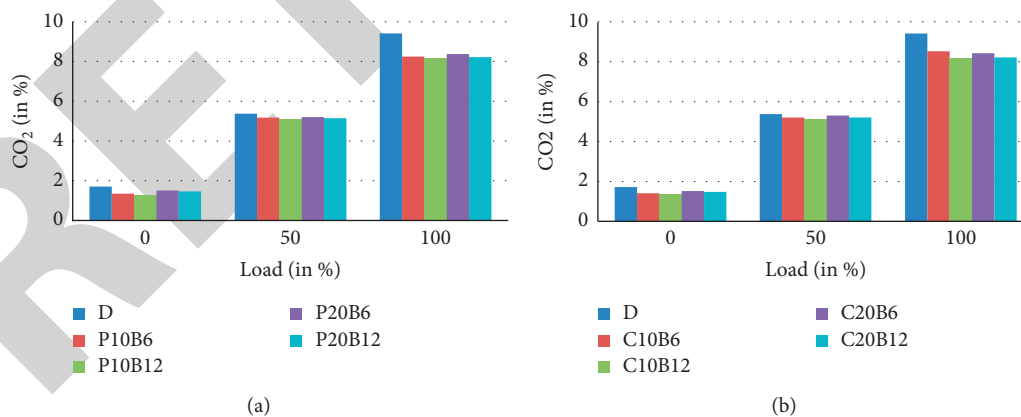


FIGURE 10: (a) CO_2 vs load for PPME samples (b). CO_2 vs load for CIME samples.

cushioning effect at the land spaces of piston rings and flame quenching [7].

5.1.5. Smoke/Opacity Emission. Opacity emission depicts the quantity of soot accumulation in the exhaust gases. Also, it occurs due to the result of unburned hydrocarbons and

absorption of some biotic compounds. Moreover, their rate may depend on the nature of the fuel tested. It was noticed that opacity emissions are decreasing with the increase in the concentration of butyl alcohol in the blend as depicted in Figures 12(a) and 12(b) [7, 8, 10]. This trend may arise because of the presence of O_2 molecules in the butyl alcohol [9].

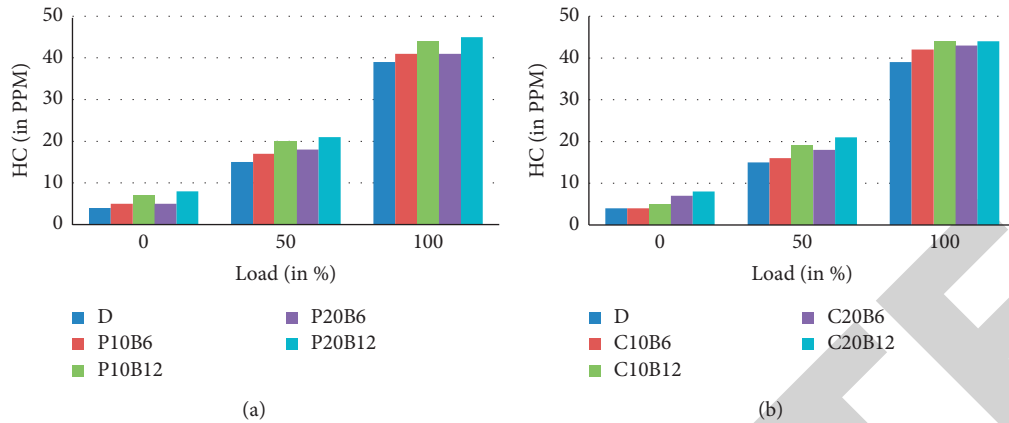


FIGURE 11: (a) HC vs load for PPME samples. (b). HC vs load for CIME samples.

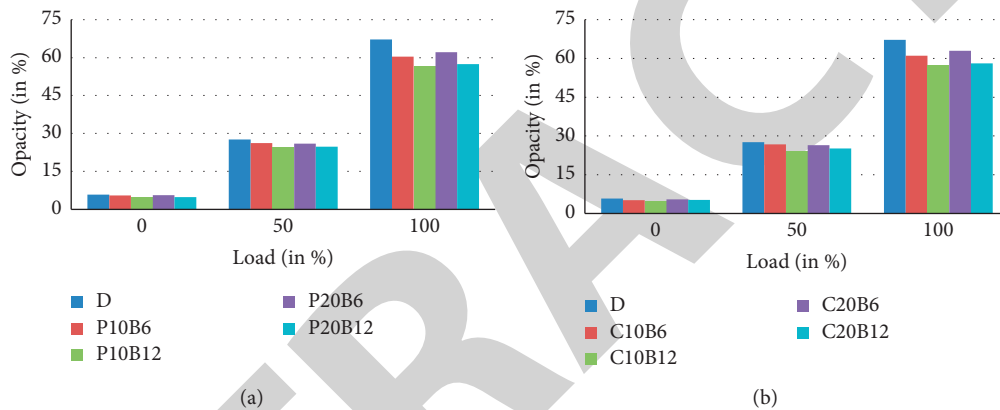


FIGURE 12: (a) Opacity vs load for PPME samples. (b). Opacity vs load for CIME samples.

5.2. Performance Analysis. In general, performance parameters such as BP, BMEP, and BTE tend to increase or remain the same with an increase in load, whereas BSFC decreases; this trend is at par with general performance of diesel engines [2–6]. In this study, the performance analysis has been carried out by connecting the test rig with IC engine soft.

5.2.1. Brake-Specific Fuel Consumption. Figures 13(a) and 13(b) show the variation of BSFC as a function of load. Here, the analysis is done at a rated speed and constant compression ratio of the same engine; that is the reason why BSFC trend relies on the trend statistics of rate of mass flow of a blend. It has been noticed that BSFC slightly increases or remains the same for all biodiesel blends in comparison with the diesel outcomes. This is because of the lower energy content in the biodiesel samples than that of diesel [9]. From the literature [7, 8, 10], it has been revealed that this increase may depend on the percentile increment of *n*-butanol in the sample. Another reason behind this trend is lower calorific value of *n*-butanol rather than a neat diesel, in which the analysis is done at the same load only, and, also, due to discrepancies in turbulence level that may lead to high cycle by cycle combustion imbalance during preliminary phases of

the combustion phenomenon [7, 8]. Although the piston has been coated with a ceramic material, *n*-butanol additive played an influencing factor in the trend statistics of brake-specific fuel consumption.

5.2.2. Mechanical Efficiency. In general, the content of diesel and additives is directly proportional to all the performance parameters like BP, BMEP, and BTE [2–6]. The higher the volume percentage of diesel and additives, the higher the performance of the engine. If volume percentage of bio-methyl esters increases, then the diesel, as well as *n*-butanol, ratio decreases in the biodiesel sample; hence, a marginal increase in performance is only observed in this investigation. During combustion process, the exhaust gas temperatures are higher for the engine with ceramic coated components than the engine under normal conditions [26–30]. When increased exhaust gases temperature is considered, it is obvious that turbocharging and consequently total thermal efficiency of the engine are increased. Otherwise, the higher the mechanical efficiency on an engine, the higher the volume % of *n*-butanol in the tested sample [7, 8, 10] (both for PPME and CIME) as noticed in Figures 14(a) and 14(b).

5.3. *Prediction Analysis.* In order to estimate the exhaust gas emissions, artificial intelligence tools such as ANN and regression analysis have been applied.

5.3.1. *Analysis Using ANN.* ANN is treated as soft computing strategy that can be assisted by the biotic neural system. The operating condition of neural networks is related to the activity of neurons in human brain, in which each activity transfers weight along with bias that can evolve one over another. ANN can be easily applied in various engineering aspects to sort out the issues in many applications, pointedly in the areas where traditional and statistical techniques are not enough to apply. It constitutes three layers (minimum) such as input, hidden, and output layers [19]. ANN has been employed as a processing strategy to study the performance and gaseous emissions in the domain of biodiesels fueled in an engine at various working conditions [11–13, 15–18, 20–25]. In the current study, ANN was applied to estimate the emission gases such as CO, CO₂, NO_x, HC, and smoke density for all blend samples. Feed forward backpropagation in combination with “TRAINLM”

training function has been used as algorithm, and mean square error treated as performance function [11, 12, 19–25]. Here, the number of hidden layers was fixed to two, whereas, for every hidden layer, neurons are varied to observe the better network architecture, in which the number of epochs at which the feasible outcomes are achieved is 1500 (based on validation). Load depicted on the engine (L), volume % of diesel oil (D), volume % of PPME or CIME (P/C), and volume % of *n*-butanol (A) were chosen as inputs, and required exhaust gases are treated as targets [11–18]. Figure 15 shows the flow process of ANN.

5.3.2. *Regression Analysis.* In addition to ANN, Minitab software is peculiarly utilized to generate second-order regression mathematical models with the experimental data the same as done in ANN [26]. The generated equations (1)–(5) are used to predict various emissions of PPME blends, whereas equations (6)–(10) are for the CIME blends based on the inputs as shown below. The predicted values of regression and ANN for all the blend ratios are tabulated, and an average of each emission parameter is extracted.

$$\text{NO}_x = -661 - 684D * D - 4121P * P - 677L * L - 1642D * A + 2157D * L + 2339P * L + 1409A * L, \quad (1)$$

$$\text{CO} = 0.609 - 0.604D * D - 3.94P * P - 0.0150L * L - 1.66D * A - 0.0220D * L - 0.0751P * L + 0.0533A * L, \quad (2)$$

$$\text{CO}_2 = 1.42 - 0.08D * D + 4.4P * P - 1.32L * L - 0.77D * A + 8.38D * L + 7.68P * L + 7.03A * L, \quad (3)$$

$$\text{HC} = 73.9 - 81.7D * D - 477P * P + 22.0L * L - 126D * A + 13.0D * L + 13.0P * L - 29.7A * L, \quad (4)$$

$$\text{opacity} = -12.7 + 20.9D * D + 126P * P + 27.2L * L + 40D * A + 30.2D * L + 42.3P * L - 26.1A * L, \quad (5)$$

$$\text{NO}_x = -889 + 1073D * D + 7579C * C - 831L * L - 2244D * A + 2291D * L + 2416P * L + 1718A * L, \quad (6)$$

$$\text{CO} = 0.061 + 0.147D * D + 0.74C * C + 0.0050L * L + 0.03D * A - 0.0535D * L + 0.0032C * L + 0.038A * L, \quad (7)$$

$$\text{CO}_2 = 5.59 - 4.77D * D - 25.3C * C - 1.27L * L - 11.1D * A + 8.77D * L + 7.25C * L + 4.29A * L, \quad (8)$$

$$\text{HC} = 17.4 - 19.6D * D - 13C * C + 24.5L * L + 2D * A + 16.1D * L - 11.2C * L + 20.3A * L, \quad (9)$$

$$\text{opacity} = 11.7 - 7.3D * D - 38C * C + 27.5L * L - 21.1D * A + 31.6D * L + 41.2C * L - 31.2A * L. \quad (10)$$

5.3.3. *Comparative Prediction Analysis.* As shown in Figures 16(a) and 16(b), the prediction accuracies of ANN are almost superior to regression analysis. ANN possessed an average prediction accuracy ranging from 92.94% to 97.95% for all the emission parameters, whereas

regression depicts 80.81% to 97.03% for all PPME blends. CIME proportions showed ANN prediction accuracy of 92.20% to 96.13% for all emissions, while regression estimates an average accuracy ranging from 87.39% to 96.13%.

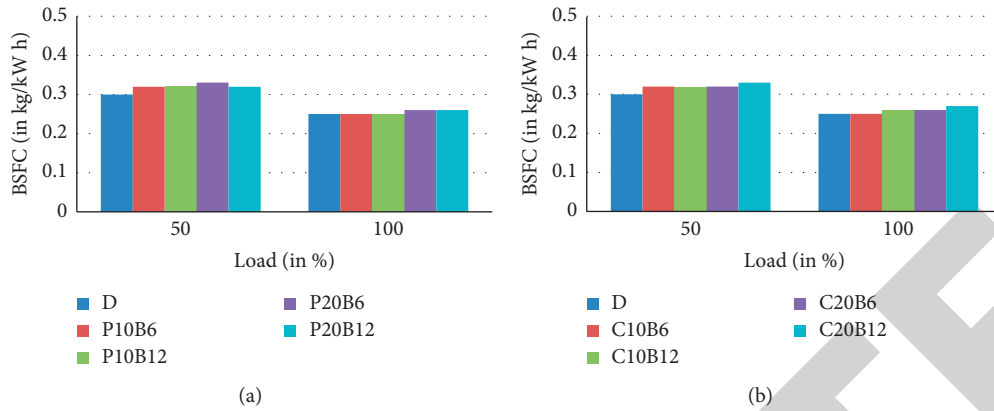


FIGURE 13: (a) BSFC vs load for PPME samples. (b). BSFC vs load for CIME samples.

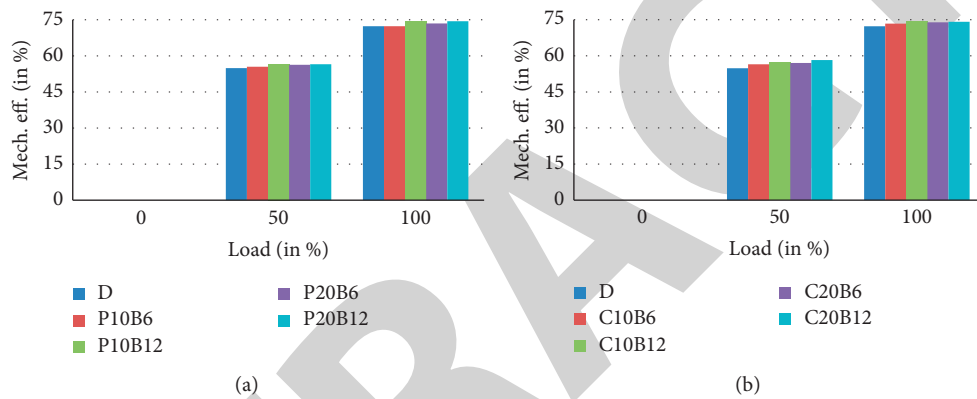


FIGURE 14: (a) Mech. eff. vs load for PPME samples (b). Mech. eff. vs load for CIME samples.

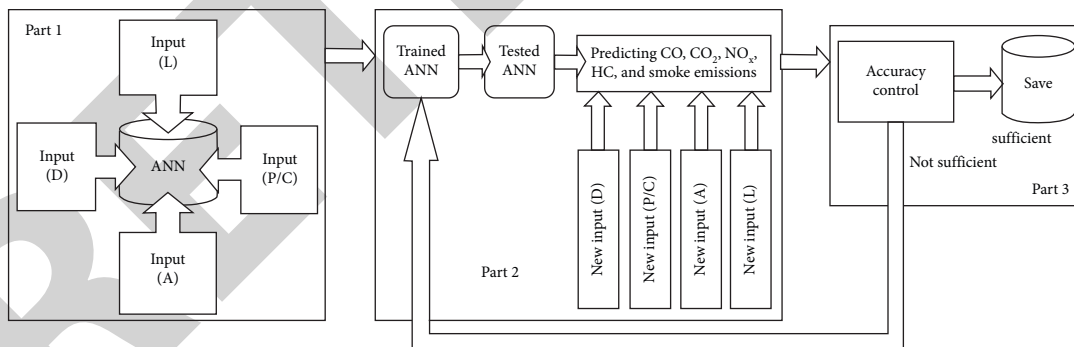


FIGURE 15: Process chart of ANN.

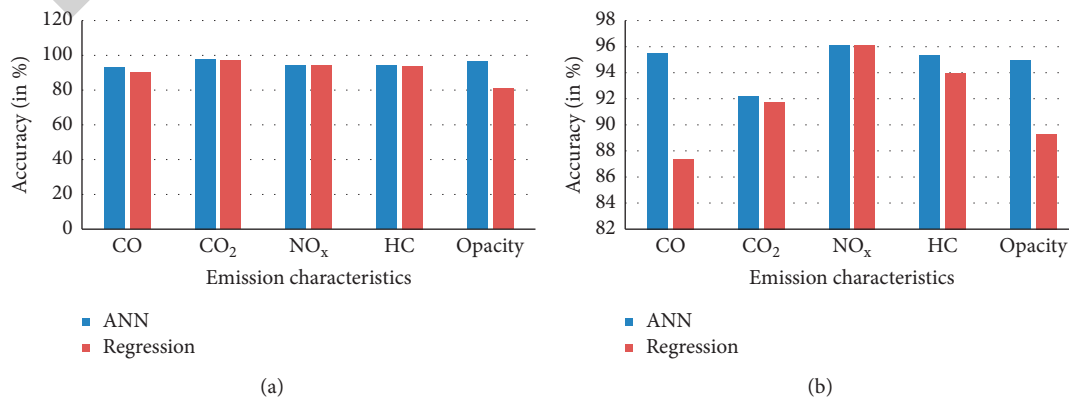


FIGURE 16: (a). Prediction chart for PPME blends. (b) Prediction chart for CIME blends.

6. Conclusion

In this study, ANN and regression analysis have been incorporated in order to optimize the working parameters of CI engine with its piston coated with ceramic material and fueled with various novel blends. Various influencing factors such as load depicted on the engine and *n*-butanol concentration on exhaust gas emissions were examined. Due to increased combustion chamber temperature of ceramic coated engine, phenomenal reduction in soot and carbon monoxide emissions has been noticed. However, *n*-butanol additive plays an influencing factor in the trend statistics, rather than the coating applied on the piston. Second-order multiregression model for each parameter is developed, and, on the other hand, the combined effects of input characteristics on engine emissions are deeply discussed. Based on the experimental investigation, the following diagnoses are made:

- (1) The existing CI engine modified with its ceramic coated piston works satisfactorily with biodiesel fuels, and the results show that it can produce less emission and improves performance.
- (2) Significant improvement was found in mechanical efficiency of the engine tested with various *n*-butanol blends, whereas brake-specific fuel consumption slightly increases with the increase in the concentration of *n*-butanol in the blend sample. This is due to the lower heating value of *n*-butanol compared with diesel fuel.
- (3) Emission parameters such as NO_x, CO, and smoke have been significantly reduced, irrespective of loads deployed on the brake drum of an engine operated with *n*-butanol blends. The higher this reduction, the higher the amount of *n*-butanol in the sample.
- (4) No significant variations were found in the statistics of CO₂ emissions. On the other side, HC emissions have been increased drastically due to cushioning and flame quenching effect.
- (5) By using ANN, 92.20–97.95% of an overall average accuracy was predicted for all emission parameters, whereas it was 80.81–97.03% by regression. Under all the circumstances, instead of the diesel fueled engine, the engine tested with P10B12 and C10B12 fuels gives optimistic responses.

Abbreviations:

ANN: Artificial neural networks
 BMEP: Brake mean effective pressure
 BP: Brake power
 BSFC: Brake-specific fuel consumption
 BTE: Brake thermal efficiency
 CI: Compression ignition
 CIME: *Calophyllum inophyllum* methyl ester
 CO: Carbon monoxide
 CO₂: Carbon dioxide
 DI: Direct injection

FAME: Fatty acid methyl esters
 H₂SO₄: Sulfuric acid
 HC: Unburned hydrocarbons
 NaOH: Sodium hydroxide
 NO_x: Oxides of nitrogen
 PPME: *Pongamia pinnata* methyl ester
 RSM: Response surface methodology.

Data Availability

The data used to support the findings of this study are included within the article.

Disclosure

This study was performed as a part of the employment at Arba Minch University, Ethiopia.

Conflicts of Interest

The authors declare that there are no conflicts of interest.

References

- [1] M. Chaker Ncibi and M. Sillanpaa, "Recent research and developments in biodiesel production from renewable bio-resources," *Recent Patents on Chemical Engineering*, vol. 6, no. 3, pp. 184–193, 2013.
- [2] B. R. Aravindh Raj, P. Jeyaraman, N. Tamil Selvam, and K. Arun Kumar, "Performance and emission evaluation of a VCR diesel engine using mahua oil methyl ester," *International Journal of Mechanical Engineering & Technology*, vol. 9, no. 3, pp. 143–155, 2018.
- [3] S. Ashraf, M. Hussain, M. W. Mumtaz, and M. Shuaib, "Biodiesel production by alkali catalyzed transesterification of chicken and beef fats," *International Journal of Alternative Fuels and Energy*, vol. 1, no. 1, pp. 14–20, 2017.
- [4] S. K. Karmee and A. Chadha, "Preparation of biodiesel from crude oil of *Pongamia Pinnata*," *Bioresource Technology*, vol. 96, no. 13, pp. 1425–1429, 2005.
- [5] K. Sureshkumar, R. Velraj, and R. Ganesan, "Performance and exhaust emission characteristics of a CI engine fueled with *Pongamia Pinnata* methyl ester (PPME) and its blends with diesel," *Renewable Energy*, vol. 33, no. 10, pp. 2294–2302, 2008.
- [6] P. L. Naik and D. C. Katpatal, "Performance analysis of CI engine using *Pongamia Pinnata* (Karanja) biodiesel as an alternative fuel," *International Journal of Science and Research*, vol. 2, pp. 445–454, 2013.
- [7] D. C. Rakopoulos, C. D. Rakopoulos, E. G. Giakoumis, A. M. Dimaratos, and D. C. Kyritsis, "Effects of butanol-diesel fuel blends on the performance and emissions of a high-speed DI diesel engine," *Energy Conversion and Management*, vol. 51, no. 10, pp. 1989–1997, 2010.
- [8] K. Nanthagopal, B. Ashok, B. Saravanan, D. Patel, B. Sudarshan, and R. Aaditya Ramasamy, "An assessment on the effects of 1-pentanol and 1-butanol as additives with *Calophyllum Inophyllum* biodiesel," *Energy Conversion and Management*, vol. 158, pp. 70–80, 2018.
- [9] P. Ramakrishnan, R. Kasimani, M. S. Peer, and S. Rajamohan, "Assessment of n-pentanol/*calophyllum inophyllum*/diesel blends on the performance, emission, and combustion characteristics of a constant-speed variable compression ratio

Retraction

Retracted: Mathematical Modeling and Analysis of Wear Behavior of AlTiN Coating on Titanium Alloy (Ti-6Al-4V)

Advances in Materials Science and Engineering

Received 26 December 2023; Accepted 26 December 2023; Published 29 December 2023

Copyright © 2023 Advances in Materials Science and Engineering. This is an open access article distributed under the Creative Commons Attribution License, which permits unrestricted use, distribution, and reproduction in any medium, provided the original work is properly cited.

This article has been retracted by Hindawi, as publisher, following an investigation undertaken by the publisher [1]. This investigation has uncovered evidence of systematic manipulation of the publication and peer-review process. We cannot, therefore, vouch for the reliability or integrity of this article.

Please note that this notice is intended solely to alert readers that the peer-review process of this article has been compromised.

Wiley and Hindawi regret that the usual quality checks did not identify these issues before publication and have since put additional measures in place to safeguard research integrity.

We wish to credit our Research Integrity and Research Publishing teams and anonymous and named external researchers and research integrity experts for contributing to this investigation.

The corresponding author, as the representative of all authors, has been given the opportunity to register their agreement or disagreement to this retraction. We have kept a record of any response received.

References

- [1] P. Sivaprakasam, A. Kirubel, G. Elias, P. Maheandera Prabu, and P. Balasubramani, "Mathematical Modeling and Analysis of Wear Behavior of AlTiN Coating on Titanium Alloy (Ti-6Al-4V)," *Advances in Materials Science and Engineering*, vol. 2021, Article ID 1098605, 9 pages, 2021.

Research Article

Mathematical Modeling and Analysis of Wear Behavior of AlTiN Coating on Titanium Alloy (Ti-6Al-4V)

P. Sivaprakasam ¹, A. Kirubel ¹, G. Elias ¹, P. Maheandera Prabu ²,
and P. Balasubramani ³

¹Department of Mechanical Engineering, College of Electrical and Mechanical Engineering, Center of Excellence-Nano Technology, Addis Ababa Science and Technology University, Addis Ababa, Ethiopia

²Department of Ocean Engineering, Indian Institute of Technology Madras, Chennai, Tamil Nadu, India

³Department of Mechanical Engineering, Sona College of Technology, Salem, India

Correspondence should be addressed to P. Sivaprakasam; shiva@aastu.edu.et

Received 29 May 2021; Revised 12 June 2021; Accepted 22 June 2021; Published 30 June 2021

Academic Editor: Samson Jerold Samuel Chelladurai

Copyright © 2021 P. Sivaprakasam et al. This is an open access article distributed under the Creative Commons Attribution License, which permits unrestricted use, distribution, and reproduction in any medium, provided the original work is properly cited.

In this study, the wear behavior of a physical vapor deposition (PVD) AlTiN coated on the titanium alloy was investigated. Response surface methodology (RSM) was used to analyze input factors, such as load (A), sliding speed (B), and sliding distance (C), while wear mass loss (WML) and coefficient of friction (COF) were considered as the response parameters. The statistical analysis shows that main factors, that is, interaction of AC and pure quadratic terms B^2 and C^2 , have maximum influences on WML. However, COF was highly affected by load, sliding speed, and interaction of AB and quadratic term A^2 . The present work attempts to carry out empirical modeling to predict output response on WML and COF. Desirability-based optimization technique was employed to obtain minimum WML and COF. Microscopy images of the wear tracks reveal visible grooves and scratches that confirm abrasive wear to be the primary wear mechanism accompanied by adhesive wear. The investigation concluded that AlTiN has better wear resistance properties and can be used to coat titanium implants for biomedical application. The result shows that the minimum WML and COF have been found at applied load 15 N, sliding speed at 0.5 m/s, and sliding distance 500 m.

1. Introduction

Surface engineering is enabling technology that meets the expectations of modern science, energy, material properties, and environmental friendliness. The technology allows for the altering of materials surfaces to have enhanced properties [1]. PVD technique is a vaporization coating method that involves transforming the coating material into the gaseous phase by using resistive heating, electron beam, etc., to deposit on the surface of the substrate [2, 3]. Many studies have considered different coating techniques for clinical purposes. PVD, CVD, sol-gel coating, and self-assembly are some of the deposition methods for biomedical applications [2–5]. However, PVD has become widely used on various medical devices, including surgical tools, orthopedic

implants, pacemakers, and orthodontic appliances, to deposit wear-resistant single or multilayer coatings. PVD's importance is focused on its ability to change a device's surface features unaffected the underlying material's properties or biomechanical functionality. Chen and Thouas [6] highlighted that lower modulus and high corrosion resistance characteristics of Ti-alloy make the material have superior biocompatibility property than stainless steel cobalt alloys. The advantage in elemental composition similarity is taken between Ti-6Al-4V substrate and TiN coating, where diffusion or adhesion property is expected to occur between materials to yield improved sliding wear resistance [7]. AlTiN films are suitable as ideal wear-resistant coatings because of their higher strength, low coefficient of friction, and chemical inertness [8]. Szala et al. [9] investigated the

sliding wear mechanism of AlTiN (PVD) coated stainless steel substrate (grade AISI 304). The results showed that AlTiN-coated samples exhibited 24 times sliding wear resistance and two times decrease in friction coefficient than the uncoated substrates. Furthermore, it was observed that grooving, microscratching, microploving, and smearing were the main types of sliding wear mechanisms.

In the aircraft sector, titanium alloys are utilized for landing systems, fasteners, engine components, airframes, and other applications. The Ti-6Al-4V alloy stands out among these alloys because of its high strength-to-weight ratio, corrosion resistance, and low density [10]. Ti and Ti alloys are lightweight and have improved biocompatibility and corrosion resistance, making them popular in medical and dental applications [11]. Protecting Ti-6Al-4V substrates with PVD coatings has been shown to improve mechanical characteristics, biocompatibility, osseointegration, wear, and corrosion resistance [12].

Biomedical areas use metallic biomaterials such as stainless steels (SS 316L), cobalt-based alloys, commercially pure titanium and its alloy, Sn alloys, and Au-based materials for different purposes [4]. Titanium alloys are the most attractive biomedical metallic material under static conditions; it is more corrosion-resistant. These materials are subject to intrinsic limitations when dynamic conditions such as fretting, wear, fatigue, and chemical corrosion [7]. Generally, these alloys have a reputation for poor tribological characteristics, and they are restricted for further uses in their tribological applications. In general, as stated in the literature mentioned above, the significance of an AlTiN coating on titanium alloys is rarely mentioned. The applied force, temperature, and oxidation, all associated with the sliding contact mechanism, regulate coated surfaces' friction and wear behavior. Particularly, load, sliding velocity, and distance have a significant impact on wear behavior. Therefore, the research concentrated on the wear properties of titanium alloys coated with AlTiN.

2. Materials and Methods

2.1. Materials. Titanium alloy (Ti-6Al-4V) is used for this investigation. The cylindrical bar is cut into 20 specimens using WEDM. The specimens were mechanically grained and polished according to required standards (\varnothing 50 mm and 10 mm thickness). AlTiN is deposited using an arc evaporation technique (Oerlikon Balzers coating system, India) with an approximate deposition thickness of 2 μ m. The EN31 steel pin (6 mm diameter and length 35 mm) materials were used against the AlTiN-coated titanium alloy disc.

2.2. Response Surface Methodology (RSM). RSM is the most popular method for designing an experiment for engineering problems and predicting and optimizing a given model on surface roughness [13, 14]. RSM [15] is the best tool for analyzing the impact of factors and their interaction on the response. Table 1 shows the input variables with levels taken into account for wear studies. The input factors and levels selected based on the tribometer range and relevant literature [14]. The wear tests were carried out using face center cubic design (RSM) at random fashion as shown in Table 2.

2.3. Sliding Wear Test. For the sliding wear test, an American Society for Testing Materials (ASTM) G99 guideline is followed. A pin on disc (DUCOM) tribometer is used to test the coated substrate material's sliding wear and friction behavior (Figure 1). The experiment is conducted at ambient temperature and humidity under dry sliding conditions. The pin on the disc tribometer consists of a stationary pin prepared of EN31 steel, which is harder than the coating material, held vertically and pressed with a specific load against a rotary sample. Figures 2(a)–2(c) show the test samples for uncoated, coated with AlTiN and wear test, respectively. The test was performed based on the design of experiments using RSM. The wear mass loss was calculated by analytical balance (0.0001 g least count) before and after wear tests. Acetone is used for cleaning the surface of the disc and pin. COF is calculated by frictional force/applied force.

3. Results and Discussion

3.1. Statistical Analysis. The statistical analysis is applied to analyzing the responses as per input factor combinations, coefficients estimation, and model adequacy checking and predicting the responses [14]. The factors considered for the study were load, sliding speed, and sliding distance. The WML and COF were taken as response parameters. The face-centered cubic design was employed using Design Expert software. The experimental results of the wear test coated on titanium alloy were presented in Table [2].

3.1.1. Mathematical Models for WML and COF. The input trials developed the mathematical models for WML and COF. Wear mass loss (Y_{WML}) and COF (Y_{COF}) are represented using quadratic equations, as shown in (1) and (2), respectively. WML and COF predictions are based on the mathematical models with a coding unit as given in equation [1, 2].

Model equation of WML:

$$Y_{WML} = 49.11 + 18.90 \times A + 3.10 \times B + 17.50 \times C + 12.37 \times AC + 7.44 \times B^2 - 7.56 \times C^2. \quad (1)$$

Model equation of COF:

TABLE 1: Wear test factors and their levels.

Factors	Levels		
	Level 1	Level 2	Level 3
A: load (N)	15	30	45
B: sliding speed (m/s)	0.5	1	1.5
C: sliding distance (m)	500	1000	1500

TABLE 2: Experimental results of wear test.

S. No.	Input factors			Responses	
	Load N	Sliding speed m/s	Sliding distance m	WML mg	COF
1	30	1	1000	55	0.4041
2	15	0.5	500	24	0.2247
3	30	1	1500	56	0.3925
4	30	0.5	1000	49	0.4198
5	45	0.5	500	35	0.3864
6	45	1.5	1500	100	0.2523
7	30	1.5	1000	63	0.4223
8	30	1	1000	49	0.4205
9	15	1.5	1500	40	0.4414
10	30	1	1000	46	0.4131
11	45	1	1000	68	0.3105
12	45	0.5	1500	96	0.3879
13	15	0.5	1500	33	0.2483
14	30	1	1000	52	0.4239
15	45	1.5	500	39	0.2463
16	15	1	1000	26	0.3304
17	15	1.5	500	26	0.449
18	30	1	1000	48	0.4212
19	30	1	500	26	0.4132
20	30	1	1000	50	0.4115

$$Y_{\text{COF}} = 0.41 - 0.011 \times A + 0.014 \times B - 0.087 \times AB - 0.086 \times A^2. \quad (2)$$

The applied load (A), sliding speed (B), sliding distance (C), the interaction of A and C , and pure quadratic terms B^2 and C^2 have the greatest influence on WML; according to the quadratic equation for WML (equation (1)), applied load (A), sliding speed (B), the interaction of A and C , and pure quadratic term A^2 have foremost influences on COF (equation (2)).

3.1.2. Model Adequacy Testing. The following graphical analysis was used to validate the adequacy of the model. Figures 3 and 4 show the residual plot for WML and COF. The residuals fall in a straight line in the normal probability plot for the WML and COF (Figures 3(a) and 4(a)), which clearly shows the errors are normally distributed, and no outliers are presented. The residuals are dispersed, suggesting that they are independent, as shown in Figures 3(b) and 4(b). There is no peculiar structure in Figures 3(c) and 4(c), indicating that the model is correct. The model adequacy test results confirm that the experimental and predicted values well fit each other. The R^2 and R^2 (adj) values for WML are 0.9836 and 0.9761 and those for COF are 0.9829 and 0.9783, respectively. The R^2 values agree with R^2

(adj) values, indicating that model data fit with experimental values. In both models, both R^2 and R^2 (adj) values are above 95%, which allows the model to fit the prediction of the solution.

3.2. Analysis of Wear Mass Loss. ANOVA analysis is used to evaluate input factors on WML. The ANOVA for WML simplified model is shown in Table 3. The P values indicate the confidence level, which is less than 0.05. It shows that the model has more than a 95% confidence interval. The coefficient of determination (R^2) value of the WML model is 0.9836. Hence, the developed model is acceptable, and the predicted values fit the measured results. Insignificant factors are eliminated from the full quadratic model by the backward elimination process. Minimum mass loss is desirable since it indicates less wear amount. The minimum WML was found at 15 N, 0.5 m/sec, and 500 m.

WML has been increased while the load and sliding distance has been increased. The higher wear mass loss occurred at a high level of load and sliding distance. From Figures 5 and 6, AlTiN-coated surface are deforms marginally when subjected to a 15 N load. As the load and sliding



FIGURE 1: Pin-on-disc tribometer.

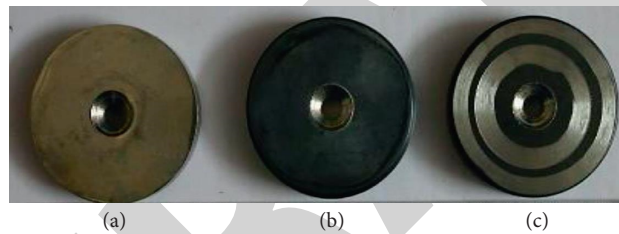


FIGURE 2: Titanium alloy test samples. (a) Uncoated. (b) Coated. (c) Wear test.

distance increase, the abrasive wear increases, resulting in greater wear mass loss. Asperities compress between the sliding surfaces, resulting in a blunt surface and increased contact area, leads to higher wear mass loss as the sliding distance increases.

The sliding speed has less influence on wear mass loss. The experimental observation shows that the maximum wear mass loss recorded was 100 mg. Fan et al. [16] can also support these results, where the adhesive strength of PVD (arc ion implant) coated AlTiN was found to be 39.7 N, which is lower than the load applied in this study. This clearly explains the significant effect of the applied load on WML. Figures 5 and 6 show the interactive effect of load and sliding distance on WML. From the figures, when applied load increases, mass loss tends to increase. Similarly, mass loss also increases as sliding distance increases.

3.3. Analysis of Coefficient of Friction. ANOVA Table 4 for COF shows that load and sliding speed and its interaction influence the response. It is evident that an increase in sliding speed results in a linear increase in COF, while an increase in applied load results in a parabolic (progressive) increment in COF (Figures 7 and 8). This phenomenon was also observed by Yousfi [17], where it was assumed that it is the cause of COF instability. In addition, a recent study by

Bahi et al. [12] showed that the COF for TiN/TiO₂ multilayer coating of Ti-6Al-4V substrate to be unstable COF as sliding distance increases. From Figure 7, it can be understood that there is a tendency for COF to decrease as load increases. The COF decreases as load increases, and related findings were observed by Dejun et al. [18]. Slight variation in COF was observed, which attributes to the galling effect [17] and an increase in the sliding distance [12]. This also confirms that AlTiN was an excellent choice of material for a substrate subjected to increased load under dry conditions.

The coefficient of friction is expected to increase as load increases between sliding surfaces, particularly between materials of high hardness. Lattice constraint is minimized due to the solid solution hardening of aluminum which attributes to the property of improved hardness of AlTiN coatings [3]. Adhesion strength is the energy required to separate a coating from its substrate. The addition of Al in TiN hard-facing improved resistance to elastic deformation. Furthermore, according to the literature [19, 20], the hardness to elastic modulus (H/E) values are also used to indicate wear initiation. Resistance to abrasion and higher hardness and resistance to elastic deformation are exhibited when H/E values are high. With a higher load, the rate of forming the tribo-layer will be faster as the temperature in the contact area rises, causing plastic deformation on the surface; thus, the coefficient of friction will decrease [21, 22].

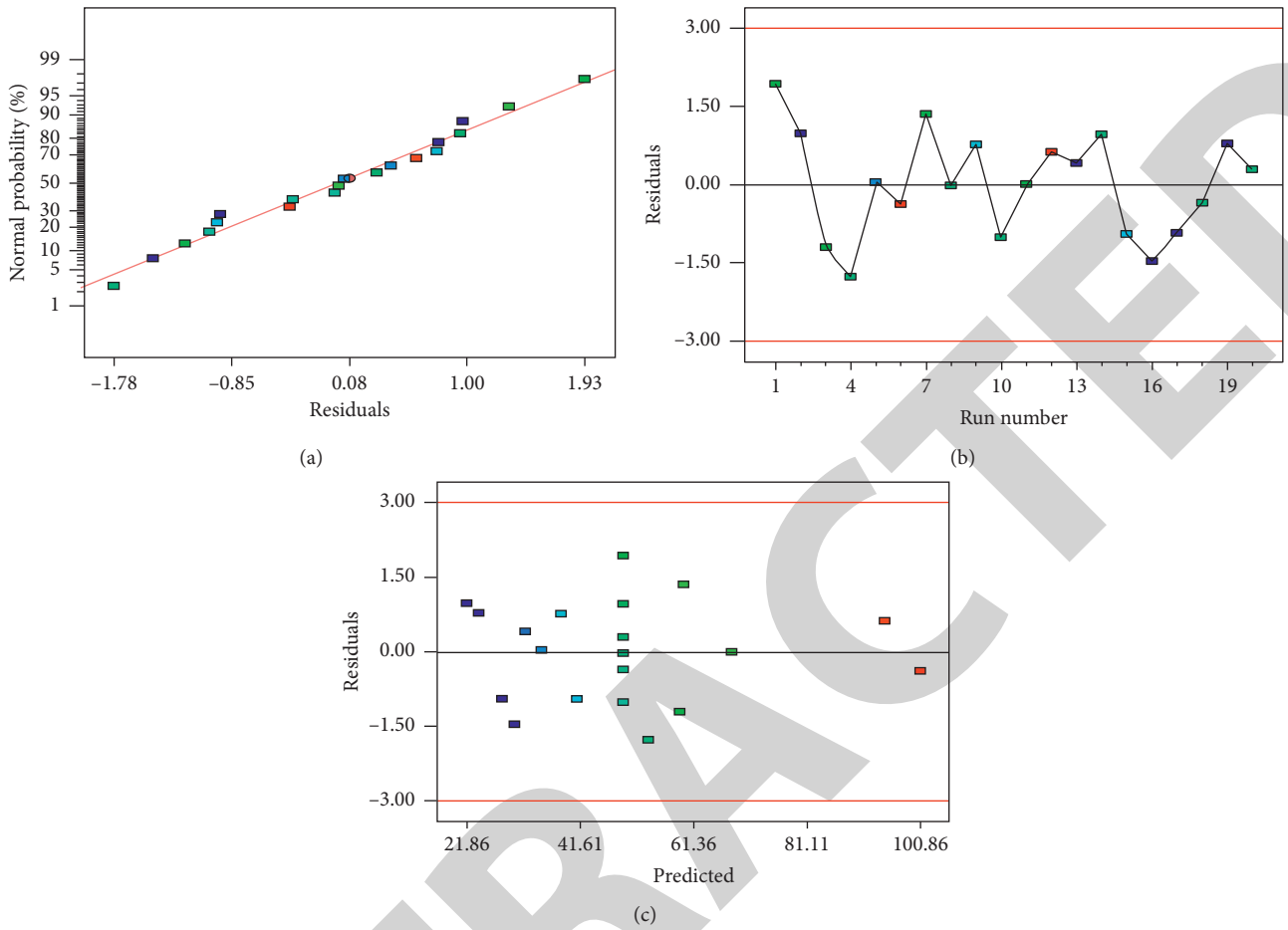


FIGURE 3: Residual plot for WML. (a) Normal probability plot. (b) Residuals versus run number. (c) Residuals versus predicted values.

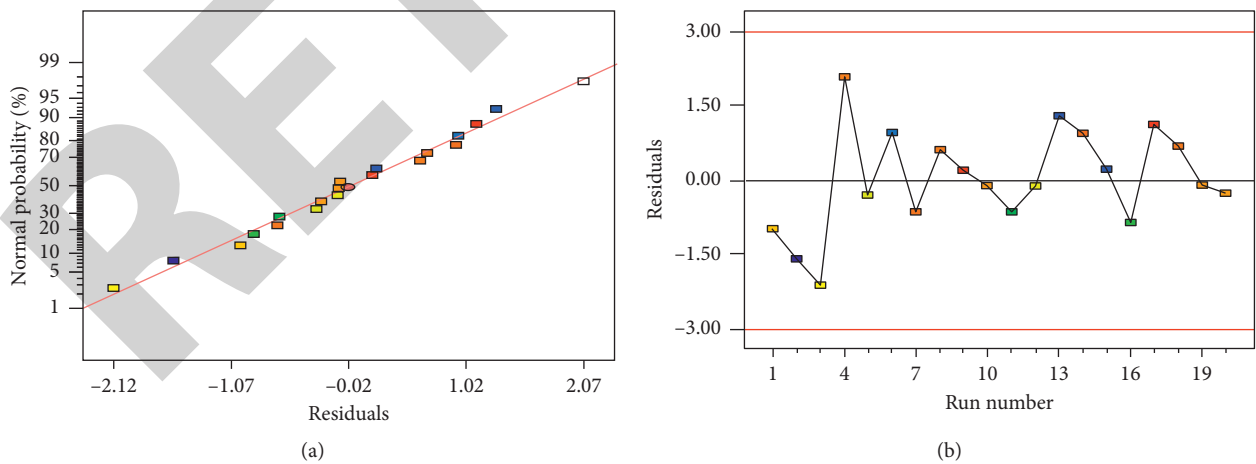
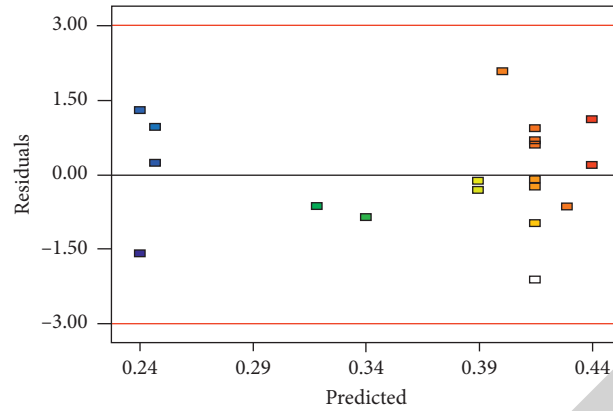


FIGURE 4: Continued.



(c)

FIGURE 4: Residual plot for COF (a) Normal probability plot. (b) Residual versus run number. (c) Residuals versus predicted values.

TABLE 3: ANOVA for WML.

Source	Sum of square	Degree of freedom	Mean square	F value	p value prob > F	
Model	8180.888	6	1363.481	130.2729	<0.0001	Significant
A	3572.1	1	3572.1	341.2939	<0.0001	
B	96.1	1	96.1	9.18181	0.0097	
C	3062.5	1	3062.5	292.6045	<0.0001	
AC	1225.125	1	1225.125	117.0537	<0.0001	
B ²	177.0125	1	177.0125	16.91254	0.0012	
C ²	183.0125	1	183.0125	17.48581	0.0011	
Residual	136.0625	13	10.46635			
Lack of fit	86.0625	8	10.75781	1.075781	0.4905	
Pure error	50	5	10			
Cor total	8316.95	19				

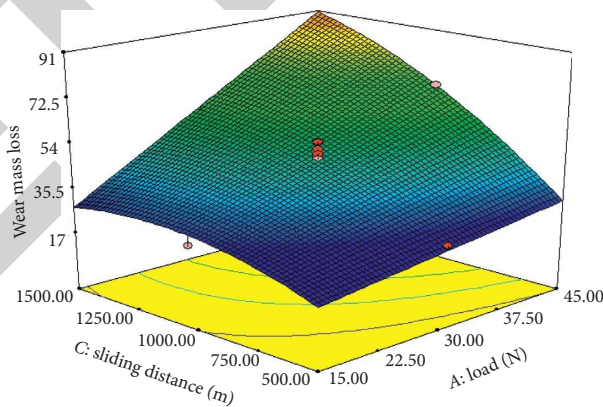


FIGURE 5: 3D surface plot of WML.

The main wear mechanism of AlTiN coating for abrasion wear is seen when microscopy pictures have been analyzed. Abrasive and adhesive wear mechanisms were observed in Figure 9, based on the direction of wear. It might be inferred that the primary wear mechanism of AlTiN coating is abrasive wear accompanied by adhesive wear. Also, the wear track contains more groves and scratches.

The desirability-based optimization technique was employed for finding the optimal combination for the wear

test [14]. The objective function for the wear test is minimum wear mass loss and minimum COF. The optimal conditions for the wear test were load at 15 N, sliding speed at 0.5 m/s, and sliding distance at 500 m.

The test results are validated based on the optimal processing parameters through a confirmation test. With a desirability value of 0.971, the optimal combinations for lower wear mass loss and COF are 15 N applied load, 0.5 m/s sliding speed, and 500 m sliding distance (Table 5). Table 5

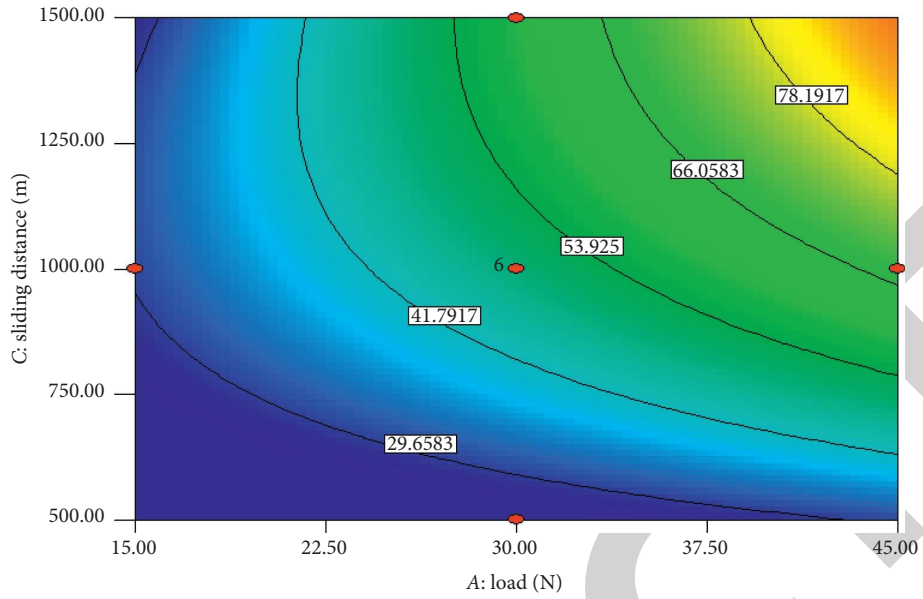


FIGURE 6: Contour plot-WML.

TABLE 4: ANOVA for COF.

Source	Sum of square	Degree of freedom	Mean square	F value	p value prob > F	
Model	0.100749	4	0.025187	215.370	<0.0001	Significant
A	0.001219	1	0.001219	10.4217	0.0056	
B	0.002079	1	0.002079	17.7801	0.0007	
AB	0.060048	1	0.060048	513.4588	<0.0001	
A ²	0.037403	1	0.037403	319.82	<0.0001	
Residual	0.001754	15	0.000117			
Lack of fit	0.001475	10	0.000147	2.6382	0.1479	
Pure error	0.000279	5	5.59×10^{-05}			
Cor total	0.102503	19				

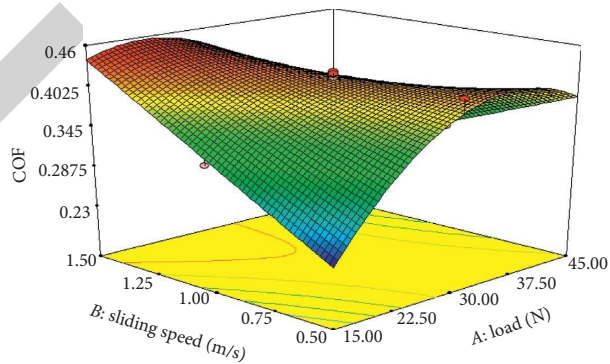


FIGURE 7: 3D surface plot of COF.

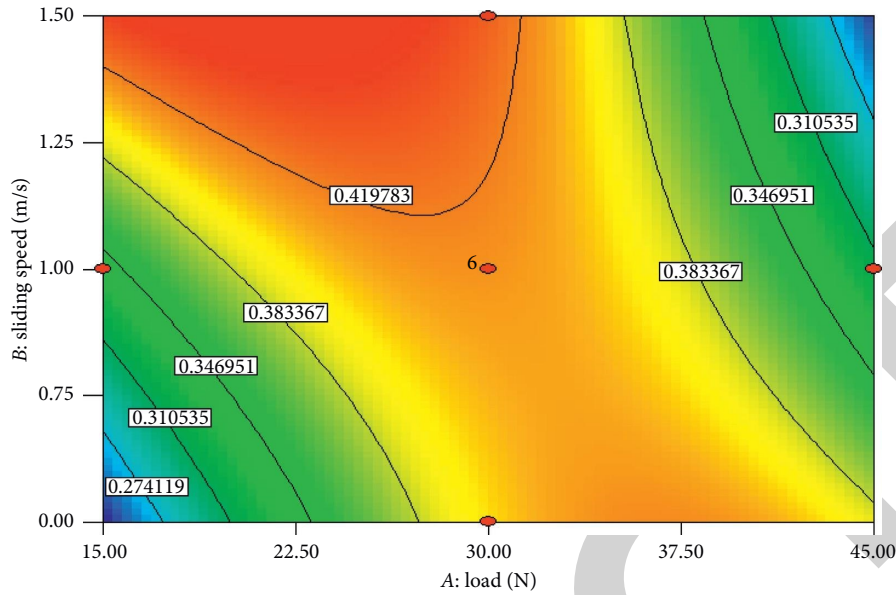


FIGURE 8: Contour plot of COF.

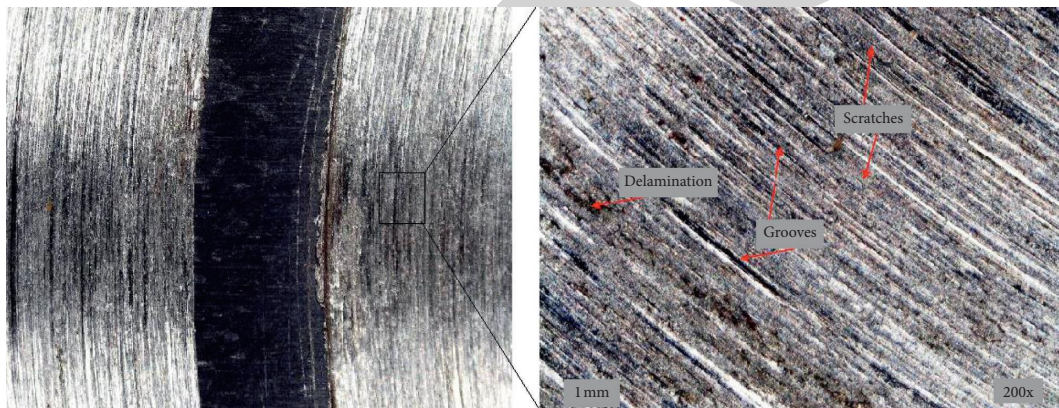


FIGURE 9: Microscope images of wear tracks.

TABLE 5: Optimum conditions for sliding parameter of AlTiN-coated titanium alloy.

Response	Goal	Desirability	A	B	C	Predicted value	Experimental value
WML	Minimum	0.971	15	0.5	500	21.934	23.00
COF	Minimum	0.971	15	0.5	500	0.2377	0.2320

shows that, at 95% confidence intervals, the predicted and test values are in good agreement.

4. Conclusion

The tribological behavior of AlTiN-coated titanium alloy against EN-31 was examined under room temperature and dry sliding conditions. The scientific results are summarized as follows.

ANOVA was performed to determine the significance of AlTiN-coated titanium alloy tribology behavior. The statistical analysis shows that applied load (A), sliding speed (B), sliding

distance (C), the interaction of A and C, and pure quadratic terms B^2 and C^2 have maximum influences on WML.

Applied load (A), sliding speed (B), the interaction of A and B, and pure quadratic term A^2 have maximum influences on COF.

The higher wear mass loss 100 g could be found at 45 N applied load, 1.5 m/s sliding speed, and 1500 m sliding distance.

Desirability-based optimization techniques were employed for the sliding wear behavior of AlTiN-coated titanium alloy. The result shows that the minimum WML and COF have been found at applied load 15 N, sliding speed at 0.5 m/s, and sliding distance 500 m.

Retraction

Retracted: Effect of Manganese Ions on Spectroscopic and Insulating Properties of Aluminophosphate Glasses

Advances in Materials Science and Engineering

Received 26 December 2023; Accepted 26 December 2023; Published 29 December 2023

Copyright © 2023 Advances in Materials Science and Engineering. This is an open access article distributed under the Creative Commons Attribution License, which permits unrestricted use, distribution, and reproduction in any medium, provided the original work is properly cited.

This article has been retracted by Hindawi, as publisher, following an investigation undertaken by the publisher [1]. This investigation has uncovered evidence of systematic manipulation of the publication and peer-review process. We cannot, therefore, vouch for the reliability or integrity of this article.

Please note that this notice is intended solely to alert readers that the peer-review process of this article has been compromised.

Wiley and Hindawi regret that the usual quality checks did not identify these issues before publication and have since put additional measures in place to safeguard research integrity.

We wish to credit our Research Integrity and Research Publishing teams and anonymous and named external researchers and research integrity experts for contributing to this investigation.

The corresponding author, as the representative of all authors, has been given the opportunity to register their agreement or disagreement to this retraction. We have kept a record of any response received.

References

- [1] B. Kassa, J. Leta Tesfaye, B. Bulcha et al., "Effect of Manganese Ions on Spectroscopic and Insulating Properties of Aluminophosphate Glasses," *Advances in Materials Science and Engineering*, vol. 2021, Article ID 6253069, 11 pages, 2021.

Research Article

Effect of Manganese Ions on Spectroscopic and Insulating Properties of Aluminophosphate Glasses

B. Kassa,¹ J. Leta Tesfaye,^{1,2} B. Bulcha,¹ R. Kiran,³ T. Deepak,⁴ Dayanand Lal,⁵ S. Venkatesh,⁶ and R. Krishnaraj^{ID 2,7}

¹Physics Department, College of Natural and Computational Science, Dambi Dollo University, Dembi Dollo, Ethiopia

²Centre for Excellence, Indigenous Knowledge, Innovative Technology Transfer and Entrepreneurship, Dambi Dollo University, Dembi Dollo, Ethiopia

³Electrical and Computer Engineering, Dambi Dollo University, Dembi Dollo, Ethiopia

⁴Department of Accounting and Finance, Dambi Dollo University, Dembi Dollo, Ethiopia

⁵Department of Computer Science and Engineering, GITAM University, Bangalore, India

⁶Mechanical Engineering, National Institute of Technology, Tiruchirappalli, India

⁷Department of Mechanical Engineering, Dambi Dollo University, Dembi Dollo, Ethiopia

Correspondence should be addressed to R. Krishnaraj; prof.dr.krishnaraj@dadu.edu.et

Received 18 May 2021; Revised 7 June 2021; Accepted 22 June 2021; Published 29 June 2021

Academic Editor: Samson Jerold Samuel Chelladurai

Copyright © 2021 B. Kassa et al. This is an open access article distributed under the Creative Commons Attribution License, which permits unrestricted use, distribution, and reproduction in any medium, provided the original work is properly cited.

The melt-quenching technique was used to produce $39\text{CdO}-10\text{Al}_2\text{O}_3-(51-x)\text{P}_2\text{O}_5: x\text{MnO}$ glasses ($x = 0, 0.1, 0.2, 0.3,$ and 0.4 wt.%). Various stability factors were calculated and presented from DTA analysis. The stability of the glass network appears to increase with the increase of MnO concentration, according to the findings. IR spectral analysis of these glasses exhibited several symmetrical and asymmetrical bands due to phosphate groups. The observed change in these band intensities with the rise in MnO concentrations, ranging from 0.1 wt.% to 0.4 wt.%, shows an increase in the stability of the glass network. Optical absorption analyses of these glasses revealed an absorption band that shifted from 500 to 488 nm as the concentration of manganese oxide (MnO) increased from 0.1 wt.% to 0.4 wt.%, indicating that Mn^{2+} ions were gradually converted into Mn^{3+} ions. EPR spectra of these glasses were characterized by two signals due to Mn^{2+} and Mn^{3+} ions. Observations on these signal intensity variations revealed an increase in stability of the glass network with the increase of MnO concentration from 0.1 wt.% to 0.4 wt.%. Parameters, which describe the insulating characteristics, for example, dielectric constant, ϵ , dielectric loss, $\tan \delta$, and AC conductivity σ_{ac} , were determined in relation to frequency (10^3 Hz to 10^5 Hz) and temperature (20°C to 400°C) and presented in the dielectric analysis of these glasses.

1. Introduction

The dielectric constant, loss $\tan \delta$, and AC conductivity, as well as the dielectric breakdown strength of the glasses, are used to determine their insulating character and understand the structural features over such a wide frequency and temperature range [1]. In recent years, a number of studies have investigated a number of inorganic glasses under this way, resulting in useful information [1–3].

Phosphate glasses may be used for a variety of uses, including bone transplantation, hazardous waste

containment, high electron conductors, laser host components, low-temperature seals, metallic seal materials, bio-glasses, diametric purposes, and solid state electrolytes, among others [4–7]. They have significant physical properties, such as a low melting temperature, high heat transfer coefficient, high ultraviolet transmission, lower glass transition temperature, minimum softening temperature, high ionic conductivity, and biocompatibility [8]. Addition of Al_2O_3 to phosphate glasses improves their chemical durability and modifies their physical properties for more commercial applications [9, 10].

Transition metals-doped glasses have interesting optical, luminescent, semiconducting, memorizing, and photo-conducting properties [11, 12]. Manganese ion is an intriguing transition metal ion although it can be present in a number between valence states (Mn^{3+} and Mn^{2+}) of different glass matrices [13]. The quantitative characteristics of modifiers and glass formers, size of both ions in the glass structure, field strength, and mobility of the modifier cation, among some other factors, determine the amount of manganese contained in the glass in different forms and valence states [14]. Mn^{2+} has an electronic configuration of 3d5, which corresponds to a half-filled d shell. The impact of manganese on the thermal, physical, structural, and optical properties of glasses has been the subject of numerous studies [15, 16]. Moreover, manganese ions are well known to have a significant impact on the electric, magnetic, and optical properties of glasses; there seem to be numerous important studies on manganese ions' environment in different inorganic glass systems available [17].

The main objective of this paper is to integrate manganese ions and their impact on structural integrity (namely, different band positions ranges between 487 and 1215 cm^{-1} ; optical band gap energy) and insulating character of CdO- Al_2O_3 - P_2O_5 : MnO glasses through a thorough investigation of dielectric constant ϵ^1 , loss $\tan \delta$, and AC conductivity σ_{ac} within the spectrum of frequency 10^3 Hz to 10^5 Hz as well as within the temperature range 20–400°C.

2. Experimental Works

Glasses with compositions 39CdO-10 Al_2O_3 -(51-x) P_2O_5 : xMnO (0–0.4 mol %) were made using the traditional melt quenching techniques, and the samples were labeled as CAPM_0: 39CdO-10 Al_2O_3 -51 P_2O_5 , CAPM_1: 39CdO-10 Al_2O_3 -50.9 P_2O_5 : 0.1 MnO, CAPM_2: 39CdO-10 Al_2O_3 -50.8 P_2O_5 : 0.2 MnO, CAPM_3: 39CdO-10 Al_2O_3 -50.7 P_2O_5 : 0.3 MnO, and CAPM_4: 39CdO-10 Al_2O_3 -50.6 P_2O_5 : 0.4 MnO, respectively. Subsequently, the glasses were made using a technique called rapid melt quench, by which the amorphous solid is formed during the melt-quenching process through the gradual toughening (i.e., rise in viscosity) of a melt.

In this experiment, the glasses were made using the melt-quenching method. The starting materials CdO, Al_2O_3 , P_2O_5 , and MnO that were used in the making of the present glass systems were of analar grade (greater than 99.9% purity). After polishing, the final glasses' measurements were 1.0 cm \times 1.0 cm \times 2.0 cm. For this dielectric analysis, various parameters, namely, dielectric constant δ , dielectric loss $\tan \delta$, and AC conductivity δ_{ac} , were investigated over a broad temperature spectrum and also as a function of wavelength. All these parameters, which were used in this analysis, were measured using LCR Meter (Hewlett-Packard Model-4263B).

3. Results and Discussion

3.1. Results. From the measured values of density d , average molecular weight \bar{M} , and refractive index n_d of CdO- Al_2O_3 - P_2O_5 : MnO glasses, various other physical parameters, such

as manganese ion concentration N_i , mean manganese ion separation R_i , polaron radius R_p , molar volume V_M , electron polarizability α_e , reflection loss R , and molar refractivity R_M , were calculated and presented in Table 1.

The dopant ion concentration (N_i) could be obtained from

$$N_i \left(\frac{\text{ions}}{\text{cm}^3} \right) = N_A M (\text{mol } \%) \frac{d}{\bar{M}} \quad (1)$$

The calculated values of N_i , the interionic distance r_i and polaron radius r_p of dopant ions can be evaluated by the following equations [17]:

$$\text{interionic distance } r_i (\text{\AA}) = \left(\frac{1}{N_i} \right)^{(1/3)}, \quad (2)$$

$$\text{polaron radius } r_i (\text{\AA}) = \frac{1}{2} \left(\frac{\pi}{6N_i} \right)^{(1/3)}.$$

Using the refractive index of the glass, the theoretical dielectric constant (ϵ) was determined:

$$\epsilon = n_d^2. \quad (3)$$

The Fresnel formula was used to calculate the reflection loss from the glass surface based on the refractive index:

$$R = \left[\frac{(n_d - 1)}{(n_d + 1)} \right]^2. \quad (4)$$

The following formula was used to calculate the molar refractivity R_M for each glass:

$$R_M = \left[\frac{(n_d - 1)}{(n_d + 2)} \right] V_m. \quad (5)$$

The following formula was used to measure the molar volume of the glass samples:

$$V_m = \frac{\bar{M}}{d}. \quad (6)$$

Using the following formula, the electronic polarizability α_e was determined:

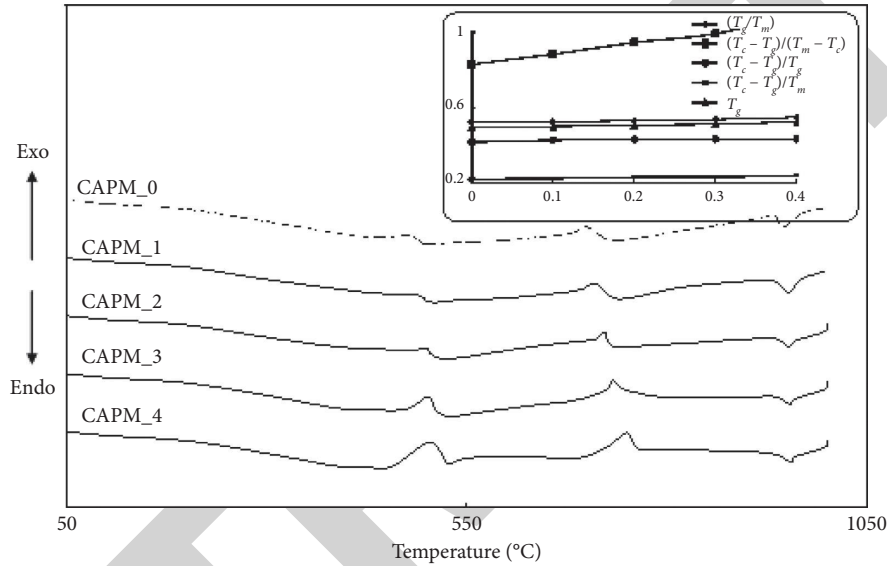
$$\alpha_e = \frac{3(n_d^2 - 1)}{4\pi N_i (n_d^2 + 2)}. \quad (7)$$

The number of manganese ions per unit volume is given by the symbol N_i .

3.1.1. Differential Thermal Analysis (DTA). As shown in Figure 1, the glass transition temperature T_g , which is between 492 and 523°C, causes an inflection in the spectra and differential thermal analysis (DTA) traces of pure and MnO-doped CdO- Al_2O_3 - P_2O_5 , through which glasses were observed at temperatures ranging from 30 to 1000°C. The crystallization temperature T_c at 698°C to 750°C causes a well-defined exothermic effect, which is accompanied by a well-defined endothermic effect, and melting temperature

TABLE 1: Different physical characteristics of CdO-Al₂O₃-P₂O₅: MnO glasses.

Physical parameters	CAPM_0	CAPM_1	CAPM_2	CAPM_3	CAPM_4
Molecular mass on average, \bar{M}	125.481	125.418	125.368	125.351	125.312
Density, d (g/cm ³)	5.351	5.360	5.362	5.371	5.382
Molar volume, V_M	23.449	23.398	23.379	23.338	23.283
Refractive index, n_d	1.553	1.572	1.605	1.643	1.692
Manganese ion concentration, N_i ($\times 10^{19}$ ion/cm ³)	—	0.672	1.345	2.017	2.691
Interionic distance, R_i (Å)	—	1.141	0.905	0.791	0.718
Polaron radius, R_p (Å)	—	0.352	0.444	0.509	0.560
Electron polarizability, α_e ($\times 10^{-19}$ ion/cm ³)	—	0.117	0.061	0.043	0.034
Dielectric constant, ϵ	2.402	2.464	2.560	2.689	2.856
Reflection loss, R	0.046	0.049	0.053	0.058	0.065
Molar refractivity, R_M	3.601	3.721	3.892	4.083	4.332

FIGURE 1: DTA traces of CdO-Al₂O₃-P₂O₅: MnO glasses. Inset shows the variation of T_g/T_m , K_{g1} , $(T_c - T_g)/T_g$, $(T_c - T_g)/T_m$, and T_g with MnO concentration.

T_m due to the endothermic effect in the range of 945°C to 956°C. Based on the observed values of T_g , T_c , and T_m , various stability factors of glasses, namely, T_g/T_m , $(T_c - T_g)/T_g$, and $(T_c - T_g)/T_m$ and the glass forming capacity parameter, which was developed by Hruby, $K_{g1} = (T_c - T_g)/(T_m - T_c)$, were calculated and are presented in Table 2.

The difference of various stability parameters, T_g/T_m , $(T_c - T_g)/T_g$, $(T_c - T_g)/T_m$, and K_{g1} , with MnO concentration is depicted in the inset of Figure 1. These curves display a growing trend in the stability factors in MnO concentrations increasing from 0.1 wt.% to 0.4 wt.%, implying that the glass network becomes more stable as MnO concentration rises.

3.1.2. IR Studies. Figure 2(a) represents the room temperature recordings of pure infrared spectra and manganese oxide-doped CdO-Al₂O₃-P₂O₅ glasses. Different IR bands corresponding to phosphate and aluminate structural groups appear in the glass matrix as the concentration of manganese oxide increases. Table 3 shows the data on different band positions from the IR spectra of these glasses.

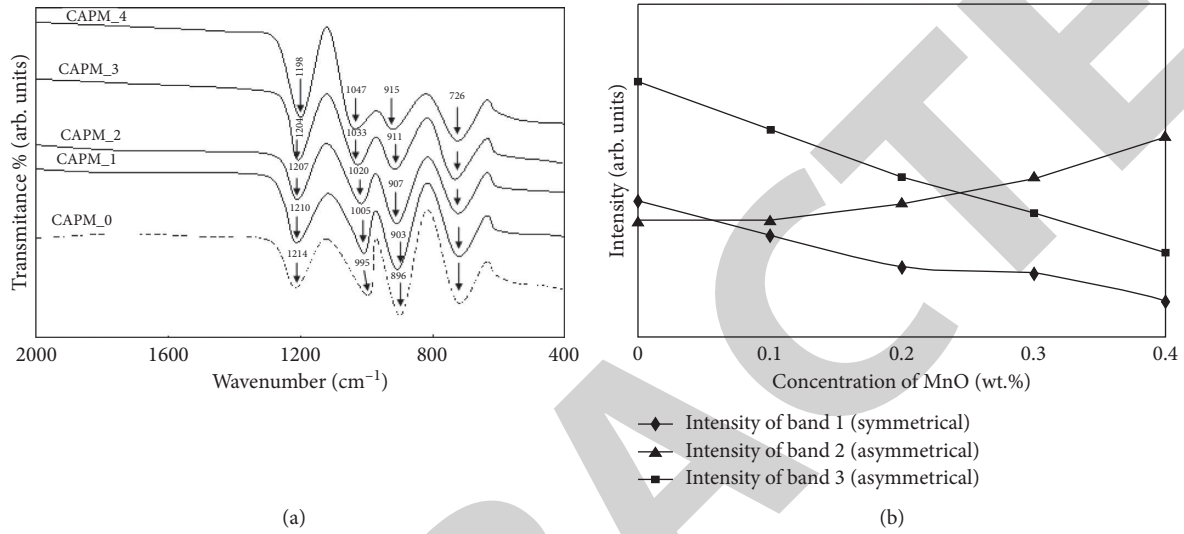
For this specific network of glasses, the infrared transmission spectra were recorded for glasses as shown in Figure 3, and the conventional bands were caused due to the following:

- (i) The O-P-O symmetric stretching vibrations in the range of 1198–1214 cm⁻¹ (band 1)
- (ii) The asymmetrical stretching of PO₄³⁻ groups in the region between 995 cm⁻¹ and 1047 cm⁻¹ (band 2)
- (iii) The asymmetrical bending vibrations of P-O-P groups in the range of 896–915 cm⁻¹ (band 3)
- (iv) The vibrations of AlO₄ groups in the region between 700 cm⁻¹ and 750 cm⁻¹

The frequency of the band 1 (symmetrical band) changes towards lower frequency as the MnO concentration in the glass matrix increases from 0.1 wt.% to 0.4 wt.%, according to the IR-Spectra. Bands 2 and 3 (symmetrical bands) change towards higher frequency as strength decreases, suggesting a decrease in asymmetric stretching and increase in symmetrical stretching in phosphate units, indicating increased polymerization/stability of the glass network. In the presence

TABLE 2: Data on DTA analysis of CdO-Al₂O₃-P₂O₅: MnO glasses.

Glasses	T_g (°C)	T_c (°C)	T_m (°C)	T_g/T_m	$(T_c - T_g)/(T_m - T_c)$	$(T_c - T_g)/T_g$	$(T_c - T_g)/T_m$
CAPM_0	493.0	698.0	945.0	0.5216	0.829	0.415	0.216
CAPM_1	499.0	712.0	953.0	0.5236	0.883	0.426	0.223
CAPM_2	505.5	723.0	953.0	0.530	0.945	0.430	0.228
CAPM_3	511.5	732.0	954.0	0.536	0.993	0.431	0.230
CAPM_4	523.6	750.0	956.0	0.547	1.099	0.432	0.236

FIGURE 2: (a) IR spectra of CdO-Al₂O₃-P₂O₅: MnO glasses. (b) Variation of symmetrical and asymmetrical band intensities for pure and MnO-doped CdO-Al₂O₃-P₂O₅.TABLE 3: Data from the infrared spectra of different band positions CdO-Al₂O₃-P₂O₅: MnO glasses.

Glasses	O-P-O units (cm ⁻¹) band 1	PO ₄ ³⁻ units (cm ⁻¹) band 2	P-O-P units (cm ⁻¹) band 3	AlO ₄ units (cm ⁻¹)
CAPM_0	1214	995	896	726
CAPM_1	1210	1005	903	726
CAPM_2	1207	1020	907	726
CAPM_3	1204	1033	911	726
CAPM_4	1198	1047	915	726

of some MnO concentration in the glass network, however, no shift in the band location of AlO₄ groups is observed. The difference between symmetrical and asymmetrical band intensities for pure and MnO-doped CdO-Al₂O₃-P₂O₅ glasses is depicted in Figure 2(b).

3.1.3. Optical Absorption Studies. Figure 3(a) shows the optical absorption spectra of various materials CdO-Al₂O₃-P₂O₅: MnO glasses. The spectra of MnO-doped glasses exhibit two absorption bands resulting from Mn²⁺ transition (around 500 nm) ${}^6A_{1g}(S) \rightarrow {}^4T_{1g}(G)$ and Mn³⁺ transition (around 490 nm) ${}^5E_g \rightarrow {}^5T_{2g}$.

There is a change in band positions from 500 to 488 nm as the concentration of MnO rises from 0.1 wt.% to 0.4 wt.%, suggesting the incremental conversion of Mn²⁺ ions into Mn³⁺ ions.

Figure 3(b) presents Urbach plot of CdO-Al₂O₃-P₂O₅: MnO glasses. Data on various band positions from the optical absorption spectra are shown in Table 4.

The optical band gap E_{opt} can be decided based on Urbach plot $(\alpha h\nu)^{1/2}$ versus $h\nu$, which is related by

$$\alpha(\nu) = \alpha_0 \left[\frac{h\nu - E_{opt}}{h\nu} \right]^2, \quad (8)$$

where α_0 is a constant that is proportional to the length of the band tailing and E_{opt} is the optical band gap energy [12].

Finally, MnO concentrations were increased from 0.1 wt.% to 0.4 wt.%. The observed band positions and measured optical band gaps for these glass series indicate a development in the glass network and an insulating character. A similar trend was also observed from other studies (namely, DTA, IR, and EPR) of CdO-Al₂O₃-P₂O₅: MnO glasses.

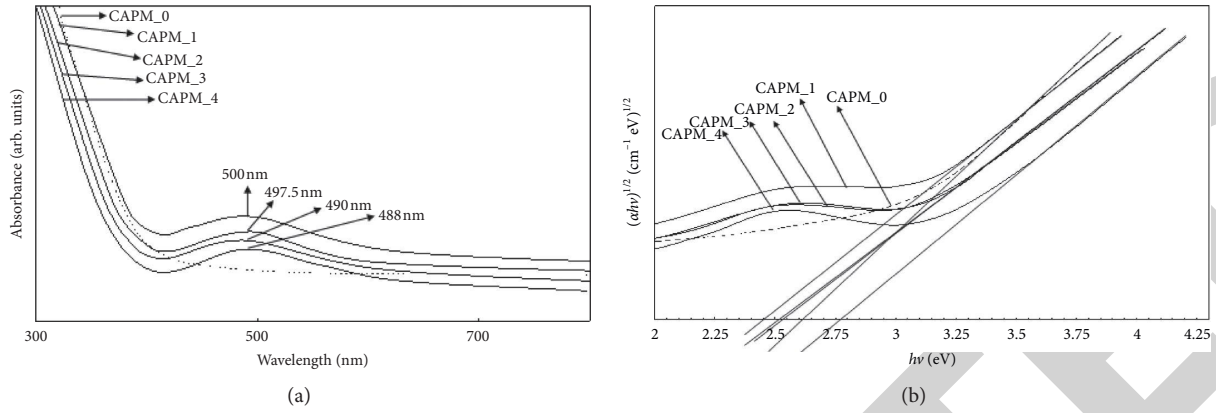


FIGURE 3: (a) Optical absorption spectra of CdO-Al₂O₃-P₂O₅: MnO glasses. (b) Urbach plots of CdO-Al₂O₃-P₂O₅: MnO glasses.

TABLE 4: Data on various band positions from the optical absorption spectra of CdO-Al₂O₃-P₂O₅: MnO glasses.

Glass	Band edge λ (nm)	Band position λ (nm) due to Mn ²⁺ transitions ${}^6A_{1g}(S) \rightarrow {}^4T_{1g}(G)$	Band position λ (nm) due to Mn ³⁺ transition ${}^5E_g \rightarrow {}^5T_{2g}$	Optical band gap energy E_{opt}	Urbach energy ΔE (eV)
CAPM_0	320.5	—	—	2.56	0.61
CAPM_1	315.7	500	—	2.44	1.03
CAPM_2	308.0	497.5	—	2.52	0.89
CAPM_3	301.5	—	490	2.53	0.67
CAPM_4	300	—	488	2.75	0.55

3.1.4. EPR Studies. Figure 4 shows the EPR spectra of CdO-Al₂O₃-P₂O₅: at room temperature, MnO glasses were registered. The spectra are characterized by two intense resonance signals; one of them is roughly oriented approximately $g = 2.01$ (signal 1) with a six-line hyperfine structure that is typical of independent Mn²⁺ ions, and the other is focusing at $g = 4.3$ (signal 2), which is a characteristic of isolated Mn³⁺ ions.

As MnO concentration is increased from 0.1 wt.% to 0.4 wt.%, the strength of signal 2 increases at the expense of signal 1, indicating that Mn²⁺ ions are converted to Mn³⁺ ions. As the MnO concentration is raised from 0.1 wt.% to 0.4 wt.%, there is a transformation of Mn²⁺ ions into Mn³⁺ ions observed in the current glass method, which is an indicative of increased covalent nature over that of ionic.

Furthermore, this suggests that the glass polymerization increases with improved stability with MnO concentrations increasing from 0.1 wt.% to 0.4 wt.% in the glass matrix.

3.1.5. Dielectric Studies. Figures 5(a)–5(c), respectively, show the variations of dielectric loss $\tan \delta$, dielectric constant ϵ , and AC conductivity δ_{ac} of CdO-Al₂O₃-P₂O₅: MnO glasses with temperature (20°C to 400°C) measured as a function of different frequencies at 1 kHz, 10 kHz, and 100 kHz.

Dielectric constant ϵ is observed to increase with temperature (with glass) at any frequency for all glasses; in addition, the value of the dielectric constant decreases as the MnO content rises from 0.1 wt.% to 0.4 wt.%. However, at any given temperature and MnO content in the glass

network, it was observed that the dielectric constant reduces as the frequency is increased (Figure 5(a)). A similar trend is observed for dielectric loss $\tan \delta$ variations (Figure 5(b)).

The ac conductivity σ_{ac} of these glasses is calculated using the following at various temperatures:

$$\sigma = \omega \epsilon_0 \epsilon \tan \delta, \quad (9)$$

where ϵ_0 is the vacuum dielectric constant) for various frequencies.

The graph of $\log \sigma_{ac}$ against $1/T$ is depicted in Figure 5(c) for all glasses at different frequencies. δ_{ac} of these glasses is found to increase with temperature and frequency; in addition, it is observed that δ_{ac} increases with rises in MnO content from 0.1 wt.% to 0.4 wt.% (Figure 3). Similar results were reported for MnO containing various glass matrices [3, 18]. Data on dielectric constant, dielectric loss, and AC conductivity of CdO-Al₂O₃-P₂O₅: MnO glasses at 1 kHz, 10 kHz, and 100 kHz for temperatures 20°C and 400°C are presented in Table 5.

3.2. Discussion. In general, glass properties are determined by its composition and, to a large degree, its structure. Aluminophosphate glasses doped with MnO are a mixture of network formers and modifiers with a complex composition [4, 5, 9, 10, 19]. P₂O₅ is a well-known network former composed of PO₄ structural units, in which one of the four oxygen atoms in the PO₄ tetrahedron is doubly bonded to the phosphorous atom [15]. By bridging oxygen atoms, the PO₄ tetrahedrons are joined together in chains or rings by covalent bonding. Cross bonds between metal cations and

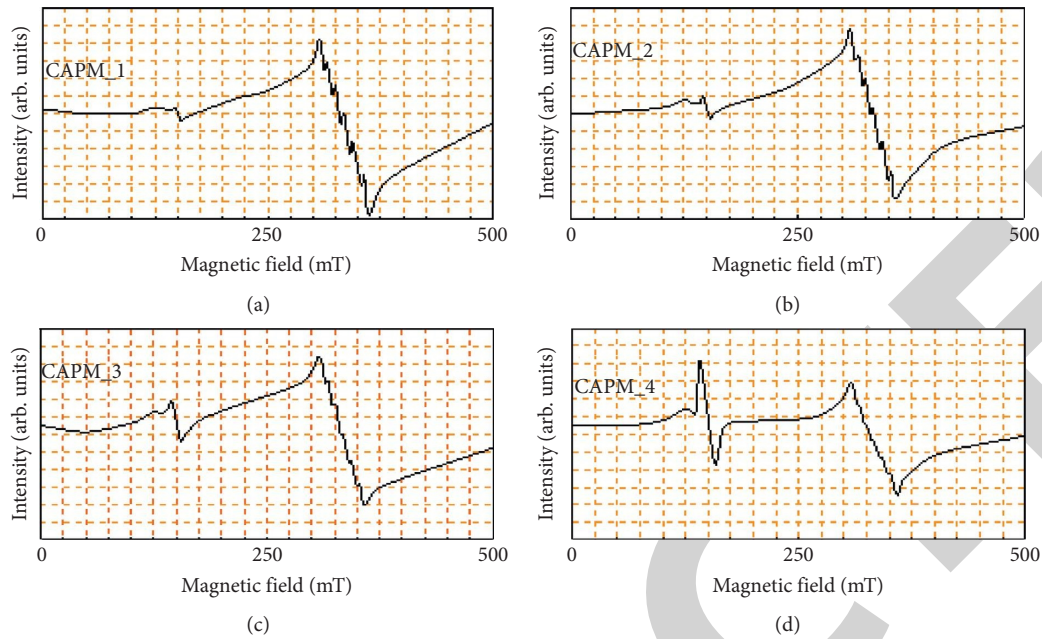


FIGURE 4: EPR spectra of CdO-Al₂O₃-P₂O₅: MnO glasses.

two nonbridging oxygen atoms of each PO₄ tetrahedron connect neighboring phosphate chains [14].

It is well known that adding a modifier oxide such as CdO to a P₂O₅ glass matrix causes the conversion of sp₂ planar PO₃ units to more stable sp₃ tetrahedral PO₄ units, as well as the formation of nonbridging oxygen atoms [20]. The bands observed at ~1200 cm⁻¹ and ~1040 cm⁻¹ result from symmetrical straining vibration ($\nu_s(\text{O-P-O})$) groups of nonbridging oxygen in phosphate chain and normal vibrational mode of asymmetric straining ($\nu_{as}(\text{PO}_4^{3-})$) group vibrations, respectively [20, 21]. Another band in the vicinity of 895 to 980 cm⁻¹ due to P-O-P bending vibration that corresponds to tendency of asymmetric straining of phosphate group [20] was also observed.

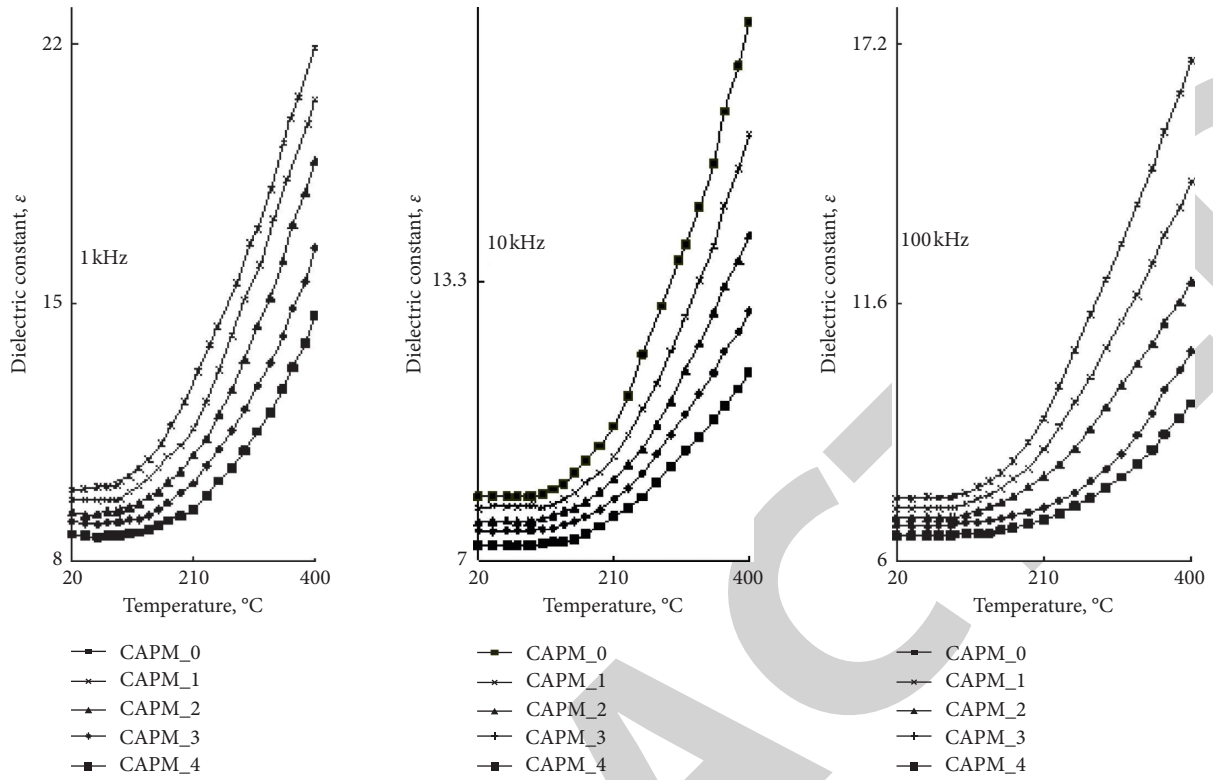
Three conventional phosphate bands were visible in the spectra of these lenses due to (i) O-P-O group symmetric straining vibrations in the range 1198–1214 cm⁻¹ (band 1), (ii) PO₄³⁻ group asymmetrical straining vibrations in the range 995–1047 cm⁻¹ (band 2), and (iii) P-O-P group asymmetrical bending vibrations in the range 896–915 cm⁻¹ (band 3). In addition, a band due to AlO₄ group vibrations with a fixed band position at 726 cm⁻¹ was observed for all glasses. From the IR spectral studies of these glasses, it was observed that as the MnO concentration rises from 0.1 wt.% to 0.4 wt.% in the glass matrix, the frequency of the symmetrical band (band 1) of phosphate units shifts towards a reduction in frequency as its intensity increases, and the asymmetrical bands 2 and 3 migrate towards higher frequencies as their intensities decrease, while they shift towards lower frequencies as their intensities decrease. This suggests a reduction in the degree of asymmetric stretching and increase in symmetrical stretching in phosphate units, MnO concentrations were increased from 0.1 wt.% to 0.4 wt.%, and there is also a rise in polymerization or stability

in the glass network. However, there is no observed change in the band position of AlO₄ groups at any concentration of MnO in the glass network.

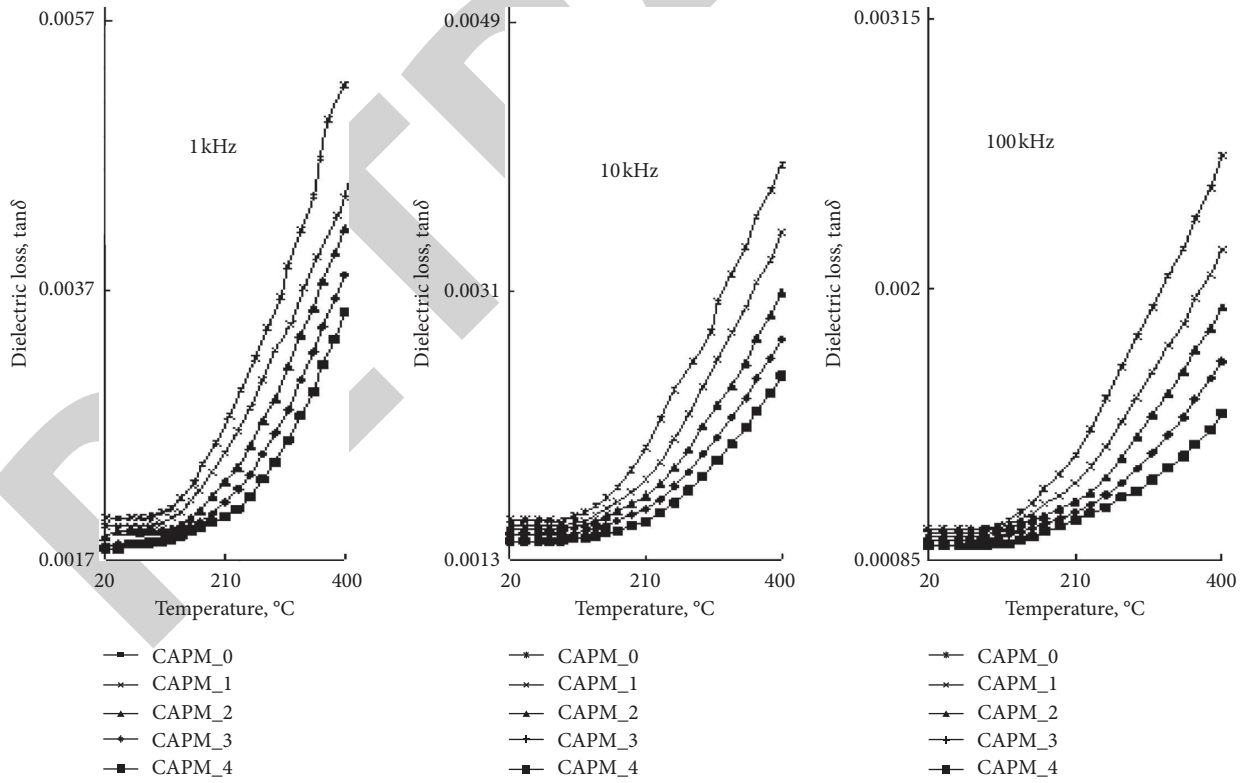
Spectra of optical absorption MnO-doped two distinct absorption bands can be seen in the glasses resulting from Mn²⁺ transition (around 500 nm) ${}^6A_{1g}(S) \rightarrow {}^4T_{1g}(G)$ and Mn³⁺ transition (around 490 nm) ${}^5E_g \rightarrow {}^5T_{2g}$. The band at 500 nm arises from intraconfigurational transitions due to Mn²⁺ ions [14, 22]. These detected bands due to Mn²⁺ ions were hidden, beyond 0.1 wt.% of MnO concentration. Due to the presence of Mn³⁺ ions, a new strong absorption spectrum with a limit at around 490 nm has emerged [15, 18, 23, 24]. It was observed that the optical band gap increases as the concentration of manganese oxide (MnO) increases from 0.1 wt.% to 0.4 wt.%, whereas the Urbach energy decreases, which indicates improvement in the insulating character and hence the glass network's strength.

Electron spin resonance gives information about the condition of valence of TM ions, local environment, and the essence of their interactions [25]. Since many of those Mn²⁺ compounds were octahedral and have a top spin structure with five unpaired electrons, they have a top spin arrangement, and an ESR signal with a g value close to the free electron value of 2.0023 is predicted [7, 25]. Signal at $g \sim 2.01$ due to Mn²⁺ ions shows an octahedral symmetrical environment with the bond dominantly ionic [15, 25, 26].

In the present study, at room temperature, the EPR spectroscopy of all these glasses was recorded by E11Z Varian X-band ($\nu = 9.5 \text{ GMZ}$) ESR Spectrometer. The spectra are characterized by two intense resonance signals; one of them is centered at approximately $g = 2.01$ (signal 1) with a six-line hyperfine sequence that is typical of independent Mn²⁺ ions, and the other is centered at $g = 4.3$ (signal 2), which is a characteristic of isolated Mn³⁺ ions



(a)



(b)

FIGURE 5: Continued.

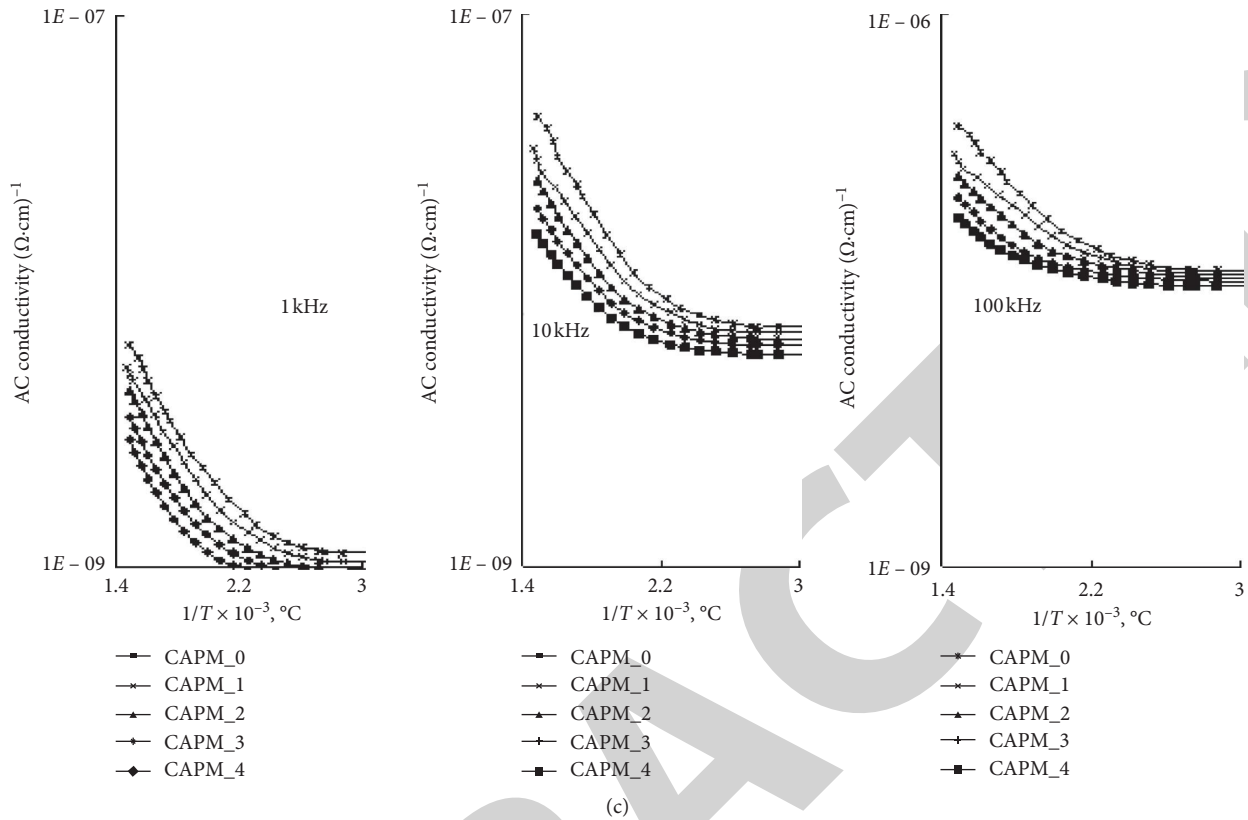


FIGURE 5: (a) Variation of dielectric constant with temperature at different frequencies for CdO-Al₂O₃-P₂O₅: MnO glasses. (b) Variation of dielectric loss with temperature at different frequencies for CdO-Al₂O₃-P₂O₅: MnO glasses. (c) Variation of AC conductivity with reciprocal temperature at different frequencies for CdO-Al₂O₃-P₂O₅: MnO glasses.

[26]. The presence of a resonance signal at $g=2.01$ is because of the existence of the Mn²⁺ ion in an area similar to octahedral symmetry. As MnO concentration is increased from 0.1 wt.% to 0.4 wt.%, the strength of signal 2 increases at the cost of signal 1, which is a sign that Mn²⁺ ions are being converted to Mn³⁺ ions. These samples' spectra are identical to those recorded for manganese ions doped in a variety of glass systems [15, 18, 27].

Ionic, dipolar, electronic, and space charges all contribute to a material's dielectric constant. Polarization is determined by the purity and perfection of the lenses [1, 28]. At very low temperatures, the effect of space charge polarizations is negligible, but it is within the low frequency range, and there is a significant difference [28]. The dipolar alignment effects in the glasses can be observed at up to 106 Hz. Retrieving our information, we find that ϵ is slightly frequency-dependent even at room temperature for pure as well as MnO-doped glasses. This is because of the dielectric constant and loss being influenced by space charge polarization. For temperature changes of around 400°C, for many solids, the reduction within the electronic dielectric constant is found to be less than 3% [29]. The defects in glasses can only increase ϵ and $\tan\delta$. As the temperature rises, space charge polarization becomes more dominant and therefore increases [1, 28, 29]. As this form of polarization decreases

with frequency, the change in ϵ and $\tan\delta$ at higher frequencies and temperature is lower [30–38].

The values increased by up to 0.5% with the addition of MnO, and $\tan\delta$, σ_{ac} , and ϵ are found to decrease at any temperature and frequency. Modifiers, such as octahedral Mn²⁺ ion, weaken the glass network by creating paths for free ions to migrate through, accumulating space charge and increasing disorder. The space charge polarization increases as the glass network becomes weaker, resulting in a reduction in dielectric parameters (i.e., MnO concentration ranging from 0.1 to 0.4). In MnO-doped glasses, the decrease of these parameters in this concentration range suggests that the Mn³⁺ ions present in these glasses (as demonstrated by measurements of optical absorption) establish cross-linkages, where Al-O-Mn bonds are formed by combining a portion of AlO₃ unit ions with a portion of AlO₃ unit ions. This is also logical because Al³⁺ and the oxidation state of Mn³⁺ ions are nearly identical, and their ionic radii are nearly similar (0.51 Å and 0.66 Å, respectively). As a result of these cross-links, the space charge polarization of glasses with MnO concentrations decreases, resulting in lower dielectric parameter values. As a result of increased concentration of MnO in the lenses, the existence of the \tan variation often supports that the bulks of the magnesium oxide in the glasses CAPM_1 and CAPM_2 are in the Mn²⁺ state, which acts as modifiers, and in the

glasses CAPM_3 and CAPM_4, they are in the Mn^{3+} state, which act as formers.

4. Conclusion

The conclusions drawn from different physical studies and spectroscopic properties of $CdO-Al_2O_3-P_2O_5: MnO$ glasses are summarized as follows.

- (i) The increase of MnO content from 0.1 wt.% to 0.4 wt.% improved glass network stability in the temperature range of 30–1000°C, according to DTA traces registered in the temperature range of 30–1000°C.
- (ii) With the improvement due to MnO content increase from 0.1 wt.% to 0.4 wt.%, the IR spectra measured at room temperature showed a rise in the symmetrical bands' intensity (band 1) at the expense of asymmetrical bands (bands 2 and 3); the observed trend indicates that the glass network's stability has improved.
- (iii) The gradual transformation of Mn^{2+} ions into Mn^{3+} by increasing MnO concentrations from 0.1 wt.% to 0.4 wt.% was observed in EPR spectra measured at room temperature, indicating an enhanced covalent atmosphere of manganese ions as well as an improvement in the consistency of the glass network.
- (iv) The MnO production was increased from 0.1 wt.% to 0.4 wt.% with an improvement in MnO content percent, and optical absorption spectra showed a shift in the concentration of Mn^{3+} ions at the cost of Mn^{2+} ions, as well as a rise throughout the optical band gap; the observed pattern shows an increase in insulating character and thereby the stability of the glass network.
- (v) At 105 Hz, the dielectric constant of glass M_0 (pure glass) is determined to be 7.36 at room temperature and it was frequency-oriented, with lower frequencies having comparatively higher values. With an improvement in MnO concentration of up to 0.4 wt.%, the dielectric constant value decreases with introduction of MnO. The variance of dielectric loss of frequency at different temperatures reveals a consistent pattern across all glasses.
- (vi) The space charge polarization increases as the glass network becomes weaker, resulting in higher measures of dielectric parameters. As more Mn^{3+} is added to the network of glasses, the space charge polarization decreases, resulting in a decrease in the measures of the dielectric parameters of the glasses.
- (vii) For all types of glasses at different frequencies, δ_{ac} of these glasses is found to increase with temperature and frequency; in addition, it is observed that as δ_{ac} decreases, MnO content was increased from 0.1 wt.% to 0.4 wt.%. This indicates that high proportion of Mn^{2+} in glass CAPM_1 (taking

modifier positions) and high proportion of Mn^{3+} in glass CAPM_4 (when glass former position high insulating character was considered).

- (viii) Finally, the results from various studies made on $CdO-Al_2O_3-P_2O_5: MnO$ glasses reveal an improved stability of the glass network with increase in MnO content from 0.1 wt.% to 0.4 wt.%.

Data Availability

The data used to support the findings of this study are included within the article.

Disclosure

This study was performed as a part of the employment of the authors.

Conflicts of Interest

The authors declare that they have no conflicts of interest.

References

- [1] G. Sahaya Baskaran, M. V. Ramana Reddy, D. Krishna Rao, and N. Veeraiyah, "Dielectric properties of $PbO-P_2O_5-As_2O_3$ glass system with Ga_2O_3 as additive," *Solid State Communications*, vol. 145, no. 7-8, pp. 401–406, 2008.
- [2] P. Bergo, W. M. Pontuschka, J. M. Prizon, C. C. Motta, and J. R. Martinelli, "Dielectric properties of barium phosphate glasses doped with transition metal oxides," *Journal of Non-crystalline Solids*, vol. 348, pp. 84–89, 2004.
- [3] Y. H. Elbasha, M. Ibrahim Ali, H. A. Elshaikh, and A. G. E.-D. Mostafa, "Influence of CuO and Al_2O_3 addition on the optical properties of sodium zinc phosphate glass absorption filters," *Optik-International Journal for Light and Electron Optics*, vol. 127, pp. 7041–7053, 2016.
- [4] H. Liu, Y. Lu, Y. Qu, H. Lu, and Y. Yue, "Effect of the content of Al_2O_3 on structure and properties of calcium-phosphate glasses: two experimental case studies," *Journal of Non-Crystalline Solids*, vol. 450, pp. 95–102, 2016.
- [5] C. N. Santos, K. Yukimitu, A. R. Zanata, and A. C. Hernandez, "Thermoluminescence of aluminophosphate glasses in the metaphosphate composition," *Nuclear Instruments and Methods in Physics Research Section B: Beam Interactions with Materials and Atoms*, vol. 246, no. 2, pp. 374–378, 2006.
- [6] R. Oueslati Omrani, A. Kaoutar, A. El Jazouli et al., "Structural and thermochemical properties of sodium magnesium phosphate glasses," *Journal of Alloys and Compounds*, vol. 632, pp. 766–771, 2015.
- [7] R. M. Krishna, J. J. Andre, J. L. Rao, and W. E. Antholine, "Structural investigations of Mn^{2+} ions in alkali barium borophosphate glasses by EPR and optical absorption techniques," *Materials Research Bulletin*, vol. 34, no. 10-11, pp. 1521–1525, 1999.
- [8] J. Holubová, Z. Černošek and E. Černošková, "Structural investigation and physical properties of $Ga_2O_3-ZnO-P_2O_5$ glasses," *Journal of Non-crystalline Solids*, vol. 454, pp. 31–38, 2016.
- [9] S. V. Stefanovsky, O. I. Stefanovsky, M. I. Kadyko, I. A. Presniakov, and B. F. Myasoedov, "The effect of Fe_2O_3 substitution for Al_2O_3 on the phase composition and structure

Retraction

Retracted: A Comparative Study on Crack-Healing Ability of Al₂O₃/SiC Structural Ceramic Composites Synthesized by Microwave Sintering and Conventional Electrical Sintering

Advances in Materials Science and Engineering

Received 26 December 2023; Accepted 26 December 2023; Published 29 December 2023

Copyright © 2023 Advances in Materials Science and Engineering. This is an open access article distributed under the Creative Commons Attribution License, which permits unrestricted use, distribution, and reproduction in any medium, provided the original work is properly cited.

This article has been retracted by Hindawi, as publisher, following an investigation undertaken by the publisher [1]. This investigation has uncovered evidence of systematic manipulation of the publication and peer-review process. We cannot, therefore, vouch for the reliability or integrity of this article.

Please note that this notice is intended solely to alert readers that the peer-review process of this article has been compromised.

Wiley and Hindawi regret that the usual quality checks did not identify these issues before publication and have since put additional measures in place to safeguard research integrity.

We wish to credit our Research Integrity and Research Publishing teams and anonymous and named external researchers and research integrity experts for contributing to this investigation.

The corresponding author, as the representative of all authors, has been given the opportunity to register their agreement or disagreement to this retraction. We have kept a record of any response received.

References

- [1] M. Mohankumar, A. N. Shankar, T. S. Karthik et al., "A Comparative Study on Crack-Healing Ability of Al₂O₃/SiC Structural Ceramic Composites Synthesized by Microwave Sintering and Conventional Electrical Sintering," *Advances in Materials Science and Engineering*, vol. 2021, Article ID 3170697, 8 pages, 2021.

Research Article

A Comparative Study on Crack-Healing Ability of Al₂O₃/SiC Structural Ceramic Composites Synthesized by Microwave Sintering and Conventional Electrical Sintering

Madhan Mohankumar ¹, A. N. Shankar ², T. S. Karthik ³, R. Saravanakumar ⁴,
Hemakesavulu Oruganti ⁵, S. Venkatesa Prabhu ⁶ and N. Rakesh ⁷

¹Department of Mechanical Engineering, Velammal Engineering College, Anna University, Chennai, Tamil Nadu, India

²Department of HSE & Civil Engineering, University of Petroleum & Energy Studies, Dehradun, India

³Department of Electronics and Communication Engineering, Aditya College of Engineering and Technology, Surampalem, Andhrapradesh, India

⁴Department of Wireless Communication, Institute of Electronics and Communication Engineering, Saveetha School of Engineering, Saveetha Institute of Medical and Technical Sciences, Chennai, Tamil Nadu, India

⁵Department of Electrical and Electronics Engineering, Annamacharya Institute of Technology & Sciences, Rajampet, Andhra Pradesh, India

⁶Department of Chemical Engineering, College of Biological and Chemical Engineering, Addis Ababa Science and Technology University, Addis Ababa, Ethiopia

⁷Department of Mechanical and Industrial Engineering, University of Technology and Applied Sciences, Nizwa, Oman

Correspondence should be addressed to S. Venkatesa Prabhu; venkatesa.prabhu@aastu.edu.et

Received 30 May 2021; Revised 10 June 2021; Accepted 14 June 2021; Published 22 June 2021

Academic Editor: Samson Jerold Samuel Chelladurai

Copyright © 2021 Madhan Mohankumar et al. This is an open access article distributed under the Creative Commons Attribution License, which permits unrestricted use, distribution, and reproduction in any medium, provided the original work is properly cited.

This study was conducted to assess and compare the crack-healing ability of conventional electrical sintered and microwave sintered Al₂O₃/x wt. % SiC (x = 5, 10, 15, and 20) structural ceramic composites. The crack-healing ability of both conventional electrical sintered and microwave sintered specimens was studied by introducing a crack of ~100 μm length by Vickers's indentation and conducting a heat treatment at 1200°C for dwell time of 1 h in air. The flexural or bending strength of sintered, cracked, and crack-healed specimens was determined by three-point bending test, and the phase variations by X-ray diffraction and SEM micrographs before and after crack-healing of both the sintering methods were studied and compared. The results show that almost all the specimens recovered their strength after crack-healing, but the strength of microwave sintered Al₂O₃/SiC structural ceramic composites has been shown to be better than that of conventional electrical sintered Al₂O₃/SiC structural ceramic composites. The microwave sintered crack-healed Al₂O₃/10 wt. % SiC specimen shows higher flexural strength of 794 MPa, which was 105% when compared with conventional electrical sintered Al₂O₃/10 wt. % SiC and crack-healed Al₂O₃/10 wt. % SiC specimen. It was found by X-ray diffractogram that before crack-healing, all the conventional electrical sintered samples have SiO₂ phase which reduce the crack-healing ability and microwave sintered samples with 15 and 20 wt. % SiC show lesser SiO₂ phase and 5 and 10 wt. % SiC samples have no SiO₂ phase before crack-healing. However, after crack-healing treatment, all the samples have distinct SiO₂ phase along with Al₂O₃ and SiC phases. Microwave sintered Al₂O₃/10 wt. % SiC specimen cracks were fully healed which was evident in SEM micrographs.

1. Introduction

In recent years, more concentration has been given to the structural ceramics with exemplary mechanical, chemical, and thermal properties [1]. However, structural ceramics are responsive to the existence of surface cracks by reason of their brittle nature. Moreover, steadfastness of structural ceramics considerably declined because of crack growth during machining or in service [2]. Crack-healing might be an effective way to overcome the effects of cracks and to recuperate the strength of structural ceramics. During the past decades, crack-healing nature of various ceramic composites by heat treatment was researched by the material researchers. Gupta [3] synthesized thermally shocked MgO and observed the crack-healing ability from 1400°C to 1650°C. Nakao et al. [4] found excellent crack-healing ability in Al₂O₃/30 vol% SiC composite, mullite/15 vol% SiC composite, and Si₃N₄/20 vol% SiC composite when heat treated at 1200°C for 1 hour dwell in air. The cracks created by machining in Al₂O₃, Si₃N₄, and mullite ceramics reinforced with SiC could be healed at 1200°C, 1300°C, and 1300°C, respectively, with the dwell time of 1 hour in air [5]. Lee et al. [6] showed that the indentation crack of ~100 μm was healed by conducting a healing treatment at 1300°C for 1 hour in air including a second phase SiC particles into Sc₂O₃ and AlN. Nam and Hwang [7] found that the optimal crack-healing condition for ZrO₂/SiC was 800°C for 5 hours in air.

Ando et al. [8] and Takahashi Koji et al. [9] found that the SiC present in Si₃N₄/SiC ceramic composite has the ability to heal the surface crack of length ~100 μm at 1200°C or 1300°C temperature with a dwell time of 1 h in air. Nakao et al. [10] observed the crack-healing in Al₂O₃/SiC whiskers/SiC particles ceramic composite and Al₂O₃/SiC whiskers ceramic composite at 1300°C with 1 hour soaking time in air due to the formation of SiO₂ by the oxidation of SiC phase and healing of the surface crack length below 250 μm and below 200 μm, respectively. The SiO₂ formed by oxidation of SiC was bonded with the crack surface, and crack-healing was achieved with a soaking time of 1 hour in air.

Later, material researchers investigated the crack-healing ability of high dense Al₂O₃/SiC ceramic composite synthesized by hot pressing sintering. However, formation of SiO₂ phase during sintering of ceramics depreciates the healing ability, as well as it affects the quality of the material. Mandal et al. [11] found that ~32% of SiC gets oxidized and converted into SiO₂ and depreciates the product quality significantly during the conventional sintering process. To overcome this limitation, structural ceramics are synthesized by using microwave heating because it elicits very low SiO₂ formation than other conventional sintering process. Microwave sintering is viewed as a prevailing method than conventional sintering processes because it can provide enhanced mechanical properties and better finer microstructure with minimum energy consumption [12, 13]. Microwave sintering has been successfully used to synthesize Al₂O₃-based structural ceramics with constructive mechanical properties [14–22]. In order to produce crack-healing in Al₂O₃/SiC structural ceramic composites, the

presence of SiC phase after sintering process was very much needed. As per above investigation, crack-healing was mostly in need of the formation of SiO₂ during healing process. In this study, crack-healing ability of conventional electrical sintered and microwave sintered Al₂O₃/x wt.% SiC (x = 5, 10, 15, 20) ceramic composite materials was compared.

2. Experimental Procedure

α-Al₂O₃ particles (average grain size = 3 μm, 99.5% purity, sigma Aldrich) and β-SiC particles (average grain size = 1 μm, 99% purity sigma Aldrich) were used as the starting materials. To advance the homogeneity of the raw materials, the mixtures of Al₂O₃ with different wt.% of SiC (5, 10, 15, and 20) were ball milled along with isopropyl alcohol medium using WC ball at 300 rpm for 6 hours. After milling, the homogeneous mixture was desiccated at 80°C and sieved through 200 mesh. All the four homogeneous powders were compacted into square plate (45 mm × 45 mm × 3 mm) in uniaxial cold press at 60 MPa for 30 seconds discretely. One set of plates was sintered in an electric resistance heating furnace with MoSi₂ as heating elements under the following condition: temperature = 1500°C; heating rate = 10°C per minute; and dwell time = 300 minutes. One more set of plates were sintered in a microwave furnace with 2.45 GHz, and it consists of magnetron as the microwave source element with SiC-based susceptor materials as supplementary heating elements under the following condition: temperature = 1500°C, holding time = 15 minutes, and input power ranging from 0.9 to 2.4 kW. Both sintering processes use an air atmosphere. A noncontact type infrared sensor was used to measure the temperature in microwave furnace and Eurotherm (Model 2416) microprocessor-based PID controller with digital indicator was used to control the temperature. In both the sintering methods, conventional electrical furnace sintering and microwave sintering method, specimens were cooled in the furnace itself. The sintered plates were cut into rectangular bar (45 mm × 4 mm × 3 mm) specimens. One face of the specimen was well polished using diamond paste in lapping machine. A semielliptical crack of ~100 μm was made on two set of conventional electrical sintered and microwave sintered specimens at the centre by Vickers indenter with a load of 29.4 N. From the review article [23], the optimum condition for crack-healing an Al₂O₃/SiC ceramic composite to recover its full strength is annealing at 1200°C for 60 minutes in air. Therefore, one set of cracked specimens was subjected to crack-healing treatment in an electric resistance heating furnace with MoSi₂ as heating elements and another set was kept as cracked for investigation. The flexural strength of smooth, cracked, and crack-healed specimens was determined by the three-point bending test based on the ASTM C1161 standard with a support span (*L*) of 40 mm length with a speed of 0.5 mm/min. Three specimens were used in each condition to calculate the flexural strength. Figure 1 shows the schematic diagram of three-point bending test, and the flexural strength was calculated using the following equation:

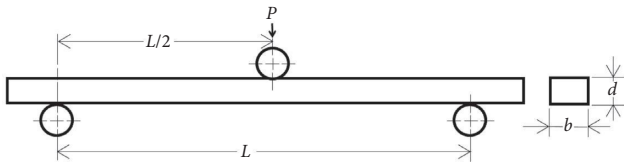


FIGURE 1: Schematic diagram of the three-point bending test.

$$S = \frac{3PL}{2bd^2}, \quad (1)$$

where P is the break force, L is the outer (support) span, b is the specimen width, and d is the specimen thickness.

X-ray diffraction (XRD-SmartLab, Japan) was used to study the various phase composition of smoothed and crack-healed specimen synthesized by both the conventional electrical sintering and microwave sintering method. The X-ray diffraction was done using Cu-K beta radiation with 30 mA electric current and 45 kV accelerated voltage. The micrographs of cracks before and after healing were scanned by scanning electron microscopy (FESEM, Supra-55, Carl Zeiss, Germany).

3. Result and Discussion

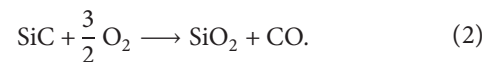
3.1. Microstructure. Figure 2 shows the microstructure and morphological of Al_2O_3 with four different wt.% of SiC composites synthesized by conventional electrical sintering. As a result of the presence of more intergranular SiC particles in samples with 15 and 20 wt. % SiC (Figures 2(c) and 2(d)), the voids are more than 5 and 10 wt. % SiC (Figures 2(a) and 2(b)) samples. Figures 2(a) and 2(b) confirm that cluster of Al_2O_3 is more than that in Figures 2(c) and 2(d) because of lesser amount of SiC particles.

Microstructures of microwave sintered $\text{Al}_2\text{O}_3/\text{SiC}$ ceramic composite samples are shown in Figure 3. It was noticeable that with increase in SiC content, the voids are increased but microwave effect reduces the voids by increasing the density. Figures 3(a) and 3(b) show clump of dense Al_2O_3 phase, and Figure 3(c) shows glassy prismatic structure. It is fascinating to notice that uniform agglomeration is noticed more in the microstructures of microwave sintered $\text{Al}_2\text{O}_3/\text{SiC}$ ceramic samples than microstructures of conventional sintered $\text{Al}_2\text{O}_3/\text{SiC}$ ceramic samples.

3.2. Flexural Strength. The relationship between the wt. % of SiC in $\text{Al}_2\text{O}_3/\text{SiC}$ ceramic composite and the flexural strength of smoothed, precracked, and crack-healed specimen synthesized by conventional electrical sintering and microwave sintering is given in Table 1. In all the cases, the flexural strength of microwave sintered specimen was more than that of the conventional electrical sintered specimen, indicating that microwave heating enhances the flexural strength by grain refinement which was evident in the microstructure. The flexural strength of crack-healed specimens of both the conventional electrical and microwave sintering is higher than that of the smooth specimens

of both the methods. Likewise, when comparing the flexural strength of cracked specimens of both the methods with that of the crack-healed specimens of both conventional electrical and microwave sintered methods, crack-healed samples show higher flexural strength than cracked specimens. This indicates that all specimens recovered flexural strength and showed that the cracks were healed partially or completely. The higher flexural strength of 794 MPa was obtained for microwave sintered crack-healed $\text{Al}_2\text{O}_3/10$ wt.% SiC structural ceramic composite. The flexural strength of crack-healed $\text{Al}_2\text{O}_3/10$ wt. % SiC sample synthesized by the microwave sintered method was improved up to 105%, when correlated with flexural strength crack-healed $\text{Al}_2\text{O}_3/10$ wt. % SiC specimen synthesized by conventional electrical sintering. Restoring full strength through oxidation has also been suggested by Koji Takahashiet al. [6] and Nakao et al. [10]. They synthesized ceramic composites based on Al_2O_3 and found that the inclusion of secondary-phase SiC particles improves crack-healing through oxidation and restores flexural strength.

3.3. Phase Variation after Crack-Healing. XRD pattern of conventional electrical sintered and microwave sintered $\text{Al}_2\text{O}_3/\text{SiC}$ ceramic materials before and after crack-healing heat treatment at 1200°C with a dwell time of 1 h in air is shown in Figure 4. XRD patterns of all the samples before and after the crack-healing heat treatment show Al_2O_3 and SiC as two main phases. After crack-healing heat treatment process, the clear sharp peaks of SiO_2 were detected in the diffraction pattern of all the samples, indicating that $\text{Al}_2\text{O}_3/\text{SiC}$ ceramic material gets suffered by oxidation. The reaction due to oxidation of SiC by crack-healing heat treatment for the formation of new phases could be described in the following equation:



However, XRD pattern of conventional electrical sintered samples shows clear sharp peaks of SiO_2 phase before the crack-healing heat treatment and some smaller peaks in microwave sintered $\text{Al}_2\text{O}_3/20$ wt. % SiC sample. XRD pattern before and after crack-healing reveals that amount of SiC particles available for crack-healing reaction was more in samples synthesized by microwave sintering than samples synthesized by conventional electrical sintering. SiC phase was still detectable in the samples after crack-healing because SiC particles on the surface and cracks are only exposed to air and get oxidized into SiO_2 and the SiC particles within the surfaces are not getting oxidized. In previous studies, it was also observed that a SiO_2 phase forms in all four traditional sintering compositions, but only a small amount of SiO_2 forms in 15 and 20 wt.% of SiC composites synthesized by microwave sintering due to the shorter sintering time [19, 20].

3.4. SEM Micrographs. SEM micrographs of radial cracks produced by Vickers indentation in conventional electrical sintered $\text{Al}_2\text{O}_3/\text{SiC}$ structural ceramics before and after

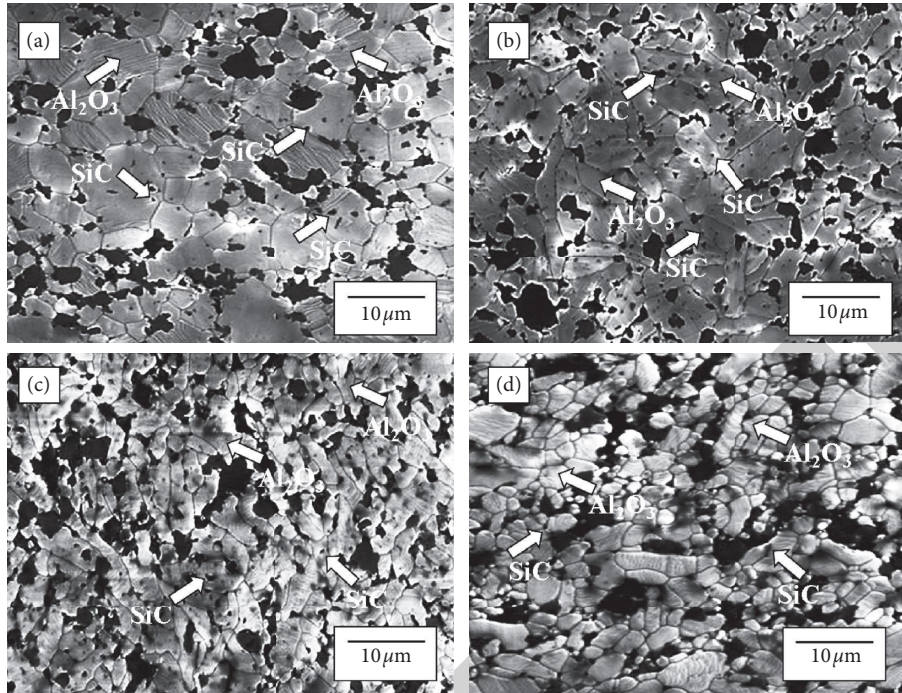


FIGURE 2: SEM figures of conventional electrical sintered $\text{Al}_2\text{O}_3/x\text{wt.}\% \text{SiC}$ samples: (a) 5 wt. %SiC; (b) 10 wt.%SiC; (c) 15 wt.%SiC; (d) 20 wt.%SiC.

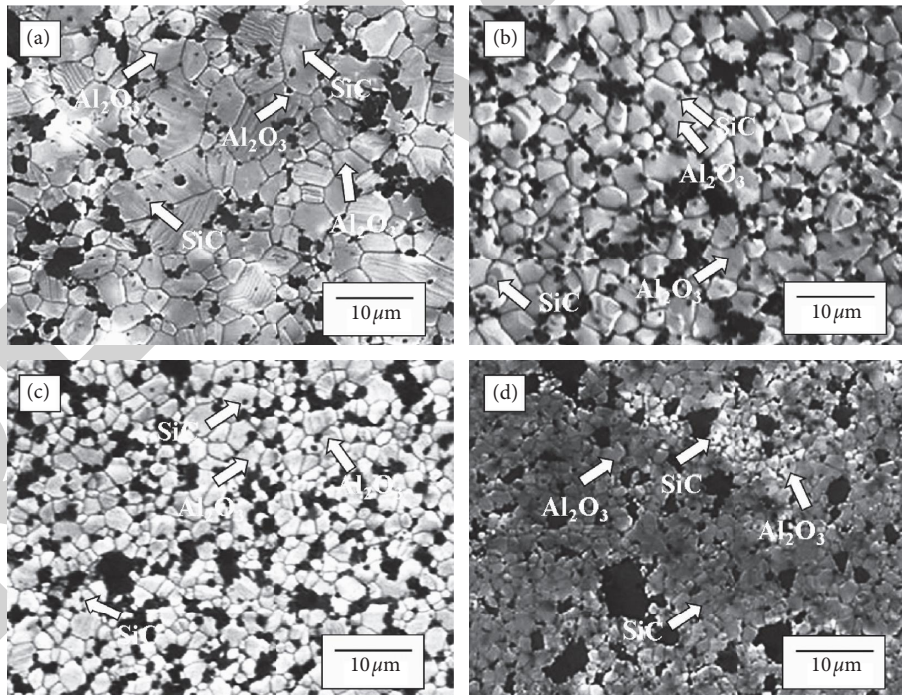


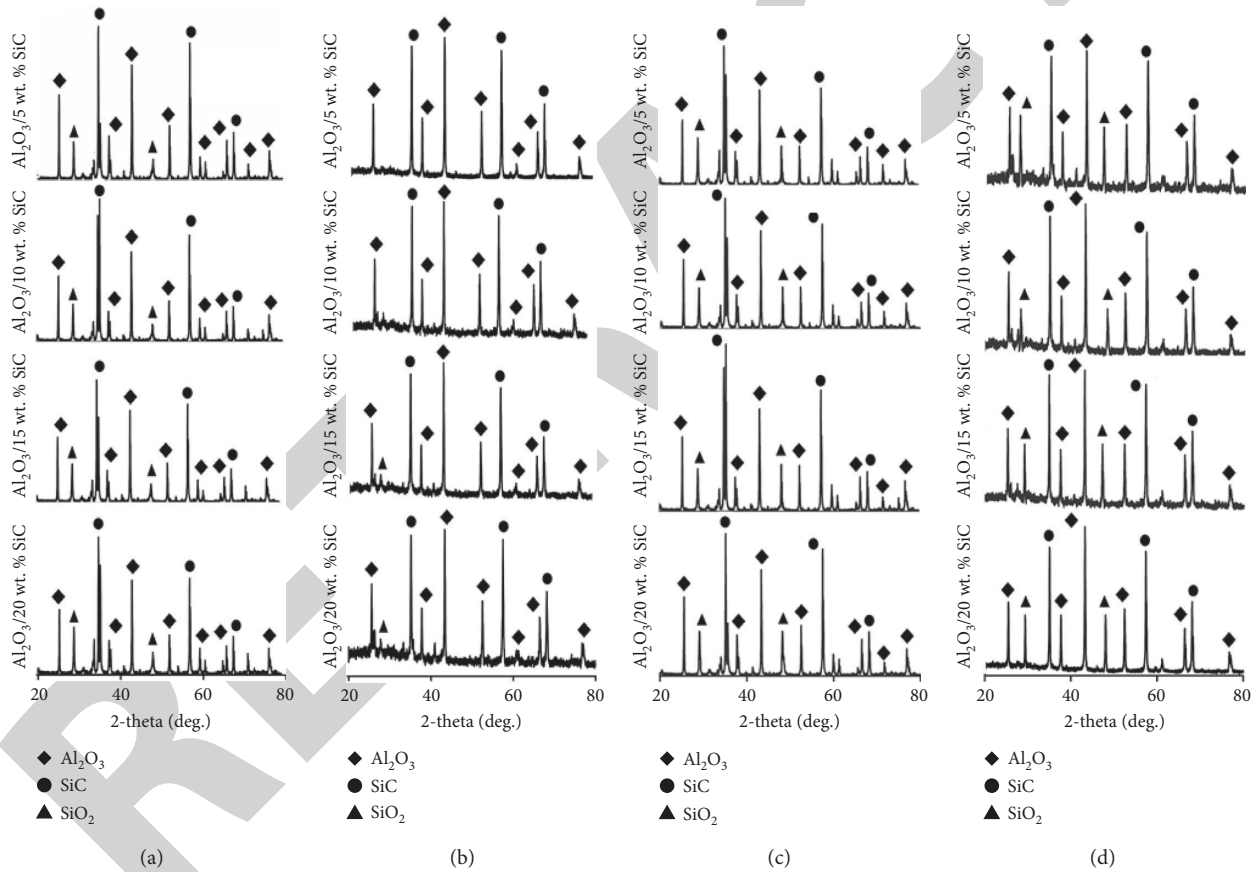
FIGURE 3: SEM figures of microwave sintered $\text{Al}_2\text{O}_3/x \text{ wt.}\% \text{SiC}$ samples: (a) 5 wt. % SiC; (b) 10 wt.% SiC; (c) 15 wt.% SiC; (d) 20 wt.% SiC.

crack-healing are shown in Figure 5. After crack-healing heat treatment at 1200°C for 1h in air, the surface of specimen became rough due to the oxidation of the particles. Healing occurs in the radial cracks produced by Vickers indentation which is shown in Figure 5. However, the radial cracks are not healed for the entire length, and the

cracks with minimum width are healed completely in all the conventional electrical sintered samples. This incomplete healing in conventional electrical sintered sample is primarily because of the nonavailability of more SiC secondary-phase particles in the cracked region. The reason for this was oxidation of SiC particles into SiO_2 during the sintering of

TABLE 1: Flexural strength of smooth, cracked, and crack-healed conventional electrical sintered and microwave sintered $\text{Al}_2\text{O}_3/\text{SiC}$ ceramic composites.

Condition	Wt. % of		Flexural strength σ in MPa	
	Al_2O_3	SiC	Conventional electrical sintering	Microwave sintering
Smooth specimen	95	5	302 ± 23	318 ± 32
	90	10	592 ± 34	624 ± 38
	85	15	512 ± 18	543 ± 28
	80	20	467 ± 42	508 ± 18
Cracked specimen	95	5	212 ± 38	203 ± 33
	90	10	242 ± 26	257 ± 42
	85	15	287 ± 18	312 ± 18
	80	20	262 ± 28	315 ± 22
Cracked + healed	95	5	427 ± 32	488 ± 41
	90	10	758 ± 24	794 ± 32
	85	15	647 ± 14	658 ± 34
	80	20	596 ± 21	623 ± 26

FIGURE 4: XRD pattern of $\text{Al}_2\text{O}_3/x$ wt.% SiC: (a) conventional electrical sintered sample; (b) microwave sintered sample; (c) crack-healed conventional electrical sintered sample; (d) crack-healed microwave sintered sample.

green consolidated sample in conventional electrical sintering, which was evident by the detection of clear SiO_2 peaks in the XRD patterns of all four composition before the crack-healing process. The oxidation of SiC particles can be reduced by minimizing the holding time during the sintering process, but this will cause the reduction in the density of $\text{Al}_2\text{O}_3/\text{SiC}$ structural ceramics synthesized by conventional electrical sintering.

Figure 6 shows the SEM micrographs of radial cracks produced by Vickers indentation in microwave sintered $\text{Al}_2\text{O}_3/\text{SiC}$ structural ceramics before and after crack-healing. Similar to conventional electrical sintered samples, after crack-healing heat treatment at 1200°C for 1h dwell time in air, the surface of specimen became rough due to oxidation of the particles. Because of the less SiC content in the ceramic structure, the radial cracks are not healed for the entire

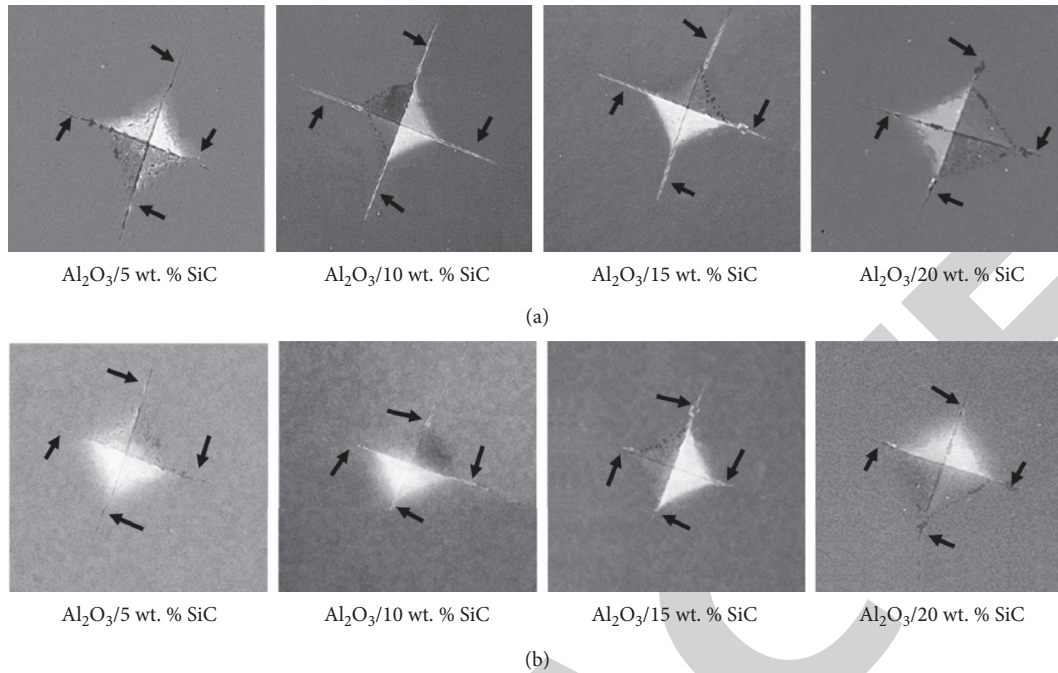


FIGURE 5: SEM micrographs of radial cracks by Vickers indentation in conventional electrical sintered $\text{Al}_2\text{O}_3/\text{SiC}$ structural ceramics (a) before crack-healing and (b) after crack-healing.

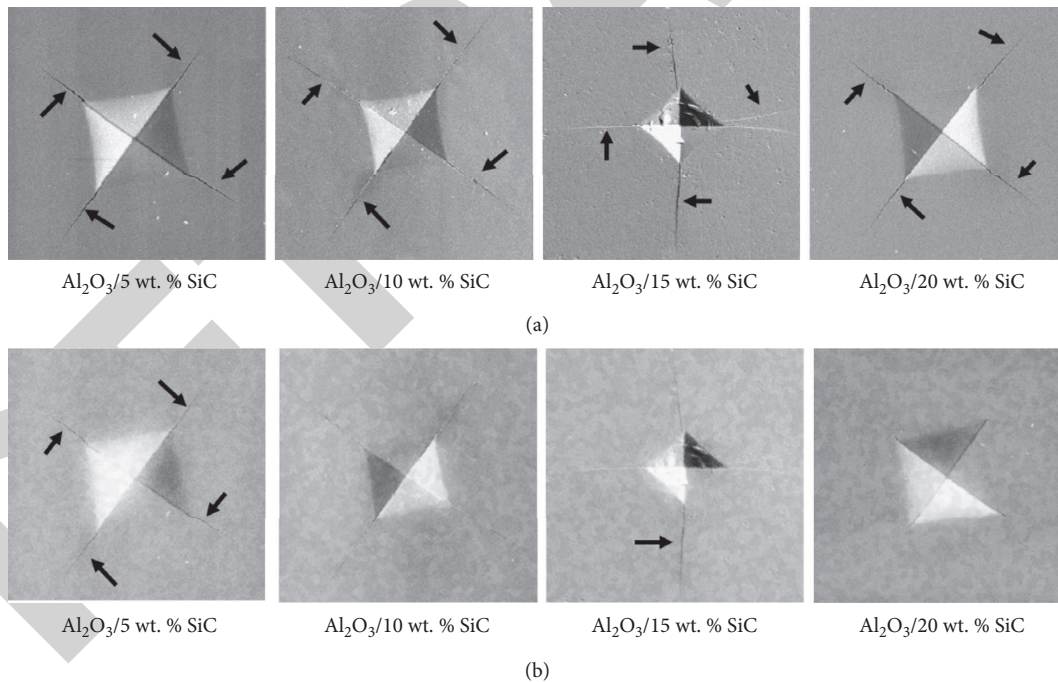


FIGURE 6: SEM micrographs of radial cracks produced by Vickers indentation in microwave sintered $\text{Al}_2\text{O}_3/\text{SiC}$ structural ceramics (a) before crack-healing and (b) after crack-healing.

length in $\text{Al}_2\text{O}_3/5$ wt.% SiC structural ceramics which is indicated in Figure 6 by arrow marks in after crack-healing. Mostly, all the radial cracks are healed in others $\text{Al}_2\text{O}_3/\text{SiC}$ ceramic composites with 10, 15, and 20 wt.% SiC. This complete healing was due to the availability of more SiC

particles after the microwave sintering. The oxidation of SiC particles was very negligible in microwave sintering because of its volumetric heating and lesser holding time. Due to this, crack-healing ability of microwave sintered samples increases than conventional electrical sintered sample. In the

SEM micrograms of both conventional electrical sintered and microwave sintered samples after crack-healing, spongy appearance is present all over the surface due to the oxidation of SiC particles, and the surface after crack-healing heat treatment become rough when compared with sample surface without crack-healing heat treatment.

4. Conclusion

In this research, crack-healing ability of conventional electrical sintered and microwave sintered $\text{Al}_2\text{O}_3/x$ wt.% SiC ($x = 5, 10, 15,$ and 20) ceramic composites was discussed and compared. For this, the crack length of approximately $100\ \mu\text{m}$ was produced by the Vickers indentation method. The crack-healing condition of 1200°C for 1h in air was used, which was identified from the review.

- (i) SEM microstructures reveal that with increase in SiC wt.%, the voids also increase in the samples synthesized by both the conventional electrical sintering and microwave sintering methods. Due to volumetric heating and less sintering time in microwave sintering process, the samples synthesized by this method show uniform agglomeration than samples synthesized by the conventional electrical sintering method.
- (ii) The higher flexural strength of 794 MPa was obtained for microwave sintered crack-healed $\text{Al}_2\text{O}_3/10$ wt. % SiC structural ceramic composite, which was 105% when compared with conventional electrical sintered crack-healed sample. In all the cases, microwave sintered sample is superior than conventional electrical sintered sample. The improvement in flexural strength after healing in microwave sintered $\text{Al}_2\text{O}_3/\text{SiC}$ sample might have resulted from the availability of more SiC particles than conventional electrical sintered $\text{Al}_2\text{O}_3/\text{SiC}$ sample because, during the synthesise of ceramic material by conventional electrical sintering, SiC particles get oxidized into SiO_2 . This will reduce the crack-healing ability and amount of strength recovery when compared with microwave sintered $\text{Al}_2\text{O}_3/\text{SiC}$ ceramics.
- (iii) The two main phases detected before and after the crack-healing in XRD pattern are Al_2O_3 and SiC phases. After crack-healing heat treatment process at 1200°C for 1h dwell in air, the SiC particles in the samples get oxidized and form SiO_2 phase and it was clearly visible by the sharp peaks in the diffractogram.
- (iv) At 1200°C for 1 hour dwell in air, the crack-healing mechanism was attributed by the formation of SiO_2 phase in $\text{Al}_2\text{O}_3/\text{SiC}$ structural ceramic materials. Results of microstructure analysis indicated that the crack was healed completely in microwave sintered Al_2O_3 with 10, 15, and 20 wt. % SiC by the oxidized product. In all other cases, the radial cracks are partially healed, but strength was recovered when compared with smooth specimen.

Data Availability

The data used to support the findings of this study are included within the article.

Disclosure

It was performed as a part of the Employment of Addis Ababa Science and Technology University, Addis Ababa, Ethiopia.

Conflicts of Interest

The authors declare that they have no conflicts of interest.

References

- [1] Y. Liu, C. Huang, H. Liu, B. Zou, P. Yao, and L. Xu, "Effect of nano-additives on microstructure and mechanical properties of Ti(C, N)-TiB₂-WC composite ceramic cutting tool materials," *Key Engineering Materials*, vol. 589-590, pp. 337-341, 2014.
- [2] S. Herbert and M. Toshimichi, "High-speed machining," *CIRP Annals*, vol. 41, pp. 637-643, 1992.
- [3] T. K. Gupta, "Crack healing in thermally shocked MgO," *Journal of the American Ceramic Society*, vol. 58, p. 143, 1957.
- [4] W. Nakao, Y. Chiba, K. Iwata, Y. Nishi, and K. Ando, "Strengthening of ceramics surface by crack healing and Electron beam irradiation," *International Journal of Applied Ceramic Technology*, vol. 8, no. 2, pp. 383-389, 2011.
- [5] K. Takahashi, K. Ando, and W. Nakao, "Crack-healing ability of structural ceramics and methodology to guarantee the reliability of ceramic components," in *Advances in Ceramics - Characterization, Raw Materials, Processing, Properties, Degradation and Healing*, IntechOpen, London, UK, 2011.
- [6] S.-K. Lee, K. Ando, and Y.-W. Kim, "Effect of heat treatments on the crack-healing and static fatigue behavior of silicon carbide sintered with Sc₂O₃ and AlN," *Journal of the American Ceramic Society*, vol. 88, no. 12, pp. 3478-3482, 2005.
- [7] K. W. Nam and J. R. Hwang, "The crack healing behavior of ZrO₂/SiC composite ceramics with TiO₂ additive," *Journal of Mechanical Science and Technology*, vol. 26, no. 7, pp. 2093-2096, 2012.
- [8] K. Ando, K. Takahashi, S. Nakayama, and S. Saito, "Crack-healing behavior of Si₃N₄/SiC ceramics under cyclic stress and resultant fatigue strength at the healing temperature," *Journal of the American Ceramic Society*, vol. 85, no. 9, pp. 2268-2272, 2002.
- [9] K. Takahashi, Y.-S. Jung, Y. Nagoshi, and K. Ando, "Crack-healing behavior of Si₃N₄/SiC composite under stress and low oxygen pressure," *Materials Science and Engineering*, vol. 527, no. 15, pp. 3343-3348, 2010.
- [10] W. Nakao, M. Ono, S.-K. Lee, K. Takahashi, and K. Ando, "Critical crack-healing condition for SiC whisker reinforced alumina under stress," *Journal of the European Ceramic Society*, vol. 25, no. 16, pp. 3649-3655, 2005.
- [11] S. Mandal, A. Seal, S. K. Dalui, A. K. Dey, S. Ghatak, and A. K. Mukhopadhyay, "Mechanical characteristics of microwave sintered silicon carbide," *Bulletin of Materials Science*, vol. 24, no. 2, pp. 121-124, 2001.
- [12] D. K. Agrawal, "Microwave processing of ceramics," *Current Opinion in Solid State & Materials Science*, vol. 3, no. 5, pp. 480-485, 1998.

Retraction

Retracted: Computational Investigations of Fixed-Free and Fixed-Fixed Types Single-Wall Carbon Nanotube Mass Sensing Biosensor

Advances in Materials Science and Engineering

Received 26 December 2023; Accepted 26 December 2023; Published 29 December 2023

Copyright © 2023 Advances in Materials Science and Engineering. This is an open access article distributed under the Creative Commons Attribution License, which permits unrestricted use, distribution, and reproduction in any medium, provided the original work is properly cited.

This article has been retracted by Hindawi, as publisher, following an investigation undertaken by the publisher [1]. This investigation has uncovered evidence of systematic manipulation of the publication and peer-review process. We cannot, therefore, vouch for the reliability or integrity of this article.

Please note that this notice is intended solely to alert readers that the peer-review process of this article has been compromised.

Wiley and Hindawi regret that the usual quality checks did not identify these issues before publication and have since put additional measures in place to safeguard research integrity.

We wish to credit our Research Integrity and Research Publishing teams and anonymous and named external researchers and research integrity experts for contributing to this investigation.

The corresponding author, as the representative of all authors, has been given the opportunity to register their agreement or disagreement to this retraction. We have kept a record of any response received.

References

- [1] K. Umaphathi, Y. Sangeetha, A. N. Shankar et al., “Computational Investigations of Fixed-Free and Fixed-Fixed Types Single-Wall Carbon Nanotube Mass Sensing Biosensor,” *Advances in Materials Science and Engineering*, vol. 2021, Article ID 3253365, 13 pages, 2021.

Research Article

Computational Investigations of Fixed-Free and Fixed-Fixed Types Single-Wall Carbon Nanotube Mass Sensing Biosensor

K. Umapathi ¹, Yalamanchili Sangeetha ², A. N. Shankar ³, P. Vidhyalakshmi ⁴,
R. Ramkumar ⁵, S. Balakumar ⁶ and D. Magdalinmary ⁷

¹Department of Electrical and Electronics Engineering, M.Kumarasamy College of Engineering, Karur, India

²Department of Information Technology, VR Siddhartha Engineering College, Vijayawada-7, Andhra Pradesh, India

³Department of HSE & Civil Engineering College, University of Petroleum & Energy Studies, Dehradun, Uttarakhand, India

⁴Department of Electronics and Instrumentation Engineering, Kongu Engineering College, Perundurai, Tamilnadu, India

⁵Department of Electrical and Electronics Engineering, K.Ramakrishnan College of Technology, Trichy, Tamilnadu, India

⁶Faculty of Electrical and Computer Engineering, Arba Minch University, Arbaminch, Ethiopia

⁷Department of Electrical and Electronics Engineering, Sri Krishna College of Technology, Coimbatore, Tamilnadu, India

Correspondence should be addressed to S. Balakumar; sbk25dec@gmail.com

Received 10 May 2021; Accepted 4 June 2021; Published 22 June 2021

Academic Editor: Samson Jerold Samuel Chelladurai

Copyright © 2021 K. Umapathi et al. This is an open access article distributed under the Creative Commons Attribution License, which permits unrestricted use, distribution, and reproduction in any medium, provided the original work is properly cited.

Using carbon nanotubes for sensing the mass in a biosensor is recently proven as an emerging technology in healthcare industry. This study investigates relative frequency shifts and sensitivity studies of various biological objects such as insulin hormone, immunoglobulin G (IgG), the most abundant type of antibody, and low-density lipoproteins (LDL) masses using the single-wall carbon nanotubes as a biomass sensor via continuum mechanics. Uniform distributed mass is applied to the single-wall carbon nanotube mass sensor. In this study, fixed-free and fixed-fixed type single-wall carbon nanotubes with various lengths of relative frequency shifts are studied. Additionally, the sensitivity analysis of fixed-free and fixed-fixed type CNT biological mass sensors is carried out. Moreover, node shapes studies are performed. The sensitivity results show better, if the length of the single-wall carbon nanotube is reduced.

1. Introduction

After discovering carbon nanotubes (CNT's) [1, 2], its utilization is found to be in diverse range of applications, such as nanomechanical resonators and nanobiological sensors. The unique great physical properties of the carbon nanotube lead to various usage in different fields such as nanoelectromechanical systems and actuators. [3–6]. The use of CNT in medical fields is enormous. Applications of CNT in electrochemical sensing [7–14], nanoactuators [15, 16], and nanosensors [5, 6, 17] are demonstrated. Nanomechanical resonators have been demonstrated in weigh cell, biomolecules, and gas molecules [18]. There is an increasing attention of CNTs in biological applications [5, 6, 19–21]. Difficulties of experimental and advantages of the theoretical modeling of nanoscale devices and CNTs are explained [3–5, 18, 22, 23].

By using CNT-based sensors, the sensing of volatile organic compounds related to human diseases is demonstrated [24], glucose oxidase (GOD) sensing using CNT is performed [25], and the extraordinary low detection limit of CNT working electrodes is shown [26]. Producing biosensors using CNT is an emerging trend. Many articles show the modeling techniques of elastic continuum mechanics concepts for analyzing the vibration of carbon nanotubes. The theory of the mechanical behaviors of materials dealing with continuous mass is called as continuum mechanics. There are two significances for the continuum modeling approach. It needs less work of the computational process than the molecular dynamics modeling, and nanostructures behavior analysis is much cheaper through the continuum model. Continuum beam and shell models have been elaborately studied. The beam theory concepts implemented using the single-wall carbon nanotube are explored [10]. The elastic

material properties and continuum models of carbon nanotubes have been studied [11].

The theory of mass recognition using CNT resonators is on the basis of the proven fact that the resonant frequency is sensitive to CNT resonator mass, which includes self-mass of the CNT resonator and attached mass. The change of attached mass on the CNT resonator triggers a change to the resonant frequency [27]. The sensitivity defined as the ratio of frequency shift to unit mass loaded is a linear function with the square of the mode number. Advantages of distributed mass load spanning the entire sensor surface in biological and chemical applications were discussed [28–30].

Innovations in microfabrication and nanofabrication technologies are permitting to attain significantly smaller mechanical transducers with micro-sized and nano-sized moving elements whose deformation and vibration are sensitively altered upon molecular adsorption. This type of mechanical biosensors is known as nanomechanical biosensors. The utilization of well-established semiconductor engineering allows the batch production of arrays of numerous nanomechanical systems. In general, all the nanomechanical biosensors are cantilever-shaped. So, developing the cantilever or bridge-type mechanical nanobiosensor is getting an important role in emerging medical industry.

In this study, we developed a computationally efficient single-wall carbon nanotube as a biological mass sensor with the continuum mechanics method using the finite element method. Using the biological objects such as insulin hormone, immunoglobulin G (IgG), and low-density lipoproteins (LDL) masses as a distributed load, the mass sensing investigations are carried out. In this study, fixed-free and fixed-fixed type single-wall carbon nanotubes with various lengths of relative frequency shifts and sensitivity analysis are examined. Additionally, the sensitivity analysis of fixed-free and fixed-fixed type CNT biological mass sensors is carried out.

2. Vibration Analysis of the CNT Model with Distributed Mass

Euler-Bernoulli theory is used to model SWCNT as resonators via continuum mechanics [31–33]. The motion of free vibration equation can be expressed as

$$EI \frac{\partial^4 u(x, t)}{\partial x^4} + \rho A \frac{\partial^4 u(x, t)}{\partial x^4} = 0, \quad (1)$$

where $u(x, t)$, E , I , and ρ are considered as the transverse deflection, Young's modulus, second moment of the cross-sectional area A , and the density of SWCNT, respectively. The fundamental frequency can be expressed as

$$f_n = \frac{1}{2\pi} \sqrt{\frac{k_{eq}}{m_{eq}}}, \quad (2)$$

where k_{eq} is the equivalent stiffness, and m_{eq} is the first mode vibration of attached mass with SWCNT mass. In this study, two different boundary constraints named as fixed-free and

fixed-fixed type is considered for the mass sensing analysis of the biosensor.

2.1. Analysis of SWCNT with Fixed-Free Boundary Condition. Figure 1 shows SWCNT with fixed-free boundary condition. By taking into account, the length L of SWCNT is perturbed with the uniform mass M , i.e., at $x=L$. The resonance frequencies of fixed-free SWCNT can be attained from

$$f_j = \frac{\lambda_j^2}{2\pi} \sqrt{\frac{EI}{\rho AL}}, \quad (3)$$

where λ_j values are acquired [34] and expressed the subsequent transcendental equation

$$\cos \lambda \cosh \lambda + 1 = 0. \quad (4)$$

The mode shapes of vibrations can be attained as

$$Y_j(\xi) = \left(\cosh \lambda_j \xi - \cos \lambda_j \xi \right) - \left(\frac{\sinh \lambda_j - \sin \lambda_j}{\cosh \lambda_j - \cos \lambda_j} \right) \cdot \left(\sinh \lambda_j \xi - \sin \lambda_j \xi \right), \quad (5)$$

where $\xi = x/L$ is the length of CNTs along normalized coordinate. The first mode of vibration is significant for the sensing applications, and the value is $\lambda_1 = 1.8751$ [35]. The value is attained by executing the transcendental (4).

$$k_{eq} = 12.36 \frac{EI}{L^3}; \quad (6)$$

$$m_{eq} = \rho AL + 4M.$$

Since we have applied distributed load where

$$M = m \times \gamma L, \quad (7)$$

$$f_n = \frac{1}{2\pi} \sqrt{\frac{k_{eq}}{m_{eq}}} = \frac{1}{2\pi} \frac{\alpha_k \beta}{\sqrt{1 + \alpha_m \Delta M}}, \quad (8)$$

where

$$\alpha_k = 3.5,$$

$$\alpha_m = 4,$$

$$\Delta M = \frac{M}{\rho AL}, \quad (9)$$

$$\beta = \sqrt{\frac{EI}{\rho AL^4}}.$$

2.2. Analysis of SWCNT with Fixed-Fixed Boundary Condition. For the fixed-fixed boundary condition shown in Figure 2, the motion and the natural frequency equations are followed by (1) and (2), respectively.

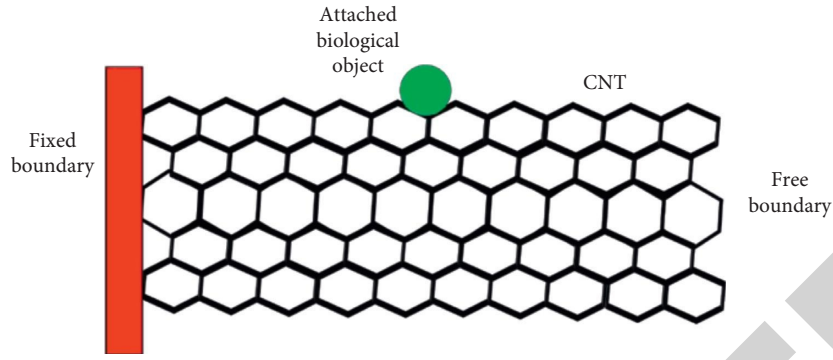


FIGURE 1: SWCNT with fixed-free boundary condition.

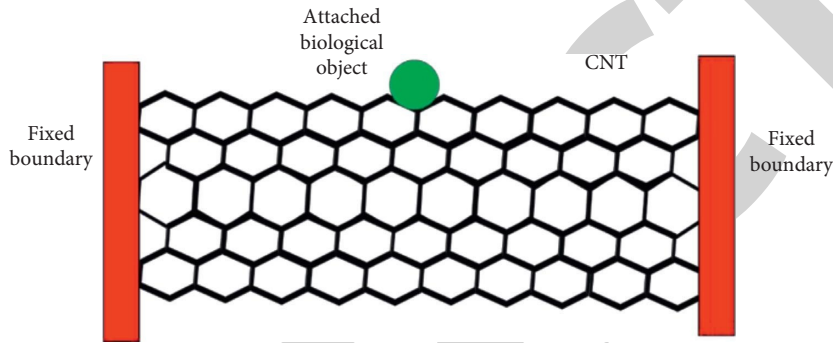


FIGURE 2: SWCNT with fixed-fixed boundary condition.

Moreover, the λ_j values are attained [34] by executing

$$\cos \lambda \cosh \lambda + 1 = 0. \quad (10)$$

The mode shape of vibration is stated as

$$Y_j(\xi) = (\cosh \lambda_j \xi - \cos \lambda_j \xi) - \left(\frac{\cosh \lambda_j - \cos \lambda_j}{\sinh \lambda_j - \sin \lambda_j} \right) (\sinh \lambda_j \xi - \sin \lambda_j \xi), \quad (11)$$

where $\xi = x/L$, and the value of first mode vibration is $\lambda_1 = 4.7300$ [35]. Using equation (6), the mode shape normalizing is carried out.

$$k_{eq} = 500.56 \frac{EI}{L^3}; \quad (12)$$

$$m_{eq} = \rho AL + 2.52M.$$

Since we have applied distributed load and $M = m \times \gamma L$,

$$f_n = \frac{1}{2\pi} \sqrt{\frac{k_{eq}}{m_{eq}}} \quad (13)$$

$$= \frac{1}{2\pi} \frac{\alpha_k \beta}{\sqrt{1 + \alpha_m \Delta M}},$$

where

$$\alpha_k = 22.37,$$

$$\alpha_m = 2.52,$$

$$\Delta M = \frac{M}{\rho AL}, \quad (14)$$

$$\beta = \sqrt{\frac{EI}{\rho AL^4}}.$$

2.3. Analysis of Mass Detection. For the free vibrations of CNT substituting $\Delta M = 0$ in (8), the resonant frequency is attained as

$$f_{0n} = \frac{1}{2\pi} \alpha_k \beta. \quad (15)$$

From (13) and (15), the resonant frequency shift attained due to the distributed attached mass can be expressed as

$$\Delta f = f_{0n} - f_n \quad (16)$$

$$= f_{0n} - \frac{f_{0n}}{\sqrt{1 + \alpha_m \Delta M}},$$

and the added mass actual value can be attained as

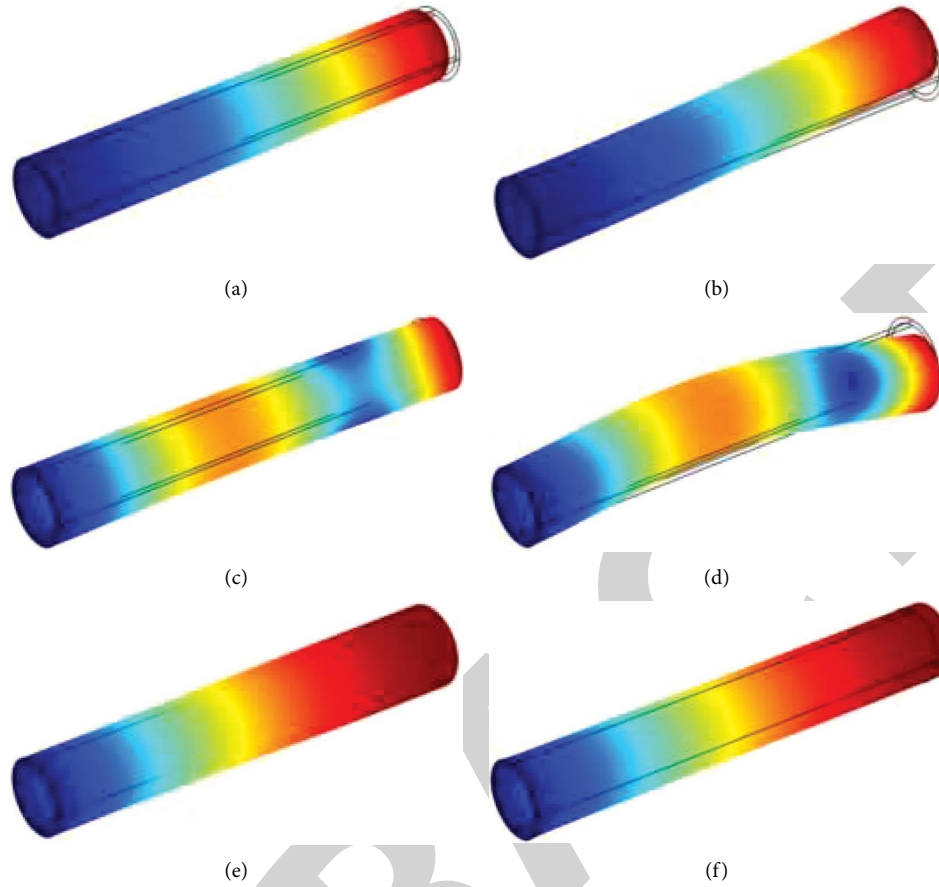


FIGURE 3: Fixed-free carbon nanotube fundamental frequency analysis for L/D ratio 7.2. (a) Fundamental frequencies F1, (b) F2, (c) F3, (d) F4, (e) F5, and (f) F6.

$$M = \frac{\rho AL}{\alpha_m} \frac{(\alpha_k^2 \rho^2)}{(\alpha_k \beta - 2\pi \Delta f)^2} - \frac{\rho AL}{\alpha_m} \quad (17)$$

The (17) relates the added mass with the shift of frequency.

3. Model Validation

Figures 3 and 4 show the fixed-free and fixed-fixed based CNT models' mode shapes for 6 fundamental frequency levels for the length to diameter ratio 7.27 for getting the precision of our model. To find the accuracy of the present CNT model, initially, our finite element CNT model is verified with previous molecular dynamics and commercially available finite element model for the same material properties and the dimensions.

Figure 5 shows the fundamental frequency comparisons for the present FEM work with the existing work. The results are compared with the previous study and will be agreed with that study. The values of the existing work and present work are given in Table 1. From the table, it has been clearly demonstrated that our model CNT provides minimum discrepancy compared to the previous length to diameter ratio studies, and it provides the assurance to take on further

studies as a biological mass sensor. The value of E and ρ is taken as 1:0 TPa and 2:24 g/cc, respectively [53].

4. Results and Discussion

4.1. Resonant Frequency Analysis for Fixed-Free Boundary.

The continuum mechanics single-wall CNT is modelled as fixed-free beam, where one end is to be fixed and other end is to be free. Figure 6 shows the fixed-free type CNT. Distributed load is uniformly applied on CNT. The fixed-free CNT is initially assumed straight and no extensile and loaded the distributed forces uniformly. From this technique, the mechanical behavior of the nanoresonator biosensor solutions provided is accurate and reliable. Using this system, the mode shapes analysis and frequency shift studies of the nanobiosensor are performed. Figure 7(a) shows SWCNT from fundamental frequency to six changes of frequencies without attaching any mass on CNT. In the fixed-free mode, the length of the carbon nanotube is changed from 2 nm to 20 nm to obtain the various results and mode shapes analysis up to 6 levels. The diameter of the carbon nanotube is 1.1 nm for all the studies in this work. The change of frequencies is in GHz. To understand SWCNT as a nanobiomass sensor, in this study, three

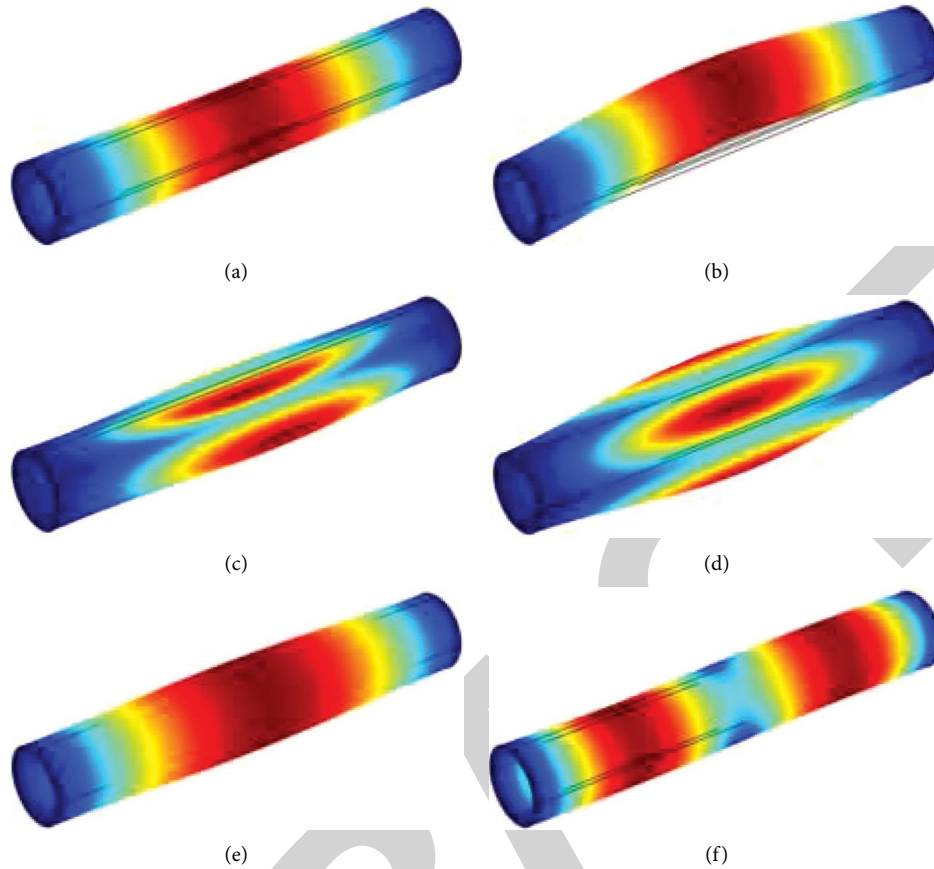


FIGURE 4: Fixed-fixed carbon nanotube fundamental frequency analysis for L/D ratio 7.2. (a) Fundamental frequencies F1, (b) F2, (c) F3, (d) F4, (e) F5, and (f) F6.

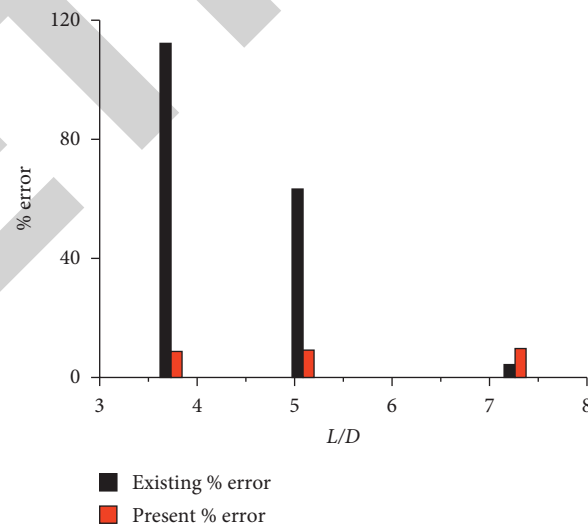


FIGURE 5: Fundamental frequency comparisons for the present FEM work with existing works.

biological objects insulin hormone, immunoglobulin G (IgG), the most abundant type of antibody, and low-density lipoproteins (LDL) masses are considered. The mass values

of insulin hormone 9.644 zg, immunoglobulin G 249.081 zg, and low-density lipoproteins 4981.620 zg are taken into account for the analysis. Compared to different

TABLE 1: Fundamental frequency comparisons for the present FE work with existing MD work.

<i>L/D</i>	Fundamental frequencies	MD [17]	FE [27]	% error	Present	% error
3.727	F1	10.315	10.769	-4.40	9.409	-8.78
	F2	10.315	10.769	-4.40	9.411	-8.75
	F3	10.478	16.859	-60.90	9.945	-5.08
	F4	10.478	22.224	-112.10	9.946	-5.07
	F5	15.796	22.224	-40.69	14.589	-7.63
5.090	F1	6.616	6.683	-4.04	6.561	-0.82
	F2	6.616	6.884	-4.05	6.561	-0.82
	F3	9.143	12.237	-33.84	8.329	-8.89
	F4	9.143	14.922	-63.21	8.333	-8.85
	F5	11.763	14.924	-26.87	10.986	-6.60
7.272	F1	3.800	3.900	-2.63	3.845	1.19
	F2	3.800	3.900	-2.63	3.845	1.20
	F3	8.679	8.659	-0.23	7.840	-9.65
	F4	8.679	9.034	-4.09	7.844	-9.61
	F5	8.801	9.034	-2.65	8.189	-6.94

Present work provided better error results than previous works.



FIGURE 6: Fixed-free boundary fundamental frequency analysis (one end is fixed and another one end is free).

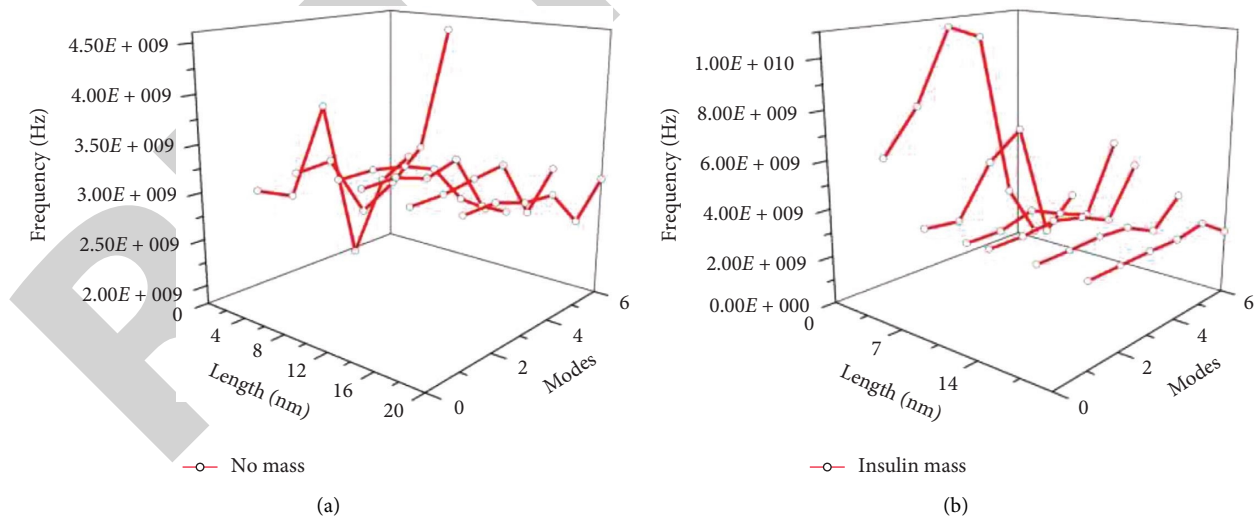


FIGURE 7: Continued.

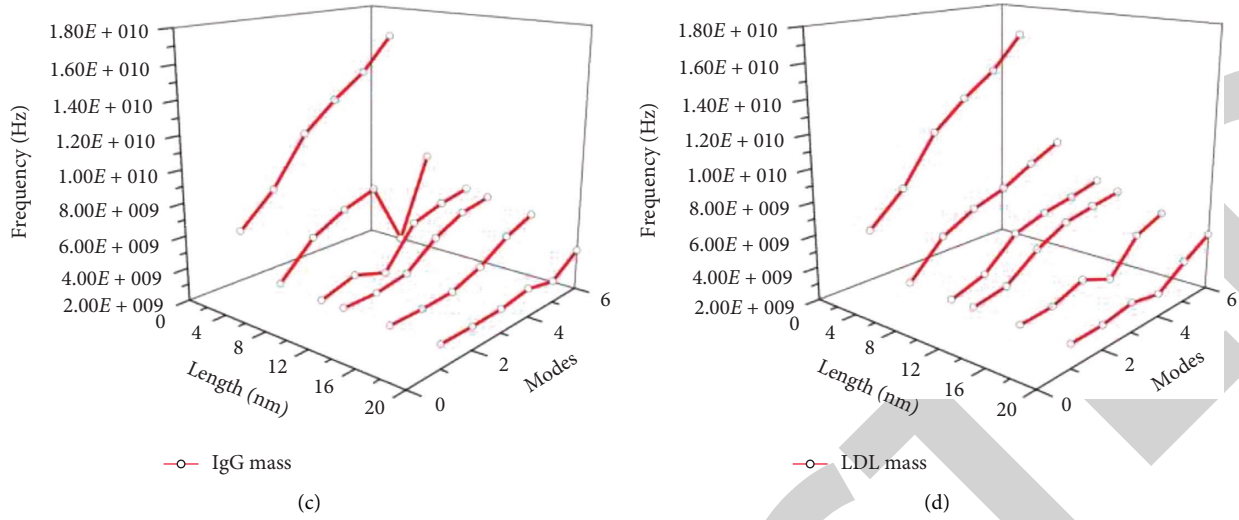


FIGURE 7: (a) Fixed-free boundary fundamental frequency for CNT with no mass and frequency shift analysis for (b) insulin, (c) IgG, and (d) LDL biological objects mass attached.



FIGURE 8: Fixed-fixed boundary fundamental frequency analysis (both the ends are fixed).

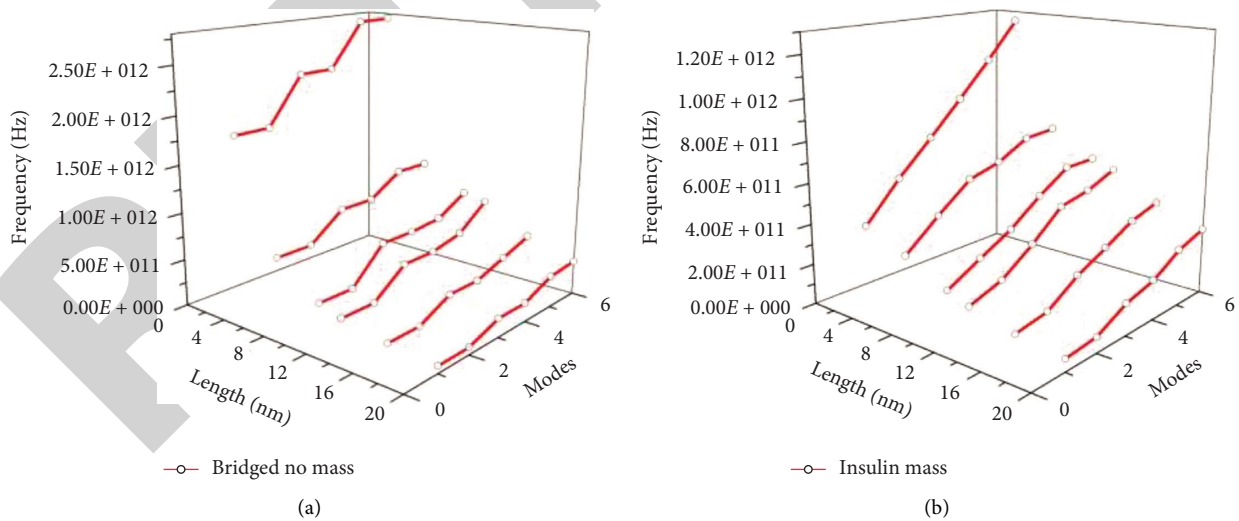


FIGURE 9: Continued.

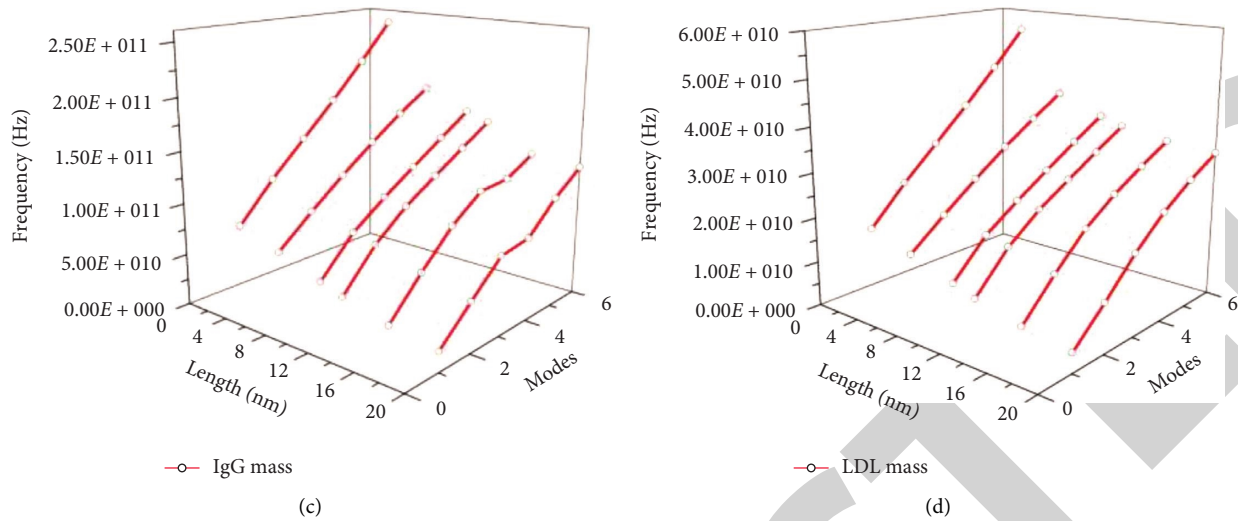


FIGURE 9: (a) Fixed-fixed boundary fundamental frequency for CNT with no mass and frequency shift analysis for (b) insulin, (c) IgG, and (d) LDL biological objects mass attached.

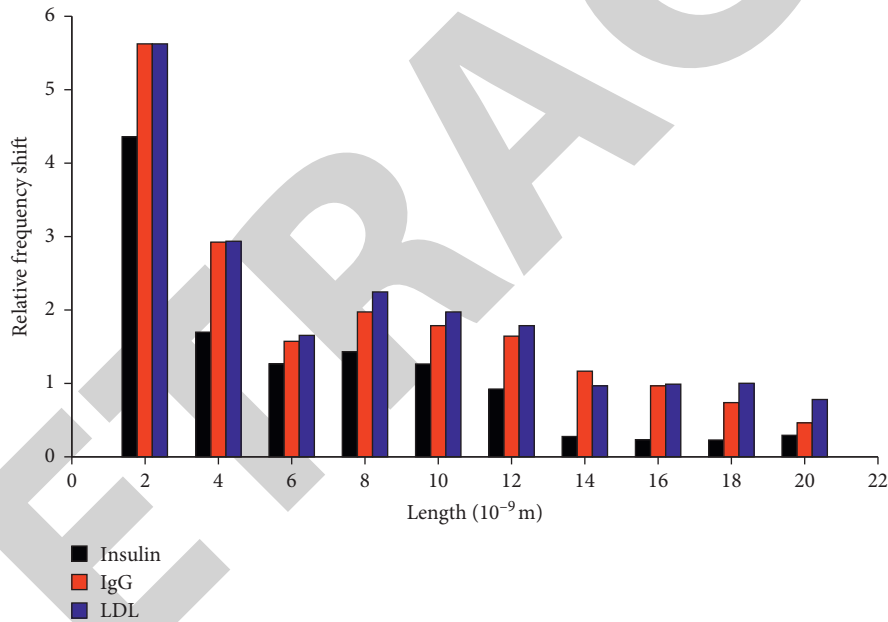


FIGURE 10: Comparisons of fixed-free boundary relative frequency shift analysis for CNT.

distributed uniform masses attached with fixed-free SWCNT, the frequency changes occurred reasonably. The mode shape and frequency shift changes are shown in Figures 7(b)–7(d). From the results, it can be understood that the lower dimensions CNT highly varied rather than higher dimensions CNT.

4.2. Resonant Frequency Analysis for Fixed-Fixed Boundary.

Both the boundary ends of SWCNT is fixed and is investigated with the no mass and with the added mass of insulin hormone, immunoglobulin G, and low-density lipoproteins independently for the various length of CNT. While adding mass on the bridge-type SWCNT, mode shapes variations are very high. Figure 8 shows the

fixed-fixed type CNT. Figures 9(a)–9(d) show SWCNT resonant frequency with no mass and the insulin hormone, immunoglobulin G, (IgG), and low-density lipoproteins (LDL) masses.

From the results, compared to no mass CNT resonant frequency and the insulin hormone, IgG, and LDL masses, it can be understood that when the mass of objects increases, the resonant frequency of CNT reduces. The higher mass of the low-density lipoproteins (LDL) resonant frequency is lower than others.

4.3. Comparisons of Relative Frequency Shift Analysis for Fixed-Free and Fixed-Fixed Type CNT.

To identify various biomasses sensing for different biological objects, the

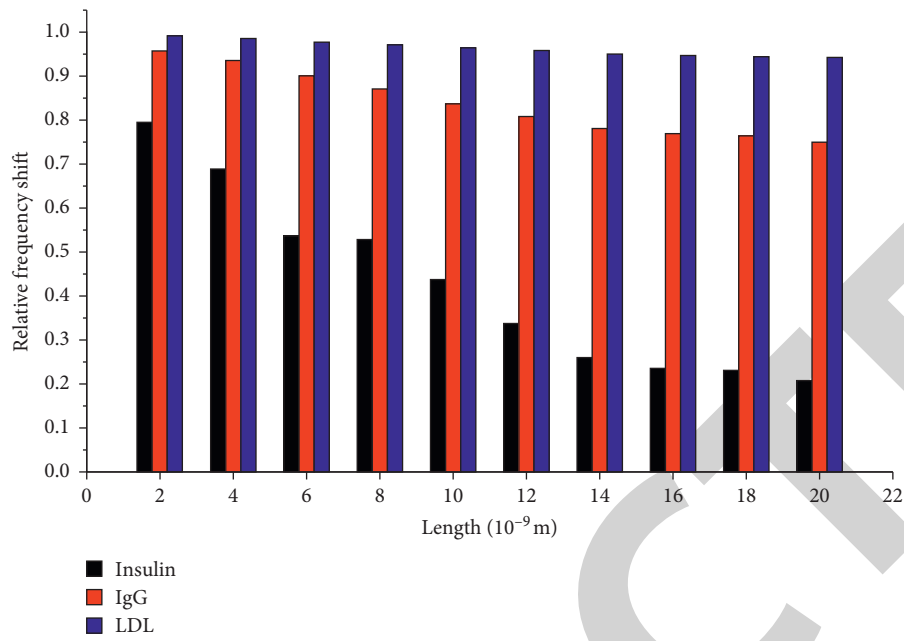
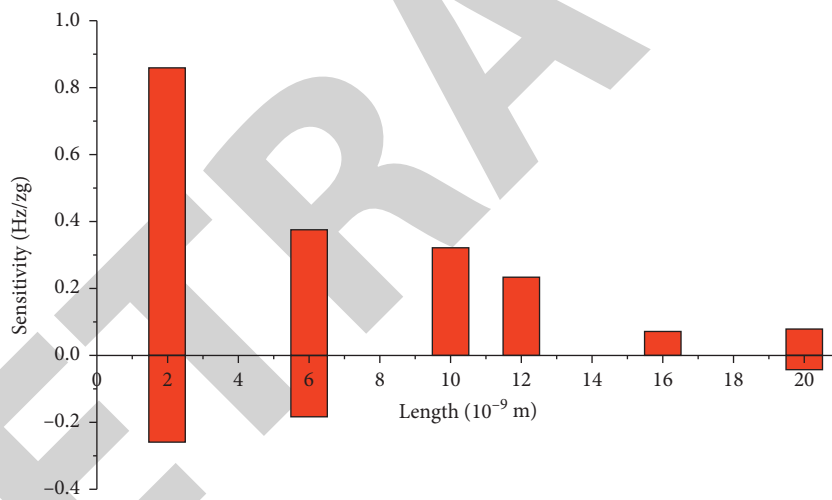


FIGURE 11: Comparisons of fixed-fixed boundary relative frequency shift analysis for CNT.



(a)

FIGURE 12: Continued.

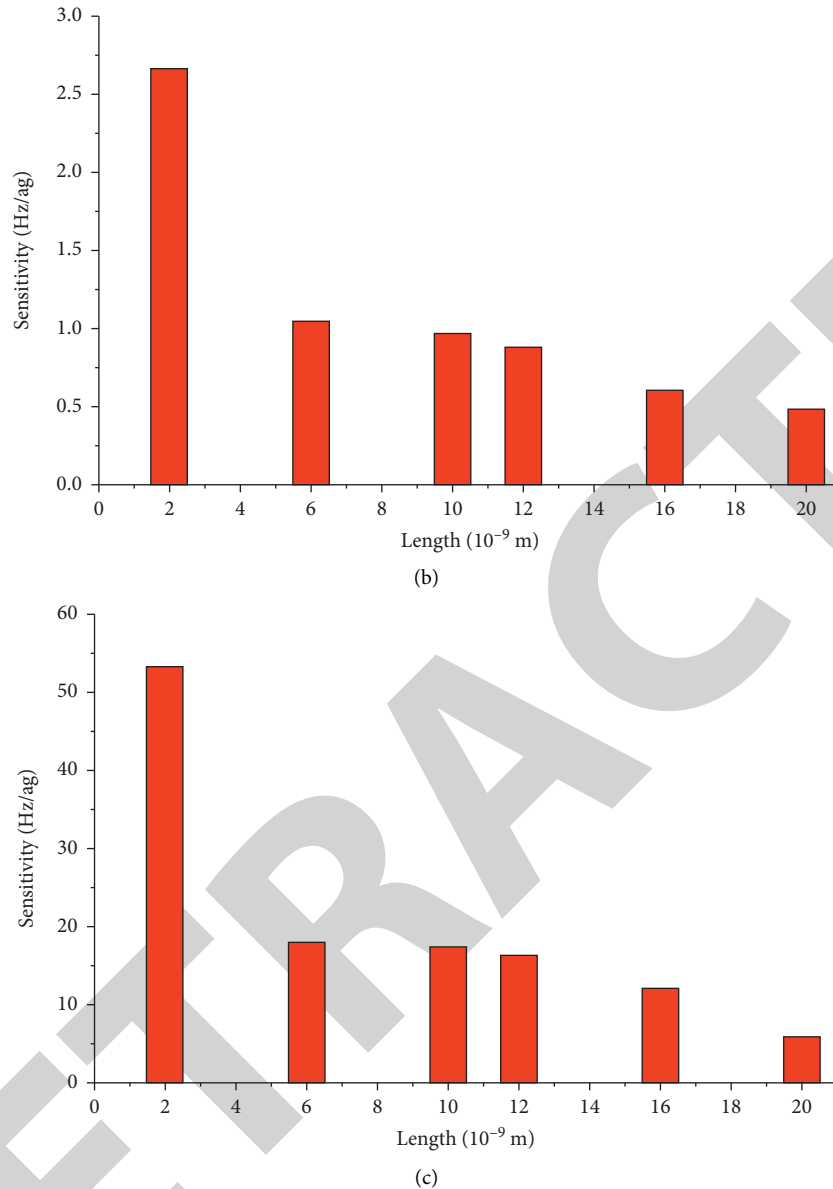


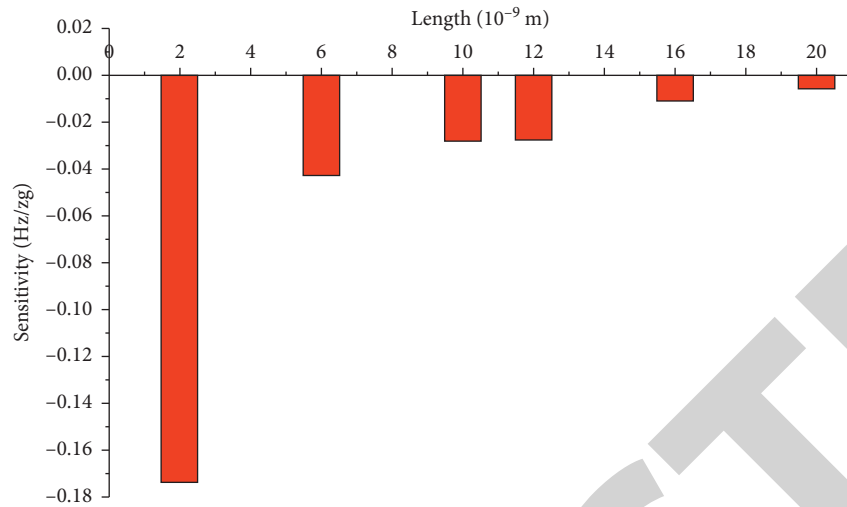
FIGURE 12: Fixed-free boundary sensitivity analysis for (a) insulin, (b) IgG, and (c) LDL biological objects mass attached.

frequency shift studies are carried out for fixed-free and fixed-fixed SWCNT. Figure 10 shows the frequency shift results of the insulin, IgG, and LDL biological sensing output on fixed-free SWCNT. Figure 10 shows that when the length of the CNT is reduced, the frequency shift is increased. But the length of CNT 6–12 nm provides better variation frequency shift for biosensing.

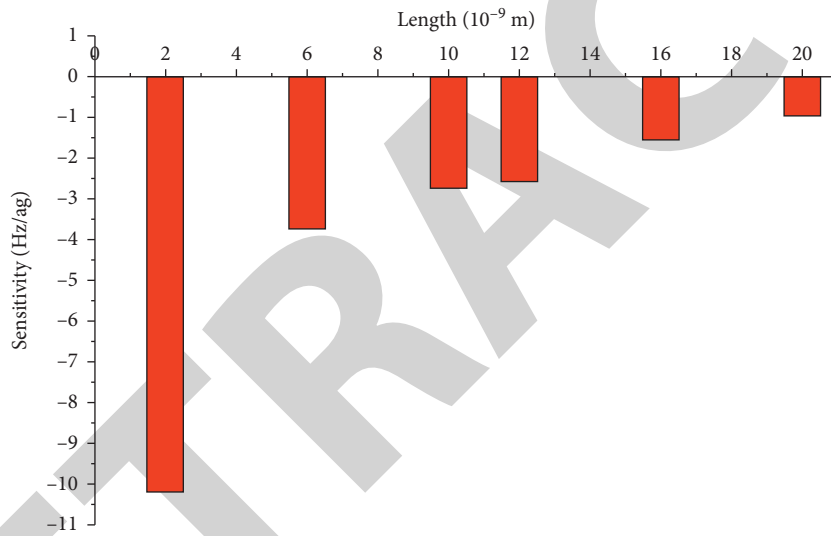
Figure 11 shows the results of the fixed-fixed type SWCNT frequency shift for various biological objects. Since both the ends are fixed, the relative frequency shift results show the clear difference between all the length of CNTs and insulin, IgG, and LDL mass sensing. Reducing the length of the CNT provides higher shifts rather than higher length CNTs.

4.4. Sensitivity Analysis for Fixed-Free and Fixed-Fixed Type CNT. To investigate the accuracy of biomass sensing for different biological objects, the sensitivity studies are important. Figures 12(a)–12(c) show insulin, IgG, and LDL sensing for the fixed-free CNT. Based on the mass of the insulin, IgG, and LDL, the sensitivity level has been varied, and it can be clearly identified. The sensitivity level gets high, when the length of CNT is reduced. When adding the low mass of insulin, the zeptogram level sensitivity is achieved, and when the mass increased for IgG and LDL, attogram sensitivity is attained.

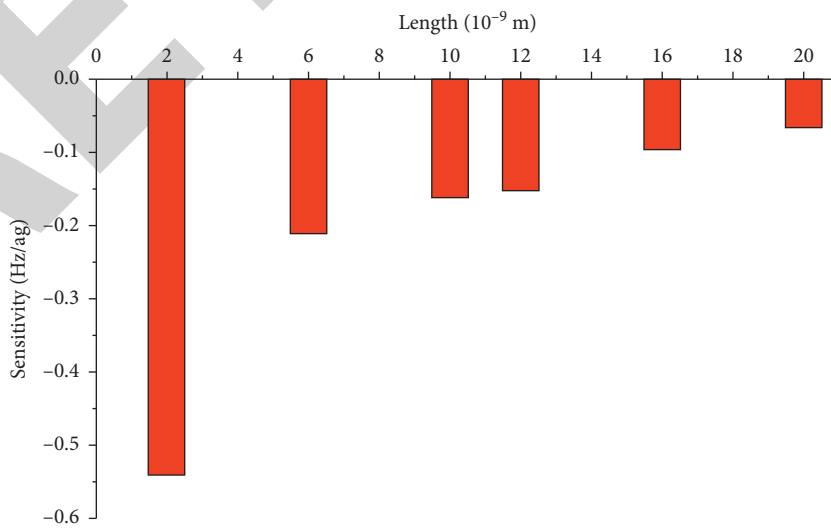
Figures 13(a)–13(c) show insulin, IgG, and LDL sensing for the fixed-fixed CNT. Insulin sensitivity is lower than IgG



(a)



(b)



(c)

FIGURE 13: Fixed-fixed boundary sensitivity analysis for (a) insulin, (b) IgG, and (c) LDL biological objects mass attached.

and LDL. Compared to the fixed-free type, the sensitivity is reduced in the fixed-fixed type CNT.

5. Conclusion

Biological sensing with the one-dimensional nanostructure is one of the vital roles in clinical and healthcare industries. In this study, we have modelled computationally efficient single-wall carbon nanotube as a biological mass sensor with the continuum mechanics technique using a finite element numerical package. The investigations are carried out using the resonant frequency analysis method. To prove the accuracy of the model, the SWCNT model is tested with the previous study [27]. Insulin hormone, immunoglobulin G (IgG), and low-density lipoproteins (LDL) masses are considered for analyzing as a biological mass sensor. In this study, fixed-free and fixed-fixed type single-wall carbon nanotubes with various lengths of relative frequency shifts are studied for insulin, IgG, and LDL. Additionally, the sensitivity analysis of fixed-free and fixed-fixed type CNT biological mass sensor is carried out. This study clearly shows that the change of biological object masses will change the frequency shift and the sensitivity of the SWCNT sensor. From the outcomes, it can be understood that SWCNT can be employed as a high-accuracy biological mass sensor for various biological objects when reducing the length of CNTs. While attaching the biological objects in the CNT nanobiosensor, the complications in measuring high number of vibration modes and loss of mechanical energy in liquids have to be explored in future.

Data Availability

The data used to support the findings of this study are included within the article.

Conflicts of Interest

The authors declare that they have no conflicts of interest.

References

- [1] S. Iijima, "Helical microtubules of graphitic carbon," *Nature*, vol. 354, no. 6348, p. 56, 1991.
- [2] S. Iijima and T. Ichihashi, "Single-shell carbon nanotubes of 1-nm diameter," *Nature*, vol. 363, no. 6430, pp. 603–605, 1993.
- [3] P. M. Ajayan, "Nanotubes from carbon," *Chemical Reviews*, vol. 99, no. 7, pp. 1787–1800, 1999.
- [4] P. M. Ajayan, J.-C. Charlier, and A. G. Rinzler, "Carbon nanotubes: from macromolecules to nanotechnology," *Proceedings of the National Academy of Sciences*, vol. 96, no. 25, Article ID 14199, 1999.
- [5] Y. Lin, S. Taylor, H. Li et al., "Advances toward bio-applications of carbon nanotubes," *Journal of Materials Chemistry*, vol. 14, no. 4, p. 527, 2004.
- [6] L. Gu, T. Elkin, X. Jiang et al., "Single-walled carbon nanotubes displaying multivalent ligands for capturing pathogens," *Chemical Communications*, vol. 7, no. 7, p. 874, 2005.
- [7] G. Maduraiveeran and M. Sasidharan, "Electrochemical sensor and biosensor platforms based on advanced nanomaterials for biological and biomedical applications," *Biosensors and Bioelectronics*, vol. 103, pp. 113–129, 2018.
- [8] Z. Zhu, "An overview of carbon nanotubes and graphene for biosensing applications," *Nano-Micro Letters*, vol. 9, no. 3, p. 25, 2017.
- [9] M. M. Rahman, M. A. Hussein, M. Abdel Salama, and M. Abdullah, "Fabrication of an l-glutathione sensor based on PEG-conjugated functionalized CNT nanocomposites: a real sample analysis," *New Journal of Chemistry*, vol. 41, Article ID 10761, 2017.
- [10] N. W. Shi Kam, M. O'Connell, J. A. Wisdom, and H. Dai, "Carbon nanotubes as multifunctional biological transporters and near-infrared agents for selective cancer cell destruction," *Proceedings of the National Academy of Sciences*, vol. 102, no. 33, Article ID 11600, 2005.
- [11] N. Wong Shi Kam and H. Dai, "Single walled carbon nanotubes for transport and delivery of biological cargos," *Physica Status Solidi (B)*, vol. 243, no. 13, pp. 3561–3566, 2006.
- [12] L. s. Lacerda, S. Raffa, M. Prato, A. Bianco, and K. Kostarelos, "Cell-penetrating CNTs for delivery of therapeutics," *Nano Today*, vol. 2, no. 6, pp. 38–43, 2007.
- [13] M. Prato, K. Kostarelos, and A. Bianco, "Functionalized carbon nanotubes in drug design and discovery," *Accounts of Chemical Research*, vol. 41, no. 1, pp. 60–68, 2008.
- [14] H. Wang, L. Gu, Y. Lin et al., "Unique aggregation of anthrax (bacillusanthracis) spores by sugar-coated single-walled carbon nanotubes," *Journal of the American Chemical Society*, vol. 128, no. 41, Article ID 13364, 2006.
- [15] C. Li and T.-W. Chou, "Single-walled carbon nanotubes as ultrahigh frequency nanomechanical resonators," *Physical Review B*, vol. 68, no. 7, p. 3, 2003.
- [16] R. H. Baughman, C. Cui, A. A. Zakhidov et al., "Carbon nanotube Actuators Carbon," *Science*, vol. 284, no. 5418, pp. 1340–1344, 1999.
- [17] C. Li and T.-W. Chou, "Mass detection using carbon nanotube-based nanomechanical resonators," *Applied Physics Letters*, vol. 84, no. 25, pp. 5246–5248, 2004.
- [18] J. Chaste, A. Eichler, J. Moser, G. Ceballos, R. Rurali, and A. Bachtold, "A nanomechanical mass sensor with yoctogram resolution," *Nature Nanotechnology*, vol. 7, no. 5, pp. 301–304, 2012.
- [19] S. C. Tsang, J. J. Davis, M. L. H. Green, H. A. O. Hill, Y. C. Leung, and P. J. Sadler, "Immobilization of small proteins in carbon nanotubes: high-resolution transmission electron microscopy study and catalytic activity," *Journal of the Chemical Society, Chemical Communications*, no. 17, p. 1803, 1995.
- [20] J. Jason, M. Davis, L. H. Arcolm et al., "The immobilisation of proteins in carbon nanotubes," *Inorganica Chimica Acta*, vol. 272, no. 1–2, p. 261, 1998.
- [21] S. S. Wong, E. Joselevich, A. T. Woolley, C. L. Cheung, and C. M. Lieber, "Covalently functionalized nanotubes as nanometre- sized probes in chemistry and biology," *Nature*, vol. 394, no. 6688, pp. 52–55, 1998.
- [22] T. Hornig, "Analytical solution of vibration analysis on fixed-free single-walled carbon nanotube-based mass sensor," *Journal of Surface Engineered Materials and Advanced Technology*, vol. 2, no. 1, pp. 47–52, 2012.
- [23] R. C. Haddon, "Carbon nanotubes," *Accounts of Chemical Research*, vol. 35, no. 12, p. 997, 2002.
- [24] C. H. Park, V. Schroeder, B. J. Kim, and T. M. Swager, "Ionic liquid-carbon nanotube sensor arrays for human breath related volatile organic compounds," *ACS Sensors*, vol. 3, no. 11, pp. 2432–2437, 2018.

Retraction

Retracted: Synthesis, Mechanical, and Tribological Performance Analysis of Stir-Casted AA7079: ZrO₂ + Si₃N₄ Hybrid Composites by Taguchi Route

Advances in Materials Science and Engineering

Received 26 December 2023; Accepted 26 December 2023; Published 29 December 2023

Copyright © 2023 Advances in Materials Science and Engineering. This is an open access article distributed under the Creative Commons Attribution License, which permits unrestricted use, distribution, and reproduction in any medium, provided the original work is properly cited.

This article has been retracted by Hindawi, as publisher, following an investigation undertaken by the publisher [1]. This investigation has uncovered evidence of systematic manipulation of the publication and peer-review process. We cannot, therefore, vouch for the reliability or integrity of this article.

Please note that this notice is intended solely to alert readers that the peer-review process of this article has been compromised.

Wiley and Hindawi regret that the usual quality checks did not identify these issues before publication and have since put additional measures in place to safeguard research integrity.

We wish to credit our Research Integrity and Research Publishing teams and anonymous and named external researchers and research integrity experts for contributing to this investigation.

The corresponding author, as the representative of all authors, has been given the opportunity to register their agreement or disagreement to this retraction. We have kept a record of any response received.

References

- [1] G. Jegan, P. Kavipriya, T. Sathish, S. Dinesh Kumar, T. Samraj Lawrence, and T. Vino, "Synthesis, Mechanical, and Tribological Performance Analysis of Stir-Casted AA7079: ZrO₂ + Si₃N₄ Hybrid Composites by Taguchi Route," *Advances in Materials Science and Engineering*, vol. 2021, Article ID 7722370, 15 pages, 2021.

Research Article

Synthesis, Mechanical, and Tribological Performance Analysis of Stir-Casted AA7079: $ZrO_2 + Si_3N_4$ Hybrid Composites by Taguchi Route

G. Jegan,¹ P. Kavipriya,¹ T. Sathish,² S. Dinesh Kumar,³ T. Samraj Lawrence ,⁴ and T. Vino¹

¹Department of Electronics and Communication Engineering, Sathyabama Institute of Science and Technology, Chennai 600 119, Tamil Nadu, India

²Department of Mechanical Engineering, Saveetha School of Engineering, SIMATS, Chennai 600 125, Tamil Nadu, India

³Department of Mechanical Engineering, St. Peter's Institute of Higher Education and Research, Avadi, Chennai 600 054, Tamil Nadu, India

⁴Department of Information Technology, College of Engineering and Technology, Dambi Dollo University, Dambi Dollo, Oromia Region, Ethiopia

Correspondence should be addressed to T. Samraj Lawrence; samrajlawrencet@gmail.com

Received 24 May 2021; Accepted 8 June 2021; Published 19 June 2021

Academic Editor: Samson Jerold Samuel Chelladurai

Copyright © 2021 G. Jegan et al. This is an open access article distributed under the Creative Commons Attribution License, which permits unrestricted use, distribution, and reproduction in any medium, provided the original work is properly cited.

Currently, the aluminum alloys are utilized more in level of all industries for different applications; furthermore, industries need high-strength alloys for making innovative components. For those reasons, many researchers hope to prepare hybrid aluminum metal matrix composites at various composition levels. In this experimental work, we intended to prepare the hybrid metal matrix composites such as aluminum alloy 7079 with reinforcement of $ZrO_2 + Si_3N_4$ through stir-casting process. Major findings of this work, as to optimize the stir-casting process, can be to continually conduct wear test and evaluate the microhardness of the stir-casted specimens. Optimization of stir-casting process parameters is a preliminary work for this research by Taguchi tool. The chosen parameters are % of reinforcement (0%, 4%, 8%, and 12%), agitation speed (450 rpm, 500 rpm, 550 rpm, and 600 rpm), agitation time (15 min, 20 min, 25 min, and 30 min), and molten temperature (700°C, 750°C, 800°C, and 850°C). The prepared stir-casted materials are tested by wear analysis and microhardness analysis, through Pin-on-Disc wear tester and Vickers hardness tester, respectively. Wear parameters are optimized, the minimum wear rate is evaluated, and also the wear worn-out surfaces are examined through SEM analysis.

1. Introduction

Aluminum alloys provide excellent mechanical properties for all types fabrication process, as well as machinability characteristics; further, its strength can be increased by adding reinforcement particles. Addition of hard ceramic particles offers good strength of the alloy materials and also enhances the mechanical properties.

Wang et al. [1] investigated the tribological and mechanical strength of the magnesium matrix composites; they prepared the AZ91 magnesium alloy with accumulation of graphite particles. Graphite is added at 5%, 10% of volume fraction levels to the magnesium alloy, and compared to

both levels of volume fraction, the 10% reduces the wear rate. On the contrary, 10% of graphite can decrease the mechanical strength such as yield strength, tensile strength, and elongation. In the base alloy using 5% of graphite, it can be simply refined well in condition and form a uniform mixture.

Fenghong et al. [2] prepared the aluminum hybrid metal matrix composites with the addition of silicon carbide and tungsten carbide using stir-casting process. The authors are evaluating the mechanical strength and wear properties of the composites in a detailed experimental work. In the microstructural study, silicon carbide and tungsten carbide particles are mixed in an unvarying manner into the

aluminum alloy material. Higher hardness values are examined in all measurements due to extreme merger of the reinforcement particles to the base materials. Wear resistance of the composites is enormously increased for the massive fusion of the hard particles in the stir-casting process.

Palanikumar et al. [3] carried out the wear analysis of aluminum alloy 6061 with addition of boron carbide and mica material; the composites are synthesized by stir-casting process. They conducted the wear test to examine the wear rate, as well as coefficient of friction of the stir-casted composite specimens. In the friction stir-casting process, the 70 μm of boron carbide particles and 10 μm of mica particles are added. For their investigations, the parameters of dry sliding wear test are chosen as applied load of 10 N, 20 N, and 30 N. Finally, the better wear reduction rate and coefficient of friction were obtained in the AA6061/B₄C/Mica composites in contrast with AA6061/B₄C composites.

Singh and Chauhan [4] investigated the wear performance of the aluminum matrix composites, namely, aluminum alloy together with silicon carbide and red mud prepared by stir-casting method. Statistical approach (Taguchi) is involved for their investigations, and parameters are preferred as percentage of red mud fraction, particle size and applied load, sliding distance, and sliding velocity. In their analysis, the sliding distance has chief parameter of influence in the wear loss examination; similarly, the applied load has extreme role of coefficient friction analysis. For this analysis, enhanced wear resistance was obtained through increasing level of red mud percentage and decrease of load and sliding distance.

Kurapati et al. [5] conducted the wear study of the aluminum alloy 2024 with added different percentage level of fly ash and silicon carbide. Reinforcement percentage of the fly ash and silicon carbide is taken in equivalent weight fraction with different percentage levels (5%, 10%, and 15%). The authors considered L27 orthogonal arrays for their investigation. Wear resistance of the composites is increased by the increase of applied load and sliding distance. Among the three parameters, the applied load was the higher influencing factor on the wear test compared to other factors such as sliding time and percentage of reinforcement.

Stir-casting process was highly involved to enhance the mechanical properties and strengthening of different alloy materials for reinforcement of hared particles [6–8]. Process parameters of the stir-casting method have a powerful role in the composite preparation, and each parameter is involved on its own characters [3, 9–11]. Combined parameters are modifying the result of the composites. Wear analysis has an extremely important role in the alloy materials to find the wear resistance. Generally, the wear test is conducted in either dry or wet conditions. In the wear test, important parts are to be considered such as weight loss, frictional force worn-out surfaces, and coefficient of friction [12–14]. Microhardness test involves measuring the hardness of the materials effectively and precisely. Compared to other hardness tests, the Vickers hardness test is the best suited method to measure the hardness, because the accuracy of testing and damage of the specimen is less [15–18]. In this

research, linked to all factors and deep study of literature, the aluminum metal matrix composites are chosen. For this experimental work, we considered the base material as aluminum alloy 7079 with reinforced particles of zirconium oxide (ZrO₂) and silicon nitride (Si₃N₄). Hybrid composites are prepared through stir-casting process, and the process parameters of the stir-casting are optimized by Taguchi route [19]. The main objectives of this work are to find the mechanical and tribological characteristics of the AMMC's for analysis of compaction characteristics of the powders. Hence, the stir-casted composites are tested by Pin-On-Disc apparatus for estimating of wear rate; further, the Vickers microhardness is used to measure the hardness value of the stir-casted part [20–22].

2. Materials

X-ray Fluorescence (XRF) technique was used to measure the elemental composition of the aluminum alloy material (AA7079).

Aluminum alloy 7079 material was selected for this study due to high corrosion resistance, extreme strength, better ductility, and excellent thermal and electrical properties [23–25]. These alloys are originally in wrought alloy, and it has extreme machinability nature. Highly stressed components used in the machineries, mobile industry apparatus, hydraulic valves manufacturing, and air wings parts are fabricated by AA7079 alloy. Zirconium oxide and silicon nitride particles are chosen as reinforced particles of this study. Exceptional strength of the reinforced particles is added to base material, and it can increase the strength of the base material [26–28]. Table 1 presents the chemical elements presents in the base material such as aluminum alloy AA7079.

3. Experimental Procedure

In the initial stage, the aluminum alloy and reinforced particles are stir-casted by using stir-casting process, and the process is to be controlled by influencing various process parameters. Further, the wear test and microhardness test are to be conducted [29–31]. Table 2 presents the different parameters and their levels of the stir-casting process. The L16 OA was executed; four parameters are used to cast the aluminum metal matrix hybrid composites, namely, % of reinforcement, agitation speed (rpm), agitation time (min), and molten temperature (°C).

Figure 1 illustrates the stir-casting process equipment and the setup. In this work, liquid state stir-casting is selected for obtaining homogeneous mixture of base materials and reinforced particles. AA7079 plates are sliced into small sizes and put into the 5 kg capacity of the crucible; further, the crucible is placed inside of the stir-casting machine [32–34]. Heating up the crucible using different temperature levels (700°C, 750°C, 800°C, and 850°C) is done up to melting the aluminum alloy. At the same time, the reinforced particles (zirconium oxide and silicon nitride) are preheated in the muffle furnace using of crucible, and both particles are taken with the same weight ratio but different percentage

TABLE 1: Chemical opus of aluminum alloy (AA7079).

Material	% of composition
Cr	0.2
Cu	0.5
Fe	0.2
Mg	3.5
Mn	0.24
Si	0.25
Zn	4.0
Ti	0.7
Al	Remaining

TABLE 2: Stir-casting process parameters and its levels.

S. no.	Parameters	Level 1	Level 2	Level 3	Level 4
1.	% of reinforcement	0	4	8	12
2.	Agitation speed (rpm)	450	500	550	600
3.	Agitation time (min)	15	20	25	30
4.	Molten temperature (°C)	700	750	800	850



FIGURE 1: Stir-casting process equipment and setup.

levels [35]. Further, both base material and reinforced particles are mixed well in the stir-casting machine with the aid of stirrer and various agitation speeds (450 rpm, 500 rpm, 550 rpm, and 600 rpm). Different agitation time periods (15 min, 20 min, 25 min, and 30 min) were maintained to obtain the homogeneous mixture of the composites. Finally, the molten material in the crucible was poured in the die for required shapes.

3.1. Wear Test. Constant levels of parameters are used to stir-casting the wear test specimens such as 8% of reinforcement, 600 rpm of agitation speed, 30 min of agitation time, and 850°C of molten temperature [36]. Table 3 presents the wear test parameters and its levels, and the parameters are, namely, % of reinforcement, applied load (N), disc speed (m/s), and sliding distance (m). All the parameters are having different set of value levels.

Wear test was conducted in the Pin-On-Disc apparatus for the model of DUCOM, and the wear of the specimens is

TABLE 3: Wear test process parameters and their levels.

S. no.	Parameters	Level 1	Level 2	Level 3	Level 4
1.	% of reinforcement	0	4	8	12
2.	Applied load (N)	15	25	35	45
3.	Disc speed (m/s)	1.0	1.5	2.0	2.5
4.	Sliding distance (m)	1000	1200	1400	1600

tested by dry sliding mode. The dry sliding wear test apparatus was illustrated in Figure 2, and different loads were applied based on the parameter involvement. All sixteen specimens are wear-tested as per the American Society of Testing Materials (ASTM G99) standard procedure, and the dimensions of the specimen were 40 mm in length and 12 mm in diameter.

Each specimen was tested by using different parameters based on the L16 Orthogonal Array arrangement. Figure 3 illustrates the wear test specimen of the 16 numbers.

3.2. Vickers Microhardness Test. Vickers microhardness testing is one of the optical measurement arrangements. The specimens are prepared as per the ASTM E-384 standards. The diamond indenter was used to measure the hardness value of the specimens by applying little amount of load, and the indentation was made on the surface of the specimen. Normally, the load variation in the Vickers hardness test is 10 gm to 1 kgf, and for this test, the 0.5 kgf load was applied. Figure 4 presents the microhardness test specimen of this experimental work.

4. Results and Discussion

4.1. Wear Test. Table 4 presents the experimental summary of wear test, and the minimum wear rate was obtained as 0.228 mm³/m for the contribution of 12% of reinforcement, 25 N of applied load, 2 m/s of disc speed, and 1000 m of sliding speed.

Table 5 presents the response table for means of wear test, and Table 6 presents the response table for S/N ratios of the wear test. All the input values are changed into mean and S/N ratio values of the wear test through Design of Experiments. From the wear test, the % of reinforcement was the extremely influenced parameter for effects in the wear test followed by sliding distance, applied load, and disc speed. The optimal parameter of the wear test was recorded as 12% of reinforcement, 25 N of applied load, 1.5 m/s of disc speed, and 1000 m of sliding speed.

Figures 5 and 6 illustrate the main effects plot for mean and S/N ratios of the wear test. Without reinforcement, the specimen was highly affected from the wear; hence, the wear rate was more. Further, increasing reinforcement percentage, the wear rate was reduced. At last, the higher percentage of reinforcement (12%) offered minimum wear rate. In applied load condition, initially, the wear rate was high in lower applied load; further, increasing applied load (25 N), the wear rate can be reduced suddenly. Once again, increasing applied load from 25 N to 45 N, the wear rate was increased. In disc speed condition, 1.5 m/s offered minimum level of wear rate; further, increasing disc speed, the wear



FIGURE 2: Stir-casting process equipment and setup.



FIGURE 3: Image of wear test specimens.



FIGURE 4: Image of Vickers microhardness test specimens.

rate also increased. For the sliding distance condition, the minimum level of sliding speed (1000 rpm) is recorded as lower wear rate, and continually increasing sliding distance, the wear rate was increased.

Figure 7 demonstrates the residual plots for wear rate. In the residual plot, all four graphs explain the parameters influence in single view. In normal probability plot, all

sixteen points touch the probability line, with few of them nearer to the line, and it can be reflected in the result of the wear rate, as conducted experimental runs were precise. In the fits plot, the points were scattered uniformly, and within the limits, this can register the selected parameters, and the response values are accurate. From the histogram plot, the all rectangle boxes are extremely close to each other. In the order plot, the points crossed the mean line both positively and negatively simultaneously. From these conditions, the experiment was conducted in an excellent way, and usage of the parameters was effective.

Figure 8 illustrates the experimental runs versus wear rate of the wear test. From the wear test, the experimental and predicted values are analyzed. In sixteen experimental runs, most of the experimental values are within the limit of predicted values; few were nearer and crossed the predicted values.

Figures 9(a)–9(c) illustrates the surface plot of the wear test. Figure 9(a) demonstrates the % of reinforcement versus the applied load. From this plot, the minimum wear was registered as the influence of minimum level of applied load and maximum level of reinforcement. Figure 9(b) presents the applied load versus the disc speed. In this plot, the maximum level of applied load and minimum level of disc speed offered minimum wear rate. Figure 9(c) exemplifies the disc speed versus the sliding distance. From this plot, the moderate level of disc speed and the minimum sliding distance offered minimum wear rate. Figure 9(d) represents the sliding distance versus the % of reinforcement. In this plot, the minimum sliding distance and maximum reinforcement percentage offered lower wear rate.

Figures 10(a)–10(p) illustrate the 3D Profilometric images of the wear specimens in sixteen numbers. These images were converted from the SEM images, and the colors simply identified the wear worn-out surfaces. Blue with white color represents the microns level of wear that can take place, the green color illustrates the moderate level of wear that took place, and finally the red color noticed that the high wear occurred on the surface of the specimens. In the color bar range of wear was marked in microns level. Figure 10(g) shows the minimum wear, Figures 10(h)–10(j) and 10(o) show the moderate wear, and Figures 10(a), 10(b), 10(d), and 10(k) show the high wear.

4.2. Vickers Microhardness Test. Table 7 illustrates the experimental summary of Vickers microhardness test, and the maximum hardness was recorded as 122 VHN. The maximum hardness values were obtained by the influence of the parameters 12% of reinforcement, agitation speed of 450 rpm, agitation time of 30 min, and molten temperature of 750°C.

Table 8 presents the response table for means of Vickers hardness test, and Table 9 presents the response table for S/N ratios of the Vickers hardness test. For these tables, all the input values are converted into mean and S/N ratio values of the Vickers hardness test through Design of Experiments. In the Vickers hardness test, the % of reinforcement was the

TABLE 4: Experimental summary of wear test.

Exp. runs	% of reinforcement	Applied load (N)	Disc speed (m/s)	Sliding distance (m)	Wear rate (mm ³ /m)
1	0	15	1.0	1000	0.572
2	0	25	1.5	1200	0.379
3	0	35	2.0	1400	0.792
4	0	45	2.5	1600	0.823
5	4	15	1.5	1400	0.548
6	4	25	1.0	1600	0.697
7	4	35	2.5	1000	0.418
8	4	45	2.0	1200	0.815
9	8	15	2.0	1600	0.734
10	8	25	2.5	1400	0.483
11	8	35	1.0	1200	0.392
12	8	45	1.5	1000	0.582
13	12	15	2.5	1200	0.676
14	12	25	2.0	1000	0.228
15	12	35	1.5	1600	0.346
16	12	45	1.0	1400	0.286

TABLE 5: Response table for means (wear test)

Level	% of reinforcement	Applied load (N)	Disc speed (m/s)	Sliding distance (°C)
1	0.6415	0.6325	0.4868	0.4500
2	0.6195	0.4468	0.4638	0.5655
3	0.6477	0.4870	0.6423	0.5273
4	0.3840	0.6265	0.6000	0.6500
Delta	0.2575	0.1858	0.1785	0.2000
Rank	1	3	4	2

TABLE 6: Response table for signal to noise ratios (wear test)—smaller is better.

Level	% of reinforcement	Applied load (N)	Disc speed (m/s)	Sliding distance (°C)
1	4.249	4.041	6.749	7.493
2	4.428	7.681	6.893	5.435
3	5.461	6.739	4.832	6.111
4	9.083	4.761	4.748	4.183
Delta	4.834	3.640	2.145	3.310
Rank	1	3	4	2

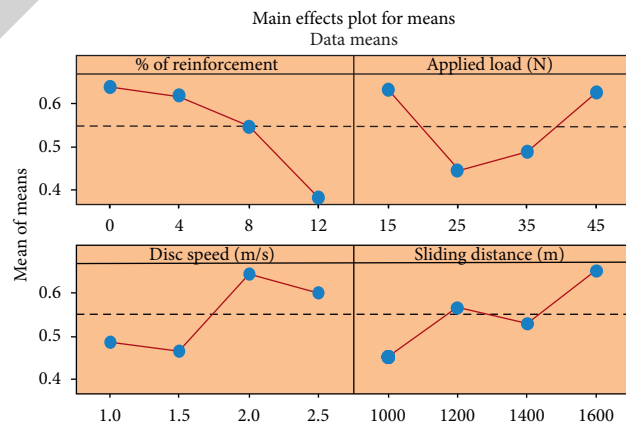


FIGURE 5: Main effects plot for means (wear test).

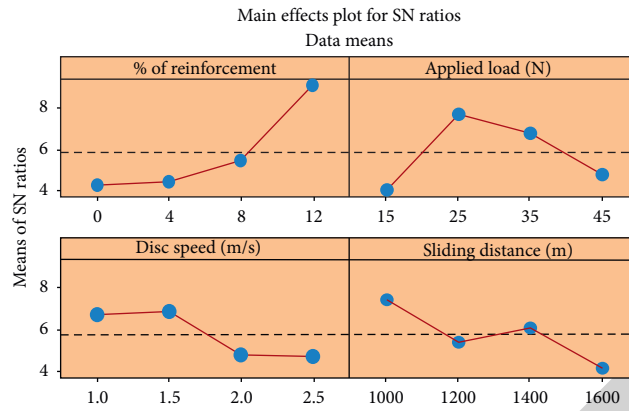


FIGURE 6: Main effects plot for S/N ratios (wear test).

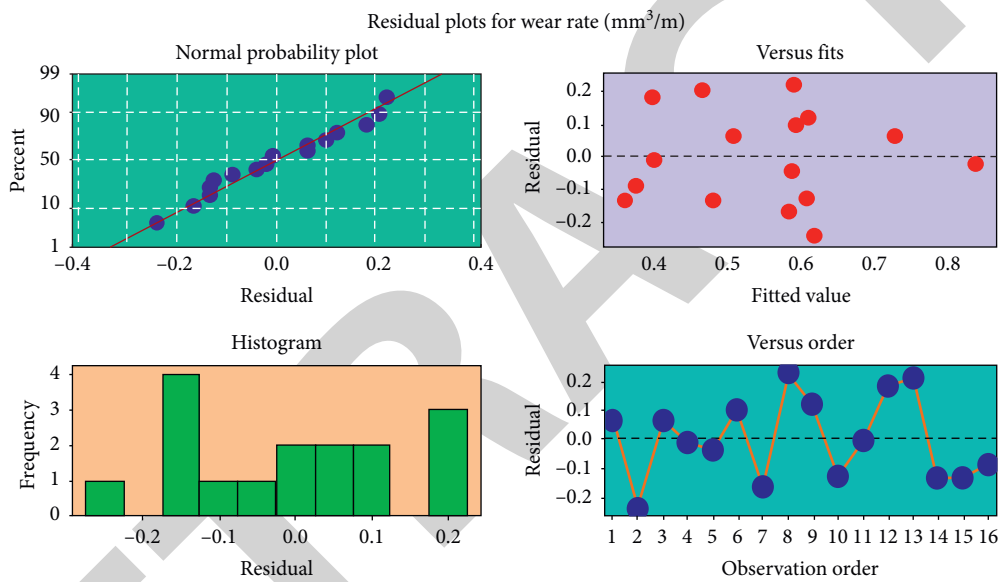


FIGURE 7: Residual plots for wear rate.

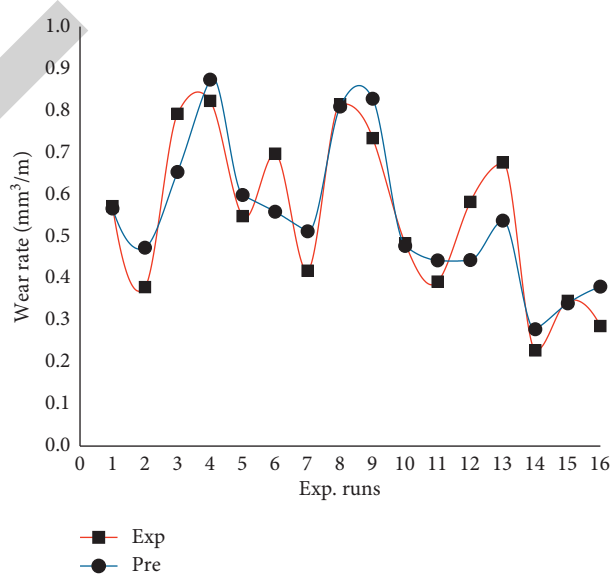


FIGURE 8: Experimental runs versus wear rate.

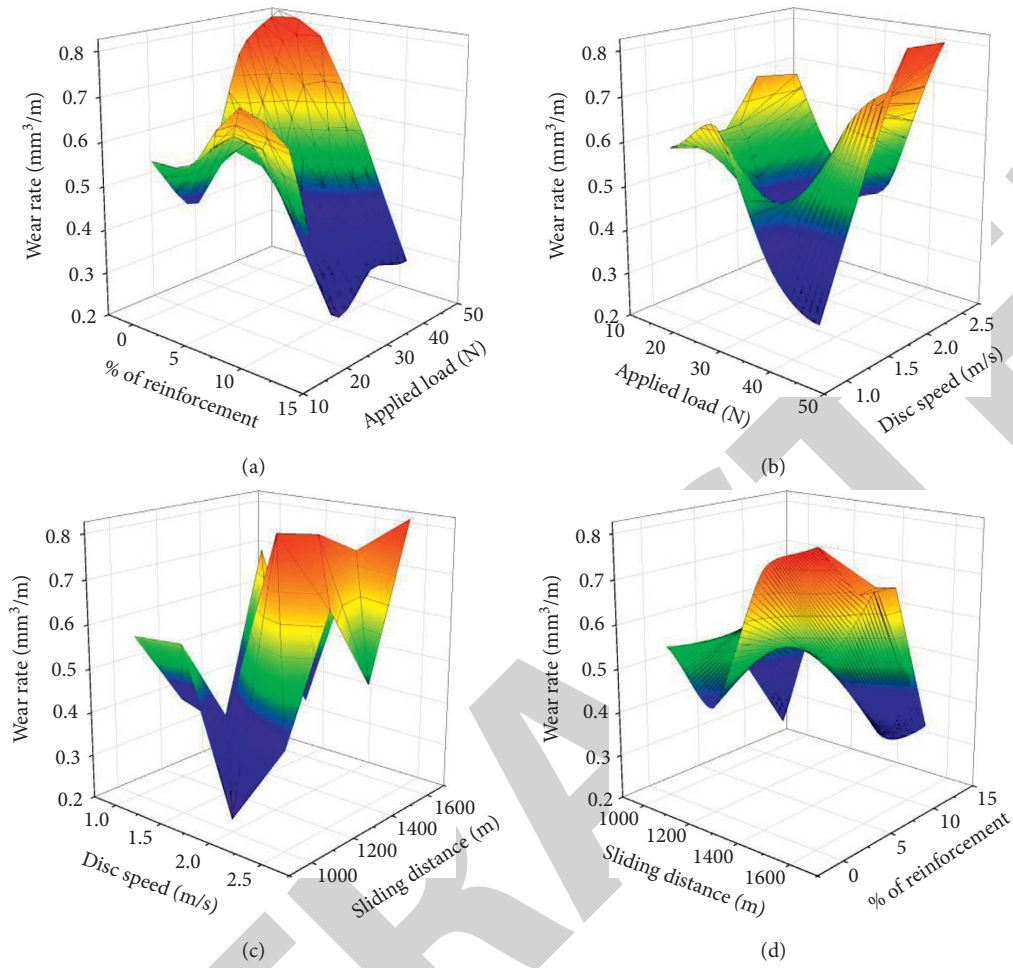


FIGURE 9: (a) % of reinforcement versus the applied load. (b) Applied load versus the disc speed. (c) Disc speed versus the sliding distance. (d) Sliding distance versus % of reinforcement.

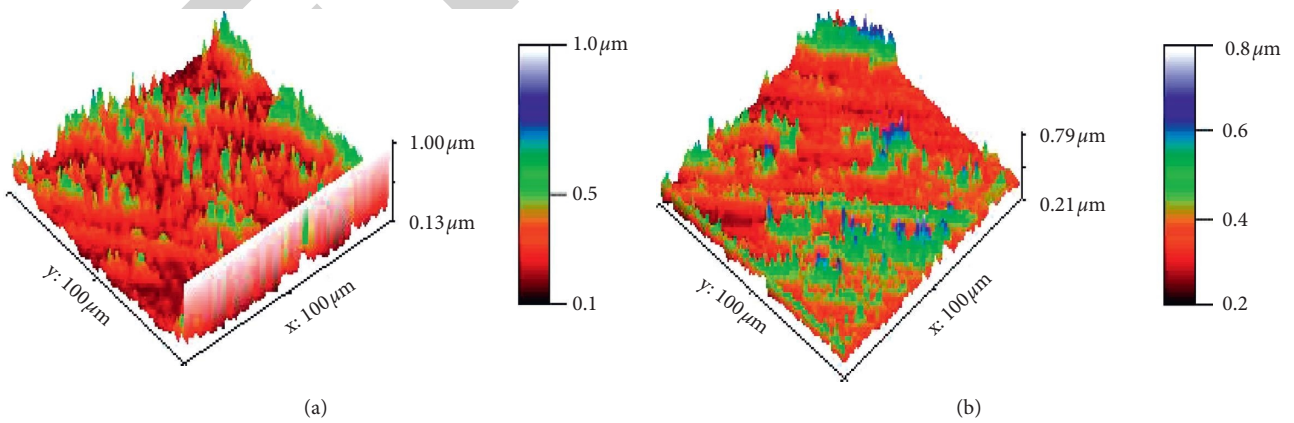


FIGURE 10: Continued.

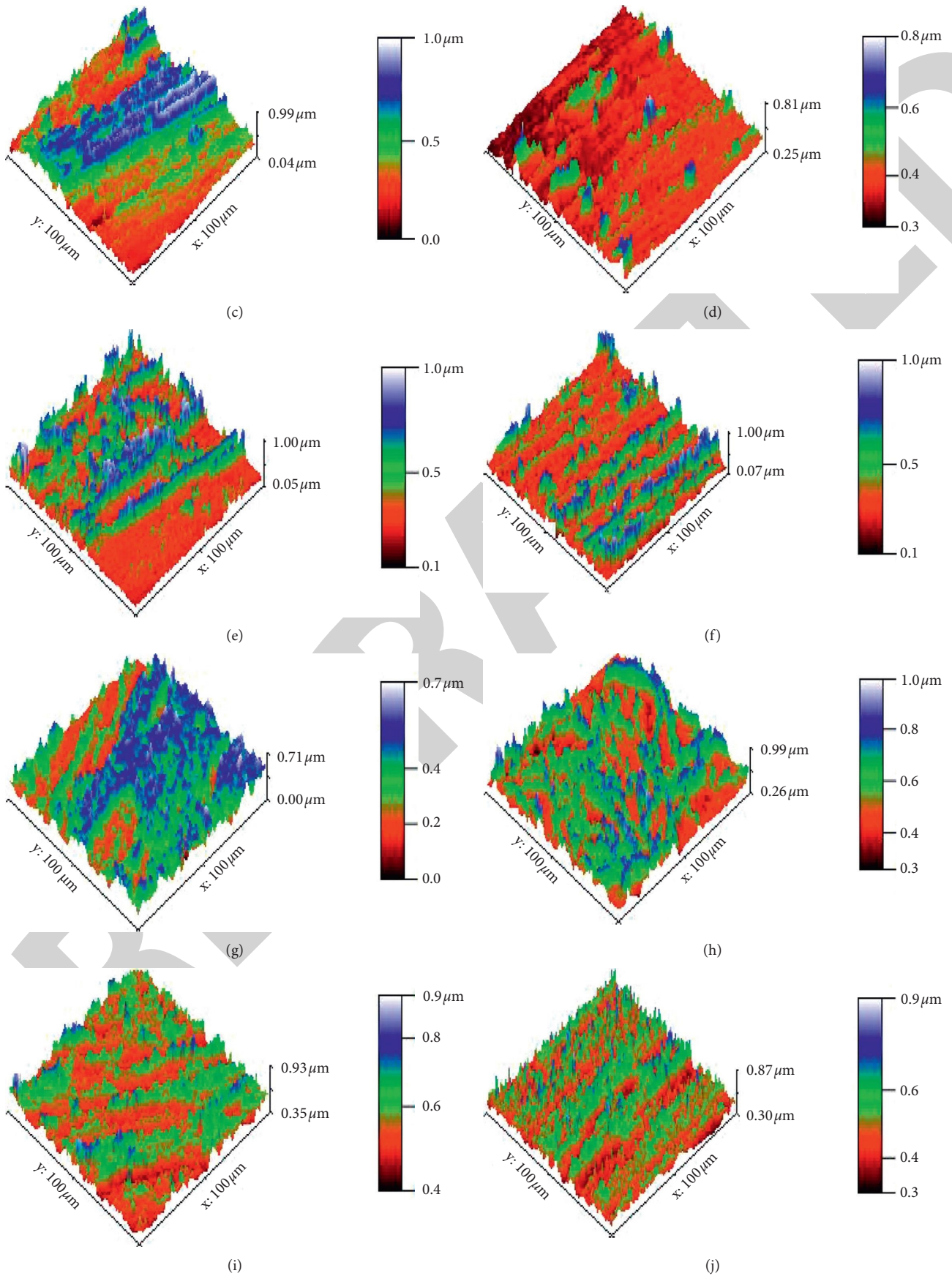


FIGURE 10: Continued.

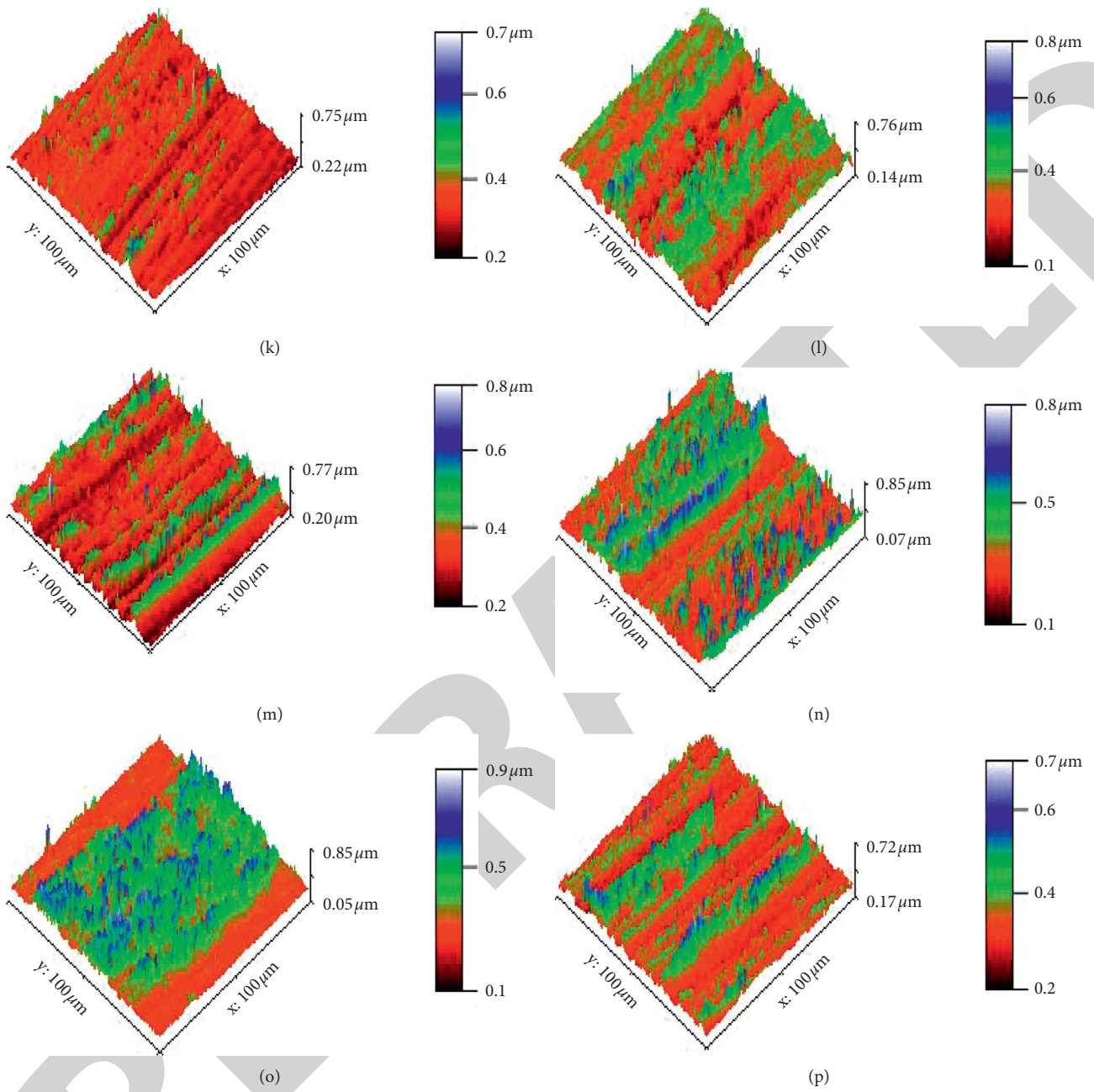


FIGURE 10: 3D Profilometric images: (a) (S-1). (b) (S-2). (c) (S-3). (d) (S-4). (e) (S-5). (f) (S-6). (g) (S-7). (h) (S-8). (i) (S-9). (j) (S-10). (k) (S-11). (l) (S-12). (m) (S-13). (n) (S-14). (o) (S-15). (p) (S-16).

TABLE 7: Experimental summary of Vickers hardness test.

Exp. runs	% of reinforcement	Agitation speed (rpm)	Agitation time (min)	Molten temperature (°C)	Vickers hardness (VHN)
1	0	450	15	700	107
2	0	500	20	750	99
3	0	550	25	800	112
4	0	600	30	850	110
5	4	450	20	800	114
6	4	500	15	850	108
7	4	550	30	700	115
8	4	600	25	750	118

TABLE 7: Continued.

Exp. runs	% of reinforcement	Agitation speed (rpm)	Agitation time (min)	Molten temperature (°C)	Vickers hardness (VHN)
9	8	450	25	850	120
10	8	500	30	800	121
11	8	550	15	750	117
12	8	600	20	700	113
13	12	450	30	750	122
14	12	500	25	700	116
15	12	550	20	850	121
16	12	600	15	800	115

TABLE 8: Response table for means (Vickers hardness test).

Level	% of reinforcement	Agitation speed (rpm)	Agitation time (min)	Molten temperature (°C)
1	107.0	115.8	111.8	112.8
2	113.8	111.0	111.8	114.0
3	117.8	116.3	116.5	115.5
4	118.5	114.0	117.0	114.8
Delta	11.5	5.3	5.3	2.8
Rank	1	2	3	4

TABLE 9: Response table for signal to noise ratios (Vickers hardness test); larger is better.

Level	% of reinforcement	Agitation speed (rpm)	Agitation time (min)	Molten temperature (°C)
1	40.58	41.26	40.96	41.06
2	41.11	40.88	40.94	41.11
3	41.42	41.30	41.32	41.25
4	41.47	41.14	41.36	41.18
Delta	0.89	0.42	0.41	0.21
Rank	1	2	3	4

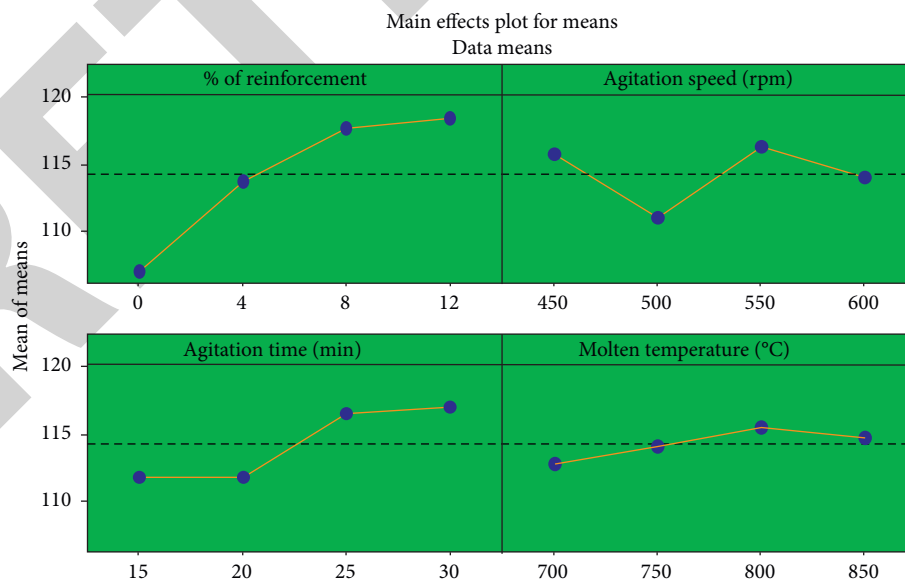


FIGURE 11: Main effects plot for means (Vickers hardness test).

particularly influenced parameter for effects in the Vickers hardness test continued by agitation speed, agitation time, and molten temperature. Optimal parameter of the Vickers

hardness test was found as 12% of reinforcement, 550 rpm of agitation speed, 30 min of agitation time, and 800°C of molten temperature.

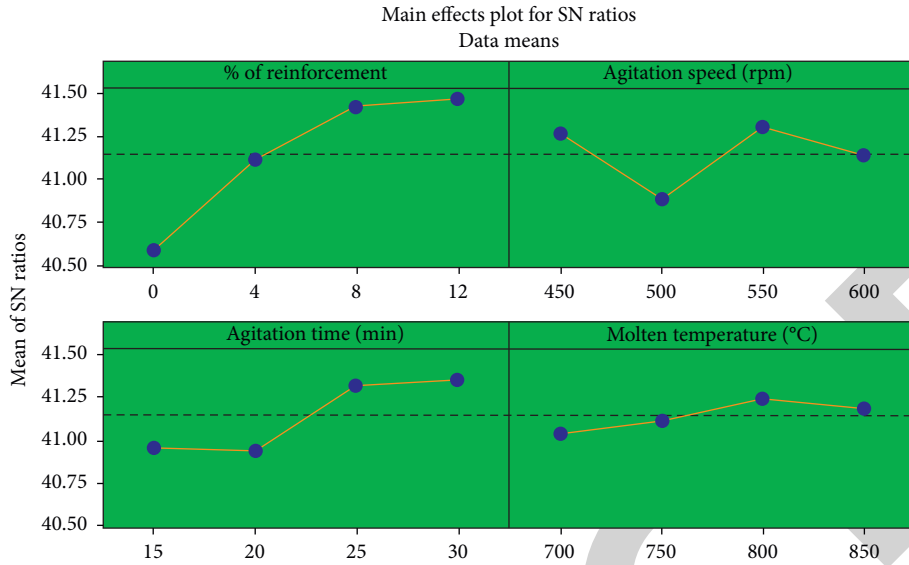


FIGURE 12: Main Effects plot for S/N ratios (Vickers hardness test).

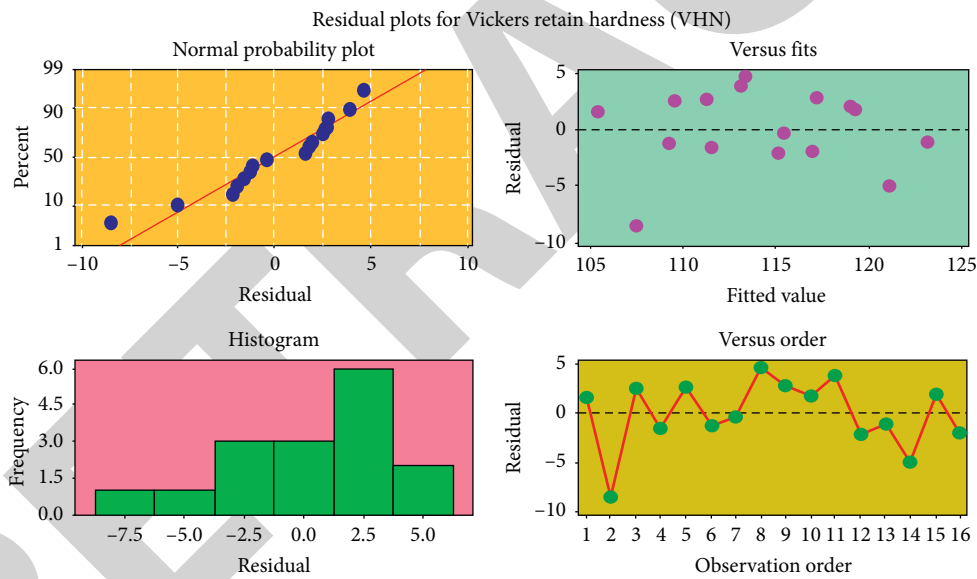


FIGURE 13: Residual plots for Vickers hardness.

Figures 11 and 12 exemplify the main effects plot for mean and S/N ratios of the Vickers hardness test. Increasing reinforcement percentage, the microhardness value was increased. Finally, the higher percentage of reinforcement (12%) provided maximum microhardness. In agitation speed state, initially, the microhardness was high in lower agitation speed; further, increasing agitation speed (500 rpm), the microhardness value was reduced suddenly. Increasing agitation speed from 500 rpm to 550 rpm, the microhardness was increased. In agitation time state, increasing gradually the agitation time, the microhardness value was increased; 30 min of agitation time provided the maximum hardness values. For the molten temperature condition, the minimum level of molten temperature was

registered as lower microhardness, and constantly increasing molten temperature, the microhardness increased. Finally, the 800°C offered maximum microhardness values.

Figure 13 displays the residual plots for Vickers hardness. In the residual plot, the microhardness level and the parameters influence are clearly exemplified in single observation. For the normal probability plot, all sixteen points are lying on the probability line few of them nearer to the line, and it can be replicated in the effect of the microhardness such as carrying out experimental runs. In the fits plot, the points were distributed unvaryingly, and within the limits, the chosen parameters can be recorded, and the response values are perfect. From the histogram plot, all rectangle boxes are extremely close and touch each other. In

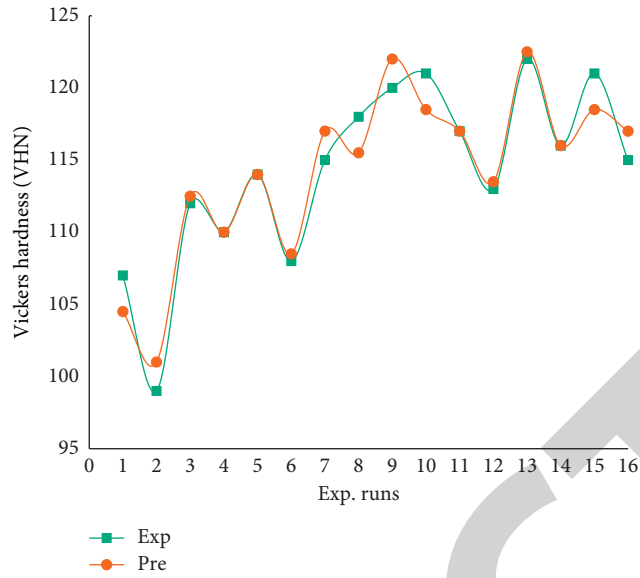


FIGURE 14: Experimental runs versus Vickers microhardness.

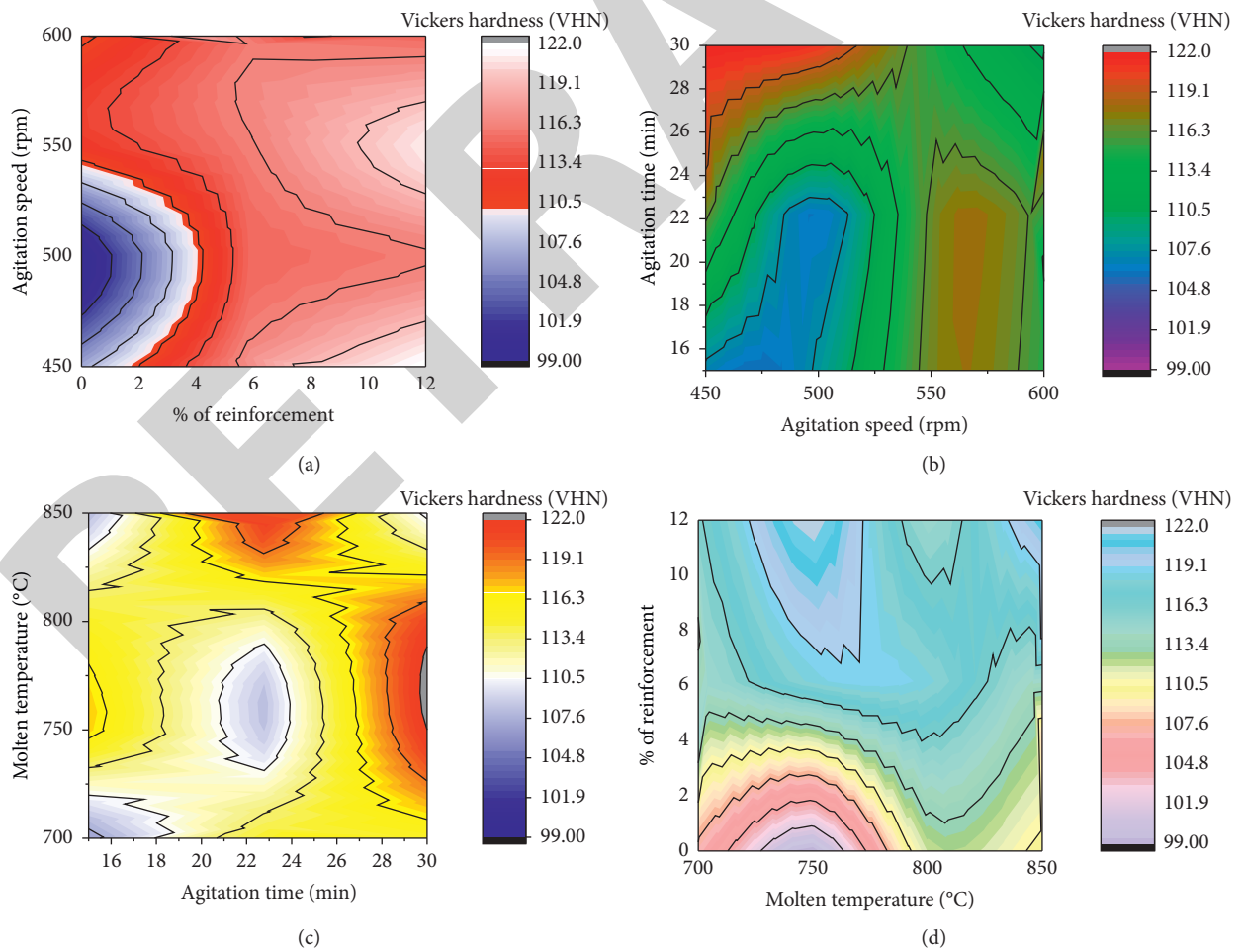


FIGURE 15: (a) Contour plot: % of reinforcement. (b) Contour plot: agitation speed. (c) Contour plot: agitation speed. (d) Contour plot: molten temperature versus % of reinforcement.

the order plot, all points crossed simultaneously the mean line both positively and negatively. From these conditions, the experiment carried out was done in an exceptional manner, and using the parameters was efficient.

Figure 14 illustrates the experimental runs versus Vickers microhardness. From the Vickers microhardness test, the experimental and predicted values are evaluated. In the sixteen experimental runs, the majority of the experimental values are within the limit of the predicted values; few were nearer and crossed the predicted values.

Figures 15(a)–15(d) present the contour plot of the Vickers microhardness test. Figure 15(a) shows the correlation between % of reinforcement and agitation speed, and the higher reinforcement percentage and moderate agitation speed offered excellent microhardness. Figure 15(b) illustrates the connection between agitation speed and agitation time, and the minimum agitation speed and higher agitation time provided maximum hardness value. Figure 15(c) demonstrates the relationship between agitation time and molten temperature, and the maximum agitation time and moderate molten temperature were recorded as maximum hardness value.

Figure 15(d) reveals the correlation between molten temperature and % of reinforcement, and the moderate molten temperature and higher reinforcement were registered as maximum hardness value.

5. Conclusions

Aluminum alloy 7079 with the addition of zirconium oxide and silicon nitride (AMCs) hybrid composites was prepared through stir-casting process. Further, the wear test was conducted by Pin-On-Disc with Taguchi statistical approach. Finally, the wear worn-out surfaces and Vickers microhardness were examined thoroughly. The output result of this experimental work was concluded and demonstrated as follows:

- (i) From the wear test, the minimum wear rate was recorded as $0.228 \text{ mm}^3/\text{m}$, the contribution of reinforcement 12%, applied load 25 N, disc speed 2 m/s and sliding speed 1000 m, which offered minimum wear rate. In the wear test, the % of reinforcement was the exceptionally influenced parameter for effects in the wear test followed by sliding distance, applied load, and disc speed. Optimal parameter of the wear test was registered as 12% of reinforcement, 25 N of applied load, 1.5 m/s of disc speed, and 1000 m of sliding speed.
- (ii) In the surface plot analysis, the minimum level of applied load and maximum level of reinforcement offered minimum wear rate. Further, the maximum level of applied load and minimum level of disc speed offered minimum wear rate. Correlation between two parameters, the minimum sliding distance and maximum reinforcement percentage, offered lower wear rate.
- (iii) For the Vickers microhardness test, the maximum hardness was recorded as 122 VHN. The maximum

hardness values were obtained by the influence of the parameters, which are 12% of reinforcement, agitation speed of 450 rpm, agitation time of 30 min, and molten temperature of 750°C . In the Vickers hardness test, the % of reinforcement was the predominantly influenced parameter for effects in the Vickers hardness test, followed by agitation speed, agitation time, and molten temperature. Optimal parameter of the Vickers hardness test was recorded as 12% of reinforcement, 550 rpm of agitation speed, 30 min of agitation time, and 800°C of molten temperature.

- (iv) From the contour plot analysis, the higher reinforcement percentage and moderate agitation speed offered exceptional microhardness. Further, the minimum agitation speed and higher agitation time presented the maximum hardness value. Finally, the maximum agitation time and moderate molten temperature were recorded as maximum hardness value.

Data Availability

The data used to support the findings of this study are included within the article. Should further data or information be required, these are available from the corresponding author upon request.

Disclosure

This study was performed as a part of the Employment of College of Engineering and Technology, Dambi Dollo University, Oromia Region, Ethiopia.

Conflicts of Interest

The authors declare that there are no conflicts of interest regarding the publication of this paper.

Acknowledgments

The authors appreciate the supports from Dambi Dollo University, Ethiopia, and Sathyabama Institute of Science and Technology, Chennai. The authors thank Saveetha School of Engineering, Chennai, for the technical assistance in the design of experiment process.

References

- [1] C.-R. Wang, K.-K. Deng, and Y. Bai, "Microstructure, and mechanical and wear properties of Grp/AZ91 magnesium matrix composites," *Materials*, vol. 12, no. 7, pp. 1190–1206, 2019.
- [2] C. Fenghong, C. Chang, W. Zhenyu, T. Muthuramalingam, and G. Anbuechziyan, "Effects of silicon carbide and tungsten carbide in aluminium metal matrix composites," *Siliconindia*, vol. 11, no. 6, pp. 2625–2632, 2019.
- [3] K. Palanikumar, S. Eaben Rajkumar, and K. Pitchandi, "Influence of primary B_4C particles and secondary mica particles on the wear performance of $\text{Al6061/B}_4\text{C/mica}$ hybrid

- composites,” *Journal of Bio and Tribo-Corrosion*, vol. 5, no. 3, Article ID 77, 2019.
- [4] J. Singh and A. Chauhan, “Investigations on dry sliding frictional and wear characteristics of SiC and red mud reinforced Al2024 matrix hybrid composites using taguchi’s approach,” *Proceedings of the Institution of Mechanical Engineers—Part L: Journal of Materials: Design and Applications*, vol. 233, no. 9, pp. 1923–1938, 2018.
 - [5] V. B. Kurapati, R. Kommineni, and S. Sundarrajan, “Statistical analysis and mathematical modeling of dry sliding wear parameters of 2024 aluminium hybrid composites reinforced with fly ash and SiC particles,” *Transactions of the Indian Institute of Metals*, vol. 71, no. 7, pp. 1809–1825, 2018.
 - [6] S. Koksai, F. Fici, R. Kayikci, and O. Savas, “Experimental optimization of dry sliding wear behavior of in situ AlB2/Al composite based on Taguchi’s method,” *Materials and Design*, vol. 42, pp. 124–130, 2012.
 - [7] L. Natrayan, V. Sivaprakash, and M. S. Santhosh, “Mechanical, microstructure and wear behavior of the material AA6061 reinforced SiC with different leaf ashes using advanced stir casting method,” *International Journal of Engineering and Advanced Technology*, vol. 8, pp. 366–371, 2018.
 - [8] M. Udayakumar, S. Aravindan, and K. Rajkumar, “Wear performance of Al-SiC- B₄C hybrid composites under dry sliding conditions,” *Materials and Design*, vol. 47, pp. 456–464, 2013.
 - [9] R. Pandiyarajan, P. Maran, S. Marimuthu, and K. C. Ganesh, “Mechanical and tribological behavior of the metal matrix composite AA6061/ZrO₂/C,” *Journal of Mechanical Science and Technology*, vol. 31, no. 10, pp. 4711–4717, 2017.
 - [10] J. Singh and A. Chauhan, “Overview of wear performance of aluminium matrix composites reinforced with ceramic materials under the influence of controllable variables,” *Ceramics International*, vol. 42, no. 1, pp. 56–81, 2016.
 - [11] V. Kavimani, K. S. Prakash, T. Thankachan, S. Nagaraja, A. K. Jeevanantham, and J. P. Jhon, “WEDM parameter optimization for silicon@r-GO/magnesium composite using taguchi based GRA coupled PCA,” *Siliconindia*, vol. 12, no. 5, pp. 1161–1175, 2020.
 - [12] D. Bandhu, A. Thakur, R. Purohit, R. K. Verma, and K. Abhishek, “Characterization & evaluation of Al7075 MMCs reinforced with ceramic particulates and influence of age hardening on their tensile behavior,” *Journal of Mechanical Science and Technology*, vol. 32, no. 7, pp. 3123–3128, 2018.
 - [13] M. H. Faisal and S. Prabakaran, “Investigation on mechanical and wear properties of aluminium based metal matrix composite reinforced with B₄C, Gr and fly ash,” in *Advanced Manufacturing and Materials Science*, pp. 379–385, Springer, Berlin, Germany, 2018.
 - [14] R. S. Bhatia and K. Kudlipsingh, “An experimental analysis of aluminium metal matrix composite using Al₂O₃/B₄C/Gr particles,” *International Journal of Advanced Research in Computer Science*, vol. 8, no. 4, pp. 83–90, 2017.
 - [15] P. V. Reddy, P. R. Prasad, D. M. Krishnudu, and E. V. Goud, “An investigation on mechanical and wear characteristics of Al 6063/TiC metal matrix composites using RSM,” *Journal of Bio- and Tribo-Corrosion*, vol. 5, no. 4, p. 90, 2019.
 - [16] A. Prasad Reddy, P. Vamsi Krishna, and R. N. Rao, “Tribological behaviour of Al6061-2SiC-xGr hybrid metal matrix nanocomposites fabricated through ultrasonically assisted stir casting technique,” *Siliconindia*, vol. 11, no. 6, pp. 2853–2871, 2019.
 - [17] S. Suresh, G. H. Gowd, and M. L. S. D. Kumar, “Mechanical and wear characterization of Al/nano-SiC NMMCs by liquid state process,” *Journal of Bio- and Tribo-Corrosion*, vol. 5, no. 2, pp. 43–53, 2019.
 - [18] K. K. Alaneme and K. O. Sanusi, “Microstructural characteristics, mechanical and wear behaviour of aluminium matrix hybrid composites reinforced with alumina, rice husk ash and graphite,” *Engineering Science and Technology, an International Journal*, vol. 18, no. 3, pp. 416–422, 2015.
 - [19] L. Natrayan and M. S. Kumar, “Influence of silicon carbide on tribological behaviour of AA2024/Al₂O₃/SiC/Gr hybrid metal matrix squeeze cast composite using Taguchi technique,” *Materials Research Express*, vol. 6, no. 12, Article ID 1265f9, 2020.
 - [20] S. Aribi, A. Fakorede, O. Ige, and P. Olubambi, “Erosion-corrosion behaviour of aluminum alloy 6063 hybrid composite,” *Wear*, vol. 376–377, pp. 608–614, 2017.
 - [21] K. Hemalatha, C. James, L. Natrayan, and V. Swamynadh, “Analysis of RCC T-beam and prestressed concrete box girder bridges super structure under different span conditions,” *Materials Today: Proceedings*, vol. 37, pp. 1507–1516, 2021.
 - [22] G. Elango, B. K. Raghunath, and K. Palanikumar, “Experimental analysis of the wear behaviour of hybrid metal-matrix composites of LM25Al with equal volumes of SiC+ TiO₂,” *Materials Technology*, vol. 48, no. 6, pp. 803–810, 2014.
 - [23] S. K. Chourasiya, G. Gautam, and D. Singh, “Mechanical and tribological behavior of warm rolled Al-6Si-3Graphite self lubricating composite synthesized by spray forming process,” *Siliconindia*, vol. 12, no. 4, pp. 831–842, 2020.
 - [24] V. Paranthaman, K. Shanmuga Sundaram, and L. Natrayan, “Influence of SiC particles on mechanical and microstructural properties of modified interlock friction stir weld lap joint for automotive grade aluminium alloy,” *Silicon*, pp. 1–11, 2021.
 - [25] S. Banerjee, S. Poria, G. Sutradhar, and P. Sahoo, “Dry sliding tribological behavior of AZ31-WC nano-composites,” *Journal of Magnesium and Alloys*, vol. 7, no. 2, pp. 315–327, 2021.
 - [26] W. Yu, D. Chen, L. Tian, H. Zhao, and X. Wang, “Self-lubricate and anisotropic wear behavior of AZ91D magnesium alloy reinforced with ternary Ti₂AlC MAX phases,” *Journal of Materials Science & Technology*, vol. 35, no. 3, pp. 275–284, 2019.
 - [27] T. Sathish and N. Sabarirajan, “Synthesis and optimization of AA 7175—zirconium carbide (ZrC) composites machining parameters,” *Journal of New Materials for Electrochemical Systems*, vol. 24, no. 1, pp. 34–37, 2021.
 - [28] S. E. Rajkumar, K. Palanikumar, and P. Kasiviswanathan, “Influence of mica particles as secondary reinforcement on the mechanical and wear properties of Al/B₄C/mica composites,” *Materials Express*, vol. 9, no. 4, pp. 299–309, 2019.
 - [29] A. Pai, S. S. Sharma, R. E. D’Silva, and R. G. Nikhil, “Effect of graphite and granite dust particulates as micro-fillers on tribological performance of Al 6061-T6 hybrid composites,” *Tribology International*, vol. 92, pp. 462–471, 2015.
 - [30] V. Paranthaman, K. Shanmuga Sundaram, and L. Natrayan, “Effect of silica content on mechanical and microstructure behaviour of resistance spot welded advanced automotive TRIP steels,” *Silicon*, Article ID 1, 2021.
 - [31] K. S. Selvaraj and G. Prabu, “Investigation of the mechanical properties of a squeeze-cast LM6 aluminium alloy reinforced with a zinc-coated steel-wire mesh,” *Materiali in Tehnologije*, vol. 52, no. 2, pp. 125–131, 2018.
 - [32] L. Natrayan and M. Senthil Kumar, “An integrated artificial neural network and Taguchi approach to optimize the squeeze cast process parameters of AA6061/Al₂O₃/SiC/Gr hybrid

Retraction

Retracted: Investigation on Dielectric Properties of Press Board Coated with Epoxy Resin, Quartz, and Rice Husk Ash

Advances in Materials Science and Engineering

Received 26 December 2023; Accepted 26 December 2023; Published 29 December 2023

Copyright © 2023 Advances in Materials Science and Engineering. This is an open access article distributed under the Creative Commons Attribution License, which permits unrestricted use, distribution, and reproduction in any medium, provided the original work is properly cited.

This article has been retracted by Hindawi, as publisher, following an investigation undertaken by the publisher [1]. This investigation has uncovered evidence of systematic manipulation of the publication and peer-review process. We cannot, therefore, vouch for the reliability or integrity of this article.

Please note that this notice is intended solely to alert readers that the peer-review process of this article has been compromised.

Wiley and Hindawi regret that the usual quality checks did not identify these issues before publication and have since put additional measures in place to safeguard research integrity.

We wish to credit our Research Integrity and Research Publishing teams and anonymous and named external researchers and research integrity experts for contributing to this investigation.

The corresponding author, as the representative of all authors, has been given the opportunity to register their agreement or disagreement to this retraction. We have kept a record of any response received.

References

- [1] B. S., K. T. S., S. M. et al., "Investigation on Dielectric Properties of Press Board Coated with Epoxy Resin, Quartz, and Rice Husk Ash," *Advances in Materials Science and Engineering*, vol. 2021, Article ID 9839770, 7 pages, 2021.

Research Article

Investigation on Dielectric Properties of Press Board Coated with Epoxy Resin, Quartz, and Rice Husk Ash

Banumathi S. ¹, Karthik T. S. ², Sasireka M. ³, Kiran Ramaswamy ⁴, Vishnu J. ¹,
Yuwan M. K. ¹, Kavin R. R. ¹ and Sathish Kumar S. ¹

¹Department of Electrical and Electronics Engineering, M.Kumarasamy College of Engineering, Anna University, Karur, Tamilnadu, India

²Department of Electronics and Communication Engineering, Aditya College of Engineering and Technology, Surampalem, Andhrapradesh, India

³Department of Electronics and Instrumentation Engineering, Kongu Engineering College, Anna University, Perundurai, Tamilnadu, India

⁴Department of Electrical and Computer Engineering, Ambo University, Addis Ababa, Ethiopia

Correspondence should be addressed to Kiran Ramaswamy; maruthirkiran@gmail.com

Received 10 May 2021; Revised 28 May 2021; Accepted 3 June 2021; Published 17 June 2021

Academic Editor: Samson Jerold Samuel Chelladurai

Copyright © 2021 Banumathi S. et al. This is an open access article distributed under the Creative Commons Attribution License, which permits unrestricted use, distribution, and reproduction in any medium, provided the original work is properly cited.

Epoxy resin mixed with rice husk ash and quartz powder increases its dielectric strength. This paper presents the dielectric properties of the press board coated with this epoxy mixture. In this work, the press board, which is used in the transformer, is coated with three components: epoxy resin, rice husk ash, and quartz powder. The nanometer-sized quartz powder and rice husk ash are mixed in the particular ratio with the epoxy resin. The mixture of epoxy resin, quartz powder, and rice husk ash is coated on both sides of the press board. The dielectric constant, volume resistivity, and Tan Delta (dissipation factor) of the coated press board are compared with the noncoated press board. The results reveal that the coated board is having high dielectric constant and volume resistivity when compared to the noncoated board.

1. Introduction

Insulators play a major role in electrical power transmission and distribution system. As the demand for electricity is increasing day by day, transmitting extrahigh voltage or ultrahigh voltage has become indispensable. So researchers are interested in doing many research studies with insulators. In the power system, three types of insulators commonly used are solids, liquids, and gases. Dielectric property and reliability are most important characteristics of any insulator. Introducing ecofriendly insulators or using naturally available materials along with the conventional insulator with increased dielectric strength has turned into a trend. In addition to the insulating property, the excellent mechanical and thermal properties are also required for an insulator for the consistent operation of electric power apparatus [1–6].

Insulators are the one which are essential parts of high-voltage engineering and are used to separate live conductors from the earthed objects such as transmission towers in transmission system and transformer tanks in transformers. Along with the understanding of the design, consistency, and protection, the researcher must know about its physical and chemical properties because only these properties decide the dielectric property of the particular insulating material.

In high-voltage power apparatuses, epoxy resin is used extensively because of its exceptional insulating behavior towards electricity, extraordinary resistance to heat, and good mechanical properties. Nanoparticles-filled epoxy exhibits good properties when compared to the epoxy filled with micrometer filler. The epoxy material with SiO₂ shows good dielectric properties when compared to the other fillers [7–10]. Silica obtained from the materials shows good

dielectric property [11]. In this work, rice husk ash is used as a filler since it consists of SiO_2 .

Rice husk has been considered as the horticulture squander material in rice creating nations all throughout the planet. Every year tons and tons of rice husks are burned considering it as a waste, and it creates air pollution also. But these rice husks delivered silica when they are singed, and it comprises around 20 to 25 wt. % silica (SiO_2). The consuming temperature is around 500°C to 800°C [12]. The ash obtained from rice husk is rich in silica, and it has been already proved that silica has good dielectric property [8]. It is being accounted for that the change of α -quartz can be framed beneath 573°C and β -quartz from 573°C to 820°C . At lower temperature, the indistinct condition of rice husk debris silica will be shaped [10, 13].

Quartz is the most ordinary form of crystalline silica that is found in nature [14]. The insulation property of quartz ceramics is high, and it is possessing heat insulation property also. They are not expensive and available in nature. The breakdown voltage of quartz ceramics is high at atmospheric temperature and at high temperature. Dielectric permittivity is low, and its other properties such as dissipation factor and lowest thermal conductivity made it is suitable for electrical insulation [15].

Many research studies have been carried out with epoxy and silica composites as the insulating material [16, 17]. Press boards are broadly used in power transformers and instrument transformers. In addition to this, press boards are used in high-voltage switches also. Here, the transformer press board is coated with three different materials: epoxy resin, rice husk ash, and quartz powder. When the board is coated with epoxy resin, the moisture absorption can be reduced [18]. This paper reports on testing of the dielectric property and resistance of the insulating material. The difference in our insulating material is that we used the combination of rice husk ash, quartz powder, and epoxy resin coated on the press board.

2. Specimen Preparation

Materials required for preparing the specimen are press board, epoxy resin, rice husk ash, and quartz powder. The chemical structure of the materials and their properties are discussed first in this section.

2.1. Chemical Structure and Properties

2.1.1. Epoxy Resin. Epoxy resin is a fluid that has a low viscosity so it is easy to blend it. Epoxy resins have properties of low consistency, simple to frame, low shrinkage, high bond, high mechanical properties, high electrical protection, and great compound opposition. Most epoxy pitches that are broadly created are from bisphenol and epichlorohydrin [19]. The chemical structure of the epoxy resin is shown in Figure 1.

2.1.2. Quartz Powder. Quartz is a hard, translucent mineral made out of silicon and oxygen (silica dioxide), as shown in Figures 2 and 3. It is essentially perhaps the most well-

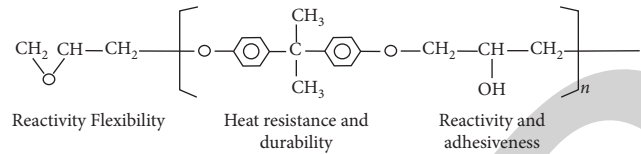


FIGURE 1: Structure of epoxy resin.



FIGURE 2: Quartz powder.



FIGURE 3: Structure of the quartz powder.

known and the second most bountiful mineral with numerous utilizations found on Earth. It is a significant part of rocks (molten, transformative, and sedimentary shakes) and structures in all temperatures. Quartz in its most flawless structure is clear or white in shading yet various contaminations inside the nuclear cross-section can make the shading change to purple, pink, earthy colored, dark, dim, green, orange, yellow, blue, or red, and sometimes, multi-color. Quartz is one of the hardest normally happening minerals and subsequently cannot be eroded without any problem. It has an exceptionally high softening point and can withstand basically high temperatures. It is synthetically steady and does not respond with different synthetics and substances. It is chemically stable and does not react with other chemicals and substances.

2.1.3. Rice Husk Ash. Removal of rice husk is one of the significant difficulties looked by mill operators all over world. Rice husk when consumed in the kettle as fuel produces debris known as rice husk debris. RHA is rice husk debris ecological waste; it contains 60% to 80% undefined silica [19]. When burnt at 500°C to 700°C , it turns into amorphous silica. It reduces the leakage current during high voltage [20–23], when used as a filler in epoxy. It is useful in various industries. Figure 4 shows the picture of rice husk ash, and the structure of rice husk is shown in Figure 5.

2.2. Specimen Preparation. Press board (IS-1576) used in the transformer (Figure 6) has thickness of about 3 mm. The press board used in the specimen is collected from the



FIGURE 4: Rice husk ash.

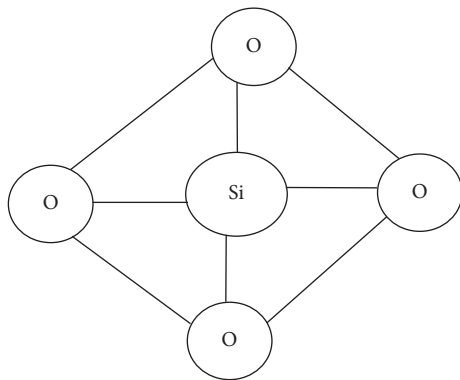


FIGURE 5: Structure of rice husk ash.

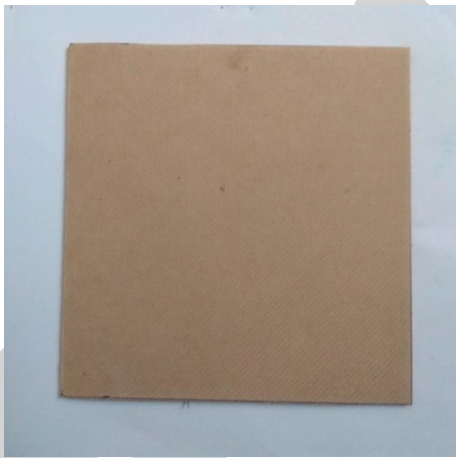


FIGURE 6: Press board used in the transformer.

distribution transformer manufacturers. The board used for this work is from Associated Transformer Private Limited, Dindugul, Tamilnadu. Epoxy resin used here is belonging to Araldite Company. This pack comes with the resin and the hardener. The mixing proportion of resin and hardener is discussed in below preparation. Quartz powder of 74 microns is actually a powdered form of quartz crystal. Rice husk ash, which is the agriculture waste, is burnt and processed to get silica content ash. The consuming temperature is around 500°C to 800°C [12]. It is being accounted for that the change of α -quartz can be framed beneath 573°C and β -quartz at 573°C to 820°C . At lower temperature, the

indistinct condition of rice husk debris silica will be shaped [20].

The press board (IS-1576) refers IS standards (Figure 1), which is to be coated with the resin mixture, is dried in sunlight for 4-5 hours to remove humidity from the board. Then, the mixture is mixed with 1 : 1 ratio of standard epoxy resin (AW 106 IN) and standard hardener (HV 953 IN) and then added the 2 : 1 ratio of quartz powder and rice husk ash, as shown in Figure 7. Then, these components are blended evenly without any bulges. The surface of the press board is cleaned to remove dust. Next, the epoxy resin mix is coated on the press board on one side evenly, as shown in Figure 8, and allowed to dry for 8-12 hours. Again, the same step is repeated on another side of the press board.

3. Experimental Setup

The basic predominant tests (dielectric constant test, Tan Delta test, and volume resistivity test) which are necessary to ensure the insulating property of any new solid insulator are performed [19, 24]. These tests were performed as per IS & IEC standards.

- (1) Dielectric constant test (IEC60250)
- (2) Tan Delta test (IEC60247)
- (3) Volume resistivity test (IEC62631-3-1)

The main importance of the test is to test the dielectric, loss dissipation, and resistance properties of the specimen.

3.1. Dielectric Constant Test. The dielectric constant of an insulating material can be defined as the ratio of the charge stored in an insulating material placed between two metallic plates to the charge that can be stored when the insulating material is replaced by vacuum or air. It is also called as electric permittivity or simply permittivity. A dielectric test is an electrical test performed on an insulator to decide the dielectric strength. The test is carried out by placing the test sample between the two electrodes, and the standard voltage is applied between the two electrodes, and the value is noted. Normally, the dielectric value of the insulator should be greater than 2. First, the noncoated press is tested, and then, the coated press board is tested, and the ratio of these values gives the dielectric constant of the material.

3.2. Tan Delta Test. The test sample on which the Tan Delta test or dissipation factor test to be conducted is first isolated from the system. A test voltage is applied across the equipment whose insulation is to be tested. The Tan Delta test is carried out by placing the test sample between two electrodes, and the ac voltage is applied. When a dielectric material is placed across the AC voltage, no power is utilized. The current will lead the voltage applied by 90° . This proves that no power loss occurred in the insulator. In most of the situation, the energy is dissipated in the insulator when the voltage is applied. This is called dielectric loss. The leakage current which is the phase angle will be less than 90° . This is



FIGURE 7: Mixture of epoxy resin, quartz powder, and rice husk ash.



FIGURE 8: Material coated using the epoxy mixture.

known as the loss angle (δ). Therefore, $\tan \delta$ is called the power factor of dielectrics.

3.3. Volume Resistivity Test. Volume resistivity is the protection from leakage current through the body of an insulating material. The higher the surface/volume resistivity, the lower the leakage current and the less conductive the material is. A standard size test is set between two anodes' plate, as demonstrated in Figure 9 and 10. For sixty seconds, a voltage is applied and the check is assessed. Surface or volume resistivity is resolved, and clear worth is given (60 seconds time).

4. Experimental Results

All the three tests, dielectric constant test, Tan Delta test, and volume resistivity test, are done with noncoated press board (NPB) and coated press board (CPB). The results obtained are discussed.

4.1. Dielectric Constant Test. The dielectric constant values of specimens are obtained for the supply voltage of 1 kV ac supply. The test results obtained for the dielectric constant

test of the specimen shows that the dielectric constant value for the coated press board is high when compared to the value of the noncoated press board. The dielectric constant of the coated press board is 3.273 (Table 1) which is higher than the dielectric constant of NPB (2.650). The dielectric constant of the epoxy-coated press board and noncoated board is plotted against supply voltage 1 kV and is shown in Figure 11.

4.2. Tan Delta Test. In the Tan Delta test, the Tan Delta value of the noncoated press board is slightly more in the value when compared to the epoxy-coated press board. The value is 0.21 for CPB, and the Tan Delta value of NCB is 0.2. If the insulation is evenly done, the loss will be almost unchanged during increase in voltage. In our case, the Tan Delta value is slightly increased for the coated press board so that the loss angle will be reduced. The values are given in Table 2, and graphical representation is given in Figure 12.

4.3. Volume Resistivity Test. The volume resistivity of the material is obtained by the test. The volume resistivity values of the specimens are obtained for the DC supply voltage of value 500 V. The output of the test shows that the volume

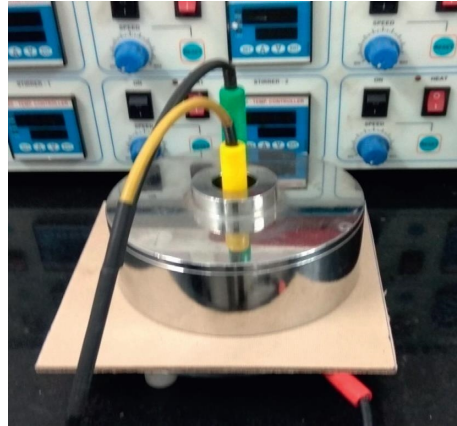


FIGURE 9: Testing of the normal press board.



FIGURE 10: Testing of the press board coated with epoxy coating.

TABLE 1: Dielectric constant of specimens (NPB and CPB).

S. No.	Specimen	Supply voltage (AC)	Dielectric constant
1	NPB	1 kV	2.650
2	CPB	1 kV	3.273

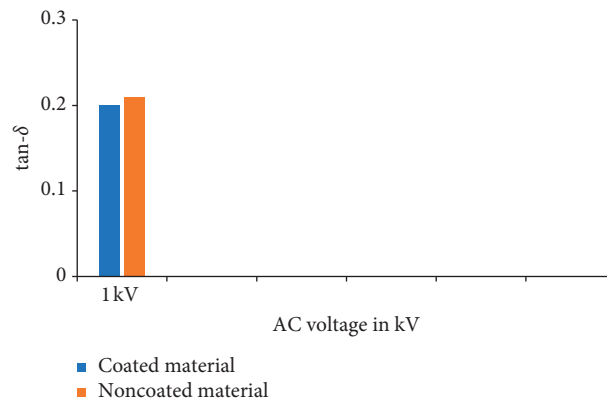


FIGURE 11: Dielectric constant of specimens (NPB and CPB) vs supply voltage.

TABLE 2: Tan delta of specimens (NPB and CPB).

S. No.	Specimen	Supply voltage (AC)	Tan Delta value
1	NPB	1 kV	0.2
2	CPB	1 kV	0.21

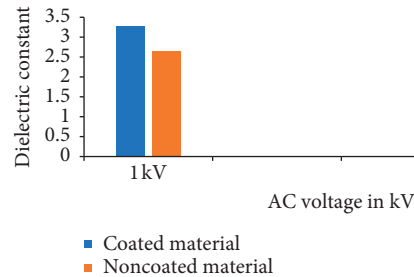


FIGURE 12: Tan Delta of specimens (NPB and CPB) vs supply voltage.

TABLE 3: Volume resistivity of specimens (NPB and CPB).

S. No.	Specimen	Supply voltage (DC)	Volume resistivity in Ω cm
1	NPB	500 V	4.96×10^{11}
2	CPB	500 V	3.18×10^{13}

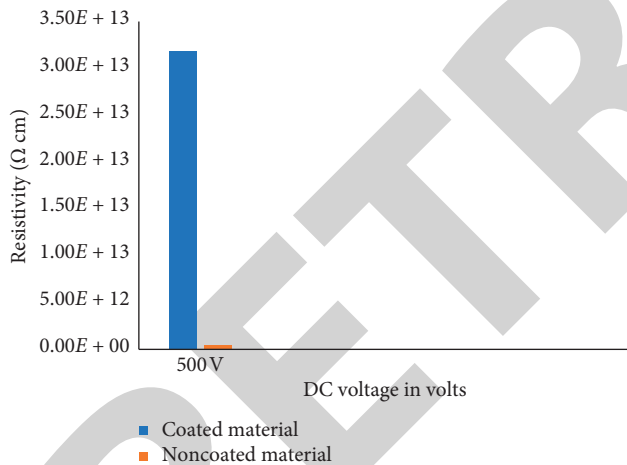


FIGURE 13: Volume resistivity of specimens (NPB and CPB) vs supply voltage.

resistivity of the epoxy-coated material is increased to $3.18 \times 10^{13} \Omega$ -cm when compared to the noncoated material $4.96 \times 10^{11} \Omega$ -cm (Table 3). The values show that the resistivity of the material is greatly increased, as shown in Figure 13.

5. Conclusion

The epoxy composite mixture coated for the transformer press board is fabricated successfully, and it is tested. The test result shows that the press board coated with epoxy resin along with quartz and rice husk ash has established a better insulation property when compared to the normal press

board. The dielectric constant of the coated press board is 3.273 at 1 kV which is higher than the noncoated press board (2.650 at 1 kV). The volume resistivity is also high $3.18 \times 10^{13} \Omega$ -cm at 500 V DC supply for the coated press board. Only the dissipation factor, i.e., Tan Delta, value of the proposed specimen is slightly higher than the NCB. Even this can be improved by proper treatment of the specimen before testing. This could be done in the future work. The coated press board has the good insulation under high voltage, and the dielectric property is also increased. These insulators can be effectively applied for high voltage application in the transformers after conducting these tests under various conditions.

Data Availability

The data used to support the findings of this study are included within the article.

Conflicts of Interest

The authors declare that there are no conflicts of interest regarding the publication of this paper.

Acknowledgments

The authors would like to thank SonaPERT (Sona Electric Power Engineering Research & Testing Centre) for providing extraordinary infrastructure and testing facility, which was helpful to complete the project in time.

References

- [1] S. Wang, Y. Chen, and J. Mao, "Dielectric strength of glass fibre fabric reinforced epoxy by nano- Al_2O_3 ," *IEEE Transactions on Dielectrics and Electrical Insulation*, vol. 27, no. 4, pp. 1086–1094, 2020.
- [2] Z.-R. Jia, Z.-G. Gao, D. Lan, Y.-H. Cheng, G.-L. Wu, and H.-J. Wu, "Effects of filler loading and surface modification on electrical and thermal properties of epoxy/montmorillonite

Retraction

Retracted: Microstructure and Fatigue Properties of 6061 Aluminum Alloy Laser-MIG Hybrid Welding Joint

Advances in Materials Science and Engineering

Received 26 December 2023; Accepted 26 December 2023; Published 29 December 2023

Copyright © 2023 Advances in Materials Science and Engineering. This is an open access article distributed under the Creative Commons Attribution License, which permits unrestricted use, distribution, and reproduction in any medium, provided the original work is properly cited.

This article has been retracted by Hindawi, as publisher, following an investigation undertaken by the publisher [1]. This investigation has uncovered evidence of systematic manipulation of the publication and peer-review process. We cannot, therefore, vouch for the reliability or integrity of this article.

Please note that this notice is intended solely to alert readers that the peer-review process of this article has been compromised.

Wiley and Hindawi regret that the usual quality checks did not identify these issues before publication and have since put additional measures in place to safeguard research integrity.

We wish to credit our Research Integrity and Research Publishing teams and anonymous and named external researchers and research integrity experts for contributing to this investigation.

The corresponding author, as the representative of all authors, has been given the opportunity to register their agreement or disagreement to this retraction. We have kept a record of any response received.

References

- [1] C. Fan, S. Yang, M. Zhu, and Y. Bai, "Microstructure and Fatigue Properties of 6061 Aluminum Alloy Laser-MIG Hybrid Welding Joint," *Advances in Materials Science and Engineering*, vol. 2021, Article ID 1933942, 12 pages, 2021.

Research Article

Microstructure and Fatigue Properties of 6061 Aluminum Alloy Laser-MIG Hybrid Welding Joint

Cong Fan ¹, Shanglei Yang ^{1,2}, Minqi Zhu,¹ and Yishan Bai¹

¹School of Materials Engineering, Shanghai University of Engineering Science, No. 333 Long Teng Road, Shanghai 201620, China

²Shanghai Collaborative Innovation Center of Laser Advanced Manufacturing Technology, No. 333 Long Teng Road, Shanghai 201620, China

Correspondence should be addressed to Shanglei Yang; yslyangshanglei@163.com

Received 6 May 2021; Accepted 4 June 2021; Published 14 June 2021

Academic Editor: Samson Jerold Samuel Chelladurai

Copyright © 2021 Cong Fan et al. This is an open access article distributed under the Creative Commons Attribution License, which permits unrestricted use, distribution, and reproduction in any medium, provided the original work is properly cited.

Laser-MIG hybrid welding of 6061-T6 aluminum alloy was carried out with ER4043 welding wire, and the microstructure and fatigue properties of the joint were studied. The grain size of HAZ is larger than that of base metal (BM) due to the influence of welding heat cycle. Snowflake-like equiaxed grains were found in the upper, middle, and lower parts of the welded joint (WJ). Based on the fatigue test with 1×10^6 cycles, the ultimate fatigue strength of BM and WJ is 101.9 MPa and 54.4 MPa, respectively. There are many pores with different sizes in WJ. The number of pores in the upper and middle parts of WJ is obviously larger than that in the lower part due to the influence of the cooling rate of the weld pool and the escape rate of pores. The porosity type is mainly metallurgical pores with regular morphology, which is mainly due to the bubbles formed by the evaporation of Mg elements and H₂O in the oxide film on the BM surface. The fatigue fracture analysis shows that the main cause of fatigue crack is the near-surface pores with 460 μm and 190 μm , respectively. The existence of pores near the surface is equivalent to the formation of a large-scale prefabricated crack, resulting in serious stress concentration. The morphology of the grains around the pores has a great influence on the initiation and propagation of the fatigue microcracks.

1. Introduction

6061-T6 aluminum alloy is a medium strength heat treatable aluminum alloy with Mg and Si as the main alloying elements. Due to the aging strengthening effect of GP region, β' phase (Q' phase) and β phase (Q''), 6061-T6 aluminum alloy has excellent mechanical properties [1, 2]. 6061-T6 aluminum alloy has good corrosion resistance, good weldability, and high strength, which is widely used in aircraft, high-speed train, and automobile structures [3]. In the manufacturing process of these structures, the fusion welding process becomes the first choice because of its high efficiency and low cost. However, due to the welding heat cycle, the grain orientation, the second phase particle behavior, and the surrounding internal stress of the traditional fusion welding processes, namely, tungsten inert gas welding (TIG) and metal inert gas welding (MIG), will change significantly. In addition, problems such as coarse structure,

defects (welding hot cracks and pores), and burning loss of strengthening alloy elements (Mg and Zn) will occur in the welded zone [4–6].

Compared with these disadvantages of MIG welding, laser welding has the advantages of high welding efficiency, small heat input, and small deformation [7–8]. In addition, it can simplify the design of welded structural parts and reduce the requirement of clamping accuracy of welded joints [9]. However, compared with iron-based materials, the characteristics of aluminum alloy materials determine that there are many low melting points of alloy components, resulting in the formation of pores and the evaporation of alloy elements in the welded joints during the laser welding of aluminum alloy, which makes the mechanical properties of laser welded joints difficult to meet the needs of industrial production [10]. In response to these problems, Steen W. M. developed laser arc hybrid welding (LAHW) [11]. LAHW is a new type of high efficient welding technology, which

perfectly combines both laser and arc thermal sources [6]. Compared with the traditional fusion welding process, LAHW has the advantages of deeper penetration, more stable welding arc, and faster welding speed [12, 13]. LAHW is a process in which laser and arc heat sources act together on the base metal. Laser can be used to guide the arc during welding to increase the utilization rate of welding heat source. As the main heat source, laser generates a keyhole in the welding pool to ensure deep fusion welding, while the molten filler material generated in the process of arc welding helps in filling the root gap, thus meeting the welding requirements of parts with large gaps [9, 14]. In addition, the use of welding wire enriches the alloying elements in the welding pool, refines the weld grain, and improves the mechanical properties of the welded joints [15].

The field has met with great success in many problems about the microstructure evolution and mechanical properties of different regions of laser arc hybrid welding joint [16–18]. These studies show that, compared with traditional welding methods (such as MIG), laser arc welding joint of aluminum alloy has smaller residual stress and greater tensile strength.

However, the application of LAHW of aluminum alloy is usually limited by porosity. It has been found that the number, size, shape, and location of metallurgical pores will be formed due to the precipitation of supersaturated hydrogen atoms during the rapid cooling process of aluminum alloy welding pool [19]. The existence of metallurgical pores near the surface reduces the effective bearing area of the joint. At the same time, serious stress concentration occurs under the action of fatigue cyclic load, which leads to the initiation of microcracks and the failure of the welded structure and greatly reduces the safety and reliability of the welded structure [20, 21]. It is worth noting that many studies successfully showed that the porosity in WJ can cause serious stress concentration through the establishment of theoretical models [22–24]. However, there is a common drawback in these models. The defect they analyzed is all single pore, which is not suitable for LAHW joint with large number of pores. In addition, the relationship between porosity and fatigue properties of LAHW joints of 6-series aluminum alloys is not fully clear. Therefore, it is necessary to study the fatigue failure of 6-series aluminum alloy LAHW joint, which has far-reaching significance for the promotion of LAHW in industrial production.

In this paper, 6061-T6 aluminum alloy with thickness of 3 mm, which is widely used in high-speed train body, is selected as BM, and laser-MIG hybrid welding process is used for connection. The microstructure and fatigue properties of WJ and BM were analyzed. The purpose of this paper is to evaluate the fatigue properties of 6061 aluminum alloy laser-MIG hybrid welded joint and discuss the fatigue failure of 6061 aluminum alloy laser-MIG hybrid welded joint from the perspective of pores forming, fatigue microcrack initiation, and propagation mechanism near the pores.

2. Materials and Methods

2.1. Materials and Welding Process. The base metal (BM) used in this test is 6061-T6 aluminum alloy, and the welding wire is ER4043. The chemical composition of BM and

welding wire is shown in Table 1. Figure 1 shows the schematic diagram of laser-MIG hybrid welding process of 6061-T6 aluminum alloy, and the welding parameters are shown in Table 2. After welding, it was cooled at room temperature, and the samples for hardness test and fatigue test were cut from the plate. The diagram of hardness test and fatigue test samples is shown in Figure 2.

2.2. Test Methods. The sample was ground to a slight scratch on the surface with sandpaper of different particle sizes from small to large. After that, the sample was polished until there was no scratch on the surface. Finally, Keller reagent (HF: HCl:HNO₃ = 1:1.5:2.5) was used to etch for about 15 s to make the final metallographic sample. The metallographic samples were observed by VHK-600 optical microscope (OM).

According to ASTM E92-2016 standard, the HV-1000 Vickers microhardness tester was used to carry out the hardness test on the cross section of the laser-MIG hybrid welded joint with the holding load of 100N and the holding time of 15 s.

According to the ASTM E466-2015 standard, the fatigue test was carried out at room temperature (25 ± 3°C) and relative humidity (40–60%) by symmetrical tension-tension cycle with sinusoidal loading waveform until the specimen reached 1 × 10⁶ cycles or fracture. The stress ratio ($R = \sigma_{\min}/\sigma_{\max}$) and load frequency were 0.1 and 15 Hz, respectively. All fatigue specimens were cyclic loaded under different stress amplitudes ($\Delta\sigma = \sigma_{\max} - \sigma_{\min}$). The ultimate fatigue strength ($N_f \geq 10^6$) of BM and welded joint (WJ) was analyzed by S-N fitting curve. All fatigue tests were carried out by Zwick/Roell Amsler HB250 hydraulic servo material testing machine, and the fatigue fracture was observed and analyzed by S-3400N scanning electron microscope (SEM).

3. Experimental Results and Analysis

3.1. Microstructure of 6061 Aluminum Alloy Laser-MIG Hybrid Welded Joint. Figures 3(a) and 3(b) show the microstructure of the base metal (BM) and heat affected zone (HAZ) in the welded joint. It can be seen from Figure 3(a) that the structure of BM is long strip, which is a typical rolled structure. The size of the grains marked by the red line in the figure was measured. The results show that the average length, average width, and aspect ratio of BM are 73.3 μm, 18 μm, and 4.07, respectively. The average length, width, and aspect ratio of HAZ grains are 82.4 μm, 22.9 μm, and 3.60, respectively. This indicates that the grain size in HAZ was coarsened obviously, and the grain length increased obviously, but the overall morphology of the grains did not change greatly. The coarse grains in HAZ were caused by the heat cycle during the welding process [25].

Figure 4(a) shows the macromorphology of the weld zone (WZ), and four positions B, C, D, and E are selected in the figure to better analyze the microstructure of WZ. Figure 4(b) shows the microscopic image near fusion zone (FZ). It can be seen from the figure that the grains grow on the surface of the BM in the semimelted state and grow along the direction of temperature gradient to the weld center in

TABLE 1: Chemical composition of 6061-T6 aluminum alloy and welding wire.

	Al	Mg	Si	Zn	Fe	Cu	Mn	Cr	Ti
6061	Bal.	0.5	0.6	≤ 0.20	≤ 0.35	≤ 0.30	≤ 0.50	≤ 0.30	≤ 0.10
ER4043	Bal.	≤ 0.05	5	≤ 0.10	≤ 0.80	≤ 0.30	≤ 0.05	—	≤ 0.2

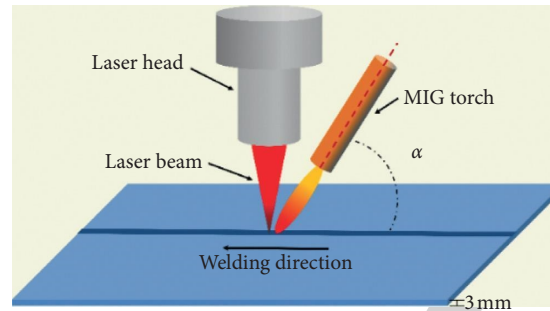


FIGURE 1: Schematic diagram of laser-MIG hybrid welding of 6061-T6 aluminum alloy.

TABLE 2: Welding parameters.

Parameters	Laser power (kW)	Current (A)	Voltage (V)	Wire feeding rate (m/min)	Welding speed (mm/s)	Defocusing amount (mm)
Values	3.0	131	18.1	8	25	-1

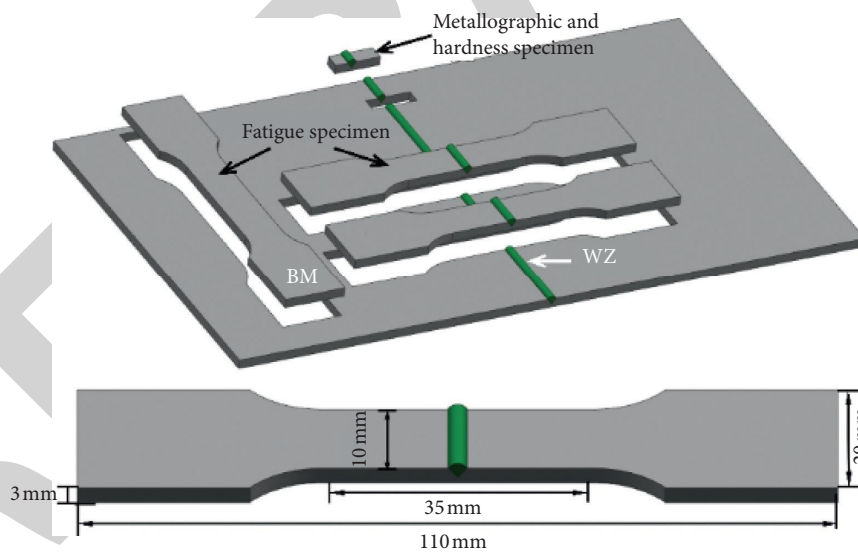


FIGURE 2: Diagram of hardness test and fatigue test samples.

the form of columnar crystals, which is a typical cocrystallization feature [26]. The elongated columnar grains in the yellow ellipse of Figure 4(b) are about $110 \mu\text{m}$ in length, but only about $30 \mu\text{m}$ in width.

Figures 4(c)–4(e) are the microstructures of the upper, middle, and lower parts of WZ. It can be found that the equiaxed grains with different sizes and morphologies are distributed in WZ. During the welding process, the undercooling in the molten pool is large, and the free crystals suspended in the molten pool can nucleate directly in the liquid metal. After

nucleation, the crystal is less constrained by the surrounding and grows divergently to form snowflake-like equiaxed grains [27]. The size of equiaxed grains in the upper part of WZ is large, about $120 \mu\text{m}$. This is because, during the process of hybrid welding, the upper part of WZ was affected by both laser and arc heat sources, and the high temperature residence time was much longer than that in other parts. The molten pool had been cooled for a long time, which leads to the coarsening of grain. In addition, some equiaxed grains in the upper part of WZ appear broken and incomplete, which may be caused by the liquid

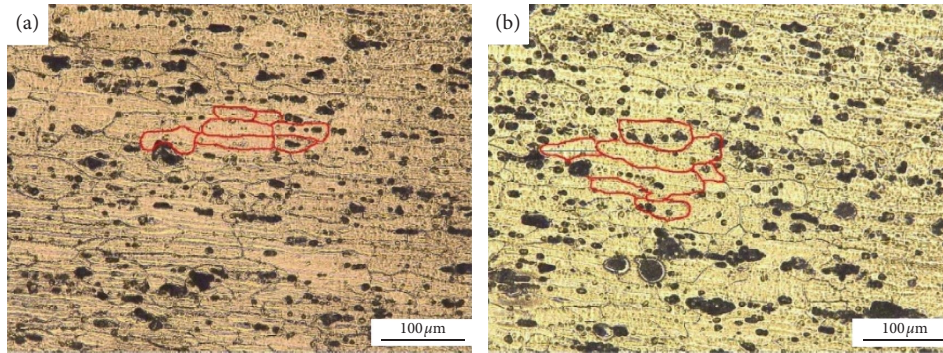


FIGURE 3: Microstructure of (a) BM and (b) HAZ in WJ.

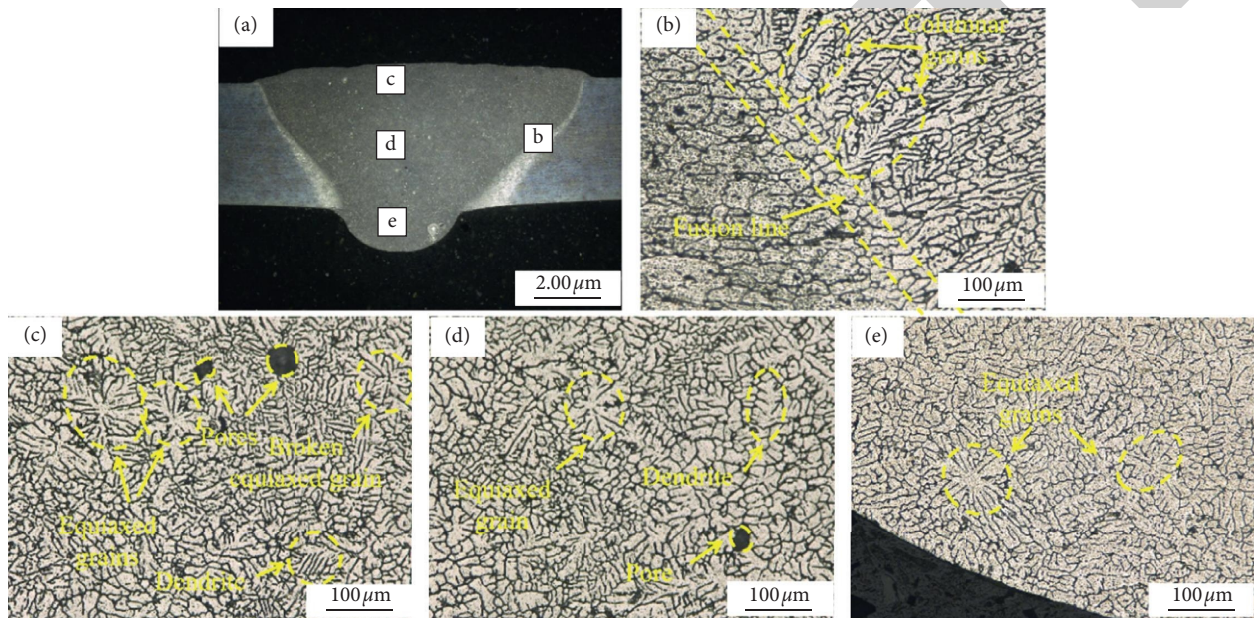


FIGURE 4: The morphology of WZ. (a) Macromorphology of WZ. (b) Microstructure of fusion zone. (c) Microstructure of the upper part of WZ. (d) Microstructure of the middle part of WZ. (e) Microstructure of the lower part of WZ.

metal being stirred by the arc during the welding process. Some of the broken equiaxed grains will grow into dendrites along the temperature gradient to the center of WZ, with the size of about $100\ \mu\text{m}$. In the lower part of WZ (Figure 4(e)), the molten pool was only affected by the laser heat source, the crystallization speed was faster, and the grains had been completely cooled without growing up, so the grain size is smaller than the middle and upper parts of WZ. Pores with diameter of $70\ \mu\text{m}$ were found in the middle and upper part of WZ. Porosity defect is the main cause of joint fatigue failure in this study, which will be analyzed in the following chapters.

3.2. Analysis of Hardness Test. Figure 5 shows the microhardness of the laser-MIG hybrid welded joint, and the hardness test direction is shown in the lower right section of the figure. Due to the uneven influence of welding heat source, the hardness values of the sample show obvious regional distribution, and the lowest hardness is located in WZ, with the lowest value being $76.5\ \text{HV}$. The reason for this phenomenon is that the main strengthening phase of 6061 aluminum alloy is β

phase (Mg_2Si), in which the boiling point of Mg is low (1107°C), which is easy to evaporate during welding. The welding wire used in this test is er4043 of Al and Si, which is difficult to supplement the evaporated Mg element, which leads to the low hardness of WZ [16]. A 3 mm softening zone (SZ) can be clearly seen in HAZ from the figure, and the minimum hardness of SZ is close to that of WZ, about $81\ \text{HV}$. The loss of hardness in SZ is due to the fact that the highest temperature of welding heat cycle in SZ cannot reach the solution temperature of β phase. At that position, only a small part of β phase was dissolved, and the remaining β phase coarsened continuously during the high temperature residence time [28]. According to Hall-Petch formula, the strengthening effect of precipitates after coarsening is poor [29]. As the measuring position gradually approached BM, the hardness value gradually increased and tended to be stable.

3.3. Analysis of Fatigue Test. Six groups of test data of WJ and BM in different stress range were obtained from fatigue test, as shown in Table 3. According to the fatigue strength

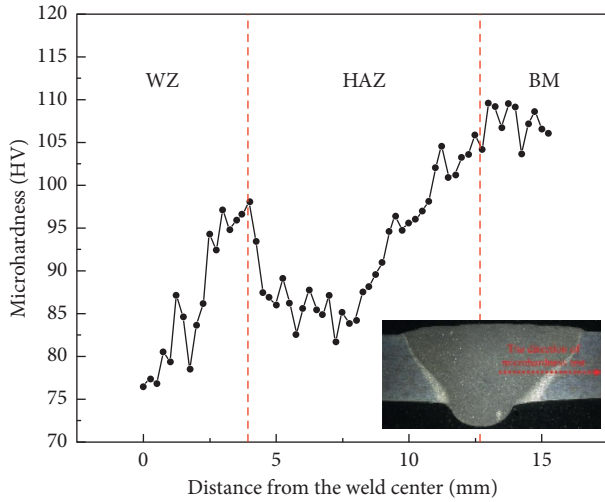


FIGURE 5: Microhardness of laser-MIG hybrid welded joint of 6061 aluminum alloy.

assessment code [30] for welded joints recommended by International Institute of Welding (II W), the test data are processed to establish the relationship between fatigue life (N) and stress (S) in fatigue test, as shown in Figure 6. The relationship between fatigue life (N) and stress amplitude ($\Delta\sigma$) can be expressed by

$$C_1 = N \times (\Delta\sigma)^k, \quad (1)$$

where C_1 is the fatigue strength coefficient at the first cycle and k is the fatigue strength coefficient. k can be obtained by fitting the experimental data with the least square method, and the fitting formula is as follows:

$$\lg N = \lg C_1 - k \times \lg \Delta\sigma. \quad (2)$$

By substituting the fatigue test data of WJ and BM into formula (2), the linear formula between fatigue life and stress amplitude of WJ and BM is obtained as follows:

$$\lg N = -0.1086 \lg \Delta\sigma + 2.38753. \quad (3)$$

$$\lg N = -0.1302 \lg \Delta\sigma + 2.78956. \quad (4)$$

According to formulas (3) and (4), the k value of BM fitting curve is slightly smaller than that of WJ, which indicates that the fatigue life of BM decreases faster with the increase of stress level. At the same time, under the condition of 1×10^6 cycles, the fatigue limits of BM and WJ are 101.9 MPa and 54.4 MPa, respectively, and the fatigue life of WJ is only 53.4% of that of BM. The welding defects in WJ and the softening phenomenon in HAZ are the main factors to reduce the fatigue life of the joint [31].

3.4. Analysis of Fatigue Fracture. Figure 7 shows the fracture morphology of BM fatigue sample with a stress amplitude of 90 MPa, and the fatigue life of the sample is 7.3×10^5 . The overall morphology of fatigue fracture (Figure 7(a)) can be divided into three typical regions, namely, fatigue source region (region I), fatigue crack propagation region (region

II), and transient fracture region (region III). The SEM image of the fatigue source area is shown in Figure 7(b), where the stress intensity factor ΔK is lower than the critical stress intensity factor ΔK_{th} [32]. The enlarged diagram of crack initiation in Figure 7(b) shows that the crack originated from the irregular impurity near the surface of BM. According to the analysis results of energy dispersive spectrometer (EDS), it can be judged that the impurity leading to crack initiation is an oxide impurity (Figure 7(c)). During the forming process of BM, the gas in the liquid phase is not discharged smoothly due to the uneven filling of the liquid metal, and the oxide impurity is formed near the surface of the material [33]. Under the action of fatigue load, these oxide impurities are easy to cause stress concentration and promote the initiation of fatigue cracks. After the crack initiation, it propagates into the grain along the direction perpendicular to the maximum normal stress direction, forming the fatigue crack propagation region (region II), as shown in Figure 7(d). In region II, approximate river patterns can be clearly observed on the fracture, which is one of the characteristics of cleavage faults. The fatigue striations and the Z-shaped secondary cracks between the fatigue strips are shown in Figure 7(e). The crack propagation direction is perpendicular to the fatigue striations. When the maximum stress intensity factor (K_{max}) exceeds the plane strain fracture toughness (K_{IC}), the fatigue specimen will fracture rapidly and form transient fracture region (region III) [32]. Figure 7(f) is the microscopic morphology of region III, and there are many dimples with different sizes in this area, which depicts the better toughness of BM. However, secondary cracks are found between the dimples, which indicates that the fatigue fracture of BM presents a certain brittleness. In conclusion, the fatigue failure mode of BM is ductile brittle mixed fracture.

The SEM images of fatigue fracture of laser-MIG hybrid welded joint with the stress amplitude of 85.5 MPa and fatigue life of 8.3×10^5 cycles are shown in Figure 8 and there are many porosity distributions in the fracture of the joint from Figures 8(a) and 8(b), and the fatigue crack originates from two large-scale pores near the weld surface. The two pores are closely adjacent with diameters of $460 \mu\text{m}$ and $190 \mu\text{m}$, respectively. The two pores are penetrated by a large secondary crack, and the initiation of secondary cracks is related to the stress concentration near the pores [27]. Secondary cracks can also be found between the WJ fatigue strips, which is similar to BM, as shown in Figure 8(c). The difference is that a granular white secondary phase with particle size of about $2 \mu\text{m}$ was found along the strike distribution of WJ secondary cracks. EDS analysis shows that the secondary phase is a Fe containing phase particle, as shown in Figure 8(d). The pinning effect of secondary phase particles on dislocation is the main cause of secondary cracks between fatigue striations [34]. The formation of secondary cracks will accelerate the growth of fatigue cracks, resulting in a significant reduction in fatigue life. Figures 8(e) and 8(f) are SEM images of WJ transient fracture region, from which the existence of pores can still be found. In addition, a large number of dimples with none distribution of secondary cracks can be observed, which indicates that the fatigue

TABLE.3: Date of fatigue tests of 6061 BM and welded joints.

Type	Samples	Maximum stress (MPa)	Stress amplitude (MPa)	Cycles	Fracture location
WJ	WJ-1	230	103.5	87186	Welded zone
WJ	WJ-2	220	99	198378	Welded zone
WJ	WJ-3	210	94.5	485937	Welded zone
WJ	WJ-4	200	90	621441	Welded zone
WJ	WJ-5	190	85.5	834052	Welded zone
WJ	WJ-6	180	81	1000000	No broken
BM	BM-1	280	126	388767	Parallel section
BM	BM-2	260	117	90957	Parallel section
BM	BM-3	240	108	101975	Parallel section
BM	BM-4	220	99	232716	Parallel section
BM	BM-5	200	90	730736	Parallel section
BM	BM-6	180	81	1000000	No broken

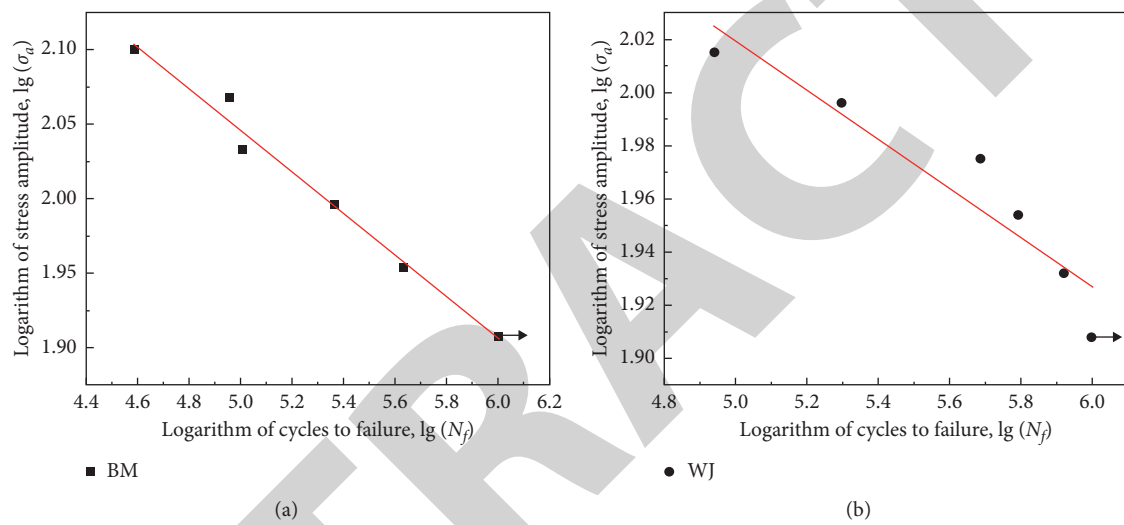


FIGURE 6: S-N fitting curve of (a) BM and (b) WJ.

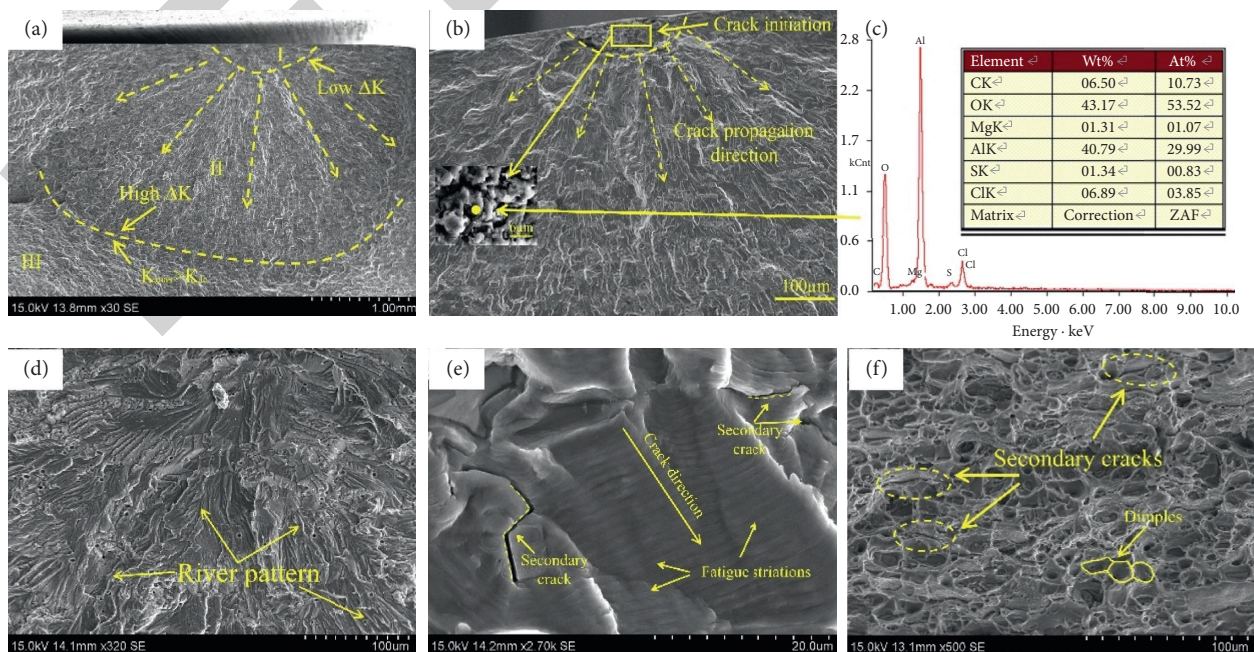


FIGURE 7: Fracture morphology of BM fatigue sample with stress amplitude of 121 MPa. (a) Overall fracture morphology. (b) Crack source. (c) Energy spectrum analysis result of yellow point in (b). (d) Fatigue crack propagation region. (e) Fatigue striation morphology. (f) Transient fracture region.

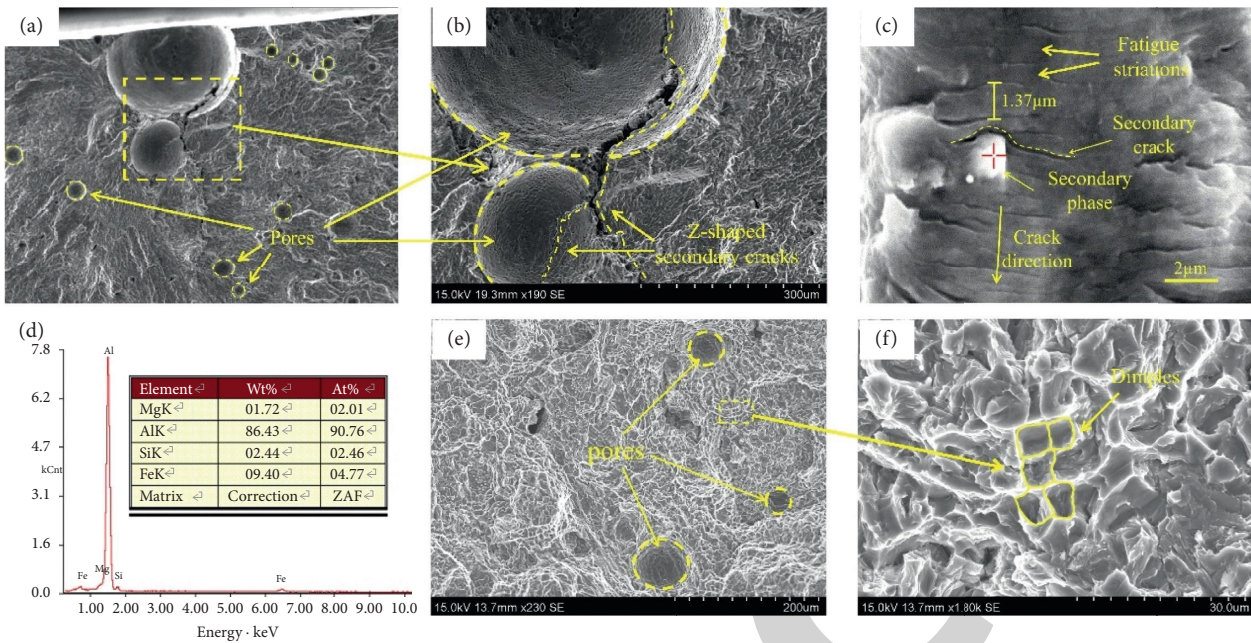


FIGURE 8: Fatigue fracture morphology of WJ under stress amplitude of 85.5 MPa. (a) Crack source and crack propagation region. (b) Partial enlargement of Figure 8(a). (c) Fatigue striations morphology in the crack propagation region. (d) Energy spectrum analysis result of the secondary phase particle in (c). (e) Transient region. (f) Partial enlargement of (e).

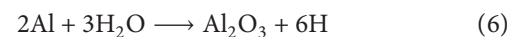
failure mode of WJ is ductile fracture mode. Based on the information in Figure 8, there are many pores in the three areas of the WJ fatigue fracture. The large number of pores would reduce the actual bearing area of the joint and cause WJ to fail in a lower fatigue life [22]. Therefore, it is extremely important to analyze the formation of pores in WJ and the initiation and propagation of cracks near the pores.

4. Discussion

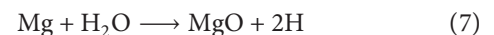
Figure 9 shows the cross section of the hybrid welded joint. It can be found that there are many different sizes of pores scattered on WZ, among which the number of pores in the upper and middle of WZ is obviously larger than that of the lower part, while the large size pores are mostly distributed in the middle part. Welding pores can be divided into metallurgical pores and process pores [35]. Metallurgical pores are generally round with smooth inner wall, which are mainly distributed in the upper and middle of WZ. The process pores are irregular in shape, and the inner wall is rough, which are generally caused by the instantaneous collapse of the keyhole of the welding heat source. In this article, the main type of pores is metallurgical pores with regular morphology, as shown in the figure.

No matter metallurgical pores and process pores, the pores in the joint would seriously break the uniformity of WZ microstructure. Liu proved that, even under low fatigue load, the peak stress near the edge of the pore is 3 times that of the defect-free state in WJ, which means that it is easy to initiate fatigue microcracks [22, 36]. In this chapter, the porosity defects of 6061 aluminum alloy laser-MIG WJ will be discussed from three aspects: porosity forming, initiation, and propagation of fatigue microcracks at the porosity.

4.1. Forming Mechanism of Metallurgical Porosity. The formation of metallurgical pores is closely related to the dissolved atomic hydrogen in the welding pool [37]. The main source of atomic hydrogen in WJ is H_2O from BM, welding wire, and the surrounding atmosphere. The base material and the welding wire ER4043 are easily oxidized, and the formed oxide film can adsorb a large amount of H_2O . H_2O will react formation formulas as follows under the compound heat source to generate atomic hydrogen:



The evaporation of alloying elements is also one of the main reasons for the formation of atomic hydrogen [35]. Si and Mg are two main alloying elements in 6061 aluminum alloy. The boiling point of Mg is only 1107 °C. Mg would evaporate rapidly and form metal vapor under the action of the composite heat source with high energy density. The formation formula is listed as follows:



H atom is easily dissolved in the molten pool at high temperature, and the solubility of atomic hydrogen decreases gradually with the decrease of temperature during welding. The solubility of atomic hydrogen in liquid phase and solid phase Al is 0.69 ml/g and 0.036 ml/g, respectively [23]. During the cooling process of the molten pool, the supersaturated hydrogen in the molten pool is gradually released with the decrease of solubility. The released atomic hydrogen is attached to the existing surface of the solute particles in the molten pool to form the bubble nucleation.

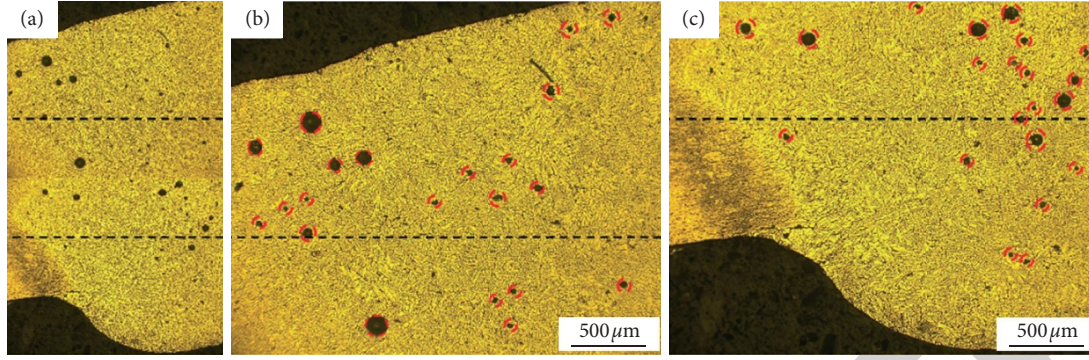


FIGURE 9: Schematic diagram of cross section of WJ. (a) Cross section of WJ. (b) Partial enlargement of cross section.

Bubbles will continue to grow after nucleation, and the growth needs to meet the formula:

$$P_h > P_0 = P_a + P_m + P_c + \frac{2\alpha}{r}. \quad (8)$$

P_h denotes the pressure in bubbles and such as hydrogen and nitrogen. The pressure in bubbles is mainly the partial pressure of hydrogen in aluminum alloy welding [38]; P_0 represents the external pressure that hinders the growth of bubbles, which is composed of atmospheric pressure P_a , and partial pressure P_m of molten metal above the bubble and partial pressure P_c of surface tension; α represents the surface tension, and the surface tension of liquid aluminum is 45 N/m; r represents the bubble radius.

It can be seen from the above formula that when the bubble is small, the additional pressure formed by the surface tension is large. However, during the welding process, there are many ready-made surfaces in the welding pool, which promotes the growth of bubbles in an oval shape and makes the bubble have a large curvature radius r , which reduces the additional pressure P_c and promotes the bubble growth. During the process of bubbles floating, the pressure from the molten pool gradually decreases, and the bubble continues to grow with the bubble radius increased. The buoyancy of bubbles increases with the increase of radius and tends to escape from the surface of molten pool. When bubbles do not escape in time before the solidification of molten pool, they will remain in WZ and become the welding pores. The formation mechanism of metallurgical pores during laser-MIG hybrid welding is shown in Figure 10.

In summary, whether pores are generated in WZ is related to the bubble escape velocity V_e and the size of the molten pool solidification rate V_s . When $V_e < V_s$, pores would appear in the weld. The bubble escape velocity can be expressed as

$$V_e = \frac{C(\rho_L - \rho_G)gr^2}{\eta}, \quad (9)$$

where C is a constant, g is the gravity acceleration, r is the bubble radius, η is the liquid metal viscosity, ρ_L is the liquid metal density, and ρ_G is the bubble density. According to the above formula, (1) the fast welding speed of hybrid welding and the strong thermal conductivity of 6061 aluminum alloy

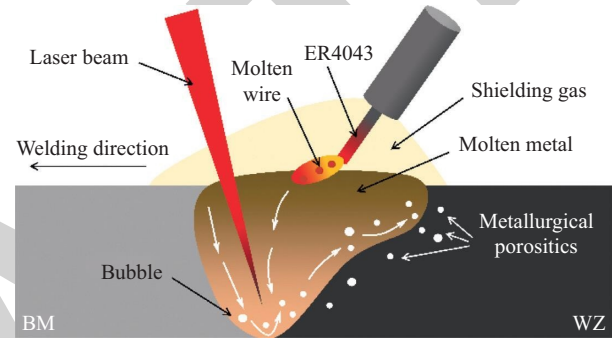


FIGURE 10: Formation mechanism of metallurgical pores during laser-MIG hybrid welding process.

lead to a larger V_s in the molten pool and a shorter time for bubbles to float out, which makes the joint have large porosity sensitivity. (2) The high viscosity of aluminum alloy leads to poor fluidity of molten pool, which is not conducive to the floating of bubbles and higher porosity. (3) The larger the bubble radius r is, the faster the V_e is. The larger the buoyancy of the bubble with larger radius in the molten pool is, the easier it is to escape.

Moreover, the generation of atomic hydrogen is accompanied by the formation of oxides like Al_2O_3 , MgO , as shown in formulas (6) and (7). During the solidification process of the molten pool, the oxide will be attached to the bubble, forming metallurgical pores with second phase and flocs in WZ, as shown in Figure 11. The EDS result shows that the oxygen content of the second phase is as high as 32.53%. According to the composition, the second phase is a metal oxide containing Al, Mg, and Mn. The oxides easily adhere to the inside of bubbles, resulting in a decrease of the buoyancy, making it difficult for bubbles to rise and escape from the molten pool [39].

4.2. Mechanism of Crack Initiation and Propagation near Pores. Fatigue crack initiation is related to the stress distribution at the initiation site, which can be reflected by the stress intensity factor K during crack initiation. The larger the K value is, the easier the crack initiation is [40]. As shown in Figure 8(a), two large pores at the crack source induce fatigue cracks, and their arrangement direction is perpendicular to the direction of fatigue stress loading. The study

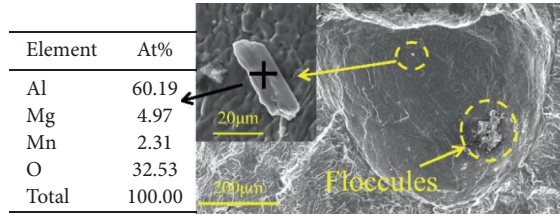


FIGURE 11: Metallurgical pore with second phase and floccs.

shows that when the arrangement direction of two close pores is perpendicular to the external stress loading direction, their stress field has obvious coupling effect and increases the stress concentration [41]. Since the pores are far smaller than W , a theoretical model with semicircular pores on the surface of an infinite subjected can be established according to Griffith's theory and the distribution of pores in Figure 8(a) to calculate the stress concentration at the pores, as shown in Figure 12 and the object is subjected to uniform external stress in the upper and lower directions. There is a semicircular pore P_1 near the surface of the object to simulate the pore on the surface of the sample, and the pore P_2 is close to P_1 in the model. The existence of P_1 and P_2 is equivalent to prefabricating microcracks near the surface of the specimen. According to the formula of stress intensity factor, when there is a semielliptical crack on the surface of an infinite object [42], it can be deduced that the K at P_1 is as follows:

$$K = \frac{1.1\sigma\sqrt{\pi L}}{\Phi}. \quad (10)$$

$$\Phi = \int_0^{\pi/2} \left(\cos^2 \beta + \frac{a^2}{b^2} \sin^2 \beta \right)^{1/2} d\beta, \quad (11)$$

where σ is the uniform tensile stress, L is the distance from the pore tip to the surface, Φ is the second kind of elliptic integral, and a and b are the long radius and short radius of the ellipse. Because the analysis object of this model is semicircular pore, the distance between the tip of the pore and the surface is equal to r , that is, $r = L$. In addition, the long radius and short radius of the semicircle are equal, so $a = b = r$, that is, $\Phi = 1.57$. Thus, formula (11) can be simplified as follows:

$$K = \frac{1.1\sigma\sqrt{\pi L}}{1.57} \approx 0.7\sigma\sqrt{\pi L}. \quad (12)$$

It can be seen from the above formula that the stress intensity factor K at P_1 increases with the increase of the distance L from the pore tip to the surface. The existence of hole P_2 increases the length of the precrack, increases the stress concentration near the surface of the object, and makes the crack easily formed.

The above analysis shows that the stress concentration at the tip of the pores is large, and cracks are easy to occur, but the actual situation is different from the above analysis. Referring to the crack initiation position shown in Figure 8(b), the crack is not exactly initiated at the tip,

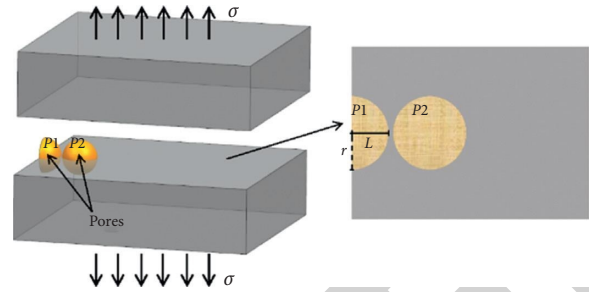


FIGURE 12: The schematic diagram of the theoretical model with pores on the surface of an infinite subject.

but slightly deviated. It can be seen from the local amplification in Figure 8(b) (Figure 13) that there are many convex grains on the inner surface of the pore and obvious grooves at the grain boundary. On the circumference of the interface between the pores and the material matrix, the grain boundary groove will inevitably exist. These grooves also produce stress concentration, and the degree of stress concentration is determined by the shape and size of the groove. Assuming that fine equiaxed grains are evenly distributed around the pores, the grooves must exist near the circumference, and the grain boundary depression on the circumference will further increase the distance L from the pores to the sample surface and increase the degree of stress concentration. Under the action of fatigue load, a microcrack occurs at the deviation from the tip of the pore and expands to both sides, as shown in Figure 14(a). According to the principle of energy optimization, the crack propagates along the grain boundary after initiation. However, in addition to equiaxed grains with uniform distribution, there are also columnar and dendritic grains with long strips. When the crack propagation meets a strip grain, the energy required for the crack propagation along the grain is greater than that through the grain, and the crack propagates in a transgranular manner, as shown in Figure 14(b).

The crack propagates in a Z-shaped way after initiation, as shown in Figure 15. Based on the fatigue crack propagation model proposed by Laird [43], the Z-shaped propagation mechanism of fatigue crack is analyzed, as shown in Figure 15. The propagation process can be divided into five steps: (1) the crack tip presents a closed state when the cyclic load is 0. (2) The crack turns to an open state under the application of tensile stress. At the same time, a certain slip system at the crack tip is activated, and the crack slip creates new microcracks along 45° . (3) When the tensile stress reaches the peak value, the slip zone expands to the maximum extent, the crack tip becomes semicircular, and the phenomenon of passivation occurs. The crack after passivation is difficult to propagate in the original direction. (4) Another slip system at the crack tip is activated in a new direction and is inducing microcracks under the action of compressive stress. (5) The crack is passivated again during its propagation. The above process is repeated continuously to form the Z-shaped propagation.

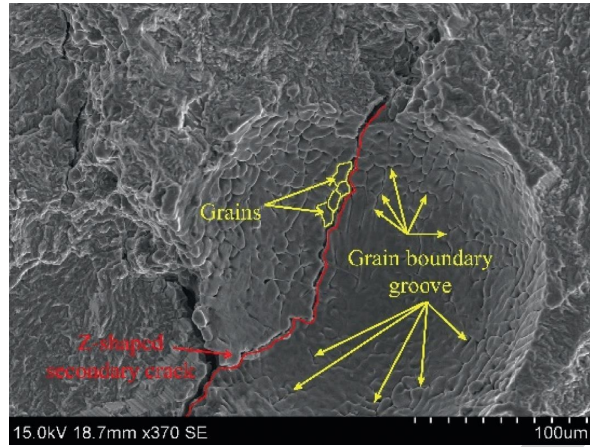


FIGURE 13: Partial enlargement of Figure 8(b).

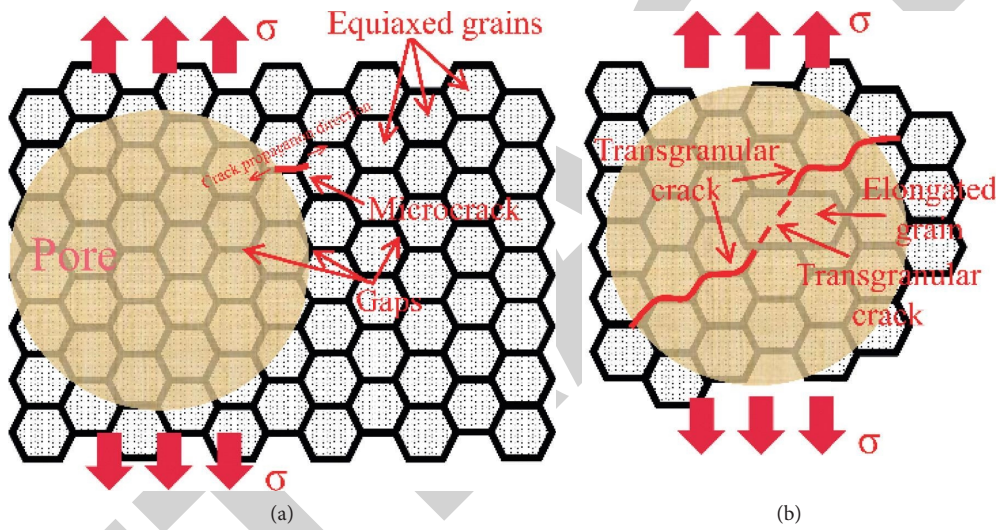


FIGURE 14: Mechanism of initiation and propagation of cracks at pores.

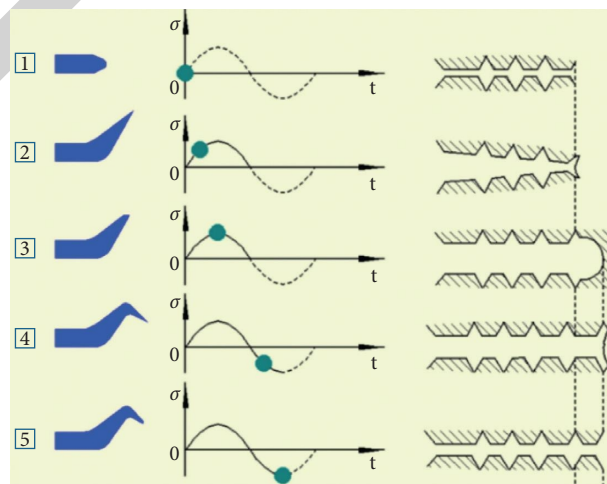


FIGURE 15: Z-shaped propagation of fatigue crack.

5. Conclusion

- (1) Snowflake equiaxed grains are found in WZ of 6061 aluminum alloy laser-MIG hybrid welded joint, and the grains in the upper part of WZ are coarser than those in other parts. The grain morphology of HAZ is close to that of BM, but the size is coarse. The lowest hardness position is WZ, which is 76.5 HV. There is a softening zone of about 3 mm in HAZ, and the lowest hardness of softening zone is 81 HV.
- (2) Under the condition of 1×10^6 cycles, the fatigue life of BM decreases faster with the increase of stress level. The fatigue limits of BM and WJ are 101.9 MPa and 54.4 MPa, respectively. The fatigue strength of WJ is only 53.4% of BM. Oxide impurity and surface pores are the main initiation for fatigue cracks in BM and WJ, respectively.
- (3) The type of pores in the joint is mainly metallurgical pores. The atomic hydrogen produced by H_2O in the oxide film of BM surface and the evaporation of Mg element are supersaturated in the molten pool and attached to the existing surface of the solute to form bubbles. When the escape velocity of bubbles is less than the cooling rate of molten pool, the bubbles that cannot escape form pores in WZ. Oxides produced during the formation of atomic hydrogen result in pores containing second phases and flocs.
- (4) The existence of pores is equivalent to prefabricating cracks in WJ. The existence of multiple near-surface pores will increase the size of prefabricated cracks, which expands the stress intensity factor and increases the stress concentration. The grain boundary grooves inside the pores will further expand the stress concentration and make the cracks initiate away from the tip of the pores. After the crack initiation, it will propagate along the grain boundary in Z shape. When elongated grains are encountered during propagation, the crack would propagate in a transgranular manner to save energy.

Data Availability

The data used to support the findings of this study are included within the article.

Conflicts of Interest

The authors declare that they have no conflicts of interest.

Acknowledgments

This project was sponsored by the National Natural Science Foundation of China (51971129) and the Shanghai Natural Science Foundation of China (19ZR1421200). This support is gratefully acknowledged.

References

- [1] C. D. Marioara, S. J. Andersen, J. Jansen, and H. W. Zandbergen, "Atomic model for GP-zones in a 6082 Al-Mg-Si system," *Acta Materialia*, vol. 49, no. 2, pp. 321–328, 2001.
- [2] J. S. de Jesus, A. Loureiro, J. M. Costa, and J. M. Ferreira, "Effect of tool geometry on friction stir processing and fatigue strength of MIG T welds on Al alloys," *Journal of Materials Processing Technology*, vol. 214, no. 11, pp. 2450–2460, 2014.
- [3] S. D. Ji, X. C. Meng, J. G. Liu, L. G. Zhang, and S. S. Gao, "Formation and mechanical properties of stationary shoulder friction stir welded 6005A-T6 aluminum alloy," *Materials & Design (1980–2015)*, vol. 62, pp. 113–117, 2014.
- [4] I. Bunaziv, O. M. Akselsen, A. Salminen, and A. Unt, "Fiber laser-MIG hybrid welding of 5 mm 5083 aluminum alloy," *Journal of Materials Processing Technology*, vol. 233, pp. 107–114, 2016.
- [5] L. Huang, D. Wu, and X. Hua, "Effect of the welding direction on the microstructural characterization in fiber laser-GMAW hybrid welding of 5083 aluminum alloy," *Journal of Manufacturing Processes*, vol. 31, pp. 514–522, 2018.
- [6] H. Huang, P. Zhang, and H. Yan, "Research on weld formation mechanism of laser-MIG arc hybrid welding with butt gap," *Optics & Laser Technology*, vol. 133, Article ID 106530, 2021.
- [7] Q. Chu, R. Bai, H. Jian, Z. Lei, N. Hu, and C. Yan, "Microstructure, texture and mechanical properties of 6061 aluminum laser beam welded joints," *Materials Characterization*, vol. 137, pp. 269–276, 2018.
- [8] B. Fu, G. Qin, X. Meng, Y. Ji, Y. Zou, and Z. Lei, "Microstructure and mechanical properties of newly developed aluminum-lithium alloy 2A97 welded by fiber laser," *Materials Science and Engineering: A*, vol. 617, pp. 1–11, 2014.
- [9] B. Acherjee, "Hybrid laser arc welding: state-of-art review," *Optics & Laser Technology*, vol. 99, pp. 60–71, 2018.
- [10] J. Liu, H. Zhu, Z. Li, W. Cui, and Y. Shi, "Effect of ultrasonic power on porosity, microstructure, mechanical properties of the aluminum alloy joint by ultrasonic assisted laser-MIG hybrid welding," *Optics & Laser Technology*, vol. 119, Article ID 105619, 2019.
- [11] W. M. Steen, "Arc augmented laser processing of materials. (USA)," *Vacuum*, vol. 31, no. 6, p. 277, 1981.
- [12] S. Yan, Y. Nie, and Z. Zhu, "Characteristics of microstructure and fatigue resistance of hybrid fiber laser-MIG welded Al-Mg alloy joints," *Applied Surface Science*, vol. 298, pp. 12–18, 2014.
- [13] I. Bunaziv, O. M. Akselsen, J. Frostevarg, and A. F. H. Kaplan, "Laser-arc hybrid welding of thick HSLA steel," *Journal of Materials Processing Technology*, vol. 259, pp. 75–87, 2018.
- [14] W. Suder, S. Ganguly, S. Williams, and B. Y. B. Yudodibroto, "Penetration and mixing of filler wire in hybrid laser welding," *Journal of Materials Processing Technology*, vol. 291, Article ID 117040, 2021.
- [15] R. Li, Z. Li, and Y. Zhu, "A comparative study of laser beam welding and laser-MIG hybrid welding of Ti-Al-Zr-Fe titanium alloy," *Materials Science and Engineering: A*, vol. 528, no. 3, pp. 1138–1142, 2011.
- [16] S. H. Yan, B. B. Xing, H. Y. Zhou et al., "Effect of filling materials on the microstructure and properties of hybrid laser welded Al-Mg-Si alloys joints," *Materials Characterization*, vol. 144, pp. 205–218, 2018.
- [17] A. H. Faraji, M. Moradi, M. Goodarzi et al., "An investigation on capability of hybrid Nd:YAG laser-TIG welding technology for AA2198 Al-Li alloy," *Optics and Lasers in Engineering*, vol. 96, pp. 1–6, 2017.
- [18] S. H. Yan, H. Y. Zhou, B. B. Xing et al., "Crystal plasticity in fusion zone of a hybrid laser welded Al alloys joint: from nanoscale to macroscale," *Materials & Design*, vol. 160, pp. 313–324, 2018.

Retraction

Retracted: Studying the Effect of Metallic Precursor Concentration on the Structural, Optical, and Morphological Properties of Zinc Sulfide Thin Films in Photovoltaic Cell Applications

Advances in Materials Science and Engineering

Received 26 December 2023; Accepted 26 December 2023; Published 29 December 2023

Copyright © 2023 Advances in Materials Science and Engineering. This is an open access article distributed under the Creative Commons Attribution License, which permits unrestricted use, distribution, and reproduction in any medium, provided the original work is properly cited.

This article has been retracted by Hindawi, as publisher, following an investigation undertaken by the publisher [1]. This investigation has uncovered evidence of systematic manipulation of the publication and peer-review process. We cannot, therefore, vouch for the reliability or integrity of this article.

Please note that this notice is intended solely to alert readers that the peer-review process of this article has been compromised.

Wiley and Hindawi regret that the usual quality checks did not identify these issues before publication and have since put additional measures in place to safeguard research integrity.

We wish to credit our Research Integrity and Research Publishing teams and anonymous and named external researchers and research integrity experts for contributing to this investigation.

The corresponding author, as the representative of all authors, has been given the opportunity to register their agreement or disagreement to this retraction. We have kept a record of any response received.

References

- [1] S. Abel, J. Leta Tesfaye, R. Kiran et al., "Studying the Effect of Metallic Precursor Concentration on the Structural, Optical, and Morphological Properties of Zinc Sulfide Thin Films in Photovoltaic Cell Applications," *Advances in Materials Science and Engineering*, vol. 2021, Article ID 7443664, 6 pages, 2021.

Research Article

Studying the Effect of Metallic Precursor Concentration on the Structural, Optical, and Morphological Properties of Zinc Sulfide Thin Films in Photovoltaic Cell Applications

S. Abel,¹ J. Leta Tesfaye,^{1,2} R. Kiran,³ T. Deepak,⁴ A. Usha Ruby,⁵ S. Venkatesh,⁶
and R. Krishnaraj^{2,7} 

¹Physics Department, College of Natural and Computational Science, Dambi Dollo University, Dambi Dollo, Ethiopia

²Centre For Excellence, Indigenous Knowledge, Innovative Technology Transfer and Entrepreneurship, Dambi Dollo University, Dambi Dollo, Ethiopia

³Electrical and Computer Engineering, Dambi Dollo University, Dambi Dollo, Ethiopia

⁴Department of Accounting and Finance, Dambi Dollo University, Dambi Dollo, Ethiopia

⁵Department of Computer Science and Engineering, GITAM University, Bangalore, India

⁶Mechanical Engineering, National Institute of Technology, Tiruchirappalli, India

⁷Department of Mechanical Engineering, Dambi Dollo University, Dambi Dollo, Ethiopia

Correspondence should be addressed to R. Krishnaraj; prof.dr.krishnaraj@dadu.edu.et

Received 7 May 2021; Accepted 31 May 2021; Published 9 June 2021

Academic Editor: Samson Jerold Samuel Chelladurai

Copyright © 2021 S. Abel et al. This is an open access article distributed under the Creative Commons Attribution License, which permits unrestricted use, distribution, and reproduction in any medium, provided the original work is properly cited.

Thin films of zinc sulfide (ZnS) with different concentrations of zinc acetate have been made by chemical bath deposition technique in acidic medium (pH = 5) on glass substrate using zinc acetate and sodium sulfide as sources of Zn^{+2} ion and S^{-2} ion, respectively, and ethylenediaminetetraacetate as complexing agents and sulfuric acid to adjust pH value at a constant deposition temperature of 85°C, and the deposition time of 90 minutes was used. The effect of the concentration of metallic precursor on the structural, morphological, and optical properties of chemical bath deposited zinc sulfide thin films was investigated in this study. The XRD result confirmed mixed phases of crystalline and amorphous structure dominating other phases, which is witnessed by larger crystallite size than other phases. It reveals that the thin films had hexagonal structure at the medium concentration with preferred orientation along (111) plane, and at lower and higher concentration, it showed that film has an amorphous structure in nature. The crystallinity of all the phases significantly enlarged with increasing the zinc precursor concentration. The SEM micrographs showed high-pitched edged irregular-shaped grains covering the substrate with pinholes and bangs. The optical properties investigated by the UV-VIS spectrometer specified a decrease in the optical bandgap of the films between 3.5 eV and 2.6 eV as the zinc acetate concentration in the solution increased from 0.1 to 0.2 M. It showed that the zinc sulfide had high absorption in the UV radiation. The main finding of this paper is that metallic precursor concentration has a significant role in the optical, morphological, and microstructural properties of the cobalt sulfide thin films, which are most suitable for photovoltaic applications.

1. Introduction

In today's world, most of the energy comes from fossil fuel, coal, oil, and gas, besides electricity and nuclear power. However, if they are not sustainable, the emissions from the combustion of fossil fuel increase the concentration of CO_2 in the atmosphere that enhances the greenhouse effect. This,

in turn, leads to global warming which could have adverse consequences on the food production and water supply [1]. Solar energy, on the other hand, is a clean energy option that is significantly cleaner, providing a solution to many of the environmental and social issues linked to fossil and nuclear fuels. As a result, solar energy technologies have clear environmental advantages over traditional energy sources,

leading to the long-term sustainability of human activities. Their primary benefit is reduced carbon dioxide (CO₂) pollution and, in most cases, the absence of any air pollution or harmful chemicals during their service. Furthermore, due to their critical position in photovoltaic technology, optical switches, and solar cell processing, metal sulfide semiconducting thin films have gained a lot of attention in recent years. Hence, ZnS thin films can be substitute chalcogenides. Since it has direct bandgaps in the absorption area, they are ideal for high photosensitivity in the infrared range, solar panels, large coefficients of optical absorption, and excellent semiconductor characteristics stability. However, the limited reports on the chemical bath deposition in the acid medium of ZnS show that most of the depositions are carried out in alkaline baths and have not been given yet to the chemical bath deposition of ZnS thin films [2]. Therefore, it is anticipated that novel chemical bath deposition routes for ZnS can be established if sufficient attention is given. The researchers, therefore, inspire the use of acidic zinc (Zn(Ac)₂·2H₂O) and sodium sulfide (Na₂S) as important complexing agents to compare the advanced thin films of the ZnS semiconductor material to synthesize and characterize zinc sulfide thin films utilizing chemical bath process deposition of acidic medium [3]. There are many deposition methods to synthesize ZnS thin films. However, it is widely accepted that the high quality of thin films deposited by CBD can be deposited in vast areas [1]. ZnS thin films were deposited using chemical bath deposition. The high resistivity and low optical transmittance of such materials' films restrict their use as optical materials for thermoelectric materials, necessitating the need to develop their optical and electrical properties [4]. Furthermore, there is a scarcity of knowledge on the structural, morphological, and optical properties of ZnS thin films in an acidic medium (pH = 5). Thin films deposited in a simple (alkaline) environment usually produce oxides or hydroxides, which can degrade the film's consistency [5]. It will be hard to manufacture high-quality ZnS thin films inside of an alkaline chemical soak environment unless the challenge of ZnS deposition is overcome [6–10]. The impact of hydroxide is minimized when ZnS is deposited in an acidic chemical bath. For most metal ions widely used in CBD, it is fair to conclude that no hydroxide is available under such conditions and also that deposition occurs through an ion-by-ion process [11–14]. The aim of this research was to look at ZnS thin films deposited under different defined temperatures for photovoltaic cell applications.

2. Experiment

Before the experiment, the chemicals used to make the chemical soak were of experimental chemical agent grade (AR) from Aldrich, which had a purity of 99.9%. Zinc acetate (Zn(Ac)₂·2H₂O) and sodium sulfide (Na₂S) were used as precursors for Zn²⁺ and S²⁻ sources, respectively. For the main chemical process, TEA has been used as a complexing agent, and sulfuric acid (H₂SO₄) has been used to change the pH to 5. Substrates were cleaned with detergent and H₂O until being ultrasonically cleaned with acetone, alcohol, and

deionized (DI) water and then dried in the air before deposition. Chemical concentrations were calculated as follows: 0.1, 0.2, and 0.3 M of (Zn(Ac)₂·2H₂O) and 0.1 M of (Na₂S) in equal volume quantitative relation, and TEA was taken as complexing agent. Initially, the solution was prepared by separately solubilizing chemicals in filtered water using magnetic stirring.

After preparing all of the solutions, they were mixed together, and the maximum hydrogen ion concentration was regulated by adding caustic soda to the solution. The mixture was heated to 85°C, and clean SLG substrates were submerged in it. Figure 1 depicts a graphical representation of chemical bath deposition. For deposition of ZnS thin films, 0.1, 0.2, and 0.4 M of Zn(Ac)₂·2H₂O and 0.1 M of Na₂S were drawn in equivalent volume quantitative relation. The same technique was used to deposit ZnS film on a substrate at various concentrations of zinc sulfate over a 90-minute period. The accumulated films were separated from the solution, washed in DI water to eliminate the ions, dried in the air, and stored for characterization.

Once making ready all the solutions, they were mixed, and the final hydrogen ion concentration was controlled by adding a caustic soda. Clean SLG substrate was immersed within the solution and heated to 85°C. A schematic diagram of the deposition by chemical bath is shown in Figure 1. For deposition of ZnS thin films, 0.1, 0.2, and 0.4 M of Zn(Ac)₂·2H₂O and 0.1 M of Na₂S were taken in equal volume quantitative relation. The same procedure was followed for deposition of film at different concentrations of zinc sulfate for 90 minutes. ZnS film was deposited on the substrate. Deposited films were removed from the solution, rinsed in DI water to remove the ions from the film, dried in air, and preserved for characterization.

3. Results and Discussion

3.1. Characterization. The physical properties of deposited ZnS thin films were investigated using a PANalytical X'Pert specialist X-ray diffraction device with copper (Cu), which has K radiation with an X-ray emission wavelength of 1.5418 in the range of 0.1 to 0.3 M. Using the Scherer relationship, mean crystallite sizes were estimated to be compatible with the increase of peaks. A scanning electron microscope was used to investigate the morphology of the surface (SEM). The LAMBDA 950 UV/Vis/NIR Spectrophotometer was used to investigate the UV characteristic [14–16].

3.2. X-Ray Diffraction. The activity structural analysis of as-deposited, processed thin films on glass substrate was performed using the X-ray diffraction (XRD) technique [17]. The spectra of the as-deposited ZnS film are shown in Figure 2. At 0.1, 0.2, and 0.3 M, Figure 2(a) reveals optical phenomena with sharp peaks at 25.23°, 18.99°, and 38.51°, suggesting the amorphous existence of the as-deposited film. The area units (111), (110), and (100) will be calculated by evaluating measured “*d*” values with experimental “*d*” values of normal crystal-shaped ZnS crystal corresponding phases [18].

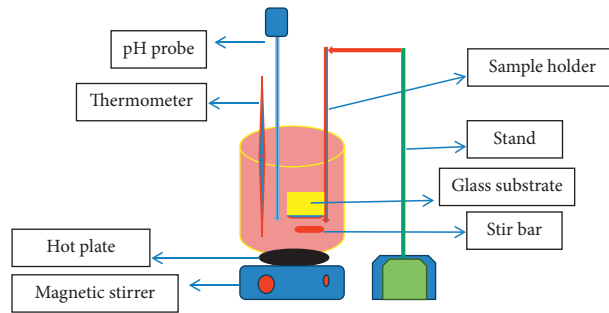


FIGURE 1: Setup of chemical bath deposition technique.

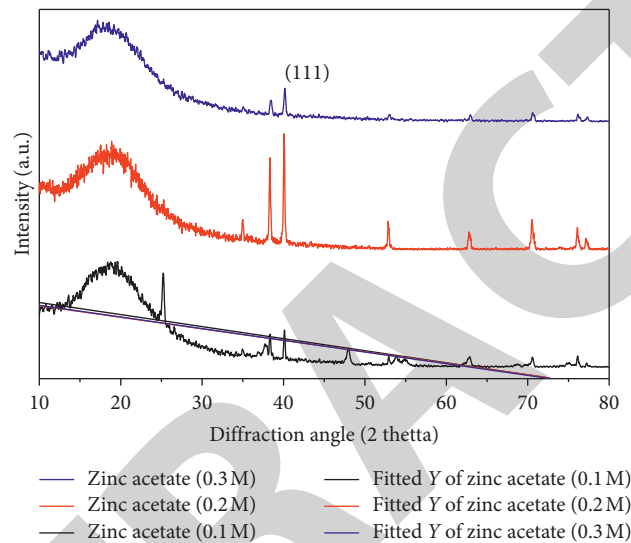


FIGURE 2: XRD patterns of deposited ZnS thin film at different zinc acetate concentrations.

Figure 2 shows the surface morphologies of ZnS thin films of different concentrations of metallic precursor. The microstructure of thin films is significantly influenced by changes in zinc acetate concentration. All the films are free from cracks and cover the substrate completely. For 0.1 M acetate, the SEM micrographs consisted of nearest to hexagonal grains at topmost with compact background grains. The scanning electron microscope micrographs of ZnS film deposited by 0.2 M zinc acetate consist of a chain of sharp irregular-shaped grains over a flat background morphology. The formation of collars between jots indicates the porousness of grains. In the case of ZnS thin films deposited by 0.3 M zinc acetate, the background morphology is similar to that deposited by 0.1 M zinc acetate; however, the large top surface grains become polygonal in shape. The two main thin film deposition mechanisms in chemical bath deposition are named ion-by-ion and cluster-by-cluster deposition mechanisms. The cations and anions bind to the substrate first and then engage in chemical reactions to form the film in the ion-by-ion process, while in the cluster-by-cluster mechanism, the ions react and form a deposit within the solution before adhering to the substrate [18].

Table 1 shows the film's FWHM of diffraction peaks and size distribution. The synthesis of a crystal isometric formed ZnS thin film is adjusted using this analysis. As a result, the

findings are in accordance with those obtained previously [19, 20]. The intensity of the peak corresponding to part (111) is found to be significantly higher than that of other peaks, indicating that this is the most common alignment for treated film in this region. When the concentration of zinc acetate increased from 0.1 M to 0.2 M, the peaks are increasingly formed, and when it is increased to 0.3 M, it becomes less peak; this shows that, at higher concentration, the ZnS thin films changed from crystalline to amorphous structure. This result agrees with the previous report [21].

3.3. Scanning Electron Microscope. As shown in Figure 3, the smooth background layer for ZnS thin films deposited by 0.1, 0.2, and 0.3 M of zinc acetate could be formed by an ion-by-ion deposition mechanism [19]. However, the top layers with large grains signify the clusters of grains initially grown within the solution and adsorbed to the substrate at the final phase of the deposition. As the idea of reporters, it showed that high concentration, temperature, and deposition time lead to cluster-by-cluster deposition [22].

Fine elongated particles of various sizes are evenly distributed around the substrate. The surface is also covered with small agglomerates of varying sizes. It is difficult to get an accurate estimate of particle size. It is also possible to see

TABLE 1: Parameters of XRD spectra for ZnS thin films at different zinc acetate concentrations.

2 theta (degree)	d (Å)	Concentration (M)	hkl	FWHM (Rad)	Grain size (nm)
25.23	3.36	0.1	(111)	1.19	22.3
18.99	2.69	0.2	(110)	8.41	24.5
38.51	1.91	0.3	(100)	0.87	30.2

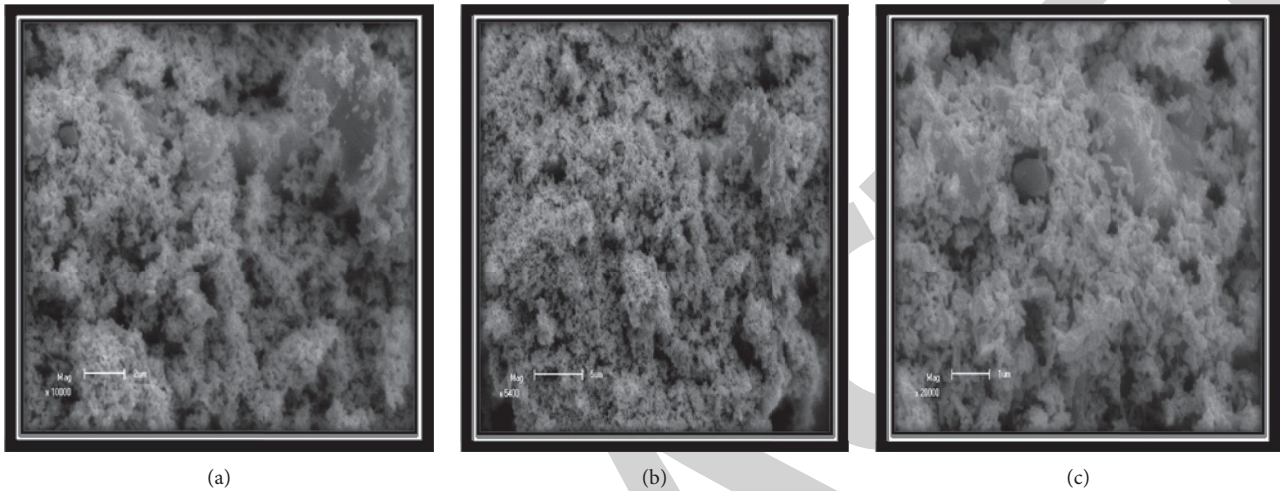
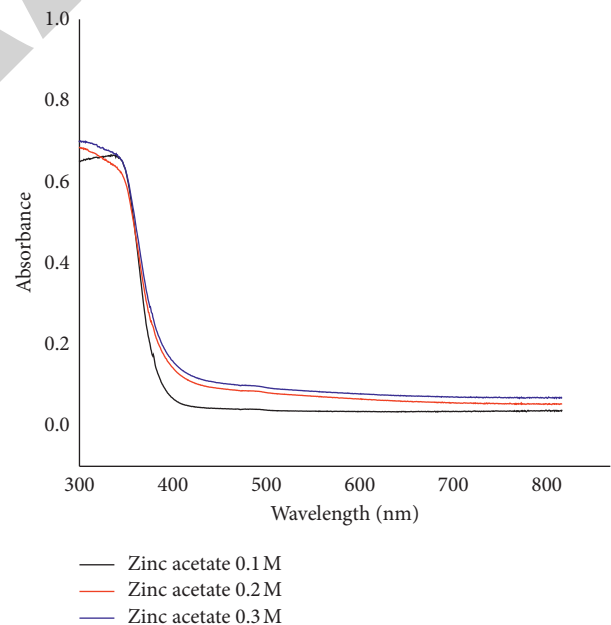


FIGURE 3: Scanning electron microscopic images of ZnS thin films at different zinc acetate concentrations: (a) 0.1 M, (b) 0.2 M, and (c) 0.3 M.

some microporous gap between the fine particles. The porous structure of films will help boost the redox balance [23, 24].

3.4. Optical Absorption Study. The optical absorption of zinc sulfide thin films formulated from various zinc acetate concentrations was calculated throughout the range of wavelength of 450 to 2250 nm. The absorbance of the films significantly increased with increasing the cobalt acetate concentration within the considered range of wavelength. The apparent wavelength spectrum is where the films' maximum absorption is observed.

As shown in Figure 4, the bandgap of the films is determined by extrapolating the linear portion of a $(h\nu)^2$ versus (h) curve. As the amount of zinc acetate solution increased from 0.1 M to 0.3 M, the bandgap of the films reduced from 3.5 eV to 2.6 eV. The decrease in bandgap may be due to an increase in crystallite size as the concentration of zinc acetate in the deposition bath is increased [25]. All ZnS thin films have high absorbance in the visible light area and bandgaps in the range of 3.5 eV to 2.6 eV, making them candidate materials for absorber layers in thin-film solar cells as well as effective visible light photocatalysts [26–31].

FIGURE 4: Plots of variation of optical absorption (αt) versus wavelength films using different zinc acetate concentrations (0.1, 0.2, and 0.3 M).

4. Conclusion

The chemical bath deposition (CBD) method was implemented by changing parameters and using an 80°C deposition temperature and a 90-minute deposition time for the synthesis of ZnS thin films. Different characterization techniques were used to classify thin films that were deposited. The surface morphology of a ZnS thin film indicates that as the amount of zinc acetate is increased, the grain size increases, and the optical bandgap energy decreases from 3.5 eV to 2.6 eV, which is ideal for a photoabsorber.

Data Availability

The data used to support the findings of this study are included within the article.

Conflicts of Interest

The authors declare that there are no conflicts of interest.

References

- [1] M. Cao, X. Zhang, J. Ren et al., "Chemical bath deposition of SnS: Cu/ZnS for solar hydrogen production and solar cells," *Journal of Alloys and Compounds*, vol. 863, Article ID 158727, 2021.
- [2] C. M. Venkatraman, R. Krishnaraj, M. Sakthivel, K. Kanthavel, and R. Palani, "Enhanced ERP for paper machines," *International Journal of Scientific & Engineering Research*, vol. 2, pp. 1–10, 2011.
- [3] M. Balamurugan, R. Krishnaraj, M. Sakthivel, K. Kanthavel, and R. Palani, "Computer aided modeling and optimization analysis," *International Journal of Scientific & Engineering Research*, vol. 2, pp. 1–8, 2011.
- [4] M. M. Thilak, R. Krishnaraj, M. Sakthivel, K. Kanthavel, and R. Palani, "Transient thermal and structural analysis of the rotor disc of brake," *International Journal of Scientific & Engineering Research*, vol. 2, pp. 1–4, 2011.
- [5] Z. D. Khefacha, Z. Benzarti, M. Mnari, and M. Dachraoui, "Electrical and optical properties of $Cd_{1-x}Zn_xS$ ($0 < x < 0.18$) grown by chemical bath deposition," *Journal of Crystal Growth*, vol. 260, no. 3, pp. 400–409, 2020.
- [6] M. G. Deepan, K. Kanthavel, and R. Krishnaraj, "Optimization of shaft design under fatigue loading using Goodman method," *International Journal of Scientific & Engineering Research*, vol. 2, no. 2011, pp. 1–5, 2011.
- [7] P. Dharmalingam, K. Kanthavel, R. Sathiyamoorthy, M. Sakthivel, R. Krishnaraj, and R. Elango, "Optimization of cellular layout under dynamic demand environment by simulated annealing," *International Journal of Scientific & Engineering Research*, vol. 3, pp. 1–7, 2012.
- [8] S. Varatharajan, R. Krishnaraj, M. Sakthivel, K. Kanthavel, M. Deepan, and M. GandPalani, "Design and analysis of single disc machine top and bottom cover," *International Journal of Scientific & Engineering Research*, vol. 2, pp. 1–6, 2011.
- [9] L. Tesfaye Jule, K. Ramaswamy, N. Nagaprasad, V. Shanmugam, and V. Vignesh, "Design and analysis of serial drilled hole in composite material," *Materials Today: Proceedings*, vol. 45, pp. 5759–5763, 2021.
- [10] L. Tesfaye Jule, K. Ramaswamy, B. Bekele, A. Saka, and N. Nagaprasad, "Experimental investigation on the impacts of annealing temperatures on titanium dioxide nanoparticles structure, size and optical properties synthesized through sol-gel methods," *Materials Today: Proceedings*, vol. 45, pp. 5752–5758, 2021.
- [11] G. Hodes, *Chemical Solution Deposition of Semiconductor Films*, CRC Press, Boca Raton, FL, USA, 2020.
- [12] N. Arif and C. S. Fun, "Impact on development of ZnS nanoparticles thin film deposited by chemical bath deposition and spin coating," *International Journal of Advanced Engineering and Nano Technology*, vol. 4, no. 5, Article ID 024521, 2020.
- [13] S. S. Yesilkaya, U. Ulutas, and H. M. AbdAlqader, "Effect of Na doping on the properties of ZnS thin films and ZnS/Si heterojunction cells," *Materials Letters*, vol. 288, Article ID 129347, 2021.
- [14] A. Garrido-Hernández, D. Y. Medina-Velazquez, A. D. J. Morales-Ramírez et al., "Effect of europium on the blue-green emission of ZnS thin films by polyol and dip-coating technique," *Materials Science in Semiconductor Processing*, vol. 121, Article ID 105403, 2021.
- [15] K. Naseema, K. Ribin, N. Navya, and P. Prasannan, "Thermal conversion of CBD grown ZnS thin films to ZnO," *Zeitschrift für Naturforschung A*, vol. 76, no. 1, pp. 65–73, 2021.
- [16] U. P. Onochie, S. C. Ikpeseni, H. I. Owamah et al., "Analysis of optical band gap and Urbach tail of zinc sulphide coated with aqueous and organic dye extracts prepared by chemical bath deposition technique," *Optical Materials*, vol. 114, Article ID 110970, 2021.
- [17] J. A. Vargas-Rueda, A. R. Alonso, M. Meléndez-Zamudio, and M. Meléndez-Lira, "Chemical stability diagrams as a powerful tool to the synthesis of Cu_2SnS_3 thin films by chemical bath deposition," *Materials Chemistry and Physics*, vol. 265, Article ID 124478, 2021.
- [18] C. S. Vall, M. Chaik, A. Tchenka et al., "Effect of chromium percentage doping on the optical, structural, morphological and electrical properties of ZnS: Cr thin films," *Physica E: Low-Dimensional Systems and Nanostructures*, vol. 130, Article ID 114694, 2021.
- [19] K. Benyahia, F. Djeflal, H. Ferhati et al., "Microstructured ZnO-ZnS composite for earth-abundant photovoltaics: elaboration, surface analysis and enhanced optical performances," *Solar Energy*, vol. 218, pp. 312–319, 2021.
- [20] A. Slonopas, N. K. Dhar, H. Ryan, J. P. Ferrance, P. Norris, and A. K. Sood, "Efficient optimization of the optoelectronic performance in chemically deposited thin films," *Thin Film Processes: Artifacts on Surface Phenomena and Technological Facets, Books on Demand*, vol. 99, p. 107, 2017.
- [21] P. O. Offor, S. N. Ude, G. M. Whyte et al., "Effect of concentration of trisodium citrate complexing agent on spray-synthesized ZnS thin films," *Materials Today: Proceedings*, vol. 36, pp. 133–140, 2021.
- [22] A. F. Abdulrahman, S. M. Ahmed, S. M. Hamad, and A. A. Barzinjy, "Effect of growth temperature on morphological, structural, and optical properties of ZnO nanorods using modified chemical bath deposition method," *Journal of Electronic Materials*, vol. 50, no. 3, pp. 1–14, 2021.
- [23] K. H. Maria, P. Sultana, and M. B. Asfia, "Chemical bath deposition of aluminum doped zinc sulfide thin films using non-toxic complexing agent: effect of aluminum doping on optical and electrical properties," *AIP Advances*, vol. 10, no. 6, Article ID 065315, 2020.
- [24] J. Kim, C. R. Lee, V. K. Arepalli, S. J. Kim, W. J. Lee, and Y. D. Chung, "Role of hydrazine in the enhanced growth of zinc sulfide thin films using chemical bath deposition for Cu

Retraction

Retracted: Steady-State Flow Characteristics and End Clearance Optimization of Internal Gear Grease Pump

Advances in Materials Science and Engineering

Received 26 December 2023; Accepted 26 December 2023; Published 29 December 2023

Copyright © 2023 Advances in Materials Science and Engineering. This is an open access article distributed under the Creative Commons Attribution License, which permits unrestricted use, distribution, and reproduction in any medium, provided the original work is properly cited.

This article has been retracted by Hindawi, as publisher, following an investigation undertaken by the publisher [1]. This investigation has uncovered evidence of systematic manipulation of the publication and peer-review process. We cannot, therefore, vouch for the reliability or integrity of this article.

Please note that this notice is intended solely to alert readers that the peer-review process of this article has been compromised.

Wiley and Hindawi regret that the usual quality checks did not identify these issues before publication and have since put additional measures in place to safeguard research integrity.

We wish to credit our Research Integrity and Research Publishing teams and anonymous and name external researchers and research integrity experts for contributing to this investigation.

The corresponding author, as the representative of all authors, has been given the opportunity to register their agreement or disagreement to this retraction. We have kept a record of any response received.

References

- [1] X. Li, L. Tang, and M. Qian, "Steady-State Flow Characteristics and End Clearance Optimization of Internal Gear Grease Pump," *Advances in Materials Science and Engineering*, vol. 2021, Article ID 8293040, 16 pages, 2021.

Research Article

Steady-State Flow Characteristics and End Clearance Optimization of Internal Gear Grease Pump

Xinjian Li , Lingfeng Tang, and Ming Qian

School of Mechanical Engineering, Anhui Polytechnic University, Wuhu, Anhui 241000, China

Correspondence should be addressed to Xinjian Li; 2190130115@stu.ahpu.edu.cn

Received 9 April 2021; Accepted 13 May 2021; Published 28 May 2021

Academic Editor: Samson Jerold Samuel Chelladurai

Copyright © 2021 Xinjian Li et al. This is an open access article distributed under the Creative Commons Attribution License, which permits unrestricted use, distribution, and reproduction in any medium, provided the original work is properly cited.

The internal gear grease pump is a mechanical device used for transfer of high viscosity fluid. The existing clearance between the end faces of the internal or external gear and the floating side plate might cause pump leakage during operation. In order to obtain the optimal end clearance of the internal gear grease pump, the rheological features of the lubricating lithium-based grease for various temperatures are explored via rotating rheometer. Shear force and apparent viscosity are chosen as monitored experimental parameters. The experimental data is fitted to obtain grease rheological features at various temperatures. The end clearance flow field model and the leakage model are established. Fluent software is employed for solving the flow field model and exploring the effect of temperature, end clearance, and speed on grease leakage. Superior grease flow performance is observed with an increase in temperature, which makes it to easier for the grease to leak from the end clearance. With an increase in the end clearance and the working pressure of the pump, an increase in leakage is also observed. Furthermore, it is found that rotational speed also affects the pump leakage. The leakage mechanism is obtained by combining the rheological features of the grease at the end clearance. The mathematical model method is utilized to solve for the optimal value of the end clearance.

1. Introduction

The compact structure and small flow pulsation of the internal gear pump contribute to its wide usage in industrial fields that require high precision, energy saving, high environmental noise, and high reliability. Similar to other types of pumps, internal gear pump leakage, as well as the end leakage, is often problematic. The end clearance of the internal gear pump is formed by the friction pair between the end faces of internal and external gears and the floating side plate. Thus, successful prevention of end leakage can significantly improve the volumetric efficiency of the pump.

Schweiger et al. [1] established the flow field model of the end clearance and radial leakage of the internal gear pump. The authors employed numerical simulations to explore the effect of temperature on the end clearance and radial clearance leakage. The leakage will cause the power loss of the internal gear pump. Guo [2] used the CFD method to numerically simulate the pressure field and the velocity field and analyzed the effects of extrusion power loss, pressure

and viscous power loss, rotation speed, and tooth width on flow field characteristics. Zeng [3] established the geometric relationship during the meshing process, and the unloading area expression was obtained by using the geometric pattern expansion method with the variable f as the independent variable. A few scholars [4–7] also applied different algorithms to optimize the parameters of internal gear pump. However, when grease is employed as the pump medium, which is a non-Newtonian fluid and has unique rheological features, it is necessary to investigate its physical properties. Bingham [8] studied the plastic fluids and found that when the stress exceeded the yield strength of the material, it maintained a proportional relationship with strain. This observation is now called the Bingham model. Herschel and Bulkley [9] utilized three parameters to establish a theoretical model of the relationship between grease shear stress and shear rate. This model was named the H-B model. Radulescu [10] and Radulescu employed the Bingham model to investigate the application of calcium-based and lithium-based lubricating grease. The authors found that the H-B

model provided better correlation of rheological features of the two greases with the experimental data. Many studies have been conducted on mechanisms of grease change, structure, and application of laws in engineering practice. Mohamed [11] used high-resolution transmission electron microscope (HRTEM) and scanning electron microscope (SEM) to study the microstructure of CNTs and lithium lipids. Hamrock and Dawson [12] found that when the grease is subjected to higher shear stress, the viscosity of the grease maintains a linear change within a certain range. When the influence of grease fiber content on the rheological features ranged from 2% to 16%, it was found that the soap fiber content negatively correlates with grease rheological index, while positive correlation is observed with grease yield stress [13]. Wang et al. discovered BN nanoparticles can not only produce lubricating film to protect friction pairs, but also their layered structure is easy to cause sliding of the friction pairs under the action of friction [14]. Simultaneously, the pipeline or transportation equipment grease temperature increase caused by friction also affects the internal structure of the grease. The variation of physical entanglement caused by short heat treatment changed the tribological properties of the lithium-based lubricating grease [15]. On the other hand, many domestic researchers have not specifically studied the influence of grease as medium on pump performance.

In this paper, a rotating rheometer is employed to explore the rheological features of lithium-based lubricating grease at the end clearance with consideration of different temperatures. Fluent software is used to simulate the flow field of the model and to explore the effects of temperature, end clearance, and rotational speed on the end clearance leakage. Based on the basic equations of fluid dynamics, as well as the grease rheological model, the end clearance leakage model of the internal gear grease pump is developed. The mathematical model method is employed to optimize the end clearance and investigate the leakage mechanism.

2. Research on the Rheological Features of Grease

In order to study the pump leakage mechanism at the end clearance, it is necessary to study the rheological features of the grease and explore the influence of the grease characteristics on the end clearance leakage itself. The NLGI 1 lubricating grease is usually used in internal gear pumps [16]. Performance parameters of several lubricating greases are shown in Table 1.

Based on data provided in Table 1, it can be concluded that the lithium-based lubricating grease, calcium-based lubricating grease, and complex calcium-based lubricating grease have higher penetration, but according to the temperature set by the experiment, calcium-based lubricating grease cannot meet the temperature requirements, and the water resistance of complex calcium-based lubricating grease is not suitable for the experimental environment. Therefore, lithium-based lubricating grease is selected as the experimental material.

2.1. Test of Rheological Features of Grease. The NLGI 1 lithium-based lubricating grease is selected as the experimental material, while the rotating rheometer (MCR302) is employed for the test (Figure 1). The H-B model is used to investigate the viscosity and grease shear rate stress variation at different temperatures and shear rates. Experimental temperature was in the range of 25°C to 85°C, while the shear rates controlled by the rotating rheometer were within the range of 0.01 s⁻¹ to 100 s⁻¹.

2.2. Grease Flow Characteristics Analysis. According to Figure 2(a), the shear stress of NLGI 1 lithium-based lubricating grease increases with the shear rate. Lubricating grease is a structural colloidal dispersion system. Its saponified structure causes the grease to have a certain structural strength. As a result, it demonstrates solid non-flowing characteristics in the early stage and mainly undergoes elastic deformation. After the early stage, the grease starts to show viscous flow. The shear stress curve plotted against the shear rate conforms to the power law [17]. On the other hand, Figure 2(b) demonstrates that the apparent viscosity of the grease gradually decreases with an increase in the shear rate. By comparing the curves on Figures 2(a) and 2(b), it can be observed that viscosity decreases with an increase in temperature. However, unstable regions in the flow curve are present due to the wall slip effect, which influences the grease flow [18].

In order to discuss the changes of apparent viscosity of grease more intuitively, a set of grease viscosity data can be selected, and logarithmic coordinates can be replaced with the ordinary ones. The result is shown in Figure 3.

Based on the experimentally obtained grease flow curves, it can be observed that the H-B model can accurately characterize the viscous flow characteristics of the grease [9]. Therefore, the H-B model is employed for data fitting to obtain the rheological parameters (τ_0 , k , n) of NLGI 1 lithium-based lubricating grease at various temperatures. The specific values are shown in Table 1.

Based on the data provided in Table 2, it can be concluded that the yield strength, consistency coefficient, and shear thinning index of the grease decrease with the increase in temperature. This shows that an increase in temperature enhances the grease flow performance and further increases the leakage of the end clearance.

2.3. Change Mechanism of Grease Rheological Features. Figure 4 shows the micromorphology of NLGI 1 lithium-based lubricating grease observed under the scanning electron microscope. It can be observed that the grease fibers are entangled into a network structure. This structure itself hinders the flow of grease, but it can enhance it when accompanied by continuous shearing force and temperature increase. Considering that the grease is affected by the shear stress and frictional heat [15, 19], it is necessary to fully consider the influence of the rheological features of the grease leakage in the end clearance zone.

TABLE 1: Performance parameters of various lubricating greases.

Type of greases	Temperature (°C)	Penetration (0.1 mm)	Drop point (°C)	Water resistance
Lithium-based lubricating grease	-20~120	325	178	Better
Calcium-based lubricating grease	-10~60	322	80	Better
Graphite calcium-based lubricating grease	-10~600	265	80	General
Complex calcium-based lubricating grease	-10~150	310	180	Worse

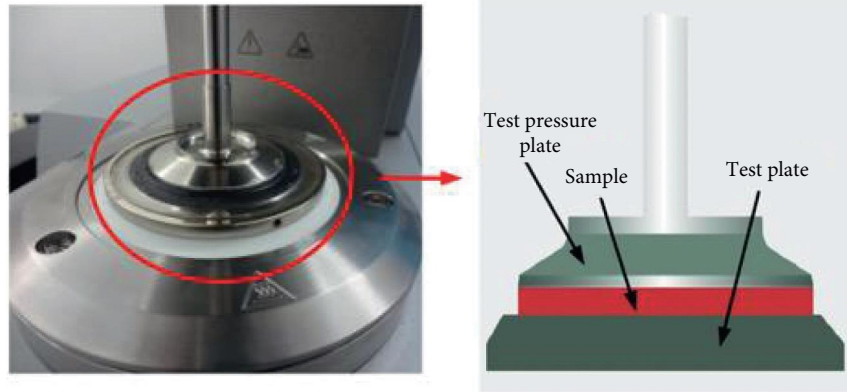


FIGURE 1: MCR 302 rotating rheometer and test module.

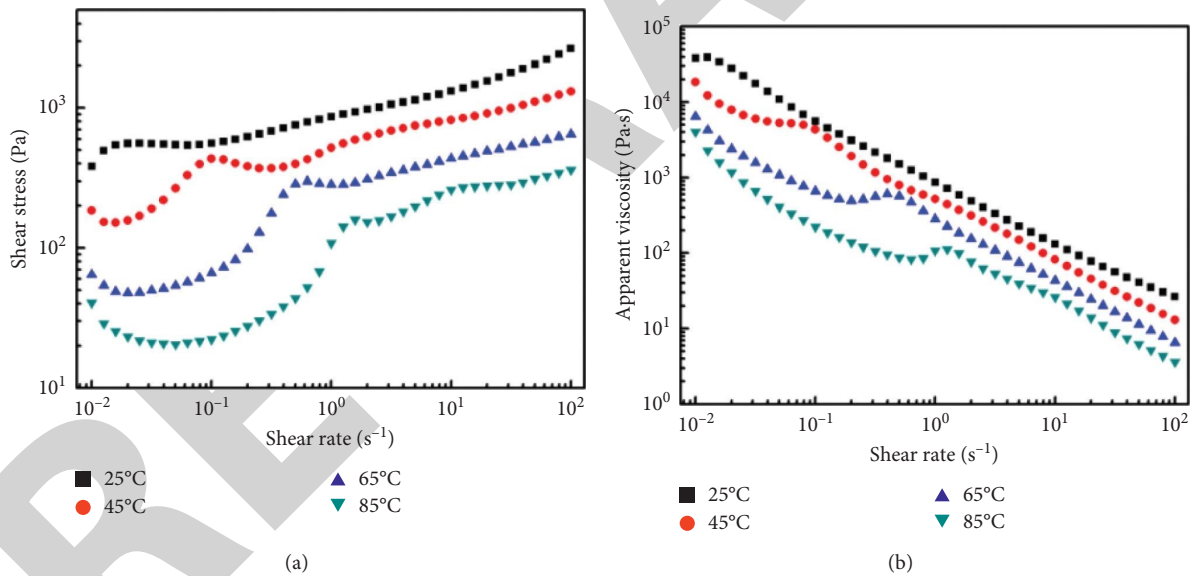


FIGURE 2: Variation of shear stress and apparent viscosity of the grease with shear rate at different temperatures for (a) curve of the shear stress with the shear rate and (b) curve of the apparent viscosity with the shear rate.

Figure 5 depicts the frequency sweep curve with frequency ($\tan \delta$) of the storage modulus (G') and loss modulus (G'') of NLGI 1 lithium-based lubricating grease at various temperatures. It can be observed that, in the entire frequency sweep area, the storage modulus of the grease at each temperature is greater than the loss modulus. Furthermore, the higher the temperature, the greater the values of the storage modulus and loss modulus. Therefore, the

entanglement of NLGI 1 lithium-based grease can be characterized by the platform modulus (G_N^0) [12]. The platform modulus of the lubricating grease can be obtained by extrapolating from the experimental data of the grease frequency sweep, which can be expressed by the following formula:

$$G_N^0 = [G']_{\tan \delta \rightarrow \text{minimum}} \quad (1)$$

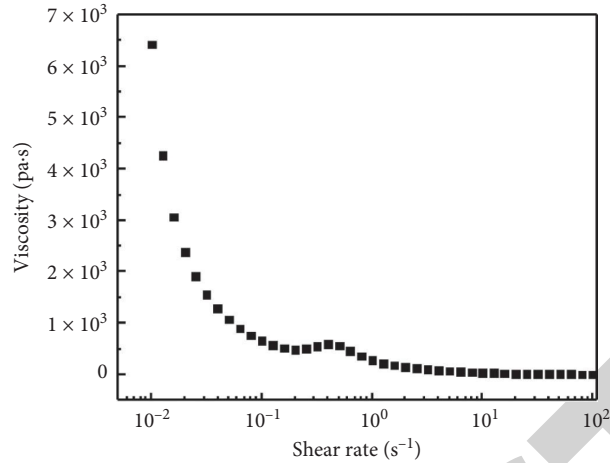


FIGURE 3: Curve of the apparent viscosity of NLGI 1 lithium-based lubricating grease as a function of the shear rate.

TABLE 2: Rheological parameters of NLGI 1 lithium-based lubricating grease at various temperatures.

Temperature (°C)	Yield strength (Pa)	Consistency coefficient (Pa S ⁿ)	Shear thinning index
25	542	286.40	0.43
45	350	136.51	0.45
65	283	43.25	0.48
85	132	27.44	0.49

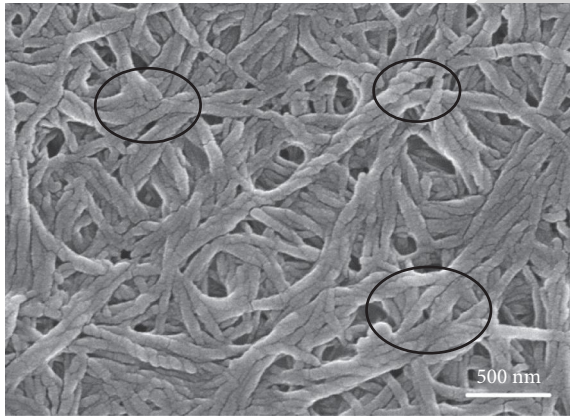


FIGURE 4: Micromorphology of NLGI 1 lithium-based lubricating grease.

3. Numerical Simulation of the Flow Field at the End Clearance of the Internal Gear Grease Pump

In order to explore the leakage mechanism of the end clearance with greater accuracy, the clearance flow field model is established, the ICEM CFD software is employed to divide the mesh, and Fluent software is used to solve the model.

3.1. Meshing the Flow Field Model. The end clearance leakage of internal gear pump conforms to the double disc leakage model. The leakage area of the external gear is defined as the area from the root circle of the external gear to the gear shaft. The leakage area of the internal gear is defined as the area

from the root circle of the internal gear to the outer circle of the gear. It should be noted that the leakage area is not a complete disc, but rather a disc fraction falling between the angles of the internal and external gear leakage of 131.718° and 158.09° , respectively. The clearance values are taken as 0.03 mm, 0.04 mm, 0.05 mm, and 0.06 mm. Figure 6 depicts the flow field model.

The ICEM CFD preprocessing software is utilized to mesh the flow field model. In Figure 6, it can be observed that the grid has a certain periodicity. Therefore, the flow field model can be divided into periodic meshes [19], which can simplify the flow field model for the purpose of obtaining higher-quality grid. Three boundary layers are added to the grid, which is shown in Figure 7.

3.2. Boundary Conditions. During the operating process of the internal gear pump, the leakage of the end clearance occurs mainly due to the flow resulting from pressure difference. The pressure inlet of the pump is rated at 25 MPa, while the pressure outlet is rated at 0.1 MPa. The specific boundary conditions are presented in Table 3.

3.3. Analysis of Simulation Results. Temperature simulation parameters are selected according to Table 1. The simulation is carried out via *Fluent* software with the lubricating grease rheological parameters at 25°C, 45°C, 65°C, and 85°C. The simulation results are exported by Tecplot 360 EX 2015 R1 and its own postprocessing software, as shown in Figure 8:

According to Figure 8, the grease traverses in a laminar flow and is symmetrically distributed within the clearance. With an increase in pump temperature, the clearance grease

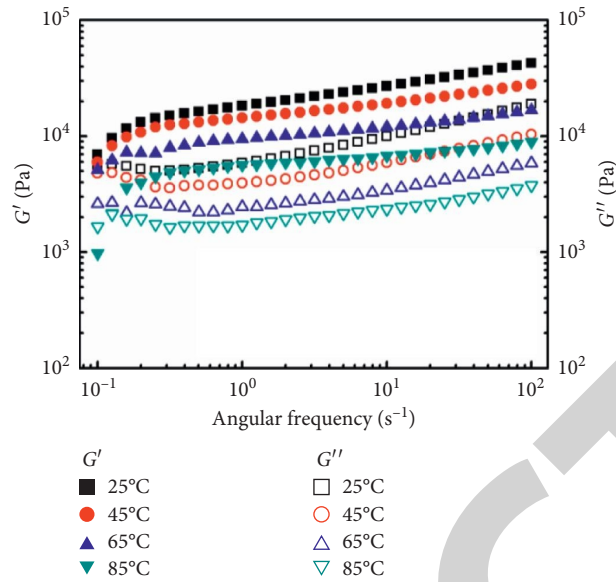


FIGURE 5: Frequency sweep curve of NLGI 1 lithium-based lubricating grease at different temperatures.

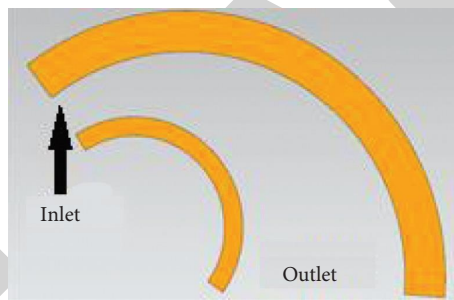


FIGURE 6: Flow field model of end clearance of internal gear pump.

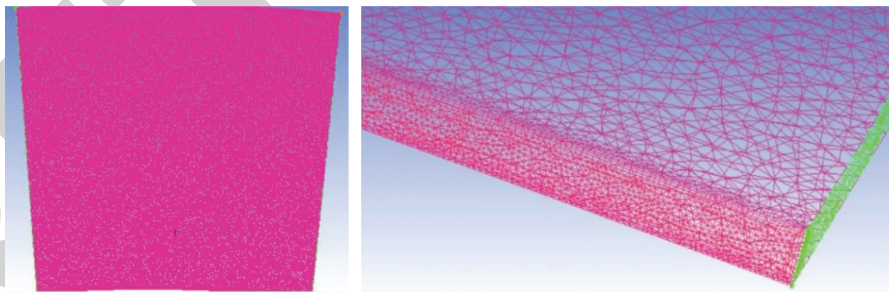


FIGURE 7: End clearance flow field grid.

TABLE 3: Boundary conditions of numerical simulation.

Calculation conditions	Parameter
Density	900 kg/m ³
Inlet	25 MPa
Outlet	0.1 MPa
Upwind	Second-order upwind
Method	Simple

flow rate increases significantly. In combination with Figure 9, it can be observed that the grease flow increases under pressure after overcoming its yield strength from the inlet to the outlet. Due to the high shear rate at the wall, the grease reaches its yield strength and gradually forms a flow core. Then, the grease forms a plug flow in the clearance. With an increase in the shear rate, the size of the flow core decreases. Finally, the flow becomes laminar. It can be concluded from

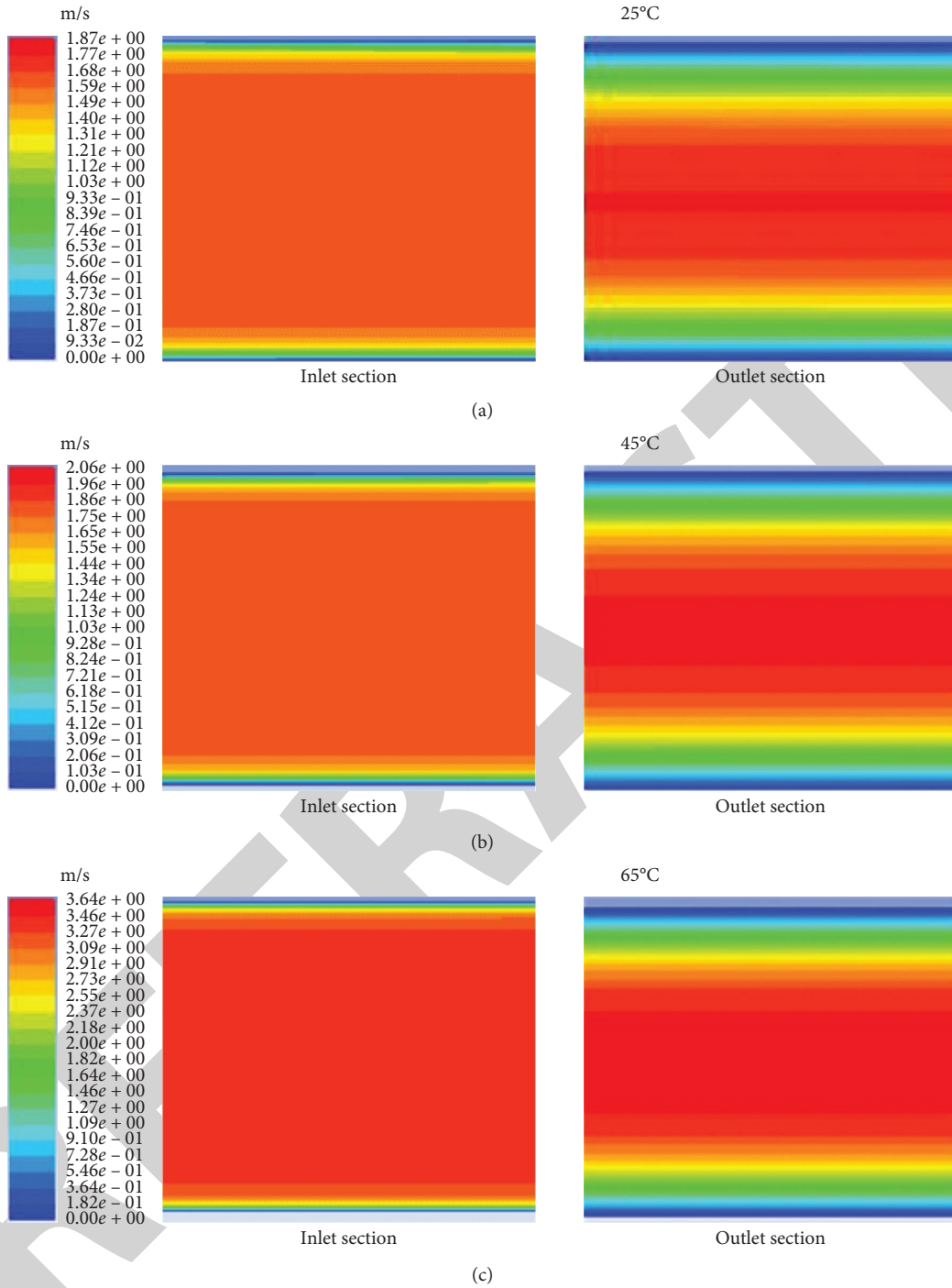


FIGURE 8: Continued.

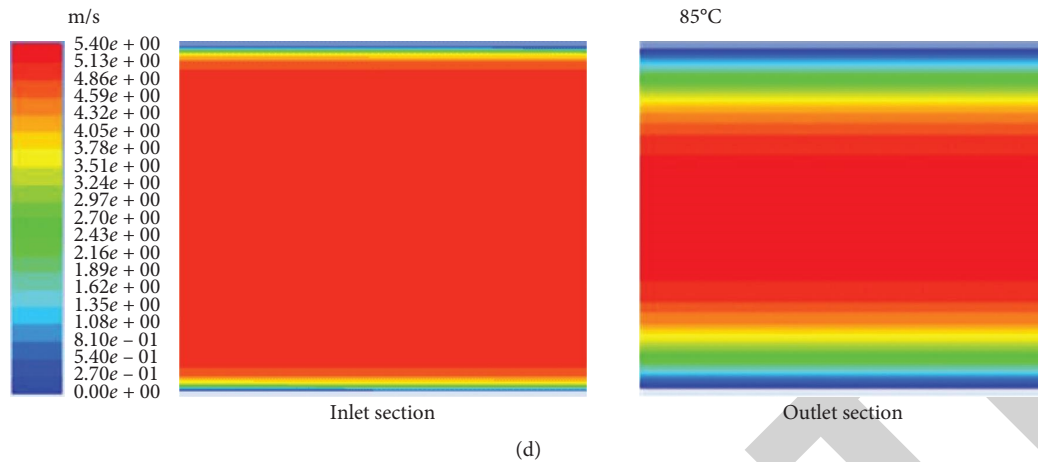


FIGURE 8: Vectors of velocity at inlet and outlet section at 25°C–85°C.

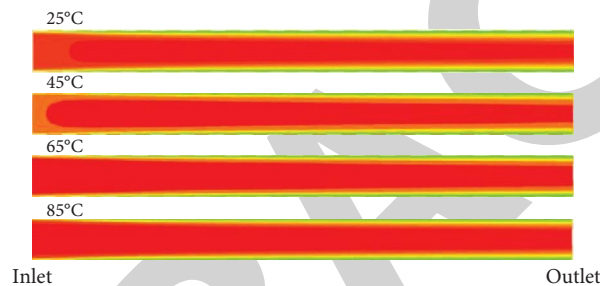


FIGURE 9: Vectors of velocity at radial section at 25°C–85°C range.

Figure 9 that, at 25°C, a sudden pressure drop at the inlet is observed, which then uniformly changes, as illustrated in Figure 10. At 65°C and 85°C, the pressure changes more evenly from the inlet to the outlet. Generally speaking, the lower the temperature is, the more the pressure will be consumed during the inlet phase.

Based on the aforementioned results, it can be concluded that, with an increase in temperature, grease and end clearance leakage flow characteristics are both increased. However, this does not necessarily mean that lower temperatures are preferable. Although the leakage is reduced in the low temperature regions, the yield strength and viscosity of the grease are increased. This results in an upsurge in the required starting torque, as well as generated fluid friction. After comprehensive consideration, 65°C is chosen as the optimal pumping temperature.

Numerical clearance effect simulation results are shown in Figures 11 and 12. The clearances are taken as 0.04 mm, 0.05 mm, and 0.06 mm, while a temperature of 65°C is utilized for numerical simulation.

It can be clearly seen from Figure 11 that the clearance value increase causes a surge in the end clearance grease flow rate. This suggests that the flow at the inlet and the outlet of the clearance will occupy more areas. When the pressure gradient remains unaltered, the shear rate of the grease at the wall increases with an increase in the clearance value. The apparent viscosity of the grease decreases with an increase of the shear rate; that is, the grease will flow more easily at the

clearance while gradually increasing its flow rate [19]. Figure 12 also verifies this point. With an increase in the clearance value, the leakage section will also grow. Due to the combined influence of the two, the end clearance leakage will increase significantly.

In order to explore the effect of rotation speed on the leakage at the end clearance, the rotation speeds of 1000 min⁻¹, 1500 min⁻¹, and 2000 min⁻¹ are employed, while the temperature is kept at 65°C. The results are shown in Figure 13.

From Figure 13, it can be seen that the grease flow is still laminar in the clearance region. However, the velocity distribution along the clearance direction is no longer symmetrical. This is caused by the plate drag effect formed by the rotation of the gear side, which increases the flow speed of the grease on the gear side, making it greater than that of the floating side plate, whose effect can be neglected.

From Figures 14(a)–14(c) and Figure 15, it can be seen that the end clearance leakage flow gradually increases in the internal gear leakage area with the rotational speed, and the pressure difference between two adjacent teeth of pressure transition zone becomes larger with the increase of the pump rotary speed [20]. In the external gear leakage area, with an increase in the rotational speed, the clearance flow leakage gradually decreases. This phenomenon occurs because the direction of the centrifugal force generated by the gear rotation is opposite to the flow direction generated by the grease pressure. Therefore, the higher the rotational speed is,

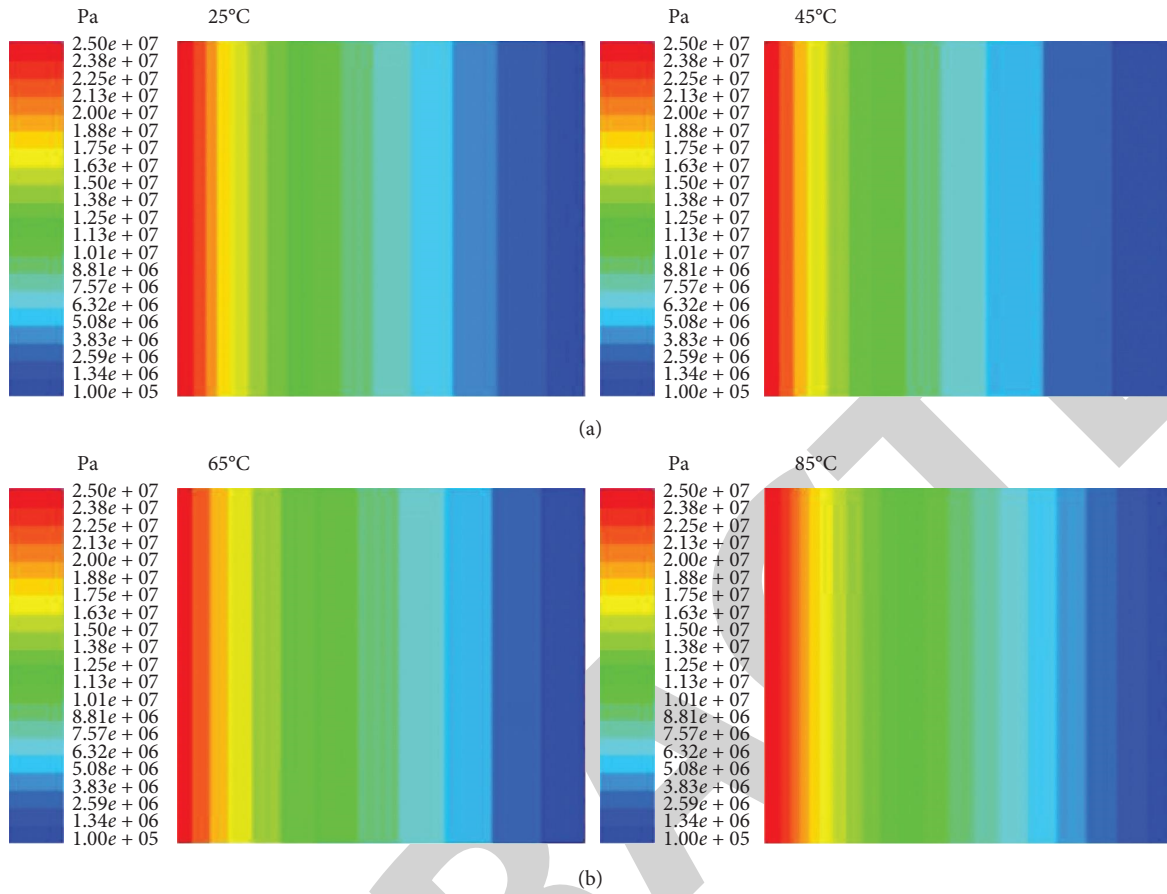


FIGURE 10: Vectors of pressure from inlet to outlet at 25°C–85°C.

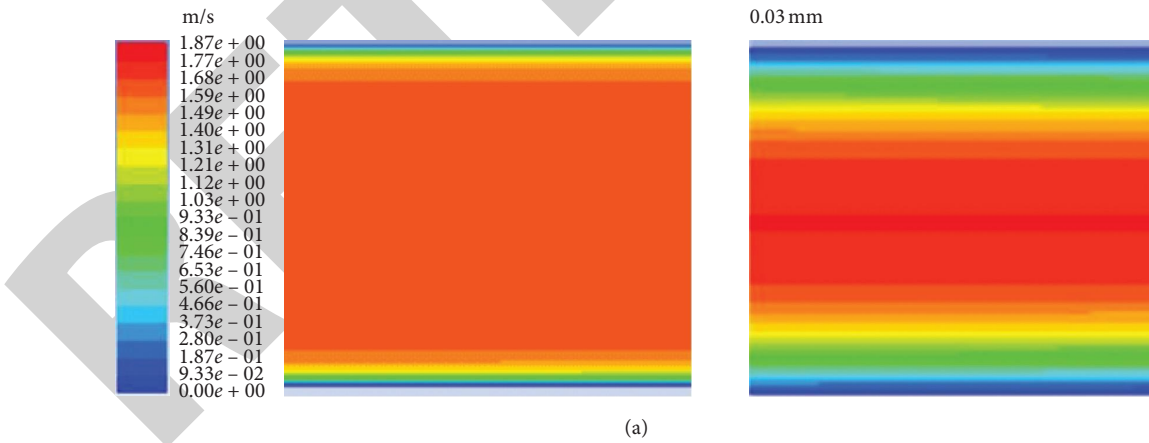


FIGURE 11: Continued.

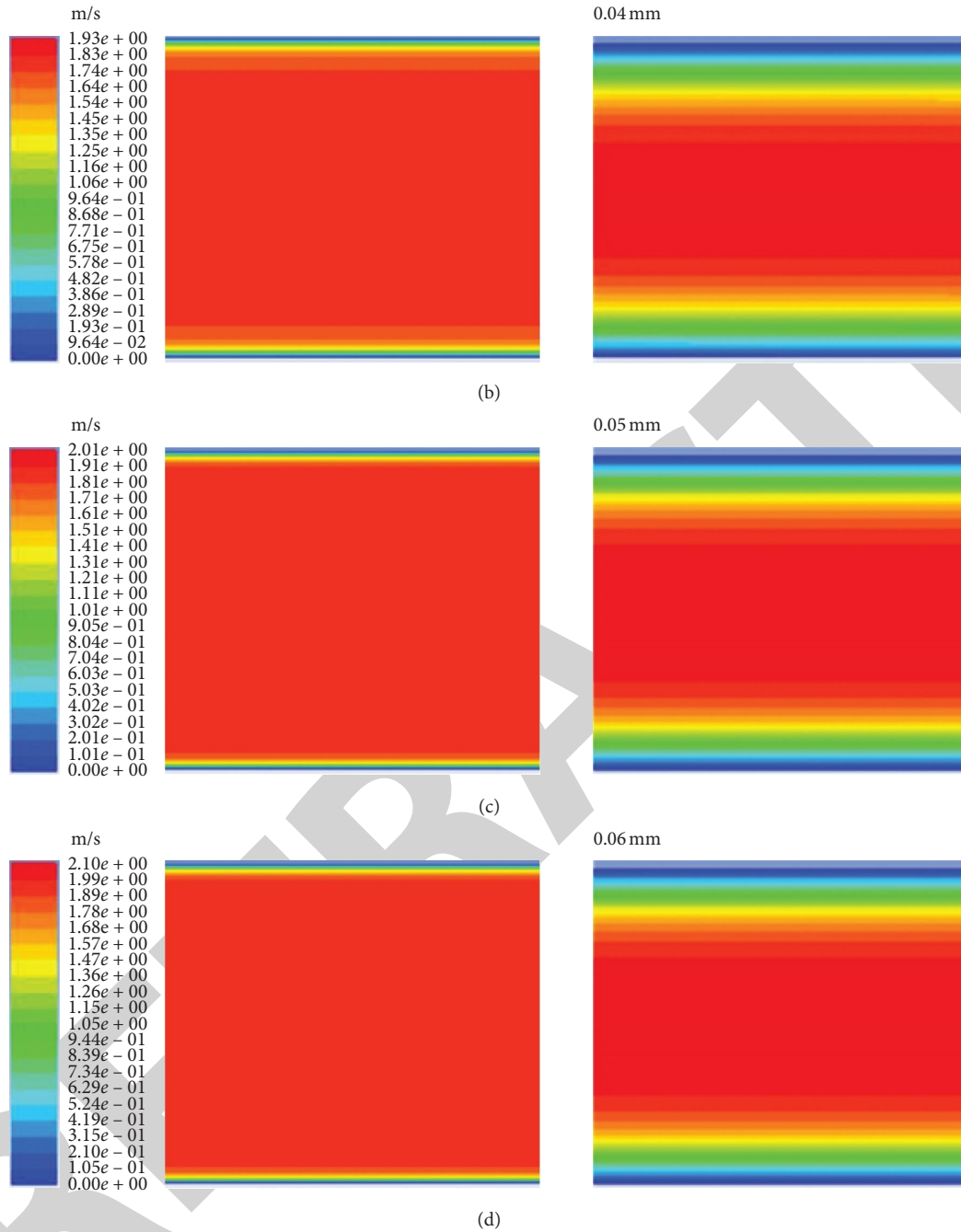


FIGURE 11: Vectors of velocity at inlet and outlet of end clearance flow field under different clearances.

the greater the leakage flow restrained in the external gear area is.

To summarize, the direction of the centrifugal force generated by the gear rotation in the internal gear area is the same as the grease flow direction due to pressure variation. Thus, as the rotational speed increases, the leakage in the internal gear area will also gradually increase. On the other hand, the grease flow direction due to pressure variation is opposite to the centrifugal force in the leakage area of the external gear. Hence, the leakage flow will decrease as the speed increases. Considering the behavior of the flow leakage

in the internal and the external gear areas, it can be concluded that the increase of rotational speed will reduce the leakage of end clearance.

4. Leakage Model Establishment and Leakage Mechanism Analysis

Main type of internal leakage is the internal gear pump leaking at its end clearance. Due to the peculiar rheological features of grease, it is necessary to establish an adequate mathematical model of end clearance leakage to accurately

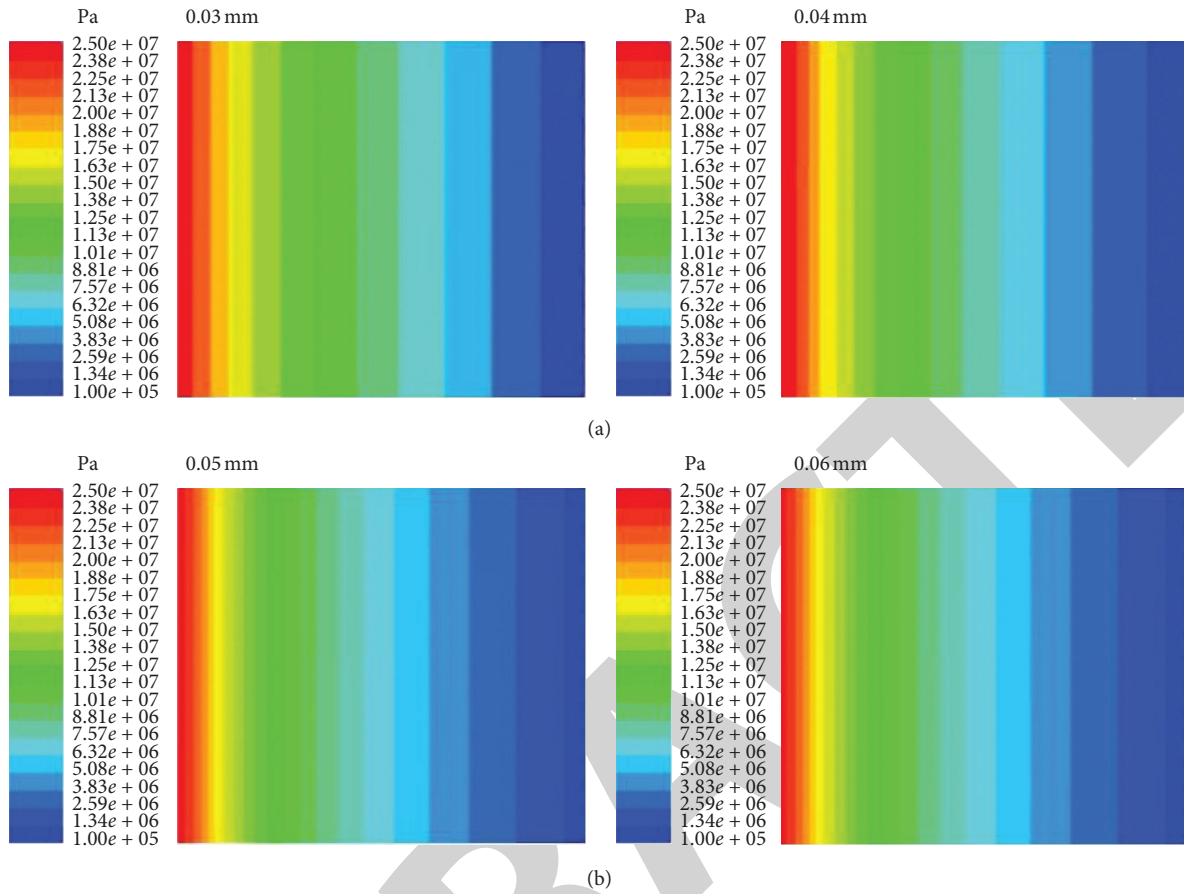


FIGURE 12: Vectors of pressure at inlet and outlet of end clearance flow field under different clearances.

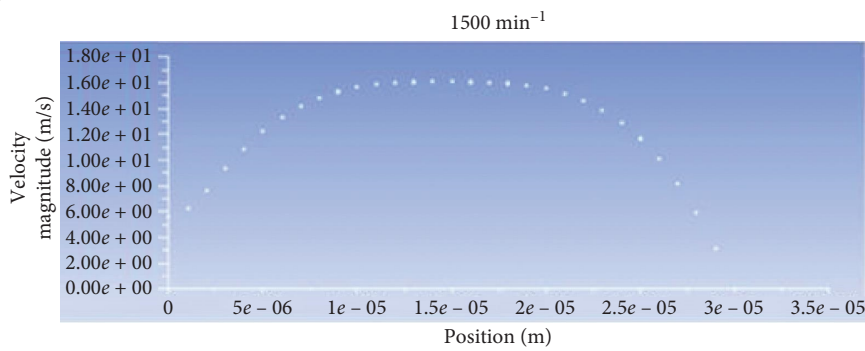
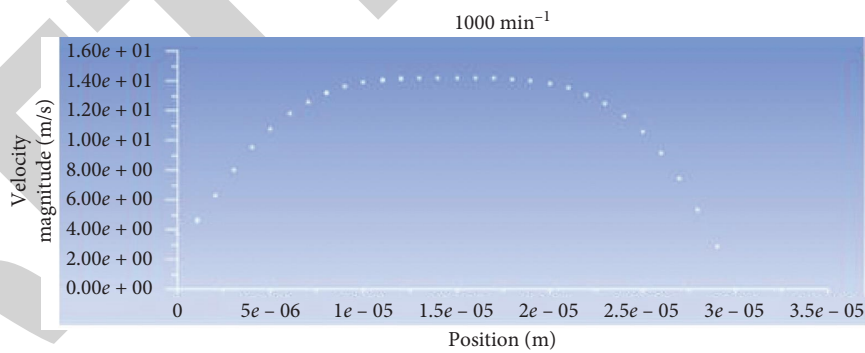


FIGURE 13: Continued.

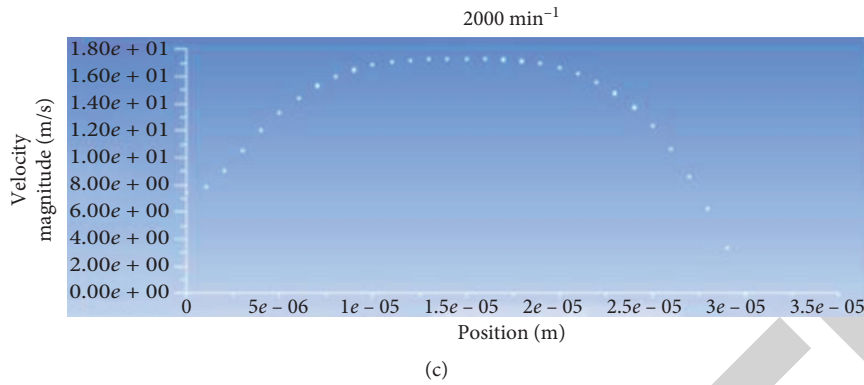


FIGURE 13: Speed scatter plot of the outlet of the internal gear area along the clearance direction at each speed.

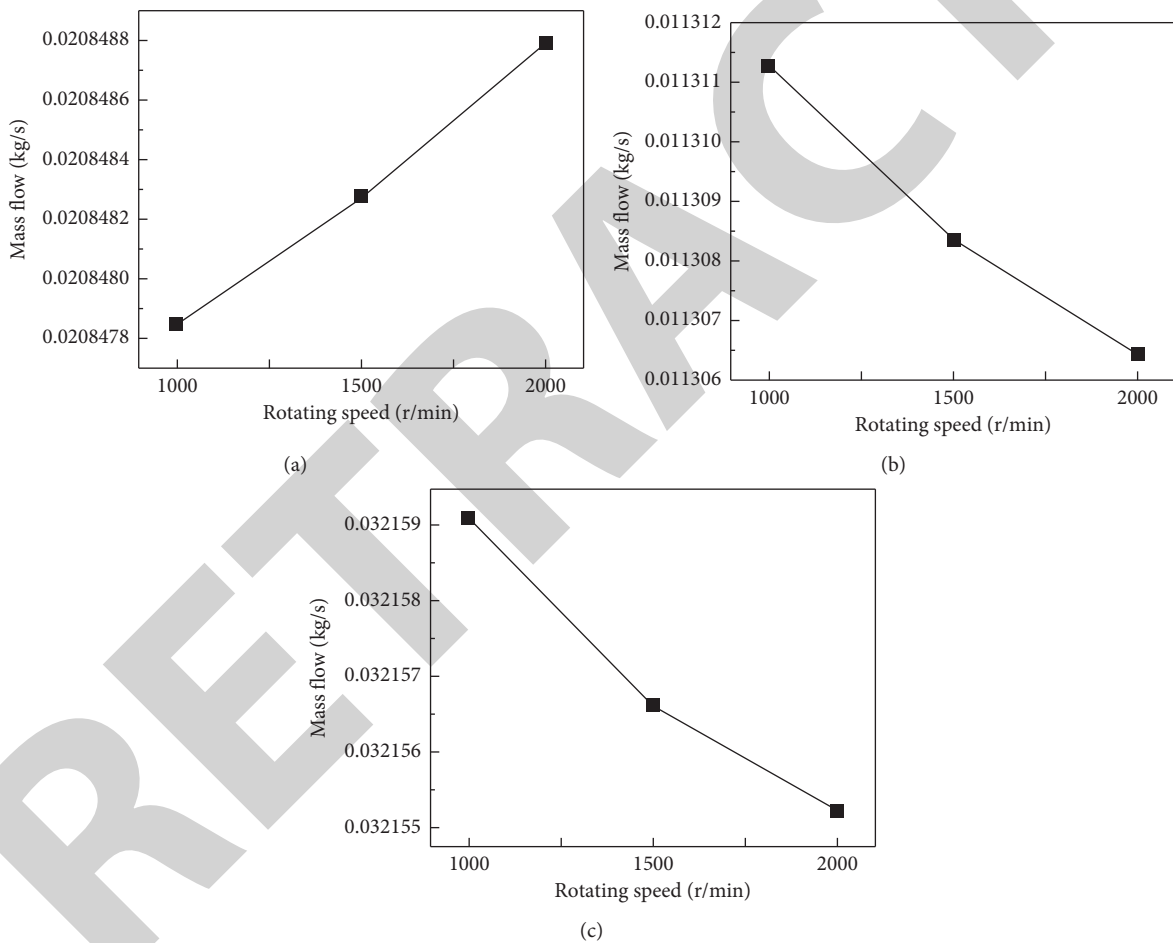


FIGURE 14: Leakage flow curve of end clearance at different speeds. (a) Leakage curve of internal gear area. (b) Leakage curve of external gear area. (c) Total leakage curve of end clearance.

explore the end clearance leakage mechanism of the internal gear grease pump.

4.1. Leakage Model Establishment. With grease being a non-Newtonian fluid with its own flow constitutive equation, the flow of grease follows the basic equations of fluid mechanics.

Since grease is an incompressible fluid, the following leakage model can be employed:

Continuity equation:

$$\frac{\partial \rho}{\partial t} + \nabla \cdot (\rho v) = 0. \tag{2}$$

Equation of motion:

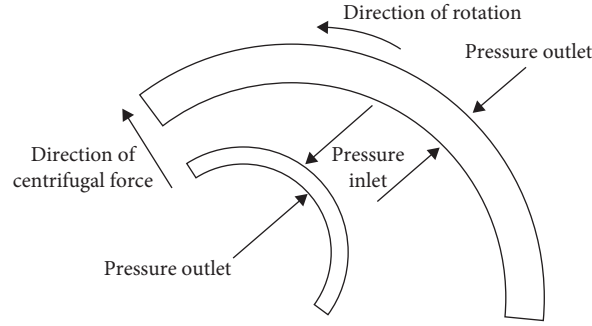


FIGURE 15: Schematic diagram of the influence of rotational speed on end clearance leakage.

$$\rho \frac{Dv}{Dt} = -\nabla \cdot p + \nabla \cdot \sigma + \rho f. \quad (3)$$

Energy equation:

$$\rho_{cv} \frac{DT}{Dt} = -\nabla \cdot q + \sigma : \nabla v. \quad (4)$$

According to the research content provided in Section 2, the viscosity and flow of grease are influenced by the shear rate. Figure 16 shows the relationship between the flow pattern of the grease at the plate clearance and the shear rate.

When the external force received by the grease increases and eventually exceeds the yield strength, the grease starts to flow simultaneously with the shear rate value being largest at the wall. However, in the center area, the grease still has a plug flow state, which is called a flow core. With an increase in the shear rate, the flow core eventually disappears, and the grease obtains laminar flow state between the plate clearance.

Pan et al. [21] analyzed the flow of grease and found that the Reynolds number of the conventional grease flow differs from the critical Reynolds number by two orders of magnitude. This observation contributed to the fact that the internal gear pump had a smaller end clearance during high pressure operation of the gear pump. When the working conditions were stable, the grease flow eventually turned laminar at the end clearance. Figure 17 depicts flow field model of clearance leakage, where the plate length is denoted as L , the width as b , and the clearance size as δ .

Based on the rectangular coordinate system, the basic equation of the grease flow pattern at the plate clearance is expanded and solved. Following the expansion, equations (2)–(4) can be written as follows:

Continuity equation:

$$\frac{\partial \rho}{\partial t} + \frac{\partial(\rho v_x)}{\partial x} + \frac{\partial(\rho v_y)}{\partial y} + \frac{\partial(\rho v_z)}{\partial z} = 0. \quad (5)$$

Equation of motion:

x direction:

$$\rho \left(\frac{\partial v_x}{\partial t} + v_x \frac{\partial v_x}{\partial x} + v_y \frac{\partial v_x}{\partial y} + v_z \frac{\partial v_x}{\partial z} \right) = -\frac{\partial p}{\partial x} + \frac{\partial \tau_{yx}}{\partial y} + \frac{\partial \tau_{zx}}{\partial z} + \rho f_x. \quad (6)$$

y direction:

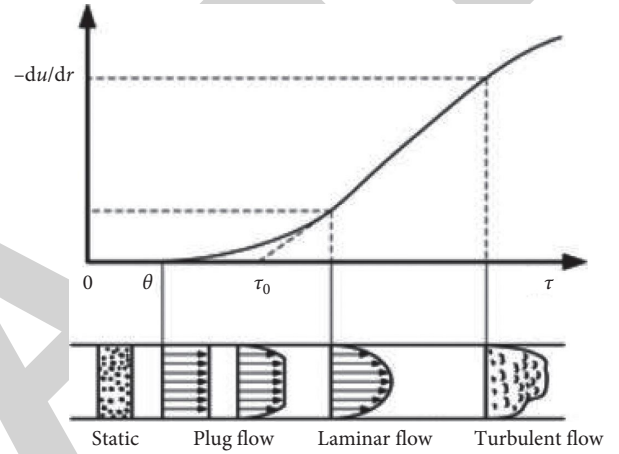


FIGURE 16: Flow pattern of grease flat extrusion.

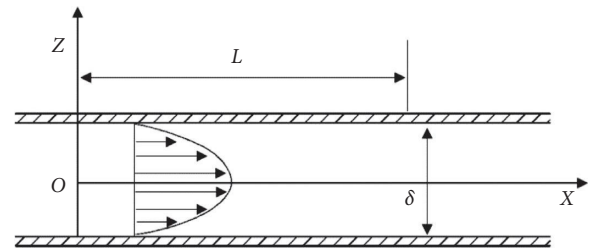


FIGURE 17: Flow field model of clearance leakage.

$$\rho \left(\frac{\partial v_y}{\partial t} + v_x \frac{\partial v_y}{\partial x} + v_y \frac{\partial v_y}{\partial y} + v_z \frac{\partial v_y}{\partial z} \right) = -\frac{\partial p}{\partial y} + \frac{\partial \tau_{xy}}{\partial x} + \frac{\partial \tau_{zy}}{\partial z} + \rho f_y. \quad (7)$$

z direction:

$$\rho \left(\frac{\partial v_z}{\partial t} + v_x \frac{\partial v_z}{\partial x} + v_y \frac{\partial v_z}{\partial y} + v_z \frac{\partial v_z}{\partial z} \right) = -\frac{\partial p}{\partial z} + \frac{\partial \tau_{xz}}{\partial x} + \frac{\partial \tau_{yz}}{\partial y} + \rho f_z. \quad (8)$$

Energy equation:

$$\rho_{cv} \frac{DT}{Dt} = -\left(\frac{\partial q_x}{\partial x} + \frac{\partial q_y}{\partial y} + \frac{\partial q_z}{\partial z}\right) + \left(\tau_{xx} \frac{\partial v_x}{\partial x} + \tau_{yy} \frac{\partial v_y}{\partial y} + \tau_{zz} \frac{\partial v_z}{\partial z}\right) + \left(\tau_{xy} \frac{\partial v_y}{\partial x} + \tau_{xz} \frac{\partial v_z}{\partial x} + \tau_{yz} \frac{\partial v_z}{\partial y}\right). \quad (9)$$

4.2. *Model Solving.* Following the simplification of the equation according to the actual boundary conditions, the aforementioned equations can be written as follows:

Continuity equation:

$$\frac{\partial v_x}{\partial x} = 0. \quad (10)$$

Equation of motion:

$$\frac{\partial p}{\partial x} = \frac{\partial \tau_{zx}}{\partial z}. \quad (11)$$

H-B model:

$$\tau = \tau_0 + k\dot{\gamma}^n. \quad (12)$$

where τ is the shear stress during grease flow, τ_0 is the shear yield strength, k is the consistency coefficient, $\dot{\gamma}$ is the shear rate, and n is the grease shear thinning index.

According to the content of Chapter 2, the grease flow characteristics conform to the H-B model. Combined with the H-B model, the shear force of the grease can be obtained:

$$\tau_{zx} = \tau = \tau_0 + k(\dot{\gamma})^n = \tau_0 + k\left(\frac{\partial v_x}{\partial z}\right)^n. \quad (13)$$

Equation (13) can then be solved for the flow pattern of the grease at the plate clearance:

$$\tau_{zx} = z \frac{\partial p}{\partial x} + C_1. \quad (14)$$

When $z=0$, v_x reaches the maximum value. $\tau_{zx} = 0$ is inserted into equation (12), while equation (14) is substituted into (12).

$$\tau_0 + k\left(\frac{\partial v_x}{\partial z}\right)^n = z \frac{\partial p}{\partial x}. \quad (15)$$

By solving equation (15), the following expression is obtained:

$$v_x = \frac{n}{n+1} \left(\frac{z \frac{\partial p}{\partial x} - \tau_0}{k} \right)^{n+1/n} \cdot k \left(\frac{\partial p}{\partial x} \right)^{-1} + C_2. \quad (16)$$

By substituting $z = \pm \delta/2$ and $v_x = 0$ into equation (16), C_2 can be obtained:

$$C_2 = -\frac{n}{n+1} \left(\pm \frac{\delta}{2k} \frac{\partial p}{\partial x} - \frac{\tau_0}{k} \right)^{n+1/n} \cdot k \left(\frac{\partial p}{\partial x} \right)^{-1}. \quad (17)$$

For $-\delta/2 \leq z \leq 0$ and $0 < z \leq \delta/2$, v_x is equal to

$$v_x = \frac{n}{n+1} \left(\frac{1}{k} \right)^{1/n} \left(\frac{\partial p}{\partial x} \right)^{-1} \left[\left(z \frac{\partial p}{\partial x} - \tau_0 \right)^{n+1/n} - \left(-\frac{\delta}{2} \frac{\partial p}{\partial x} - \tau_0 \right)^{n+1/n} \right], \quad -\frac{\delta}{2} \leq z \leq 0, \quad (18)$$

$$v_x = \frac{n}{n+1} \left(\frac{1}{k} \right)^{1/n} \left(\frac{\partial p}{\partial x} \right)^{-1} \left[\left(z \frac{\partial p}{\partial x} - \tau_0 \right)^{n+1/n} - \left(\frac{\delta}{2} \frac{\partial p}{\partial x} - \tau_0 \right)^{n+1/n} \right], \quad 0 < z \leq \frac{\delta}{2}. \quad (19)$$

By deriving for z in equations (18) and (19), the shear rate equation becomes

$$\frac{dv_x}{dz} = \left(\frac{1}{k} \right)^{1/n} \left(z \frac{\partial p}{\partial x} - \tau_0 \right)^{1/n}. \quad (20)$$

Finally, by combining equation (20) and the H-B model, the distribution of the shear stress is obtained:

$$\begin{aligned} \tau_{zx} = \tau &= \tau_0 + k(\dot{\gamma})^n = \tau_0 + k \left[\left(\frac{1}{k} \right)^{1/n} \left(z \frac{\partial p}{\partial x} - \tau_0 \right)^{1/n} \right]^n \\ &= z \frac{\partial p}{\partial x}, \quad -\frac{\delta}{2} < z \leq \frac{\delta}{2}. \end{aligned} \quad (21)$$

From equation (21), it can be noticed that the shear stress varies linearly with z value, and the shear stress is related to

the pressure gradient $\partial p/\partial x$ [22], which indicates that the stress distribution of the grease at the clearance is related to the working pressure of the pump. When the working pressure of the pump increases, the shear stress and the power loss due to viscous friction increase accordingly.

5. End Clearance Optimization

The end clearance leakage of the internal gear grease pump rises with an increase in clearance value. On the other hand, if the clearance is too small, it will cause wearing of the floating side plate and the end face of the gear. This, in turn, will increase the clearance, as well as the leakage, while simultaneously reducing the service life of the pump. When optimizing the design of the end clearance, two factors are usually considered. One is the power loss caused by the flow leakage, while the other one is the friction caused power loss.

5.1. Power Loss of Flow Leakage. Due to the high internal pressure of the pump, the grease will leak towards the low-pressure zone through the end clearance, causing the energy and power losses of the pump. According to Wang [14] research, the trapped oil volume changed on parabolic rule with the increase of tooth turning angle. The angle of the trapped oil reduced on linear relationship with the increase of spiral angle. The power loss caused by the flow leakage can be expressed by

$$q = \frac{\pi \delta^3 \Delta p}{6\mu \ln(r_x/r_y)} \cdot \frac{\varphi}{2\pi}, \quad (22)$$

where μ is the fluid viscosity, r_x and r_y are the internal and external gear radius parameters, respectively, δ is the value of the end clearance, and Δp is the pressure difference due to leakage between the inlet and outlet. φ is the envelope angle of gear leakage area. By substituting the parameters of the internal and the external gear leakage, total leakage can be obtained:

$$P_q = q\Delta p = \frac{\delta^3 \Delta p^2}{6} \cdot \frac{\dot{\gamma}}{\tau_0 + k\dot{\gamma}^n} \cdot \left[\frac{\varphi_1}{\ln(r_2/r_1)} + \frac{\varphi_2}{\ln(r_4/r_3)} \right], \quad (23)$$

where q is the end clearance leakage flow, r_1 is the root circle radius of the internal gear, r_2 is the external circle radius of the internal gear, r_3 is the root circle radius of the external gear, r_4 is the radius of the gear shaft, and r_5 is the addendum circle radius of the external gear, φ_1 is the envelope angle of internal gear leakage area, and φ_2 is the envelope angle of external gear leakage area.

5.2. Power Loss of Internal Friction. The power loss area of internal friction is divided into the leakage area of the internal gear and the leakage area of the external gear. The power loss area of internal friction of the external gear includes the area from the root circle of the external gear to the gear shaft, as well as the root circle to the addendum circle. The power loss area of internal friction of the internal gear includes the root circle of the internal gear to the outer circle area of the gear shaft's internal gear and the area from the root circle to the addendum circle.

Internal fluid friction force at the end clearance can be calculated by taking the external gear as an example:

$$dF = \tau_0 + k\dot{\gamma}^n dA, \quad (24)$$

where F is the internal friction force of fluid at end clearance, and A is a small area from the root circle to the gear shaft. The shape of the floating side plate can be regarded as a semicircular one. A small area from the root circle to the gear shaft is taken:

$$dA = \pi r dr, \quad (25)$$

where r is the radius of the internal or the external gear. Assuming that the angular velocity of the gear is ω , the linear velocity of the small area is

$$v = \omega r. \quad (26)$$

Therefore, the power loss area of internal friction between the tooth circle and the gear shaft is

$$\begin{aligned} P_1 &= \int_{r_4}^{r_3} dP_+ = \int_{r_4}^{r_3} \omega r dF \\ &= \frac{1}{3} \tau_0 \pi \omega (r_3^3 - r_4^3) \left(\frac{k\pi \omega^{n+1} \delta^{-n}}{n+3} \right) (r_3^{n+3} - r_4^{n+3}). \end{aligned} \quad (27)$$

The shape of the floating side plate is approximately semicircular. Thus, only half of the total area of the internal and external gears contains friction clearance with the floating side plate.

$$dA = \frac{\pi r dr}{2}. \quad (28)$$

The friction power loss from the root circle to the addendum circle area can be calculated as

$$\begin{aligned} P_2 &= \int_{r_3}^{r_5} dP_{f+} = \int_{r_3}^{r_5} \omega r dF_f \\ &= \frac{1}{6} \tau_0 \pi \omega (r_5^3 - r_3^3) \left(\frac{k\pi \omega^{n+1} \delta^{-n}}{2n+6} \right) (r_5^{n+3} - r_3^{n+3}). \end{aligned} \quad (29)$$

In a similar manner, the friction power losses from the root circle to the outer circle of the internal gear, P_3 , as well as the friction power loss from the root circle to the addendum circle of the internal gear, P_4 , are

$$P_3 = \frac{1}{3} \tau_0 \omega \pi (r_2^3 - r_1^3) + \left(\frac{k\pi \omega^{n+1} \delta^{-n}}{n+3} \right) (r_2^{n+3} - r_1^{n+3}), \quad (30)$$

$$P_4 = \frac{1}{6} \tau_0 \pi \omega (r_1^3 - r_6^3) + \left(\frac{k\pi \omega^{n+1} \delta^{-n}}{2n+6} \right) (r_1^{n+3} - r_6^{n+3}), \quad (31)$$

where r_6 is the addendum circle radius of the internal gear.

In summary, the total friction power losses at the end clearance of the internal gear grease pump can be obtained as

$$P_f = 2(P_1 + P_2 + P_3 + P_4). \quad (32)$$

5.3. Mathematical Model Establishment. The optimal end clearance value of the internal gear grease pump mainly considers the flow leakage and friction induced power losses. The objective function is the minimum end clearance leakage total power loss. The mathematical model of the optimal end clearance is then

$$F(X) = P = \min(P_q + P_f), \quad (33)$$

where P_q is the power loss caused by the flow leakage and P_f is the power loss caused by friction. The constraint conditions are

$$\begin{cases} 25^\circ\text{C} \leq T \leq 85^\circ\text{C}, \\ \delta_{\min} \leq \delta \leq \delta_{\max}, \\ 600 \text{ r/min} \leq n \leq 2000 \text{ r/min}, \end{cases} \quad (34)$$

where T is the working temperature, δ is the end clearance, and n is the rotational speed of the pump.

Substitute the data in Table 4 into equation (33), and the optimal clearance is calculated as $\delta^* = 0.0000124 \text{ m} = 0.0124 \text{ mm}$.

TABLE 4: Calculation parameters of power loss of end clearance.

Parameter	Unit	Value
Yield strength, τ_0	Pa	283
Consistency coefficient, k	Pa·S ⁿ	43.25
Shear thinning index, n	1	0.48
Root circle radius of internal gear, r_1	mm	30.45
Outer circle radius of internal gear, r_2	mm	36
Addendum circle radius of internal gear, r_6	mm	24.66
Root circle radius of external gear, r_3	mm	15.01
Gear shaft radius, r_4	mm	12.5
Addendum circle radius of external gear, r_5	mm	20.1
Leakage envelope angle of internal gear, φ_1	rad	0.732π
Leakage envelope angle of external gear, φ_2	rad	0.88π
Variation in pressure, Δp	Pa	2.49×10^7
Pressure gradient $\partial p / \partial x$	Pa/m	4.49×10^9

6. Conclusions

In this paper, numerical and theoretical investigations have been conducted to study the rheological features of NLGI 1 lithium-based lubricating grease. Fluent software was employed to simulate the model flow field and explore the effects of temperature, end clearance size, and rotational speed on the end clearance leakage. Based on the rheological features of the grease, parameters and laws influencing the end clearance leakage of the internal gear grease pump were explored. The following conclusions are made:

- (1) The relationship curve between the shear stress and the shear rate of NLGI 1 lithium-based lubricating grease conforms to the characteristics of the H-B model curve, while its rheological features can be utilized as data parameters for numerical simulations.
- (2) The grease will flow only when the applied external force is greater than its structural strength. With an increase in temperature, the entangled structure of the grease is transformed, which has a beneficial effect on grease fluidity.
- (3) The entangled network structure of grease has a dynamic evolution process. When the shear stress stops or the temperature decreases, its entangled structure can restore to its original shape.
- (4) The end clearance leakage flow increases linearly with an increase in the pump temperature. The optimal temperature for pump operation is 65°C. When both clearance and temperature values are uniform, the end clearance leakage decreases as the rotational speed rises.
- (5) It can be concluded that the grease end clearance flow pattern is laminar. End clearance grease flow is determined by its rheological features (τ_0 , k , n) and the gear pump's operating parameters (δ , $\partial p / \partial x$). The mathematical model of the optimal end clearance is established, based on which an optimal clearance of $\delta^* = 0.0124$ mm is determined.

Data Availability

The data used to support the findings of this study are included within the article.

Conflicts of Interest

The authors declare that they have no conflicts of interest.

Acknowledgments

This work was supported by the Natural Science Foundation of Anhui Province Education Department (KJ2017ZD12 and KJ2016SD05), the University Synergy Innovation Program of Anhui Province (GXXT-2019-004), and Teaching Research Project of Anhui Education Department (2019jyxm0229).

References

- [1] W. Schweiger, W. Schoefmann, and A. Vacca, "Gerotor pumps for automotive drivetrain applications: a multi domain simulation approach," *SAE International Journal of Passenger Cars-Mechanical Systems*, vol. 4, no. 3, pp. 1358–1376, 2011.
- [2] S. Guo, D. Chen, and X.-Q. He, "Calculation of unloading area of internal gear pump and optimization," *Mathematical Problems in Engineering*, vol. 2020, Article ID 7319871, 2020.
- [3] Q.-l. Zeng, Z.-y. Sun, L.-r. Wan, Y. Yang, H.-z. Dai, and Z.-k. Yang, "Research and comparative analysis of flow field characteristics and load-independent power losses of internal and external gear pairs," *Mathematical Problems in Engineering*, vol. 2020, Article ID 8860588, 19 pages, 2020.
- [4] S. YuanJing, Q. ZhiYuan, and Z. GuoChao, "Optimization design of internal gear pump based on improved particle swarm optimization," *Journal of Mechanical Strength*, vol. 41, no. 06, pp. 1378–1383, 2019.
- [5] J. Zhang, S. Wang, X. Jiang, and X. Chen, "Optimization design of multi-teeth parallel internal gear pump based on genetic algorithm," *Modern Manufacturing Engineering*, vol. 04, pp. 115–118+152, 2018.
- [6] K. Gu, Z. Wang, G. Li, and X. Liu, "Optimization of geometric parameters of the straight conjugate internal gear pump based on GA," *Journal of Electronic Science and Technology*, vol. 30, no. 06, pp. 39–42, 2017.
- [7] C.-f. Wang and C.-x. Zhou, "Optimum design of external gear pump with matlab," *Mechanical Engineering*, vol. 07, pp. 119–120, 2011.
- [8] E. C. Bingham, *Fluidity and Plasticity*, McGraw-Hill, New York, NY, USA, 1922.
- [9] W. H. Herschel and R. Bulkeley, "Measurement of consistency as applied to rubber-benzine solutions," *Proceedings of the American Society of Testing Materials*, vol. 26, pp. 621–633, 1926.
- [10] A. V. Radulescu, "Radulescu I Rheological models for lithium and calcium greases," *Mechanika*, vol. 59, no. 3, pp. 67–70, 2006.
- [11] A. Mohamed, "Rheological behavior of carbon nanotubes as an additive on lithium grease," *Journal of Nanotechnology*, vol. 2013, Article ID 279090, 1385 pages, 2013.
- [12] B. J. Hamrock and D. Dowson, *Ball Bearing Lubrication*, pp. 243–252, Wiley & Sons, New York, NY, USA, 1981.
- [13] S. K. Yeong, P. F. Luckham, and T. F. Tadros, "Steady flow and viscoelastic properties of lubricating grease containing various thickeners concentrations," *Journal of Colloid and Interface Science*, vol. 274, no. 1, pp. 285–293, 2004.
- [14] T. Wang, Z. Li, J. Li, and Q. He, "Impact of boron nitride nanoparticles on the wear property of lithium base grease," *Journal of Materials Engineering and Performance*, vol. 29, no. 8, pp. 4991–5000, 2020.